ISRES Publishing

The Eurasia Proceedings of Science, Technology, Engineering & Mathematics

EPSTEM

VOLUME 26 IConTES CONFERENCE

ISSN: 2602-3199

ISBN: 978-625-6959-24-8

IConTES 2023: 7th International Conference on Technology, Engineering and Science (IConTES)

November 16 - 19, 2023

Antalya, Turkey

Edited by: Prof.Dr. Mehmet Özaslan - Gaziantep University, Turkey

IConTES 2023 NOVEMBER

Volume 26, Pages 1-809 (November 2023)

The Eurasia Proceedings of Science, Technology, Engineering & Mathematics (EPSTEM)

e-ISSN: 2602-3199

Address: Istanbul C. Cengaver S. No 2 Karatay/Konya/TURKEY

Website: www.isres.org

Contact: isrespublishing@gmail.com

Conference: IConTES 2023: 7th International Conference on Technology, Engineering and Science (IConTES)
Conference website: https://www.2023.icontes.net
Dates: November 16 – 19, 2023
Location: Antalya, Turkey
Edited by: Prof. Dr. Mehmet Özaslan

About Editor
Prof Dr. Mehmet Ozaslan
Department of Biology, Gaziantep University, Turkey
Website: mehmetozaslan.com
Email: ozaslanmd@gantep.edu.tr

Language Editor
Assoc. Prof. Dr. Kagan Buyukkarci
Department of English Language Education, Suleyman Demirel University, Turkey
Email: kaganbuyukkarci@sdu.edu.tr

ORGANIZING COMMITTEE

Editorial Policies

ISRES Publishing follows the steps below in the procedings book publishing process.
In the first stage, the papers sent to the conferences organized by ISRES are subject to editorial oversight. In the second stage, the papers that pass the first step are reviewed by at least two international field experts in the conference committee in terms of suitability for the content and subject area. In the third stage, it is reviewed by at least one member of the organizing committee for the suitability of references. In the fourth step, the language editor reviews the language for clarity.

Review Process

Abstracts and full-text reports uploaded to the conference system undergo a review procedure. Authors will be notified of the application results in three weeks. Submitted abstracts will be evaluated on the basis of abstracts/proposals. The conference system allows you to submit the full text if your abstract is accepted. Please upload the abstract of your article to the conference system and wait for the results of the evaluation. If your abstract is accepted, you can upload your full text. Your full text will then be sent to at least two reviewers for review. The conference has a double-blind peer-review process. Any paper submitted for the conference is reviewed by at least two international reviewers with expertise in the relevant subject area. Based on the reviewers' comments, papers are accepted, rejected or accepted with revision. If the comments are not addressed well in the improved paper, then the paper is sent back to the authors to make further revisions. The accepted papers are formatted by the conference for publication in the proceedings.

Aims & Scope

In the 21st century, developments in science and technology have led to significant changes in the field of engineering. Creativity and design skills are at the center of studies in the field of engineering today. The main focus of this conference is original studies in the field of engineering. In addition, technology and basic science studies that are directly or indirectly related to engineering are also accepted at the conference.

The aim of the conference is to bring together researchers and administrators from different countries, and to discuss theoretical and practical issues in all fields of Engineering.

Articles: 1-89

CONTENTS

The Eurasia Proceedings of Science, Technology, Engineering & Mathematics (EPSTEM)
ISSN: 2602-3199

The Eurasia Proceedings of Science, Technology, Engineering & Mathematics (EPSTEM), 2023

Volume 26, Pages 1-12

IConTES 2023: International Conference on Technology, Engineering and Science

Artificial Intelligence Technologies and Applications Used in Unmanned Aerial Vehicle Systems

Mustafa Cosar
Hitit University

Abstract: An Unmanned Aerial Vehicle (UAV) is an autonomous airborne platform characterized by fundamental flight capabilities, including take-off and landing procedures, navigation, route tracking, and mission execution. UAVs serve civilian and military purposes across various domains, undertaking tasks that surpass human capabilities. These vehicles come in diverse hardware and software configurations, comprising essential components such as take-off and landing systems, navigation modules, emergency response mechanisms, sensory apparatus, imaging instrumentation, and energy supply systems. UAVs exhibit the capability for flight management, target identification, and mission analysis, drawing on data collected from preloaded datasets, control centers, and real-time environmental cues. Leveraging various artificial intelligence (AI) algorithms, UAVs autonomously process instantaneous data, incorporating methodologies such as artificial neural networks, image processing algorithms, learning algorithms, and optimization techniques. This paper analyses data analytics methodologies and AI technologies used by UAVs. Furthermore, an image processing application using a Convolutional Neural Network (CNN) algorithm is implemented to provide object recognition. The object recognition rate of the application developed in Python language was calculated with an accuracy of 0.7107. This finding shows that by using AI algorithms to analyze images acquired through onboard sensors, the UAV's capability to conduct critical operations such as target acquisition, obstacle avoidance and collision avoidance can be improved.

Keywords: UAV, AI, Machine learning, Image processing, Object recognition

Introduction

In recent years, a significant spotlight has been cast on the advancement of systems, underpinned by the contributions of Information Technologies (IT), engineered to provide support in endeavors exceeding human capabilities or encompassing substantial risk. These systems are predominantly identified as robotic systems or AI systems.

The term "Robot," which means "heavy and tedious labor" in Czech, was first coined by Karel Čapek in 1921. The word "Robotics" was first used in 1950 by the science fiction writer Isaac Asimov. Robotics is a software and hardware system utilized to control, disassemble, and assemble a robotic object according to its programmed instructions (Ozfırat, 2009). In the architecture of robotic systems, there are physical components encompassing mechanical, electrical, electronic, and computational modules, along with software components such as operating systems, control software, communication protocols, and task-specific software (Cosar, 2023).

The terms "Robot" and "Robotics" are often used interchangeably, but they do have some conceptual distinctions. "Robot" typically refers to a self-moving entity, whereas "Robotics" encompasses the system that constitutes such an entity. With the addition of AI, these systems become autonomous and capable of collecting data, learning, and solving problems independently. When a robotic system can emulate human behaviors, demonstrating the ability to perform these behaviors, it signifies its intelligence and learning capabilities.

The concept of AI was initially delineated by John McCarthy in 1956 as the 'science and engineering devoted to the creation of intelligent machines, especially intelligent computer programs' (McCarthy, 2007). AI systems are conceptualized to improve upon the present state, identify optimal solutions to problems, and automatically calculate and execute them. Progressing significantly beyond their initial capabilities, AI systems have currently advanced to a level where they can engage in meaningful conversations with humans and provide diverse recommendations, thus functioning at the level of a proficient assistant.

UAVs, commonly known as drones, represent autonomous aerial platforms capable of independently executing a wide spectrum of operations, including takeoff, flight, mission execution, and landing, occasionally making autonomous decisions. UAVs have gained significant traction in both military and civilian domains due to their versatility and advantages, being deployed for tasks such as observation, monitoring, transportation, search and rescue (Cosar, 2022). UAVs, commonly referred to as drones, can operate in two primary modes: remote-controlled and semi-autonomous, or fully autonomous. In the former, they are under remote human control, while in the latter, they exhibit a high degree of autonomy, often assisted by advanced AI technologies, enabling them to independently manage all aspects of their missions.

This study commences by providing an overview of the general architectures and components inherent to UAV systems. It subsequently delves into the realm of AI technologies and their current applications, which bestow upon UAVs their advanced capabilities. Finally, the study presents a practical application in image processing, specifically for object recognition. The article's structural organization unfolds as follows: The second section navigates through the conceptual framework surrounding UAVs and AI technologies, offering insights into exemplary applications and summarizing the pertinent literature. The third section meticulously elucidates the methodology of the exemplar application, expounding on the dataset employed for image processing, the AI algorithm applied, and the algorithmic underpinnings of the program developed using the Python programming language. The fourth section divulges the outcomes of running the Python program, particularly focusing on the achieved accuracy rate in object recognition and the visual outputs. In conclusion, the final section provides an exhaustive assessment that encompasses a retrospective analysis, the current state of affairs, and prospective outlook regarding the technologies under discussion. This study is positioned to make substantial contributions to forthcoming research initiatives within the realms of UAVs and AI technologies.

Conceptual Framework

UAV Systems

UAVs are autonomous aerial robotic systems capable of independently performing takeoff, flight, mission execution, and landing activities, and, in some cases, making autonomous decisions. They consist of mechanical and electronic hardware components, flight control systems, and software components designed for various purposes. In addition, they are equipped with sensors that can collect real-time data from both their own components and the external environment. Moreover, they possess communication modules that facilitate communication with other UAVs, particularly in swarm missions and with ground control centers.

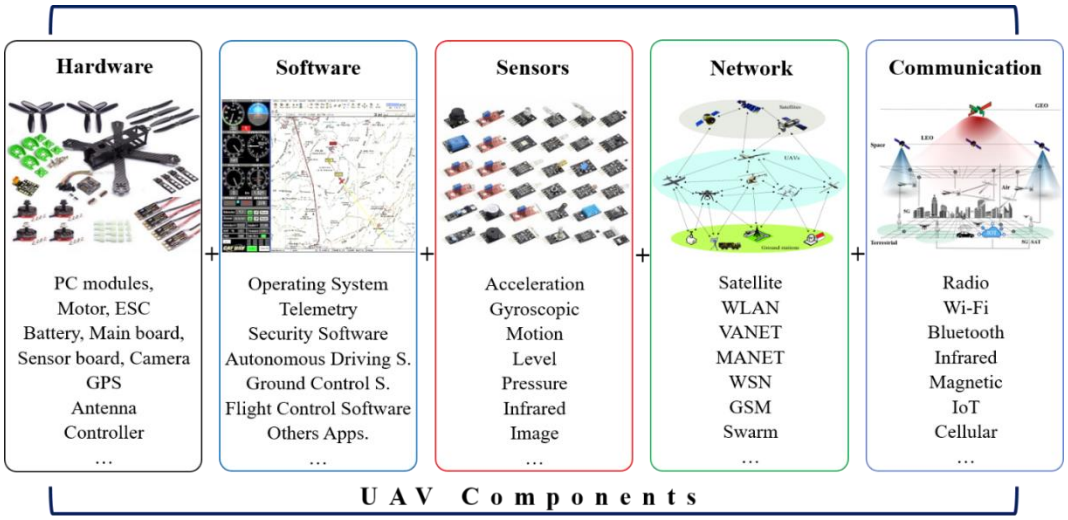

Figure 1. Components of a UAV (Cosar, 2022)

Within a UAV system, the software components encompass autonomous navigation software, image capture and processing software, mapping and route planning software, communication software, mission protocol software, and cybersecurity software. Figure 1 depicts the components of a UAV, as updated from Cosar (2022). Each heading in the figure is accompanied by sub-components. All of these components play various roles in making AI operational. Particularly noteworthy are the sensor components that have the ability to detect internal and external environmental parameters, enabling learning through data analytics and facilitating autonomous decision-making. In addition to these components, UAV systems include a fuselage and wings, which enable the UAV to stay aloft and fly. Under the fuselage, various materials are used for the chassis and connection elements. Another essential component that should not be overlooked is the power source, engine, and power transmission lines that provide energy to the mechanical and electronic components.

UAVs are classified into various categories based on their physical characteristics, wing structure, shapes, and intended applications. UAVs are categorized by their physical attributes into Fixed-Wing, Rotary-Wing, Flapping-Wing, and VTOL (Vertical Take Off and Landing). Furthermore, they undergo a separate classification based on payload capacity and whether they are designed for military or civilian purposes.

The most critical component of a UAV system is the flight control system. This component, organized as a module in terms of both software and hardware, processes data collected from the ground station, the UAV itself, and the surrounding environment during pre-flight, in-flight, and post-flight operations. The flight control system utilizes sensors to collect and process data, subsequently transmitting commands to other UAV components and relaying information to the ground station's computer system via the telemetry module.

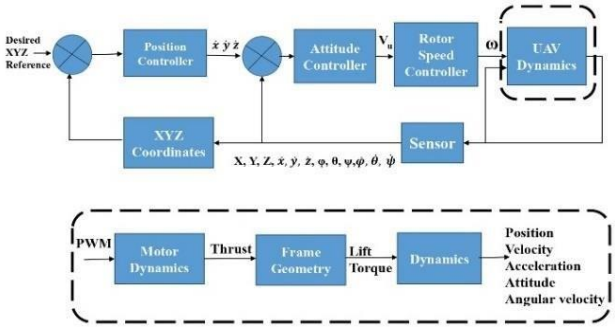

Figure 2. Block diagram of UAV flight control system (Hegde et al., 2020)

Figure 2 illustrates a block diagram of a rotary-wing UAV's flight control system, responsible for managing flight based on parameters such as altitude, distance, coordinates, wing rotation speed, and other variables. This system initially performs measurement and calculation processes to reach ideal position values based on the UAV's position during takeoff, landing, and flight. Subsequently, it calculates the disparities between the current state, as derived from data collected through sensor communication, and the desired state. Based on these calculated values, it initiates crucial processes such as mission and route optimization, triggering the autonomous decision-making process. This loop continuously operates throughout the mission.

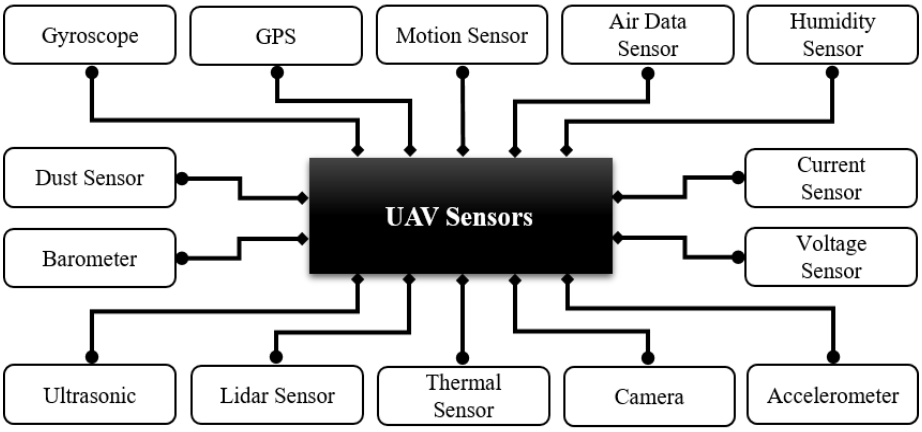

Figure 3. Some sensors found in UAV architecture

One of the most influential components in the convergence of UAVs with AI is the sensors depicted in Figure 3. This component serves as the UAV's sensory organs, providing the data that assists in situational analysis. Below, we introduce the most commonly used sensors in UAV applications.

- GPS Sensor (Global Positioning System Sensor): GPS sensors are employed to determine the UAV's geographical location on Earth, facilitating navigation and route planning. They are essential for mapping flight paths, reaching designated waypoints, and accomplishing mission objectives.
- IMU Sensor (Inertial Measurement Unit Sensor): IMU sensors measure the UAV's speed, acceleration, and angular movements. This data is crucial for maintaining flight stability, refining position calculations, and enabling precise maneuvering during flight.
- Camera Sensor: UAVs use cameras for tasks such as image and video recording, observation, mapping, and object recognition. Camera sensors are utilized to capture and analyze visual data.
- LiDAR Sensor (Light Detection and Ranging Sensor): LiDAR sensors are employed to create high-resolution 3D maps, detect objects, and measure distances accurately. They are particularly valuable for tasks like terrain mapping and environmental sensing.
- Thermal Sensor: Thermal cameras detect temperature variations and are used for operations such as search and rescue, fire monitoring, and identifying water resources.
- Gyro Sensor (Gyroscope Sensor): Gyro sensors are used to detect changes in orientation and rotation. They contribute to maintaining the UAV's stability during flight and enabling precise maneuvers.
- Radar Sensor: Radar sensors are used to monitor air traffic, avoid other aircraft, and ensure safe landings at airports.
- Ultrasonic Sensor: Ultrasonic sensors measure the distance to the ground and are crucial for automatic landings and obstacle avoidance systems.
- Pressure Sensor: UAVs employ pressure sensors to measure atmospheric pressure, providing crucial data for altitude determination and weather analysis.
- Magnetic Field Sensor: A magnetic field sensor is a vital component used for detecting changes in magnetic fields, which aids in orientation and navigation within UAV systems.
- Humidity Sensor: Humidity sensors are utilized to measure atmospheric moisture levels, offering valuable insights into environmental conditions and weather phenomena during UAV missions.
- Current Sensor: Current sensors play a fundamental role in monitoring the electrical current flowing through various components in the UAV's electrical system, ensuring both safety and operational efficiency.
- Voltage Sensor: Voltage sensors are pivotal for measuring electrical potential differences, allowing for the continuous monitoring of the electrical system's status and performance.
- Infrared Sensor (IR Sensor): Infrared sensors capture infrared radiation, enabling thermal imaging and object detection, particularly under low-light conditions, facilitating enhanced situational awareness.
- Compass Sensor: Compass sensors serve as a navigational aid, determining the UAV's orientation concerning Earth's magnetic field, thereby contributing to accurate heading control.
- Distance Sensor: Distance sensors are instrumental in gauging the range between the UAV and objects in its vicinity. They are indispensable for applications such as obstacle avoidance, terrain mapping, and precise landing procedures.

These sensors collectively bolster the sensory capabilities of UAVs, allowing them to undertake a diverse array of tasks and interact effectively with their surroundings.

Artificial Intelligence

AI is the discipline of science and engineering related to the imitation or development of thinking, learning, decision-making and problem-solving abilities that model human behavior in software and hardware systems of computer science. AI possesses a wide range of applications, including the performance of complex tasks, big data analysis, object recognition, natural language processing, autonomous decision-making, and predictive modeling. This technology enables a multitude of innovative applications spanning various domains, from industrial processes to healthcare services, automation systems to intelligent assistants.

Figure 4 depicts the systematic assessment of AI applications over a sequence of stages. The process commences with the transition from extensive repositories of big data, progressing towards meticulously curated, categorized, correlated, processed, and analyzed datasets. Subsequently, leveraging learning techniques, the dataset undergoes profound knowledge extraction. Ultimately, this acquired knowledge facilitates the generation of decisions and actions. It is imperative to acknowledge that this process imposes an additional

burden in terms of hardware and software resources. Notably, the computation speed for parameter adjustments and the computational requirements for data processing introduce supplementary expenses and computational workloads for UAVs.

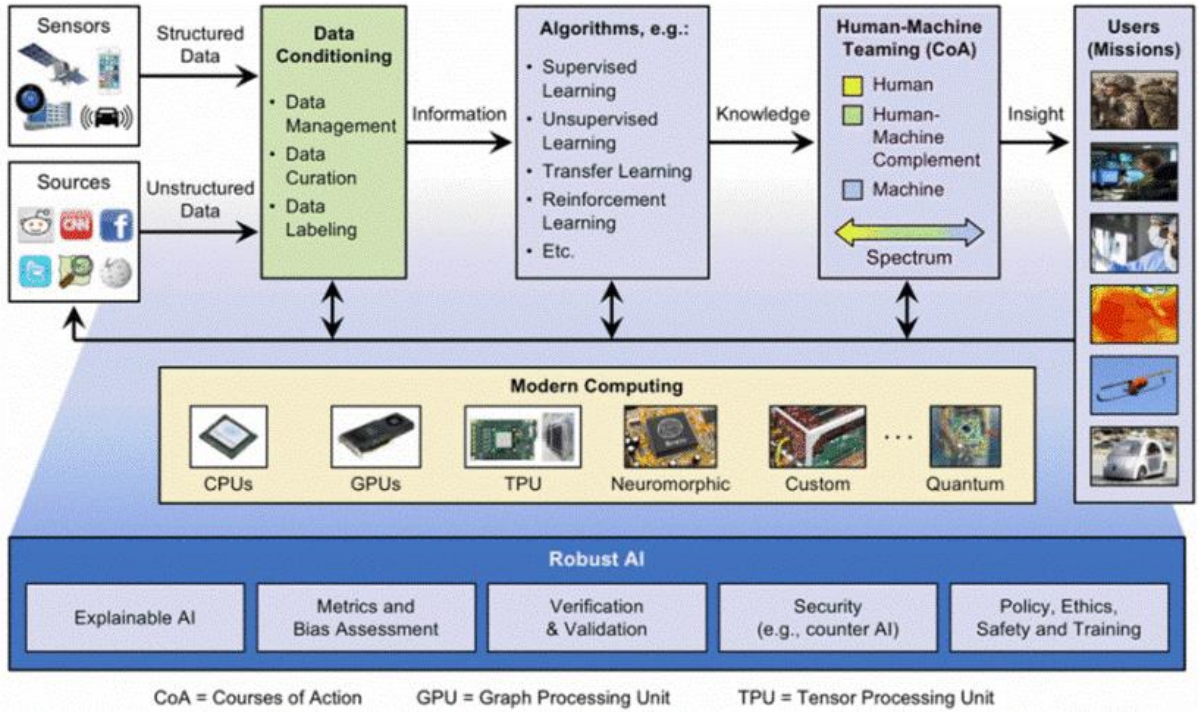

Figure 4. Architecture of a AI system (Reuter et al., 2020)

UAV and AI

AI technologies are prominently employed in processes demanding cognitive functions, such as speech recognition, image perception, autonomous navigation, and positioning. UAV systems have harnessed these AI capabilities to act autonomously and make decisions. In the early stages of UAV utilization, rudimentary challenges were addressed through human-assisted expert systems. As technology evolved, integrating human pilot behaviors to mimic analogous responses, particularly for critical decision-making, became a common practice. In recent times, the growing demand for mission diversity, speed, and energy efficiency necessitates the exploration of alternative technologies. In this context, AI technology emerges as the primary solution. This is attributed to the UAV's requirement to process dynamic environmental variables continuously and in real-time during flight.

Two distinct operational principles for UAVs and AI technologies exist, dependent on data collection and processing methods. The first, Off-board processing, hinges on data transfer and processing between the UAV and an external computer within the environment. However, this method is susceptible to external influences as the entire process occurs through a communication medium. The second approach is Onboard processing, whereby the UAV autonomously initiates data processing using its in-built hardware and software. In onboard processing, it is not possible to change pre-existing image processing rules and add new ones. Therefore, such UAVs are generally preferred in non-dynamic missions. Decision-making rules are generally straightforward, void of temporal constraints, and do not accommodate event prioritization or hierarchies' dependent on other events (Boubeta Puig et al., 2018).

The integration of AI with modules responsible for UAV flight control, encompassing image recognition, object tracking, and various information-based processes, has yielded favorable outcomes. Despite the augmented demand on software, hardware, and energy systems, the empowerment of UAVs designed for low-tolerance, sensitive tasks with robust machine and deep learning processes significantly enhances mission performance, rendering them indispensable.

UAVs face a plethora of challenges, including adverse weather conditions, energy consumption optimization, payload capacity management, mission risk mitigation, route obstacle avoidance, inherent design-related factors,

cyber threats, and the dynamic nature of environmental conditions. To effectively contend with these adverse circumstances, the implementation of an autonomous system capable of independent decision-making is imperative. In this context, AI technology assumes a pivotal role in facilitating real-time situation analysis and decision-making processes.

Table 1. AI technologies used by the UAV during the mission and the application process

Task	Implementation	AI Technologies
Object recognition and tracking	It is used for autonomous UAVs that have a decision-making mechanism by real-time image processing. Noise and unwanted effects are removed from the pure image collected by the camera and other image sensors, and the simplest and clearest image is obtained. From these images, decision-making processes such as object recognition, object tracking and obstacle avoidance are initiated.	▪ Artificial Neural Networks (ANN) ▪ Nearest Neighbors (KNN) ▪ CNN ▪ Graph Neural Networks ▪ Support Vector Machine (SPV) ▪ Machine Learning (ML) ▪ Deep Learning (DL) ▪ Reinforcement Learning (RL) ▪ Markov decision process, ▪ Q-Learning (Q-L) ▪ Swarm AI Algorithms ▪ Evolutionary Computing (EC) ▪ Genetic Algorithms ▪ Gravitational Search Algorithm (GSA) ▪ Optimization Algorithms ▪ Heuristic and Meta-Heuristic Algorithms (Bee Colony, Ant Colony, Particle Swarm Opt...)
Target classification	It is used to minimize target deviations in adverse environmental conditions and areas with heavy signal traffic.	
Path planning	It is used to determine alternative routes by processing parameters such as speed, duration, path loss and target distance during the UAV's mission.	
Energy consumption	It is used to control energy consumption during landing, take-off and flight time and to prevent unnecessary consumption.	
Takeoff, landing and maneuvering	It is used to perform actions such as anomaly detection, obstacle avoidance and collision avoidance that do not comply with the functioning of the system.	
Communication	It aims to improve the quality of the signal, its transmission, and its resistance to distortion during the communication phase of the UAV with the control centre and other UAVs.	
Task optimization	It is used to increase communication, interaction and coordination in single and swarm flights of the UAV. It is generally effective in flight speed, flight duration, energy utilization and path planning.	
Flying object detection	It is used for activities such as detection, avoidance and interception by processing radar, sound, image and thermal scan data for the detection of other flying systems on the route.	
Cyber security	It is used in the detection and prevention of cyber threats and attacks against the UAV's position, swarm interaction and communication systems.	

Table 1 provides a list of AI technologies used in UAV applications. This table provides summary information about the purposes for which AI technologies are used and what kind of improvements they make. Column 3 of the Table 1 lists the most commonly used AI algorithms and optimization methods. It is possible to expand the lines of this table as the use of AI technologies becomes widespread.

Literature

Gonzales et al. (2016) conducted image processing via thermal imagery to detect, classify, and monitor wildlife in forests or open areas using drones. Zhang et al. (2018) wanted to provide cellular wireless network service by optimizing UAV positions with ML algorithms. In the Ucan base station model, they managed to reduce the energy consumption of IHs by 20-80%. Sarıbas et al. (2018) were able to real-time, accurately determine vehicle positions using the EPPC, YOLO Tiny, and YOLOv2 algorithms with a 84.49% accuracy rate based on image data collected by UAVs. Polvara (2018) successfully executed the landing of an UAV on a moving ship. The evaluation of variables was carried out for landing at a non-fixed and irregularly moving point in this application.

In the study by Line (2018), autonomous landing was performed on a moving vehicle with a QR code. Zhang et al. (2018) proposed a ANN detection algorithm using three signal features for UAV RF signals: improved slope, improved kurtosis, and improved skewness. The recognition rates of SVM, KNN, RBFNN, SOMNN, and BPNN were found to be 0.9106, 0.8828, 0.9252, 0.8459, and 0.9368, respectively.

Venturini et al. (2021) approached mission optimization in UAV swarms by using a scaled Reinforcement Learning (RL) approach in a simulation environment, achieving a success probability of approximately 0.65 to 0.7. Poudel and Moh (2021) proposed a hybrid algorithm that combines probabilistic roadmap and optimized artificial bee colony (ABC) for determining the optimal route in an environment with various obstacles through data collection over the network. The proposed algorithm was found to provide energy efficiency and packet transmission efficiency.

Tlili et al. (2022) proposed an AI-supported model for detecting errors and abnormalities during cyberattacks on UAVs. The model used the Long Short-Term Memory (LSTM) algorithm, resulting in accuracy values of 0.955 in attack detection and 0.824 in error tolerance. Boone et al. (2023) ran a ML algorithm to detect buildings in aerial images obtained from low-flying UAVs. Through image processing on maps, the model achieved a mean Average Precision (mAP) of 0.3 and an Intersection of Union (IoU) accuracy of 88%.

Method

In this study, an image processing application was developed using a classification algorithm, which is one of the AI technologies. A deep neural network model was constructed in order to classify low-resolution images available in the Keras and Tensorflow libraries through ML, and images were tested. The CIFAR-10 dataset was used as the dataset. The CNN algorithm was employed as the classification algorithm. The application's computer software was coded in the Python programming language.

Dataset

The CIFAR-10 dataset, created by the Canadian Institute for Advanced Research, was utilized. This dataset consists of 10 different object classes and contains 60,000 image sets for training and 10,000 image sets for testing, each with a size of 32x32 pixels. These images have pixel values ranging from 0 to 255. The dataset is well-suited for performing analyses as successful as those conducted by humans using AI methods (Hope et al., 2017). During the application, the value ranges were normalized to the range of 0 to 1 to process the data more effectively.

Image Classification Algorithm

In the digital environment, images are modeled as numerical three-dimensional matrices. The image processing process is carried out on this matrix using mathematical and statistical computations. CNN is a neural network based mainly on image or video type media data models. This network is an extended version of ANN used to extract features by creating a grid-like matrix structure on visual datasets.

The basic components of the architecture of the method include the 1^{st} layer convolutional layer, 2^{nd} layer pooling layer and 3^{rd} fully connected layer. How many of these layers will be used may vary depending on the type of data to be processed and the purpose of the application. Here is a mathematical model of a CNN: In this equation, X represents the input data, F represents filters, W represents the weight matrix, b represents bias, and σ represents the activation function, producing output Y. Convolution and pooling operations can be further detailed with parameters defining dimensions and indices.

Convolutional Layer

Convolutional layers perform the convolution of special filters on input data. Mathematically, in these layers, each filter conducts a dot product with the input data. The result is called feature maps. Mathematically, the convolution process can be expressed as follows. X is the input data, F represents the filters, * represents the convolution process, and Y represents the feature map. The mathematical calculation model of this process is given in Formula 1.

$$Y = X * F \tag{1}$$

Pooling Layer

Pooling layers are used to downsize feature maps and highlight important features. The most commonly used pooling operation is max-pooling. Mathematically, max-pooling can be expressed as:

$$Yi,j = max(Xi',j') \tag{2}$$

Fully Connected Layers

These layers flatten feature maps and connect them with consecutive layers. Mathematically, these layers produce an output by multiplying the input vector with *a* weight matrix and applying an activation function. The first fully connected layer often includes an activation function (Raitoharju, 2022).

$$Yi,j = \sigma(WX + b) \tag{3}$$

In Formula 3, *Y* is the output function, *W* is the weight matrix of the image, *X* is the input vector, and *b* is the bias. Additionally, σ represents the activation function. CNNs typically include these basic components and often consist of multiple convolution and pooling layers. When combined, these layers can extract and classify complex image features.

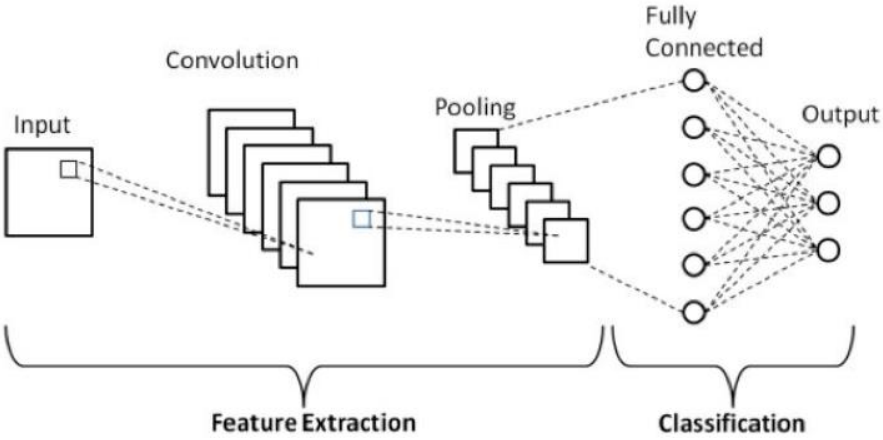

Figure 5. Schematic diagram of a basic CNN architecture (Phung & Rhee, 2019)

CNNs have distinct advantages over other pattern recognition algorithms as they integrate both feature extraction and classification processes. Figure 5 illustrates a basic schematic representation of the image processing procedure using a fundamental CNN algorithm. Figure 5, a simplified diagram of the image processing process, consists of five different layers. The number of layers varies depending on the application type and image complexity. These layers are assessed within two distinct segments. The first segment involves feature extraction and the second segment pertains to classification.

The feature extraction segment includes image resizing, weight matrix creation, and size reduction without losing the basic information of the image. At the end of this process, the feature map of the image is created. The second segment is created to classify image features. In this process, for each object category, there is an output neuron that represents the classified version of the image (Phung & Rhee, 2019).

Computer Algorithm of the Model

In calculating the accuracy of the model, the number of iterations was determined as 10. Then, coding process in Python language was started. The pseudo code of the application is presented below as Algorithm_1.

Algorithm_1. Pseudo code of the Image Processing Application

1. Import necessary libraries: TensorFlow, Keras and Matplotlib libraries
2. Load CIFAR-10 dataset
3. Define class names:
   Create a list of class names for the CIFAR-10 dataset, representing different categories like 'Airplane,' 'Automobile,' 'Bird,' etc.
4. Normalize the data:
   Scale the pixel values of the images in both training and test datasets to be between 0 and 1 by dividing by 255.
5. Create a convolutional neural network (CNN) model:
   Create the model: tf.keras.models.Sequential().
   Conv2D layers add with ReLU activation functions and MaxPooling layers to build the CNN layers.
   Flatten the data and add Dense layers for classification.
   The final Dense layer has 10 units, representing the 10 different classes.
6. Compile the model as a matric:
   optimizer, cross-entropy loss-gain, and determine 'accuracy'
7. Model's training:
   Use the training images and labels to train the model for 10 epochs with model.fit().
   The model's performance is evaluated on the test dataset during training.
8. Evaluate the test model's performance:
   The test loss and test accuracy using model.evaluate() calculate, and print the test accuracy.
9. Make predictions:
   Use the trained model to make predictions on the test images.
10. Visualize predictions and true labels:
    Create a 5x5 grid for displaying test images with their predicted and true labels.
    Loop through the test images, plot them, and label each image with its predicted and true class names.
    Use 'green' for correct predictions and 'red' for incorrect predictions.
11. Display the plot using plt.show().

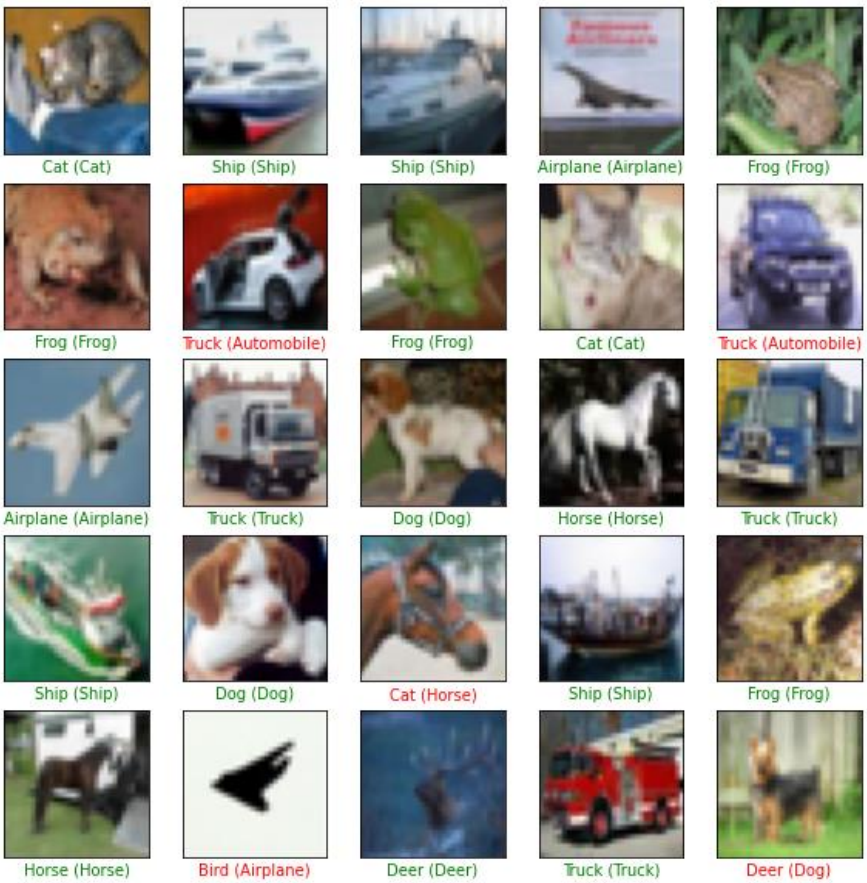

Figure 6. Object recognition matrix obtained from image processing with CNN algorithm

After training, the accuracy of the model is evaluated on test images. In such applications, where recognition is attempted with AI algorithms on the dataset of images obtained from camera images, the quality of the UAV's image capture and recording features directly affects the results. Therefore, the complexity and duration of the UAV's flight mission may change its accuracy performance.

Results and Discussion

Based on the obtained results, the application was coded using the Python programming language. When the relevant code was executed, the AI algorithm's image processing accuracy value (Test accuracy) was determined to be 0.7106999754905701. As a result of the image processing, the obtained labeled abstract matching image matrix is presented in Figure 6.

Figure 6 illustrates the results of the image predictions, with green labels indicating correct predictions and red labels indicating incorrect predictions, with the true label provided in parentheses for the red ones. A lower occurrence of red labels is desirable, signifying higher accuracy in predicting new images after the learning process. This code snippet generates a 5x5 grid presenting 25 test images alongside their predicted and true labels, highlighting correct predictions in green and incorrect ones in red. Similar structures can be employed to include additional graphs. The accuracy graphs are outlined as follows.

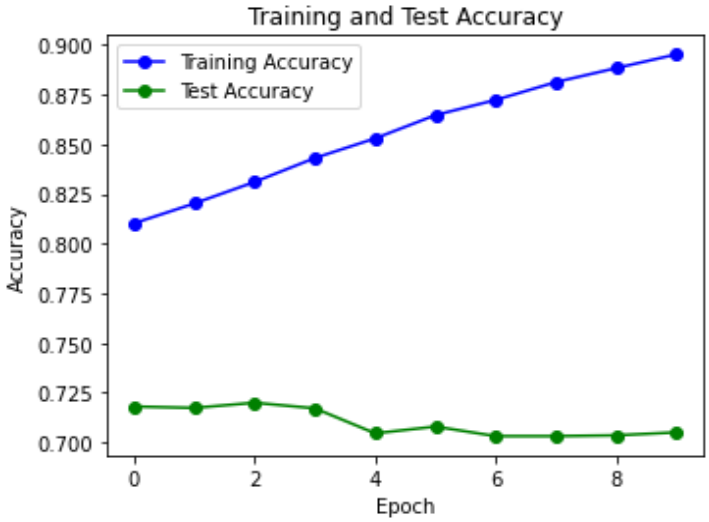

Figure 7. Image processing result accuracy values graph

When the application code is run, it creates a graph with two underlines as shown in Figure 7. This graph shows the "Training Accuracy" (in blue) and "Testing Accuracy" (in green) over trials (Epoch). These graphs show how the accuracy values change with each epoch, helping to monitor the performance of your model during training and testing.

Conclusion

In this study, an overview of AI technologies in conjunction with UAV was provided, along with contemporary applications. Subsequently, an object recognition application was implemented using AI algorithms in the image processing phase. The success rate was calculated as 0.7107.

The current structure of UAV systems imposes several constraints, including their weight, payload capacity, energy consumption, remote control limitations, and potential obstacles encountered during missions. Some of these obstacles can be overcome with pre-mission interventions, but others require real-time detection, calculation, measurement, and evaluation to make autonomous decisions. This is where AI technologies come into play, ensuring the optimal solution following a situation analysis.

AI technologies employed in UAV systems are primarily used in various stages of image processing, location accuracy computation, range and route calculation, swarm optimization, energy efficiency control, and

communication system enhancements. The variable structure, quality, and parametric size of the dataset in AI applications directly impact the decision-making process of autonomous systems. In image processing procedures, the accuracy and processing time are greatly influenced by the AI algorithm used, especially when dealing with extensive data. Additionally, the technology and capacity of hardware components used in computation and data transmission stages are also crucial.

Recent developments indicate the provision of hardware solutions aimed at enhancing computational capabilities. Processors contributing to learning capabilities stand at the forefront of these solutions. New chip technologies are developed to be energy-efficient and feature high data processing capacities. Processors like AImotive aiWare3, AlphaIC Real AI Processor-Edge, Huawei HiSilicon Ascend 310, and Tesla Full Self-Driving (FSD) are specifically designed for autonomous vehicles, equipped with AI-supported computation and algorithms.

The widespread use of IT offers opportunities for remote monitoring, control, and management. As the drawbacks of these technologies are gradually eliminated, their usage expands, fostering a positive outlook. AI technologies thus present an approach that mitigates IT-related disadvantages, particularly in the context of unmanned vehicles used for remote monitoring, control, and management on land, at sea, and in the air. These AI-equipped unmanned vehicles contribute to reduced mission duration, energy consumption, and enhanced mission success rates. The future of AI is being shaped by ongoing scientific and technological research, developments, and user preferences. Notably, regulations related to legal and ethical aspects are required to maximize the benefits of AI for humanity and minimize associated risks.

Scientific Ethics Declaration

The author declares that the scientific ethical and legal responsibility of this article published in EPSTEM Journal belongs to the author.

Acknowledgements or Notes

* This article is an updated and extended version of the abstract presented orally at the International Conference on Technology, Engineering and Science (www.icontes.net) held in Antalya/Turkey on November 16-19, 2023.

References

Boone, J., Goodin, C., Dabbiru, L., Hudson, C., Cagle, L., & Carruth, D. (2023). Training artificial intelligence algorithms with automatically labelled uav data from physics-based simulation software. *Applied Sciences*, *13*(1), 131. https://doi.org/10.3390/app13010131

Boubeta-Puig, J., Moguel, E., Sánchez-Figueroa, F., Hernández, J., & Preciado, J. C. (2018). An autonomous UAV architecture for remote sensing and intelligent decision-making. *IEEE Internet Computing*, *22*(3), 6–15.

Casas, E., Ramos, L., Bendek, E. & Rivas-Echeverría, F. (2023). Assessing the effectiveness of YOLO architectures for smoke and wildfire detection. *IEEE Access*, *11*, 96554-96583.

Cosar, M. (2022). Cyber attacks on unmanned aerial vehicles and cyber security measures. *The Eurasia Proceedings of Science, Technology, Engineering & Mathematics (EPSTEM)*, *21*, 258-265.

Cosar, M. (2023). Tedarik zinciri yönetiminde yapay zekâ ve robotik. In B. Taskın & B.Caglar (Eds.), *Tedarik zincirinde dijital donusum* (1st ed., pp.69-93). Bursa, Turkey: Ekin Publishing

Hegde, N. T., George, V.I., Nayak, C.G. & Kumar, K. (2020). Transition flight modeling and robust control of a VTOL unmanned quad tilt-rotor aerial vehicle. *Indonesian Journal of Electrical Engineering and Computer Science*, *18*(3), 1252-12651.

Hope, T., Resheff, Y.S. & Lieder, I. (2017), *Learning tensor flow: A guide to building deep learning systems.* Sebastopol, CA, USA: O'Reilly Media, Inc.

Koc, M. (2020). Derin ogrenme kullanarak iha ile hareketli bir hedefin otonom olarak yakalanması. (Master's thesis). Sabahattin Zaim University, Istanbul.

Line, V. (2018). Autonomous tracking and landing of a multirotor UAV on an outdoor ground moving platform.

McCarthy, J. (2007). What is artificial intelligence? Technical report, Stanford University. Retrieved from http://www-formal.stanford.edu/jmc/whatisai/node1.html

Ozfırat, M. K. (2009). Robotik sistemler ve madencilikte kullanımının arastırılması. *TUBAV Bilim Dergisi*, *2*(4), 412-425.

Phung V. H., & Rhee E. J. (2019). A high-accuracy model average ensemble of convolutional neural networks for classification of cloud image patches on small datasets. *Applied Sciences*, *9*(21), 4500.

Polvara, R. (2018). Vision-based autonomous landing of a quadrotor on the perturbed deck of an unmanned surface vehicle. *Drones*, *2*(2), 15.

Poudel, S., & Moh, S. (2021). Hybrid path planning for efficient data collection in UAV-Aided WSNs for emergency applications. *Sensors*, *21*. 2839.

Raitoharju, J. (2022). Convolutional neural networks. *Deep learning for robot perception and cognition* (1st ed., pp. 35-69). Massachusetts, USA: Academic Press

Reuther, A., Michaleas, P., Jones, M., Gadepally, V., Samsi, S. & Kepner, J. (2020). Survey of machine learning accelerators. *2020 IEEE High Performance Extreme Computing Conference* (HPEC), 1-12.

Sarıbas, H., Cevıkalp, H., & Kahvecıoglu, S. (2018). Car detection in images taken from unmanned aerial vehicles. *In 26th Signal Processing and Communications Applications Conference (SIU)*, 1-4. IEEE.

Tlili, F., Ayed, S., Chaari, L., & Ouni, B. (2022). Artificial intelligence based approach for Fault and Anomaly Detection Within UAVs. In L. Barolli, F.Hussain & T. Enokido (Eds.), *Advanced information Networking and Applications. AINA 2022. Lecture Notes in Networks and Systems* (p.449). Springer, Cham,

Venturini F., Mason, F., Pase, F., Chiariotti F., Testolin, A., Zanella, A. & Zorzi, M. (2021). Distributed reinforcement learning for flexible and efficient UAV swarm control. *IEEE Transactions on Cognitive Communications and Networking*, *7*(3), 955-969.

Villi, O., & Yakar, M. (2022). Insansız hava araclarının kullanım alanları ve sensor tipleri. *Turkiye İnsansız Hava Aracları Dergisi*, *4*(2), 73-100.

Zhang, H., Cao, C., Xu L., & Gulliver, T. A. (2018). A UAV detection algorithm based on an artificial neural network. *IEEE Access*, *6*, 24720-24728.

Zhang, Q., Mozaffari, M., Saad, W., Bennis M., & Debbah M. (2018). Machine learning for predictive on-demand deployment of Uavs for wireless communications. *2018 IEEE Global Communications Conference (GLOBECOM*),1-6. Abu Dhabi, United Arab Emirates.

Author Information

Mustafa Cosar
Department of Computer Engineering, Hitit University
19030, Corum/Turkiye
Contact e-mail: *mustafacosar@gmail.com*

To cite this article:

Cosar, M. (2023). Artificial intelligence technologies and applications used in unmanned aerial vehicle systems. *The Eurasia Proceedings of Science, Technology, Engineering & Mathematics (EPSTEM), 26*, 1-12.

The Eurasia Proceedings of Science, Technology, Engineering & Mathematics (EPSTEM)
ISSN: 2602-3199

The Eurasia Proceedings of Science, Technology, Engineering & Mathematics (EPSTEM), 2023

Volume 26, Pages 13-18

IConTES 2023: International Conference on Technology, Engineering and Science

Geophysical Techniques for Determination of Areas with Increased Water Saturation in Integrated Mine Waste Storage Facility

Maya Tomova
University of Mining and Geology

Atanas Kisyov
University of Mining and Geology

Abstract: The aim of this study is focused in determination of areas with increased water saturation in the integrated mine waste storage facility (IMWF) in open pit "Khan Krum" gold mine in Southeastern Bulgaria. The integrated mine waste facility (IMWF) is designed to store both dewatered process tailings and waste rock from mining. The concept of the integrated mine waste facility (IMWF) is to place thickened tailings into cells constructed from mine rock. For determination of areas with increased water saturation, is used Electrical Resistivity Tomography (ERT) – geophysical imaging technique widely applied to mineral prospecting, mining exploration and also environmental investigations. Electrical resistivity tomography is commonly used for solving complex tasks related to increasing efficiency in the open mine. In this research electrical resistivity tomography is used to detect and characterize water saturation zones by exploiting resistivity contrasts between dewatered process tailings and waste rock from mining using electrical current.

Keywords: Geophysics, Electrical resistivity, Tomography, Waste storage.

Introduction

The "Ada Tepe" open pit gold mine geological section within "Khan Krum" gold mine deposit is located 3 km south of the Krumovgrad town site, Southeastern Bulgaria, and trends in a north south direction. The morphology of the site is hilly rising in elevation from 492,4 masl abutting the major regional Krumovitsa River system, to 220 masl within the zone of mineralization. The Ada Tepe deposit is a low-sulphidation adularia-sericite gold-silver epithermal deposit formed during the Neogene within the Southern Rhodope tectonic zone and located within Paleocene sedimentary rock overlying the north-eastern end of the Kessebir core complex.

The method selected for the management of mining waste deposition usually depend on the selected extraction method, the selected mineral processing, the waste characteristics, the technical characteristics of the mine waste facility, its geographical location and the local environmental conditions (Garbarino et al., 2018). Mining and mineral processing generate waste that must be properly managed to reduce environmental risks. Several studies, for example Tayebi-Khorami et al. (2019) and Yankova (2020, 2021), have been carried out to highlights the key problems with mining and mineral processing waste and in particular tailings storage, mining waste amount reducing and safe storage. Effective waste management is the basis of sustainable development. Many experts contend the present stage of mineral-raw material industry evolution is describing by mineral deposits with complex mining-geological conditions, difficult for mining, low grade ores with complex processing, which leads to considerable waste quantities formation. Waste proper storage is critical to the planet and human health.

In the waste management early planning of „Ada Tepe" mine separate waste dump and tailings storage facility were designed but for their construction 96 ha surface area have been necessary (Eldridge et al., 2011). For

location optimizing while, considering the terrain's characteristics, the affected area, mineral deposit volume and exploitation, Kaykov and Koprev (2020) considered the ratio between waste volume and surface area to be a variable and depends on the terrain features, waste dump features design and the construction sequence.

The concept of the IMWF is to place thickened tailings into cells constructed from mine rock. The mine rock provides strength required for overall stability and also internal drainage (Eldridge et al., 2011). The study area is composed of a highly porous, poorly sorted breccia, breccia conglomerate, breccia conglomerate with quartz inclusions, metamorphic clasts and clay. This information was claimed by several drillings around the research area. The waste rock mostly consists of breccia conglomerates with occasional boulders of metamorphic rocks – amphibolites, gneiss and schists. A total of 14,950,000 tons of waste rock are expected to be produced during the life of the Ada Tepe mine.

A recent literature review (2023) found that IMWF is challenging to construct and operate. One of the challenges is operational sequence while constructing the IMWF (Eldridge et al. 2013). Aleksandrova and her team (2021) have suggested using the Critical path method (CPM) as a tool to manage the facility's construction operational sequence. Dimitrov and co-workers (2023) suggested that constructing a IMWF with wider or narrower body can manage the facility's operational sequence, and the need for contingency storage will be decreased or eliminated. The authors have designed two types of IMWF and investigated how choosing the proper form for the IMWF can help in having better control over the operational sequence. The researchers recommend building a broader construction body since thus large cells numbers can be fitted in one bench.

To minimize pond formation, the IMWF is formed into a 'honycomb' structure which reduces the drainage pathway lengths (both horizontally and vertically) and optimizes the structure's ability to drain water away. Drainage into the IMWF is collected in an under-drain system that prevents the build-up of a water table within the rock and tailings. The drainage berms have a significantly higher permeability than the tailings, and there is no ponding expected both from the supernatant water and rainfall. However, regularly strict site control is required to the peripheral high permeability berms, which has to prevent pond formation.

The following investigation is focused in determination of areas with increased water saturation in the integrated mine waste storage facility (IMWF) using Electrical Resistivity Tomography (ERT). This technology is used for imaging sub-surface structures from electrical resistivity measurements made at the ground surface. According to Dimovski et al. (2017) results illustrate the potential of electrical tomography method to provide fast and reliable information for observed area based on electrical resistivity.

Description of the Technology

A good knowledge of the waste and its behavior over time is of a great importance to ensure the environmentally safe management of extractive waste. From an environmental point of view, the main difference between the mineral in the original deposit and the corresponding mine waste is the increased possibility for various physical, chemical or biological processes which can affect the mine waste. This means that through the extraction and floatation process some parts in the original mineral resources might become more accessible in the waste. This can result in possible reactions with the environment or leakage for mine waste. Therefore, proper mine waste characterisation is the basis for successful and safe waste management. It is also important to consider changes that can occur over time (Garbarino et al., 2018).

The IMWF is sequentially constructed from the bottom up, with mine wastes placed on starting platforms at the bottom of the valley at approximately 300m elevation and then progressively built up in benches during the mine life to elevation 450 m. This approach allows the lower, completed sections of the facility to be reclaimed and closed during the life of the mining operation. This method allows on the completed section to be performed quality control for increased water saturation within the facility and also completed sections of the facility to be progressively rehabilitated and vegetated during the life of the mining operation.

One possible way for evaluating the water saturation and the ability of the IMWF to drain water away is presented in this research using Electrical Resistivity Tomography (ERT). This non-invasive geophysical technique proved itself as very productive when it comes to determine the subsurface resistivity distribution by making measurements generally on the ground surface. As stated by Hasan et al. (2021) the basic principle of ERT is based on the varying electrical conductivity of the subsurface materials, which depends on many factors, such as rock type, porosity, permeability, connectivity of pores, temperature, salinity, cation exchange capacity,

clay content, nature of the fluid/water, etc. Generally, it can be assumed that a wide range of electrical resistivity for most materials suggests the varying water content (Hasan et al., 2021).

Two-dimensional resistivity profiling is commonly used for determining the distribution of electrical resistivity in the shallow subsurface. In the field survey two electrodes are used to inject electric current into the ground and other two electrodes to measure the electric potential difference. Then, automatic computer-controlled instrumentation measures potential differences between pairs of electrodes, creates resistances by dividing by the current passed, and converts these resistances into apparent resistivities using geometrical factors determined by the relative positions of the electrodes (Park, 2009). The measurements are often carried out along a line and the observed potential differences are converted into pseudo-sections of apparent resistivities, which indicate the resistivity changes of subsurface structures (Zhou, 2014). ERT profiles consist of a modeled geological cross-sectional (2D) plot of resistivity versus depth (Ωm). Analyses of these data provide understanding of the underground resistivity anomalies such as water saturation or outline the subsurface geological structure.

Results and Interpretation

The aim of recent research is to determine areas with increased water saturation in the integrated mine waste storage facility (IMWF) using Electrical Resistivity Tomography (ERT). Apparent resistivity data were collected with a Wenner-Schlumberger array. According to Seaton and Burbey (2002) Wenner–Schlumberger configuration is considered to have good signal response, the ability to resolve horizontal and vertical structures relatively well, and greater depth of investigation than the Wenner configuration (Ward, 1990; Sharma, 1997; Reynolds, 1997; Loke, 2001).

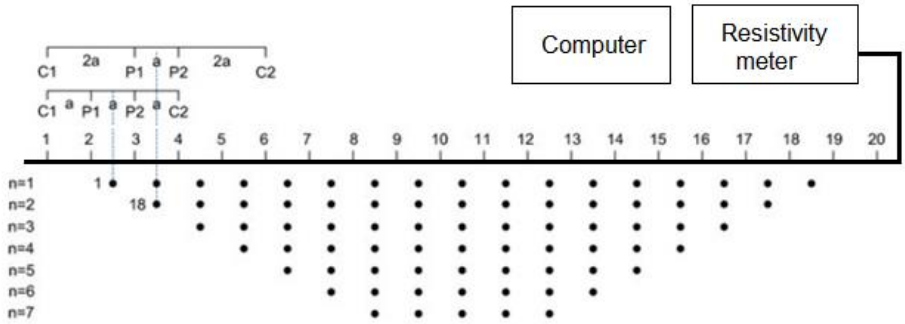

Figure 1. The Wenner–Schlumberger configuration and the sequence of measurements in ERT

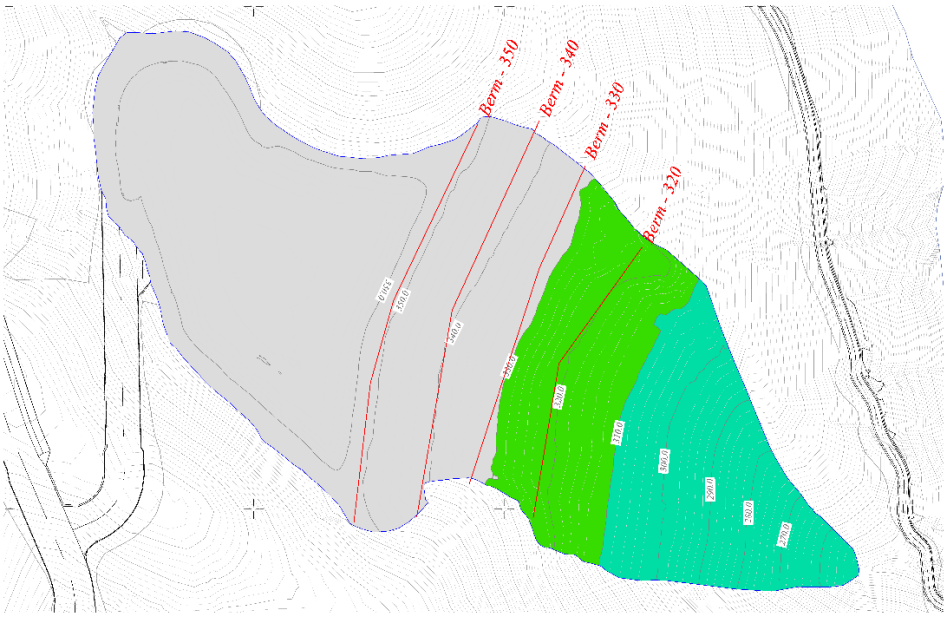

Figure 2. Field measurements situation plan

Electrical resistivity tomography data processing and modelling were done using the RES2DINV. This computer program automatically determines the 2D resistivity model for the observed data (Griffiths, 1993). The precise location of the geophysical surveying lines in the area of Integrated Mine Waste Facility is illustrated in Figure 2. The ERT field measurements were performed along 4 lines with total length of 740m.

Table 1. Total length of each line of Integrated Mine Waste Facility

Line	Line 1 (Berm 350m)	Line2 (Berm 340m)	Line 3 (Berm 330m)	Line 4 (Berm 320m)
Length, m	210	210	170	150

The interpreted ERT sections are presented below (Figure 3 to Figure 6).

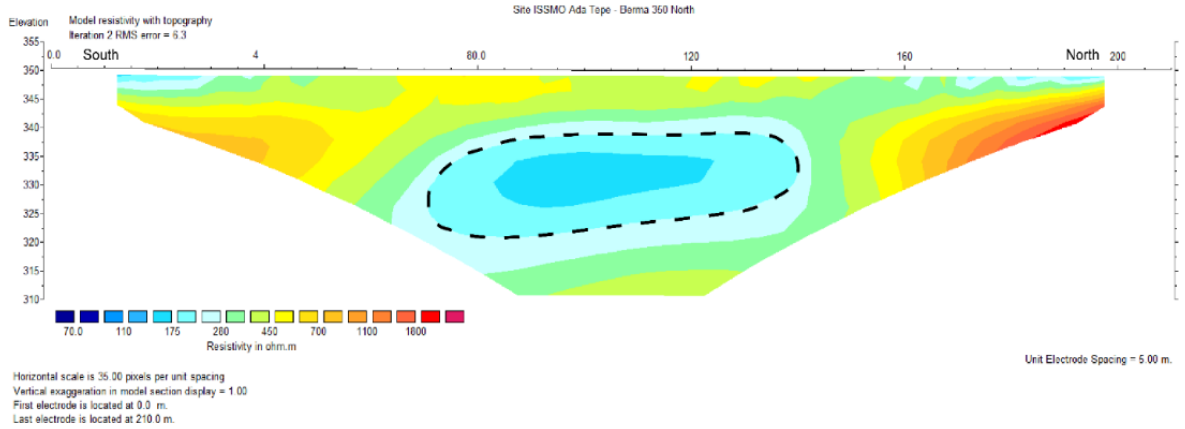

Figure 3. ERT section along Line 1 - Berm 350m

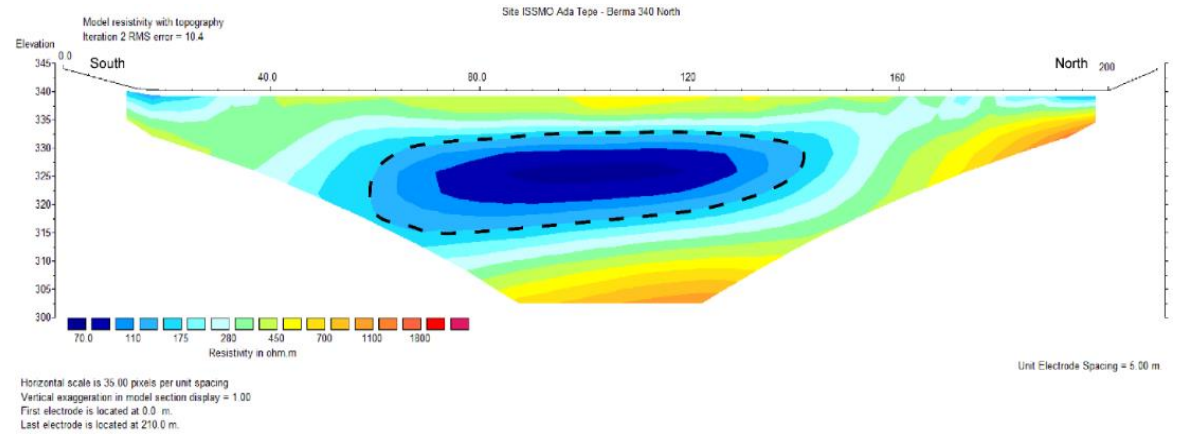

Figure 4. ERT section along Line 2 - Berm 340m

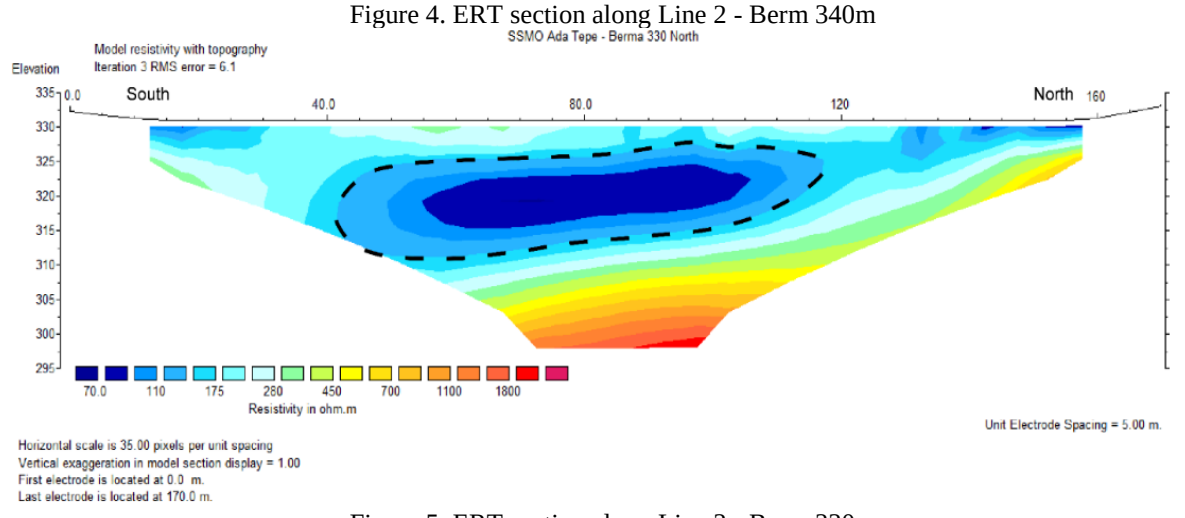

Figure 5. ERT section along Line 3 - Berm 330m

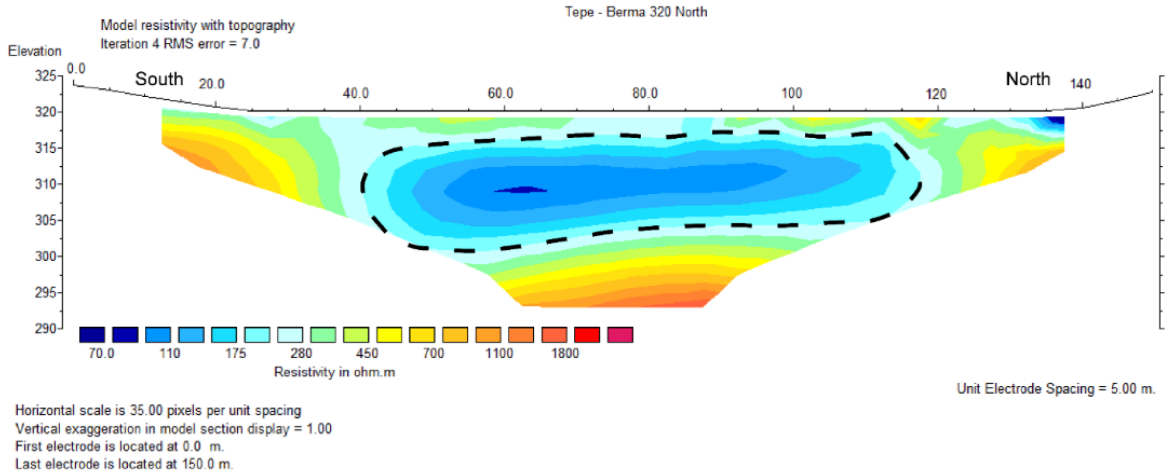

Figure 6. ERT section along Line 4 - Berm 320m

Based on interpretation of ERT lines at the IMWF can be assume that the electrical resistivity distribution in depth along all profiles is well differentiated. According to the measurement results and the interpretation of the ERT lines is considered that specific electrical resistance of the observed area varies from 70 Ωm to more than 2000 Ωm. It can be considering that along all the lines, in the central part, are distinguished zones with relatively low values of electrical resistance in the range from 70 Ωm to about 200 Ωm. Most likely, these zones mark the spatial distribution of an area with increased water saturation due to the incomplete drainage of the deposited material.

Conclusion

Mining industries are the very first link of a long supply chain. The raw materials are feedstock materials many industries and significantly contributes as such to technological development. The extractive industry has very important role in the economic and also societal development of every country. Mining and ore processing operations around the world produce significant amounts of waste, predominantly non-profitable solid residues, i.e., waste rock and tailings.

In the last few decades many efforts have been made by the mining industries to prevent, reduce and minimise as far as possible the negative impacts due to its operations. Over the years, mining waste management strategies and techniques have evolved considerably to achieve these objectives. One possible prevention, in order to minimise and reduce as far as possible the generation of mine waste, may be performed by implementing appropriate equipment and technology modifications during the extraction of the mineral resources.

The "Ada Tepe" deposit can be assuming as high-grade open pit mine, which use modern and environmentally sound methods for mine waste management as well as suitable mining techniques. Furthermore, minimising the environmental impacts contributes to making the extraction of mineral resources more environmentally responsible. So, to ensure the effectiveness and long-term stability of the IMWF is recommended monitoring the results within six months.

Scientific Ethics Declaration

The authors declare that the scientific ethical and legal responsibility of this article published in EPSTEM journal belongs to the authors.

Acknowledgements or Notes

* This article was presented as an oral presentation at the International Conference on Technology, Engineering and Science (www.icontes.net) held in Antalya/Turkey on November 16-19, 2023.

References

Aleksandrova, E. Dimitrov, L., & Kaykov, D. (2021, September 6-10). Operational sequence for constructing a combined mine waste facility. Proceedings of the *XVI International Conference of the Open and Underwater Mining of Minerals*, 7-13. Varna, Bulgaria.

Dimitrov, L., Grigorova, I., & Yankova, T. (2023). Possibilities to construct combined mine waste dump facility with better operational sequence. *The Eurasia Proceedings of Science, Technology, Engineering & Mathematics (EPSTEM), 23*. 42-49.

Dimovski, S., Stoyanov, N., Tzankov Ch., Kisyov, A., (2017). Application of electrical resistivity tomography for studying fissure-karst water-bearing complexes. Proceedings of the *9th Congress of the Balkan Geophysical Society*, 1-5. Antalya, Turkey.

Eldridge, T., Kissiova, M., Wickland, B., Ahmed, I. B., & Laurin, J.-F. (2013). Integrated mine waste storage facility, Krumovgrad gold project, Bulgaria. Proceedings of the *XV Balkan Mineral Processing Congress, Sozopol*, 356-359. Bulgaria.

Eldridge, T., Wickland, B., Goldstone, A., & Kissiova, M. (2011). Integrated mine waste storage concept, Krumovgrad gold project, Bulgaria. *Tailings and Mine Waste.*

Garbarino, E., Orveillon, G., Saveyn, H., Barthe, P., & Eder, P. (2018). Best available techniques (BAT) reference document for the management of waste from extractive industries. *Directive 2006/21/EC, 21*(3), 30- 33.

Griffiths, D. H., & Barker, R. D. (1993). Two dimensional resistivity imaging and modeling in areas of complex Geology. *Journal of Applied Geophysics*, *29*, 211-226.

Hasan, M., Shang, Y., Meng, H., Shao, P., & Yi, X. (2021). Application of electrical resistivity tomography (ERT) for rock mass quality evaluation. *Scientific Reports, 11*(1), 23683.

Kaykov, D., & Koprev, I. (2020). Rationalizing the location and design of the waste dump in the case of open pit mining. *Sustainable Extraction and Processing of Raw Materials Journal*, *1*, 42-46.

Loke, M. H. (2001). Tutorial: 2-D and 3-D electrical imaging surveys. *Course Notes for USGS Workshop "2-D and 3-D Inversion and Modeling of Surface and Borehole Resistivity Data*.

Park, J., You, Y., & Kim, H. J. (2009). Electrical resistivity surveys for gold-bearing veins in the Yongjang mine, Korea. *Journal of Geophysics and Engineering*, *6*(1), 73–81.

Reynolds, J. M. (1997). *An introduction to applied and environmental geophysics*. Wiley

Seaton, W., & Burbey, T. (2002). Evaluation of two-dimensional resistivity methods in a fractured crystalline-rock terrane. *Journal of Applied Geophysics*, *51*(1), 21-41.

Sharma, P. V. (1997). *Environmental and engineering geophysics*. Cambridge University Press

Tayebi-Khorami M., Edraki, M., Corder, G., & Golev, A. (2019). Re-thinking mining waste through an integrative approach led by circular economy aspirations. *Minerals*, *9*(286), 1-12.

Ward, S. H. (1990). Resistivity and induced polarization methods. *Geotechnical and Environmental Geophysics*, *1*, 147-189.

Yankova, T., (2020). Mineral processing waste utilization. *XX International Multidisciplinary Scientific GeoConference SGEM 2020*, *20*, 219-226. Albena, Bulgaria.

Yankova, T., (2021). Mining damaged landscape reclamation study. *XXI International Multidisciplinary Scientific GeoConference SGEM 2021*, *2*(1.1), 383-390. Albena, Bulgaria.

Zhou, B. (2014). *Electrical resistivity tomography: A subsurface-imaging technique*. Applied Geophysics with Case Studies on Environmental, Exploration and Engineering Geophysics, IntechOpen

Author Information

Maya Tomova
University of Mining and Geology “St. Ivan Rilski”
Sofia, Studentski grad, prof. Boyan Kamenov", Sofia 1700
Sofia, Bulgaria
Contact e-mail: *maya.grigorova86@gmail.com*

Atanas Kisyov
University of Mining and geology “St. Ivan Rilski”
Sofia, Studentski grad, prof. Boyan Kamenov", Sofia 1700
Sofia, Bulgaria

To cite this article:

Tomova, M., & Kisyov, A. (2023). Geophysical techniques for determination of areas with increased water saturation in integrated mine waste storage facility. *The Eurasia Proceedings of Science, Technology, Engineering & Mathematics (EPSTEM), 26*, 13-18.

The Eurasia Proceedings of Science, Technology, Engineering & Mathematics (EPSTEM)
ISSN: 2602-3199

The Eurasia Proceedings of Science, Technology, Engineering & Mathematics (EPSTEM), 2023

Volume 26, Pages 19-25

IConTES 2023: International Conference on Technology, Engineering and Science

Development of Reliable and Effective Methods of Cryptographic Protection of Information Based on the Finite Automata Theory

Altynbek Sharipbay
L.N. Gumilyov Eurasian National University

Zhanat Saukhanova
L.N. Gumilyov Eurasian National University

Gulmira Shakhmetova
L.N. Gumilyov Eurasian National University

Alibek Barlybayev
L.N. Gumilyov Eurasian National University

Abstract: This paper describes project to conduct study of cryptographic protection of information on publications in publications and development of methods for reliable and efficient cryptographic protection of information based on finite automaton models-FAM, preparation of additions to standards and management of dissertations of undergraduates and doctoral students on information security and information protection. To achieve this goal, following tasks will be solved: 1. Study of mathematical foundations of cryptology and analysis of standards for cryptographi. Results: Theory of finite fields, models of FA, descriptions of requirements of standards, proposals to standards. 2. Study of applicability of various FA models in construction of reliable and efficient cryptoalgorithms. Results: Algorithm for obtaining an inverse FA from given FA - proving applicability of FA in cryptosystem, algorithm for composing several FA - proving increase in reliability of cryptosystem using composite FA with increased number of states, algorithm for constructing equivalent FA – proving increase in efficiency of cryptosystems using equivalent FA with reduced number of states. 3. Development and verification of programs for reliable and efficient cryptosystem based on KA. Results: FA cryptographic programs and their applications in steganography, verification and testing protocols for developed programs.

Keywords: Cryptography, Information security, Finite automata, Reversibility of finite automata, Information security standards

Introduction

In era of active use of Internet, ensuring security of information becomes serious problem. Therefore, special attention is paid to ensuring confidentiality, availability and integrity of information using cryptographic methods. During COVID 19 demand for online services has increased. This led to increase in attacks and hacks (Boranbayev et al., 2018). In 2022, outside attacks on communication infrastructures have become more frequent, which required an increase in the quality of information protection. Security of every citizen and entire country depends on reliability and effectiveness of cryptographic protection. Therefore, cryptographic information protection tools developed on basis of specific methods are required.

Kazakhstan uses foreign software products (Seilova et al., 2021). State programs and Concepts (Kassymzhanova et al., 2022) require the development (Aktayeva et al., 2018) of domestic software products (Mukanov, 2023).

Based on these documents, project executors are engaged in cryptographic information protection and have certain scientific background (Shakhmetova et al., 2021; Sharipbaev et al., 2004; Sharipbaev et al., 2004; Andasova et al., 2009; Satybaldina et al., 2009; Abdymanapov et al., 2021; Sharipbay et al., 2013).

In (Sharipbaev et al., 2006; Satybaldina et al., 2009; Sharipbay et al., 2016; Sharipbay et al., 2017; Sharipbay et al., 2016), applications of finite automata (FA) in cryptography and general idea of information encryption by means of FA with output and FA without output were described. In (Shakhmetova, 2018; Shakhmetova et al., 2019), issues of using automata models without exit in cryptography were discussed, advantages and disadvantages of such models as the Domosi cryptosystem and its improved version were presented. But there was interest in FA with release (Shakhmetova et al., 2018). Many scientific papers (Sharipbay et al., 2019) have been studied and analyzed, where concept of finite automaton cryptography (FAC) was introduced.

All knowledge about FAC is presented with help of ontology, which is built for first time and provides clear understanding of using FA in cryptography and systematizes the information about this subject area obtained during study. As practical example, FAPKC ontology (Finite Automation Public Key Cryptosystems) was constructed - public key streaming cryptosystem based on FA, proposed by Tau (2008). In this ontology, process of improving FAPKC from version FAPKC0 to FAPKC4 was shown. Based on these studies, the following problems were identified:

- Absence of algorithm for constructing composition of PILT - automata.
- Large key size. For example, key length for algorithm security achieved with 512-bit RSA key is 2792 bits for FAPKC.
- Lack of evidence base for correctness of cryptographic algorithms.

Considering all weaknesses of previous cryptosystems (Bao & Igarashi, 1995; Meskanen, 2001), R. Tau proposed new asymmetric encryption algorithm FAPKC4 (Tao & Chen, 1999). It is interesting in that public key is used to encrypt plaintext and verify signature, which consists of sequential composition of reversible automata, while inverse automata are part of the private key, which is used to decrypt and sign the message. It's believed that without knowledge of secret key it's difficult to invert sequence of automata composition (Satybaldina et al., 2011). In contrast to number theory, where large number can always be decomposed into simple factors, for which order of their mutual arrangement in product is not important, in theory of FA in composition of reversible automata, both their set and the order of the mutual arrangement of reversible automata in composition matter. In other words, composition of FA from primitive automata doesn't have the commutativity property. Therefore, the task of decomposing FA composition into its constituent components is same difficult task as factoring the product of two large numbers (Sharipbay et al., 2019). Therefore, decomposition of FA into primitive automata allows you to create ultra-reliable information security systems.

As is known, main property of FA, which determines its use in encryption/decryption of information, is its reversibility. Therefore, issues of checking the reversibility of FA, algorithms for constructing FA, which were presented in works (Shakhmetova et al., 2020; Shakhmetova & Saukhanova, 2020), were investigated. In these works, problems of reversibility of several FAM were considered, such as reversibility of input-output FA and reversibility of automata that stores information, which confirms need to study problem of reversibility of other FAM as well.

It is known that in addition to FAPKC, there are other FAM in cryptography. In Abubaker (2011), it was proposed to use FA in a cryptosystem based on 128-bit key using key generation algorithm based on (DAFA - DES Augmented Finite Automaton cryptosystem, DES - Data Encryption Standard). The paper (Srilakshmi, 2012) proposes new cryptographic algorithms based on Mealy/Moore automata and recursive functions. In (da Cruz Amorim, 2016; Vieira, 2017), all characteristics of linear FA and their reversibility were studied, and new structural FAM was also presented, called PILT - Post Initial Linear Tranducer.

There are also studies in this subject area in Russia and Kazakhstan. So in works (Agibalov, 2009; Kovalev & Trenkaev, 2011; Kovalev, 2014) implementation of FAPKC on FPGAs is shown, scientists from L.N. Gumilyov ENU proposed hardware implementation of FA-cryptosystem with public key (Satybaldina et al., 2011; Satybaldina et al., 2011).

Today, there are many well-known cryptographic ciphers that have proven themselves well in information security environment, and they undoubtedly have high efficiency from computational point of view. However, rapid growth and improvement of quantum computers has increased likelihood of solving most classically difficult problems, and constant improvement of cryptanalysis has influenced development of new algorithms

for breaking classical cryptographic systems. If we take 1024-bit RSA encryption as example, then it was cracked by scientists from USA, Netherlands and Australia, who found serious vulnerability in cryptographic library implemented in GnuPG (Bernstein et al., 2017). This trend gives impetus to development of new cryptographic systems or the improvement of existing ones, using alternative mathematical models.

As result of studies of publications of domestic scientists in foreign and Kazakh publications, it can be concluded that such studies are mainly carried out as memristive cryptography (James, 2019), cryptography based on elliptic curves (Muratbekov et al., 2014; Kulmamirov et al., 2018), improvement of classical cryptographic algorithms (Gnatyuk et al., 2020; Gnatyuk et al., 2020; Biyashev et al., 2021), neural networks in cryptography (Fenina, 2021), which indicates that in Kazakhstan, research in FAC is carried out only by project executors, as described in the backlog of the project. Consequently, there are no software implementations of finite-automatic methods of cryptographic information protection, except for those that were discussed in review of existing works. Therefore, fundamental differences between project idea and existing analogues are that:

- For FAM based on PILT-automata, algorithm for constructing composition of reversible PILT-automata will developed and implemented.
- FAM will used in steganography, to protect secret text in stegacontainer, as well as in encoding/decoding of binary data.
- Proofs of correctness of cryptographic algorithms and protocols are carried out not by testing methods on specific data, but by formal proofs of verification conditions formulated in logical language.

This project provides for creation of reliable and efficient cryptosystem based on FAM, where encryption is carried out by a composition of reversible FA, and decryption by reverse sequence of reverse FA. Decomposition of an automata-encoder into simple components has exponential complexity (Agibalov, 2009), and its performance doesn't depend on the size of its transition table. Therefore, cryptographic systems based on FAM will have a significant advantage, both in terms of throughput and performance, over cryptographic methods based on numerical operations. In addition, development and verification of necessary cryptoprotocols will carried out using specification language with expressive power equivalent to expressive power of FA, which ensures correctness of created formalisms, constructiveness of algorithms and provability of their correctness. These arguments prove scientific novelty, importance and prospects of developing FAM, confirm significance of such cryptographic methods on national and international scale, and prove high scientific and technical level of proposed project, which will make significant contribution to formation of domestic scientific and technological potential.

Significance of the Project

In digital society, correct creation, use and protection of information resource ensures increase in degree of organization, and therefore, efficiency of functioning of economic systems. In turn, information resources today acquire characteristics of commodity and capital, actively participate in commodity-money relations. Therefore, urgent problem has arisen of creating domestic models and methods for protecting information resources from illegal actions that can lead to loss or distortion of valuable data and cause enormous material damage to their owners and society as a whole. In solving this problem, one cannot ignore time factor, when loss of time leads to a country lagging behind other countries. Issues of economic and national security of country depend on this. Without correct and timely solution to problem of protecting information resources, any country has no future. Results of project will be of economic and industrial interest, and will also cause great social demand among scientists and specialists working in field of information security.

For successful implementation of project, it's required to combine scientific results obtained earlier in direction of study area and results of project participants themselves into single integrated finite-automata technology for cryptographic information protection, which will include software implementation of information protection methods, teaching aid, training course and recommendations for improving state standards in field of cryptographic information protection.

Research in project is interdisciplinary, which requires knowledge in field of algebra to justify factorization of numbers, automata theory for modeling algorithms for encryption and decryption of information, mathematical logic for formulating and proving verification conditions for cryptographic algorithms and protocols, as well as information technology for programming encryption and decryption algorithms information, and standardization to prepare recommendations for improving state standards in the field of cryptographic information protection.

Due to fact that in Kazakhstan information security must be ensured, without any doubt, only by domestic cryptosystems.

Research Methods

The main scientific issue is the problem of developing reliable and efficient methods of cryptographic information protection based on the theory of finite automata, which requires a consistent study of the mathematical foundations of cryptography and the analysis of standards for the subject area of the project and the study of the applicability of various FA models in solving the problem of cryptography based on the construction of reverse FA, as well as the development and software implementation of cryptographic methods for protecting information based FA and verification of implemented programs. To study the mathematical foundations of cryptology and analyze the standards for the subject area of the project, descriptive research methods are used, and to solve other issues, the following experimental studies and works are sequentially performed: choosing a specific FA model; constructing a reverse FA to the selected FA; building a composition of the FA from a specific model; development and software implementation of data encryption methods based on various FA models; verification of programs and evaluation of their complexity, reliability and efficiency. To assess the applicability of the given FA to solve the problem of creating a reliable and efficient method of cryptographic information protection, experimental methods, software design methods, program testing methods, and formal program verification methods are used.

The most important experiments are: development and verification of the program for constructing the reverse FA given by the FA in order to determine their applicability to the creation of the required cryptosystem; development and verification of a program for constructing a composition of given FA in order to increase the reliability of the developed cryptosystem based on an increase in the number of FA and states of the resulting FA; development and verification of a program for constructing a FA equivalent to a given FA in order to increase the efficiency of the developed cryptosystem by reducing the number of states of the resulting FA.

The research used in the project as a substantiation of ways to achieve the goal of developing methods for reliable and effective cryptographic protection of information should use descriptive studies of the mathematical foundations of cryptology and analysis of standards for the subject area of the project, as well as the following experimental studies: development and verification of a program for constructing a reverse FA by given FA; development and verification of a program for constructing a composition of given FA; development and verification of a program for constructing a FA equivalent to a given FA. In addition to these methods, the project will use the methods of number theory, automata theory, the theory of algorithms and the theory of information encryption, as well as methods for constructing and verifying algorithms, methods for developing and testing software, and methods for graphical presentation of analysis results.

Methods for collecting primary information are searching the Internet and scientific and technical libraries for scientific publications and publications on models and methods of cryptology, as well as the texts of international and domestic standards and other legal documents on information security and cryptographic protection of information, specifications of cryptographic programs (possibly with online demonstration) that can be used in solving some tasks of the project with references to them. The methods of data processing are comparison with the contents of the available scientific, practical and regulatory materials, and in the absence of the latter, the found materials will be studied and stored in computer memory or in the cloud, indicating their IP addresses or mailing addresses of sources. Participants have a sufficiently high level of knowledge and experience in the subject area of the project to ensure reliability and reproducibility. They can hold scientific seminars, participate in scientific conferences and other events dedicated to the scientific direction of the project.

Conclusion

Main results of the project will be:

- correspond to international level of scientific and technical development, as they will published in rating international editions;
- ensure information security in field of information and communication technology, since reliability of created cryptosystems on KAM will be proven using composite automata;

- have a high degree of readiness for commercialization, since effectiveness of created cryptosystems on KAM will be proved by using an equivalent automaton with a minimum number of states, facilitating its software and hardware implementation;
- participate in training of highly qualified young specialists and scientists, involving bachelors, masters and PhD students in EP "Computer Science", "Artificial Intelligence Technology" and "Information Security" to solve individual project tasks as topics of their diploma and dissertation works, which is scientifically confirmed-practical significance and impact on the development of science: computer science and artificial intelligence.

In general, results of project contribute to solution of urgent tasks of socio-economic and scientific and technical development of RK, provided for in following state programs:

• "Digital Kazakhstan", which provides for the task "Ensuring information security in the field of ICT";
• "Development of Education and Science of the Republic of Kazakhstan", which provides for tasks to ensure a safe and convenient learning environment; increasing the effectiveness of R&D and integration into the global educational and scientific space.

Scientific Ethics Declaration

The authors declare that the scientific ethical and legal responsibility of this article published in EPSTEM journal belongs to the authors.

Acknowledgements

* This article was presented as an oral presentation at the International Conference on Technology, Engineering and Science (www.icontes.net) held in Antalya/Turkey on November 16-19, 2023.

* This research is funded by the Science Committee of the Ministry of Education and Science of the Republic of Kazakhstan (Grant No. AP19677422).

References

Abdymanapov, S. A., Muratbekov, M., Altynbek, S., & Barlybayev, A. (2021). Fuzzy expert system of Information security risk assessment on the example of analysis learning management systems. *IEEE Access*, *9*, 156556-156565.

Abubaker, S. (2011). *Probabilistic, lightweight cryptosystems based on finite automata*. (Doctoral dissertation).

Agibalov, G. P. (2009). *Finite automata in cryptography. Prikladnaya Diskretnaya Matematika, 11*, 43-73.

Aktayeva, A., Niyazova, R., Muradilova, G., Makatov, Y., & Kusainova, U. (2018). Cognitive computing cybersecurity: social network analysis. In *International Conference on Convergent Cognitive Information Technologies* (pp. 28-43). Cham: Springer International Publishing.

Andasova, B. Z., Satybaldina, D. Zh., & Sharipbaev, A. A. (2009). Analysis of cryptographic protocols based on modal logics. *Bulletin of ENU. L.N. Gumilyov*, *4*(71), 50-57.

Bao, F., & Igarashi, Y. (1995). Break finite automata public key cryptosystem. In *International Colloquium on Automata, Languages, and Programming* (pp. 147-158). Berlin, Heidelberg: Springer

Bernstein, D. J., Breitner, J., Genkin, D., Groot Bruinderink, L., Heninger, N., Lange, T., ... & Yarom, Y. (2017). Sliding right into disaster: Left-to-right sliding windows leak. In Proceeding 19th *International Conference, Cryptographic Hardware and Embedded Systems–CHES 2017* (pp. 555-576). Taipei, Taiwan.

Biyashev, R. G., Kapalova, N. A., Dyusenbayev, D. S., Algazy, K. T., Wojcik, W., & Smolarz, A. (2021). Development and analysis of symmetric encryption algorithm Qamal based on a substitution-permutation network. *International Journal of Electronics and Telecommunications*, *67*(1), 127-132.

Boranbayev, A., Boranbayev, S., Nurusheva, A., & Yersakhanov, K. (2018). The modern state and the further development prospects of information security in the Republic of Kazakhstan. In *Information Technology-New Generations: 15th International Conference on Information Technology* (pp. 33-38). Springer International Publishing.

da Cruz Amorim, I. D. F. (2016). *Linear finite transducers towards a public key cryptographic system* (Doctoral dissertation.) Universidade do Porto (Portugal)

Fenina, O. (2021). The application of neural networks in cryptography. In Proceedings of the *4th International Conference on Mathematics and Statistics* (pp. 48-58).

Gnatyuk, S., Akhmetov, B., Kozlovskyi, V., Kinzeryavyy, V., Aleksander, M., & Prysiazhnyi, D. (2020). *New secure block cipher for critical applications: Design, implementation, speed and security analysis. In Advances in artificial systems for medicine and education III* (pp. 93-104). Springer International Publishing.

Gnatyuk, S., Kinzeryavyy, V., Iavich, M., Odarchenko, R., Berdibayev, R., & Burmak, Y. (2020*). Studies on cryptographic security and speed analysis of new advanced block cipher* (pp. 202-213). ICST

James, A. P. (2019). An overview of memristive cryptography. *The European Physical Journal Special Topics, 228*(10), 2301-2312.

Kassymzhanova, A. A., Usseinova, G. R., Baimakhanova, D. M., Ibrayeva, A. S., & Ibrayev, N. S. (2022). Legal framework for external security of the Republic of Kazakhstan. *International Journal of Electronic Security and Digital Forensics, 14*(2), 209-222.

Kovalev, D. S. (2014). Optimization of FPGA implementations of finite-automatic cipher systems. In *Collection of Scientific Articles of the All-Russian Scientific and Practical Conference* (pp. 38-44). Barnaul: FPGAs, Signal Processing Systems.

Kovalev, D. S., & Trenkaev, V. N. (2011). FPGA implementation of finite automata public key cryptosystem. *Prikladnaya Diskretnaya Matematika*, *13*, 33-34.

Kulmamirov, S. A., & Aksholak, G. I. (2018). Analysis of encrypted digital signature algorithms based on elliptic curves. In Proceedings of the *International Practical Internet Conference "Actual Problems of Science*

Meskanen, T. (2001). *On finite automaton public key cryptosystems.* Turku Centre for Computer Science.

Mukanov, A. (2023). The main indicators of the state program digital Kazakhstan. In Proceedings of the *7 th International Scientific and Practical Conference Current Issues and Prospects for the Development of Scientific Research, 32* (151), 25-38.

Muratbekov, M. M., Abdymanapov, S. A., & Altynbek, S. A. (2014). Using the properties of Abelian groups to build cryptosystems on elliptic curves of odd order. *Bulletin of KazUEFMT, 1,* 105-109.

Satybaldina, D. Zh., & Sharipbaev, A. A. (2009). Application of fuzzy set theory to information Security Risk Analysis. In Abstracts of the *Third Congress of the World Mathematical Society of Turkic Countries,* (p. 216).

Satybaldina, D. Zh., & Sharipbaev, A. A. (2009). Information security risk assessment based on fuzzy logic. In Proceedings of the *II All-Russian Conference "Knowledge - Ontologies – Theories* (pp. 216-220). Novosibirsk.

Satybaldina, D. Zh., Sadykov, A. A., & Adamova, A. D. (2011). Hardware-software implementation of a cryptosystem based on finite automata. *Bulletin of L.N. Gumilyov atyndagy ENU Khabarshysy*, (2).

Satybaldina, D., Sharipbayev, A., & Adamova, A. (2011). *Implementation of the finite automaton public key cryptosystem on FPGA.* (pp. 167-173). WOSIS.

Satybaldina, D., Sharipbayev, A., Sadykov, A., & Adamova, A. (2011). FPGA implementation of the Finite Automaton Public Key Cryptosystem. In Book of abstracts of the *Third International Conference on Control and Optimization with Industrial Applications* (COIA 2011) (pp. 42-43). Ankara, Turkey.

Seilova, N., Kungozhin, A., Ibrayev, R., Gorlov, L., Ospanov, Z., Itemirov, R., & Kiyashko, I. (2021). About cryptographic properties of the Qalqan encryption algorithm. In *Ceur Workshop Proceedings "Cybersecurity Providing in Information and Telecommunication Systems II—CPITS-II*, 206-215.

Shakhmetova, G. B. (2018). Automata without exit in cryptography. In *XIII International Scientific Conference of Students and Young Scientists Science and Education* (pp. 767-770).

Shakhmetova, G. B., & Saukhanova, Zh. S. (2020). On algorithms that determine reversible finite automata with memory. In *XV International Scientific Conference* (pp. 496-500). Ǵylym Jáne Bilim-2020 Shakhmetova, G. B., Saukhanova, Zh. S., & Sharipbay, A. A. (2019). The use of finite automata without exit in information encryption. *Bulletin of the State University, 1*(85), 138-143.

Shakhmetova, G. B., Saukhanova, Zh. S., Sharipbay, A. A., & Ulyukova, G. B. (2020). The use of reversible automata in asymmetric cryptosystems. *Bulletin of AUPET, 1*(48), 118-123.

Shakhmetova, G. B., Sharipbay, A. A., Saukhanova, Zh. S., & Isabaeva, G. Zh. (2018). The use of finite automata for the development of asymmetric ciphers. *In Proceedings of the V International Scientific and practical conference "intelligent information and communication technologies - a means of implementing the third industrial revolution in the light of the strategy* (pp. 286-288).

Shakhmetova, G., Saukhanova, Z., Udzir, N. I., Sharipbay, A., & Saukhanov, N. (2021). Application of pseudo-memory finite automata for information encryption. In *IntelITSIS*, 330-339.

Sharipbaev, A. A., & Satybaldina, D. Zh. (2006). On finite-automatic models for the design of cryptosystems. In Proceedings of the *11th International Interuniversity in Mathematics and Mechanics, dedicated to the 10th anniversary of the ENU. L.N.* (p.214). Gumilyov Kazakhstan, Astana.

Sharipbaev, A. A., Bekbulatova, K., & Satybaldina, D. Zh. (2004). Security of public key algorithms. In Proceedings of *the International Scientific and Practical Conference Valikhanov Readings-9* (Volume 4, pp. 149-152). Kokshetau.

Sharipbaev, A. A., Kaplina, S. A., & Satybaldina, D. Zh. (2004). Methods for designing block ciphers. In Proceedings of the *International Scientific and Practical Conference Valikhanov Readings-9* (Volume 4, pp. 164-167). Kokshetau.

Sharipbay, A. A. (2016). Automatic models in cryptography. *Bulletin of KazNU Series of Mathematics, Mechanics, Computer Science, 3-1* (90), 96-104.

Sharipbay, A. A. (2016). Automatic models of encoders in electronics and cryptography. In Proceedings of the *V International Scientific and Practical Conference Informatization of Society* (pp. 402-411). Astana

Sharipbay, A. A. (2017). Genetic cryptographic algorithm of asymmetric information encryption. *In International Scientific Conference Computer Science and Applied Mathematics Part II*, Almaty (pp. 144-151).

Sharipbay, A. A., Omarbekova, A. S., & Niyazova, R. S. (2013). Cryptology. *MYURK, 1413*

Sharipbay, A. A., Saukhanova, Z. S., Shakhmetova, G. B., & Saukhanov, N. S. (2019). Application of finite automata in cryptography. In Proceedings of the *5th International Conference on Engineering and MIS*, 1-3.

Sharipbay, A. A., Saukhanova, Zh., Shakhmetova, G. B., & Saukhanova, M. S. (2019). Ontology of finite automaton cryptography. *Ontology of Design, 9*(1), 36-49.

Srilakshmi, S. (2012). On finite state machines and recursive functions application to cryptosystems.

Tao, R. (2008). *Finite automata and application to cryptography.* Chicago: Springer.

Tao, R., & Chen, S. (1999). The generalization of public key cryptosystem FAPKC4. *Chinese Science Bulletin, 44*, 784-790.

Vieira, J. B. (2017). *Finite transducers in public key cryptography.* Universidade do Porto (Portugal)

Author Information

Altynbek Sharipbay
L.N. Gumilyov Eurasian National University
Pushkin street 11, Astana, Kazakhstan
Contact e-mail: *sharalt@mail.ru*

Zhanat Saukhanova
L.N. Gumilyov Eurasian National University
Pushkin street 11, Astana, Kazakhstan

Gulmira Shakhmetova
L.N. Gumilyov Eurasian National University
Pushkin street 11, Astana, Kazakhstan

Alibek Barlybayev
L.N. Gumilyov Eurasian National University
Pushkin street 11, Astana, Kazakhstan

To cite this article:

Sharipbay, A., Saukhanova, Z., Shakhmetova, G., & Barlybayev, A. (2023). Development of reliable and effective methods of cryptographic protection of information based on the finite automata theory. *The Eurasia Proceedings of Science, Technology, Engineering & Mathematics (EPSTEM), 26*, 19-25.

The Eurasia Proceedings of Science, Technology, Engineering & Mathematics (EPSTEM)
ISSN: 2602-3199

The Eurasia Proceedings of Science, Technology, Engineering & Mathematics (EPSTEM), 2023

Volume 26, Pages 26-37

IConTES 2023: International Conference on Technology, Engineering and Science

Novel Comparative Study of Covid-19 Detection from X-ray and CT Scan Images Using CNN and MLP Neural Networks

Belhia Souaad
UDL University of Sidi Bel Abbes

Al Jahmani Souha
UDL University of Sidi Bel Abbes

Bahram Tayeb
University of Saida

Adjoudj Reda
UDL University of Sidi Bel Abbes

Abstract: The coronavirus has caused the deaths of millions of people and has endangered the entire healthcare system. In order to count positive cases and stop the disease from spreading, Rapid clinical results may prevent the COVID-19 from spreading and help medical professionals treat patients while working under challenging circumstances.. Normal disease diagnosis using a laboratory test requires equipment and takes some time with the use of X-ray and chest CT Scan images, artificial intelligence techniques are extensively used to categorize the COVID-19. In this study we present an automatic detection approach for COVID-19 infection based on Chest CT and X-ray images using a Multilayer Perceptron (MLP) Neurons Network and a Convolutional Neural Network (CNN). The two models are evaluated in two classes, COVID-19 and normal images, for detection by Chest X-ray images we obtained 95,7% accuracy using MLP model and 90% accuracy using CNN model. For detection by Chest CT image we obtained, 80,60 % accuracy using the MLP model and 88,49 % accuracy using the CNN. The experimental results indicate that the proposed approach can achieve high accuracy in detecting COVID-19 from X-ray images, demonstrating the potential of using machine learning techniques in medical diagnosis.

Keywords: COVID-19, MLP Neural Network, X-rays images, CT Scan image, Machine learning, CNN.

Introduction

In 2019, the tale coronavirus (COVID-19) Begin to spread in China as the starting point, and also in many other countries across the world (Scudellari, M (2020). Early automatic diagnosis of this disease could be very helpful in limiting its spread. Machine Learning is one artificial intelligence method that can help in the detection of COVID-19 infections in medical images like chest X-rays. An X-ray is an imaging technique used to investigate fractures, bone displacement, pneumonia, and tumors. X-rays have been used for many decades and provide an impressively fast way of seeing the lungs, making them a useful tool in the detection of COVID-19 infections [3 (Boudrioua et al., 2020)- (Narin et al., 20201). They are capable of producing images that depict lung damage, such as that caused by Coronavirus (COVID19) pneumonia (Apostolopoulos , I. D et al, 2020).

CT scans make use of the principles of X-ray in an advanced manner to examine the soft structures of the body. It is also used to get clearer images of organs and soft tissues (Wang, 2020) – (Kroft Ljm et al., 2019). Changes in chest radiography pictures such as X-ray and CT scan were detected even before clinical signs of COVID-19

appeared in several studies (Chan et al., 2020). We need an expert radiotherapist to examine the x-rays because they contain very small details. Even if some cases are a failure due to poor vision (Belhia et al., 2022)

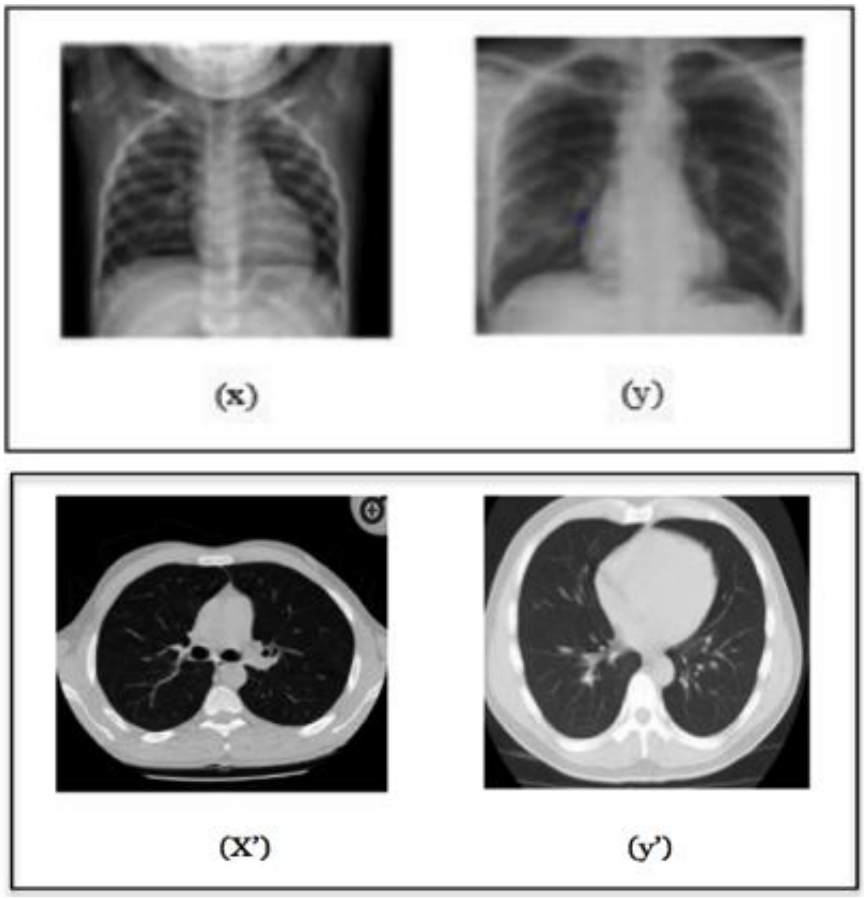

Figure 1**.** (x) Normal chest image and (y) Covid 19 affected chest image (x') Normal CT scan image and (y') COVID-19 affected CT scan image.

From Figure1 it is very difficult to detect COVID-19 infection. But artificial intelligence techniques can classify them by training with labeled data. Thus, we use machine learning (Kishore et al., 2018). In this work, we present an automatic detection system to classify chest X-ray and CT Scan images as from COVID-19 patients or normal patients using perceptron neural network (MLP) compared with Convolutional Neural Network (CNN). The research findings indicate that COVID-19 can be detected more accurately through X-ray images than CT scan images, with a detection rate of over 90%, demonstrating a superior diagnostic performance. With the same methods (CNN and MLP).

This study is structured as follows:. Section II describes the technique's suggested methodology (Multi-layer Perceptron MLP) and Convolutional neural network (CNN), including the dataset, classification processes, and metrics used to evaluate the approach. The results are discussed in Section III. The conclusion and future prospects are presented in Section IV.

Methodology

In most cases, we always require a medical diagnosis based on multiple expert medical opinions. several medical opinions help to reach a more reliable conclusion. Following the same principle, two models MLP and CNN have been adopted in our proposed work.

Model Architecture

Three main modules are distinguished in this architecture (Figure 2). Each one has a distinct role and task that will act and interconnect in the order listed below:

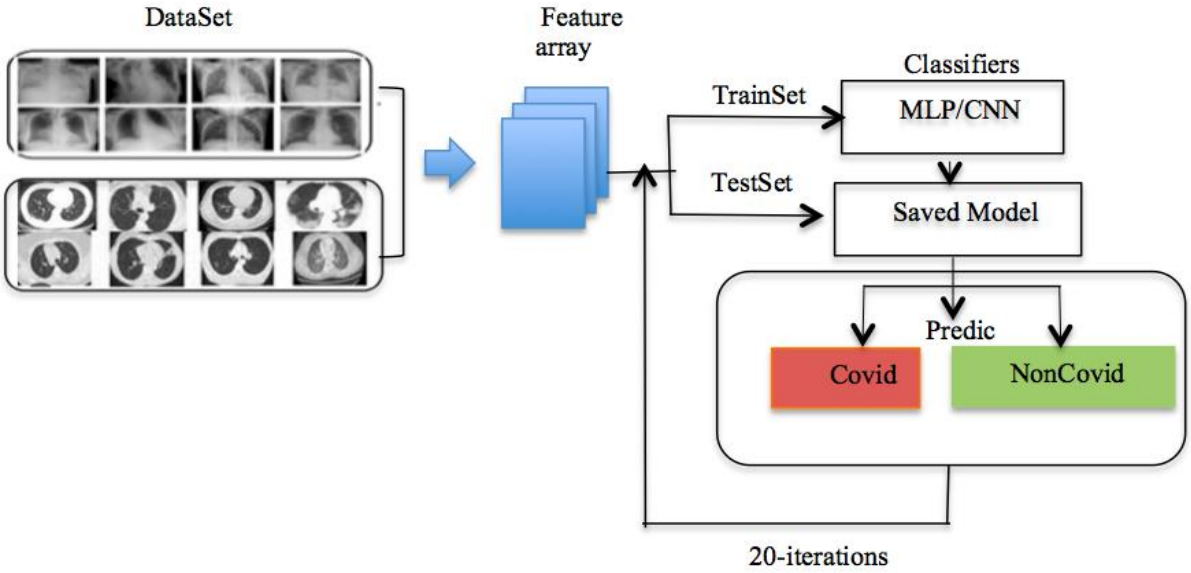

Figure 2. A description of the COVID 19 detecting system

Perceptron Neural Network

A Multi-layer perceptron (MLP) is a feed forward neural network that has been supplemented. The three types of layers depicted in Figure. 3 are input, output, and hidden layers. The first layer receives the information that is going to be processed. Tasks like prediction and classification are under the output layer's purview. The multilayer perceptron has between the input layer and the output layer one or more so-called "hidden" layers. The number of layers correlates to the network's weight matrices. A multilayer perceptron is therefore better suited to deal with nonlinear types of functions. Similar to a feed forward network, data flows forward from the input to the output layer to train the neurons, the back propagation learning technique is utilized. MLPs are meant to approximate any continuous function and can handle issues that aren't linearly separable (Abirami et al., 2020)

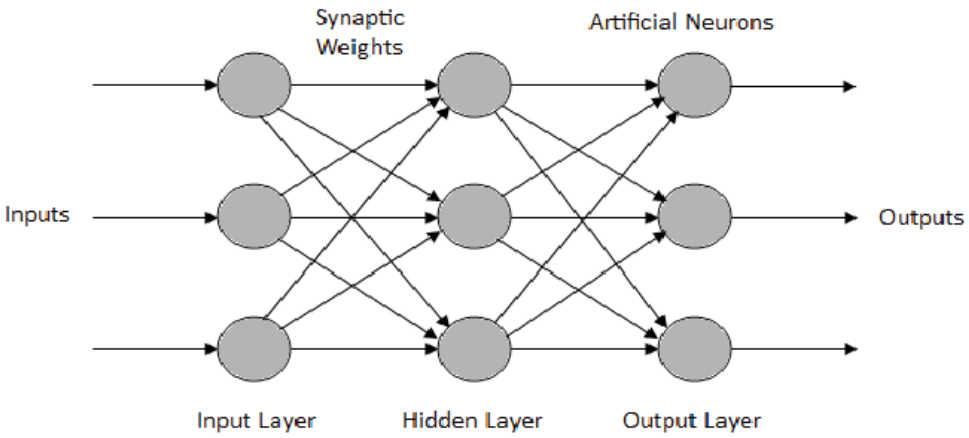

Figure 3. Basic architecture of multilayer neural network.

Each neuron in the output and hidden layers computes the following:

$$A(x) = F(n(2)+E(2)j(x)) \quad (1)$$

$$Z(x) = F(x)=d(n(1)+E(1)x) \quad (2)$$

With the parameters as shown in Table 1 (Abirami et al., 2020).

Table 1. Summarize network parameters.

Parameters	Description
$n(1), n(2)$	Bias vectors
E(1) , E(2)	Weight matrices
F , d	Activation functions
$q = \{E(1), n(1), E(2), n(2)\}$	is the set of parameters to be learned.
$\tanh(a) = \frac{e^{a} - e^{-a}}{e^{a} + e^{-a}}, sigmoid(a) = \frac{1}{1+e^{-a}}$	Are two common choices ford

Our model consists of four Multilayer Perceptron layers in a Dense layer, followed by a Rectified Linear Unit (ReLU) and sigmoid activation function:

- (ReLU): a deep neural network's classification function that is utilized as an activation function for a multi-layer perceptron MLP learning network (Yamashita et al 2018). We accomplish this by taking the activation of the penultimate layer *hn1* in a neural network, then multiply it by weight parameters θ to get the raw scores *oi* (2)

$$T(O) = Max(O, o_i) \text{ Where}$$

$T(O)$ is the ReLU function

- Sigmoid is an activation function that receives a real value as input and returns a probability between 0 and 1..It appears to be in the shape of a 'S'.

$$S(Z) = \frac{1}{1+e^{-Z}}$$

The data is moves from the input layer to the hidden layers. Each layer simply multiplies the inputs by the weights, adds a bias, and applies an activation function to the result before passing the output to the next layer. We keep going till we get to the last layer (Xavieret al., 2020). The activation functions ReLU and Sigmoid were used in our study.

A multi-layer neural network was created for the classification task, with the first layer having 128 neurons (the number of nodes varies depending on the size of the data), two hidden layers with 64 neurons each, and a final layer to divide cases into COVID-19 and no-COVID-19 categories. For this layer, we used a binary classifier (0 and 1): 0 for COVID-19 cases and 1 for normal cases.

Convolutional Neural Network *(*CNN*)*

A CNN or ConvNet convolutional neural network is a type of acyclic (feed-forward) artificial neural network, in which the connection pattern between neurons is inspired by the visual cortex of animals. CNN is a mathematical construction generally composed of three types of layers: (Convolutional layer), the pooling layer (Pooling layer) and the fully connected layer (Fully-connected layer).

The role of the convolutional layer consists in extracting the relevant information from the image (characteristics) thanks to a convolution operation the rectified linear unit layer (ReLU) is an activation function that is used on all elements of the volume to eliminate all negative values and keep positive values. It aims to introduce non-linear complexities to the network. The pooling step is a down sampling technique. Generally, a pooling layer is inserted regularly between the correction and convolution layers. By reducing the size of the feature maps, and therefore the number of network parameters, this speeds up the computation time and reduces the risk of over-fitting.

Fully-connected layer FC Fully-connected layer This layer is at the end of the network. It allows the classification of the image from the characteristics extracted by the succession of processing blocks. It is entirely connected, because all the inputs of the layer are connected to the output neurons of this one (Yamashita et al 2018), (Belhia et al, 2022)**.**

Nonlinear Activation Function

The rectified linear unit (ReLU) is presently which is used as a activation function, which simply computes the function: $g(x) = max(0, x)$ as seen in Figure 4, and then is forwarded through a nonlinear activation function sigmoid in the final layer (output layer).

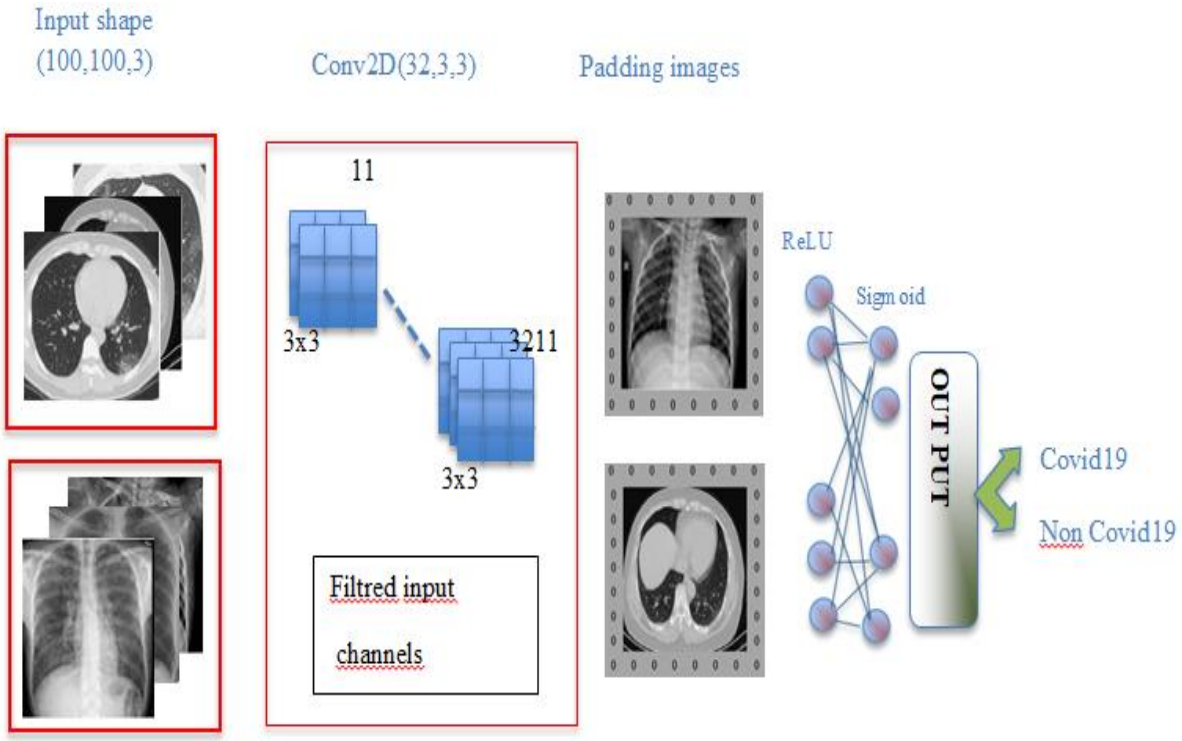

Figure 4. Diagram of the pretrained models for COVID-19 detection.

The planned CNN design will be presented in this part. As previously stated, this network is made up of an input layer, 8 layers of hidden blocks, and then a classification layer. The input images of this network are sized as (100, 100, 3), while the output can be one of two different classes: COVID-19, or normal. The proposed model consists of 8 convolutional layers and 6 pooling layers. Filters of (3x3) size with padding are applied to each convolutional layer, and each pooling layer implements a max-pooling window of (2 x 2) size. The terms "Conv2D," "MaxPool2D," and "FC" refer to the convolution, pooling, and fully connected layers, respectively, in the following. (The filter has dimensions of 3 height and 3 width, Convolution over volume (color image — 3 channels) with a filter of 3 x 3, The models were trained using the Adam optimizer and the cross-entropy loss function. and the table 2 explains the architecture of our suggested CNN.

Table 2. The architecture of our suggested CNN

Layers	Layers type	Output shape
Image-input	Input-layer	[(None, 100, 100, 3)]
Layer-1	Conv2D	(None, 100, 100, 32)
Layer-2	Conv2D	(None, 100, 100, 64)
Layer-3	MaxPool2D	(None, 50, 50, 64)
Droput-0	Dropout	(None, 50, 50, 64)
Layer-4	Conv2D	(None, 50, 50, 64)
Layer-5	MaxPool2D	(None, 25, 25, 64)
droput-1	Dropout	(None, 25, 25, 64)
Layer-6	Conv2D	(None, 25, 25, 128)
Layer-7	MaxPool2D	(None, 12, 12, 128)
droput-2	Dropout	(None, 12, 12, 128)
Flatten	Flatten	(None, 18432)
Layer-8	Dense	(None, 64)
Droput-3	Dropout	(None, 64)
Predictions Dense	Dense	(None, 2)

Dataset Preparation

X-Ray Images COVID-19 and Normal Individuals

For this research, we worked on different data-sets (Joseph ,P C et al , 2020).these open source public data-sets contain X-ray images of COVID-19 positive patients, patients having bacterial pneumonias (MERS, SARS, and ARDS.) Also the data-set used has been taken from two different sources Kaggle and GitHub making our data contains X-ray images of different patients from two data-set.

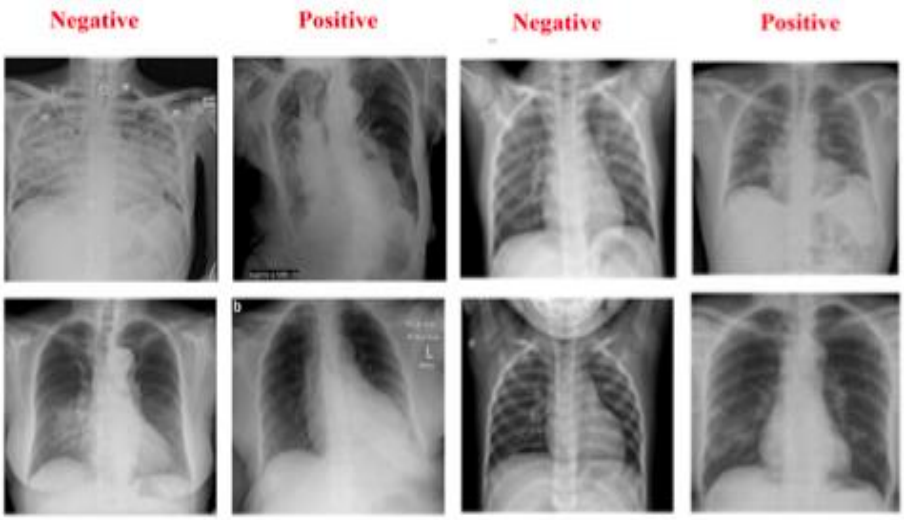

Figure 5. Illustrates some of the dataset's examples. Normal cases are on the first row, whereas COVID-19 cases are on the second. (Xavier et al., 2020).

In this study, we used a dataset which contains 538 of COVID-19 and 180 Normal X-ray images. The COVID-19 X-ray and normal X-ray images are collected from the GitHub repository and Kaggle repository. The dataset was examined in the proposed model. We use this dataset for the proposed machine learning architectures MLPNN and CNN for detection of COVID19 cases.

Chest CT Scan Dataset COVID-19 and Normal İndividuals

This is a large public COVID-19 (SARS-CoV-2) chest CT scan dataset, containing a total of 8439 CT scan, including 7495 positive cases (COVID-19 infection) and 944 negative cases (normal and not COVID-19). The data is available as 512×512 pixel PNG images and was collected from real patients at the radiology centers of University Hospitals in Tehran, Iran. Which 718 of CT Scan images are used in this work including 538 positives case and 180 negatives cases (Mustafa et al., 2021). In order to create a consistent and robust model, the same number of samples with a total of cases must be guaranteed for each class. In this study, we used the chest X-Ray and CT scan images available in the Github and Kaggle (Joseph, P. C ,2020) repositories. The publicly accessible database contains X-ray and CT scan for both classes, , i.e.Non-COVID-19 images and COVID-19 infected images. Figure 6 and 7 show X-ray and CT scan for COVID-19 and non-COVID-19. The sample images involved in this comparative analysis are listed in Table 3.

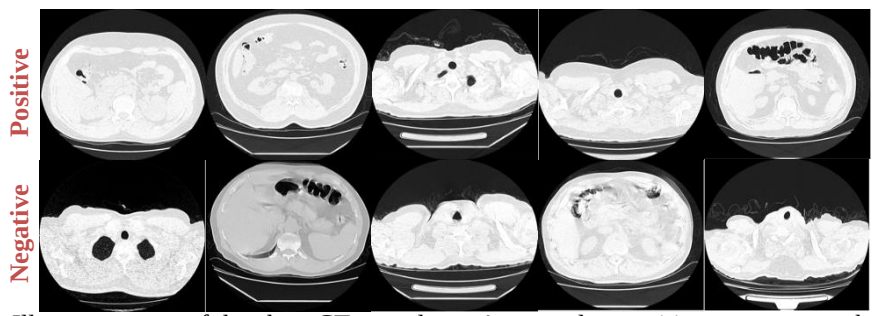

Figure 6. Illustrates some of the chest CT scan dataset's examples. positive cases are on the first row, whereas negative cases are on the second.

Table 3. Dataset and class.

Dataset	Class	Train data	Test data	Type
X-Ray images	COVID-19 /Non-COVID-19	501	217	jpg, png , jpeg
CT images	COVID-19 /Non-COVID-19	501	217	png

Classification Module

Module, which specializes exclusively in image classification. The module's output must be a single probability value between 0 and 1 indicating the presence or nonappearance of Covid19 internationally, — for example as a function of the entire image as a whole. For starters, this module will allow us to globally classify the sample into two classes: images with Covid cases and images without any trace of Covid19, and its output will have a direct influence on the detection module's predictions (Belhia,S,2022).

Evaluate the Results

Model Validation

There are several ways to validate model performance. The confusion matrix is one of the most widely used techniques. The diagonal values of the matrix represent correct predictions for each class, while other cell values represent a number of incorrect predictions. The performance of deep transfer learning models was measured using Performance Metri Criteria. They are as follows:

Performance Metric

For the performance of deep transfer learning models, criteria were utilized. These are the following:

Table 4. Performance metric

Equation	Number
Accuracy = (VB + VA) / (VB + VA + FB + FA)	(1)
Recall = VA / (VA + FB)	(2)
Specificity = VB / (VB + FA)	(3)
Precision = VA / (VA+ FA)	(4)
F1-Score = 2x((Precision x Recall)/(Precision + Recall))	(5)

In Equation (1) and (5), VA, FA, VB, and FB denote the number of True Positives, False Positives, True Negatives, and False Negatives, respectively. Given a test dataset and model, VA is the proportion of positive (Covid-19) that the model correctly labels as Covid-19; FA is the proportion of negative (normal) that the model incorrectly labels as positive (Covid-19); VB is the proportion of negative (normal) that the model correctly labels as normal, and FB is the proportion of positive (COVID-19) that the model incorrectly labels as negative (normal) (Narin et al., 2021).

Result

The experimental setup and detail as well as the experimental results are presented in this section. In the "Experimental details" subsection, we explain the MLP and CNN implementation specifics, including the data used, the architectures, and the training and testing procedures. In the "Experimental results" subsection, we report on the performance of the suggested method (MLP) and compare it to a CNN.

Experiment Setup

Python 3.8.8 programming language has been used to develop The MLP and CNN architecture and it is executed on intel®core™ i5-6200GHz processor with 8.00 GB of RAM. All experiments were performed on a jupyter notebook.

Experiments Details Using (MLP and CNN) for X-Ray Images

For MLP model we used the Adam optimizer to optimize model weights and minimize the categorical cross-entropy loss function, after training the model for 20 epochs. We also employed the Early Stopping technique to avoid overfitting by stopping training after the validation score stopped improving (Early Stopping callbacks (patience = 10 epochs)). Our network is good, as our training history graphic demonstrates, based on our training data:

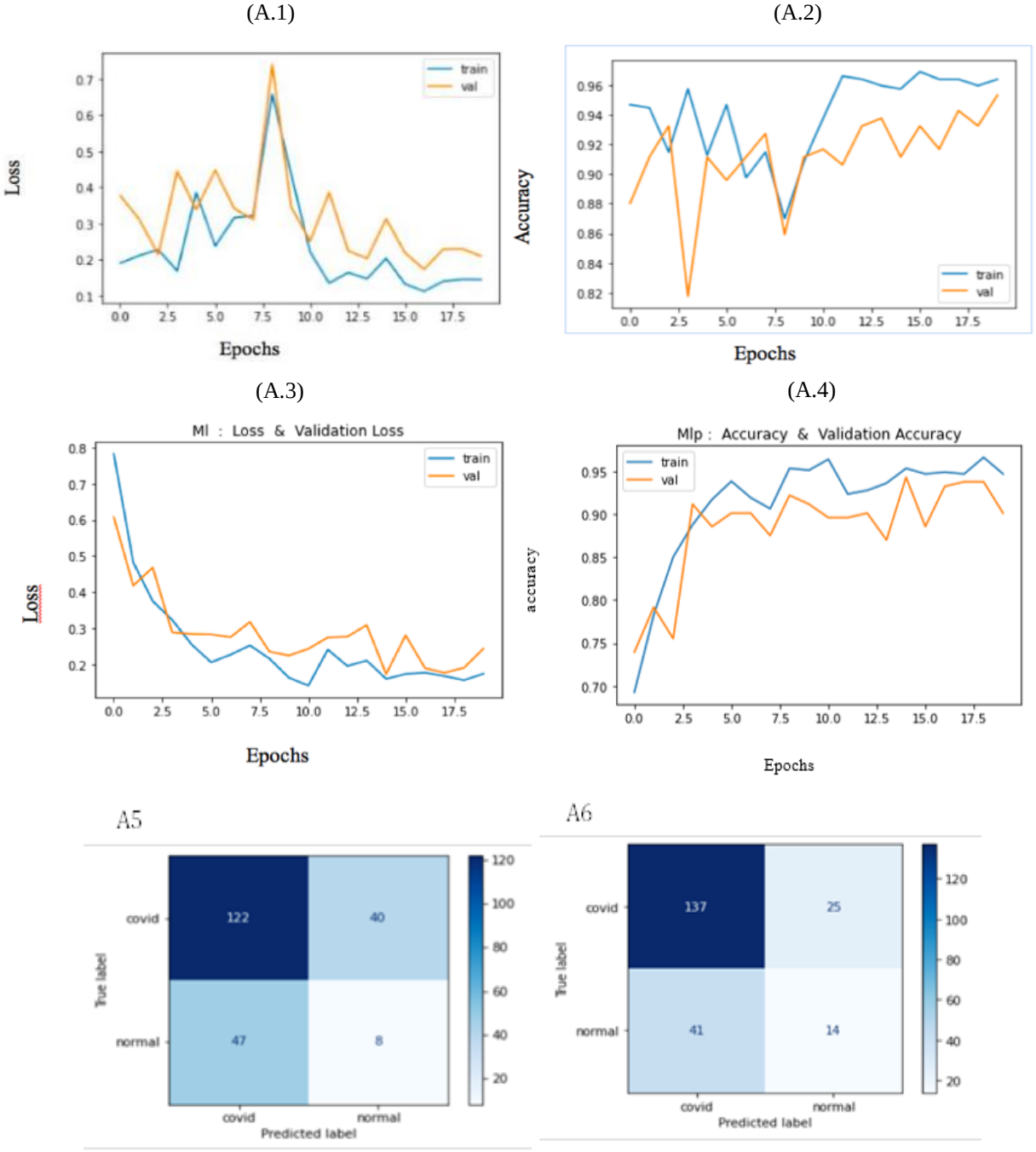

Figure 7. Experiments details using (MLP and CNN) for X-ray images

Figure A.1. depicts the examination of training and testing results with the loss. This Machine learning training history plot with accuracy curves shows that our model performs excellently on our Covid-19 X-ray training data, which was used in our Keras/TensorFlow model. Figure A.2. describes the training and testing result analysis with the Accuracy, which illustrates the model accuracy for our model as it improves with subsequent epochs. Figure A.3. and A.4. discuses the result analysis of training and testing with the Accuracy and loss for CNN Model (see Figure 7). Figure A.5 is Confusion matrix for the Ensembling (MLP) and Figure A.6.is Confusion matrix for the Ensembling (CNN).

In Figure A.5 The confusion matrix demonstrates that our proposed model successfully classified 122 of the Covid19 patients based on the X-ray pictures. Only 40 of the Covid19 patients were incorrectly classed as normal. Similarly, 8 cases were accurately identified based on X-ray pictures. Only 47 patients were misidentified as Covid19. In Figure A.6 We can examine the confusion matrix with model CNN, which shows that the model pre-trained model classified 137 of the Covid-19 as True Positive, while only 25 were incorrectly classified as normal. and 14 patients were accurately classified as Covid19, whereas 41 were incorrectly labeled as Covid19.

Experimental Results of X-Ray Images Data

From Figure (A.1) , we discuss the analysis of the results of training and testing with accuracy which shows the model accuracy for our model (MLP) as it improves with successive epochs and when comparing with the analysis of the CNN results in Figure (A.3) and (A.4), we deduce the MLP register of the model good results than CNN. In the second phase of our experiments, we compared the MLP to a standard CNN trained on the same data. The CNN architecture is presented in Table 5.

Table 5. Description a comparison of different models' performance in detecting Covid-19 from dataset X-ray images**.**

Method	Data	Loss	Accuracy	Validation loss	Validation Accuracy
MLP	X-ray img	0,144	0,957	0,209	0,957
CNN	X-ray img	0,174	0,90	0,244	0,901

Experiments Details Using (MLP and CNN) Model for CT Scan Images

Experimental Results of CT Scan Images Data

Our model is perfect on the Covid-19 Chest CT Scan training data utilized in our Keras/TensorFlow model, as shown in Figure (B.1) Machine Learning Training MLP History Plot Showing Accuracy Curves. The result analysis of MLP training and testing with the loss is covered in Figure (B.2). Our network is robust, as shown by the training Covid-19 CT Scan data plot in our training history. Figures (B3) and (B4) display CNN result analysis of training and testing, and we reach the conclusion that the CNN record of the model performed MLP in terms of results.

Table 6**.** Description a comparison of different models' performance in detecting Covid-19 from dataset CT scan images

Method	Data	Loss	Accuracy	Validation loss	Validation Accuracy
MLP	CT images	0,465	0,806	0,579	0,796
CNN	CT images	0,307	0,883	0,320	0,921

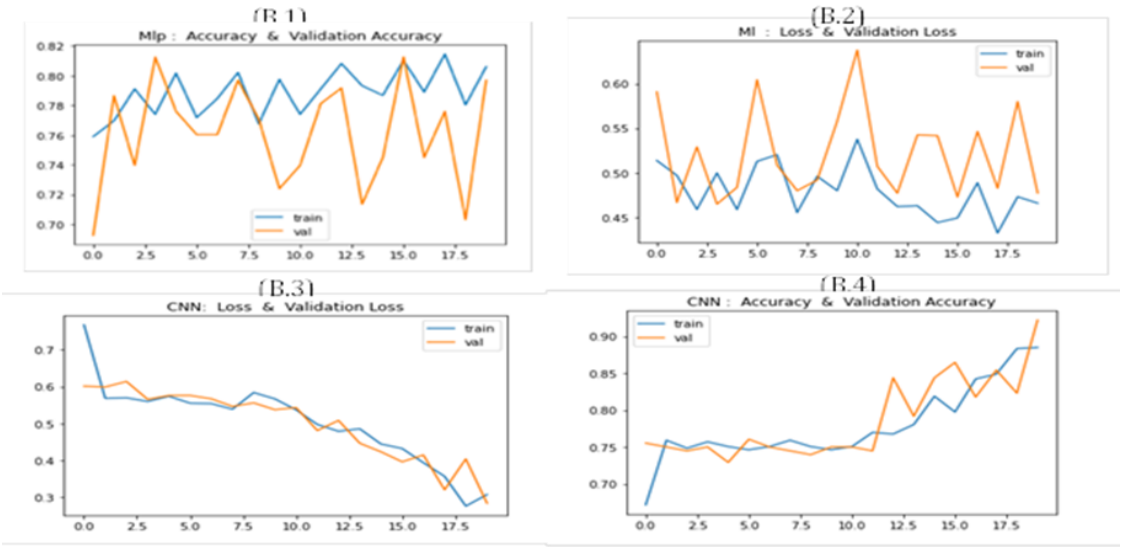

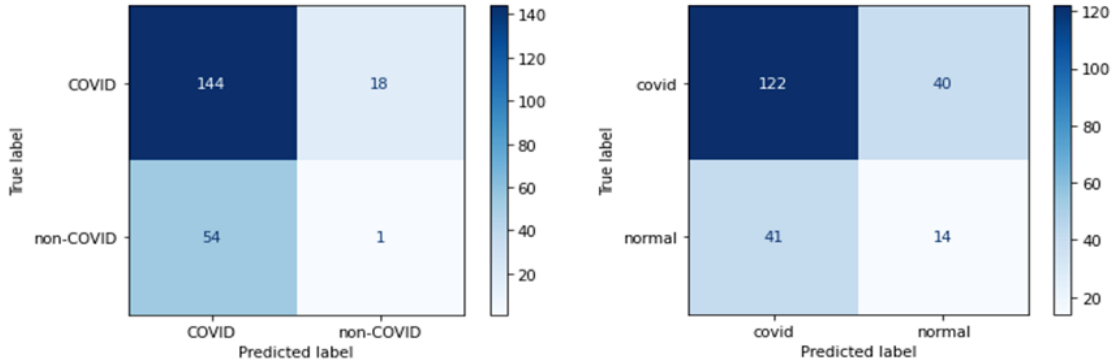

Figure 8. Experimental results of CT scan ımages data

Figure B.1. Machine learning training MLP history plot. Figure B.2. The result analysis of MLP training and testing with the loss. Figure B.3. Discusses the CNN result analysis of training and testing with the loss. Figure B.4 Show Accuracy Validation Accuracy with CNN model. Figure B.5. Confusion matrix for the Ensembling (MLP). Figure B.6. Confusion matrix for the Ensembling (CNN).

Figure B.5 of confusion matrix shows that 144 of the Covid19 patients were correctly identified using our suggested model and the CT images. 18 of the Covid19 patients were the only ones who were misclassified as normal. Similar to this, just 1 case could be correctly identified using CT images. Covid19 was mistakenly assigned to 54 patients.

Examining the confusion matrix with model CNN in Figure B.6 reveals that 122 of the COVID-19 were wrongly identified as True Positives, while 40 were accurately classified as normal. and however 41 patients were misclassified with Covid19, 14 patients had the correct classification.

Discussion

In this work we have studied the superior features and limitations of the suggested model compared to state-of-the-art models. It is, however, crucial to emphasize that due to differences in the datasets as well as the database size, simulation techniques and parameters, an individual comparison is not feasible. Despite the fact that both strategies MLP and CNN produced good outcomes with little difference, using X-ray and CT Scan images . As shown in the Table 5 and Table 6 , the MLP achieves an accuracy of 95,7% for X-ray images and 80.60% for CT scan images, while the CNN achieves an accuracy of 90% for X-ray images and 88.49% for CT scan images.

We noted that our proposed model MLP was perfect on X-ray images data However the CNN model performs better than the MLP on CT Scan images. It should be noted that the suggested model will be tested using the COVID-19 X-ray and CT Scan database. Given the amount of positive COVID-19 cases worldwide, one may claim that the database is insufficient. These results will definitely improve with the increased dataset. it is clear that the proposed model learned the COVID-19 infections very well leading to fewer false detections. Moreover, existing models are more complex than the proposed model.

Conclusion

This study examined the usefulness of pre-trained MLP in predicting Covid-19 from X-rays and CT scans. Another CNN model was used to evaluate the performance of the MLP model. For COVID-19 testing, these approaches can save RT-PCR test kits and costs and represent a rapid tool for RT-PCR testing. Our study uses personalized CNN and MLP approaches to support rapid diagnosis of people infected with COVID-19. Both models are evaluated in two classes, COVID-19 images and normal images. As a result, the COVID19 identification accuracy rate is 95.7% for X-ray images using MLP and 90% using CNN model, the Covid19 detection performance rate is 80.60% for CT Scan images with MLP and 88.49% with CNN.

Experimental results indicate that MLPs and CNNs can achieve high accuracy in detecting COVID-19 from X-ray images and CT images, demonstrating the potential of using machine learning techniques in the medical

diagnosis. We also used chest X-ray images and CT images to train, test and compare the studied models and found that these models performed well for both types of images, there was no big difference in the performance rate. In the future, we will pay special attention to the classification of patients with other lung diseases.

Scientific Ethics Declaration

The authors declare that the scientific ethical and legal responsibility of this article published in EPSTEM journal belongs to the authors.

Acknowledgements or Notes

* This article was presented as a poster presentation at the International Conference on Technology, Engineering and Science (www.icontes.net) held in Antalya/Turkey on November 16-19, 2023.

References

Abirami, S., & Chitra, P (2020). *The digital twin paradigm for smarter systems and environments: The industry use cases* (Volume 117, 1 st ed.). Advances in Computers.

Apostolopoulos, I. D., & Bessiana, T. (2020). Covid-19: Automatic detection from x-ray images utilizing transfer learning with convolutional neural networks. *Physical and Engineering Sciences in Medicine*, *43*, 635-640.

Bedad, F., Adjoudj, R., & Bousahba, N. (2022). Study of the robustness of a transformation-based multi-biometric template schemes protection, *International Journal of Computing Digital Systems, 11*(1), 335-344.

Belhia, S., & Gafour.A. (2012). Feature level fusion in multimodal biometric identification. *Second International Conference on the Innovative Computing Technology (INTECH 2012)*.Morroco.

Belhia, S., Al Jahmani.S., & Adjoudj, R. (2022). Automatic detection of Covid-19 based in artificial intelligence tools. *Turkish Journal of Computer and Mathematics Education*, *13*(3), 668-680.

Boudrioua, Ms., & Boudrioua, A. (2020, May 4). Predicting the COVID-19 epidemic in Algeria using the SIR model. *medRxiv.* Retrieved from https://www.medrxiv.org/

Chan, J. F. W., Yuan, S., Kok, K. H., &…Yuen, K. W. (2020). A familial cluster of pneumonia associated with the 2019 novel coronavirus indicating person-toperson transmission : a study of a family cluster. *Lancet, 395*(10223), 514–523.

Chaudhary, M. (2020, August 28). Activation functions: Sigmoid, tanh, relu, leaky relu, softmax. Retrieved from https://medium.com/@cmukesh8688/activation-functions-sigmoid-tanh-relu-leaky-relu-softmax-50d3778dcea5

Cohen, J. P., Moorrison, P., Dao, L., Roth, K., Duong, T. Q., & Ghassemi, M. (2020). Covid-19 image data collection: Prospective predictions are the future. *Melba Journal*, *1*(2020).

Damilakis, J., Adams, J. E., Guglielmi, G., & Link, T. M. (2010). Radiation exposure in X-ray-based imaging techniques used in osteoporosis. *European Radiology*, *20*(11), 2707–2714.

Ghaderzadeh, M., Asadi, F., Jafari, M., Bashash, D., Abolghasemi, H., & Aria, M. (2021).Deep convolutional neural network–based computer-aided detection system for Covid-19 using multiple lung scans: design and implementation study. *Journal of Medical Internet Research, 23*(4).

Hemdan, E. E. D., Shouman, M. A., & Karar, M. E. (2020). Covidx-net: A framework of deep learning classifiers to diagnose Covid-19 in xray images. *ArXiv.*

Imran, M., Sattar, M. U., Khan, H. W., Ghaffar, A., & Mushtaq, H. (2022). Selecting a better classifier using machine learning for Covid-19. *International Journal of Computing and Digital Systems, 11*(1), 955-962.

Kishore, P.V.V., Vijay Kumar, K. V. K., Eepuri, K. K., Sastry, A. S.C. S., Kumar, D. A., & Prasad, M. V. D. (2018). Indian classical dance action identification and classification with convolutional neural networks. *Advancess in Multimedia, 28*(1), Article ID 5141402, https://doi.org/10.1155/2018/5141402

Kroft, L. J. M., van der Velden, L., Giron, I. H., Roelofs, J. J. H., de Roos, A., & Geleijns, J. (2019). Added value of ultra–low-dose computed tomography, dose equivalent to chest X-ray radiography, for diagnosing chest pathology. *Journal of Thoracic Imaging, 34*(3), 179–186.

Mahesh, P., Prathyusha, Y. G., Sahithi, B., & Nagendram, S. (2021). Covid-19 detection from chest x-ray using convolution neural networks. *Journal of Physics Conference Series, 1804.*

Mahmud, T., Rahman , M. A., & Fattah, S. A. (2020). CovXNet: A multi-dilation convolutional neural network for automatic Covid-19 and other pneumonia detection from chest X-ray images with transferable multi-receptive feature optimization. *Computers in Biology and Medicine*, *122*, 103869.

Narin, A., Kaya, C., & Pamuk, Z. (2021). Automatic detection of coronavirus disease (covid-19) using x-ray images and deep convolutional neural networks. *Pattern Analysis and Applications. 24*(3), 1207-1220.

Ohata, E. F., Bezerra, G. M., das Chagas, V. S., Neto, A. V. L., Albuquerque, A. B., & de Albuquerque, V. H. C. (2021). Automatic detection of Covid-19 infection using chest x-ray images through transfer learning. *IEEE/CAA Journal of Automatica Sinica, 8*(1), 239-248.

Pereira, R. M., Bertolini, D., Teixeira, L. O., Silla, C., & Costa, Y. M. G. (2020). Covid-19 identification in chest X-ray images on flat and hierarchical classification scenarios. *Computer Methods and Programs in Biomedicine, 194*(17), 105532.

Scudellari, M. (2020, March 31). Hospitals deploy ai tools to detect Covid- 19 on chest scans. IEEE Spectrum. Retrieved from https://spectrum.ieee.org/

Subasi, A., Quershi, S. A., Brahimi, T., & Serireti, A. (2021). Chapter 14 – "covid-19 detection from X-ray images using artificial intelligence. *Artificial intelligence and big data analytics for smart healthcare* (pp. 209-224).

Togacar, M., Ergen, B., & Comert, Z. 2020). Covid-19 detection using deep learning models to exploit Social Mimic Optimization and structured chest X-ray images using fuzzy color and stacking approaches. *Computers in Biology and Medicine Journal, 121*, 103805.

Wang, L., D., & Wong, A. (2020). Covid-net: A tailored deep convolutional neural network design for detection of COVID-19 cases from chest Xray images. *Scientific Images, 10*, 19549.

Wang, N., Liu, H., & Xu, C. (2020). Deep learning for the detection of Covid-19 using transfer learning and model integration. *10th International Conference on Electronics Information and Emergency Communication (ICEIEC)*. IEEE.

Yamashita, R., Nishio, M., Do, R. K. G., & Togashi, K. (2018). Convolutional neural networks: an overview and application in radiology, *Insights into Imaging, 9*, 611—629.

Author Information

Belhia Souaad
Computer Science Department,
University of Sidi Bel Abbes, 22000.
Algeria,
Contact e-mail: *souad.belhia@univ-sba.dz*

Aljahmani Souha
Computer Science Department,
University of Sidi Bel Abbes, 22000.
Algeria,

Bahram Tyeb
Computer Science Department,
Moulay Tahar University, Saida, 20000.
Algeria,

Adjoudj Reda
Computer Science Department,
University of Sidi Bel Abbes, 22000.
Algeria,

To cite this article:

Belhia, S., Aljahmani, S., Bahram., & Adjoudj, R. (2023). Novel comparative study of Covid-19 detection from x-ray and ct scan ımages usıng cnn and mlp neural networks. *The Eurasia Proceedings of Science, Technology, Engineering & Mathematics (EPSTEM), 26,* 26-37.

The Eurasia Proceedings of Science, Technology, Engineering & Mathematics (EPSTEM)
ISSN: 2602-3199

The Eurasia Proceedings of Science, Technology, Engineering & Mathematics (EPSTEM), 2023

Volume 26, Pages 38-48

IConTES 2023: International Conference on Technology, Engineering and Science

Aircraft Firefighting Capabilities Using Suspended Containers

Milen Atanasov
Georgi Benkovski Bulgarian Air Force Academy

Abstract: In the world, the fight against forest and industrial fires is carried out by both ground based equipment and aircraft – airplanes and helicopters. Each of these has its specific advantages and disadvantages. The use of aviation containers for extinguishing fires is an alternative to existing methods at the moment. They are particularly effective in the initial outbreaks of fires in hard-to-reach areas and fires caused by toxic substance, as well as in limiting the growth of their spread. The advantage is that they can be targeted at a specific place and, depending on the type of fire, can be filled with the corresponding fire-fighting substance. These containers can be hung on airplanes and helicopters depending on their load capacity. They are used in the following way, after their targeted drop from the aircraft at a specific effective height, the container is destroyed and a fire-fighting substance is poured onto the burning surface. The moment of release of the aviation fire-fighting container is determined depending on the flight conditions and the targeting system of the aircraft used. For this purpose, mathematical modelling of the process of using the aviation container was carried out, mathematical models for the movement of the aircraft and the aviation fire-fighting container were compiled, and a mathematical model of the targeting system was created.

Keywords: Aircraft, Fires, Aviation containers

Introduction

At present, aerial firefighting is done by fixed-wing aircraft and helicopters. The substances used for extinguishing fires are liquid (water, foam), solid (powdery, bulk) and gaseous (fire extinguishing aerosols, carbon dioxide, etc.). Helicopters and fixed-wing aircraft are used to fight fires from the air. Nearly 1,000 aircraft have been contracted for each fire season in the US in recent years, with an annualized cost of over US$250 million in recent years. Helicopters used to fight fires can be type tankers or carry buckets. Buckets are always filled by dipping into dams, lakes, rivers or artificial reservoirs. The most popular bucket is the flexible Bambi Bucket.

Some of the most popular firefighting helicopters are the Bell 204, Bell 205, Bell 212, Boeing Vertol 107, Boeing Vertol 234, Sikorsky S-70, "Firehawk" and Sikorsky with flexible charging hose. Today, the largest firefighting helicopter in the world is the Mi-26, using the Bambi bucket. Tanker-type firefighting aircraft are divided into the following groups: single-engine air tankers (SEAT) with a capacity of up to 3,000 liters (Air Tractor AT-802; air tankers with a capacity of 7,500 liters to 15,000 (P2V, HC-130H, BAe- 146, MD-87, C-130Q, RJ85, C-130 H & J); air tankers with a capacity of more than 15,000 liters (DC-XNUMX). The use of an aviation container with a capacity of 500 liters (Figure 1) for extinguishing fires is proposed. (Velikov, 2022).

At a height of 100 m, the aviation container is disconnected and the fire extinguishing agent is dispersed. 8 containers with a total volume of 4000 l can be loaded onto a Su 25 type aircraft. Until now, the "Bambi Bucket" type bucket has a capacity of 3000 l, and 6 containers with a total volume of 3000 l can be loaded onto a Mi-17 helicopter. Aviation containers for extinguishing fires are launched from aircraft having targeting systems with an electronic computing machine.

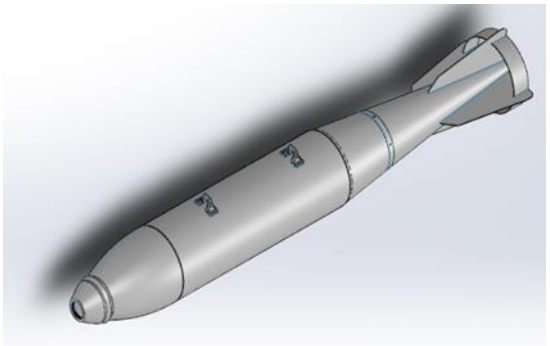

Figure 1. Aviation container type (Velikov, 2022)

Method

With the help of mathematical modelling, the areas of conditions under which aviation containers are launched for fire extinguishing have been determined and the accuracy of reaching the point where the fire-fighting mixture is ejected from the container has been calculated. For this purpose, mathematical models and algorithms have been created: for the movement of the aviation container, for the movement of the aircraft, of the targeting system, of the aiming process, for calculating the accuracy of hitting when using built-in targeting systems and when using suspended targeting containers equipped with a tracking system.

Modelling the Aiming Process of Dropping an Aviation Container for Fire Extinguishing

In many cases, mathematical modelling of complex systems is the only means of studying their effectiveness. This is because it is not possible to analyse and evaluate such systems with laboratory, natural experiments or analytical methods. Modelling makes it possible to study and simulate the functioning of systems in arbitrary conditions. In doing so, numerous variations can be made between system parameters and external conditions to obtain an arbitrary situation. The block principle of mathematical modelling is used to study the aiming process for launching an aviation firefighting container, because it is necessary to model the joint operation of the sight and the aircraft. The studied target system is a dynamic system that is non-linear and non-stationary. In order to make a quantitative assessment of this system, it is necessary to carry out mathematical modelling of the aiming process.

Mode Continuously Computed Impact Point

To solve the task of aiming for the release of an aviation container, it is necessary to bring the aircraft to one of the possible points in which, when the container is released, it falls at the point where the fire-fighting mixture is ejected from it. In modern aviation aiming systems, depending on the flight conditions, the location of the target relative to the aircraft, the type of manoeuvre used for launching, the system for indicating the aiming parameters and the design features of the aircraft, the following mode are used: Continuously Computed Impact Point - CCIP and the Continuously Computed mode Release Point - CCRP (Atanasov, 2014).

When using the CCIP mode, the pilot piloting the aircraft must align the aiming marker with the target and release the container. According to the current flight parameters of the aircraft, the ballistic task is solved, in which the coordinates of the fall of the container are calculated - X_h, Z_h in the HUD coordinate system - $Ox_hy_hz_h$ (Stoĭkov & Atanasov, 2009). The necessary target sighting angles Bh and Eh in the considered coordinate system are determined using the following expressions (Figure 2):

$$B_h = \operatorname{arctg}\frac{Z_h}{X_h};$$
$$E_h = \operatorname{arctg}\left(\frac{H}{X_h}\cos B_h\right). \quad (1)$$

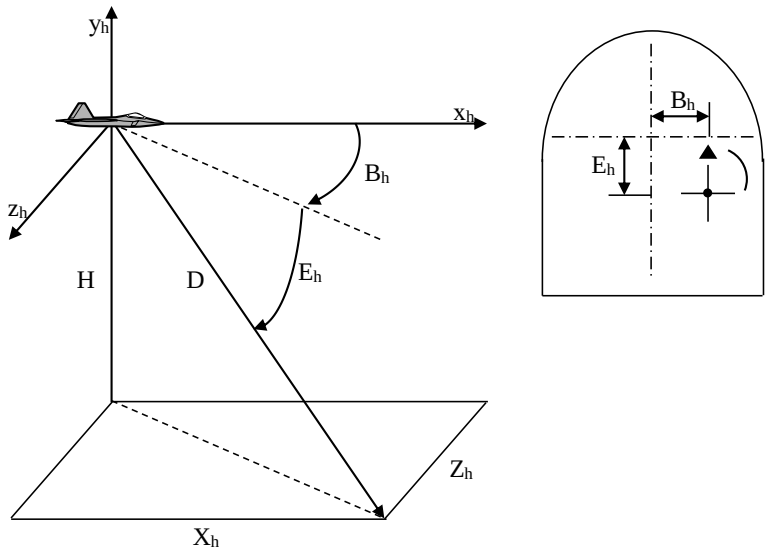

Figure 2. Aiming scheme in CCIP mode

Mode Continuously Computed Release Point

When aligning the reticle with the target, its initial coordinates are calculated. The current coordinates of the target are calculated after integrating the ground speed. Aiming parameters are calculated by the on-board computer. Azimuth aiming is done by automatic or director control of the aircraft, and range aiming is done automatically. When p=x–X=0, the on-board computer sends a signal to automatically launch the aviation container. The accuracy of solving the targeting task depends on the accurate solution of the ballistic task and the accurate calculation of the coordinates of the target relative to the aircraft. The error in determining the current coordinates of the target increases as the path increases, i.e. as the integration time increases.

Mathematical Model of the Targeting Process with the CCIP and CCRP Modes

The block diagram of the aiming process when launching an aviation container using the CCIP and CCRP modes is shown in Figure 3 (Atanasov, 2014). In Figure 3 the following models are shown:

- Aircraft model;
- Ballistic model;
- Mathematical model of a targeting system using the CCIP and CCRP modes.

The structural diagram of the targeting system consists of the blocks for:

- Determination the coordinates of the target x, z;
- Calculation of the X, Z coordinates of the hit of the container;
- Determination of aiming angles E_h and B_h;
- Convertion the target's current coordinates;
- Head-up display (HUD);
- Formation of aiming parameters.

Depending on the input parameters, in the block which determines the current coordinates of the target, the coordinates x, z are determined. In the block for determining the coordinates X and Z, they are functionally connected to: the distance A_0 to the fall point, the time of the fall of the container and the wind speed $\tilde{U}$. The block for determining the corners E_h and B_h, converts the X and Z coordinates into angular (E_h and B_h) into a coordinate system of HUD - $Ox_hy_hz_h$. The block for converting the coordinates of the target transforms the coordinates X and Z into angular (βh and εh) into the coordinate system of $Ox_hy_hz_h$. The target parameter indicator shows the angles E_h and B_h. The parameter forming block determines the aiming parameters p and q, depending on the mode used - CCIP and CCRP.

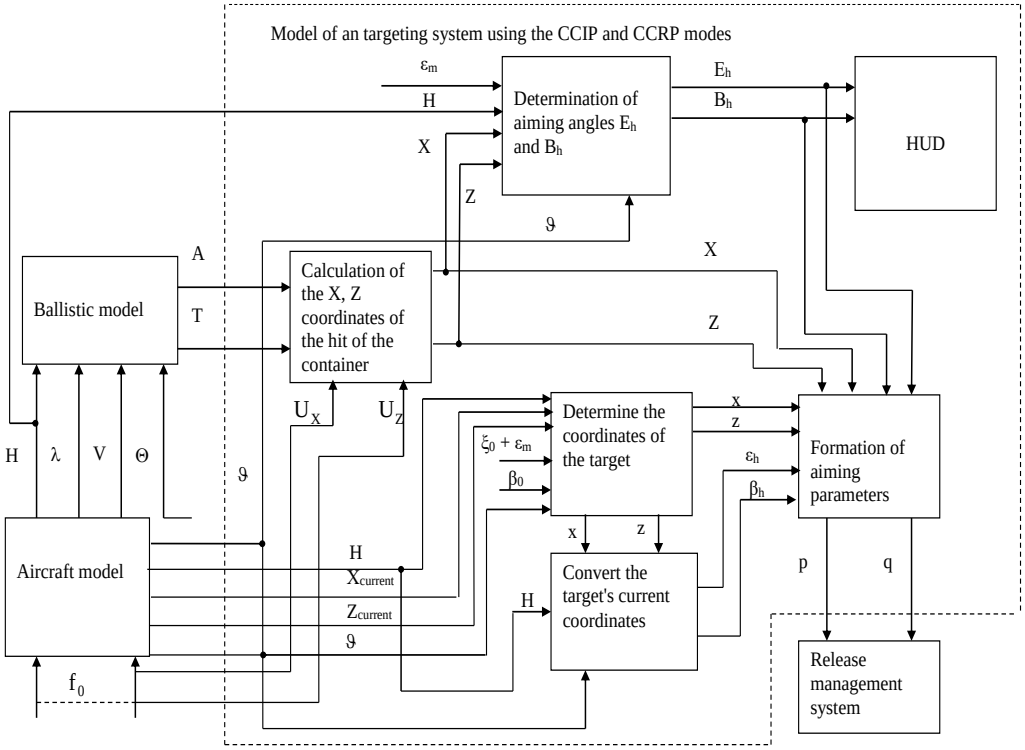

Figure 3. Flowchart of the targeting process when dropping an aviation container using the CCIP and CCRP modes

As a result of solving the targeting task using the CCIP and CCRP modes, the conditions of dropping an aviation container for firefighting are determined $f(t_d)=[V(t_d), H(t_d), E_h(t_d), B_h(t_d), X(t_d), Z(t_d)]$. The algorithm is shown in figure 4 (Atanasov M., 2014).

Mathematical Model for Determining the Accuracy of Dropping an Aviation Container under the CCIP and CCRP Modes

The measured quantity $y'(t)$ is represented as a sum of the true value of the measured quantity y(t) and the error in its measurement ξ_y. The probabilistic characteristics of the error ξ_y of the measured quantity are the mathematical expectation of the error $M[\xi_y]$ and the root mean square deviation $\sigma_{\xi y}$ the error of the measured quantity ξ_y has a random component $\Delta\xi_y$ and a constant component ξ_{yc}:

(2) $$\xi_y = \Delta\xi_y + \xi_{yc}.$$

For the determination of bomb-drop accuracy, it is assumed that the errors of the measured quantities have a normal distribution law. For the measured quantity $y_j(t)$, a random number ξ_{yj} is generated which has a normal distribution law with numerical characteristics $\sigma_{\xi yj}$ and $M[\xi_{yj}]$.

For time t, the measured value $y'_j(t)$ is determined by the equation:

(3) $$y'_j(t) = y_j(t) + \xi_{yj}$$

The current parameters of the flight are determined by the set initial conditions: V, W_x, W_y, W_z, H, ψ, θ, γ, λ, β_{sl}, α. Using a random number generator, normally distributed errors with zero expectation and mean square deviation are generated for each of the measured quantities. By form. (3) the values of each of the measured quantities are determined: V', W'_x, W'_y, W'_z, H', ψ', θ', γ', λ', β'_{sl}.

When using the CCIP mode, the drop parameter is determined by the formula:

(4) $$p'(t)=\varepsilon(t) - E'(t).$$

When the condition $p'(t) \leq 0$ is met, the bomb drop error is determined ΔX:

(5) $$\Delta X=X' - x$$

After N number of realizations, $\sigma_{\Delta x}$ is determined. Provided that the CCRP mode is used, the drop parameter is determined by the formula:

(6) $$p'(t)= x'(t) - X'(t),$$

When the condition $p'(t) \leq 0$ is met, the drop error ΔX is determined.

The algorithm for determining $\sigma_{\Delta x}$ of the hit error when using the CCIP and CCRP modes under specified launch conditions V, H, λ. is shown in Figure 5 (Atanasov, 2014).

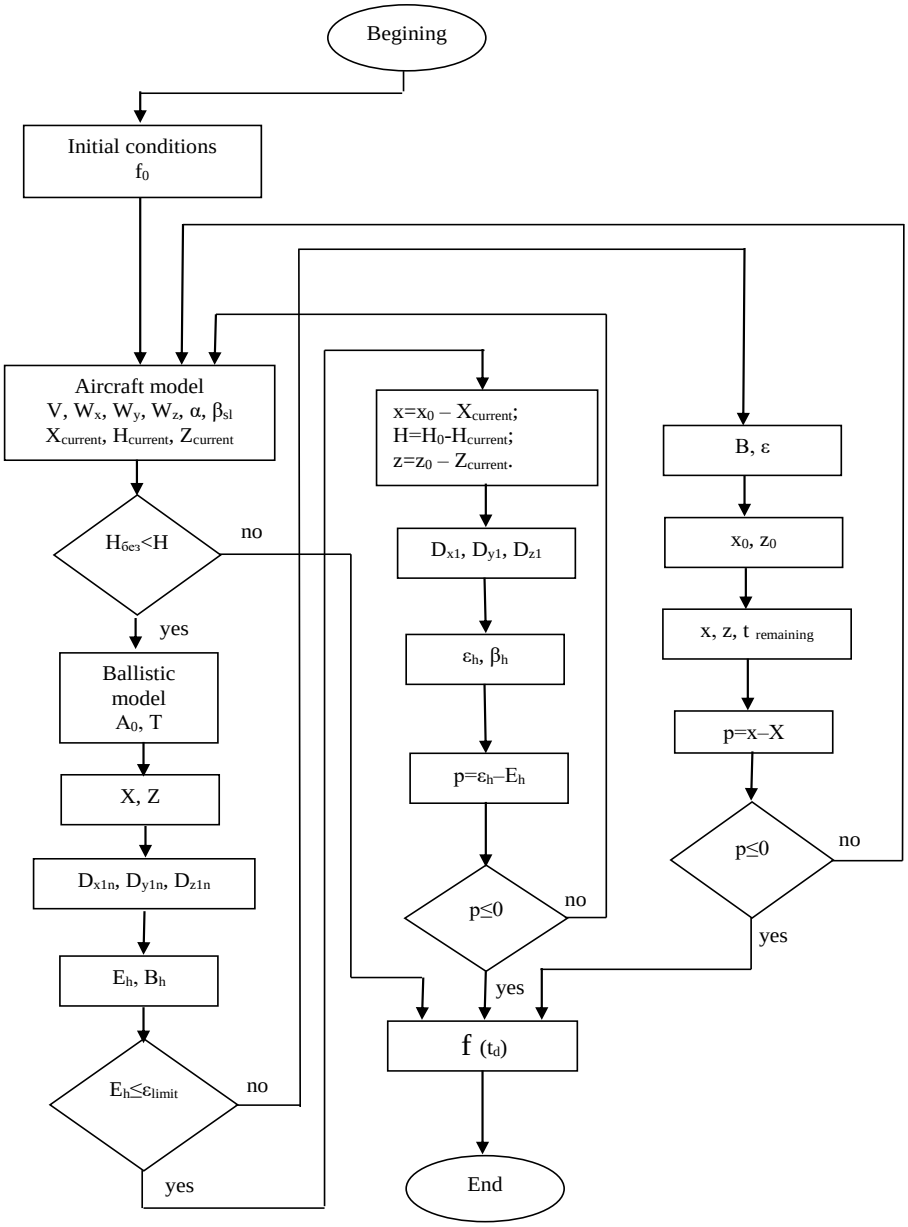

Figure 4. Algorithm of the targeting process when dropping an aviation container using the CCIP and CCRP modes

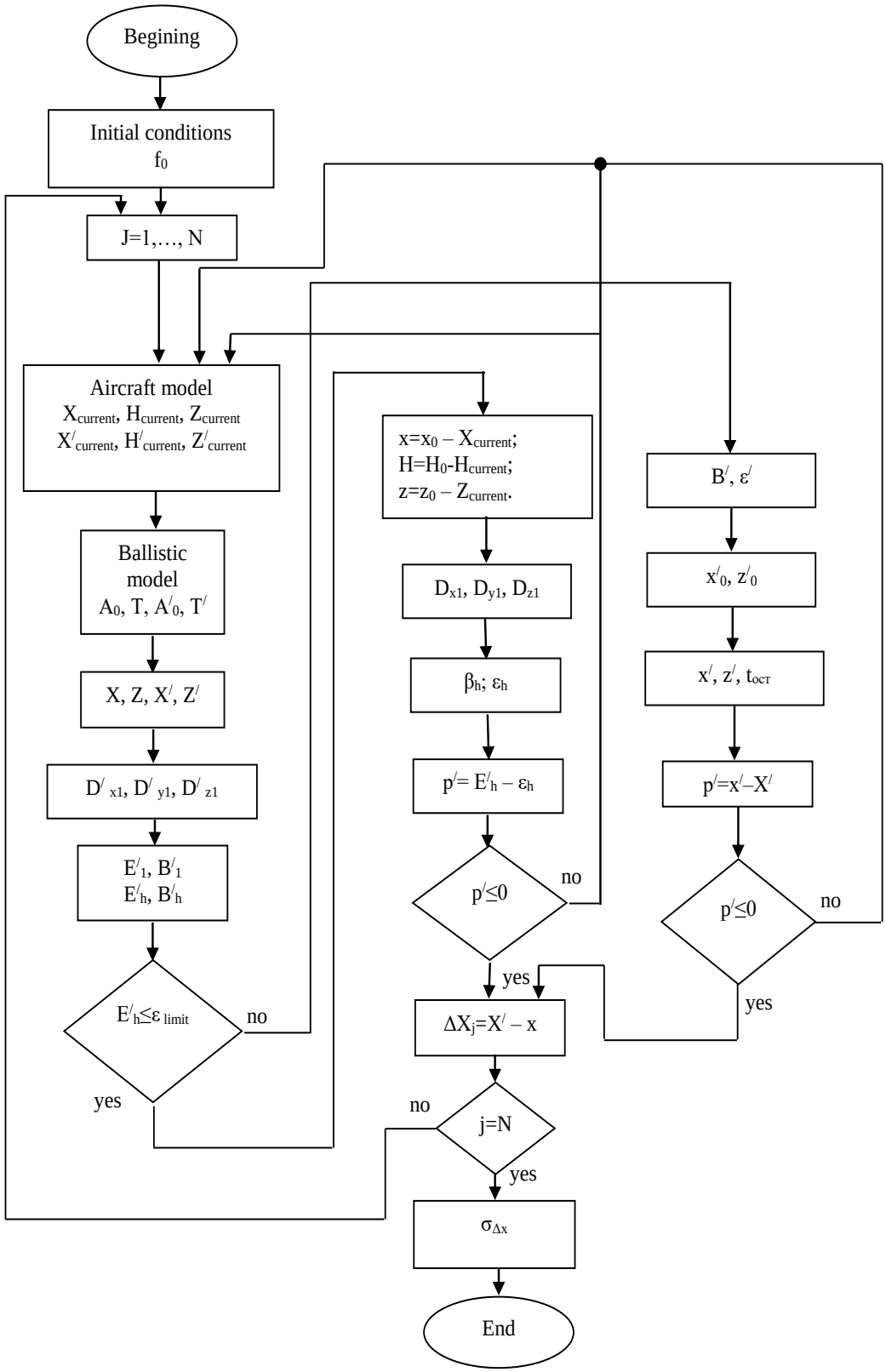

Figure 5. Algorithm for determining $\sigma_{\Delta x}$ using CCIP and CCRP modes

Modern generation 4+, 4++ and 5 aircraft can be fitted with a targeting pod designed to use high-precision weapons against ground targets. Apart from military purposes, these targeting containers can also be used for civilian purposes to accurately deliver various cargoes from the air (Atanasov, 2020; 2022). In Figure 6 an algorithm of the targeting process with a targeting pod is presented (Atanasov, 2014)

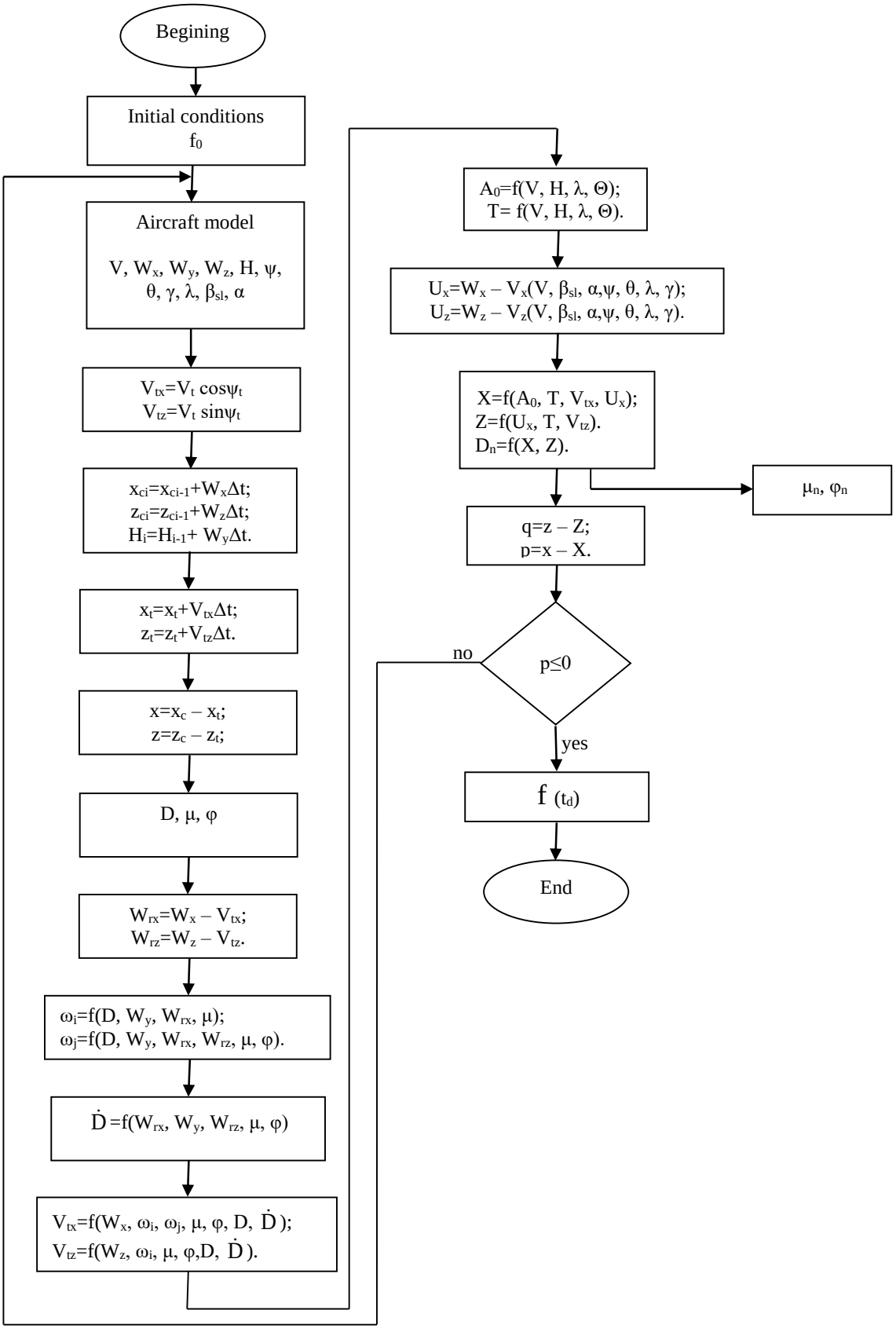

Figure 6. Algorithm of operation of the targeting process with targeting pod

The algorithm for determining $\sigma_{\Delta x}$ when using a targeting container for launching a fire extinguishing container is shown in Figure 7 (Atanasov, 2014).

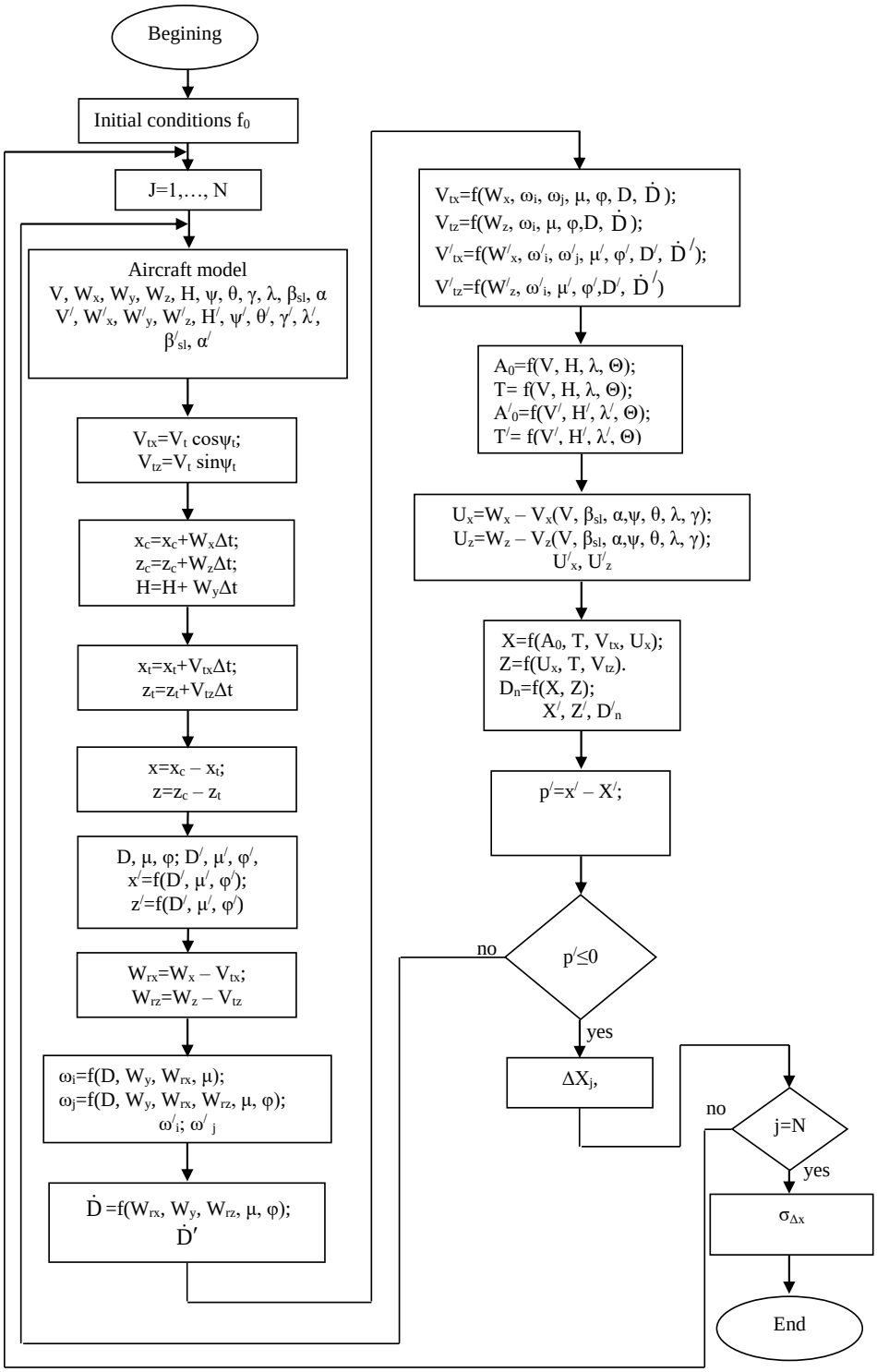

Figure 7. Algorithm for determining $\sigma_{\Delta x}$ using a targeting pod

Results and Discussion

Areas of Use of the CCIP and CCRP Modes When Using a Type Targeting System

The areas of conditions under which an aviation container is launched for firefighting using the CCIP and CCRP modes are defined. The drop is carried out from horizontal flight and diving with an angle of 20^0, from heights H=500 - 2000 m and speeds V=600 - 850 km/h. The research is carried out for launching an aviation container

with a volume of 500 l with a characteristic time Θ= 20.38 s using a type targeting system with a limiting aiming angle $\varepsilon_{limit}=|18^0|$.

From Table 1, it can be seen that the range of conditions under which the container is automatically released from horizontal flight using the CCRP mode (angle values are in grey) is greater than that under which the CCIP mode is used (manual drop). The CCIP launch mode is used for the entire range of speeds (V=600 – 850 km/h.) at a height of H=500 m.

Table 1. Aiming angle when dropping an aviation container from horizontal flight

Dropping an aviation container from horizontal flight						
E_d [degr]	V=600 [km/h]	650	700	750	800	850
H=500 [m]	-17.77	-16.57	-15.52	-14.61	-13.80	-13.09
800	-21.94	-20.48	-19.21	-18.00	-17.11	-16.23
1100	-25.22	-23.58	-22.15	-20.89	-19.77	-18.77
1400	-27.96	-26.19	-24.63	-23.26	-22.03	-20.93
1700	-30.32	-28.45	-26.79	-25.33	-24.02	-22.83
2000	-32.39	-30.44	-28.71	-27.16	-25.78	-24.53

Table 2 shows the release angles E_d of the aviation container from a dive angle of 20^0. From the table it can be seen that the range of conditions under which the CCIP method is used is significantly larger than that of the CCRP method. The CCRP method is used at heights H≥1700 m with speeds V≤700 km/h.

Table 2. Aiming angle when dropping an aviation container from a dive

Dropping an aviation container from a 20^0 angle dive						
E_d [degr]	V=600 [km/h]	650	700	750	800	850
H=500 [m]	-9.77	-8.84	-8.05	-7.36	-6.77	-6.26
800	-13.04	-11.87	-10.86	-9.98	-9.21	-8.54
1100	-15.66	-14.34	-13.18	-12.16	-11.27	-10.47
1400	-17.87	-16.43	-15.16	-14.04	-13.05	-12.16
1700	-19.78	-18.25	-16.90	-15.70	-14.63	-13.67
2000	-21.46	-19.86	-18.45	-17.18	-16.05	-15.03

Accuracy of Solving the Aiming Task When Launching an Aviation Container for Firefighting

The accuracy of solving the aiming task when launching a container from a horizontal flight and diving using a type targeting system and a container targeting system for the above conditions was determined. The flight parameters are determined with the errors of the flight information sources specified in table 3 (Atanasov, 2014; Marinov & Ĭordanov, 2019), where V is the airspeed of the aircraft, H is the drop altitude, D is the distance to the point of the fire (hit point), α is the angle of attack, θ is the pitch angle, W aircraft ground speed, γ bank angle, λ pitch angle.

Table 3. Errors of flight information sources

	V, m/s	H, m	D, m	α, degr.	θ, degr.
$\sigma_\Delta \pm$	5	10	6	0,7	0,25
	W_x, m/s	W_y, m/s	W_z, m/s	γ, degr.	λ, degr.
$\sigma_\Delta \pm$	7%(W_x)	1,1	0,1	0,1	1,1

As a result of the mathematical modelling of the aiming process when launching an aviation container for firefighting, the root-mean-square deviation (RMSD) $\sigma_{\Delta x}$ of the container hit error was calculated using a type targeting system and a container targeting system.

It can be seen that when using the CCIP mode, the container hit accuracy is greater than when using the CCRP method. This is explained by the length of the velocity integration time. When the integration time is small, the hit accuracy is similar to that when using the CCIP mode (Table 4, Table 5). From table 4 and Table 5, it can be seen that in a dive, the accuracy of hitting of the air container is greater from a dive than from horizontal flight.

From Tables 4 - 7 it can be seen that when using a type targeting system and a suspended targeting system, provided that 8 containers with a total volume of 4000 litres of fire-fighting mixture can be mounted on the aircraft, will be achieved the desired fire extinguishing efficiency.

Table 4. RMSD of the hit error of the container using a type of targeting system from horizontal flight

$\sigma_{\Delta x}$ [m]	V=600 [km/h]	650	700	750	800	850
H=500 [m]	17.06	17.62	17.96	18.79	21.14	25.04
800	29.16	27.87	27.00	26.08	26.20	26.54
1100	36.11	35.58	35.47	35.18	34.70	34.03
1400	44.97	44.66	44.23	43.88	43.19	42.15
1700	54.52	53.91	53.29	52.64	51.96	51.27
2000	67.22	64.54	63.63	62.49	62.08	61.42

Table 5. RMSD of the hit error of the container using a type of targeting system from 20^0 angle dive

$\sigma_{\Delta x}$ [m]	V=600 [km/h]	650	700	750	800	850
H=500 [m]	10,73	10,78	10,91	11,10	11,34	11,62
800	12,60	13,50	14,33	15,11	15,82	16,49
1100	16,06	17,10	18,10	19,06	19,98	20,87
1400	21,15	21,62	22,22	22,96	23,82	24,80
1700	27,75	27,01	26,70	26,81	27,33	28,26
2000	35,70	33,24	31,54	30,61	30,89	31,21

When dropping an aviation container from horizontal flight and diving using a suspended targeting system, the hit accuracy achieved is greater than when using the CCRP mode with a type targeting system (Tables 4 – 7). This enables accurate dropping of aviation containers from heights above 1500 m. In this way, the accurate and safe use of aircraft in firefighting is ensured.

Table 6. RMSD of the hit error of the container using targeting pod from horizontal flight

$\sigma_{\Delta x}$ [m]	V=600 [km/h]	650	700	750	800	850
H=500 [m]	16.00	18.66	20.41	21.66	22.77	24.13
800	20.37	22.27	2442	26.02	28.02	29.25
1100	24.56	27.33	29.88	32.37	34.97	37.69
1400	28.52	31.34	34.12	36.96	39.94	43.10
1700	31.07	35.26	38.56	41.50	44.65	48.27
2000	27.39	39.36	44.32	45.92	47.77	51.86

Table 7. RMSD of the hit error of the container using targeting pod from 20^0 angle dive

$\sigma_{\Delta x}$ [m]	V=600 [km/h]	650	700	750	800	850
H=500 [m]	14.57	14.73	15.46	16.40	17.18	17.66
800	15.87	17.96	19.14	19.88	20.65	21.69
1100	18.75	20.98	22.43	23.51	24.62	25.96
1400	22.82	24.10	25.49	26.96	28.49	30.08
1700	25.28	27.27	28.88	30.40	32.11	34.13
2000	21.84	30.13	33.45	34.41	35.63	38.46

Conclusion

The following conclusions can be drawn from the research:

- Using containers for extinguishing fires is an alternative to existing means. They are suitable for limiting the spread of fire. They are suitable for use in initial outbreaks. For this purpose, it is necessary to build a national early warning system for the occurrence of fires (Marinov, 2023). This would save considerable effort and money in fighting fires.
- The advantage is that depending on the type of fire, different fire-fighting mixtures can be used to increase efficiency.
- Aviation containers can be placed on different aircraft, making them universal. In this way, more than one aircraft can be used to increase extinguishing efficiency.
- The targeting system of the aircraft allows the precise use of the aviation containers, which increases the extinguishing efficiency.

Recommendations

The research shows that when dropping an aviation fire-fighting container from an aircraft with a type targeting system from altitudes above 1000 m, it would be more effective to drop them from a dive. The use of aircraft with a targeting pod to drop an aviation container from medium altitudes from level flight will increase the accuracy and effectiveness of extinguishing incipient fires.

Scientific Ethics Declaration

The author declares that the scientific ethical and legal responsibility of this article published in EPSTEM journal belongs to the author.

Acknowledgements or Notes

* This article was presented as an oral presentation at the International Conference on Technology, Engineering and Science (www.icontes.net) held in Antalya/Turkey on November 16-19, 2023.

* The research in this article was carried out in fulfilment of Task 1.1.2. "Analysis and assessment of disaster, accident, emergency and crisis management systems and development of science-based proposals for their improvement" from the National Scientific Program "Security and Defence", adopted by RMS No. 731 of 21.10.2021. and according to Agreement No. D01-74/19.05.2022.

References

Atanasov, M. (2020). Mathematical model and algorithm of operation of a system for release of load from airplane. *Aerospace Research in Bulgaria, 32,* 64-74.

Atanasov, M. (2022). Mathematical model for operation of aviation systems for delivery of special means to air and earth objects. *Aerospace Research in Bulgaria*, *34.* 138-148.

Atanasov, M. (2014). *Tochnost na reshavane na zadachata na pritselvane s neupravlyaemi aviatsionni bombi.* Monografiya, Pleven.

Johnson, R. (2011, September 7). The federal government grounded half its firefighting planes just weeks before the Texas wildfires. Retrieved from https://www.businessinsider.com

Marinov, A. (2023). Hohmann orbit transfer analysis aeronautical research and development. *Bulgarian Air Force Academy*, *2,* 46-51.

Marinov A., & Iordanov, G. (2019). Senzori za otchitane na parametrite na poleta, *Godishna Mezhdunarodna Nauchna Konferentsiya Na Fakultet*, 69-76.

Stoĭkov, O., & Atanasov, M. (2009). Aviatsionni pritselni sistemi – Pŭrva chast. *Disertatsiya Dolna Mitropoliya*

Velikov R., (2022), Izsledvane na efektivnostta na aviatsionnite sredstva za gasene na pozhari. *Disertatsiya, Dolna Mitropoliya.*

Author Information

Milen Atanasov
Georgi Benkovski Bulgarian Air Force Academy
St. St. Ciril and Methodius 1, 5855, Dolna Mitropolia
Bulgaria
Contact email:*matanasov@afacad.bg*

To cite this article:

Atanasov, M. (2023). Aircraft firefighting capabilities using suspended containers. *The Eurasia Proceedings of Science, Technology, Engineering & Mathematics (EPSTEM), 26,* 38-48.

The Eurasia Proceedings of Science, Technology, Engineering & Mathematics (EPSTEM)
ISSN: 2602-3199

The Eurasia Proceedings of Science, Technology, Engineering & Mathematics (EPSTEM), 2023

Volume 26, Pages 49-59

IConTES 2023: International Conference on Technology, Engineering and Science

Evaluation of the Seismic Response of Reinforced Concrete (RC) Buildings Considering Soil-Structure-Interaction Effects

Adnane Brahma
University of Science and Technology Houari Boumediene (USTHB)

Mohamed Beneldjouzi
University of Science and Technology Houari Boumediene (USTHB)

Mohamed Hadid
National High School of Public Works (ENSTP)

Mustapha Remki
Earthquake Engineering Applied Research Center (CGS)

Abstract: The dynamic response of the structure is influenced by soil-structure interaction (SSI), and is distinct from the fixed-base one. When stiff structures are supported by soft to very soft soil, SSI has a substantial effect. This work intends to investigate the effects of SSI using various estimation techniques in order to quantify the foundation damping effect on the response of reinforced concrete (RC) buildings. Generalized and completely viscous damping formulas were utilized to estimate the damping of the soil-foundation system. The investigated structures are 4, 8, and 12-story RC buildings built on very soft soil in a high seismic zone. In comparison to the fixed base condition, the study demonstrated an increase in the natural period, damping of the system, and a decrease in base shear. The study's response parameters are compared to those obtained in accordance with ASCE7-16 code provisions.

Keywords: Foundation damping, SSI, RC building, Base shear, ASCE7-16

Introduction

Seismic analysis of civil structures is often made with the assumption of a fixed base corresponding to rigid-rock. This assumption becomes invalid in the case of flexible base, due to the added flexibility provided to the SFS system (Avilés & Pérez Rocha, 2011). When subjected to seismic motion, the structural response and the free-field ground displacement are not independent of each other. The seismic waves excite the structure, which in turn, modifies the input ground motion. This difference in motion is due to interaction between the foundation, the geological backgrounds underlying and surrounding the foundation, and the superstructure. Dynamic response analysis of foundations supporting structures subjected to seismic excitations is, hence, a key step in structural seismic design and plays a substantial role in the analysis of soil-foundation-structure (SFS) system.

The effect of SSI is more significant in short-period low-rise buildings in contrast to long-period high-rise structures. Buildings considered in this study are low-to-mid-rise resting on soft soil, and are expected to exhibit SSI effects that would alter the response of the buildings considered.

This study evaluates the seismic response of RC multi-story buildings accounting for soil-foundation-structure interaction (SFSI) effects and examines their direct impact on the key parameters of seismic design.

Two approaches were used to calculate the damping foundation. The first one is that provided by the NIST-GCR (2012) provisions and the second is proposed by Givens et al. (2016). The first solution is entirely expressed in terms of real-valued variables, whereas the second involves complex variables and results in complex-valued expressions that are employed with the modular foundation damping solutions. The buildings selected are designed first based on the Algerian Seismic Rules (RPA99, 2003) for their fixed base condition and then designed again according to the substructure approach, which consists of replacing soil deposits with an appropriate spring-dashpot system to model the soil flexibility. Findings show that SFSI is beneficial for the structure and results in a reduction of global base shear force due to a lengthening of the fundamental vibrating period, which leads to a reduced spectral acceleration. Comparison with ASCE7-16 code provisions allowed confirmation of the results of the study.

Soil-Structure Model Considered

SSI effects produce kinematic interaction effects related to the inability of foundation to follow the ground motion due to the greater foundation's stiffness in comparison with soil's stiffness, and inertial interaction effects resulting in inertial forces developed within the structure due to the existence of structural and foundation masses.

Most technics for analyzing SSI interaction effects are mainly based on two methods: (1) the direct method, in which the soil and the structure are included in the same model and are analyzed as a complete and unique system; and (2) the substructure method, which involves dividing the SFS system into separate parts that are combined to formulate the complete problem solution.

According to pioneering works in the field (Stewart & Fenves, 1998), figure 1.b illustrates the retained SFS rheological model, where the superstructure is represented by a single degree of freedom (1-DOF) system with a height h, mass m, stiffness k and viscous damping factor c. This system is connected to a rectangular foundation of dimensions L and B ($L \geq B$). Following the substructure approach, the soil deposits are replaced by a discrete spring-dashpot system described by impedance functions, which reflect the stiffness and the energy dissipation effect mobilized during a seismic excitation given the soil flexibility.

The base of the structure is allowed to move with respect to the free-field motion with u_0 value and to rotate through an angle θ (Figure 1.b). After replacing the soil deposits by impedance functions, the system is converted into an equivalent SFS system, where the stiffness K_u and K_θ and damping factors c_u and c_θ correspond, respectively, to the translation according to x axis, and rocking about y axis modes (coupling terms, mass and mass moment of inertia of the foundation are neglected).

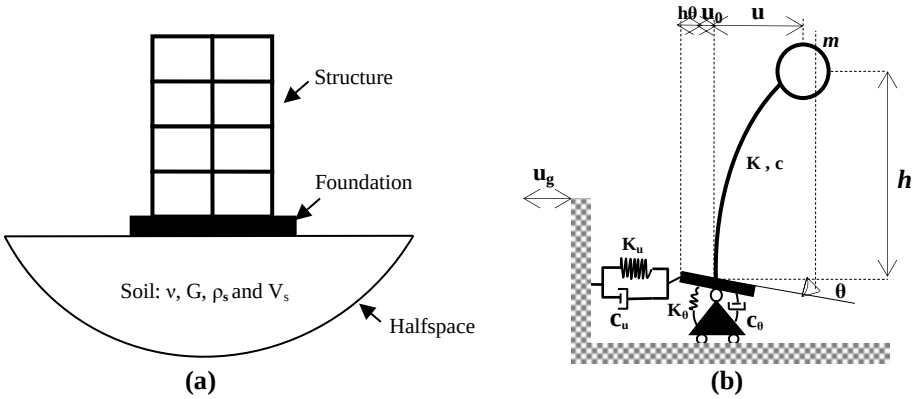

Figure 1. SFS model: (a) Simplified model and (b) Rheological model.

Several authors (Stewart et al., 1999 among others), have shown that the system of Figure 1.b may adequately represent approximate model of a structure with several DOFs having several vibration modes, but whose global response is dominated by the fundamental mode. In such a model, h and m represent, respectively, the effective height and mass associated with the first mode of vibration. Previous studies (Jennings & Bielak, 1973; Stewart

& Fenves, 1998) have shown that the influence of higher modes on the effect of SFSI is negligible. The model of figure 1.b is therefore well suited to the dynamic SFSI analysis of multi-story RC buildings. In this model, the total displacement, u_t of mass m is given by:

$$u_t = u_g + u_0 + h\theta + u \tag{01}$$

Where, u_t, $u_g$and u_0 are, respectively, the total displacement, the displacement of the foundation and the displacement of the ground; u represents the amplitude of the relative displacement of mass m with respect to a moving benchmark attached to the rigid base, and θ, the rotation of the foundation relative to an axis perpendicular to the study plane

Effects of the Foundation Flexibility

In a building resting at a shallow depth on soft soil deposits, the flexible base effect is represented using dynamic frequency-dependent impedances. The latter define stiffness and energy dissipation of the system caused by radiation of waves and by hysteretic action of the ground for the various degrees of freedom, which are limited, in the case of the present study, to the modes of translation according to the x-axis and the rocking around the y-axis. The first consequence of the SFSI effects is the vibration period lengthening of the system initially with fixed base, due to the flexibility introduced by the underlying soil deposits.

If T represents the natural period of the structure in its fixed-base condition, and $\widetilde{T}$ represents the period of the modified structure which approximates the flexibly supported system, it can be shown (Veletsos & Meek, 1974) that:

$$\frac{\widetilde{T}}{T} = \sqrt{1 + \frac{k}{k_x} + \frac{kh^2}{k_{yy}}} \tag{02}$$

Equation (2) may be applied to fundamental mode dominated multi-degree-of-freedom structures considering the first mode effective parameters (modal mass, modal stiffness and effective building height). k_x, represents the lateral translational stiffness of the foundation; and k_{yy}, denotes the rocking stiffness of the foundation; k, is the stiffness of the superstructure corresponding to the first mode of vibration along the x axis; m and h, correspond, respectively, to the modal mass and effective height of the structure. $\widetilde{T}$ /T is a ratio greater than 1, which denotes the vibration period lengthening of the system initially on a fixed base.

Impedance Functions and Damping of the Soil

Impedance Functions

Impedance functions are complex expressions representing the stiffness and the frequency-dependent radiative and material damping characteristics in an SFSI problem, analyzed through the substructure approach. Their classic form is given by:

$$K_j^d = K_j^s(k_j + i\omega c_j) \tag{03}$$

$$K_j^s = k_j^0 \alpha_j \eta_j \tag{04}$$

Where K_j^d is the complex-valued dynamic impedance function; j indicates the mode of displacement (translation or rotation); k_j^0, represents the static stiffness of the foundation at zero-frequency for mode j; k_j and c_j denote, respectively, the stiffness and frequency-dependent damping coefficient for mode j and ω, the circular frequency (rad/s). Also, the static stiffness of the foundation is affected by correction coefficients (α_j and η_j), to account, respectively, for the dynamic and embedment effects of the foundation when it is the case.

The determination of impedance functions is one of the most critical steps involved in substructure approach. For practical applications, they are generally treated as independent of frequency. The most common values of their terms are those corresponding to zero-frequency (static components). Several authors have proposed

solutions for impedance functions for different modes of displacement (Veletsos & Wei, 1971;Pais & Kausel, 1988). The terms of the impedance functions used in this study are those of Pais and Kausel (1988) (Table 1).

Table 1. Equations for shallow foundation stiffness and damping of Pais and Kausel (1988)

Degree of freedom	Static stiffness	Dynamic stiffnesses
Translation along x-axis	$K_{Hx}^{s} = \frac{GB}{2-\nu}\left[6.8\left(\frac{L}{B}\right)^{0.65} + 2.4\right]$	$\overline{K}_{Hx}^{d} = K_{Hx}^{s}(k + ia_0c)$ $k = 1.0$; $c = \frac{4(\frac{L}{B})}{K_{Hx}^{s}/GB}$
Rocking about y-axis	$K_{Ry}^{s} = \frac{GB^3}{1-\nu}\left[3.73\left(\frac{L}{B}\right)^{2.4} + 0.27\right]$	$\overline{K}_{Ry}^{d} = K_{Ry}^{s}(k + ia_0c)$ $k = 1.0 - \frac{0.55a_0^2}{b+a_0^2}$; $b = 0.6 + \frac{1.4}{(\frac{L}{B})^3}$ $c = \frac{\left(\frac{4\alpha}{3}\right)(\frac{L}{B})^3}{K_{Ry}^{s}/GB^3}\frac{a_0^2}{f+a_0^2}$ $f = \frac{1.8}{1.0 + 1.75(\frac{L}{B} - 1)}$

In table 1, $a_0 = \frac{\omega B}{V_s}$ is the dimensionless frequency; $\alpha = \sqrt{2(1-\nu)/(1-2\nu)} \leq 2.5$ and G = $\rho_s V_s^2$, is the elastic shear modulus. The damping ratios are defined as:

$$\beta_j = \frac{a_0 c_j}{2k_j} \tag{04}$$

Damping

The total damping, β_{SSI}, associated with the soil-foundation interaction is composed of the contribution of two damping types: (1) viscous damping related to the superstructure, and (2) the foundation damping accounting for the hysteretic (material) damping along with radiative (geometric) damping.

Hysteretic damping relates to the physical nonlinearities of the soil and characterizes the energy dissipation by friction between its particles, whereas the radiation damping reveals the seismic energy reflected into the ground in the form of waves, when the incident seismic field meets the elements of the foundation. Indeed, the foundation elements behave as a rigid body with a stiffness much greater than that of soil deposits. Foundation damping is a direct contributor to the flexible-base system damping, β_{ssi}, the following expression for the calculation of the SFS system total damping as follows(Wolf, 1985;Veletsos & Meek, 1974):

$$\beta_{ssi} = \beta_f + \frac{\beta_{st}}{\left(\frac{\tilde{T}}{T}\right)_{eff}^2} \tag{05}$$

Where β_f, is the total foundation damping, and β_{st}, the viscous damping ratio related to the superstructure. In this study we used two expressions for foundation damping. The first was developed by the authors for (NIST GCR, 2012) can write as follows:

$$\beta_f = \left[\frac{\left(\frac{\tilde{T}}{T}\right)^2 - 1}{\left(\frac{\tilde{T}}{T}\right)^2}\right]\beta_s + \left(\frac{1}{\left(\tilde{T}/T_x\right)^2}\right)\beta_x + \left(\frac{1}{\left(\tilde{T}/T_{yy}\right)^2}\right)\beta_{yy} \tag{06}$$

The second expression is proposed by (Givens et al., 2016)as follows:

$$\beta_f = \frac{1}{\left(\tilde{T}/|\bar{T}_x|\right)^2}(\beta_x + \beta_s) + \frac{1}{\left(\tilde{T}/|\overline{T_{yy}}|\right)^2}(\beta_{yy} + \beta_s) \tag{07}$$

Where β_s, Is the soil hysteretic damping ratio, β_x and β_{yy} are damping ratios related to radiation damping from translational and rotational modes (described further in section above). T_x, T_{yy}, $|\bar{T}_x|$ and $|\overline{T_{yy}}|$ are fictitious vibration periods, complex and real-valued respectively calculated as if the only source of the vibration was foundation translation or rotation, as follows:

$$\begin{cases} |\bar{T}_x| = 2\pi\sqrt{\dfrac{m}{|\bar{k}_x|}} \\ |\overline{T_{yy}}| = 2\pi\sqrt{\dfrac{mh^2}{|\overline{k_{yy}}|}} \end{cases} ; \quad \begin{cases} T_x = 2\pi\sqrt{\dfrac{m}{k_{x,surf}}} \\ T_x = 2\pi\sqrt{\dfrac{mh^2}{k_{x,surf}}} \end{cases}$$

The complex-valued impedance functions as follows:

$$\bar{k_j} = k_j[1 + 2i(\beta_j + \beta_s)] \tag{12}$$

Where: k_j and c_j are dimensionless parameters functions of a_0, ν = Poisson's ratio; j indicates the mode of displacement (translation or rotation) (Table 1).

Design Provisions

The concepts described in the preceding sections have provided the basis of the SSI design. For buildings analyzed without regard for SSI, the total lateral force or base shear, V, is expressed according to the Algerian Seismic Rules (RPA99, 2003) in the case of the equivalent static method is expressed as:

$$V = C_s W \tag{13}$$

in which, W, the total weight of the building. including the dead weight and the effective portion of the design live load. and ,C_s, the lateral force coefficient which represents the ratio of the effective spectral acceleration for the system, is defined by the following ratio (RPA99, 2003) :

$$C_s = \frac{ADQ}{R} \tag{14}$$

Where, *A* is the zone acceleration coefficient, *D* is the dynamic amplification factor, *Q* is the quality factor and *R*, is the behavior factor. In the present study, parameters needed in the C_s formula were calculated following the section 4.2.3 of the RPA99: *A* = 0.25; *D* = 2.2 (fixed base); *Q* = 1.2 and *R* = 3.5; *D* has been assessed based on appropriate formula of structural period, provided by the RPA99 provisions.

The variation of C_s with T is represented by a function which is initially constant and then decreases with increasing T. As a result, consideration of soil-structure interaction in this case will reduce the design values of the lateral forces, shears and overturning moments below the levels applicable to a rigid-base condition. In this regard, (ASCE7-16, 2007) proposes expression which aims to consider reduction in the global base shear force, which has been used in accordance to RPA99 provisions as follows:

$$\tilde{V} = V - \Delta V \geq \alpha V \tag{15}$$

$$\alpha = 0.5 + \frac{R}{15} \quad for \quad 3 \leq R \leq 6 \tag{16}$$

Where $\tilde{V}$, is the reduced base shear force, V, is the base shear force in the fixed base condition and ΔV, the base shear force reduction:

$$\Delta V = \left[C_s - \tilde{C}_s \left(\frac{\beta_{st}}{\beta_{ssi}}\right)^{0.4}\right] \bar{W} \tag{15}$$

Where C_s and $\tilde{C}_s$, the lateral force coefficients corresponding to the fundamental natural periods of the fixed-base and the elastically supported systems, respectively; β_{ssi} the percentage of critical damping for the structure-foundation-soil system; and $\bar{W}$ is the effective weight of the structure. The base shear force of the structure considering SFSI effects in the case of the response spectrum method is given by the following expression:

$$\tilde{V}_{mod} = S_a(\tilde{T})M^* \tag{16}$$

In which, M^* is the fundamental mode mass and S_a, the spectral acceleration corresponding to the flexible base period $\tilde{T}$.

Soil and Superstructure Modeling

The structures studied are multi-story reinforced concrete structures with 4, 8 and 12 storey, as a total height H= 12.8, 25.6 and 38.4 m respectifly. located in a zone of high seismicity (zone III, according to RPA99 version 2003). The buildings has mixed bracing (moment frames-shear walls) and is based on a RC mat foundation. The floors are RC two ways slab, and the wall infill of the hollow bricks. Ground and upper stories are of the same height h=3.2 m. Building structural elements are given in Table 2.

Table 2. Dimensions in Cm of building's structural element

Element		R+3	R+7		R+11		
		1-4	***1-4***	***4-8***	***1-4***	***4-8***	***8-12***
Column	C1 (a×b)	40×40		40×40			40×40
	C2 (a×b)		50×50			50×50	
	C3 (a×b)				60×60		
Beam	b (b×h)	30×40	30×40		30×40		
Slab	D (e)	20	20		20		
Wall	W (aw)	20	20		20		
E (MPA)	23500						
ν	0.3						
ρ (t/m3)	2.5						

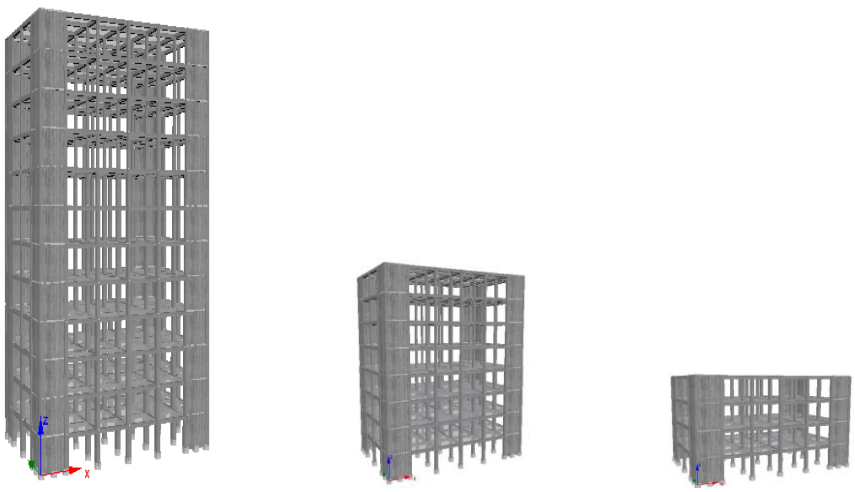

R+11 **R+7** **R+3**

(a)

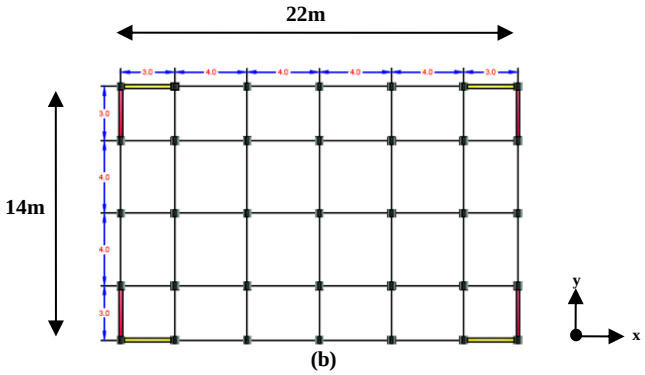

Figure 2. (a) 3D FE models of the studied buildings made with SiesmoStruct ver 2020. (b) Plan view

Table 3. Results of the first mode (fundamental mode)

Buildings	T_i (s)	M^* (ton)	H^* (m)
R+3	0.3	1671.98	8.96
R+7	0.83	3158.16	17.92
R+11	1.38	4944.38	26.88

The soil is classified into the S4 category (according to (RPA99, 2003) ver 2003) and is assumed to be homogeneous with linear elastic behavior. It is characterized by its weight density ρs = 17 KN/m^3, its elastic shear modulus G = 244800 KN/m^2, its Poisson's ratio, ν = 0.4 and its hysteretic damping ratio, βs = 7%. The shear wave velocity within the soil deposits is V_S = 120 m/s (very soft site category).

Results and Discussion

In this section, parameters needed for the ISFS analysis are calculated. Also shown in Figure 3b are stiffness and damping predictions using Pais and Kausel (1988) half space equations adapted for elastic and homogenous soil profiles following recommendations in (NIST GCR, 2012). Using the impedance ordinates in Figure 3b, we compute foundation damping using (Eq,16), for excitation in the x-direction. Table 4 clearly shows that the Givens approach produces higher foundation damping than the approach mentioned in NIST guidelines, especially for low rise (R+3) (high frequency) structures.

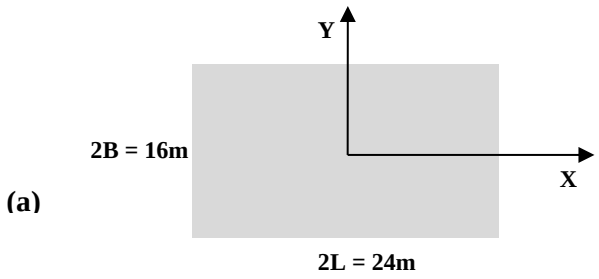

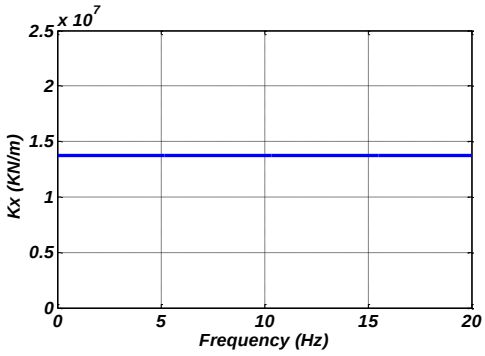

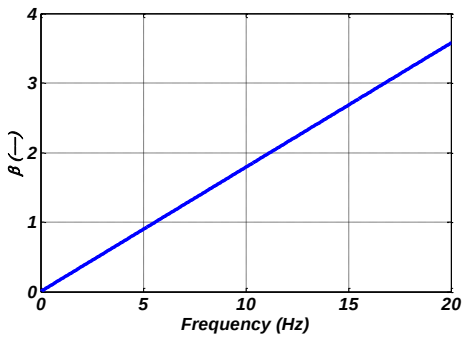

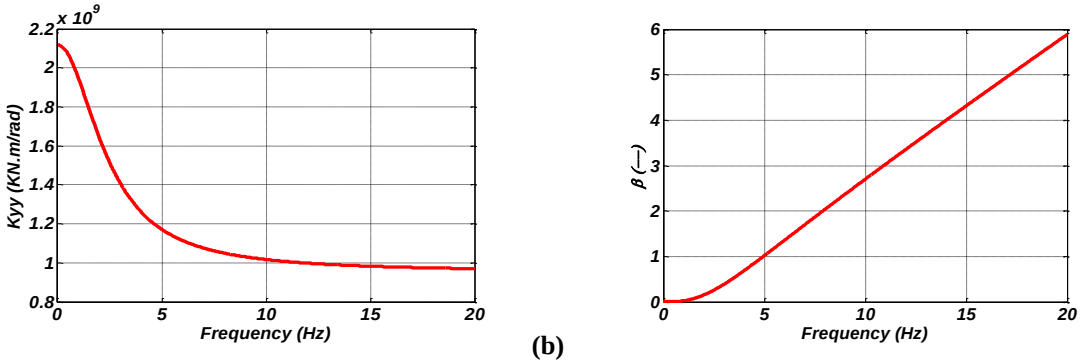

(b)

Figure 3. (a) plan view of assumed foundation geometry; (b) frequency-dependent foundation stiffness's for translation (k_x), rotation (k_{yy}), and associated radiation damping terms (β_x and β_{yy}) for y-component excitation. Foundation stiffness and damping results are shown from closed form expressions for a soil half space adapted to the present conditions following guidelines in NIST (2012).

Table 4. Parameters used in ISFS analysis

Symbole	R+3 Nist-GCR2012	R+3 Givens-2016	R+7 Nist-GCR2012	R+7 Givens-2016	R+11 Nist-GCR2012	R+11 Givens-2016
$\boldsymbol{K_i}$ (KN/m)	732669.067		180799.503		102393.634	
$\boldsymbol{K_x}$ $\times 10^7$ (KN/m)	1.377	-	1.377	-	1.377	-
$\boldsymbol{K_{yy}}\times 10^9$ (KN.m/rad)	2.118	-	2.118	-	2.118	-
$\lvert\bar{\boldsymbol{k}}_{\boldsymbol{x}}\rvert\times 10^7$ (KN/m)	-	2.292	-	1.585	-	1.482
$\lvert\bar{\boldsymbol{k}}_{\boldsymbol{yy}}\rvert\times 10^9$ $(KN.m/rad)$	-	3.673	-	4.585	-	4.829
$\boldsymbol{\alpha_x}$	1.0		1.0		1.0	
$\boldsymbol{\alpha_{yy}}$	0.64		0.89		0.95	
$\widetilde{\boldsymbol{T}}$ (s)	0.312		0.847		1.41	
$\widetilde{\boldsymbol{T}}/\boldsymbol{T}$	1.04		1.02		1.02	
a_0	1.395		0.504		0.303	
$\boldsymbol{\beta_x}$	0.59		0.21		0.13	
$\boldsymbol{\beta_{yy}}$	0.48		0.039		0.009	
$\boldsymbol{T_x}$ *(sec)*	0.069	-	0.15	-	0.26	-
$\boldsymbol{T_{yy}}$ *(sec)*	0.062	-	0.146	-	0.264	-
$\lvert\bar{\boldsymbol{T}}_{\boldsymbol{x}}\rvert$*(sec)*	-	0.0536	-	0.0886	-	0.1146
$\lvert\bar{\boldsymbol{T}}_{\boldsymbol{yy}}\rvert$ *(sec)*	-	0.0499	-	0.1374	-	0.2579
$\boldsymbol{\beta_{rd}}$	0.049	-	0.004	-	0.0012	-
$\boldsymbol{\beta_f}$	0.059	0.034	0.009	0.006	0.007	0.004
$\boldsymbol{\beta_{ssi}}$ (%)	11%	8%	5.7%	5.4%	5.5%	5.2%

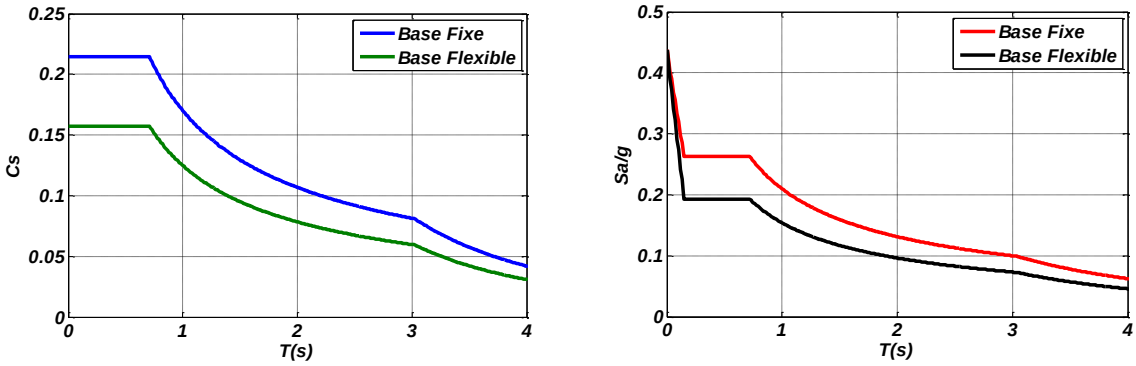

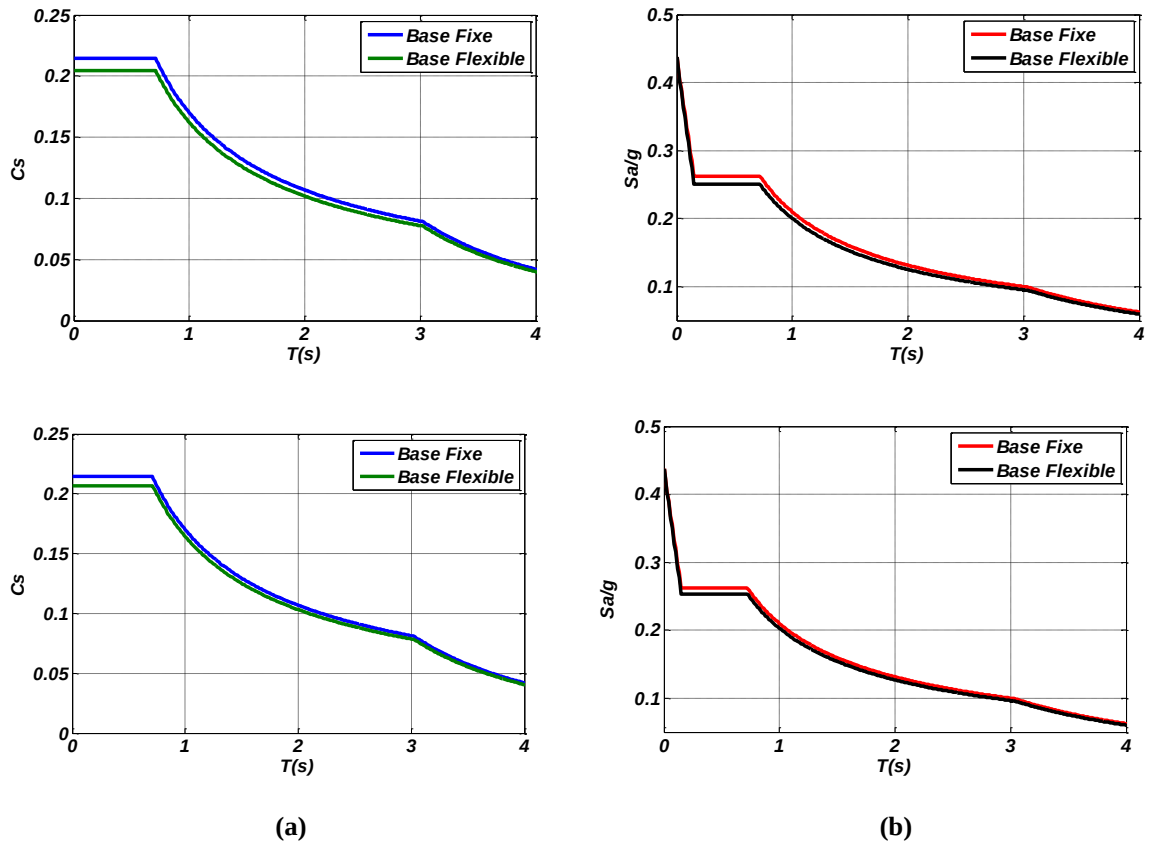

Figure 4. (a) Reduction of the seismic response coefficient in the case of fixed and flexible base conditions, (b) Design response spectrums corresponding to the S4 site for fixed and flexible base conditions according to RPA99 provisions.

It is clear, from obtained results that consideration of flexible support is beneficial for the seismic structural response and results in a reduction in the design base shear force. This reduction is relatively important in the case of the equivalent static method, which could be explained by the very soft nature of the S4 site having resulted in a high damping effect.

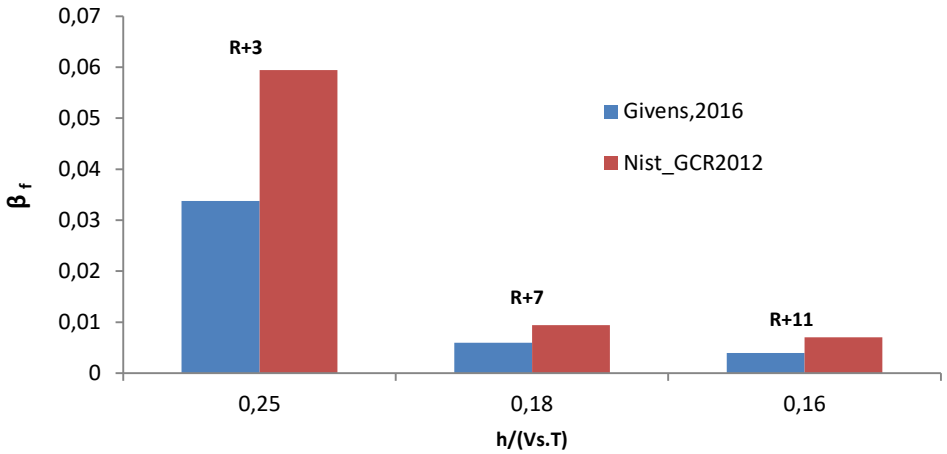

Figure 5. Comparison of foundation damping solutions based on NIST provisions (2012) Eq (6), and Givens (2016) Eq (7).

Figure 5 clearly shows that the damping calculated with the approach using generalized damping formulas (which takes into account the hysterical and viscous components (Givens' approach)) is lower than that calculated with the approaches adopted in NIST-GCR2012, particularly for low-rise building (R+3).

Table 5. Fixed and flexible base shear force reduction in equivalent static method retained by the RPA99 provisions.

	Equivalent static force procedure					
	NIST-2012			Givens-2016		
	R+3	R+7	R+11	R+3	R+7	R+11
$V\ (KN)$	3518,32	5932,24	6617,53	3518,32	5932,24	6617,53
$\Delta V\ (KN)$	1600,77	681,83	559,82	1098,79	421,98	281,74
$\tilde{V}\ (KN)$	2580,10	5250,41	6057,71	2580,10	5510,26	6335,79
α	0.733	0.733	0.733	0.733	0.733	0.733
$\alpha V\ (KN)$	2580,10	4350,31	4852,85	2580,10	4350,31	4852,85
Reduction in V (%)	**26,67**	**11,49**	**8,46**	**26,67**	**7,11**	**4,26**

Table 6. Fixed and flexible base shear force reduction in response spectrum method retained by the RPA99 provisions.

	Response spectrum procedure					
	NIST-2012			Givens-2016		
	R+3	R+7	R+11	R+3	R+7	R+11
$V\ (KN)$	4478,52	7551,22	8423,53	4478,52	7551,22	8423,53
$\Delta V\ (KN)$	1192,18	448,08	401,47	731,52	305,52	236,05
$\tilde{V}\ (KN)$	3286,33	7103,15	8022,06	3746,99	7245,7	8187,48
Reduction in V (%)	**26,62**	**5,93**	**4,77**	**16,33**	**4,05**	**2,80**

Table 5 and 6 clearly shows that reduced base shear forces from the two methods are in good agreement whereas the reduction rate is important and relates to the RPA99 equivalent static method. Indeed, the latter considers the total structural weight in the design of base shear force, which, consequently, leads to an important fixed base shear force, unlike to most of seismic codes retaining only 70% of the total structure's weight, to reflect the structural weight mobilized by the first mode of the structure. In addition, disparity in the rates refers partially to regulatory aspects and dynamic effect neglected in the equivalent static method.

Conclusion

Seismic design of buildings is mostly carried out with the assumption of perfect embedding at a rigid base. Unlike buildings on fixed base, flexible base has an obvious effect on the seismic buildings' behavior and offers a prominent reduction in the internal forces produced within the superstructure, especially for massive low-rise buildings. As a first observation, results found in the study show that SSI effects has a beneficial influence on the structural response and reflect what one would expect from the analysis of coupled site-structure systems relative to the corresponding fixed-base ones.

It is clearly observed, in the light of the results, that flexible-base structural response allows reducing amplification expected from site effects, and the fixed base hypothesis retained by the RPA99 and by the most of seismic codes associated with site effects leads, overall, to an over estimation of the structural response and hence of the seismic damage.

Scientific Ethics Declaration

The authors declare that the scientific ethical and legal responsibility of this article published in EPSTEM journal belongs to the authors.

Acknowledgements or Notes

* This article was presented as an oral presentation at the International Conference on Technology, Engineering and Science (www.icontes.net) held in Antalya/Turkey on November 16-19, 2023.

References

Asce. (2007). Minimum design loads and associated criteria for buildings and other structures. *American Society of Civil Engineers, 1877*, 7-16.

Avilés, J., & Pérez Rocha, L. E. (2011). Use of global ductility for design of structure-foundation systems. *Soil Dynamics and Earthquake Engineering*, *31*(7), 1018–1026.

Givens, M. J., Mylonakis, G., & Stewart, J. P. (2016). Modular analytical solutions for foundation damping in soil-structure interaction applications. *Earthquake Spectra, 32(*3), 1749–1768.

NIST GCR. (2012). Soil-structure interaction for building structures. *National Earthquake Hazards Reduction Program (NEHRP), 12*.

Jennings, P., & Bielak, J. (1973). Dynamics of building-soil interaction. B*ulletin of Tile Seismological Society of America*, *63*(1), 9–48.

Pais, A., & Kausel, E. (1988). Approximate formulas for dynamic stiffnesses of rigid foundations. *Soil Dynamics and Earthquake Engineering, 7*(4), 213–227.

RPA99. (2003). Règles Parasismiques Algériennes, D.T.R. –B.C. 2.48. *National Center of Earthquake Applied Research (CGS).*

Stewart, J. P., & Fenves, G. L. (1998). System identification for evaluating soil-structure interaction effects in buildings from strong motion recordings. *Earthquake Engineering and Structural Dynamics, 27*(8), 869–885.

Veletsos, A. S., & Wei, Y. T. (1971). Lateral and rocking vibration of footings. J*ournal of the Soil Mechanics and Foundations Division, 97*(9), 1227–1248.

Veletsos, A. S., & Meek, J. W. (1974). Dynamic behaviour of building-foundation systems. *Earthquake Engineering & Structural Dynamics, 3*(2), 121–138.

Wolf, J. P. (1985). *Dynamic soil-structure interaction*. New Jersey: Prentice-Hall Inc.

Author Information

Adnane Brahma
University of Science and Technology Houari Boumediene (USTHB)
Algiers, Algeria
Contact e-mail: abrahma@usthb.dz

Mohamed Beneldjouzi
University of Science and Technology Houari Boumediene (USTHB)
Algiers, Algeria

Mohamed Hadid
National High School of Public Works (ENSTP)
Algiers, Algeria

Mustapha Remki
Earthquake Engineering Applied Research Center (CGS)
Rue Kaddour Rahim, BP 252, Hussein Dey, Alger, 16040
Algeria

To cite this article:

Brahma, A., Beneldjouzi, M., Hadid, M., & Remki, M. (2023). Evaluation of the seismic response of reinforced concrete (RC) buildings considering soil-structure-interaction effects. *The Eurasia Proceedings of Science, Technology, Engineering & Mathematics (EPSTEM), 26,* 49-59.

The Eurasia Proceedings of Science, Technology, Engineering & Mathematics (EPSTEM)
ISSN: 2602-3199

The Eurasia Proceedings of Science, Technology, Engineering & Mathematics (EPSTEM), 2023

Volume 26, Pages 60-66

IConTES 2023: International Conference on Technology, Engineering and Science

Optimization of EMC Filter for a Variable Speed Drive System in Electric Aircraft

Houcine Miloudi
Djillali Liabès University of Sidi Bel-Abbès

Mohamed Miloudi
Relizane University

Mohammed Hamza Bermaki
Djillali Liabès University of Sidi Bel-Abbès

Abdelkader Gourbi
APELEC, ISTA, Oran University

Abdelber Bendaoud
Djillali Liabès University of Sidi Bel-Abbès

Abstract: In recent years, static converters are in constant evolution, and they have occupied an increasing role within aeronautical on-board networks. This development results in an increase in the power density of the onboard network and a reduction in the volume of the components. This development in electrical technologies creates problems related to electromagnetic pollution. To avoid polluting their environments, the power electronics designer will have to provide effective devices and means to mitigate the levels of emissions from their equipment. This work focuses on electromagnetic compatibility (EMC) problems appearing in power converters on board future more electric aircraft. The work deals with the aircraft EMC issue, and then the reduction of electromagnetic pollution from a variable speed drive system. With the standards used in the aeronautical fields, type DO 160D, the optimization approach consists in bringing the level of emissions of the current generated towards the network and the load Induction motor) below the EMC standard in the whole range of frequencies 150 kHz -30 MHz.

Keywords: Aircraft, Do-160d Standard, Electromagnetic compatibility, Optimization.

Introduction

Electromagnetic interference (EMI) is an inevitable occurrence in electrical and electronic systems. In adjustable-speed AC motor drive systems, a crucial component is the PWM inverter, widely utilized in industrial and aircraft applications. This inverter serves as a major source of conducted noise emissions, especially common mode (CM) noise, leading to significant noise current issues, particularly at high frequencies (HF). (Jettanasen, 2010). The EMI caused by switching power supplies interferes with the normal operation of other sensitive equipments and may cause operating faults (Miloudi et al., 2012). the Electromagnetic interference analysis within the system aircrafts is an important part of system design (Yanyan et al., 2020).

For the reduction of conducted emissions, we can cite two methods, the first being filtering by passive elements, and the second being the use of active filters (Yongbin et al., 2016). Certain EMI filter design approaches simplify the process by disregarding the noise source and termination impedances. Meanwhile, other methods

consider these factors but simplify them as purely resistive elements (Miloudi et al., 2012). In this paper the crucial aspects of electromagnetic protection for aircraft electromechanical systems in intricate electromagnetic environments are examined in conducted electromagnetic interference.

EMI in Variable Speed Drive System

The subject of our study is a variable speed drive system. This type of drive is currently available in the market, utilizing IGBT power transistors with switching speeds 20 times faster, and its conventional topology is presented in Figure 1. It consists of an Input Rectifier bridge, a voltage inverter, all connected through a continuous capacitive bus, and the load comprised of a three phase induction motor and its power cable. The rapid switching in power converter represents a significant cause of Electromagnetic Interference (EMI) (Feloups et al., 2023), posing challenges in complying with EMC regulations. To adhere to these regulations, EMI filters are frequently incorporated into the converter front end (Ashritha et al., 2018). Variable speed drives are required to adhere to regulations concerning both conducted and radiated disturbances. These standards ensure that a system can operate effectively within its environment without generating electromagnetic disturbances that are disruptive to nearby equipment (Zeghoudi et al., 2022).

In this work, we will focus specifically on common mode currents, which refer to currents flowing between the power module and the ground. The simultaneous presence of parasitic capacitances and high voltage gradients across these capacitances causes the circulation of a current. Capacitive coupling is one of the methods through which electromagnetic disturbances are transmitted. Therefore, quantifying the parasitic capacitances of a power module provides an indication of the module's susceptibility to disturbances. The common mode current is caused by variations in the common mode voltage generated by the inverter, and it is responsible for radiated disturbances. It can be calculated based on the knowledge of the common mode voltage imposed by the inverter and the common mode impedances of the system.

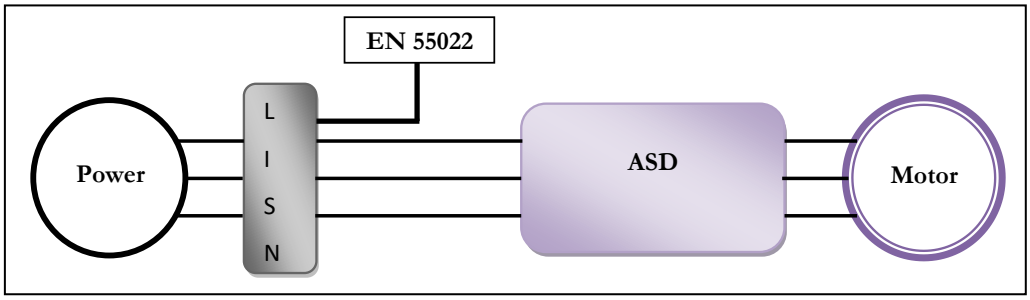

Figure 1. Adjustable speed drive structure

Common Mode Disturbances (CM): these emissions are generated by the flow of a capacitive current that propagates in all conductors in the same direction, and the return path is through the ground. This current is primarily due to the parasitic capacitances of the system excited by the dV/dt generated by power switches.

DO-160D Standard

RTCABO-160D, which stands for "Environmental Conditions and Test Procedures for Airborne Equipment," establishes a set of baseline environmental test conditions (categories) and the relevant testing procedures for airborne equipment (Borgstrom, 1998). This aeronautical standard aims to quantify electromagnetic noise at the input and output of the static converter in the radio frequency band (150 kHz – 30 MHz).

EMI Filter Configuration

In power conversion systems employing switches, the inherent rapid changes in voltage (dv/dt) and current (di/dt) during switching operations can generate substantial electromagnetic interference (EMI) noises. Conventionally, passive EMI filters are applied to mitigate these disruptive switching noises (Penugonda., 2021).

The configuration of a Common mode CM filter ideally comprises series inductors in each phase followed by parallel capacitors, as illustrated in Figure 2. The winding of these inductors is designed in opposite phases to neutralize the flux produced by CM current (Chaiyan et al., 2010) .

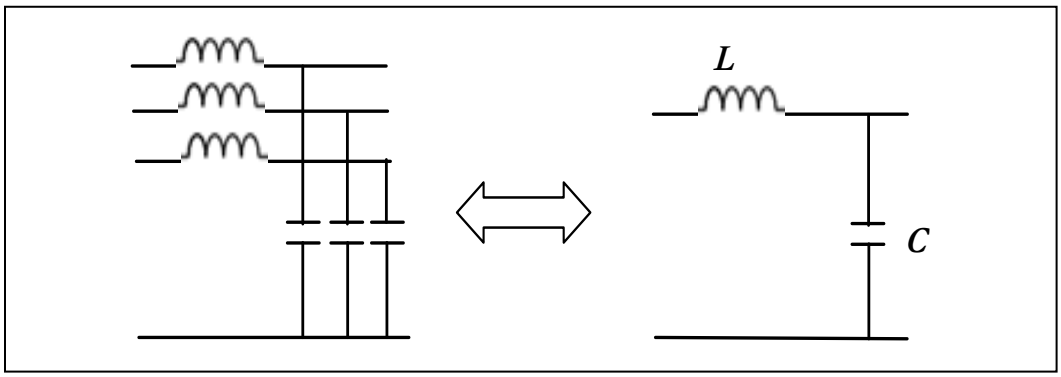

Figure 2. EMC filter (LC configuration)

The EMC filter in LC configuration can be given by the relation:

$$Z(p) = X_L * p + \frac{1}{X_C * p}$$

A passive filter solely relies on passive components to mitigate conducted disturbances, as noted by various researchers (Jon et al., 2021; Penugonda et al., 2021). These filters operate without the need for an external power supply. This approach enables strategic alteration of the disturbance propagation path, impeding their circulation, as demonstrated in studies by (Gregorio et al., 2017). for standard aspect the passive filters can be positioned upstream drive. An EMC filter designed to minimize the circulation of PEMs (Power Electronics Modules) generated by the converter outside of it will be positioned between the LISN and the converter input (Figure 3).

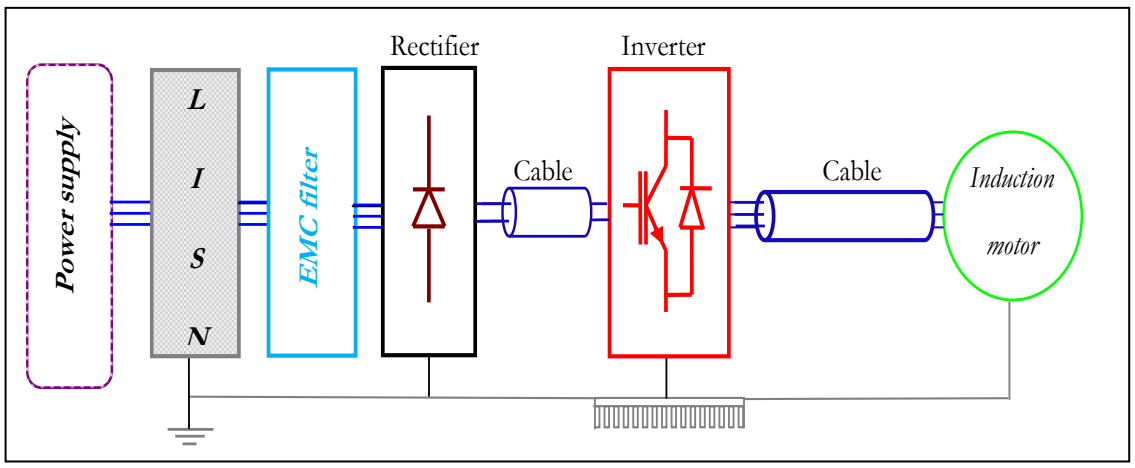

Figure 3. Input EMC filter on of ASD

The CM filter is placed upstream of the network, a technique commonly employed by modern variable speed drive systems. The combination of high impedance (inductance) and low impedance (capacitance) pathways effectively channels disruptive currents along routes that do not interfere with the network. When striving to optimize EMC performance, incorporating EMC constraints involves evaluating the level of emissions (spectrum envelope) at the input of the variable speed drive in relation to the limit specified by the DO-160D standard for the corresponding frequency.

In this study, the optimization approach consists of reducing the emission levels exceeding the limit of EMC standard to below it over the entire corresponding frequency range.
The optimization flowchart is shown in Figure 4.

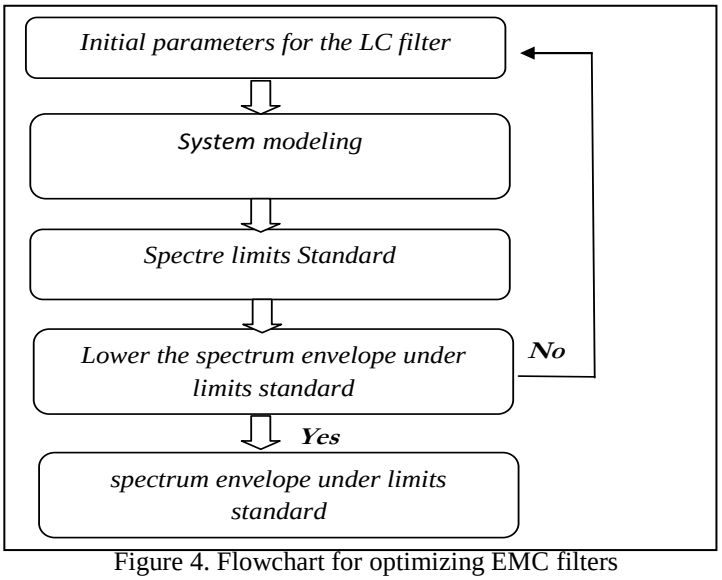

Figure 4. Flowchart for optimizing EMC filters

Results and Discussion

This optimization method aims to lower the emissions generated by the current flowing into the network, ensuring they stay within the EMC standard, specifically in the frequency range of 150 kHz to 30 MHz. Examining the influence of the filter placed before the inverter on the common mode currents circulating throughout the system is crucial. The optimized values for the EMC filter elements are determined through this analysis: L_{CM}=2.8 mH, C_{CM}=0.8 pF.

EMC Filter Performance

In the first, the spectral estimates are referenced to DO-160D standard, the aerospace standard used for evaluating conducted disturbances in the analyzed system, and they measure electromagnetic noise at both the input and output of the variable frequency drive.

Spectrum of Common Mode Currents in the Input of the ASD System

The common mode current in the input of the variable speed drive system is well reduced, over the entire frequency range imposed by standard DO-160D (Figure 6).

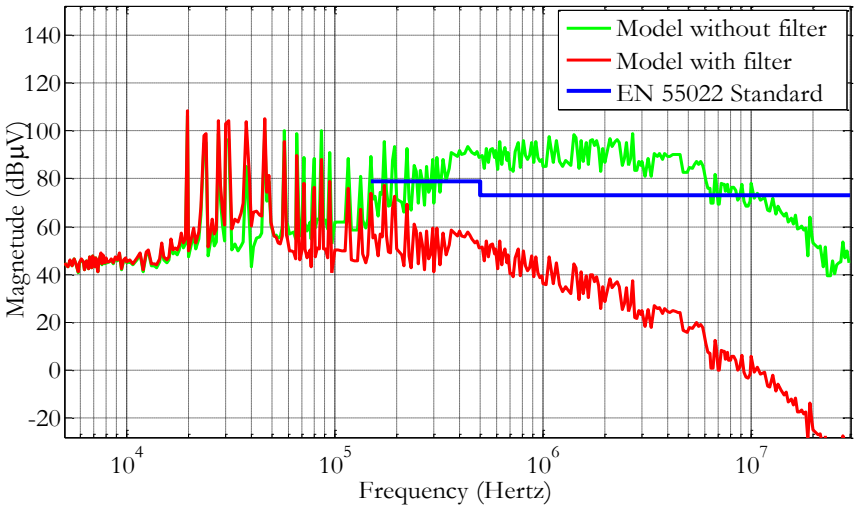

Figure 5. Currents in the input of the ASD system

To see the effectiveness of the presence of the EMC filter at the input of inverter, we show in figure 6 the spectrum of the current.

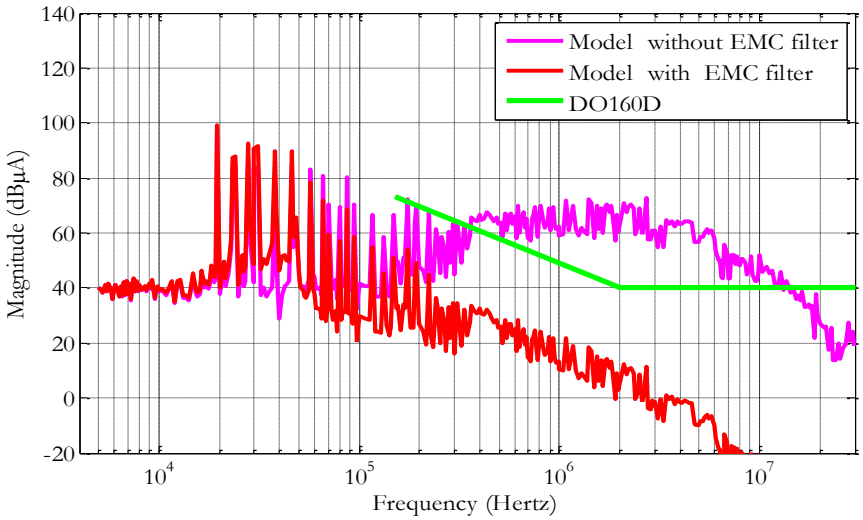

Figure 6. Currents in the input of inverter (with/ without EMC filter)

An input filter is a circuit component used to suppress electromagnetic interference (EMI) or radio frequency interference (RFI) in ASD system. It's often employed to meet electromagnetic compatibility (EMC) standards, which specify the acceptable levels of electromagnetic emissions from electronic devices.

The common mode current can cause electromagnetic interference and needs to be controlled to comply with EMC standards. The proposed filter suggests that the input filter has a positive effect on reducing interference at this specific frequency. From figures 5 and 6, the system still meets the EMC standard requirements. The emission levels remain within the acceptable limits set by the standards,

EMC Filter Effect on the Common Mode Current Generated to the Motor

The figure 7 presents the CM current generated to the motor, in order to see the effect of an EMC filter.

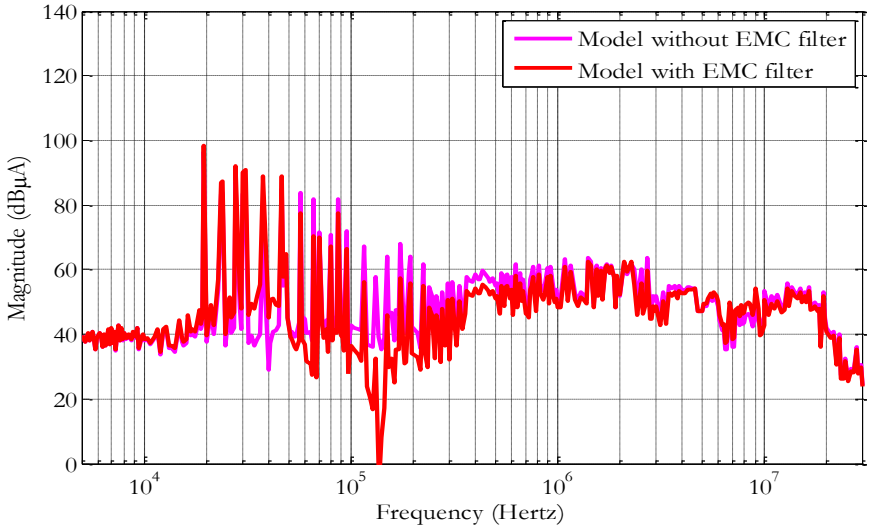

Figure 7. Currents in the motor

As we have seen previously, the results assert that despite the presence of the input filter, there is no significant change in the spectrum of common mode current in the motor. This means that the filter doesn't affect the distribution of interference across different frequencies (Figure 7).

Conclusion

Improving electromagnetic compatibility acts on the side of the sources by trying to reduce the disturbances they emit. The filter presented with an inductance alone is sufficient to limit disturbances and keep the spectra below the corresponding limits. Therefore, the inductance significantly attenuates conducted electromagnetic disturbances (PEMs), and the capacitance of the filter remains secondary to the inductance in reducing conducted emissions, the common mode choke acts as a barrier, hindering the flow of common mode current by elevating the impedance on the network side. Meanwhile, capacitors, grounded and providing low high-frequency impedance, create a preferred pathway for current return. This arrangement ensures the containment of disturbances.

In the frequency range considered, the proposed EMC filter is particularly effective for the normative aspect, and gives best EMC performance. But unfortunately, there is no action on the motor overvoltage, and also it does not make it possible to reduce the common mode currents circulating in the motor.

Scientific Ethics Declaration

The authors declare that the scientific ethical and legal responsibility of this article published in EPSTEM journal belongs to the authors.

Acknowledgements or Notes

This article was presented as the poster presentation at the International Conference on Technology, Engineering and Science (www.icontes.net) held in Antalya/Turkey on November 16-19, 2023.

References

Ashritha, M., & Sudheer, M. L. (2018). CM noise cancellation in near unity power factor converter. *15th International Conference on ElectroMagnetic Interference & Compatibility (INCEMIC*), 1-4. Bengaluru, India.

Borgstrom, E. J. (1998). An overview of the EMC requirements in RTCA/DO-160D. *International Symposium on Electromagnetic Compatibility. Symposium Record, 2*, 702- 707. Denver, Colorado, USA.

Chu, Y., Wang, S., & Wang, Q. (2016). Modeling and stability analysis of active/hybrid common-mode EMI filters for DC/DC power converters journal articles. *Journal of IEEE Transactions On Power Electronics, 31*(9), 6254- 6263.

Feloups, C. E. S., Adhena, H. H., Moonen, N., Thomas, D., & Leferink, F. (2023). Investigating the CM noise generated by different configurations of multiple forward converters. *International Symposium on Electromagnetic Compatibility – EMC Europe,* 1-6. Krakow, Poland.

González-Ramos, J., Angulo, I., Fernández, I., Arrinda, A., & Vega, D. D. L. (2021). Characterization of the potential effects of emc filters for power converters on narrowband power line communications journal articles. *Journal of Electronics (MDPI), 10*, 152.

Jettanasen, C. (2010). Passive common-mode EMI filter adapted to an adjustable-speed AC motor drive. 2010 *Conference Proceedings IPEC* (pp.1025-1030). Singapore.

López, G., Ignacio, J., More Sánchez, E., Martínez, C., & Martín, F. (2017). Effects and countermeasures in narrowband power-line communications networks: A practical approach journal articles. *Journal of Energies*, *10*, 1238

Miloudi, M., Bendaoud, A., Miloudi, H., Nemmich, S., & Slimani, H. (2012). Analysis and reduction of common-mode and differential-mode EMI noise in a Flyback switch-mode power supply (SMPS)," *20th Telecommunications Forum (TELFOR*), 1080-1083. Belgrade, Serbia.

Penugonda, S. (2021). Reduction of mode conversion of differential-mode noise to common-mode noise by printed Circuit Board Modification for Unbalanced EMI Filter Network. *IEEE International Joint EMC/SI/PI and EMC Europe Symposium*, 261-264. Newyork, NY.

Penugonda, S. Z., Xu, Y., Guo, M., Ouyang, M., Kim, J., Lee, J., Ha, H., Lee, S., Yun, J. F., & Kim, H. (2021). Reduction of mode conversion of differential-mode noise to common-mode noise by printed circuit board modification for unbalanced EMI filter network. Proceedings of the *2021 Joint IEEE International Symposium on EMC/SI/PI, and EMC Europe*. Raleigh, Caroline: Nord, États-Unis.

Wang, Y., Gao, K., Xing, J., & Jiang, T. (2020). A new method of EMI estimation among low altitude aircrafts on sea surface. *IEEE International Conference on Computational Electromagnetics (ICCEM)*, 138-140. Singapore.

Zeghoudi, A., Bendaoud, A., Slimani, H., Miloudi, H., Miloudi M., & Chikhi, N. (2022). Experimental measurement of common and differential modes for variable speed drive DC motor. *19th International Multi-Conference on Systems, Signals & Devices (SSD)*, 532-537. Sétif, Algeria.

Author Information

Houcine Miloudi
APELEC, Djillali Liabès University
Sidi Bel-Abbès, Algeria
Contact e-mail: *el.houcine@yahoo.fr*

Mohamed Miloudi
APELEC, Relizane University
Relizane University, Algeria

Mohammed Hamza Bermaki
APELEC, Djillali Liabès University
Sidi Bel-Abbès, Algeria

Abdelkader Gourbi
APELEC, ISTA, Oran University,
Oran University, Algeria

Abdelber Bendaoud
APELEC, Djillali Liabès University
Sidi Bel-Abbès, Algeria

To cite this article:

Miloudi, H., Miloudi, M., Bermaki, M. H., Gourbi, A., & Bendaoud, A. (2023). Optimization of EMC filter for a variable speed drive system in electric aircraft. *The Eurasia Proceedings of Science, Technology, Engineering & Mathematics (EPSTEM), 26,* 60-66.

The Eurasia Proceedings of Science, Technology, Engineering & Mathematics (EPSTEM)
ISSN: 2602-3199

The Eurasia Proceedings of Science, Technology, Engineering & Mathematics (EPSTEM), 2023

Volume 26, Pages 67-74

IConTES 2023: International Conference on Technology, Engineering and Science

Assessment of the Ecological Footprint of Industrial Processes: An Integrated Approach to Life Cycle Analysis

Vessela Petrova
University of Mining and Geology

Abstract: The ecological footprint is crucial in assessing industrial processes and is essential for understanding their impact. The integrated approach to life cycle assessment is essential for studying these footprints. The scientific paper describes a comprehensive approach to assessing the environmental footprint of industrial operations using life cycle analysis. The study's goal is to examine the environmental implications of various stages in the life cycle of industrial products or processes. A life cycle analysis framework is provided, which encompasses all processes from raw material extraction to product manufacture and consumption, as well as waste and recycling possibilities. Each phase is evaluated in terms of energy use, material consumption, and environmental impact. Concrete steps for implementing an integrated approach to life cycle analysis in industrial environments are presented, as are examples of the methodology's implementation in various areas of production. The article emphasises the need for incorporating environmental considerations into decision-making processes and assists organisations in identifying opportunities for optimising and reducing their environmental footprint.

Keywords: Ecological footprint; Life cycle analysis, Industrial processes, CO_2 emissions

Introduction

One of the most significant challenges facing humanity is environmental degradation and how to deal with it. Intensification of various forms of pollution, reduction of biodiversity, depletion of natural resources—all these processes pose a serious threat to ecosystems and human health. Industrial processes have a significant impact on the environment due to the large volume of production, the use of resources, and the emissions they generate. They constitute one of the main causes of environmental pollution and the ecological challenges we face. (Chambers et al., 2004)

Ecological Footprint

The ecological footprint is a summary indicator of the consumption of natural resources (energy and materials), just as economic indicators provide a framework for the financial economy. Prof. William Rees and Dr. Mathis Wackernagel developed the idea of an "ecological footprint" in the early 1990s (Wackernagel & Rees, 1996). Ecological footprint analysis is rapidly gaining popularity and is now widely used by governmental and non-governmental organisations. Its applications include policy analysis, performance benchmarking, education and public awareness, and scenario development. (Bastianoni et al., 2006) By its nature, the ecological footprint considers the use of the planet's renewable resources. The ecological footprint considers only the ecological component without engaging with the social and economic dimensions of sustainability. (Bergmark, 2022) Environmental footprint assessment plays an important role for industrial processes due to a number of significant aspects:

- Identification of environmental impacts: focus on the real environmental impacts of industrial processes. This includes greenhouse gas emissions, air and water pollution, the use of resources such as energy and water, and other parameters. By clearly defining and quantifying these impacts, businesses can understand where the main problem areas are concentrated and focus on them for improvement.
- Identification of opportunities for optimisation and environmental improvement: marking potential opportunities for optimisation and reduction of the negative impact on the environment By analysing the different phases of the life cycle, businesses can identify key points for improvement, such as energy efficiency, material efficiency, waste recycling, etc. This allows them to innovate, change production processes, and prioritise sustainable practices.
- Meeting environmental requirements and regulations: in many countries and regions, various environmental requirements and regulations are imposed on industrial activities. Environmental footprint assessment helps businesses meet these requirements and adhere to regulatory standards. This not only helps them avoid legal penalties but also proves their commitment to sustainability and environmental responsibility.
- Improvement of corporate image and competitiveness: marking a positive effect on the corporate image and competitiveness of enterprises Consumers and customers are increasingly paying attention to environmental aspects and looking for products and services that are good for the environment. Companies that actively work to reduce their environmental footprint have the opportunity to portray themselves as sustainable and responsible and attract consumers who share similar values.

Life Cycle Assessment

The first Life Cycle Assessment study was conducted in the 1960s in packaging studies, primarily focused on energy use rather than emissions (Samani, 2023). Life cycle analysis is a methodology for assessing the environmental impacts of products or processes from the beginning to the end of their life cycle. The process includes all phases related to raw materials, production, use, waste treatment, and final disposal or recycling. Life cycle analysis uses a systematic and quantitative approach to assess various impacts, such as energy consumption, greenhouse gas emissions, water and air pollution, and other parameters, in order to determine the overall ecological footprint of products or processes. (Ventura, 2022)

Ecological Footprint and Life Cycle Analysis are different but interrelated methods for measuring and evaluating the environmental impacts of products, services, organisations, and even human lifestyles. The relationship between them is that both methods are used to assess environmental impacts but focus on different aspects and scales. They are used to identify the key factors that contribute to the environmental burden and to identify opportunities for improvement and reduction of negative impacts. Table 1 presents a brief comparative analysis of the concepts.

Table 1. A comparative analysis of the concepts of ecological footprint assessment and life cycle analysis, (Author's research)

	Ecological Footprint Assessment	Life Cycle Analysis
Methodology	A method of measuring human consumption of natural resources and comparing it with the ability of planet Earth to restore them.	A method of assessing the environmental impacts of products and services throughout their life cycle, including production, use, and disposal.
Focus	It focuses on summing up all resources used by man and emissions produced by man's activities into a single number (global acres) expressed in area or land surface units.	It focuses on specific products or processes and analyses all stages of their life cycle, including raw materials, production, transport, and final processing.
Application	It is used to assess the sustainability of human lifestyles and to compare them with the Earth's biological capacity.	It is used to identify key areas where the sustainability of products or services can be improved.

The link between the methods occurs when life cycle analysis is used to analyse the life cycle of a specific product or service in order to determine its ecological footprint. Thus, life cycle analysis can provide detailed data on the impact of a product in different phases of its life cycle, which can then be aggregated and compared to the global ecological footprint of human lifestyles. This helps identify specific ways to reduce the environmental footprint of products and services.

Life cycle analysis, also called "life cycle environmental impact assessment," is a technique for identifying inputs of raw materials, energy, chemicals, etc. and outgoing waste, pollutants, recycling, etc. in the product life cycle and assessing potential environmental impacts. (Seol et al., 2021) Raw materials, water resources, and energy are inputs, and air emissions, water system emissions, solid waste, etc. in the production process, the use process, and the disposal process are the outputs. Figure 1 illustrates the technique with inputs and outputs, and the considered structure can be applied to various industrial processes.

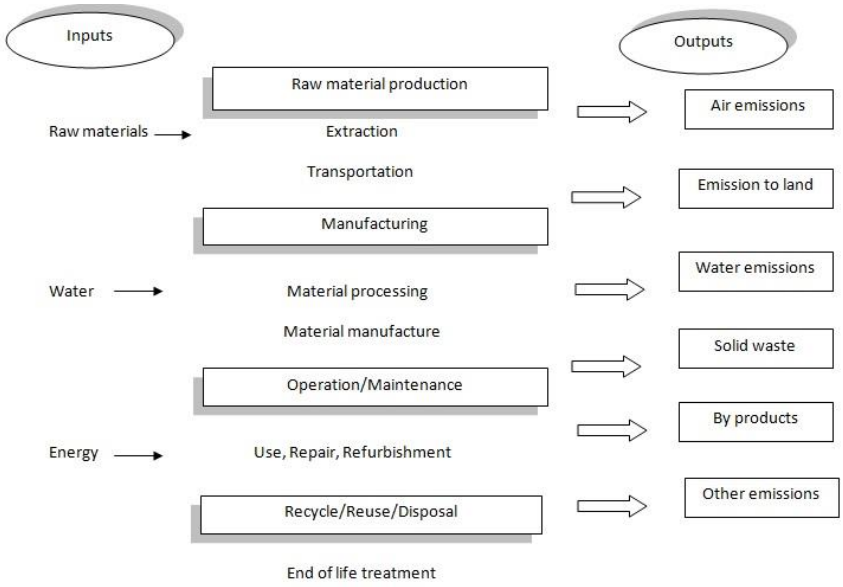

Figure 1. Life cycle assessment technique

Tools Used in Life Cycle Analysis

Life cycle analysis involves the use of various tools that are designed to measure and assess the environmental impacts of products or processes throughout their life cycle. Figure 2 highlights the main tools used in life cycle analysis.

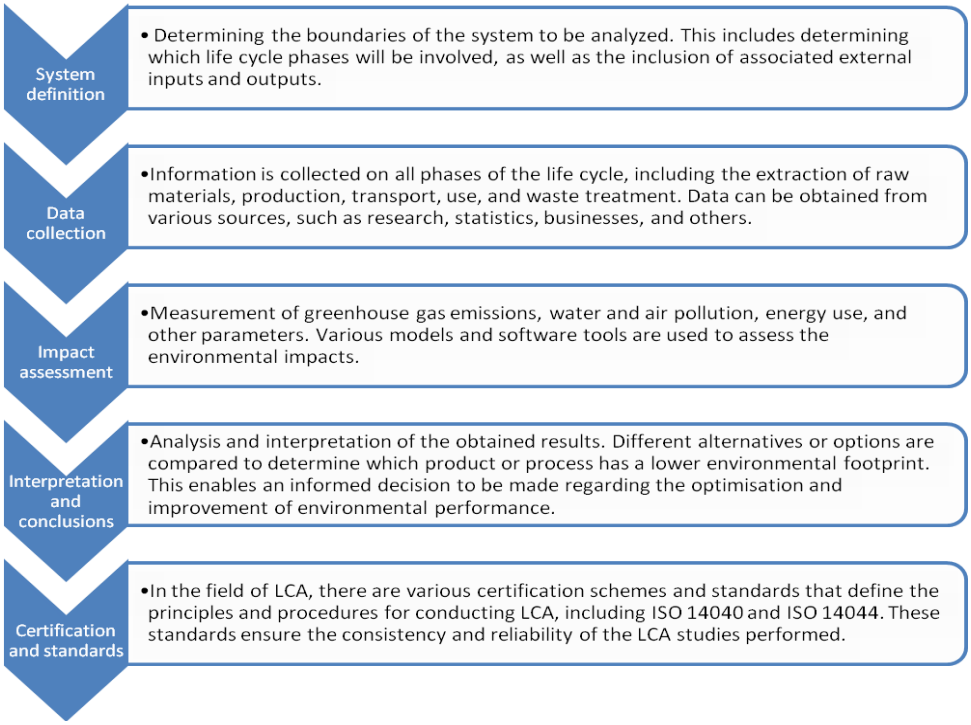

Figure 2. Tools for implementing life cycle analysis

The presented tools are used in combination to perform a complex and comprehensive life cycle analysis of products or processes. They help to understand and assess environmental impacts and identify opportunities for improvement and optimisation in accordance with the principles of sustainable development.

Indicators for Ecological Footprint Assessment

Environmental footprint assessment indicators are specific measures that are used to measure the impact of products or processes on the environment. (Vargas Gonzales et al., 2019) Different indicators can be used in an industrial context, and it is most important to choose those that are most appropriate for the specific sector or product. In general, these are:

- Energy efficiency: measures the energy efficiency of the product or process. It can be measured as the ratio of input energy to useful output or as the energy expenditure per unit of product.
- Water footprint: measures the water consumption or pollution associated with the product or process. The total amount of water used during the entire life cycle of the product or process is measured.
- Greenhouse gas emissions measure the amount of greenhouse gases emitted, such as CO_2, CH_4, and N_2O. It is used to estimate the carbon footprint of the product or process and its impact on climate change.
- Air and water pollution: measures the amount and types of pollution that is generated by the product or process and has an impact on air and water quality.
- Waste and recycling refers to the amount of waste that is generated by the product or process, as well as the possibilities of recycling materials and components. (Dimov et al., 2020)

When comparing different indicators and their applicability in the industrial context, it is important to take into account the specific needs and characteristics of the sector or product. Some indicators may be better suited to measuring climate impact, while others are better suited to assessing resource consumption or water and air pollution. It is important to choose indicators that are relevant to the specific industry and can provide information that can be used to improve and optimise the environmental footprint. (Vanham et al., 2019)

Application of the Integrated Approach to Life Cycle Analysis in Industrial Environments

The integrated life cycle analysis approach has wide applications in industrial processes, playing an important role in the management of environmental sustainability and the optimisation of products and processes. (Schaubroeck et al., 2021) Some of the main applications of the integrated life cycle analysis approach in industrial settings are:

- Design of products: allows assessment of their potential impact on the environment from the early stages of development. This includes choosing appropriate materials, processes, and technologies to reduce the adverse environmental impact throughout the product's life cycle.
- Supplier and supply chain management helps industrial enterprises assess and manage the environmental impact of their suppliers. This includes assessing energy consumption, greenhouse gas emissions, and other environmental parameters of supply, as well as supporting supply chain sustainability and responsibility.
- Process management provides an opportunity to assess and optimise the environmental footprint of industrial processes, including identifying environmental risks, measuring emissions and waste, optimising resource consumption (energy, water, and raw materials), and introducing more sustainable technologies and methods.
- Decision-making process: provides information and analysis that supports the decision-making process in industrial environments. This allows companies to balance and consider environmental, economic, and social aspects when choosing alternatives and strategies.

Communication and marketing enable businesses to communicate their efforts to optimise the environmental footprint of their products and processes to consumers and other stakeholders. This can have a positive effect on the image and positioning of the brand, as well as provide a competitive advantage in the market. The use of the integrated approach to life cycle analysis in industrial environments contributes to achieving sustainable and responsible entrepreneurship, reducing the adverse impact on the environment, and improving the environmental performance of products and processes.

Industrial Examples in the Field

The integrated life cycle analysis approach is used in various industries and processes in order to manage the ecological footprint and achieve sustainability. (Bockin et al., 2022)

- Assessment of the ecological footprint of food production, including assessment of soil and water pollution from agriculture, greenhouse gas emissions from food production and transport, and the impact of packaging and food chain waste. (Dilawar et al., 2019)
- Assessment of the environmental footprint in the automotive industry, in the production of cars and their components This includes measuring greenhouse gas emissions from production, in-use fuel, and electricity consumption, as well as recycling and waste disposal options for cars.
- Assessment of the ecological footprint in construction and in the production of building materials and processes This includes measuring the energy efficiency of buildings, the impact on air and water quality, waste management, and the possibilities of recycling materials.
- Evaluation of the ecological footprint in the field of information technologies and in the production of electronic devices and computer systems. This includes measuring the energy efficiency of devices, sources of materials and components, waste management, and electronics recycling options.
- Assessment of the ecological footprint in the textile industry in the production of textile products and materials, including the processing of textiles and the use and disposal of clothing. This includes measuring energy efficiency, water and chemical use, and opportunities to recycle textile waste.

Identification of the Key Factors Influencing the Ecological Footprint and Opportunities for Optimisation

Identifying the key factors that influence the ecological footprint is an important step in the process of environmental analysis and management. There may be different factors that apply to specific industries or processes, but here are some of the general key factors:

- Energy consumption: The energy used during production, transport, use, and disposal of products is one of the main factors affecting the ecological footprint. Identifying energy-efficient methods and technologies can significantly reduce the footprint. Optimisation opportunities include using energy-saving electrical appliances, improving thermal insulation, using energy-efficient lighting and heating systems, and implementing processes to optimise energy operations.
- Water consumption: Water is another important factor to consider when evaluating the ecological footprint. Identifying methods to optimise water resources reduce losses, and reuse water can contribute to reducing the footprint. Optimisation occurs by using technologies to reduce water consumption, recycle and reuse water, and optimise wastewater treatment and disposal processes.
- Sources of greenhouse gas emissions: greenhouse gas emissions such as carbon dioxide (CO_2), methane (CH_4), and nitrogen oxide (NOx) have a significant impact on climate change. Identifying and reducing emissions from various sources, such as manufacturing, transportation, heating, and cooling, is an important goal in reducing the footprint.
- Waste management: Effective waste management, including recycling, re-engineering, and the use of secondary raw materials, is a key factor in reducing the environmental footprint. Identifying methods to reduce waste and move towards sustainable waste management systems is essential.
- Use of raw materials: The use of raw materials, including extraction, processing, and transportation, also has an important impact on the ecological footprint. Identifying sustainable sources of raw materials, optimising material flows, and reducing excess consumption can reduce the footprint. Optimisation opportunities include choosing materials with lower energy and water consumption during production, fewer emissions of harmful substances, and better degradability or recyclability.
- Innovation in processes: The research and implementation of innovative processes and technologies can lead to a significant reduction of the ecological footprint. For example, the development of green and sustainable production methods, the use of renewable energy sources, the development of processes for circularity and wear resistance of materials, as well as the application of eco-design principles, can contribute to reducing the footprint.

Researches

An author's study was carried out, which tracks CO_2 as a leading factor in environmental pollution. Statistical methods were used for data processing. Figure 3 tracks the progression of carbon emissions released from industrial processes.

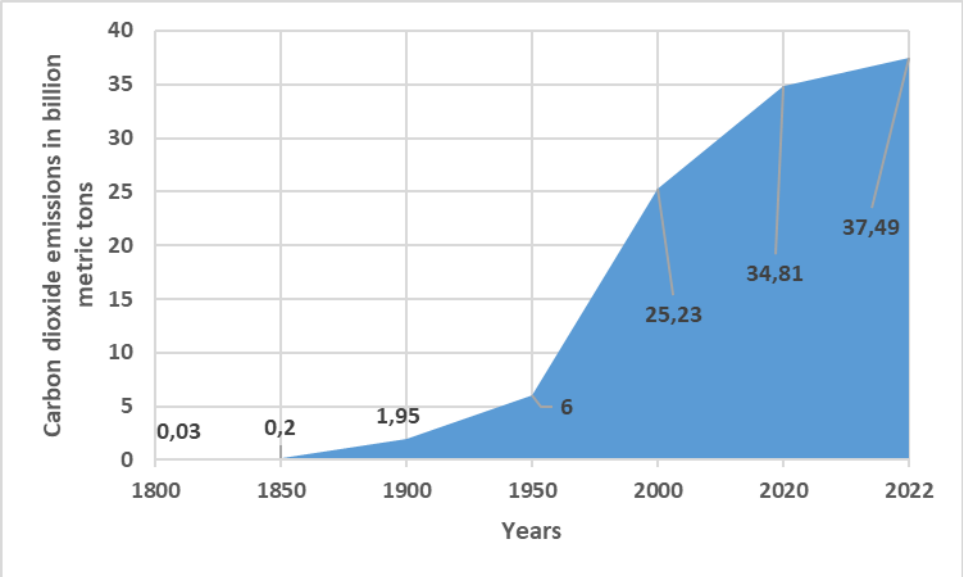

Figure 3. Levels of carbon dioxide emissions, released from industrial processes, in billion metric tons, (Author's research)

The dramatic increase in emissions with the onset and development of the industrial revolution is impressive. These processes are well supported in the scientific literature. CO_2 emissions are often linked to global warming and climate change, which are fundamental challenges for the world today. Therefore, today the world is undertaking efforts, including international agreements such as the Paris Agreement, to reduce emissions and limit climate change.

Nevertheless, the size of the population also has a significant role in determining the quantity of carbon emissions. There exists a robust and very significant association between pollution and population. The graphical representation of the dependence is depicted in Figure 4.

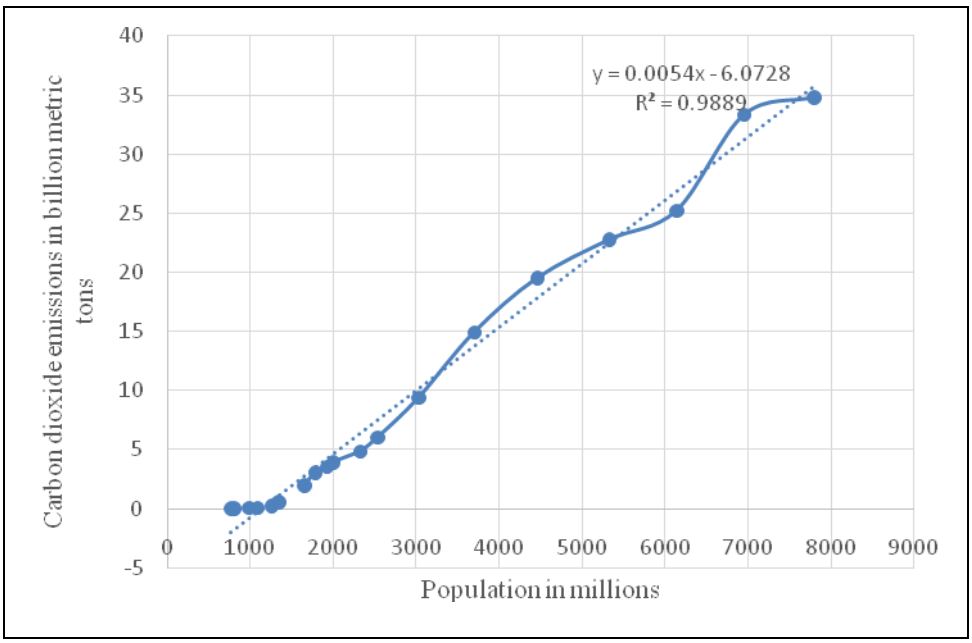

Figure 4. Correlation between carbon dioxide emissions and world population, (Author's research)

The equation illustrating the relationship and the coefficient of determination R^2=0.9889 are also shown. Based on this model, it is possible to make predictions regarding the projected pollution levels in the year 2050,

coinciding with an estimated global population of 9735 million individuals. According to the estimate, it is anticipated that carbon emissions would reach a value of 519.6388.

A larger population leads to increased energy consumption, requires larger production capacities and implies greater mobility, which in turn leads to higher levels of greenhouse gas emissions. In practice, population growth leads to an increase in energy consumption for heating, cooling, lighting, transportation, etc. In addition, increased consumption of food, goods and services also contributes to carbon emissions associated with agriculture, industry and transport. To reduce the carbon emissions associated with population growth, strategies for sustainable development and efficient use of resources are needed. (Global Footprint Network, 2017) This may include promoting energy efficiency in buildings, promoting renewable energy sources, improving public transport, moving towards more sustainable and ecological production and consumption models. In addition, education and public awareness play an important role in consciously reducing carbon emissions. Raising environmental awareness and promoting responsible consumption are essential to achieving a sustainable future.

Conclusion

The evaluation of the ecological footprint is essential for industrial processes, as it allows the identification of opportunities for optimisation and reduction of the footprint. By using methods and tools such as energy efficiency, waste and water management, sustainable material selection, and process innovation, industrial companies can reduce their negative impact on the environment and achieve sustainable practices. In turn, the integrated approach to life cycle analysis provides a complex and systematic methodology for assessing the ecological footprint of industrial processes. It includes consideration of all phases of the life cycle of a product or process, from raw material extraction to waste treatment, and applies quantitative assessment to various aspects such as greenhouse gas emissions, energy and water consumption, and air and water pollution. Identifying the key factors that influence the ecological footprint is of great importance in carrying out the assessment. This includes an analysis of energy efficiency, waste management, greenhouse gas emissions, and water resource use. Identifying these factors allows companies to focus on specific areas for improvement and implement targeted optimisation measures. The use of the integrated life cycle analysis approach in industrial environments has been applied in various industries and processes. For example, in the production of food products, an assessment of the ecological footprint of raw materials, production and packaging processes, as well as waste management, is carried out. In the field of electronics, life cycle analysis is used to assess the energy efficiency of devices, e-waste management, and the use of rare materials. The research done proves the correlation between the levels of CO_2 emissions with the world population and, in this context, the effectiveness of ecological footprint and life cycle assessment, which analyse in detail various aspects such as energy and material efficiency, greenhouse gas emissions, recycling, and others.

Scientific Ethics Declaration

The author declares that the scientific ethical and legal responsibility of this article published in EPSTEM journal belongs to the author.

Acknowledgements or Notes

* This article was presented as an oral presentation at the International Conference on Technology, Engineering and Science (www.icontes.net) held in Antalya/Turkey on November 16-19, 2023.

References

Bastianoni, S., Galli, A., Niccolucci, V., & Pulselli, R. M. (2006). *The ecological footprint of building construction*. UK: WIT press.

Bergmark, P., & Zachrisson, G. (2022). Towards considering planetary boundaries in life cycle assessments of ICT. *International Conference on ICT for Sustainability, ICT4S 2022* (pp.128-139). IEEE.

Bockin, D., Goffetti, G., Baumann, H., Tillman, A.M., & Zobel, T. (2022). Business model life cycle assessment: a method for analysing the environmental performance of business. *Sustainable Production and Consumption*, *32*(20), 112–124.

Chambers, N., Simmons C., & Wackernagel, M.(2004). *Sharing nature's interest: Ecological footprints as an indicator of sustainability.* London, Great Britain: Sterling Earthscan

Husain, D., Garg, P., & Prakash, R. .(2019). Ecological footprint assessment and its reduction for industrial food products. *International Journal of Sustainable Engineering*, *14*(1), 26-38.

Dimov, E., Bakyrdjieva, R., & Stratiev, N. (2020). The mining industry and the recycling of raw materials as an important element of the Bulgarian economy. *Journal of Mining and Geological Sciences*, *63*, 289-292.

Global Footprint Network (GFN) .(2017). Ecological wealth of nations. Retrieved from http://www.footprintnetwork.org/content/ documents/ecological_footprint_nations/ecological.html

Samani, P. (2023). Synergies and gaps between circularity assessment and life cycle assessment (lca). *Science of The Total Environment, 903,* 166611.

Schaubroeck, T., Schaubroeck, S., Heijungs, R., Zamagni, A., Brandao, M., & Benetto, E. (2021). Attributional & consequential life cycle assessment: definitions, conceptual characteristics and modelling restrictions. *Sustainability, 13*(13), 1–47.

Seol, Y., Seungjoo, L., Jong-Young, L., Jung-Geun, H., & Gigwon, H. (2021). Excavation method determination of earth-retaining wall for sustainable environment and economy: Life cycle assessment based on construction cases in Korea. *Sustainability, 13*(5), 2974.

Vanham, D., Leip, A., Galli, A., Kastner, T., Bruckner, M., Uwizeye, A., van Dijk, K., Ercin, E., Dalin, C., Brandao, ˜ M., Bastianoni, S., Fang, K., Leach, A., Chapagain, A., Van der Velde, M., Sala, S., Pant, R., Mancini, L., Monforti-Ferrario, F., CarmonaGarcia, G., Marques, A., Weiss, F., & Hoekstra, A.Y. (2019). Environmental footprint family to address local to planetary sustainability and deliver on the SDGs. *Science of the Total Environment, 693.* 133642.

Vargas Gonzalez, M., Witte, F., Martz, P., Gilbert, L., Humbert, S., Jolliet, O., van Zelm, R., & L'Haridon, J. (2019). Operational life cycle impact assessment weighting factors based on planetary boundaries: applied to cosmetic products. *Ecological Indicators*, *107*(2), 105498.

Ventura, A. (2022). Transition life cycle assessment: A new method to face ecological transition. *Frontiers in Sustainability, 3.* 801668.

Wackernagel, M., & Rees, W. (1996). *Our ecological footprint: Reducing human impact on the earth*. Gabriola Island, British Columbia: New Society.

Author Information

Vessela Petrova
University of Mining and Geology "St. Ivan Rilski"
Sofia, Bulgaria
Contact e-mail: *vessela.petrova@mgu.bg*

To cite this article:

Petrova, V. (2023). Assessment of the ecological footprint of industrial processes: An integrated approach to life cycle analysis. *The Eurasia Proceedings of Science, Technology, Engineering & Mathematics (EPSTEM), 26,* 67-74.

The Eurasia Proceedings of Science, Technology, Engineering & Mathematics (EPSTEM)
ISSN: 2602-3199

The Eurasia Proceedings of Science, Technology, Engineering & Mathematics (EPSTEM), 2023

Volume 26, Pages 75-85

IConTES 2023: International Conference on Technology, Engineering and Science

Numerical Study of the Thermal and Hydraulic Characteristics of the SiO_2 –Water Nanofluid through a Backward-Facing Step

Rahima Benchabi
University of Mentouri Brothers

Ahsene Lanani
University of Mentouri Brothers

Abstract: The work of this paper is devoted to the two-dimensional numerical investigation of the turbulent forced convection through backward-facing step. Two cases are taken into account. For the first, the bottom wall is smooth; but for the second case, it is corrugated with a triangular base containing ten corrugations. A uniform heat flux is imposed on the bottom wall. A flow of a nanofluid consisting of silicon dioxide SiO_2 nanoparticles dispersed in a base fluid (water) flows through this step.The flow equations were discretized by the finite volume method. For modeling turbulence, the K-ε-RNG model was applied to analyze Reynolds number effect, the volume fraction and the size of the particle. Numerical simulations were conducted for various Reynolds between 10,000 and 40,000; volume fractions of nanoparticles which vary from 0 to 5% and particle diameter dp equal to 30; 50 and 70 nm. We noted that the obtained findings are in good conformity with those of the literature.

Keywords: Forced convection, Turbulent flow, Backward-facing step channel, Corrugated channel, SiO_2 – water Nanofluid.

Introduction

The improvement of heat transfer is a key objective in several applications, and to do this, a large number of researchers have conducted a multitude of numerical and experimental tests relating to the description of the phenomena governing the modes of heat transfer. Chronologically, ideas for improvement began to affect mainly the geometry of systems at the macroscopic scale, and the physico-chemical nature of convective media fields. Attempts at improvement have sometimes touched on the microscopic aspect of the process. But the emergence and rapid expansion of nanoscience and nanotechnology in the second half of the 20th century meant that convection became a major part of this new trend, and thus another aspect of improvement. It is at the nanometric dimension of the material, of the convective medium, that much of the recent work has focused on developing a more efficient heat transfer fluid to reduce energy consumption. Among the topical solutions found, note that of nanofluids (Choi & Eastman, 1995). These nanofluids are colloidal solutions formed by particles of nanometric size (1 to 100 nm), with metal bases or metal oxides suspended in a basic liquid (pure water; E-G; oils; etc…). The presence of nanoparticles in base fluids changes their thermal conductivity and viscosity. A great deal of work has been carried out in this area by many authors. They have experimentally and numerically studied nanofluids; convection and heat exchange in various corrugated channels.

Hilo et al. (2020) have numerically investigated a turbulent forced convection flow in a straight and wavy channel using three bases (zigzag, triangular and trapezoidal) on two backward-facing step

channel with pure water as the working fluid. The authors investigated the effects of corrugated design and geometric parameters like the pitch of the channel, amplitude and Re number on velocity vectors, temperature contours, pressure drop and mean Nu number. The results indicate that the combination of a wavy wall and a backward-facing step increases Nu by up to 62% at a Reynolds number of 5000, with a slight increase in pressure drop. This study also showed that the greatest enhancement in heat transfer rate compared to a backward-facing step could be achieved using a trapezoidal wavy bottom with an amplitude height and channel pitch of 4 mm and 20 mm, respectively.

A numerical study of laminar flow by forced convection in an isothermally heated wavy channel with a triangular base, utilizing Cu-water nanofluid, has been conducted (Ahmed et al., 2011). Simulations are performed for volume fractions varying from 0 to 5% and Re from 100 to 1000. The findings reveal that the average Nu number rises with the Re number and nanoparticles volume fractions; but this increase is associated with an increase in the pressure drop. It was also found that the use of nanofluid in wavy channels can be suggested as an appropriate method for achieving enhanced heat exchange efficiency, which may lead to the design of more compact heat exchangers. In (Ahmed et al., 2013(a)), the authors have performed a numerical simulation of the laminar forced convection heat exchange of Cu-water nanofluid in a trapezoidal corrugated channel. They were interested in the effect of concentration in the range of 0% to 5%, the Reynolds number varying between 100 and 700 and the geometric parameters effect such as amplitude and wavelength of the channel corrugation on the pressure drop and the mean Nu. Numerical findings show that the mean Nusselt value increases with nanoparticle volume fraction, Reynolds number and amplitude of the corrugated channel, while the pressure drop also increases. In addition, as the wavelength of the wavy channel rises, the mean Nu decreases and the pressure drop increases. These findings also reveal that the utilization of the copper-water nanofluid in place of conventional fluids using the trapezoidal channel can lead to a further improvement in heat exchange. It may therefore be possible to design more compact, thermally efficient heat exchangers. Ahmad et al. (2013b) considered a numerical study of a forced convection laminar flow using the Al_2O_3-water nanofluid in a triangular channel. The study was conducted for Re ranging from 100 to 800, nanoparticle volume fractions between 0% and 5% and diameters equal to 30, 50 and 70 nm. The findings showed that the Nu increases with the Re and volume fraction of the nanoparticles, but that the pressure drop also increases. Similarly, as nanoparticle size reduces, the Nu increases, while nanoparticle size has no effect on pressure drop. In (Ahmed et al., 2014), the authors have investigated heat exchange numerically in a straight, wavy channel with three bases (trapezoidal, triangular and sinusoidal) using the CuO-water nanofluid. These researchers examined the effect of concentration in the 0-5% range, with Re in the 100-800 range. The findings indicate an improvement in the heat exchange with the increased nanoparticles volume fraction of and increased Re for all shapes of the channel. This study also showed that the trapezoidal channel offers the highest Nu, followed by the sinusoidal, then the triangular and finally the straight channel.. Furthermore, dimensionless pressure drop rises with nanoparticle volume fraction, while it decreases with increasing Re for all shapes of the channel. Khoshvaght-Aliabadi (2014) has numerically investigated forced convection heat transfer and flow in an undulating sinusoidal channel by using the Al_2O_3-water nanofluid. The author examined the influence of geometric factors such as channel height and length, the wavelength, the amplitude of the corrugations, the angles of phase shift for different Reynolds numbers varying from 6000 to 22000 and volume fractions of the nanoparticles varying from 0% to 4%. The findings indicate that nanofluid flow inside sinusoidal channels provides greater values of the Nu relatively to the base fluid, while the values obtained for the nanofluid friction factor and the base fluid are practically the same. Ahmad et al. (2015) conducted an experimental investigation followed by a numerical study of convective heat exchange flow using a SiO2-water nanofluid with three wavy channel shapes (trapezoidal, sinusoidal and straight channel) for Re numbers ranging from 400 to 4000 and different volume fractions equal to 0%, 0.5% and 1%. Numerical and experimental results revealed that the average Nu increased as the nanoparticle volume fraction increased, and that the pressure drop also increased. The authors also found the first channel gave the greatest heat exchange, then the second and finally the third. In (Selimefendigil & Oztop, 2017), the authors have numerically analyzed the laminar forced convection heat exchange of Cu-water nanofluid in a V-shaped channel via a backward-facing step. The authors studied the influences of Re, wave length and height, nanoparticle volume fraction, flow pulsation amplitude and frequency, and heat exchange. The findings demonstrate that the mean Nu rises with Re, as well as with corrugation length and height. The mean Nu increases with the addition of nanoparticles, although the degree of improvement is related to the volume fraction of nanoparticles. The forced convection and turbulent

flow characteristics of various kinds of nanoparticles (Al_2O_3, CuO, SiO_2, ZnO) and water as a basic fluid in a straight channel and two configurations of trapezoidal symmetry and zigzag shape have been investigated (Ajeel et al., 2018). Simulations are performed for volume fractions ranging from 0% to 8%; particle diameter varies from 20 nm to 80 nm and Re between 10000 and 30000. The results show that the best nanofluid was SiO_2, monitoring of Al_2O_3, ZnO and CuO-water and that also the symmetry profile of the trapezoidal channel has a significant effect on thermal efficiency in comparison with the zigzag profile. Ajeel et al. (2019a) have carried out a simulation of turbulent flow by forced convection using the ZnO-water nanofluid in a wavy channel with various rib shapes (semicircular, trapezoidal and house). Simulations are carried out for Re in the range 10,000 - 30,000 and volume fractions varying from 0% to 8%. The findings obtained by the study indicate that the Nu and the pressure drop are 1 to 4 times higher for the wavy channels than for the straight channel and that also among wavy channels, the trapezoidal offers the best thermal efficiency, followed by semicircular and triangular. Experimental and numerical investigations were conducted by Ajeel et al., (2019b). The authors focused the improvement of heat exchange in various shapes of wavy channels (semicircular, trapezoidal and straight) using Al_2O_3 as nanoparticles for Re varying from 10000 to 30000 and volume fractions of the Al_2O_3 nanofluid of 0%, 1% and 2%. The results showed that the Nu, the pressure drop for all mid-channel shapes, increases with increasing Re and nanoparticle volume fractions. The research also showed that the new type of trapezoidal corrugated channel is experimentally and numerically confirmed as the best choice for obtaining thermal enhancement in heat exchange devices. Ajeel et al. (2020) studied the heat exchange characteristics of SiO_2-water nanofluid flowing through a house-shaped corrugated channel under a uniform heat flux equal to $10\,kW/m^2$ and Re varying from 10000 to 30000. In their study, the nanoparticle concentration varies from 0% to 8%. The effect of geometric parameters, involving height-to-width ratio (h/W), height-to-length ratio (p/L) and ratio (e/r) on temperature and flow characteristics were the focus of the study. The results demonstrated that increasing the Re and the height/width ratio of the wavy channel had a marked influence on enhancing the mean Nu and the pressure drop. Also, when p/L increases the heat transfer decreases. Mohammed et al. (2016) conducted numerical study on laminar flow and heat exchange of distilled SiO_2-water nanofluid through a wavy channel backward facing step, using the finite difference method for a range of Re varying between 100 and 1500 and a volume fraction of nanoparticles from 0 to 1%. The findings showed that the Nu and the coefficient of friction increase when the amplitude of the wavy channel increases. The study also demonstrated that as the volume fraction of nanoparticles increases, the Nu also rises considerably, with only a modest increase in the friction coefficient.

Our study involves the numerical simulation of two-dimensional forced convection turbulent flow using the Ansys-Fluent computer code, on the one hand, and the K-ε-RNG turbulence model, on the other, through a smooth, then undulating, downward step. The bottom surface is exposed to a constant flow of heat, during a turbulent flow using water as the base fluid for a nanofluid in which spherical nanoparticles of SiO_2 are dispersed at different diameters ($dp = 30$, 50 and 70 nm) and different volume fractions equal to 0%; 1%; 3% and 5%. The principal objective of our research is to demonstrate the influence of nanofluids on thermal efficiency in forced convection, for Reynolds numbers of 10,000, 20,000, 30,000 and 40,000.

Mathematical Modeling

Physical Model

The investigated physical model is depicted in figures 1 and 2. It is a symmetrical, triangular-based wave channel with total channel length, $L_{Total} = 0.2\,m$, including the heights, Hmin and Hmax. The wavelenght of the corrugation is denoted by λ. In addition, the length of the upstream and downstream undulations is $L = 0.04\,m$.

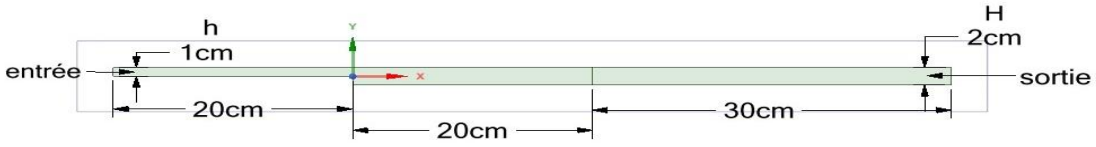

Figure 1. Smooth channel with backward-facing step

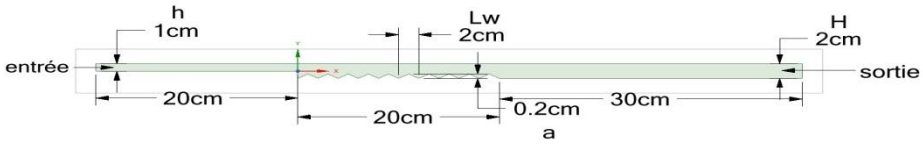

Figure 2. Triangular based corrugated channel with backward-facing step

Flow Equations

The nanofluid under consideration is supposed to be Newtonian and incompressible; viscous dissipation is negligible ($\Phi = 0$) and the fluid's physical characteristics (ρ, u, k, C_p) are constant. The flow equations can be formulated as:

Continuity equation

$$\frac{\partial \bar{U}}{\partial x} + \frac{\partial \bar{V}}{\partial y} = 0 \tag{1}$$

x - Momentum equation

$$\bar{U}\frac{\partial \bar{U}}{\partial x} + \bar{V}\frac{\partial \bar{U}}{\partial y} = -\frac{1}{\rho_{eff}}\frac{\partial \bar{P}}{\partial x} + \frac{\partial}{\partial x}\left[2(\nu_{eff} + \nu_t)\frac{\partial \bar{U}}{\partial x}\right] + \frac{\partial}{\partial y}\left[(\nu_{eff} + \nu_t)\left(\frac{\partial \bar{V}}{\partial x} + \frac{\partial \bar{U}}{\partial y}\right)\right] \tag{2}$$

y - Momentum equation

$$\bar{U}\frac{\partial \bar{V}}{\partial x} + \bar{V}\frac{\partial \bar{V}}{\partial y} = -\frac{1}{\rho_{eff}}\frac{\partial \bar{P}}{\partial y} + \frac{\partial}{\partial y}\left[2\left(\nu_{eff} + \nu_t\right)\frac{\partial \bar{V}}{\partial y}\right] + \frac{\partial}{\partial x}\left[\left(\nu_{eff} + \nu_t\right)\left(\frac{\partial \bar{V}}{\partial x} + \frac{\partial \bar{U}}{\partial y}\right)\right] \tag{3}$$

Energy equation

$$\bar{U}\frac{\partial \bar{T}}{\partial x} + \bar{V}\frac{\partial \bar{T}}{\partial y} = \frac{\partial}{\partial \mathrm{x}}\left[\left(\frac{\nu_{eff}}{Pr} + \frac{\nu_t}{\sigma_t}\right)\frac{\partial \bar{T}}{\partial \mathrm{x}}\right] + \frac{\partial}{\partial \mathrm{y}}\left[\left(\frac{\nu_{eff}}{Pr} + \frac{\nu_t}{\sigma_t}\right)\frac{\partial \bar{T}}{\partial \mathrm{y}}\right] \tag{4}$$

Equation l'énergie cinétique turbulente.

$$\bar{U}\frac{\partial k}{\partial x} + \bar{V}\frac{\partial k}{\partial y} = \frac{\partial}{\partial \mathrm{x}}\left[\left(\nu_{eff} + \frac{\nu_t}{\sigma_k}\right)\frac{\partial k}{\partial \mathrm{x}}\right] + \frac{\partial}{\partial \mathrm{y}}\left[\left(\nu_{eff} + \frac{\nu_t}{\sigma_k}\right)\frac{\partial k}{\partial \mathrm{y}}\right] + P_k - \varepsilon \tag{5}$$

Equation taux de dissipation de l'énergie cinétique.

$$\bar{U}\frac{\partial \varepsilon}{\partial x} + \bar{V}\frac{\partial \varepsilon}{\partial y} = \frac{\partial}{\partial \mathrm{x}}\left[\left(\nu_{eff} + \frac{\nu_t}{\sigma_\varepsilon}\right)\frac{\partial \varepsilon}{\partial \mathrm{x}}\right] + \frac{\partial}{\partial \mathrm{y}}\left[\left(\nu_{eff} + \frac{\nu_t}{\sigma_\varepsilon}\right)\frac{\partial \varepsilon}{\partial \mathrm{y}}\right] + (C_{\varepsilon 1}(P_k) - C_{\varepsilon 2}\varepsilon)\frac{\varepsilon}{k} \tag{6}$$

Where $P_k = \nu_t\left(\frac{\partial \overline{U_i}}{\partial x_j} + \frac{\partial \overline{U_j}}{\partial x_i}\right)\frac{\partial \overline{U_i}}{\partial x_j}$

Dimensionless Numbers

Reynolds Number

$$Re = \frac{UD_h}{\nu} \tag{7}$$

Nusselt Number

$$Nu = \frac{hD_h}{K} \tag{8}$$

Boundary Conditions

- Inlet of the channel

A velocity is imposed at the inlet of the channel, given by:

$$U_{eff} = \frac{Re \times \mu_{eff}}{D_h \times \rho_{eff}} \quad (9)$$

A constant temperature is subject at the inlet $T_{eff} = 300°K$

Turbulent kinetic energy k and turbulent dissipation rate ε are expressed as follows:

$$k = \frac{3}{2} U^2 I^2 \quad (10)$$

Where $I = 0.16 Re^{-1/8}$ and $Re = \frac{UD_h}{\nu}$

$$\varepsilon = C_\mu^{3/4} \frac{k^{3/2}}{l} \quad (11)$$

Where $l = 0.07L$ and $L = D_h$

- Outlet the of channel

$\frac{\partial U}{\partial x} = 0$; $\frac{\partial V}{\partial x} = 0$; $\frac{\partial T}{\partial x} = 0$; $\frac{\partial \mathrm{k}}{\partial \mathrm{x}} = 0$; $\frac{\partial \varepsilon}{\partial \mathrm{x}} = 0$

A heat flux $\varphi = 4000 w/m^2$ is imposed on the bottom wall of the backward-facing step.

Property of the Nanofluid

The thermo-physical characteristics of the SiO2-Water nanofluid employed in this research are:

Density

$$\rho_{nf} = (1 - \varphi)\, \rho_f + \varphi \rho_P \quad (12)$$

Heat Capacity

Model of Xuan & Roetzel (2000):

$$(\rho Cp)_{nf} = (1 - \varphi)\, (\rho Cp)_f + \rho Cp)p \quad (13)$$

Effective Dynamic Viscosity

Model of Corcione (2010):

$$\frac{\mu_{nf}}{\mu_f} = \frac{1}{1 - 34{,}87 (\frac{d_p}{d_f})^{-0.3} \varphi^{1.03}} \quad (14)$$

Where d_p is the diameter of the SiO_2 particle and df is the diameter of the water.

Effective Thermal Conductivity

Model of Maxwell (1882):

$$K_{eff} = K_{statistique} + K_{brownien} \quad (15)$$

Where: $$K_{statistique} = \frac{K_p+2K_{bf}+2\phi(K_p-K_{bf})}{K_p+2K_f-\phi(K_p-K_{bf})}K_{bf} \quad (16)$$

$$K_{brownien} = 5\times10^4\beta\phi\rho_{bf}Cp_{bf}\sqrt{\frac{K_BT}{\rho_p d_p}}f(T,\phi) \quad (17)$$

$$f(T,\phi) = (2.8217\times10^{-2}\phi + 3.917\times10^{-3})\left(\frac{T}{T_0}\right) + (-3.0669\times10^{-2}\phi - 3.391123\times10^{-3})$$

Numerical Modeling

The flow equations and heat exchange are solved by the finite volume method. In order to simulate and calculate the fluid flow properties of the studied problem, the CFD calculation code ANSYS FLUENT 2019 was used. This code offers extensive solutions for the most complicated geometries. The precision and stability of the results of our simulation depends on the quality of the mesh, so a mesh independence test has been carried out for different numbers of nodes.

Discretization Schemes

The discretization schemes used in this study are presented in the table1.

Table1. Discretization schemes

Variable	Nature of scheme
Pressure	Standard
Velocity and pressure coupling	Simple
Momentum Quantity	Second order upwind
Energy	Second order upwind

Mesh Effect and Validation

Mesh Effect

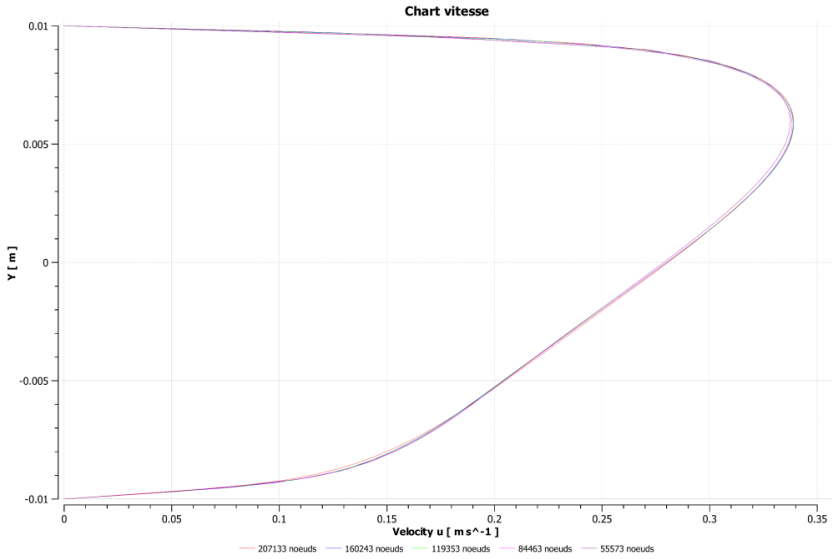

Figure 03. Velocity profiles for different mesh sizes, at Re=10000 and ϕ=0% at station x=10cm.

To demonstrate the influence of the mesh size on the solution, five mesh sizes were examined 55573; 84463; 119353; 160243 and 207133 for Re = 10000 and $\phi = 0\%$. The effect of the nodes number on the solution is expressed by the profile of the axial velocity. Figure 3 illustrates the change in the axial component of the velocity. It is noticed that the curves of the various meshes have an identical pace and that the profiles not dependent on the number of nodes.So our choice fell on mesh 4; to save time and preserve computer capacity. Note also that this mesh captures better the dynamic and thermal boundary layers near solid walls.

Validation of the Results

The numerical simulation validation is required to verify the precision of the numerical findings obtained by the ANSYS FLUENT 2019 calculation code. Our results were compared with the Dittus Boelter correlation. Figure 4 shows the change in the average Nu versus Re for a smooth channel filled with water. It can be seen that average Nusselt values rise with Re, and that there is also good concordance between our findings and the calculation by the Dittus Boelter correlation.

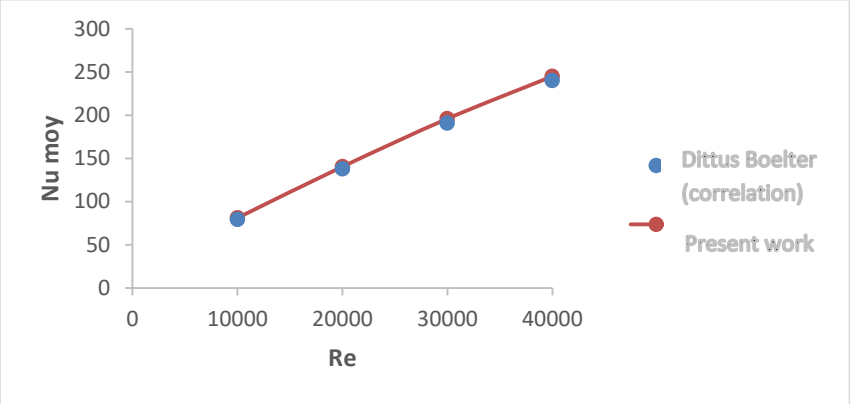

Figure 04. Variation of average Nu versus Re

Results Discussion

This section is devoted to showing the findings obtained by numerical simulation using the Ansys-Fluent computer code, where the impact of Re, volume fraction and particle size will be studied.

Reynolds Number Effect

The pressure drop of the nano-fluid SiO_2 and water for different Re in the smooth and corrugated backward facing step is shown in Figure 5 (a) and (b). These figures show an increase in pressure drop with rising Re.. This is caused by an increase in the average velocity, which translates into a greater velocity gradient near the walls, and hence into greater shear stress. We also note that the pressure drop values are very high for SiO_2, especially for Re values of 30000 and 40000.

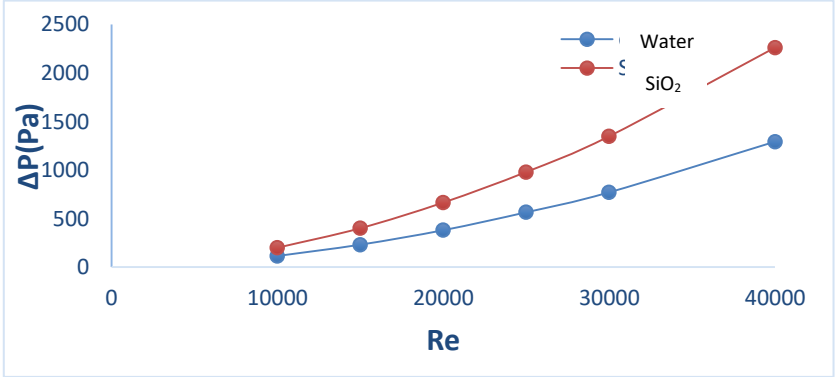

(a)

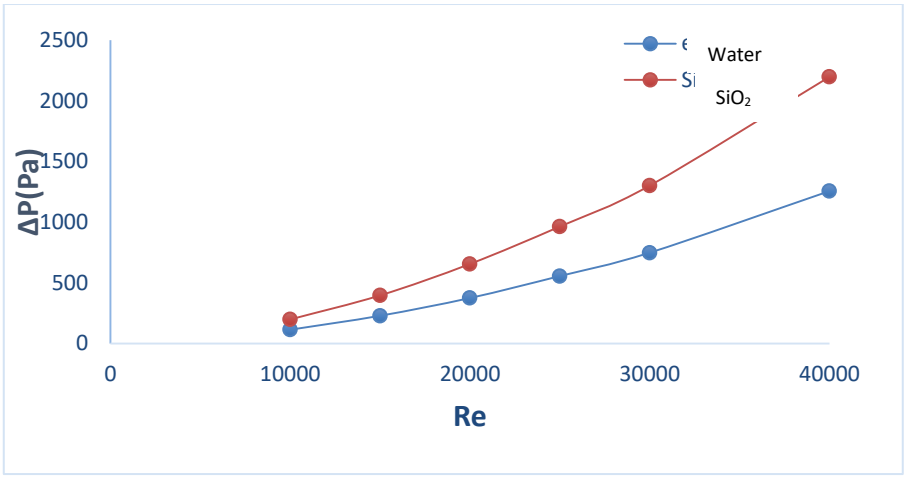

(b)

Figure 5. Pressure drop versus Reynolds : (a) Smooth backward facing step, (b) Corrugated backward-facing step

Figure 6 shows the change of the average Nu versus Re for water and SiO_2 with volume fraction equal to 3% and diameter $dp = 30nm$. We can see that the Nu rises proportionally with the Re due to the improved fluid particle motion, where we can clearly see that the Nu values are high for $Re = 40000$ compared to those for Re =10000. We can therefore say that the rate of heat exchange is improved.. These figures also show that the mean Nu for SiO_2 is higher than for water in both the smooth and corrugated backward facing step cases.

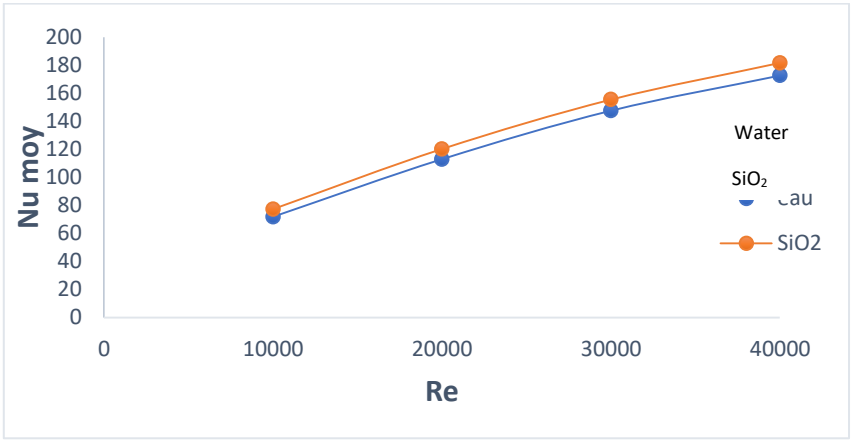

(a)

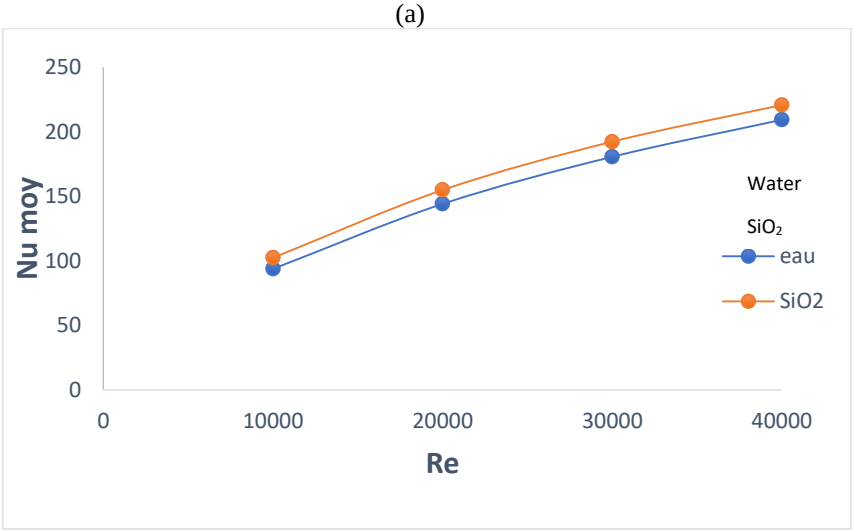

(b)

Figure 6. Mean Nu versus Re

Size of the Particle Effect

Figure 7 illustrates the influence of particle diameter on the average Nu versus Re with various particle diameters ($dp = 30nm$, 50nm and 70nm) and $\phi = 3\%$, in a smooth and corrugated channel with a triangular base. In the case of the smooth channel, the Nu rises with increasing Re and decreasing particle size; the Nusselt number values are much higher for $dp = 30nm$ than those corresponding to $dp = 30nm$ and 70nm. This is due to the increased exchange surface, nanoparticle aggregation and stronger Brownian motion for smaller nanoparticle diameters, leading to higher nanofluid thermal conductivity. The larger the nanoparticles, the weaker this Brownian motion will be, as they will be more difficult to move due to their greater inertia, and will have a lower displacement speed and therefore more efficient heat transfer when the particle size decreases. The same applies to the corrugated channel, but at higher values.

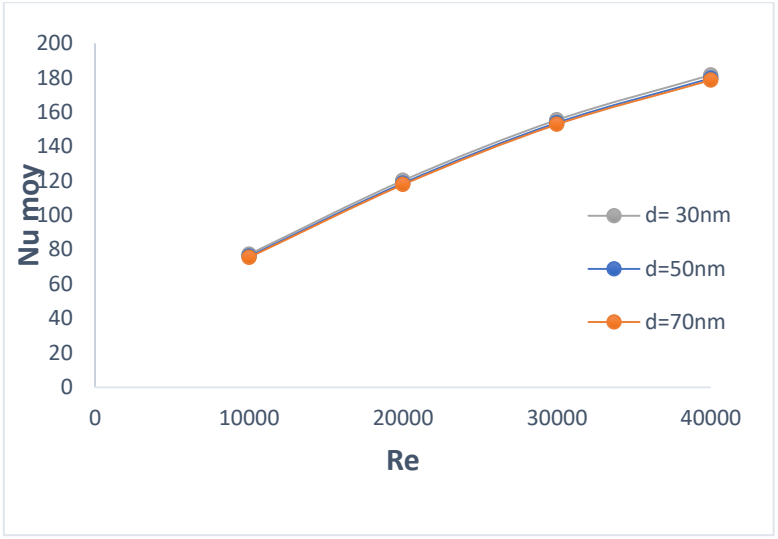

(a)

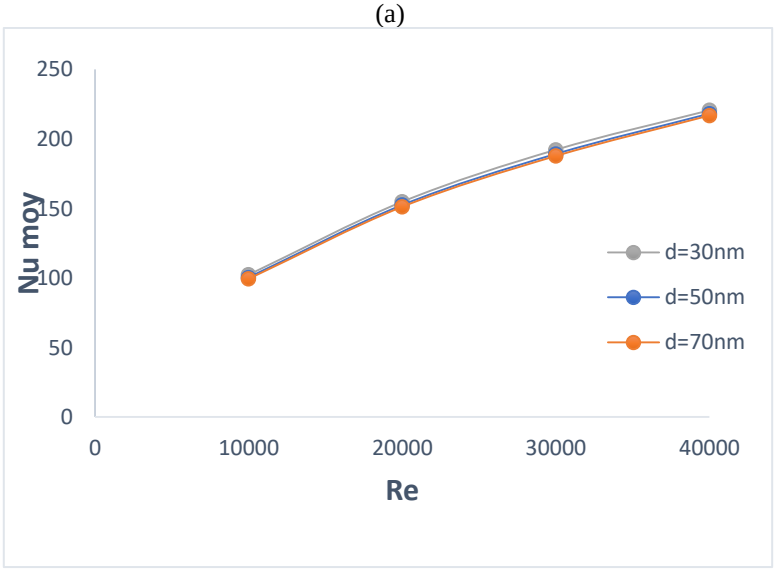

(b)

Figure 7. Average Nu for various particle diameters with $\phi = 3\%$: (a) Smooth backward facing step, (b) corrugated backward facing step

Conclusion

In this work, we have numerically investigated the two-dimensional heat exchange by turbulent forced convection for water and the SiO_2-water nanofluid inside a smooth, corrugated channel with a triangular base whose bottom wall is subjected to a constant heat flow. The effect of Re and oxide particle size on thermal and hydraulic behavior through the smooth, corrugated channel with two backward-facing steps has been investigated. The obtained findings show that:

- An increase in Reynolds number results in an increase in Nu and pressure drop.
- The SiO_2-water nanofluid with the 3% fraction provides the best heat transfer enhancement, and oxide nanoparticles offer a high performance for increasing the Nu compared with water.
- Nu is affected by Re, an increase in the latter leads to a rise in the Nu, and the corrugated channel provides the highest Nu values compared with the smooth channel.
- Particle diameter has a significant influence on the Nu. Smaller particle diameters tend to increase both Nusselt number and pressure drop.

Scientific Ethics Declaration

The authors declare that the scientific ethical and legal responsibility of this article published in EPSTEM journal belongs to the authors.

Acknowledgements or Notes

* This article was presented as an poster presentation at the International Conference on Technology, Engineering and Science (www.icontes.net) held in Antalya/Turkey on November 16-19, 2023.

* This research was partially supported by the Algerian MESRS.
Project research N°: A11N01UN250120200005.

References

Ahmed, M. A., Shuaib, N. H., Yusoff, M. Z., & Al - Falahi, A. H. (2011). Numerical investigations of flow and heat transfer enhancement in a corrugated, channel using nanofluid. *International Communications in Heat and Mass Transfer*, *38*(10), 1368–1375.

Ahmed, M. A., Yusoff, M. Z., & Shuaib, N. H. (2013). Effects of geometrical parameters on the flow and heat transfer characteristics in trapezoidal-corrugated channel using nanofluid. *International Communications in Heat and Mass Transfer*, *42*, 69–74.

Ahmed, M. A., Yusoff, M. Z., Ng, K. C., & Shuaib, N. H. (2014). Effect of corrugation profile on the thermal–hydraulic performance of corrugated channels using CuO–water nanofluid. *Case Studies in Thermal Engineering*, *4*, 65–75.

Ahmed, M. A., Yusoff, M. Z., Ng, K. C., & Shuaib, N. H. (2015). Numerical and experimental investigations on the heat transfer enhancement in corrugated channels using SiO_2–water nanofluid. *Case Studies in Thermal Engineering*, *6*, 77–92.

Ahmed, M. A., Yusoff, M. Z., Shuaib, N. H., & Ng, K. C. (2013). A numerical study of laminar forced convection flow of Al_2O_3-water nanofluid in triangular-corrugated channel. *IOP Conference Series: Earth Environmental Science*, *16*(1). p. 012149), IOP Publishing.

Ajeel, R. K., Salim, W.S-I.W. & Hasnan, K. (2019). Experimental and numerical investigations of convection heat transfer in corrugated channels using alumina nanofluid under a turbulent flow regime. *Chemical Engineering Research and Design*, *148*, 202–217.

Ajeel, R. K., Salim, W.S-I.W. & Hasnan, K. (2020). Numerical investigations of heat transfer enhancement in a house shaped corrugated-channel: Combination of nanofluid and geometrical parameters. *Thermal Science and Engineering Progress*, *17*, 100376.

Ajeel, R. K., Salim, W.S-I.W., & Hasnan, K. (2018). Thermal and hydraulic characteristics of turbulent nanofluids flow in trapezoidal-corrugated channel: Symmetry and zigzag shaped. *Case Studies in Thermal Engineering*, *12*, 620–635.

Ajeel, R. K., Salim, W.S-I.W., & Hasnan, K. (2019). Thermal performance comparison of various corrugated channels using nanofluid: Numerical study. *Alexandria Engineering Journal*, *58*, 75–87.

Choi, S., & Eastman, J. A. (1995). *Enhancing thermal conductivity of fluids with nanoparticles*. Argonne National Laboratory, Lemont.

Corcione, M. (2010). Heat transfer features of buoyancy-driven nanofluids inside rectangular enclosures differentially heated at the sidewalls. *International Journal of Thermal Sciences*, *49*, 1536-1546.

Hilo, A. K., Abu Talib, A., & Iborra, A. A. (2020). Effect of corrugated wall combined with backward-facing step channel on fluid flow and heat transfer. *Energy*, *190*, 116294.

Khoshvaght-Aliabadi, M. (2014). Influence of different design parameters and Al_2O_3-water nanofluid flow on heat transfer and flow characteristics of sinusoidal-corrugated channels. *Energy Conversion and Management, 88,* 96–105.

Maxwell, J. C. (1882). *A treatise on electricity and magnetism* (2nd ed.). Oxford, UK: Clarendon Press.

Mohammed, K. A., Abu Talib, A. R., Abdul Aziz, N., & Ahmed, K. A. (2016). Three dimensional numerical investigations on the heat transfer enhancement in a triangular facing step channels using nanofluid. *Materials Science and Engineering, 152. No. 1,* p. 012057. IOP Publishing.

Selimefendigil, F., & Oztop, H. F. (2017). Forced convection and thermal predictions of pulsating nanofluid flow over a backward facing step with a corrugated bottom wall. *International Journal of Heat and Mass Transfer, 110,* 231–247.

Xuan, Y., & Roetzel, X. (2000). Conceptions for heat transfer correlation of nanofluids. *International Journal of Heat Mass Transfer, 43,* 3701–3707.

Author Information

Rahima Benchabi
University of Mentouri Brothers
Constantine 1, 25000, Algeria
Contact e-mail : *benchabi.rahima@umc.edu.dz*

Ahsene Lanani
University of Mentouri Brothers
Constantine 1, 25000, Algeria

To cite this article:

Benchabi, R., & Lanani, A. (2023). Numerical study of the thermal and hydraulic characteristics of the SiO_2 - water nanofluid through a backward-facing step. *The Eurasia Proceedings of Science, Technology, Engineering & Mathematics (EPSTEM), 26,* 75-85.

The Eurasia Proceedings of Science, Technology, Engineering & Mathematics (EPSTEM)
ISSN: 2602-3199

The Eurasia Proceedings of Science, Technology, Engineering & Mathematics (EPSTEM), 2023

Volume 26, Pages 86-92

IConTES 2023: International Conference on Technology, Engineering and Science

Effect of Slag on the Porosity and Microstructure of HPC Reinforced with Hybrid Steel Fiber

Aldjia Boutiba
University of Tizi Ouzou

Rabah Chaid
University of Boumerdes

Laurent Molez
Laboratory of Civil Engineering and Mechanics, INSA Rennes

Abstract: Due to their structural and economic performance, high performance metal fiber concretes are increasingly used in construction, but with the addition of metal fibers, workability decreases as the amount of fibers added increases. In order to improve workability, a larger quantity of fines should be used than for ordinary concrete. The use of granulated slag reduces the amount of clinker needed to make cement. It is considered that granulated slag improves the workability of concrete. According to Manai, this is due to the very low rates of water adsorption by the granulated slag grains at the start of mixing. Also, the addition of granulated slag has a positive effect on the porosity, but also on the microstructure of the hydrates. These two characteristics are factors determining the compressive strength and durability of the cement paste. The aim of this study is to define the effect of blast furnace slag on the porosity and microstructure of high performance fibre-reinforced concrete. The results of SEM and DRX observation of the microstructure of the concrete samples show that the addition of ultra-fine granulated slag resulted in a relative improvement in porosity and microstructure.

Keywords: Characteristics, Fibers, HPC, Slag,

Introduction

The characteristics of the microstructure, that is to say the total porosity and the distribution of the pore sizes, but also the microstructure of the hydrates, are factors determining the compressive strength and the durability of the cement paste (Aïtcin, 2001). The porosity may be connected or occluded, and the pore size distribution may vary widely. These different parameters influence the permeability of concrete.

In recent years, high performance concretes (HPC) have been used extensively worldwide. With HPC, it is possible to build with less formwork, less concrete to place and less reinforcement than with ordinary concrete (Escadeillas,2006), (Ezeldin & Balaguru, 1982). With the increase in compressive strength, the HPC becomes less ductile or more fragile. The latter leads to design and dimensioning problems for certain types of structures. The most evoked track in the literature to overcome this weakness in tensile behavior is the addition of metal fibers to the concrete formulation (Rossi et al., 1987; Swam & Mangat, 1974).

The change in the rheological behaviour of fresh concrete when fibres are added to its matrix is an important factor. For a given matrix (paste and aggregates), workability decreases as the amount of fibre added increases. To improve workability, a larger quantity of fines (sand and cement) should be used than for ordinary concrete

- Selection and peer-review under responsibility of the Organizing Committee of the Conference

(Feldman,1983). The presence of fly ash or granulated slag reduces the size of the largest pores. Indeed the Pozzolanic reactions lead to the formation of secondary CSH and reduce porosity, which is good for durability (Mindess**,** 1984). The presented work is achieved at the laboratory of civil engineering, mechanical engineering (materials) of INSA-Rennes, France. The purpose of our study is to determine the porosity and microstructure of High performance concrete reinforced with a mixture of short fibers and fibers with end hooks, as well as a 15% substitution of cement by blast furnace slag. The dosage in slag optimized in previous studies is 15% (in place of cement). This content induces mechanical strength at 28 days very high (Chaid, 2006).

Materials and Methods

The materials used for making concrete study are:

Portland cement without mineral additives CEM I 52.5 PM ES CP2 of Lafarge France. The chemical and mineralogical composition are shown in Table 1.

Table 1. Chemical and mineralogical composition of cement used

Elements	CaO	SiO_2	Al_2O_3	Fe_2O_3	MgO	K_2O	Na_2O	SO_3	RI	PAF	CaO_L
%	66.60	22.40	2.96	2.33	0.95	0.15	0.10	2.13	0.20	1.59	0.50
Minerals		C_3S		C_2S		C_3A			C_4AF		
%		65.3 %		18.6		4.35			7.14		

A blast furnace slag plant in El-Hajar-Annaba Algeria is an amorphous granular ground to a specific surface area greater than that of cement; whose chemical composition and physical characteristics are reported in Table 2.

Table 2. Chemical composition and physical characteristics of slag

Elements	CaO	SiO_2	Al_2O_3	Fe_2O_3	MgO	K_2O	Na_2O	SO_3	RI	PAF
%	39.77	41.69	7.05	1.41	5.49	0.44	0.10	0.15	0.12	0.11
Physical characteristics			Density			2.99 g/cm^3,				
			Specific surface area			8500 cm^2 / g.				

The aggregates used are silica sand crushed (0/2) and two fractions of silica gravels crushed (2/6) and (6/12). Their physical properties are presented in Table 3.

Table 3. Physical properties of aggregates

Types	Sand	Gravels 2/6,3	Gravels 6 /12
Actual density ρr (Kg/m 3)	2604,00	2620,00	2645,71
Apparent density ρapp (Kg /m 3)	1555,53	1365,63	1338,79

The admixture is a superplasticizer, Sika ViscoCrete TEMPO 9. We used a mixture of short fibers and fibers with end hooks (Dramix RC-80/50BN) shown in Figures 1 and 2. These fibers are added at ratio of 0.35% of volume per cubic meter of concrete. The formulation of the concrete submitted to the tests (studied concrete) is achieved with the method of Dreux-Gorisse while using the software concrete lab free of the LCPC. After convenience tests, the composition of basis kept for these concretes is presented in Table 4.

Figure 1. Short fibres.

Figure 2. Fibres with end hooks.

Table 4. Concrete mixes

Constituents	Quantity (kg/m^3)
Cement	446
Slag	66.9
Gravel 6/12	891.9
Gravel 2/6	85.2
Sand 0/2	738.3
Water	155.6
Admixtures	0.34% of the weight of the cement

The specimens of the studied concretes with slag but without fibers, concrete with slag without fibre and concrete with slag and fibers are placed, after demoulding, in water total immersion at a temperature of 20 °C. The abbreviations used for the different concretes are:
HPC: Control concrete without the slag or fibers,
HPCS: Concrete with the slag but without fibers,
HPCSF: Concrete with the slag and fibers.

Results and Discussion

Characterization of the Fresh Concrete Capillarity, Water Porosity and Density

The results of the cone slumping tests of fresh concrete are summarized in Table 5. The measured slump for the different concretes was between 13 and 14 cm, which corresponds to a plastic vibrated concrete of subsidence class S3, with a good consistency according to the NF-EN 206[9] standard. The addition of fibres resulted in a loss of HPCMF slump when using the same amount of superplasticizer. However, the increase in the quantity of admixture has led to an improvement in the subsidence of this type of concrete.

Table 5. Fresh concrete characteristics

Quantity of superplasticizer	Characteristics	Types of concrete		
		HPC	HPCS	CSF
The same quantity of superplasticizer for the 3 concretes	Abrams cone slumping in (cm)	13	14	10
Increased the quantity of superplasticizer for HPCSF	Abrams cone slumping in (cm)	14	14	13

Capillarity, Water Porosity and Density

For capillarity, water porosity and density tests on high performance concretes made with the same quantity of superplasticizer. The retention periods are 6 and 24 months. After these deadlines the test bodies are dried in an air-conditioned room (50% relative humidity, 20°C).

Porosity Accessible to Water and Density

The porosity accessible to water determines almost all the properties of concrete, and, first of all, its mechanical resistance: when the porosity increases due to the degradation of the concrete, its resistance decreases (Baron, 1992). The average values of the porosities accessible to water and of the densities determined for the concretes studied are represented in figure 03. The porosity of non-fibre-reinforced concrete is lower than that of fibre-reinforced concrete. It is generally accepted that the incorporation of fibers in a HPC leads to a decrease in compactness due to the reduction of rheological properties (Ladaoui, 2010).

The porosity of fibre-reinforced concrete (HPCSF) decreased slightly by 1.36% between 6 months and 2 years, because when the cement hydrates, the hydrates formed block the pores and reduce porosity. Density increases with decreasing water-accessible porosity; this is verified for both types of concrete.

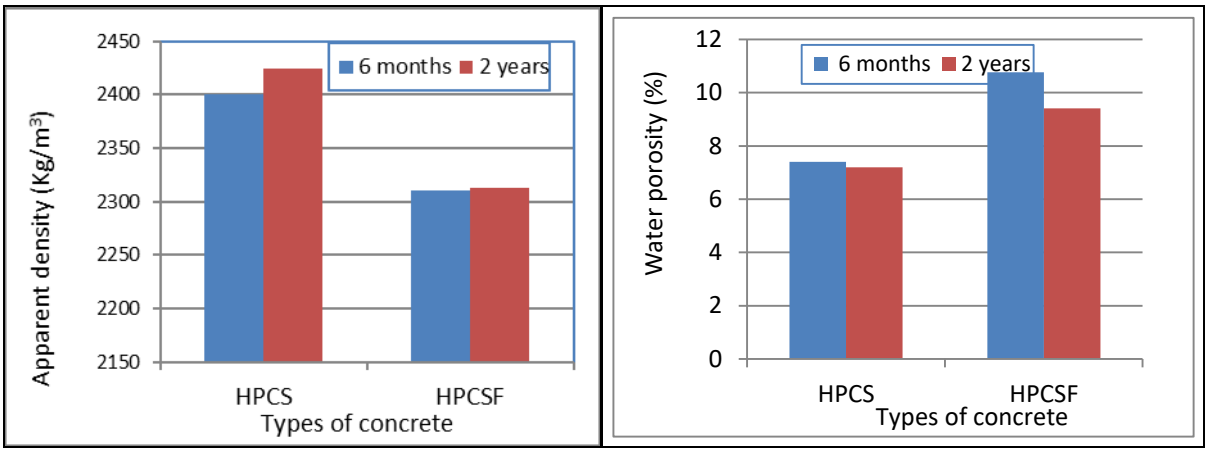

Figure 3. Porosity accessible to water and apparent density variation of the different concretes.

Capillary water absorption

Concrete is indeed a material that has capillary pores whose size varies according to its composition characteristics (W/B ratio, mineral additions, etc.). When a liquid comes into contact with this type of pore, surface tensions cause the liquid to rise inside by capillary action. The test of water absorption by capillarity involves placing the lower surface of the specimen (bottom of the mould) to the contact of water and to follow according to the time, the evolution of the mass. Figure 04 illustrates the evolution of water absorption by capillarity of the survey concretes according to the time.

After 6 and 24 months of storage, the gotten results show that in the first hours of the test (up to 8 hours), the capillary coefficients of absorption of the concretes fibers and non fibers are globally similar. But after 24 hours, the fibre-reinforced concretes show a slightly higher water absorption than the non-fibre-reinforced concretes. The capillary absorption coefficient after 2 years of storage for the two types of concrete is slightly higher, compared to those stored for 6 months.

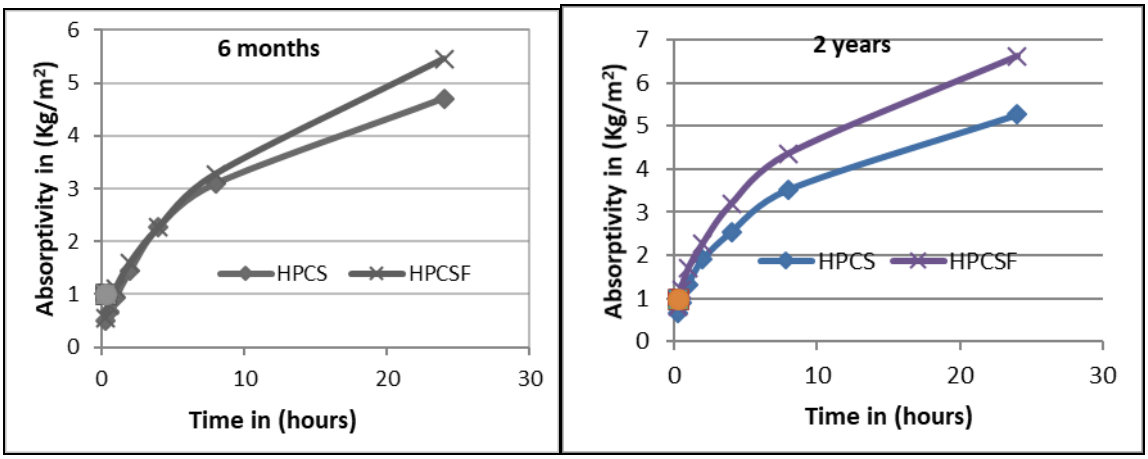

Figure 4. Absorption capillary coefficients of the different concretes,

Microstructure of Specimens Concrete Examined by SEM

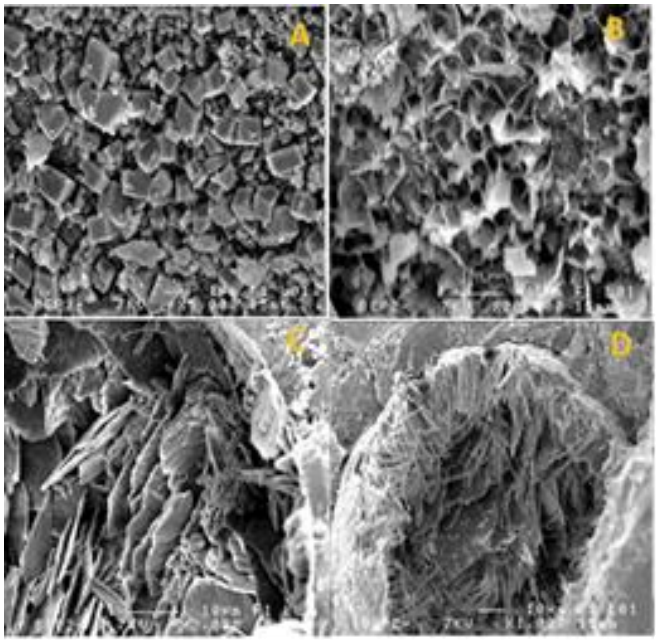

Figure 5. Micrographs of the microstructure of HPC after 6 months of conservation.

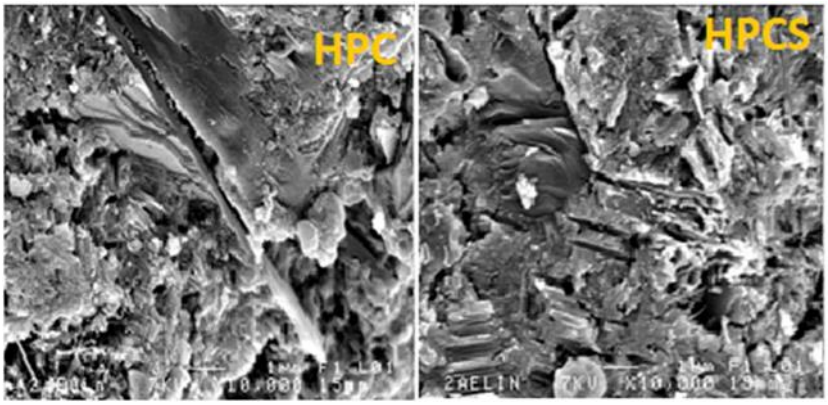

Figure 6. SEM observation of the internal microstructure of HPC and HPCS after 2 years of conservation.

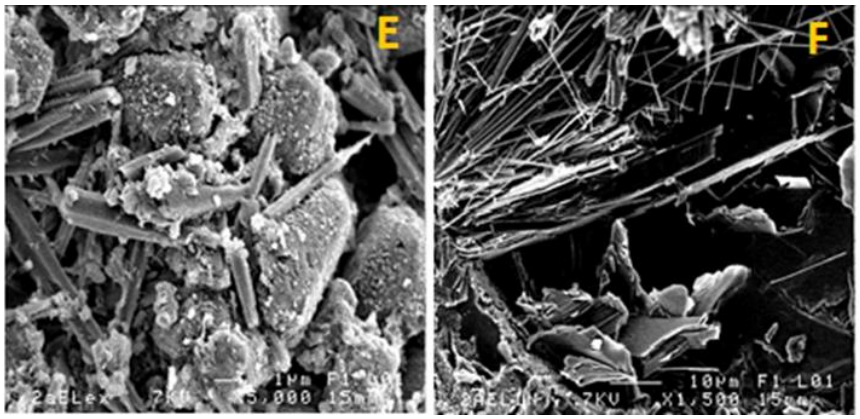

Figure 7. SEM observation of the internal and external microstructure of HPCS after 2 years of conservation.

In order to support the hypotheses formulated regarding the performance of our study concretes, observations with a Scanning Electron Microscope are carried out on HPCS concrete specimens after 6 months of hardening. Figure 5 shows for the external microstructure, the presence of carbonates crystallised in rhomboid (A). For the internal microstructure, we find CSH in sponges (B), ettringite, which crystallised in fine needles and tablets of portlandite (C and D). SEM observations at x10,000 magnification, carried out on samples of HPC and HPCS

after two years of hardening figure 6, show a relatively improved microstructure in concrete with added slag (HPCS), with relatively more densified interfaces and rich in CSH, characteristic of HPC with added active cementitious materials. For the external microstructure of the HPCS concrete after two years of hardening (Figure 7), we note the presence of ettringite in short needles (E) of the same type as that formed in healthy HPC [1]. While the internal phases of the concrete present fine needles of ettringite (F), with CSH of high compactness (Figure 6).

Conclusion

The main objectives of our work were, on the one hand, to evaluate the influence of reinforcement by mixed metal fibre and the substitution of 15% of cement by granulated blast furnace slag on the porosity and microstructure of high performance fibre-reinforced concrete. The addition of fibers resulted in a loss of HPCSF subsidence for the same amount of super plasticizer. Nevertheless, the increase in the quantity of admixture has led to an improvement in the workability of this type of concrete. The porosity of fibre-reinforced concrete (HPCSF) decreased slightly by 1.36% between 6 months and 2 years, because when the cement hydrates, the hydrates formed block the pores and reduce porosity.

Density increases with decreasing water-accessible porosity; this is verified for both types of concrete. After 6 and 24 months of storage, the gotten results show that after 24 hours of the test, the fibre-reinforced concretes show a slightly higher water absorption than the non-fibre-reinforced concretes. The micrographs of the cementitious matrix show a relatively improved microstructure in concrete with added slag (HPCS).

Scientific Ethics Declaration

The authors declare that the scientific ethical and legal responsibility of this article published in EPSTEM journal belongs to the authors.

Acknowledgements or Notes

* This article was presented as a poster presentation at the International Conference on Technology, Engineering and Science (www.icontes.net) held in Antalya/Turkey on November 16-19, 2023.

References

Aïtcin, P. C. (2001). *Concretes high performance*. Paris, France: Eyrolles.

Baron, J., & Oliver, J. P. (1992). *Introduction to the durability of concrete*. *The durability of concrete*. Paris: ENPC press.

Chaid, R. (2006). *Formulation, characterization and durability of the BHP to the additions local cimentious*. (Doctoral dissertation). Polytechnic National School, Algiers.

Escadeillas, G. (2006). The éco-materials in the construction: Stakes and perspectives. *The scientific days of the French-speaking Regrouping for research and the formation on the concrete (RF) 2B* (7 th ed.).

Ezeldin, A., & Balaguru, P. (1982). Normal and high-strength fiber reinforced concrete under compression. *Journal of Materials in Civil Engineering, 4*(4), 415-429.

Feldman, R. F. (1983). Significance of porosity measurements on blended cement performance. In V. M. Malhatro (Ed.), *1st International Conference on the Use of Fly Ash, Silica Fume, Slag and other Mineral by-Products in Concrete, Montebello* (pp. 415-433). Canada.

Ladaoui, W. (2010). *Experimental survey of the long-term behavior of the HPC destined to the works of storage of the radioactive garbage* (Doctoral dissertation). Toulouse, France: University of Toulouse III-Paul Sabatier.

Mindess, S. (1984). Relationship between strength and microstructure for cement based materials: A overview. *Materials Research Society Proc, 42,* 53-68.

NF EN 206. (2014). *Concrete - specification, performance, production and conformity*. AFNOR.

Rossi, P., Acker, P., & Mailer, Y. (1987.) Effect of steel fibers at two different stages: the material and structure. *Materials and Structures, 20*(6), 436-439.

Swamy, R. N., & Mangat, P. S. (1974). Compatibility of steel fiber reinforced concrete. *Cement and Concrete Research, 8*(5), 34-35.

Author Information

Aldjia Boutiba
Mouloud Mammeri University
Route de Hasnaoua BP 47, Tizi Ouzou, Algeria
Contact e-mail: *boualdjedi@ yahoo.fr*

Rabah Chaid
M'Hamed Bougarra University
Cité Frantz. Fanon, 35000 Boumerdes, Algeria

Laurent Molez
INSA Rennes
20 Av. des Buttes de Coesmes, 35700 Rennes, France

To cite this article:

Boutiba, A., Chaid, R., & Molez, L. (2023). Effect of slag on the porosity and microstructure of HPC reinforced with hybrid steel fiber. *The Eurasia Proceedings of Science, Technology, Engineering & Mathematics (EPSTEM), 26*, 86-92.

The Eurasia Proceedings of Science, Technology, Engineering & Mathematics (EPSTEM)
ISSN: 2602-3199

The Eurasia Proceedings of Science, Technology, Engineering & Mathematics (EPSTEM), 2023

Volume 26, Pages 93-99

IConTES 2023: International Conference on Technology, Engineering and Science

Validation of the Ruees-Voight Homogenisation Model for Glass Powder-Based Eco-Concretes

Benbakhti Abdeldjalil
University Centre of Maghnia

Benfrid Abdelmoutalib
University of Djillali Liabes

Chatbi Mohamed
University of Djillali Liabes

Harrat Zouaoui Rabie
University of Djillali Liabes

Bachir Bouiadjra Mohamed
University of Djillali Liabes

Abstract: In view of the ecological challenge that our planet has been facing in recent years, environmental protection has become an issue for researchers and scientists in all fields, through the reduction of discharges from factories and the recycling of waste. Among the most common solid waste is glass waste, which is attracting the attention of recycling specialists in various sectors, particularly construction, by incorporating it into the composition of concrete and reusing it as building materials. The aim of our work is to use the RUEES-Voigt homogenization model to estimate the values of the mechanical properties of an eco-concrete based on glass powder and to compare them with the results found experimentally for a replacement of (5% , 10% ,15%,20 ,25%,30%,35%) of the quantity of cement by glass powder with a particle diameter of 2.79 µm. Very interesting experimental results were obtained which validate the effective RUEES-Voigt model proposed, which opens up the possibility of using other homogenization models.

Keywords: Glass powder-based concrete, Environmental protection, Ruees-Voight homogenisation model, Experimental validation.

Introduction

The number one environmental issue is ecological living and environmental protection. The rate of waste is increasing rapidly, as daily use and needs demand many things, as well as industrial needs. One type of waste is glass. First of all it is necessary to give some statics about glass waste. (Planet scope, 2022) states that glass waste represents 13% of all European waste, and that 11.5 million tons of glass in Europe have been reported, lately 70% of glass recycling has been attributed.

Waste key figures (2019) states that around 2025 ,80 000 tons of flat glass will be rejected and recycled by a factor of 56% in the industry sector. In the field of civil engineering and public works, a wide range of studies have been carried out on the subject of glass recycling for the manufacture of concrete using glass powder, as it is rich in silica and can therefore replace cement as well as silica sand. In brief, we cite some of the work that has been undertaken on this subject. The mechanical properties of glass powder are obtained from (KLA

Instruments) who characterized the modulus of elasticity according to the grain size (diameter) of the glass particle for a diameter of d=2.79 µm The modulus of elasticity is experimentally estimated as Eg= 67.31 GPa.

These values will be used in this paper with a poisson's ratio noted in several materials science books that n=0.3. (Khalil et al., 2018) , this study consists of using waste glass to formulate a concrete , the two researchers replace between (10%-15%-20%-25%-30%) of cement by glass powder (75µm) ,the results show that glass powder works as a pozzolan material and the mechanical behavior improves and reaches the maximum at 15% P.V [4]. Dalia Shakir Atwan prepares concretes based on glass waste of 3 diameters (600um, 2.36 mm, 4.75 mm) to replace the fine aggregate of the grading curve by (10%,20%,30%). He found that strength improved when the waste became very fine as a powder (Atwan, 2017). Yassen et al. (2019):work on a concrete based on glass powder, they replaced between (10%,15%,20 and 25%) of cement by P.V (between 75µm and 300µm), they concluded that concrete strength and elastic modulus improve and the optimal value at 20%. Naje et al. (2019) studied the behavior of a waste glass-based concrete; they replaced between 10% and 30% of sand with crushed waste glass (smaller than 5mm). They found that it is possible to replace 30% of sand with glass waste with an increase in the mechanical characteristics of concrete.

Boukhelf et al.(2020) studied the effect of partial replacement of cement by alternatives derived from waste glass and silica fume on the hygrothermal behavior of concrete (Boukhelf et al., 2020). Benbakhti et al.(2016) analyzed functionally graded slabs.(Benbakhti et al.,2017). Benfrid et al. (2023) evaluated the limitation and performance under thermomechanical loading of an eco concrete panel using an analytical model. under thermomechanical loading of an eco concrete panel using an analytical model(Benfrid et al., 2023). It can be seen that most scientific reviews are based solely on the experimental part; moreover, they do not give a known homogenization rule such as the model of (Voigt, 1889) or the model of (RUEES, 1929), or the model that combines the two, called the (RUESS-Voigt) model (Fatima AOUISSI, 2019). In this work, we are interested in applying the (RUESS-Voigt) homogenization model, which must be identical to the experimental resultsbased on an eco-concrete based with 5% , 10% ,15%,20 ,25%,30% and 35% of the quantity of cement replaced by glass powder with a particle diameter of 2.79 µm, the work plan is illustrated in the form of an organization chart in Figure 1.

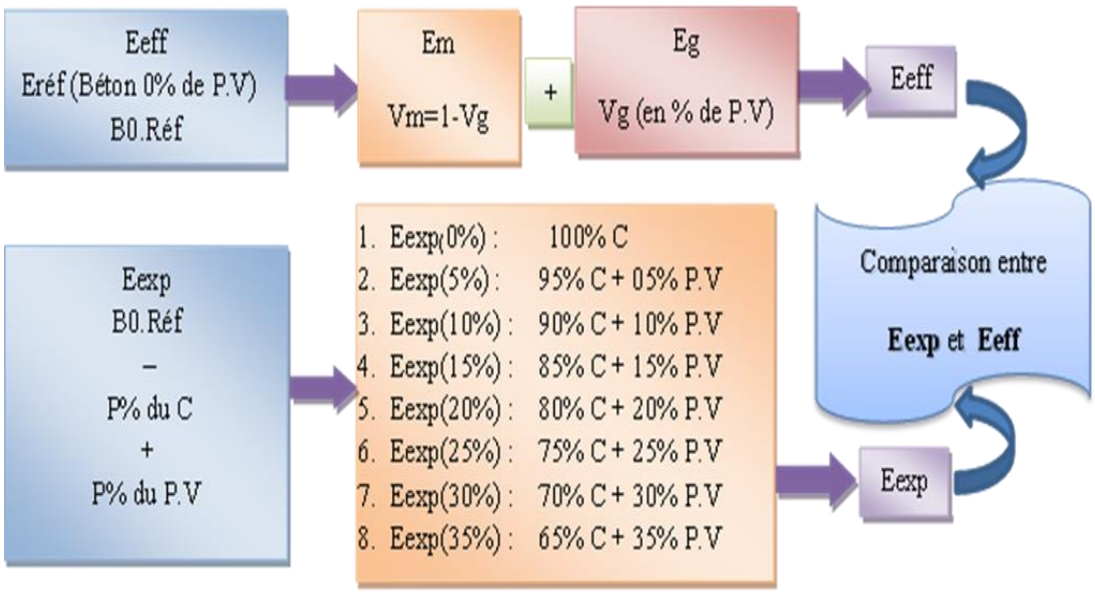

Figure 1. Paper organization

Homogenization Models

It is assumed that the reference concrete with 0% P.V. (matrix) and glass powder is the reinforcement. Knowing that "The total volume of matrix plus reinforcement is equal to unit 1".

$$V_g + V_m = V \quad (1)$$

2-1-Model de REUSS-Voigt [8] :

$$E_p = E_m + V_g^{\frac{2}{3}}(E_g - E_m) \quad (2)$$

$$\frac{1}{E_s} = \frac{1}{E_m} + V_g^{\frac{2}{3}}\left(\frac{1}{E_g} - \frac{1}{E_m}\right) \quad (3)$$

$$E_{rv} = E_m + V_g^{\frac{1}{3}}(E_s - E_m) \quad (4)$$

With

Em: Modulus of elasticity of concrete.
Eg: Modulus of elasticity of glass powder.
Ep : The modulus of elasticity of the parallel part determined by the VOIGT model.
Es : The modulus of elasticity of the part in series determined by the REUSS model.
Erv : The modulus of elasticity determined by the REUSS / VOIGT model.
Eexp : Modulus of elasticity of concrete obtained from experiments.
V : Total volume of mix.
Vm : Concrete volume.
Vg : Glass powder volume.
C: Cement.
P.V: Percentage of glass powder.
Fcj: Compressive strength of concrete at age j:(days).
B.ref: A reference concrete with 0% P.V.
d: Diameter.
Note: E units are taken in [GPa] and Fc in [MPa].

Table 1. Centre the caption above the table (Benmansour at al, 2014)

Chemical and mineralogical composition of cement, %.		Physical and mechanical characteristics of cement	Unit	Values		
CaO	54.92	Apparent density	kg/m^3	1020		
SiO_2	24.02	Absolute density	kg/m^3	3000		
Al_2O_3	5.47	Normal consistency	%	27		
Fe_2O_3	2.83					
SO_3	≤ 3.5	Surface Spécifique Blaine	cm^2/g	3480		
MgO	0.93	Start of cement setting	h et mn	1 h 40		
CaOlibre	1.35	End of cement setting	h et mn	4 h 50		
C_3S	62.12	Mechanical resistance		2 j	7j	28 j
C_2S	16.57					
C_3A	5.71	Compression	MPa	70	24.17	30.25
C_4AF	9.30	Bending	MPa	2.97	5.3	8.12

Experimental Processes

Concrete Preparation

Materials Used

To carry out this work, we used an electric concrete mixer with a capacity of 200 L, cylindrical molds (32×16) cm^3 for making the test specimens, an electric plastic (cellophane) grinder and an electric vibrator.

Materials

Cement

For this work, a cement of the type CPJ - CEM II/A 42.5 was used, complying with Algerian standards. The mineral composition was calculated using the revised Bogue formula, and the results are presented in Table 1 (Benmansour et al., 2014).

Glass Powder

To prepare a glass powder, a 0.5 kg grinding machine (High Speed Powder Machine Electric) was used, followed by sieving through 300 µm fine aggregates. This powder must be fine in accordance with regulations (ASTM-C 1260).

In this case, colored glass was used, as experimental studies by the Colombian Civil Engineering Department show that colored glass is more resistant than non-colored glass, as it reduces the alkali _ silicate reaction (Meyer et al., 2001). We only use pass-throughs with a diameter equal to or less than 300µm to make our concrete.

Aggregates

The standard classification (ASTM: C-294-69) gives a specification of aggregate constituents. The standard (ASTM: C33-87) provides a particle size analysis for sand and gravel [15]. In this formulation, only gravel up to 1 cm in size is used. Table N°02 shows the gravel gradings purely from western Algeria, approved and authorized by the Algerian Ministry of Minerals, and Table N°03 shows the gradings for sand.

Table 2. Granulometric analysis of the gravels used

Sieve diameter	Standard requirements	Percentage of passersby
75 mm	-----	100%
63 mm	-----	100%
50 mm	-----	100%
37.5 mm	-----	100%
25 mm	-----	100%
19 mm	100%	100%
12,5 mm	90%-100%	95%
9,5 mm	40%-70%	68%
4,75 mm	0%-15%	11%
2,36 mm	0%-5%	4%

Table 3. Granulometric analysis of the used sand

Sieve diameter	Standard requirements	Percentage of passersby
4,75 mm	95%-100%	97%
2,36 mm	80%-100%	87%
1,18 mm	50%-85%	65,7%
600 µm	25%-60%	55,4%
300 µm	10%-30%	29%
150 µm	02%-10%	7.3%

Mixing Water

In this case, a quantity of water distilled by evaporation is prepared to avoid any disturbance in the results, with a ratio of water quantity to cement E/C=0.3.

Sample Preparation

Concrete Formulation

Table N° 04 presents the formulation used in the various mixes, for the benefit of the work we will use a super plactifying admixture and we will ensure a concrete dosage of 300 kg/m3, while replacing the quantity of cement progressively by the different percentage of glass powder as explained in figure 1.

Table 4. Granulometric analysis of the used sand

	Cement (kg)	Glass powder (kg)	Sand (0/5)(Kg)	Gravel (3/8) (Kg)	water (l)	admixture (Kg/m3)
B0%	300	0	833,5	831,5	140	33,5
B5%	285	5	833,5	831,5	140	33,5
B10%	270	10	833.5	831,5	140	33,5
B15%	255	15	833.5	831,5	140	33,5
B20%	240	20	833.5	831,5	140	33,5
B25%	225	25	833,5	831,5	140	33,5
B30%	210	30	833.5	831,5	140	33,5
B35%	195	35	833.5	831,5	140	33,5

Forming Concrete Specimens

The standard (ASTM-C-192-180) clearly specifies sample preparation:

1- Mixing.

2- Sampling in two successive layers with vibration.

3- Adjust the level and finish the edges of the molds with a trellis.

4- Measuring plastic to prevent evaporation.

5- Demold after 24 h.

6- Place the samples in a vat of water for 7 days.

Compressive Crushing of Concrete

Crushing is carried out in accordance with the standard (B.S 1981.PART(5) /1983). For short-term ageing (7, 14 and 28 days) and also for long-term ageing (56, 90, 120, 150 days) to check the behaviour of glass powder based concrete.

Table 5. Short- and long-term compressive strength and modulus of elasticity determined experimentally.

		Short term			Long term			
Type	Age	7 j	14 j	28 j	56 j	90 j	120 j	150j
B0%	fc (MPa)	28,7	34,1	42,3	44,9	46,1	46,2	46,3
	E (GPa)	33,67	35,67	38,32	39,01	39,44	39,47	39,50
B5%	fc (MPa)	28,1	39,9	41,9	45,1	47,6	47,7	47,9
	E (GPa)	33,44	37,59	38,20	39,15	39,86	39,89	39,95
B10%	fc (MPa)	27,7	38,6	40,9	47,9	49,6	49,9	49,8
	E (GPa)	33 ,28	37,17	37,89	40,55	40,41	40,49	40,47
B15%	fc (MPa)	26,5	38,1	40,2	48,1	48,9	49,1	49,3
	E (GPa)	32,79	37,01	37,23	40	40,22	40 ,38	40,4
B20%	fc (MPa)	26	37,4	38,8	50,1	51,8	51,9	52
	E (GPa)	32,58	36 ,78	37,24	50,55	41	41,03	41,05
B25%	fc (MPa)	25,7	36,7	38,1	51,8	52	52,1	52,3
	E (GPa)	32,46	36,55	37,01	41	41,06	41,08	41,13
B30%	fc (MPa)	25,1	36	36,8	52,1	52, 3	52,6	52,7
	E (GPa)	32,20	36,32	37,01	41	41,06	41,08	41,13
B35%	fc (MPa)	22,4	30,7	28,7	28	27,8	25	23,9
	E (GPa)	31,01	34 ,44	33,67	33,40	33,32	32,16	31,68

Results and Discussion

Long- and short-term compression tests were carried out on (32×16) cm3 cylindrical specimens to determine the mechanical properties of different specimens with different percentages of glass powder replacement (5%, 10%, 15%, 20, 25%, 30%, 35%). The results for crush resistance and young's modulus of elasticity are shown in Table 5. Table 6 illustrates the results obtained by applying the formulas of the homogenization law proposed by Ruess Voigt for different percentages of replacements and for concrete at 7, 14, 28, 56, 90, 120 and 150 days.

Table 6. the effective short- and long-term modulus of elasticity by RUESS-VOIGT.

		Short term			Long term			
Type	Age	7 j	14 j	28 j	56 j	90 j	120 j	150j
B0%	E (GPa)	28	35	43	45	46	46	46
B5%	E (GPa)	28,21	35,17	43,13	41,12	46,11	46,11	46,11
B10%	E (GPa)	28,63	35,55	43,41	45,38	46,36	46,36	46,36
B15%	E (GPa)	29,20	36,05	43,80	45,74	36,70	46,70	46,70
B20%	E (GPa)	29,91	36,67	44,29	46,18	47,13	47 ,63	47,13
B25%	E (GPa)	30,73	37,40	44,86	46,71	47,63	48,20	47,63
B30%	E (GPa)	31,61	38,23	45,52	47,31	48 ,28	48,21	48,20
B35%	E (GPa)	32 .73	39,17	46,25	47,98	48,85	48.22	48,28

A comparison of Tables 5 and 6 shows that the longitudinal elastic modulus E values calculated analytically by Ruess Voigt's law are very close to the values assessed by the laboratory test for concretes with low replacement ratios of 5, 10 and 15, but the difference in values starts to increase for replacement ratios of 20% and above, and is more noticeable for long-term results.

Conclusion

From this study, we can see that the RUESS-VOIGT model is the 'homogenization' model that comes closest to estimating the short-term mechanical cleanliness of an eco-concrete based on glass powder with diameters ranging from 75 µm to 300 µm, with a low percentage of replacement. This model can be applied to rates of up to 20% replacement of cement by glass powder to estimate the mechanical behavior of eco-concrete.

Recommendations

Further studies can be carried out to assess the accuracy of this homogenization law for determining the mechanical properties of eco-concretes based on glass powder, but replacing the fine aggregates by different percentages of the latter.

Scientific Ethics Declaration

The authors declare that the scientific ethical and legal responsibility of this article published in EPSTEM journal belongs to the authors.

Acknowledgements or Notes

* This article was presented as a poster presentation at the International Conference on Technology, Engineering and Science (www.icontes.net) held in Antalya/Turkey on November 16-19, 2023.

References

Aouissi, F. (2019). *Mechanical behavior of concrete prediction and optimization.* (Doctoral dissertation). Université BLIDA 1. Retrieved from https://www.planetoscope.co

ASTM C1260. (2022). *Standard test method for potential alkali reactivity of aggregates (mortar-bar method)*. https://www.astm.org/c1260-21.html

ASTM-C294. (2019). *Standard descriptive nomenclature for constituents of concrete aggregates*. https://global.ihs.com/doc_detail.cfm?document_name=ASTM%20C294&item_s_key=00014509

ASTM-C294. (2021). *Test method for effect of organic impurities in fine aggregate on strength of mortar*.

Atwan, D. S. (2017). Effect of particle size of waste glass on compressive strength and modulus of rupture of concrete mix. *Al-Nahrain Journal for Engineering Sciences (NJES), 20*(4), 970-975.

Benbakhti, A., Bouiadjra, M. B., Retiel, N., & Tounsi, A. (2016). A new five unknown quasi-3D type HSDT for thermomechanical bending analysis of FGM sandwich plates. *Steel and Composite Structures, 22*(5), 975-999.

Benfrid, A., Benbakhti, A., Harrat, Z. R., Chatbi, M., Krour, B., & Bouiadjra, M. B. (2023). Thermomechanical analysis of glass powder based eco-concrete panels: Limitations, performance evaluatio. *Periodica Polytechnica Civil Engineering, 67*(4), 1284–1297.

Benmansour, N., Agoudjil, B., Gherabli, A., Kareche, A., & Boudenne, A. (2014). Thermal and mechanical performance of natural mortar reinforced with date palm fibers for use as insulating materials in building. *Energy Build, 81* (2014) 98–104.

Boukhelf, F., Cherif, R., Trabelsi, A., Belarbi, R., & Bouiadjra, M. B. (2021). On the hygrothermal behavior of concrete containing glass powder and silica fume. *Journal of Cleaner Production, 318,* 128647.

Khalil, W. I., & Al-Obeidy, N. F. (2018). Some properties of high strength sustainable concrete containing glass powder waste*. Diyala Journal of Engineering Sciences, 11*(2), 42-32.

Meyer. C., Egosi, N., & Andela, C. (2001). *Concrete with waste glass as aggregate*. In *Recycling and reuse of glass cullet* (pp. 179-188). Thomas Telford Publishing.

Naje, A. G., Rahem, S. A., Thabit, N. H., & Abd, H. J. (2019). Effect of adding different concentrations of waste glass on some properties of concrete*. Journal Irac of Sciences and Technology*, *10*(2), 35-42.

Reuss, A. (1929). Berechnungder fließgrense von mischkristallen auf grund der plastizitätsbedingung für Einkristalle. Z. Angew. *Math. Mech., 9*(1), 49–58.

Voigt, W. (1889). Ueber die Beziehung zwischen den beidene Elastizitatskonstanten Isotroper Korper*. Annalan derPhys., 38,* 573–587.

Yassen, M. M., Mahmoud, A. S., & Hama, S. (2019). Effectiveness of glass wastes as powder on some hardened properties of concrete. *Al-Nahrain Journal for Engineering Sciences NJES, 22*(1)*,* 14-17.

Author Information

Benbakhti Abdeldjalil
University Centre of Maghnia, Algeria
Contact e-mail: *Jalil7benbakhti@gmail.com*

Benfrid Abdelmoutalib
Laboratory for Advanced Structures and Materials in Civil Engineering and Public Works, Faculty of Technology, University of Djillali Liabes Algeria

Chatbi Mohamed
Laboratory for Advanced Structures and Materials in Civil Engineering and Public Works, Faculty of Technology, University of Djillali Liabes Algeria

Harrat Zouaoui Rabie
Laboratory for Advanced Structures and Materials in Civil Engineering and Public Works, Faculty of Technology, University of Djillali Liabes Algeria

Bachir Bouiadjra Mohamed
Laboratory for Advanced Structures and Materials in Civil Engineering and Public Works, Faculty of Technology, University of Djillali Liabes Algeria

To cite this article:

Abdeldjalil, B., Abdelmoutalib, B., Mohamed, C., Rabie, H.Z., & Mohamed, B.B. (2023). Validation of the ruees-voight homogenization model for glass powder-based eco-concretes. *The Eurasia Proceedings of Science, Technology, Engineering & Mathematics (EPSTEM), 26,* 93-99.

The Eurasia Proceedings of Science, Technology, Engineering & Mathematics (EPSTEM)
ISSN: 2602-3199

The Eurasia Proceedings of Science, Technology, Engineering & Mathematics (EPSTEM), 2023

Volume 26, Pages 100-108

IConTES 2023: International Conference on Technology, Engineering and Science

Robustness of the Fuzzy Adaptive Speed Control of a Multi-Phase Asynchronous Machine

Bessaad Taieb
Hassiba Benbouali University Chlef

Benbouali Abderrahmen
Hassiba Benbouali University Chlef

Taleb Rachid
Hassiba Benbouali University Chlef

Abstract: Fuzzy controllers are a powerful tool for controlling complex processes. However, its robustness capacity remains moderately limited because it loses its property for large ranges of parametric variations. In this paper, the proposed control method is designed, based on a fuzzy adaptive controller used as a remedy for this problem. For increase the robustness of the vector control and to maintain the performance of the five-phase asynchronous machine despite the presence of disturbances (variation of rotor resistance, rotor inertia variations, sudden variations in the load etc.), by applying the method of behaviour model control (BMC). The results of simulation show that the fuzzy adaptive control provides best performance and has a more robustness as the fuzzy (FLC) and as a conventional (PI) controller.

Keywords: Five-phase, Asynchronous machine, Vector control, Fuzzy adaptive control, Behaviour model control (BMC).

Introduction

The DC machine was for a long time the most used for its capacity of speed variation and its great flexibility of operation. Its control is simple because the two magnitudes torque and flux are naturally decoupled. Nevertheless, the DC machine has many disadvantages related to its mechanical commutate. Indeed, the collector increases the cost of manufacture and maintenance of the machine and limits its use in explosive and/or corrosive environments. This is why researchers have turned to the control of alternating current machines. The growth in electrical energy consumption and high power electrical applications have led to the use of multi-phrase machines (whose number of phases is greater than three) to segment the power. In addition to this advantage, multi-phrase machines have several other advantages such as power segmentation without increasing the currents per phase and the minimization of iron losses. Through these advantages, the multi-phrase machine is used in several applications, especially in the field of high power, among other things, in wind power generation.

Multi-phase machines have obvious potential because of their reliability and their possibility of operating in degraded operation. Despite all these advantages, its control remains quite complicated compared to that of the DC machine, because its mathematical model is nonlinear and strongly coupled. Modern control techniques lead to a control of asynchronous machines comparable to that of the DC machine. Among these techniques, we find direct torque control, state feedback control, vector control and adaptive control. These techniques use both conventional and modern regulators which make the controls mentioned above robust.

Traditionally, because of its simplicity, a PI controller is used for both current and speed regulation. However, the main disadvantage of using PI controller is that performance degrades under external disturbances and machine parameter variations. To solve this problem, several researchers have proposed intelligent controllers like fuzzy logic, sliding mode control, adaptive control and neural network control. The authors concluded that fuzzy controller has capable of improving the tracking performance under external disturbances and more robust control method than usual PI control. However, the speed adjustment is carried out using a fuzzy controller but its capacity of robustness remains moderately limited, because it loses its property for the large ranges of parametric variations (speed for example). To overcome this problem, is reasonable to combine the adaptive control with the fuzzy robust controller.

Behavior Model Control Principals

In this paper, the "mod" subscript is used to define model values (e.g. Y_{mod} , the model output). P(S) and M(S) are transfer functions. The Behavior Model Control aims to define a complementary control function (value) to that defined by the main controller in order to enhance the control algorithm performance. It requires at least two controllers, a model and the process to be controlled (Fig. 1).

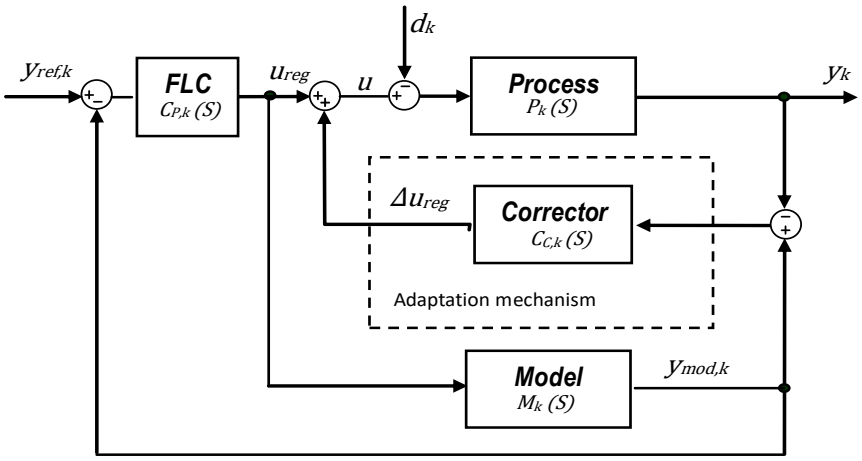

Figure 1. Behavior model control (Functional block)

According to the set-point (reference) Y_{ref} , the main controller $C_p(S)$ delivers an output value u_{reg} . The issued control value u_{reg} from the main controller is applied to a predefined model M(S) called the Behavior Model(BM). The BM define a model output value Y_{mod}. The second controller called "The Behavior Controller or the Adaptation Corrector" uses the gap between the process output value Y and the model output value Y_{mod} , to define the complementary control function (value) Δu_{reg}.

By cancelling the error (Y - Y_{mod}), the process behaviour becomes similar to that of the predefined model, hence the term Behavior Model Control. The complementary control function (value) Δu_{reg} is added to the output value u_{reg} and then applied to the process P(S) as an input value.

As a result, this auxiliary control algorithm increases the robustness of the global control algorithm; it indirectly rejects various disturbances, facilitates the synthesis of classical control and allows the linearization of a non-linear process through a linear model.

It should be noted that the main controller serves to eliminate the error between the set-point (reference) Y_{ref} and output value. This later, can be the output of the model Y_{mod} or that of the process Y. Therefore, one can define two structure of BMC: BMC based on the predefined model output, and BMC based on the process output. According to the scheme of Fig. 1, the following expressions are deduced:

$$\begin{cases} Y(S) = \left[U_{reg}(S) + \Delta U_{reg}(S) - d\right]P(S) \\ \Delta U_{reg}(S) = \left[M(S) + U_{reg}(S) - Y(S)\right]C_C(S) \end{cases} \quad (1)$$

Following the calculation, one arrive at the system that expresses the process output Y as well as that of the model Y_{mod}.

$$\begin{cases} Y(S) = \dfrac{P(S)(1+M(S).C_c(S))}{1+P(S).C_c(S)} U_{reg}(S) \\ \qquad - \dfrac{P(S)}{1+P(S).C_c(S)}.d \\ Y(S) = M(S).U_{reg}(S) \end{cases} \tag{2}$$

Where d : represents the disturbance.

In order to simplify this system, the correction controller $C_C(S)$ must satisfy the following assumptions:

$$\begin{cases} |M(S).C_c(S)| >> 1 \\ |P(S).C_c(S)| >> 1 \end{cases} \tag{3}$$

After simplification, the following is obtained:

$$\begin{cases} Y(S) = M(S).U_{reg}(S).\dfrac{1}{C_c(S)}.d \\ Y_{mod}(S) = M(S).U_{reg}(S) \end{cases} \tag{4}$$

Which gives the following result:

$$Y(S) = Y_{mod}(S) - \frac{1}{C_C(S)}.d \tag{5}$$

The process output (Y) is the same as that of the model (Y_{mod}) at small disturbance. If this disturbance $\dfrac{d}{C_c(S)}$ is negligible compared to the process output Y, it follows perfectly the model output. This condition is written:

$$\frac{d}{C_c(S)} << M(S).U_{reg}(S) \tag{6}$$

Considering the return coming from the model output Y_{mod}, the system (2) becomes:

$$\begin{cases} Y_{\text{mod}}(S) = \dfrac{M(S).C_p(S)}{1+M(S).C_p(S)}.Y_{ref}(S) \\ Y(S) = \dfrac{P(S)(1+M(S).C_c(S))}{M(S)(1+P(S).C_c(S))}.Y_{mod}(S) \\ \qquad - \dfrac{P(S)}{1+P(S).C_c(S)}.d \end{cases} \tag{7}$$

To simplify the transfer function $\dfrac{Y}{Y_{mod}}$, let us suppose the following hypothesis:

$$|M(S).C_c(S)| >> 1 \tag{8}$$

Correction Controller (Used in The Speed Loop)

The correction controller used in the speed loop allows to cancel the error between the output speed of the machine Ω and that of the model Ω_{mod}. So it is very convenient to use this error as well as its derivative as inputs to this corrector. By integrating the output of the latter, we obtain the correction signal ΔT_e which allows the two machines to have a similar behavior to that of the model. The internal structure of the "Correction Controller" block FLCR is identical to that of an FLC (Main Controller), i.e it consists of three blocks: Fuzzification (F), Knowledge Base and the Inference (I) and defuzzification (D).

where : u represents the stator currents ($i_{sd}$and i_{sq}) and speed Ω for the five-phase machine.

As with the design process of the main controller FLC, each input is represented by seven fuzzy sets. This leads to a rule base of forty-nine (49) rules. The inference method used is that of Mamdani (Max-Min). While defuzzification is achieved by the Center of Area (COA) method is employed. The membership functions of input variables E and ΔE respectively and output variable, which are with conventional triangular shapes. Each membership is divided into seven and three fuzzy sets for speed and stator currents respectively (Fig.2).

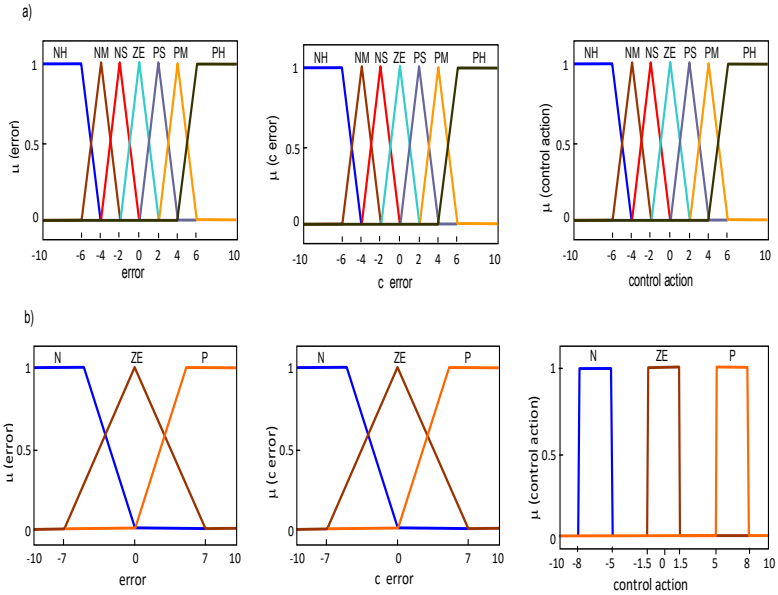

Figure 2. Membership functions of input/output variables: a) Speed,b) Currents

Mathematical Model for Five-Phase Asynchronous Machine

The electric equation of a five-phase an asynchronous machine in the natural base is given by the following expression for each phase:

$$\begin{cases} [V_s] = [R_s][I_s] + \dfrac{d[\phi_s]}{dt} \\ [V_r] = [R_r][I_r] + \dfrac{d[\phi_r]}{dt} \end{cases} \qquad (9)$$

Where: $[V_s] = [v_{sa}\ v_{sb}\ v_{sc}\ v_{sd}\ v_{se}]$; $[I_s] = [i_{sa}\ i_{sb}\ i_{sc}\ i_{sd}\ i_{se}]$; $[V_r] = [v_{ra}\ v_{rb}\ v_{rc}]$; $[I_r] = [i_{ra}\ i_{rb}\ i_{rc}]$;

$R_s = R_{sa} = R_{sb} = R_{sc} = R_{sd} = R_{se}$; $R_r = R_{ra} = R_{rb} = R_{rc}$;

$[\phi_s]=[\phi_{sa}\ \phi_{sb}\ \phi_{sc}\ \phi_{sd}\ \phi_{se}]$; $[\phi_r]=[\phi_{ra}\ \phi_{rb}\ \phi_{rc}]$

The model of five-phase an asynchronous machine is as follows after converting Phase variables into *d-q* variables:

$$\begin{cases} V_{sd} = [R_s]i_{sd} - \omega_s \phi_{sq} + \dfrac{d\phi_{sd}}{dt} \\ V_{sq} = [R_s]i_{sq} + \omega_s \phi_{sd} + \dfrac{d\phi_{sq}}{dt} \\ V_{rd} = [R_r]i_{rd} - (\omega_s - \omega_r)\phi_{rq} + \dfrac{d\phi_{rd}}{dt} \\ V_{rq} = [R_r]i_{rq} + (\omega_s - \omega_r)\phi_{rd} + \dfrac{d\phi_{rq}}{dt} \end{cases} \quad (10)$$

The electromagnetic torque for asynchrounous machine is equal to:

$$T_e = \frac{5}{2} pL_m(\phi_{rd}.i_{sq} - \phi_{rq}.i_{sd}) \quad (11)$$

On the other hand, the mechanichal equation of the machine is:

$$J\frac{d\Omega_r}{dt} = T_e - T_r - f_m.\Omega_r \quad (12)$$

This set of equations allows characterizing the electromechanical behaviour of a five-phase PMSM machine.

Indirect Vector Control for Five-Phase Asynchronous Motor Drive

Vector control technique aims to make equivalence between the five-phase asynchronous motor drive and DC motor. This objective can be achieved by controlling the q-axis flux component to zero. Stator flux and rotor flux orientation are examples of field oriented control techniques for an asynchronous machine. The stator current space vector for an asynchronous machine has two components i_{sd} and i_{sq}.

The i_{ds} produces the rotor flux component and i_{qs} produces the torque-producing component in rotor flux orientation. The rotary flow direction control model is given by the following equation:

$$\begin{cases} i_{rq} = 0 \\ i_{rd}^{*} = \phi \end{cases} \quad (13)$$

The simplified model of the machine as follows:

$$\begin{cases} \sigma L_s \dfrac{di_{sd}}{dt} = -\left(R_s + \dfrac{L_m^2}{L_r^2}R_r\right)i_{sd} + \sigma L_s \omega_s i_{sq} + \dfrac{L_m}{L_r.T_r}\phi_r + V_{sd} \\ \sigma L_s \dfrac{di_{sq}}{dt} = -\left(R_s + \dfrac{L_m^2}{L_r^2}R_r\right)i_{sq} - \sigma L_s \omega_s i_{sd} - \dfrac{L_m}{L_r.T_r}\omega_r \phi_r + V_{sq} \\ \dfrac{d\phi_r}{dt} = \dfrac{L_m}{T_r}i_{sd} - \dfrac{1}{T_r}\phi_r \\ T_e = p\dfrac{L_m}{T_r}\phi_r i_{sq} \\ \omega_r = \dfrac{M}{T_r}.\dfrac{1}{\phi_r}.i_{sq} \\ J\dfrac{d\Omega_r}{dt} = T_e - L_r - f\Omega_r \end{cases} \quad (14)$$

With $T_s = L_s / R_s$: stator time constant ; $T_r = L_r / R_r$: rotor time constant ; $\sigma = 1 - \frac{L_m^2}{L_r.L_s}$: Total leakage coefficient.

Dynamic Model of Flux and Torque

The rotor flux and the electromagnetic torque can be estimated from the currents i_{sd} and i_{sq} , stator quantities accessible from the measurement of real currents stator subject to the realization of the Park transformation.

$$\begin{cases} \hat{\phi}_r + T_r \frac{d}{dt}\hat{\phi}_r = L_m i_{sd} \\ \hat{T}_e = p\frac{L_m}{T_r}\hat{\phi}_r i_{sq} \\ \hat{\omega}_s - \omega_r = \frac{L_m}{T_r}.\frac{1}{\hat{\phi}_r}.i_{sq} \\ \hat{\theta}_s = \int \hat{\omega}_s dt \end{cases} \Rightarrow \begin{cases} \hat{\phi}_r = \frac{L_m}{1+T_r} i_{sd} \\ \hat{T}_e = p\frac{L_m}{T_r}\hat{\phi}_r i_{sq} \\ \hat{\omega}_s - \omega_r = \frac{L_m}{T_r}.\frac{1}{\hat{\phi}_r}.i_{sq} \\ \hat{\theta}_s = \int (p\Omega_r \frac{L_m}{T_r}.\frac{1}{\hat{\phi}_r}.i_{sq})dt \end{cases} \quad (15)$$

Decoupling by Compensation

The decoupling principle amounts to defining two new control variables v_{sd1} and v_{sq1} such as v_{sd1} only acts on i_{sd} and v_{sq1} on i_{sq}. So, we can write the voltages v_{sd} and v_{sq} as a function of v_{sd1} and v_{sq1} as follows:

$$\begin{cases} v_{sd} = v_{sd1} - e_1 \\ v_{sq} = v_{sq1} - e_2 \end{cases} \quad (16)$$

With:

$$\begin{cases} e_1 = \sigma L_s \omega_s i_{sq} + \frac{L_m R_r}{L_r^2}\phi_r \\ e_2 = -\sigma L_s \omega_s i_{sd} - \frac{L_m}{L_r}\omega_s \phi_r \end{cases} \quad (17)$$

Defluxing

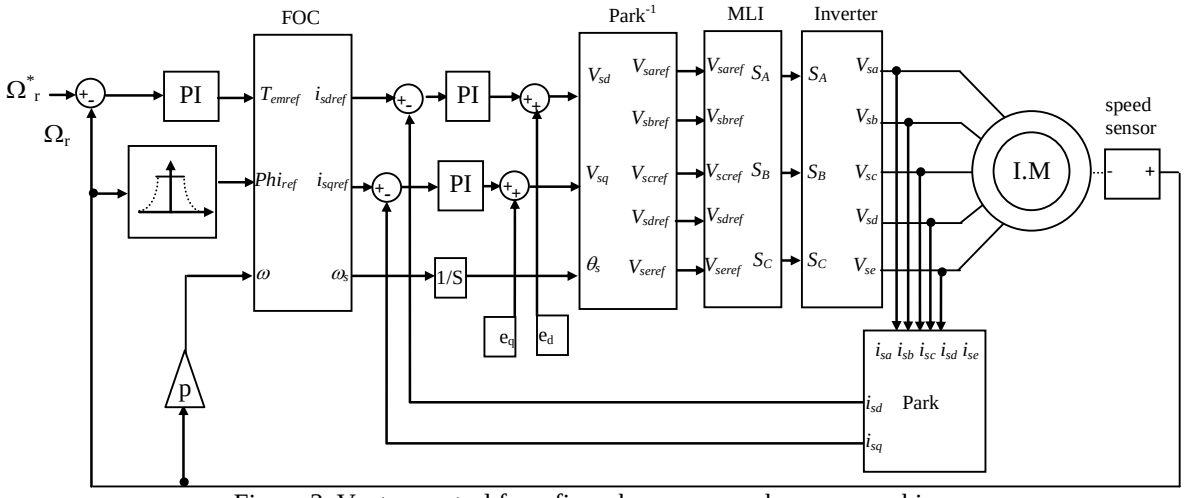

Figure 3. Vector control for a five-phase an asynchronous machine.

The defluxing block are written as follows

$$\phi_r^* = \begin{cases} \phi_{rn} & if \quad \Omega_r < \Omega_{rn} \\ \dfrac{\phi_{rn}\Omega_{rn}}{\Omega_r} & if \quad \Omega_r > \Omega_{rn} \end{cases} \qquad (18)$$

A system illustration of the vector control of five-phase an asynchronous motor is given in Figure 3.

Results and Discussion

Fig. 4 shows the performances of the behaviour model control of a five-phase an asynchronous induction machine. The simulation results are intended to simulate the application of fuzzy adaptive controller (BMC) on the speed control of a five-phase induction machine. The first step is reserved for the simulation of the no-load start, followed by the application of a load torque equal of 20 Nm at t = 2s, with a reversal of direction of rotation at time t = 3s from +100 rad / s to -100 rad / s under a speed of 50 rad / s (five-phase IM). The responses in terms of speeds, torques and stator currents are illustrated in Fig. 4. It is clear that the dynamic performances of five-phase IM are acceptable.

System Robustness

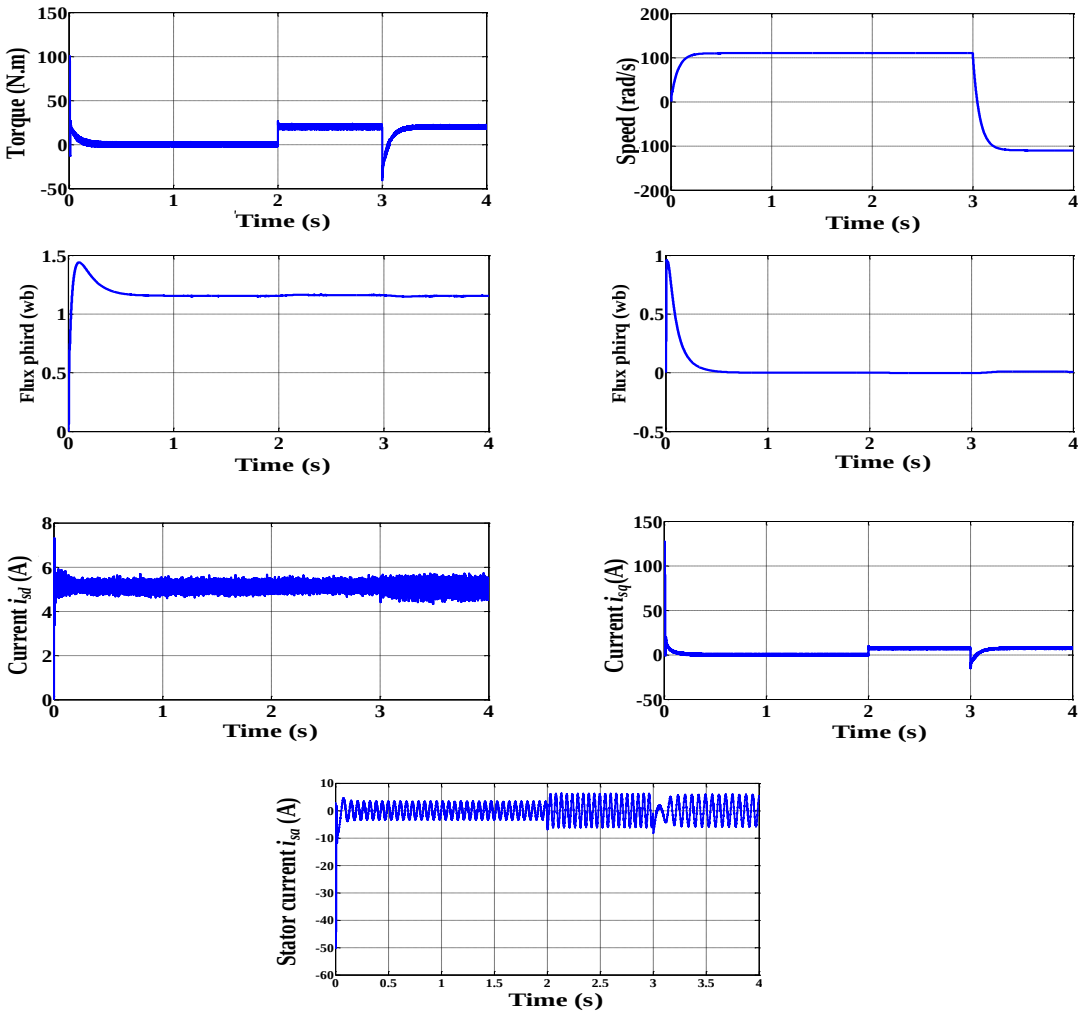

Figure 4. Indirect vector control performance of the five-phase IM with fuzzy adaptive regulators in speed reversal

Figs. 5, the five-phase an asynchronous I.M driver controlled by BCM, FLC and conventional PI of the system under variation of the load and inertial moment (200% *Jn*). At the bottom of the Fig.5, it shows that with BMC, the process is less disturbed by an external disturbance than by compared to the conventional control (PI) and the FLC control. In addition, it is noted that the BMC provides means to better control the transient error due to external disturbance. Finally, the speed response is without overshoot, without static error and with very fast disturbance rejection. Despite internal and external disturbances, the adaptive control maintains the desired performance.

Variation of Rotor Inertia J=200% Jn

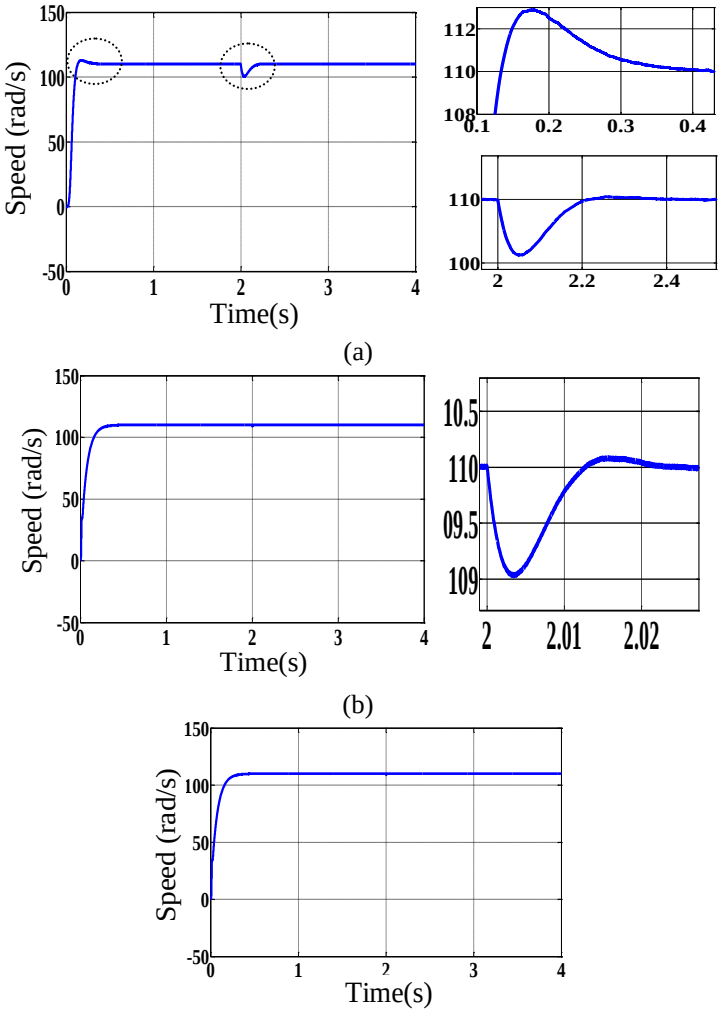

Figure 5. Comparison between BMC, FLC and PI conventional
a) PI, b) FLC, c) BMC)

Conclusion

The work carried out is a numerical simulation of the adaptive control within the direct vector control of a voltage-fed asynchronous machine. The proposed adaptive control is with a reference model whose adaptation mechanism is in parallel with the FLC of the inner loop. The performance of the fuzzy logic adaptive controller has been tested. The results obtained by simulation show that BMC is very robust with respect to the disturbances due to the variations of the load, the moment of inertia. The speed response correctly follows the chosen reference model despite the disturbances.

Induction Motor Data

Rated power P_n= 3kW, nominal currant I_n= 3.6/6.2A, stator resistance R_s= 2.5Ω, rotor resistance R_r=1.9Ω, stator inductance L_s= 0.24H, rotor inductance L_r= 0.24H, mutual inductance L_m= 0.226H, rated phase stator voltage V_n = 380V, pole pair number P=2, rotor speed N = 1499tr/min, viscous friction coefficient K_f= 0.0006Nms/rad, Rotor inertia J= 0.031kg.m2.

Scientific Ethics Declaration

The authors declare that the scientific ethical and legal responsibility of this article published in EPSTEM journal belongs to the authors.

Acknowledgements or Notes

* This article was presented as a poster presentation at the International Conference on Technology, Engineering and Science (www.icontes.net) held in Antalya/Turkey on November 16-19, 2023.

References

Bessaad, T., Taleb, R., & Bachir, G. (2016) Fuzzy Speed Controller design of multi-machines system, *Rev. Roum. Sci. Techn.–Électrotechn. et Énerg*, *61*(1), *Bucarest.*

Bounadja, M., Mellakhi, A., & Belmadani, B. (2007). A high performance PWM inverter voltage-fed induction machines drive with an alterative strategy for speed control. *Serbian Journal of Electrical Engineering*, *4*(1), 13-22.

Fang, Y., Fei, J., & Hu, T. (2018). Adaptive backstepping fuzzy sliding mode vibration control of flexible structure. *Journal of Low Frequency Noise. Vibration and Active Control*, *37*(4), 1079-2096.

Fei, J., & Lu, C. (2018). Adaptive fractional order sliding mode controller with neural estimator. *Journal of the Franklin Institute*, *355*(5), 2369-2391.

Han, H. (2018). Fuzzy approximator based adaptive controller design using Nussbaum type function. *IEEJ Transactions on Electrical and Electronic Engineering*, *13*(7), 1020-1026.

Khaw, A. L. Y., Wong, J., & Lim, Y. S. (2018). Fuzzy controlled energy storage system for improving reliability of electricity supply during islanding of photovoltaic systems. *International Transactions on Electrical Energy Systems*, *28*(10), e2604.

Levi, E. (2008). Multiphase electric machines for variable-speed applications. *IEEE Trans. Ind. Electron*, *55*(5), 1893–1909.

Shihabudheen, K. V., Raju, S. K. G. & Pillai, N. (2018). Control for grid-connected DFIG-based wind energy system using adaptive neuro-fuzzy technique. *International Transactions on Electrical Energy Systems*, *28*(5).

Vulturescu, B., Bouscayrol, A., Hautier, J. P. Guillaud, X. & Ionescu, F. (2000). Behaviour model control of DC machine. *Conference Espoo (Finland)*, 427-431.

Author Information

Bessaad Taieb
Hassiba Benbouali University of Chlef
Hssania Chlef, Algeria
Contact e-mail: *t.bessaad@univ-chlef.dz*

Benbouali Aderrahmen
Hassiba Benbouali University of Chlef
Hssania Chlef, Algeria

Taleb Rachid
Hassiba Benbouali University of Chlef
Hssania Chlef, Algeria

To cite this article:

Taieb, B., Aderrahmen, B., & Rachid, T. (2023). Robustness of the fuzzy adaptive speed control of a multi-phase asynchronous machine. *The Eurasia Proceedings of Science, Technology, Engineering & Mathematics (EPSTEM), 26*, 100-108.

The Eurasia Proceedings of Science, Technology, Engineering & Mathematics (EPSTEM)
ISSN: 2602-3199

The Eurasia Proceedings of Science, Technology, Engineering & Mathematics (EPSTEM), 2023

Volume 26, Pages 109-113

IConTES 2023: International Conference on Technology, Engineering and Science

Investigation of the Temperature Field during Radial-Shear Rolling of Technical Copper

Abdrakhman Naizabekov
Rudny Industrial Institute

Sergey Lezhnev
Rudny Industrial Institute

Yevgeniy Panin
Rudny Industrial Institute

Abstract: Radial-shear rolling is one of the most promising methods of metal forming, allowing to develop a level of strain in the rolled bar sufficient to obtain an ultrafine-grained structure. At the same time, it has already been theoretically and experimentally confirmed that after metal processing by this method, a gradient distribution of grain size is observed in the cross section of the rod, which is a consequence of the laminar-turbulent flow of metal in the deformation zone. This work, carried out within the framework of grant №AP14869128, funded by the Science Committee of the Ministry of Science and Higher Education of the Republic of Kazakhstan, is devoted to the study of the temperature field during radial-shear rolling of M1 technical copper at an initial workpiece temperature of 20°C. To study the temperature distribution over the bar cross section, finite element modeling of radial-shear rolling of M1 technical copper was performed in the Deform program. A rod with a diameter of 30 mm and a length of 150 mm was set as the initial workpiece. It was decided to conduct three passes of radial-shear rolling with compression of 3 mm per pass. In addition to studying the temperature fields on the workpiece, the temperature distribution on the rolls was also considered. Analysis of the simulation results showed that the temperature distribution over the cross-section of the rod has a gradient character.

Keywords: Radial-Shear rolling, Gradient distribution, Simulation, Temperature, Rod

Introduction

Scientific works on obtaining high-quality metal with various methods of severe plastic deformation (SPD) are among the most cited publications in the world (Valiev et al., 2000; Valiev & Langdon, 2006; Sakai et al., 2014). The implementation of SPD due to the intensification of shear and alternating strains makes it possible to achieve the refinement of the initial structure to an ultrafine-grained state and obtain unique mechanical characteristics, which are sometimes paradoxical (Tsuji et al., 2002; Valiev et al., 2002). At the same time, the most well-known SPD methods – high-pressure torsion (HPT) and equal-channel angular pressing (ECAP) - allow deforming samples of limited geometric dimensions, which significantly reduces the possibility of using these methods on an industrial scale.

For the possibility of deformation of long-length samples, a number of ECAP-based combined processes have been developed, which also ensure the continuity of the process (Naizabekov et al., 2020; Naizabekov et al., 2019). However, their implementation requires the modernization of existing rolling or drawing equipment. From this point of view, the most promising SPD method for deforming long workpieces is radial-shear rolling,

which has been studied in many works, including in recent years (Petrova et al., 2023; Lezhnev et al., 2023; Mashekov et al., 2021).

The main content of these studies is the influence of this method on the structure and properties of the processed material and the study of the stress-strain state. At the same time, very little attention is paid to such a factor as the distribution of temperature fields in the workpiece at various geometric and technological parameters of the process. This work is devoted to the study of this problem.

Method

The study of the temperature fields distribution in the workpiece during radial-shear rolling was carried out using FEM modeling in the Deform program. The parameters of the SVP-08 mill from the Rudny Industrial Institute were used as the geometry of the rolls. M1 copper alloy was chosen as the workpiece material at a temperature of 20°C. To study the influence of geometric and technological parameters of the process, it is advisable to vary their values. The following conditions were simulated:

1) The workpiece diameter was 30 mm, the rolls rotation speed was 100 rpm, compression is 1 mm;
2) The workpiece diameter was 30 mm, the rolls rotation speed was 100 rpm, compression is 1.5 mm;
3) The workpiece diameter was 30 mm, the rolls rotation speed was 50 rpm, compression is 1.5 mm;
4) The workpiece diameter was 20 mm, the rolls rotation speed was 100 rpm, compression is 1.5 mm.

The workpiece length in all models was equal to 100 mm, the friction coefficient at the contact of the workpiece and the rolls was equal to 0.5. The heat exchange coefficient of the workpiece with the tool was 5000 W /(m^2 • °C); the heat exchange coefficient of the workpiece with the environment was 0.002 W/(m^2 • °C).

Results and Discussion

To analyze the temperature distribution in the workpiece, a cross section was made at a distance of 50 mm from the front end. The temperature measurement was carried out at the moment of deformation of this section in the deformation zone of the rolling rolls. At the same time, the "point tracking" tool was used, measuring the temperature from the center of the workpiece to the contact zone of the metal with the roll.

When considering Model 1 with a workpiece diameter of 30 mm, a roll rotation speed of 100 rpm and a compression of 1 mm, an extremely uneven temperature distribution was noted over the entire section of the workpiece (Figure 1a). The center of the workpiece heats up to 32°C, while the surface zone heats up to 124°C, i.e. the temperature difference under these conditions is 92°C. For comparative analysis, this model was adopted as the basic one.

In Model 2, with an increase in compression in the rolls up to 1.5 mm (Figure 1b), a general increase in temperature was indicated in the entire section of the workpiece. The central zone of the rod heats up to 54°C, while the surface zone heats up to 191°C, i.e. the temperature difference under these conditions is 137°C. The general increase in temperature over the entire section of the workpiece is a direct consequence of an increase in absolute compression. However, the increase in the temperature difference between the center and the surface is due to a change in the kinematic parameters at the contact of the workpiece and the tool. Due to the fact that the rolls have a mushroom shape, with increasing compression, the length of the deformation focus also increases, while the metal receives a higher linear velocity.

All subsequent models had an increased compression value in rolls of 1.5 mm. When the rolls rotation speed decreased to 50 rpm (Model 3 – Figure 1b), a significant decrease in the temperature difference between the center and the surface was noted. With almost identical heating of the central area of the workpiece to 55°C, the surface of the workpiece in the area of contact with the rolls warmed up to 133°C, i.e. the temperature difference under these conditions is 78°C.

Thus, it can be said that the change in compression affects the temperature change over the entire workpiece section, and the change in rolls rotation speed affects the temperature change mainly in the surface layers. Also, these differences may be the result of the fact that when the compression changes, the configuration of the deformation zone in the rolls changes.

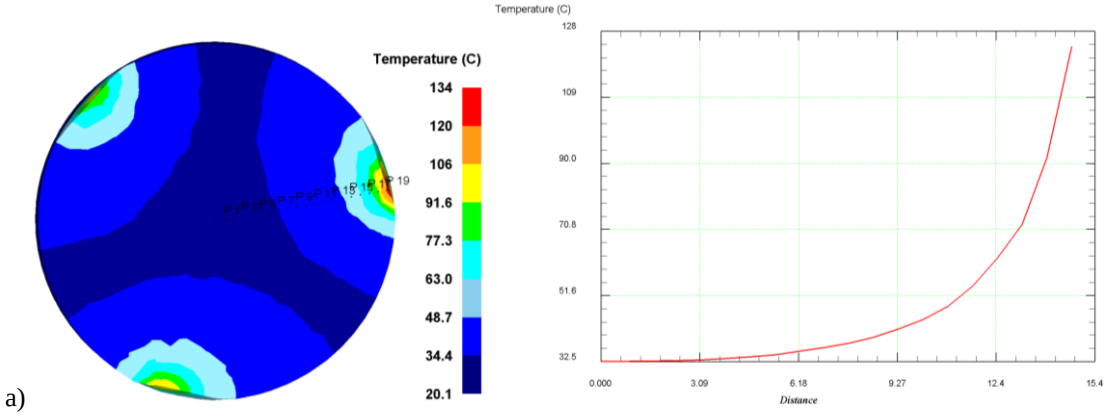

a)

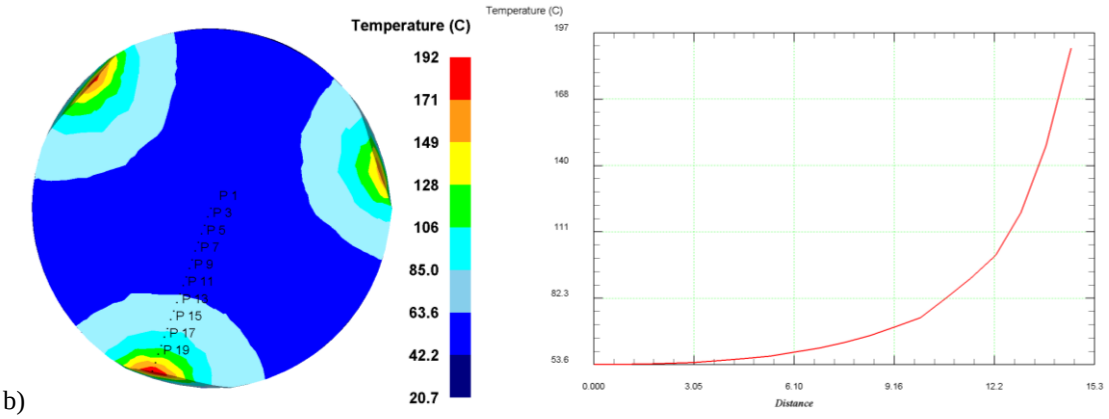

b)

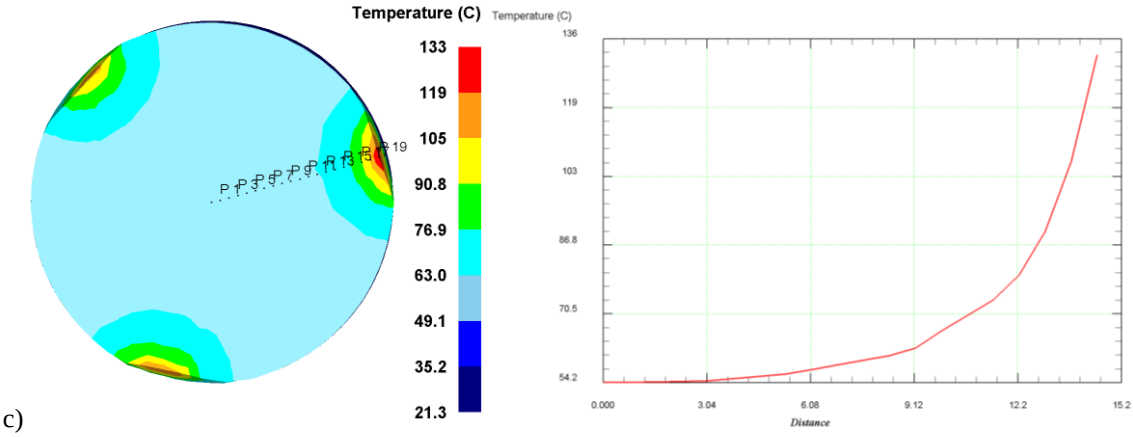

c)

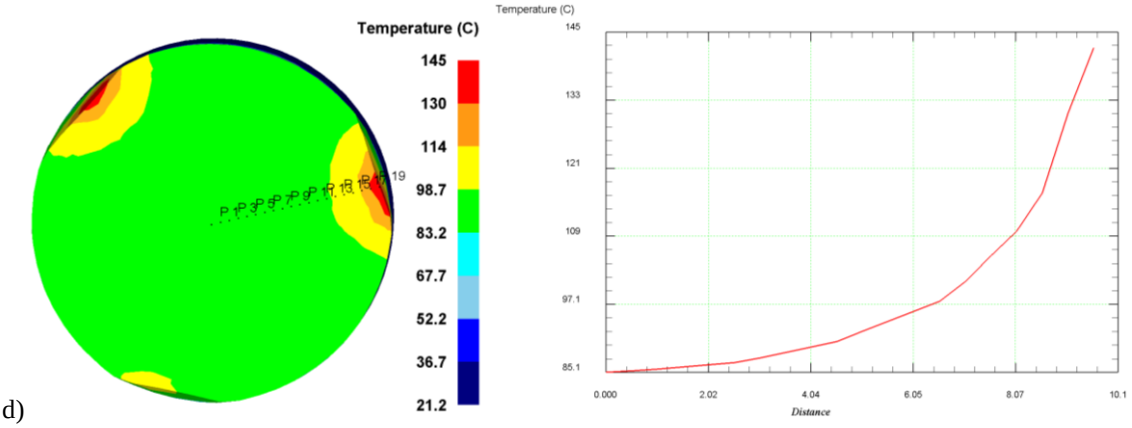

d)

Figure 1. Temperature distribution in the workpiece section: a – model 1; b – model 2; c – model 3; d – model 4

To verify this statement, Model 4 was considered, where a workpiece of a smaller diameter of 20 mm was used to change the parameter of the deformation zone (Figure 1g). In this model, the center of the workpiece is heated to 85°C, while the surface zone is heated to 143°C, i.e. the temperature difference under these conditions is 58°C. A more uniform temperature distribution with increased compression and rotation speed of the rolls became possible due to the fact that due to a decrease in the initial diameter of the rolls, the location of the deformation zone on the radial-shear rolling mill shifts to a more gentle area of the rolls, where kinematic conditions are more uniform. It is this factor that makes it possible to obtain a sufficiently smooth surface of the workpiece without screw edges, even at high compressions.

Conclusion

The study of the temperature distribution in the workpiece during radial-shear rolling has shown that the overall temperature level and the nature of its distribution over the cross-section depend on both the geometric parameters of the process and the technological parameters. At the same time, it was noted that a change in the parameters affecting the change in the configuration of the deformation focus leads to a change in the temperature distribution gradient between the center and the surface. Information about these patterns will allow you to control the temperature change in the required conditions.

Scientific Ethics Declaration

The authors declare that the scientific ethical and legal responsibility of this article published in EPSTEM journal belongs to the authors.

Acknowledgements or Notes

* This article was presented as an poster presentation at the International Conference on Technology, Engineering and Science (www.icontes.net) held in Antalya/Turkey on November 16-19, 2023.

* This research was funded by the Science Committee of the Ministry of Science and Higher Education of the Republic of Kazakhstan (Grant № AP14869128).

References

Lezhnev, S., Panin, E., Tolkushkin, A., Kuis, D., & Kasperovich, A. (2023). Development and computer simulation of a new technology for forming and strengthening screw fittings. *Journal of Chemical Technology and Metallurgy*, *58*(5), 955-960.

Mashekov, S., Nurtazaev, E., Mashekova, A., & Abishkenov, M. (2021). Extruding aluminum bars on a new structure radial shear mill. *Metalurgija*, *60*(3-4), 427-430.

Naizabekov, A., Lezhnev, S., Panin, E., Volokitina, I., Arbuz A., Koinov, T., & Mazur, I. (2019). Effect of combined rolling–ECAP on ultrafine-grained structure and properties in 6063 Al alloy. *Journal of Materials Engineering and Performance*, *28*(1), 200-210.

Naizabekov, A., Volokitina, I., Lezhnev, S., Arbuz A., Panin, E. & Volokitin, A. (2020). Structure and mechanical properties of AISI1045 in the helical rolling–pressing process. *Journal of Materials Engineering and Performance*, *29*(1), 315-329.

Petrova, A. N., Rasposienko, D. Yu., Astafyev, V. V. & Yakovleva, A. O. (2023). Structure and strength of Al-Mn-Cu-Zr-Cr-Fe ALTEC alloy after radial-shear rolling. *Letters on Materials*, *13*(2), 177-182.

Sakai, T., Belyakov, A., Kaibyshev, R., Miura, H. & Jonas, J. J. (2014). Dynamic and post-dynamic recrystallization under hot, cold and severe plastic deformation conditions. *Progress in Materials Science*, *60*(1), 130-207.

Tsuji, N., Ito, Y., Saito, Y., & Minamino, Y. (2002). Strength and ductility of ultrafine grained aluminum and iron produced by ARB and annealing. *Scripta Materialia*, *47*(12), 893-899.

Valiev, R. Z., & Langdon, T. G. (2006). Principles of equal-channel angular pressing as a processing tool for grain refinement. *Progress in Materials Science*, *51*(7), 881-981.

Valiev, R. Z., Alexandrov, I. V., Zhu, Y. T., & Lowe, T. C. (2002). Paradox of strength and ductility in metals processed by severe plastic deformation. *Journal of Materials Research*, *17*(1), 5-8.

Valiev, R. Z., Islamgaliev, R. K. & Alexandrov, I. V. (2000). Bulk nanostructured materials from severe plastic deformation. *Progress in Materials Science*, *45*(2), 103-189.

Author Information

Abdrakhman Naizabekov
Rudny Industrial Institute
38 50 let Oktyabrya str., Rudny, Kazakhstan

Sergey Lezhnev
Rudny Industrial Institute
38 50 let Oktyabrya str., Rudny, Kazakhstan

Yevgeniy Panin
Rudny Industrial Institute
38 50 let Oktyabrya str., Rudny, Kazakhstan
Contact e-mail: *ye.panin@tttu.edu.kz*

To cite this article:

Naizabekov, A., Lezhnev, S., & Panin, Y. (2023). Investigation of the temperature field during radial-shear rolling of technical copper. *The Eurasia Proceedings of Science, Technology, Engineering & Mathematics (EPSTEM), 26*, 109-113.

The Eurasia Proceedings of Science, Technology, Engineering & Mathematics (EPSTEM)
ISSN: 2602-3199

The Eurasia Proceedings of Science, Technology, Engineering & Mathematics (EPSTEM), 2023

Volume 26, Pages 114-120

IConTES 2023: International Conference on Technology, Engineering and Science

Statistical Analysis of an RC Elevated Tank Damage by a Nonlinear Approach

Ourdia Ider
Mouloud Mammeri University

Amar Aliche
Mouloud Mammeri University

Hocine Hammoum
Mouloud Mammeri University

Karima Bouzelha
Mouloud Mammeri University

Abstract: In the seismic field, the seismic performance of a structure reflects its damage level under a given seismic demand. Thus, to evaluate this performance, many analysis and design techniques are used, such as nonlinear approach commonly called Pushover is used in this research. On the other hand, predicting the damage level is a random process, where only a probabilistic approach would allow predicting it, as the level of uncertainty, related to the seismic action is important. For this purpose, a statistical study was conducted through simulations with large number of seismic accelerations, generated from a probabilistic distribution law, inspired from the Monte Carlo method, to evaluate the damage rates corresponding to each damage domain. The results revealed the influence of the seismic zone and the location of the structure on the damage rate observed after seismic loading.

Keywords: Seismic acceleration, Performance, Damage, Pushover analysis, Statistical study, Monte Carlo.

Introduction

In the field of seismic engineering, the concept of damage is used to express the various responses of structures to the loads they experience throughout their lifecycle. This concept refers to a structure's susceptibility to damage caused in various ways, including excessive forces such as earthquakes, strong winds, or storms. Assessing damage requires qualifying and quantifying the expected level of damage in order to compare it to the maximum acceptable threshold.

In this context, mastering damage to achieve greater safety and security requires a better understanding and, consequently, better control and/or reduction of the multiple sources of uncertainty that one may encounter (Lemaire, 2005; Aoues, 2008; Aliche et al., 2019). It is within the framework of this overarching challenge that the present work is situated, with its primary objective being to propose an approach that combines nonlinear static analysis and probabilistic analysis to account for the uncertainties surrounding the assessment of structural damage levels under dynamic loading. For the purposes of probabilistic analysis, the Monte Carlo simulation method is employed in this research. A numerical example is presented to illustrate the calculation method described, along with an analysis and discussion of the obtained results.

Damage Assessment of an RC Elevated Tank

In this study, we propose a methodology for estimating the damage that can occur in an RC elevated tank under the influence of seismic loading. The approach developed is inspired by the concept presented in the RISK-EU method adopted for RC tanks. This approach will then be coupled with a probabilistic analysis process that considers the random nature of seismic loading to determine the estimate of the damage probability of occurring to our structure.

Assessment Methodology

It is common practice today to estimate the performance of a civil engineering structure by a deterministic approach on the (Sa, Sd) plane using nonlinear calculation methods. This procedure allows the construction of pushover curves for the studied structure by applying the capacity spectrum method, which then provides the maximum displacement of the structure during seismic loading (Hammoum et al, 2016). This parameter, considered as a key element, and helps to determine the state of damage in the RC structure through an associated damage index. The literature offers several models for characterizing structural degradation, such as the RISK-EU method. The principle of this method is to identify damage domains based on the maximum displacement that develops at the top of the tank under seismic action. We get inspired from of the RISK-EU method and FEMA 273 code, and we propose a classification of damage domains for RC elevated tank (Table 1). Consequently, there are six damage levels ranging from the green domain 1 to total failure of the structure corresponding to the red domain (see Table 1).

Table 1. Proposed Damages Domains for Elevated Tanks.

Degrees and damage domains	Formulas for differents spectrals displacements limits
Green 1 Domain (Negligible Damages)	$Sd < 0.4\ \delta e$
Green 2 Domain (Minor Damages)	$0.4\ \delta e \leq Sd < 0.8\ \delta e$
Orange 1 Domain (Moderate Damages)	$0.8\ \delta e \leq Sd < \delta e + 0.25\ (\delta u - \delta e)$
Orange 2 Domain (Signifiant Damages)	$\delta e + 0.25\ (\delta u - \delta e) \leq Sd < 0.75\ \delta u$
Orange 3 Domain (Severe Damages)	$0.75\ \delta u \leq Sd < \delta u$
Red Domain (Complete Structural Collapse)	$Sd \geq \delta u$
δe : Elastic limit displacement	
δu : Ultimate limit displacement	

The drawback of this approach lies in the fact that each step of the structure damage assessment process is affected by uncertainties primarily related to the definition of the hazard. To address this issue and better estimate the probability of damage to our structure, an approach based on the use of a probabilistic model that takes into account the uncertainties in seismic loading is developed. This approach, accurately estimates the degree of damage to an RC elevated tank by employing the Monte Carlo simulation method. Two types of seismic behaviour coefficients are considered for this purpose.

Probabilistic Concept

Damage Criterions and Limit State Functions

The evaluation of vulnerability involves quantifying the damages that can occur in a structure or structural component following a given seismic load. In the case of an elevated tank, which is considered as an inverted pendulum with mass concentrated at the top, its stability is affected by ground motion at the base during seismic loading, resulting in a maximum displacement, Sd, at the top, thus resulting damage to certain structural components or complete structural collapse. However, to quantify the probability of a certain level of damage occurrence, considering the non-linear behaviour of the structure and the variability in seismic loading, we employ the Monte Carlo method (Lemaire, 2005).

Random Variable

The modeling of the nonlinear behaviour of an RC elevated tank is affected by numerous uncertainties, which can sometimes be difficult to estimate quantitatively. Accounting for these uncertainties leads to a certain

complexity in the formulation. Therefore, a simplification focused on essential parameters becomes essential. In this study, where the probability of reaching or exceeding a damage level is calculated, the parameter that exerts the most influence on the structure's behaviour is the seismic loading. This variable is considered as the primary source of uncertainty in our study and follows a probability distribution law.

Goodness-of-Fit Test

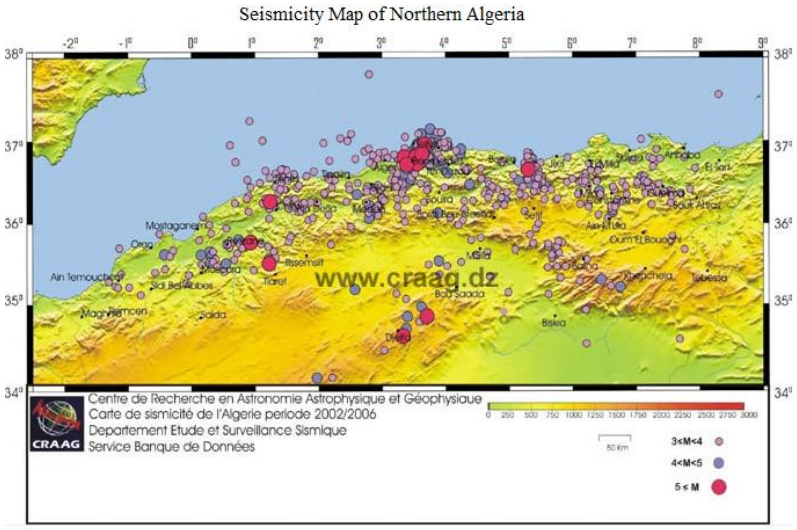

Figure 1. Seismicity map of Northern Algeria

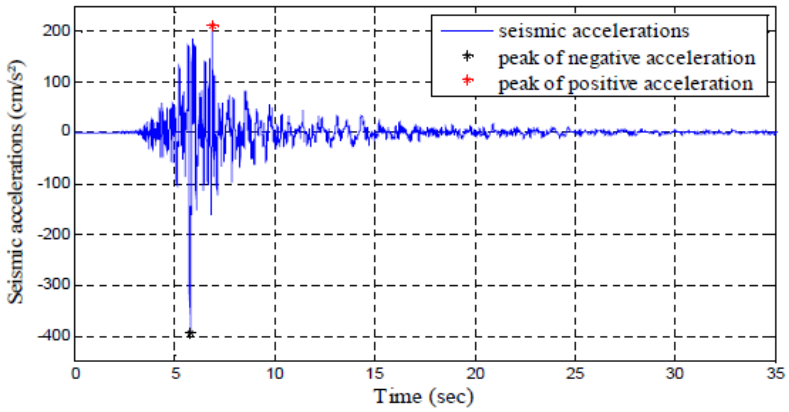

Figure 2. Accelerogram recorded at the Kheddara Dam Site (CGS) (Aliche et al., 2016)

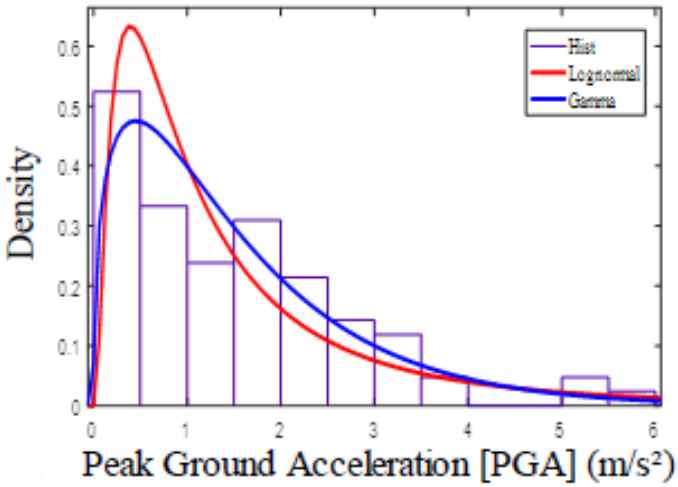

Figure 3. Histogram of peak accelerations and probability distribution laws.

To determine the type of distribution of accelerations, we perform a statistical analysis based on Kolmogorov-Smirnov (K-S) tests (Ahmadi et al, 2015). These tests are conducted using a database composed of 45 accelerograms recorded following the May 21st, 2003 earthquake in Boumerdes, Algeria, by various seismographs installed by the National Center for Applied Research in Seismic Engineering (CGS) in the central region of Algeria (see Figure 1). In Figure 2, we provide an example of an accelerogram recorded at the Kheddara dam site (50 km east of Algiers) and used for the statistical analysis (Hammoum et al, 2021).

The result of the goodness-of-fit test, namely the K-S Test, indicates that the gamma distribution is the most appropriate for approximating the distribution of the peaks accelerations sample (Table 2). The shape and scale parameters of the distribution are, respectively, k = 1.41427 and θ = 1.08846.

The representation of the sample density along with the overlay of the cumulative distribution function on the sample (Figure 3) confirms the choice of the distribution law. In fact, the gamma distribution appears to be much more suitable than the log-normal distribution.

Table 2. Kolmogorov-Smirnov Goodness-of-Fit test results for acceleration

Distribution Laws	P-values	k-s stat	Test Decision
Log normal	0.6737	0.0769	accepted
Gamma	0.6987	0.0753	accepted

Practical Application

Description of the Studied Elevated Tank

To apply the methodology described above, we consider a concrete elevated tank with a capacity of 200 m3 and a support height of H=15m. The tank is located in seismic zone IIa and on a loose soil site (S3). The behavior coefficient provided by RPA is R=2, and the value of R obtained through the nonlinear approach is R=2.63 (Ider, 2023). A three-dimensional finite element model has been developed to simulate the tank's behaviour under lateral loading of the progressive thrust type, using the ETABS© software.

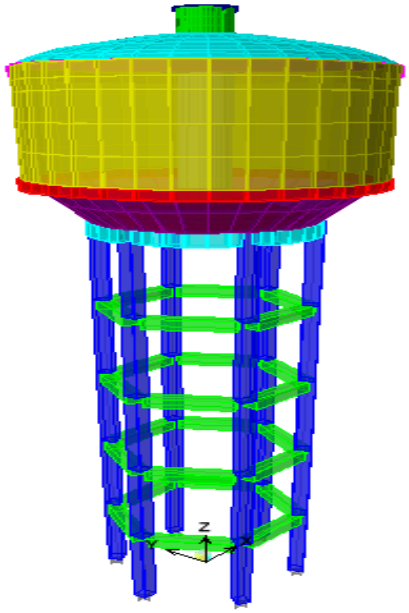

Figure 4. Finite element modelling of the RC elevated tank

Performance Point Evaluation

For each spectrum representing a simulated seismic loading, we obtain the displacement induced at the top of the structure, considering two types of seismic behaviour coefficients, namely R_{RPA}=2 and $R_{power\ law}$ which varies depending on the seismic zone (Table 3) (Ider, 2023). Figure 5 displays the maximum displacements experienced by the tank for 150,000 seismic loading simulations.

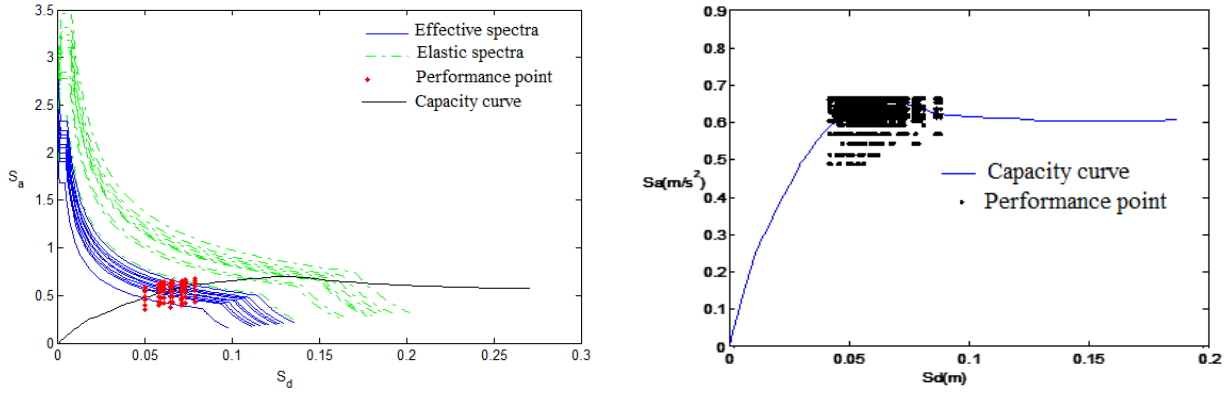

Figure 5. Performance points in the form of a scatterplot from the 150000 simulations.

Influence of the Seismic Zone and the R Coefficient on the Level of Damage

The probabilistic analysis of the seismic vulnerability of the tank, which was the subject of the deterministic study, is carried out by varying its location from Zone I to Zone III. The results of calculating the probability of damage to the study tank are given in the following table 3 (Table 3):

Table 3. Probabilistic variation of the damage level of a support tank with H=15m for different R.

R - RPA		**R=2**			
zone		I	II a	II b	III
		0.12	0.2	0.25	0.3
Pf	Green 1 Domain	0	0	0	0
	Green 2 Domain	0.05758	0	0	0
	Orange 1 Domain	0.846213333	0.03386667	0	0
	Orange 2 Domain	0.09616	0.95366667	0.13144667	0
	Orange 3 Domain	4.66667E-05	0.01246667	0.80427333	0.00771333
	Red Domain	0	0	0.06428	0.99228667

R-law Power		**R=2.05**	**R=2.63**	**R=2.98**	**R=3.35**
zone		I	II a	II b	III
		0.12	0.2	0.25	0.3
Pf	Green 1 Domain	0	0	0	0
	Green 2 Domain	0.115846667	0	0	0
	Orange 1 Domain	0.821846667	0.47072	0	0
	Orange 2 Domain	0.06226	0.52928	1	1
	Orange 3 Domain	4.66667E-05	0	0	0
	Red Domain	0	0	0	0

The results of the damage analysis of the tank under consideration in our application, identified by evaluating each simulation using the damage index as defined by the limit state functions for failures or damages, are presented in Table 3. These results are also summarized by presenting a histogram illustrating the probability distribution of damage occurrences within the elevated tank. Thus, the Figure 6 illustrates the probability distribution of tank damage based on the two values of the behaviour coefficient considered. This representation provides a detailed insight into the statistical distribution of damage within the sample used. It is evident that for both coefficients (R-RPA and R-Power Law), the probability of damage occurrence in the structure is significantly different.

The structure is at risk of experiencing Orange 2-type damages with a probability of 95.36% in the case of a coefficient (RRPA =2). However, with a coefficient of (R-Power Law = 2.63), the risk of damage is 52.92% in the Orange 2 domain and 47.07% in the Orange 1 domain. this comes from the fact that the coefficient proposed

in the calculation code overestimates the seismic risk, resulting in significant displacements, unlike the R-Power Law coefficient. Moreover,the results have demonstrated that the probability of damage occurrence is highly sensitive to changes in the seismic zone

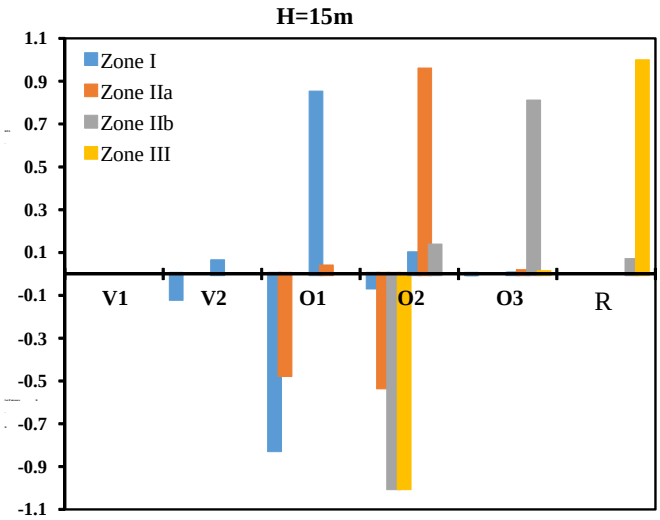

Figure 6. Probabilistic histogram of the variation in damage level of a support tank with H=15m for different R and seismic zone..

Conclusion

The concept of probabilistic analysis and the notion of damages are employed in this research to assess the probabilities of damage to the elevated tank subject of this study, within each of the predefined domains outlined in Section 1. Two behaviour coefficients are used, namely R=2 as recommended by the RPA, and the R values obtained from the power law. The limit state functions are defined by the damage domains associated with the spectral displacement Sd.

The random variable associated with seismic action is generated by a Gamma distribution, deduced from a statistical analysis performed on a sample of peak accelerations obtained from 45 accelerograms recorded following the Boumerdes earthquake in 2003. The results have highlighted a redistribution of the risk probabilities of damage occurrence between the value of R=2 and the values derived from the power law. Furthermore, the results have shown that the probability of damage occurrence is highly sensitive to changes in the seismic zone.

Scientific Ethics Declaration

The authors declare that the scientific ethical and legal responsibility of this article published in EPSTEM journal belongs to the authors.

Acknowledgements or Notes

* This article was presented as a poster presentation at the International Conference on Technology, Engineering and Science (www.icontes.net) held in Antalya/Turkey on November 16-19, 2023.

References

Ahmadi, H., Mohammadi, A. H., & Yeganeh, A. (2015). Probability density functions of SCFs in internally ring-stiffened tubular KT-joints of offshore structures subjected to axial loading. *Thin-Walled Structures, 94*, 485-499.

Aliche, A. (2016). *Contribution à l'analyse de l'évolution de la vulnérabilité des réservoirs en béton dans leur cycle de vie* (Doctoral dissertation). Université de Tizi Ouzou-Mouloud Mammeri.

Aliche, A., Hammoum, H., & Bouzelha, K. (2019). Mecano-reliability analysis applied to RC tank under seismic loads according to the Algerian seismic standard. *Asian Journal of Civil Engineering, 20*(3), 395-408.

Aoues, Y. (2008). *Optimisation fiabiliste de la conception et de la maintenance des stuctures.* (Doctoral dissertation). Université Blaise Pascal-Clermont-Ferrand II.

DTR/B-C 2–48–2003.National seismic code for building design and construction, R.P.A 99/ Version 2003.

Hammoum, H., Aliche, A., Bouzelha, K., Aoues, Y., Amiri, O., & Mehani, Y. (2021). Fragility analysis of concrete elevated water tanks under seismic loads. *Frattura ed Integrità Strutturale, 15*(57), 93-113.

Hammoum, H., Bouzelha, K., & Slimani, D. (2016). Seismic risk of RC water storage elevated tanks: Case study. A. S. H. Makhlouf & M. Aliofkhazeri (Eds.), *Handbook of Materials Failure Analysis with Case Studies from the Chemicals, Concrete and Power Industries* (pp.187-216). Butterworth-Heinemann.

Ider, O. (2023). *Evaluation of the global behavior coefficient R for elevated tanks.* (Doctoral dissertation). Mouloud Mammeri University of Tizi-Ouzou. Algeria.

Lemaire, M. (2013). *Structural reliability.* John Wiley & Sons.

Author Information

Ider Ourdia
Civil Engineering Department, Mouloud Mammeri University, 15 000 Tizi-Ouzou, Algeria

Aliche Amar
Civil Engineering Department, Mouloud Mammeri University, 15 000 Tizi-Ouzou, Algeria
Contact e-mail: amar.aliche@ummto.dz

Hammoum Hocine
Civil Engineering Department, Mouloud Mammeri University, 15 000 Tizi-Ouzou, Algeria

Bouzelha Karima
Civil Engineering Department, Mouloud Mammeri University, 15 000 Tizi-Ouzou, Algeria

To cite this article:

Ider, O., Aliche, A., Hammoum H., & Bouzelha, K. (2023). Statistical analysis of an RC elevated tank damage by a nonlinear approach. *The Eurasia Proceedings of Science, Technology, Engineering & Mathematics (EPSTEM), 26,* 114-120.

The Eurasia Proceedings of Science, Technology, Engineering & Mathematics (EPSTEM)
ISSN: 2602-3199

The Eurasia Proceedings of Science, Technology, Engineering & Mathematics (EPSTEM), 2023

Volume 26, Pages 121-134

IConTES 2023: International Conference on Technology, Engineering and Science

Seismic Hazard Map of ASEAN Countries towards Risk Assessment and Sustainability of Structures and Infrastructures

Noor Sheena Herayani Harith
Universiti Malaysia Sabah

Azlan Adnan
Universiti Teknologi Malaysia

Abstract: This study contains the most recent seismic hazard map of Southeast Asia. This area is located to the south of the Eurasian plate. The Ring of Fire that surrounds the region makes it one of the most active in terms of earthquakes and volcanoes. Malaysia, Indonesia, Thailand, Singapore, the Philippines, Myanmar, Vietnam, Laos, Cambodia, and Brunei are among the countries being studied. The goals of this project are to provide Peak Ground Acceleration (PGA) values for all regions in ASEAN countries, and then to create seismic zoning maps for these countries so that zones with non-seismic regions can be identified and zones with no special steel reinforcement-detailing requirements can be specified. The final step is to create design response spectra. Based on each nation's most recent body of literature, the PGA hazard map is created. There are two maps that need to be created, one for 10% and one for 2% probability of exceeding. The PGA contours of all the compiled maps were then reconstructed, and the baseline colours were compared to an Indonesia seismic hazard map. The maximum PGA value for Southeast Asia is as high as 0.8g at 10% and 2.0g at 2% probability of exceedance, respectively, whereas the minimum PGA value is typically equal to 0.0g at both 10% and 2% probability of exceedance. The design response spectrum distribution of the stable with moderate earthquake region from 0 to 4 s (including West Malaysia, Sabah and Sarawak of East Malaysia) and the distribution of spectra for active earthquake regions including Indonesian cities (including Acheh, Padang and Palu) are plotted. Then, the design response spectra for the selected cities in regions of moderate seismicity and active earthquakes are integrated.

Keywords: Sustainable structure, Earthquake asian, Seismic hazard

Introduction

Southeast Asia is lying within the Pacific Ring of Fire, an area with frequent seismic and volcanic activity. It is flanked on the west by the seismically active Indonesian Volcanic Arc (200-300 km away), which marks the inter-plate boundary (subduction zone) between the Indo-Australian and Eurasian Plates, and on the east by the Eurasian and Philippines Plates. These plates interact in complex ways, resulting in a diverse set of geological characteristics and seismic hazards. Metcalfe (2017), Shah et al. (2018), Pilia et al. (2023), Holt et al. (2018), Lallemand (2016), Khin et al. (2017) on Cummins (2017), Triyoso et al. (2022), and others have investigated Southeast earthquake hazards. Large earthquakes originating in these volcanic arcs have been felt across Southeast Asia. The regular occurrence of tremors inside the country and its surrounding region appears to indicate that ASEAN countries such as Malaysia, Brunei, Indonesia, the Philippines, Singapore, Myanmar, Vietnam, Laos, Thailand, and Cambodia face seismic risk. The question now is whether seismic variables should be included in infrastructure planning and design, as well as the degree of risk and its regional variation. These questions have gone unanswered thus far due to a dearth of seismic knowledge and seismic data. As a result, the magnitude of seismic hazard is unknown. It is unknown whether such a risk should be included in the design of future structures and infrastructure. This is exacerbated by the fact that ASEAN nations are quickly

developing and critical transportation systems are being built at a rapid pace. Long-term ground vibrations produced by distant earthquakes may also endanger these structures.

One of Southeast Asia's most notable tectonic features is the Sunda Trench, a deep oceanic trench that extends along the western shores of Sumatra and Java. The Eurasian and Indo-Australian continents are separated by this trench, which is a hotspot for earthquakes and volcanic activity. The subduction of the Indo-Australian plate beneath the Eurasian plate, in particular, is responsible for the formation of the Indonesian archipelago and many active volcanoes in the region (Lemenkova, 2020, 2021). Another notable tectonic feature of Southeast Asia is the Philippine Mobile Belt, a zone of dynamic deformation that comprises the Philippine Sea plate and numerous smaller microplates. This area is also known for frequent earthquakes, many of which are triggered by the subduction of the Philippine Sea plate beneath the Eurasian plate, as reported by Rangin (2016) and Suzuki et al (2017). The tectonic setting of Southeast Asia is complex and active, with multiple plates and microplates interacting in various ways (Li et. al., 2021; Hua et.al.,2022). This creates a high level of seismic and volcanic activity, putting people and infrastructure in the region at risk.

The Southeast Asia seismic hazard map, created previously by Petersen et al., (2007), is a vital tool for understanding the potential of earthquakes occurring in the region. Peak Ground Acceleration (PGA) hazard maps of 10% and 2% in 50 years were released by Petersen et al. (2007). The most recent hazard map is also available from Pagani et al. (2018, 2020) and published geographic distribution of the PGA with a 10% likelihood of being surpassed in 50 years, estimated under reference rock conditions (shear wave velocity, V, of 760-800 m/s). Despite being published in Pagani et al. (2018, 2020), the data map initially shows different values in contrast to MS EN1998:2015 (2017) for the Malaysia region. The most recent hazard map is also available from Pagani et al. (2018, 2020) and published geographic distribution of the PGA with a 10% likelihood of being surpassed in 50 years, estimated under reference rock conditions. Despite being published in Pagani et al. (2018, 2020), the data map initially shows different values in contrast to MS EN1998:2015 (2017) for the Malaysia region. This could be linked to an updated Malaysian database that includes local seismic sources, as discovered by Shoushtari et al. (2018) and Harith et al. (2023).

The seismic hazard map depicts the likelihood and intensity of earthquakes in different parts of Southeast Asia. Based on the information supplied by the map, governments and emergency responders may prioritise resources and prepare for possible disasters. The seismic danger map was constructed by using a variety of data sources, including prior seismic activity, geological surveys, and satellite photography (Morell et al., 2020; Xu et al., 2022). Statistics are used to assess which areas are most vulnerable to earthquakes and to estimate the potential damage caused by an earthquake in each area. On the map, a color-coded system is utilised to illustrate the level of seismic danger posed by each region. The bright colour represents the probability of an earthquake occurring in a location, while the low colour represents the probability of a small earthquake occurring in a region. The map also includes information on the probable repercussions of earthquakes, such as the possibility that buildings and infrastructure would be destroyed. The seismic hazard map for Southeast Asia is a vital resource for regional decision-makers and first responders. It contributes to the process of making decisions on infrastructure development, emergency planning, and disaster response. For example, the image might be used to evaluate whether areas require additional strengthening of building norms and standards to ensure that buildings can resist the effects of earthquake. This study aims to create the most recent seismic hazard map by incorporating all Southeast Asian nations (Malaysia, Brunei, Indonesia, the Philippines, Singapore, Myanmar, Vietnam, Laos, Thailand, and Cambodia).

Active Earthquake Region (Indonesia, Philippines, and Myanmar)

A region characterised by frequent earthquakes and ongoing tectonic activity is referred to as an active earthquake region. Consisting of the earth's surface, tectonic plates are constantly shifting and interacting with one another. The Earth's crust may experience pressures and strains where these plates converge, which may result in earthquakes. In comparison to other Southeast Asian nations, Indonesia, the Philippines, and Burma have the highest earthquake activity. Indonesia is prone to a high level of seismic and volcanic activity, with earthquakes and volcanic eruptions happening on a regular basis across the archipelago. The Indonesian archipelago and the region's many active volcanoes are the result of the subduction of the Indo-Australian plate beneath the Eurasian plate (Hutchings & Mooney, 2021). Indonesia is situated in the Ring of Fire, a seismically active region that encircles the Pacific Ocean. On December 26, 2004, a magnitude 9.1 earthquake off the coast of Sumatra caused one of the most devastating earthquakes to strike Indonesia. The earthquake triggered a series of tsunamis that affected several countries in the region, including Indonesia, Sri Lanka, India, and Thailand. The earthquake and resulting tsunamis killed more than hundreds of thousand people, making it one of the

deadliest natural disasters in history. On September 28, 2018, a magnitude 7.5 earthquake struck off the coast of Sulawesi, an Indonesian island. The earthquake triggered a massive tsunami, wreaking havoc and killing thousands of people. Movement along the Palu-Koro Fault, a strike-slip fault that runs through the island of Sulawesi, caused the earthquake.

The Philippines is situated on the boundary between the Philippine Sea Plate and the Eurasian Plate and is prone to a high degree of seismic and volcanic activity. Active fault systems in the country, such as the Philippine Fault System and the Marikina Valley Fault System, pose significant earthquake hazards to the region. The Philippines is also located on the Ring of Fire and is highly prone to earthquakes due to its location on the intersection of several tectonic plates. Every year, thousands of earthquakes strike the country, with many of them being minor tremors that go unnoticed. However, there have been several devastating earthquakes in the country's history. On July 16, 1990, a magnitude 7.8 earthquake struck the island of Luzon, resulting in one of the deadliest earthquakes to strike the Philippines. The earthquake caused widespread devastation and the deaths of thousands of people. More recently, on October 15, 2013, a magnitude 7.2 earthquake struck the island of Bohol, causing extensive damage and killing hundreds of people. Volcanic activity also causes earthquakes in the Philippines. For example, Mount Pinatubo's eruption in 1991 caused a magnitude 7.8 earthquake, resulting in several deaths and widespread damage.

Myanmar is located on the boundary of the Indian Plate and the Eurasian Plate, which makes it an active earthquake region. The Sagaing fault, which runs north-south through the country, in particular, is a major source of seismic activity. The collision of these two plates is responsible for the tectonic activity in Myanmar, which has resulted in the formation of the Himalayan Mountain range and other mountain ranges in the region. Myanmar is vulnerable to earthquakes due to the region's tectonic activity, and the country has previously experienced several significant earthquakes. One of the most devastating earthquakes in Myanmar's recent history occurred on August 24, 2016. The 6.8 magnitude earthquake occurred in central Myanmar, near the town of Chauk. The earthquake was felt throughout the country as well as in neighbouring Thailand and Bangladesh. The earthquake caused widespread damage to buildings, roads, and other infrastructure, and at least three people were killed.

Stable Continental Region (Malaysia, Singapore, Thailand, Vietnam, Laos, Cambodia and Brunei)

A stable continental region is a tectonically stable area of the Earth's crust that does not experience significant geological activity such as earthquakes or volcanic eruptions. These regions are typically found deep within tectonic plates, far from the boundaries where plates collide or move apart. Malaysia, Singapore, Thailand, Vietnam, Laos, Cambodia, and Brunei are examples of stable continental regions. A moderate earthquake is one with a Richter magnitude of 5.0 to 5.9 on the Richter scale. This magnitude earthquake can cause noticeable shaking and minor damage to buildings and other structures. Malaysia is located on the Sunda Plate, which is prone to earthquakes caused by the Indian Plate subduction beneath the Eurasian Plate. The region is also impacted by active far-fault systems, such as the Sumatran fault, which poses a significant earthquake risk. On June 5, 2015, Malaysia was struck by a powerful earthquake with a magnitude of 6.0. The earthquake struck in the country's east, near the borders with Brunei and Kalimantan, and was felt throughout the region. The earthquake damaged buildings and infrastructure, particularly in the Sabah town of Ranau. The earthquake in Sabah, Malaysia, was caused by movement along the Ranau Fault, which runs through the country's northern region. Malaysia is also close to the Sunda Megathrust, which is a subduction zone where the Indo-Australian Plate is being pushed beneath the Sunda Plate. The Sumatran Fault is a major fault system located off the western coast of Sumatra, Indonesia, and about 300 kilometres from Malaysia. The fault is a transform fault that divides the Indian-Australian Plate to the west from the Sunda Plate to the east. The fault system stretches for about 1,800 kilometres and is known to be a source of significant seismic activity in the area. On December 26, 2004, the Sumatran Fault caused one of the most notable earthquakes in Malaysia. This 9.1 magnitude earthquake was one of the largest ever recorded and triggered a devastating tsunami that caused significant damage and loss of life throughout Southeast Asia. While Malaysia did not feel the full force of the 2004 earthquake and tsunami, there was significant seismic activity because of the event.

Singapore is in Malaysia's southern region, which is generally considered to be earthquake-free. Singapore is located on the stable Sunda Shelf, which is less prone to earthquakes than the rest of Southeast Asia. While Singapore has had earthquakes in the past, most of them were minor and did not cause significant damage. With a magnitude of 6.1, one of the most notable earthquakes to have struck Singapore occurred on February 4, 2018. The earthquake struck off the coast of Java, Indonesia, and was felt in several parts of Singapore.

Thailand is situated on the Indochina block, which is bordered by the Eurasian Plate to the north, the Indian Plate to the west, and the Australian Plate to the south. Thailand has experienced a number of significant earthquakes in the past, the most recent occurring on May 5, 2014. The quake had a magnitude of 6.0 and occurred in the northern region of the country near the Myanmar border. The earthquake was felt throughout the region and caused significant damage to buildings and infrastructure. The quake in Thailand was caused by movement along the Mae Tha Fault, which runs through the country's northern region. The Mae Tha Fault is a major source of seismic activity in Thailand and can produce magnitude 7 or greater earthquakes. Thailand is situated near the Mae Tha Fault and the subduction zone where the Indian Plate is being pushed beneath the Eurasian Plate, resulting in the formation of the Himalayas and the associated seismic activity in the region.

Vietnam is situated on the eastern margin of the Eurasian Plate and is surrounded by the South China Sea. The principal cause of tectonic activity in Vietnam is the collision between the Eurasian Plate and the Philippine Sea Plate, which generates a complex system of fault zones and volcanic activity in the region. Vietnam is also located close to the subduction zone where the Philippine Sea Plate is being pushed beneath the Eurasian Plate, resulting in the formation of the Ryukyu Islands and the associated seismic and volcanism. Vietnam has experienced several significant earthquakes in the past, with the most recent one occurring on July 6, 2021. The earthquake had a magnitude of 6.2 and occurred in the province of Son La in the country's northwest. Several regions of the country, including Hanoi, felt the earthquake, which caused damage to buildings and roads.

Laos is located on the Southeast Asian Tectonic Plate, which is surrounded by several active plate boundaries. Numerous significant earthquakes have occurred in the country, including a magnitude 6.8 quake in 2011 that caused widespread destruction and fatalities. Laos is situated on the Indochina block, which is bordered by the Eurasian Plate to the north, the Indian Plate to the west, and the Australian Plate to the south. On November 21, 2019, Laos experienced a significant earthquake with a magnitude of 6.1. The earthquake occurred in the northern portion of the nation near the Thai border and was felt throughout the region. The earthquake resulted in several fatalities and extensive damage to buildings and infrastructure, particularly in Muang Nan. The Laos earthquake was caused by movement along the Xayaburi Fault, which runs through the country's northern region. The Xayaburi Fault is a major source of seismic activity in Laos and can produce magnitude 7 or greater earthquakes.

Cambodia is bordered by several active plate boundaries. Several significant earthquakes have occurred in Cambodia, including a magnitude 5.5 earthquake that caused damage and fatalities in 2021. Cambodia is situated on the Indochina block, which is bordered by the Eurasian Plate to the north, the Indian Plate to the west, and the Australian Plate to the south. On December 13, 2019, an earthquake with a magnitude of 6.1 occurred in Cambodia. Particularly in Kampot, the earthquake caused damage to buildings and infrastructure. The quake in Cambodia was caused by movement along the Prek Kampi Fault, which runs through the country's southern region. The Prek Kampi Fault is a major source of seismic activity in Cambodia and can produce magnitude 7.0 or greater earthquakes.

Brunei is in Southeast Asia share its boundaries with Sarawak, Malaysia and situated on the northern edge of the island of Borneo. While there have not been any major earthquakes reported in Brunei in recent years, the potential for seismic activity exists due to its location near the plate boundary. Earthquakes in this region can range in magnitude and can be felt over a wide area, depending on their depth, location, and the type of rock and soil in the area. To prepare for earthquakes, it is important for Brunei to have measures in place to mitigate their impact. This includes developing building codes that are designed to withstand seismic activity, as well as emergency response plans and public education campaigns to promote earthquake safety. Nevertheless, the region has experienced several moderate earthquakes in the past, including a magnitude 6.0 quake in 2015 that was felt across the nation. Brunei is located on the northern coast of Borneo, which is near several active faults from Sabah and Sarawak. Despite this, earthquakes in Brunei are uncommon and typically of low magnitude.

Methodology

Several procedures and methodologies using geological, seismological, and geotechnical data go into creating a seismic hazard map. Seismic hazard mapping is a complex process that calls for precise knowledge of the local geology and tectonics, in addition to sophisticated modeling and analysis tools. Using these methods to create a thorough seismic hazard map can help reduce the damage caused by earthquakes and keep residents and vital infrastructure safe. The seismic hazard map developed by each Southeast Asian country was the starting point for this research. The map includes two different levels of potential overshoot: 10% and 2%. The most up-to-date map data was collected to create a composite hazard map for all Southeast Asian nations.

Figure 1 illustrates the step-by-step process that must be followed to carry out the current project activities. The seismic hazard maps for Southeast Asian countries (including Malaysia, Indonesia, Thailand, Singapore, the Philippines, Myanmar, Vietnam, Laos, Cambodia, and Brunei) were collected at the beginning of the activity. These maps were created based on the most recent results that were published. After that, every map will be compiled so that the values of Peak ground Acceleration (PGA) can be observed. There will also be a comparison made between these PGA values and other previously published seismic hazard maps for the Southeast Asian region. After obtaining the parameters of the PGA, the next step is to combine all the seismic hazard maps into a single map. This will be done as part of the activity. The map is going to be made into two different types, including one with a 10% probability of exceedance and another with a 2% probability. Finally, the design response spectra will be generated using the data findings based on the latest literature.

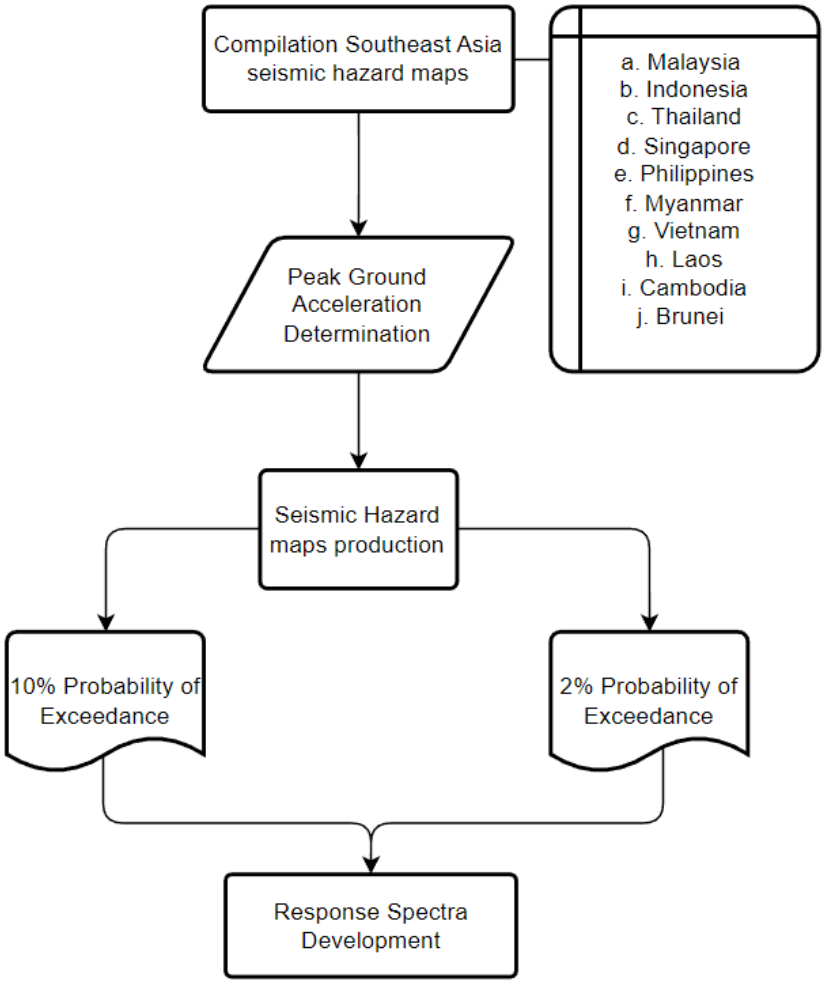

Figure 1. The flow of track development of the study

Review of Seismic Hazard Map in Asian Countries

Petersen et al. (2007) and Pagani et al. (2018) initially compiled seismic hazard maps for Southeast Asia. Pagani et al. (2018) presents the latest version of the hazard component for the Global Earthquake Model (GEM). The most recent research and data on seismicity, fault sources, and ground motion have been incorporated into this model to provide an up-to-date assessment of the risk of earthquakes occurring all over the world. This article discusses the hazard maps that were generated because of using the GEM model and presents the methodology that was used to generate them along with any associated uncertainties. The earliest documentation for the Southeast Asia Seismic Hazard Maps can be found in Petersen et al. (2007)'s publication. These maps, which provide estimates of the likelihood and intensity of earthquakes in Southeast Asia, were developed by the United States Geological Survey (USGS).

Pagani et al. (2018)'s GEM model incorporates the most up-to-date research and data to provide a global assessment of earthquake hazard. Southeast Asia Seismic Hazard Maps, on the other hand, were developed by

Petersen et al. (2007) and are more than a decade older than the GEM model. While the Southeast Asia Seismic Hazard Maps developed by Petersen et al. (2007) use simpler ground motion prediction equations based on older research, the GEM model presented by Pagani et al. (2018) uses a more sophisticated methodology that incorporates ground motion prediction equations based on the latest research. Pagani et al. (2018) maps of seismic risk. Most of the highest PGA values in Southeast Asia are found within the Ring of Fire, which includes Myanmar, Indonesia, and the Philippines. Some regions of Thailand, Cambodia, Vietnam, and Borneo have the world's lowest PGA values.

Guidelines for designing buildings to withstand earthquakes can be found in Eurocode 8, and their development is described in the MS EN1998:2015 (2017) is Malaysia National Annex. This report examines Malaysia's general regulations, seismic actions, and rules for buildings with the overarching goal of ensuring that all structures in the country are adequately prepared to withstand seismic activity. Two additional maps of East Malaysia complement the Malay Peninsula or West Malaysia map (Sabah and Sarawak). The 10% probability of West Malaysia and East Malaysia exceeding is depicted in Figure 4. The range of PGA values in Malaysia is 0.00 g to 0.16 g. Sabah, in East Malaysia, has the highest PGA contributions compared to West Malaysia and Sarawak, also in East Malaysia. The concentrated contours on these three maps indicate areas where local fault influence has been detected. The results for the 2% probability of exceeding are shown in Figure 5. Sabah, East Malaysia has the highest PGA values, ranging from 0.02 to 0.25g. The 2% probability of exceeding PGA values in the Malaysia region falls between 0.00 and 0.25g.

Irsyam et al. (2017) create a map showing earthquake hotspots and fault lines across Indonesia. The map can be used to inform earthquake preparedness and response strategies by revealing the expected frequency and intensity of earthquakes in various regions of Indonesia. There is only a tiny fraction on both maps where the PGA value is 0.00 - 0.05g. The PGA value for most of Indonesia falls between 0.05 and 0.8g with a 10% chance of exceeding, and between 0.05 and 2.0g with a 2% chance of exceeding. A probabilistic seismic hazard analysis model for the Philippines is described in Penarubia et al. (2020). The model incorporates several variables, including seismic sources and soil conditions, to make predictions about the frequency and severity of earthquakes in various parts of the country. To lessen the destruction caused by earthquakes, this data can be used to modify building codes and emergency procedures.

South of West Malaysia, on an island, is the city-state of Singapore. Wenqi and Pan (2020) provide a probabilistic evaluation of Singapore's seismic risk. The assessment considers several variables, including regional seismicity and soil geology, to provide an estimate of the frequency and magnitude of earthquakes in Singapore. The results of the study can be used to modify the city-building state's codes, emergency response strategies, and other precautions against earthquake damage. Ten percentile PGA values in Singapore range from 0.048 g to 0.052 g. Meanwhile, the PGA values range from 0.143 g to 0.146 g at a 2% chance of exceedance. The risk of natural disasters, such as earthquakes, in Cambodia is evaluated in the Country Report Cambodia (2015). The purpose of this report is to help businesses prepare for natural disasters by pinpointing the areas of the country that are most at risk. The report only includes one map, and that map is the GSHAP map for a threshold of 10% exceedance. Figure 12 displays the PGA values for all of Cambodia, which range from 0.4 to 0.8g.

Ornthammarath et al. (2010) provide a probabilistic evaluation of Thailand's seismic risk. The likelihood and intensity of earthquakes in various regions of Thailand are estimated by considering several factors, including seismic sources and soil conditions. The results of the study can be used to modify building codes, improve emergency preparedness, and take other preventative steps against earthquake damage. The PGA map from 0.0 to 0.3g (10% probability of exceeding). However, at a 2% chance of exceeding, the PGA values are between 0.00 and 0.70g. Pailoplee and Charusiri (2017) use a seismicity approach to look at seismic activity and risks in Laos. The goal of the study is to find out which parts of the country are most likely to be affected by earthquakes and to come up with ways to lessen the effects of earthquakes. The Laos seismic hazard map shows that the PGA are between 0.0 and 0.24g with a 10% chance of being greater. At a 2% chance of going over, the PGA shows that the values are between 0.0 and 0.4g.

A seismic risk assessment for Myanmar is provided by Nanthaporn and Pailoplee (2017). The study considers a variety of factors, including seismic sources and soil conditions, to estimate the probability and intensity of earthquakes in various regions of Myanmar. This data can be utilized to inform building codes, emergency response plans, and other measures designed to mitigate the effects of earthquakes. PGA map with a 10% probability of exceeding values between 0.0 and 0.2g and 2% probability of exceeding the PGA values places them between 0.0 and 0.35g. Nguyen and Pham (2014) provide a probabilistic assessment of the seismic hazard in the South-Central region of Vietnam. The evaluation considers various factors, such as the seismicity of the

region and the geological characteristics of the soil, to estimate the probability and magnitude of earthquakes in the region. The assessment provides information that can be used to inform building codes, emergency response plans, and other measures designed to reduce the impact of earthquakes in the region. The 10% probability of exceeding within the ranges 0.0 to 0.198g and the 2% probability of exceeding within the ranges 0.0 to 0.24g. The Brunei Country Report (2015) assesses the risk of natural disasters, such as earthquakes, in Brunei. The purpose of this report is to identify the areas of the country most susceptible to natural disasters and to develop business continuity plans to mitigate their effects. Since the Brunei map uses Modified Mercalli Intensity (MMI), Figure 1 displays the USGS Approximate Correlation Between MMI and PGA extracted from Chock et al. (2006). Brunei has an MMI between I and IV. The conversion will be roughly between 0.0017 and 0.039g PGA.

Results

In many regions of the world, including Malaysia, Brunei, Indonesia, Philippines, Singapore, Myanmar, Vietnam, Laos, Thailand, and Cambodia, the compilation of seismic hazard data is a crucial aspect of earthquake risk assessment and disaster management. Due to their location on the Pacific Ring of Fire, an area with intense tectonic activity, these Southeast Asian countries are susceptible to seismic activity. Seismic hazard compilation entails gathering information on past earthquakes, fault lines, and geological structures in the region to generate earthquake hazard maps. These maps can then be used to evaluate the probability of earthquakes with varying magnitudes and frequencies. In recent years, these nations have experienced a number of devastating earthquakes and their associated effects, including loss of life, population displacement, and infrastructure damage. Consequently, there is a growing need for accurate seismic hazard maps to strengthen the region's resilience to future seismic events. Numerous entities, including government agencies, academic institutions, and international organizations, have contributed to the compilation of seismic hazard maps for these nations. These efforts have resulted in a better understanding of the region's seismic activity and have contributed to the development of earthquake mitigation strategies.

Results PGA for 10% and 2% Probability of Exceedance

This study will provide an overview of the seismic hazard compilation efforts for Southeast Asian countries namely, Malaysia, Indonesia, Thailand, Singapore, the Philippines, Myanmar, Vietnam, Laos, Cambodia, and Brunei as well as highlight the key findings and implications of these studies for two distinct parameters, namely 10% and 2% probability of exceedance. The colour of each contour is determined by Irsyam et al. (2017)'s PGA map colour code. The minimum PGA ranges from 0.00 to 0.05 g, while the maximum exceeds 0.80 g. In the development of seismic hazard maps for Southeast Asian countries, the 10% probability of exceedance is an important metric. This metric represents the likelihood that an earthquake of a certain magnitude or greater will occur within a specified period, typically 50 years. In these nations, the 10% probability of exceeding is frequently used as the basis for seismic building codes and design requirements. This entails that buildings, bridges, and other infrastructure must be designed to withstand the ground motion and other seismic effects anticipated from earthquakes with a 10% probability of exceedance. Figures 2 and 3 show the final compilation of seismic hazard maps for 10% and 2% probability of exceedance, respectively.

In general, the 10% probability of PGA value varies for these nations based on their tectonic setting, seismicity, and geology. The 10% probability of PGA value may be greater in regions with high seismic activity and strong ground motions than in regions with lower seismic activity and weaker ground motions. For instance, in the Philippines, which is situated in the Pacific Ring of Fire and is prone to large earthquakes, the 10% probability of PGA value varies between 0.0g and 0.8g depending on the location. Depending on the location in Indonesia, which is also situated within the Pacific Ring of Fire, the 10% probability of PGA value ranges are the same as Philippines. The 10% probability of PGA value is generally low and moderate in Malaysia, ranging from 0.0g to 0.15g. Similarly observed in Myanmar, the PGA values are the same as Malaysia. In contrast, in Cambodia, Singapore and Brunei, which is situated in a relatively low earthquake activities and stable tectonic environment, the 10% probability of PGA value ranges from 0.0g to 0.05g. In Laos, the PGA value is in the range of 0.1 to 0.25g, Vietnam is 0.0 to 0.2g and Thailand is 0.0 to 0.3g. The 2% probability of PGA value may be greater in regions with high seismic activity and strong ground motions than in regions with lower seismic activity and weaker ground motions. In the Philippines, the 2% probability of PGA value varies between 0.0g and 2.0g. Depending on the location in Indonesia, the 2% probability of PGA value ranges are the same as Philippines. The 10% probability of PGA value is generally low and moderate in Malaysia, ranging from 0.00g to 0.25g.

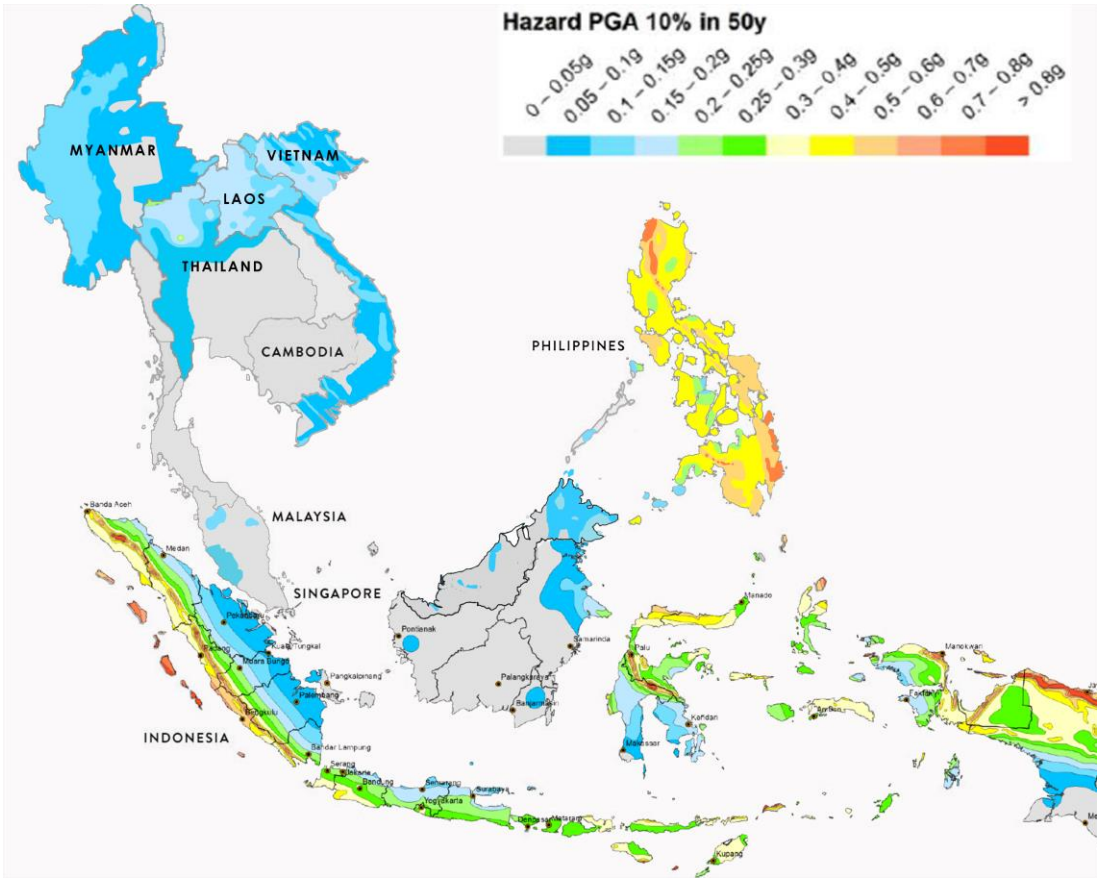

Figure 2. Final compilation of Southeast Asia seismic hazard map at 10% probability of exceedance in 50-year design period

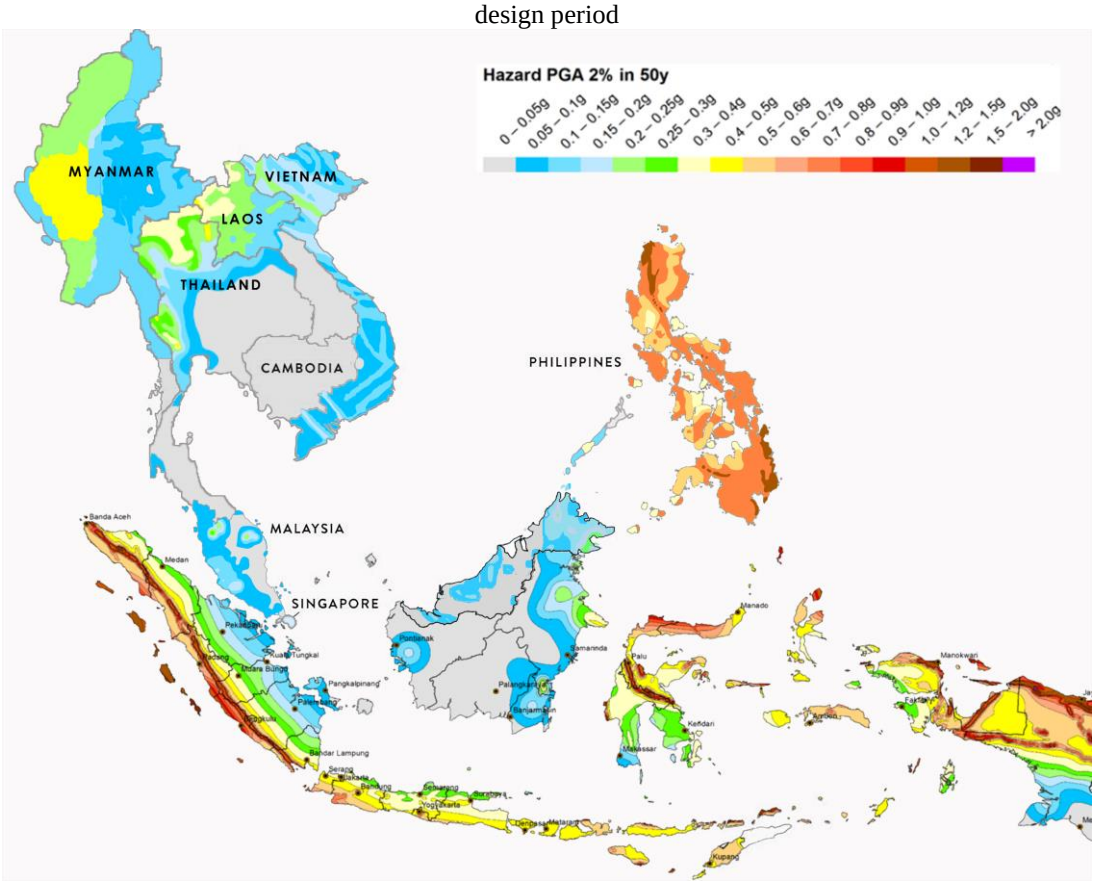

Figure 3. Final compilation of Southeast Asia seismic hazard map at 2% probability of exceedance in 50-year design period

Similarly observed in Myanmar, the PGA values are the same as Malaysia. In contrast, in Cambodia, Singapore and Brunei, which is situated in a relatively low earthquake activities and stable tectonic environment, the 10% probability of PGA value ranges from 0.0g to 0.05g. In Laos, the PGA value is in the range of 0.0 to 0.5g, Vietnam is 0.0 to 0.25g and Thailand is 0.0 to 0.5g. It is essential to note that the 10% and 2% probability of PGA value is only one metric used in seismic hazard evaluation and design. Depending on the application and design requirements, other metrics, such as spectral acceleration and response spectra, may also be employed.

Design Response Spectra of Southeast Asia

Response spectrum are graphical representations of the greatest acceleration, velocity, or displacement that a structure can experience during an earthquake. Generally, these spectra are developed for a particular geographical region, taking the geology and seismicity of the region into account. Response spectra are vital for building design and earthquake engineering because they measure the possible effects of an earthquake on a structure. By evaluating the reaction spectrum, engineers can estimate the maximum acceleration, velocity, and displacement that a structure may experience during an earthquake and design it to withstand these forces.

Design response spectra are often stated in terms of spectral acceleration, which is the greatest acceleration that a structure is anticipated to experience during an earthquake at a specific time interval. The design response spectrum is defined by a variety of criteria, including the seismic hazard level at the site, the building code requirements, and the intended use and occupancy of the building. In building design, the design response spectra are utilized to compute the seismic design forces that a structure must be able to endure. Engineers utilize design response spectra to determine the maximum acceleration, velocity, and displacement that a structure is likely to encounter during an earthquake, and then design the structure to withstand these forces. Design response spectra are a vital aspect of seismic design codes, which provide instructions for developing earthquake-resistant structures. By calculating the seismic design forces using the design response spectrum, engineers can ensure that structures are designed to resist earthquake forces and provide a safe environment for people.

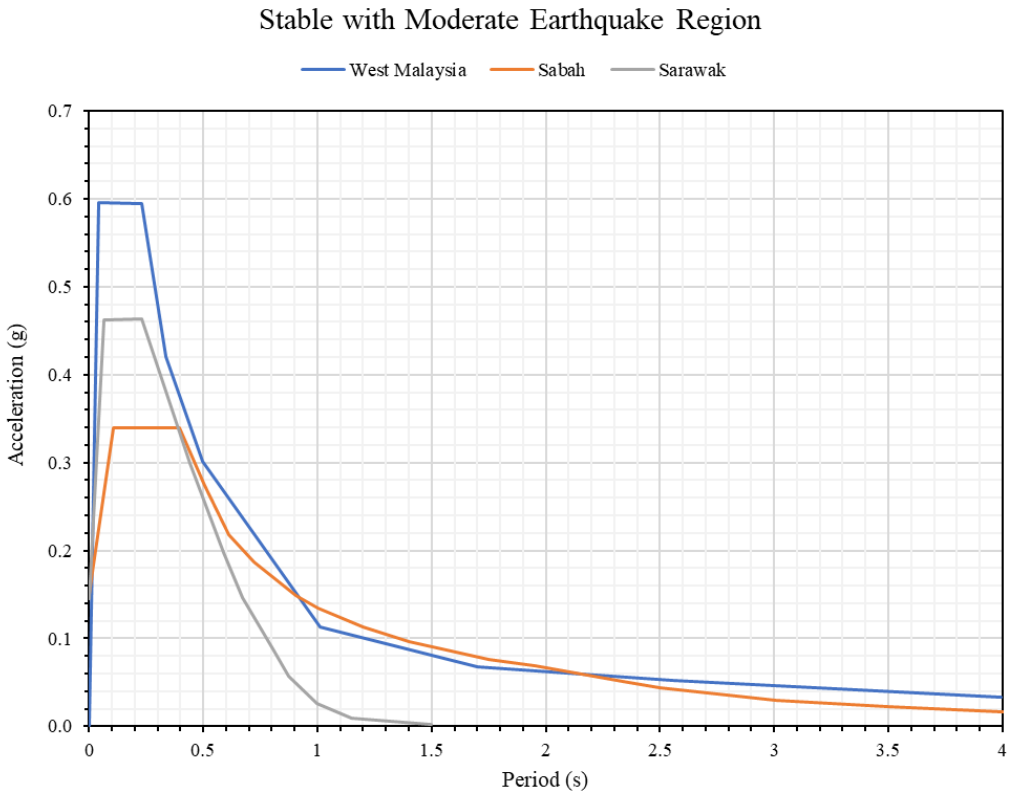

Figure 4. Design response spectra plotted at stable continental region by taking Malaysia as an example (the line shows three cities chosen for analysis (West Malaysia, Sabah and Sarawak)

The design response spectra are successfully derived from MS EN1998:2015 (2017) and Desain Spektra Indonesia (2021) for the current project. The design response spectra are centered on two design categories: the first type is stable with moderate earthquake region and second type is active earthquake region. Figure 4

depicts the spectrum distribution of the Malaysia region from 0 to 4 s (including West Malaysia, Sabah and Sarawak of East Malaysia). Figure 5 illustrates the distribution of spectra for active earthquake regions including Indonesian cities (including Acheh, Padang and Palu).

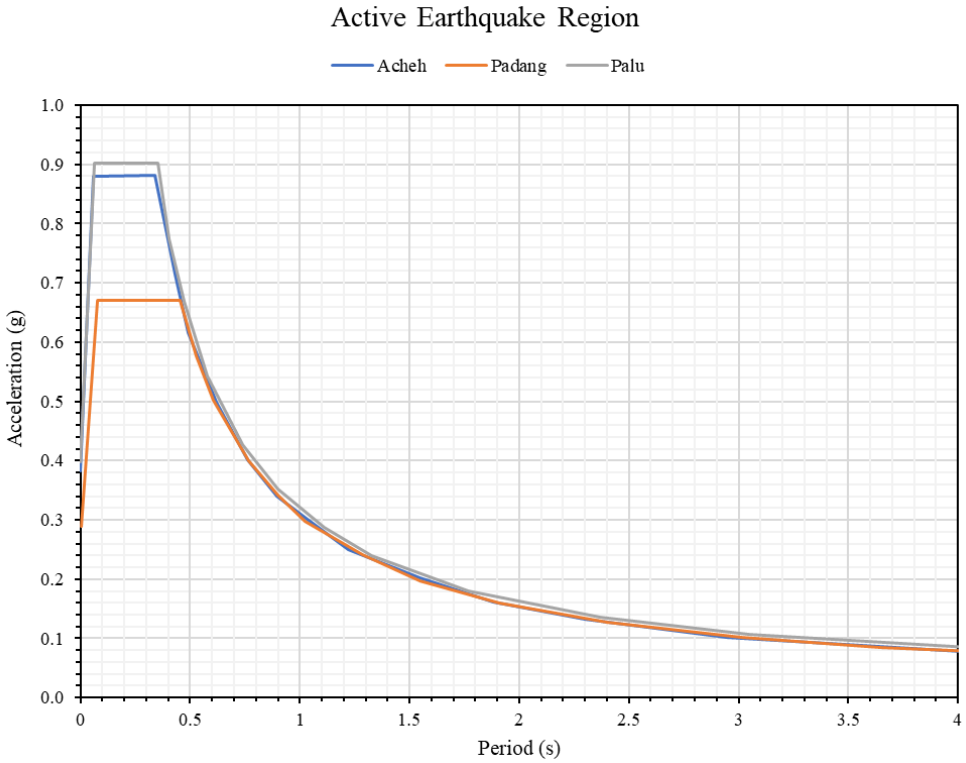

Figure 5. Design response spectra plotted at active earthquake region by taking Indonesia as an example, the line shows three cities chosen for analysis (Acheh, Padang and Palu)

Discussion

The Petersen et al. (2007) has limited results showed whereas in Indonesia, the PGA map only shows at Sumatra region only with no results found in other part Indonesia. Thus, the comparison displays the results from the region of Sumatra. In addition, a small portion of East Malaysia has been omitted from the report. Therefore, the results will be compared with what has been display in the report only. In the Philippines region, no PGA values have been calculated. Pagani et al. (2018) published at 10% probability of exceedance with no map for 2% probability of exceedance. Consequently, the comparison was based solely on the 10% probability of exceeding. Table 1 shows the comparison of PGA values for 10% and 2% probability of exceedance. Meanwhile, Figures 7 and 8 show the variation of PGA values in comparison to previous study by Petersen et al. (2007) and Pagani et al. (2018).

Table 1. Summary and comparison of peak ground acceleration values at 10% probability of exceedance in 50-year design period for Southeast Asia countries (unit g).

Country	10 % Probability of Exceedance			2% Probability of Exceedance		
	Petersen et al. (2007)	Pagani et al. (2018)	This Study	Petersen et al. (2007)	Pagani et al. (2018)	This Study
Malaysia	0.001-0.15	0.02-0.2	0.0-0.15	0.001-0.15	-	0.0-0.25
Indonesia	0.2-0.9	0.0-1.5	0.0-0.8	0.15-1.1	-	0.0-2.0
Thailand	0.01-0.15	0.0-0.35	0.0-0.3	0.02-0.35	-	0.0-0.5
Singapore	0.02-0.05	0.0-0.01	0.0-0.05	0.10-0.15	-	0.1-0.15
Philippines	-	0.08-1.5	0.0-0.8	-	-	0.0-2.0
Myanmar	0.02-0.6	0.02-1.5	0.0-0.15	0.02-1.1	-	0.0-0.5
Vietnam	0.02-0.05	0.0-0.35	0.0-0.2	0.10-0.15	-	0.0-0.25
Laos	0.02-0.05	0.0-0.35	0.1-0.25	0.02-0.3	-	0.0-0.5
Cambodia	0.02-0.05	0.0-0.05	0.0-0.05	0.10-0.15	-	0.0-0.05
Brunei	0.001-0.04	0.0-0.02	0.0-0.05	0.06-0.1	-	0.0-0.05

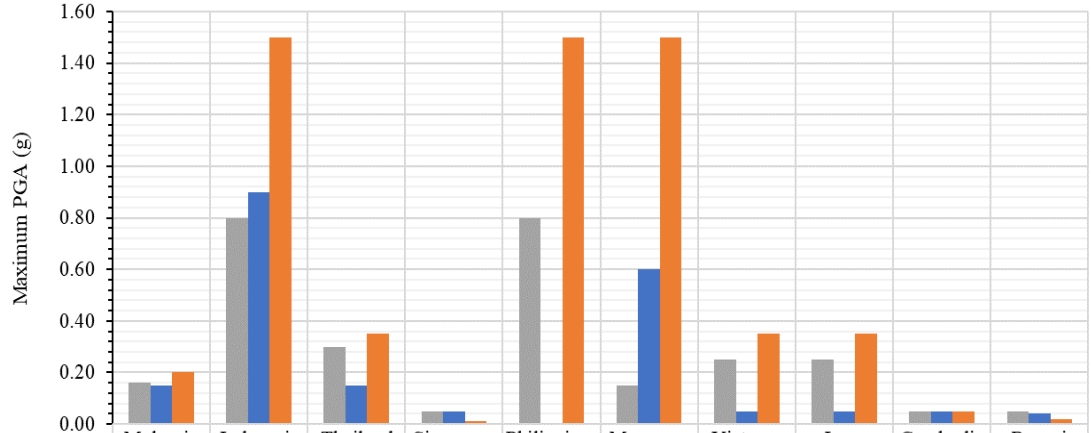

	Malaysia	Indonesia	Thailand	Singapore	Philippines	Myanmar	Vietnam	Laos	Cambodia	Brunei
This Project	0.16	0.80	0.30	0.05	0.80	0.15	0.25	0.25	0.05	0.05
Petersen et al. (2007)	0.15	0.90	0.15	0.05	0.00	0.60	0.05	0.05	0.05	0.04
Pagani et al. (2018)	0.20	1.50	0.35	0.01	1.50	1.50	0.35	0.35	0.05	0.02

Figure 7. Comparison of maximum PGA values at 10% probability of exceedance for Southeast Asia countries

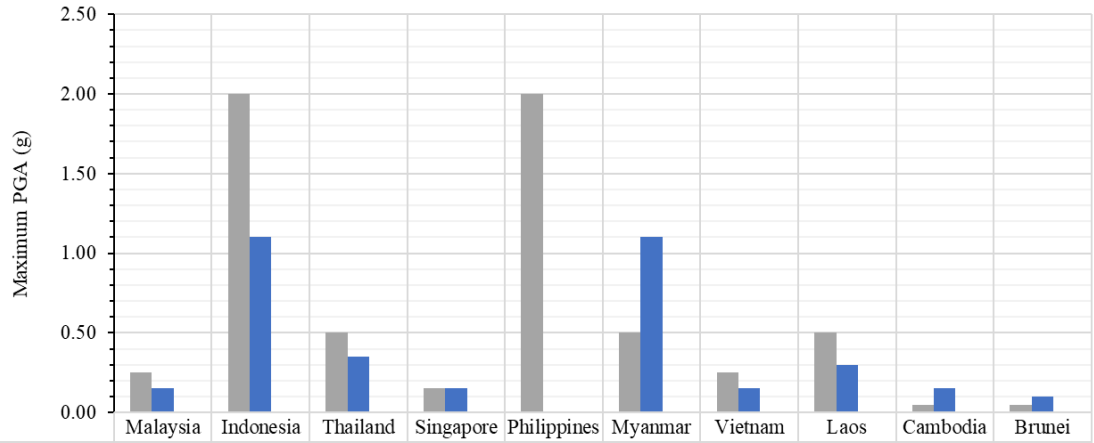

	Malaysia	Indonesia	Thailand	Singapore	Philippines	Myanmar	Vietnam	Laos	Cambodia	Brunei
This Project	0.25	2.00	0.50	0.15	2.00	0.50	0.25	0.50	0.05	0.05
Petersen et al. (2007)	0.15	1.10	0.35	0.15	0.00	1.10	0.15	0.30	0.15	0.10
Pagani et al. (2018)	0.00	0.00	0.00	0.00	0.00	0.00	0.00	0.00	0.00	0.00

Figure 8. Comparison of maximum PGA values at 2% probability of exceedance for Southeast Asia countries

Conclusion

In conclusion, seismic hazard data compilation is critical for earthquake risk assessment and disaster management in several Southeast Asian countries, including Malaysia, Brunei, Indonesia, Philippines, Singapore, Myanmar, Vietnam, Laos, Thailand, and Cambodia. These countries are in the Pacific Ring of Fire, which is a highly tectonically active region, making them prone to seismic activity. The 10% probability of PGA value varies depending on the tectonic setting, seismicity, and geology of each country. Regions with high seismic activity and strong ground motions have a greater 10% and 2% probability of PGA value compared to regions with lower seismic activity and weaker ground motions. For example, in the Philippines, which is prone to large earthquakes and situated in the Pacific Ring of Fire, the 10% probability of PGA value ranges from 0.0g to 0.8g meanwhile 2% probability of PGA value ranges from 0.0g to 2.0g depending on the location. The same range of 10% probability of PGA value is observed in Indonesia. Meanwhile, Malaysia and Myanmar have low to moderate 10% probability of PGA values ranging from 0.0g to 0.15g. The 2% probability of PGA values ranging from 0.0g to 0.25g for Malaysia, and 0.0g to 0.5g for Myanmar. On the other hand, Brunei, Singapore, and Cambodia, located in a relatively low earthquake activity and stable tectonic environment, have a 10% probability of PGA value ranging from 0.0g to 0.05g and 2% from 0.0 to 0.05g except Singapore, 0.1 to 0.15g. Laos has a 10% and 2% probability of PGA value in the range of 0.1 to 0.25g and 0.0 to 0.5g, respectively, Vietnam ranges from 0.0 to 0.2g and 0.0 to 0.25g for 10% and 2% probability, respectively, and Thailand ranges from 0.0 to 0.3g for 10% probability and 0.0 to 0.5g for 2% probability. However, the 10% and 2% probability of PGA value is only one metric used in seismic hazard evaluation and design. Depending on the application

and design requirements, other metrics such as spectral acceleration and response spectra may also be employed. The design response spectra for seismic hazard evaluation and design in the Asian region are divided into two categories based on the level of seismic activity: stable with moderate earthquake region and active earthquake region. The spectrum distribution for selected cities in regions of moderate seismicity and active earthquakes, including West Malaysia, Sabah, Sarawak of East Malaysia, and Indonesian cities such as Acheh, Padang, and Palu, have been integrated for the range of 0 to 4 seconds. These spectra distributions are an essential aspect of earthquake risk assessment and disaster management, which can aid in the development of effective strategies for mitigating the impact of seismic events in the region.

Recommendations

It is recommended to provide details about the specific methods used to generate the seismic hazard map and associated design response spectra. Adding more information about the data sources, modeling techniques, and assumptions made during the analysis would make the study more transparent and credible. Providing some context about the potential consequences of not properly accounting for seismic hazards in building design and construction (e.g., increased risk of collapse, injury, and death) would make the study's findings more impactful. Since current study does not mention any sensitivity analyses performed to assess the robustness of the results or any assumptions made about the underlying seismicity or tectonic activity of the region, thus being transparent about these issues would make the study more reliable and useful.

Scientific Ethics Declaration

The authors declare that the scientific ethical and legal responsibility of this article published in EPSTEM journal belongs to the authors.

Acknowledgements or Notes

The author would like to acknowledge the Ministry of higher education for funding the project through the Fundamental Grant Scheme (FRGS), FRGS/1/2020/TK0/UMS/02/11 and internal grant, Universiti Malaysia Sabah (UMS) through the Geran Bantuan Penyelidikan Pascasiswazah (UMSGreat), GUG0554-1/2022 and GUG0555-1/2022.

References

Adam, F.H., Leigh, H.R., Thorsten, W.B., & Claudio, F. (2018). Slab interactions in 3-D subduction settings: *The Philippine Sea Plate Region. Earth and Planetary Science Letters, 489,* 72-83.

Chock, G., Kindred, T., Robertson, I. N., Iinuma, G., Nicholson, P. G., Lau, E., & Brandes, H., & Sarwar, A., Medley, E., & Pino, J. D., Okubo, P., Holmes, W., Hirshorn, B., & Sumada, J (2006). *Compilation of observations of the october 15, 2006 Kiholo Bay (Mw 6. 7) and Mahukona (Mw 6.0) earthquakes, Hawai'i* (report).

Country Report Brunei. (2015). *Natural disaster risk assessment and area business continuity plan formulation for industrial agglomerated areas in the ASEAN region*. AHA Centre, Japan International Cooperation Agency.

Country Report Cambodia. (2015). *Natural disaster risk assessment and area business continuity plan formulation for industrial agglomerated areas in the ASEAN region*. AHA CENTRE, Japan International Cooperation Agency.

Cummins, P. R. (2017). Geohazards in Indonesia: Earth science for disaster risk reduction – introduction. *Geological Society, London, Special Publications, 441* (1), 1

Desain Spektra Indonesia. (2021). Direktorat bina teknik permukiman dan perumahan, direktorat jendera Cipta karya and kementerian pekerjaan umum dan perumahan rakyat. Retrieved from https://rsa.ciptakarya.pu.go.id/2021/

Harith, N.S.H., & Tongkul, F. A. (2023) Seismic hazard curve as dynamic parameters in earthquake building design for Sabah, Malaysia. *Buildings*, *13*(2), 318.

Hua, Y., Zhao, D., & Xu, Y.G. (2022). Azimuthal anisotropy tomography of the Southeast Asia subduction system. *Journal of Geophysical Research: Solid Earth*, *127*(2).

Hutchings, S. J., Mooney, W. D. (2021). The seismicity of Indonesia and tectonic implications. *Geochemistry, Geophysics, Geosystems, 22(9).*

Irsyam, M., Widiyantoro, S., Natawidjaja, D.H., Meilano, I., Rudyanto, A., Hidayati, S., Triyoso, W., Hanifa, N.R., Djarwadi, D., Faizal, L., & Sunarjito, S. T. (2017). *Peta Sumber dan Bahaya Gempa Indonesia Tahun 2017.* Retrieved from https://sianipar17.files.wordpress.com/2018/12/nsha_2017.pdf

Lallemand, S. (2016). Philippine sea plate inception, evolution, and consumption with special emphasis on the early stages of Izu-Bonin-Mariana subduction. *Progress in Earth and Planetary Science, 3*(15), 1-27.

Lemenkova, P. (2020). Analysis of the difference in depths and variation in slope steepness of the Sunda trench, Indonesia, east Indian Ocean. *Revista De Geomorfologie, 22*(1), 21–41.

Lemenkova, P. (2021). Java and Sumatra segments of the Sunda trench: Geomorphology and geophysical settings analysed and visualized by GMT. *Glasnik Srpskog Geografskog Drustva, 100* (2), 1-23.

Li, J., Weiwei, D., Jian, L., Yigang, X., Fansheng, K., Sanzhong, L., Xiaolong, H., Zhiyuan, Z. (2021). Dynamic processes of the curved subduction system in Southeast Asia: A review and future perspective. *Earth-Science Reviews, 217*(8).

Metcalfe, I. (2017). Tectonic evolution of Sundaland. *Bulletin of the Geological Society of Malaysia, 63*, 27 – 60.

Morell, K.D., Styron, R., Stirling, M., Griffin, J., Archuleta, R., & Onur, T. (2020). Seismic hazard analyses fromgeologic and geomorphic data: Current and future challenges. *Tectonics,39*(10).

MS EN 1998-1:2015. (2017). *Malaysia national annex to eurocode 8: Design of structures for earthquake resistance - Part 1: General rules, seismic actions and rules for buildings.* Department of Standards Malaysia. Retrieved from https://ir.unimas.my/id/eprint/36083/

Nguyen, H.P., & Pham, T.T. (2014). Probabilistic seismic hazard assessment for the South Central Vietnam. *Vietnam Journal of Earth Sciences 36*, 451-461.

Ornthammarath, T., Pennung, W., Kawin, W., Saeed, Z., Ragnarm S., & Carlo, G.L. (2010). Probabilistic seismic hazard assessment for Thailand. *Bull Earthquake Engineering, 9(2),* 367-394.

Pagani, M., Garcia Pelaez, J., Gee, R., Johnson, K., Poggi, V., Silva, V., Simionato, M., Styron, R., Vigano, D., Danciu, L., Monelli, D., Weatherill, G. (2018). Global earthquake model (gem) seismic hazard Map (version 2018.1 - December 2018).

Pagani, M., Garcia-Pelaez, J., Gee, R., Johnson, K., Poggi, V., Silva, V., Simionato, M., Styron, R., Vigano, D., Danciu, L., Monelli, D., Weatherill, G. (2020). The 2018 version of the global earthquake model: Hazard component. *Earthquake Spectra, 36*, 226-251.

Pailoplee, S., & Charusiri, P. (2017). Analyses of seismic activities and hazards in Laos: A seismicity approach. *Terrestial Atmospheric Oceanic Sciences, 28*(6), 843-853.

Peñarubia, H.C., Johnson, K.L., Styron, R.H., Bacolcol, T.C., Sevilla, W.I.G., Perez, J.S., Bonita, J.D., Narag, I.C., Solidum, R.U., Pagani, M.M.Jr., & Allen, T. (2020). Probabilistic seismic hazard analysis model for the Philippines. *Earthquake Spectra, 36*, 44-68.

Petersen, M., Stephen, H., Charles, M., Kathleen, H., James, D., Nicolas, L., Anthony, C., David, L., & Kenneth, R. (2007). *Documentation for the Southeast Asia seismic hazard maps.* Administrative Report September 30, 2007. U.S. Department of the Interior U.S. Geological Survey. Retrieved from https://pdf.usaid.gov/pdf_docs/pnads391.pdf

Pilia, S., Rawlinson, N., Hall, R., Cornwell, D.G., Gilligan, A., & Tongkul, T. (2023). Seismic signature of subduction termination from teleseismic P- and S-wave arrival-time tomography: The case of northern Borneo. *Gondwana Research, 115,* 57–70.

Rangin, C. (2016). Rigid and non-rigid micro-plates: Philippines and Myanmar-Andaman case studies. *Comptes Rendus Geoscience, 348*(1), 33-41,

Shah, A. A., Qadri, T., & Khwaja, S. (2018). Living with earthquake hazards in South and Southeast Asia. *ASEAN Journal of Community Engagement, 1*(2), 1-24.

Shoushtari, A.V., Adnan, A., & Zare, M. (2018). Incorporating the local faults effects in development of seismic ground-motion hazard mapping for the Peninsular Malaysia region. *Journal of Asian Earth Sciences, 163*, 194-211.

Somsa-ard, N., & Pailoplee, S. (2013). Seismic hazard analysis for Myanmar. *Journal of Earthquake and Tsunami,7*(4), 1350029.

Suzuki, S., Rolando, E.P., Tomas, A.T., Graciano, P.Y., Carla, B.D., Mayumi, U., & Keisuke, I. (2017) Development of the Philippine mobile belt in northern Luzon from Eocene to Pliocene. *Journal of Asian Earth Sciences, 142*, 32-44.

Triyoso, W., Sahara, D.P., Sarsito, D.A., Natawidjaja, D.H., & Sukmono, S. (2022). Correlation dimension in Sumatra island based on active fault, earthquake data, and estimated horizontal crustal strain to evaluate seismic hazard functions (shf). *GeoHazards, 3*, 227-241.

Wenqi, D., & Pan, T-C (2020). Probabilistic seismic hazard assessment for Singapore. *Natural Hazards, 103,*2883–2903.

Xu, S., Dimasaka, J., Wald, D.J. & Noh, H.Y. (2022). Seismic multi-hazard and impact estimation via causal inference from satellite imagery. *Nature Communications,.13*(1), 7793.

Author Information

Noor Sheena Herayani Harith
Faculty of Engineering, Universiti Malaysia Sabah, Jalan UMS, 88400 Kota Kinabalu, Sabah, Malaysia
Natural Disaster Research Centre (NDRC), Universiti Malaysia Sabah, Jalan UMS, 88400 Kota Kinabalu, Sabah, Malaysia
Contact e-mail: *sheena@ums.edu.my*

Azlan Adnan
School of Civil Engineering, Universiti Teknologi Malaysia, 81310 Skudai, Johor Bahru, Johor, Malaysia

To cite this article:

Harith, N.S.H., & Adnan, A. (2023). Seismic hazard map of ASEAN countries towards risk assessment and sustainability of structures and infrastructures. *The Eurasia Proceedings of Science, Technology, Engineering & Mathematics (EPSTEM), 26*, 121-134.

The Eurasia Proceedings of Science, Technology, Engineering & Mathematics (EPSTEM)
ISSN: 2602-3199

The Eurasia Proceedings of Science, Technology, Engineering & Mathematics (EPSTEM), 2023

Volume 26, Pages 135-141

IConTES 2023: International Conference on Technology, Engineering and Science

Tensile Property of Carbon Reinforced Epoxy Composites for Different Directions

Selahattin Selek
OSTIM Technical University

Yusuf Sahin
OSTIM Technical University

Abstract: Due to higher chemical stability, higher strength/stiffness, lower density, and good corrosion resistance, carbon fiber-reinforced polymeric composites (CFRPs) have been increased numbers of areas such as aircraft industry, automotive industry, ship making and packing industry, turbines, compressors, wind blades besides implant applications. Epoxy based composites are developed using carbon fiber reinforcements by vacuum controlled resin transfer (VARTM) molding method by Twill carbon fiber [K3T] with 200 gr and Plain carbon fiber [K3P] with 200 gr. Composite plates are produced in the dimension of 500 mm x 500 mm with 0.8 mm thickness. According to the ASTM D3039, standard test samples are cut with CNC machine. Tensile tests are conducted at three different fiber directions like 0^0-45^0- 90^o, respectively. Their mechanical properties are determined. Experimental results indicated that fiber direction significantly affected the tensile behavior of tested samples. Average tensile strength of CFRPs was obtained around 470 MPa for 0 degree to x-axis, and testing lasted about 44 s. For 90^o direction, tensile strength of carbon fiber composites reached to 520 MPa, which is slightly higher than the previous one while trial period was around 50 s. For 45^o tested samples, a completely different behavior was observed because stress-strain curve showed the elastic-plastic behavior. Its tensile strength measured was about 120 MPa average value while the trial lasted about 145 s.

Keywords: Carbon fiber, Plain fiber, Twill fiber, Fiber direction, Tensile strength

Introduction

Since fiber reinforced polymeric composites (FRPCs) have higher strength/rigidity, higher corrosion, lightweight, fire retardant associated with dimensional stability, lower cost, easy production when compared with steel structures, concretes and other building materials, FRPCs have been found many applications such as airplane, sport, marine and automotive industries (Soutis et al., 2005; Sahin, 2022; Sahin&Patrick, 2018). In general, FRPCs consists of the matrix like epoxy, polyester, vinyl ester while fibers such as glass, carbon, basalt fiber, and kevlar used as reinforcements. The development of composite materials design and manufacturing technology is one of the most important tasks in the history of materials. Researcher and scientific engineering people interested in new method to provide larger and quality components like Vacuum Assisted Resin Transfer Method (VARTIM) approach, particularly for fiber-reinforced polymeric materials (Mallick, 2007; Sahin, 2022; Sanchez, 2012; Bodaghi et al., 2016). For metals and composites, tensile tests have been used as a standard testing to evaluate the mechanical properties like tensile and Young's modulus and compare qualitatively with different materials. The mechanical property of composites show different characteristics based on types of fiber/matrix (Ma et al., 2017; Ma et al., 2018; Turla et al.,2014), Nano-addition (Agarwal et al., 2014; Zhang et al., 2019; Xu & Hoa, 2008), interface bonding (Liu et al., 2014; Li et al.,2013), applied methods (Sahin, 2021; Cecen &Sarıkant, 2008), stacking sequence (Ary Subagia et al., 2014; Zhang et al., 2012; Yusuff et al., 2021), orientation effect (Rahmani et al., 2012; Kaleemulla & Siddeswarappa,2010; Agrawal & Bhattacharya, 2021;

GuruRaja & HariRao,2013) and characterization (Shokrieh &Omidi, 2009; Paive et al., 2006; Cecen & Sarıkanat, 2008; Pandy et al., 2011) in making composites.

For the case of fiber orientation, it also affects the properties of composites (Agarwal et al.2014; Rahmani et al.2014; Kaleemulla &Siddeswarappa, 2010). The highest mechanical properties were obtained for longitudinal direction of the fibers (Ozsoy, 2015). Shokrieh and Omidi (2009) indicated significant increases in strength as strain rate increased for glass fiber reinforced epoxy. Paive et al. (2006) showed that the highest strength was provided for F584/PW samples with reinforced with Plain Weave (PW) and Eight Harness Satin (8HS) fabrics while the highest elastic modulus was obtained for F584/8HS samples. Agarwal et al. (2021) revealed that higher property for tensile and flexural test were achieved with first [(0/0/0/0)] and fifth [0/+90/-90/0)] configurations in CFRPs. GuruRaja et al. (2013) indicated that the $0/90^o$ samples indicated the considerable increase in elasticity modulus of composites, followed by $60/30^o$ oriented samples for carbon/glass hybrid composites. Çecen and Sarıkanat (2008) showed that longitudinal direction (0^o) was about 54% larger than that of 45^o directed for glass-fabric based polyester composites. Pandy et al. (2011) indicated that higher tensile stress was provided for satin weave T300 carbon reinforced composite while lower strength was provided for hybrid composite. In hybrid epoxy composite, plain carbon fabrics, 8H satin weave in addition to glass fabrics were used.

From the above literature review, large numbers of studies carried out over mechanical behavior of FRPCs using different fillers and factors. There are some other works conducted to determinethe effects of fiber directions, but limited numbers of investigations for tensile properties of composites produced through VARTM were studied (sahin 2021, 2022; Sanchez et al., 2013; Bodaghi et al., 2016; Cecen&Sarıkanat, 2008). Therefore, the purpose of the study is to characterize tensile property for CFRP composites fabricated using VARTIM with different orientations such as 0^o, 45^o, $0/90^o$ subjected to tensile loading in accordance with ASTM standard.

Experimental Details

Materials

CFRC composites were produced through Vacuum Assisted Resin Infusion Transfer Molding (VARTIM) method. Carbon dry fabric with plain-weave type (K3P), Twill carbon (K3T), plain basalt fiber (K3P). Areal weight of woven carbon is 200 g/m^2, selected as reinforcement, average diameter is about 10 μm. Thermosetting bisphenol-A epoxy resin (F-1564) and hardener (F-3487) were mixed in 3:1 ratio. The properties of carbon fabrics used for VARTIM approach were indicated in Table 1. In manufacturing the composites, total of three plies of plain carbon fabrics were stacked on release film of aluminum mold.

The composite specimen size was about 500 mm × 500 mm × 0.8 mm fabricated with a square laminate. A releasing agent was applied on mold for providing quality surface roughness and removing the laminate easily. Sealant tape, peel ply, vacuum bag was used for completing process. Preform was prepared using fabrics like carbon. Vacuum will be continued until the resin has run out. 1 at pressure was applied at inlet port to remove the resin-rich layer. Flow direction should be along flow media.

Table 1. The properties of glass/carbon fabrics, epoxy used for VARTIM approach

Materials	Plain Carbon Fabric (CF)	Glass fiber (GF)	Epoxy resin (EP)
Fabric weight (g/m^2)	200	220	-
Fabric thickness (mm)	0.32	0.15	-
Warp construction/fill	12/13	22/26	-
Monofilament diameter (μm)	7-10	10-18	-
Density (g/cm^3)	1.78	2.60	1.15
Modulus of elasticity (GPa)	230	80-90	30-50
Tensile strength (MPa)	4900	1380-3200	73

Fig.1 shows some basic elements used in preparing of composite in VARTIM technique. Theseare mostly release film, infusion mesh (a), peel ply, (b) vacuum bag or nylon film, (c) vacuum sealant tape (yellow), infusion vacuum hose and spiral house, T-connector and finally carbon fibers or any other fibers.

The mechanical tests like tensile test according to ASTM D3039 were performed using the composites using universal mechanical testing machine with 100 kN load cell capacity. Specimens were prepared for mechanical

testing by cutting from the epoxy laminate panels with a CNC-machining. Samples were cut from the plate according to 0-45-0/90^{o} direction withrectangle shape. The specimen was measured about 18 mm in width, 179 mm in length, 1.0 mmin thickness. Head speed rate was 10 mm/min.

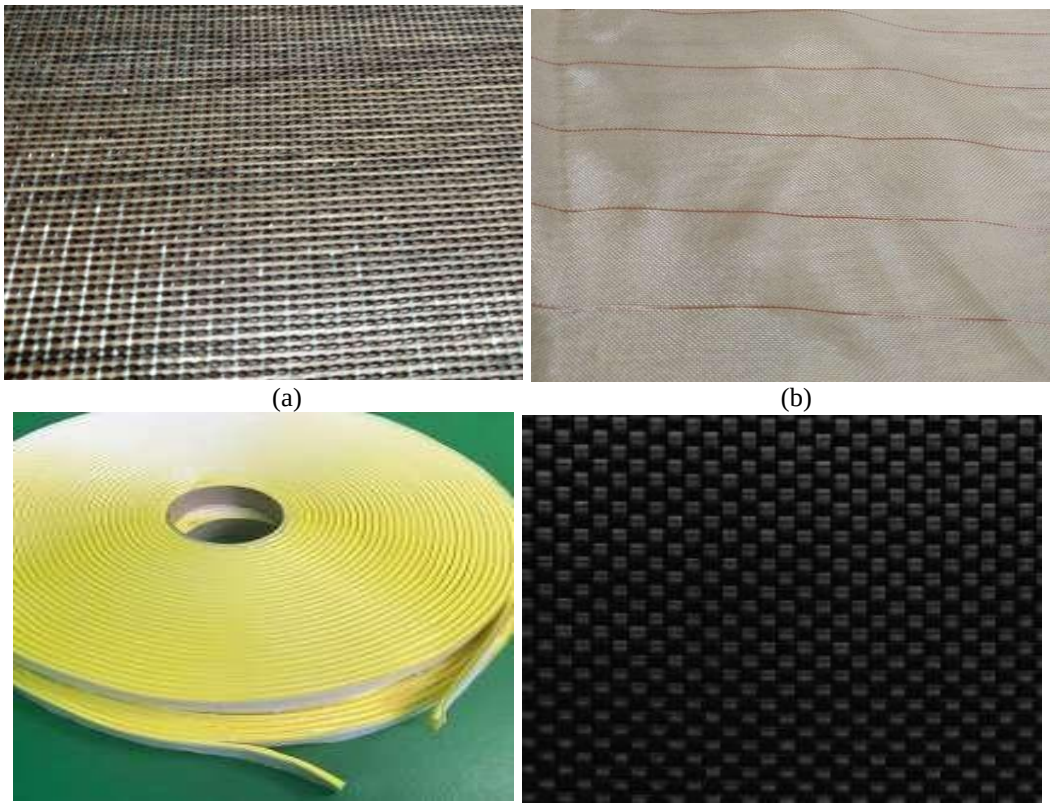

(a) (b)

(c) (d)

Figure 1. Some elements used in preparing of composite in VARTIM technique.
(a) Infusionmesh, (b) Peel ply, (c) Sealant tape, (d) Carbon fiber.Mechanical testing

Results and Discussion

Tensile Strength of Composites

Typical stress versus time curves for the carbon fiber reinforced epoxy composites when loaded in tension load was indicated in Fig. 2, 3 and Fig. 4 for 0^{o} orientation (longitudinal), 30^{o} (angle-ply) orientation of composite and 90^{o} design, respectively. The tensile stress was provided by getting maximum load as a failure for all tested samples.

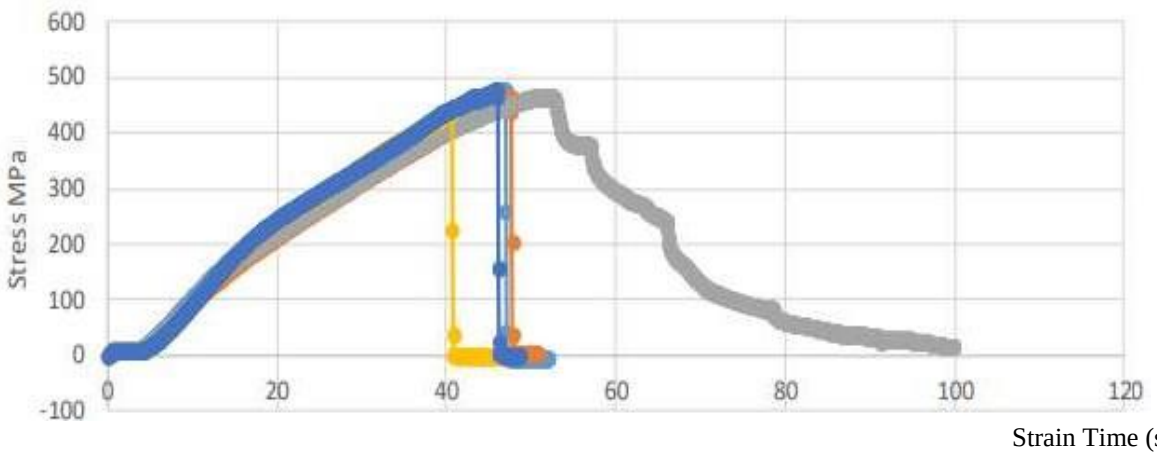

Figure 2. Stress vs. Time curves for CFRCs with plain carbon tested along 0^{o} orientation.

Let's look at each one separately. Fig. 2 shows the experimental results of stress vs. time graphwhen tested at 10 mm/min head speed in 0^o orientation. It is observed that this figure exhibited almost linear behavior to failure before the load reached its maximum level due to having higher mechanical properties. The fiber reinforced composite samples indicated an around maximumstress of 460 - 480 MPa but for trial 3, average strain to failure is found to be increased a little bit more due to not achievement enough interface bonding between fiber and resin. It is observed that there was a decreasing trend in testing time or strain rate for trial 4 samples and test was lasted about 45 s.

Fig. 3 showed a typical tensile stress - time behavior of woven CFRPs subjected to tensile tests at 10 mm/min speed. This is obviously indicated more linear behavior to failure before the loadreached its maximum level. The results showed that maximum strength achieved was around 480 – 520 MPa and average failure time was 45s for these tested samples. The tensile strengthincreased slightly more when fibers orientated in $0/90^o$. This might be related to formation of enough interface bonding between the fiber/resin due to production method, its process parameters. The test duration was about 50s. The composite laminates using epoxy matrix reinforced with carbon fabrics showed the highest tensile strength/highest elastic modulus were obtained for F584/PW sample and for F584/8HS sample, respectively (Paive et al., 2006).

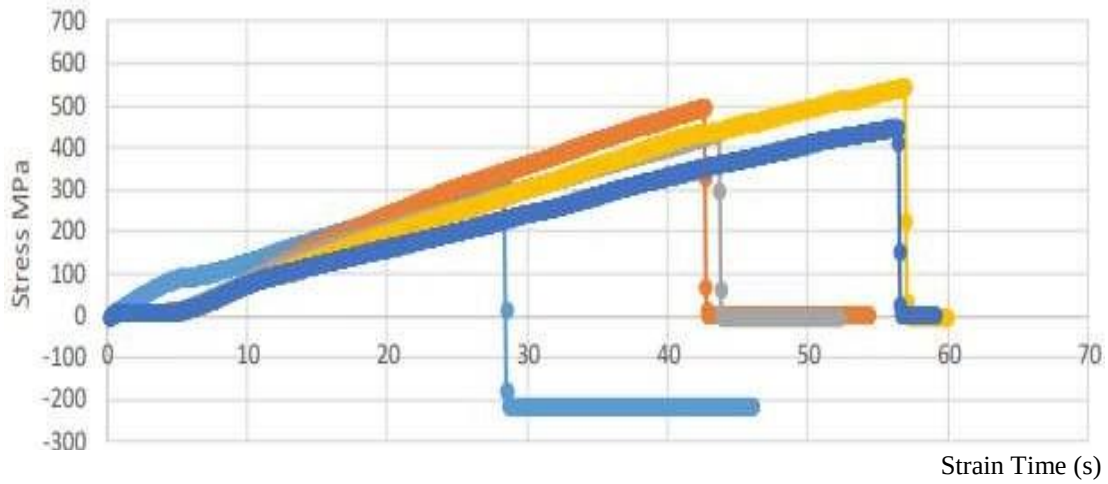

Figure 3. Stress vs. Time curves for CFRCs tested along 90^o orientation.

Fig. 4 revealed stress vs. time curves for CFRCs when tested along 30^o orientation. The mechanical behavior of composite was fully different way when compared to the previous two composites because in first indication, non-linear behavior was observed with gradual increase by forming concave curve, (elastic-plastic) after reaching to peak point around 110 MPa, and then dropped to about 60 - 80 MPa in tensile stress and average strain time to failure is around 140s. Second indication was that the layers were subjected to change angle in aligning their selves in application of load direction. As the load applied, it was limited with bending and shear force, and finally this resulted in debonding of adhesion and fracture of the specimens (Korkmaz et al., 2016).

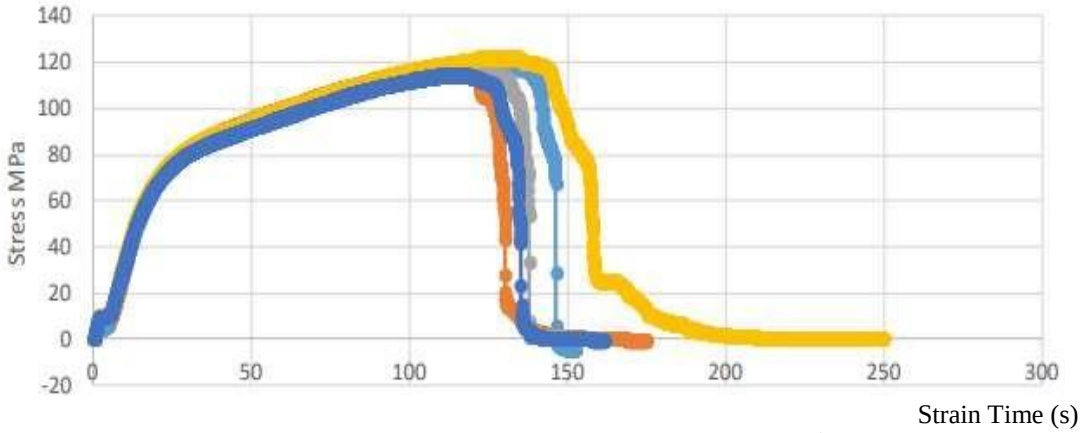

Figure 4. Stress vs. Strain times curves for CFRCs tested along 45^o orientation.

Other reason is that the transfer of load is achieved through the resin instead of fibers. Final one was to obtain higher strain time, which is about 140-145 s that are very higher than those of other composites. The higher strain time to failure was because of subjecting the fibers distortion along the warp and weft direction. This also another indication that elastic modulus seems to be smaller than other samples. On the other hand, due to generating more energy, this composite is supposed to be tougher than those of others.

Conclusion

The following conclusions were drawn out from present study on tensile strength and fracture behavior of FRPC composites.

- Among the orientation effects for three types of CFRPs, the 90^o oriented samples indicated higher tensile stresses (485 MPa), followed by 0^o oriented samples (460 MPa) and 45^o oriented samples (115 MPa), respectively. There was no significant difference between first and second oriented samples.

- Based on tensile stress obtained here, the improvements in 90^o and 0^o orientation in CFRP composite were about 321%, 300% compared to 45^o orientation, respectively.

However, strain time of the 0^o samples was found to be around 40s while the toughness energy of samples of 45^o were the highest about 140s. The improvements in angle ply orientation is about 250%. The reason was that fibers propagated through zigzag way along the 45^o fibers/matrix interface that resulted in higher crack propagation energies. A similarrate was provided for other composite samples.

Scientific Ethics Declaration

The authors declare that the scientific ethical and legal responsibility of this article published in EPSTEM journal belongs to the authors.

Acknowledgements

*This article was presented as an oral presentation at the International Conference on Technology, Engineering and Science (www.icontes.net) held in Antalya/Turkey on November 16-19, 2023.

*This work is achieved in the LRTAPM, laboratory of advanced technology in mechanical engineering of badji Mokhtar-Annaba University, in collaboration with the LEM3, material mechanics and microstructure studies of the University of Lorraine, Metz, France. Financial support are due to the delegated ministry of scientific research (MDRS) of the Algerian ministry of higher education and scientific research (MESRS) under the CNEPRU research projet-LRTAPM: A11N01UN230120140056 (Annaba).

References

Agarwal, G., Patnaik, A.,& Sharma, R.K.(2014). Mechanical and thermo–mechanical properties of bi-directional and short carbon fiber reinforced epoxy composites, *Journal of Eng. Sci. Technol. Taylor's University*, *9*(5), 590-604.

Agrawal, S.A., & Bhattacharya, S. (2021). Mechanical performance of woven carbon reinforced epoxy compositeswith varied orientation angle. *J. Metals Materials and Minerals, 31*(1), 82-87.

Ary Subagia, I. D. G., Kim, Y., Tijing, L.D., Kim, C.S., & Shon, H.K. (2014). Effect of stacking sequence on the flexural properties of hybrid composites reinforced with carbon and basalt. *Compos. Part B, 58*(1), 251-258.

Bodaghi,M., Cristóvão,C., Gomes,R., & Correia,N.C. (2016). Experimental characterization of voids in high fiber volume fraction composites processed by high injection pressure RTM. *Compos Part A: Appl. Sci. Manufacturing, 82*(1), 88-99.

Cecen, V., & Sarıkanat, M. (2008). Experimental characterization of traditional composites manufactured by vacuum assisted resin transfer molding. *Journal of Applied Polymer Science, 107*(3), 1822-1830.

GuruRaja, M.N., &Hari Rao, A.N. (2013). Influence of angle ply orientation on tensile properties carbon/glass hybrid composites. *Journal of Minerals and Materials Characterization and Engineering, 1*(5), 231-235.

Kaleemulla, K.M.&Siddeswarappa, B.(2010). Influence of fiber orientation on the in-plane mechanical properties of laminated hybrid polymer composites. *Journal of Reinforced Plastics Composites, 29*(12), 1900-1914.

Korkmaz,N., Cakmak, E., Dayık, M. (2016). Dokuma karbon elyaf takviyeli karbon Nano tup- epoksi kompozit malzemelerin mekanik ve termal karakterizasyonu. *Suleyman Demirel Universitesi Fen Bilimleri Enstitusu Dergisi, 20* (2), 338-353.

Li, M., Gu, Y., Liu, Y., Li, Y., Zhang, Z. (2013). Interfacial improvement of carbon fiber/epoxy composites using a simple process for depositing commercially functionalized carbon nanotubes on the fibers. *Carbon, 52*(1),109-121.

Liu, W.B., Zhang, S., Li, B., Yang, F., Jiao, W.C, Hao, L.F., &Wang, R.G. (2014). Improvement in interfacial shear strength and fracture toughness for carbon fiber reinforced epoxy composite by fiber sizing. *Poly. Composite,* 35(3), 482-488.

Ma, Y., Jin, S., Yokozeki, T., Ueda, M., Yang, Y., Elbadry, E., &Hamada, H. (2017). A comparative study of the mechanical properties and failure behavior of carbon fiber/epoxy and carbon fiber/polyamide 6 unidirectional composites. *Composite Structers, 160*(1), 89-99.

Ma, Y., Yang., Sugahara, T., & Hamada, H., (2016). A Study on the failure behavior and mechanical properties of unidirectional fiber reinforced thermosetting and thermoplastic composites. *Compos Part B: Engineering, 99*(1), 162-172.

Mallick, P.K. (2007). *Fiber reinforced composites*: *Materials, manufacturing, and design* (3rd ed.). New York, NY: CRC Press.

Ozsoy, N., Mimaroğlu, A., & Ozsoy, M. (2015). Comparison of mechanical behavior of carbon and glass fiberreinforced epoxy composites. *Acta Physic a Polonic A, 127*,1032-1034.

Paiva, J.M.F. da, Mayer, S., & Rezende, M.C., (2006). Comparison of tensile strength of different fabric reinforcedepoxy composites. *Journal of Materials Research, 9* (1), 83-89.

Pandya, K.S., Veerraju, Ch., & Naik, N.K., (2011). Hybrid composites made of carbon and glass woven fabricsunder quasi-static loading. *Materials &. Design,32*(7), 4094-4099.

Phong, N.T., Gabr, M.H., Okubo, K., Chuong, B., Fujii, T. (2013). Improvement in the mechanical performances of carbon fiber/epoxy composite with addition of anno- (Polyvinyl alcohol) fibers. *Composite Structures, 99*, 380-387.

Rahmani, H., Najafi, S.H.M., Saffarzadeh-Matin, S., & Ashori, A. (2014). Mechanical properties of carbon fiber/epoxy composites; Effects of number of plies, fiber contents and, angle-ply layers. *Polyp. Eng. Sci., 54*(11), 2461-2476.

Sahin, Y. (2022). *Cam, karbon & hibrit takviyeli epoksi kompozitlerin uretimi ve mekanik ozelliklerinin iyileştirilmesi*. Nişantasi Universitesi Bilimsel Arastirma Projeleri Koordinasyon Birimi (Nishbap). Bilimsel Araştirma Projesi Sonuc Raporu, BAP 2020. Istanbul, Turkey.

Sahin, Y. (2022). *Introduction to composite materials* (4th ed.). Ankara, Turkey: Seckin Publication,

Sahin, Y., & Patrick, D.B.(2018). Development of epoxy composites containing basalt and carbon fabrics and their mechanical behaviours. *International Journal of Metallurgy and Metal Physics, 3*(2), 25.

Sahin, Y., Alsayed, M., & Nur Gunturk, M.M. (2021). Production processing of fabric reinforced composites by vacuum-assisted resin transfer molding. *Internatıonal innov. approaches in engineering and technology* (pp. 115-128). In Y. Sahin & S.Yalcınkaya (Eds.,). Istanbul Turkey: Guven Plus Grup A.S Publishing.

Sanchez., Campo, M., Jimenez-Suarez, A., & Urena, A. (2013). Effect of the carbon nanotube functionalization on flexural properties of multiscale carbon fiber/epoxy composites manufactured by VARIM. *Compos. Part B: Engineering,45*(1), 1613-1619.

Shokrieh, M.M., & Omidi, M. J. (2008). Tension behavior of unidirectional glass/epoxy composites under differentstrain rates. *Composite Structures, 88*(4), 595-601.

Souris, C.(2005). Fiber reinforced composites in aircraft construction. *Progress in Aerospace Sciences, 41*(2), 143–151.

Turla, P., Kumar, S.S., Reddy, P.H., & Shekar, K. C. (2014). Processing and flexural strength of carbon fiber and glass fiber reinforced epoxy-matrix hybrid composite. *Int. B.Eng. Res. Technology, (IJERT), 3*(4), 394-398.

Xu, Y. & Hoa, S.V. (2008). Mechanical properties of carbon fiber reinforced epoxy/clay nanocomposites. *Compos.Sci. Technology, 68*(3-4), 854-861.

Yusuff, I., Sarifuddin, N., Norbahiyah, S., Ali, A.M., & Ismail, H. (2021). Tensile and flexural properties of woven carbon-kenaf fiber reinforced epoxy matrix hybrid composite: Effect of hybridization and stacking sequences. *AIPConf. Proceedings, 2267*(1).

Zhang, J., Chaisombat, K., He, S., & Wang, C.H. (2012). Hybrid composite laminates reinforced with glass/carbonwoven fabrics for lightweight load bearing structures. *Materials &. Design, 36*(1), 75-80.

Zhang, S., Hao, A., Nguyen, N., Oluwalowo, A., Liu, Z., Dessureault, Y., Park, J.G., &Liang, R. (2019). Carbon nanotube/ carbon composite fiber with improved strength and electrical conductivity via interface engineering. *Carbon,144*, 628-638.

Author Information

Selahettin Selek
Ostim Technical University
Department of Mechanical Engineering
Ostim, Yeni Mahalle, Ankara, Turkey

Yusuf Sahin
Ostim Technical University
Department of Mechanical Engineering
100 Yıl Blv.55/F, Ostim, Yeni Mahalle, Ankara, Turkey
Contact e-mail: *yusuf.sahin@ostimteknik.edu.tr*

To cite this article:

Selek, S., & Sahin, Y. (2023). Tensile property of carbon reinforced epoxy composites for different directions. *The Eurasia Proceedings of Science, Technology, Engineering & Mathematics (EPSTEM), 26*, 135-141.

The Eurasia Proceedings of Science, Technology, Engineering & Mathematics (EPSTEM)
ISSN: 2602-3199

The Eurasia Proceedings of Science, Technology, Engineering & Mathematics (EPSTEM), 2023

Volume 26, Pages 142-148

IConTES 2023: International Conference on Technology, Engineering and Science

Multilayered Inhomogeneous Beams under Torsion and Bending: An Analytical Study of Energy Dissipation

Victor Rizov
University of Architecture

Abstract: The present theoretical paper is devoted to the problem of energy dissipation in multilayered inhomogeneous beam structures of visoelastic behaviour. In particular, our attention is concentrated on studying the energy dissipation for the case of a beam that is loaded simultaneously in torsion and bending. Both torsion and bending moments which are applied on the beam change with time so that the angles of twist and rotation of the beam end vary continuously with time. The viscoelastic mechanical behaviour of the beam under torsion is treated by a viscoelastic model that has two linear springs and a linear dashpot. The model is under time-dependent shear stress. The viscoelastic behaviour of the beam under bending is modelled in a similar way. An analytical approach of deriving the energy dissipation is applied. The approach treats a multilayered beam that has an arbitrary number of layers of different thicknesses and material properties. The layers are longitudinally inhomogeneous. An investigation of the energy dissipation is carried-out to clarify the effect of the parameters of the time-dependent bending and torsion moments, the material inhomogeneity and the beam size on the energy dissipation.

Keywords: Energy dissipation, Beam structure, Multilayered material, Viscoelastic behaviour, Torsion

Introduction

The multilayered structural materials are produced usually by adhesively bonded layers of different materials (Kim et al., 1999; Finot & Suresh, 1996; Rzhanitsyn, 1986). The layers may have also different thickness (Kaul, 2014; Lloyd & Molina-Aldareguia, 2003; Rizov, 2018). The multilayered materials are known with various useful properties which make them especially suitable for use in engineering applications with complex requirements. For instance, they have relatively high strength-to-weight and stiffness-to-weight ratios. Thus, the multilayered materials are applied with great success for building-up light-weight structures. Multilayered materials are often an object of study of engineering science (Dolgov, 2005, 2016; Rizov, 2021; Sy et al., 2015; Sy et al., 2020). Although the concept of multilayered materials is not a new one, there are some aspects of the mechanical behaviour of the multilayered materials especially when they are used for manufacturing of members of various mechanisms and load-bearing engineering structures which need further clarification.

Such aspect is the energy dissipation in multilayered structural members of viscoelastic behaviour when loaded simultaneously in torsion and bending. It should be noted here that publications on energy dissipation usually are concerned with multilayered viscoelastic beam structures loaded in pure bending (Narisawa, 1987; Rizov, 2021). However, beams under simultaneous action of torsion and bending moments are frequently used as members of various engineering structures. Besides, in some cases the loading varies continuously with time.

The aim of the present paper is to study analytically the energy dissipation in a multilayered viscoelastic beam structure under torsion and bending. The layers of the beam are continuously inhomogeneous in longitudinal direction. Thus, the material properties (in particular, the moduli of elasticity and the coefficient of viscosity of the viscoelastic model) are continuously distributed in each layer along the beam length. The torsion and

- Selection and peer-review under responsibility of the Organizing Committee of the Conference

bending moments which act on the beam change with time so that the angles of twist and rotation of the end of the beam are continuous functions of time. The energy dissipation is derived. An investigation of the effects of the parameters of the time-dependent bending and torsion moments, the material inhomogeneity and the beam size on the energy dissipation is carried-out.

Theoretical Analysis

Consider the multilayered beam structure whose configuration is shown in Fig. 1.

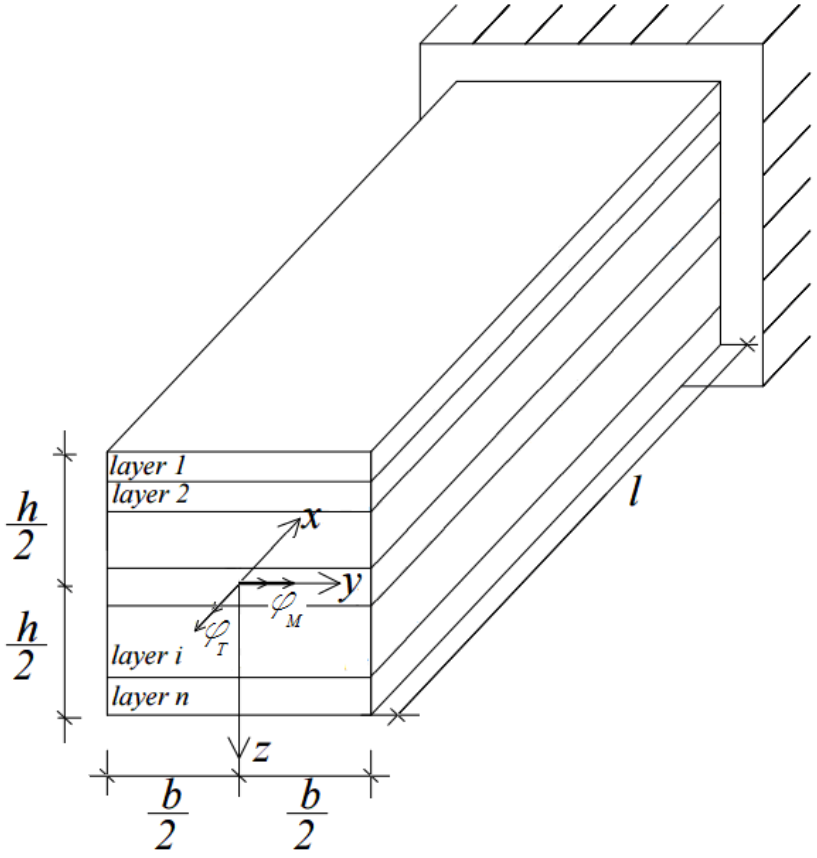

Figure 1. Multilayered beam structure.

The beam has n layers. Each layer has individual thickness and material properties. The width and thickness of the beam are b and h, respectively. The beam is subjected to torsion so that the variation of the angle of twist, φ_T, (Fig. 1) with time, t, is given by

$$\varphi_T = \varphi_{T0}\cos(\omega t), \tag{1}$$

where φ_{T0} and ω are parameters. Besides, the beam is also under bending moment so that the variation of the angle of rotation, φ_M, with time can be described by

$$\varphi_M = \varphi_{M0}\cos(\omega t), \tag{2}$$

where φ_{M0} is a parameter.

The beam under consideration has linear viscoelastic mechanical behaviour. The beam response to torsion is treated by the viscoelastic model shown in Fig. 2.

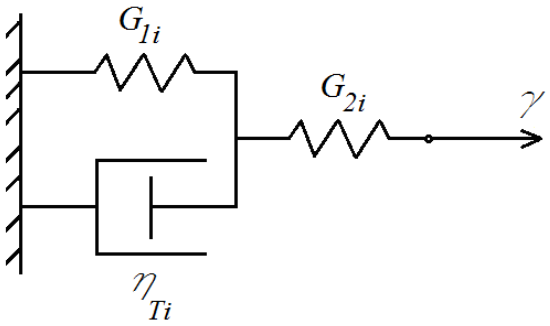

Figure 2. Viscoelastic model.

The two springs of the viscoelastic model have shear moduli, G_{1i} and G_{2i}. The coefficient of viscosity of the dashpot is η_{Ti} (Fig. 2). It should be specified here that the subscript, i, refers to the *i*-th layer of the beam structure. The layers of the beam are made by materials exhibiting continuous inhomogeneity in longitudinal direction. Thus, G_{1i}, G_{2i} and η_{Ti} change continuously along the *x*-axis. The changes of G_{1i}, G_{2i} and η_{Ti} are defined by

$$G_{1i} = G_{1Bi} e^{\delta_{1i} \frac{x}{l}}, \tag{3}$$

$$G_{2i} = G_{2Bi} e^{\delta_{2i} \frac{x}{l}}, \tag{4}$$

$$\eta_{Ti} = \eta_{TBi} e^{\delta_{3i} \frac{x}{l}}, \tag{5}$$

where

$$0 \le x \le l, \tag{6}$$

$$i = 1, 2, ..., n. \tag{7}$$

In formulas (3) – (6), G_{1Bi}, G_{2Bi}, η_{TBi}, δ_{1i}, δ_{2i} and δ_{3i} are parameters, l is the longitudinal size of the beam structure. The model in Fig. 2 is under shear strain, γ, that is given by

$$\gamma = \gamma_0 \cos(\omega t), \tag{8}$$

where γ_0 is a parameter. The time-dependent shear modulus, $\tilde{G}_i(t)$, of the viscoelastic model is defined by

$$\tilde{G}_i(t) = \frac{\tau_i}{\gamma}, \tag{9}$$

where τ_i is the shear stress in the model.

The bending response of the beam structure is treated by a viscoelastic model that has the same components like the model in Fig. 2. The only difference is that G_{1i}, G_{2i}, η_{Ti}, γ and γ_0 are replaced with E_{1i}, E_{2i}, η_{Mi}, ε and ε_0, respectively (here, E_{1i} and E_{2i} are the moduli of elasticity of the two springs, η_{Mi} is the coefficient of viscosity, ε is the linear strain, ε_0 is a parameter). The change of E_{1i}, E_{2i} and η_{Mi} along the beam length is given by

$$E_{1i} = E_{1Bi} e^{\delta_{4i} \frac{x}{l}}, \tag{10}$$

$$E_{2i} = E_{2Bi} e^{\delta_{5i} \frac{x}{l}}, \tag{11}$$

$$\eta_{Mi} = \eta_{MBi} e^{\delta_{6i} \frac{x}{l}}, \tag{12}$$

where E_{1Bi}, E_{2Bi}, η_{MBi}, δ_{4i}, δ_{5i} and δ_{6i} are parameters. The time-dependent modulus of elasticity, $\tilde{E}_i(t)$, of the viscoelastic model in this case is presented by

$$\tilde{E}_i(t) = \frac{\sigma_i}{\varepsilon}, \tag{13}$$

where σ_i is the normal stress in the model.

The unit dissipated energy, u_{0Ti}, in the *i*-th layer of the beam due to torsion is defined by

$$u_{0Ti} = \int_0^t \tau_{\eta Ti} \dot{\gamma}_{\eta T} dt, \tag{14}$$

where $\tau_{\eta Ti}$ and $\gamma_{\eta Ti}$ are the shear stress and the shear strain in the dashpot of the viscoelastic model, respectively.

The dissipated energy, U_T, due to the torsion of the beam is obtained by

$$U_T = l \sum_{i=1}^{i=n} \iint_{(A_i)} u_{0Ti} dA, \tag{15}$$

where A_i is the area of the cross-section of the *i*-th layer.

The unit dissipated energy, u_{0Mi}, in the *i*-th layer in the context of the beam response to bending is given by

$$u_{0Mi} = \int_0^t \sigma_{\eta Mi} \dot{\varepsilon}_{\eta M} dt, \tag{16}$$

where $\sigma_{\eta Mi}$ and $\varepsilon_{\eta M}$ are the normal stress and the linear strain in the dashpot of the viscoelastic model, respectively.

The unit dissipated energy (16) is integrated to derive the dissipated energy, U_M, in the beam due to bending, i.e.

$$U_M = l \sum_{i=1}^{i=n} \iint_{(A_i)} u_{0Mi} dA. \tag{17}$$

The dissipated energy, U, due to torsion and bending is equal to the sum of U_T and U_M, i.e.

$$U = U_T + U_M , \tag{18}$$

where the integrals (15) and (17) are solved by the MatLab.

Numerical Results

Numerical results are derived assuming that $n = 4$, $b = 0.008$ m, $h = 0.012$ m, $l = 0.450$ m, $\varphi_{T0} = 0.004$ rad, $\varphi_{M0} = 0.006$ rad and $\omega = 0.0003$.

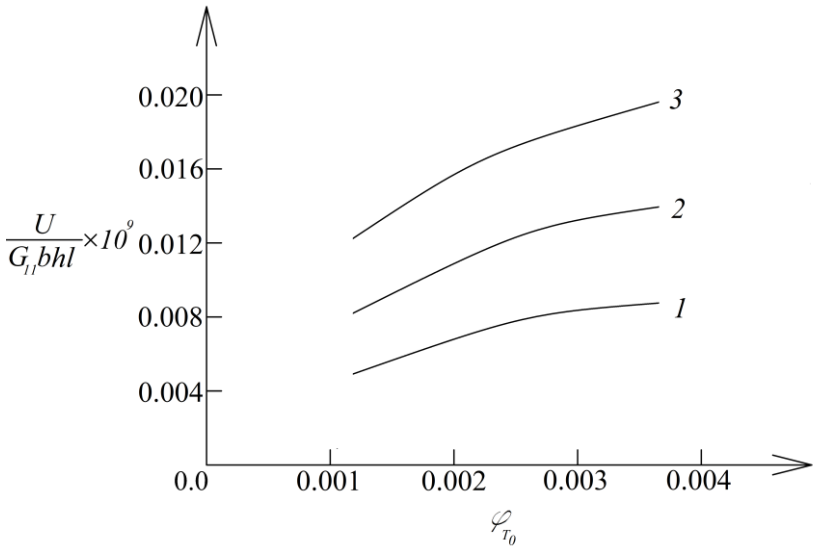

Figure 3. Dissipated energy versus φ_{T0} (curve 1 – at $\delta_{11} = 0.3$, curve 2 – at $\delta_{11} = 0.5$ and curve 3 – at $\delta_{11} = 0.7$).

The results are shown in form of various graphs in Fig. 3, Fig. 4 and Fig. 5 illustrating how the dissipated energy in the beam structure changes with varying of different parameters of the loading, the beam size, the distribution of moduli of elasticity and the coefficients of viscosity in the length direction of the layers.

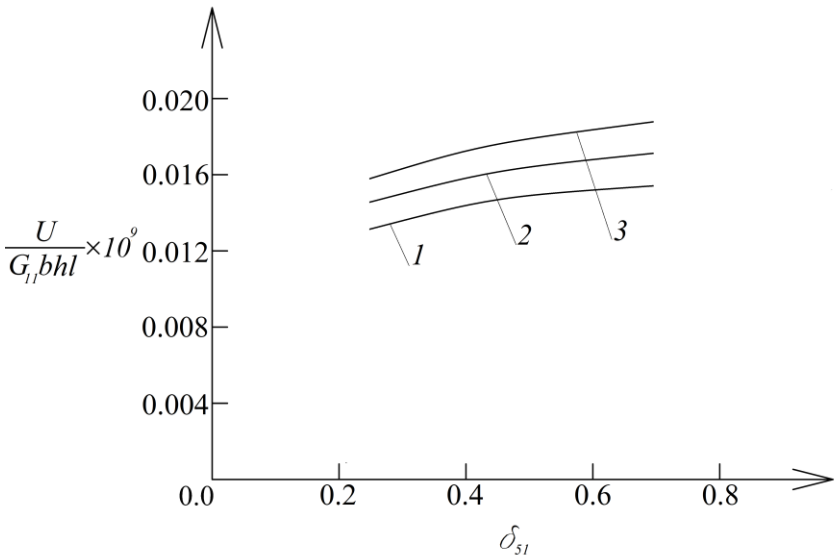

Figure 4. Dissipated energy versus δ_{51} (curve 1 – at $\varphi_{M0} = 0.002$ rad, curve 2 – at $\varphi_{M0} = 0.004$ rad and curve 3 – at rad).

Results illustrating variation of the dissipated energy induced by changing the parameter, φ_{T0}, at different values of the parameter, δ_{11}, are depicted in Fig. 3. From the results in Fig. 3 it becomes clear that there is a significant influence of both parameters, φ_{T0} and δ_{11}, on the dissipated energy. It can be seen that the dissipated energy grows with growing of φ_{T0} (Fig. 3). The growth of δ_{11} also causes growth of the dissipated energy.

Figure 4 gives plots of the dissipated energy versus the para $\varphi_{M0} = 0.006$meter, δ_{51}, for three values of the parameter, φ_{M0}. The results show that increase of δ_{51} produces an increase of the dissipated energy (Fig. 4).

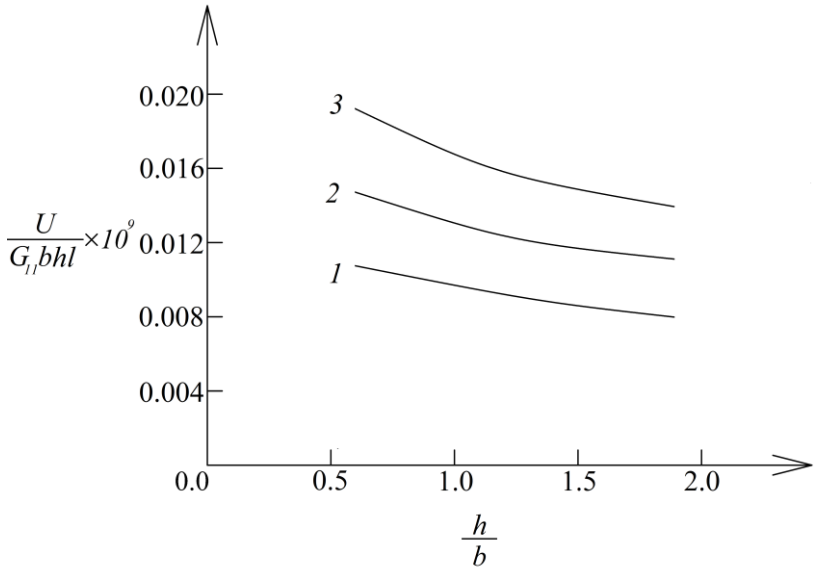

Figure 5. Dissipated energy versus h/b ratio (curve 1 – at $l/b = 20$, curve 2 – at $l/b = 40$ and curve 3 – at $l/b = 60$).

The same character has the dependence of the dissipated energy on the parameter, φ_{M0}, i.e. increase of φ_{M0} leads to growth of the dissipated energy (Fig. 4).

Figure 5 visualizes the dependence of the dissipated energy upon the beam sizes (the latter are represented by h/b and l/b ratios). It can be observed in Fig. 5 that as a result of increase of h/b ratio the dissipated energy reduces. However, increase of l/b ratio induces a growth of the dissipated energy (Fig. 5).

Conclusion

A theoretical study of the energy dissipation in a multilayered inhomogeneous beam structure of viscoelastic behaviour under time-dependent bending and torsion is performed. The study reveals that:

1) the dissipated energy grows with growing of φ_{T0};

2) increase of φ_{M0} leads also to growth of the dissipated energy;

3) the growth of the parameter, δ_{11}, causes growth of the dissipated energy;

4) increase of δ_{51} produces an increase of the dissipated energy;

5) the dissipated energy reduces when h/b ratio increases;

6) increase of l/b ratio induces a growth of the dissipated energy.

Recommendations

It is recommendable in a future work to develop further the present dissipation analysis by considering non-linear viscoelastic behavior.

Scientific Ethics Declaration

The author declares that the scientific ethical and legal responsibility of this article published in EPSTEM journal belongs to the author.

Acknowledgements or Notes

* This article was presented as an oral presentation at the International Conference on Technology, Engineering and Science (www.icontes.net) held in Antalya/Turkey on November 16-19, 2023.

References

Dolgov, N. (2005). Determination of stresses in a two-layer coating. *Strength of Materials, 37*(4), 422-431.

Dolgov, N. (2016). Analytical methods to determine the stress state in the substrate–coating system under mechanical loads. *Strength of Materials, 48*(5), 658-667.

Finot, M., & Suresh, S. (1996). Small and large deformation of thick and thin-film multilayers: effect of layer geometry and compositonal gradients. *Journal of Mech. Phys. Solids, 44*(5), 683-721.

Kaul, A. B. (2014). Two-dimensional layered materials: Structure, properties, and prospects for device applications, *Journal of Materials Research, 29*(03), 348-361.

Kim, J. S., Paik, K.W., & Oh, S. H. (1999). The multilayer-modified Stoney's formula for laminated polymer composites on a silicon substrate. *Journal of Applied Physics, 86, 5474–5479.*

Lloyd, S.J., & Molina Aldareguia, J. M. (2003). Multilayered materials: A palette for the materials artist. *Philos Trans. R. Soc. Lond. A, 361*(1813), 2931-2949.

Narisawa, I. (1987). *Strength of polymer materials*. Chemistry.

Rizov, V. I. (2021). Delamination analysis of multilayered beams exhibiting creep under torsion. *Coupled Systems Mechanics, 10,* 317-331.

Rizov, V. I. (2021). Energy dissipation in viscoelastic multilayered inhomogeneous beam structures: An analytical study. *Materials Science Forum, 1046,* 39-44.

Rizov, V.I. (2018). Analysis of cylindrical delamination cracks in multilayered functionally graded non-linear elastic circular shafts under combined loads. *Frattura ed Integrità Strutturale, 12*(46), 158-170.

Rzhanitsyn, A.R. (1986). *Built-up bars and plates*. Stroyiizdat.

Sy, N. N., Lee, J., & Cho, M. (2015). Efficient higher-order zig-zag theory for viscoelastic laminated composite plates. *International Journal of Solids and Structures, 62,* 174-185.

Sy, N. N., Lee, J., & Cho, M. (2020). A coupled hygrothermo-mechanical viscoelastic analysis of multilayered composite plates for long-term creep behaviors. *Composite Structures, 242*(3), 112030.

Author Information

Victor Rizov
Department of Technical Mechanics
University of Architecture, Civil Engineering and Geodesy
1 Chr. Smirnensky blvd.
1046 – Sofia, Bulgaria
Contact e-mail: *V_RIZOV_FHE@UACG.BG*

To cite this article:

Rizov, V. (2023). Multilayered ınhomogeneous beams under torsion and bending: An analytical study of energy dissipation. *The Eurasia Proceedings of Science, Technology, Engineering & Mathematics (EPSTEM), 26,* 142-148.

The Eurasia Proceedings of Science, Technology, Engineering & Mathematics (EPSTEM)
ISSN: 2602-3199

The Eurasia Proceedings of Science, Technology, Engineering & Mathematics (EPSTEM), 2023

Volume 26, Pages 149-155

IConTES 2023: International Conference on Technology, Engineering and Science

Effect of Using Nano-TiO_2 on the Rheological Properties of Cementitious Systems

Hatice Gizem Sahin
Bursa Uludag University

Fatih Eren Akgumus
Bursa Uludag University

Ali Mardani
Bursa Uludag University

Abstract: Self-cleaning concrete (SCC) was developed that can reduce air pollution by utilizing its photocatalytic property. Due to this feature, polluting materials are broken down into H_2O and CO_2, which are completely harmless, without the need for any additional carrier gas. For this purpose, it was emphasized that semiconductor oxides with photocatalytic properties such as TiO_2, ZnO, CdSe and WO_3 are used in the production of SCC. Compared to other oxides, it was determined that nano-TiO_2 is more commonly preferred. However, it was emphasized that the use of nano-TiO_2 due to the high surface area/volume ratio increases the water requirement and the risk of agglomeration of cementitious systems. This situation directly affects the rheological properties of SCC. In this study, the effects of nano-TiO_2 utilization ratio change on the rheological properties of cementitious systems were investigated. For this purpose, a total of 4 mixtures were prepared by substituting nano-TiO_2 with 28 nm at a rate of 0, 0.5, 1 and 1.5% by weight of cement. The rheological properties of the prepared mixtures were evaluated according to the dynamic yield stress (DYS), apparent viscosity (AV) and structural build-up (A_{thix}) parameters. It was understood that the DYS, AV and A_{thix} values of the mixtures increased with the increase of nano-TiO_2 utilization ratio.

Keywords: Self-cleaning concrete, nano-TiO_2, Rheological properties, Structural build-up

Introduction

As urbanization becomes more widespread, it was understood that environmental pollution has significantly increased, leading to a decrease in air quality (Mardani-Aghabaglou, 2016; Sezer et al., 2016; Yigit et al., 2020; Mardani-Aghabaglou et al., 2018). The fact that these issues stem from numerous parameters was emphasized. It was observed that a significant number of studies related to the reduction of pollutants within the framework of the European Green Deal are currently underway. In a study conducted by Nath et al. (2016), the presence and quantity of volatile organic compounds such as C, N, and S oxides resulting from industrialization were emphasized as directly affecting air quality. In this context, it was emphasized that issues such as global warming, pollution risk, acid rain, and changes in concrete surface color have increased, while human health was significantly adversely affected (Beeldens, 2006). Several methods were implemented to mitigate these adversities.

In this study, the color change of concrete surfaces due to pollutants was examined. In this regard, it was understood that the application of photocatalysis, which accelerates the natural degradation process, holds the potential to be a solution to this problem (Yang et al., 2000). The use of photocatalysts in cementitious systems was observed to preserve the aesthetic properties of concrete, purify it from pollutants, and maintain the same

- Selection and peer-review under responsibility of the Organizing Committee of the Conference

color and texture (Visali et al., 2021). It was emphasized that semiconductors are the most suitable photocatalysts due to their photocorrosion resistance and wide bandgap energies (Castro Hoyos et al., 2022; Liang et al., 2019).

It was reported that TiO_2, due to its low cost, non-toxic nature, and good thermal stability, is the most commonly used semiconductor photocatalyst (Yuranova et al., 2007; Yasmina et al., 2014). There were sufficient studies on the impact of TiO_2 (nT) usage on the self-cleaning and mechanical properties of concrete mixtures (Wang et al., 2019). However, it was found that there is a lack of information in the literature regarding the impact of nT usage on the rheological properties and thixotropic behavior of cementitious systems (Li et al., 2020). Observations have revealed that in a limited number of conducted studies, conflicting results were reported. Various researchers have noted that the use of nano-materials, which increases the risk of agglomeration due to their high surface area, directly affects the flow performance of cementitious systems (Song et al., 2021; Mohseni et al., 2015; Temel et al., 2023). It was understood that this situation necessitates the determination of rheological properties that provide information about the homogeneity and workability of cementitious systems containing nT (Talero et al., 2017).

Many researchers have reported that the increase in the use of nano-materials and their usage rate in cementitious systems generally has a negative impact on their rheological properties (Nazar et al., 2020). However, it was determined that a definitive conclusion on this matter has not been reached in mixtures containing nT. This study investigates the impact of the usage rate of nT on the rheological properties and thixotropic behavior of cement paste mixtures.

Materials and Methods

CEM I 42.5 Portland cement was used as the binder. The chemical components provided by the manufacturer, along with some of the physical and mechanical properties of the used cement, are presented in Table 1.

Table 1. Some properties of the cement.

Oxides (%)						
SiO_2	Al_2O_3	Fe_2O_3	CaO	MgO	$Na_2O+0,658\ K_2O$	SO_3
18	4.75	3.58	63	1.4	0.7	3.11
Specific Gravity	Surface Area (cm^2/g)	Compressive Strength (MPa)		Setting Time (minutes)		
		7-Day	28-Day	Initial	Final	
3.06	3441	42.8	51.8	170	240	

Table 2 displays a few of the nT's properties that were supplied by the manufacturer.

Table 2. Some properties of the used nT in the study

Value	Units	28 nm NT
Purity	%	>99
Size	nm	28
Specific Surface Area	m^2/g	>60
Loss of Weight in Drying	%	2 max.
Loss of Weight in Ignition	%	5 max.
pH	-	5.5-7.0
Color	-	White

A water reducing admixture (WRA) was used to achieve the desired flow performance. Some characteristics of the WRA provided by the manufacturer, are shown in Table 3.

Table 3. Some properties of WRA

Density (g/cm^3)	Solid Content (%)	pH	Chlorine content (%)	Na_2O ratio (%)
1.060	32	2-5	<0.1	<10

Preparation of Mixtures

In addition to the control, a total of four different paste mixtures were prepared by adding nT at a rate of 0.5%, 1%, and 1.5% by weight of the cement. In order to achieve the desired flow performance, WRA was added to all mixtures at a rate of 0.15% by weight of the binder. The selection of these ratios took into account the measurement capacity of the rheometer used and the prevention of segregation in the mixtures. The mixture ratios are shown in Table 4. The nT utilization ratio was used for the nomenclature of the mixtures. For example, the mixture containing 1.5% nT is named 1.5-nT.

Table 4. Amounts of prepared mixtures

Mixture	Cement	nT	w/b	WRA (%)
C	1	-	0.35	0.15
0.5-nT	0.95	0.5		
1.0-nT	0.90	1		
1.5-nT	0.85	1.5		

Method

The rheological parameters of the paste mixtures were measured, including the DYS and AV values. Furthermore, the thixotropic behavior of the mixtures was examined by calculating the structural build-up development (A_{thix}).

Determination of Rheological Properties

For rheological measurements, an MCR52-Anton Paar rheometer with an 8 mm ball was used, as shown in Figure 1-a. The rheological measurement method applied in the study is depicted in Figure 1-b.

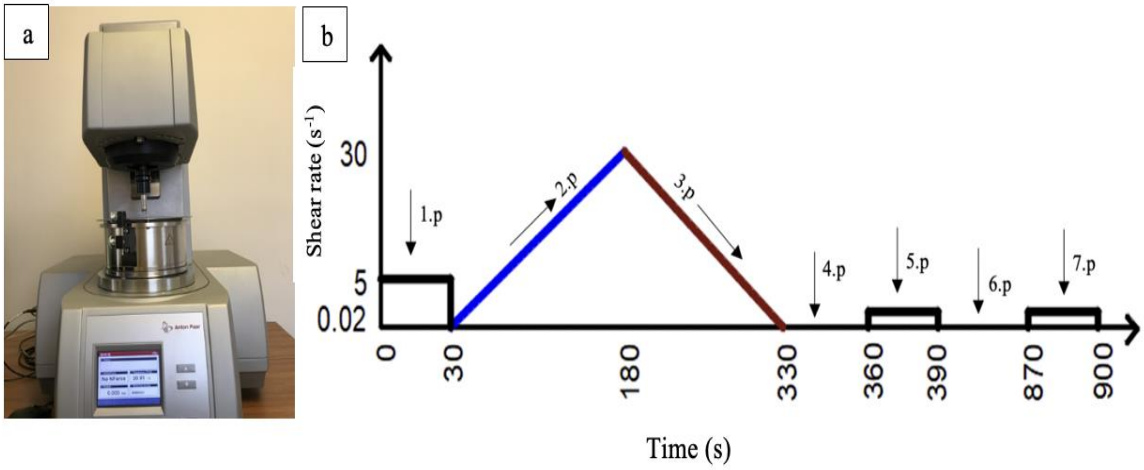

Figure 1. (a) Rheometer and (b) rheological measurement system

In order to determine the rheological measurements, shear stress-shear rate and AV-shear rate graphs were obtained for each mixture, considering the data obtained in the 3rd period as shown in Figure 1-b. The Herschel-Bulkley model was used in the analysis of rheological data.

The shear stress/AV-shear rate graph for the C and 1.5-nT mixtures is shown in Figure 2.

Measurement of Thixotropic Behavior

Using the static yield stress values obtained from this test, the structural build-up development (A_{thix}) of the mixture was determined (Sahin & Mardani, 2022).

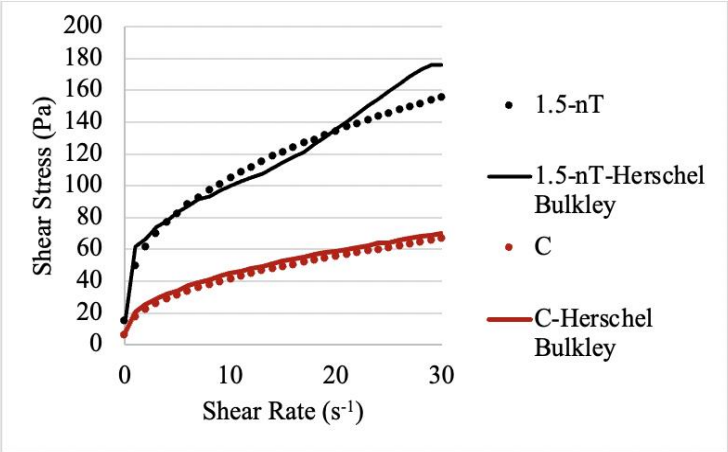

(a)

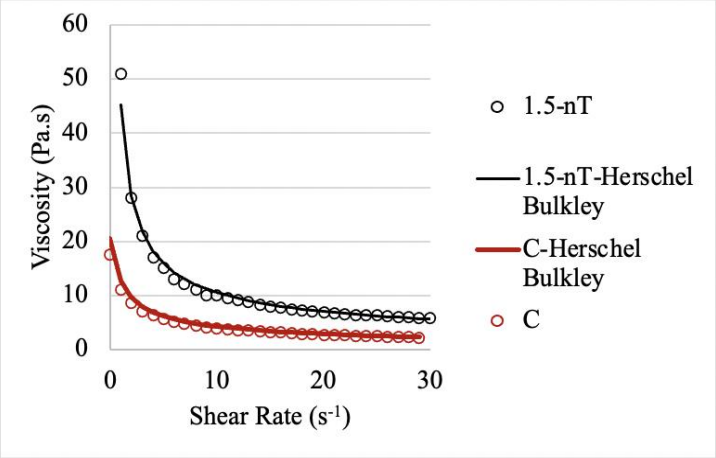

(b)

Figure 2. (a) DYS-shear rate and (b) AV-shear rate for the 1.5-nT mixtures

Results and Discussion

Rheological properties and thixotropic values are shown in Table 5. The addition of nT to paste mixtures generally rises their rheological properties and thixotropic values, regardless of the utilization ratio. The rise in the total surface area due to the addition of nT was reported by various researchers to lead to an rised risk of agglomeration, thus potentially negatively affecting the flow performance of cementitious systems (Nazari et al., 2012; Wiesner et al., 2017). It was emphasized by many researchers that in the system, as the content of fine materials rises and the total surface area rises, the water requirement of the mixture also rises (Mardani-Aghabaglou et al., 2017; Senff et al., 2014). Furthermore, various researchers have emphasized that nT can accelerate the formation of nuclei in the matrix, potentially rising the hydration rate and, consequently, leading to a rise in heat of hydration (Lee et al., 2013; Zhang et al., 2015). In this case, various researchers have expressed that the rise in the amount of evaporating water may negatively affect the rheological properties of the mixtures (Yang et al., 2023; Sun et al., 2020).

With a rise in the nT utilization ratio from 0.5% to 1.5%, the DYS, AV, and A_{thix} values of the mixture rised by 76%, 133%, and 60%, respectively. De Matos et al. (2022) reported that in 3D-printed concrete mixtures containing nT at 0.25, 0.50, 0.75, 1, and 1.5% ratios, a rise in the nT utilization ratio had a negative impact on the rheological properties of the mixtures. It was reported that this phenomenon is due to the high surface area of nT and its reduction of the interparticle spacing (Bergold et al., 2013). However, in another study conducted by Jiang et al. (2018), it was measured that an rise in the nT utilizatioın ratio resulted in a decrease in the AV

value of the mixtures. This phenomenon is due to the lubricating and ball-bearing role of spherical particles between the cement flocculation structures.

Table 5. Rheological and thixotropic values of mixtures

Mixture	DYS (Pa)	AV (Pa.s)	A_{thix} (Pa/s)
C	7.8	2.3	0.04
0.5-nT	8.7	2.4	0.05
1.0-nT	10.3	2.6	0.07
1.5-nT	15.3	5.6	0.08

Conclusion

The results obtained from the materials used and the experiments conducted are listed below:

- Regardless of the utilization ratio, the addition of nT generally resulted in a rise in the rheological properties and thixotropic values of the paste mixtures.
- A rise in the nT utilization ratio was observed to enhance the rheological properties of cement paste mixtures and improve their structural build-up behavior.

Scientific Ethics Declaration

The authors declare that the scientific ethical and legal responsibility of this article published in EPSTEM journal belongs to the authors.

Acknowledgements

This article was presented as an oral presentation at the International Conference on Technology, Engineering and Science (www.icontes.net) held in Antalya/Turkey on November 16-19, 2023.

* The authors would like to thank to Bursa Uludag University Scientific Research Projects Coordination Center (BAP) for their support under the grant number FOA-2022-1135. The first author thanks to TUBİTAK 2211-A program for the support received during their doctoral studies. Additionally, the second author is thankful for the scholarship provided under the project with TUBİTAK grant number 222M245.

References

Beeldens, A.(2006). An environmentally friendly solution for air purification and self cleaning effect: the application of TiO2 as photocatalyst in concrete. *In: Proceedings of Transport Research Arena Europe*, Goteborg, Sweden

Bergold, S. T., Goetz-Neunhoeffer, F., & Neubauer, J. (2013). Quantitative analysis of C–S–H in hydrating alite pastes by in-situ XRD. *Cement and Concrete Research*, *53*, 119-126.

de Matos, P., Zat, T., Corazza, K., Fensterseifer, E., Sakata, R., Mohamad, G., & Rodríguez, E. (2022). Effect of TiO2 nanoparticles on the fresh performance of 3d-printed cementitious materials. *Materials*, *15*(11), 3896.

Jiang, S., Shan, B., Ouyang, J., Zhang, W., Yu, X., Li, P., & Han, B. (2018). Rheological properties of cementitious composites with nano/fiber fillers. *Construction and Building Materials*, *158*(1), 786-800.

Lee, B. Y., Jayapalan, A. R., & Kurtis, K. E. (2013). Effects of nano-TiO2 on properties of cement-based materials. *Magazine of Concrete Research*, *65*(21), 1293-1302.

Li, H., Ding, S., Zhang, L., Ouyang, J., & Han, B. (2020). Effects of particle size, crystal phase and surface treatment of nano-TiO2 on the rheological parameters of cement paste. *Construction and Building Materials*, *239*.

Liang, X., Cui, S., Li, H., Abdelhady, A., Wang, H., & Zhou, H. (2019). Removal effect on stormwater runoff pollution of porous concrete treated with nanometer titanium dioxide. *Transportation Research Part D: Transport and Environment, 73,* 34-45.

Mardani-Aghabaglou, A. (2016). *Investigation of cement-superplasticizer admixture compatibility* (Doctoral dissertation). Izmir, Ege University, Engineering Faculty, Civil Engineering Department.

Mardani-Aghabaglou, A., Ozen, S., & Altun, M. G. (2018). Durability performance and dimensional stability of polypropylene fiber reinforced concrete. *Journal of Green Building*, *13*(2), 20-41.

Mardani-Aghabaglou, A., Son, A. E., Felekoglu, B., & Ramyar, K. (2017). Effect of cement fineness on properties of cementitious materials containing high range water reducing admixture. *Journal of Green Building*, *12*(1), 142-167.

Mohseni, E., Ranjbar, M. M., & Tsavdaridis, K. D. (2015). Durability properties of high-performance concrete incorporating nano-TiO2 and fly ash. *American Journal of Engineering and Applied Sciences*, *8*(4), 519-526.

Nath, R. K., Zain, M. F. M., & Jamil, M. (2016). An environment-friendly solution for indoor air purification by using renewable photocatalysts in concrete: A review. *Renewable and Sustainable Energy Reviews*, *62*, 1184-1194.

Nazar, S., Yang, J., Thomas, B. S., Azim, I., & Rehman, S. K. U. (2020). Rheological properties of cementitious composites with and without nano-materials: A comprehensive review. *Journal of Cleaner Production*, *272*, 122701.

Nazari, A., Montazer, M., & Moghadam, M. B. (2012). Introducing covalent and ionic cross-linking into cotton through polycarboxylic acids and nano TiO2. *Journal of The Textile Institute*, *103*(9), 985-996.

Rojas A.M., Manzano, M. A., & Maury-Ramírez, A. (2022). Challenges and opportunities of using titanium dioxide photocatalysis on cement-based materials. *Coatings*, *12*(7), 968.

Senff, L., Tobaldi, D. M., Lemes-Rachadel, P., Labrincha, J. A., & Hotza, D. (2014). The influence of TiO2 and ZnO powder mixtures on photocatalytic activity and rheological behavior of cement pastes. *Construction and Building Materials*, *65*, 191-200.

Sezer, A., Boz, A., & Tanrinian, N. (2016). An investigation into strength and permittivity of compacted sand-clay mixtures by partial replacement of water with lignosulfonate. *Acta Psyhica Polonica Series a*, *130*(1).

Song, H., & Li, X. (2021). An overview on the rheology, mechanical properties, durability, 3D printing, and microstructural performance of nanomaterials in cementitious composites. *Materials*, *14*(11).

Sun, J., Tian, L., Yu, Z., Zhang, Y., Li, C., Hou, G., & Shen, X. (2020). Studies on the size effects of nano-TiO2 on Portland cement hydration with different water to solid ratios. *Construction and Building Materials*, *259*.

Sahin, H., & Mardani, A. (2022). Effect of cement C3A content on some fresh state properties and compressive strength of 3D printing concrete mixtures. *Journal of Uludag University Faculty of Engineering*, *27*(2), 831-846.

Talero, R., Pedrajas, C., González, M., Aramburo, C., Blázquez, A., & Rahhal, V. (2017). Role of the filler on Portland cement hydration at very early ages: Rheological behaviour of their fresh cement pastes. *Construction and building Materials*, *151*, 939-949.

Temel, M., Taskır, İ.S., Sahin, H.G., & Mardani A. (2023). Effect of nano-TiO2 fineness and utilization ratio on the Water Absorption Capacity of Mortar Mixture. *Ulugh Beg International Congress of Science and Engineering Knowledge.* Uzbekistan

Visali, C., Priya, A. K., & Dharmaraj, R. (2021). Utilization of ecofriendly self-cleaning concrete using zinc oxide and polypropylene fibre. *Materials Today: Proceedings*, *37*, 1083-1086.

Wang, J. H., Chen, C. C., & Wang, H. W. (2019). Grouping and time-series notifying of periodic data in a real-time streaming system for smart toy claw machine. *Journal of Systems Architecture*, *92*, 12-22.

Wiesner, M. R., & Bottero, J. Y. (2017). *Environmental nanotechnology: applications and impacts of nanomaterials*. McGraw-Hill Education.

Yang, F., Xie, J., Wang, W., Wang, W., & Wang, Z. (2023). The role of nano-TiO2 on the mechanical properties and hydration behavior of C2S, C3S and C4A3S‾. *Construction and Building Materials*, *388*, 131558.

Yang, J., Li, D., Zhang, Z., Li, Q., & Wang, H. (2000). A study of the photocatalytic oxidation of formaldehyde on Pt/Fe2O3/TiO2. *Journal of Photochemistry and Photobiology A: Chemistry*, *137*(2-3), 197-202.

Yasmina, M., Mourad, K., Mohammed, S. H., & Khaoula, C. (2014). Treatment heterogeneous photocatalysis; factors influencing the photocatalytic degradation by TiO2. *Energy Procedia*, *50*, 559-566.

Yigit, B., Salihoglu, G., Mardani-Aghabaglou, A., Salihoglu, N. K., & Ozen, S. (2020). Recycling of sewage sludge incineration ashes as construction material. *Journal of the Faculty of Engineering and Architecture of Gazi University*, *35*(3), 1647-1664.

Yuranova, T., Sarria, V., Jardim, W., Rengifo, J., Pulgarin, C., Trabesinger, G., & Kiwi, J. (2007). Photocatalytic discoloration of organic compounds on outdoor building cement panels modified by photoactive coatings. *Journal of Photochemistry and Photobiology A: Chemistry*, *188*(2-3), 334-341.

Zhang, R., Cheng, X., Hou, P., & Ye, Z. (2015). Influences of nano-TiO2 on the properties of cement-based materials: Hydration and drying shrinkage. *Construction and Building Materials*, *81*, 35-41.

Author Information

Hatice Gizem Sahin
Bursa Uludag University, Faculty of Engineering,
Department of Civil Engineering, Nilufer/Bursa/Turkey

Fatih Eren Akgumus
Bursa Uludag University, Faculty of Engineering,
Department of Civil Engineering, Nilüfer/Bursa/Turkey

Ali Mardani
Bursa Uludag University, Faculty of Engineering,
Department of Civil Engineering, Nilufer/Bursa/Turkey
Contact e-mail: ali.mardani16@gmail.com

To cite this article:

Sahin, H.G., Akgumus, F.E., & Mardani, A. (2023). Effect of using nano-TiO_2 on the rheological properties of cementitious systems. *The Eurasia Proceedings of Science, Technology, Engineering & Mathematics (EPSTEM)*, *26*, 149-155.

The Eurasia Proceedings of Science, Technology, Engineering & Mathematics (EPSTEM)
ISSN: 2602-3199

The Eurasia Proceedings of Science, Technology, Engineering & Mathematics (EPSTEM), 2023

Volume 26, Pages 156-165

IConTES 2023: International Conference on Technology, Engineering and Science

Examining the Performance of the Heat Exchanger in a Heat Pump Clothes Dryer

Fazıl Erinc Yavuz
Haier Europe – Renta Elektrikli Ev Aletleri San ve Dıs Tic. Ltd. Sti

Vasıf Can Yildiran
Haier Europe – Renta Elektrikli Ev Aletleri San ve Dıs Tic. Ltd. Sti

Sebastian George Colleoni
Haier Europe

Abstract: The performance of the newly designed fin and tube heat exchanger placed within the heat pump tumble dryer (HPTD) has been numerically and experimentally investigated. A new heat exchanger (HX) has one inlet and one outlet for the refrigerant side. However, after insertion into the evaporator, the flow splits into two different branches and reaches a lower pressure than the standard one. Also, due to the separation more tube bundles can be fitted in the same amount of volume. Due to increased tube bundles, total heat transfer is increased. This behavior can be seen with numerical and experimental results. Also, the fin structures on the heat exchanger were removed from the model to avoid increasing the solution grid density. In this region, it was defined as a porous structure to accommodate the pressure drop. To solve the problem, the program called ANSYS-FLUENT was utilized to solve the problem, and the PISO algorithm was employed to solve the pressure-velocity pair. While air at a specified temperature was passed around the exchanger, water was circulated on the inner surface instead of the refrigerant gas to observe the temperature change.

Keywords: CFD, Tumble dryer, Heat exchanger, Evaporator, Porous media, Heat transfer

Introduction

Energy consumption of household appliances has a big impact on climate, water usage and resource consumption because of their electricity usage. To reduce these consumptions academicians and engineers are working tirelessly. Due to increasing number of tumble dryers is also impact on the total consumption. In this study, effect of newly developed heat exchanger is investigated as an evaporator in the heat pump tumble dryer.

Heat exchangers widely investigated in literature and finding a higher capacity in same volume is essential for household appliances, but increasing the capacity is not always comes with the better results, because of the flow resistance on the air side or some other adverse effects.

In a study that conducted conjugated heat transfer simulation in a fin and tube heat exchanger, they indicate that, increasing turbulence effect have a positive effect on heat transfer rate due to the increase in the heat exchange coefficient as expected with an increased power needs on the air flow side (Välikangas & Karvinen, 2018). On another study, frost formation was investigated numerically and experimentally, they have used porous media assumption and they have found frost layer formation has significant effect on heat transfer between air and fins (Lenic et al., 2009). Beside Lenic and his team study, in the literature there are lots of frost layer formation study with porous media assumption (O'Neal & Tree, 1984; Sami & Duong, 1989; Lee et al., 2003; Yao et al., 2004).

The other studies, has widely investigated the arrangement of refrigerant circuits, configuration of fins and tubes and operating conditions (Liu et al., 2004; Lu et al., 2011). In other study, experimental study has been conducted and compared with the well-known correlations such as Dittus-Boelter, Blasius, Gnielinski and Haaland with maximum difference 7.5% (Siddique & Alhazmy, 2008). In our study, refrigerant circuit on fin and tube heat exchanger has been taken from CAD model and fins are modelled as a porous media for a comparison test.

Method

This study consists of three phases. First one is design phase, for three-dimensional CAD model Creo Parametric has been used. Pipe designs were created according to the design constraints of the current plastic basement, also inlet and outlet pipe location were decided according to the same plastic part. Second phase can be summarized at CFD studies, in this phase capacity comparison and air flow distribution were conducted. For this phase commercial CFD solver ANSYS Fluent had been used.

Third phase can be called as prototype creation and experimental study. For prototype phase, producibility of the design were investigated with the supplier of relevant part. Afterwards, tumble dryer was built with the prototype evaporators and tests were conducted. In first test, current configuration and new configuration had been tested under same ambient conditions and comparison were conducted. In second test energy consumption test had been conducted according to relevant standard (IEC 61121 – Tumble Dryers for Household Use-Methods for Measuring the Performance).

Design Phase

At the beginning of the study, the investigation on current evaporator was conducted which is shown on left side of Figure 1. Green arrows show the air flow and blue lines shows the refrigerant flow. Solid lines show the right-side u-bends of the evaporator while the dashed lines show the left-side u-bends. First idea is adding more pipes to the evaporator to enhance heat transfer capacity. However, due to the mechanical and producibility restrictions such as minimum bending radius of Al or Cu pipe and geometrical constraints this idea was cancelled. Second idea was splitting the refrigerant flow into two different branches at the entrance of the evaporator and with that split dimension between the pipes (h) can be reduced and more pipes can be added into the system. After the investigation of couple of design parameters, final heat exchanger design was created, and the figure of refrigerant flow is shown on the right side of Figure 1.

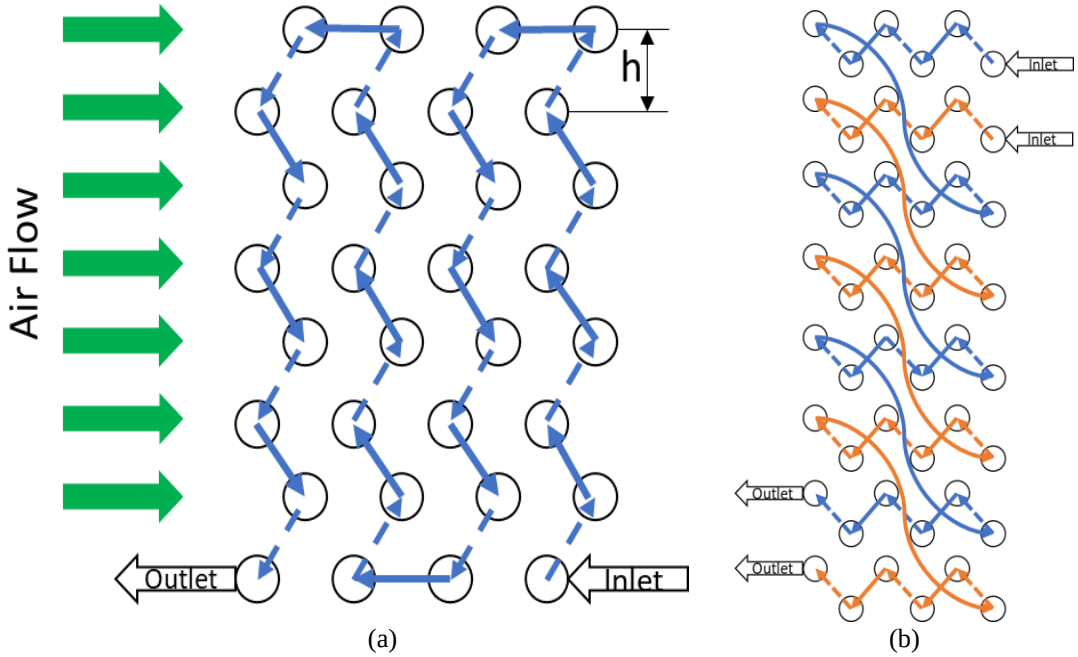

(a) (b)

Figure 1. Heat exchanger refrigerant circuit comparison a) Current b) New design

Simulation Phase

Three-dimensional model of the current and new evaporator placed in the cavity and two analyses were conducted under same input and boundary conditions. ANSYS Fluent commercial software was used as a solver and solution had been conducted under steady-state conditions. Due to the high mesh requirement, fins are modelled as a porous medium. In an earlier study, evaporator porous zone has been modeled and the constants for the porous zone has achieved and validated with the pressure difference test that was conducted by our team. In Figure 2 pressure drop values at different velocities has given.

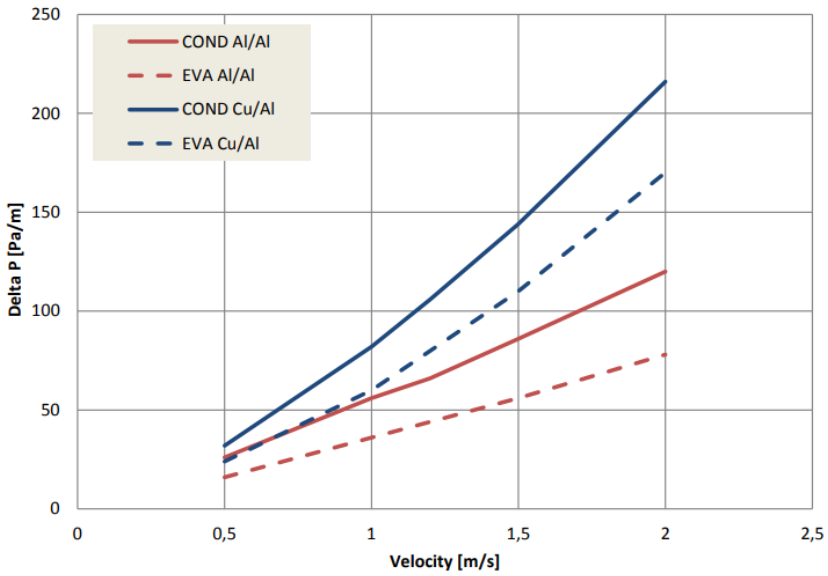

Figure 2. Pressure drop on the condenser and evaporator for different air velocity values

The cavity was generated in ANSYS SpaceClaim and the solution geometry is shared in Figure 3. To solve the problem mesh generation is needed. The mesh is generated on Fluent Mesh software with approximately 6.5 million cells. The mesh visual is shared in Figure 4. Five different meshes were generated in Fluent Mesh and analysis were conducted for the mesh independency study, which is shared in Figure 5. The difference between tests and analyses were found approximately 0.3%. The rest of the analyses were conducted under same mesh properties.

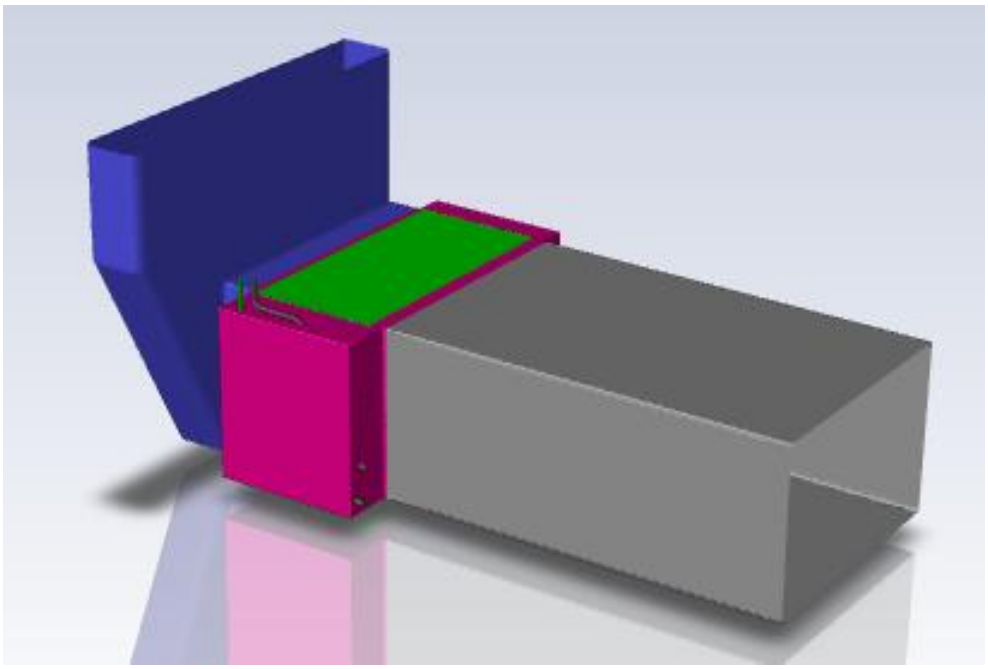

Figure 3. Solution domain

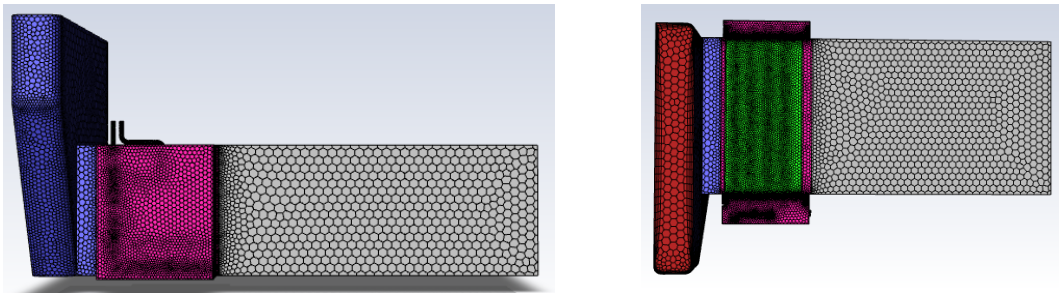

Figure 4. Mesh visual from front and top view

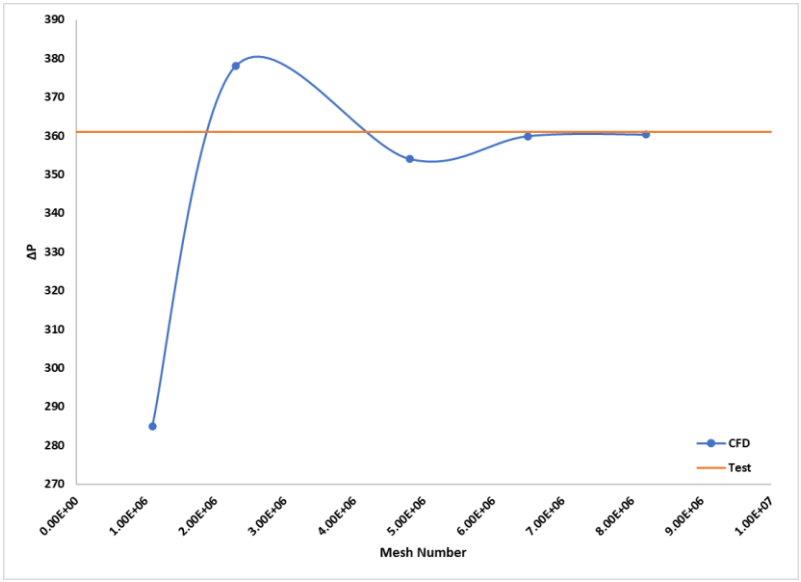

Figure 5. Mesh ındependency

For air flow side, air assumed as dry air and ideal gas assumption were used. For refrigerant side, due to the complexity of multi-phased analysis, water was used instead of refrigerant. Two cases were conducted under same input and boundary conditions which is shown at Figure 6.

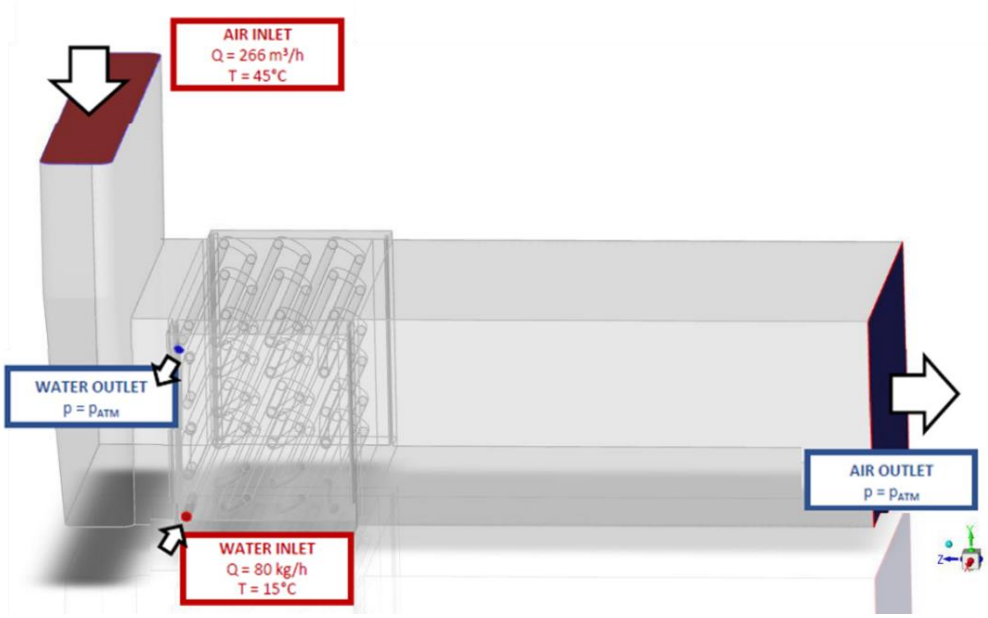

Figure 6. Inputs and boundary conditions

The flow of water and air are turbulent, therefore k- ω SST turbulence model (Menter,1993) was used. Equations of turbulence model is shared in below.

$$\rho\frac{\partial k}{\partial t}+\rho u_i\frac{\partial k}{\partial x_j}=P-\ \beta^*\rho k\omega+\frac{\partial}{\partial x_j}\left[(\mu+\sigma_k\mu_T)\frac{\partial k}{\partial x_j}\right] \quad [1]$$

$$\rho\frac{\partial \omega}{\partial t}+\rho u_i\frac{\partial \omega}{\partial x_j}=\frac{\gamma\rho}{\mu_T}P-\ \beta\rho\omega^2+\frac{\partial}{\partial x_j}\left[(\mu+\sigma_\omega\mu_T)\frac{\partial \omega}{\partial x_j}\right]+2\rho(1-F_1)\frac{\sigma_{\omega 2}}{\omega}\frac{\partial k}{\partial x_j}\frac{\partial \omega}{\partial x_j} \quad [2]$$

For the solution of velocity-pressure couple Reynolds Averaged Navier-Stokes (RANS) Equations (Wilcox, 1998) were used and shown in below. PISO solution algorithm was used for the solution of velocity-pressure couple.

$$\left(\frac{\partial v_x}{\partial x}+\frac{\partial v_y}{\partial y}+\frac{\partial v_z}{\partial z}\right)=0 \quad [3]$$

$$\rho U\left(\frac{\partial U}{\partial x}+\frac{\partial V}{\partial x}+\frac{\partial W}{\partial x}\right)=-\frac{\partial P}{\partial x}+\mu\left(\frac{\partial^2 U}{\partial x^2}+\frac{\partial^2 U}{\partial y^2}+\frac{\partial^2 U}{\partial z^2}\right)-\mu\left(\frac{\partial\overline{u\prime^2}}{\partial x^2}+\frac{\partial\overline{u\prime v\prime}}{\partial x\partial y}+\frac{\partial\overline{u\prime w\prime}}{\partial x\partial z}\right) \quad [4]$$

$$\rho V\left(\frac{\partial U}{\partial y}+\frac{\partial V}{\partial y}+\frac{\partial W}{\partial y}\right)=-\frac{\partial P}{\partial y}+\mu\left(\frac{\partial^2 V}{\partial x^2}+\frac{\partial^2 V}{\partial y^2}+\frac{\partial^2 V}{\partial z^2}\right)-\mu\left(\frac{\partial\overline{u\prime v\prime}}{\partial x\partial y}+\frac{\partial\overline{v\prime^2}}{\partial y^2}+\frac{\partial\overline{v\prime w\prime}}{\partial y\partial z}\right) \quad [5]$$

$$\rho W\left(\frac{\partial U}{\partial z}+\frac{\partial V}{\partial z}+\frac{\partial W}{\partial z}\right)=-\frac{\partial P}{\partial z}+\mu\left(\frac{\partial^2 W}{\partial x^2}+\frac{\partial^2 W}{\partial y^2}+\frac{\partial^2 W}{\partial z^2}\right)-\mu\left(\frac{\partial\overline{u\prime w\prime}}{\partial x\partial z}+\frac{\partial\overline{v\prime w\prime}}{\partial y\partial z}+\frac{\partial\overline{w\prime^2}}{\partial z^2}\right) \quad [6]$$

$$\rho C_p\left(U\frac{\partial T}{\partial x}+V\frac{\partial T}{\partial y}+W\frac{\partial T}{\partial z}\right)=k\left(\frac{\partial^2 T}{\partial x^2}+\frac{\partial^2 T}{\partial y^2}+\frac{\partial^2 T}{\partial z^2}\right) \quad [7]$$

Experimental Phase

After the design and numerical studies, prototype phase was started. Then, two configurations have been assembled one with the current evaporator and the other one with the new evaporator. Two different tests were conducted. One test can be called as temperature difference test which is not normative, and the only thing can be seen is the temperature deviations with the other reference machines. The second test is normative test and it is conducted according to IEC 61121 – Tumble Dryers for Household Use-Methods for Measuring the Performance Standard.

Results and Discussion

Results of Simulation

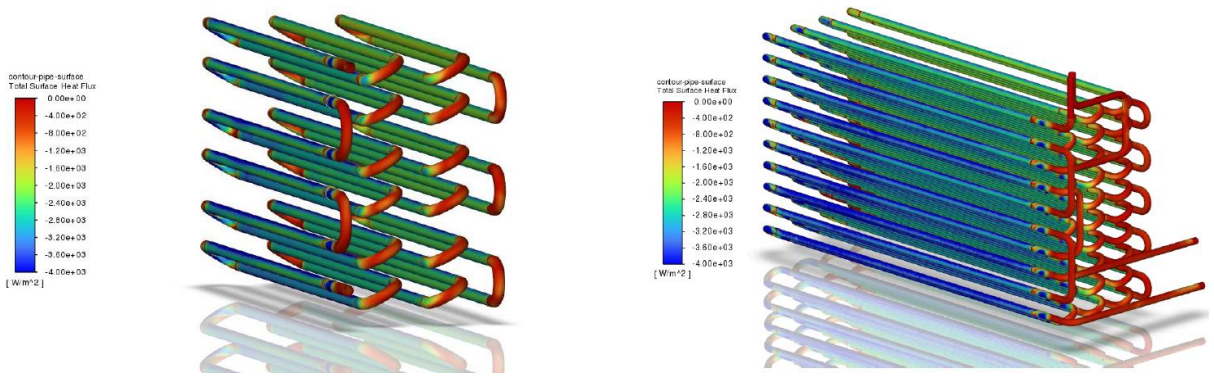

(a) (b)

Figure 7. Heat flux contour of the pipes a) Current b) New evaporator.

The simulations show that new design has an improvement not only for the heat exchange but also flow dynamics. Due to the higher pipe numbers of new design more uniform flow at the evaporator has achieved. Also, heat exchange amount of the evaporator is increased. Figure 7 indicates that with new pipe the system has supplied high heat fluxes for higher surface area even if the maximum flux is not changed. Due to the higher contact surface, outlet temperature of the evaporator is increased. It can be seen at Figure 8.

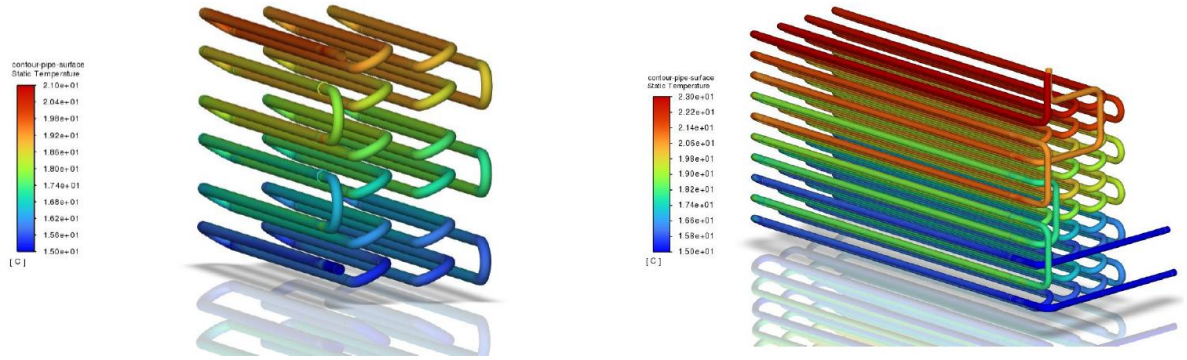

(a) (b)

Figure 8. Temperature contour of the pipes a) Current b) New evaporator.

For the air side, at the entrance no essential difference has been observed. It is due to that; the entrance region of the flow did not be changed. Figure 9 shows the velocity distribution on the evaporator inlet region.

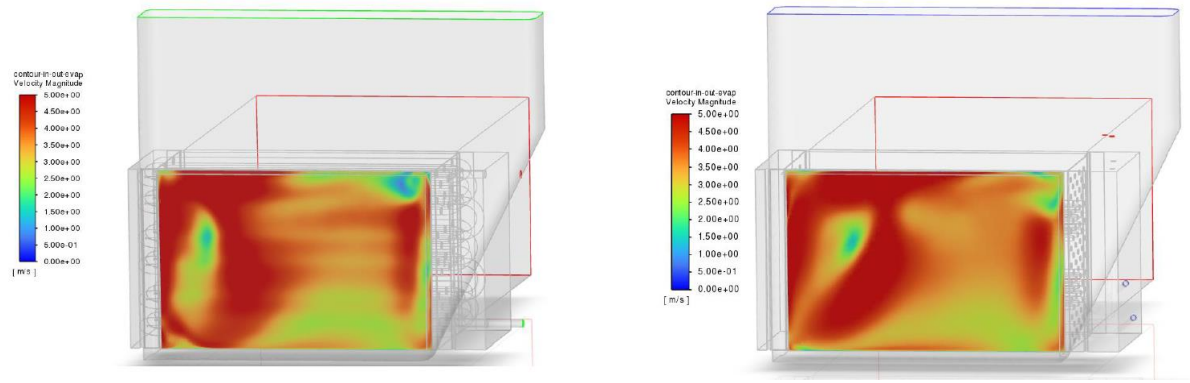

(a) (b)

Figure 8. Velocity distribution contour on the evaporator ınlet a) Current b) New evaporator.

However, due to the higher contact surface lower outlet velocities has achieved, but more uniform velocity distribution is achieved. Figure 9 shows the velocity distribution on the evaporator outlet region.

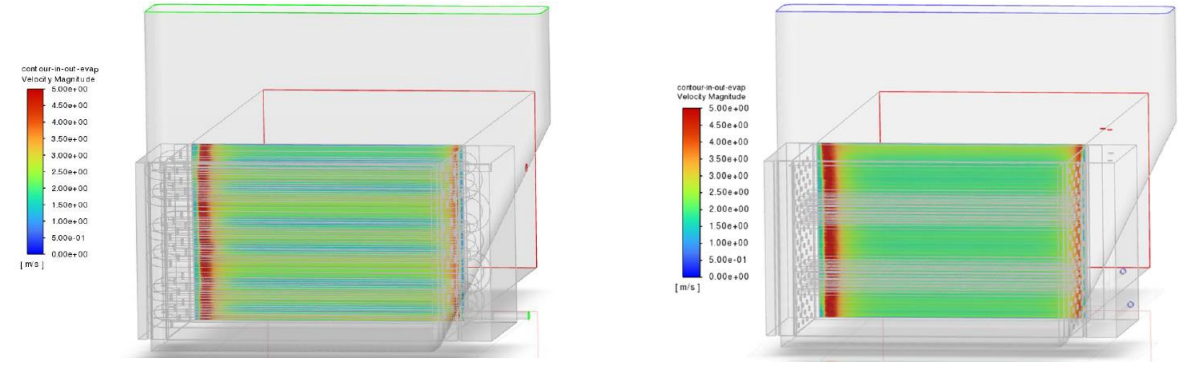

(a) (b)

Figure 9. Velocity distribution contour on the evaporator outlet a) Current b) New evaporator.

The uniformity analysis for the flow side has been conducted and the average velocity values taken from three different planes as following, inlet, middle, outlet. Also, every plane has splitted into four different equal

regions to understand which of the area receive more flow than the others. Figure 10 shows four different regions which velocity values are taken.

Figure 10. Velocity distribution regions

The results show that, with new evaporator the system can receive more uniform airflow then the current one. Results can be seen at Table 1 and also histogram values is shared in Figure 11.

Table 1. Velocity distribution ınside the evaporator

Plane	Region	Current Production (m/s)	Percentage of Current Production	New Evaporator (m/s)	Percentage of New Evaporator
Inlet	Top-Left	0.018812	23.9%	0.019424	24.9%
	Top-Right	0.018996	24.2%	0.019606	25.1%
	Bottom-Left	0.020061	25.5%	0.019452	25%
	Bottom-Right	0.020731	26.4%	0.019479	25%
Middle	Top-Left	0.018446	24.4%	0.019397	24.9%
	Top-Right	0.018536	24.5%	0.019775	25.3%
	Bottom-Left	0.019074	25.2%	0.019346	24.8%
	Bottom-Right	0.019512	25.8%	0.019511	25%
Outlet	Top-Left	0.018442	24.3%	0.019346	24.8%
	Top-Right	0.018251	24%	0.019729	25.3%
	Bottom-Left	0.019536	25.7%	0.019325	24.8%
	Bottom-Right	0.019680	25.9%	0.019511	25%

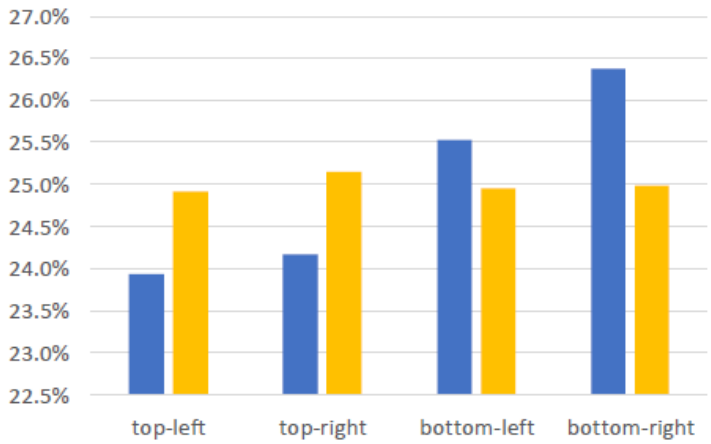

Figure 11. Average velocity distribution on the regions

On the thermal side, new evaporator has 60% increase on the temperature difference on the air side and the total heat exchange is increased 63.4%. In Table 2 summary of the thermal measurements is shared.

Table 2. Summary of the thermal measurements

Cycle	Measurement	Unit	Current Evaporator	New Evaporator
Air Cycle	Mass Flow	kg/h	296.1	296.1
	Avearage T Inlet	°C	45.0	45.0
	Average T Outlet	°C	40.2	37.3
	ΔT	°C	4.8	7.7
	Pipe Surface External	m²	0.0359	0.0484
	Pipe Surface Internal	m²	0.1510	0.2604
	Total Pipe Surface	m²	0.1868	0.3087
	Q Pipe External	W	51.9	47.4
	Q Pipe Internal	W	339.5	592
	Q Pipe Total	W	391.4	639.4
Water Cycle	Mass Flow	kg/h	80.0	80.0
	Avearage T Inlet	°C	15.0	15.0
	Average T Outlet	°C	19.2	21.9
	ΔT	°C	4.2	6.9

Result of Experiments

After the convincing results phase of the simulations, prototype was started and the test that was mentioned in the method section. First test was conducted under same ambient conditions (25°C, 55% r.h.) in this test, two prototypes were built and the only different thing in these prototypes are evaporators. Then, compressor supplied with the electricity and heating on condenser and cooling on the evaporator is observed for 100s. Thermocouples or infrared temperature measurement devices fixed to their positions and tests conducted, respectively. The results show that with new evaporator all system temperatures go down due to the higher capacity of the new evaporator, the comparison results shared in the Figure 12.

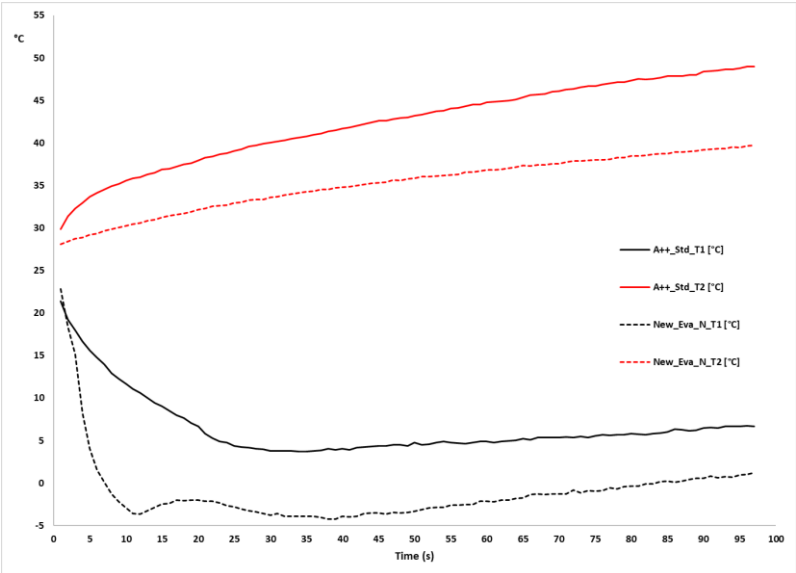

Figure 12. Comparison of temperatures on the evaporator and condenser

After short temperature comparison test, complete machines were built, and tests are conducted according to IEC 61121 standard. Three full load and four half load tests were conducted as stated in standard. Results of one full load and one half load test is shared in Figure 13. On the tests three temperature measurements are taken. T1 temperature on the air temperature and placed between evaporator exit and condenser inlet. T2 Placed at the drum outlet where the air takes humidity from wet clothes. T3 placed on the blowing pipe of the compressor. All temperature measurement shows that with new evaporator all system temperature goes down due to the increased evaporator capacity. However, due to the condenser capacity and compressor capacity remained same the system could not take the humidity from machines and eventually total drying time is elongated with the higher energy consumption. However, these tests indicates that with higher condenser capacity or with the optimized cycle this evaporator can reduce the cycle and/or energy consumption.

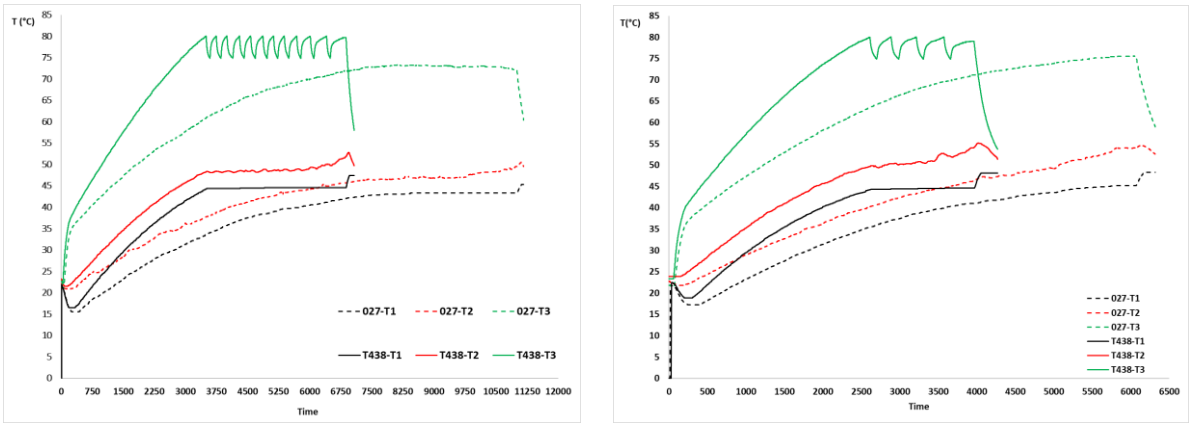

(a) (b)

Figure 13. Temperature comparison on the IEC 61121 test. a) Full load b) Half load

Conclusion

It can be clearly said, the new evaporator has higher capacity from the current one. However, without calibrated or optimized system, our current system could not supply the evaporator well enough. Study also shows that splitting the flow creates a chance to increasing the pipe number and therefore increased exchanger capacity, also with new evaporator more uniformed air flow can be attained. Further research on the evaporator, such as coating the fins with a specific feature, is ongoing. In addition, on the condenser side, a study is ongoing to increase the capacity of the same volume as the current condenser.

Scientific Ethics Declaration

The authors declare that the scientific ethical and legal responsibility of this article published in EPSTEM journal belongs to the authors.

Acknowledgements or Notes

* This article was presented as an oral presentation at the International Conference on Technology, Engineering and Science (www.icontes.net) held in Antalya/Turkey on November 16-19, 2023.

*We extend our gratitude to Renta Electric Home Appliances Industry and Foreign Trade Ltd. and our affiliated company, Haier Europe, for their contributions to our work.

References

IEC 61121(2002). *Tumble dryers for household use-methods for measuring the performance* (3r ed.). Webstore.

Lee, K. S., Jhee, S., & Yang, D. K. (2003). Prediction of the frost formation on a cold flat surface. *International Journal of Heat and Mass Transfer, 46*(20), 3789-3796.

Lenic, K., Trp, A., & Frankovic, B. (2009). Transient two-dimensional model of frost formation on a fin-and-tube heat exchanger. *International Journal of Heat and Mass Transfer, 52*(1-2), 22-32.

Liu, J., Wei, W., Ding, G., Zhang, C., Fukaya, M., Wang, K., & Inagaki, T. (2004). A general steady state mathematical model for fin-and-tube heat exchanger based on graph theory. *International Journal of Refrigeration, 27*(8), 965-973.

Lu, C. W., Huang, J. M., Nien, W. C., & Wang, C. C. (2011). A numerical investigation of the geometric effects on the performance of plate finned-tube heat exchanger. *Energy Conversion and Management, 52*(3), 1638-1643.

Menter, F. (1993). Zonal two equation kw turbulence models for aerodynamic flows. In *23rd Fluid Dynamics, Plasmadynamics, and Lasers Conference* (p. 2906).

ONeal, D. L., & Tree, D. R. (1984). Measurement of frost growth and density in a parallel plate geometry. *Ashrae Transactions, 90*(2), 278-290.

Sami, S. M., & Duong, T. (1989). Mass and heat transfer during frost growth. *ASHRAE Transactions, 95*, 158-165.

Siddique, M., & Alhazmy, M. (2008). Experimental study of turbulent single-phase flow and heat transfer inside a micro-finned tube. *International Journal of Refrigeration, 31*(2), 234-241.

Välikangas, T., & Karvinen, R. (2018). Conjugated heat transfer simulation of a fin-and-tube heat exchanger. *Heat Transfer Engineering, 39*(13-14), 1192-1200.

Wilcox, D. C. (1998). *Turbulence modeling for CFD* (Volume 2, pp. 103-217). La Canada, CA: DCW industries.

Yao, Y., Jiang, Y., Deng, S., & Ma, Z. (2004). A study on the performance of the airside heat exchanger under frosting in an air source heat pump water heater/chiller unit. *International Journal of Heat and Mass Transfer, 47*(17-18), 3745-3756.

Author Information

Fazıl Erinc Yavuz
Haier Europe – Renta Elektrikli Ev Aletleri San ve Dıs Tic. Ltd. Sti
Organize sanayi bolgesi 22. Cadde No: 4
Odunpazarı/Eskisehir Turkiye
Contact e-mail: *erinc.yavuz@haier-europe.com*

Vasıf Can Yildiran
Haier Europe – Renta Elektrikli Ev Aletleri San ve Dıs Tic. Ltd. Sti
Organize sanayi bolgesi 22. Cadde No: 4
Odunpazarı/Eskisehir Turkiye

Sebastian George Colleoni
Haier Europe
Via Privata Eden Fumagalli 20861 Brugherio MB Italy

To cite this article:

Yavuz, F.E., Yildiran, V.C., & Colleoni, S.G. (2023). Examining the performance of the heat exchanger in a heat pump clothes dryer. *The Eurasia Proceedings of Science, Technology, Engineering & Mathematics (EPSTEM), 26*, 156-165.

The Eurasia Proceedings of Science, Technology, Engineering & Mathematics (EPSTEM)
ISSN: 2602-3199

The Eurasia Proceedings of Science, Technology, Engineering & Mathematics (EPSTEM), 2023

Volume 26, Pages 166-175

IConTES 2023: International Conference on Technology, Engineering and Science

Enhancing Driver Comfort and Control: A Proposal for Customizable Gas and Brake Pedal Sensitivity

Huseyin Karacali
TTTech Auto Turkey

Efecan Cebel
TTTech Auto Turkey

Nevzat Donum
TTTech Auto Turkey

Abstract: Despite spectacular advancements in automotive industry, a significant gap exists within the domain of driver-vehicle interaction like the fixed response force of the accelerator and brake pedals. Nowadays, although there are studies on safety especially for pedals, the issue of customizing the pedal hardness has not become widespread. In this study, a method for customizing the accelerator and brake pedals is suggested. The proposed system improves driving comfort and experience by allowing drivers to customize their preferred pedal level. Utilizing an accessible tuner for stepwise adjustments, drivers can fine-tune the pedal response force until it matches their comfort and driving style. Moreover, our system includes numbered preset buttons, which enable drivers to save their preferred force profiles. This feature not only accommodates the unique preferences of individual drivers but also eases transitions between different drivers sharing the same vehicle. By just a push of a button, drivers can recall their saved profiles, ensuring consistent comfort and control across different driving sessions. By incorporating this system to the car, we aim to revolutionize driver-vehicle interactions, moving away from the traditional standardized approach towards a personalized driving experience. This novel solution holds promise in expanding driving comfort, improving vehicle control, and potentially enhancing driving safety. Furthermore, it creates new avenues for research into the effects of tailored pedal forces on driving efficiency and fatigue, thus shaping the future trajectory of automotive design.

Keywords: Gas and brake pedal, Sensitivity, Driving efficiency, Driver comfort

Introduction

Personalization is essential for addressing user needs in today's rapidly expanding and changing technological world. By offering them specialized solutions, personalization has the ability to improve people's interactions with technology. By supplying automobiles that are in line with drivers' choices and demands, personalization in the automotive industry offers a distinctive driving experience. The trend of personalization aims to cater to individual demands in the automotive sector, ranging from the interior and exterior design of vehicles to their technological features. This trend was the biggest motivation in creating this study. It is known that there have been ongoing studies for years regarding personalization in vehicles and specialized systems around the driver. In a past study, issues such as improving user experiences while driving and driver-based automotive user interface design were discussed. At this point, the point that issues such as entertainment, comfort and driving assistants are specifically designed for the driver is mentioned (Kern & Schmidt, 2009). In another paper, the active fatigue state of the driver was observed, and the adaptive cruise control system values were dynamically changed accordingly, thus this appears as a customized study focused on the driver (Chen et al., 2014). Automatic adjustment of the mirrors according to the driver's perspective, placing the driving parts in optimum

positions according to the driver's physical characteristics, and voice commands or other functions can be performed in the vehicle with the driver's voice identity. Adjusting the seat and mirror angles are just two simple examples of car customization features.

The ability to customize the stiffness of gas and brake pedals in vehicles holds significant importance as it allows drivers to fine-tune their driving experience based on their personal preferences and comfort levels. Moreover, it is crucial in ensuring optimal control and responsiveness, enabling drivers to tailor their driving dynamics to suit their individual needs and driving styles. Another important motivation and starting point while doing this study was the studies in the literature on pedal feel and stiffness. The idea of recording pedals specifically for the driver and then applying them to the personalization and profiling trend in the automotive industry has been the leading aim of this study. If we look at past studies on pedal sensitivity, a dynamic model was developed regarding the feel of the brake pedal and as a result of the simulations, it was stated that the brake system in that study was usable (Meng et al., 2015). In our study, it was thought that each driver could have a gas or brake pedal sensitivity that they felt comfortable with, and improvements were made accordingly. In another study, it was aimed to provide stable brake feeling and an optimization model was developed. This system, which is suitable for cable brake systems, provides the opportunity to adjust the brake pedal feeling differently (Aleksendric et al., 2015). As a result of the pedal hardness being adjustable, the driving comfort and performance of at least 2 drivers driving the same vehicle will be improved. In addition, a single driver can set different modes according to himself and save them for different paths.

It has been observed that some automobiles on the market have an adjustment for the firmness or height of the brake and gas pedals, according to various research that has been done on the subject (Lexus Parts, n.d.). Finding the appropriate setting for each driver will be a hassle, as many of the previous studies offered a mechanical solution and lacked user-specific customization. In our study, since the pedal hardness of the profile is kept digitally in a system, it is possible to switch between profiles with a single key. The pedal stiffness study is of a nature that improves the automotive sector, which is affected by the transition from centralization to personalization in technology. It aims to increase driving comfort and efficiency.

Materials

Potentiometer

A potentiometer is a variable resistor that can be used to control the flow of electric current. It consists of a resistive element, such as a metal wire or a carbon strip, with a movable contact called a wiper. The wiper is connected to a terminal, and the two ends of the resistive element are connected to the other two terminals. (Potentiometer, 2023).

The working principle of a potentiometer is based on the potential drop across any section of a wire is directly proportional to the length of the wire, provided the wire is of a uniform cross-sectional area and a uniform current flow through the wire.

When a constant current flows through a potentiometer, the potential difference between the wiper and either end of the resistive element is proportional to the distance between the wiper and that end. This means that the potentiometer can be used as a voltage divider (Analog Devices, n.d.). Potentiometers are used in a wide variety of applications such as volume controlling device, brightness controlling device. In this study, it is also used as a controller for the sensitivity of the gas and brake pedals.

Analog Digital Converter (ADC)

An Analog-to-Digital Converter (ADC) is an electronic circuit that converts analog signals into digital data. This circuit enables varying continuous voltage or current signals to transform from the analog world to digital data (Storr, 2023). The converted data is applicable to be processed by microcontrollers or other digital systems.

The potentiometer used to determine the hardness of the accelerator pedal produces an analog signal. The ADC measures the analog signal from the potentiometer at a specific sampling rate. The sampling process ensures that the analog signal is measured at regular intervals. These intervals represent the continuous variation of the signal, and the value of the analog signal is obtained at a specific time (Agarwal, 2021).

Microcontroller Unit (MCU)

Microcontrollers (MCUs) or other control units are employed. MCUs are integrated circuits utilized for processing, controlling, and managing analog and digital signals. The MCU receives the digital signal from the potentiometer and processes it according to a specific algorithm or programming logic (Brain, 2000). This programming is employed to evaluate data related to the position of the accelerator pedal, control power transmission, or perform other relevant functions (tutorialspoint, n.d.).

Gas and brake pedal sensitivity system was implemented using the NXP S32K148 microcontroller platform. The NXP S32K148 is a 32-bit microcontroller centered around the ARM Cortex-M4 core, specifically designed for applications in the automotive industry. This microcontroller meets the high-quality standards required by the automotive sector, ensuring reliable performance even in the challenging automotive electronics environment. It adheres to the AEC-Q100 standards, and it is fully compliant with the safety requirements outlined in ISO 26262. These qualities make it a suitable choice for integration into safety-critical systems (NXP, n.d.).

Non-Volatile Memory (NVM)

Non-volatile memory (NVM) is a type of computer memory that can keep data even when the power is turned off. This is unlike volatile memory, such as DRAM, which loses its data when the power is turned off. NVM is typically used for long-term storage, such as in hard drives, solid-state drives (SSDs), and memory cards. It is also used in some embedded systems, such as those found in cars and other devices ("Non-volatile memory", 2023). In this study, non-volatile memory was used to permanently retain pedal sensitivity data that the driver has set and saved. The use of NVM has become inevitable since data needs to be stored in situations such as when the vehicle is not in use or there is a power cut.

Method

In this study, an MCU-based system design is presented to increase the comfort of the drivers and customize the driving experience by adjusting the sensitivity of the accelerator/brake pedal. The system has the ability to adjust the response characteristics of the accelerator and brake pedals according to the preferences of the drivers. The block diagram describing the system in a simple way is shown in Figure 1.

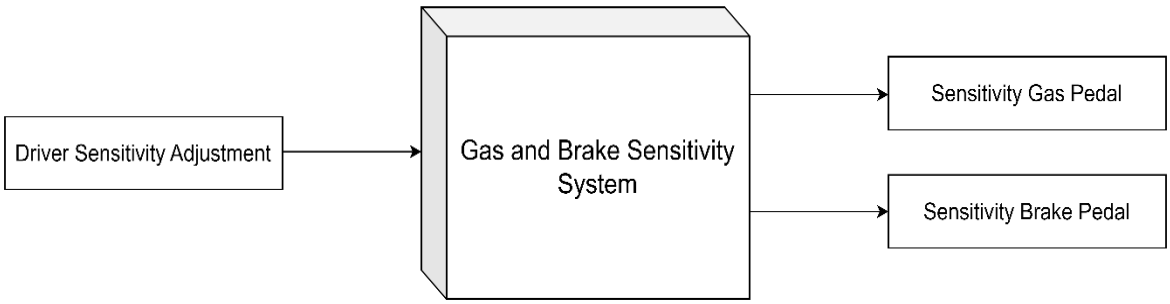

Figure 1. Gas and brake pedal sensitivity system high level block diagram

The system employs potentiometers to ascertain the sensitivity levels of the accelerator and brake pedals. Potentiometers generate a voltage output that varies in proportion to the force applied by the driver on the pedals. This voltage signal is then read by an ADC unit connected to the NXP S32K148 MCU. The MCU is responsible for converting the analog voltage signal acquired via the ADC into digital data for further processing. The driver's determined sensitivity level can be stored within the system as a personalized profile, and this registration process is typically facilitated through designated buttons.

This procedure allows the driver to fine-tune their pedal sensitivity to craft a bespoke driving experience. For instance, if a driver desires a more delicate throttle response, the system can be configured to deliver increased acceleration when the pedal is lightly depressed. Similarly, analogous sensitivity adjustments can be made for the brake pedal.

The user interface of the system presents a platform for the driver to adjust these preferences, enabling them to save these settings within a profile. These profile settings can then be stored for later retrieval, offering a customized driving experience tailored to individual preferences. This system empowers drivers to personalize their driving experience, enhancing both comfort and control, ultimately resulting in a more enjoyable time behind the wheel. The user interface of the system is shown in Figure 2.

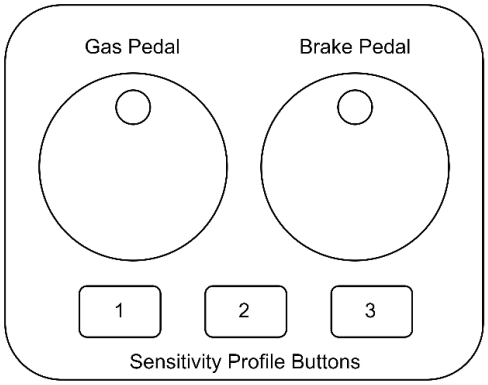

Figure 2. Gas and pedal sensitivity system user interface prototype

The driver initiates the system's recording mode by pressing and holding down the designated profile button. The duration of the button press is scrutinized to determine if the driver has commenced profile recording. An interrupt handler is employed to identify when the button has been held down for an extended period. It is considered that the driver has executed a long press when the predefined LONG_PRESS event threshold is surpassed. Upon detecting this long button press, the system transitions into recording mode. Figure 3 illustrates the flowchart showing the capture processes of button events.

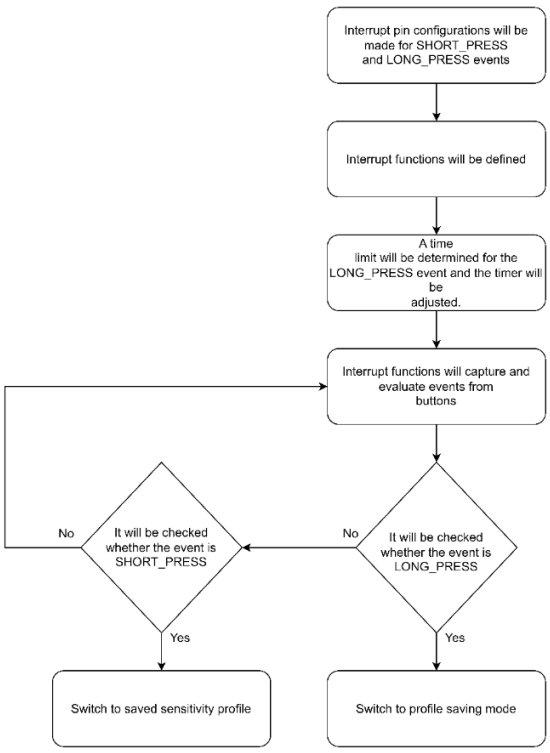

Figure 3. Button press event flow chart

To communicate this transition, the user LED associated with the selected profile blinks, signaling to the driver that the system has entered recording mode. The flashing user LED serves as a visual indicator to convey the system's recording status to the driver. Once the system has entered recording mode, the driver gains the ability to fine-tune the sensitivity of the accelerator and brake pedals to suit their personal comfort preferences. These sensitivity adjustments are executed by manipulating potentiometers. The data output from these potentiometers is captured and subsequently processed through the ADC.

In essence, this sequence of events allows the driver to record their preferred pedal sensitivity settings within the chosen profile while providing a clear visual indication through the user LED that the system is actively recording. This ensures a seamless and user-friendly means of customizing the driving experience.

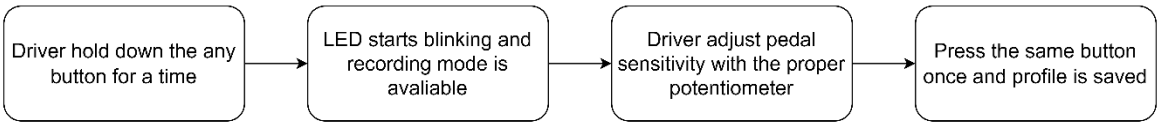

Figure 4. Setting and saving sensitivity for a profile flowchart

In this research project, a system is employed to finely adjust the sensitivity of both the accelerator and brake pedals. To ensure that the digitally configured pedal sensitivity settings are retained in memory, it is imperative to convert the values set with these potentiometers into a digital format on the platform. This critical task is accomplished through the utilization of the ADC integrated within the MCU.

The first pivotal step in this process is the meticulous configuration of the ADC settings. The ADC module embedded within the MCU necessitates a thorough configuration, encompassing the selection of the ADC's operating mode, resolution, reference voltage, and various other parameters. The configuration process is executed with careful reference to the comprehensive documentation provided by the MCU's manufacturer.

For the operating mode of the ADC, the 'continuous conversion mode' is deliberately chosen. In this mode, the ADC incessantly samples and transforms an analog input signal into a precise digital representation. This continuous operation ensures that when the driver initiates the pedal sensitivity adjustment, the ADC diligently reads and translates the analog values throughout the duration of this process.

The configuration of the ADC settings is a critical precursor to the successful digitization of pedal sensitivity settings, guaranteeing a highly responsive and accurate means of translating the driver's preferences into a digital format for further processing and system memory retention. Another crucial aspect of ADC configuration pertains to the setting of ADC resolution. ADC resolution defines the number of digital bits allocated to represent the amplitude of an analog input signal. It essentially dictates the precision or granularity of the digital representation. In this specific research, the ADC embedded within the MCU is configured with a resolution of 4096. It's worth noting that the MCU's documentation specifies a 12-bit ADC with a precision ranging from 2 to 12 bits. By selecting a 12-bit resolution, the system ensures a high degree of precision in translating the analog input signals into their digital counterparts.

Moving on, the definition of the reference voltage value is the next critical configuration step. Given that the MCU's documentation designates the ADC's reference voltage as 3 Volts, the reference voltage is meticulously set to precisely 3 Volts. Consequently, this establishes the full-scale range of the ADC, ensuring that it effectively covers the entire spectrum of voltages within its operational capacity.

The second facet of ADC configuration involves the setup of General-Purpose Input/Output (GPIO) pins that are designated for ADC operations. The selection and configuration of these GPIO pins are fundamental to the successful integration of the ADC into the system. This configuration process is executed through the utilization of specific software libraries designed for this purpose. By carefully designating and configuring the relevant GPIO pins, the system ensures seamless communication between the analog input sources, such as the potentiometers responsible for pedal sensitivity adjustments, and the ADC module within the MCU. This critical step is pivotal in enabling the ADC to accurately sample and convert the analog input signals into digital data, facilitating the precise adjustment of pedal sensitivity settings as per the driver's preferences.

The final and crucial step entails initiating a continuous loop responsible for reading the analog signals that have been fine-tuned using the potentiometers connected to the ADC. The system must maintain an uninterrupted transition from analog to digital conversion as long as the driver is adjusting the pedal sensitivity settings. To achieve this, the previously configured ADC settings are integrated into the software, and the loop is set into motion.

Even at this juncture, the software permits the definition of the delay duration between two successive analog data readings. This delay, often referred to as the sampling rate, plays a pivotal role in the precision of the digital conversion process, as it determines how frequently the ADC samples the analog input.

The obtained unit voltage value is derived through a systematic process. Initially, the read analog value is divided by the ADC's resolution. This division yields a normalized value that reflects the unit voltage change per digital bit. Subsequently, the final calibrated digital value is calculated by multiplying this normalized value by the reference voltage value, which has previously been established as 3 Volts.

In essence, this final step in the process ensures that the system consistently and accurately translates the analog adjustments made by the driver into precise digital representations. This continuous loop operation guarantees that the pedal sensitivity settings can be tailored to the driver's preferences with a high degree of accuracy and responsiveness, facilitating a finely tuned driving experience. The algorithm created for reading the data from the potentiometer is shown in Figure 5.

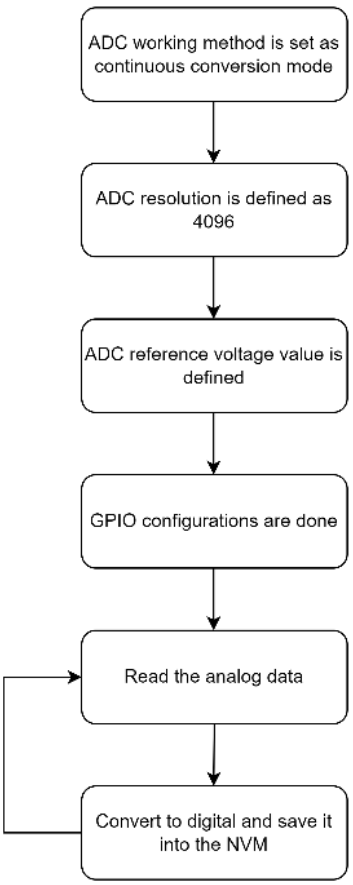

Figure 5. Flowchart for reading potentiometer data

Once the driver has fine-tuned the sensitivity settings to their preference, they finalize the profile recording process by activating the save function through the profile button. In this scenario, the system detects a SHORT_PRESS event triggered by the button press. With the SHORT_PRESS event, the system proceeds to store the gas and brake pedal sensitivity data, meticulously customized by the driver, into the NVM. This storage ensures that the driver's preferred settings are retained and can be recalled in future usage.

To provide feedback to the driver and confirm the successful completion of the recording process, the user LED is employed. The user LED, which typically blinks during the recording process, transitions into a continuous and steady illumination state as the SHORT_PRESS event is detected, signaling the completion of the recording procedure. This serves as a visual indicator to communicate to the driver that their personalized pedal sensitivity settings have been securely saved and that the recording operation has been successfully executed.

The data saving operation takes place on NVM while creating the profiles in the study. This internal memory of the MCU selected within the scope of the project was managed by the flash driver functions. In addition to simple flash operations such as reading, writing and deleting, operations such as partitioning and allocating depending on the number of drives in the initialization section also had to be handled. As shown in Figure 6, the operations performed on NVM in different use cases are presented.

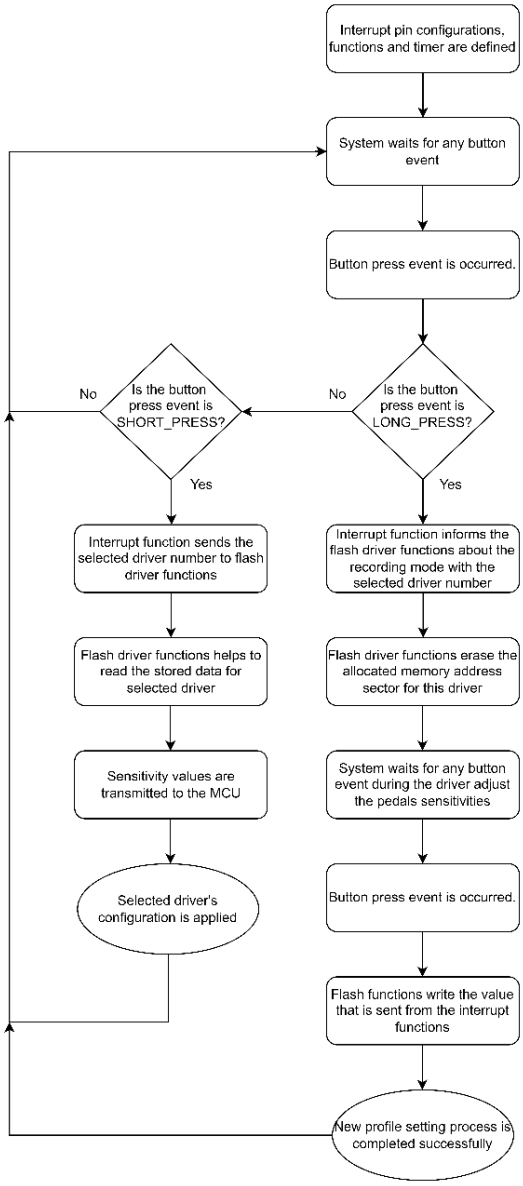

Figure 6. Flowchart for NVM management for different cases

This endeavor to tailor the sensitivity of both the gas and brake pedals also encompasses a mechanical component. This mechanical system is intricately controlled by the ADC values derived from potentiometers. The heart of this mechanical arrangement lies in the presence of springs positioned behind both the gas and brake pedals. These springs are designed to exhibit bidirectional movement, achieved through the adjustment of a screw mechanism that interfaces with a potentiometer, offering a remarkable 4096 distinct digital positions. In other words, this system allows for the controlled extension and compression of these springs within a defined range.

At the minimum potentiometer value, the spring is stretched to a point where its mechanical properties remain unimpaired, rendering the pedal at its softest configuration. Conversely, at the highest potentiometer value, the spring is compressed to its maximum extent, resulting in the stiffest pedal configuration possible. This design affords the driver the flexibility to finely calibrate the pressure applied to the pedal, enabling them to choose between a softer or firmer pedal feel. By adjusting the potentiometer, the driver can pinpoint the precise level of sensitivity that suits their preferences and record it within their personal profile.

Figure 7 illustrates the overarching structure of the system, featuring a preliminary design that incorporates the pedal-side components, providing a visual representation of this mechanical mechanism. This fusion of mechanical and electronic elements ensures a highly customizable and responsive driving experience, catering to the distinct preferences of each driver.

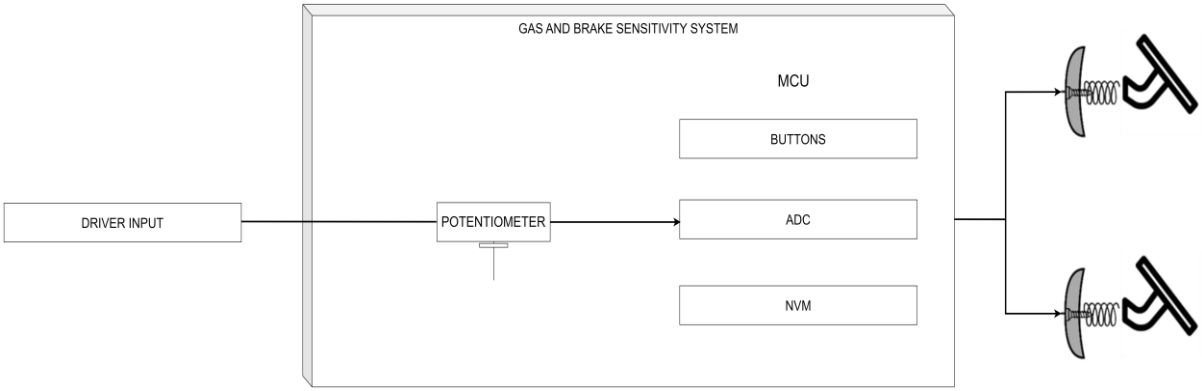

Figure 7. General design of the system

The innovative system design presented herein empowers drivers with a unique and sophisticated capability—the ability to finely calibrate the sensitivity of both the gas and brake pedals. This advanced feature not only prioritizes driver comfort but also offers a wealth of advantages, including the personalization of the driving experience and an enhancement in overall operational efficiency.

Moreover, this customization extends to an enhancement in driving efficiency. With the ability to adjust pedal sensitivity, drivers can optimize their driving style for various road conditions and driving scenarios. For instance, in stop-and-go traffic, a softer pedal response may reduce fatigue, while in sportier driving situations, a firmer pedal feel could enhance control and responsiveness. The system's adaptability enables a dynamic response to changing driving conditions, thus increasing driving efficiency and safety.

Results and Discussion

Customizable vehicle systems offer significant advantages to the driver during the act of driving. These systems allow drivers to tailor their vehicles to their preferences. Such systems not only enhance the driver's comfort but also increase driving safety. In this context, studies have been conducted to investigate the impact of adjustable pedal systems, which are part of customizable vehicle systems, on driver comfort. In a study, twenty volunteers were tested in small and large vehicles equipped with adjustable pedals at three pedal positions. Observations revealed that the use of adjustable pedals in both vehicles was influenced by factors such as visibility, knee-steering wheel contact, and arm posture. It was observed that the amount of heel lifting decreased when the short-statured group transitioned from the normal to comfortable/maximum tolerable positions. The results underscore the utility of adjustable pedals, particularly for short-statured drivers in large vehicles (Parenteau et al., 2000).

Our system, allowing drivers to adjust the stiffness of the gas and brake pedals to enhance their driving comfort and efficiency, stands out with its ease of use and straightforward integration. The methodologies employed in the development of this system, are meticulously detailed in the Method section. The tools, devices, and technologies harnessed for the implementation of this study are comprehensively outlined in the Materials section. This research project is intrinsically geared towards enhancing both driver comfort and vehicle performance by the creation of distinct driver profiles.

The system, designed to cater to the preferences of three different drivers, utilizes a combination of buttons, each assigned unique functions, and rotary knobs that facilitate the adjustment of pedal stiffness. This integration allows for the digital storage of customized profiles for each driver, enabling swift activation of their respective settings prior to commencing a drive.

A significant achievement of this study is the mitigation of the issue of pedal stiffness disparities encountered across different vehicles. Additionally, the driving experience is markedly enhanced by the ability to fine-tune pedal sensitivity, thus ensuring each driver's personal comfort is accommodated, even within the same vehicle. Beyond these accomplishments, this research project introduces a pioneering perspective on the evolution from centralized to decentralized structures within the technology sector.

In addition to the visionary outlook this study offers in terms of pedal stiffness personalization, it carries the potential to contribute to emerging technical concepts that are increasingly being integrated into a myriad of projects. Notably, the study lends itself to the realm of machine learning. Here, the system, after a driver configures their pedal settings, can continuously monitor and record data pertaining to fuel consumption and vehicle performance in relation to the force exerted on the pedals. Utilizing machine learning algorithms, the system can then make recommendations for optimizing settings, thereby not only enhancing vehicle performance but also elevating the overall driving experience.

Additionally, in a previous study, the effect of the adjustable pedal structure on causing an accident based on the in-vehicle control mechanisms and the changes that may occur on the driver's side were examined. According to this study, it was concluded that this pedal adjustment was not a serious threat, since the in-vehicle control mechanisms caused very few accidents during the year in North Carolina. Since pedal adjustment will not occur during the journey, this work cannot be a factor in the accident. Moreover, as a result of this study, it was concluded that pedal adjustment provides a slight improvement in issues such as speed, control and lane keeping. Therefore, these results will be similar for driver-specific pedal sensitivity adjustments (Young et al., 2001).

In summary, this research project represents a fusion of innovative methodologies and advanced technologies, culminating in a system that provides unprecedented personalization of pedal stiffness. The implications extend beyond enhanced driver comfort, encompassing the realms of vehicle performance and the broader adoption of decentralized technological frameworks, offering a glimpse into the future of personalized and intelligent automotive systems.

Scientific Ethics Declaration

The authors declare that the scientific ethical and legal responsibility of this article published in EPSTEM journal belongs to the authors.

Acknowledgements or Notes

* This article was presented as an oral presentation at the International Conference on Technology, Engineering and Science (www.icontes.net) held in Antalya/Turkey on November 16-19, 2023.

We would like to extend our sincerest appreciation to Huseyin Karacali, the Software Architect, for his exceptional mentorship and inspiring influence. Moreover, we would like to acknowledge the invaluable assistance rendered by TTTech Auto Turkey throughout the developmental stages of this project.

References

Agarwal, T. (2021, January 29). Analog to digital converter: Block diagram, types & its applications. Retrieved from https://www.elprocus.com/analog-to-digital-converter/

Aleksendric, D., Cirovic, V., & Smiljanic, D. (2015). *Brake pedal feel control model*. SAE Technical Paper Series.

Analog Devices. (n.d.). *Definition of potentiometer*. Retrieved from https://www.analog.com/en/design-center/glossary/potentiometer.html

Brain, M. (2000). *How microcontrollers work*. Retrieved from https://electronics.howstuffworks.com/microcontroller1.htm

Chen, L. k., Dai, C. C, & Luo, M. f. (2014). Investigation of a driver-oriented adaptive cruise control system. *International Journal of Vehicle Design, 66*(1), 20-.42.

Kern, D., & Schmidt, A. (2009). Design space for driver-based automotive user interfaces. Proceedings of *the 1st International Conference on Automotive User Interfaces and Interactive Vehicular Applications.*

Lexus Parts. (n.d.). *Pedal height adjustment switch this fits your Lexus GX 460*. Retrieved from https://parts.lexus.com/p/Lexus__GX-460/Pedal-Height-Adjustment-Switch

Meng, D., Zhang, L., & Yu, Z. (2015). A dynamic model for brake pedal feel analysis in passenger cars. Proceedings of the *Institution of Mechanical Engineers, Part D: Journal of Automobile Engineering, 230*(7), 955–968.

Non-volatile memory. (2023b, September 7). In *Wikipedia*. Retrieved from https://en.wikipedia.org/wiki/Non-volatile_memory

NXP. (n.d.). *S32K148-Q176 automotive general-purpose evaluation board*. Retrieved from https://www.nxp.com/design/development-boards/automotive-development-platforms -platforms

Parenteau, C. S., Shen, W., & Shah, M. (2000). *The effectiveness of adjustable pedals usage*. SAE Technical Paper Series.

Potentiometer. (2023, September 6). In *Wikipedia.* Retrieved from https://en.wikipedia.org/wiki/Potentiometer

Storr, W. (2023, March 17). *Analogue to digital converter (ADC) basics*. Retrieved from https://www.electronics-tutorials.ws/combination/analogue-to-digital-converter.html

Tutorials Point. (n.d.). Microcontrollers - overview. Retrieved from https://www.tutorialspoint.com/microprocessor/microcontrollers_overview.htm

Young, D. E., Schmidt, R. A., Ayres, T. J., & Trachtman, D. (2001). Risk and driver behavior with adjustable pedals. *Proceedings* of the *Human Factors and Ergonomics Society Annual Meeting*, *45*(23), 1656–1660.

Author Information

Huseyin Karacali
TTTech Auto,
Turkey

Efecan Cebel
TTTech Auto, Turkey
Contact e-mail: efecan.cebel@tttech-auto.com

Nevzat Donum
TTTech Auto,
Turkey

To cite this article:

Karacali, H., Cebel, E., & Donum, N. (2023). Enhancing driver comfort and control: A proposal for customizable gas and brake pedal sensitivity. *The Eurasia Proceedings of Science, Technology, Engineering & Mathematics (EPSTEM), 26*, 166-175.

The Eurasia Proceedings of Science, Technology, Engineering & Mathematics (EPSTEM)
ISSN: 2602-3199

The Eurasia Proceedings of Science, Technology, Engineering & Mathematics (EPSTEM), 2023

Volume 26, Pages 176-182

IConTES 2023: International Conference on Technology, Engineering and Science

Proposal for an Inspection Tool for Damaged Structures after Disasters

Akkouche Karim
University of Tizi Ouzou

Nekmouche Aghiles
National Center For Applied Research in Earthquake Engineering

Bouzide Leyla
University of Tizi Ouzou

Abstract: This study focuses on the development of a multifunctional Expert System (ES) called post-seismic damage inspection tool (PSDIT), a powerful tool which allows the evaluation, the processing and the archiving of the collected data stock after earthquakes. PSDIT can be operated by two user types; an ordinary user (engineer, expert or architect) for the damage visual inspection and an administrative user for updating the knowledge and / or for adding or removing the ordinary user. The knowledge acquisition is driven by a hierarchical knowledge model, the Information from investigation reports, and those acquired through feedback from expert / engineer questionnaires are part**.**

Keywords: Disaster, Damaged structures, Damage assessment, Expert system.

Introduction

In Algeria the post-seismic survey is usually conducted by simplified approaches, based on the evaluation form. This form is the result of field experience, refined after several successive earthquakes. Indeed, the visual inspections as well as the evaluations are established with a common and standard language for the damages description. However, the experience gained during the various earthquakes (in particular the Boumerdes earthquake, Algeria, 21 May 2003) shows that several problems may arise during this damage assessment phase. Among these problems, we distinguish on the one hand, those related to the subjectivity of some results due to non-compliant inspections (Anagnostopoulos & Moretti, 2008) and on other hand, those related to the short time allowed for the inspection process due the need for the occupants to return their homes shortly after the occurrence of the earthquake (Allali, 2018). To remedy these imperfections, the only solution is to bring improvements to the inspection tools. Moreover, in order to appreciate effectively the degradation state after an earthquake and reduce the risk, we have to design new more sophisticated inspection tools (Bosi et al., 2011; Baggio et al., 2007).

Several strategies have been adopted the field of damage detection; with high resolution imagery (Bechtoula & Ousalem, 2005; Saito, 2004). and artificial intelligence theory-based systems (Anagnostopoulos & Moretti, 2008; Akkouche et al., 2019; Boukri et al., 2013; Churilov, 2009). All these techniques represent an important technological advance in this field, and their applications represent a success with the post-event management managers. On the other hand, they have no interest in the general public immediate needs, which is of paramount importance for their life safety and for the post-event situation management. Indeed, the survivor's participation in the damage assessment can be, in this situation, of a precious help. In this paper, a knowledge-based expert system PSDIT for the structures diagnosis undergoing seismic damage is proposed. This approach insists to answer the omissions made by the organisms (CTC, CGS… etc.), PSDIT is developed using object-

oriented programming tools. PSDIT data and knowledge are collected from different sources. The damage level estimation is based on mathematical models developed in the first part of the study (Akkouche et al., 2019).

Post-Seismic Damage Assessment

In Algeria, to evaluate post-seismic damage, an intuitive procedure based mainly on visual observation is used. This procedure consists of filling in the form given in Figure 1.

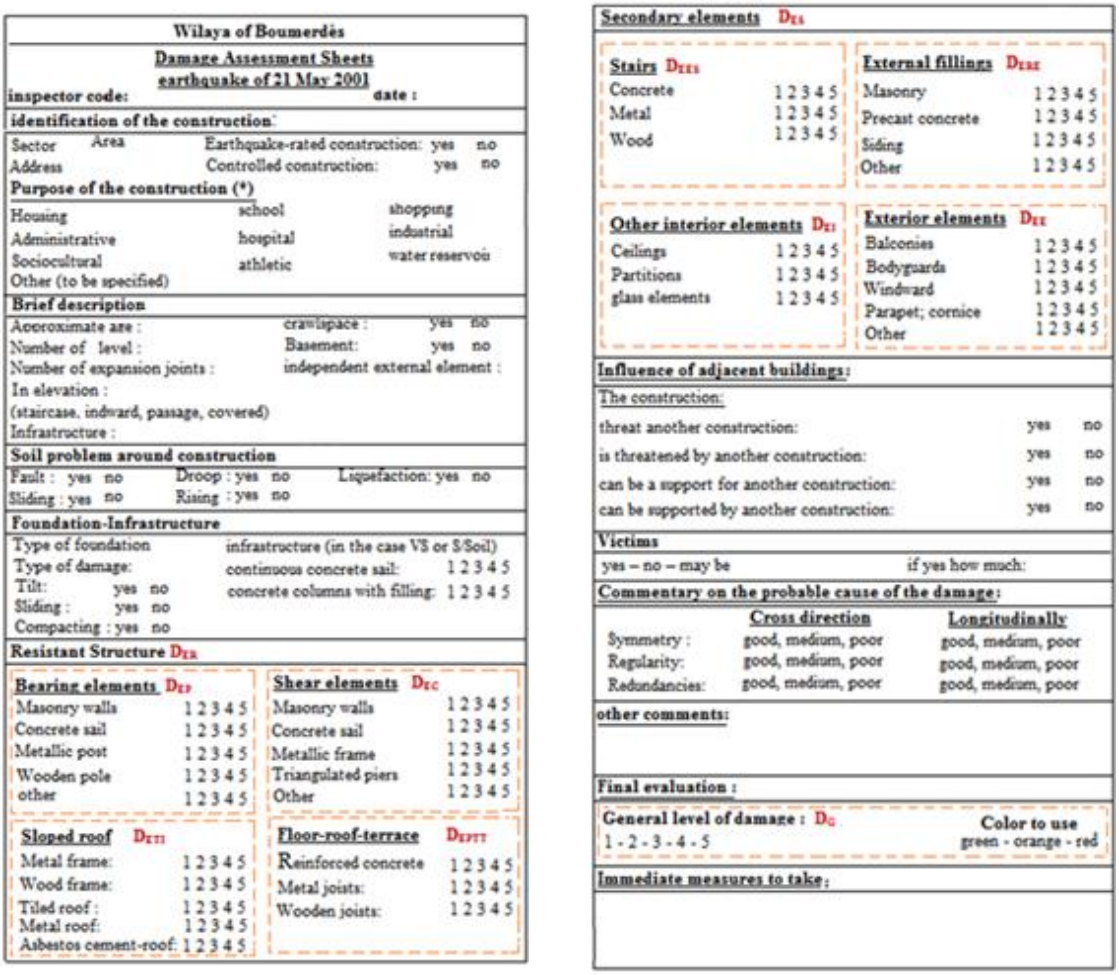

Wilaya of Boumerdès

Damage Assessment Sheets
earthquake of 21 May 2001

inspector code: date :

identification of the construction:

Sector Area — Earthquake-rated construction: yes no
Address — Controlled construction: yes no

Purpose of the construction (*)

Housing — school — shopping
Administrative — hospital — industrial
Sociocultural — athletic — water reservoir
Other (to be specified)

Brief description

Approximate are : — crawlspace : yes no
Number of level : — Basement: yes no
Number of expansion joints : — independent external element :
In elevation :
(staircase, indward, passage, covered)
Infrastructure :

Soil problem around construction

Fault : yes no — Droop : yes no — Liquefaction: yes no
Sliding : yes no — Rising : yes no

Foundation-Infrastructure

Type of foundation — infrastructure (in the case VS or S/Soil)
Type of damage: — continuous concrete sail: 1 2 3 4 5
Tilt: yes no — concrete columns with filling: 1 2 3 4 5
Sliding : yes no
Compacting : yes no

Resistant Structure D_{ER}

Bearing elements D_{EP}

Masonry walls	1 2 3 4 5
Concrete sail	1 2 3 4 5
Metallic post	1 2 3 4 5
Wooden pole	1 2 3 4 5
other	1 2 3 4 5

Shear elements D_{EC}

Masonry walls	1 2 3 4 5
Concrete sail	1 2 3 4 5
Metallic frame	1 2 3 4 5
Triangulated piers	1 2 3 4 5
Other	1 2 3 4 5

Sloped roof D_{ETI}

Metal frame:	1 2 3 4 5
Wood frame:	1 2 3 4 5
Tiled roof :	1 2 3 4 5
Metal roof:	1 2 3 4 5
Asbestos cement-roof:	1 2 3 4 5

Floor-roof-terrace D_{ETT}

Reinforced concrete	1 2 3 4 5
Metal joists:	1 2 3 4 5
Wooden joists:	1 2 3 4 5

Secondary elements D_{ES}

Stairs D_{ESS}

Concrete	1 2 3 4 5
Metal	1 2 3 4 5
Wood	1 2 3 4 5

External fillings D_{ESE}

Masonry	1 2 3 4 5
Precast concrete	1 2 3 4 5
Siding	1 2 3 4 5
Other	1 2 3 4 5

Other interior elements D_{EI}

Ceilings	1 2 3 4 5
Partitions	1 2 3 4 5
glass elements	1 2 3 4 5

Exterior elements D_{EE}

Balconies	1 2 3 4 5
Bodyguards	1 2 3 4 5
Windward	1 2 3 4 5
Parapet; cornice	1 2 3 4 5
Other	1 2 3 4 5

Influence of adjacent buildings:

The construction:

threat another construction:	yes no
is threatened by another construction:	yes no
can be a support for another construction:	yes no
can be supported by another construction:	yes no

Victims

yes – no – may be — if yes how much:

Commentary on the probable cause of the damage:

	Cross direction	Longitudinally
Symmetry :	good, medium, poor	good, medium, poor
Regularity:	good, medium, poor	good, medium, poor
Redundancies:	good, medium, poor	good, medium, poor

other comments:

Final evaluation :

General level of damage : D_G — **Color to use**
1 - 2 - 3 - 4 - 5 — green - orange - red

Immediate measures to take:

Figure 1. The evaluation form used in Algeria (Akkouche et al., 2019).

This procedure considers a five-level damage scale (ranging from D1 to D5), similar to the damage scale given by EMS-98 (Grunthal & Levret, 2001)"Thus, concerning the assessment of the construction elements damage level (structural elements, non-structural elements and foundation system), it is done on five damage categories, varying from a slight damage (noted D1) to a high damage (noted D5). However, concerning the construction external elements (the construction ground, adjacent structures), these are evaluated by "Yes", in the case where the threat exists and "No" in the opposite case, which represent respectively the scale bounds (D1 and D5). Then, depending on the damage observed on the different components, a global damage category D_G will be attributed to the structure.

Architecture of the Proposed System

Our proposed system Expert System for assessment damage is a rule based ES which has been developed using JESS, the Java Expert System Shell. The user of the ES is first presented with a set of questionnaires to access the assessment damages. The questionnaires are presented in simple Frensh, which the user has to answer in affirmative or negative. According to the information provided by the user, the ES makes use of the RETE

algorithm to match the pattern facts with the rules. Once a certain rule is matched, the rule is fired and according to the rules stored in the knowledge base, the user is presented with an assessment.

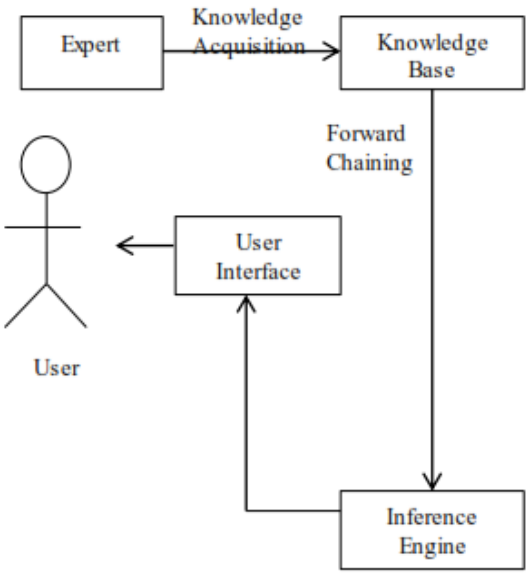

Figure 2. Architecture of the proposed system.

Knowledge Acquisition

The first and foremost work for building an Expert System is preparing a knowledge base for the system (Churilov, 2009). The primary source of information was interaction with experts and postgraduate students of the civil engineering department of the Mouloud MAMMERI University. The second source of acquisition of knowledge was from the internet.

Knowledge Representation

For knowledge representation, we used the JESS to represent facts and form the rules. First we present the questions before the user asking if the component has suffered from the damages mentioned in the scientific work (Akkouche et al., 2019). The user either puts his answer as yes or no. We also take a global counter for the purpose of storing our cumulative weight age score.

The RETE Algorithm

The RETE algorithm is the core of the Java Expert System Shell forsearching patterns in the rules. It is one of the most used algorithms for pattern searching. It highly speeds up the searching process by limiting the effort to recompute the conflicts after a rule is fired (Liao, 2005). The RETE algorithm is implemented as directed acyclic graphs which are used to match rules to facts (Grunthal & Levret, 2001).

Expert's Know-How

Knowledge is represented by the facts use and rules as modalities.

The Facts

The facts represent all the damage that may occur after a seismic event, such as; cracks, concrete bursting ... etc. In this study, they differ from one user to another. In the evaluation case by owner, a fact is represented by a question. That is, a direct question reflecting the damage (s) visible or invisible by deduction. Thus, it can describe a state, a situation or a damage sign, as illustrated in Figure 6.

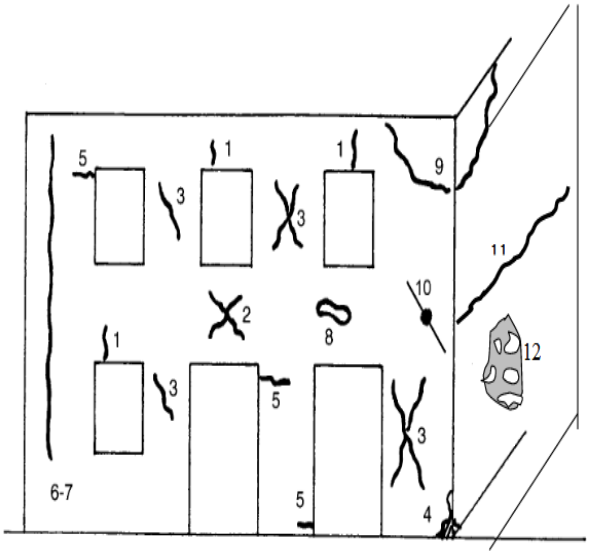

Figure 3. Example of damaged structures

When the apparent damage is not represented in a direct way by the question asked (example, the disorders of different natures manifest on the same element). This damage will be created by combination with other questions. Depending on the nature, the position, the diffusion and the disorders importance, each element is classified according to the EMS-98 scale. Then, from these different results, the constructions can be classified in three categories of different damages Table 1.

Table 1. The different damage classes

Color	V_1	V_2	O_3	O_4	R_5
Symbol	D_1	D_2	D_3	D_4	D_5
Meaning	Very slight damages	Slight damages	Importants damages	Very important damages	Collapse (partial or total)

The Rules

The introduction of these models given by (Akkouche et al., 2019): for the estimation of the damage level and (Morgan et al., 2006) for the estimation of number of victim's) in the BC was made in the form of production rules, as given by the program next

- der (DER):- dep (DEP), dec (DEC), deptt (DEPTT), deti (DETI),
    A is a * DEP, B is b * DEC,
    C is c * DEPTT, D is d * DETI,
    E is e * DEP * DEC,
    F is f * DEP * DEPTT,
    G is g * DEC * DEPTT,
H is h * DEP * DETI,
I is i * DEC * DETI,
J is j * DEPTT * DETI,
K is k * DEP * DEC * DEPTT,
L is l * DEP * DEC * DETI,
M is m * DEP * DEPTT * DETI,
N is n * DEC * DEPTT * DETI,
DER is A + B + C + D + E + F + G + H + I + J + K + L + M + N.
des (DES):- dees (DEES), dere (DERE), dei (DEI), deex (DEEX),
A is o * DEES, B is p * DERE,
C is q * DEI,
D is r * DEEX,
E is s * DEES * DERE,
F is t * DERE * DEI,

G is u * DERE * DEEX,
H is v * DEES * DEI,
I is w * DEES * DEEX,
J is x * DEI * DEEX,
K is y * DEES * DERE * DEI,
L is z * DEES * DERE * DEEX,
M is a1 * DEES * DEI * DEEX,
N is a2 * DERE * DEI * DEEX,
DES is A + B + C + D + E + F + G + H + I + J + K + L + M + N.
dg (der(DER), denr (DENR), DG):- der(DER), denr (DENR),
A is a3 * DER,
B is a4 * DENR,
C is a5 * DER * DENR,
DG is A + B + C + 1.
-nah (NAH) (a(i) (a(I)), rd2(RD2), rd3, d4, d5 (RD3,D4, D5), rvict (Rvict)
A is b1 * a(I)
B is b2 * RD2
C is b3 * RD3, D4, D5
D is b4 * Rvict
NAH is A+B+C-D.

Validation of the PSDIT Tool

The validation of the proposed model is established by comparing the calculated DG with PSDIT and the estimated category of DG (given in the form), on a set of ten constructions (see Table 2).

Table 2. The level of component damage.

Building Number	Damage reported on components							
	Structural				Non structural			
	D_{EP}	D_{EC}	D_{EPT}	D_{TI}	D_{ESC}	D_{ERE}	D_{EI}	D_{EE}
1	3	4	2	2	3	2	2	2
2	2	4	3	3	4	4	4	4
3	3	1	4	4	4	3	1	3
4	4	3	4	3	3	3	3	4
5	2	2	1	2	2	4	2	1
6	4	4	2	2	4	3	2	2
7	1	1	1	1	3	2	3	4
8	1	1	2	2	3	1	3	4
9	3	3	2	2	2	2	1	4
10	5	2	2	3	3	2	1	4

The constructions selected for the validation of the model come from the forms that were not used in the identification procedure (the establishment of the models). The comparison of the global damage values D_G obtained by the calculation, and those instinctively estimated by the investigators using the resemblance formula given by the EMS 98 scale definitions highlighted, the subjectivity of the evaluation process (after the Boumerdes earthquake, 2003).

Referring to the results given in Table 2, it was found that for constructions 1, 2, 4 and 7, the model reproduces the expert's decision with an insignificant margin of error ranging from [3% to 7.5%]. While, for constructions 5 and 6, the model approaches the experimental results with a percentage difference ranging from [18.7% to 26.1%], i.e. an inaccuracy of (+ or -) one degree of damage. On the other hand, the biggest difference was observed on constructions 3, 8, 9 and 10. This divergence of 33,1% with 50% demonstrates the importance of the inaccuracy, as an error of (+ or -) two or three degrees of damage is noted. Despite the fact that the same category of damage (very significant) was attributed to the first 05 constructions (see Table 3), a significant difference is noted in terms of damage recorded on the various elements (see Table 2), for example: the same decision was made for the 1st and the 5th construction (vis-à-vis the maintenance or the discontinuation of usage), whereas, in the detail of the inspection, a lag of 20% in terms of damage significance was recorded on the 1st construction compared to the 5th.

Table 3. The overall damage level

Building Number	D_G Global Damage form of evaluation	Proposed model	Gap (%)
1	4	3,88	3
2	4	4,27	6,3
3	4	2	50
4	4	3,70	7,5
5	4	3,25	18,7
6	3	4,06	26,1
7	3	3,16	5,1
8	2	2,99	33,1
9	2	3,48	43,4
10	2	3,53	42,5

Conclusion

The PSDIT use should bring great interest in the pos-seismic emergency management. Indeed, it allows non-expert engineers to benefit from the experience and skills of experts in the assessment damages field. After identification, the PSDIT classifies and processes all the information needed to manage the situation. These results are gathered in tables that include the number of damaged buildings, number of the homeless people, the number of casualties and missing people. This work is done following different scales: structure, district and city. Among the results generated by the PSDIT:

• Immediate measures, in relation to the damage levels DG of structures,
• The arrangements to be made by the authorities for the victims' management, such as, the number of reception centers in the short and long term for the homeless, the care centers for the wounded (beds number, staff number ... etc.),
• The budget estimate dedicated for the victims' compensation, since the tool can inform us about state of the structural elements and non-structural separately.

Scientific Ethics Declaration

The authors declare that the scientific ethical and legal responsibility of this article published in EPSTEM journal belongs to the authors.

Acknowledgment or Notes

* This article was presented as a poster presentation at the International Conference on Technology, Engineering and Science (www.icontes.net) held in Antalya/Turkey on November 16-19, 2023.

* The authors would like to thank the Algerian institution; the National Earthquake Engineering Research, CGS and The Constructions Technical Control offices, CTC, Algeria, in particular the Tizi-Ouzou CTC and Boumerdes CTC

References

Akkouche, K., Hannachi, N. E., Hamizi, M., Khelil, N., Djouzi, K., & Daoui, M. (2019).Knowledge-based system for damage assessment after earthquake: Algerian buildings case. *Asian Journal of Civil Engineering, 20*(2), 769-784.

Allali, S. A., Abed, M., & Mebarki, A. (2018). Post-earthquake assessment of buildings damage using fuzzy logic. *Engineering Structure, 166*, 117-127.

Anagnostopoulos, S., & Moretti, M. (2008). Post-earthquake emergency assessment of building damage, safety and usability- Part 1: Technical issues. *Soil Dynamics and Earthquake Engineering, 28*(3), 223–232.

Ayala, D. F. D., & Paganoni, S. (2011). Assessment and analysis of damage in L'Aquila historic city centre after 6th april 2009. *Bulletin of Earthquake Engineering, 9*(1), 81–104.

Baggio, C., Bernardini, A., Colozza, R., Corazza, L., Della-Bella, M., & Di Pasquale, G., (2007). *Field manual for post-earthquake damage and safety assessment and short term counter measures (AeDES).* Luxembourg: Office for Official Publications of the European Communities.

Barkavi, T., & Natarajan, C. (2018). Knowledge-based decision support system for identification of crack causes in concrete buildings. *Asian Journal of Civil Engineering, 19*(2), 111-120.

Bechtoula, H., & Ousalem, H. (2005). The 21 May 2003 Zemmouri (Algeria) earthquake: Damages and disaster responses. *Journal of Advanced Concrete Technology, 3*(1), 161-174.

Bignami, C. (2014). *Earthquake damage assessment from VHR data: Case studies.* Encyclopedia of Earthquake Engineering.

Bosi, A., Marazzi, F., Pinto, A., & Tsionis, G. (2011). *The L'Aquila (Italy) earthquake of 6 April 2009: Report and analysis from a field mission*. Luxemburg: Publications Office of the European Union. Retrieved from https://publications.jrc.ec.europa.eu

Boukri, M., Farsi, A M., Mebarki, N. & Belazougui, M. (2013). Development of an integrated approach for Algerian building seismic damage assessment. *Structural Engineering and Mechanics, 47*(4), 471-493.

Carreño, M. L., Cardona, O. D., & Barbat, A. H. (2010). Computational tool for post-earthquake evaluation of damage in buildings. *Earthquake Spectra, 26*(1), 63–86.

Chiriou, L. (2005). Damage assessment of the 2003 Bam, Iran earthquake using Ikonos imagery. *Earthquake Spectra, 21*(1), 219–224.

Churilov, S. (2009). *Expert system for seismic vulnerability assessment of masonry structures, protection of historical building*s (pp. 1449-1454). London: Taylor & Francis Group.

Grunthal, G., & Levret, A. (2001). *European macro seismic scale 1998 (EMS-98), cahiers du centre Européen de géodynamique et de séismologie*. Luxembourg: Conseil de l'Europe.

Liao, S. H. (2005). Expert system methodologies and applications—a decade review from 1995 to 2004," *Expert Systems with Applications, 28*, 93–103.

Morgan, O., Tidball-Binz, M., & Van-Alphen, D. (2006). "*Management of dead bodies after disasters: A field manual for first responders,"* Washington, D. C: PAHO. Retrieved from https://www.icrc.org/en/doc/assets/files/other/icrc_002_0880.pdf

Saito, K., Spence, R., Going, C., & Markus, M. (2004). Using high-resolution satellite images for post-earthquake building damage assessment: A study following the 26 january 2001 Gujarat earthquake. *Earthquake Spectra, 20*(1), 145–169.

Yamazaki, F., & Matsuoka, M. (2007). Remote sensing technologies in post-disaster damage assessment. *Journal of Earthquake Tsunami, 1*(3), 193–210.

Author Information

Akkouche Karim
Civil Engineering Department, Mouloud MAMMERI University of Tizi Ouzou, Tizi-Ouzou, CO 15000 Algeria,
Contact e-mail: *karim.akkouche@ummto.dz*

Nekmouche Aghiles
National center for applied research in earthquake engineering, Alger, CO 16000 Algeria.

Bouzide Leyla
Civil Engineering Department, Mouloud MAMMERI University of Tizi Ouzou, Tizi-Ouzou, CO 15000 Algeria,
Contact e-mail: *bouzid_ley@ymail.com.*

To cite this article:

Karim, A., Aghiles, N., & Leyla, B. (2023). Proposal for an inspection tool for damaged structures after disasters. *The Eurasia Proceedings of Science, Technology, Engineering & Mathematics (EPSTEM), 26*, 176-182.

The Eurasia Proceedings of Science, Technology, Engineering & Mathematics (EPSTEM)
ISSN: 2602-3199

The Eurasia Proceedings of Science, Technology, Engineering & Mathematics (EPSTEM), 2023

Volume 26, Pages 183-189

IConTES 2023: International Conference on Technology, Engineering and Science

TRIAC Based Isolated AC Load Drive Equivalent Circuit Design of Solid-State Relay

Gonca Uslu - Ozkucuk
OSTIM Technical University

Abstract: Electronic main boards generally provide the supply and control functions of a system. All electronic main boards include inputs and outputs and are designed according to the design requirements. In this study, a safe and low-cost switching mode power supply (SMPS) board is designed using a flyback converter topology to drive the AC and DC outputs. The triode for alternating current (TRIAC)-based safe and low-cost main board includes a flyback configured transformer with additional winding for driving the TRIAC as an AC output switch in noise immune quadrants II and III. TRIAC is used to switch AC outputs instead of a relay, and the isolation distances of the safety criteria are provided by an optocoupler. In this way, the relay usage is over, and one TRIAC and one optocoupler do the same work that is done by one relay. In this way, the cost of the AC output switch decreases. In addition, the number of AC switches covering the area on the printed-circuit board (PCB) of the mainboard decreases. The flyback topology is designed with half-wave rectified and the transformer is designed with extra winding for producing negative voltage with respect to primer reference for providing negative gate current of TRIAC. TRIAC-based AC output switched, safe, and low-cost main boards can be used for white good main boards, automation (PLC) applications, and automotive electronic control systems. This study provides cost-effective solutions in these areas.

Keywords: TRIAC, Flyback converter, Power electronic, Circuit design

Introduction

Main boards are used in almost every moment of our lives. Most electronic devices include a mainboard with a converter topology, which has different capacities from µW levels to MW. Middle- and high-segment power converters and mainboards are generally used for energy systems, especially in renewable areas such as solar and wind or hybrid applications (Bayrak, 2015; Bayrak & Kabalci, 2016).

The flyback topology is a highly preferred SMPS topology for most mainboards because of its simple, isolated, and efficient structure. There are important design works on flyback topology in the literature. Generally, studies on isolated flyback topology focus on different aims. When we study the literature from the main board design perspective of an isolated flyback converter, we can see the classical topology and traditional methods in the constructions. Most of the designs include an input section of DC or AC type with full wave rectifier bridge diode and filter block, isolated flyback transformer according to needs, switching element and feedback section from seconder side (with an opto-coupler) or primer side regulation (Chang & Chen, 2013; Coruh et al., 2010; Reshma et al., 2016). Multiple DC output designs are commonly used and are more suitable for a main board design because all DC voltage levels (3.3 V, 5 V, 7.2 V, 12 V, etc.) for driving the microcontroller and other auxiliary elements in the main board are produced in multiple output designs (Hashjin, 2017; Myderrizi & Ozbey, 2014). When we examine the literature on AC TRIAC switches with flyback, we find much work on TRIAC dimming flyback converters for led driver applications. These systems include a controlled TRIAC dimmer on the input line to obtain smooth brightness (Moon et al., 2014; Zhang et al., 2012). These systems are related to the control of the driver, but our design TRIAC usage aim is related to safe AC output switching They are completely different applications. Our main idea is to integrate a TRIAC as an AC output switch to a flyback

topology, which is modified to drive the TRIAC in noise immune quadrants II and III in a mainboard frame (*Fundamental Characteristics of Thyristors*).

In this study, we designed a main board that can be used for daily life electronic devices such as whitegoods, small household appliances, automation, and automotive main boards. Our system works with a one-phase AC mains source input or can be modified with respect to a DC source input for automotive applications. The designed system includes a modified flyback topology for driving AC outputs with a TRIAC and provides the isolation of primer–seconder distance safety criteria. The power capacity of the system is determined up to 10W. This means that, designed mainboard can drive DC outputs up to nearly 8 W from the seconder winding and up to nearly 10 (ten) TRIACs from the extra TRIAC drive winding for 10 AC outputs. This main board topology can be integrated in all white goods and small household appliances, or it can be used as a mainboard for a middle segment automation system.

Design Specifications

Determining the design specification of the system is a critical step because theoretical calculations of the design are performed according to these specifications. In this system, a 10 W output power flyback converter is designed. The designed mainboard can drive DC outputs up to 8 W from a seconder winding and up to 10 (ten) TRIACs (with 20 mA gate current) from extra TRIAC drive winding for 10 AC outputs. The system specifications are described in Table 1.

Table 1. System specification table

System specification	Value
Min. and Max. input voltage	$V_{line,min}$: 170V $V_{line,max}$: 265V
Input voltage frequency	f_L: 50Hz
Max. output power	10W
Design efficiency	0.85

The designer determined these specifications according to the project needs. This board is designed for European grid AC mains with 220–230 V, 50 Hz, and system immunity of AC mains tolerances are determined as 25%; therefore, maximum and minimum input voltages are determined with respect to this consideration. In addition, the design includes an extra winding to produce negative voltage with respect to the primer Notr line. In this way, we can obtain DC and AC outputs that are driven by a TRIAC with a negative gate current. TRIAC driving is performed by a control signal that triggers the TRIAC gate with respect to zero cross moments using an optocoupler. TRIAC driving circuit is shown in Figure 1.

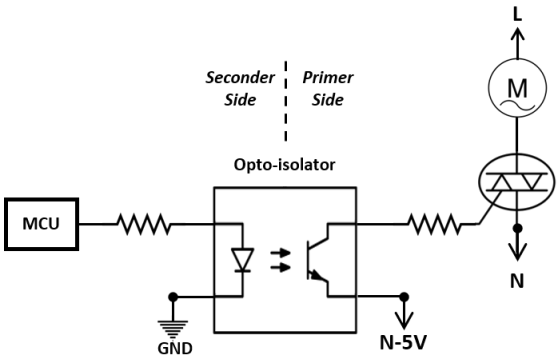

Figure 1. TRIAC driving schematic

Theoretical Analysis and Design

The flyback topology contains important basic elements. They are input capacitance (bulk capacitance), switching element, transformer primer-seconder inductance, output diode, and output capacitance. The important problem in the design work is determining these elements and the extra TRIAC winding circuit. In this section, the theoretical values of these important elements and other design parameters of the system are

calculated with respect to the formulas given below (Hart, 2010; Rashid, 2011). The system general block diagram is shown in Figure 2.

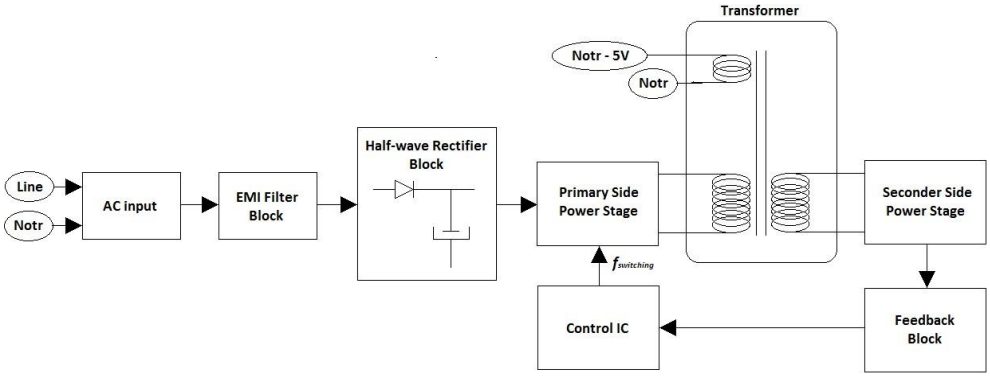

Figure 2. Block schematic of proposed design

Input capacitance is an important energy storage element in the design. Therefore, first maximum and minimum DC voltages on the capacitor and input power must be determined. Generally, European grid AC mains with 220–230 V, 50 Hz system uses 1 uF per watt. This generalisation comes from 50 Hz sinus waveform rectifying. In our design, we use a half-wave rectifier because of the usage of Notr as primer ground. If we want a DC voltage from 50 Hz sinus wave, we must keep the DC link voltage ripple at a certain value. This value is related to the ripple time and one-period time ratio (Dch). Generally, this ratio is selected as 0.2 or 0.25 (Hart, 2010; Rashid, 2011). If it is greater than 0.25, the system discharge time is larger and the energy of the primer does not compensate for the seconder.

The input power is shown in Equation (1):

$$Po = \frac{P_{in}}{Eff} \tag{1}$$

The minimum and maximum DC voltages on the capacitor are given by Equations (2) and (3), respectively:

$$2V_{DC_{min}} = \sqrt{2\left(V_{line_{min}}\right)^2 - \frac{P_{in}(1 - D_{ch})}{C_{bulk} f_L}} \tag{2}$$

$$2V_{DC_{max}} = \sqrt{2} V_{line_{max}} \tag{3}$$

The switching element is a metal oxide semiconductor field effect transistor (MOSFET). The selection of the MOSFET depends on the drain–source voltage capacity. The voltage drop on the drain-source of the MOSFET depends on maximum DC voltage on the primer capacitor plus the reflected voltage from the seconder side to the primer side. The maximum duty cycle of the MOSFET is determined by the relationship between the minimum primer DC voltage and the reflected voltage. The maximum duty cycle (D_{max}) must be selected intelligently. If D_{max} is selected as a small value, the stress on the switching MOSFET decreases but the stress on the output diode increases. Therefore, there is a trade-off between D_{max} and stress on the MOSFET and output diode. In our design, we selected the maximum duty cycle of the MOSFET as 0.33. This value provides the optimum stress on the MOSFET and output diode.

The reflected voltage is shown in Equation (4):

$$V_{Reflected} = \frac{D_{max}}{1 - D_{max}} V_{DC_{min}} \tag{4}$$

MOSFET drain-source nominal voltage is shown in Equation (5):

$$V_{DS_{nom}} = V_{DC_{max}} + V_{Reflected} \tag{5}$$

Transformer primer inductance is another important parameter in the design. The flyback converter can operate in discontinuous conduction mode (DCM) and continuous conduction mode (CCM) according to the input voltage level and load condition. The worst case for both the DCM and CCM working modes is full load with a minimum input voltage. Primer inductance calculations were performed in accordance with this consideration.

Primer inductance is shown in Equation (6):

$$L_{primer} = \frac{\left(V_{DC_{min}} D_{max}\right)^2}{2 P_{in} f_{sw}} \tag{6}$$

After this stage MOSFET current capacity is determined with respect to calculated primer inductance value.

Nominal MOSFET drain-source current is shown in Equation (7):

$$I_{nominal} = \frac{P_{in}}{V_{DC_{min}} D_{max}} \tag{7}$$

Primer current ripple is shown in Equation (8):

$$\Delta I = \frac{V_{DC_{min}} D_{max}}{L_{primer}\, f_{sw}} \tag{8}$$

Maximum MOSFET drain-source current is shown in Equation (9):

$$I_{DS_{peak}} = I_{nominal} + \frac{\Delta I}{2} \tag{9}$$

Seconder inductance of the transformer is determined by the winding turns ratio because the input and output voltages are directly proportional to the winding ratio. In addition, the transformer core type, dimensions, output power level, and frequency are another factor for seconder inductance. In this design, we selected seconder inductance and extra Notr-5V winding inductance as 30 (thirty) times smaller than the primer inductance because the system works at 220 V and 50 Hz under optimum conditions. Thus, the primer DC voltage is equal to 154V, as shown in Equation (3), under this condition. The seconder voltage was 5 V, and the ratio between the primer and seconder was nearly 30. This value provides the work of the system effectively. The selection of the output diode depends on the nominal current and reverse voltage of the diode. The output diode is selected with respect to these considerations.

Nominal current value of output diode is shown in Equation (10):

$$I_{out_{nom}} = I_{DS} \sqrt{\frac{1 - D_{max}}{D_{max}}} \frac{V_{reflected}}{V_{out} + V_{f_{diode}}} \tag{10}$$

Maximum reverse voltage on the output diode is shown in Equation (11):

$$V_{D_{nom}} = V_{out} + \frac{V_{DC_{max}} \left(V_{out} + V_{f_{diode}}\right)}{V_{reflected}} \tag{11}$$

These calculations show the limit values of the output diode selection. The selection of the diode must be performed with margins for a reliable design. If the output diode is selected with current and reverse voltage smaller than the theoretical results, design does not work reliable. The output capacitor is another important element in the design and depends on the ripple current of the output.

Output capacitor ripple current is shown in Equation (12):

$$I_{cap} = \sqrt{{I_{out_{nom}}}^2 - {I_{average}}^2} \tag{12}$$

The calculated capacitor ripple current must be smaller than the selected capacitor ripple currents All calculations and selected components with margins for reliable design values are listed in Table 2.

Table 2. Theoretical analysis results table

Parameters	Theoretical Values	Selected Values
V_{DCmin}	120.2V	-
V_{DCmax}	187.3V	-
C_{bulk}	11.76uF	12uF, 400V
V_{DSnom}	247.4V	250V
I_{DSpeak}	0.606A	3.5A
L_{primer}	186.6uH	200u
$L_{seconder}$	6.05uH	7u
$L_{extra\_winding}$	6.05uH	7u
I_{outnom}, V_{Dnom}	4.56A, 22.54V	6A, 60V
I_{cap}, $C_{seconder}$	4.09A	300uF, 6.3V

Simulation Results

The proposed design is simulated in the LT Spice simulation program with respect to the calculated and selected values in the theoretical analysis and design section. The system contains a flyback converter with a feedback line from the seconder and a 5 V, 2 A DC output. In addition, the system is designed to be completely safe, which means that there is no electrically conductive element between the primer and seconder. Extra TRIAC driving winding produces nearly negative 5 V according to the primer ground (Notr). The LT spice circuit schematic is shown in Figure 3.

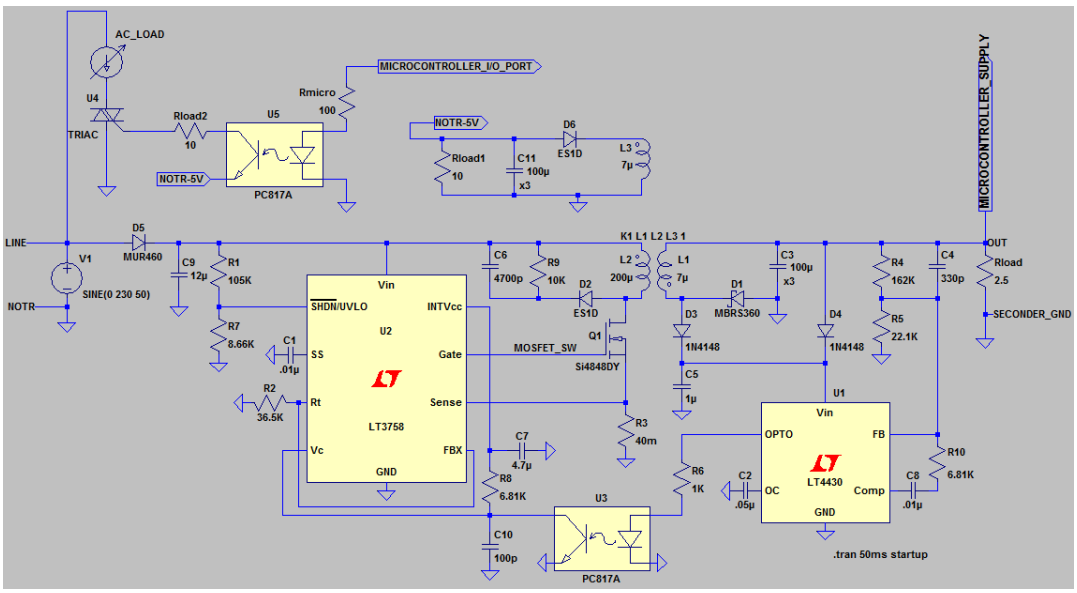

Figure 3. LT Spice designed circuit

In this section, the designed LT Spice circuit is run and the obtained results are interpreted. In the simulations, LT components are mostly used, and the parameters of the components are reset according to Table. 2. The feedback of the system is taken by a seconder DC output of 5 V, and the switching frequency of the SMPS IC is 350 kHz.

The simulation time of the design is 50 ms. A seconder DC output 5 V, 2 A, and extra TRIAC winding Notr-5V is obtained successfully in Figure 4. When we examine Fig. 4, with a second DC output of 5 V, the stability of the system is observed at 4th msec. Seconder DC output 5 V is obtained exactly 5 V but primer extra TRIAC winding Notr-5V is obtained nearly negative value -5V certain negative value is -4.70V because feedback is taken from seconder side DC output 5V. We can obtain 10 W DC output power for DC loads and 2.35W for TRIAC gate driving for AC loads. This system can drive five TRIACs with a gate current of 50 mA. The number of TRIACs can be increased if a low gate current-triggered TRIAC is preferred.

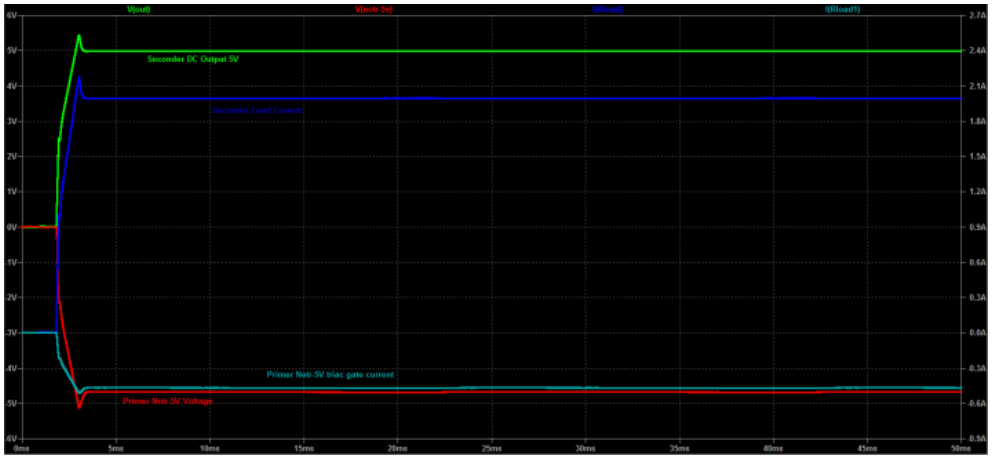

Figure 4. DC output 5 V and extra winding Notr-5V with currents under full load

The system input is 230 V, 50 Hz AC, and a half-wave rectifier is used to obtain the DC bulk capacitor voltage. The input values are shown in Fig. 5. When we examine Fig. 5, 12uF bulk capacitor is sufficient for obtaining DC voltage from the half-wave rectifier block. The system works in the DCM mode, and the inrush current is at acceptable levels according to the input diode. The design works under less stress and is stable.

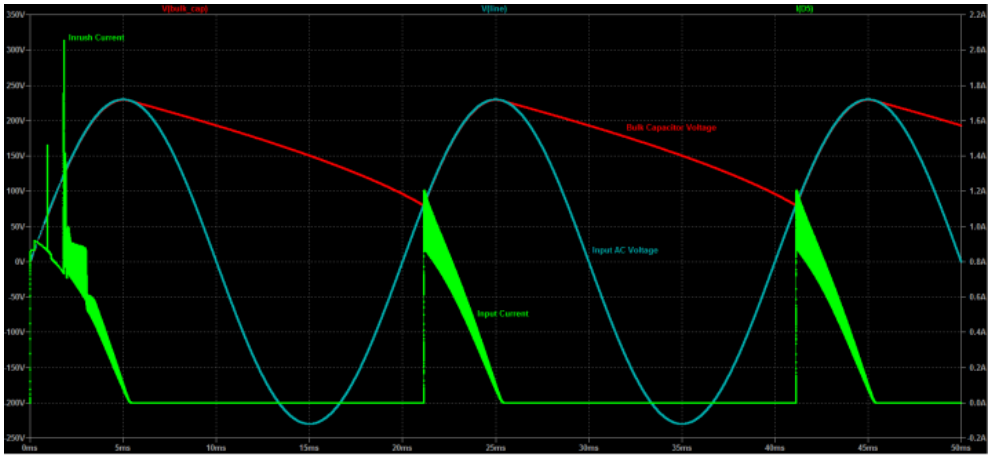

Figure 5. AC input, bulk capacitance voltage, and input current

Conclusion

In this study, we have two main advantages over the traditional main board design with flyback topology. We eliminated relay usage for AC loads in the main boards. One TRIAC and one optocoupler with the help of an extra TRIAC winding do the same work by providing safety criteria instead of relay. In this way, the cost of the system decreases and the PCB design is more compact and smaller than the traditional design. The energy consumption of one relay is greater than that of one TRIAC. If we consider more than one AC output system, the energy consumption decreases in our new design topology.

Scientific Ethics Declaration

The author declares that the scientific ethical and legal responsibility of this article published in EPSTEM journal belongs to the author.

Acknowledgements or Notes

* This article was presented as an oral presentation at the International Conference on Technology, Engineering and Science (www.icontes.net) held in Antalya/Turkey on November 16-19, 2023.

References

Bayrak, G. (2015). A remote islanding detection and control strategy for photovoltaic-based distributed generation systems. *Energy Conversion and Management*, *96*, 228-241.

Bayrak, G., & Kabalci, E. (2016). Implementation of a new remote islanding detection method for wind–solar hybrid power plants. *Renewable and Sustainable Energy Reviews*, *58*, 1-15.

Chang, C.J. , & Chen, C. L. (2013). An isolated output-feedback scheme with minimized standby power for SMPS. *IEEE Transactions on Power Electronics*, *28*(11), 5140-5146.

Coruh, N., Urgun, S., & Erfidan, T. (2010). Design and implementation of flyback converters. 2010 5*th IEEE conference on industrial electronics and applications*, *Fundamental Characteristics of Thyristors*. Retrieved from http://www.littelfuse.com.

Hart, D. W. (2010). *Power electronics*. McGraw-Hill.

Hashjin, S. A. (2017). *Cok cıkıslı yalıtılmıs flyback donusturucu tasarımı ve uygulaması*. (Master'thesis) Gazi University, Ankara, Turkey.

Moon, S., Koo, G.-B., & Moon, G.-W. (2014). Dimming-feedback control method for TRIAC dimmable LED drivers. *IEEE Transactions on industrial Electronics*, *62*(2), 960-965.

Myderrizi, I., & Ozbey, E. (2014). A low power multiple output switch-mode power supply with wide input range. *Analog Integrated Circuits and Signal Processing*, *81*, 431-441.

Rashid, M. H. (2011). *Power electronics handbook, Devices, circuits and applications* .(3rd ed.). Elsevier.

Reshma, K., Sreenath, R., & Pai, N. (2016). Design and implementation of an isolated switched-mode power supply for led application. *International Conference on Computation of Power, Energy Information and Commuincation (ICCPEIC)*

Zhang, J., Zeng, H., & Jiang, T. (2012). A primary-side control scheme for high-power-factor LED driver with TRIAC dimming capability. *IEEE transactions on power electronics*, *27*(11), 4619-4629.

Author Information

Gonca Uslu-Ozkucuk
OSTIM Technical University, Vocational School of Higher Education, Department of Electricity and Energy, Electricity Program, Ankara, Turkey
Ostim, 100. Yıl Blv., 55/F, 06374
Ostim Osb/Yenimahalle/Ankara, Turkey
Contact e-mail: *gonca.usluozkucuk@ostimteknik.edu.tr*

To cite this article:

Uslu-Ozkucuk, G. (2023). TRIAC based isolated AC load drive equivalent circuit design of solid-state relay. *The Eurasia Proceedings of Science, Technology, Engineering & Mathematics (EPSTEM), 26,* 183-189.

The Eurasia Proceedings of Science, Technology, Engineering & Mathematics (EPSTEM)
ISSN: 2602-3199

The Eurasia Proceedings of Science, Technology, Engineering & Mathematics (EPSTEM), 2023

Volume 26, Pages 190-201

IConTES 2023: International Conference on Technology, Engineering and Science

An Adapted Technology Acceptance Model (TAM 5) Framework to Enhance User Acceptance and Experience

Motasem Armouti
Applied Science Private University

Suhair AlHajHassan
Applied Science Private University

Khalid Alsamara
Chicago State University

Abstract In the rapidly evolving technological landscape, many companies invest in developing solutions that often fail to gain user acceptance. Understanding the reasons behind these failures is crucial, thus various iterations of the Technology Acceptance Model (TAM) have been introduced namely: TAM, TAM 2, TAM 3, and TAM 4 IE. Applying these models has shed light on a significant portion of the factors influencing technology acceptance. Nevertheless, it suggests that numerous other factors remain unexplored and need further consideration. This research proposes the Technology Acceptance Model 5 (TAM 5) as an advanced version with additional dimensions and factors to further investigate, aiming to enhance technology acceptance. TAM 5 includes three primary dimensions: First, applying Hybrid Agile-Waterfall software development approach, merging the strengths of both methodologies, to enhance the development process and user satisfaction; Second, applying Hybrid Work Settings of Working from Home (WFH) and Working from Office (WFO), enhancing team collaboration and problem-solving, thereby facilitating technology acceptance; and finally, consideration of Cultural factors, Social customs and traditions, and Time zone differences (CST), all of which may influence technology acceptance. To assess the effectiveness of TAM 5, a questionnaire designed and validated by experts was administered to respondents in the software industry, including professionals from various roles and experience levels. The results were analyzed using multiple regression, and the weights indicate that applying the Hybrid Agile-Waterfall development approach and the Hybrid Work Settings had a significant positive impact on technology acceptance with β values of 0.333 and 0.344 respectively. Cultural factors and traditions had a significant negative influence on technology acceptance with β value of -0.848, while the impact of time zone differences was found to be insignificant with a negligible β value. In conclusion, TAM 5 reveals key dimensions that impact technology acceptance rates, providing valuable insights for businesses and researchers to better understand and address the challenges related to user acceptance of technology in contemporary society.

Keywords: Technology acceptance model (TAM), User acceptance, Hybrid Agile-Waterfall approach, Work from Home (WFH), Work from Office (WFO).

Introduction

Technology has invaded our daily lives and has become a vein for individuals, organizations and even governments. Hundreds of thousands of applications and solutions emerged during the last few years and forced themselves into our communities and changed our way of life, social behavior, learning scheme, and our personality including how we run businesses, conduct trade, and much more. Among these applications are social media platforms, FinTech, healthcare, Enterprise Resource Planning (ERP), e-government, smart cities,

Internet of Things (IoT), and Industrial Internet of Things (IIoT) to name a few. This high volume of competition to make the public accept one application or solution over the other is becoming exceptionally important, acting as cross-roads between success and failure, between making a profit or a loss, and between contributing something of value to society versus being ineffective. Therefore, having criteria in place for accepting technology (i.e., software application) shapes the entire process of building applications, design, development, quality assurance, user experience and interface, deployment, and delivery.

Technology Acceptance Model (TAM), introduced by Fred Davis in 1986, is the art of delivering a software product in a way that is accepted and satisfactory to those who will use it, the end-users. It consists of two major beliefs: Perceived Usefulness (PU) and Perceived Ease of Use (PEOU) which drive people or organizations to accept or reject a software application (Lai, 2017; Legris et al., 2001).

The Standish Group report (1999) estimated that in 1998, the cost of canceled Information Technology (IT) projects was USD 75 billion (Chulkov & Desai, 2005). Another Standish Group study found that only 29 percent of projects succeed. The Royal Society of Engineering and British Computer Society found that 84 percent of projects fail while in the public sector, project failures are a lot more common in comparison to the private sector. The cost of failures is huge and overwhelming. Failures of Information Systems (IS) projects in both the public and private sectors cost around USD 150 billion per annum in the United States and USD 140 billion in the European Union (Gauld, 2007).

In addition to the User Experience (UX), it is very clear that missing a Technology Acceptance Model (TAM), which is the acceptance criteria from the plan of designing and developing the software, plays a significant role in project failure and the rejection of the product as it does not fulfill the end-user requirements. This has been a major issue for software providers and customers alike, resulting in undesirable consequences, such as legal actions, increased spending on products that are unusable, time wasted on development, deployment, and implementation for both providers and customers, and the search for alternatives which again, may end in the same results.

To overcome the challenges surrounding the rejection of software by end users, Technology Acceptance Model 5 (TAM 5) is proposed by this research with additional factors that contribute to enhancing the technology acceptance rates. The following research questions were identified and have been answered through the journey of this research work:

RQ1: How does the hybrid Agile-Waterfall development approach affect technology acceptance?
RQ2: How does the hybrid work setting of Work from Home (WFH) and Work from Office (WFO) affect technology acceptance?
RQ3: How do cultural factors and social customs affect technology acceptance?
RQ4: How does the time zone difference affect technology acceptance?

The remainder of the paper is structured as follows. Section 2 provides a review of the state of the art of related work. The proposed TAM 5 framework is presented in Section 3. Section 4 discusses the main results of the research work. Finally, Section 5 summarizes the work and the main contributions of this paper and opens possible directions for further research.

Related Work

Technology Acceptance Model (TAM)

TAM plays a significant role in the success or failure of a particular software application. To reflect how critical TAM could be, let's take healthcare devices, such as remote patient monitoring, glucose monitoring, Parkinson's disease monitoring, and heart rate monitoring to name a few. These are application-operated devices that depend entirely on technology and are essential to provide patient care by health care providers, which makes it even more essential to be accepted by users.

Another example is NASA spaceships which have no room for technology flaws especially when they are on a mission to space with astronauts aboard spaceships with their lives at stake. The Standish Group conducted a study in 1998 and found that 26% of all Management Information Systems (MIS) projects were completed with requirements met, within budget and on time (Legris et al., 2001). This indicates that 74% of MIS projects were either incomplete or partially delivered or cancelled. It also indicates that the acceptance rate is not satisfactory,

and the impact of this rejection is high in developers' time and effort and in the cost of developing such applications, given developers are forced to rework the rejected parts resulting in increased spending on wages, third party software licensing, and utilities, etc. Therefore, it is very important to find models and techniques that can enhance technology acceptance. Original TAM structure is shown in Figure 1.

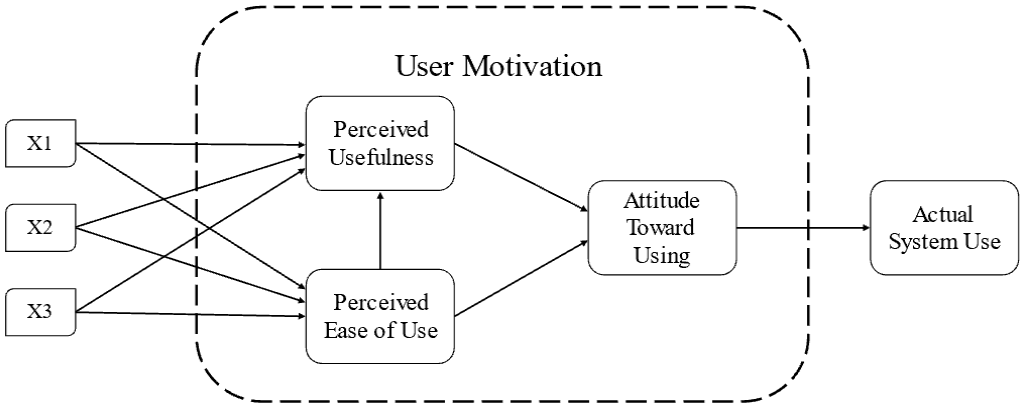

Figure 1. Technology acceptance model (Davis 1986; Adapted from Lai, 2017)

Enhanced TAMs

TAM is the cornerstone for future work to enhance the TAM framework or build on it to come up with better frameworks such as TAM2, TAM3, and TAM 4 IE. TAM2 was proposed by Venkatesh and Davis (2000) where four constructs were considered (1) job relevance, (2) output quality, (3) result demonstrability, and (4) perceived ease of use.

Venkatesh and Bala (2008) developed an integrated model of technology acceptance - TAM3 where they combined the model of the determinants of perceived ease of use and TAM2. TAM3 was developed using the four different determinants of perceived usefulness and perceived ease of use including (1) social influence, (2) system characteristics, (3) the individual differences, and (4) facilitating.

TAM4 IE was the outcome of theoretical and empirical research conducted in previous studies and has the following five aspects: (1) subjective perception, (2) perceived usability, (3) perceived usefulness, (4) future expectations, and (5) facilitating conditions (Prietch and Filgueiras, 2015).

The Proposed Model (TAM 5)

The research proposed model is composed of three dimensions that altogether construct TAM 5 as illustrated in Figure 2. The first dimension is applying a Hybrid Development Approach that combines waterfall and agile development models, merging the strengths of both methodologies, to enhance the development process and user satisfaction, the second dimension is adopting a Hybrid Work Setting that combines work from home and work from office styles, enhancing team collaboration and problem-solving, and the third dimension consists of considering multiple factors; Cultural factors, Social customs and traditions, and Time zone differences, all of which may influence technology acceptance. These dimensions and factors and their influence on technoogy acceptance will be described in detail in the next subsections.

Dimension One: Hybrid Software Development Approach

The first dimension of TAM 5 is applying the hybrid software development methodology which combines waterfall and agile models, where the agile model is the primary structure of the software development cycle and waterfall is applied where applicable within different sprints or iterations. Large projects can be challenging to manage and frequently fall short of stakeholder expectations. Although agile methods have generated sound interest in the business world, little research has been done on how they should be implemented in large environments that involve outsourcing, numerous programs, projects, and methodologies; a situation that is currently viewed as extremely difficult in the business world.

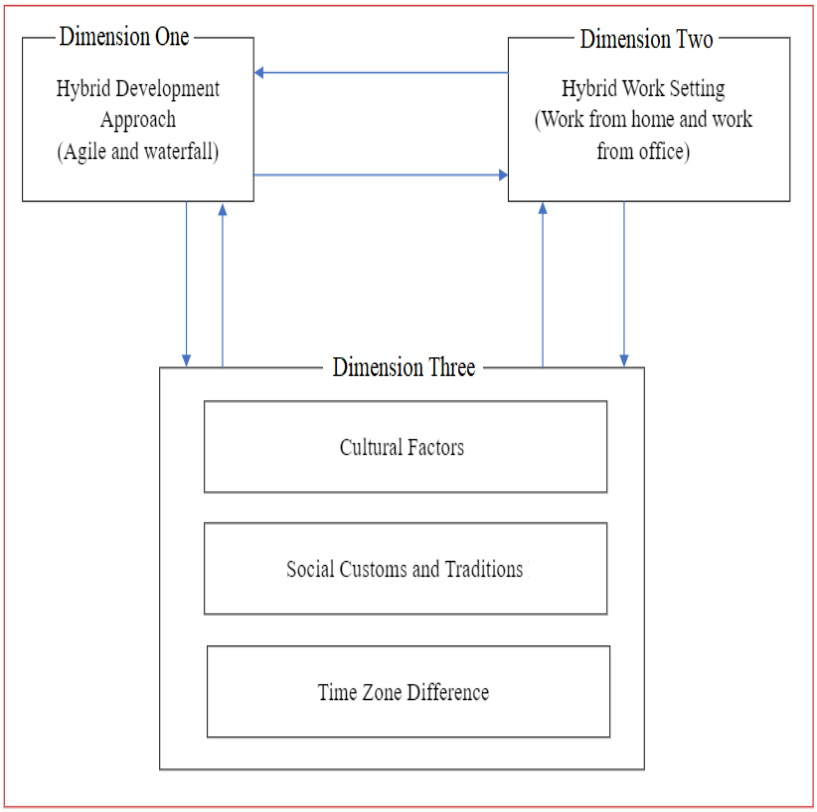

Figure 2. Technology acceptance model 5 (TAM 5)

Since it is generally accepted that no one methodology can be used to serve all projects, both agile and non-agile techniques must be customized and integrated to suit various projects. This highlights the fact that, in order to meet these issues, a software development capacity may blend agile and traditional components to produce a hybrid software development process (Gill et al., 2018).

The composite approach splits the project into several increments; each of which will have a set of the project lifecycle stages. Each increment will combine the best attributes of available software development processes (Waterfall, Iterative, and Agile) together used to develop and manage application software development (Al-Maharmeh & Unhelkar, 2008).

One of the 12 principles of the Agile manifesto is to “enable face-to-face interactions”, but with the widespread use of remote work and adoption of work from home flexibility after the COVID-19 pandemic, face-to-face interactions were not much of a practice as it was pre-COVID. This led to mixing working from home style with working from office which may have an impact on technology acceptance rate as will be discussed in the next section.

Dimension Two: Hybrid Work Setting

The global pandemic of COVID-19 precipitated a widespread adoption of remote work practices. It pushed people worldwide to start working from home and led to teachers and students adopting remote teaching and learning, commonly known as online work and study. Post the pandemic, people, employers, and employees alike, willingly adapted the working from home style, yet working from office has tangible effects on productivity and knowledge exchange among employees. This led several companies to adopt a hybrid work setting of mixing work from home and work from office work styles.

Psychiatrist Edward Hallowell refers to a short meetup at a co-worker's desk as a 'human moment' which is "a face-to-face encounter that allows for empathy, emotional connection, and nonverbal cues to complement what is actually said". With remote communications, the connection is severely weakened, and nonverbal signals are more difficult to pick up on. People are more likely to empathize with each other and are often energized in human moments which support organizational culture and collaboration (Fayard et al., 2021).

Therefore, the second dimension proposed by TAM 5 is applying the hybrid work setting that enforces both work from home and work from office styles, where several weekly hours are mandatory to be worked from office and team members can meet to tackle pressing issues that can be resolved much faster and more efficiently during face-to-face meetings. Concurrently, it allows team members to work remotely, providing them with a degree of flexibility, which is anticipated to positively influence the rate of technology acceptance.

Dimension Three: Cultural Factors, Social Customs, and Time Zone Differences (CST)

Several scholars and researchers introduced new factors they believed had an impact on the original model of TAM. In this research, TAM 5 introduces new factors and investigates their substantial impact on technology acceptance rates.

Cultural Factors

Several cultural factors have a genuine impact on technology acceptance. Some cultural factors that may affect the productivity of teams and therefore decrease the acceptance rate are: (1) having children, elderly or other family members to care for, especially while working from home, which were found to have a negative impact on remote workers' physical and psychological well-being, (2) difference in weekend days, and (3) following different calendars, e.g., Gregorian, Hijri (Islamic), etc., which can potentially disrupt effective communication within a team. These variations in scheduling preferences and cultural practices can introduce complexity and hinder seamless coordination among team members, impacting their ability to collaborate and communicate efficiently, and consequently affects technology acceptance.

Social Customs

Social customs and traditions also have an impact on technology acceptance rate. Some factors are religious occasions like the month of Ramadan, Eid Al Fitr, and Eid Al Adha in Muslim majority countries, and Christmas holiday in other countries. Having different days off and holidays among diverse team members would also affect teams productivity and the overall technology acceptance rate. For example, in Ramadan, the working hours are reduced by 25%, six hours instead of eight hours per day for the private sector and may be more than that for the public sector, followed by three days holiday which reduces the productivity of employees and may have a negative impact on technology acceptance.

Time Zone Differences

A critical factor that needs attention for virtual teams scattered around the world is the different time zones and the difficulties associated with it, such as, delay in communication, the mental stress at the end of a working day in one zone which is a fresh start of the working day in another zone. Companies are asking their employees to change their working hours to start in the afternoon, which would be the morning of their teammates in another time zone, to have more interactions, meetings, etc. This inconvenient change is neither sustainable nor comfortable for many employees, especially for families who have caregiving responsibilities, so adopting a mixture of work from home and work from office may enhance the productivity of the developers and teams and consequently increasing technology acceptance.

Results and Discussion

One of the most common methods of collecting data in research is questionnaires. However, it is a challenge to validate that the collected data is reliable and reflects realistic results. In this research, in order to assess the effectiveness of TAM 5 model, data was collected and acquired in the form of a questionnaire that was developed and validated by experts to address the proposed factors and are subject to arbitration. The questionnaire was administered to respondents in the software industry, including professionals from various roles and experience levels, and a total of 115 participants took part in the survey.

A complete quantitative data analysis was carried out to answer and assess the research hypothesis and research questions. Statistical Package for the Social Science (SPSS) was used to analyze the data and the questionnaire

responses. SPSS is a powerful statistical software platform that provides efficient statistical data analysis. The collected responses of 115 were examined by SPSS prior to the data analysis and it was determined that they were fit for the analysis.

Analyzing the Items of the Development Approach

According to Table (1) below, about half of the organizations adopt Agile framework (Scrum, Kanban, Extreme Programming (XP), Lean) development approach with percent (47.8%), also (46.1%) of the organizations in the study sample adopt Hybrid (Agile & Waterfall) development approach, while only (4.3%) of the organizations adopt Waterfall development approach. Finally, (1.7%) of the organizations adopt other development approach.

Table 1. Means, SD, and percentages-development approach

Statement Number	Items	M	SD	Percent
1	Agile framework (Scrum, Kanban, XP, Lean)	2.02	1.009	47.8
2	Waterfall			4.3
3	Hybrid (Agile & Waterfall)			46.1
4	Other			1.7

Table (2) below demonstrates values of means, standard deviation, and MI for the Development Approach. The second statement "Adopting the Agile development approach increases the technology acceptance rate (i.e., enhances user acceptance)" ranked first among the items being rated by the study sample, as it has the highest mean (4.16), expressing a high level of agreement, while the third statement "Adopting the Waterfall development approach increases the technology acceptance rate (i.e., enhances user acceptance)" ranked the lowest among the items being rated by the study sample, as it has the least mean (2.79), also expressing a moderate level of agreement. The overall assessment degree of the Development Approach dimension is rated by a mean of 3.704. This value expresses a high level of agreement among the study sample.

Table 2. Means, SD, and MI for development approach (arranged in a descending order)

Statement Number	Items	M	SD	MI	Level	Rank
2	Adopting the Agile development approach increases the technology acceptance rate (i.e., enhances user acceptance)	4.16	0.67	83.2%	High	1
4	The productivity of development teams would increase and lead to the enhancement of the technology acceptance rate (i.e., enhances user acceptance)	4.10	0.754	82.0%	High	2
1	Adopting the Hybrid (Agile & Waterfall) development approach increases the technology acceptance rate (i.e., enhances user acceptance)	3.77	0.872	75.4%	High	3
3	Adopting the Waterfall development approach increases the technology acceptance rate (i.e., enhances user acceptance)	2.79	0.996	55.8%	Moderate	4
	Overall Mean	3.704	0.491	74.1%	High	

Means description (1 – 1.8 v. low, 1.81 – 2.6 low, 2.61 – 3.40 Moderate, 3.41 – 4.20 high, and 4.21 – 5 v. high)

Analyzing the Items of Work Settings

According to Table 2 below, about half of the organizations' work setting was Hybrid (WFO and WFH), i.e., mixture of hours between working from the office and working from home with percent (49.6%), also (40.9%) of the organizations' adopted Work from Office (WFO) work style, i.e., working specific number of hours in

office forced by work policy, while (9.6%) of the organizations' work style was Work from Home (WFH), i.e., working only from home.

Table 2. Means, SD, and percentages-work settings

Statement Number	Items	M	SD	Percent
1	Work from Office (WFO), i.e., working specific number of hours in office forced by work policy.	2.09	0.951	40.9
2	Work from Home (WFH), i.e., working only from home, such as during COVID-19 lockdown.			9.6
3	Hybrid (WFO and WFH), i.e., mixture of hours between working from office and working from home.			49.6
4	Other			0

Table 3 below demonstrates the values of means, standard deviation, and MI for the Work Settings. The third statement "Implementing a Hybrid (WFO and WFH) policy by my organization would increase my work productivity" ranked first among the items being rated by the study sample, as it has the highest mean (4.17), expressing a high level of agreement, while the fifth statement "Implementing a Work from Home policy by my organization would enhance the overall technology acceptance rate (i.e., enhances user acceptance)" ranked the lowest among the items being rated by the study sample, as it has the least mean (3.3), expressing a moderate level of agreement. The overall assessment degree of the Work Style dimension is rated by a mean of 3.615. This value expresses a high level of agreement among the study sample.

Table 3. Means, SD, and MI for work settings (arranged in a descending order)

Statement Number	Items	M	SD	MI	Level	Rank
3	Implementing a Hybrid (WFO and WFH) policy by my organization would increase my work productivity	4.17	0.764	83.4%	High	1
6	Implementing a Hybrid (WFO and FH) policy by my organization would enhance the overall technology acceptance rate (i.e., enhances user acceptance)	3.87	0.884	77.4%	High	2
4	Implementing a Work from Office policy by my organization would enhance the overall technology acceptance rate (i.e., enhances user acceptance)	3.54	0.901	70.8%	High	3
1	Employing a Work from Office policy by my organization would increase my work productivity	3.43	1.036	68.6%	High	4
2	Implementing a Work from Home policy by my organization would increase my work productivity	3.37	1.021	67.4%	Moderate	5
5	Implementing a Work from Home policy by my organization would enhance the overall technology acceptance rate (i.e., enhances user acceptance)	3.3	0.936	66%	Moderate	6
	Overall Mean	3.615	0.467	72.3%	High	

Means description (1 – 1.8 v. low, 1.81 – 2.6 low, 2.61 – 3.40 Moderate, 3.41 – 4.20 high, and 4.21 – 5 v. high)

Analyzing the Items of Cultural Factors

Table 4 below demonstrates the values of means, standard deviation, and MI for the Cultural Factors. The first statement "Having children, elderly or other family members to care for while working from home would decrease my productivity" ranked first among the items being rated by the study sample, as it has the highest mean (3.55), expressing a high level of agreement, while the fourth statement "Working with diverse team members that have different holiday occasions such as Ramadan, Eid holidays, and Christmas with different days off would decrease the overall technology acceptance rate (i.e., reduces user acceptance)" ranked the lowest among the items being rated by the study sample, as it has the least mean (3.01), expressing a moderate level of agreement. The overall assessment degree of the Cultural Factors dimension is rated by a mean of 3.2. This value expresses a moderate level of agreement among the study sample.

Table 4. Means, SD, and MI for cultural factors (arranged in a descending order)

Statement Number	Items	M	SD	MI	Level	Rank
1	Having children, elderly or other family members to care for while working from home would decrease my productivity	3.55	1.028	71%	High	1
2	Having children, elderly or other family members to care for while working from home would decrease the overall technology acceptance rate (i.e., reduces user acceptance)	3.21	0.96	64.2%	Moderate	2
3	Working with diverse team members that have different holiday occasions such as Ramadan, Eid holidays, and Christmas with different days off would decrease team productivity	3.03	1.123	60.6%	Moderate	3
4	Working with diverse team members that have different holiday occasions such as Ramadan, Eid holidays, and Christmas with different days off would decrease the overall technology acceptance rate (i.e., reduces user acceptance)	3.01	1.004	60.2%	Moderate	4
	Overall Mean	3.2	0.762	64%	Moderate	

Means description (1 – 1.8 v. low, 1.81 – 2.6 low, 2.61 – 3.40 Moderate, 3.41 – 4.20 high, and 4.21 – 5 v. high)

Analyzing the Items of Time Zone Difference

According to Table 5 below, most of the respondents worked with virtual teams in different time zones in their organizations with percentage (75.7%). Table 6 below demonstrates the values of means, standard deviation, and MI for the Time Zone Difference factor.

Table 5. Means, SD, and percentages-time zone differences

Statement Number	Items	M	SD	Percent
1	No	1.76	0.431	24.3
2	Yes			75.7

Table 6. Means, SD, and MI for time zone (arranged in a descending order)

Statement Number	Items	M	SD	MI	Level	Rank
1	Working with virtual teams in different time zones would be a challenge facing development team members	3.83	0.819	76.6%	High	1
3	Being flexible to collaborate with other team members in different time zones other than my own would increase the overall technology acceptance rate (i.e., enhances user acceptance)	3.57	0.849	71.4%	High	2
2	Being flexible to collaborate with other team members in different time zones other than my own would increase my productivity	3.5	0.931	70%	High	3
	Overall Mean	3.63	0.624	72.7%	High	

Means description (1 – 1.8 v. low, 1.81 – 2.6 low, 2.61 – 3.40 Moderate, 3.41 – 4.20 high, and 4.21 – 5 v. high)

The first statement “Working with virtual teams in different time zones would be a challenge facing development team members” ranked first among the items being rated by the study sample, as it has the highest

mean (3.83), expressing a high level of agreement, while the second statement "Being flexible to collaborate with other team members in different time zones other than my own would increase my productivity" ranked the lowest among the items being rated by the study sample, as it has the least mean (3.5), expressing a high level of agreement. The overall assessment degree of the Time Zone dimension is rated by a mean of 3.63. This value expresses a high level of agreement among the study sample.

Model of Measurement

The model of measurement with its 4 variables (i.e., independent factors) measured by 17 measurement items was assessed using Confirmatory Factor Analysis (CFA), which is a quantitative technique used to analyze the efficacy of measurement models where the number of factors and their direct relationship are specified (Price, 2023). CFA is available on Analysis of a Moment Structures – statistical software (AMOS) as depicted in Figure (3). According to Chen (2007) the model showed a satisfactory model fit concerning major model fit indices. Model fit statistics for the primary measurement model are shown in Table 7 below.

Table 7. Final measurement model fit

X^2	X^2/DF	SRMR	CFI	TLI	GFI	IFI	RMSEA
95.522	1.151	0.079	0.976	0.96	0.913	0.979	0.036

Table 7 shows that the value of Standardized Root Mean Squared Residual (SRMR) is less than 0.08, indicating an excellent model fit (Hu & Bentler, 1999). The Comparative Fit Index (CFI) value is greater than 0.95 indicating an excellent fit for the model (Kline, 2005). The Tucker Lewis Index (TLI) value is greater than 0.90, indicating an excellent fit as well (Sharma et al., 2005). The Goodness of Fit Index (GFI) and Incremental Fit Index (IFI) values are greater than 0.90, also indicating an excellent fit for the model (Hu & Bentler, 1999). Also, the Root Mean Square Error of Approximation (RMSEA) is less than 0.1, which indicates an excellent fit for the model (Brown, 2015). As indexes suggest a sufficient fit of the model to the current data, the hypothesized model is fitted.

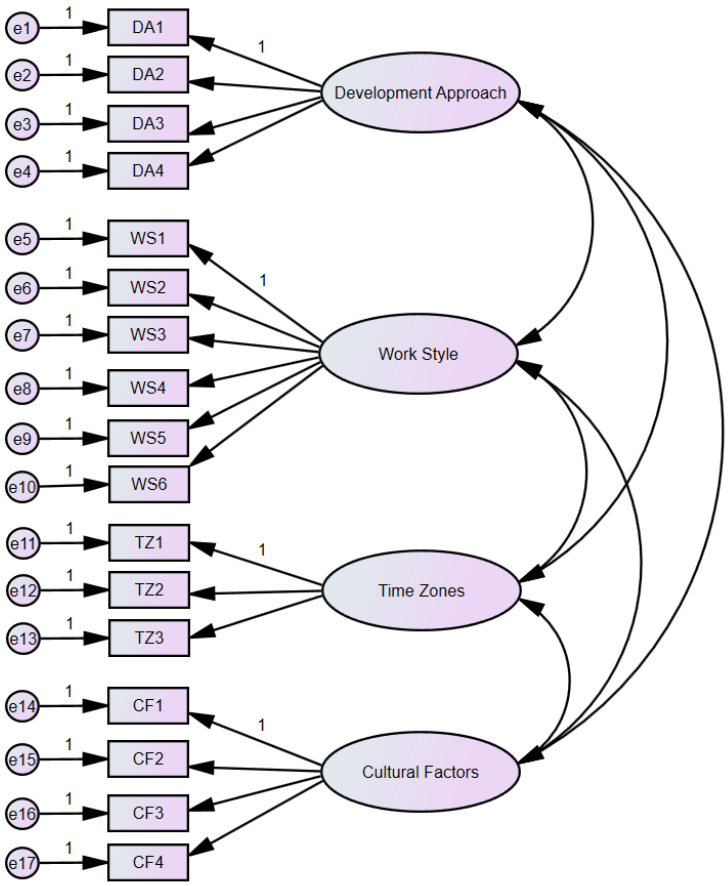

Figure 3. Confirmatory factor analysis (CFA) model

Testing the Research Questions

To test the research questions, the variance-based Structural Equation Model (SEM), is used because of its ability to model relationships between multiple dependent and independent variables at the same time which is required in this research (Henseler, 2017).

Testing RQ_1: How does the hybrid Agile-Waterfall development approach affect technology acceptance?

The result of the SEM is presented in Table (8) below shows the following: Hybrid Agile-Waterfall development approach can explain 24.5% of the variation in technology acceptance, the R^2 value equals 0.245, which indicates the ability of the independent variable to explain changes in the dependent variable. According to the regression weights, Hybrid Agile-Waterfall development approach has a significant positive effect on technology acceptance, since the critical ratio value is greater than 2 and the p-value (0.001) is less than 0.01, the path is significant (Byrne, 2013). The effect size of Hybrid Agile-Waterfall development approach on technology acceptance is 0.333.

Table 8. Structural Equation Modelling Regression Weights-Development Approach

			Estimate	S.E.	C.R.	P	Effect	R^2
TA	←	Hybrid (Agile-Waterfall)	.819	.258	3.179	.001	0.333	0.245

S.E. = Standard errors of the regression weights, C.R. = Critical Ratio, P = p-value (*<0.05, **<0.01, ***<0.001)

Testing RQ2: How does the hybrid work style of work from home (WFH) and work from office (WFO) affect technology acceptance?

The result of the SEM is presented in Table (9) below. Hybrid work settings of work from home (WFH) and work from office (WFO) can explain 11.8% of the variation in technology acceptance, the R^2 value equals 0.118, which indicates the ability of the independent variable to explain changes in the dependent variable. According to the regression weights, Hybrid work settings of work from home (WFH) and work from office (WFO) has a significant positive effect on technology acceptance, since the critical ratio value is greater than 2 and the p-value (0.001) is less than 0.01, the path is significant (Byrne, 2013). The effect size of Hybrid work settings of work from home (WFH) and work from office (WFO) on technology acceptance is 0.344.

Table 9. Structural Equation Modelling Regression Weights-Work Settings

			Estimate	S.E.	C.R.	P	Effect	R^2
TA	←	Hybrid work settings	.923	.437	2.114	.035	0.344	0.118

S.E. = Standard errors of the regression weights, C.R. = Critical Ratio, P = p-value (*<0.05, **<0.01, ***<0.001)

Testing RQ3: How do cultural factors and social customs affect technology acceptance?

In this research, we assumed that cultural factors such as having children or elderly family members to care for have a negative impact on technology acceptance rate and the results proved this assumption. The result of the SEM is presented in table (10) below. Cultural factors can explain 71.9% of the variation in technology acceptance, the R^2 value equals 0.719, which indicates the ability of the independent variable to explain changes in the dependent variable. According to the regression weights, Cultural factors have a significant negative effect on technology acceptance, since the critical ratio value is less than -2 and the p-value (0.001) is less than 0.01, the path is significant (Byrne, 2013). The effect size of cultural factors and social customs on technology acceptance is -0.848.

Table 10. Structural Equation Modelling Regression Weights-CST

			Estimate	S.E.	C.R.	P	Effect	R^2
TA	←	CF	-3.725	1.499	-2.485	.013	-0.848	0.719

S.E. = Standard errors of the regression weights, C.R. = Critical Ratio, P = p-value (*<0.05, **<0.01, ***<0.001)

Testing RQ4: How does the time zone difference affect technology acceptance?

The result of the SEM is presented in Table (11) below. Time zone difference can explain 1.7% of the variation in technology acceptance, the R^2 value equals 0.017, which indicates the ability of the independent variable to explain changes in the dependent variable. According to the regression weights, the time zone difference has an insignificant effect on technology acceptance, since the critical ratio value is less than 2 and the p-value (0.211) is greater than 0.05, the path is insignificant (Byrne, 2013).

Table 11. Structural Equation Modelling Regression Weights-Time Zone Differences

			Estimate	S.E.	C.R.	P	Effect	R^2
TA	←	TZ	6.606	5.286	1.250	.211	-	0.017

S.E. = Standard errors of the regression weights, C.R. = Critical Ratio, P = p-value (*<0.05, **<0.01, ***<0.001)

Conclusion and Future Directions

The Technology Acceptance Model explored various factors that proved to have a significant impact on increasing technology acceptance and adoption, however it still needs improvement and enhancement to bring aboard more factors that contribute to the technology acceptance to achieve better results in both user acceptance and experience. The constant change in technology and human social behavior makes this an on-going process as it needs to be revised as new technologies emerge and human needs change and evolve.

This research has proposed TAM 5 model which consists of applying a hybrid development approach consisting of agile and waterfall models, adopting a hybrid work setting combining work from home and work from office styles, and the following additional factors: cultural factors, social customs and traditions, and time zone difference. This research aimed at investigating the impact of applying TAM 5 factors on technology acceptance.

It was concluded that applying the Hybrid Development Approach and the Hybrid Work Settings have a significant positive effect on technology acceptance rate. On the other hand, Cultural Factors and Social Customs and Traditions were found to have a significant negative impact on technology acceptance rate, while the Time Zone Difference Factor has an insignificant effect on technology acceptance rate. In conclusion, TAM 5 has revealed key dimensions that impact technology acceptance rates, providing valuable insights for businesses and researchers to better understand and address the challenges related to user acceptance of technology in contemporary society.

The technology acceptance rate is influenced by an indefinite and evolving array of factors, given the constant emergence of new technologies. This suggests that ongoing research can reveal additional and novel factors in the future, including those that may influence unemployment rates and the economy, since the introduction of new technology is closely linked to employment, as it creates fresh job prospects. Finally, this proposed research will be further evaluated by conducting a case study to apply TAM 5 factors on a software development company to evaluate these factors impact on technology acceptance rate.

Scientific Ethics Declaration

The authors declare that the scientific ethical and legal responsibility of this article published in EPSTEM journal belongs to the authors.

Acknowledgements or Notes

* This article was presented as an oral presentation at the International Conference on Technology, Engineering and Science (www.icontes.net) held in Antalya/Turkey on November 16-19, 2023.

References

Al-Maharmeh, M., & Unhelkar, B. (2008). Investigation into the creation and application of a composite application software development process framework (CASDPF). *Fifth International Conference on Information Technology: New Generations*, Las Vegas.

Brown, T. A. (2015). *Confirmatory factor analysis for applied research* (2nd ed.). The Guilford Press.

Byrne, B. M. (2013). *Structural equation modeling with AMOS: Basic concepts, applications, and programming*. Routledge.

Chen, F. F. (2007). Sensitivity of goodness of fit indexes to lack of measurement invariance. *Structural Equation Modeling: A Multidisciplinary Journal*, *14*, 464-504.

Chulkov, D. V., & Desai, M. S. (2005). Information technology project failures. Applying the bandit problem to evaluate managerial decision making. *Information Management & Computer Security, 13*(2), 135-143.

Fayard, A. L., Weeks, J., & Khan, M. (2021). Designing the hybrid office. *Harvard Business Review, 99*(2), 114-123.

Gauld, R. (2007). Public sector information system project failures: Lessons from a New Zealand hospital organization. *Government Information Quarterly, 24*, 102-114.

Gill, A., Henderson-Sellers, B., & Niazi, M. (2018). Scaling for agility: A reference model for hybrid traditional-agile software development methodologies. *Information Systems Frontiers, 20*, 315–341.

Henseler, J. (2017). Bridging design and behavioral research with variance-based structural equation modeling. *Journal of Advertising, 461*, 178-192, 2017.

Hu, L., & Bentler, P. (1999). Criteria for fit indexes in covariance structure analysis: Conventional criteria versus new alternatives. *SEM, 6*(1), 1-55.

Kline, R. B. (2005). *Principles and practice of structural equation modeling* (2nd ed.). Guilford Press.

Lai, P. (2017). The literature review of technology adoption models and theories for the novelty technology. *Journal of Information Systems and Technology Management, 14*(1), 21-38.

Legris, P., Ingham, J., & Collerette, P. (2001). Why do people use information technology? A critical review of the technology acceptance model. *Information & Management, 40*, 191-204.

Price, L. R. (2023). Confirmatory factor analysis: foundations and extensions. Retrieved from https://www.sciencedirect.com/topics/socialsciences/confirmatoryfactoranalysis#:~:text=Quantitative%20Research%20and%20Educational%20Measurement&text=Confirmat

Prietch, S. S., & Filgueiras L. V. L. (2015). Technology acceptance evaluation by deaf students considering the inclusive education context. In *Human-Computer Interaction–INTERACT 2015: 15th IFIP TC 13 International Conference*, Bamberg, Germany.

Sharma, S., Mukherjee, S., Kumar, A., & Dillon, W. (2005). A simulation study to investigate the use of cutoff values for assessing model fit in covariance structure models. *Journal of Business Research, 58*(7), 935-943.

Authors Information

Motasem Armouti
Applied Science Private University
Amman, Jordan

Suhair AlHajHassan
Applied Science Private University
Amman, Jordan
Contact e-mail: *su_hassan@asu.edu.jo*

Khalid Alsamara
Chicago State University
Chicago, Illinois, USA

To cite this article:

Armouti, M., AlHajHassan, S. & Alsamara, K. (2023). An adapted technology acceptance model (TAM 5) framework to enhance user acceptance and experience. *The Eurasia Proceedings of Science, Technology, Engineering & Mathematics (EPSTEM), 26*, 190-201.

The Eurasia Proceedings of Science, Technology, Engineering & Mathematics (EPSTEM)
ISSN: 2602-3199

The Eurasia Proceedings of Science, Technology, Engineering & Mathematics (EPSTEM), 2023

Volume 26, Pages 202-207

IConTES 2023: International Conference on Technology, Engineering and Science

The Effects of Technological Aspects on the Formation and Transformation of Cities: The Case of Amman

Bushra Zalloom
Zarqa University

Abstract: The contemporary world is dominated by the power of technology and capitalism ideology (called techno-capitalism in this paper). The techno-capitalism transforms various cityscapes worldwide into unsocial hubs for economic purposes and giant realms for play. This transformation weakens social cohesiveness and harms the cityscape by causing poverty, inequality, and a loss of identity, even if it enhances the possibility that the city will enter the global market, and stimulate economic growth as well as innovation. This paper aims to discuss the evolution of cities by studying the reasons behind their continuous dynamics and exploring the influences and effects of techno-capitalism. To achieve the research aims, Amman's case study will be studied and analyzed to explore the effects of technological and non-technological aspects on the formation and transformation of the cityscape. At the conclusion, the paper will propose some strategies to preserve the uniqueness of the city while keeping up with modern technology.

Keywords: Technology, Capitalism, City transformation, City identity

Introduction

Since the 19th century, technical advancements have accelerated, fuelling urbanization's fast rise. They expedited the transformation of the spatial and social boundaries and distinctions caused by time and location. The effects of new technologies fundamentally alter the current urban structure and its primary purposes, paving the way for the arrival of different kinds of functions that affect the cityscape. Many primary roles that were dominant and have been for thousands of years changed as a result of digital technology.

Previous studies confirm that the cityscape of traditional cities is a product of the social and cultural aspects that represent its sociocultural characteristics. During the last decades, these various urban landscapes worldwide have been transformed into what is known as the High-tech international style. Technology and capitalism played a vital role in this transformation and their influences are observed in the built environment as well as the cityscape. The use of new technology, globalization, and economic boom have affected the urban process and development. The macro-scale sensitivity of urban fabric as well as the micro-scale uniqueness of the architectural style have been transformed to fulfil capitalism's demands and reflect modernity, power, and prosperity. As a result, many cities started to change their image, and local government was convinced to adopt a techno-capitalism perspective on city planning and design.

This paper provides an analysis of how urban structure has been affected by techno-capitalism and transformed by focusing on the case of Amman, the capital city of Jordan, and discussing the causes and effects of this transformation. First, it discusses the influences of technological factors on urban form, then, it analyzes the formation and transformation of Amman's cityscape during the last decades, and finally, some strategies to preserve the uniqueness of the city while keeping up with modern technology are proposed.

Method

The case study method has been used to achieve the research aim of studying the effects of technological aspects on the formation and transformation of cities. The case of Amman is analyzed to explore the impacts of technological and non-technological aspects on the cityscape. The review of existing literature is made to comprehend the main aspects that affect the formation of Amman and to understand the effects of modern technology on the cityscape and social life. The physical features have been recognized by conducting site visits to analyze the design of the high-rises in Amman, their construction, the used materials, and their impacts on surroundings areas.

Results and Discussion

The Influences of Technological Factors on Urban Form

Technology, according to Geyer (2002) does not determine historical evolution or social changes on its own; rather, it reflects how society might evolve in certain ways by utilizing technical potential. Technology creates the boundaries between reality and new cybernetic spaces in modern cities, it produces virtual analogs that shape new social norms and requirements (Mozuriunaite, 2016). Using technology in architectural design and construction provides the same growth pattern, the same high-rise building style, and the same cityscape without referencing the locality, therefore, the image of the city doesn't represent the individuality of the location, and the viability of social systems is harmed by this placelessness. As a result, the city's identity and traditional culture are subject to adaptation and change (Zalloom, 2018). The techno-capitalism effectively translated commercial concerns into new urban forms while ignoring the significance of spatial interactions (Madanipour, 2001). The risk of losing one's unique identity in the global environment is due to the globalization of urban form (Antrobus, 2009).

Lin (2010), Kostof (2009) and Oktay (2002) and others claim that a city's identity is influenced by the links it establishes with the outside world. The identity of the city is significant in forging ties in the modern era of globalization. Therefore, city administrators who want to modify their cities must be aware of how their environment is seen to attract investments (Antrobus, 2009). Cities should be redesigned to meet the demands of modern technology without harming their identity, they may be viewed from several perspectives as centers for business and creative industries (Sassen, 2006), as realms of play (Stevens, 2007), or as spaces for consumption (Lin 2010). Information technology plays a vital role in branding the city and its urban spaces as a modern hub for technology that attracts investments.

Formation and Transformation of Amman's Cityscape

Following the Second World War, two schools of thought emerged and influenced Amman's architecture. Jordanian architects who received their education in the West attempted to apply modernist architectural concepts (Pilder, 2011), however, those who received their education at Jordanian institutions applied the Arab-Islamic architecture as a model for creating a new Jordanian style. These various viewpoints enrich the city's architectural language and represent Amman as a hub for architectural innovation.

Figure 1. Transformation of Amman's skyline from humble to high-rises

Amman, once known as the city of hats and steps, by the time it is known as the city of circles. The history of Amman's development is defined by its eight circles; starting from the First circle in Jabal Amman district

through the Eighth circle in Wadi al-Saier district (GAM, 2022). Zalloom (2018) reviewed the historical development of Amman and stated that local socio-spatial aspects formed the cityscape, which includes its natural assets, such as "the hilly topography, and the Amman Stream", and its built environment, such as "the humble skyline, the grand stairs, and the natural stone cladding." Amman was identified by its humble skyline with four-story buildings cladded with stone, the emerging technology transformed its skyline into an exhibition of electing Hi-Tech styles cladded with glass (Figure 1.). Additionally, the lack of construction codes and conservation policies turned parts of the city into displays of electing design with no respect for urban identity.

The techno-capitalism philosophy uses its ideology to reshape the universe in accordance with its own limited viewpoint. The economic crisis of the twenty-first century had a huge impact on the physical, social, and cultural elements. The transnational mobility of capital brought particular practices among diverse geographic zones where the built environment is invested for consumption and production (Madanipour, 2001). Similarly, the influx of migrants during the Gulf Wars in 1990 and 2003 had a great effect on Amman as they significantly changed the city's physical, sociocultural, and economic qualities (UN, 2005). By purchasing real estate, making commercial investments, and introducing new consuming habits, the newcomers helped Amman's economy. The city rapidly developed new cafes, restaurants, hypermarkets, and malls that provided WI-FI connections to satisfy the users' needs, in addition to expanding existing telecommunication and modern infrastructure in response to the new, rising consumption pattern (Pilder, 2011). The development of a new urban (digital technologies) paradigm is enabled by new communications systems, which connect operational city systems.

Figure 2. The emerged International High-Tech style of high-rises in Amman

Figure 3. Using huge areas of glass in cladding the facades of buildings

Furthermore, the information technology revolution has changed the use of construction materials to represent modern aesthetics; several shops, for instance, replaced the local stone with enormous quantities of glass, and sometimes with colorful aluminum composite sheets known as Alucobond sheets (Zalloom, 2020). The growth of high-rises and retail centers with luxurious facilities and infrastructure for the elite is an obvious illustration of urban reformation and the formation of spatial organization (Al-Faouri, 2011). These high-rises are made of irregular and cubic glass pieces. Showcase glass-unit and aluminum-sheeted buildings, which display a standardized architecture while supporting technology and its innovative successes (Figure 2, Figure 3). High-rise buildings were viewed by decision-makers as a crucial answer for meeting the demand for residential projects, addressing the rapid growth in land value, and lowering the infrastructure costs associated with

horizontal expansion. Even if the economic factor is important, no effort has been made to preserve the urban form's general characteristics.

The micro-scale of architecture and the macro-scale of urban landscape were impacted by this transformation and began to adopt the Hi-Tech style which is also known as the global style. As a result, the city becomes an exhibition of different architectural languages that reflect power and prosperity. Buildings represent techno-capitalism, promote the environment that suits the consumer capital, and symbolize technical signifiers inside and outside them (Figure 4). The culture of globalization threatens the cityscape as ready-made products are installed everywhere, and privately built structures with various Hi-Tech designs dominate how the city is perceived.

Figure 4. The use of technology inside various types of buildings

The socio-spatial character of Amman was presented through its outdoor spaces, squares, markets, and piazzas. Public steps were built along pedestrian walkways to enhance the city's distinctive urban character as it slowly grew from its center. Today, working from home makes life and work easier. People who live in one region might be employed by firms in another region by using technology. Digital communications have established themselves in both the industrial and service sectors. Electronic mail quickly takes the role of paper mail and minimizes people's movement and the use of transportation (Mozuriunaite, 2016; Juceviþius, 2007). Moreover, the great demand for real estate has caused spatial and social division since rising land and property values are forcing residents to move to the city's outskirts, where costs are still reasonable. All these factors affected the role of public spaces.

The benefits of new technology lead to new transportation requirements and societal behaviours that have an impact on the existing urban infrastructure. The spread of the internet and virtually active systems alter social mores, a nation's cultural legacy, and how its citizens use cities (Mozuriunaite, 2016). This type of technological advancement causes a reaction that will inevitably have an impact on other variables. Physical movement and living in an urban environment are no longer necessary for intellectual work. This type of digital mobility reduces interpersonal interactions and socializing. Cities that are growing assimilate, change, and shrink as a result of the mixing and interdependence of their physical structures.

Recommendations: Strategies to Preserve the Uniqueness of the City

This section suggests some strategies to preserve the uniqueness of the city while keeping up with modern technology. The study shows that Amman's recent history serves as an example of how techno-capitalism influences urban identity and helps in spreading the High-tech architectural style. The failure of modernist and regionalism architects, as well as the impact of local businesses in reshaping the city, were clear indications of a lack of policy and the absence of a defined strategy or vision for the growth of the city. The Amman case confirms that technology, as well as capitalism, have affected the cityscape and created a fragmented cityscape that harms social life. Therefore, a comprehensive approach is required to fulfil the investment needs and implement technology while preserving the identity of the city and its lure.

Practical tactics to control the city and its distinctiveness should be used, and new forms of governance must be connected to novel approaches to preserve the uniqueness of the city. This is how urban threats may be transformed into urban threads. The initial stage is creating a city-wide agenda by conducting a thorough

evaluation of how existing public areas are currently operating. Each district should be included in this evaluation, along with residents and other shareholders. Such a district-by-district strategy motivates locals and decision-makers to revisit their neighborhoods and discover unanticipated opportunities. Spaces that are not being used or are being used inefficiently can be discovered and upgraded. Social innovation strengthens the sense of place identity by giving a chance to expand the public realm for public participation, ingenuity, cohesion, and creativity. Where place-making is well-established, the community and the local cooperation are the experts in the process of developing sustainable, dynamic, and distinctive public spaces that really benefit the residents.

Further steps are taken by various cities to develop the urban form and strengthen their cultural heritage, including direct investment in cultural tradition to enhance the area's unique character; promoting quality of life and place distinctiveness worldwide to attract businesses and skilled labor; preserving the historical customs and values; scheduling festivals in the historical context; hiring knowledgeable tour guides; restoring ancient public places and giving them various purposes that the residents may experience and enjoy in their everyday lives. In addition to addressing the physical component, these activities bring new usages for the built environment.

These strategies can additionally include reshaping the social fabric through enhancing social activities, comprehensive governance for the developments and their amenities, and finally, public involvement in decision-making and planning. The public viewpoints are the most valuable sources of knowledge because they can precisely choose what makes their cities an attraction.

Scientific Ethics Declaration

The author declares that the scientific ethical and legal responsibility of this article published in EPSTEM journal belongs to the author

Acknowledgements or Notes

* This article was presented as an oral presentation at the International Conference on Technology, Engineering and Science (www.icontes.net) held in Antalya/Turkey on November 16-19, 2023.

* The author acknowledges the Scientific Research Deanship at Zarqa University for supporting this research.

References

Al-Faouri, R. (2011). *Assessment of the economic impact of ICT on: Real estate, renting and business activities, the case of Jordan*. Amman: Ministry of Information and Communications Technology.

Antrobus, D. (2009). Three stories of Salford: transformation, identity and metropolitan peripheries. *North West Geography, 9*(2).

GAM. (2022). *Amman story*. Retrieved from www.aCmmancity100.jo/en/content/story-amman

Geyer, H. (2002). *International handbook of urban systems: Studies of urbanization and migration in advanced and developing countries*. Edward Elgar Publishing

Juceviþius, G. (2007). *Innovative cities and region: monograph*. Kaunas: Technologija.

Kostof, S. (2009). *The city shaped: urban patterns and meanings through history*. London: Thames & Hundson Ltd.

Lin, R. (2010). *Urban renaissance: A blueprint for creative city Tainan*. (Unpublished master's thesis). Erasmus University, Rotterdam.

Madanipour, A., & Hull, A. (2001). *The governence of place: Space and planning processes* (1st ed.). Burlington: Ashgate Publishing Company.

Mozuriunaite, S. (2016). *Technological factors determining transformation of urban functions in Lithuanian cities*. Proceeding from *WMCAUS 2016 Conference*, *161*, 1899-1903.

Oktay, D. (2002). The quest for urban identity in the changing context of the city: Northern Cyprus. *Cities, 19*(4), 261–271

Pilder, A. (2011). *Urbanization and identity: The building of Amman in the twentieth century*. (Unpublished master's thesis). Oxford: Miami University.

S-assen, S. (2006). Urban sociology in the 21st century. In D. Bryant & L. Peck (Ed.), *Locality and social life* (pp.476-486). London: SAGE Publication.

Stevens, Q. (2007). *The ludic city: Exploring the potential of public spaces*. Oxford: Routledge.

United Nations- UN. (2005). *Urbanization and the changing character of the Arab city*. New York, NY: ESCWA.

Zalloom, B. (2018). Tracing the cityscape transformation under capitalism: The case study of Amman. *Journal of Urban Regeneration & Renewal, 12*(1), 54-71

Zalloom, B. (2020). The importance of studying human perception when designing high-rises and their surrounding environment: The case study of Amman city. *Journal of Urban Regeneration & Renewal, 14*(2), 172-186.

Author Information

Bushra Zalloom
Associate Professor, School of Architecture,
Zarqa University, Zarqa, Jordan
Contact e-mail: *bzalloom@zu.edu.jo*

To cite this article:

Zalloom, B. (2023). The effects of technological aspects on the formation and transformation of cities: The case of Amman. *The Eurasia Proceedings of Science, Technology, Engineering & Mathematics (EPSTEM), 26*, 202-207.

The Eurasia Proceedings of Science, Technology, Engineering & Mathematics (EPSTEM)
ISSN: 2602-3199

The Eurasia Proceedings of Science, Technology, Engineering & Mathematics (EPSTEM), 2023

Volume 26, Pages 208-216

IConTES 2023: International Conference on Technology, Engineering and Science

Adapted FMECA for Supporting Maintenance Actions

Suzana Lampreia
Portuguese Naval Academy, Naval Research Centre – CINAV

Valter Vairinhos
Portuguese Naval Academy, Naval Research Centre – CINAV

Victor Lobo
Portuguese Naval Academy, Naval Research Centre – CINAV

Teresa Morgado
ISEL, Lisbon School of Engineering, Polytechnic Institute of Lisbon

Abstract: In a Navy ship the knowledge of the equipment's and systems state are a pillar and a necessity for operation success. Nowadays equipment's are monitored with multiple sensors, and data are storage and processed through automatic systems. However, the data is not always useful, and most of the times it is never putted into useful data. The maintenance management in the organization understudy are made based in the maintenance management system and based in the opportunity and attributed missions considering good sense decision of the responsible engineers. The actual systems allow decision based on registered data. With this study, we intend to develop a FMECA risk analysis considering a selection of a navy ship equipment's. The FMECA methodology will be adapted to include various severity parameters and data from equipment's condition control. The result of adapted FMECA will give the risk of the equipment operation. For that, considering some maintenance action doesn´t occurred in time, it would be defined some strategies of mitigating the risk. With this methodology, we intend to build a support decision making system for the maintenance management based on risk.

Keywords: FMECA, Maintenance, Decision, Condition control

Introduction

Maintenance is a necessity of current equipment´s and systems in various industrial contexts. In the Portuguese Navy ships represent complex systems with amounts of installed sensors and data produced by the modern mechanical and electronic systems.

To maintained equipment and systems operationality many preventives and sometimes corrective actions may be taken. In the organization there is a strong and well stablished maintenance plan that allows the ships good performance. But there are some procedures that can be enhanced with the objective of optimizing maintenance performance and well cost management.

The motivation of this study is centered on the:

- Environment of scarce resources, human and material for ships maintenance.
- Need to implement a leaner maintenance system.
- Develop a dynamic maintenance support system based in a decision-making software.

This work are divided in chapters where at first it was made a state of the art in the area of ship maintenance and the methodologies that may be applied to treat data, then it was focus on the Failure Mode, Effects and Critically Analysis, it is also exposed actual organization in surface ships in the Portuguese Navy, then the methodology of monitoring and treat data it is present, follow by the case study with FMECA applied to propulsion diesel engines, and then the results are present and some mitigating strategies are exposed.

Maintenance Management Based on Data

There are some environments, because of timing, economic context, localization of the ships, that does not allow performing some maintenance actions, in that case prioritize maintenance, assuming that not all maintenance can be performed (US Navy, 2015) can be one logic strategy to concretize only what must essentially be do it to maintain a ship navigating with a good level of operationality.

The maintenance that is not performed should be reallocated also according to future prioritization. To implement these strategies, decision trees were used by US Navy (2015), so it is believed that is possible to implement some techniques that it will enhance maintenance management also in Portuguese Navy.

In the naval industry, the Fragility and Criticality (FaC) methodology is used to study the probability of any maintenance being discontinued (Button, 2015; Martin et al., 2017). The criteria from condition monitoring maintenance should be detailed, for example: in flight hours of a helicopter, it should be discriminated the time it flies over sea in a saline environment and the time it flies over land (Tinda et al, 2021). The condition based maintenance should be used in substitution of the maintenance based in functioning time (Tinda et al, 2021).

The factors that influence decisions about maintenance on warships are the need of reduce costs and the difficulties on scheduling maintenance given the availability of shipyards (Blanton, 1997). A qualitative analysis of the life cycle status of surface ships of the United Kingdom Royal Navy (RN) was made to reducing costs in the military (Ford et al., 2015). US Navy surface ships was being modernized considering that it was intended to be implemented a fault prediction system (Lee, 2020). The ship maintenance strategies should be integrated and planned when project and construction is made, if it is so, may be the process of future maintenance intervention will be agile and adaptive (Eckstein, 2020).

To carry out a maintenance planned system on ships three steps were proposed by Cullum et al. (2018): “Risk Assessment-Condition Monitoring and Machine Learning”, “Maintenance Scheduling-Decision Theory” and “Quantify Availability and Overall Maintenance Cost”. Some methodology regarding these three steps may be implemented in the Portuguese Navy. A computerized maintenance management system (CMMS) was proposed to be applied in military ships, considering automation and respective sensors (Dragos et al., 2020). The actions before its implementation:

- ✓ Planning.
- ✓ Software preparation vs control attributes.
- ✓ Process for obtaining the data.

If ships maintain a record of anomalies to prevent the occurrence of similar damages, it will be possible to measure performance of the implemented maintenance and make proposals for improvement (Alhouli, 2011). Certain statistical methodologies can effectively contribute to the implementation of condition based maintenance. Lampreia et al. and Vairinhos et al. (2015) had applied respectively modified control charts and biplots for data analysis.

The Implemented System in the Organization

The Portuguese Navy (Marinha, 1984) has implemented a data collection and processing system since the 1980s, computerized in the 1990s, with software, SICALN, first in an MS-DOS environment, and later in an ORACLE environment. This system is now also being evaluated for possible enhancement and substitution.

In the Data Collection and Treatment System (SRTD), there is no systematic statistical treatment of the collected data, it is only available for consulting. “The life cycle of a ship is defined as the period of time elapsed from its conception to its alienation. (Marinha, 2020) To keep the ships operational, during their life cycle there may be maintenance interventions that can have three stages of maintenance (Marinha, 2020) :

- The 1st stage;
- The 2nd stage;
- The 3rd stage;
- These processes of maintenance and recovery of the operationally of the means are possible through the technical coordination of the various organization members involved.

The Portuguese Navy Maintenance organization inspired in the current normative but adapted to its reality consists in the preventive maintenance and corrective maintenance, the first it is subdivided in the systematic and the conditioned, and the second: the current, eventual, urgent, and very urgent. Sometimes in the corrective maintenance another maintenance "figure" appears, the contingency maintenance, where only the essential corrections are made do accomplished some ship mission.

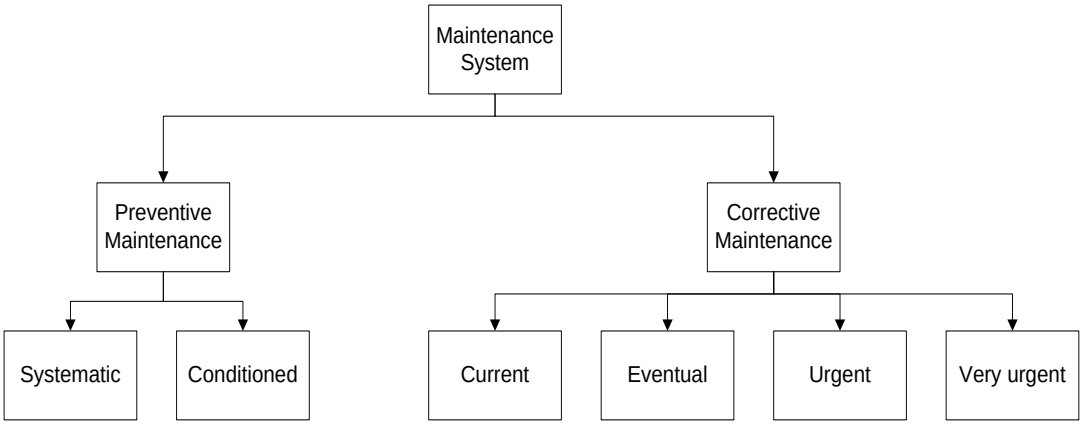

Figure 1. Maintenance organization

The current model maintenance management is considered to have the following general characteristics:

- It is a strong model in Normative and organizational basis.
- It is inflexible.
- The crossing of data is done based on the common sense of the maintenance project managers.

It was a very strong and good maintenance management plan when ship´s Navy came in the seventies and eighties, but nowadays need some upgrade to treat data from equipment´s. It is believed that the actual work may contribute for enhance the maintenance management in surface ships.

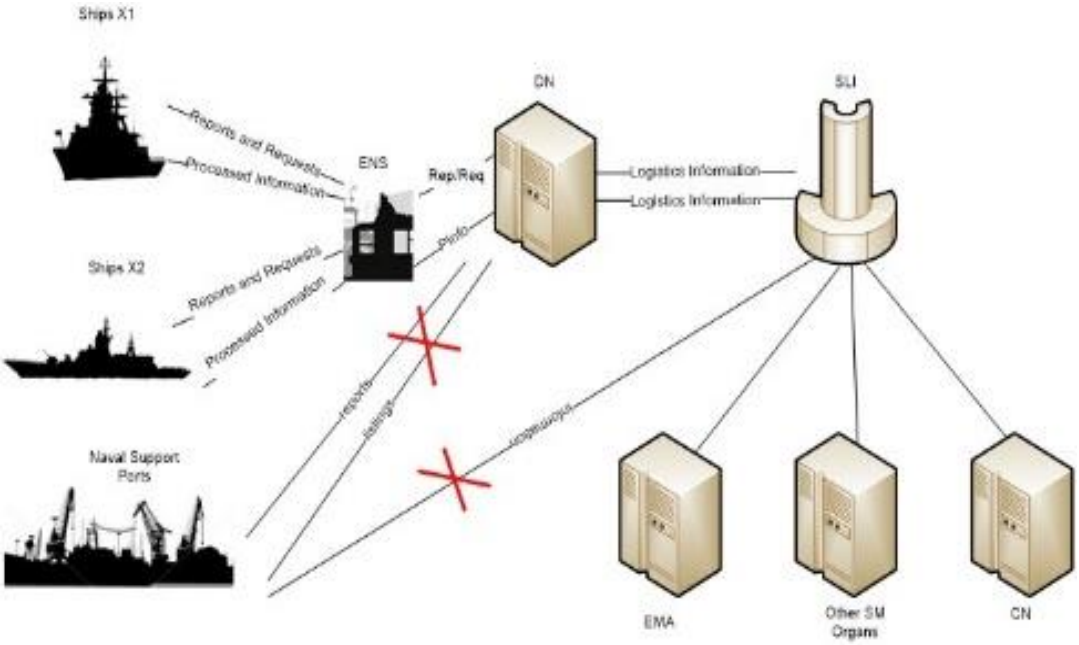

Figure 2. SRTD flux

In the actual SRTD flux, a request or report it is generated in the ships which represents the first level for maintenance in the ship, this procedure is made in the SICALN, then the Administrative Command with its specialist made the first triage and decide if it is a work for the operational workshop or for the Shipyard. If it is not for the operational workshop the work it is forwarded to the Technical Direction, after evaluation the request is sent to the Shipyard.

Methodology

The methodology to proceed to the study begin with the equipment selection for the study, then the sensors selection, the data selection, then the FMEA is applied, then define the levels of FMECA parameters, then decide which control condition parameters will contribute for the results, then calculate the FMECA-CC and if the results are not acceptable it should return to the beginning of the process, if it are the results should be crossed with the results of others equipment's, and then it is decided if we should proceed to a maintenance action or not, if not, the we should monitor the equipment state by continuously observing the results of FMECA-CC, if yes we procced to a maintenance action.

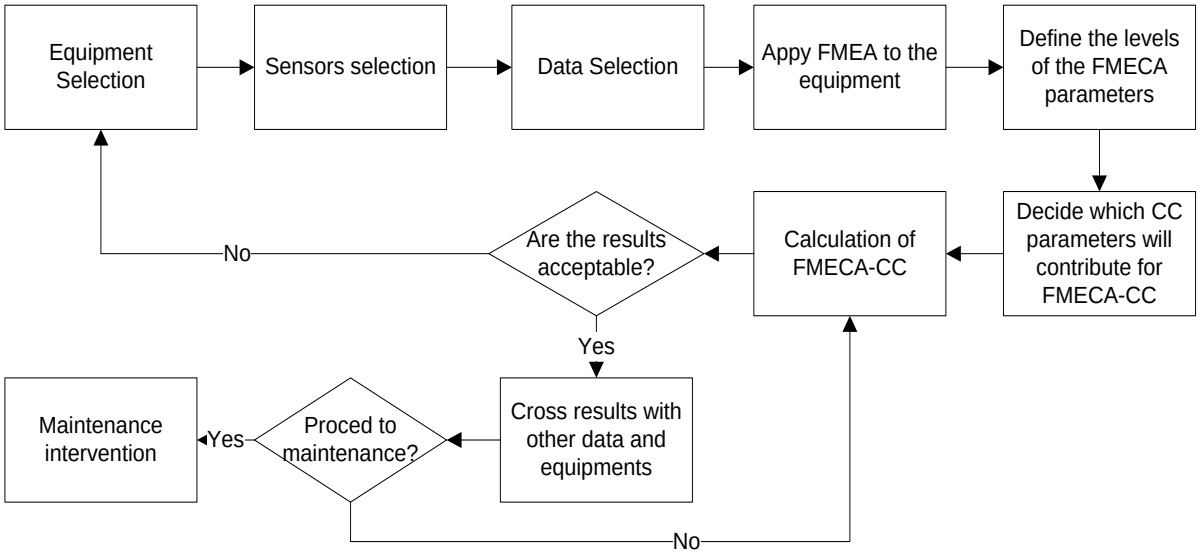

Figure 3. FMECA-CC methodology

Case Study

The maintenance life cycle is defined as the "time elapsed between entry into service and the end of the first interim overhaul, or between the completion dates between two consecutive interim overhauls." (Marinha[i], 2020). The maintenance plan for Portuguese Navy ship under study, is a 5-year cycle, where the first 23 month correspond to an operational state, then a small revision with the duration of 2 months, then another 23 months on an operational state, and finally a period of intermediate revision of 12 months considering docking of 5 months.

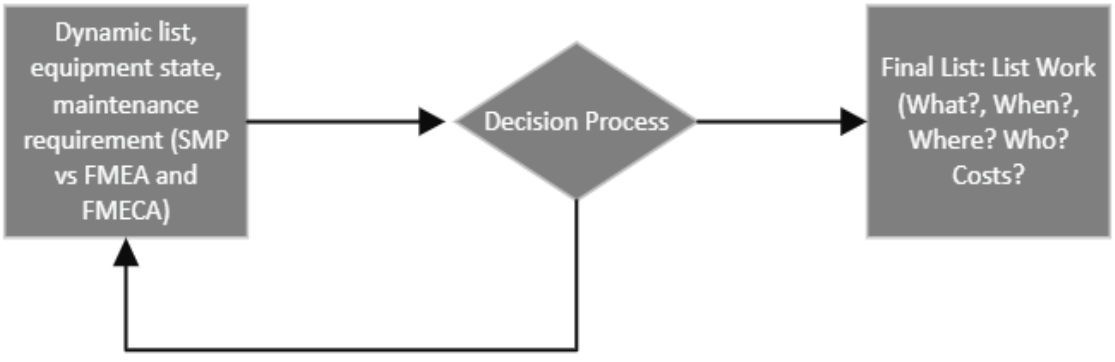

Figure 4. Basis decision process

Basis decision process starts with the equipment and its sensors, Fig. 4, where it should exist a dynamic list which is fed by the equipment's sensors and by the registering of some maintenance action in the SRTD and maybe another systems, based on what the FMEA and FMECA are built.

The equipment´s selected to be exposed in this study are two diesel engines from ship with combined propulsion. The characteristics of the selected diesel engines (Diesel engines 1163 TB83) are:

- 12 cylinders in V;
- 1163 - Engine series, 100 strokes from a cylinders in litters;
- T – Turbocharger engine;
- B – Air cooler, with cooled pistons;
- 8 – Maritime propulsion engine;
- 3 – Project digit;

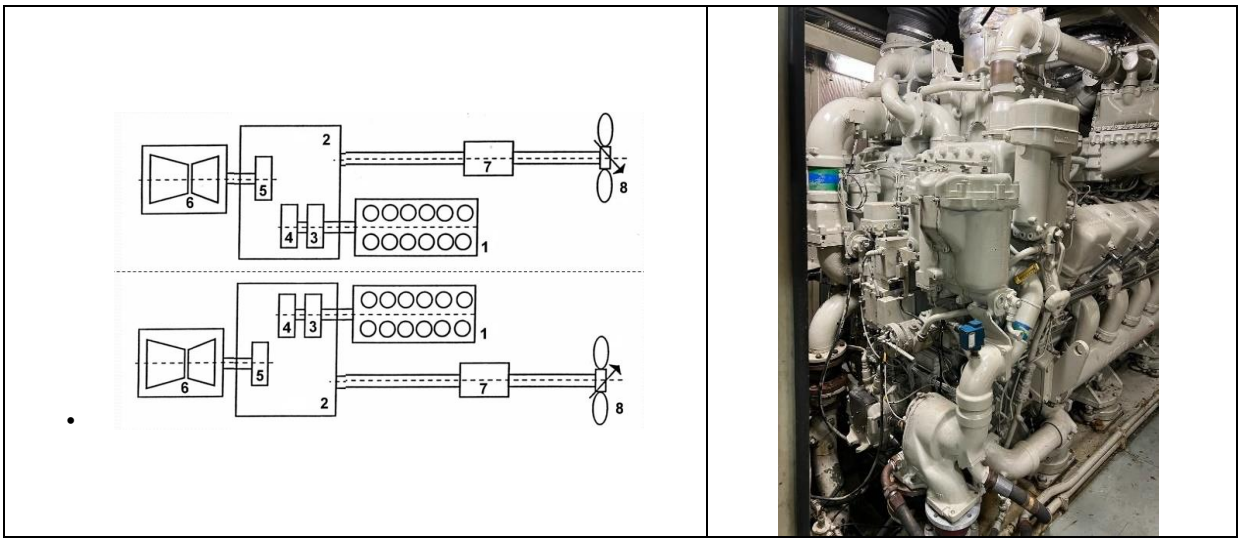

Figure 5. Propulsion system and engines understudy

For risk assessment various methodologies may be used. In the maintenance area Failure Mode and Effect Analysis (FMEA) and Failure Mode, Effects and Critically Analysis (FMECA) may be one of the applicable methodologies. First and before the risk evaluation it was applied a FMEA, Table 1. It was used the data from the existing maintenance plan system, and the aspect, impact and how to detect was developed according to the perception of the authors.

Table 1 – Applying FMEA for risk analysis on propulsion diesel engines.

Man.Act. Motors	Aspect	Impact	How detect
Verify evacuation gas colors, condensations, obstructions, etc	Inadequate gas color	Inadequate fuel mixture/Valves out of tune	Observing gas outsider methodology
While sailing, check the color of the exhaust gases, condensation, obstructions, etc.	Inadequate gas color	Out of calibration injectors/Excessive fuel consumption	Observing gas outsider methodology

Then to calculate the FMECA results it was used equation nr 1. Where the O it's the probability of occurrence, S the severity and D de detection facility.

$$RPN_{DM}=O*S_m*D* \quad (1)$$

It was considered 5 Severities: Safety, Environmental, Equipment, Personnel, Operational; and for FMECA overhaul calculus the mean of it $St=mean(S_S;S_E;S_{eq};S_P;S_O)$.

Results

On Table 2 we observe the results of FMEA and FMECA. It is to be referred that although the results, the FMEA, data and even the risk evaluation, should be, in the future work, verified using the opinion of other specialist that can attribute some other leve

Table 2. Applying FMECA for risk analysis

Man.Act. Motors	Aspect	Impact	How detect	S_S	S_E	S_{Eq}	S_P	S_O	O	D	FMECA	CCV	CCT	CCP	CCTex	FMECA_CC
Verify evacuation gas colors, condensations, obstructions, etc	Inadequate gas color	Inadequate fuel mixture/Valves out of tune	Observing gas outsider methodology	1	4	5	3	1	1	1	2,8	1	1	3	1	5
While sailing, check the color of the exhaust gases, condensation, obstructions, etc.	Inadequate gas color	Out of calibration injectors/Excessive fuel consumption	Observing gas outsider methodology	1	5	5	5	4	1	1	4	3	2	3	3	10

The scales of St are stated in table 3, where it was considered five levels of severity, security severity, environment severity, equipment severity, severity on people and operational severity.

Table 3. Applying FMEA for risk analysis

Value Atribution	Security Severity (SS)	Environment Severity (SE)	Equipment Severity (SEq)	Severity on People (SP)	Operational Severity (SO)
0,1	No impact	No impact	No impact	No impact	No impact
1	Light impact	Light impact	Light impact	Light impact	Light impact
2	Impact medium severity	Impact medium severity	Equipment operating without security systems	Impact on health	Severe impact
3	Severe impact	Severe impact	Equipment operating in general degraded mode	Impact on health with absence from service	Ship limited
4	Inoperative Ship	Impact on the interior of the ship	Equipment operating in general degraded mode	Permanent health damage	Limop ship at risk of imminent failure
5	Impact on ship safety	Aggravated internal and external impact	Ship INOP_Equipment inoperative without redundancy	Life risk	Inoperative Ship

For the parameterization of the occurrence and detection it was defined 6 levels of value attribution, Table 4.

Table 4. Levels of occurrence and detection

Value Atribution	Ocurrence (O)	Detection (D)
0,1	Occurred more than 10 years ago	Easy detection
1	It occurred between 5 and 10 years ago	Detection difficulty medium low
2	Occurred less than 5 years ago	Medium difficulty detection
3	Occurred less than 1 year ago	Detection difficulty medium high
4	Occurred less than 6 months ago	Deteção dificuldade extremamente alta
5	Permanently	Not detectable (Till something goes wrong)

For the FMECA-CC it was considered various scales for condition control: CC-CCV for vibration (Root mean Square (RMS) values; CCT for thermography and CCTex where the text from SRTD is considered for respective equipment, Table 5.

Table 5. CC cathegorization

Value Atribution	Vibration (CCV)	Termography (CCT)	Operating Parameters (Temperatures or Pressures) (CCP)	Detection Text about engine and corrective maintenance
1	Low level	Low level (no difference)	Low level	No occurrence in the last 5 years
2	Low medium level	Low medium level (1º - 4ºC difference from normal)	Low medium level	Occurred once in the last 5 years
3	Middle level	Average level (4º - 15ºC difference from normal)	Middle level	Occurred between 2 and 5 times in the last 5 years
4	High middle level	Medium high level (difference 15ºC and maintains)	High middle level	Occurred 5 to 10 times in the last 5 years
5	High level	High level (difference >15ºC from normal) star_border	High level	Occurred more than 10 times in the last 5 years

FMECA vs FMECA-CC

Comparing the results of traditional FMECA and FMECA-CC it was verified a higher sensibility of FMECA-CC, Table 6, where the data from equipment condition control are used. So condition control data will allow an adjustment of the results of the originally FMECA.

Table 6. Comparing traditional FMECA and FMECA-CC

Diesel Propulsion Engines – Maintenance activity	Aspect	Impact	How detect	FMECA	FMECA_ CC
While sailing, check the color of the exhaust gases, condensation, obstructions, etc.	Inappropriate gas color	Inadequate fuel mixture/Valves out of tune	Method of observing gases abroad	2,8	5
While sailing, check the color of the exhaust gases, condensation, obstructions, etc.	Inappropriate gas color	Out of calibration injectors/Excessive fuel consumption	Method of observing gases abroad	4	10
While sailing, check the color of the exhaust gases, condensation, obstructions, etc.	Inappropriate gas color	Fuel carryover/fire risk	Method of observing gases abroad	4	7
While sailing, check the color of the exhaust gases, condensation, obstructions, etc.	Inappropriate gas color	Lack of rim seal/lubrication oil carryover/fire risk	Method of observing gases abroad	4	6

Also, the study in others equipment´s may be considered for implementing FMECA-CC, equipment´s like Air Compressor & Oil and Marine Gasoil Centrifugal purifier. If the knowledge of overall equipment´s is a reality, may the decision be to proceed to parallel maintenance during maintenance to main engines. If decision is to proceed to an intervention in the diesel engine, and if the risk in the compressor is high and it can be done during the engine maintenance. The same for centrifugal purifier or other equipment´s.

Although the obtained results, not only the equipment's state, but also the opportunity to proceed to a maintenance in the operational period of the ship and the material and personal resources are important and to be accounted in the maintenance process. Strategies for mitigating the calculated risk may be when some

anomaly is detected and there is no possibility of intervention, the equipment's monitor should be more frequent and some minor maintenance intervention (contingency), without put the equipment out of service, may be made.

Conclusions and Future Work

In an environment of scarce material and human resources a dynamic maintenance management may be a solution for optimize the resources. Before implementing a dynamic maintenance management system, the previous data and implemented processes were analyzed. FMEA and FMECA may be a base for a maintenance decision support system applied to equipment system plan.

The registered information considered for the decision support system applying an FMECA-CC are: equipment´s maintenance system plan, the condition control data (Vibrations/thermography/parameters/data-text registered-DSM58). Application of dynamic work lists may lead to maintenance optimization and consequently reducing cost in material and personnel.

For future work the FMECA must be validated on job, Finish the data analysis using the risk analysis methodology, finish the FMECA analysis and integrate other related equipment´s and choose the best methodology for the presented data.

Scientific Ethics Declaration

* The authors declare that the scientific ethical and legal responsibility of this article published in EPSTEM journal belongs to the authors.

Acknowledgements or Notes

* This article was presented as an oral presentation at the International Conference on Technology, Engineering and Science (www.icontes.net) held in Antalya/Turkey on November 16-19, 2023.

* This work is supported by Portuguese Naval Academy and CINAV and acknowledged for the collaboration of Lisbon School of Engineering, Polytechnic Institute of Lisbon.

References

Alhouli, Y. (2011). *Development of ship maintenance performance measurement framework to assess the decision making process to optimise in ship maintenance planning*. (Doctoral dissertation). Faculty of Engineering and Physical Sciences, School of Mechanical, Aerospace and Civil Engineering.

Blanton, G. (1997). The future of navy ship Maintenance – one point of view. *Journal Ship Production and Design, 13* (2), 147-152.

Button, W., Martin, B., Sollinger, J. M., & Abraham, T. (2015). *Assessment of surface ship maintenace requirements*. Santa Monica, California: Rand Corporation

Cullum, J., Binns, J., Lonsdale, M., Abbassi, R. & Garaniya, V. (2018). Risk-based maintenance scheduling with application to naval vessels and ships. *Journal of Ocean Engineering 148*, 476-485.

Dong, H., & Tsai, S. (2021). An empirical study on application of machine learning and neural network in English learning. *Mathematical Problems in Engineering, 2021*(1), 1- 9.

Dragos, S., Pucarea, A., Cotorcea, A. & Florin, N. (2020). Maintenance onboard ships using computer maintenance management system. *Scientific Bulletin of Naval Academy, 23*(1).

Ford, G., McMahon, C. & Rowley, C. (2015). An examination on significant issues in naval maintenance. The fourth *International Conference on Thought-life Engineering Services, 38,*197-203.

Lampreia S., Requeijo J., Dias J., & Vairinhos, V. (2015). Implementation of MEWMA control chart in equipment condition monitoring. *Journal of Vibration Engineering & Technologies, 3*(6), 667-677.

Lee, C. (2020). Just in: Navy looking for better approaches to ship maintenance. Retrieved from https://www.nationaldefensemagazine.org/articles/2020/8/25/navy-works-to-tackle-ship-maintenance,

Marinha. (2020). Ciclos de manutenção das unidades navais e helicópteros (ILDINAV801). *Direção de Navios*.

Marinha. (1984). *Manual do sistema de recolha e tratamento de dados (srtd) (ILMANT512)*. Direção de Navios.

Martin, B, McMahon, M., Riposo, J., Kallimani, J., Bohman, A., Ramos, A., & Schendt, A. (2017). *A strategic assessment of the future of U.S. navy ship maintenance: Challenges and opportunities.* Santa Monica, California: Rand Corporation.

Vairinhos, V., Parreira, R., Lampreia, S., Lobo, V., & Galindo, P. (2018). Vibration analysis based in HJ-biplots. *International Journal of Prognostics and Health Management*, 1-10.

Author Information

Suzana Lampreia
CINAV- Escola naval/ Naval Research Centre - Portuguese Naval Academy.
Base Naval de Lisboa, 2810-001 Almada, Portugal
Contact e-mail: *suzanalampreia@gmail.com*

Valter Vairinhos
CINAV- Escola naval/ Naval Research Centre - Portuguese Naval Academy.
Base Naval de Lisboa, 2810-001 Almada, Portugal

Victor Lobo
CINAV- Escola naval/ Naval Research Centre - Portuguese Naval Academy.
Base Naval de Lisboa, 2810-001 Almada, Portugal

Teresa Morgado
ISEL, Lisbon School of Engineering, Polytechnic Institute of Lisbon.
Rua Conselheiro Emídio Navarro, 1 1959-007 Lisboa, Portugal

To cite this article:

Lampreia, S., Vairinhos, V., Lobo, V., & Morgado, T. (2023). Adapted FMECA for supporting maintenance actions. *The Eurasia Proceedings of Science, Technology, Engineering & Mathematics (EPSTEM), 26*, 208-216.

The Eurasia Proceedings of Science, Technology, Engineering & Mathematics (EPSTEM)
ISSN: 2602-3199

The Eurasia Proceedings of Science, Technology, Engineering & Mathematics (EPSTEM), 2023

Volume 26, Pages 217-224

IConTES 2023: International Conference on Technology, Engineering and Science

Assessing the Effects of Alluvial Transport in the Kizilirmak River on Dams with Local, Photogrammetric and Remote Sensing Methods

Oyku Alkan
Graduated Istanbul Technical University

Muntaha Kassim Alzubade
University of Technology of Baghdad

Mehmet Nurullah Alkan
Hitit University

Abstract: Naturally transported sand, clay, and gravel-like blocks by rivers cause a decrease in water flow and flow velocity. Additionally, uncontrolled disposal of waste materials into the riverbed increases adverse effects and endangers natural life. Over time, the alluvium generated by natural and external factors in river and creek beds leads to flood risks that pose a significant threat to life and property. These sediments, known as alluvium, accumulate in favorable locations in valleys and form alluvial beds with spread movement to broader areas. In Turkey, interventions in river branches and creek beds, as well as insufficient preventive measures, have kept floods a hot topic. To eliminate these issues, it is crucial for every organization to take comprehensive measures and increase environmental awareness by addressing similar areas in large projections. The Kızılırmak River, originating from the Kızıldag slopes in the İmranlı district of Sivas province and passing through the Çorum province before reaching the Black Sea at Bafra Cape, also harbors alluvial risks and adverse effects. It holds significant importance for energy production with 12 dams and hydroelectric power plants (HES) on the river. Additionally, the Pirinçli Hydroelectric Power Plant, with a transmission structure of 13,756 meters between Dodurga district of Çorum province and Güvercinlik and Kumbaba Villages, plays a vital role in electricity production in the region. The Pirinçli HES is located downstream of the Obruk Dam constructed by the State Hydraulic Works (D.S.I.) on the Kızılırmak River. It is known that a significant portion of the sediment accumulation between Güvercinlik Dam and Kumbaba Dam occurred before the construction of the Obruk Dam. Hence, preventing risks that could lead to environmental adversities is of paramount importance. In this study, a combined fieldwork was conducted using different methods to determine the areas where sediments accumulated and the alluvial material being transported cuts off the flow velocity of the Kızılırmak River and causes accumulations between the Güvercinlik Dam and Kumbaba Dam. For this purpose, terrestrial measurements, photogrammetric and remote sensing methods were combined and evaluated together to ensure the integrity of the obtained data.

Keywords: Drone photogrammetry, Risk assessment, HEPP, Environmental threats, Remote sensing

Introduction

Blocks such as sand, clay and pebbles carried naturally by streams cause the flow of water and the flow rate to decrease. In addition, waste materials left uncontrolled in the river bed increase the negativities and endanger the natural life.Flood risks caused by these alluviums, which arise from natural and external factors that form in river and stream beds over time, greatly threaten the safety of life and property. These sediments, called alluviums and accumulated in suitable places over time, occupy the ground floor in most of the valleys and form alluvial deposits by spreading to larger areas. Coastal erosion that occurs in waterways as a result of the

construction of structures in coastal areas near estuaries, which are the source of sediment supply, can negatively affect the lives of local residents (Tak et al.,2020). In order to evaluate risks in rivers, a detailed analysis is required whether changes in the flow regime are associated with sudden climate changes. It is important to record hydrogeomorphological basin changes because these processes can occur very quickly and lead to flood events that affect the entire living environment (Salandra et al.,2022).

Floods in Turkey, which occur as a result of interventions in river branches and stream beds and inadequate precautions, always remain hot on the agenda. In order to eliminate the negative effects experienced, it is of great importance for each organization to consider similar areas in wide projections, to always take precautions and to increase environmental awareness. In this context, river bed composition needs to be regularly monitored and updated due to various factors For this purpose, to extract river bed features precisely, UAV-based orthophoto maps are created using photogrammetric techniques. (Liu,2023) .

The Kızılırmak River, which originates from the foothills of Kızıldağ in the İmranlı district of Sivas Province, passes through the borders of Çorum province and reaches the Black Sea from the Bafra cape, also contains alluvial risks and negativities. It has an important place with its energy production with 12 dams and HEPPs on the river. Obruk Dam in Dodurga district of Çorum province and Pirinçli Hydroelectric Power Plant (HEPP), which has a 13756 m long transmission structure located between Güvercinlik and Kumbaba Villages, plays an important role in the region in terms of electricity production. Pirinçli HEPP is located downstream of the Obruk Dam built by DSI on the Kızılırmak River. It is known that the majority of the conflicts between Güvercinlik Dam and Kumbaba Dam took place before the construction of the Obruk Dam. In this case, it is of great importance to prevent risks that may lead to environmental negativities.

Objective

Detection of areas where the sediment accumulated between Güvercinlik Dam and Kumbaba Dam and the alluvial material being transported interrupt the flow rate of the Kızılırmak River and cause accumulations.In this study, a composit fieldwork was conducted using varied methods to determine the areas where sediments accumulated and the alluvial material being transported cuts off the flow velocity of the Kızılırmak River and causes accumulations between the Güvercinlik Dam and Kumbaba Dam. For this purpose, terrestrial measurements, photogrammetric and remote sensing methods were combined and evaluated together to ensure the integrity of the obtained data.

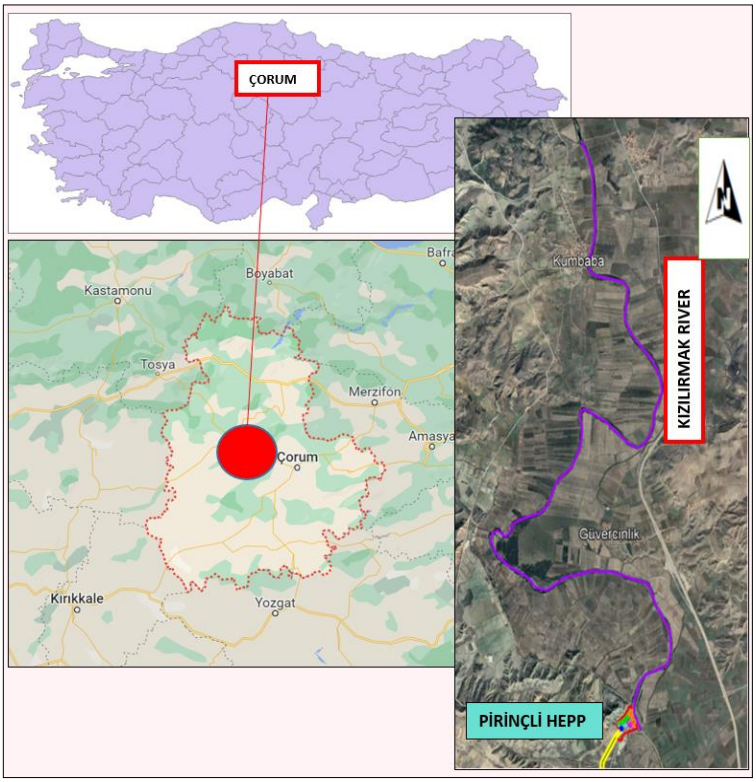

Figure 1. Location of the study area

Study Area and Assessment of Current Situation

The length between Güvercinlik Weir, built next to Pirinçli HEPP, and Kumbaba Weir is around 13 km. In the examinations carried out on this area along the river flow, it was observed that the excessive alluvial material formed in places especially filled the stream beds and blocked the water flow. While the existing Kızılırmak River capacity (Obruk Dam Maximum production capacity) is on average 400 m3/sec, it is estimated that it cannot even carry 100 m3/sec of water due to the fullness of alluvial material. The study area, which was created for the purpose of measuring and determining the depths of the areas where this flow obstacle is concentrated in its current state, is on the Kızılırmak River line in Dodurga District of Corum Province; In the geographical coordinates of 40.51'29.24"N, 34.51'27.98"E Güvercinlik Weir and 40.55'22.04"N, 34.50'52.13"E Kumbaba Weir, it covers the Güvercinlik and Kumbaba settlement areas and the river areas on the tail water side of the Pirinçli HEPP power plant pointed at the satellite image (Figure 1).

Method

Terresterial, Photogrammetric and Remote Sensing

Various methods were used in field studies and the integrity of the data obtained was ensured. For this purpose, terrestrial measurements were evaluated using photogrammetric and remote sensing methods. The work program including all methods is shown in the flow chart (Figure 2).

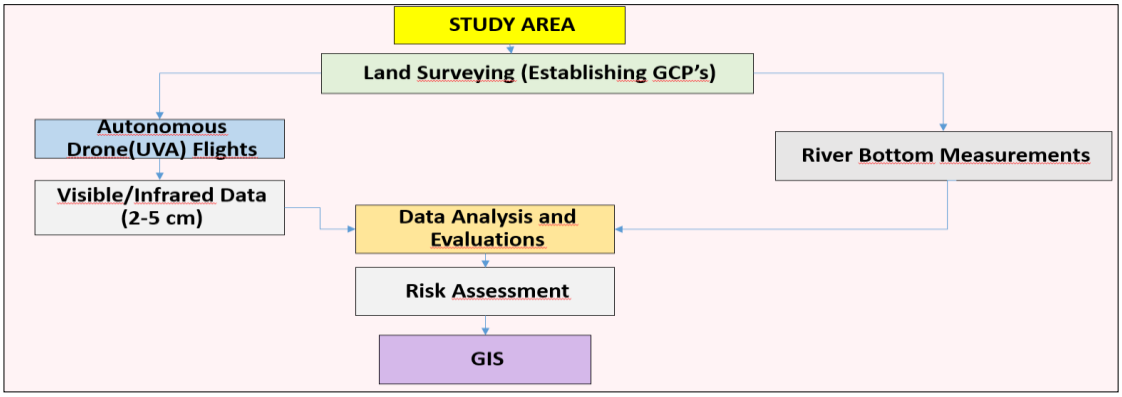

Figure 2. Flow chart of the work schedule

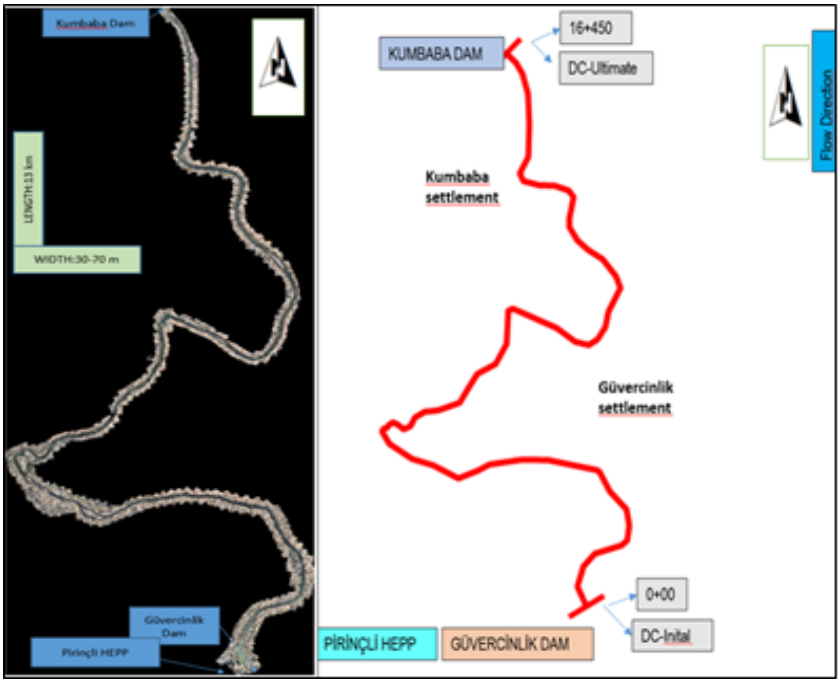

Figure 3. Mosaic image and sattelite image of the study area

Drone Mapping

The length of the Kızılırmak River between Güvercinlik and Kumbaba dams is 13 km, and its width varies between 30-70 m. Orthophoto map production of the study area was made with the 3D drone mapping method as dsm_ortho (Figure 3). 11 planned flights were made for the 13 km area, 27 GCPs (Ground Control Points) were established and coordinate measurements were carried out on a 3D plane, in the TUSAGA Active system. In addition, the study was designed to form a basis for the cadastral map of the region.

River Bottom Measurements

River depth measurements were obtained as DCP (Depth Control Points) in the form of a test point every 50 meters. Test measurements were carried out at 236 DCPs each measuring point for 0+050 to 13+000 is coordinated in three dimensions (Table 1). Measurements were started by taking the Pirinçli HEPP power plant tailwater and completed at the Kumbaba Dam. The depth was measured as 2.40 m at the initial point and 1.20 m at the ultimate point (Figure 4).

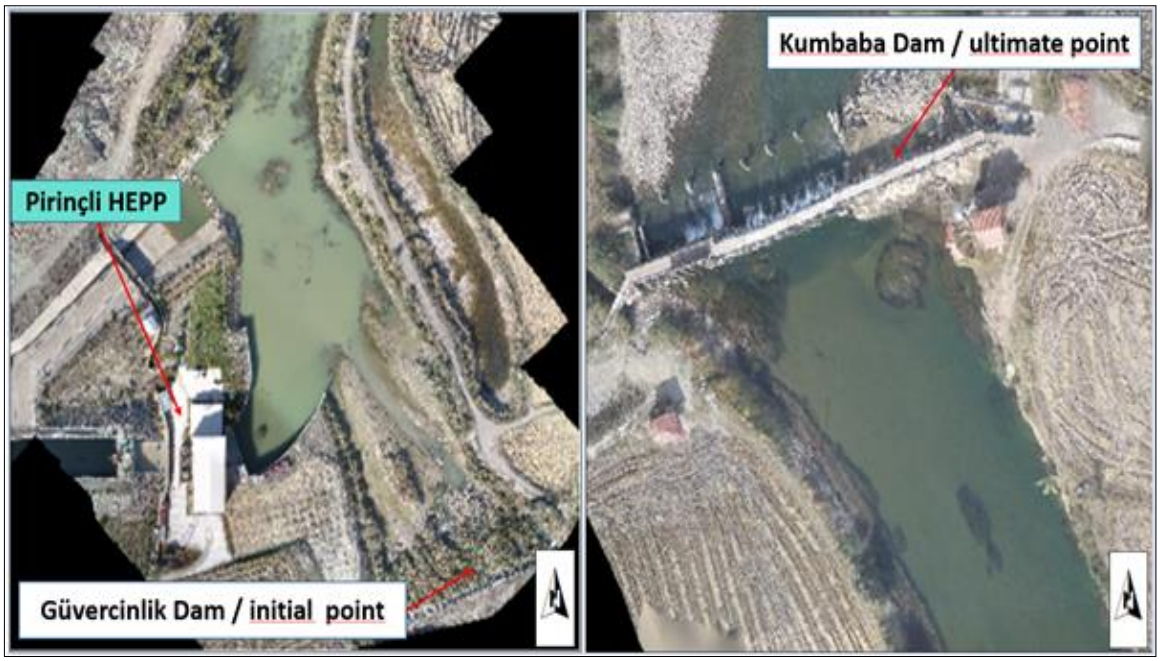

Figure 4. Rendered drone images of initial and ultimate points

Table 1. Brief of the DCPs

4+950	20	5+000	30	3+150	40	0+100	50	3+100	60	0+600	70	0+450	80	0+150	85	4+800	90	1+050	100	0+850	110	0+400	120	0+700	130	1+000	140	0+800	150
5+150	20	4+950	30	3+200	40	0+500	50	3+350	60	4+800	70	1+650	80			5+500	90	1+300	100	3+400	110	0+650	120	1+150	130	1+200	140	0+950	150
5+200	20	5+000	30	3+250	40	0+550	50	4+500	60	4+600	70	2+650	80			6+750	90	1+350	100	4+450	110	1+100	120	1+900	130	1+250	140	1+700	150
		5+100	30	3+300	40	1+600	50	5+350	60	5+700	70	2+700	80			7+200	90	2+500	100	4+650	110	2+600	120	2+550	130	8+700	140	1+750	150
		6+450	30	5+050	40	4+850	50	5+400	60	6+100	70	4+750	80			7+250	90	3+500	100	5+600	110	3+450	120	7+350	130	9+700	140	1+800	150
		6+500	30	5+250	40	4+900	50	5+650	60	6+350	70	4+450	80			7+550	90	3+550	100	6+700	110	3+600	120	9+400	130	9+800	140	1+850	150
		12+70(	30	5+300	40	4+900	50	6+000	60	8+400	70	4+550	80			7+600	90	4+650	100	8+650	110	3+650	120	10+650	130	9+900	140	2+750	150
				6+200	40	5+450	50	6+550	60	8+550	70	4+700	80			8+500	90	4+700	100	9+550	110	3+700	120	10+700	130	13+200	140	3+050	150
				6+400	40	5+850	50	6+950	60	8+600	70	4+750	80			9+500	90	4+850	100	9+600	110	4+400	120	11+400	130			3+750	150
				6+650	40	5+900	50	7+700	60	10+150	70	5+750	80			10+000	90	7+900	100	9+650	110	4+600	120	12+050	130			6+600	150
				7+650	40	6+150	50	8+000	60	10+400	70	5+800	80			10+300	90	8+150	100	9+750	110	6+250	120	12+450	130			7+750	150
				7+950	40	9+000	50	9+250	60	10+500	70	5+950	80			11+100	90	8+900	100	9+850	110	6+800	120	13+300	130			8+850	150
				8+450	40	9+150	50	12+25(	60	11+150	70	6+050	80			11+300	90	10+100	100	10+250	110	7+100	120	13+450	130			9+450	150
				8+950	40	9+200	50			11+200	70	8+200	80			12+900	90	10+450	100	11+050	110	7+150	120					9+950	150
				12+65(	40	10+200	50			12+850	70	8+250	80			14+200	90	10+550	100	11+650	110	7+500	120					11+800	150
				14+50(	40	12+600	50			13+850	70	9+300	80					10+900	100	11+700	110	10+350	120					13+250	150
						14+000	50					9+350	80					11+350	100	12+950	110	10+600	120					13+550	150
												10+050	80					12+200	100	13+400	110	11+250	120					13+600	150
												11+750	80					12+400	100	15+300	110	13+000	120					13+800	150
												12+300	80					12+550	100	15+750	110	14+450	120					13+900	150
												12+350	80					12+750	100	15+800	110	15+450	120					14+650	150
												12+500	80					13+350	100	15+850	110	15+650	120					14+850	150
TOTAL:236 test points												13+950	80					14+150	100	15+900	110	15+700	120					14+900	150
												14+050	80					15+350	100			15+950	120					15+150	150
												14+100	80					15+400	100			16+000	120					15+250	150
												14+550	80									16+450	120					15+500	150
																												15+600	150
																												16+150	150
cm	20		30		40		50		60		70		80		85		90		100		110		120		130		140		150
sum	3		7		16		17		13		16		26		1		15		24		23		26		13		8		28

In the study, which was carried out to identify risky areas where the alluvial material accumulated and sedimented between the Güvercinlik and Kumbaba dams of the Kızılırmak River disruption of the flow rate and the water level was high. The km-depth/measurements obtained as 50 m intervals at DCPs which are considered as test points including 150 cm depths. Distribution of Depth Control Points of test points measured every 50 m is graphed (Figure 5).

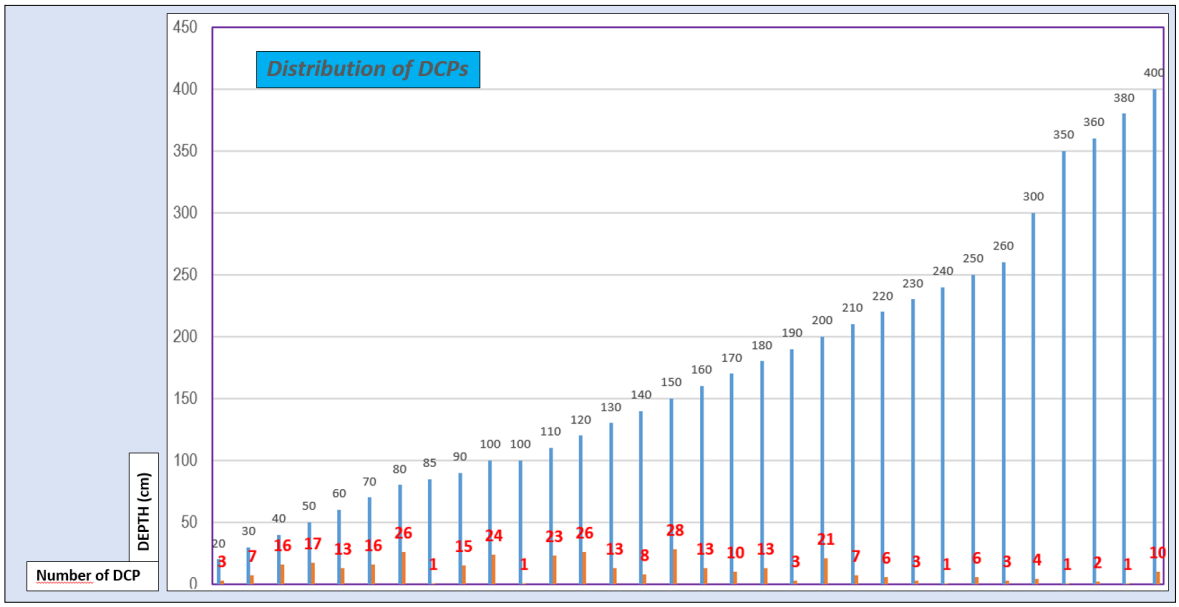

Figure 5. Distribution of the depth control points

Drone images of the lowest and highest depth obtained from the model created for the study area (Figure 6).

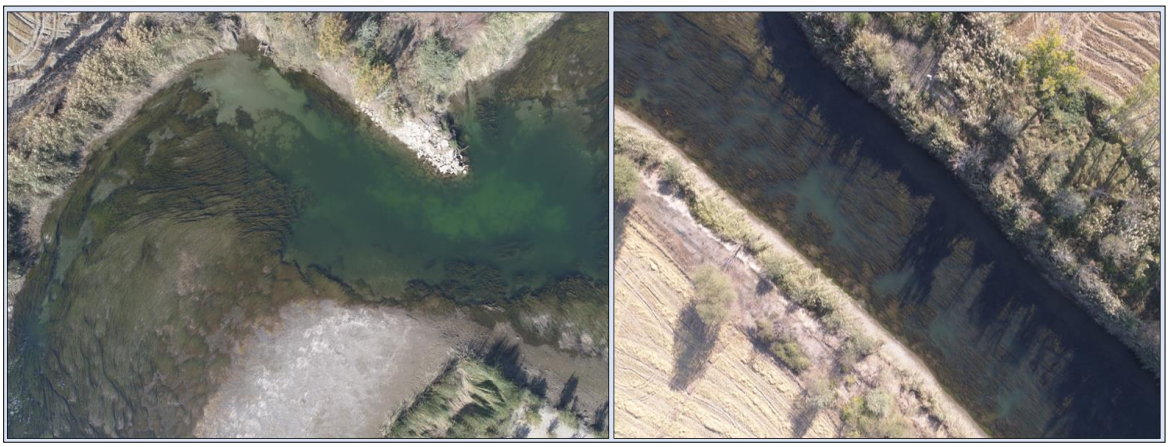

Figure 6. Lowest and highest depths among the dams

Images of sand islands formed by alluvial materials in the region are shown as examples of risk areas (Figure 7)

Figure 7. Risky areas with high potential for impact on the environment

Results and Discussion

Data Analysis and Evaluations

The lowest depth between the dams measured as 20 cm with 3 test points are at the 5th km.The highest depth measured 4 m with 10 test points where it exceeded the limit were determined at 1.5 and 3 km and at 10, 11 and 12 km The scatter plot of the measurements are generated (Figure 8).

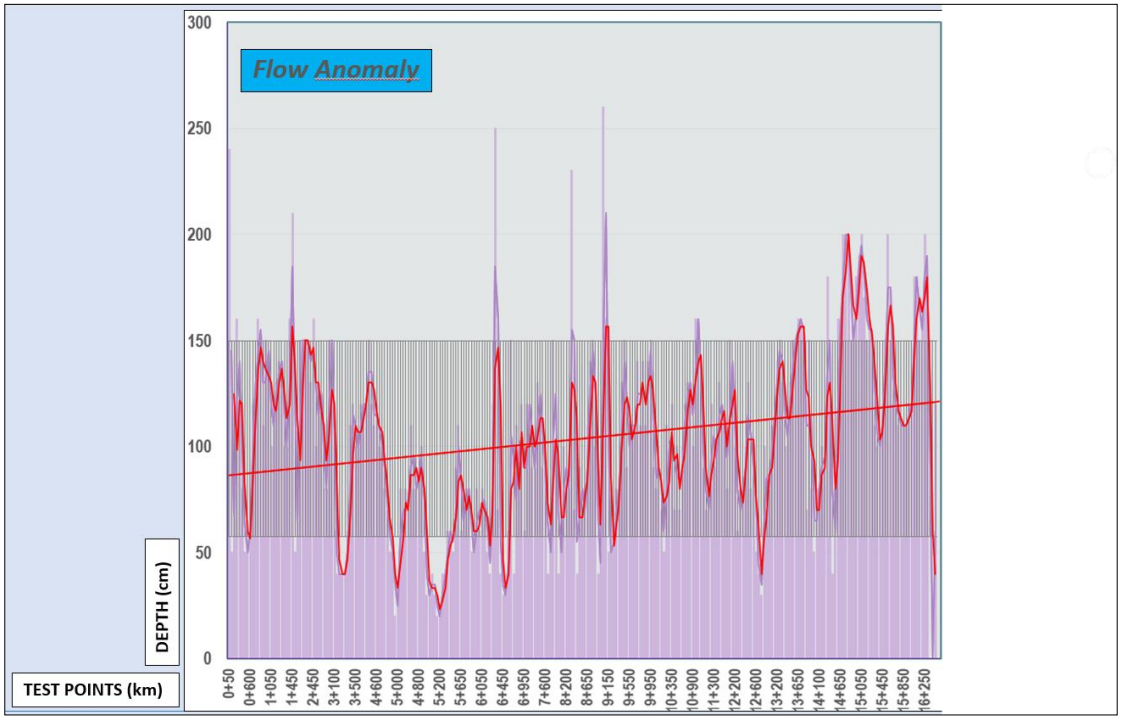

Figure 8. Scatter plot of the measurements generated

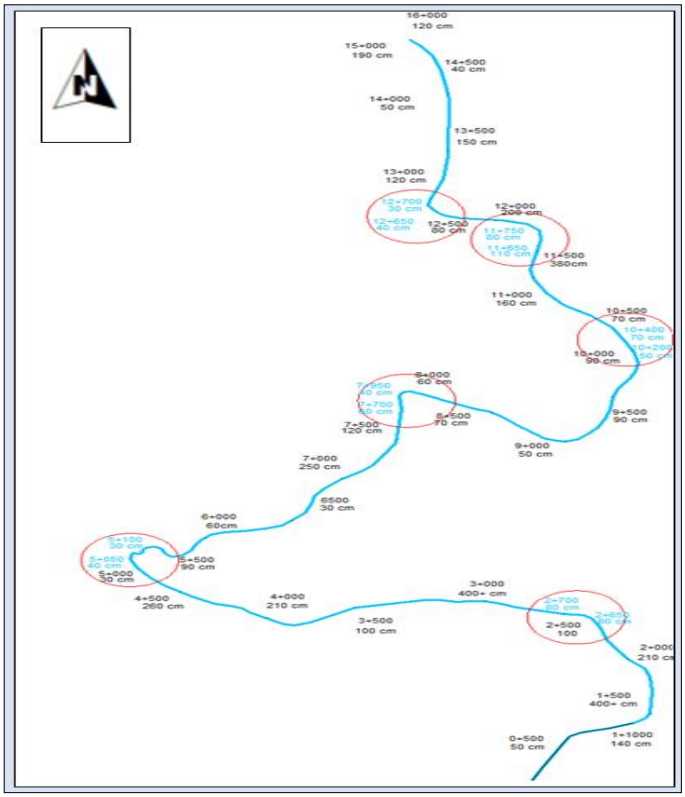

Figure 9. Risky areas on the depth measurement line

Depth values taken from depth measurements every 500 m, as well as risky areas where the depth falls to 50 cm or less are marked on the measurement line. As a result of the analysis carried out by processing and evaluating the data, areas that occurred in the six test regions and could pose a risk were identified (Figure 9). Orthophoto mosaics were created from images superimposed with depth measurements to define hydromorphological units marked risky areas on the ortophoto image and satellite image compared (Figure 10).

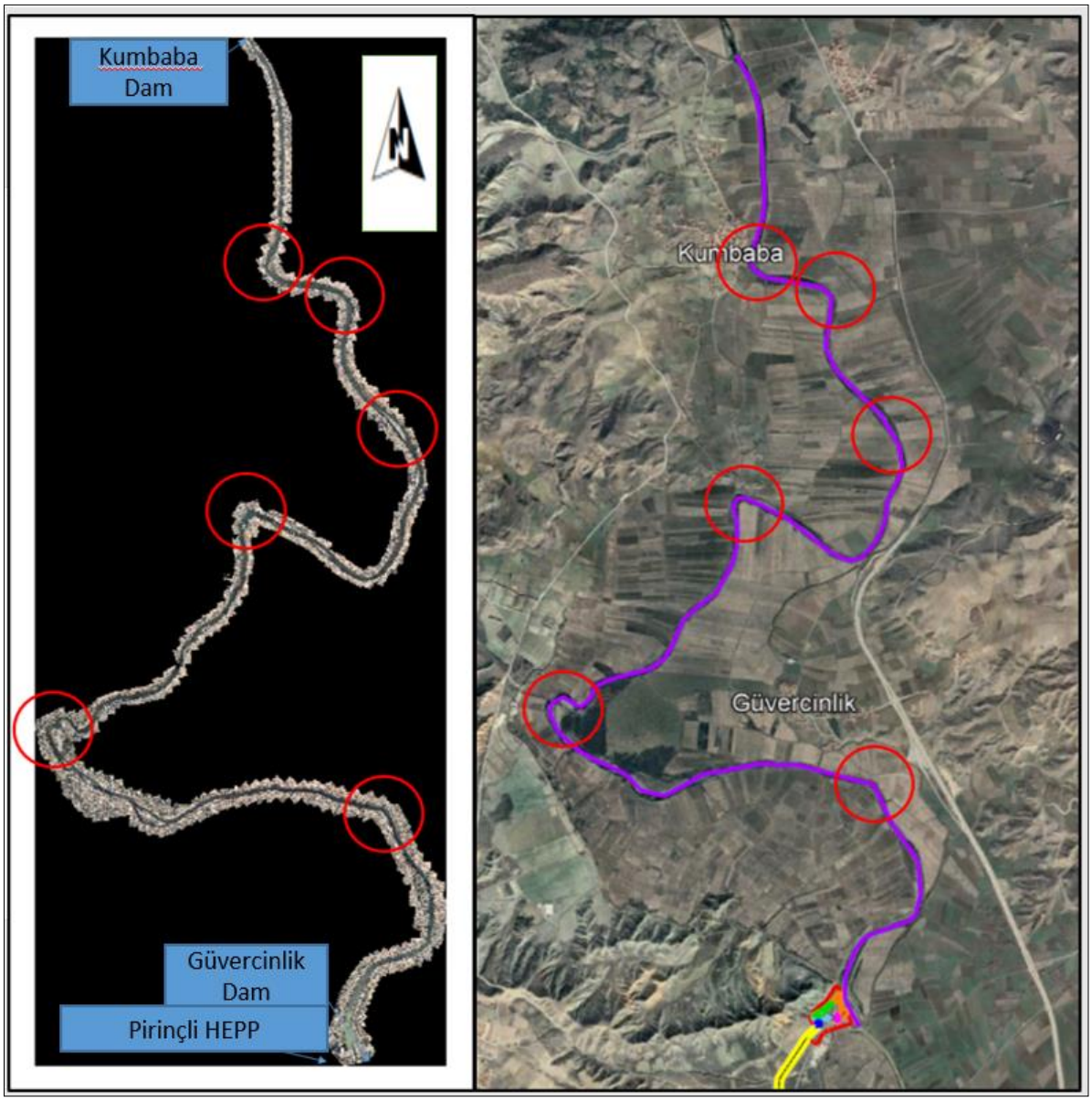

Figure 10. Mosaic image (Visible/infrared drone footage focusing on potential risk areas)

Conclusion

Of the depth measurements made at 341 points, 236 have a depth of 150 cm. It is seen that there are excessive alluvial accumulations in these areas. It has been observed that the values obtained from depth measurements between the dams are not distributed homogeneously in the anomaly graph, areas with high depth are located side by side with areas with low depth. These areas are considered to be particularly high risk. Considering that the average amount of water that Obruk Dam will release at its maximum production is 400 m3/sec, it is obvious that the river bed between Güvercinlik and Kumbaba Dams cannot carry this amount of water and that it will cause floods along with the connected streams on the side branches and threaten the safety of life and property.It is known that the alluvial material that forms the current situation was transported to the region before the construction of the Obruk Dam. Since the transports that may come from Obruk Dam will be detained/blocked by the existing dams.

Recommendations

When the study is evaluated in terms of its rich data, integrity of its methods and environmental quality It is anticipated that this planned work will be permanent in the long term.

Scientific Ethics Declaration

The authors declare that the scientific ethical and legal responsibility of this article published in EPSTEM journal belongs to the authors.

Acknowledgements or Notes

* This article was presented as an oral presentation at the International Conference on Technology, Engineering and Science (www.icontes.net) held in Antalya/Turkey on November 16-19, 2023.

References

Ahn, Y., Shin, B., & Kim, K. H. (2017) Shoreline change monitoring using high resolution digital photogrammetric technique. *Journal of Coastal Research, 79*, 204–208.

Alkan, o. (2019). *Statistical accuracy analysis of remote sensing methods used for mineral deposits and geothermal research in Middle-North Anatolia region.* (Doctoral dissertation).

Arnall, A. (2020) Where land meets sea: Islands, erosion and the thing-power of hard coastal protection structures. *Environment and Plannig E: Nat. Space*, *6*(1), 69–86.

Liu, L. (2023). Drone-based photogrammetry for riverbed characteristics extraction and flood discharge modeling in Taiwan's mountainous rivers. *Measurement, 220*. 113386.

Salandra, M., Roseto, R., Mele, D., Dellino, P., & Capolongo, D. (2022). Probablistic hydro- geomorphological hazard assessment based on UAV- derived high-resolution topographic data: The case of Basento river (Southern Italy). *Science of the Total Environment, 842*(3)

Srivastava, S., Seng, K.P., Ang, L.M., Pachas, N. A. & Lewis, T. (2022). Drone-based environmental monitoring and image processing, *Sensors*, *22*(20), 7872.

Suska, K. (2023). Drones in fish fauna assessment of rivers. *Ecohydrology & Hydrobiology*, 1642-3593.

Tak, W.J., Jun, K.W., Kin, S.D., & Lee, H.J. (2020). Using drone and LiDAR to assess coastal erosion and shoreline change due to the construction of coastal structures. *Coastal Research*, *95*, 674-678.

Author Information

Oyku Alkan
Graduated Istanbul Technical University
Istanbul, Turkiye
Contact e-mail: *oyku*.alk*@gmail.com*

Muntaha Kassim Alzubade
University of Technology,
Baghdad, Iraq

Mehmet Nurullah Alkan
Hitit University,
Corum, Turkiye

To cite this article:

Alkan, O., Alzubade, M.K., & Alkan, M.N. (2023). Assessing the effects of alluvial transport in the Kizilirmak river on dams with local, photogrammetric and remote sensing methods. *The Eurasia Proceedings of Science, Technology, Engineering & Mathematics (EPSTEM), 26*, 217-224.

The Eurasia Proceedings of Science, Technology, Engineering & Mathematics (EPSTEM)
ISSN: 2602-3199

The Eurasia Proceedings of Science, Technology, Engineering & Mathematics (EPSTEM), 2023

Volume 26, Pages 225-233

IConTES 2023: International Conference on Technology, Engineering and Science

CFD Investigation of Shell and Tube Heat Exchanger: Impact of Various Tube Bundle Combinations on Heat Transfer Coefficient and Pressure Drop

Sara Sahrane
National Higher School of Technology and Engineering BP 12

Slimane Niou
National Higher School of Technology and Engineering BP 12

Abstract: Shell and tube heat exchangers play a crucial role in various industries, including chemical processing, oil and gas, power generation, and HVAC systems. These exchangers are widely used for transferring heat between two fluids while maintaining their separation. The design of a shell and tube heat exchanger consists of a bundle of tubes enclosed within a larger shell. The hot fluid flows through the tubes, while the cold fluid circulates around them in the shell, facilitating efficient heat transfer and pressure drop of the system. The performance of a shell and tube heat exchanger is influenced by various factors, including the configuration of the tube bundle. The choice of different tube bundle combinations can significantly impact the overall performance of the heat exchanger. In this paper, a numerical study is conducted to examine the effects of two combination of circular and square tube bundle with the simple arrangement: i) circular, ii) square, on a shell and tube heat exchanger. COMSOL Multiphysics is employed to model and simulate this heat exchanger under various mass flow rates. The result shown that the combined geometry heat exchanger exhibits the highest overall heat transfer coefficient compared to heat exchangers with single arrangements. The pressure drop on the tube and shell side was also studied for all cases of heat exchangers. The placement of circular tubes in the center and near the shell has a significant effect on heat transfer and pressure losses. It has been demonstrated that the tubes located at the ends of the shell have a much greater impact on heat transfer compared to the tubes positioned in the center.

Keywords: Shell and tube heat exchanger, Tube bundle, Square tube, Circular tube, Heat transfer Coefficient.

Introduction

Heat exchangers are pivotal components in a wide array of industries and engineering disciplines, including chemical, petroleum, food processing, nuclear power plants, thermal power plants, and electric power plants. They play a vital role in the transmission and recovery of energy(Master et al., 2003).

Among various heat exchanger types, shell and tube heat exchangers are the most widely employed, accounting for 35% to 40% of the usage (Zhang et al., 2009), This popularity can be attributed to their numerous advantages, including ease of maintenance, high efficiency, compact design, and robustness. Shell and tube heat exchangers consist of two primary components: tubes and a shell. Tubes are responsible for conveying aggressive fluids, whether hot or cold, compressible or incompressible, and especially those at high pressures. The shell facilitates the circulation of fluids at lower pressures and typically incorporates longitudinal and/or transverse baffles. The inclusion of baffles serves to extend the fluid's path within the shell, increase turbulence, and enhance heat transfer. Nonetheless, baffles introduce certain drawbacks, such as increased flow resistance, induced vibrations, and areas of stagnant flow along the shell's periphery (Unverdi, 2022) .

To enhance the performance of shell and tube heat exchangers, many researchers have conducted extensive investigations. Some recent studies have focused on the shell side, particularly examining baffles' characteristics such as material type, quantity, shape, and cutting angles. For instance, El-Said et al. (2021) delved into the impact of varying baffle geometries segmental curved baffles (convex core baffles with convex peripheral baffles , convex peripheral baffles with concave core baffles,) A conventional STHE with straight baffles (SB) is also studied for comparison on exchanger performance. Abbasian Arani and Moradi (2019) explored the combination of disk baffles with other types of drawn baffles. Another avenue of research has concentrated on the tube side, which involves fewer parameters.

The arrangement of tubes significantly influences the energy efficiency of tube and shell heat exchangers. Kallannavar et al. (2020) investigated the effects of four tube arrangements (30°, 90°, 60°, and 45°) in the context of a tube and shell heat exchanger with circular tubes.Meloukı et al. (2013) presented a Comparative numerical study of the influence of square and cylindrical tubes in an aligned bundle on the thermal performance of a tube-and-shell heat exchanger. Ibrahim and Gomaa (2009) and Matos et al. (2004) conducted a comparative analysis of 12 elliptical and circular tubes, demonstrating that elliptical tubes enhance heat transfer by 20% compared to circular tubes, especially within a Reynolds number range of 300 to 800. Tao et al. (2007) performed a numerical investigation on a tube and shell heat exchanger with elliptical tubes, revealing a remarkable 30% increase in heat transfer efficiency compared to circular tubes.

This manuscript's primary objective is to assess the impact of varying tube cross-sections (two combination of circular and square tube bundle with the simple arrangement circular and square) on the hydro-thermal performance of a tube and shell heat exchanger. This assessment is conducted using numerical software for design, modeling, and simulation, which combines heat transfer and fluid mechanics based on the Navier-Stokes equations and the k-ε turbulence model.

Method

Geometrical Model

The exchanger under investigation in this study is categorized as a multi-tube heat exchanger and features a bundle containing 37 tubes. It operates with a single pass on the tube side and a single pass on the shell side, with a counterflow configuration. The shell of the exchanger is equipped with four vertical single segment baffles, each having a 25% cut. The 3D representation of this exchanger's geometry was created using COMSOL Multiphysics 5.5 software, as illustrated in Figure 1.

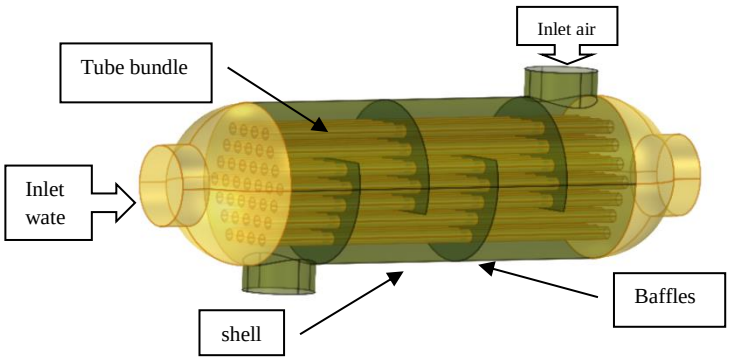

Figure 1. Numerical model of the shell and tube exchanger

The hot fluid (water) enters the shell at of 80°C while the cold fluid (air) enters the tubes with a temperature of 5°C. Table 1 shows the thermo-physical properties of the two fluids.

Table 1. Thermophysical properties of shell and tube heat exchanger

Properties	Fluid		
	water	air	unit
T_{inlet}	80	5	°C
Thermal conductivity	0.6562	0.02401	(W/m.K)
Density	971.8	1006	(kg/m^3)
Specifc heat capacity	4194	1006	(J/Kg K)
Dynamic viscosity	3.54×10^{-4}	1.75×10^{-5}	(Pa s)

The exchanger's overall geometry remained consistent across the cases under examination, with variations introduced solely to the tube bundles, as depicted in Figure 2. Detailed dimensional specifications for these heat exchangers can be found in Table 2.

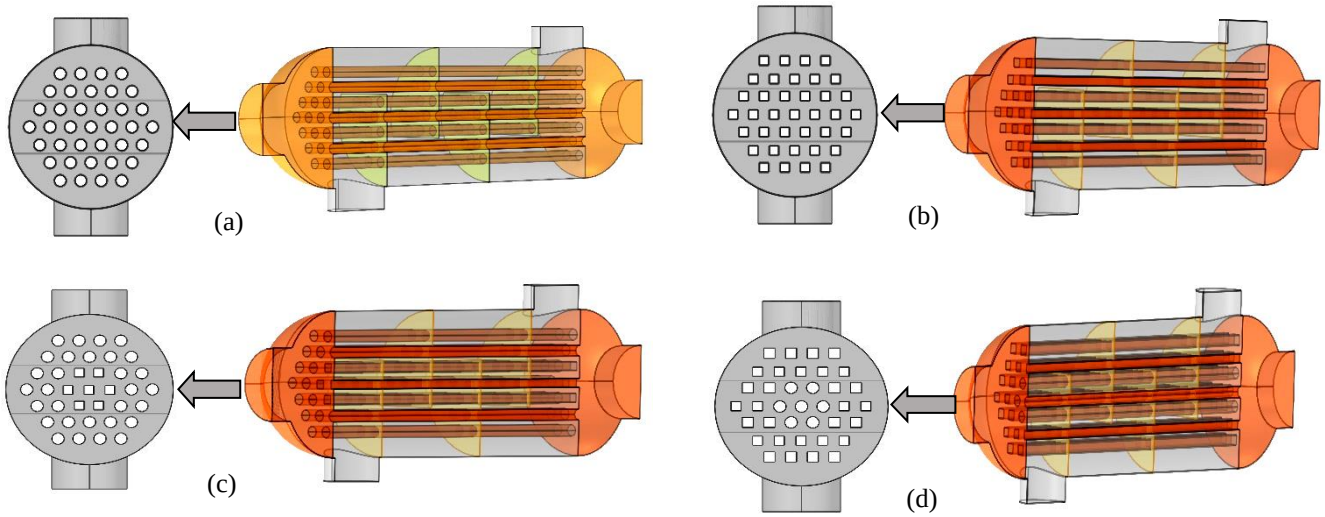

Figure 2. Cross sectional models of shell and tube exchanger : (a) circular , (b) square , (c) combined cir-sqr ,(d) combined sqr-cir

Table 2. Size of heat exchanger

Propertie	Value	Unit
Shell diameter	200	mm
Tube diameter	15	mm
Length shell /tube	500	mm
Number of tubes	37	
Number of baffles	4	

Mathematical Model

Heat Transfer Coefficient

The overall heat transfer coefcient is calculated by the following equation (He et al., 2016) :

$$U = \frac{1}{\frac{1}{hi}+\frac{di\ln(\frac{de}{di})}{2\lambda}+\frac{1}{he}} \qquad (1)$$

hi : convective transfer coefficients for the tube side, he : convective transfer coefficients for the shell side, k : thermal conducivity of the tube, d_i : inner diameters of the tube, d_e: outer diameters of the tube.

Pressure Drop in Shell Side

The pressure drop in the shell side can be obtained using the following equation (2)(Sarkar & Bhattacharyya, 2012) :

$$\Delta P = f\frac{D_S}{D_e}(N_b+1)\frac{1}{2}\rho V^2$$

$$f = \exp(0.576 - 0.19 ln R_{es})$$

$$D_e = \frac{4\left(\frac{\sqrt{3}P_t^2}{4} - \frac{\pi d_0^2}{8}\right)}{\frac{\pi d_0}{2}}$$

$$Re_s = \frac{\rho u_m D_e}{\mu} \qquad (2)$$

ΔP: pressure drop in shell side **Re_s**: Reynold's number in shell, **f** = friction factor, **D_s** : Sell diameter, **D_e**: equivalent diameter for the triangular pitch,, **N_b** : number of bafe, **ρ**= density of the fluid, **μ**= dynamic viscosity of the fuid, **u_m**: velocity of the fuid,,**V** : mean fow velocity, **P_t**: tube pith ,d_0: outer diameters of the tube.

Turbulent Fow k–ε Model:

The turbulent flow model (k - ε) is widely used in the literature to the study the turbulent flows with very high Reynolds numbers [12]. It is a model with two partial differential equations: i) turbulent kinetic energy (k) and ii) dissipation (ε). COMSOL uses the Navier - Stokes equations as the basic equations to solve the fluid flow models (3) :

$$\rho(\mu.\nabla)\mu = \nabla.[-PI + (\mu + \mu_T)(\nabla\mu + (\nabla\mu)^T - \frac{2}{3}(\mu + \mu_T)(\nabla.\mu)I - \frac{2}{3}\rho kI] \qquad (3)$$
$$\nabla.(\rho\mu) = 0$$

ρ : density (kg/m^3) ; μ : Dynamic viscosity (kg/m/s) ; P : fluid pressure (Pa)
k : Turbulent kinetic energy (m²/s²) et μ_T : turbulent viscosity (Pa.s).
The turbulent kinetic energy is defined as follows (4):

$$\rho(\mu.\nabla)k = \nabla.\left[\left(\mu + \frac{\mu_T}{\sigma_k}\right)\nabla k\right] + p_k - \rho\varepsilon \qquad (4)$$

σ_k : the turbulent Prandtl number; ε : Turbulent dissipation(m²/s²)
Turbulent dissipation is the rate at which velocity fluctuations dissipate. It is defined by the equation (5) :

$$\rho(u.\nabla)\varepsilon = \nabla.\left[\left(\mu + \frac{\mu_T}{\sigma_\varepsilon}\right)\nabla\varepsilon\right] + C_{e1}\frac{\varepsilon}{k}p_k - C_{e2}\rho\frac{\varepsilon^2}{k} \qquad (5)$$

u : fuid flow velocity,.

For a turbulent flow, the viscosity is defined by the equation (6) :

$$\mu_T = \rho C_\mu \frac{k^2}{\varepsilon} \qquad (6)$$

The production of turbulent kinetic energy may be expressed by equation (7):

$$P_k = \mu_T\left[\nabla u:(\nabla u + (\nabla u)^T) - \frac{2}{3}(\nabla.u)^2\right] - \frac{2}{3}\rho k\nabla.u \qquad (7)$$

The constants used in the equations for turbulent kinetic energy, turbulent dissipation and turbulent viscosity are: C_{e1}=1.44, C_{e2}=1.92, C_μ=0.99, σ_k = 1, σ_ε =1.3

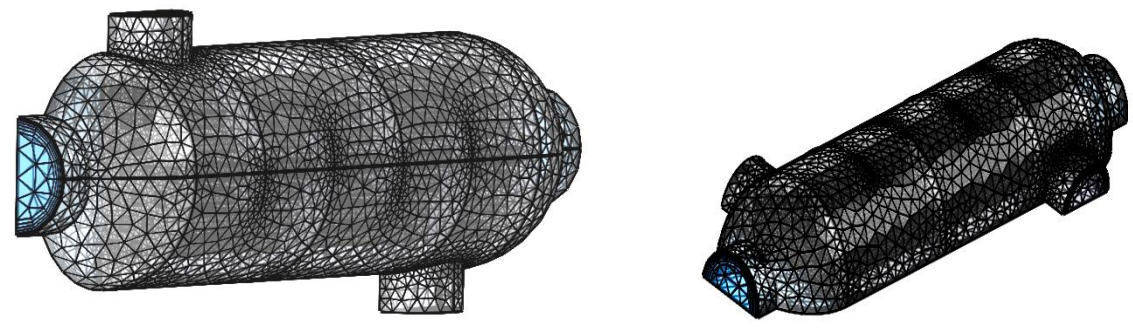

Figure 3**.** The meshed model used in the numerical calculations of heat exchangers

Mesh Control

The computational grid was created with the aid of COMSOL software. To discretize the volume of the shell and tube assembly, a free unstructured tetrahedral mesh was employed, as illustrated in Figure 3. A mesh sensitivity analysis was conducted to determine the optimal quantity and size of mesh elements, aiming to minimize computational expenses.

Results and Discussion

Temperature Evolution

In Figure 4, we observe the 3D temperature contours within the heat exchanger for the different geometries. Heat transfer within the shell and tube exchanger occurs through two primary modes: conduction and convection. Conduction is facilitated by the separating walls between the two fluid streams, which include the tube plate inside the exchanger, the shell wall, and the baffles. On the other hand, convection is responsible for heat transfer between the cold fluid (air) and the inner surfaces of the tubes, as well as between the hot fluid and the external surfaces of the tubes and the interior of the shell.

Temperature distribution is remarkably uniform throughout the exchanger. The lowest temperature within the tube bundle corresponds to the outlet temperature of the cold fluid, which is 320.68, 320.75,322.33 and 322.6K for the combined square- circular, square, circular and combined circular-square geometries and, respectively. Notably, the heat transfer performance is higher in the exchanger with a combined geometry with square - circular geometry compared to the other geometries. This observation can be attributed to the specific characteristics of the combination between square and square geometry.

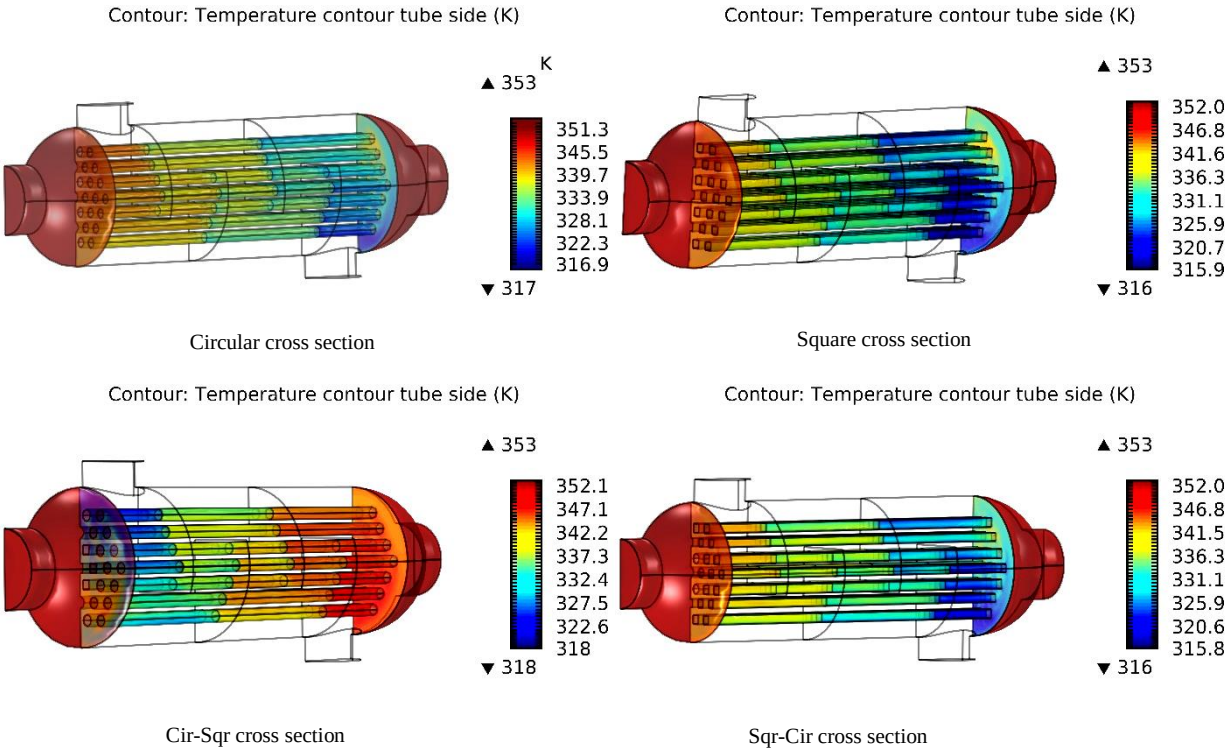

Figure 4. Temperature contour tube side of different heat exchangers

Velocity Evolution

In Figure 5, velocity contours are depicted within the cross-sectional areas of various geometries, namely: square, circular, and the combined circular-square configurations. Notably, the highest velocity values within these heat exchanger geometries were observed proximate to the edges of the baffles. Specifically, for the square section, the velocity reached 3.48 m/s, whereas for the circular section, it measured 3.04 m/s. In the case

of combined geometries, the velocities were noted at 2.97 m/s for the circular-square arrangement (cir-sqr) and 3.07 m/s for the square-circular arrangement (sqr-cir).

This accelerated flow pattern on the shell side can be primarily attributed to the restricted flow area between the shell and the baffle plates. Importantly, it is worth noting that this phenomenon predominantly impacts the shell side and does not significantly affect the tube side of the heat exchanger

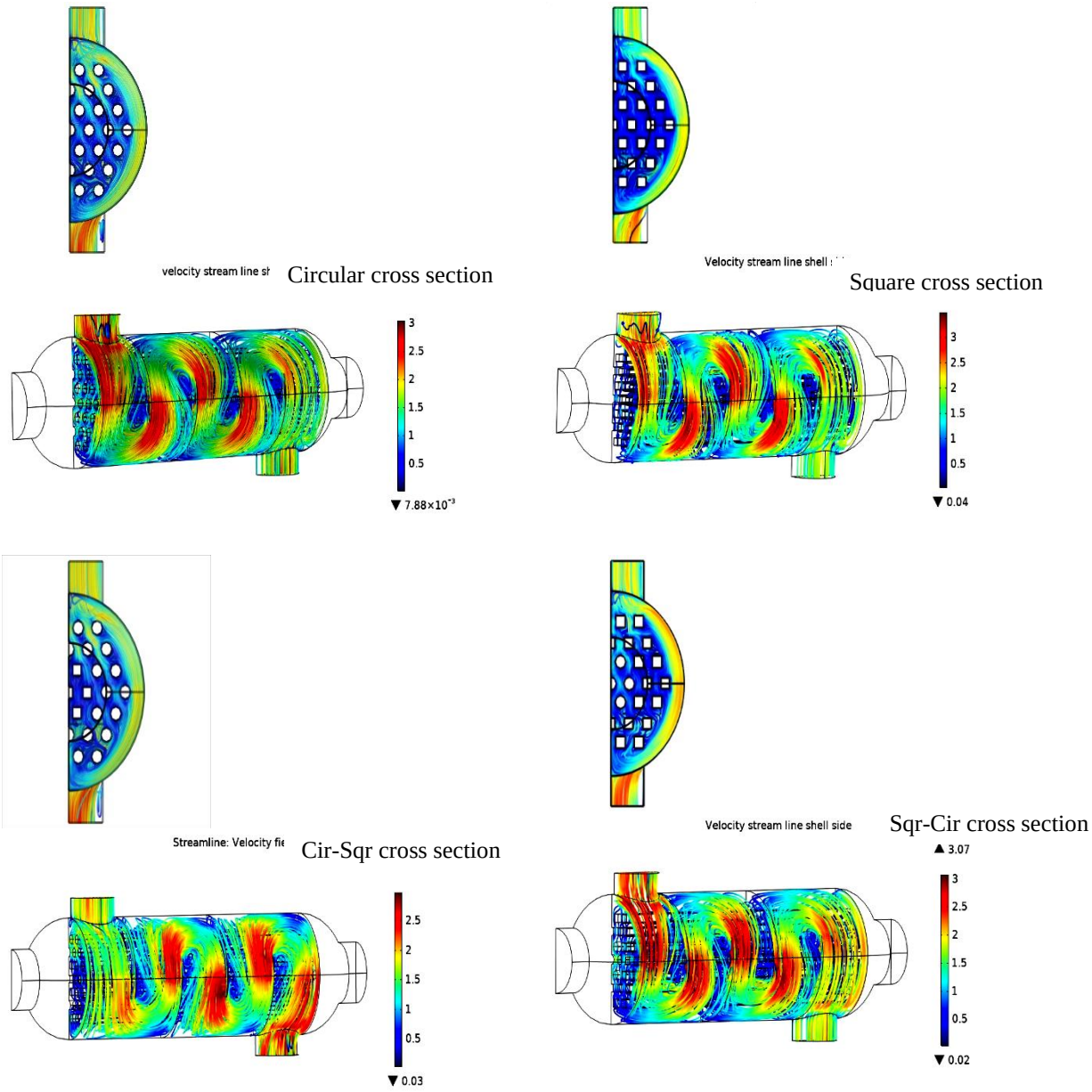

Figure 5. Streamline velocities on the shell side of various heat exchangers

Heat Transfer Coefficient

Figure 6 provides a graphical representation illustrating the correlation between the global heat transfer coefficient and the Reynolds number for four distinct heat exchanger geometries: square, circular, and two combined circular-square configurations. The relationship observed demonstrates a direct proportionality between the global heat transfer coefficient and the Reynolds number. Notably, the point of maximum Reynolds number signifies the juncture of the highest mass flow rate, consequently resulting in the most substantial heat transfer coefficient.

Among the investigated geometries, the heat exchangers featuring a circular section exhibit the most remarkable heat transfer performance, boasting a coefficient of 10.458 W/m²·K. This surpasses the performance of the other geometries. This superiority in heat transfer efficiency can be attributed to the circular geometry's reduction in cross-sectional area on the shell side. This reduction leads to an augmented flow rate, enabling a more rapid and efficient transfer of heat to the cold fluid.

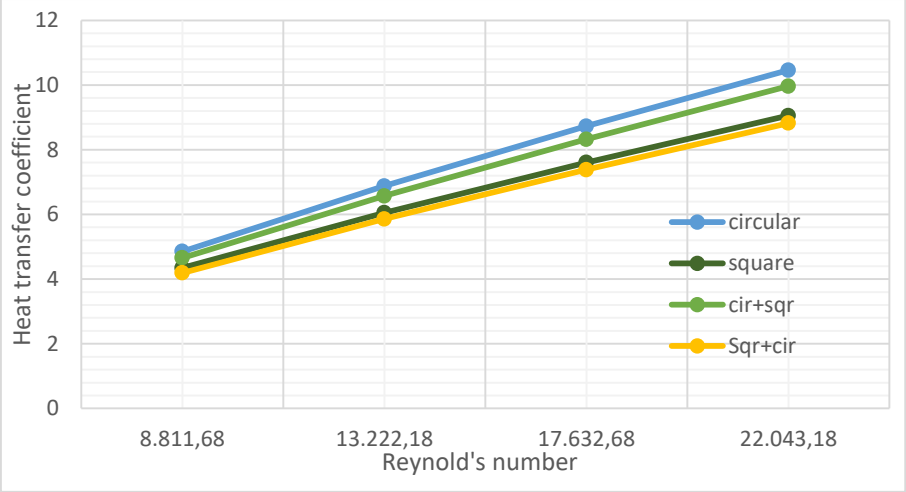

Figure 6. The overall heat transfer coeffcient in the different geometries:

Pressure Drop in Shell Side

According to the findings presented in Figure 8 which delineates the relationship between pressure drop on the shell side and the Reynolds number across various cross-sectional shapes (square, circular, and a fusion of circular and square geometries), provide compelling evidence of a direct proportionality between pressure drop and Reynolds number. Notably, the heat exchanger employing the combined circular-square cross-section exhibits the highest pressure drop, signifying a substantial impact on the system's hydraulic resistance.

In contrast, both the circular geometry and the combined circular-square configuration demonstrate significantly lower pressure drops, registering at 20.434 Pa and 21.512 Pa, respectively. This divergence in pressure drop performance is attributed to the nuanced flow dynamics induced by distinct cross-sectional shapes. The introduction of a square cross-section geometry is observed to augment the formation of recirculation zones, thereby amplifying frictional effects on the shell side. Consequently, this phenomenon leads to an appreciable elevation in pressure drop, emphasizing the influence of cross-sectional geometry on the heat exchanger's hydraulic behavior

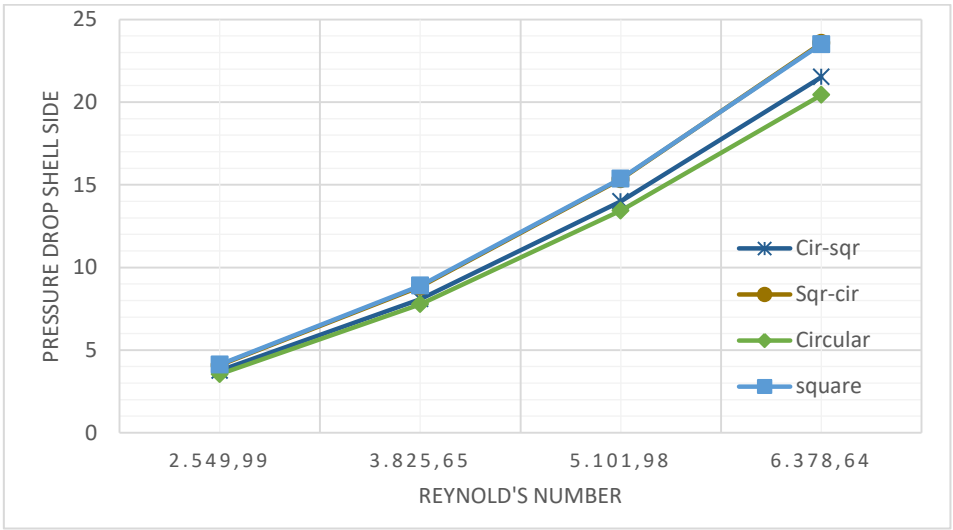

Figure 7. Pressur drop shell side in the different geometries

Conclusion

The performance of the heat exchanger was assessed through simulations conducted using Comsol Multiphysics 5.5 software, employing the (k, ε) model. The results of the simulations for heat exchangers with single arrangements unequivocally favored the circular geometry, showcasing the highest heat transfer coefficient. The combination of square and circular tubes, strategically positioned at the center and ends of the heat exchanger, was the chosen configuration. This combined arrangement was comprehensively evaluated for its energy-related characteristics, including the overall heat transfer coefficient and the pressure drop on the shell side. The study's findings can be distilled into the following key points:

- Geometric variations in the tube configuration directly impact both the overall heat transfer coefficient and pressure drop on the tube and shell sides.
- Parameters such as flow velocity, tube cross-sectional area, flow rate, and Reynolds number exert significant influence on these heat transfer characteristics.
- Notably, minimizing pressure drop translates to reduced pump power requirements, consequently augmenting the overall system efficiency.
- The strategic placement of tubes, particularly with circular tubes at the ends and square tubes at the center, emerged as the superior configuration, outperforming the reverse arrangement (square at the ends and circular at the center)

Scientific Ethics Declaration

The authors declare that the scientific ethical and legal responsibility of this article published in EPSTEM journal belongs to the authors.

Acknowledgements or Notes

* This article was presented as a poster presentation at the International Conference on Technology, Engineering and Science (www.icontes.net) held in Antalya/Turkey on November 16-19, 2023.

References

Abbasian Arani, A. A., & Moradi, R. (2019). Shell and tube heat exchanger optimization using new baffle and tube configuration. *Applied Thermal Engineering*, *157*. 113736.

El-Said, E. M. S., Elsheikh, A. H., & El-Tahan, H. R. (2021). Effect of curved segmental baffle on a shell and tube heat exchanger thermohydraulic performance: Numerical investigation. *International Journal of Thermal Sciences*, *165*. 106922.

He, Z., Fang, X., Zhang, Z., & Gao, X. (2016). Numerical investigation on performance comparison of non-Newtonian fluid flow in vertical heat exchangers combined helical baffle with elliptic and circular tubes. *Applied Thermal Engineering*, *100*, 84–97.

Ibrahim, T. A., & Gomaa, A. (2009). Thermal performance criteria of elliptic tube bundle in crossflow. *International Journal of Thermal Sciences*, *48*(11), 2148–2158.

Kallannavar, S., Mashyal, S., & Rajangale, M. (2020). Effect of tube layout on the performance of shell and tube heat exchangers. *Materials Today: Proceedings*, *27*, 263–267.

Master, B. I., Chunangad, K. S., & Pushpanathan, V. (2003). Heat exchanger fouling and cleaning : fundamentals and applications fouling mitigation using helixchanger heat exchangers. *Heat Exchanger Fouling and Cleaning: Fundamentals and Applications*, 1–6.

Matos, R. S., Vargas, J. V. C., Laursen, T. A., & Bejan, A. (2004). Optimally staggered finned circular and elliptic tubes in forced convection. *International Journal of Heat and Mass Transfer*, *47*(6–7), 1347–1359.

Minist, P., Sup, E., & Facult, R. S. (2013). *Etude numérique comparative de l ' influence entre des tubes carré et cylindrique d ' un faisceau aligné , sur les performances thermique d ' un échangeur tube et calandre Proposé et dirigé par* .

Sarkar, J., & Bhattacharyya, S. (2012). Application of graphene and graphene-based materials in clean energy-related devices Minghui. *Archives of Thermodynamics*, *33*(4), 23–40.

Tao, Y. B., He, Y. L., Wu, Z. G., & Tao, W. Q. (2007). Three-dimensional numerical study and field synergy principle analysis of wavy fin heat exchangers with elliptic tubes. *International Journal of Heat and Fluid*

Flow, *28*(6), 1531–1544.

Unverdi, M. (2022). Prediction of heat transfer coefficient and friction factor of mini channel shell and tube heat exchanger using numerical analysis and experimental validation. *International Journal of Thermal Sciences*, *171*, 107182.

Zhang, J. F., Li, B., Huang, W. J., Lei, Y. G., He, Y. L., & Tao, W. Q. (2009). Experimental performance comparison of shell-side heat transfer for shell-and-tube heat exchangers with middle-overlapped helical baffles and segmental baffles. *Chemical Engineering Science*, *64*(8), 1643–1653.

Author Information

Sara Sahrane
LTSE, Energy Systems Technology Laboratory, National Higher School of Technology and Engineering BP 12, 23052 Annaba, Algeria
Contact e-mail: *s.sahrane@ensti-annaba.dz*

Slimane Niou
LTSE, Energy Systems Technology Laboratory, National Higher School of Technology and Engineering BP 12, 23052 Annaba, Algeria

To cite this article:

Sahrane, S., & Niou, S. (2023). CFD investigation of shell and tube heat exchanger: Impact of various tube bundle combinations on heat transfer coefficient and pressure drop. *The Eurasia Proceedings of Science, Technology, Engineering & Mathematics (EPSTEM)*, *26*, 225-233.

The Eurasia Proceedings of Science, Technology, Engineering & Mathematics (EPSTEM)
ISSN: 2602-3199

The Eurasia Proceedings of Science, Technology, Engineering & Mathematics (EPSTEM), 2023

Volume 26, Pages 234-241

IConTES 2023: International Conference on Technology, Engineering and Science

Optimization of Energy Consumption of the Debutanizer Column, Using Genetic Algorithm

Ahmed Ould Brahim
Mohammed V University in Rabat

Souad Abderafi
Mohammed V University in Rabat

Abstract: In the light of the emissions associated with fossil fuel combustion and their associated health and environmental impacts, natural gas is becoming increasingly attractive when compared with other fuels. The separation of natural gas liquids (NGL) in gas processing is energy-intensive, which is performed by a series of column among them the debutanizer column. This latter is used to separates C4 cuts and lighter components from NGL, typically gasoline, requiring modeling and optimization to reduce energy consumption. This work presents a rigorous methodology for modeling and optimization energy consumption of debutanizer column. This methodology is to develop a statistical model that will be used to test the variation of the energy consumed by the process, depending on columns parameters that have a great influence on this consumption. An experimental design was implemented and the data required for modeling were obtained by numerical simulations studies of debutanizer column, basing on Peng-Robinson (PR) thermodynamic model. Simulation results were validated successfully and the resulting model will be operated, using a genetic algorithm. The genetic algorithm modeling allows us determining the optimal values of reflux ratio and pressure of column, which provide savings in energy consumption for NGL separation process.

Keywords: Energy consumption, Genetic algorithm, distillation column, NGL separation

Introduction

Throughout the world, oil and gas are fossil energy sources exploited until now in various industrial processes such as the manufacture of chemicals, sugar mills, cement factories, the phosphate industry and others. They are also used as fuel in combustion engines. This intense demand raises the problem of global warming, due to greenhouse gas emissions, on the one hand and on the other hand, the risk of exhaustion of oil and natural gas reserves. The use of renewable energy resources, such as solar energy, wind energy and biomass are not yet economically competitive solutions to replace fossil fuels, as they are under development. As a result, industrial processes still need to be optimized to minimize their energy consumption and increase their efficiency. Refineries are among the most energy-consuming industries and this consumption leads to high operating costs and significant greenhouse gas emissions, polluting the environment.

The separation of petroleum fractions or gases is carried out, mainly, using different unit operations based on distillation columns. These operations occupy an essential place in the entire manufacturing process for oil and gas products in particular, and often constitute a major part of the manufacturing cost. High energy consumption is one of the main characteristics of distillation. This consumption can reach 50% of the total energy required of a distillery and represents approximately 3% of global energy consumption (Tgarguifa et al., 2017, 2018). It is therefore necessary to optimize this unit and improve its performance, to have a more efficient and less energy-consuming separation process. The separation of liquid natural gases (LNG) is carried out by a series of three columns, called deethanizer, depropanizer and debutanizer, which requires large energy consumption (Mandis et

al., 2022). The debutanizer is used to separate butane cuts (C4) and lighter components of LNG, generally gasoline (Chun & Kim, 2013). The most widely used separation technique is distillation, which is one of the most important separation units in the chemical and process industries (Jones, 2015). Its disadvantage is that its energy consumption accounts for more than 70% of the total energy consumption of the industry (Liu et al, 2017).

Many researchers have generally used different methods to optimize the energy consumption of the distillation column. Kiss et al. (2012) proposed energy-efficient distillation technologies, allowing the right choice to be made for a given separation task at the early stages of design. Practically, many methods are used to optimize the distillation column of certain mixtures containing butane. Osuolale and Zhang (2014) developed a neural network-based strategy for modeling and optimization of energy efficiency in the distillation column applied to different separation mixtures and in particular to that containing butane. Jung et al. (2012) sought to improve the energy efficiency of the LNG separation process, by testing various complex configurations such as double prefractionator arrangement, double wall separation column (DDWC) and agrawal arrangement. The comparison of these three configurations with the conventional method allowed them to recommend the DDWC integrating the debutanizer and the deisobutanizer. Response surface methodology (RSM) coupled with the Box-Behnken design technique was used to optimize the separation of a ternary mixture of normal C4-C6 paraffin from the split-wall column (Sangal et al, 2013). Based on the Petlyuk sequence and using a multi-objective genetic algorithm, Gutiérrez-Antonio and Briones-Ramírez (2009) developed a tool for optimizing distillation columns. This tool has been tested on different ternary mixtures; three of them contain butane and propane. From the results obtained, the authors concluded that the method can be generalized to optimize chemical and petrochemical installations.

Tavan et al. (2016) used the MSR and the desirability function to study the effects of temperature, operating pressure and feed stage on the deethanizer column relating to new modernized installations. This study shows that production capacity has been improved, using optimal parameters. Concerning the optimization of the debutanizer column, we distinguished the work which consists of examining the concept of internal heat integration (Jana, 2010). This method allowed an improvement in energy consumption, by developing a new configuration incorporating additional costs linked to the purchase of new equipment. This work aims optimize the debutanizer column and study the performance of the industrial process of a natural gas separation unit. To do this purpose, data available in the literature relating to an industrial liquefied gas separation unit were exploited (Luyben, 2013).

Industrial Process

Natural gas is a fossil fuel present naturally in gaseous form in the porous rocks of the subsoil. It is a mixture whose main constituent is methane (CH4) but we also find ethane, propane as well as butane. Liquid hydrocarbons recovered from LNG are generally separated by three columns (Figure 5.1). The deethanizer separates ethane from propane and heavier components. The depropanizer separates propane from butanes and heavier components. The debutanizer separates the butane from the residues from the previous column. It is the separation of completely miscible liquid mixtures based on the boiling point difference and volatility of the components in the mixture. However, the lightest products are obtained at the top of the column and the heaviest components remain at the bottom of the distillation column. We conventionally carry out a sequential distillation of C2 to C4, from gasoline (Gasoline C5+), followed by the distillation of iC4, from nC4 (James, 2009). Figure 5.1 shows the three separation columns each equipped with a partial condenser and a reboiler. Based on an example of an industrial LNG separation process (Luyben, 2013), the operation of these three units is described and their operating conditions are grouped together in table 5.1.

Deethanizer

The charge for the first column of the process, derived from the demethanizer, is composed of traces of C1, small quantities of hydrocarbons of type C2, C3, C4 and C5+. This charge feeds the deethanizer column, on stage 15, minimizing the charge of the refrigerated condenser. This 1.23 m diameter column is made up of 31 stages operating at 21 bar to be well under the critical pressure of ethane which is 48 bar. At this pressure, the reflux rate temperature is 264 K, requiring cooling to 1.734 MW. The base of the column is at 363 K, so a low temperature heat source is required (2.108 MW). The C2/C3 separation is not difficult. The design specifications are 1 mol% C3 in the distillate and 0.34 mol% C2 in the bottoms. The required reflux rate is 1.258. The purity of the ethane product is 97.06%.

Depropanizer

The second column of the process is the depropanizer made up of 51 stages. The residual current from the dethanizer feeds the column at stage 24, which minimizes the use of the reboiler. This column operates at 17 bar, to reach a reflux temperature equal to 322 K. For cooling the condenser, water is used. The depropanizer column is a distillation column intended to separate propane from other components depending on the volatility of the substances. The composition of the distillation and bottoms products also depends on the feed composition introduced into the feed tray. The design specifications are 0.6 mol% C4 (sum of iC4 and nC4) in the distillate and 0.1 mol% of C3 in the funds. The required reflux ratio is 2.114 and the reboiler capacity is 1.656 MW of low pressure steam.

Debutanizer

The debutanizer is the main column used to separate butane from LNG containing C3 to C7 hydrocarbons (Luyben. 2013). This column is equipped with 30 stages, a condenser and a reboiler. The feed to the column derived from the depropanizer is composed of traces of C3, quantities of the hydrocarbon type, C4 and C5 +. This mixture feeds the debutanizer column with a total molar flow rate equal to 142.4 k mol/h, at stage 16, which minimizes the reboiler's tasks. The separation in the debutanizer is carried out between butane and gasoline with a reflux rate of 2.2 at 322 K. At the top of this column, butane (iC4 / nC4) is obtained at 7.1 atm and at the bottom a gasoline cut containing hydrocarbon chains, type C5+, is obtained. Subsequently, the downstream deisobutanizer column separates isobutane (iC4) from normal butane (nC4), due to the lower volatility of iC4/nC4 (Ould Brahim & Abderafi, 2021).

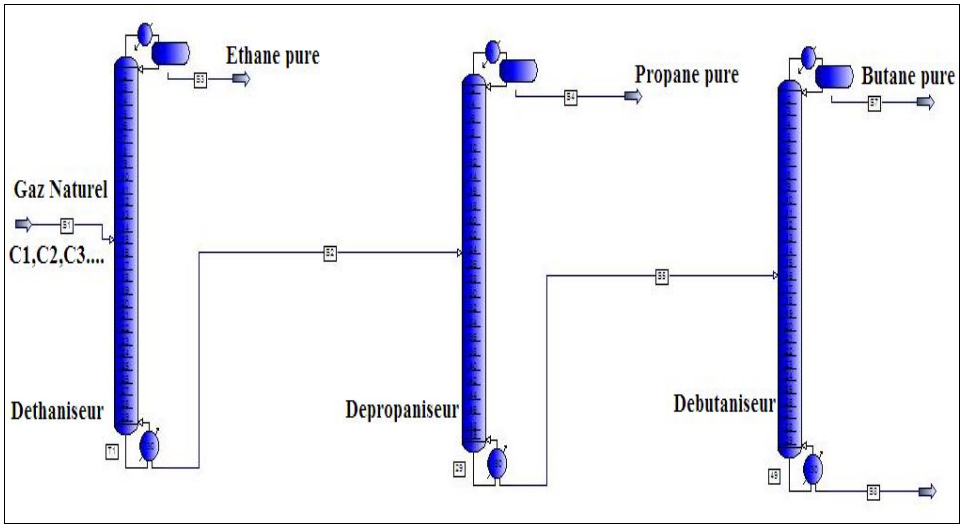

Figure 1. Diagram relating to the LNG separation process

Table 1. Operating conditions of the LNG separation process (Luyben, 2013)

Component	Alimentation	Deetahnizer	Depropanizer	Debutanizer
Methane	0.0096	0.0196		
Ethane	0.4779	0.9706	0.0066	
Propane	0.2613	0.0097	0.9875	0.0018
i-Butane	0.0664		0.0057	0.4605
n-Butane	0.0757		0.0002	0.5354
i-Pentane	0.0379			0.002
n-Pentane	0.0287			0.0002
Hexane	0.0287			
Hepthane	0.0139			
F (kg/h)	24487.096			
T (°C)	35.05			
P (bar)	25.1			
Pureté		0.9706	0.9875	0.9959
Q_R(MW)		2.20	1.60	1.02
Q_c(MW)		1.80	1.60	1.30

Method

Sensitivity Analysis

Based on the literature, the main factors which influence the distillation process and which can potentially be modified by the operator are the feed rate, reflux rate and column pressure (Jobson, 2014). Concerning the first parameter, for a separation column to operate properly, good contact must be maintained between the liquid and the vapor at each plate of the column. At low flow rates, there will be insufficient liquid on the trays or liquid will pass through perforations in the tray. At too high a flow rate, the space between the plates will be filled with liquid which causes clogging of the column. In both cases, the separation efficiency will be reduced or even interrupted. However, the effect of the pressure at the top of the column and the reflux rate on the thermodynamic efficiency were tested. To perform the LNG separation column simulation, all column operating variables are kept fixed except reflux rate and pressure, allowing their effects on energy consumption to be tested of the reboiler and the condenser, as well as on the purity. Operating parameters vary depending on the separation unit. In our previous work (Ould Brahim & Abderafi, 2016), different pressure values, generally applied in refineries, were tested. For the dethanizer, the pressure was varied from 16 to 23 atm and for the depropanizer, the pressure was varied from 14 to 19 bar. Optimal values are obtained by sensitivity analysis.
In this study, the same procedure described was followed, for the choice of intervals. We sought to find the values which make it possible to obtain more or less a balance between the separation efficiency and the energy requirements of the column. Therefore, the reflux rate was varied between 1.1 and 2.53 and the pressure between 5.3 and 8.23 atm. These operating variables do not have the same dimensions, which makes it difficult to compare their coefficients. Normalized (or coded) values are used; Table 2 shows the coded variables for reflux rate and pressure. This method of coding can increase the precision of the models in order to obtain homogeneous equations and simple calculation procedures. Note, that the statistical models can only be used within the ranges of operating variables used; no extrapolation is permitted. The central composite plane was chosen, modifications in this area consist of choosing the axial values on the faces and defining only one focal point, because all variables are deterministic in the case of digital experiment design. In this case, nine experiments are generated by the experimental design.

Table 2. Variables codées, pour le taux de reflux et lapression

X_i	Code X_i	-1	0	1
Taux de reflux (RR)	X_{RR}	1.1	1.819	2.53
P(atm)	X_P	5.3	6.765	8.23

Genetic Algorithm

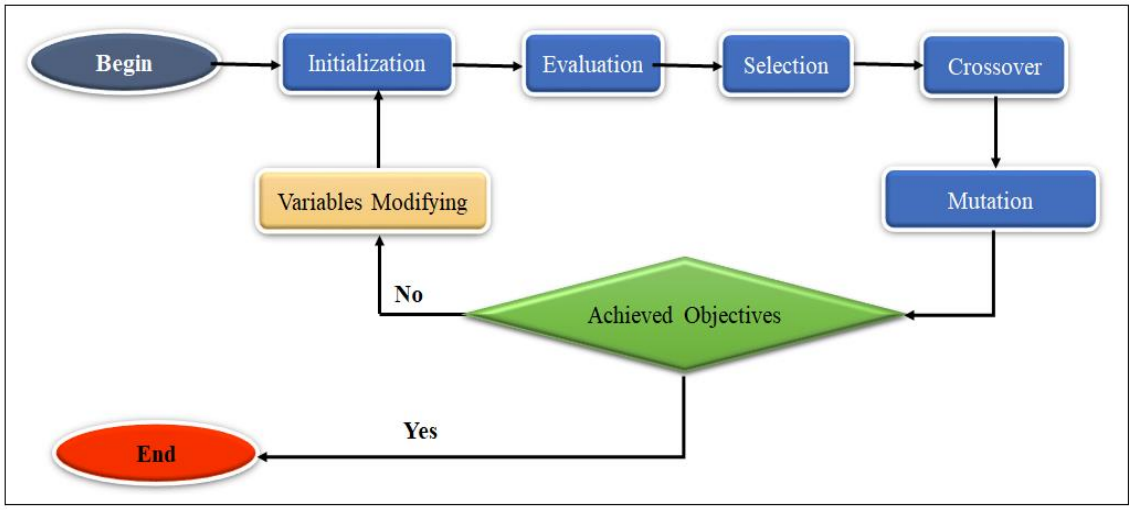

Figure 2. Genetic algorithm procedure

The genetic algorithm is based primarily on perceptions of natural evolution and the biological principles of natural selection (Alam et al., 2020). It is one of the simple and easy-to-use optimization methods that has allowed them to be applied in several engineering fields. To achieve the objective of the studied system, GA manages the problem by following different steps efficiently (Figure 2). The calculation of the genetic algorithm

begins by initializing the independent variables with random values, Initially, a population, which consists of a certain number of individuals, is generated randomly within the lower and upper bounds of the decision variables (constraints). Then, the evaluation is carried out to ensure the availability of a solution. Furthermore, three evolution operators in genetic algorithms are applied. The first is selection which involves choosing the individuals best suited to the problem, followed by crossover to ensure the reproduction of the particularities of the chosen individuals and finally, mutation which is a random alteration of the particularities of an individual. If the objective is achieved, the results are considered; otherwise, the reset is performed with other variables and the calculation is restarted from the beginning, until convergence (Lambora et al., 2019). The optimization problem studied consists of minimizing the amount of heat from the condenser and reboiler as a function of the reflux rate and pressure at the head of the debutanizer column, using the optimization technique based on the algorithm genetic.

Model Simulation and Procedure

The set of equations that govern the operation of the distillation column is obtained basing on the equations of mass and energy balances and equilibrium conditions to be fulfilled by every stage of the process (Tgarguifa et al., 2017). Each stage, receives a diet feed, a fluid flow from the upper stage and a steam flow of the lower tray, a liquid extraction, a steam extraction and a heat input can be considered. The fugacity coefficient, φ_i, is obtained by a thermodynamic model like an equation of state (EOS). Among the many cubic EOS of Van der Waals type currently available, the equation proposed by Peng and Robinson is widely used due to its simplicity and flexibility, for hydrocarbons fractions (Peng & Robinson, 1976).

Following the numerical experimental plan, the calculation of the heating powers of the condenser and the reboiler as well as the purity was carried out, using the Pro II simulation software. This calculation was carried out by simulation of the debutanizer column, choosing the model descibed above. The data on the LNG separation feed conditions necessary for this simulation were used.

Results and Discussion

Simulation Model Validation

Firstly, the data in Table 1 are used to test the accuracy of the simulation model for a distillation column. The thermodynamic model which is the Penge-Robinson equation of state was chosen, for the prediction of the process properties, using the Pro II process simulation software. The accuracy of the model was tested by comparing the predicted values of reboiler and condenser heat quantity, and product purity, to experimental data, for the three columns studied. The calculated results are compared by calculating the relative error, using the following equation:

$$E(\%) = \frac{|V_e - V_c|}{V_e} \times 100 \qquad (5.1)$$

Where, V_c and V_e are the calculated values and experimental values, respectively. The results obtained are grouped in table 3. This table shows comparison between calculated and experimental values. This comparison allows us to note that the results are satisfactory, if we consider the experimental error. However, the model used is reliable and can be used to conduct numerical simulation and for process optimization.

Table 3. Comparison between calculated and experimental values

	Déethanizeur			Dépropanizeur			Débutaniseur		
	V_e	V_c	E (%)	V_e	V_c	E(%)	V_e	V_c	E(%)
E_r (MW)	2,108	2,20	4,3	1,611	1,600	0,6	1,02	1,00	1,96
E_c (MW)	1,734	1,7	1,9	1,656	1,600	3	1,301	1,30	0,08
Pureté	0,970	0,974	0,3	0,987	0,995	7	0,9959	0,9937	0,002
	Ethane			Propane			Butane		

Debutanizer Optimization by GA

The GA method described above was followed to optimize the responses and exactly determine the optimal values with their coordinates. Using MATLAB software, the simulation data obtained were used with the GA. The reflux rate and the pressure at the top of the column were used as research variables, to minimize the energy consumption of the condenser and reboiler and taking into account the purity of the butane, as a constraint equal to 0.99. At the end of the execution of the algorithm (after 176 iterations), several solutions are obtained, with some redundant values which is due to the fact that the algorithm chooses an initial population randomly. Figure 3 shows the pareto front giving different solutions of optimal values relating to the energy consumption of condenser and reboiler obtained from GA. This figure shows-that the minimum value of fitness is equal to 2.06 for reboiler and 2.263 for condenser. These values correspond to reflux rate of 1,105 and pressure of 5.301 atm; it allows to deduce that the minimum consumption of the condenser is equal to 0.984 MW and that of the reboiler is equal to 0.614 MW. These obtained optimal values are compared with their corresponding experimental values given in table 1 for debutanizer. This comparison clearly shows a reduction in energy consumption of 39.8% for the reboiler and 24.31% for the condenser. The use of optimal variables allows a gain in total operating energy equal to 38.37%.

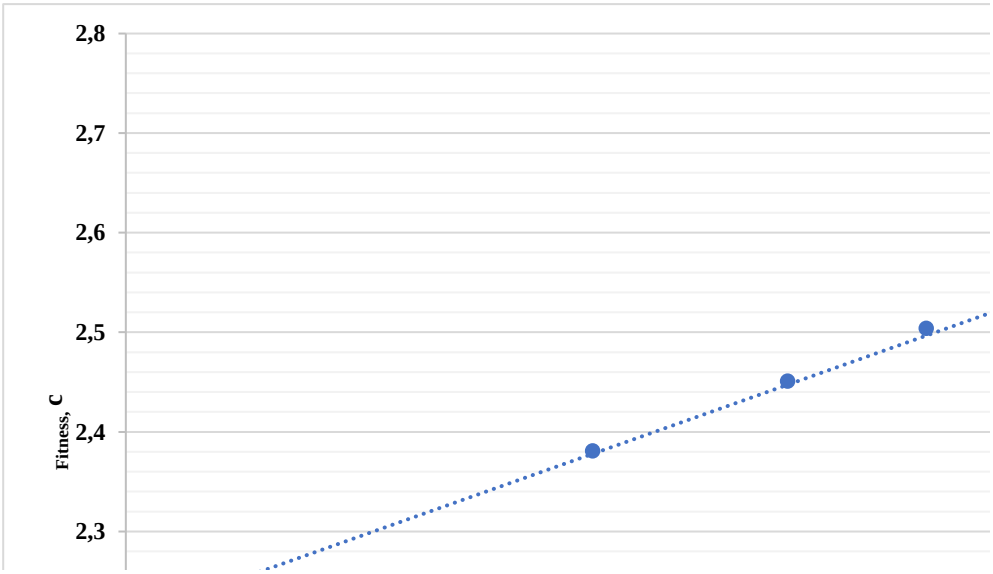

Figure 3. Pareto front obtained from GA.

Overall Process Performance

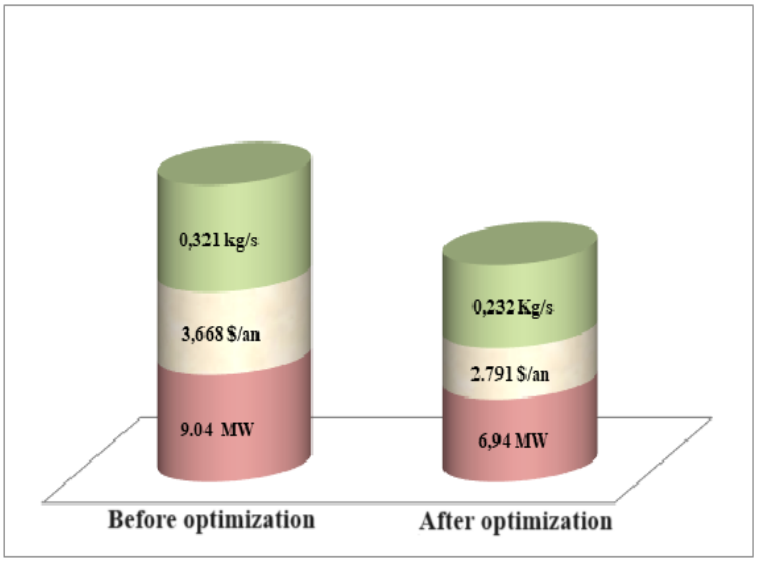

Figure 4. Comparison of the LNG separation process, before and after optimization

To evaluate the performance of the overall LNG separation process, the optimal values of pressure and reflux rate, obtained for the two columns of the Deethanizer and depropanizer in our previous work (Ould Brahim and Abderafi, 2016) and those of the debutanizer found in this study. These values were used to calculate the energy consumed, the operating cost and the concentrations of greenhouse gas emissions, for the studied LNG separation process. The energy cost used for steam production was $0.028/kWh; this cost was estimated based on the average price of industrial fuel, which corresponds to $300/tonne in September 2016, according to the International Energy Agency. The electricity cost used in the calculation was $0.0672/kWh, obtained from the US Energy Information Administration in October 2016. The results obtained from these parameters are compared to those of the process before optimization (Figure 4). This comparison shows us that the quantity of total energy consumed was reduced by 23.26%, the operating cost by 23.91% and CO2 emissions by 27.73%. These results allow us to conclude on the performance of the optimized LNG process.

Conclusion

In this work, particular attention was paid to the debutanizer of the NGL separation unit. Its optimization was successfully carried out using Genetic Algorithm, by testing the effect of variation in pressure and reflux rate on the energy consumption of the condenser and reboiler, by simulation. The results showed that the industrial process is sensitive to the operating conditions studied and particularly the reflux rate has a significant effect on the energy consumption of the distillation column. Then, the performance of the optimized NGL separation process showed a reduction in the amount of total energy consumed, operating cost and greenhouse gas emissions by 23.26%, 23.91% and 27.73%, respectively. The evaluation results showed us a reduction in energy consumption which is accompanied by a reduction in operating costs and greenhouse gas emissions.

Recommendations

The performance of the industrial liquefied gas separation process can be further improved if renewable energies are exploited to minimize their energy consumption and increase their efficiency. For this, it is recommended to carry out a technico-economic study, to have a separation process that is more efficient, less energy-consuming, respectful of the environment and low-cost production.

Scientific Ethics Declaration

The authors declare that the scientific ethical and legal responsibility of this article published in EPSTEM journal belongs to the authors.

Acknowledgements or Notes

* This article was presented as a poster presentation at the International Conference on Technology, Engineering and Science (www.icontes.net) held in Antalya/Turkey on November 16-19, 2023.

References

Alam, T., Qamar, S., Dixit, A., & Benaida, M. (2020) Genetic Al-gorithm: Reviews, implementations, and applications. *International Journal of Engineering Pedagogy (iJEP)*.

Chun, H. H., & Kim, Y. H. (2013). Application of a divided wall column for gas separation in floating liquefied natural gas plant. *Korean Journal of Chemical Engineering*, *30*(7), 1473–1479.

Gutiérrez Antonio, C., & Briones Ramírez, A. (2009). Pareto front of ideal Petlyuk sequences using a multi objective genetic algorithm with constraints. *Computers & Chemical Engineering*, *33*(2), 454-464.

Jana, A.K. (2010). Heat integrated distillation operation. *Applied Energy*, *87*, 1477–94.

Jobson, M. (2014). Energy considerations in distillation. In A. Gorak (Ed.), *Distillation fundamentals and principles* (pp. 225-270). Elsevier

Jones, D.S.J. (2015). Atmospheric and vacuum crude distillation units in petroleum refineries. In S. A. Treese & P. R. Pujado (Eds.), *Handbook of petroleum processing* (2nd ed., pp.125–198). Springer

Jung, Y., Van N., Long D., Woldetensay M.G., & Lee, M. (2012) A study of complex distillation arrangements for improved depropanizing, debutanizing and deisobutanizing dractionation of NGL. *Computer Aided Chemical Engineering*. *31*, 680-684.

Kiss, A., Servando, J., Flores, L., Carlos, A., & Infante, F. (2012). Towards energy efficient distillation technologies - making the right choice. *Energy*, *47*(1), 531-542.

Lambora, A., Gupta, K., & Chopra, K. (2019). Genetic algorithm- a literature review. *International Conference on Machine Learning, Big Data, Cloud and Parallel Computing (Com-IT-Con).* India.

Liu, X.G., He, C., Chen, J.J., Zhang, B.J., & Chen, Q.L. (2017). A new retrofit approach to the absorption-stabilization process for improving energy efficiency in refineries. *Energy*, *118*, 1131-1145.

Mandis, M., Chebeir, J. A., Romagnoli, J.A., & Baratti, R. (2022). Effect of the demethanizer improved control strategy on the separation train for the NGL separation process. *IFAC PapersOnLine*, *55*(7), 889–894.

Osuolale, F.N., & Zhang, J. (2014). Energy efficient control and optimization of distillation column using artificial neural network. *Chemical Engineering Transactions*, *39*, 37-42.

Ould Brahim, A., & Abderafi, A. (2021). Energy efficiency improvement of debutanizer column, for NGL separation. *International Journal of Environmental Science and Development*, *12*(9), 255-260.

Ould Brahim, A., & Abderafi, A. (2016). Optimisation of the energy efficiency and the CO2 reduction, for the NGL separation. *International Renewable and Sustainable Energy Conference (IRSEC*), 822-827. Marrakech, Morocco.

Peng, D.Y.,. & Robinson, D.B. (1976) A new two-constant equation of state. *Industrial & Engineering Chemistry Fundamentals, 15*(1), 59–64.

Sangal, VK., Kumar, V., & Mishra, M. I. (2013)**.** Optimization of a divided wall column for the separation of C4-C6 normal paraffin mixture using Box-Behnken design. *Chemical Industry & Chemical Engineering Quarterly*, *19*(1) 107−119.

Smith, R. (1995). *Chemical process design.* Newyork, NY: McGraw-Hill.

Tavan, Y., Hosseini, S.H., & Kargari, A. (2016). An increased production capacity by a retrofitted industrial deethanizer column. *Journal of Natural Gas Science and Engineering*, *30*, 248-255.

Tgarguifa, A., Abderafi, S., & Bounahmidi, T. (2018). Energy efficiency improvement of distillery, by replacing a rectifying column with a pervaporation unit. *Renewable Energy*, *122*, 239-250.

Tgarguifa, A., Abderafi, S., & Bounahmidi, T. (2017). Energetic optimization of Moroccan distillery using simulation and response surface methodology. *Renewable and Sustainable Energy Reviews*, *75*,415-425.

Author Information

Ahmed Ould Brahim
Mohammadia Engineering Scool, Mohammed V University in Rabat
Av. Ibn Sina, B.P. 765, Rabat-Agdal, Morocco

Souad Abderafi
Mohammadia Engineering Scool, Mohammed V University in Rabat
Av. Ibn Sina, B.P. 765, Rabat-Agdal, Morocco
Contact e-mail: *abderafi@emi.ac.ma*

To cite this article:

Brahim, A. O. & Abderafi, S., (2023). Optimization of energy consumption of the debutanizer column, using genetic algorithm. *The Eurasia Proceedings of Science, Technology, Engineering & Mathematics (EPSTEM), 26,* 234-241.

The Eurasia Proceedings of Science, Technology, Engineering & Mathematics (EPSTEM)
ISSN: 2602-3199

The Eurasia Proceedings of Science, Technology, Engineering & Mathematics (EPSTEM), 2023

Volume 26, Pages 242-253

IConTES 2023: International Conference on Technology, Engineering and Science

New Generation Space Vehicle Operations in the United Arab Emirates – An Airspace and Risk Assessment

Oliver Lehmann
Abu Dhabi University

Ramy El-Jabi
Abu Dhabi University

Kirk Webster
Abu Dhabi University

Aya Rachdi
Abu Dhabi University

Abstract: Air Transport is a highly technocentric and rapidly evolving industry. While certain legacy systems persist, more advanced technological concepts for carrying payloads and passengers further, faster, and more efficiently place this particular industry at the forefront of the most cutting-edge research and development initiatives in the fields of autonomous systems, artificial intelligence, cybersecurity, and advanced communication, navigation, surveillance applications. While drone technologies and applications have been widely and comprehensively addressed in recent years, the incipient hypersonic and suborbital commercial transport sector has received disproportionately less academic attention. Although certain suborbital passenger transport concepts such as the German Aerospace Center's SpaceLiner are proposed for the more distant future, other concepts have reached operational status. A recent addition into the foray has been Blue Origin and its vertically launched New Shepherd autonomous vehicle. The United Arab Emirates, an increasingly active spacefaring nation, has signaled its interest. Among the nation's highly ambitious short and long-term initiatives is the idea of launching space tourism flights from its own soil. Blue Origin, along with other candidates, has emerged as a contender to operate its New Shepard vehicle from a UAE-based spaceport. This paper explores how Next Generation Space Vehicle Operations (NGSVO) could impact a highly dense and compact airspace when operating from and to a UAE spaceport. Preliminary results suggest that under certain circumstances, NGSVOs may indeed affect existing Air Traffic Management (ATM) operations and pose increased safety risks while leading to higher fuel consumption and larger carbon dioxide footprints of regular air traffic. To establish a benchmark for future comparisons, the current study applies traditional airspace segregation methods to the UAE airspace to accommodate a specific type of NGSVO. Operational gains may be deduced by comparing the results of future studies applying more advanced ATM concepts to those reported in the current study.

Keywords: Space vehicle operation, Space port, Risk assessment, Air traffic management

Introduction

The approach used here includes using a simplified air traffic event model calculation to gauge how a number of UAE air traffic parameters are impacted by NGSVO; Analyzing these parameters will provide information on how many, and to what extend flights will be impacted by the space vehicle passing over and through the airspace. Elements of the UAE airspace and airway route network are used in our calculations, and space vehicle trajectories and the potential spaceport location are integrated into these. Continuing, the calculations also apply

the relevant hazard protection areas associated with the space vehicle in order to separate these from regular air traffic. Such hazard areas are based on recognized risk assessment methods.

Finally, such research aims to understand how today's ATM environment is going to be affected and how ATM systems and ATC controllers might deal with NGSVO, in order to achieve the intensive dynamic re-routing of the prevailing air traffic required with the lowest possible detriment.

Preliminary results have shown that it is a considerable challenge to seamlessly implement next generation space vehicles into today's ATM. However, the as part of new operating concepts demonstrated horizontal launches of space vehicles from a carrier plane are also an interesting control tool. Particularly, the navigational performance of the glider during descent, approach and landing continues to be challenging for a safe and efficient operation which does not threaten and obstruct other users of the airspace. Highly frequented air spaces such as those on which this investigation is based, this challenge applies even more to.

It had to be determined on what data basis the investigation should be founded. To make the most realistic assumptions possible, publicly available radar data was used (Flightradar24, 2022), since pure flight plan data doesn't represent the actual route flown. The considerations of this initial investigation were focused on an exemplary traffic hour. To account for a worst-case scenario, an hour with the maximum number of flights was selected. Data from the years 2019/2020 were not considered representative due to the ongoing COVID19 pandemic. After analyzing the available data, 6:00 p.m. to 7:00 p.m. from December 19th, 2018 was selected as a traffic hour with a very high number of flights within UAE airspace (peak hour) (Lehmann et al., 2022). The data used in the further course is shown in Figure 1.

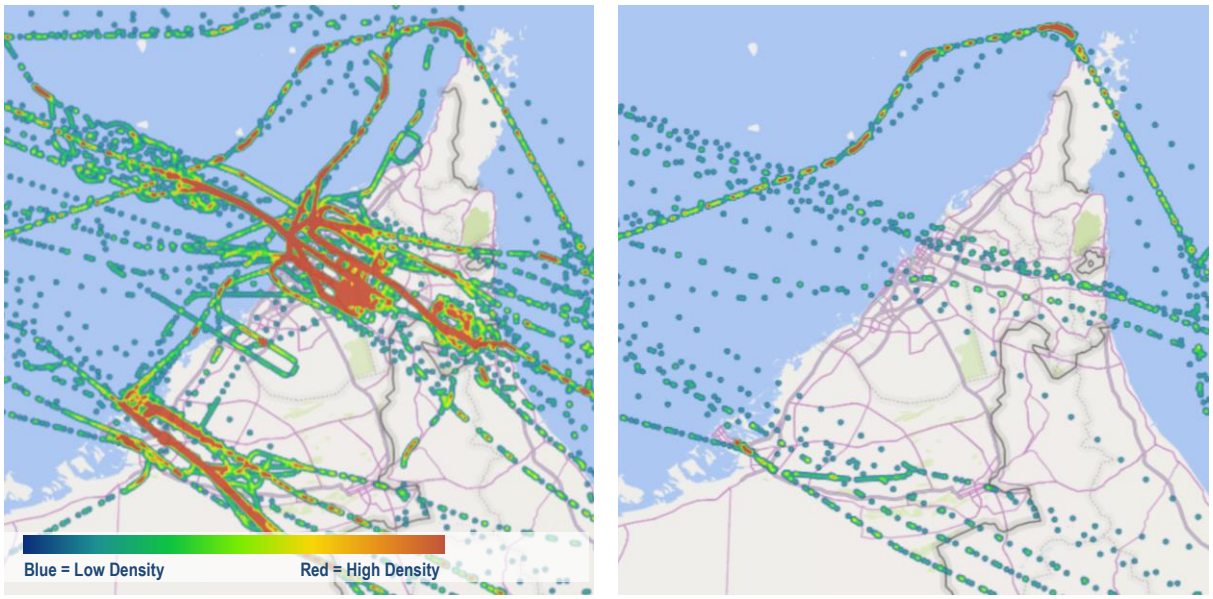

Figure 1. Heat map - Density of air traffic (Lehmann et al., 2022)

For Figure 1 unmodified position data was used. A higher density of air traffic (red color) commonly means that, among other things, higher impacts from NGSVO can be expected in this area. Further, Figure 1 shows the density of Air Traffic (qualitative) in the reference period (peak hour); All Flights (left); Only UAE Overflights (right).

In total 20,740 data sets have been evaluated, these could be assigned to in total 233 different flights within the reference hour, as well as to position data (latitude/longitude) the altitude and the direction of flight, the Callsign, the ADS-B identifier and the flight number were also included in the data.

It bears remembering that 5% to 10% of the flights which were actually conducted are not present in the data Federal Aviation Administration (2022); (Flightradar24, 2022). This may be due to missing or non-functioning or inactive ADS-B equipment of the aircraft or alternatively insufficient receiver coverage on the ground. This means that real Air Traffic in total can also be around 5% to 10% higher during any selected peak hour. For the here discussed analysis, however, this is noncritical. In the further course of the project, our database is to be expanded to include official ATC data (Lehmann et al., 2022).

Impact on Civil Aviation Airspace

Method

Model and Data

The current approach implements a simplified air traffic event model calculation to simply count the number of commercial passenger flights impacted by the temporary closure of a portion of UAE airspace. A flight is considered to be impacted if its usual passage through a portion of the airspace coincides with the closure of that airspace, forcing the flight to be rerouted, delayed, or subjected to other air traffic flow management measures. This can be considered as a simplified and accessible alternative to conducting more advanced airspace analyses using a dedicated fast time simulation platform. While future studies will make use of such resources, the current approach is suitable for the purpose of establishing a benchmark.

Historical UAE airspace flight data is provided by the Flightradar24 internet-based aircraft flight tracking service that collects data from a large ADS-B network along with other sources such as MLAT, radar data, as well as schedule and flight status data (Federal Aviation Administration, 2022). This information is combined with UAE eAIP data to derive useful flight parameters such as aircraft position, points of origin/destination, ATS routes flown, as well as bearing and distance to/from key points such as the reference spaceport location.

Two data sources provide space vehicle trajectory and flight parameters. The first is a study describing the results of a simulation campaign of nominal SS2 flights (Llanos et al., 2018), in which distance flown, altitude, and speed of simulated nominal flights are provided, among other data. The second source is the flight data recorded on Flightradar24 during SS2's test flight in California on July 11, 2021 (Flightradar24, 2022).

Space Vehicle Trajectory

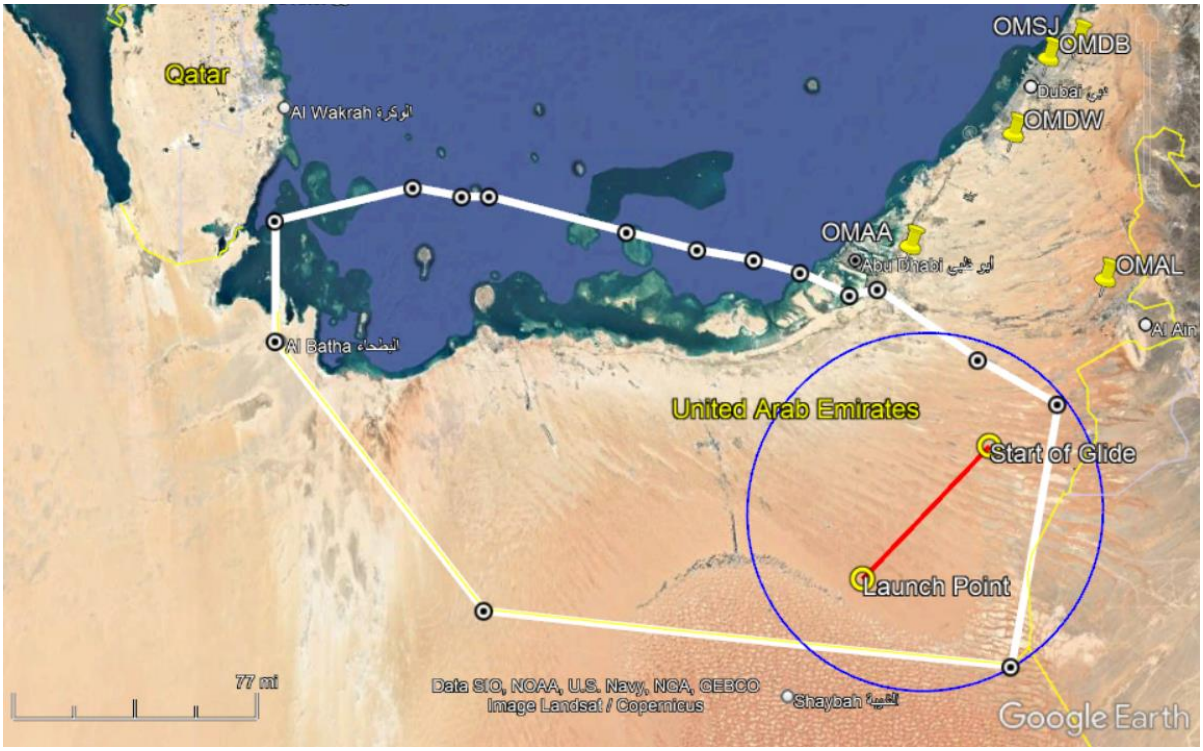

Figure 2. Proposed SS2 trajectory (red) and related assessment area (blue)

For the current hypothetical use case, the following scenario will be considered: SS2 will be transported by the carrier aircraft from the future Al Ain Spaceport to a launch point around 100 NM southwest of the spaceport, within the OMR 54 restricted area, and will be released above 40,000 feet for the secondary launch. Upon its return, SS2 will enter the glide phase at around 49 NM from the launch point, and around 50 NM from the Spaceport. The distance of 49 NM represents the maximum distance flown by the SS2 between the launch point

and the top of glide during a simulation campaign in one study (Llanos et al., 2017). SS2 will then return to the Spaceport as a glider. Figure 2 shows the proposed SS2 trajectory (red segment), OMR 54 restricted airspace (white trapezoid), along with the airspace closure (blue circle) as defined further below.

Large portions of airspace have been historically blocked to protect civil aviation traffic from the passage of space vehicles, from slightly before until slightly after the planned time of operations (Tinoco et al., 20210; Young et al., 2017). The dimensions of the temporary airspace closure typically depend on the flight characteristics of the specific type of space vehicle and the nature of the operation. More specifically, the temporary airspace closure must be large enough to account for off-nominal events such as the inflight breakup or explosion of the space vehicle, leading to a debris field spanning relatively large areas. Since a debris dispersal model for SS2 was not available for the current study, the approach taken in Lehmann et al. (2022) is applied: a circular airspace closure is defined having a similar surface area of a trapezoidal operating range near the Cecil Spaceport in Florida (USA), as defined in Llanos et al. (2017).

As explained in Lehmann et al. (2022), the application of a debris dispersal model based on a known inflight breakup, namely the Space Shuttle Columbia accident, is not appropriate in this case. The proposed circular area is centered at the mid-point of SS2's trajectory (between the secondary launch from the carrier aircraft and the top of glide). The hypothetical horizontal launch corridor between the Al Ain Spaceport and the launch and reentry operating area in OMR 54 will be excluded from the impact analysis based on the same rational presented in Llanos et al. (2017) and Lehmann et al. (2022). This serves as an adequate approximation for the UAE scenario and allows to derive some preliminary insights. Figure 2 shows the airspace closure (blue circle), the OMR 54 restricted airspace (white trapezoid), along with the proposed SS2 trajectory (red segment) as defined further above.

Results and Discussion

Assessment Results

Prior to identifying affected flights, it would be useful to present overall traffic data in the UAE Airspace. The following figures provide an overview of traffic demand and controller workload during the defined peak hour. A total of 233 fights were counted in the UAE airspace during the defined peak hour. This includes 61 overflights through the UAE airspace, 78 departures from UAE airports, and 94 arrivals into UAE airports. Here, "UAE airports" refers to Abu Dhabi International Airport (OMAA), Dubai International Airport (OMDB), Al Maktoum International Airport (OMDW), and Sharjah International Airport (OMSJ) only.

Premilitary insights on the number of potentially impacted flights may be derived by analyzing the traffic demand within the defined assessment area. 12 flights passed through the assessment area during the peak hour, all of which were overflights passing through the UAE airspace. None of these flights were departing from or arriving to UAE airports. This may indicate the need to implement common relevant air traffic flow management measures such as rerouting of overflights. While such measures would not be required for UAE terminal traffic in this specific case, other scenarios involving SVO flight trajectories closer to major UAE airports would most likely have an impact on terminal traffic as well. Table 1 shows the affected flights.

Table 1. Flights affected by the proposed airspace closure

Operator	Call Sign	Aircraft	From	To
Air India	AIC975	A320	GOI	KWI
Air India Express	AXB321	B738	CCJ	RUH
Air India Express	AXB773	B738	CNN	DOH
Jet Airways	JAI524	B738	BOM	RUH
Jet Airways	JAI552	B738	BOM	DOH
Jet Airways	JAI560	B738	BOM	DOH
Jet Airways	JAI566	B738	TRV	DMM
Oman Air	OMA673	B788	MCT	JED
Oman Air	OMA677	B738	MCT	MED
Saudi Arabian Airlines	SVA3759	A332	DEL	JED
Saudi Arabian Airlines	SVA705	B772	KHI	JED
Saudi Arabian Airlines	SVA773	A333	BOM	JED

Table 2 below lists the ATS routes that intersect the assessment area:

Table 2. Affected ATS routes

Affected ATS Routes	Affected
LUDID-M628-RIGIL-M628-PEKEM	AXB321 OMA673 SVA3759
M628-RIGIL-M628-PEKEM	SVA705 SVA773
RIGIL-M628-PEKEM	JAI524
SODEX-ELUDA-N563-NOBTO-N563-PARED-SIGMO-N563-TAPTO-N563-VUXOD-N563-KUGTO-N563-BOSEV-L565-UKUVO-G462-OXARI-G462-PURLI-G462	AIC975
SODEX-N563-ELUDA-N563-NOBTO-N563-PARED-N563-SIGMO-N563-VUXOD-N563-P899-LAGVU-P899-MEKRI-P899-VATIG-P899-KUMSI	AXB773
SODEX-N563-ELUDA-N563-NOBTO-N563-PARED-N563-SIGMO-N563-VUXOD-N563-RUKOS-P899-LAGVU-P899-MEKRI-P899-VATIG-P899-KUMSI-MEKMA	JAI552
SODEX-N563-ELUDA-N563-NOBTO-N563-PARED-SIGMO-PUVUT-N563-VUXOD-N563-ORMID	JAI566
SODEX-N563-ELUDIA-N563-SIGMO-N563-VUXOD-N563-P899-LAGUV-P899-VATIG-P899-KUMSI-P899-MEKMA	JAI560

Discussion of Results

The above analysis assumes that the entire assessment area would be closed to regular air traffic during the peak hour. This implies that appropriate ATFM measures (mostly rerouting) would need to be applied to all 12 flights identified above. On the other hand, the launch point location and the flight direction were chosen strategically to ensure that most of the assessment area falls within the OMR 54 restricted airspace. This is categorized as a permanent restriction from ground level to unlimited, for military purposes. Although civil aviation aircraft are occasionally permitted to transit through OMR 54 on pre-agreed ATS routes, it wouldn't be unusual for these routes to become unavailable on occasion, forcing aircraft to adopt alternate routes.

It's worth noting that while the proposed assessment area somewhat overlaps the airspaces of Oman and Saudi Arabia, this situation may be dealt with either through agreements between the concerned parties or by adjusting the location of the launch point and the direction of flight in order to contain the assessment area entirely within UAE airspace. The latter approach would potentially lead to higher levels of impact, as described in Lehmann et al. (2022).

Furthermore, while the assessment area considered in the current study assumes that OMR 54 would be made available for such SVOs, it is certainly not a forgone conclusion. Hence, while the current specific scenario may not represent a significant impact on traffic movements and controller workload, the actual flight trajectory could potentially be much closer to major UAE airports, in which case the impact on both overflights and arriving/departing aircraft would likely be significant. In such circumstances, NGSVOs may indeed affect existing Air Traffic Management (ATM) operations and pose increased safety risks while leading to higher fuel consumption and larger carbon dioxide footprints of regular air traffic.

Impact on Flight Safety

Risk Assessment Methodology

With continued enhancements in not only navigating regulations but also exploring gaps within the systems associated with space operations, governments across the globe have been working with industry to find solutions that will make this new commercial endeavor safe and viable for the public. Since Blue Origin and Virgin Galactic have done successful commercial passenger launches, and with SpaceX continued launches to the international space station, these government entities have relaxed some of the regulation pertaining to such launches but still requires that these companies maintain detailed records associated with these launches. Technology is also aiding in better identifying gaps that could potentially harm the system but with constant revamping of safety measures, these launch systems are poised to carry passengers to the edge of space and back to earth safely.

Table 3. Adopted Risk Assessment Process

Prosedure	Task
1. Identify the Threats, Vulnerabilities, Hazards/Risks	• SS2 takeoff to predetermined altitude and separation process. • SS2 does not separate from the transport vehicle. • SS2 does not ignite for the next phase of flight due to computer glitch. • Separation is outside normal parameters/or identified launch area. • Loss of one or both aircrafts • Equipment functional failures • Structural failures and Human errors
2. Understand the impact of these threats, vulnerabilities, and risks on the organization	• Loss of occupants of both aircrafts • Colliding with another aircraft during the separation and return phase of orbiter. • Debris field beyond containment area • Civilian harm or injury below • Legal matter associated with the loss of the vehicle and occupants. • Possible environmental contamination due to flammable/explosive fuel leakage or wreckage • Environment (or external) events, such as Orbital Debris impacts dispersion
3. Create or use a model for risk analysis	• Bow-tie Analysis • Failure Mode and Effect Analysis (FMEA) • Decision Tree Analysis • Fault Tree Analysis (FTA)
4. Sample the model to understand the threats, vulnerabilities, and risks more fully	• Ensure manual control of ignition system if necessary. • Automate the drag system to reduce human error. • Coordinate with ATC to facilitate the liftoff and separation process • Review Flight Data to include trajectory and speed • Internal monitoring of the flight crew during the entire flight process • Analyze Cockpit Voice Recorder (CVR) • Review deviations from flight path if any
5. Analyze the results obtained from the above steps	• Results of Analysis • Review of Flight Data
6. Implement a risk management plan to manage the threats, vulnerabilities and risks based on the results of the risk analysis	• Mitigation plan to reduce likelihood of hazardous activities • Redesign of parts or activities if necessary as deemed by the analyzed data
7. Review and Revise	• Review current plans and update as required

It is the operations of these SVO and their integration into the current airspace system that creates risks that must be understood and mitigated. The process of integration is a complex one and requires input from industry as well as using system engineering to design safety measures for the system itself. System engineering is defined as "a methodology that supports the containment of the life cycle cost of a system. System engineering can be viewed as the art and science of developing an operable system capable of meeting requirements within often opposed constraints" (NASA, 2007). The process must be flexible and should demand recurring evaluations to ensure that benchmarks are met and that they satisfy the evolution of these vehicles as well as growth in the surrounding areas of the launch site.

Risk cannot be eliminated altogether but can be mitigated through risk controls using system engineering (during the design phase), along with other risk analysis tools and methods. These methods tend to follow a step function in which the risk is constant until changes in the design, process, or operation are addressed. Conventional theory suggests that risk can increase when trading safety margin for perceived gains such as increased performance which ultimately increases the risk for the underlying areas of the launch vehicle. Utilizing a system engineering approach can reduce the chance and effects of failures that could be inherent to the design of the system which ultimately could place the vehicle and operation at risk.

Before further reviewing some of the risks associated with high-risk recreational activities, we must first define risk. Risk is the chance or probability of a hazardous situation that may lead to harm to a person, users, environment, property, equipment loss, or harmful effects on the environment (Canadian Centre for Occupational Health and Safety, 2021). The hazardous situation may also be called a failure mode, and it is triggered by a failure cause. The risk itself is assessed by the severity of the harm and the probability of the harm happening.

The risk assessment process includes:

1. Identify threats, vulnerabilities, and risks.
2. Understand the impact of these threats, vulnerabilities, and risks on the organization.
3. Create or use a model for risk analysis.
4. Sample the model to understand the threats, vulnerabilities, and risks more fully.
5. Analyze the results obtained from the above steps.
6. Implement a risk management plan to manage the threats, vulnerabilities and risks based on the results of the risk analysis.
7. Review and revise.

Although Failure Mode and Effects Analysis FMEA will not be used in this paper, it should be noted that when FMEA and Risk Analysis are completed in harmony, with their key differences, attributes and interconnected relationship considered, risk management process stands to benefit in terms of efficiency and effectiveness, saving both time and resources (Congenius, 2021). Further guidance on risk assessment methodology can also be found in the ICAO Safety Management Manual Doc 9859 (2018).

Adopted Approach for SpaceShip Two

In the case of SS2, the assessment is as shown in Table 3. Below (Figure 3) is an example of risk impact/probability chart that consists of varying degrees of risk probability and risk impact:

Risk Assessment Matrix		**Impact**			
		Minor 1	**Moderate 2**	**Major 3**	**Critical 4**
Likelihood	**76% -100% 4**	**4 Medium**	**8 High**	**12 Very High**	**16 Extreme**
	51% - 75% 3	**3 Medium**	**6 High**	**9 High**	**12 Very High**
	26% - 50% 2	**2 Low**	**4 Medium**	**6 High**	**8 High**
	0% - 25% 1	**1 Very Low**	**2 Low**	**3 Medium**	**4 Medium**

Figure 3. Adopted risk assessment matrix

The corners of the risk impact/probability matrix show varying extremes that typically have the most actionable items and will shed light on the possibilities of inherent risks:

- **Low probability/ low impact:** Risks in this area are both low probability and low impact, so no attention is needed.
- **High probability/ low impact:** Risks poses a moderate threat to operations. Although risk should be minimized, in this corner, it can be easily managed if it occurs.

- **Low probability/ high impact:** Risks will have a high impact on operations, but the probability of the event materializing is unlikely. Preventative steps should already be in place should an event occur. Contingency plans should also be in place to minimize the severity of the impact should the risk manifest.
- **High probability/ high impact:** Risks in this category represent the highest-priority risks and should be given the most attention because they have a higher probability of occurring which would have a negative impact on operations (Indeed, 2022).

With the use of Temporary Flight Restrictions (TFRs), SpaceShip Two could be segregated from other arriving or departing traffic, ensuring that there is a slight modification to the flight structure to protect both spaceship two and the overlying traffic. As suggested for future studies, the dynamic opening and closing of the surrounding airspace might be a temporary but viable solution for the future growth of SVO. Any integration solution must include characteristics associated with the suborbital launch platform. Some of the characteristics identified includes, launch system reliability, timing, and trajectory (Unverzagt, 2020).

Refinement of Assessment Scenario

To better understand the status of the airspace in Al Ain and the surrounding areas within the UAE, we must first look at the uses of the current airspace. By reviewing the flight data available which includes takeoffs and landing as well as overflights, points the project in a direction that will provide the data necessary to aid in the integration of SVO. Mitigation strategies must be incorporated to ensure that in the event of an unforeseen catastrophic failures, the debris field will be contained within the specified NM buffer zone on either side of the launch trajectory but could be expanded as needed. During liftoff from the designated spaceport the mated aircraft will be under the guidance of air traffic control and will follow the established procedures as it attempts to get to its designated altitude for separation above 50,000 ft.

During the initial ascent, there should be no other commercial traffic above Spaceship two ignition altitude, where the aircraft would have no problems getting to its position to begin the weightlessness phase before its return. During the return phase of Spaceship two, the craft should still follow the same parameters to return once below 50,000 ft. Although now a glider, it should be able to circumnavigate whatever aircraft might be in the vicinity with the help of Air Traffic Control (ATC) to get back to its landing position at Al Ain Spaceport. This can only be done through coordinated information sharing between managers of the airspace and launch providers. The authors are aware that the current effective airspace rules, do not recognize the type of glider described here (see ICAO Annex 2; Chapter 3.2.2). As a result, suitable supplements, preferably at the ICAO level, must be defined. The aviation law issue to be derived from this is not part of this technical paper and will be examined separately.

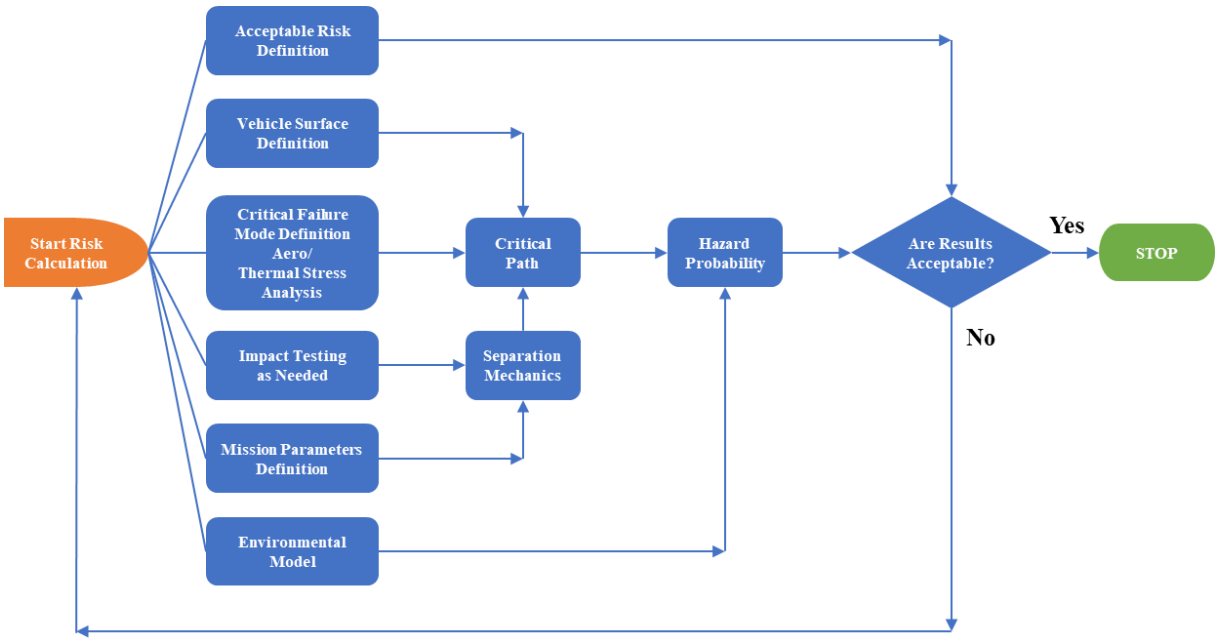

Figure 4. On-orbit impact analysis methodology
Committee on Space Shuttle Meteoroid/Debris Risk Management (1997)

In a recent white paper submitted by Air Line Pilot Association (ALPA) to one of their annual conferences, "the challenge to date has been to develop a data-exchange mechanism to pass this information to the other parties involved. The FAA's space data integrator (SDI) under development is a move in this direction and would serve as a testbed for what could potentially be used in the UAE to facilitate suborbital space launches in and around the region. According to reports, SDI would provide controllers and traffic managers with situational awareness of a spaceflight mission through real time data on vehicle state and operational status, calculate the location and extent of potential hazard areas, and provide visibility into mission progress. SDI will afford the capability for FAA and, by extension, other airspace users to benefit from a detailed level of knowledge of a space mission as it progresses through shared airspace. In addition, the real-time, detailed view provided by SDI allows alert and execution of contingencies if off-nominal events occur" (Air Line Pilots Association, 2020).

There are multiple risk assessment strategies to choose from across varying industries. The risk assessment associated with spaceship two and the transport aircraft comes from a complex set of systems that if not implemented correctly, would affect not only other users within the airspace, but could negatively impact the surrounding environment.

Launch & reentry operation window as short as possible –

- Avoid peak traffic times
- Optimize launch & reentry trajectories as far as possible
- Optimize air space usage alongside restricted areas which could include military operation areas (MOA).
- Ensure real time monitoring and direct communication, connecting all involved stakeholders with ANSP managers and ATC facilities (Kaltenhaeuser et al., 2015)

Analysis and optimization of SVO scenarios and concepts regarding air traffic impacts as suggested by Kaltenhaeuser et al., 2015 can be seen below:

- Improved ATC procedure design
- Support of Spaceport site evaluation
- Integration of SVO Mission management and ATM
- Improved SVO implementation into AIM (e.g. System Wide Information Management)
- Provision of adequate evaluation and validation capabilities

Conclusion

Further study will require more precise definition of the space vehicle's 4D trajectory within the surrounding airspace in the region, as well as a more precise definition of flight restriction areas along the SV trajectory. After reviewing the latest dataset, it was recognized there were slight deviations from prescribed flight path in terms of vehicle heading. An investigation into the cause of these deviations is warranted to further define both the prescribed trajectory as well as define the hazard protection areas. Such restriction areas would be based on traffic separation criteria for such high-risk operations as well as hazard areas relating to abnormal events such as the inflight breakup or explosion of the space vehicle, leading to a debris field spanning relatively large areas. The primary objective during this next stage is the application of a more accurate debris dispersal model to define more precise hazard protection areas, allowing for a less conservative approach, possibly leading to reduced impacts on regular air traffic within the UAE airspace and beyond.

The risk assessment methodology presented in our initial research was further expanded to incorporate analyses of both internal and external risks relating to NGSVO within UAE airspace (Lehmann et al., 2021). This paper was updated to review other possible solutions to this burgeoning problem to finally integrate SVO traffic with normal commercial traffic into the UAE airspace. As the problem is further researched, the hope is that it will present a more concrete solution that will solve the issue once and for all.

Outlook

Future research will involve the use of a fast-time simulation platform and a more comprehensive dataset allowing for a more detailed analysis of the UAE, Oman, Saudi and surrounding airspaces, and the impact of inserting NGSVO trajectories. We will then be able to consider how modern and emerging ATM concepts such

as Trajectory Based Operation (TBO), Advanced Flexible Use of Airspace (AFUA), dynamic sectorization, and the role of aircraft-ground datalink requirements could support the situation. The impact of re-routings on overall fuel consumption and CO2 emissions of the air traffic in airspaces across the region will be expanded and investigated.

Scientific Ethics Declaration

The authors declare that the scientific ethical and legal responsibility of this article published in EPSTEM Journal belongs to the authors.

Acknowledgement

*This article was presented as an oral/poster presentation at the International Conference on Technology, Engineering and Science (www.icontes.net) held in Antalya/Turkey on November 16-19, 2023.

*This project was supported and funded by the Abu Dhabi Department of Education and Knowledge (ADEK) Award for Research Excellence (AARE) 2018.

References

Air Line Pilots Association. (2020). *ALPA white paper: Safe integration of commercial space operations into the U.S. national airspace system and beyond*. Retrieved from https://www.alpa.org/-/media/ALPA/Files/pdfs/news-events

Canadian Centre for Occupational Health and Safety (2021). *Hazard and risk*. Retrieved from: https://www.ccohs.ca/oshanswers/hsprograms/hazard_risk.html

Committee on Space Shuttle Meteoroid/Debris Risk Management (1997); *Protecting the space shuttle from meteoroids and orbital debris.* Washington, D.C.: National Academy Press, Sciences, Engineering, Medicine.

Congenius. (September 23, 2020). Risk analysis vs FMEA: How knowing the difference benefits your risk management. Retrieved from https://congenius.ch/

Cooke, B., & Williams, P. (2004). *Construction planning, programming and control*. Oxford: Blackwell Publishing. Retrieved from: https://www.stakeholdermap.com/risk/risk-assessment.html#cooke

Federal Aviation Administration. (2014). *Management of space vehicle operations in the national airspace System concept of operations*. Retrieved from https://www.faa.gov

Federal Aviation Administration. (2022). Air traffic technology Retrieved from: https://www.faa.gov/air_traffic/technology/equipadsb/research/airspace/

Flightradar24. (2022). Commercial data services. Retrieved from https://www.flightradar24.com/commercial-services/data-services

Health and Safety Executive. (2016). Risk management online. Retrieved from: https://www.hse.gov.uk/risk/index.htm

Air Line Pilots Association (2018). *Addressing the challenges to aviation from evolving space transportation*

ICAO. (2021) – *Rules of the air – Annex 2* (10th ed.). Amendment.

ICAO. (2018). *Safety management manual doc 9859* (4th ed.).

Indeed, (October 12, 2022). *How to use a risk assessment matrix*. Retrieved from indeed.com

Industry High Level Group (2019). *Aviation benefits report 2019* Retrieved from: https://www.icao.int/sustainability/Documents.pdf

Kaltenhaeuser, S., Luchkova, T., Klay, N., & Ang, R. (2019). Assessment of the impact of air launch operations on air traffic in Europe. *5th Annual Space Traffic Management Conference.* Austin, Texas

Kaltenhaeuser, S., Morlang, F., Hampe J., & Schmitt, D. (2015). Air traffic management and space transportation: System wide information management and integration into European airspace. *ICAO/ UNOOSA Aerospace Symposium*

Lehmann, O., El-Jabi, R., Webster, K., & Rachdi, A. (2021). Integration of space vehicle operations into the United Arab Emirates air traffic management – An impact analysis. Proceedings of the *32nd ICAS Congress.* Shanghai, China

Lehmann, O., El-Jabi, R., Webster, K., & Rachdi, A. (2022): New generation space vehicle operations in the United Arab Emirates – An airspace and risk assessment. Proceedings of the *33rd ICAS Congress*. Stockholm; Sweden

Llanos, P. J., & Seedhouse, E. (2017). Integrating spaceship two into the national airspace system. In *AIAA SPACE and Astronautics Forum and Exposition* (p. 5358).

Llanos, P., Seedhouse, E., & Hays, C. (2018). Nominal spaceship two flights conducted by scientist-astronaut candidates in a suborbital space flight simulator. *4th Annual Space Traffic Management Conference*. Daytona Beach, Florida

Luchkova, T., Kaltenhaeuser, S., & Morlang, F. (2016). Air traffic impact analysis design for a suborbital point-to-point passenger transport concept. *3rd Annual Space Traffic Management Conference*. Daytona Beach, Florida

Martin, J.N. (1997) *Systems engineering handbook: A process for developing Systems and Products*. (Lucent Technologies.

Millard, S. (2010). Over-flight risk considerations for the launch of an ELV rocket to an ISS inclination. *AIAA Atmospheric and Space Environments Conference.* Federal Aviation Administration

NASA. (2007) *Systems engineering handbook*. Washington, D.C.: NASA Headquarters. Retrieved from https://soma.larc.nasa.gov/mmx/pdf_files

National Research Council (1997). *Protecting the space shuttle from meteoroids and orbital debris*. Boeing North American Inc. Retrieved from https://www.nap.edu

Tinoco, J. K., Yu, C., Firmo, R., Castro, C. A., Moallemi, M., & Babb, R. (2021). Sharing airspace: Simulation of commercial space horizontal launch impacts on airlines and finding solutions. *Journal of Space Safety Engineering, 8*(1), 35-46.

Turner, R. (2000). *Gower handbook of project management* (4 th ed.). Aldershot: Gower.

Unverzagt, R. M. (2020). *Airspace integration in an era of growing launch operations. Center for space Policy and strategy*. Retrieved from https://aerospace.org/sites/default/files/2020-10/Unverzagt_AirspaceIntegration_20200929.pdf

Wolf, C. (1978). *A theory of "non-market failure": Framework for implementation analysis.* Santa Monica, CA: The Rand Corporation.

Young, J. E., Kee, M. G., & Young, C. M. (2017). *Effects of future launch and reentry operations on the national airspace system. Journal of Air Transportation, 25*(1), 8-16.

Annex 1.Abbreviations

ADEK.....Abu Dhabi Department of Education and Knowledge (UAE)
ADS-B.....Automatic Dependent Surveillance – Broadcast
AFUA .....Advanced Flexible Use of Airspace
AIP.....Aeronautical Information Publication
ALPA.....Air Line Pilot Association
ANSP.....Air Navigation Service Provider
ATC.....Air Traffic Control
ATFM.....Air Traffic Flow Management
ATM.....Air Traffic Management
CCOHS.....Canadian Center for Occupational Health and Safety
FAA.....Federal Aviation Authority
ICAO .....International Civil Aviation Organization
MBRSC .....Mohammed Bin Rashid Space Centre
MLAT.....pseudo-range Multilateration
MOU.....Memorandum of understanding
NGSVO .....New Generation Space Vehicle Operations
NM.....Nautical Miles
OMAA.....Abu Dhabi International Airport
OMAL .....Al Ain International Airport
OMSJ.....Sharjah International Airport
SDI.....Space Data Integrator
SS2.....Scaled Composites Model 339 SpaceShip Two (The Spaceship Company)
SV.....Space Vehicle
SVO.....Space Vehicle Operations
TBO.....Trajectory Based Operation
TFR.....Temporary Flight Restrictions
UAE.....United Arab Emirates

Annex2. Definition

"Dwell time" means the period during which a launch vehicle's instantaneous impact point is over a populated or other protected area.

"Launch vehicle" means:
a) a vehicle built to operate in, or place a payload or human beings in, outer space; and
b) a suborbital rocket.

"Protected area" means an area of land not controlled by a launch operator that is a populated area, is environmentally sensitive or contains a vital national asset.

"Suborbital trajectory" means the intentional flight path of a launch vehicle, reentry vehicle, or any portion thereof, whose vacuum instantaneous impact point does not leave the surface of the Earth.

"Suborbital rocket" means a vehicle, rocket-propelled in whole or in part, intended for flight on a suborbital trajectory, and the thrust of which is greater than its lift for most of the rocket-powered portion of its ascent.

"United Arab Emirates" means the seven Emirates of the United Arab Emirates.

Author Information

Oliver Lehmann
Abu Dhabi University
P.O. Box 59911
Abu Dhabi, United Arab Emirates

Ramy El-Jabi
Abu Dhabi University
P.O. Box 59911
Abu Dhabi, United Arab Emirates
Contact e-mail: *ramy.el-jabi@adu.ac.ae*

Kirk Webster
Abu Dhabi University
P.O. Box 59911
Abu Dhabi, United Arab Emirates

Aya Rachdi
Abu Dhabi University
P.O. Box 59911
Abu Dhabi, United Arab Emirates

To cite this article:

Lehmann, O., El-Jabi, R., Webster, K., & Rachdi, A. (2023). New generation space vehicle operations in the United Arab Emirates – An airspace and risk assessment. *The Eurasia Proceedings of Science, Technology, Engineering & Mathematics (EPSTEM), 26,* 242-253.

The Eurasia Proceedings of Science, Technology, Engineering & Mathematics (EPSTEM)
ISSN: 2602-3199

The Eurasia Proceedings of Science, Technology, Engineering & Mathematics (EPSTEM), 2023

Volume 26, Pages 254-261

IConTES 2023: International Conference on Technology, Engineering and Science

dsPIC Implementation and Performances Evaluation of Adaptive Filters for System Identification

Benziane Mourad
University of Bouira

Arabi Abderrazak
University of Setif

Medjedoub Smail
University of Bouira

Ayad Mouloud
University of Setif

Saoudi Kamel
University of Bouira

Abstract: This paper aims to implement and evaluate performances of adaptive filters applied to linear systems identification on a dsPIC platform. To do so, we considered two different applications: the identification of DC motor transfer function and the acoustic echo cancellation. For the DC motor case, real-time identification is not necessarily required. However, for the acoustic echo cancellation case, real-time identification is crucial, making execution time a key parameter in this scenario. We have implemented three adaptive algorithms: LMS, NLMS, and RLS. The first two are known for their computational simplicity, while RLS is recognized for its convergence speed. Performances evaluation is primarily based on accuracy and computation speed. A comparison is carried out in both cases to determine which algorithm is more suitable for each application. The results obtained showed that RLS is better suited for the DC motor case, while NLMS is more suitable for acoustic echo cancellation, particularly when the impulse response of the echo path is long.

Keywords: Systems identification, dsPIC implementation, Adaptive algorithms, LMS, NLMS, RLS, Real-time.

Introduction

Adaptive methods in signal processing aim to automatically adapting processing operators to the statistical properties of signals and systems, as well as their temporal variations. This processing aims to eliminate, or at least reduce, the effect of temporal variations in the properties of signals and systems. Without these variations, there would be no need for adaptivity; one could simply calculate the "optimal filter" once and deploy it (Benesty & Huang, 2000). These methods have known significant growth since the 1960s, motivated by the development of digital processing and the continuous increase in the processing power of Digital Signal Processors (DSPs), allowing the real-time implementation of increasingly sophisticated algorithms at higher speeds processing (Paulo & Diniz, 2013). They have reached a certain level of maturity both in terms of algorithm development and implementation, as well as from the perspective of theoretical tools for performance analysis (Diniz, 2020).

The applications of this approach to processing using adaptive filters are numerous, including system identification, inverse modeling, interference elimination, and predictive filtering (Ghauri & Sohail, 2013). Adaptive filtering algorithms can be categorized into two main groups: LMS, known for their simplicity but limited performance, and RLS, offering significantly better performance at the cost of higher computational complexity (Haykin, 2014). Implementing such algorithms in specific processors, such as dsPIC, ensures their proper operation with improved performance (Colak et al., 2015; Siddiqui et al., 2015; Uriz et al., 2012).

The objective of this work is to implement three basic adaptive algorithms: the LMS, its normalized version NLMS, and the RLS, on a dsPIC microcontroller in the context of linear system identification. We have chosen two different applications: the DC motor, which is a simple linear system, and its identification does not require real-time processing, and echo cancellation, where real-time processing is essential. Evaluating the performance of these algorithms in terms of executing time and accuracy allows us to study their adaptation for the two selected examples.

This paper is organized as follows: Section 2 outlines the methodology used for system identification for the two selected systems. Section 3 presents the mathematical formulation of the three conventional adaptive algorithms. Finally, results are discussed in Section 4.

System Identification Using Adaptive Filters

Presentation of Systems

In this work we have chosen two different systems:
The first one is the DC motor, it has a mathematical model represented by the transfer function given by:

$$G(s) = \frac{K}{s(Ts+1)} \tag{1}$$

The discrete time model is given by

$$d(n+1) = -ad(n) - bd(n-1) + cx(n) \tag{2}$$

$$d(n+1) = \mathbf{h}^T \begin{bmatrix} d(n) & d(n-1) & x(n) \end{bmatrix} \tag{3}$$

Where:

$\mathbf{h}^T = \begin{bmatrix} a & b & c \end{bmatrix}$: impulse response to be identified.

The figure 1 shows the block diagram of DC motor identification.

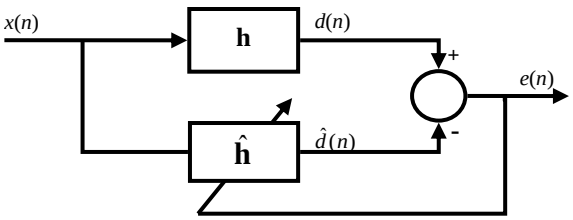

Figure 1. Block diagram of DC motor identification

For this case, the adaptive algorithm tries to find the vector **h**=[*a b c*] minimizing the error signal between desired signal *d*(*n*) and estimated signal $\hat{d}(n)$ (Ogata, 2010). The second system is the echo cancellation. The principle of echo cancellation based on adaptive filtering is shown in figure 2. The general concept is to estimate the echo signal $\hat{d}(n)$ from the far-end signal *x*(*n*) using an adaptive filter. This is a typical example of system identification where the system to be identified is the impulse response of the echo path (Vaseghi, 2000).

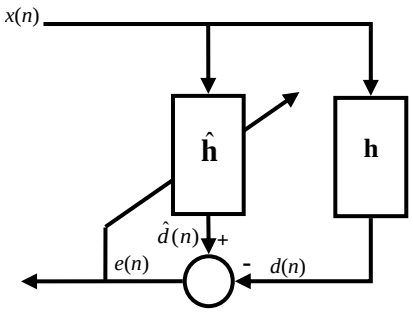

Figure 2. Block diagram of echo canceller

The microphone signal $d(n)$ is obtained as follow:

$$d(n) = \mathbf{h}^T \mathbf{x}_L(n) \tag{4}$$

Where:

$\mathbf{h}^T = \left[h_0\ h_1\ \ldots\ h_{L-1} \right]$: impulse response of the echo-path with a tap-length L.

$\mathbf{x}_L^T(n) = \left[x(n)\ x(n-1)\ \ldots\ x(n-L+1) \right]$: vector of L past samples of the far-end signal.

The echo cancellation is obtained by subtracting the estimate of echo signal $\hat{d}(n)$ from the microphone signal $d(n)$, the estimated echo signal is a combination of fad-end signal $x(n)$ and coefficients of adaptive filter $\hat{\mathbf{h}}$ as following:

$$\hat{d}(n) = \mathbf{h}^T \mathbf{x}_L(n) \tag{5}$$

Where:

$\mathbf{h}^T(n) = \left[h_0(n)\ h_0(n) \ldots h_{L-1}(n) \right]$

We get the error signal:

$$e(n) = d(n) - \hat{d}(n) \tag{6}$$

$$e(n) = d(n) - \mathbf{h}^T \mathbf{x}_L(n) \tag{7}$$

Ideally, this error is equal to zero.

Algorithms

In 1959, engineers Bernard Widrow and Marcian Hoff developed an adaptive filtering algorithm called the Least Mean Square (LMS) algorithm. It has become one of the most widely used algorithms in various applications such as channel equalization, echo cancellation, and noise reduction. The principle of LMS is to adjust the coefficients of a filter to minimize the mean squared error between the desired signal and the output signal (estimated signal). One of the advantages of the LMS algorithm is its computational simplicity, which makes it an attractive solution for many users. The following equations describe the LMS algorithm for updating the adaptive filter weights at each iteration (Gay et al., 2000).

$$\mathbf{w}(n+1) = \mathbf{w}(n) + \mu \mathbf{x}(n) e(n) \tag{8}$$

$x(n)$: vector of input signal with the same length of adaptive filter;
$\mathbf{w}(n)$: Vector filter coefficients at time n ;

μ : step size ;

The Normalized LMS (NLMS) is a variant of the LMS algorithm used in signal processing to estimate adaptive filters. Like the LMS algorithm, NLMS iteratively adjusts the filter coefficients based on the prediction error between the actual and estimated filter outputs. The main difference between LMS and NLMS is the normalization of the coefficients updating. In fact, NLMS uses normalization based on the input power of the filter, which improves the algorithm's convergence especially in noisy environments. By the use of the normalized step-size parameter μ in LMS, we obtain another algorithm called Normalized LMS (NLMS). The formula used to calculate the weight update vector is as follows:

$$\mu(n) = \frac{\beta}{c + \|x(n)\|^2} \tag{9}$$

With:

$\mu(n)$: step size at time n.
β : normalized step size ($0 < \beta < 2$)
c : a small constant to avoid division by zero when x(n) is equal to zero.

The Recursive Least Squares (RLS) algorithm implements an exact least squares solution recursively. The Wiener solution for a finite-length adaptive filter is given by:

$$w_{opt} = R^{-1}P \tag{10}$$

Where R is the autocorrelation matrix of the inputs, and P is the cross-correlation between the inputs and the reference signal. At each time interval, RLS recursively estimates R^{-1} and P based on all previous data and calculates the weight vector as follows:

$$w_n \underline{\underline{\text{def}}} R^{-1}P_n \tag{11}$$

The best current approximation of the Wiener solution can be expressed as follows in the coefficients updating formula:

$$\mathbf{w}_n = \mathbf{w}_{n-1} + \mu_n R_{n-1}^{-1} a_n \mathbf{x}_n \tag{12}$$

Where:

$$a_n = d(n) - \mathbf{w}_{n-1}^T \mathbf{x}_n$$

$$\mu_n = \frac{\lambda^{-1}}{1 + \lambda^{-1}\mathbf{x}_n \mathbf{x}_n^T R_{n-1}^{-1}}$$

λ : is a constant slightly less than 1, called forgetting factor.

Results and Discussion

Matlab Simulation

First, a simulation is performed in Matlab to select the parameter values for each algorithm before the implementation in the dsPIC. We will implement the two system identification examples using adaptive filters based on the basic LMS, NLMS, and RLS algorithms.

DC motor Identification

The first system is the DC motor, which has a second-order transfer function, meaning we have three coefficients to identify. To achieve this, we will use the signal x(n) as the excitation signal, which is given by:

$$x(n) = \sin(0.1n) + \sin(0.2*n) + \sin(0.3n) + 3\sin(n) \tag{13}$$

In this case, the length of the adaptive filter is 3. The number of samples in the signal $x(n)$ is 16000. After several simulations, we have chosen the following parameters:

- LMS (μ=0.05)
- NLMS (β=0.5, C=0.00001)
- RLS (λ=0.95, δ=0.005).

The comparison criterion in this case is the square error between the system output and the output of the adaptive filter, given by:

$$SE(n) = \left[d(n) - \hat{d}(n) \right]^2 \tag{14}$$

By setting the target for this error to 0.0001, we obtained the following results:

Table 1. SE obtained with Matlab simulation for DC motor model

Algorithm	Number of necessary iterations	SE after 200 iterations	SE after 1000 iterations
LMS	1127	$2.04*10^{-4}$	$0.69*10^{-4}$
NLMS	385	$7.76*10^{-4}$	$7.12*10^{-9}$
RLS	133	$0.01*10^{-4}$	$2.15*10^{-23}$

It's evident that the RLS algorithm demonstrates better convergence compared to LMS and NLMS, meaning it reaches the desired SE error after a lower number of iterations.

Echo Canceller

For the echo canceller, the goal in this case is to identify the impulse response of the echo path to be able to estimate the echo signal and subtract it from the transmit signal. We have used an impulse response composed of 128 samples (Figure 3). For the excitation signal (far-end signal), we have chosen an audio signal sampled at 8 KHz and consisting of 40000 samples (Figure 4).

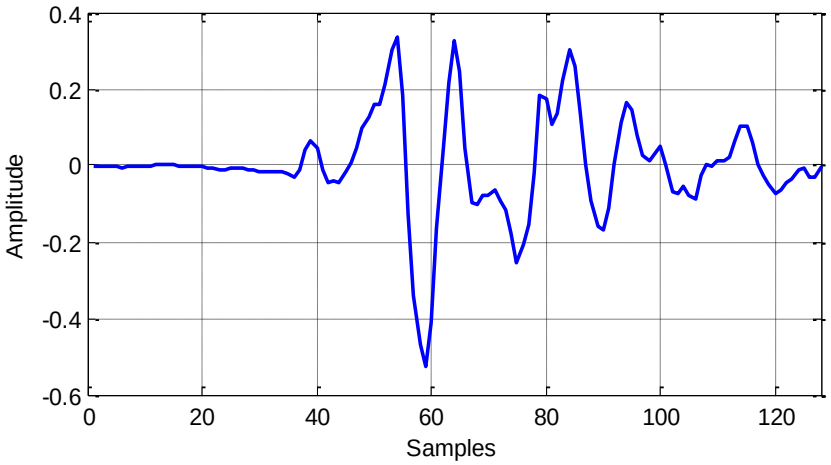

Figure 3. Impulse response of echo path

We proceeded in the same manner to set the parameters for each algorithm to ensure good convergence, this time based on misalignment as the evaluation criterion, with its expression given by:

$$Mis(dB) = 10\log_{10}\left[\frac{\left\| \hat{\mathbf{h}}(n) - \mathbf{h} \right\|^2}{\left\| \mathbf{h} \right\|^2} \right] \tag{15}$$

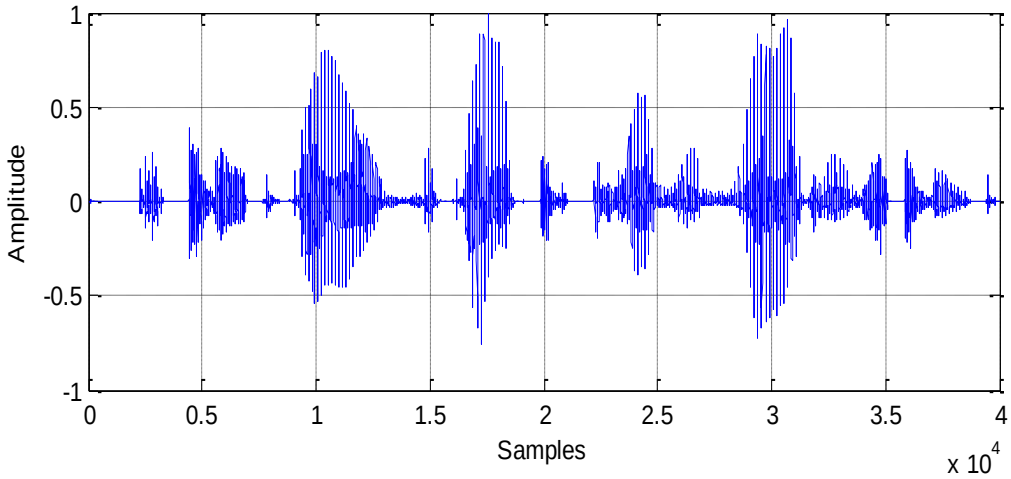

Figure 4. Far-end signal

In this case, the length of the adaptive filter is 128, and the number of samples in the signal x(n) is 40000. After several simulations, we chose the following parameters:

- LMS (μ=0.05)
- NLMS (β=0.6, C=0.09)
- RLS (λ=0.95, δ=0.005)

By setting the misalignment objective to -15dB, we obtain the results presented in the table 2:

Table 2. Misalignements obtained with Matlab simulation

Algorithm	Number of necessary iterations	Misalignement after 10000 iterations	Misalignement after 20000 iterations
LMS	17480	-5.024 dB	-17.03
NLMS	5500	-25.71 dB	-36.36
RLS	2375	-127.1 dB	-212.5

We observe that the RLS algorithm consistently shows good convergence, even with a longer impulse response than in the first case.

Implementation and Performances Evaluation

In this step, we will implement the three algorithms for the two selected systems on a dsPIC. The dsPIC is a fast 16-bit microcontroller designed for signal processing applications. This component is used in various embedded applications and is suitable for real-time signal processing tasks, particularly for linear system identification that requires real-time adaptation of adaptive filter coefficients. Among the microcontrollers in this family, we have chosen the dsPIC33FJ64MC804, which integrates more than 35 programmable digital I/Os and over 6 analog inputs [14]. The programming is done using an advanced language, specifically C++, and a compiler dedicated to dsPIC. The objective of this implementation is to evaluate the performance in terms of execution speed and accuracy.

Accuracy Analysis

The calculation accuracy is evaluated based on the results obtained in Matlab for defining the parameters of each algorithm. The tables 3 and 4 summarize the results obtained for the DC motor and the echo canceller, respectively.

The difference between the results obtained with Matlab and on the dsPIC is primarily due to that Matlab uses 64-bit floating-point calculations, while the dsPIC performs calculations using 16 bits. In comparison to the results obtained, the calculation precision of the dsPIC is more than sufficient for the two implemented systems.

Table 3. SE obtained for DC motor model on dsPIC

Algorithm	SE after 200 iterations	SE after 1000 iterations	SE after 1000 iterations
LMS	0.1032	0.0002	$<10^{-6}$
NLMS	0.0033	$<10^{-6}$	$<10^{-6}$
RLS	$<10^{-6}$	$<10^{-6}$	$<10^{-6}$

Table 4. SE obtained for echo canceller on dsPIC

Algorithm	SE after 10000 iterations	SE after 20000 iterations	SE after 30000 iterations
LMS	0.0303	$0.96*10^{-4}$	$0.11*10^{-4}$
NLMS	$0.03*10^{-4}$	$0.02*10^{-4}$	$<10^{-6}$
RLS	$<10^{-6}$	$<10^{-6}$	$<10^{-6}$

Processing Speed

The tables 5 and 6 represent the results obtained for the processing speed in the cases of the DC motor and the echo canceller, respectively.

Table 5. Execution time of DC motor identification

Algorithm	Execution time of one iteration (µs)	Number of necessary iterations	Necessary time for identification (ms)
LMS	7.25	17480	126
NLMS	8.5	5500	46.7
RLS	17	2375	40.3

Table 6. Execution time of echo canceller system

Algorithm	Number of necessary iterations	Exeution time of 1 iteration (µs)
LMS	17480	19.5
NLMS	5500	20.75
RLS	2375	45

For the DC motor identification, we have calculated the execution time for one iteration and the total time required for identification based on the error margin set during the Matlab simulation. It's clear that RLS has the shortest identification time among the three algorithms (40.3 ms), despite its longer iteration execution time (17 µs), thanks to its high convergence speed.

In the case of the echo canceller, execution time plays a crucial role since it's a real-time application where execution must occur within the sampling period of the processed signal. For telephony applications, the sampling frequency is typically 8 KHz, which corresponds to a sampling period of 125 µs. All three algorithms meet this constraint and have execution times below 125 µs. It's worth noting that execution time would increase if a longer adaptive filter were used to improve precision.

Conclusion

In this study, the implementation of three adaptive filtering algorithms was carried out on a dsPIC for the identification of linear systems. Two different systems were considered: the DC motor, requiring the identification of three coefficients, and an echo canceller, where identification was performed on the 128 samples of the echo path's impulse response. The objective of this study is to evaluate performance in terms of execution time and accuracy.

The results showed that LMS has a slow convergence rate and low execution time due to its simplicity. Therefore, it is not recommended for real-time applications requiring fast adaptive filter convergence. These algorithms are better suited for cases where identification can be done offline, as in the DC motor case where the time required for identification is not critically important. The performance of LMS was improved with its normalized version, NLMS, which has faster adaptive filter convergence. Considering its performance compared to its simplicity, NLMS is widely used in many applications. RLS exhibited the fastest convergence

speed. Its major drawback is its computational complexity, especially for adaptive filters with long impulse responses. However, with current advancements in specialized processors for complex calculations, RLS is becoming increasingly viable for various applications.

Scientific Ethics Declaration

The authors declare that the scientific ethical and legal responsibility of this article published in EPSTEM journal belongs to the authors.

Acknowledgements or Notes

This article was presented as an oral presentation at the International Conference on Technology, Engineering and Science (www.icontes.net) held in Antalya/Turkey on November 16-19, 2023.

References

Benesty, J., & Huang, Y. (2003). *Adaptive signal processing-application to real-world problems*. Berlin : Springer.

Colak, I. S. (2015). Controller design for a limited angle torque motor and dsPIC implementation In *OPTIM, ELECTROMOTION Conference* (pp.649-654). Side, Turkey

Diniz, P. S. R. (2020). *Adaptive filtering*. Switzerland AG: Springer Nature

Gay, S. L., Steven, L., & Benesty, J. (2000). *An introduction to acoustic echo and noise control, acoustic signal processing for telecommunication* (pp.1-19). Boston, MA: Springer

Ghauri, S. A., & Sohail, M. F. (2013). System identification using LMS, NLMS and RLS. *2013 IEEE Student Conference on Research and Development (SCOReD*). Retrieved from http://www.microchip.com

Haykin, S., (2014). *Adaptive filter theory* (5 th ed.). NJ: Pearson Education.

Ogata, K., (2010). *Modern control engineering* (5th ed.). Prentice Hall.

Paulo, S., & Diniz, R. (2013). *Adaptive filtering, algorithms and practical implementation* (4th ed.). Newyork, NY: Springer

Siddiqui, R. A., Grosvenor, R. I., & Prickett, P.W. (2015). dsPIC-based advanced data acquisition system for monitoring, control and security applications. *12 th International Bhurban Conference on Applied Science and Technology.* Islamabad, Pakistan.

Uriz, A. J. (2012). An Implementation in dsPIC of a denoising algorithm based on the discrete wavelet transform. *Andean Region International Conference.*

Vaseghi, S. V. (2000) *Echo cancellation, in advanced digital signal processing and noise reduction*, (pp.396–413). Newyork, NY: John Wiley & Sons

Author Information

Benziane Mourad
University of Bouira, Algeria
Contact e-mail : *m.benziane@univ-bouira.dz*

Arabi Abderrazak
University of Sétif, Algeria

Medjedoub Smail
University of Bouira, Algeria

Ayad Mouloud
University of Sétif, Algeria

Saoudi Kamel
University of Bouira, Algeria

To cite this article:

Mourad, B., Abderrazak, A., Smail, M.., Mouloud, A., & Kamel, S. (2023). dsPIC implementation and performances evaluation of adaptive filters for system identification. *The Eurasia Proceedings of Science, Technology, Engineering & Mathematics (EPSTEM), 26*, 254-261.

The Eurasia Proceedings of Science, Technology, Engineering & Mathematics (EPSTEM)
ISSN: 2602-3199

The Eurasia Proceedings of Science, Technology, Engineering & Mathematics (EPSTEM), 2023

Volume 26, Pages 262-271

IConTES 2023: International Conference on Technology, Engineering and Science

Improve Image Classification Using Data Optimization

Djamel Berrabah
Djillali Liabes University

Yacine Gafour
Ibn Khaldoun University

Abstract: Image classification is a fundamental task in machine learning that involves assigning labels or classes to images based on their content. It is often performed using convolutional neural networks (CNNs). These networks are capable of learning and generalizing patterns from large amounts of data. However, if the data is not sufficiently voluminous, overfitting can occur. In such cases, it is recommended to turn to classical machine learning techniques. Moreover, the data that was insufficient for deep learning may exceed the processing capacity of the machine. This can pose significant challenges in terms of storage, memory availability, and computational power required to perform the learning operations. Our proposed approach involves addressing these challenges by optimizing the content of the dataset. This optimization is performed while preserving the essential information necessary for classification. Indeed, identical or highly similar are identified, grouped together and represented by the most representative one among them. At the same time, their sizes can be reduced. Furthermore, another significant challenge in our proposed approach revolves around managing class imbalances within the dataset. Our approach has been evaluated and the results are promising.

Keywords: Unsupervised linear/non-linear dimensionality reduction, data visualization technique unsupervised learning algorithm, dataset optimization

Introduction

In the contemporary digital age that defines our times, we find ourselves amidst a vast wealth of visual data, comprising a diverse array of images and graphical information. At the core of this visual content lies a fundamental challenge: how to accurately and efficiently extract meaningful information from these images? The answer to this question is pivotal for a multitude of applications, ranging from facial recognition to disease detection in medical X-rays, as well as the classification of objects within complex scenes. Over the past few decades, machine learning and in particular deep learning have revolutionized the way we approach image classification. Deep neural networks, such as convolutional networks (CNN), have achieved remarkable performance in image recognition. However, beyond the power of the algorithms, a crucial element has emerged: the quality and composition of the dataset on which these models are trained. Moreover image classification using deep learning models on small datasets can be a difficult task, since these models typically require large amounts of data to generalize effectively. Although there are solutions to overcome this problem, such as data augmentation, transfer learning, etc., the performance of the image classifier may not be as high as with sets of larger data. However, there are several techniques and strategies that can be used to improve image classifier performance even with limited data. By carefully applying these techniques, it is still possible to create a reasonably effective image classifier with a small dataset. Imagine you are

training a machine learning model using data. You can compare it to a student learning from examples. The more examples (data) this student has, and the more diverse they are, the better they can generalize and make accurate decisions. That's why the quality and variety of data are essential. To optimize the model, it's necessary to carefully select the data, eliminate low-quality data, and ensure that the training dataset is representative of the real-world situations.

In this paper, we will delve into an essential yet often overlooked aspect of image classification. We will explore why the composition of the dataset can impact the model's performance, as well as the efforts made by researchers and practitioners to enhance the accuracy, reliability, and generalization of results. We will discuss improving the quality of datasets and the tangible consequences of their optimization on model performance (Hinton & Salakhutdinov, 2006). We will demonstrate how subtle adjustments to the dataset can significantly affect an algorithm's ability to discern and categorize images with unparalleled precision. Beyond pixel nuances, dataset optimization also delves into semantic and contextual dimensions. This article will showcase sophisticated methods for preprocessing, data augmentation, and dataset cleaning deployed to address these challenges. This paper is organized as follow: In section 2, some dimensionality reduction algorithms, are briefly reviewed. The detailed description of the proposed approach can be found in Section 3. Section 4 presents experiments conducted to validate the efficacy of the proposed method, while Section 5 presents the conclusions and outlines future work.

Related Works

Keeping only the most important images or data points is a crucial step in dataset reduction. It helps to focus on the information that is relevant to the specific task, reducing noise and improving model efficiency. Representing data in a feature space that enhances class separability is fundamental in classification tasks. Feature engineering aims to transform the data into a format where different classes are distinguishable, making it easier for machine learning algorithms to make accurate predictions. The decision to keep or discard data should be a balance between data reduction and maintaining the essential information. It's essential to avoid overfitting (using too much data) and underfitting (using too little data) to ensure the model's generalization. The approach for dataset reduction and feature engineering can vary depending on the specific domain and problem. Different tasks may require different strategies. Overall, the statement emphasizes the importance of thoughtful data preprocessing, which can significantly impact the success of machine learning models, especially in classification tasks.

The field of dimensionality reduction offers a range of techniques, each with its strengths and applications (Dutta & Ghosh, 2016). t-distributed stochastic neighbor embedding (t-SNE) (van der Maaten & Hinton, 2008), independent component analysis (ICA) (Comon, 1994), and multidimensional scaling (MDS) (Cox & Cox, 1994) are indeed some of the well-established and widely used methods, but there are many others, including Isomap (Tenenbaum et al., 2000), LLE (Roweis & Saul, 2000), and autoencoders (Wang et al., 2020), to name a few. The choice of dimensionality reduction method often depends on the specific problem, the nature of the data, and the goals of the analysis. For instance, some methods are excellent for linear dimensionality reduction, while others are often preferred for visualizing high-dimensional data in a lower-dimensional space. In t-SNE, the main idea is to visualize and cluster high-dimensional data while preserving local similarities, making it effective for revealing data structure in lower dimensions (Zhang & Izquierdo, 2006). However, it can be computationally expensive and slow for very large datasets, limiting its practicality in such cases. Independent Component Analysis is commonly used in blind source separation, but it may not perform well when the underlying assumptions about source independence are violated in the data. One of its disadvantages is its sensitivity to these underlying assumptions, which may not always hold in real-world data, potentially leading to inaccurate results. Multidimensional Scaling is a technique for visualizing high-dimensional data while preserving data point distances, but it can be computationally demanding for large datasets. This computational intensity makes it less practical for very large datasets, potentially leading to longer processing times. Isomap, Locally Linear Embedding (LLE), and autoencoders are all dimensionality reduction techniques used to map high-dimensional data into lower-dimensional spaces. Isomap and LLE emphasize preserving local data structures, while autoencoders utilize neural networks to learn efficient representations. However, these methods may require careful tuning and can be sensitive to the choice of hyperparameters and the specific characteristics of the dataset, making them less straightforward for some applications. Some of these methods have been combined to create new techniques, including Uniform Manifold Approximation and Projection (UMAP) (McInnes et al., 2018). UMAP combines elements from Isomap and t-SNE and is recognized for its capability to capture both local and global structures within data. However, it is computationally intensive and

sensitive to hyperparameter choices, which can affect result quality and introduce non-deterministic behavior. Dimensionality reduction techniques discussed and so on, such as Isomap, LLE, t-SNE, and UMAP, have been used effectively for data visualization (Yousaf et al., 2020; Hajibabaee et al., 2021) and classification (Milošević et al., 2022; Shi et al., 2019) tasks. These techniques can provide encouraging results when applied to well-structured and low-noise data. However, as the statement correctly points out, their performance can be less reliable when confronted with noisy or real-world data, where the data may be less well-behaved or exhibit more complex structures. In such cases, additional data preprocessing or specialized methods may be required to mitigate the impact of noise and improve performance.

Proposed Approach

Large image datasets have become increasingly common across various fields, necessitating the reduction of image datasets to improve the efficiency and computational performance of image processing tasks. These tasks encompass activities like classification, object detection, and image retrieval. The primary objective when working with these datasets is to optimize dimensionality while retaining crucial information (as depicted in Figure 1). By reducing dimensionality, algorithms become more computationally efficient, resulting in faster and more manageable processing, all while preserving essential image details. A multitude of techniques for dimensionality reduction has been developed, and the choice of the most suitable method depends on the specific characteristics of the dataset and the desired outcome of the image processing task. Our approach serves as a preprocessing step, conducted prior to commencing the image classification process (Figure 1). In this paper, we introduce two distinct optimization approaches for reducing the image dataset: Horizontal and Vertical optimizations. These strategies are tailored to address the challenges posed by the dataset's volume

Figure 1. Image classification process using an optimized dataset

Vertical Optimization

Principal Component Analysis (PCA) and clustering are two distinct techniques commonly employed in data analysis and machine learning. They can be effectively used in conjunction to comprehend and structure data. PCA, as elucidated by Jolliffe and Cadima (2002), stands as a widely adopted linear dimensionality reduction method celebrated for its ease of implementation and versatile applications across various domains. PCA operates by harnessing eigenvectors to capture linear variations within high-dimensional data. It adeptly unveils the underlying lower-dimensional structure of data points distributed along or in proximity to a linear subspace. This is achieved by identifying linear combinations of the original variables, referred to as principal components, which encapsulate a significant portion of the data's variance (as depicted in Figure 1). As a result, PCA emerges as a potent technique for dimensionality reduction and the extraction of pivotal insights from extensive datasets."

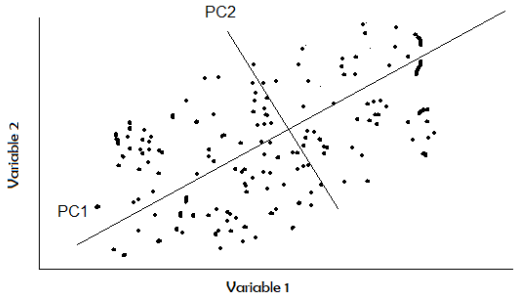

Figure 1. Generating PCA dimensions

In the context of image processing, an image can be regarded as a high-dimensional dataset, where each pixel represents a feature. When applying PCA to images, we treat them as matrices, with pixel intensity values corresponding to the matrix elements. The PCA algorithm then analyzes the covariance matrix of the image data and computes the associated eigenvectors and eigenvalues. These eigenvectors, often referred to as principal components, represent the directions of maximum variance in the image data, effectively forming a set of basis vectors spanning the image space. The corresponding eigenvalues indicate the significance or weight of each eigenvector in representing the image data.

By selecting a subset of principal components with the largest eigenvalues, we can effectively reduce the dimensionality of the image data while preserving the most significant information. In summary, PCA in image processing offers a way to reduce dimensionality while retaining essential information. The fundamental concept behind this technique is to decrease dataset dimensionality while preserving as much variability, both statistical and strategic information, as possible (Jolliffe & Cadima, 2002).

PCA can be used as a preprocessing step before applying clustering algorithms to data. A lower number of principal components that explain a significant portion of the variance are typically selected (e.g., 95% of the variance). The clustering algorithm is applied to the transformed data after reducing its dimensionality. Thus, the clustering algorithm will group similar data points based on the principal components instead of the original features (Figure 2). As a result, the results of clustering can be interpreted in the lower-dimensional space, which make it easier to understand the structure of data and the relationships between clusters. By combining PCA and clustering, it is possible to potentially improve the quality of clusters, reduce the impact of noise, and gain a better understanding of data.

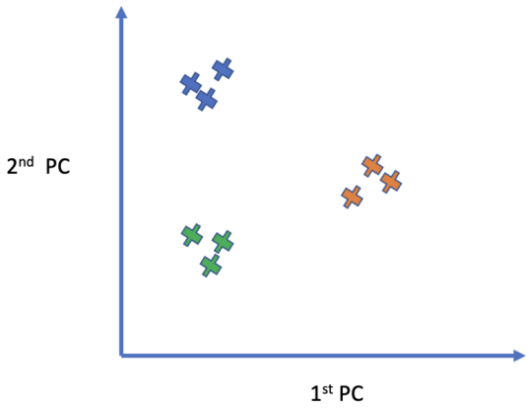

Figure 2. PCA clustering

Horizontal Optimization

K-means (Garbade & Michael, 2018) stands as a widely used unsupervised clustering technique with applications spanning various domains, including image processing and computer vision. Its significance is prominently visible in tasks like image segmentation and classification. The central objective of K-means is to partition a dataset into 'k' distinct groups or clusters, ensuring that images within the same cluster share similarities while those across different clusters exhibit dissimilarities (Figure 3). In the realm of K-means, each observation is represented as a point in an n-dimensional space, with 'n' signifying the number of descriptive variables or features. The algorithm's mission is clear: group similar data points and unveil concealed patterns in the dataset. This is achieved by identifying a fixed number of clusters ('k') within the dataset. The K-means algorithm embarks on this journey with an initial set of centroids, randomly selected as the starting points for each cluster. It then iteratively calculates to optimize the positions of these centroids.

Utilizing K-means clustering to eliminate redundant images presents a pragmatic method for mitigating data redundancy within an image dataset. First, relevant features are extracted from each image using Ho-LBP (Gafour et al., 2020). These features will serve as the basis for comparing and clustering images. Then, the K-means clustering algorithm is applied to the feature vectors extracted from the images. The number of clusters (K) chosen will

determine the level of image redundancy reduction. Within each cluster created by K-means, images that are similar to each other are considered to be potentially redundant or near-duplicates. Determining which images are redundant depend on the similarity threshold. Images with feature vector similarities that exceed this threshold are considered duplicates. Once duplicates are identified within clusters, redundant images are eliminated. Reducing the number of images in a dataset using K-means can be a challenging task. In practice, our objective is not the complete removal of redundant images but rather the reduction of dataset size. It's worth noting that eliminating all redundancy entails the deletion of a portion of the data, which could result in valuable information loss. This is especially critical when the deleted data plays a significant role in analysis or addresses class balancing concerns.

K-means Algorithm for Dataset optimization:

- **Feature Extraction**: Initially, we extract meaningful features from input images by employing the Ho-LBP descriptor.
- **Vectorize Images**: The extracted features are transformed into a suitable format for K-means clustering. Typically, each image is represented as a feature vector in a high-dimensional space based on these extracted features.
- **K-means Clustering**: Apply the K-means algorithm to cluster the feature vectors associated to images into 'k' clusters. The choice of 'k' depends on how many images are to be retained in the reduced dataset (or to eliminate from the input dataset).
- **Cluster Centroids**: After K-means clustering, 'k' cluster centroids are obtained. These centroids represent the most representative images in each cluster.
- **Cluster Labeling:** After clustering, each image is assigned to one of the 'K' clusters based on its similarity to the cluster's centroid.
- **Thresholding:** A similarity threshold is set to determine when two images are considered duplicates. Images with feature vector similarities exceeding this threshold are marked as duplicates.
- **Duplicate Detection:** Within each cluster, images that are very similar are likely duplicates or near-duplicates. Images within the same cluster are compared to identify and flag potential duplicates.
- **Selecting Representative Images**: To reduce the dataset, one (or more) image(s) can be chosen from each cluster to represent that cluster. These selected images will form the reduced dataset.
- **Eliminate Duplicates:** The elimination process concerns images having probable duplicates or near-duplicates. This elimination is done according to the degree of similarity. the images with the greatest degree of similarity will be the first candidates to be eliminated.

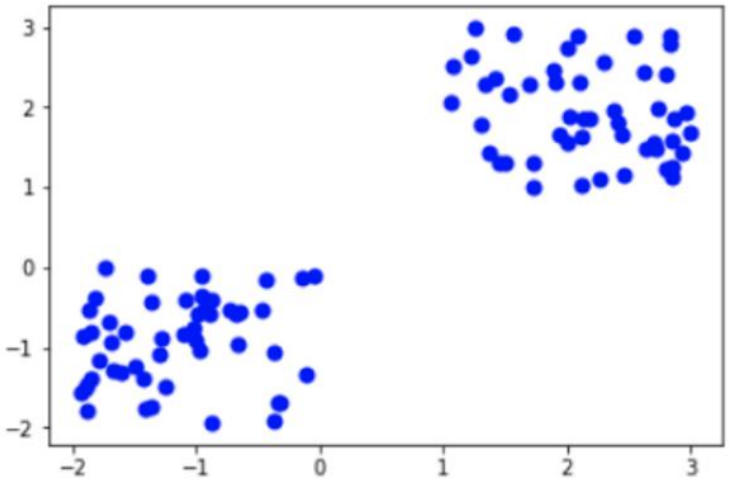

Figure 3. How data is displayed on two-dimensional space

It is necessary to know that the K-means algorithm is applied in our approach in a somewhat specific way. In its original version, the algorithm attempts to organize the dataset into a specified number of clusters. But Image Datasets are already organized into clusters (classes). So what is the role of this algorithm in our proposal approach?

As said above, our aim is the deduplication of similar images, more precisely, those containing the same information or almost. In this case, k-means is not applied globally but in a particular way. This means that the same class is divided into clusters to eliminate redundant images.

Hybrid Solution

In the preceding subsections, we explored two approaches to dataset optimization: horizontal and vertical. As previously discussed, the central challenge lies in optimizing the dataset while preserving vital strategic information. Both Principal Component Analysis (PCA) and K-means are powerful techniques for dataset optimization, each with its own unique strengths and applications.

In horizontal optimization, PCA takes center stage. Its primary role is to reduce data dimensionality, effectively reducing the number of variables in a dataset while retaining critical information. This can be particularly valuable for mitigating noise, enhancing model performance, and simplifying complexity. However, a key consideration is the potential loss of strategic image information if the number of principal components becomes excessively small.
In contrast, vertical optimization involves the use of K-means, a clustering algorithm aimed at partitioning data into coherent groups or clusters based on similarity. This approach is instrumental in uncovering underlying patterns and trends within the data, facilitating a deeper understanding of dataset characteristics. Nevertheless, it carries the risk of losing the images themselves, which are deemed strategic information.

Recognizing these challenges and trade-offs, we have explored the concept of hybridization as a viable solution. Our goal is to synergize the advantages of both approaches, leveraging PCA's proficiency in reducing dimensionality and K-means' expertise in cluster analysis. This hybrid solution strives to produce cleaner datasets with diminished noise levels, offering the potential for a well-organized cluster framework, ultimately augmenting modeling effectiveness.

Experimental Studies

In the forthcoming section, we will showcase the results of our experiments, in which we assess the performance of our approaches. We utilized the Ho-LBP descriptor and employed the SVM classification algorithm. These methods were implemented using The Extended Yale Face Database B. The experiments were executed on a system with a 2.5 GHz Intel Core i5 CPU, 8GB of RAM, and a 64-bit Windows operating system.

Dataset

The Extended Yale Face Database B (EYFB) is a renowned resource in the realm of computer vision and facial recognition. It features grayscale images of individuals captured under diverse lighting conditions, offering a challenging dataset for testing and advancing face recognition algorithms. With images of numerous subjects, each portrayed in varying poses and lighting scenarios, EYFB presents a real-world complexity that makes it a benchmark for evaluating the robustness and accuracy of facial recognition systems. Researchers frequently employ this dataset to assess and enhance the performance of algorithms for face detection, feature extraction, and identity verification. The Extended Yale Face Database B comprises a collection of 16,128 grayscale face images featuring 28 human subjects. Each subject is portrayed in 9 distinct poses and under 64 varying illumination conditions. These images are presented at a resolution of 192x168 pixels.

The lighting conditions in the database vary from frontal lighting to extreme side lighting, including cast shadows. This wide range of lighting variations makes the database challenging and suitable for evaluating the robustness of face recognition algorithms. The Extended Yale Face Database B is often used by researchers and developers in the field of computer vision and face recognition to evaluate and compare the performance of their algorithms. It provides a standardized benchmark for testing face recognition methods under varying lighting conditions. It's worth noting that while the Extended Yale Face Database B is a useful resource for research and development, it's important to ensure that any use of the database complies with the licensing terms and conditions associated with its distribution.

Experimental Results and Discussion

In practice, principal components are intricate combinations of features that adeptly represent data while preserving its unique characteristics, all while ensuring that information overlap is minimized. Original features often exhibit substantial redundancy, underscoring the effectiveness of Principal Component Analysis (PCA) in dimensionality reduction (Granato et al., 2018). When data is projected into a lower-dimensional subspace using principal components as axes, similar data points tend to naturally cluster together (as illustrated in Figure 2). This clustering phenomenon arises because the data representation explicitly aligns with axes that maximize variance (Granato et al., 2018). This approach facilitates the reduction of image sizes within the dataset, all while retaining representative samples. It proves particularly invaluable when dealing with large datasets, offering the means to create smaller, more manageable subsets for experimentation or the training of machine learning models. In a similar vein, K-means clustering, another widely used technique, groups similar data points together, contributing to efficient data organization and analysis in various domains (Garbade & Michael, 2018).

Scenario No. 1: Classification without Optimization

This experimentation (classification without optimization) will be used to compare the results in Table 1 with the other experiments in which the dataset is optimized. The goal is to assess the effectiveness of each optimization type.

Table 1. Classification result without dataset optimization

Precision	Time
61.56	248.44

Scenario No. 2: Classification after Applying PCA

This time, we applied PCA to the dataset before classification. As shown in Table 2 describing the results, the parameter 'C' represents the number of components to describe the training data. With C = 2, the accuracy dropped to 19%. However, with C = 10, accuracy increased to 56%, though it remained lower than the results in Table 2 for classification without optimization. When using C = 20, we achieved the same accuracy as the unoptimized classification, which proves that strategic information has been well preserved. Simultaneously, the execution time has undergone noticeable changes.

Table 2 Classification results after applying PCA

C	Precision (%)	Time (sec)
2	19.23	245.39
10	56.40	244.56
20	61.56	246.11

Scenario No. 3: Classification after Applying K-Means Algorithm

When applying K-means clustering for dataset reduction, it's crucial to make thoughtful choices regarding the features you use and the value of 'k,' which represents the number of clusters or groups in which the data will be partitioned. These choices can significantly impact the quality of the reduced dataset and its effectiveness for downstream tasks.

In this scenario, we utilize K-means for dataset optimization. As depicted in Table 3, we observed a substantial reduction in computation time, amounting to 30 seconds and 40 seconds, respectively, for each experiment, while maintaining the same number of images to be eliminated. Specifically, with K = 9, we achieved a more significant reduction in computation time. Furthermore, it's worth noting that the accuracy remained unchanged, and the number of rows (images) was unaltered, even though the number of clusters was modified. It's essential to highlight

that the accuracy consistently remained at 59.67%. In each experiment, 290 rows (images) were removed from the final dataset (see Table 3).

Table 3. Classification after applying K-means algorithm

S	K	Nb of eliminated Img	Precision (%)	Time(sec)	Clustering time
0.2	9	290	59.67	211.23	231.35
0.2	18	290	59.67	220.50	230.11

Scenario No. 4: Classification after Applying PCA then K-Means Algorithm

In this scenario, we considered re-running scenario 3 by incorporating PCA before implementing the K-means algorithm. We observed that the results were nearly identical, except for the clustering time, which was reduced by more than half. The significant advantage of this approach lies in the substantial reduction in the overall execution time of the process, as the clustering time accounts for a significant portion of the total duration, without affecting the other performance metrics.

Table 4. Classification after applying PCA then K-means algorithm

S	C	K	Eliminated Img	Precision (%)	Time(sec)	Clustering time
0.2	2	9	290	59.67	212.55	75.13
0.1	2	18	290	59.67	220.50	80.22

Getting similar or nearly identical results in various scenarios is a positive indicator. This demonstrates that dataset reduction or optimization was carried out while preserving crucial information.

Scenario No. 5: Classification after Applying PCA then K-Means Algorithm and then PCA

In this final scenario, we incorporated PCA both before calculating the distances between images to identify duplicates and prior to the image classification process. The results, as depicted in Table 5, demonstrate a minimum calculation time of 82 seconds with a 51% precision rate for parameters s = 0.1, c = 2, and k = 18. When using s = 0.05, c = 2, and k = 9, we achieved a precision of 56% with a calculation time of 121 seconds. It's important to note that outcomes vary depending on the parameter settings. In Figure 4, we visualize the optimization process for a dataset class. Each color corresponds to a cluster, with Y representing the centroids and X representing the redundant images. Figure 4 makes it evident that as images get closer in distance, the need for elimination becomes more pronounced.

Table 5. Classification after applying PCA then K-means algorithm and then PCA

S	C	K	Eliminated Img	Precision (%)	Time(sec)	Clustering time
0.1	2	4	3994	52.08	85.00	72.30
0.5	2	5	3660	56.07	100.42	94.17
0.5	2	9	2994	56.25	121.99	96.08
0.5	2	18	2101	57.85	154.11	120.15
0.5	2	18	4070	51.67	82.47	117.43

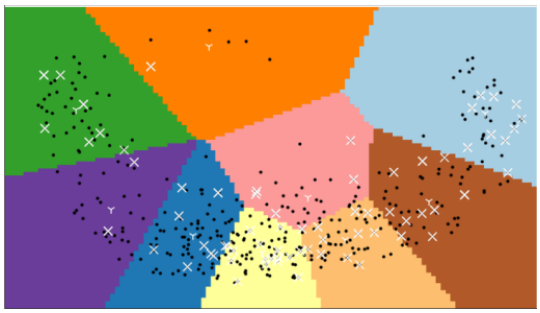

Figure 4. Kmeans clustering and images to be eliminated

In the context of our experiments, we observed the interplay between precision, computation time, and various optimization scenarios. Precision exhibited a slight, nearly negligible decrease, and computation time remained consistently variable, contingent on the specific test and its corresponding parameters. Among the scenarios tested, Scenario N°5 stood out as particularly intriguing due to its varying precision and computation time across different parameter values. In Scenario N°5, the distinction from Scenario N°4 lies in the reduction of image size within clusters through PCA. We then computed distances between these reduced images to eliminate duplicates. The introduction of PCA prior to clustering and distance calculation yielded a significant reduction in computation time. Furthermore, we noted that Scenarios N°4 and N°3 yielded nearly identical results since both involved the elimination of the same number of images. There was no discernible difference between the outcomes of Scenario N°2 and Scenario N°1.

Conclusion and Future Works

The combined use of PCA and K-means in dataset reduction presents a powerful approach for enhancing efficiency and maintaining data quality. PCA effectively reduces dimensionality by preserving essential information, and K-means clustering refines dataset organization. This synergy optimizes data while minimizing redundancy. However, the choice of parameters and feature selection plays a pivotal role in achieving the desired results. When thoughtfully applied, this method streamlines data processing, accelerates computations, and streamlines machine learning models, making it a valuable asset in the realm of data optimization.

Through these experiments, we have been able to observe the potential of eliminating redundant data. By using PCA thoughtfully, we achieved satisfactory results. It's worth noting that the success of this experiment could vary depending on the choice of dataset, algorithms, and implementations. Therefore, conducting a variety of experiments is essential to solidify our assessment of the proposed dataset optimization technique.

The challenge of class imbalance is significant. It occurs when one or more classes have considerably fewer data samples than others, leading to an unequal distribution. This can result in models performing well on the majority class but poorly on the minority class, causing inaccurate and biased predictions. Addressing class imbalance is crucial for model fairness and accuracy.

Notice that K-means clustering is just one of many techniques for identifying duplicate images. Depending on the size and characteristics of the dataset, we think using other methods like perceptual hashing (e.g., pHash) method may also be suitable for duplicate image detection. It's important to choose the right feature representation and similarity metric for comparing images, as this will affect the clustering results and the threshold for identifying duplicates. Also, the choice of 'K' should be guided by the diversity of the dataset and the expected number of distinct duplicate groups.

Scientific Ethics Declaration

The authors declare that the scientific ethical and legal responsibility of this article published in EPSTEM journal belongs to the authors.

Acknowledgements or Notes

* This article was presented as an oral presentation at the International Conference on Technology, Engineering and Science (www.icontes.net) held in Antalya/Turkey on November 16-19, 2023.

References

Comon, P. (1994) Independent component analysis: A new concept?. *Signal Processing*, *36*(3), 287-314.
Cox, T. & Cox M., (1994). *Multidimensional scaling.* London: Chapman & Hall.

Dutta, S., & Ghosh, A. K. (2016) On some transformations of high dimension, low sample size data for nearest neighbor classification. *Mach Learn, 102*, 57–83.

Gafour, Y., Berrabah, D., & Gafour, A. (2020). A novel approach to improve face recognition process using automatic learning. *International Journal of Computer Vision and Image Processing (IJCVIP), 10*(1), 42-66.

Garbade, Dr., & Michael, J. (2018) Understanding K-means clustering in machine learning. Medium, towards data science. Retrieved from https://towardsdatascience.com/understanding-kmeans-clustering-in-machine-learning

Granato, D., Santos, J. S., Escher, G. B., Ferreira, B. L., & Maggio, R. M. (2018). Use of principal component analysis (PCA) and hierarchical cluster analysis (HCA) for multivariate association between bioactive compounds and functional properties in foods: A critical perspective. *Trends in Food Science & Technology, 72*, 83–90.

Hajibabaee, P., Pourkamali-Anaraki, F., & Hariri-Ardebili, M. A. (2021). An empirical valuation of the t-SNE algorithm for data visualization in structural engineering. *20th IEEE International Conference on Machine Learning and Applications (ICMLA*), 1674-1680. Pasadena, CA, USA.

Hinton, G. E., & Salakhutdinov, R. R. (2006) Reducing the dimensionality of data with neural networks. *Science, 313* (5786), 504–507.

Jolliffe, I.T., & Cadima, J. (2016) Principal component analysis: a review and recent developments. *Philos Trans A Math Phys Eng Sci., 374*(2065).

McInnes, L., Healy, J., Saul, N., & Großberger, L. (2018). UMAP: Uniform manifold approximation and projection. *Journal of Open Source Software, 3*(29), 861.

Milošević, D., Medeiros, A. S., Piperac, M. S., Cvijanović, D., Soininen, J., Milosavljević, A., & Predić, B. (2022). The application of uniform manifold approximation and projection (UMAP) for unconstrained ordination and classification of biological indicators in aquatic ecology. *Science of The Total Environment, 815*.

Roweis, S. T., & Saul, L. K. (2000). Nonlinear dimensionality reduction by local linear embedding. *Science, 290* (5500), 2323-2326.

Shi, X., Yang, H. U. I., Xu, Z., Zhang, X., & Farahani, M. R. (2019). An independent component analysis classification for complex power quality disturbances with sparse auto encoder features. *IEEE Access, 7*, 20961-20966.

Tenenbaum, J. B., de Silva, V., & Langford, J. C. (2000). A global geometric framework for nonlinear dimensionality reduction. *Science, 290* (5500), 2319-2323.

Van der Maaten, L.J.P., & Hinton, G.E. (2008). Visualizing high-dimensional data using t-SNE. *Journal of Machine Learning Research, 9*(86), 2579-2605.

Wang, K., Su, G., Liu, L., & Wang, S. (2020). Wavelet packet analysis for speaker-independent emotion recognition, *Neurocomputing, 398*(4), 257-264.

Yousaf, M., Rehman, T.U. & Jing, L. (2020) An extended isomap approach for nonlinear dimension reduction. *Sn Computer Science, 1*, 160.

Zhang, Q., & Izquierdo, E. (2006). A multi-feature optimization approach to object-based image classification. In: H. Sundaram, M. Naphade, J. R., Smith, Y. Rui (Eds)., *Image and video retrieval. CIVR 2006. Lecture notes in computer science* (*p.*4071). Springer, Berlin, Heidelberg.

Author Information

Djamel Berrabah
Djillali Liabes University
Sidi Bel Abbes, Algeria
Contact e-mail: *berrabdjamel@gmail.com*

Yacine Gafour
Ibn Khaldoun University
Tiaret, Algeria

To cite this article:

Berrabah, D., & Gafour, Y. (2023). Improve image classification using data optimization. *The Eurasia Proceedings of Science, Technology, Engineering & Mathematics (EPSTEM), 26,* 262-271.

The Eurasia Proceedings of Science, Technology, Engineering & Mathematics (EPSTEM)
ISSN: 2602-3199

The Eurasia Proceedings of Science, Technology, Engineering & Mathematics (EPSTEM), 2023

Volume 26, Pages 272-278

IConTES 2023: International Conference on Technology, Engineering and Science

Verification the Stressed State of the Ships' Hull during Separate Water Descent

Yordan Denev
Technical University of Varna

Abstract: This study evaluates the stressed state of the ship's hull during its welding of separate water descent parts. Separate descent of ship hull is applicable for small and medium sized ship yards (SME), where shipbuilding facilities have restrictions on length and lifting capacity. In the paper different scenarios are developed for verification. It is assumed that separately launched sections of the ship's hull are free of heels and trim, i.e., pre-ballasted, and any initial deformation in connected structures has been eliminated during the stage of hull assembly. In different scenarios, there are varying factors directly related to the strength of the ship, its construction materials, as well as those that have an impact on the production processes. Two of most used welding methods in ship building are analyzed- submerged arc welding and gas metal arc welding. The analysis shows that the stressed state of the ship's hull closely depends on the initial tense state, thickness of plate elements and welding method.

Keywords: Small and medium sized ship yard, Launching, Hull assembly, Thickness, Welding, Strength

Introduction

The pursuit of constantly increasing the deadweight(DWT) of ships on a global scale has an influence on the market conditions of shipbuilding companies. Increased DWT improves operational efficiency of the ship [https://www.dnv.com/expert-story/maritime-impact/Ticket-to-trade-increasing-deadweight-for-improved efficiency.html] emissions, which influence the individual CO2 emissions in the atmosphere and is used, monitoring the annual operation performance index. Increasing the deadweight is not always achieved at the expense of the length. It can also be accomplished by increasing the draft and reducing the freeboard, but this is within certain limits. This measure is easily implementable for already constructed ships. However, for ships that are yet to be built, this measure has certain limitations in ship yard production facilities.

With the emergence of this trend, a significant number, including the smaller and medium-sized shipbuilding enterprises, have become non-competitive in the market. Each shipbuilding company has developed and successfully implemented technological processes for ship hull construction as a whole. The main methods for constructing ship hulls are block, sectional, and block-sectional. Analysis of sectional and block-sectional shipbuilding methods with preliminary developed and evaluated criteria is done in (Денев, 2020). Some ship yards need to reorient their activities or seek ways to withstand this global trend. One possible solution to overcome the problem is the separate launching of the ship into the water. This method allows the construction of relatively larger ships under limited production conditions.

Hull Separate Water Descent

The separate launching of the ship's hull into the water and the subsequent assembly and welding of the individual parts together is a complex technological process compared to performing these tasks in a dry dock.

The main stages of the process are presented in Fig.1. to Fig.4 (Шевелевич, 1974). Separately launched parts are with different light weights and they are with trim independently of each other, Fig.1.

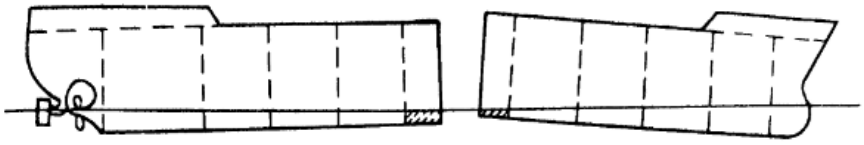

Figure 1. Ship's hull parts launching

To eliminate the trim and for easy connection of each part, they are ballasted. Ballasting is carried out by forcibly filling the tanks based on a pre-calculated calculation, fig.2.

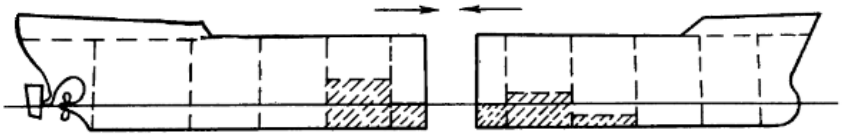

Figure 2. Ballasting the separately water descent parts

When the ballasting operations are finished, the next step is that parts connect each other by help of fixed strips and elastic jacks and partly welding seams, fig.3.

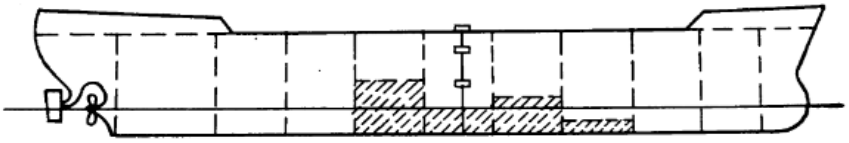

Figure 3. Connected each one to other with fixed devices

Welding process of outer shell plating continues with mounting of additional construction in connected areas providing water tightness of the welding seam and partly ballast discharging, фиг.4. One more method for welding is underwater welding of bull weld seam but it requires additional equipment and personal skills.

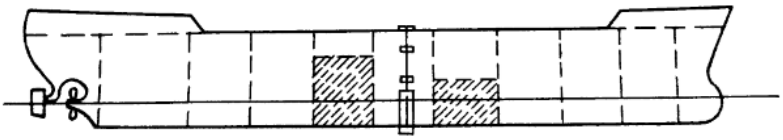

Figure 4. Welding and partly debalasting of hull parts in welding seam area

The most appropriate welding method for this case is shielded metal arc welding and the gas metal arc welding process.

Methodology

Separately, water descent ship hulls parts have to be welded together to provide structural strength and identity. For manual metal arc welding (SMAW) and gas metal arc welding (GMAW), processes are calculated and we analyzed. The welding parameters are calculated for plate thickness range from 8mm to 20 mm.

Considering that stressed ship condition closely depends on actual forces in the shipbuilding process, which are mainly welding forces, it is necessary for a proper calculation of welding current the value depends on heat input in the area of the welding seam. Welding current value is selected based on shielded electrode diameter, while electrode diameter is selected by plate thickness and seam area. The heat input in welding seam is calculated by:

$$q_e = I * U * \eta, W$$

Where: I- welding current, A; U- voltage, V; η- efficiency coefficient, form MMAW η=0.7, while for GMAW η=0.8 (Weman, 2003). https://www.materialwelding.com/what-is-efficiency-in-welding-welding-efficiency-for-smaw-gmawtig-fcaw-and-saw/

Shown in fig.5, the curves for SMAW are nearly parallel and double S- shaped. In areas between 12 and 14 mm and 18 and 20 mm, there are no none from the curve. That corresponds with non- changing welding parameters for thicknesses in relevant areas.

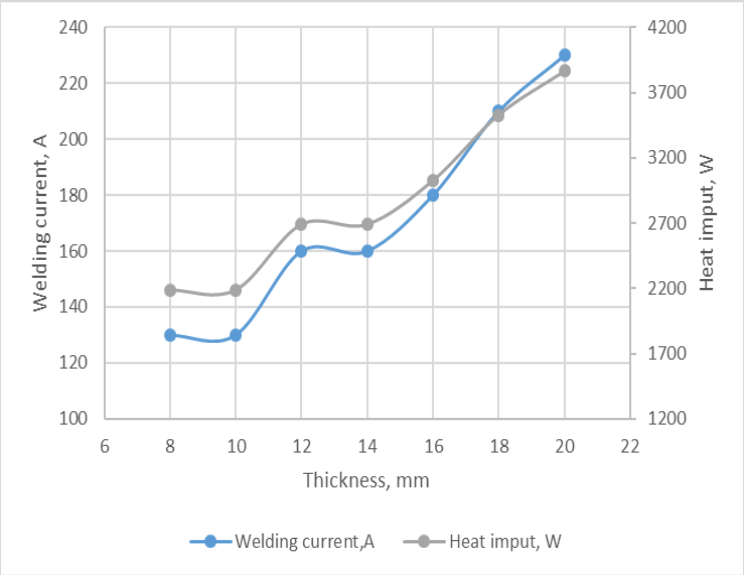

Figure 5.Welding parameters in SMAW process

Different are curves of GMAW, shown on fig.6. Their shape is not a double S- curve. It is noticed that at 14 mm thickness the curve of welding current and heat input are very closely side by side. Welding parameters, current, wire diameter and voltage for GMAW are selected from a tabular from reference literatüre(ESAB, n.d.,& Miller, 2018). Heat input is calculated by formula (1).

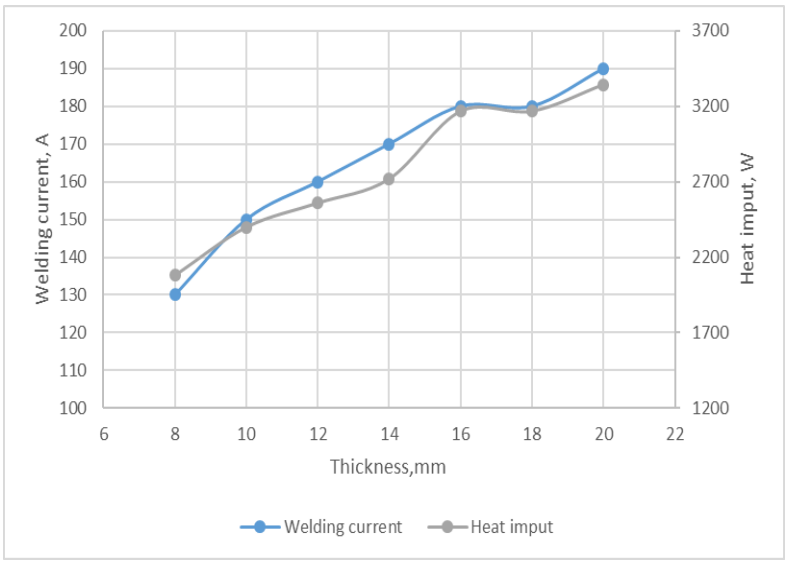

Figure 6. Welding parameters in GMAW process

Verification of Stressed Ships State

After hull parts separate water descent launching follows their watertight connected one to other by welding process. In the welding process, as a result of the high amount of heat input, stress is generated, leading to deformations in the ship's hull. Considering that the maximum allowable value of normal stresses in on the ship

hull closely depends on material, for steel ships with length more than 90m, according[GL rules] is calculated by following formulae:

$$[\sigma] = \frac{175}{k}, N/mm^2$$

Where: k- material factor, k=1 for shipbuilding steel(St235),
The permissible value of normal stress for ships with length less than 90m is calculated by:

$$[\sigma] = \frac{18.5\sqrt{L}}{k}, N/mm^2$$

Where: L- ships length, m

The full separate water descent process is applicable for ships with lengths more than 90m fabricated from shipbuilding steel ST235. In this context, in fig.7 and fig.8, are shown the distribution of normal stresses on the bottom and side of the ship the hull related to thickness of plates in the area of the butt welds. The actual stresses are compared with processes permissible in two welding processes.
Actual stresses in construction are calculated by:

$$\sigma = E * \frac{\Delta l}{l}$$

Where: E- Young modulus, for shipbuilding steel E=0.002kN/mm2; Δl- construction deformation, mm; l- construction welding length, mm;
Construction deformation is calculated by [Бельчук, 1961]:

$$\Delta l = \Delta_c * L, mm$$

Where Δc- construction deformation according center of gravity, L- all length of construction;
Construction deformation according center of gravity is calculated by:

$$\Delta c = \frac{3.6 * 10^{-6}\, q_e}{F}$$

Where: qe- heat input in welding seam, W; F- area of ship midship section, m2;
Increase of normal stresses on the side by about 11% in areas with higher plate thickness, Fig.7. This is due to higher welding current value and input heat, corresponding to easy melting of welding seam metal.

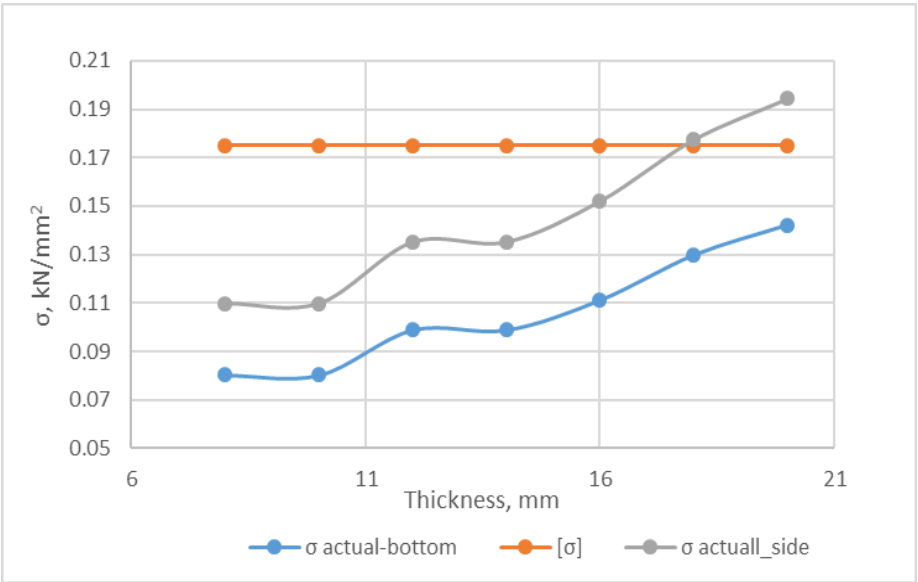

Figure7. MMA welding

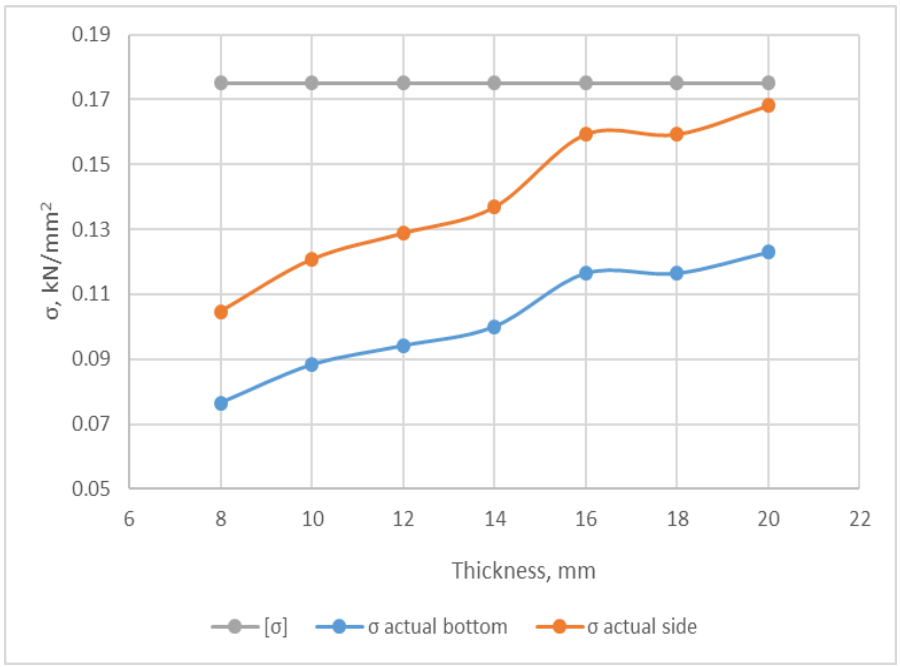

Figure 8. Gas metal arc welding

The actual stresses and stress on the hull in the bottom region is less than the maximum permissible stress value. This is due to the actual position of the ship's center of gravity and neutral axe position. The results obtained in fig. and fig. are related to the ship's hull as a whole. There is a requirement for ship hull welding afloat. The level of longitudinal stress during the welding operation is to be below 50 MPa in the concerned area; however, lower limits may be requested by the surveyor depending on the specificities of the ship and/or welding.(Bureau Veritas, 2022). For the analysis and evaluation of whether this requirement is met during welding activities for separately lowered parts of the ship's hull in Fig.9 and Fig.10, different scenarios for performing the welding operations are presented. The main task is to investigate the optimal lengths of the welds so that the stresses generated by them are minimal or absent altogether.

Different welding lengths are studied. For the bottom part of the ship's hull they are 2000, 4000 and 6000 mm, while for the side parts they are 3000, 6000 and 9000 mm and the thickness range from 8 to 20mm. In fig. and fig., maximum precaution is shown [σ]= 0.05kN/mm2. In fig. and fig. with σb2, it is noticed that this is actual stress on the bottom when we weld 2000mm of seam, σs3 is noticed that this is actual stress on the side when 3000mm is welded. In all thickness range when welding in bottom seam is by 2000mm length actual stress didn't exceed permissible,

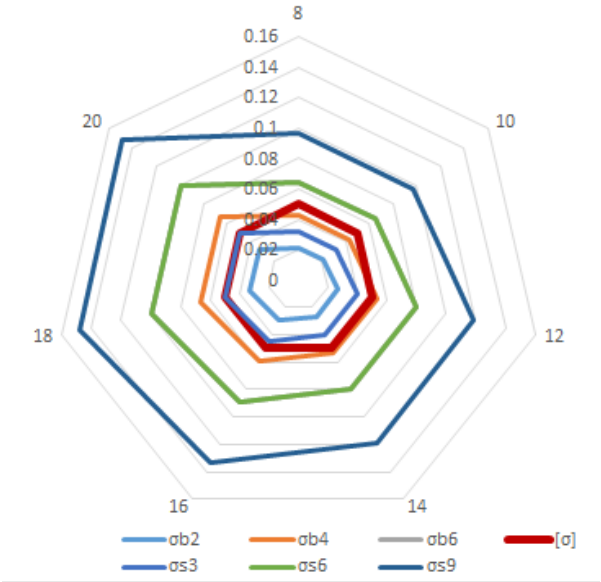

Figure 9. MMA welding

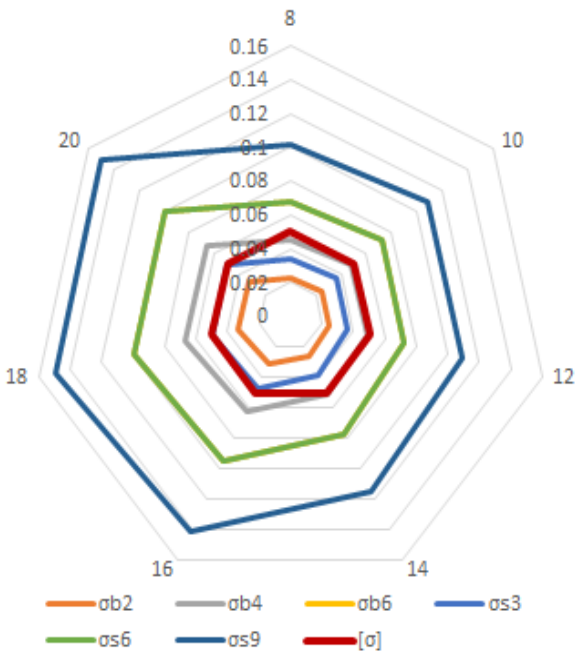

Figure 10. Gas metal arc welding

When welding on the side with a 3000 mm seam, actual stress up to 14 mm didn't exceed permissible. In other thickness ranges they are equal or near to permissible. The actual stresses on bottom and side with welding length equal and more than 6000 and 9000 mm widely exceed permissible, fig.9 and fig.10. The maximum permissible value exceeded in MMA welding is about 11% at 20 mm thickness and 9000 mm welding length at side area,fig.10. When GMAW process is used there are not waste material for environmental pollution compared with SMAW.

Conclusion

The study presents a technological possibility for shipbuilding in the conditions of small and medium-sized businesses, considering contemporary trends and environmental requirements in navigation. The proposed method enhances the competitiveness of SMEs in the market. An analysis was conducted on the stressed state of the ship's hull during the welding process of its separately lowered parts.

The normal stresses during welding were analyzed and compared with the maximum allowable values using two different methods: manual shielded metal arc welding and welding in a protective gas environment with a consumable electrode. The current stress values were examined over a wide range of thicknesses and different welding sequences in terms of the length of the weld. It was found that for weld lengths greater than 6 and 9 meters for the bottom and deck areas, the stresses exceeded the allowable limits by almost twice for both welding methods. Optimal, in terms of subsequent stress occurrences and consequent deformation occurrences in the entire thickness range, is the execution of welds with a length of 2 for the bottom area and 3 for the ship's side area.

Scientific Ethics Declaration

The author declares that the scientific ethical and legal responsibility of this article published in EPSTEM journal belongs to the author.

Acknowledgements

* This article was presented as an oral presentation at the International Conference on Technology, Engineering and Science (www.icontes.net) held in Antalya/Turkey on November 16-19, 2023.

* Infrastructure for sustaınable development of marıne research and partıcıpatıon ın the european ınfrastructure euro-argo – masrı is a project of the National roadmap for scientific Infrastructure (2020 – 2027) of Republic of Bulgaria

References

Burea Veritas. (2022). *Rules for steel ships*. Retrieved from https://marine-offshore.bureauveritas.com/nr467-rules-classification-steel-ships

DNV. (2020, May 26). *Ticket to trade increasing deadweight for improved efficiency*. Retrieved from https://www.dnv.com/expert-story/maritime-impact/Ticket-to-trade-increasing-deadweight-for-improved-efficiency.html

ESAB. (n.d.) MIG/ MAG welding, training and education GL rules.

Material Welding. (2023, July 3). *What is efficiency in welding & welding efficiency for-smaw gmawtig fcaw and saw*. Retrieved from https://www.materialwelding.com/what-is-efficiency-in-welding

Miller. (2018). *Guidelines for gas metal arc welding*. Retrieved from https://www.millerwelds.com/-/media/miller-electric/import/literature/file/guidelines-for-gas-tunsten-arc-welding-gtaw.pdf

Weman, K. (2003). *Welding process handbook* (2nd ed.). Cambridge, England: Springer

Бельчук, Г.А., & Мацкевич, В.Д. (1961) Сварка в судостроении

Денев, Й. (2020). *Строителство на кораба в ограничени производствени условия: сравнителен анализ, сп. Известия*, 53-59.

Author Information

Yordan Denev
Technical University of Varna
Studenstska 1 str. Varna, Bulgaria
Contact e-mail: *y.denev@tu-varna.bg*

To cite this article:

Denev, Y. (2023). Verification the stressed state of the ships' hull during separate water descent. *The Eurasia Proceedings of Science, Technology, Engineering & Mathematics (EPSTEM), 26*, 272-278.

The Eurasia Proceedings of Science, Technology, Engineering & Mathematics (EPSTEM)
ISSN: 2602-3199

The Eurasia Proceedings of Science, Technology, Engineering & Mathematics (EPSTEM), 2023

Volume 26, Pages 279-286

IConTES 2023: International Conference on Technology, Engineering and Science

Adsorption of Copper Ions from Aqueous Systems Using Moss Peat: Reaction Kinetics and Adsorption Isotherm

Suha T. Aldmour
Mutah University

Abstract: The removal of copper ions from aqueous systems using moss peat was investigated. Kinetic experiments were conducted at a constant temperature, pH, and initial copper concentration. The data obtained from the kinetic experiments were analysed and fitted well using the pseudo-second-order model. The data of the isotherm experiment were modelled and fitted well with the Langmuir models. This finding suggests that copper ions are chemically adsorbed on the moss peat and assume monolayer adsorption. The optimum pH for copper ion adsorption by moss peat was investigated over a range of (2-4.5), and it was found that the maximum adsorption capacity of moss peat was achieved at pH 4.5. The results of this study suggest the potential use of moss peat as an effective material for the adsorption of copper ions from aqueous solutions under a range of environmental conditions.

Keywords: Cu(II), Moss peat, Reaction kinetic, Adsorption isotherm

Introduction

Copper is a strategic element that is widely used in industries like metallurgy, fungicides, mining, electroplating, and petroleum refining (Demirbas et al., 2009; Trakal et al., 2014). However, improper disposal of industrial effluents has led to the release of copper ions, Cu^{2+}, into aquatic systems, causing toxic effects (Hossain et al., 2012b). Moreover, acute exposure to Cu^{2+} can result in several physiological issues in humans, including mental illness, schizophrenia, cardiovascular disease, Alzheimer's disease, and diseases of aging (Brewer, 2007; Faller, 2009; Hureau & Faller, 2009).

The remediation of contaminated water resources has recently attracted much interest due to the limited water resources and high water demand. There are various techniques for removing heavy metals from aqueous systems, such as cementation, reverse osmosis, electrochemical methods, and membrane filtration (Al-Saydeh et al., 2017). However, these techniques have drawbacks related to high operating costs, high energy consumption, or long duration (Gautam et al., 2014). Among these techniques, adsorption has received the most attention because of its simplicity, high removal efficiency, and cost-effective process (Davarnejad & Panahi, 2016).

The adsorption of heavy metals has been studied using a variety of adsorbents. However, carbon-rich adsorbents have shown several benefits due to their simplicity of use, availability, and environmentally friendly materials (Hossain et al., 2012a; Khatoon & Rai, 2016). Numerous studies have been carried out on the adsorption of metal ions from aqueous solutions using organic-rich adsorbents, such as banana peels, humic acid, grass, and sawdust (Rafatullah et al., 2009; Hossain et al., 2012a; Aldmour, 2018; Aldmour et al., 2019). It has been found that the adsorption capacities of these adsorbents vary significantly depending on their source. Therefore, further investigation of other adsorbents is required to assess their ability to adsorb Cu^{2+} under different conditions.

Materials and Method

- Selection and peer-review under responsibility of the Organizing Committee of the Conference

Moss Peat

The Moss peat used in this study was collected from Kekkilä Professional (Kekkilä Professional, Finland), which produces moss peat for horticulture use. Air-dried and sieved moss peat (p.z 600-850 μm) was prepared and used for characterization tests. For the batch experiments, moss peat was oven-dried to a constant mass at 105 °C.

Characterization of Moss Peat

Moss peat was characterized by moisture, ash, and volatile matter contents. The moisture content of the moss peat samples was estimated as a percentage of the air-dried samples based on ASTM standard D2974-87, method A (ASTM, 1999). The ash content of moisture-free moss peat samples was determined according to ASTM standard D1102-84 (ASTM, 2001). After ignition at 600 °C, the ash content was calculated for moss peat as a percentage of the residue relative to the initial mass of moss peat. The volatile matter content was determined according to the ASTM standard E872-82 (ASTM, 2013). Moisture-free samples were heated at 950±20 °C for 7 min, and volatile matter was calculated as a percentage of mass loss relative to the moisture-free sample. All tests in this study were performed in triplicates.

Preparation of Copper Solution

A stock solution (400 mM) of Cu^{2+} was prepared by dissolving copper sulfate pentahydrate (CuSO4.5H2O; Sigma Aldrich) in deionized water. Copper-moss peat suspensions were prepared by diluting the stock solution with deionized water to obtain the target concentrations of Cu^{2+}. All chemicals used in this study were of analytical grade.

Batch Experiments

Effect of Contact Time

To prepare copper-moss peat suspensions, moss peat (2.5 g) was mixed with 237.5 ml of deionized water. The pH of the suspensions was adjusted to ~ 4.0, using 1 M HCl or 1 M NaOH, and periodically shaken until the pH of the suspensions remained stable for at least a day. Then, the copper solution (400 mM) was adjusted to pH 4, and 12.5 ml of this solution was added to each suspension to obtain a final volume of 250 ml, and the concentration of Cu^{2+} in the final suspensions was 20 mM (1270.9 mg/l)). The samples were then maintained at 20 ±1 °C with agitation at 150 rpm for 7 hr. Throughout the experiment, samples were periodically taken from the suspensions after 0.25, 0.5, 1.5, 2, 3, 4, 5, and 7 h and then filtered using a 0.45 μM PTFE syringe filter for Cu^{2+} analysis. The data obtained from this experiment were used to identify the optimum contact time for the adsorption of Cu^{2+} and were fitted to the sorption kinetic models.

Effect of Initial Concentration of Copper

The effect of the initial Cu^{2+} concentration on the adsorption process was determined over a range of 50–300 mg/l. The pH of the suspensions was adjusted to 4, and the adsorbent dosage was 4 g/l. The remaining experimental conditions were maintained as described in Section 2.4.1, and the experiment was conducted for a period equal to the optimum contact time determined in the contact time experiment (Section 2.4.1). At the end of the experiment, the samples were collected, filtered, and analyzed for the Cu^{2+} concentration in the solution. The data obtained from this experiment were fitted to sorption isotherm models.

Effect of Initial pH

The effect of pH on the removal of Cu^{2+} from aqueous systems was studied over a pH range of 2.0 to 4.5. To adjust the initial pH of the suspensions, 1 M HCl or 1 M NaOH was used. The other experimental conditions were maintained as described in Section 2.4.1. At the end of the experiment, the samples were withdrawn, filtered, and analyzed for Cu^{2+} concentration in the solution. All batch experiments were performed in triplicates.

Copper Analyses

The residual Cu^{2+} in the aqueous solutions was measured using Atomic Absorption Spectrometry (AAS-7000 Shimadzu). A calibration curve for Cu^{2+} was constructed within the range of 0.1-2.0 mg/l using a copper standard solution obtained from Sigma-Aldrich.

Results and Discussion

Characterization of Moss Peat

The characterization of moss peat is summarized in Table 1. It was found that moss peat has a low ash content of 6.4%. In contrast, the volatile organic matter was very high. These results suggest that the large organic fraction in moss peat may play a significant role in metal adsorption. Previous studies pointed out that organic-rich materials like sewage sludge, mosses, and soil organic matter have a high content of functional groups and consequently have an abundance of binding sites for metal interaction (Won et al., 2013; González & Pokrovsky, 2014; Aldmour, 2018). Accordingly, moss peat may have a high adsorption capacity for Cu^{2+}.

Table 1 Characterization of moss peat

	Moss peat
Moisture content	54.3±0.87
Ash content (wt.% dry basis)	6.54±0.34
Volatile matter (wt.% dry basis)	92.40±0.12

Effect of Contact Time

The percentage of copper adsorbed by moss peat was calculated using the following equation:

$$\%Removal = \frac{C_o - C_e}{C_o} \times 100\% \dots\dots\dots\dots\dots (1)$$

Where: C_o and C_e are the initial and equilibrium concentrations of metal ions in the solution (mg/l), respectively. Figure 1 illustrates the impact of contact time on the percentage of Cu^{2+} removal using moss peat. It was found that within the initial 30 minutes, a rapid rate of Cu^{2+} absorption was observed, followed by a relatively slow rate until reaching the equilibrium state at 240 min. The experiment revealed that 29.2% of Cu^{2+} was removed from the solution within 30 minutes, while only 4.3% was removed within 210 minutes. These results may be due to the abundance of active sites on the adsorbent surface during the initial stage of the reaction, while the decrease in reaction rate can be attributed to limited binding sites as the reaction progresses (Kowanga et al., 2016).

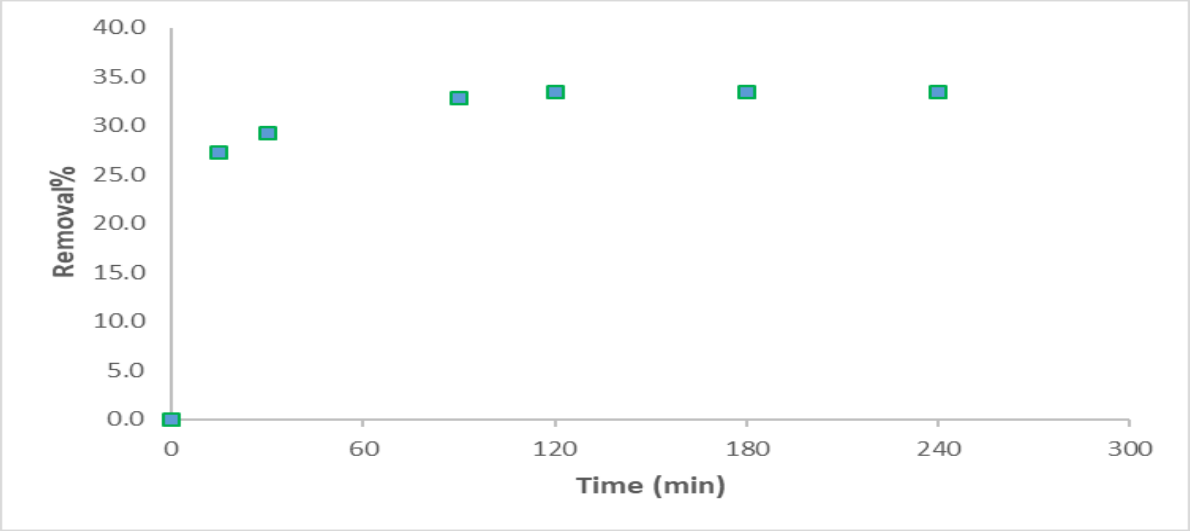

Figure 1. Percentage of Cu^{2+} removal from aqueous solution by moss peat versus time

Kinetics

The sorption mechanism and kinetic parameters were investigated using pseudo-first-order and pseudo-second-order models. The pseudo-first-order equation is expressed in its linearized form by the following equation:

$$log(q_e - q_t) = logq_e - \frac{k_1}{2.303}t \dots\dots\dots\dots\dots (2)$$

Where: qe is the amount of metal ions adsorbed per unit mass of adsorbent at equilibrium (mg/g), q_t is the amount of metal ions adsorbed per unit mass of adsorbent at variable time (mg/g), k_1 is the rate constant of the pseudo-first-order kinetic model (min^{-1}), t is the time (min). A plot of $log(q_e-q_t)$ versus t results in a straight line, and the values of a slope and intercept are used to determine the values of k_1 and q_e, respectively.
The linearized form of the pseudo-second-order kinetic equation is expressed by equation 3:

$$\frac{t}{q_t} = \frac{1}{k_2 q_e^2} + \left(\frac{1}{q_e}\right)t \dots\dots\dots\dots\dots (3)$$

Where: k_2 is the rate constant of the pseudo-second-order model (g/mg.min). A plot of t/q_t versus t gives a straight line, and the values of q_e and k_2 are calculated from the slope and intercept, respectively. The kinetics parameters of the pseudo-first-order and the pseudo-second-order models for the adsorption of Cu^{2+} on moss peat were calculated using Figures 2 and 3 and presented in Table 2. The correlation coefficient for the pseudo-second-order model was significantly greater than that for the pseudo-first-order model. This finding suggests that the pseudo-second-order model can describe the adsorption of Cu^{2+} on moss peat.

Table 2. Kinetic parameters of pseudo-first-order and pseudo-second-order models

Sorbent	Pseudo-First Order			Pseudo-Second Order		
	Calculated q_e (mg/g)	K_1 (min^{-1})	R^2	Calculated q_e (mg/g)	K_2 (min^{-1})	R^2
Moss Peat	7.77	0.0039	0.7581	61.35	0.0028	0.9989

Figure 2. Pseudo-first order kinetic model for the adsorption of Cu^{2+} on moss peat

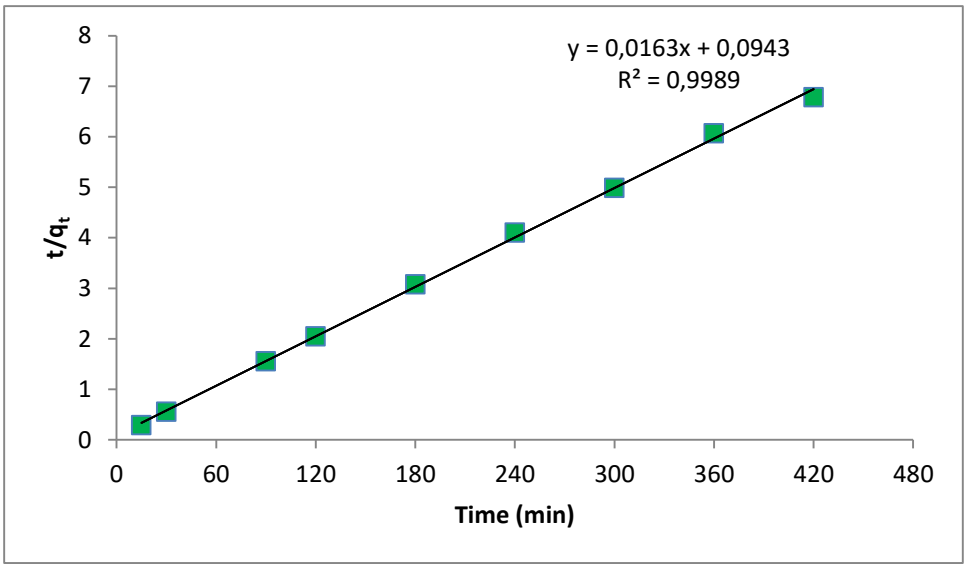

Figure 3. Pseudo-second order kinetic model for the adsorption of Cu^{2+} on moss peat

3.3 Adsorption Isotherms

Isotherm models were used to understand the adsorption mechanism of Cu^{2+} on moss peat and its maximum adsorption capacity. The two most common isotherm models, including Freundlich and Langmuir, were applied

to fit the data. The Freundlich isotherm equation is expressed in its linearized form by the following equation (Wang & Guo, 2020):

$$logq_e = logK_F + \frac{1}{n} logC_e \ldots\ldots\ldots\ldots\ldots (4)$$

Where: q_e (mg/g) is the amount of sorbate per unit mass of sorbent at equilibrium, C_e (mg/l) is the concentration of sorbate in the liquid phase at equilibrium, K_F ((mg/g)(L/mg)$^{1/n}$) is the Freundlich adsorption constant, and n (dimensionless) is an empirical parameter related to the adsorption intensity (Kılıc et al., 2013). A plot of log q_e versus log C_e gives a linear relationship, and the values of n and K_F were calculated from the slope and intercept, respectively. The linear form of the Langmuir isotherm equation is written as follows (Wang & Guo, 2020):

$$\frac{C_e}{q_e} = \frac{C_e}{q_m} + \frac{1}{K_L q_m} \ldots\ldots\ldots\ldots\ldots (5)$$

Where: q_m (mg/g) is the maximum adsorption capacity of adsorbents calculated by Langmuir model, and K_L (L/mg) is the rate adsorption constant (adsorption rate to desorption rate ratio). The plot of C_e/q_e versus C_e yields a straight line, which is used to estimate q_m and K_L values from the slope and intercept, respectively. These parameters, q_m and K_L, are then used to estimate the separation factor, R_L (dimensionless), which predicts the affinity between the metal ion and the adsorbents. R_L is calculated using the following equation (Weber & Chakravorti, 1974; Kowanga et al., 2016):

$$R_l = \frac{1}{1 + K_L C_o} \ldots\ldots\ldots\ldots\ldots (6)$$

Where: C_o (mg/l) represents the highest initial concentration of the adsorbate in the solution. Based on the value of R_L (R_L>1, R_L=1, 1>R_L>0, R_L=0), the adsorption process can be categorized as unfavorable, linear, favorable, and irreversible, respectively. The parameters obtained from the Langmuir and Freundlich models are presented in Table 3. The correlation coefficients (R^2) of the Freundlich and Langmuir models were determined to be 0.863 and 0.992, respectively. The findings of this study indicate that the equilibrium adsorption data is fitted well in the Langmuir isotherm model. This finding demonstrates that Cu^{2+} undergoes chemical adsorption on the adsorption sites of moss peat, suggesting homogeneous monolayer adsorption. Also, it was found that moss peat has a high adsorption capacity of 23.42 mg/g, which might be attributed to its high organic content. It must be pointed out that organic-rich materials with low ash content showed a high adsorption capacity for adsorbates, while those with a high ash content exhibited a low adsorption potential for adsorbates due to the covering of organic moieties by ash (Zhang et al., 2013; Inyang & Dickenson, 2015).

Table 3. Langmuir and Freundlich isotherm parameters

Adsorbent	Langmuir isotherm				Freundlich isotherm		
	q_m	K_L	R_L	R^2	N	K_F	R^2
Moss peat	23.42	0.0726	0.044	0.992	3.632	5.574	0.863

Table 4. Maximum Cu^{2+} adsorption capacity using biomass adsorbent

Adsorbent	pH	Temperature (ºC)	Dosage of adsorbent (g/l)	Maximum Adsorption capacity (mg/g)	Reference
Cellulose pulp waste	<6	22	20	4.98	(Ulmanu et al., 2003)
Active carbon	<6	22	20	6.61	(Ulmanu et al., 2003)
Compost	7.3	22	20	12.77	(Ulmanu et al., 2003)
Corn straw- biochar	5	20 ± 2	5	12.52	(Chen et al., 2011)
Hard wood-biochar	5	20 ± 2	5	6.79	(Chen et al., 2011)
Tree fern	NA*	20	5	10.6	(Ho et al., 2002)
Hazel nut husk-activated carbon	5.7	18	(2-20)	6.65	(Imamoglu & Tekir, 2008)
Moss peat	4	20 ± 1	4	23.42	This study

*NA: Not available

When comparing the maximum adsorption capacity of Cu^{2+} on moss peat to those of previous studies (see Table 4), it is noted that the adsorption capacity of moss peat is significantly higher than that of many organic-rich

adsorbents. As a result, this study suggests that moss peat may have an important implication as an adsorbent for the remediation of Cu^{2+} contaminated water. The value of R_L was determined, and it was less than 1. This result indicates that the adsorption of Cu^{2+} on moss peat is a favorable process.

Effect of pH on Copper Adsorption

pH is an important factor that influences the adsorption of metals onto sorbent surfaces. The pH has been found to have an impact on the speciation of metals in aqueous solutions, the ionic state of functional groups, the surface charge, and the characteristics of the sorbent (Hossain et al., 2012a; Yu et al., 2013). The impact of the initial pH of the suspension on the adsorption of Cu^{2+} by moss peat was examined within the pH range of 2–4.5. Within this range, copper predominantly exists in the form of Cu^{2+}, and the hydrolysis and precipitation of copper ions are not observed (Kołodyńska et al., 2012). Figure 6 shows an increase in the adsorption of Cu^{2+} by moss peat as the pH increased from 2.0 to 4.5. The maximum adsorption capacity of moss peat was observed at pH 4.5, with a value of 60.0 mg/g. The limited adsorption of Cu^{2+} at low pH can be attributed to the high concentration of hydrogen ions, which compete with Cu^{2+} for the available active sites. As the pH increases, there is a corresponding decrease in the amount of hydrogen ions, resulting in an increased availability of binding sites for Cu^{2+}.

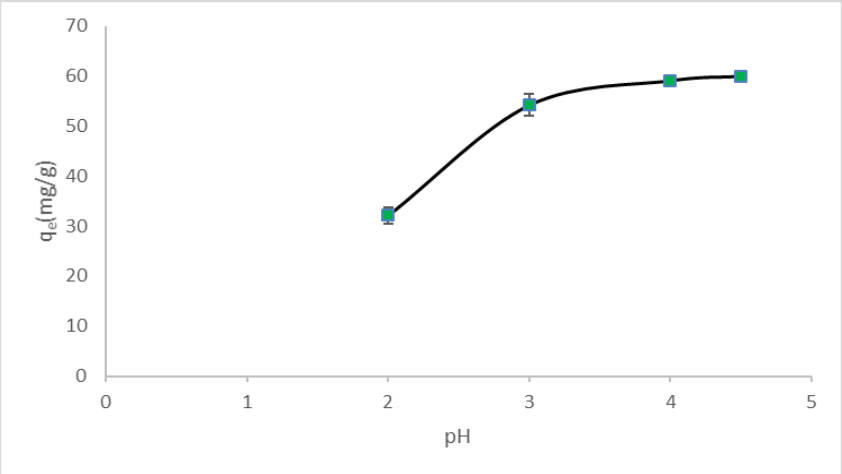

Figure 6. Effect of pH on the adsorption of Cu(II) by moss peat

Conclusion

In this research study, moss peat, the fibrous product of the anaerobic decomposition of sphagnum moss, effectively removed Cu^{2+} from aqueous solutions. A pseudo-second-order could fit the kinetic experimental data. Moreover, the Langmuir model fitted the adsorption isotherm data well, suggesting that Cu^{2+} was adsorbed chemically for the binding sites at moss peat. By comparing the adsorption capacity of moss peat for the adsorption of Cu^{2+} with other organic-rich adsorbents, moss peat can be used as an effective adsorbent under the studied environmental conditions.

Scientific Ethics Declaration

The author declares that the scientific ethical and legal responsibility of this article published in EPSTEM journal belongs to the author.

Acknowledgement

* This article was presented as an oral presentation at the International Conference on Technology, Engineering and Science (www.icontes.net) held in Antalya/Turkey on November 16-19, 2023.

* I am grateful to Mutah University/Jordan for providing me with financial support to attend this conference.

References

Al-Saydeh, S. A., El-Naas, M. H., & Zaidi, S. J. (2017). Copper removal from industrial wastewater: A comprehensive review. *Journal of İndustrial Engineering Chemistry*, *56*, 35-44.

Aldmour, S. T., Burke, I. T., Bray, A. W., Baker, D. L., Ross, A. B., Gill, F. L., & Stewart, D. I. (2019). Abiotic reduction of Cr(VI) by humic acids derived from peat and lignite: kinetics and removal mechanism. *Environmental Science and Pollution Research*, *26*(5), 4717–4729.

Aldmour, S. T. J. (2018). *Abiotic reduction of Cr (VI) by humic acids: kinetics and removal mechanism*. (Doctoral dissertation). University of Leeds

ASTM. (1999). *D 2974-87 Standard test methods for moisture, ash, and organic matter of peat and other organic soils.* (pp. 288–290). West Conshohocken: American Society for Testing and Materials.

ASTM. (2001). *D 1102-84 standard test method for ash in wood*. West Conshohocken, United States: ASTM International.

ASTM. (2013). *E872-82 standard test method for volatile matter in the analysis of particulate wood fuels.* West Conshohocken, United States: ASTM International.

Brewer, G. J. (2007). Iron and copper toxicity in diseases of aging, particularly atherosclerosis and Alzheimer's disease. *Experimental Biology and Medicine*, *232*(2), 323-335.

Chen, X., Chen, G., Chen, L., Chen, Y., Lehmann, J., McBride, M. B., & Hay, A. G. (2011). Adsorption of copper and zinc by biochars produced from pyrolysis of hardwood and corn straw in aqueous solution. *Bioresource Technology*, *102*(19), 8877-8884.

Davarnejad, R., & Panahi, P. (2016). Cu (II) removal from aqueous wastewaters by adsorption on the modified Henna with Fe3O4 nanoparticles using response surface methodology. *Separation and Purification Technology*, *158*, 286-292.

Demirbas, E., Dizge, N., Sulak, M., & Kobya, M. (2009). Adsorption kinetics and equilibrium of copper from aqueous solutions using hazelnut shell activated carbon. *Chemical Engineering Journal*, *148*(2-3), 480-487.

Faller, P. (2009). Copper and zinc binding to amyloid-β: coordination, dynamics, aggregation, reactivity and metal-ion transfer. *ChemBioChem 10*(18), 2837-2845.

Gautam, R. K., Sharma, S. K., Mahiya, S., & Chattopadhyaya, M. C. (2014). Contamination of heavy metals in aquatic media: transport, toxicity and technologies for remediation. S. Sharma (Ed.), *Removal of heavy metals present in water*. RSC Publisher.

González, A., & Pokrovsky, O. (2014). Metal adsorption on mosses: toward a universal adsorption model. *Journal of Colloid İnterface Science*, *415*, 169-178.

Ho, Y., Huang, C., & Huang, H. (2002). Equilibrium sorption isotherm for metal ions on tree fern. *Process Biochemistry*, *37*(12), 1421-1430.

Hossain, M., Ngo, H., Guo, W., & Setiadi, T. (2012a). Adsorption and desorption of copper (II) ions onto garden grass. *Bioresource Technology*, *121*, 386-395.

Hossain, M., Ngo, H. H., Guo, W., & Nguyen, T. (2012b). Removal of copper from water by adsorption onto banana peel as bioadsorbent. *International Journal of GEOMATE*, *2*(4), 227-234.

Hureau, C., & Faller, P. (2009). Aβ-mediated ROS production by Cu ions: structural insights, mechanisms and relevance to Alzheimer's disease. *Biochimie*, *91*(10), 1212-1217.

Imamoglu, M., & Tekir, O. (2008). Removal of copper (II) and lead (II) ions from aqueous solutions by adsorption on activated carbon from a new precursor hazelnut husks. *Desalination*, *228*(1-3), 108-113.

Inyang, M., & Dickenson, E. (2015). The potential role of biochar in the removal of organic and microbial contaminants from potable and reuse water: A review. *Chemosphere*, *134*, 232-240.

Khatoon, H., & Rai, J. P. N. (2016). Agricultural waste materials as biosorbents for the removal of heavy metals and synthetic dyes-a review. *Octa Journal of Environmental Research*, *4*(3), 208-229.

Kılıc, M., Kırbıyık, C., Cepeliogullar, O., & Putun, A. E. (2013). Adsorption of heavy metal ions from aqueous solutions by bio-char, a by-product of pyrolysis. *Applied Surface Science*, *283*, 856-862.

Kołodyńska, D., Wnętrzak, R., Leahy, J., Hayes, M., Kwapiński, W., & Hubicki, Z. (2012). Kinetic and adsorptive characterization of biochar in metal ions removal. *Chemical Engineering Journal*, *197*, 295-305.

Kowanga, K. D., Gatebe, E., Mauti, G. O., & Mauti, E. M. (2016). Kinetic, sorption isotherms, pseudo-first-order model and pseudo-second-order model studies of Cu (II) and Pb (II) using defatted Moringa oleifera seed powder. *The Journal of Phytopharmacology*, *5*(2), 71-78.

Rafatullah, M., Sulaiman, O., Hashim, R., & Ahmad, A. (2009). Adsorption of copper (II), chromium (III), nickel (II) and lead (II) ions from aqueous solutions by meranti sawdust. *Journal of Hazardous Materials*, *170*(2-3), 969-977.

Trakal, L., Šigut, R., Šillerová, H., Faturíková, D., & Komárek, M. (2014). Copper removal from aqueous solution using biochar: effect of chemical activation. *Arabian Journal of Chemistry*, *7*(1), 43-52.

Ulmanu, M., Marañón, E., Fernández, Y., Castrillón, L., Anger, I., & Dumitriu, D. (2003). Removal of copper and cadmium ions from diluted aqueous solutions by low cost and waste material adsorbents. *Water, air, and soil pollution*, *142*, 357-373.

Wang, J., & Guo, X. (2020). Adsorption isotherm models: Classification, physical meaning, application and solving method. *Chemosphere*, *258*, 127279.

Weber, T. W., & Chakravorti, R. K. (1974). Pore and solid diffusion models for fixed-bed adsorbers. *AIChE Journal*, *20*(2), 228-238.

Won, S. W., Choi, S. B., & Yun, Y.-S. (2013). Binding sites and mechanisms of cadmium to the dried sewage sludge biomass. *Chemosphere*, *93*(1), 146-151.

Yu, J.-X., Wang, L.-Y., Chi, R.-A., Zhang, Y.-F., Xu, Z.-G., & Guo, J. (2013). Competitive adsorption of Pb^{2+} and Cd^{2+} on magnetic modified sugarcane bagasse prepared by two simple steps. *Applied Surface Science*, *268*, 163-170.

Zhang, P., Sun, H., Yu, L., & Sun, T. (2013). Adsorption and catalytic hydrolysis of carbaryl and atrazine on pig manure-derived biochars: impact of structural properties of biochars. *Journal of Hazardous Materials*, *244-245*, 217-224.

Author Information

Suha T. Aldmour
Civil and Environment Engineering Department, Mutah University, Karak, Postal Code (61710), Jordan
Contact e-mail: *suha3112@mutah.edu.jo*

To cite this article:

Aldmour, S.T. (2023). Adsorption of copper ions from aqueous systems using moss peat: Reaction kinetics and adsorption isotherm. *The Eurasia Proceedings of Science, Technology, Engineering & Mathematics (EPSTEM)*, 26, 279-286.

The Eurasia Proceedings of Science, Technology, Engineering & Mathematics (EPSTEM)
ISSN: 2602-3199

The Eurasia Proceedings of Science, Technology, Engineering & Mathematics (EPSTEM), 2023

Volume 26, Pages 287-294

IConTES 2023: International Conference on Technology, Engineering and Science

Intelligent Integration and Fusion of Multimodal Biometric Systems

Adjoudj Reda
University of Sidi Bel-Abbès

Belhia Souaad
University of Sidi Bel-Abbès

Allal Anis
University of Sidi Bel-Abbès

Bahram Tayeb
University of Saïda

Abstract: The propagation and the frightening expansion of frauds due essentially to the easy access to high technologies make it difficult or sometimes impossible to detect these frauds and impostures. Therefore, it has become important, if not urgent, to develop identification techniques and tools that are more robust to attacks, more precise and more efficient. There are currently in Europe and some American countries very efficient biometric systems that combine two (2) modalities (photos and fingerprints in the case of biometric passports), but they remain very vulnerable, notably because of acquisition problems, data quality or the non-permanence of certain biometrics. Therefore, the systems based on biometric modality has been growing in the world for a decade. The processes of identification and identity verification of individuals have a very wide spectrum of applications in modern society and are becoming very relevant. However, the field of multi-biometrics is not new, many researchers have been working on this topic especially in the last 10 years. Scholar Google lists nearly 6000 publications on the subject, half of which since 2018. Real systems are in production, we can cite the UID program in India to enroll the 1.300 billion inhabitants with the 10 fingerprints and the two Iris. Most of the techniques consisted in generalizing classical biometric systems (with one modality) by attribute fusion (concatenation of data, statistical reduction...), by score fusion (often performed by summing up the comparison scores from each biometric system) or by decision fusion (majority vote most often). The objective of our work is to propose new techniques of fusion & multimodal biometric integration by using artificial intelligence tools and especially the application of fusion techniques such as: Brute Force Search, Support Vector Machines, neural networks, fuzzy systems, neuro-fuzzy systems, Genetic Algorithms, Particle Swarm Optimization.

Keywords: Biometric, Artificial intelligence, Pattern recognition, Image processing

Introduction

Europe and some American countries currently have high-performance biometric systems that combine two (2) modalities (photos and fingerprints in the case of biometric passports), but they remain highly vulnerable, notably due to acquisition problems, data quality or the non-permanence of certain biometrics. In our country-Algeria-, where the application of biometrics is taking its first steps, it remains primary because of a single modality (in fact, two modalities are taken, face and fingerprint, but only one modality is used (fingerprint or photo) during verification). This is highly inadequate and certainly very vulnerable. Through this paper, we hope to convince local and national authorities to opt for multimodal fusion for better performance. There's no doubt that the security and economic impact will be immense, translating into better control and mastery of

information on the security front. Nevertheless, other logistical aspects must imperatively follow: a robust, uniform national network linking all the country's relevant institutions, where citizen databases must be distributed, as well as the associated real-time applications that must follow (wireless devices, GSM, distributed d-bases...).

In another part of view, some of the limitations imposed by single-modal biometric systems, can be overcome by employing multiple biometric modalities (such as than a person's face and fingerprint or several fingers of a nobody). Such systems, known as multi-biometric systems modals, are expected to be more reliable due to the presence of multiple modalities biometrics (Hong et al., 1999). By asking the user to present a sub-random set of biometric traits (e.g. left index and fingers right means, in that order), the system ensures that a user is indeed present at the time of data acquisition. These systems can also meet the stringent performance requirements imposed by various apps. Multi-modal biometric systems address the problem of non-universality, since several features ensure sufficient coverage of the population (Jain et al., 2004), and they improve the precision of the comparison (Jain et al., 2005). In addition, multi-modal biometric systems provide anti-parody measures by making it difficult for an intruder to simultaneously mystify the multiple biometric traits of a legitimate user. Hence, the development of biometric systems based on multiple biometric traits a received considerable attention from researchers.

Modes of Operation

A multi-modal biometric system can operate in one of three different modes: serial mode, parallel mode and hierarchical mode. In fashion serial operation, the output of a biometric trait is typically used to reduce the number of possible identities before the next trait is used. This serves as an indexing scheme in an identification system. For example, a multi-modal biometric system using face and fingerprints could employ face information to search for the few best matches then use fingerprint information to converge on a single identity. It is contrary to a mode of parallel operation, where information from multiple traits is used simultaneously to run recognition. This difference is crucial. In the serial operational mode, the different biometric characteristics do not have to be acquired simultaneously. Moreover, a decision could be reached without acquisition of all traits. This reduces the overall recognition time. In the hierarchical mode, classifiers are combined in a structure tree.

Fusion in Multi-Modal Biometric Systems

A biometric system has four important modules. The sensor acquires the biometric data of the user; the extraction module extracts a set of characteristics from acquired data; the compare or the match module compares the characteristics acquired with the models stored in the database, for example, using a classifier or a comparison algorithm; the module decision-making uses the result of the previous module either to identify a person already registered or verify the identity of a person. Sanderson and other researchers (Sanderson & Paliwal, 2002) have classified fusion or the integration of information in biometric systems in two broad categories:

– The Fusion in Pre-Classification.
– Post-Classification Fusion.

Fusion or integration in pre-classification refers to merging information before the application of any classification algorithm or comparison. In post-classification integration the information is merged after the classifiers' decisions have been obtained.

State of the Art

The multi-modal approach integrating the biometric characteristics of an individual is a relatively recent field of research. Indeed, the first publications date back to 1995. This work had been carried out by Brunelli and Falavigna (Brunelli et al., 1995) who used the multi-modal approach for the identification some people. Their system consisted of two image and audio subsystems, consisting respectively of two and three classifiers, These classifiers were non-homogeneous and their outputs were then integrated after normalization. The resulting multi-modal system had a recognition rate of 98% whereas mono-modal audio sub-systems 2 and image had recognition rates 88% and 91% respectively. Duc and his team (Duc et al., 1997a) have developed a technique for merging biometric information for the authentication of persons also based on the integration of two image

and audio subsystems called experts. The novelty of this technique compared to the previous one was that it allowed to evaluate the bias provided by each sub-module and this bias was then used to calibrate and reconcile the decisions made by each subsystem. They then managed to reduce the error rate and obtain a good recognition rate of 95.50%. We should also mention the work of Jourlin and his colleagues (Jourlin et al., 1997), which also focused on the fusion or multi-modal integration of features. Here, it is a question of verification as well. They take over the ideas suggested by Dieckmann's team in 1997, as Duc indicates in his article (Duc et al, 1997b), according to which, it is possible to achieve multi-modal recognition by merging or combining audio characteristics and visual information of the contour of the face during the production process of facial expression. The resulting audio subsystem had an FA3 of 2.3% and an FR4 of 2.8%, for a recognition of 97.2%. The image system had an FA of 3.0% and a FR of 27.8%, for a recognition of 72.2%. After Merging of scores, the resulting system achieves an FA of 0.5%, an FR of 2.8% and a 96.60% recognition.

In all these studies, we notice that the multi-modal system consists of the fusion of two or three uni-modal subsystems. Without losing sight of the specificity of each subsystem involved, we will say that the multi-modal systems designed in this way are distinguished from each other by the fusion technique employee. This combination is thus done using a neural network in the case of Brunelli and Falavigna (1995), of a classifier bayesian in that of Duc (Duc et al. 1997a, 1997b), then finally of a weighted sum of the similarity scores in the Jourlin case (Jourlin et al.,1997), where the weights are obtained using a dichotomous algorithm. In all the cases, the multi-modal system has performances superior to those of each unimodal subsystem. Jourlin and his teammates use a variant of component analysis main derivative of the technique initiated by Turk and Pentland, developed in 1991. In this original version, the authors identify images of whole faces. For their experiments Turk and Pentland use faces (pictures) of size variable, taken with different lighting, sometimes with the head more or less leaning. The system then proves to be insensitive to changes in lighting with 96% correct recognition, somewhat sensitive to orientation change with 85% correct recognition and finally they get a rate of 64% recognition, following a variation in the size of the image of the face. By Compared to Brunelli and Falavigna, the performance of component analysis (ACP) are slightly higher. Compared to the work of Duc et al. (1997) Turk and Pentland's approach is much simpler mathematically, it consists of locating the corners in the input images (face, iris, and fingerprint) by applying the Harris operator (Morin, 2006). The latter is based on the contrast, i.e. at each change of contrast we consider the point as a corner, and we recover its coordinates (x and y). At the end of this step we will have a vector of points. It is therefore this technique that we will use in the extraction module of the features of our system. Consequently, very few researchers have studied the integration or combination at level of characteristics and most of them generally prefer plans of fusion in post-classification (Ross & Govindarajan, 2005; Adjoudj, 2022).

Fusion Approach Developed

In this section we will describe the approach developed for the automatic multi-modal biometric recognition of people based on the fusion of their biometric characteristics which are: the face, the iris, and the fingerprint. For this, two methods have been developed; the first is a method classic based on notions of calculating distances (Fig 2), while the second is an approach based on the use of neural networks for classification (Fig.3.b). A complete and detailed description of the two approaches will be presented in the following sections, as well as a comparative study between them. For the validation of our two methods, we tested them on two databases. Data called MIT and CMU (see next section).

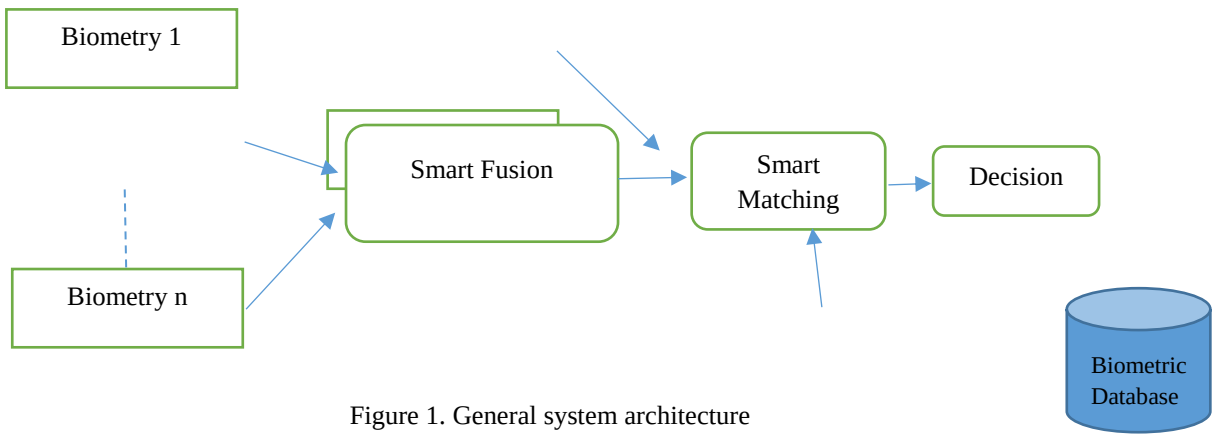

Figure 1. General system architecture

As previously said, the multi-modal biometric fusion approach consists of automatically and reliably recognize a person. By presenting his three biometric characteristics such as Input Data (face, iris, fingerprint, plus an identity in the case of verification), the result of the system will be either the validation or rejection of the proclaimed identity (in the case of a verification) or its identity, if it is already registered in the database (in the case of a identification). see Fig.1.

Developed Multi-modal Biometric Fusion System

Like any biometric system, our system is composed of the main modules which are:

– The feature extraction module (we used an operator called Harris) (Morin, 2006), (Adjoudj, 2006),

– The comparison module (Matching), two methods were used, the geometric first and which is the Euclidean distance (used especially in classical approach), the second is a neural network used for the classification (neural approach),

– And the decision module.

With only one exception which is the first module of a biometric system (the sensor). For our system (see Fig.2), we have the images ready to use.

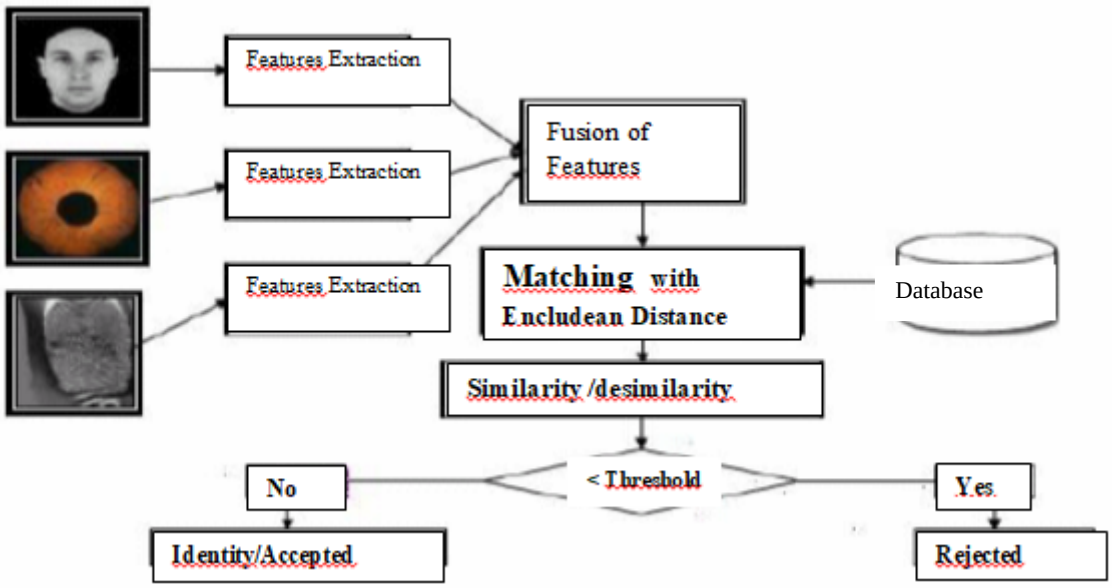

Figure 2. Schema of our system.

The Smart Distance-Based Multi-Modal Biometric Fusion Approach

The multi-modal biometric approach that will be described in this section is an approach based on the calculation of the Euclidean distance between the combined footprint/ merged (the fingerprint that we will have as a result after the integration of the three fingerprints: the face print, the iris print, and the fingerprint) of the input person, i.e. the person to be identified and all the combined fingerprints of all individuals in the database. So the person to be identified corresponds to the person in the base who has the maximum number of points similar. First of all, the system must extract useful information, i.e. locate only the points (features) in the input images, then it must construct a single vector from the three vectors obtained during the phase previous one (by a simple concatenation), and compare the latter with others which already exist in the database, if these vectors look alike then the person is identified (recognized). Algorithm shows the operation of this approach.

Smart Algorithm

Propose new techniques for multimodal biometric fusion using artificial intelligence tools.

1)- Implement independent biometric information pre-processing processes (biometric data quality):

2)- Acquisition, filtering, features extraction

3)- normalization methods (UCN Unconstrained Cohort Normalization), Min_max , etc....)

4)- application of fusion techniques: Brute Force Search, Support Vector Machines, neural networks, fuzzy systems, neuro-fuzzy systems, Genetic Algorithms, Particle Swarm Optimization ....
5)- Securing acquired data.
6)- Generalization of BioHashing.
7)- Comparison of multi-biometric data.
8)- Consideration of biometric data quality.
9)- In general, performance is analyzed using measures derived from international standardization (such as the Error Equal Rate or EER).

Fusion Step

The integration of multiple biometric modalities, or so-called multimodal systems (Ayesha et al., 2020), improves recognition efficiency. The multi-view face and fingerprint modalities were combined in this work to create the multi-view multimodal biometric framework using score-level fusion. The combination at the score level provides a perfect balance between data availability and ease of execution. The decision level indicates the insertion of a similarity matrix for all combined scores. If the application has a high score, the system must approve it (high number interest point pair).

Our research focused on parameters associated with frequency. The rationale behind selecting such parameters is based on their ability to enable the representation of the fingerprint through a fixed-size vector. The definition of this characteristic is necessary for the purpose of comparing two Bio codes and verifying their level of similarity or dissimilarity. The aforementioned comparisons suggest that there exists a fluctuating level of dependability, which may ultimately lead to the acceptance or rejection of certain practices. The Euclidean distance method is employed as a comparative technique (see next section).

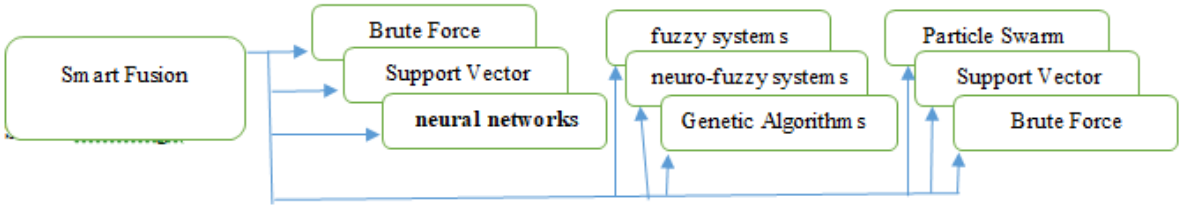

Figure 3.a. – Deferents approaches of smart fusion schema

Smart Matching Step

Matching is the core of this system, and it is the comparison of the vector merged from the input person (constructed in the previous step) with those from the database. This comparison is based on the calculation of the smart distance, so we need to measure the similarity between two individual vectors V_1 & V_2. Two individuals will be said to be close if they have roughly the same values variables. In general, the smart distance is used. Denoted *d*, it is defined as the root of the sum of the squares of the differences of the coordinates x_i, y_i, according to the formula described in [1], and as we have already used it in (Adjoudj, 2022), see Fig.2.

$$d(V_1,V_2)=\sqrt{\sum_{i=1}^{p}(x_{1i}-x_{2i})^2+(y_{1i}-y_{2i})^2} \qquad [1]$$

With: $\boldsymbol{p}$ the number of points which constitute each vector, each vector has the same size p.
$\boldsymbol{x_i, y_i}$: the coordinates of the $\boldsymbol{i^{th}}$ point of the vector to be recognized $\boldsymbol{V_1}$.
$\boldsymbol{x_i, y_i}$: the coordinates of the $\boldsymbol{i^{th}}$ point of a vector of the basis $\boldsymbol{V_2}$.

The system decides that the person to identify corresponds to the person in the database which has the maximum of similar points, i.e. the minimum distance d. So the role of identification is to confirm that it is such and such a person or say that this person does not belong to the database. This ID is parameterized by a variable threshold (see Fig.2)

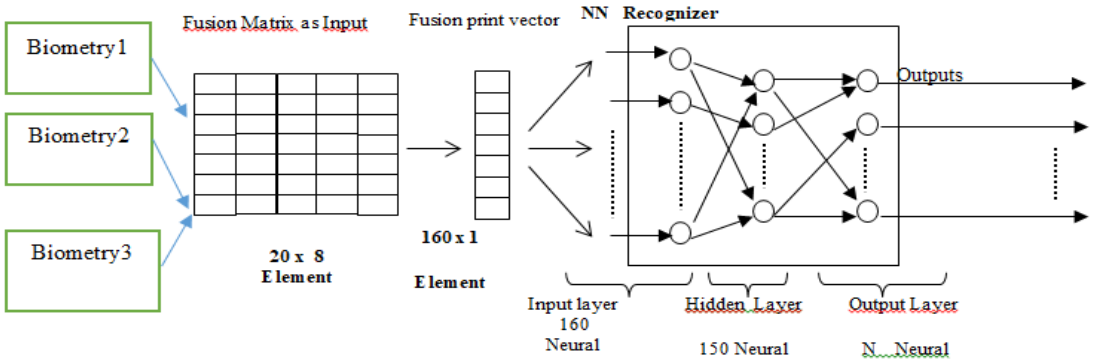

Figure.3.b – Architecture of the system with neural network approach

Validation, Implementation and Testing

We note that the volume of calculations involved and the volume of data to be processed is very high, and that it is therefore quite possible that WorkStations may be required for such implementations. For this we proceed by their differents steps :

- Selection of suitable platforms (Matlab, Java, ...)
- Use of powerful machines or workstations (Sun workstation)
- Possible use of BEAT evaluation platform,
- Possible use of specialized software such as Munitia Cyl, SFinGe, ...
- Realization of biometric systems on real data.

In this phase we will test our system, i.e. identify a person from their three biometric images or modalities (face, iris, and fingerprint). This phase proceeds as follows:

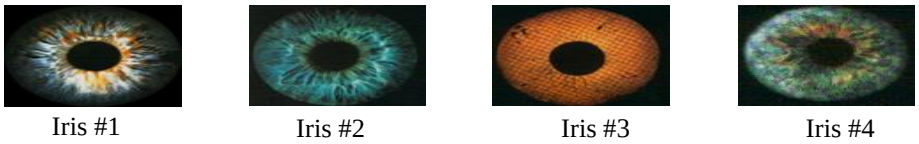

Iris #1 Iris #2 Iris #3 Iris #4

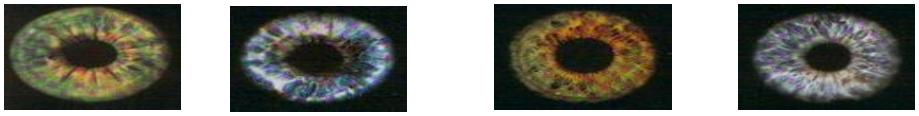

Iris #5 Iris #6 Iris #7 Iris #8

Figure.4.a.Samples from iris database.

Figure 4.b. Samples from face database.

Figure 4.c. Samples from fingerprint database.

For this, we built test groups. For the MIT database, we added different synthetic noises (tq: the noises of Salt & papper, of Speckle, of Gauss, and Poisson) to the original images (whose threshold varies between 0.03 and 0.04). For the CMU database, we have several versions of images from the face (several emotional states), we built 4 test groups with only the photo of the face which changes (emotion), the others that of the iris and that of the fingerprint remain the same.

Discussion

Neural networks are used for classification and prediction, and are systems for making input/output associations. They have the ability to learn, which gives them the appearance of universal approximators. This has been seen and observed in this approach. Compared to the first Euclidean distance-based approach, the neural approach gave encouraging results too. Admittedly, the RN recognized all the people in the training groups (which is to be expected), but in the test it gave erroneous results despite the low threshold of added noise. This system which is based on notions of smart distance to make the Matching, allowed us to obtain very good results / encouraging results and favorable. For the MIT base, he recognized all people despite the threshold of the added noise, and the same goes for the base CMU, and as a perspective, we will test our approach with the following multi-biometric databases TIMIT, XM2VTS, BANCA, NIST, FVC.

Conclusion

In this paper, first results have been obtained on a multimodal biometric fusion system that uses face, iris and fingerprint features for automatic verification. A feature-level fusion scheme was proposed, in which two different approaches were developed, the first using Euclidean distance for comparison. According to the experiments carried out, the performance of the multimodal system is superior to the individual performance of the single-mode systems. In conclusion, it should be mentioned that it is possible to combine more than three modalities with an integration of modules such as the one we have used: the only problem is to access the measurements given by each of the single-mode modules, i.e. sensors and modules, in order to extract the characteristics present. All these recommendations are avenues for future work.

Scientific Ethics Declaration

The authors declare that the scientific ethical and legal responsibility of this article published in EPSTEM journal belongs to the authors.

Acknowledgements or Notes

* This article was presented as a poster presentation at the International Conference on Technology, Engineering and Science (www.icontes.net) held in Antalya/Turkey on November 16-19, 2023.

References

Adjoudj, R. (2006). *Reconnaissance & identification of persons by automatic authentication in a high security system.* (Doctoral dissertation). University of Sidi Bel-Abbès. Retrieved from http://www-inf.univ-sba.dz

Adjoudj, R., Gafour, A. K., Boukelif, A., & Lehireche, A. (2008). La reconnaissance des visages : une comparaison entre les réseaux des neurones compétitifs et les réseaux des neurones à spike, a comparison between artificial and spike neural network for face recognition. *Revue Traitement Du Signal, 25*(6), 449-458.

Adjoudj, R. (2022). Multi-modal biometric persons recognition system. *The Eurasia Proceedings o Science, Technology, Engineering & Mathematics (EPSTEM), 21*, 558-564.

Ayesha, S., Hanif, M. K., & Talib, R. (2020) Overview and comparative study of dimensionality reduction techniques for high dimensional data. *Information Fusion, 59*, 44–58,

Bharadi, V. A., Shah, D. N., Thapa, N. T., Pandya, B H., & Cosma, G. (2018). Multi-instance ıris recognition.

Bharadi, V., Pandva, B., & Cosma, G. (2018). Multi-modal biometric recognition using human ıris and dynamic pressure variation of handwritten signatures. *Fifth International Conference on Social Networks Analysis, Management and Security (SNAMS)*.

Brunelli, R., & Falavigna, D. (1995). Person identification using multiple cues. *IEEE Transactions on Pattern Analysis and Machine Intelligence, 18*(9), 955-966.

Carrillo, C.M. (2003). *Continuous biometric authentication for authorised aircraft personnel*. (Master's dissertation). Naval Postgraduate School Monterey, California.

Duc, B., Bigun, E. S., Bigun, J., Maître, G., & Fisher, S. (1997). Fusion of audio and video information for multi-modal person authentication. *Pattern Recognition Letters, 18*(9), 35-84.

Duc, B., Maître, G., Fisher, S., & Bigun, J. (1997). Person authentication by fusing face and speech information. *International Conference on Audio- and Video-based Biometric Person Authentication*, 311-318.

Géo. (1998). Magasine scientifique Géo (pp. 67-82). Edition de l'Institut National De Géographie., France, Marseille.

Hong, L., Jain, A. K., & Pankanti, S. (1999). Can multibiometrics improve performance. *International Conference on Computing Communication Control and Automation (ICCUBEA*). IEEE.

Iyengar, S. S., Prasad, L., & Min, H. (1995). *Advances in distributed sensor technology*. Prentice Hall Edition.

Jain A. K., Flynn, P., & Ross A. (2008). *Hand book of biometrics*. Springer

Jain, A. K., Nandakumar, K., & Ross, A. (2005). Score normalization in multimodal biometric systems. *Pattern Recognition Journal*.

Jain, A. K., Ross A., & Prabhakar, S. (2004). An introduction to biometric recognition. *IEEE Transactions on Circuits and Systems for Video Technology,14*(1), 4-19.

Janakaraj, P., Jakkala, K., Bhuyan, A., Sun, Z., Wang, P., & Lee, M.(2019). Star: Simultaneous tracking and recognition through millimeter waves and deep learning. *12th IFIP Wireless and Mobile Networking Conference (WMNC)*. IEEE.

Jourlin, P., Luettin, J., Genoud, D., & Wassner, H. (1997). Acoustic-labial speaker verification. *Pattern Recognition Letters, 18*(9), 853-858.

Morin, L. (2006). *Cours de Traitement d'images*. Université de Rennes.

Nandakumar, K. (2008). *Multibiometric systems: Fusion strategies and template security*. (Doctoral dissertation). MSU, Department of Computer science. Retrieved from https://citeseerx.ist.psu.edu/document?repid

Ramírez, A. V., Hornero, G., Royo, D., Aguilar, A., &Casas, O. (2020). Assessment of emotional states through physiological signals and its application in music therapy for disabled people. *IEEE Open Access Journals.*

Ross, A., & Govindarajan, R. (2005). Feature level fusion using hand and face biometrics. In Proceedings of *SPIE Conference on Biometric Technology for Human Identification II, 5779*, 196-204. Orlando, USA.

Sanderson, C., & Paliwal, K. K. (2002). Information fusion and person verification using speech and face information, *IDIAP*.

Authors Information

Adjoudj Réda
Evolutionary Engineering and Distributed Information Systems Laboratory, EEDIS Lab.
Computer Science Department
University of Sidi Bel-Abbès, Algeria
Contact e-mail: *Adjoudj@univ-sba.dz*

Belhıa Souaad
Evolutionary Engineering and Distributed Information Systems Laboratory, EEDIS Lab.
Computer Science Department
University of Sidi Bel-Abbès, Algeria

Allal Anis
Evolutionary Engineering and Distributed Information Systems Laboratory, EEDIS Lab.
Computer Science Department
University of Sidi Bel-Abbès, Algeria

Bahram Tayeb
Evolutionary Engineering and Distributed Information Systems Laboratory, EEDIS Lab.SBA
Computer Science Department
University of Saïda, Algeria

To cite this article:

Reda, A., Souaad, B., Anis, A., & Tayeb, B. (2023). Intelligent ıntegration and fusion of multimodal biometric systems. *The Eurasia Proceedings of Science, Technology, Engineering & Mathematics (EPSTEM), 26*, 287-294.

The Eurasia Proceedings of Science, Technology, Engineering & Mathematics (EPSTEM)
ISSN: 2602-3199

The Eurasia Proceedings of Science, Technology, Engineering & Mathematics (EPSTEM), 2023

Volume 26, Pages 295-305

IConTES 2023: International Conference on Technology, Engineering and Science

Generalized Predictive Control of the Active and Reactive Stator Powers of the DFIG for Wind Energy Generation

Hacene Mellah
Bouira university

Amar Maafa
Bouira University

Hamza Sahraoui
Université Hassiba Benbouali de Chlef

Abdelghani Yahiou
Bouira University

Houria Smail
Bouira University

Abstract: This paper proposes a Generalized Predictive Control (GPC) strategy for Wind Power Generation (WPG) based on a doubly fed induction generator (DFIG). The objective is to study and apply a robust active and reactive power control strategy based on GPC of the DFIG, this is likely to optimize the energy production and improve the quality of the energy produced. In order to maximize the amount of WPG taken even when the turbine is uncertain or the wind speed varies abruptly, the design is built utilizing the Maximum Power Point Tracking (MPPT) theory. Through numerical modeling with the aid of the Matlab/Simulink software, the predictive control (GPC) of the active and reactive stator powers of the DFIG was validated. A comparison between the GPC of the GADA and the indirect method based on a typical PI controller is developed in order to illustrate the viability of the suggested method. According to the simulation results of this comparison, the suggested method is viable and has promising results.

Keywords: Generalized predictive control (GPC), Wind power generation (WPG), Doubly fed induction generator (DFIG), Active and reactive power control (ARPC).

Introduction

Energy has become increasingly important throughout time as a result of the urgent need to combat climate change and lessen our reliance on fossil fuels. Hydroelectric power, wind power, and solar power are regarded as substitutes that can fulfil our energy needs. We can benefit from the addition of these energy sources by creating jobs and stimulating the economy, especially in rural and isolated places (VO et al., 2023). Due to the obvious advantages of variable speed wind turbines (VSWT) equipped with a double-fed induction generator (DFIG) compared to other wind turbines based on other electric machines, they have drawn more attention from researchers during the past two decades (Hansen, 2023).

Doubly-Fed Induction Generator (DFIG) or known as the "double-fed asynchronous machine'. The most common arrangement for this machine's wiring is to link the stator directly to the network while feeding the

- Selection and peer-review under responsibility of the Organizing Committee of the Conference

rotor through a controlled power converter. This method is more appealing for all situations where speed variations are constrained to those around synchronization. The main benefit of this machine is that the system's power converter only needs to handle 20–30% of the total system power (Mellah & Hemsas, 2012). This means that power converter losses—and hence, production costs—can be minimized in comparison to the converter's ability to handle all power. Additionally, the DFIG in generator mode enables the production of electrical energy at constant frequency and variable mechanical speed. Additionally, she provides a broad operational range in comparison to a squirrel cage induction generator (Cheng & Zhu, 2014; Simões et al., 2015). The interested reader is referred to ref for more information about different WES (Dani et al., 2023).

The advancement of highly integrated digital control systems and the advancement of power electronics have made room for a variety of control strategies (Bektache & Boukhezzar, 2018;Shiravani et al., 2022;Pradhan et al.,2022; Davanipour & Asadipooya, 2017). Among the many control strategies discussed in specialized literature, Field-Oriented Control (FOC) of the DFIG enables the design of alternate-current speed variations that are competitive and while maintaining the efficiency and simplicity of direct current drives (Omac & Erdem, 2023; Prasad & Mulla, 2020). GPC (Shiravani et al., 2022).

However, when really difficult performances are required, conventional control method quickly reveal their limitations. In fact, one of the biggest problems with controlling processes is the presence of delays. These delays are frequently the root of issues that arise during the real time implementation of conventional methods. The idea of predictive control was developed to address this kind of issue (Bektache & Boukhezzar, 2018; Pradhan et al., 2022; Shiravani et al., 2022). We focus on the generalized predictive control (GPC) in this paper.

This paper is structured as follows: the first section provides a general overview of the wind energy conversion systems. In the second section, a modeling study of a DFIG will be presented. The purpose of the study will be to focus on the control of active and reactive power using PI regulators. The third section introduces a fast description of generalized predictive control. In the fourth section we presented some simulations results and we conclude by a conclusion. The third section introduces a fast description of generalized predictive control. In the fourth section, we presented some simulation results and concluded this paper with a conclusion.

Wind Energy Conversion Systems

A device called WECS transforms wind energy into another kind of energy. WECS can be broadly classified into two categories: those that utilize wind turbines to produce energy, which we will discuss later, and those that use windmills to pump water. According to rotational speed control, we can distinguish between two types of WECS: fixed-speed and variable-speed WECS. The first type is called fixed-speed WECS, generally with a squirrel induction generator applied with a gearbox to avoid operation at high wind speeds so as not to damage the turbine.

The second type is called variable-speed WECS, generally with a DFIG or permanent magnet synchronous generator equipped with a power electronic device (Mellah & Hemsas, 2013). Figure 1 shows the WECS based DFIG configuration. Figure 1 shows the WECS based DFIG configuration. We note that there are many ways to get electricity from: marine current (TOLA et al., 2022), ocean wave energy (Rahuna et al., 2023), ocean current energy (Silva et al., 2023).

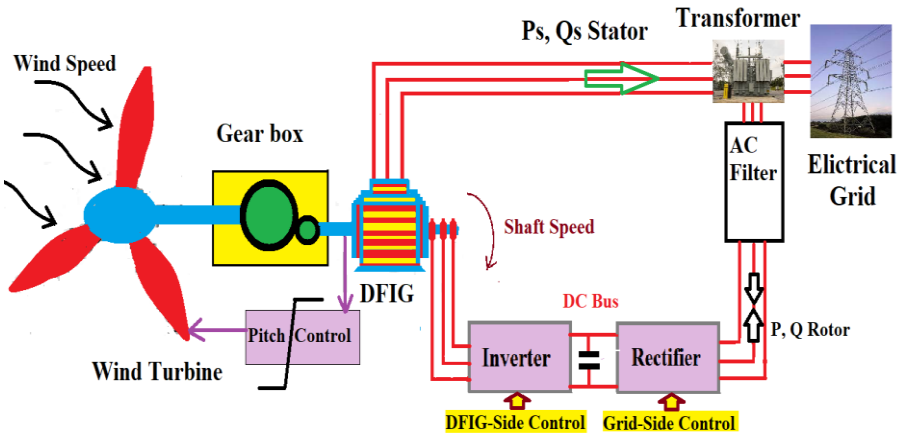

Figure 1. WECS based a DFIG configuration

Modeling of the DFIG

Modeling the electric machine is an essential step in its development. Advances in computer science and software engineering make it possible to carry out efficient modeling and to consider the optimization of electrical machines. The objective of this section is to give a short description of the modeling of the DFIG machine in the frame of reference linked to the rotating field, and it makes it possible to obtain a mathematical model adapted to the decoupled adjustment of the active and reactive powers at the level of the stator of DFIG.

Stator and Rotor Voltage Equations

In the previous conditions, the equations of the mathematical model of the DFIG in matrix form are written:
For the stator:

$$\begin{bmatrix} V_{as} \\ V_{bs} \\ V_{cs} \end{bmatrix} = \frac{d}{dt}\begin{bmatrix} \Phi_{as} \\ \Phi_{bs} \\ \Phi_{cs} \end{bmatrix} + \begin{bmatrix} R_s & 0 & 0 \\ 0 & R_s & 0 \\ 0 & 0 & R_s \end{bmatrix}\begin{bmatrix} I_{as} \\ I_{bs} \\ I_{cs} \end{bmatrix} \quad (1)$$

For the rotor:

$$\begin{bmatrix} V_{ar} \\ V_{br} \\ V_{cr} \end{bmatrix} = \frac{d}{dt}\begin{bmatrix} \Phi_{ar} \\ \Phi_{br} \\ \Phi_{cr} \end{bmatrix} + \begin{bmatrix} R_r & 0 & 0 \\ 0 & R_r & 0 \\ 0 & 0 & R_r \end{bmatrix}\begin{bmatrix} I_{ar} \\ I_{br} \\ I_{cr} \end{bmatrix} \quad (2)$$

Magnetic Equations

The magnetic equations in matrix form are given by the following expressions:

$$\begin{bmatrix} \Phi_s \\ \Phi_r \end{bmatrix} = \begin{bmatrix} [l_s] & [M_{sr}] \\ [M_{sr}] & [l_r] \end{bmatrix} \cdot \begin{bmatrix} i_s \\ i_r \end{bmatrix} \quad (3)$$

With:

$$[\Phi_s] = \begin{bmatrix} \Phi_{sa} \\ \Phi_{sb} \\ \Phi_{sc} \end{bmatrix} \; ; \; [\Phi_r] = \begin{bmatrix} \Phi_{ra} \\ \Phi_{rb} \\ \Phi_{rc} \end{bmatrix}; [i_s] = \begin{bmatrix} i_{sa} \\ i_{ab} \\ i_{ac} \end{bmatrix} \quad and \quad [i_r] = \begin{bmatrix} i_{ra} \\ i_{ab} \\ i_{rc} \end{bmatrix}$$

Mechanical Equation

$$C_{e_m} - C_r = j\frac{d\omega_m}{dt} \Rightarrow \omega_m = \frac{1}{j}(C_{e_m} - C_r) \quad (4)$$

Park Transformation

This transformation, which allows the transition from the three-phase system to the two-phase system, is carried out by matching their homopolar, direct and quadrature components to the real variables. and applied to currents, voltages, and flux makes it possible to obtain differential equations with constant coefficients, the following equation represent the voltage equation.

$$\begin{cases} V_d = Ri_d + \dfrac{d\Phi_d}{dt} - \dfrac{d\theta}{dt}\Phi_q \\ V_q = Ri_q + \dfrac{d\Phi_q}{dt} + \dfrac{d\theta}{dt}\Phi_d \\ V_o = Ri_o + \dfrac{d\Phi_o}{dt} \end{cases} \quad (5)$$

The voltage homopolar component is zero for a balanced system. From the above we obtain the following equations:

$$\begin{cases} V_{ds} = R_s i_{ds} + \dfrac{d\Phi_{ds}}{dt} - \omega_s \Phi_{qs} \\ V_{qs} = R_s i_{qs} + \dfrac{d\Phi_{qs}}{dt} + \omega_s \Phi_{ds} \\ V_{dr} = R_r i_{dr} + \dfrac{d\Phi_{dr}}{dt} - (\omega_s - \omega_m)\Phi_{qr} \\ V_{qr} = R_r i_{qr} + \dfrac{d\Phi_{qr}}{dt} + (\omega_s - \omega_m)\Phi_{dr} \end{cases} \quad (6)$$

Park Transformation Applied to the Flux

We apply the Park transformation, then we eliminate the homopolar component, and we obtain:

$$\begin{bmatrix} \Phi_{ds} \\ \Phi_{qs} \\ \Phi_{dr} \\ \Phi_{qr} \end{bmatrix} = \begin{bmatrix} L_S & 0 & L_m & 0 \\ 0 & L_S & 0 & L_m \\ L_m & 0 & L_r & 0 \\ 0 & L_m & 0 & L_r \end{bmatrix} . \begin{bmatrix} i_{ds} \\ i_{qs} \\ i_{dr} \\ i_{qr} \end{bmatrix} \quad (7)$$

State-Space Representation of the Electrical Equations

After simple mathematical operations, we get the following state space representation of the DFIG model:

$$\dot{X} = \begin{bmatrix} -(\frac{R_s}{\sigma} + \frac{L_m^2}{L_r \sigma T_r}) & (\omega_s) & (\frac{L_m}{\sigma T_r L_r}) & (\omega_m \frac{L_m}{\sigma L_r}) \\ -(\omega_s) & -(\frac{R_s}{\sigma} + \frac{L_m^2}{\sigma T_r L_r}) & -(\omega_m \frac{L_m}{\sigma L_r}) & (\frac{L_m}{\sigma T_r L_r}) \\ (\frac{L_m}{T_r}) & 0 & -(\frac{1}{T_r}) & (\omega_s - \omega_m) \\ 0 & (\frac{L_m}{T_r}) & -(\omega_s - \omega_m) & -(\frac{1}{T_r}) \end{bmatrix} X + \begin{bmatrix} (\frac{1}{\sigma}) & 0 & -(\frac{L_m}{\sigma L_r}) & 0 \\ 0 & (\frac{1}{\sigma}) & 0 & -(\frac{L_m}{\sigma L_r}) \\ 0 & 0 & 1 & 0 \\ 0 & 0 & 0 & 1 \end{bmatrix} U \quad (8)$$

Where: $\dot{X}' = [\frac{di_{ds}}{dt}, \frac{di_{qs}}{dt}, \frac{d\Phi_{dr}}{dt}, \frac{d\Phi_{qr}}{dt}]$, X' = [$i_{ds}$, i_{qs}, Φ_{dr}, Φ_{qr}], U' = [V_{ds}, V_{qs}, V_{dr}, V_{qr}], $\sigma = (L_s - \frac{L_m^2}{L_r})$ and $T_r = \frac{L_r}{R_r}$

DFIG Torque

The DFIG electromagnetic torque's expression:

$$T_{e_m} = np.\frac{L_m}{L_r}.(\Phi_{dr} i_{qs} - \Phi_{qs} i_{ds}) \quad (9)$$

So, the mechanical equation becomes:

$$\frac{d\omega_m}{dt} = \frac{1}{j}.[np(\frac{L_m}{L_r}).(\Phi_{rd} i_{sq} - \Phi_{rq} i_{sd}) - C_r] \quad (10)$$

Expressions of Active and Reactive Powers

The expressions of the active and reactive powers are given by:

$$\begin{cases} P_s = \frac{3}{2}(v_{ds}.i_{ds} - v_{qs}.i_{qs}) \\ Q_s = \frac{3}{2}(v_{qs}.i_{ds} - v_{ds}.i_{qs}) \end{cases} \quad (11)$$

Field Oriented Control Strategies

There are two methods for carrying out power control of the DFIG:

-The direct method consists of independently regulating each axis for power control. The regulators of this method directly control the rotor voltages, hence the explicit name of this type of control.
-The indirect method consists of indirectly regulating the rotor currents. The setpoint for this type of regulation is estimated from the reference powers and the feedback to the comparators will be made from the measured direct and quadrature rotor currents.

Direct Vector Control

This method requires a good knowledge of the flux module and its phase; this must be verified whatever the transitional regime carried out. It is therefore necessary to carry out a series of measures available within the process. This control mode is so called because a regulation of the stator flux is introduced by a feedback loop requiring the measurement or estimation of these variations. In its essence, direct vector control must be carried out by measuring the flux which requires the use of the sensor placed in the air gap of the machine, an operation which is generally delicate to carry out.

In order to access information concerning the amplitude and phase of the flux, it is necessary to use “hall effect” sensors previously placed under the teeth of the stator. They are mechanically fragile and cannot work in severe conditions such as vibration and excessive heating. The signals captured are tainted by harmonies and their frequency varies with speed, which requires automatic adjustable filters.

Indirect Vector Control

This method consists of estimating the rotor voltage values from the active and reactive power values. Thus, the rotor currents will be regulated indirectly. This method is so called because it does not use a flux regulation loop, and therefore it does not require the use of the sensor or estimation of the stator flux. In this method the flux vector is estimated from the measurement of the rotor currents and the rotor speed, based on the equations of the rotor circuit of the asynchronous motor in a reference system rotating in synchronism with the vector of the stator flux.

The major disadvantage of this method is the sensitivity of the estimation towards the variation of the machine parameters due to magnetic saturation and the temperature variation especially for the rotor time constant Tr. The control is based on the inversion of the of equation.

$$V_{dr} = (R_r + L_r \delta S) I_{dr} + \frac{MS}{L_s} \Phi_s - W_r L_r \delta I_{qr} \tag{12}$$

$$V_{qr} = (R_r + L_r \delta S) I_{qr} + W_r \frac{M}{L_s} \Phi_s + W_r L_r \delta I_{dr} \tag{13}$$

$$I_{dr} = \frac{\Phi_S}{M} \tag{14}$$

$$I_{qr} = \frac{Cem}{K_t \Phi_s} \tag{15}$$

Indirect Control without Power Loop

The block diagram of indirect control without power loops is presented in Figure2.

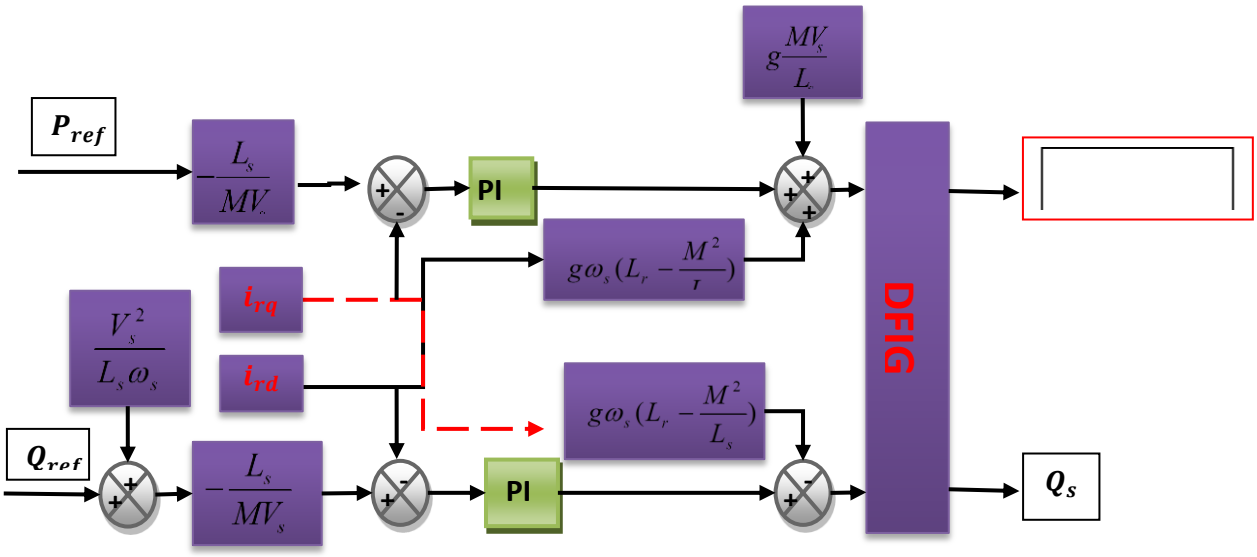

Figure 2. Block diagram of indirect control without power loops

Indirect Control with Power Loop

In order to improve the previous command, we will incorporate an additional regulation loop at the power level in order to eliminate the static error while preserving the dynamics of the system. We arrive at the block diagram presented in Fig.3 on which we clearly distinguish the two regulation loops for each axis, one controlling the current and the other the power.

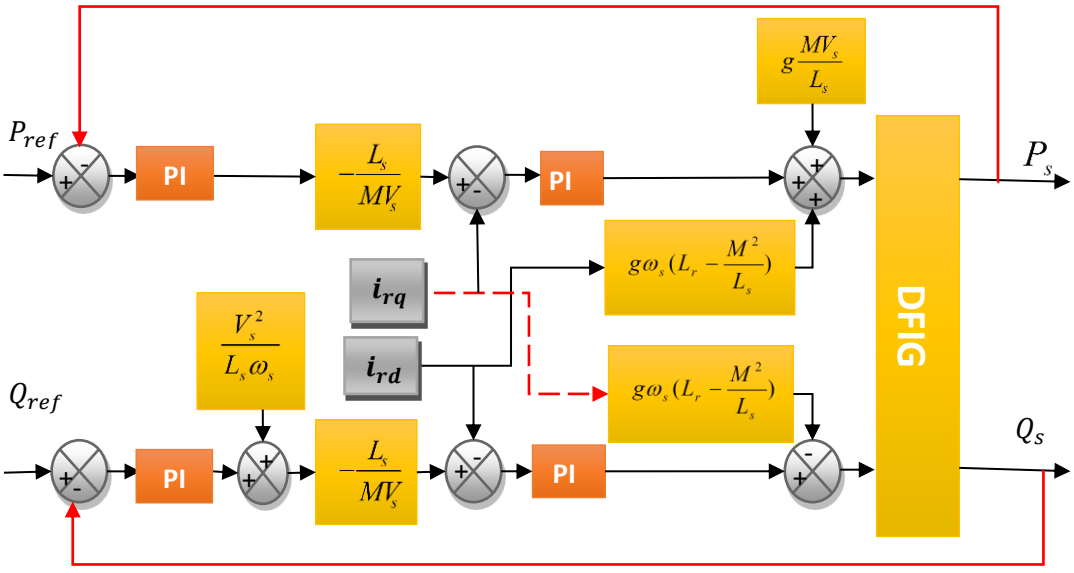

Figure 3. Block diagram of indirect control without power loops

Generalized Predictive Control (GPC)

The GPC was introduced at the end of the 1980s and is regarded as the most widely used prediction method, particularly for industrial processes (Domański, 2020). It is based on the minimization of a quadratically weighted horizon-flying criterion and depends on four parameters: the horizon of the command, the command's horizon and the factor of ponderation. However, the optimal adjustment is not guaranteed, Fig.5 show the diagram of the GPC method principle. The GPC cost function computes the performance by means of predicted errors between the reference output and the output of the system and predicted output increments (Rodrigues et al., 2020) as represented in eq.16, the interested reader is reffred to ref (Clarke et al., 1987a, 1987b)for more information.

$$J = E\left[\sum_{j=N1}^{N2}\left[y(t+j)-w(t+j)\right]^2 + \sum_{j=1}^{Nu}\lambda(j)\left[\Delta U(t+j-1)\right]^2\right] \quad (16)$$

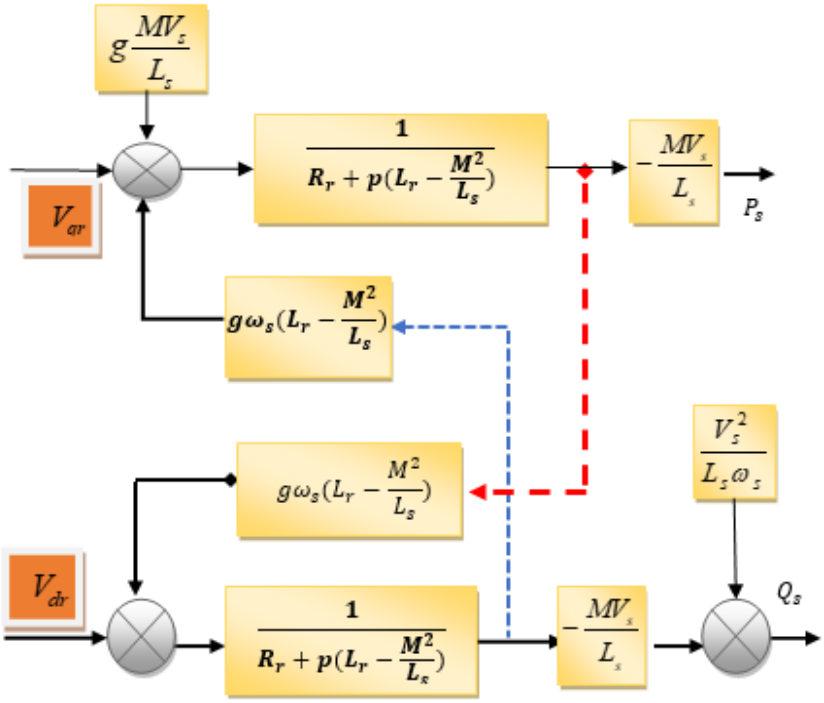

Figure 4. Block schematic of stator active and reactive power as function of rotor current of the DFIG

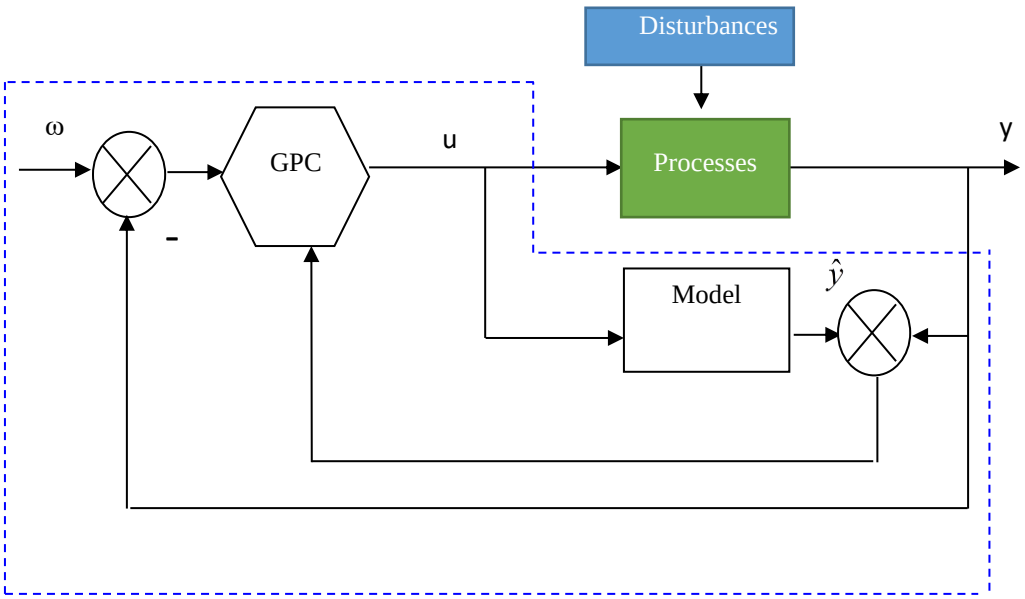

Figure 5. Diagram of the GPC Method Principle

Simulation Results

The generalized predictive control (GPC) of the active and reactive stator powers was validated by numerical simulation in the Matlab/Simulink environment. We used the same specifications for the FOC method. A comparison of the robust predictive control of the DFIG with the indirect method of classic PI is established using the same graph. Figure 6. illustrate the profile of the DFIG's enforced rotational speed.

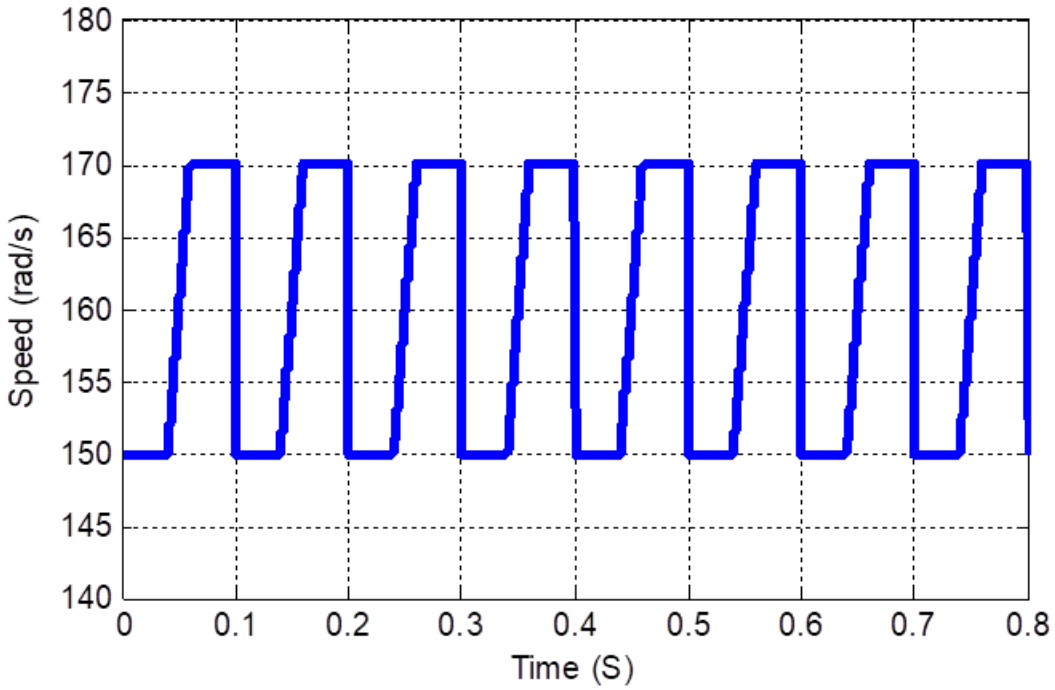

Figure 6. Profile of the DFIG's enforced rotational speed

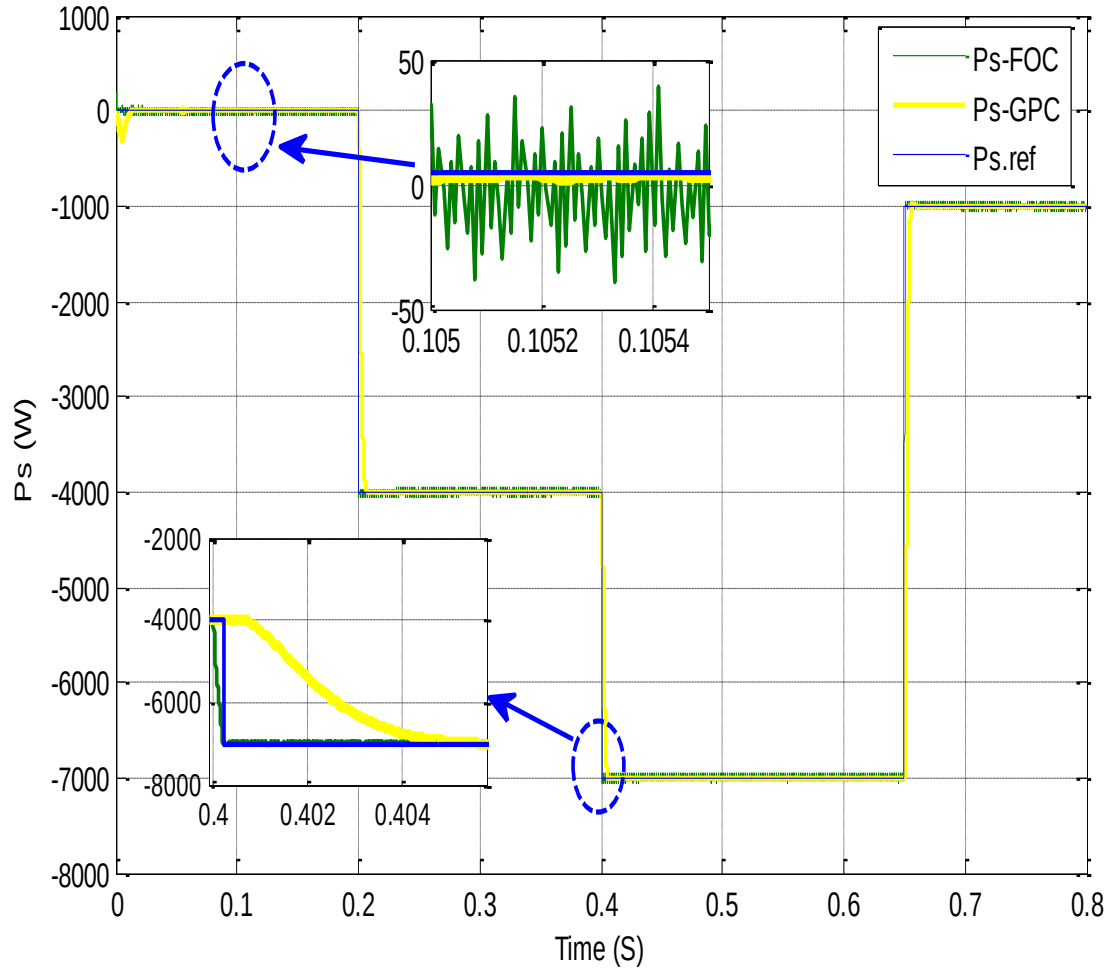

Figure 7. DFIG active power integrated to grid for the both control strategies FOC and GPC under wind variation.

Figure 7 shows the DFIG active power integrated to grid for the both control strategies FOC and GPC under wind variation, and Figure 8 shows the DFIG reactive power integrated to grid for the both control strategies FOC and GPC under wind variation. According to the simulation result, in transient-state, the FOC method quickly reaches the reference compared to the GPC for both powers, unlike in steady-state.

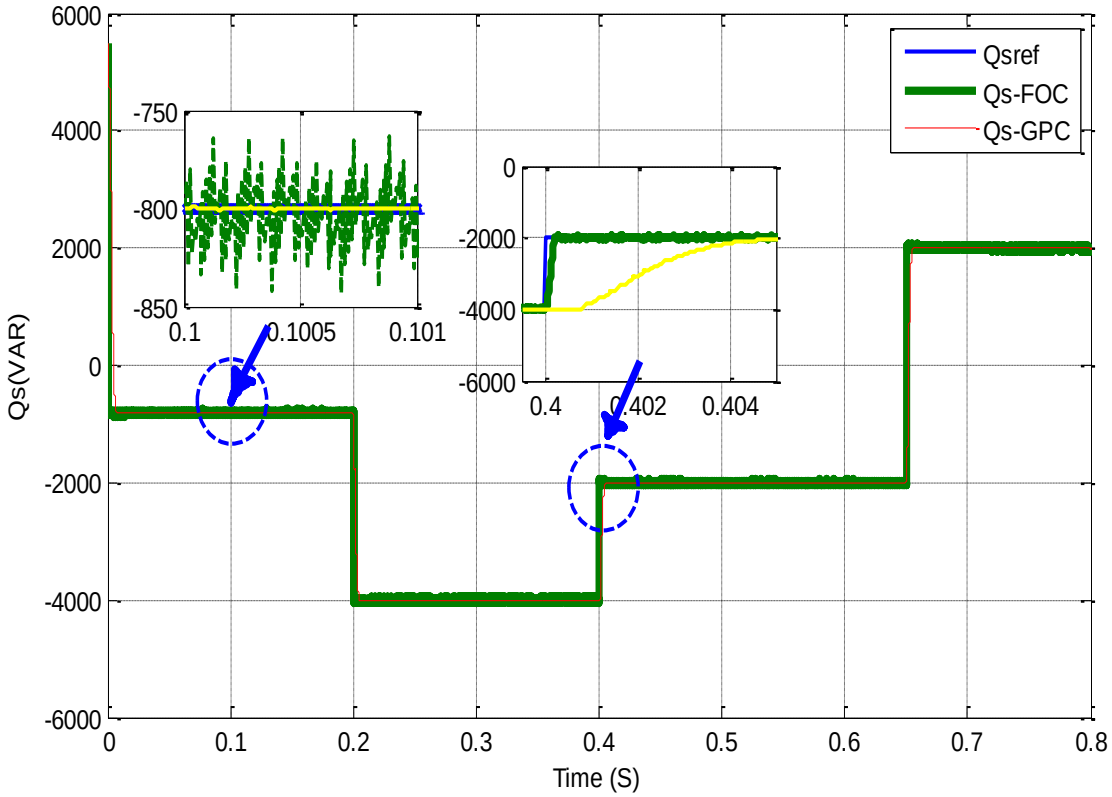

Figure 8. DFIG reactive power integrated to grid for the both control strategies FOC and GPC under wind variation.

Conclusion

In this study, we looked at a generalized predictive control method used with DFIG. We first provided the vector control based on flux orientation, then we used the Park model to represent the DFIG. Perfect understanding of the model of the system that needs to be adjusted is necessary for the vector control of the DFIG using a traditional adjustment method like PI regulators. This method produces control laws whose effectiveness is highly correlated with the accuracy of the dynamic model that characterizes the system's behavior. Since they directly affect the control computation, modelling errors or system parametric fluctuations can worsen the adjustment performance. Next, we looked at DFIG-specific generalized predictive control. According to the simulation results, performance was largely satisfactory throughout the load intervention and setpoint inversion. We produced power controls that are immune to variations in the parameters and demonstrated that adjusting the regulator's design and adjustment parameters can enhance the control process's output performance. As a result, the way the system behaves is determined by these factors. However, determining the ideal values for these factors is not always simple.

Scientific Ethics Declaration

The authors declare that the scientific ethical and legal responsibility of this article published in EPSTEM journal belongs to the authors.

Acknowledgements or Notes

* This article was presented as an oral presentation at the International Conference on Technology, Engineering and Science (www.icontes.net) held in Antalya/Turkey on November 16-19, 2023.

*The authors would like to thank the MESRS (Ministère de l'enseignement supérieur et de la recherche scientifique), Algeria. We also would like to thank the University of Bouira and Bouira and Hassiba Benbouali de Chlef for their assistance.

References

Bektache, A., & Boukhezzar, B. (2018). Nonlinear predictive control of a DFIG-based wind turbine for power capture optimization. *International Journal of Electrical Power & Energy Systems*, *101*, 92–102.

Cheng, M., & Zhu, Y. (2014). The state of the art of wind energy conversion systems and technologies: A review. *Energy Conversion and Management*, *88*(2), 332–347.

Clarke, D. W., Mohtadi, C., & Tuffs, P. S. (1987a). Generalized predictive control—Part I. The basic algorithm. *Automatica*, *23*(2), 137–148.

Clarke, D. W., Mohtadi, C., & Tuffs, P. S. (1987b). Generalized predictive control—Part II. Extensions and interpretations. *Automatica*, *23*(2), 149–160.

Dani, A., Mekrini, Z., El Mrabet, M., & Boulaala, M. (2023). *A review of different structures generators and control strategies applied to the wind turbine* (pp. 190–199). Cham: Springer Nature Switzerland.

Davanipour, M., & Asadipooya, H. (2017). Nonlinear model predictive control based on fuzzy wavelet neural network and chaos optimization. *Turkish Journal of Electrical Engineering and Computer Sciences*, *25*(5), 3569–3577.

Domański, P. D. (2020). Performance assessment of predictive control—A survey. *Algorithms*, *13*(4), 97.

Hansen, A. D. (2023). Wind turbine technologies. In *Wind Energy Engineering* (pp. 89–98). Elsevier.

Mellah, H., & Hemsas, K. E. (2012). Design and simulation analysis of outer stator inner rotor DFIG by 2D and 3D finite element methods. *International Journal of Electrical Engineering and Technology (IJEET)*, *3*(2), 457–470.

Mellah, H., & Hemsas, K. E. (2013). Simulations analysis with comparative study of a PMSG performances for small WT application by FEM. *International Journal of Energy Engineering*, *3*(2), 55–64.

Omac, Z., & Erdem, I. (2023). Rotor field-oriented control of doubly fed induction generator in wind energy conversion system. *Gazi University Journal of Science*, *36*(3), 1217–1229.

Pradhan, P. P., Subudhi, B., & Ghosh, A. (2022). A new optimal model predictive control scheme for a wind energy conversion system. *International Journal of Numerical Modelling: Electronic Networks, Devices and Fields*, *35*(3), e2976.

Prasad, R. M., & Mulla, M. A. (2020). Mathematical modeling and position-sensorless algorithm for stator-side field-oriented control of rotor-tied DFIG in rotor flux reference frame. *IEEE Transactions on Energy Conversion*, *35*(2), 631-639.

Rahuna, D., Erwandi, Kasharjanto, A., Suyanto, E. M., & Mintarso, C. S. J. (2023). Experimental study on hydrodynamic aspects of turbine which convert hydrokinetic and potential coastal wave energy. *IOP Conference Series: Earth and Environmental Science*, *1166*(1).

Rodrigues, L. L., Vilcanqui, O. A. C., Conde D., E. R., Guerero, J. M., & Sguarezi Filho, A. J. (2020). Generalized Predictive Control applied to the DFIG power control using state-space model and voltage constraints. *Electric Power Systems Research*, *182*(9), 106227.

Shiravani, F., Cortajarena, J. A., Alkorta, P., & Barambones, O. (2022). Generalized predictive control scheme for a wind turbine system. *Sustainability*, *14*(14), 8865.

Silva, R. N., Nunes, M. M., Oliveira, F. L., Oliveira, T. F., Brasil, A. C. P., & Pinto, M. S. S. (2023). Dynamical analysis of a novel hybrid oceanic tidal-wave energy converter system. *Energy*, *263*, 125933.

Simões, M. G., Farret, F. A., & Blaabjerg, F. (2015). Small wind energy systems. *Electric Power Components and Systems*, *43*(12), 1388–1405.

Tola, O. J., Tsado, J., Agbachıi E. O., Umoh, E. A., & Enesi, Y. A. (2022). Modeling and simulation of marine current energy conversion system with six-phase permanent magnet synchronous generator. *The Eurasia Proceedings of Science Technology Engineering and Mathematics*, *21*, 1–10.

Vo, T.M.N., Wang, C.N., Yang, F.C. & Nguyen, V.T.T. (2023). Renewal energy efficiency assessment. *The Eurasia Proceedings of Science, Technology, Engineering & Mathematics (EPSTEM), 23*, 556-563.

Author Information

Hacene Mellah
Bouira university
Department of Electrical Engineering, University of Bouira, Bouira, Algeria
Address of Institution or University
Contact e-mail: *has.mel@gmail.com*

Hamza Sahraoui
Department of Electrical Engineering, University of Hassiba Benbouali de Chlef, Chlef, Algérie.

Amar Maafa
Bouira University
Department of Electrical Engineering, University of Bouira, Bouira, Algeria

Abdelghani Yahiou
Bouira University
Department of Electrical Engineering, University of Bouira, Bouira, Algeria
Contact e-mail:

Houria Smail
Bouira University
Department of Electrical Engineering, University of Bouira, Bouira, Algeria

To cite this article:

Mellah, H., Maafa, A., Sahraoui, H., Yahiou, A., & Smail, H. (2023). Generalized predictive control of the active and reactive stator powers of the DFIG for wind energy generation. *The Eurasia Proceedings of Science, Technology, Engineering & Mathematics (EPSTEM), 26*, 295-305.

The Eurasia Proceedings of Science, Technology, Engineering & Mathematics (EPSTEM)
ISSN: 2602-3199

The Eurasia Proceedings of Science, Technology, Engineering & Mathematics (EPSTEM), 2023

Volume 26, Pages 306-316

IConTES 2023: International Conference on Technology, Engineering and Science

Comparative Non-Destructive Investigations of the Effects of Structural Changes After Heat Treatment of Carbon Steel Samples by Magnetic Noise and Vibration Methods

Yonka Ivanova
Sofia University

Abstract: The microstructure of some components that work for a long time at high temperatures changes, which leads to a reduction in their life cycle. Traditionally, the study of the resulting structures is carried out by mechanical tests and metallographic analysis. The application of non-destructive methods increases the possibilities to monitor the quality of the elements and to prevent destruction. The aim of the study is to detect changes in the microstructure after different heat treatment and ageing heating of materials via magnetic noise and vibration methods. To realize the goal, samples of high-quality medium carbon steel were prepared through targeted heat treatments, quenching and tempering at different temperatures, as well as ageing heating at temperatures of 700 ^{o} C for up to 16 hours by vibration and magnetic noise method. The natural frequencies and damping properties of forced longitudinal vibrations of various heat treated steel specimens were obtained and analyzed. Using magnetic noise method, the following parameters were obtained and analyzed: root mean square voltage (RMS), energy and envelope parameters of magnetic noise signals. The comparative application of several non-destructive methods increases the knowledge of methods and materials and makes it possible to establish their sensitivity in studying microstructural characteristics.

Keywords: Comparative non-destructive investigations, Magnetic noise method, Vibration method, Carbon steel, Microstructure change

Introduction

Changes in steel microstructures upon heating and cooling can affect their macroscopic properties. The processes taking place during cooling of austenite affect the type, shape, size of the obtained phases in the heat treatment process. In addition, construction materials in the industry, working under risky conditions and prolonged overheating, deteriorate their properties due to degradation of their microstructure. As a result, the mechanical properties, strength, yield strength and modulus of elasticity and hardness change (Hertzberg, 1996; Okrajni, 2010; Dobrzański et al., 2007). Many studies have been devoted to the influence of microstructure on the mechanical properties of a metal (Zieliński et al., 2017; Ghorbanhossein et al., 2020; Bhardwaj et al.,2020).

The present work presents an investigation of the influence of quenching, tempering and ageing heat treatments on the microstructure of carbon steel samples, as well as changes in their vibrational (resonance frequencies and damping coefficient) and magnetic properties (the activity and magnitude of Barkhausen magnetic noises). Therefore, in the introduction, a brief review of the scientific results in the literature regarding the effect of the materials microstructure on its vibrational and magnetic properties is made.

In physical metallurgy, studies on damping properties provide a better knowledge of the microstructure, micro or macro defects, as well as phase changes that are induced by heat treatment. Luca et al. (2011) presented an investigation of the internal friction and resonance frequencies after quenching of medium carbon ferrite-pearlite steel. After quenching, a decrease in resonance frequencies and modulus of elasticity in longitudinal oscillations

was recorded. Hamisi et al. (2018) investigated the effects of ageing on the mechanical and vibrational properties of SA516 carbide steels. The increasing the duration of heating caused degradation of the mechanical properties of the steel specimens. A decrease in their natural frequencies and an increase in damping properties were found. The effects of ageing heat treatment on the vibrational properties of a Mg-6Al-1Zn alloy were examined (Zhang et al., 1993; El-Morsy et al., 2015).

The results of an experimental and numerical study of the microstructural changes on the vibrational properties of CK35 steel was presented (Amirian et al., 2022), (Yazani et al., 2021). Experimental results indicated that the dispersion of spheroidized carbides in the ferritic matrix could increase natural frequencies and damping loss factors (Amirian, et al., 2022; Ahmadpar et al., 2021). Ageing heat treatment in the ferrite structure induces weak changes in the values of natural frequencies Yazani et al., 2021).

The magnetic noise method is applied in the study of the microstructure of ferromagnetic materials. It is based on the phenomenon that occurs when a ferromagnetic material is magnetized (Manh et al., 2020). The structure of a ferromagnetic material consists of magnetic domains separated by domain walls (Manh et al., 2020; Capo-Sanchez et al., 2004). In the absence of a magnetic field, the domains are randomly oriented. When a magnetic field is applied, the magnetic domains align in the direction of applied field by moving their domain walls (Saquet et al., 1999; Ivanova, 2022).

The time-varying magnetic field creates discontinuous magnetization changes in ferromagnetic samples, leading to the generation of magnetic Barkhausen noise (MBN) . These flux changes in the material induce a voltage in a receiver coil mounted near the Barkhausen events (Samimi et al., 2016). MBN technique had been applied for microstructure characterization such as grain boundaries, other phases, inclusions (Manh et al., 2020). The magnetic noise method is sensitive to carbon content (Capo-Sanchez et al., 2004; Samimi et al., 2016) , crystal size (Moorthy et al., 1998; Saquet et al., 1999) and different microstructures such as: ferrite, pearlite and martensite (Moorthy et al., 1998; Ivanova, 2022; Davut et al., 2009; Gur et al., 2007; Zerovnik et al., 2014).

From the overview presented above, it can be seen that the changes in metal structures may influence their mechanical, magnetic and vibration properties. Combining two or more physical research methods complements material knowledge, which is extremely important for equipment operating in risky conditions. This study is a continuation of experiments on medium carbon steel specimens after quenching and tempering (Ivanova, 2022), where using only one non-destructive method results are presented. The current work extends the study of the same type of steel subjected to ageing heat treatment at 700 degrees for 8 and 16 hours. The influence of microstructures changes after quenching, tempering and ageing on the vibration properties and magnetic properties is investigated.

This paper is organized as follows. After the introduction, which makes a brief overview of the scientific achievements on the sensitivity of the vibrational and magnetic noise methods for detecting the microstructural changes during heating, follows the section "Experimental procedure. Materials and methods". The subsection "Materials" describes the steel samples, as well as the preparation for conducting the heat treatments. The subsection "Methods" consists of two parts. The first part describes the basic concepts of vibration method through forced longitudinal vibrations. In the second part, the equipment for magnetic noise research is presented. The results of the research conducted by the two non-destructive methods are followed by a discussion and a conclusion that notes future directions in our research.

Experimental Procedure, Materials, Methods

Materials

The material used in this study is a ferrite-pearlite steel. The chemical composition of the steel was: C 0.34%, Si- 0.37%, Mn - 0.7%, P < 0.035%, Ni < 0.25%, Cr < 0.25%, S < 0.04%, Cu < 0.25%. Eighteen cylindrical steel samples with a diameter of 5.5 mm and a length of 100 mm were prepared and divided into six groups. Three groups were subjected to heat treatment, which consisted of quenching and subsequent tempering at the following temperatures: 150°C /group 2/, 250°C /group 3/, 400°C /group 4/.

The samples from groups 6 and 7 were subjected to ageing heating (spheroidization) at a temperature of 700 degrees Celsius for 8 and 16 hours (Alza, 2020; Harisha, 2018). The heat treatment modes are presented in column 2 of Table 1.

Table 1. Heat treatments of the investigated steel samples

Steel specimens	Heat treatment	Microstructure	Vickers hardness HV
Group 1	Non-heat-treated	Ferrite and pearlite	320
Group 2	Quenching T = 850°C Tempering T = 150°C	Tempered martensite	750
Group 3	Quenching T = 850°C Tempering T = 250°C	Tempered martensite	620
Group 4	Quenching T = 850°C Tempering T = 250°C	Tempered troostite	400
Group 5	Prolonged heat treatment T = 700°C Duration 8 hours	Ferrite and cementite	200
Group 6	Prolonged treatment T = 700°C Duration 16 hours	Ferrite and cementite	160

Methods

Vibration Method through Forced Longitudinal Vibrations

In the present work, experimental modal analysis by forced longitudinal vibrations is used to investigate the internal friction and dynamic characteristics of the samples. The standing waves are formed in the specimens as the result of longitudinal vibration of the sample. Generally, sound velocity in a specimen could be determined from Eq.1 (Chevalier, 2010).

$$\lambda = C/f \tag{1}$$

where C is sound velocity in a specimen, and f is resonance frequency of the first mode of vibration. The wave length λ can be calculated from Eq. 2 :

$$\lambda = \frac{2L}{n} \tag{2}$$

Where L is the length of specimen and n is the number of resonance mode. According to the positions of the node and the two antinodes corresponding to the first mode of vibration, the wave length was equal to the twice of the specimen length. Young's modulus can be obtained from the longitudinal mode vibration (Lord, 2007) . Knowing the values of Young's modulus (E) and geometric dimensions of the rod sample, we can determine the first fundamental frequency (f_1).

$$f_l = \sqrt{\frac{\pi n^2 r^2 E}{4LmK}} \tag{3}$$

Where m and r are the mass and the radius of rod, n is the mode of vibration (n = 1 for the fundamental). K is a correction factor depending on Poisson's ratio (ν) and diameter-length ratio of the rod (Lord, 2007).

$$\frac{1}{K} = 1 - \frac{\pi^2 \nu^2 r^2}{2L^2} \tag{4}$$

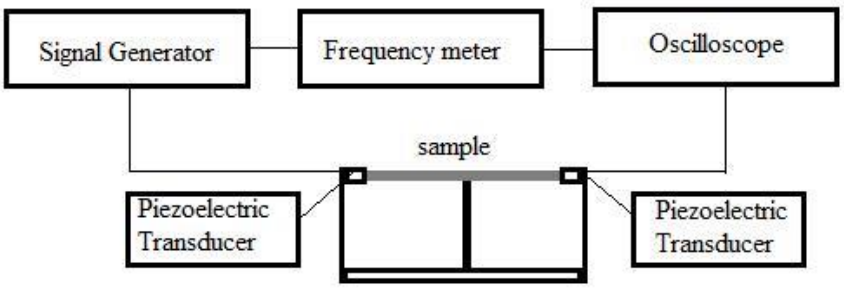

Figure 1. Block scheme of the setup for determining internal friction and damping ratio

when $2r/\lambda = nr/L >> 1$ (Lord, 2007). Figure 1 presents the setup that is applied to investigate the vibration properties of the prepared heat-treated steel samples by longitudinal forced vibration. The specimen was supported in the middle of its length between the excitation and receiving piezoelectric transducers. One transducer excited a sinusoidal vibration at one end of the specimen and the other receiving transducer recorded the response. The resonant frequency of the samples was detected with an oscilloscope and evaluated with a digital frequency meter.

The half-power bandwidth method was used to measure damping loss factor, damping ratio, internal friction and the logarithmic decrement (Hamisi et al., 2018; Yazani, 2021; Maringer, 1966).
The damping loss factor η can be defined as (Yazani, 2021):

$$\eta = \frac{W_2 - W_1}{W_r} \tag{5}$$

Where w_r is the frequency at which the peak of the curve is obtained and w_1 and w_2 are the two frequencies, for which the frequency response is $1/\sqrt{2}$ times the one at resonance. The damping ratio ξ is given by Yazani (2021) and Maringer (1966).

$$\xi = \frac{\eta}{2} \tag{6}$$

The internal friction (Q^{-1}) is obtained using bandwidth ($\Delta w = w_2 - w_1$) and is in the form of Eq. (7) (Hamisi et al., 2018; Yazani, 2021; Maringer, 1966).

$$Q^{-1} = \frac{W_2 - W_1}{W_r} \tag{7}$$

For small damping ($\xi \ll 1$), the logarithmic decrement δ is defined as (Maringer, 1966):

$$\delta = \pi Q^{-1} \tag{8}$$

Magnetic Noise Method Measurements

Acquisition of the raw MBN signal was performed by a MULTITEST-MC 04 device, given in detail in (Velev et al., 2009; Ivanova, 2022). The apparatus consists of a magnetizing module, a converter for recording magnetic noise signals and measuring the magnetic noise voltage, and a signal amplifier with several bandpass filters. A sinusoidal magnetization with a frequency of 76 Hz was applied. A cyclic sinusoidal field was induced in the sample at different magnetizing currents. Barkhausen signals were visualized and recorded using a VT DSO 2810 digital oscilloscope at a sampling rate of 100 MSPS and Multi-Instruments Pro 3.9 data acquisition software.

The software can extracted the RMS value of the Barkhausen noise (V_{RMS}) as well as the peak value (Vp). The MBN envelopes were reconstructed on based on the filtered MBN signals. The position of peak of MBN envelopes of was also analyzed. The time of appearance of MBN was calculated from envelope peak relative to the zero value of the magnetizing field. All MBN parameters were obtained by averaging sixteen consecutive pulses (eight hysteresis cycles).

Experimental Procedure

The prepared steel specimens were subjected to the heat treatments described in Table 1. After the heat treatment, the samples were cleaned of the oxide layer by surface treatment and specified in length and diameter.

Since the natural frequencies and damping properties are to be compared and analyzed, the samples should have the same dimensions and weights. The length (L=100 mm) and diameter (d=5 mm) of the samples were measured with an accuracy of 0.02 mm. After the preparation of the samples, the first resonance frequency of longitudinal oscillations was calculated. Two specimens from each group given in Table 1 are subjected to non-destructive evaluation by vibration analysis and Barkhausen magnetic noise testing.

Results and Discussion

Results of Performed Heat Treatments

The microstructure of investigated samples is shown in figure 2. The initial ferrite-pearlite structure before heat treatment is given in figure 2a. The martensitic structure obtained after quenching and low-temperature tempering T=150 ^{o}C can be observed in figure 2 b. Changes in the structure after these heat treatments can be explained by the decomposition of martensite and the beginning of the formation of iron carbides (Totten, 2006).

Martensitic structure after quenching and tempering at T=250 ^{o} C is given in figure 2c. The processes taking place during heating in the temperature range of 200-250 ^{o} C are mainly explained by the breakdown of residual austenite, as a result of which the internal stresses in the structure and hardness are reduced (Totten, 2006; (Ivanova, 2022).

The microstructure after tempering at T=350^{o} C is a finely dispersed ferrite-cementite mixture (tempered troostite) and is shown in figure 2 d. During tempering at and above 500 ^{o}C, the formed carbides coagulate and as a result a dispersed ferrite-cementite mixture is fixed, which is called tempered sorbite (figure 2e), (Ivanova, 2022). After applying a prolonged heat treatment at 700^{o}C, the pearlite regions are decomposed and the structure consists of ferrite and cementite, which are distributed in the form of irregular islands (Harisha, 2018). Hardness dropped significantly to 200-160 HV.

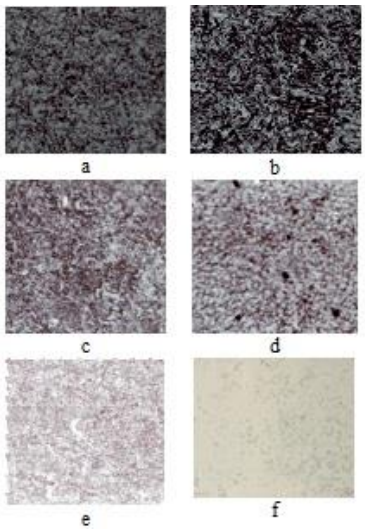

Figure 2. Microstructure of the tested samples: initial ferrite and pearlite microstructure before heat treatment (a), martensitic structure after quenching and low-temperature tempering –Group 2 (b), martensitic structure (quenching and tempering at T = 250°C)-Group 3 (c), tempered troostite – Group 4 (d), tempered sorbite - structure after quenching and tempering at T = 600°C (e); heat treated sample at 700 °C for 8 hours.

Results of the Vibration Tests

As mentioned before, two samples of each heat treatment were prepared for the vibration test. It should be noted that the samples are clamped midway between the emitting and receiving piezoelectric transducers. The emitter excites sinusoidal oscillations at one end of the sample. By changing the frequency of the sine wave through a sweep generator, the occurrence of system resonance was detected and recorded by an oscilloscope. The tests on each specimen were repeated three times and the results for the resonance frequencies were averaged.

Figure 3 shows the resulting resonance and the first resonant frequency obtained from a non-heat treated steel specimen. The vibration test results are summarized in Table 2, where are listed the values of the resonant frequencies and the widths of the resonant curves. Column 5 in Table 2 gives the relative change in the first resonance frequency compared to the initial state. Table 3 shows the experimental damping coefficients, calculated using Eqs. (6-8).

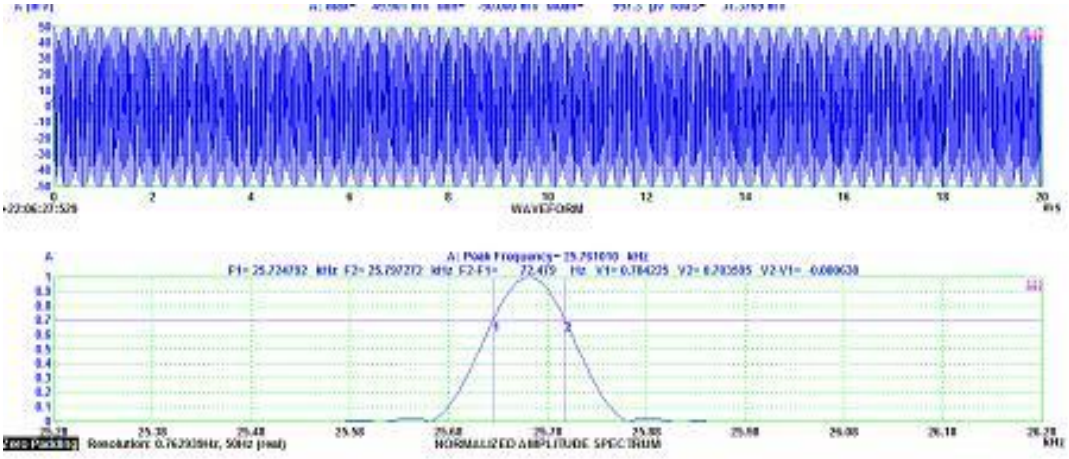

Figure 3. Results from vibration test for non-heated steel sample.

Table 2. First natural frequency of investigated steel samples

Group samples	f_r,kHz	f_1, kHz	f_2,kHz	Difference $\frac{f_{r1}-f_{ri}}{f_{r1}}$,%
1	25.761	25.724	25.797	0
2	25.437	25.400	25.474	-1.26
3	25.610	25.574	25.646	-0.59
4	25.791	25.754	25.827	0.12
5	25.810	25.764	25.837	0.19
6	25.853	25.817	25.890	0.36

According to the first natural frequency in Table 2, it is observed that after the quenching and tempering process at temperatures of 150 ^{o}C and 250 ^{o}C (groups 2 and 3), the natural frequencies are reduced compared to the untreated samples. The relative difference is the largest in group 2 and reaches 1.26%. This is probably caused by the state of internal stresses created during quenching and confirms the results in (Luca et al., 2011). Martensite is characterized by a high density of dislocations and high internal stresses. This also affects the internal friction. The logarithmic decrement increases on average by about 2.6% after quenching compared to the initial state.

Table 3. Damping coefficients of samples

Group samples	Damping ratio ξ (x10^{-3})	Internal friction Q^{-1}(x10^{-3})	Log. decrement δ(x10^{-3})
1	1.414	2.829	8.882
2	1.451	2.902	9.112
3	1.408	2.815	8.840
4	1.412	2.820	8.850
5	1.415	2.829	8.884
6	1.417	2.833	8.896

In the samples subjected to prolonged heating at 700^{o} C for 8 and 16 hours, a slight increase in natural frequencies was observed respectively 0.2% and 0.36%, compared to the initial state. According to (Yazani, 2021), this is due to the deposition of carbides during the heating of 8 h and 16 h duration. As a result of the heat treatment, the pearlite is destroyed and the structure of iron carbide layer is heterogeneously deposited on the surfaces and grows (Ahmadpar et al., 2021). The microstructure becomes softer and as a result the internal friction, the damping coefficient increases slightly (Yazani, 2021; Ahmadpar et al., 2021).

Results of MBN measurements

Figure 4 shows a part of recordings during magnetization and appearing magnetic noises at a magnetizing current of 200 mA. Depending on the various microstructures, different values of peaks (Vp) and shapes of MBN signals can be observed. The maximum amplitude and RMS values of the magnetic noises depend on the magnitude of the jumps of the magnetic domains obtained at different magnetizing currents (Ivanova, 2022).

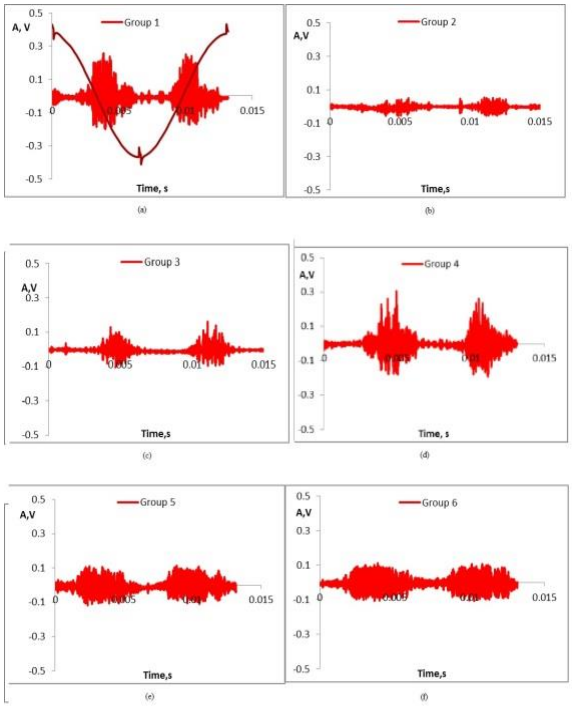

Figure 4. Magnetic noise signals at a magnetizing current of 200 mA: specimens group 1 (a), group 2 (b), group 3(c), group 4 (d), group 5 (e), group 6 (f)

Figure 5a presents the variation of RMS values of the magnetic noise on the magnetizing current *In* for the studied steel samples. The values are well distinguishable. As the magnetizing current increases, the RMS value increases. The samples subjected to quenching and low-temperature tempering, which have a structure of tempered martensite, show the lowest RMS values. In the remaining groups of samples (3, 4), an increase in the root mean square values is noticeable. This can be explained by the type of microstructures obtained: tempered martensite and troostite.

According to the research, the RMS values of the samples after prolonged heating are close to those of group 4. Figure 5 b shows the relative change of the studied parameter ($|\Delta V_{RMS}| = (V_{RMS,i} - V_{RMS,1})/V_{RMS,1}$, compared to the original untreated group 1. A very good sensitivity of the results was found at a magnetizing current of 200 mA. The relative variation in $|\Delta V_{RMS}|$ after quenching and low-temperature tempering is 50%, and after ageing treatments is from 25 to 33%.

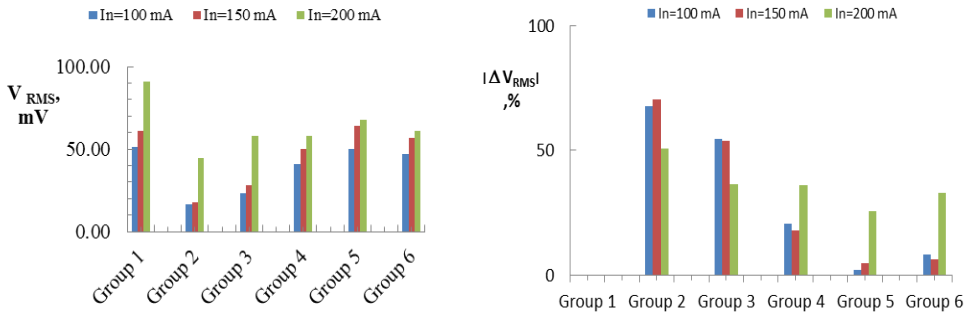

a) b)

Figure 5. Dependence of RMS parameter on the magnetizing current

In the case of half a cycle of magnetization, the sample is demagnetized and then magnetized in the opposite direction. This activates the movement of the domain walls, which overcome the obstacles posed by the different microstructural phases. The nature of the MBN signals is a consequence of the nonuniform jumps of the domain walls during the remagnetization of the ferromagnetic material. This process depends on the microstructural features, different phases, boundaries between crystallites, the presence, shape and size of carbide inclusions, etc. (Davut et al., 2009; Gur et al., 2007; Zerovnik et al., 2014). Figure 6 plots MBN

envelopes from studied samples at three values of the magnetizing current, respectively 100 mA (a), 150 mA (b) and 200 mA (c).

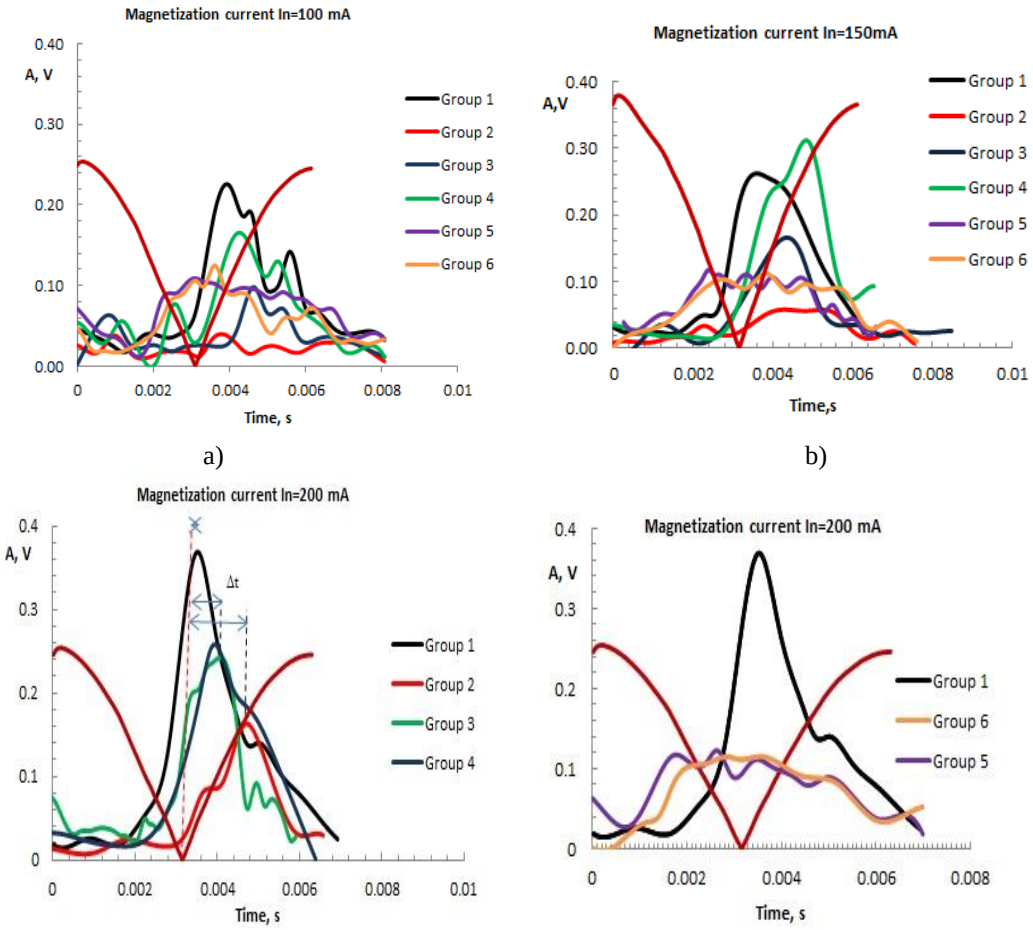

Figure 6. MBN envelopes for investigated steel samples: a) Magnetization current *In* = 100 mA; b) Magnetization current *In* = 150 mA; c) Magnetization current *In* = 200 mA; d) Results for groups 5 and 6 at *In* = 200 mA

At all three values of the magnetizing current for the samples of groups 2, 3 and 4, the following can be observed: i) different peak values; ii) shift of the MBN peak at zero value of the magnetizing field; iii) difference in MBN envelope shapes. In the tempered martensitic structures (group 2), the peak value is small and MBN envelope is wider. In the transition from tempered martensite with high hardness to a finer ferrite-pearlite structure such as troostite, an increase in the peak values, a sharpening of the MBN envelop is observed. The MBN envelopes for the samples subjected to ageing heating for 8 and 16 h are broadest and without pronounced peak values (Figure 6d).

Table 4. Parameters of MBN signals for different heat treated samples

Group samples	MaxMBN (Vp),V	Shift of MBN peak, Δt,s	Normalized MBN energy
Group 1	0.37	0.0003	1
Group 2	0.16	0.0015	0.20
Group 3	0.26	0.0007	0.58
Group 4	0.24	0.0008	0.48
Group 5	0.12	-	0.29
Group 6	0.12	-	0.27

To estimate the MBN in samples with different types of microstructure, the energy parameter can also be used. It is defined as the time integral of the MBN signal squared over the voltage. Table 4 gives parameters that characterize magnetic noise signals , which are: the peak height, the shift in the peak position of MBN envelope

($\Delta\ t$) and the MBN energy. The results for MBN energy are normalized to the energy of the unheated samples. The changes of MBN parameters when changing the heat treatment mode and microstructure are given in figures 7a, b and c.

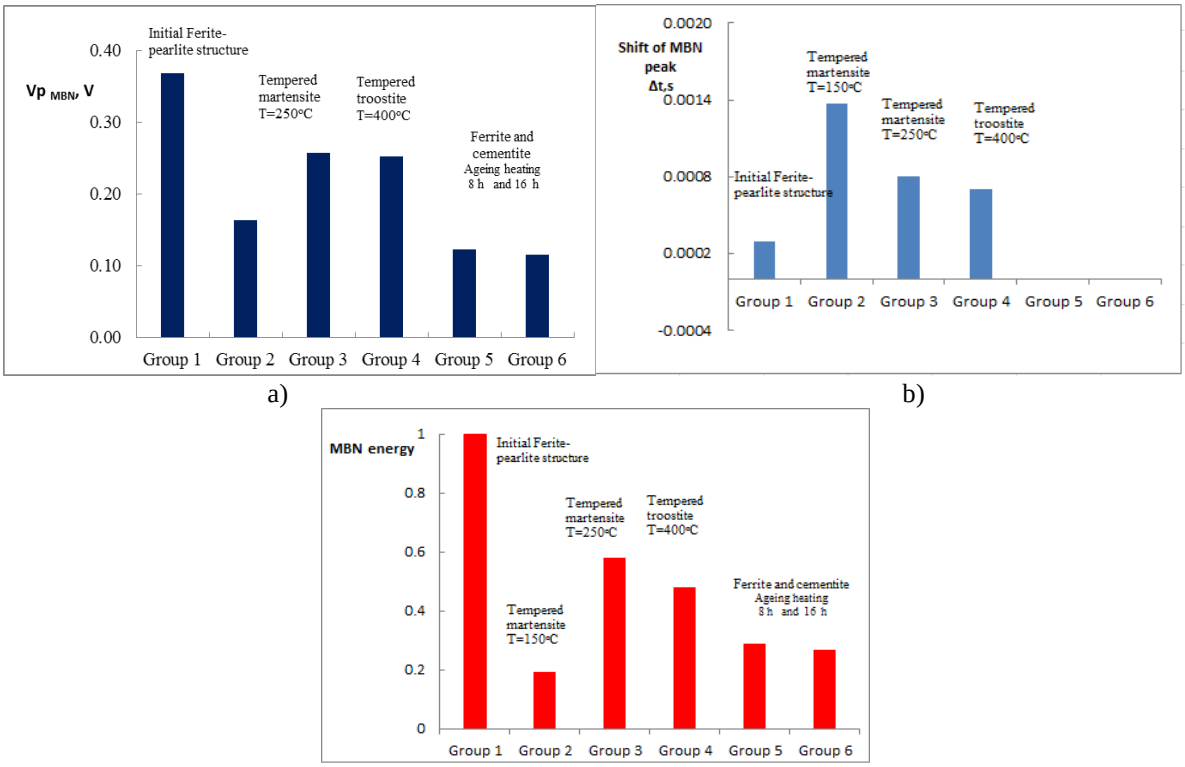

Figure 7. Parameters of MBN signals for different heat treated samples at magnetization current 200 mA: a) MBN envelope peak height; b) Shift of MBN peak; c) MBN energy

According to the literatures (Ivanova, 2022), (Davut et al., 2009), (Zerovnik et al., 2014) when magnetizing martensite, very small domains are created due to the characteristics of martensite, which has high internal stresses. Therefore, for movement of the domains, a larger value of the magnetizing field is required. From figure 7 a it can be seen that the resulting peak value of the magnetic noise is smaller and is at relatively larger values of the magnetizing current. The energy of MBN signal is the smallest, as can be noted in figure 7c. As the martensitic microstructure changes to a finer ferrite-pearlite structure such as troostite, remagnetization becomes easier. The amplitude of the MBN signal increases and the energy decreases, as can be noted in figures 7a and 7c. In the figure 7b, one can see the differences in the time delays of the samples in different states. The time delay is measured from the highest point of the envelope to the sinusoid of the magnetizing current. For specimens with higher hardness, a longer time delay is obtained. After quenching and tempering, the time of occurrence of magnetic noise increases.

The peak values of the MBN envelopes of groups 5 and 6 heated at 700 degrees for 8 and 16 hours are the smallest and are approximately 0.1 V. The MBN envelopes are the widest and very different from the others for groups 1 to 4. The energy is almost 3 times less compared to the energy of the untreated group. These results are probably due to the degradation of the microstructure, as well as the decarburization of the surface layer of the samples as a result of the prolonged heat treatment.

Conclusion

As a result of the conducted research, the sensitivity of vibration and magnetic noise methods to the microstructural changes of medium carbon steel after various types of heat treatments was established. Some vibration and magnetic properties of steel samples after quenching and tempering were obtained. The microstructural changes after ageing treatment at 700 ^{o}C for 8 and 16 hours were also investigated. The vibration method is less sensitive to microstructure changes than the magnetic noise method. After quenching and tempering, the first resonance frequency was found to increase by about 1%, and the internal friction and

logarithmic decrement by almost 2.6%. The prolonged heat treatment causes a slight increase in resonance frequency and damping properties.

In the magnetic noise method study, various parameters such as RMS and parameters of BMN envelopes were used to characterize the microstructure after quenching and tempering and ageing. The method is very sensitive to changes in the microstructure. The relative change in RMS value after quenching and low tempering is 50%. The method is also sensitive to structural changes after prolonged heat treatments. The change in RMS value is about 30%. A multiparameter approach of MBN signals was used for analysis. It was found that with the combination of parameters: MBN envelope peak height, peak shift and signal energy, the different microstructures can be quality characterized and recognized. The use of the two different physically based non-destructive methods complements the knowledge of the materials and allows an application of the methods according to their sensitivity.

Recommendations

The presented research can provide new knowledge to students and engineers to put into practice non-destructive evaluation of construction materials.

Scientific Ethics Declaration

The author declares that the scientific ethical and legal responsibility of this article published in EPSTEM journal belongs to the author.

Acknowledgements or Notes

* This article was presented as a poster presentation at the International Conference on Technology, Engineering and Science (www.icontes.net) held in Antalya/Turkey on November 16-19, 2023.

* This work has been accomplished with the financial support by the Grant No BG05M2OP001-1.002-0011-C02 financed by the Science and Education for Smart Growth Operational Program (2014-2020) and co-financed by the European Union through the European structural and Investment funds.

References

Alza, V. A. (2021). Spheroidizing in steels: Processes, mechanisms, kinetic and microstructure - A review. *IOSR Journal of Mechanical and Civil Engineering*, *18*(3), 63-81.

Amirian, A., Torshizi, S. E. M., & Dibajian, S.H. (2022). Experimental and numerical investigation of the effect of microstructural changes on the vibrational characteristics of CK35 steel. Proceedings of the *Institution of Mechanical Engineers, Part C: Journal of Mechanical Engineering Science*, *236*(3), 1363-1376.

Bhardwaj, A., Gohil, N., Gupta, A. K., & Satheesh Kumar, S. S. (2020). An experimental investigation on the influence of elevated-temperature constrained groove pressing on the microstructure, mechanical properties and hardening behavior of Ti6Al4V alloy. *Materials Science and Engineering*, *802*(2), 140651.

Capo Sanchez, J., Perez Benitez, J. A., Padovese, L. A., & Serna Giraldo, C. (2004). Dependence of the magnetic Barkhausen emission with carbon content in commercial steels, *Journal of Materials Science, 39*(4), 1367-1370.

Chevalier, Y., & Tuoriter, J. V. (2010). *Mechanics of viscoelastic materials and wave dispersion*. *Longitudinal vibration of a rod*. St. Ouen, France: Wiley

Davut, K., & Gur, C.H. (2009). Monitoring the microstructural evolution in spheroidised steel by magnetic Barkhausen noise measurements. Proceedings from *7th International Conference on Barkhausen Noise and Micromagnetic Testing, ICBM-7*. Aachen, Germany.

Dobrzański, J., Krztoń, H., & Zieliński, A., (2007). Development of the precipitation processes in low-alloy Cr-Mo type steel for evolution of the material state after exceeding the assessed lifetime, *Journal of Achievements in Materials and Manufacturing Engineering*, *23*(2), 19-22.

El-Morsy, A.W., & Farahat, A. I. Z. (2015). Effect of aging treatment on the damping capacity and mechanical properties of Mg-6Al-1Zn alloy, *The Scientific World Journal*, 1-8.

Ghorbanhosseini, S., Fereshteh Saniee, F., & Sonboli, A. (2020). An experimental investigation on the influence of elevated-temperature constrained groove pressing on the microstructure, mechanical properties, anisotropy and texture of 2024 Al sheets, *Journal of Alloys and Compounds*, *817*, 152763.

Gur, C., & Cam, I. (2007). Comparison of magnetic Barkhausen Noise and ultrasonic velocity measurements for microstructure evaluation of SAE 1040 and SAE 4140 steels. *Materials Characterization*, *58*(5), 447-454.

Hamisi, M., & Torshizi, S. (2018). Experimental study of aging effect on mechanical and vibrational properties on carbon steel SA516. *Modares Mechanical Engineering*, *18*(7), 50-55.

Harisha, S. R. et al. (2018). Study on spheroidization and related heat treatments of medium carbon alloy steels. *MATEC Web of Conferences*, *144*(6), 1-10.

Hertzberg, R.W. (1996). *Deformation and fracture mechanics of engineering materials*. (4th ed.). Hoboken: John Wiley & Sons, Inc.

Ivanova, Y. (2022). Investigation of heat-treated steels using the magnetic noise method. *The International Scientific Journal. Machines. Technologies. Materials, 16*(4) ,138-141.

Lord, J.,D. ,Morrell, R. (2007). *Measurement good practice guide 98, Elastic modulus measument*, National Physical Laboratory.

Manh, T. L et al. (2020). *Barkhausen noise for non-destructive testing and materials characterization in low carbon steels*. Duxford: Elsevier

Maringer, R. E. (1966). *Damping capacity of materials* (pp.1-11*).* Ohio*:* Battelle Memorial Institute, Columbus Laboratories.

Moorthy, V., Vaidyanathan, S., Jayakumar, T., & Raj, B. (1998). On the influence of tempered microstructure on the magnetic Barkhausen emission in ferritic steels. *Philosophical Magazine A, 77*(6), 1499- 1514.

Okrajni, J. (2010). Life and operational safety of power systems and chemical plants. *The Journal of Achievements in Materials and Manufacturing Engineering, 43* (1), 38-63.

Samimi, A., Krause, T. T., & Clapham, L. (2016). Multi-parameter evaluation of magnetic Barkhausen Noise in carbon steel. *Journal of Nondestructive Evaluatio*n, *35*(3), 35-40.

Saquet, O., Chicois, J., & Vincent, A. (1999). Barkhausen noise from plain carbon steels: Analysis of the influence of microstructure. *Materials Science and Engineering: A , 269*(1–2), 73-82.

Totten, G. E. (2006). *Steel heat treatment handbook, metallurgy and technologies*. London: Taylor and Fransis Group LLC.

Velev, G., & Markovski, A. (2009). Investigation of the structure of ferro-magnetic materials using methodology based on Barkhausen effect. Proceedings from *7th International Conference on Barkhausen Noise and Micromagnetic Testing, ICBM-7.* Aachen, Germany.

Yazani, N. M. (2021). Experimental evaluation of the effects of structural changes on the vibration properties of CK35 steel. *Acta Mechanica et Automatica, 15 (2*), 53-57.

Zerovnik, P.l., Fefer, D., & Grum, J. (2014). Surface integrity characterization based on time-delay of the magnetic Barkhausen noise voltage signal. *Journal of Mechanicai Engineering, 60*(1), 21-28.

Zieliński, A., Golański, G., & Sroka, M. (2017). Influence of long-term ageing on the microstructure and mechanical properties of T24 steel. *Materials Science and Engineering: A, 682,* 664-672.

Author Information

Yonka Ivanova
Sofia University "St. Kliment Ohridski", Faculty of Physics, Bulgaria
Institute of Mechanics at Bulgarian Academy of Sciences, Sofia, 1113, Acad. G. Bontchev Str.,bl.4, Bulgaria
Contact e-mail: *yonivan@phys.uni-sofia.*

To cite this article:

Ivanova, Y.P. (2023). Comparative non-destructive investigations of the effects of structural changes after heat treatment of Carbon Steel Samples by Magnetic Noise and Vibration Methods. *The Eurasia Proceedings of Science, Technology, Engineering & Mathematics (EPSTEM), 26,* 306-316.

The Eurasia Proceedings of Science, Technology, Engineering & Mathematics (EPSTEM)
ISSN: 2602-3199

The Eurasia Proceedings of Science, Technology, Engineering & Mathematics (EPSTEM), 2023

Volume 26, 317-326

IConTES 2023: International Conference on Technology, Engineering and Science

Finite Element Modelling of Polypropylene Fibre Reinforced Concrete Beams Reinforced with Steel under Bending

Razan Haedar Al-Marahla
AlZaytoonah University of Jordan

Muhammad Kashif Shehzad
National Highways

Nour Hider Almarahlleh
Tafila Technical University

Abstract: Application of the fibre-reinforced concrete has manifested a wider acceptability over time for its contribution towards significantly improving the flexural performance of structural members. A lot of work has been done to understand the influence of fibres on the mechanical and structural behaviour of reinforced concrete. Towards this end, several researchers have experimentally investigated the residual flexural strength to characterize the fibre-reinforced concrete. The number of influencing parameters to be investigated through experiments is mostly limited because of the time and cost implications. Consequently, validation of the experimental investigations through analytical models and further utilizing these models to study the behaviour in greater detail is a viable option for researchers. As part of this work, an analytical investigation has been performed to investigate the performance of full-scale polypropylene fibre-reinforced concrete beams. The models have been validated through comparison with the observed performance during an experimental investigation where tests on twelve full-scale FRC beams were performed. Three-dimensional finite element models of the beams under 4-point loading were prepared and the post-cracking flexural performance of FRC beams has been investigated by varying the dosage of polypropylene fibres obtained from shredding medical face masks.

Keywords: Fibre reinforced polymers, Polypropylene, Residual flexural strength, Finite element, Constitutive model

Introduction

Various types of fibres used in concrete are known to have the ability to improve and modify the mechanical properties of a cementation matrix and the flexural toughness, as reported by experiments carried out previously by (Yoo et al., 2016; Xu et al., 2020; Al Marahla & Garcia-Taengua, 2021; Yousefi et al., 2022). Several researchers (Biolzi & Cattaneo, 2017; Fallah& Nematzadeh, 2017; Lee, 2017, Abbass et al., 2018, Jhatial et al., 2018, Belmokaddem et al., 2020) examined the influence of fibres on the residual flexural parameters considering different types of fibers, aspect ratio and volume fractions following the available standards (EN 14651, 2007a; ASTM C1609, 2012). Amin and Gilbert (2018) found in their study that the addition of steel fibers to concrete increased the tension carried by the concrete, as the fibers demonstrated the ability to transmit tensile stress across cracks while inhibiting the propagation of splitting cracks.

Fibres can substantially improve the post-cracking performance of structural members after the formation of the first crack, particularly in the steel fiber reinforced concrete, which can be used to replace conventional reinforcement partially or fully (Abbass et al., 2018). However, applications of non-steel fibres has mostly

- Selection and peer-review under responsibility of the Organizing Committee of the Conference

remained limited to restraining and controlling the plastic cracking. Biolzi and Cattaneo (2017) investigated the effect of steel fibres on the instantaneous deflection and confirmed that steel fibres improved the stiffness of RC beams, and consequently reduced the deflection.

Non-metallic fibres have lower tensile strength and modulus of elasticity but lower carbon footprint compared to steel fibres (Jhatial et al., 2022). However, research has focused on investigating the influence of steel fibres on the flexural behaviour of RC members and paid little attention to non-metallic fibres. Researchers have identified synthetic fibres (a form of non-metallic fibres) as a promising material due to their low environmental impact (Cadenazzi et al., 2020).

Modelling of structural members under bending using available software has focused on the plain concrete and steel FRC. The direct post-cracking tensile behavior of steel fibre reinforced concrete is utilized as a stress-crack opening response in the available guidelines. Finite-element computations model of FRC structural application is required to economize the experimental effort and to overcome the shortfalls in existing techniques for modeling and analyzing the flexural and post-cracking performance of non-metallic FRC elements with less time and effort. Therefore, this study investigates experimentally and numerically the influence of polypropylene fibres obtained from shredding medical face masks on the flexural performance of RC members.

In this study, an experimental campaign was conducted on FRC prismatic and full-scale beams. Normal strength concrete having a water to cement ratio of 0.45 was considered with varying the volume fraction of fibres obtained from face masks. Therefore, three groups of concrete mixes were categorized by the content of 0, 0.25% and 0.5%. Parametric study on full-scale beams under flexure has been carried out considering the experimental conditions. FE models using the constitutive models obtained experimentally for modelling the behaviour of materials using DIANA software are included.

Materials and Methodology

Background Experimental Program

In this research, the influance of the inclusion of randomly oriented polypropylene fibres in concrete was evaluated. Different concrete members containing varying volume fraction of fibre (0, 0.25%, and 0.5%) were investigated experimentally. Experimentl campain comprised nothced prisms produced and tested under three point bending test complying with EN 14651 standard, and full-scale conventionally reinforced beams tested under four point bending test. Residual flexural strength obtained experimentally were employed in the charactrisation of concrete properties in FEA models.

Materials

Concrete mixes having water /cement ratio of 0.45 was used. At age of 28 days, average compressive strength of reference mixes was 36 MPa. Medical face masks with 70 GSM density were used as fibres in concrete with three different volume fractions of 0, 0.25% and 0.5%. Special cutting machine was used to shred the masks to a regular size of 40 mm length and 5 mm width. Reference mixes with fibres were adjusted by varying the superplasticizer dosage to accommodate different fibre contents. A good level of workability was observed in fresh concrete, slump value was between 120 and 150 mm. For all cases, concrete mixes were produced following the same sequence, details on the mixing sequance and testing are available in (Al Marahla et al., 2023).

Table 1. Reference mix designs

Constituents	Quantity (kg/m^3)		
	Mix 1	Mix 2	Mix 3
Water	200	200	200
Cement	417	417	417
Coarse aggregate	928	928	928
Fine aggregate	801	801	801
Superplasticizer	4	6.2	7.8
Fibres content % (masks)	0	0.25	0.5

Specimens, Test Setup and Methodology for Three Point Bending Test

For each of the FRC mixes as per the combinations listed in Table 1, ten prismatic specimens were tested under flexure. Notched prisms complying to EN 14651 (2007b) standared were prepared, cast and tested under 3PBT flexure as depicted in Figure 1.

.

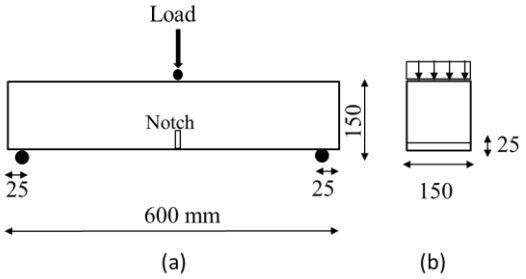

Figure 1. Specimen dimensions; (a) Elevation, (b) Cross section

Limit of proportionality (fL) and residual strength parameters f_{R1}, f_{R2}, $f_{R3,}$ and f_{R4} corresponding to fracture displacement values of 0.5, 1.5, 2.5, and 3.5 mm, respectively, were derived from this test. The load-displacement response for each case was used to define the constitutive curve in the modelling of FRC beams.

Specimens, Test Setup and Methodology for Four Point Bending Test

Full-scale beams had a dimension of 150 mm wide, 200 mm total depth and 2200 mm long with 2000 mm clear span as shown in Figure 2. In total, three different mix designs were considered in this study with the mix proportions listed in Table 1. Twelve beams were produced and tested, 4 typical beams for each concrete mix.

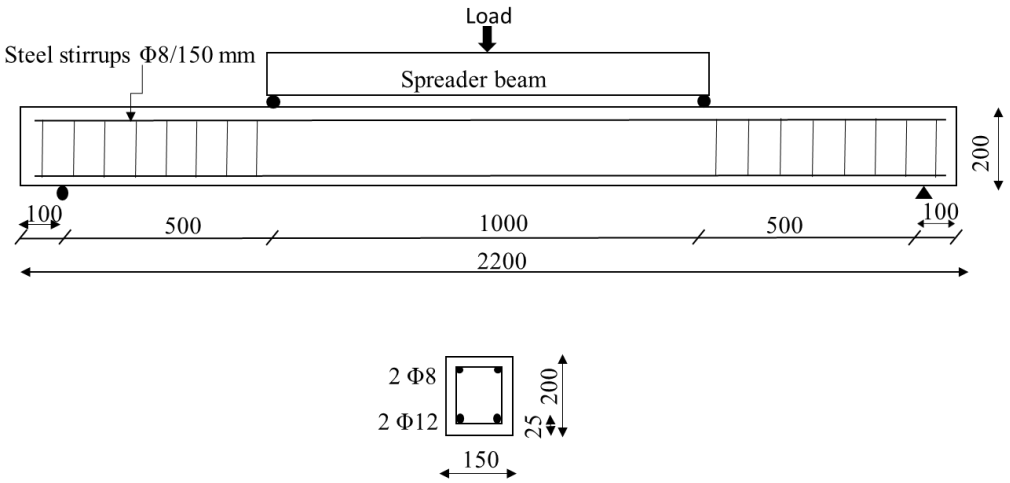

Figure 2. Beam geometry and typical cross sections

During each test, beam vertical deformations were monitored and recorded. The mid-span deflection was measured using linear variable differential transformers (LVDTs) that were connected to a data logger that recorded the mid-span deflection up to the failure load.

Finite-Element Modelling

In this investigation, a nonlinear finite element analysis was carried out to simulate the behavior of fiber-reinforced concrete beams subjected primarily to flexure. To accomplish this, the DIANA FEA software was utilized to predict the response of RC members with varying fiber contents. Three-dimensional finite element models of experimentally tested beams were created to evaluate the flexural behavior. The geometry, boundary conditions, and reinforcement details of the modelled beams were identical to those utilized in the experimental

investigations. Comparing and discussing the results derived from nonlinear FE analysis and those obtained experimentally are presented in this section.

The mechanical properties of concrete were assigned in accordance with FIB Model Code 2010. To simulate the behavior of concrete, a total strain-based cracking model with rotating crack orientation was employed. Concrete was modelled using 3D solid elements (Diana, 2017), while steel reinforcement was modelled using bar elements with bond slip interface to the surrounding concrete.

In both instances (plain and FRC), the compressive behavior of concrete was modelled using the Parabolic model (Thorenfeldt, 1987). To model the tensile behavior of reinforced concrete beams without fibers, the nonlinear post-cracking softening of concrete Hordijk model was used (Hordijk, 1992). The smeared crack approach has been adopted to represent the behavior of the materials, with standard continuum elements representing concrete (Rashid, 1968). Figure 3 below depicts the models used to predict the behavior of concrete under compression and tension.

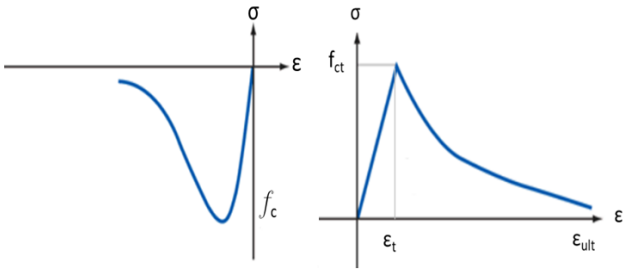

(a) (b)

Figure 3. Concrete behaviour models; (a) Torenfeldt model , (b) Hordijk model

On the basis of experiments on notched prisms, flexural parameters (residual flexural strength versus CMOD curves) were specified. In order to account for the effect of added fibers on the tensile behavior of FRC, the constitutive behavior in DIANA was modified with the parameters obtained from bending test on notched beams. The post-cracking response (stress-CMOD) were incorporated into the modeling as shown in Figure 4.

.

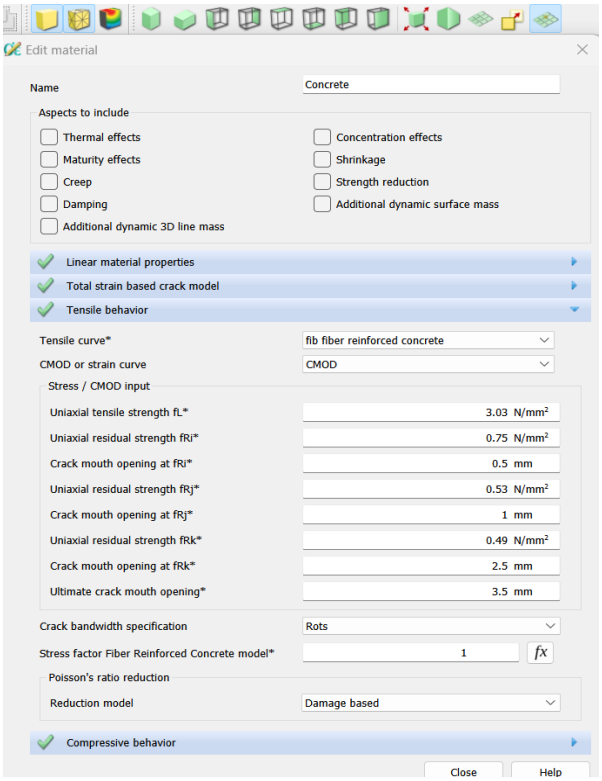

Figure 4. Tensile function of concrete using DIANA

After conducting a mesh sensitivity analysis, the 25mm mesh size was chosen to model the concrete elements considered in this study. Figure 5 shows the mesh used in this model.

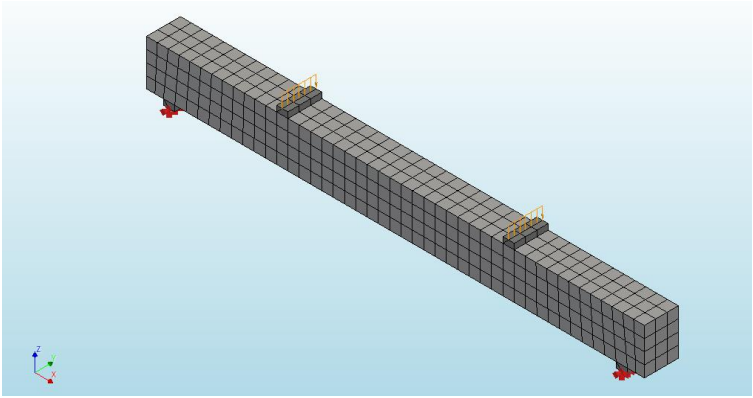

Figure 5. Mesh used in FEA for beams in DIANA

In terms of boundary conditions, beam modelled in this study was allocated simply supported conditions. Where the vertical and horizontal translations were restricted at one support, while only the vertical translation was restricted at the other support. Steel plates were used for loading and support and their linear elastic material properties were simulated. Due to the symmetry in geometry, reinforcement, boundary conditions, and loading, only one-half of the RC beam was modelled to save computational time. For obtaining capacity and post-peak behavior in DIANA FEA, the Modified Newton Raphson iterative scheme with the line search option was used, and the energy and displacement convergence norms were satisfied with a tolerance of 0.001 and 0.01, respectively.

Results and Discussion

Characterization Test (3PBT)

After the formation of a single crack at the notch's tip, prisms without fibres failed abruptly, resulting in the prisms' separation into two pieces. Whereas prisms with various volume fractions of face masks fibres demonstrated superior ductility compared to reference specimens without spontaneous splitting. Filure modes are shown in Figure 6.

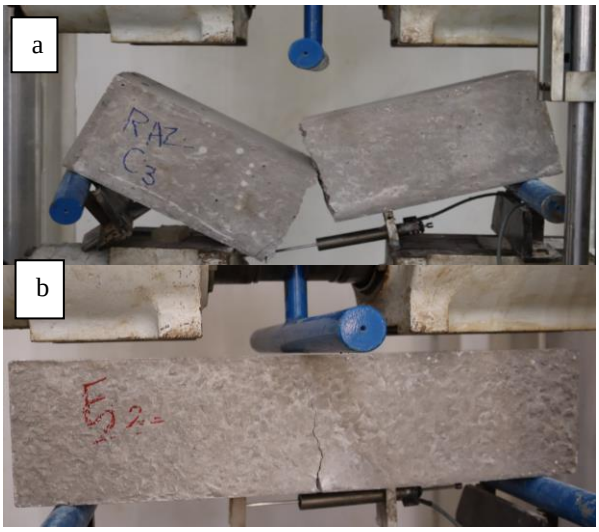

Figure 6. Failure of prisms (a) plain concrete, (b) with fibres

Residual flexural parameters obtained experimentally are presented in Table 2. Values present the average of ten different values.

Table 2. Residual flexural parameters

Fibre content (%)	f_{LOP}	f_{R1}	f_{R2}	f_{R3}	f_{R4}
0	2.46	0	0	0	0
0.25	2.69	0.42	0.38	0.37	0.36
0.50	3.03	0.75	0.53	0.49	0.46

Figure 7 presents the load-crack displacement associated with each fractional volume of fibres. Using the EN 14651 standard's proposed general formula, the vertical displacement (deflection) of a prism derived from a flexural bending test can be converted to an approximation of the CMOD. From the post-cracking behaviour of tested prisms, it was found that the limit of proportionality increased by up to 22.5% in FRC specimens exposed to the maximal dose considered in this study. This is due to the delay in crack coalescence induced by the addition of fibres to concrete mixes.

In addition, Figure 7 reveals that the addition of a higher volume fraction (0.5%) of fibers led to increase the residual parameters. At a crack width of 0.5 mm, the residual flexural ratio (f_{R1}/f_{LOP}) was 0.16 and 0.25 for fiber additions of 0.25% and 0. 5%, respectively. And (f_{R3}/f_{LOP}) values of 0.14 and 0.17, respectively, at a crack width of 2.5 mm.

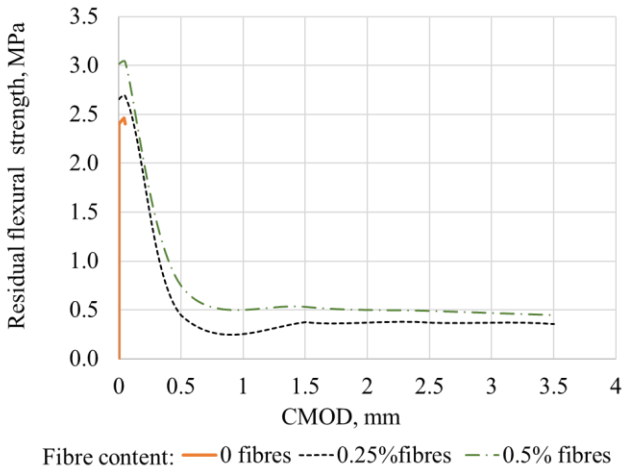

Figure 7. Load-CMOD for prisms with different dosages of polypropylene fibres

Flexural Tests (4PBT)

During the test carried out on the short-term deflection of beams, the midspan deflection of each beam was measured until failure. Table 3 presents the experimentally observed failure modes, maximal load (peak), midspan deflection, cracking loads, and number of cracks for each beam. It was observed that all beams failed in flexure under conditions of ultimate state.

Table 3. Beams results (mode of failure, deflection and cracking)

Beam	P_{max} (kN)	δ at max load	Ductility index (μ)
F01 (no fibres)	93.3	34.0	2.67
F02 (replicate)	96.4	35.1	2.54
F03 (replicate)	96.4	35.1	2.54
F04 (replicate)	97.7	38.3	2.44
F11 (with 0.25% fibres)	95.2	37.4	2.88
F12 (replicate)	96.2	31.1	4.50
F13 (replicate)	100.1	33.3	4.51
F14 (replicate)	100.9	33.2	4.32
F21 (with 0.5 fibres)	100.3	32.5	4.66
F22 (replicate)	103.7	28.7	5.58
F23 (replicate)	104.8	29.2	5.64
F24 (replicate)	106.5	30.1	5.35

However, beams made of plain concrete (F01, F02, F03, and F04) exhibited explosive concrete crushing, whereas fibre-reinforced beams with 0.25 and 0.5 percent fibres exhibited relatively ductile behavior, with the beams reaching the failure stage progressively. Previously conducted research (Shaaban et al., 2021; Hammad et al., 2022; Al Marahla et al., 2023) examined the flexural and cracking behaviour of reinforced concrete beams containing fibers. According to the authors, the addition of polypropylene fibres increased flexural fractures by up to 30% and increased stiffness.

FEA Analysis

To establish the validity of the FE models in comparison to the experimental behavior, the relationship between load and deflection and modes of failure of beams were compared. The relationship between load and deflection for experimentally measured beams and modelled beams is compared in this study. The experimentally obtained behaviour is contrasted to the behaviour obtained from models containing normal concrete (NC) and FRC.

Figure 8 illustrates the load-deflection profiles obtained experimentally and those from FEA. The results indicate a reasonable correlation between the experimental and finite element results, especially in the case of beams without fibers, where the FE model predicts a lower load at the time of failure than the experimentally determined value. The model of FRC beams indicates that the beams initially displayed a relatively stiffer behavior than reference beams. This may be due to the assumption of a perfect bond between reinforcement and concrete in the FEA.

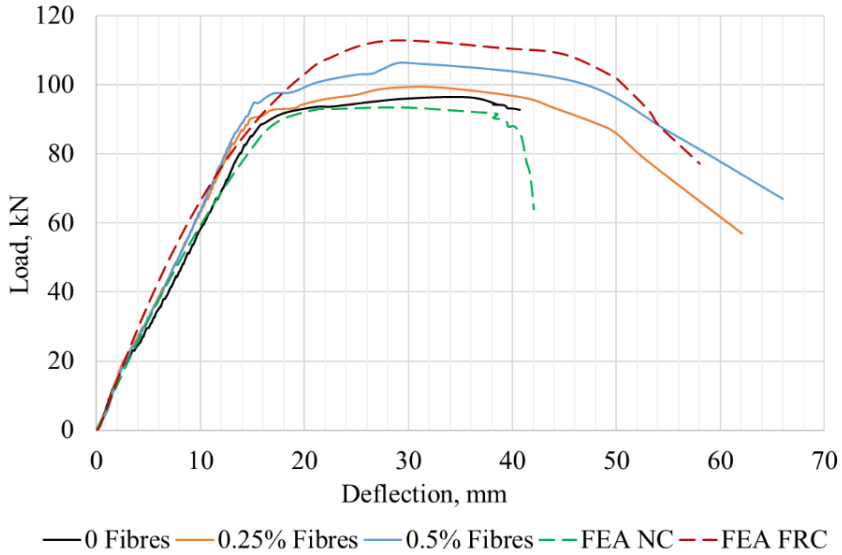

Figure 8. Comparison between mid-span deflection obtained experimentally and FEA results.

During the stage of crack formation and development, a plateau is observed where the deformation increased under a constant load prior to beam failure. While this is similar to the experimentally observed behavior, it occurred at a comparatively higher load in the FE model than in the tested beams. The experimentally determined average midspan deflection at the ultimate load for an FRC beam with a 0.5% fiber content was 29.4 mm associated with 106 kN, whereas the numerical values of midspan deflection were 28 mm associated with a vertically applied load of 114 kN. This variation in the load and deflection behaviour is attributable to the size of the fibres used, and their dispersion.

From the results of the FE models, it was observed that yielding of steel reinforcement was associated with extensive concrete cracking in the tension zone. In both modelled scenarios, this was followed by the cruching of the concrete in the compression zone, which is consistent with the experimental observations. Stresses developed in steel rebars as longitudinal reinforcement at ultimate condition is shown in (Figure 9) below.

For precise and reliable numerical modeling of the post-cracking behavior of FRC members, the results of FEA indicated that the efficacy of fibre in tension should be accounted for in concrete material properties (constitutive curve).

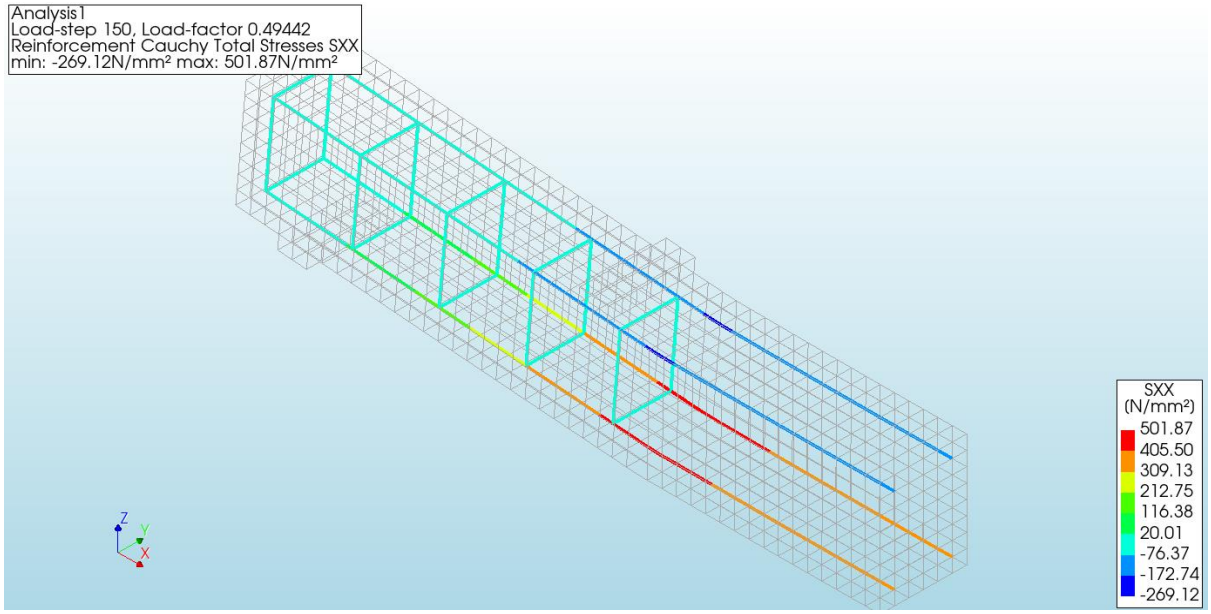

Figure 9. Stresses developed in steel reinforcement under ultimate condition.

Conclusion

In this investigation, a nonlinear finite element analysis was carried out to simulate the behavior of fiber-reinforced concrete beams under bending. DIANA FEA software was utilized to predict the response of RC members with varying fiber contents. Three-dimensional finite element models of experimentally tested beams were created, and a nonlinear static analysis was conducted to evaluate the flexural behavior. In numerical analysis, the geometry, boundary conditions, and reinforcement details of the modelled beams were identical to those utilized in the experimental investigations. Based upon the discussion and presented results, the following conclusions were drawn:

- Fibres considered in this study enhanced the post-peak ductility of the FRC prisms when compared to those prisms without fibers. Residual parameters were improved by up to 25% of peak strength due to the incorporation of fibres.
- The contribution of polypropylene fibres across the cracks can be illustrated by the residual tensile strength, and the behavior is identified as a function of the concrete's tensile strength in FEA.
- The addition of fibers to concrete mixtures substantially enhances the beams' flexural behavior, bending stiffness, and ductility. The mid-span deflections in FRC beams were lower by up to 19% when compared to the reference beams.
- The FEA results indicated that the efficacy of fibre in tension should be accounted for in concrete material properties (constitutive curve) for precise and reliable numerical modeling of the flexural and cracking behavior of FRC members.

Recommendations

Finite element (FE) analysis using available software is recommended to be incorporated in future research including the findings concluded from the experimental campaign. Moreover, the authenticity of the models in predicting the flexural behaviour and cracking performance of full scale FRC beams reinforced with steel bars can be evaluated and improved with less time and effort. The objective of FEA modelling should be to predict and investigate the influence of contributory parameters on the behaviour of members.

Scientific Ethics Declaration

The authors declare that the scientific ethical and legal responsibility of this article published in EPSTEM.journal belongs to the authors.

Acknowledgements

* This article was presented as an oral presentation at the International Conference on Technology, Engineering and Science (www.icontes.net) held in Antalya/Turkey on November 16-19, 2023.

* The authors would like to acknowledge the contribution of Al-Zaytoonah University of Jordan which collectively funded the conference registration fees and travel expenses for first author.

References

Abbass, W., Khan, M. I. & Mourad, S. 2018. Evaluation of mechanical properties of steel fiber reinforced concrete with different strengths of concrete. *Construction and Building Materials, 168***,** 556-569.

Al Marahla, R. H. & Garcia-Taengua, E. (2021). Sensitivity of the flexural performance of glass and synthetic FRC to fibre dosage and water/cement ratio. In P. Serna, A. Llano-Torre, J.R. Martí-Vargas & J. Navarro-Gregori (Eds.), *Fibre Reinforced Concrete: Improvements and Innovations* (pp.301-312).Cham. Springer International Publishing

Al Marahla, R. H., Shehzad, M. K., & Garcia-Taengua, E. (2023). Flexural and deflection behaviour of synthetic fibre reinforced concrete beams reinforced with glass fibre reinforced polymers bars under sustained service load. *Structures*, 946-955.

Amin, A., & Gilbert, R. I. (2018). Instantaneous crack width calculation for steel fiber-reinforced concrete flexural members. *ACI Structural Journal, 115*, 535-543.

ASTM C1609. (2012). *C1609/C1609M-12: Standard test method for flexural performance of fiber-reinforced concrete (using beam with third-point loading)*. West Conshohocken, USA.

Belmokaddem, M., Mahi, A., Senhadji, Y., & Pekmezci, B. Y. (2020). Mechanical and physical properties and morphology of concrete containing plastic waste as aggregate. *Construction Building Materials, 257*(1).

Biolzi, L., & Cattaneo, S. (2017). Response of steel fiber reinforced high strength concrete beams: Experiments and code predictions. *Cement and Concrete Composites, 77*, 1-13.

Cadenazzi, T., Dotelli, G., Rossini, M., Nolan, S., & Nanni, A. (2020). Cost and environmental analyses of reinforcement alternatives for a concrete bridge. *Structure Infrastructure Engineering, 16*(4), 787-802.

Diana, F. (2017). *Diana user's manual release 10.1*. In J. Manie (Ed.), DIANA FEA BV.

EN 14651. (2007a). *Test method for metallic fibre concrete–measuring the flexural tensile strength.* (pp.1-20). United Kindom, UK :British Standard Institute

EN 14651. (2007b). *Test method for metallic fibre concrete–measuring the flexural tensile strength.* (*Limit of proportionality (LOP), residual).* British Standard.

Fallah, S., & Nematzadeh, M. (2017). Mechanical properties and durability of high-strength concrete containing macro-polymeric and polypropylene fibers with nano-silica and silica fume. *Construction Building Materials, 132***,** 170-187.

Hammad, N., ElNemr, A. M., & Hassan, H. E. D. (2022). Flexural performance of reinforced alkali-activated concrete beams incorporating steel and structural macro synthetic polypropylene fiber. *Construction Building Materials, 324*(16), 126634..

Jhatial, A. A., Goh, W. I., Mastoi, A. K., Traore, A. F., & Oad, M. (2022). Environmental assessment and mechanical properties of polypropylene fibres reinforced ternary binder foamed concrete. *Environmental Science Pollution Research, 29*(2), 2985-3007.

Jhatial, A. A., Goh, W. I., Mohamad, N., Hong, L. W., Lakhiar, M. T., Samad, A. A. A., & Abdullah, R.(2018). The mechanical properties of foamed concrete with polypropylene fibres. *International Journal of Engineering Technology, 7*(3.7), 411-413.

Lee, J. H. (2017). Influence of concrete strength combined with fiber content in the residual flexural strengths of fiber reinforced concrete. *Composite Structures, 168*, 216-225.

Rashid, Y. R. (1968). Ultimate strength analysis of prestressed concrete pressure vessels. *Nuclear Engineering Design, 7*(4), 334-344.

Shaaban, I. G., Said, M., Khan, S. U., Eissa, M., & Elrashidy, K. (2021). Experimental and theoretical behaviour of reinforced concrete beams containing hybrid fibres. *Structures, 32*(2), 2143-2160.

Thorenfeldt, E. (1987). Mechanical properties of high-strength concrete and applications in design.Proceedings from *Symposium Utilization of High-Strength Concrete*. Norway.

Xu, H., Shao, Z., Wang, Z., Cai, L., Li, Z., Jin, H., & Chen, T. (2020). Experimental study on mechanical properties of fiber reinforced concrete: Effect of cellulose fiber, polyvinyl alcohol fiber and polyolefin fiber. *Construction and Building Materials, 261*, 120610.

Yoo, D. Y., Banthia, N., & Yoon, Y. S. (2016). Flexural behavior of ultra-high-performance fiber-reinforced concrete beams reinforced with GFRP and steel rebars. *Engineering Structures, 111,* 246-262.

Yousefi, M., Khandestani, R., & Gharaei-Moghaddam, N.(2022). Flexural behavior of reinforced concrete beams made of normal and polypropylene fiber-reinforced concrete containing date palm leaf ash. *Structures, 37*(9), 1053-1068.

Author Information

Razan Haedar Al Marahla
AlZaytoonah University of Jordan
St 594, Airport Rd, Amman, Jordan
r.almarahla@zuj.edu.jo

Muhammad Kashif Shehzad
National highways, UK
Leeds LS11 9AT, United Kingdom

Nour Hider Almarahlleh
Tafila Technical University
At-Tafilah, Jordan

To cite this article:

Al Marahla, R.H., Shehzad, M.K., Almarahlleh, N. H. (2023). Finite element modelling of polypropylene fibre reinforced concrete beams reinforced with steel under bending. *The Eurasia Proceedings of Science, Technology, Engineering & Mathematics (EPSTEM), 26*, 317-326.

The Eurasia Proceedings of Science, Technology, Engineering & Mathematics (EPSTEM)
ISSN: 2602-3199

The Eurasia Proceedings of Science, Technology, Engineering & Mathematics (EPSTEM), 2023

Volume 26, Pages 327-331

IConTES 2023: International Conference on Technology, Engineering and Science

Inception Model for Automatic Arabic Speech Recognition

Zoubir Talai
Badji Mokhtar University of Annaba

Nada Kherici
Badji Mokhtar University of Annaba

Abstract: Reproducing basic human abilities has always been the main purpose for Artificial Intelligence (AI) systems. Since speech is essential to people's communication, AI was applied to this major field to achieve Automatic Speech Recognition (ASR). In this paper, we focus on the inception model as a solution for Arabic speech recognition, due to its remarkable results on image classification tasks. We adapted this model for ASR problems and tried it on a dataset of spoken Arabic digits collected from social media apps and published corpora which resulted in more than 54000 utterances. A comparison between the proposed model and a traditional Convolutional Neural Network (CNN) shows the superiority of the inception model in ASR tasks. The inception model achieved 99.70% accuracy on the training dataset which is far better than the traditional CNN that achieved 87.46% on the same set, it did also great performance on the test subset with 88.96% accuracy compared to the traditional model with 84.78% recognition rate.

Keywords: Inception model, Convolution neural network, Artificial intelligence, GoogLeNet

Introduction

Automatic speech recognition (ASR) has grown to be a major field of research these last few years. A great number of commercial products were created based on the use of ASR as a user interface that proved to be useful and provides helpful assistance to humans in all kinds of everyday tasks. Consumer-targeted applications require ASR to be robust facing language dialects and noisy environments which can be challenging for such systems.

For this purpose, scholars issued several propositions using different approaches. Han et al. (2020) proposed ContextNet, a Convolutional Neural Network (CNN) combined with Recurrent Neural Network (RNN) to incorporate global context information into convolution layers with a custom scaling technique for the proposed model to achieve good accuracy in acceptable computation time. Another end-to-end model was proposed by Kriman et al. (2020), where they combined 1D time-channel separable convolution layers with batch normalization and ReLU layers to create blocks that were connected using the residual connection. They trained their model on the LibriSpeech dataset and claimed near state-of-the-art accuracy while needing fewer parameters. CNN was also used by Passricha & Aggarwal (2020) combined with Bidirectional Long Short Term Memory (LSTM) to achieve continuous speech recognition tasks. The authors experimented with different weight-sharing methods and pooling strategies to decrease Word Rate Error (WER). CNN proved also to be very efficient in the work proposed by Shahamiri (2021) where authors trained a CNN model and used it for transfer learning to create an ASR system to help people affected with Dysarthia. This medical condition is a result of paralysis of muscles involved in the articulation process hence making pronunciation for the affected individual very difficult. It was also used by Palaz et al. (2019) to estimate Hidden Markov Model (HMM) states class conditional probabilities. To achieve this goal, the authors trained a CNN model with raw speech signal to do feature extraction and initiate an HMM to finally recognize the spoken word. Houri et al. in (2021)

proposed a new approach to extract speaker characteristics by constructing CNN filters linked to the speaker. They also proposed new vectors to identify speakers, which they called convVectors. Experiments have been performed with a gender-dependent corpus (THUYG-20 SRE) under three noise conditions: clean, 9db, and 0db. Results showed that the convVectors method was the most robust. CNN was also used by Mustaqeem & Kwon (2020) where authors used it to learn discriminative features from whole utterances and then fed them to a Long Short-Term Memory (LSTM) network for sequence learning to find emotions of the speaker. Finally, Kiranyaz et al. (2021) wrote a good paper on 1D convolutional neural networks and their applications showing their advantages in ASR systems.

In this paper, we adapt the Inception Model (also called GoogLeNet) to ASR by modifying its architecture and changing its layers making them suitable for audio signal processing. These changes include one-dimensional (1D) convolution filters and 1D max pooling layers. This paper is organized into four sections. Starting with an introduction that presents the context of the study and some related works. The second section outlines the used CNN's architecture. The next section summarizes the results along with discussions. Finally, we conclude the paper with what we think of the obtained results and perspectives.

1D Convolution Neural Network

Like a conventional 2D CNN that is principally used for image classification, one-dimensional convolution networks are majorly used for signal processing problems such as Automatic speech recognition, Electrocardiogram monitoring, structural damage detection in civil infrastructure based on vibration, predictive maintenance for industrial machines…etc.

1D CNN operates the same way as 2D CNN, the first layer is dedicated to data input which generally consists of raw signal. The next set of layers is a combination of convolution/pooling layers that extract features from that signal. Finally, a fully connected network receives those features and classifies them into several classes. This last one must have in its final layer a number of neurons equal to class's number.

AlexNet

AlexNet is a deep convolutional neural network architecture that was introduced by Krizhevsky et al. (2012). It consists of 8 layers, including 5 convolutional layers and 3 fully connected layers. AlexNet uses traditional stacked convolutional layers with max-pooling in between as shown in figure 1. Its deep network structure allows for the extraction of complex features from sound files. The architecture employs overlapping pooling layers to reduce spatial dimensions while retaining the spatial relationships among neighboring features. It uses the ReLU activation function and dropout regularization, which enhance the model's ability to capture non-linear relationships within the data.

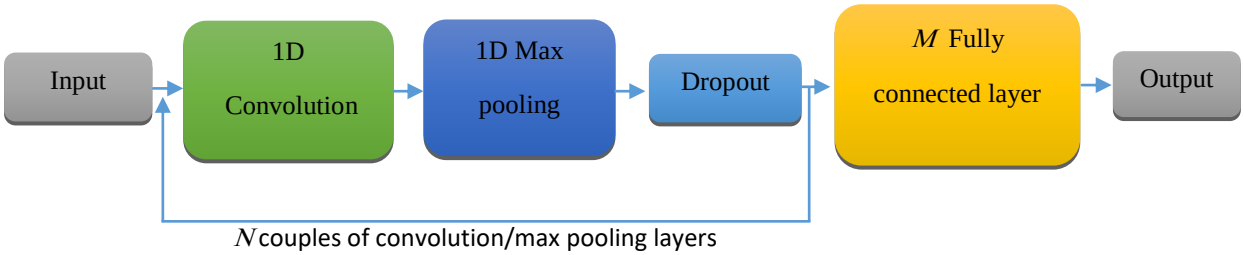

Figure 1. AlexNet architecture for ASR

Inception Model v1 (GoogLeNet)

GoogleNet, also known as Inception v1, was introduced by Szegedy et al. (2015). It was built on the success of AlexNet by introducing a number of new innovations. In GoogleNet architecture, there is a method called global average pooling used at the end of the network. This method reduces the number of parameters in the model and helps prevent overfitting. GoogleNet also introduced inception modules shown in Figure 2, which are designed to capture features at different scales and resolutions. The architecture is deeper than AlexNet and has 22 layers.

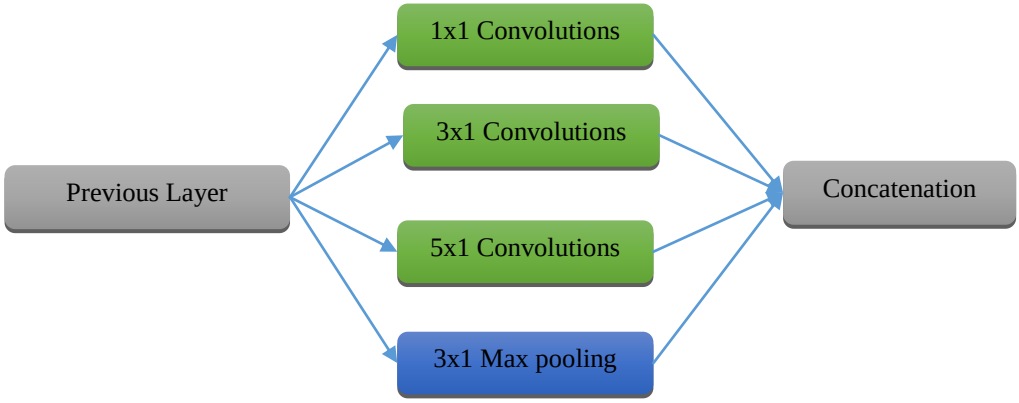

Figure 2. 1D inception block

Dataset

For experimentations, we used a dataset collected for previous work by Talai et al. (2022). We collected utterances of the first ten Arabic digits, from 107 speakers; the recordings were received via Internet and social media apps. A mixed group of people participated in the recording including women, men, and children aged from 4 to 64 years. The sound files were pretreated and converted to have segments of two seconds duration. We also resorted to data augmentation to increase the initial dataset which proved to be too small for the training of the proposed model. This operation resulted in 14 538 samples. The corpus was divided in two parts (80% + 20%), 80% was dedicated to the training/validation of the model, and 20% was kept for testing the models' performance.

Results and Discussion

To achieve good recognition using AlexNet and after several experiments, we chose to progressively increase kernel size and decrease extracted features combined with a dropout layer to avoid overfitting. As for the used GoogLeNet, we used the Inception block present in Table 2, we also chose to add one auxiliary classifier noticeable in the sequence: Average pooling – Conv1D – Dense. Note that the number of features extracted and kernel size are to be chosen meticulously so that the output size of each layer matches the input needed for the next one. Table 1 shows the used architectures.

Table 1. Used architectures

AlexNet	Inception Model
Conv1D (8, 13)	Inception(16,16,16,16,8,16)
Max-Pooling (3)	Inception(16,16,16,16,8,16)
Dropout (0.3)	Average-pooling(5)
Conv1D (16, 11)	Conv1D(32,1)
Max-Pooling (3)	Dense(10)
Dropout (0.3)	Inception(32,32,32,32,16,32)
Conv1D (32, 9)	Inception(32,32,32,32,16,32)
Max-Pooling (3)	Dense(10)
Dropout (0.3)	
Conv1D (64, 7)	
Max-Pooling (3)	
Dropout (0.3)	
Dense (256)	
Dense (128)	
Dense (10)	

After several experimentations, the best model's evolution can be seen in Figure 3. The results presented in Table 3 show the improvement gained using the Inception model. First, AlexNet's accuracy is acceptable considering the nature of input data, the simplicity of implementation, and the arguably small size of the network. Unfortunately, it stops evolving at a certain accuracy even with 50 epochs. On the other hand, the

Inception model outperforms AlexNet's results needing only 12 epochs. The combination of Inception blocks and auxiliary output layer proves that this model is efficient for automatic speech recognition tasks.

Table 2. Inception block architecture

Inception (a, b, c, d, e, f)			
Conv1D(a,1)	Conv1D(b,1) Conv1D(c,3)	Conv1D(d,1) Conv1D(e,5)	Max-Pooling(3) Conv1D(f,1)
Concatenation			

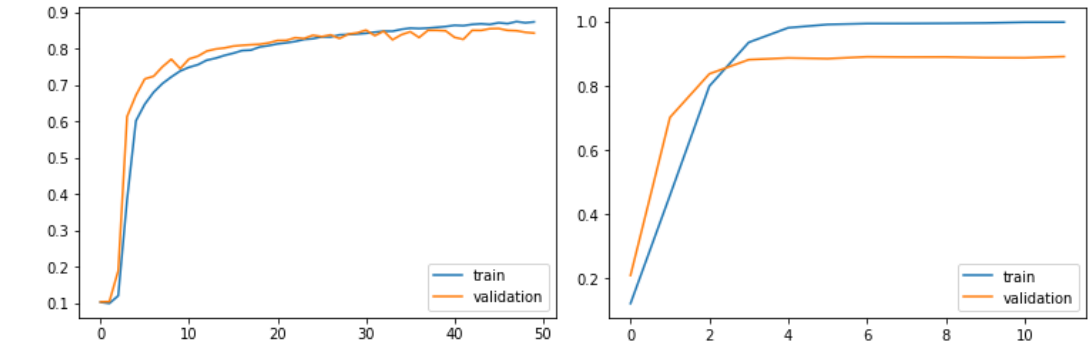

(a) (b)

Figure 3. Models' accuracy evolution: 3a AlexNet. 3b Inception Model

Table 3. Results summary

	AlexNet	**Inception Model**
Batch Size	16	32
Epochs	50	12
Accuracy achieved on training dataset	87.46%	99.70%
Accuracy achieved on the validation dataset	84.78%	88.96%

Conclusion

ASR is an exciting field that has seen significant progress in recent years. With major developments in computing power and the appearance of GPU parallel processing, even the most complex deep model can be trained in an acceptable time. This work introduces a different way of using the Inception model to achieve automatic speech recognition. We detailed the required modification to the model's architecture so it can work with sound data. The Inception model proved to be efficient for ASR tasks without needing long processing time. Inception model proved his superiority achieving 88.96% recognition rate compared to AlexNet which only had 84.78% accuracy.

References

Han, W., Zhang, Z., Zhang, Y., Yu, J., Chiu, C.-C., Qin, J., Gulati, A., Pang, R., & Wu, Y. (2020). ContextNet: improving ocnvolutional neural networks for automatic speech recognition with global context. *arXiv.*

Hourri, S., Nikolov, N. S., & Kharroubi, J. (2021). Convolutional neural network vectors for speaker recognition. *International Journal of Speech Technology*, *24*(2), 389–400.

Kiranyaz, S., Avci, O., Abdeljaber, O., Ince, T., Gabbouj, M., & Inman, D. J. (2021). 1D convolutional neural networks and applications: A survey. *Mechanical Systems and Signal Processing*, *151*, 107398.

Kriman, S., Beliaev, S., Ginsburg, B., Huang, J., Kuchaiev, O., Lavrukhin, V., Leary, R., Li, J., & Zhang, Y. (2020). Quartznet: Deep automatic speech recognition with 1D time-channel separable convolutions. *ICASSP 2020 - 2020 IEEE International Conference on Acoustics, Speech and Signal Processing (ICASSP)*, 6124–6128.

Krizhevsky, A., Sutskever, I., & Hinton, G. E. (2012). Imagenet classification with deep convolutional neural networks. *Advances in Neural Information Processing Systems*, *25*.

Mustaqeem, & Kwon, S. (2020). A CNN-assisted enhanced audio signal processing for speech emotion recognition. *Sensors*, *20*(1), 1.

Palaz, D., Magimai-Doss, M., & Collobert, R. (2019). End-to-end acoustic modeling using convolutional neural networks for HMM-based automatic speech recognition. S*peech Communication, 108*, 15–32.

Passricha, V., & Aggarwal, R. K. (2020). A hybrid of deep CNN and bidirectional LSTM for automatic speech recognition. *Journal of Intelligent Systems, 29*(1), 1261–1274.

Shahamiri, S. R. (2021). Speech vision: An end-to-end deep learning-based dysarthric automatic speech recognition system. *IEEE Transactions on Neural Systems and Rehabilitation Engineering, 29*, 852–861.

Szegedy, C., Liu, W., Jia, Y., Sermanet, P., Reed, S., Anguelov, D., Erhan, D., Vanhoucke, V., & Rabinovich, A. (2015). Going deeper with convolutions. 2015 I*EEE Conference on Computer Vision and Pattern Recognition (CVPR)*, 1–9.

Talai, Z., Bahi, H., & Kherici, N. (2022). Remote spoken Arabic digits recognition using CNN. In N. M. Mahyuddin, N. R. Mat Noor, & H. A. Mat Sakim (Eds.), Proceedings of the *11th International Conference on Robotics, Vision, Signal Processing and Power Applications* (pp. 639–645). Springer.

Author Information

Zoubir Talai
Badji Mokhtar University of Annaba
P.O Box.12, Annaba-23000 Algeria
Contact e-mail: talai_zoubir@yahoo.com

Nada Kherici
Badji Mokhtar University of Annaba
P.O Box.12, Annaba-23000 Algeria

To cite this article:

Talai, Z. & Kherici., N. (2023). Inception model for automatic arabic speech recognition. *The Eurasia Proceedings of Science, Technology, Engineering & Mathematics (EPSTEM), 26*, 327-331.

The Eurasia Proceedings of Science, Technology, Engineering & Mathematics (EPSTEM)
ISSN: 2602-3199

The Eurasia Proceedings of Science, Technology, Engineering & Mathematics (EPSTEM), 2023

Volume 26, Pages 332-340

IConTES 2023: International Conference on Technology, Engineering and Science

Validation of the Heuristic Model for SMART Management in a Medium-Sized Industrial Enterprise

Miglena Temelkova
University of Telecommunications and Post

Iliyan Bakalov
Ministry of Innovation and Growth

Abstract: This article presents the results of the approbation of a Heuristic model for SMART management in a medium-sized industrial enterprise in a specific economic entity. The main practical steps and the effects achieved as result of the introduction of the model in the selected industrial enterprise are summarized. The results achieved at different stages and the analytical assessments, the improvements, the restructuring and other strategic and operational activities leading to effective changes in the operation of the industrial unit are presented. Conclusions and inferences have been made, the most important of which is that the Heuristic Model for SMART management in the medium-sized industrial enterprise is also applicable in small industrial enterprises having a complex and multi-layered structural architecture. In order to comply with the regulation of the European Union for the protection of personal data, the name of the company is not indicated in this article, and the provided data is publicly available.

Keywords: Approbation, Heuristic model, SMART management, Industrial enterprise

Introduction

Under the conditions of Industry 4.0, the options for integrating technological network connectivity with the possibilities of the heuristic tool-kit, as well as with the possibility of upgrading the heuristic systems with the experience acquired on the basis of artificial intelligence and expert systems, give reasons to look for a definition of the concept of «a heuristic model for SMART management in the medium-sized industrial enterprise ». The author defines this model as an arbitrary algorithmic process based on a SMART tool-kit and heuristics that provides optimality or compromise improvement of management in all or in specific functional planes of the organization. This model integrates, on the one hand, the latest technological innovations such as cloud computing, mobile connectivity, large databases, artificial intelligence, additive manufacturing and the Internet of Things, and on the other hand, the business practices introduced through machine self-learning and the expert systems bringing human expertise to the algorithm of codes and data. The heuristic model for SMART management in the medium-sized industrial enterprise is a final, simplified, adequate image of a real intelligent management process and should be described in detail and decomposed into its constituent fundamental elements by defining its input-output information flows.

In the course of the approbation of the Heuristic Model for SMART management in the medium-sized industrial enterprise the specific industrial enterprise will organize its activity on the basis of the integrated and model-based analysis, assessment, forecasting, planning, organization, control. The aim is for the subject of approbation to keep its structure and work processes flexible and adaptable to the changes in the environment. On this basis, the process of testing the Heuristic Model for SMART management in the medium-sized industrial enterprise comes down to:

- analysis and assessment of the environment of the industrial enterprise and its production processes;
- study of the "production – management" relationship within the industrial entity chosen for testing the model;
- decomposing the systems of the industrial entity into subsystems and of production into processes and operations;
- determination of the mathematical foundation of the Heuristic model for SMART management in the industrial enterprise selected for implementation of the model;
- refinement of the heuristic elements in the Heuristic Model for SMART management in the industrial enterprise selected for selected for testing the model;
- creating a software information technology foundation in the industrial entity;
- selection of a specific control parameter (corresponding to the specifics of that industrial entity) in the industrial enterprise selected for testing the model.

The specified activities lead to the specific formal implementation of the Heuristic model for SMART management in the medium-sized industrial enterprise according to the individual conditions of the environment and the specifics of the activity. For the purposes of this study, the testing of the Heuristic Model for SMART management in the medium-sized industrial enterprise took place in an industrial enterprise headquartered in the city of Targovishte – i.e. a region outside the capital of Bulgaria, located in the north-eastern part of the country. The business unit in which the Heuristic model for SMART management is implemented in the medium-sized industrial enterprise was registered in 2001 with a wide scope of activities in this country and abroad:

- production, processing and sale of industrial, household and agricultural products;
- production of furniture and details from wood and timber and their marketing;
- wholesale and retail trade in goods permitted by law;
- commission and brokerage activity;
- construction and repair activities;
- electrical installation and repair work;
- hotel and restaurant management;
- entertainment, fun and amusement games;
- transport and car repair activities;
- repair of industrial and household appliances;
- trade in petroleum products;
- foreign trade activity;
- marketing and management after obtaining the necessary licenses for the relevant activities.

According to the registration, the main activity under the National Classifier of Economic Activities is the production of furniture. Based on the brief historical retrospection of the registration of the company, it becomes clear that it has over 20 years of experience in the creation of custom furniture and the implementation of assignments from partners and traders. Today, part of the company's production provides products for a well-known Swedish company - a leader in the online sales of furniture on the Scandinavian market. A check with the Information System for the management and monitoring of funds from the European Union in Bulgaria showed that the company is a beneficiary of four projects under Operational Programme "Innovations and Competitiveness". The funding agreed for these projects amounts to BGN 2,085,924.50, and the amounts actually received, based on verified activities and expenditure justification documents are BGN 1,379,379.10.

The economic entity chosen for the testing of the Heuristic model for SMART management in a medium-sized industrial enterprise is a small industrial enterprise with a total workforce of 35 employees. The turnover of the company varies from BGN 1,852,000 in 2019 to BGN 2,199,000 in 2020 (https://portal.registryagency.bg). The company's assets amount to nearly BGN 2,000,000.

At the same time, the company selected for testing the Heuristic Model for SMART management in a medium-sized industrial enterprise is one of the formal exceptions to the generally accepted definition of a medium-sized industrial enterprise. This exception is defined by the European Commission, which assumes that "if an enterprise has access to significant additional resources it might not be eligible for the status of a small or medium-sized enterprise" (European Union, 2020). This means that the size of the economic entity is not the only factor to consider when defining an enterprise as a small or medium-sized enterprise. Therefore, the more complex structure of the company, its access to significant resources, including through EU funds, the object of its activity, the presence of a real substantial transformation process, are essential factors in defining its type.

The reason for choosing the company in which the testing of the Heuristic Model for SMART management in a medium-sized industrial enterprise took place as the subject of the study is related to its rapid development and the potential it shows for growth and expansion of the market share in the external environment, including on the international market. The company's strategic priorities indicate that it has focused its activities on expanding its structure and markets. It is clear from the mentioned arguments that the company has the capacity to restructure into a medium-sized industrial enterprise. This is also the main reason for choosing it as the subject of the testing of the Heuristic Model for SMART management. The aim is to analyse the ability, through the introduction of the model, of the industrial enterprise to accelerate its formal growth to a medium-sized industrial enterprise, and the introduction of the Heuristic model for SMART management is accepted by the company's management as a first step in the achievement of this strategic goal. The purpose of the approbation of the Heuristic Model for SMART management in the selected industrial enterprise can be synthesized as follows:

- reduction of resource intensity;
- increasing the capacity and production workload;
- increasing adaptability;
- sustainability of processes;
- optimization of stocks and warehouse stocks;
- optimization of the need for production land;
- planning sustainability.

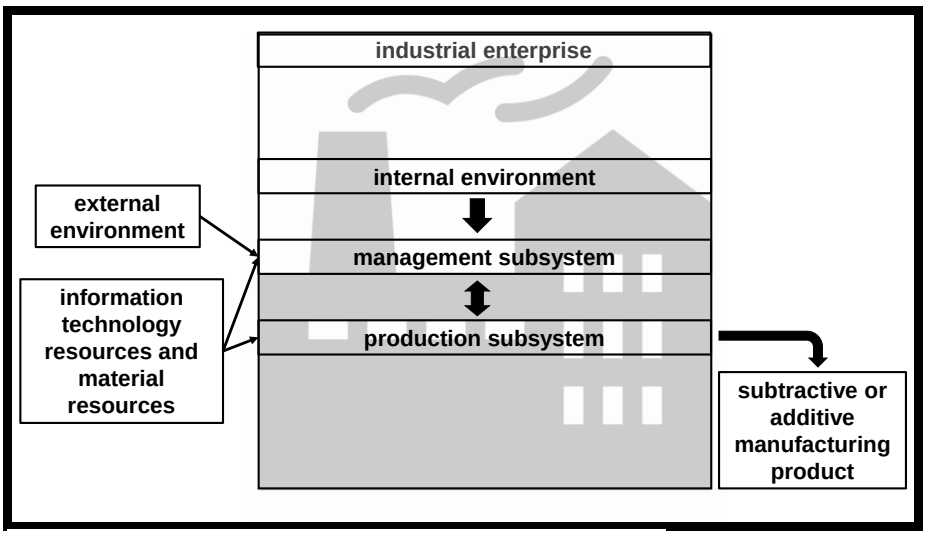

Figure 1. Structure of the industrial enterprise subject to approbation of the Heuristic Model for SMART management in the medium-sized industrial enterprise (developed by the authors)

The company chosen for testing the Heuristic model for SMART management in a medium-sized industrial enterprise is a unique production system, the constituent elements of which are production equipment and information and analytical equipment, technological processes, technical means of control and management and people involved in the service and management of the production process. The input materials (chipboard, timber, locks, hinges, fasteners and other elements) are transformed under the influence of the dispositive factors of production and the management subsystem into a final commodity product (Figure 1.). On this basis, it implements industrial production activities, which, taking into account the conditions of limited resources and organizational and structural complexity, determine its strategic priorities in time and space. (Temelkova, 2010).

Testing of the Heuristic Model for SMART Management in a Medium-Sized Industrial Enterprise

The testing of the Heuristic Model for SMART management in a medium-sized industrial enterprise in the selected company requires passing the stages described above in the article. The first stage of the testing is related to an analysis of the environment of the subject in which the model is tested.

The analysis and assessment of the environment of the industrial enterprise requires study of the environment external to the company using a set of strategic tools:

- The Political, Economic, Social, Technological Analysis indicates that the factors related to an increase in the cost of production per unit of production negatively affect the company's activity. At the same time, the factors leading to better quality parameters of production and to options for larger production volumes are evaluated positively.
- The Industry Analysis of the "Furniture Manufacturing" sector indicates that its attractiveness is moderate, as it is influenced by the moderate rates of demand and profitability in the sector. At the same time, the high supply in the industry and the low degree of regulation of supply through barriers to entry into the industry lead to the need to search for sustainable tools to minimize the cost of production of a product unit.
- The Competitive Analysis highlights three groups of competitors of the investigated enterprise: companies similar to the investigated enterprise; companies specializing in a narrow product niche; regionally operating companies.
- The study of the driving forces of competition of the analysed economic entity, according to Michael Porter's model, reveals that the forces of competition act intensively, that the access of new players to the industry is facilitated, and the power of suppliers and consumers is moderate. Thus the possibility of the company's products to be replaced by substitute goods is tangible. This necessitates a search for options to increase the added value of production.
- Competitor Profiling gives a clear and accurate view of the strengths and weaknesses of the investigated company which enables to estimate its potential and vulnerability. It is evident from the assessment of the company's competitive advantages that it also has the potential to gain better market positions and capacity. (Figure 1).

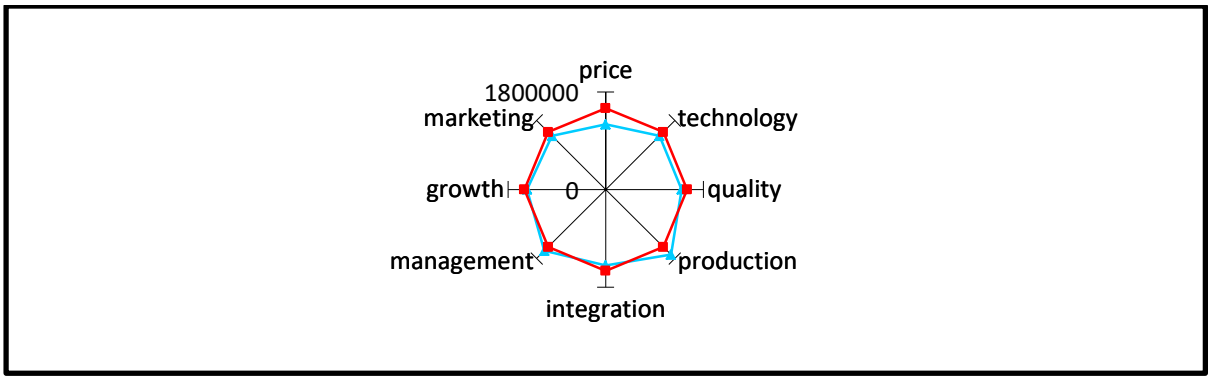

Figure 2. Competitive profile of the investigated company, object of approbation the Heuristic Model for SMART management in the medium-sized industrial enterprise is introducted (developed by the authors)

- Pressure Analysis defines several main groups with specific interests: owners, managers, workers and employees who are part of the internal environment of the industrial enterprise, and suppliers, consumers, society, who are part of the external environment of the company. There is a match between the interests of owners and managers and an indirect match between their interests and the interests of the company's employees and suppliers. Optimizing costs and profits would lead to the satisfaction of the interests of all studied groups of the community.

Table 1. Key Success Factors Analysis of the investigated company where the Heuristic Model for SMART management in the medium-sized industrial enterprise is introducted (developed by the authors)

Factor	Priority Requirements to Achieve Success in the Sector
Proposal of a Suitable Product/Furniture	modern design innovative form long product line colour variety warranty
Offering at an Affordable Price	delivery and assembly high quality custom design specialized stores
Offering at a Suitable Place	website opportunity to choose proper customer service consulting clients

The internal environment of the company, subject of the testing of the Heuristic model for SMART management in a medium-sized industrial enterprise, is investigated using a set of analytical tools:

- Key Success Factors Analysis is based on a company's fulfilment of the requirements of three factors leading to success in that economic sector. The success in the industry and the growth of the company to a medium-sized enterprise is a realistic strategic move based on the optimization of the production by reducing the resource intensity and by increasing the capacity and the market share (Table 1).
- The Strategic Product Analysis indicates that custom production increases during the summer months, and it is the weakest at the beginning of the calendar year. Regarding standardized products, it is observed that they are in the "growth" stage of the life cycle, which substantiates the thesis that the company has the potential to expand its market share.
- Analysis by the Boston Consulting Group provides information on the strategic positions of the manufactured products on the market and in the company itself: the "cash cow" products are the kitchen units, the wardrobes and the bedrooms; the "star" product is the shelves; "dilemma" products are the chests of drawers.
- The activities in the industrial enterprise subject of analytical analysis which add more value and require significant costs were identified using the Value - Chain Analysis technique: the production operations for converting raw materials and materials into finished products through processing, cutting, assembly, testing, and the internal logistics encompassing the receiving, warehousing, storage and distribution of material resources.
- The studies of the production activity in the industrial enterprise made with the Ratio Analysis technique show positive changes in the production and the sales by products, a positive rate of change of the increase in the number of personnel, a positive indicator of stock turnover, profitability higher than one, very good current liquidity.
- The study using the Strategic Position Analysis technique provides information that the company holds good positions in the sector in terms of market, production, personnel, economic and financial indicators. The most unfavourable is its marketing positioning, although it is close to the average positions in the industry.
- According to the Vulnerability Analysis, the supply and the cost are at risk, although the risk is not particularly tangible. This necessitates strategic moves to reduce the production costs in a sustainable manner.
- The Critical Success Factors Analysis technique used in the study of the company points to the need to reduce production costs and optimize profit.

The analyses of the environment show unequivocally that the selected company in which the Heuristic model for SMART management in a medium-sized industrial enterprise was implemented has a good competitive position, is in a good financial condition, realizes a sustainable market presence and market share which determines the indisputable presence of potential for expansion of the activity. However, the expansion of the activities requires a higher profitability of the production process. This would be possible if the production costs, which determine the cost, are reduced and the production is increased based on the innovations introduced in the company through the funding from the European Regional Development Fund. The «production - management» relationship in the industrial subject chosen for the testing of the model has to be studied using two main tools:

- A balanced system of indicators that shows the need to implement financial and non-financial indicators in the analysed company and, on this basis, to determine the efficiency as a function of indicators leading to a qualitative change in the financial and the organizational and technical state of the industrial enterprise;
- Brown's framework of process assessment which links the production process in the industrial enterprise with efficiency as an indicator that supports the sustainable production process and the development of the company.

The relational dependencies between the "management" and "production" subsystems in the industrial enterprise are identified on the basis of the studies and analysis made with the Balanced System of Indicators and the Brown Framework for measuring processes in the company in which the Heuristic Model for SMART management in a medium-sized industrial enterprise was implemented. (Table 2) The decomposition of the production process into operations in the studied economic entity highlights the following features:

- the operations are combined in parallel and sequentially;
- the average duration of each operation is 14.50 minutes;
- the movement of components and semi-finished goods is in parallel and sequential;
- the average time required for movement of components and semi-finished goods is 0.15 hours;

- theaverage machine setup time is 0.09 hours;
- the type of technological routes is in parallel and sequential;
- the average production time per product unit is 2.17 hours.

Table 2. Intersection points between the «production» and «management» subsystems in the industrial enterprise selected for implementation of the Heuristic Model for SMART management in the medium-sized industrial enterprise (adapted by the author by Temelkova, 2010)

Industrial Enterprise Selected for the Testing		
Subsystem	Elements	Intersection Points
Management	Strategic Management	planning organizing the coordination between production and management motivating staff reporting control
	Work Processes	processing and transfer of information
	Investments	efficiency
	Productivity	number of products by type
	Marketing	quality price market share
	Innovation	innovative technologies digitization
	Human Resources	remuneration
Production	Operating Management	planning of production organization of production, coordination and logistics production report control
	Production Process	operations time
	Logistics	supply procurement forwarding
	Technology	resource intensity
	Human Resources	remuneration

The analyses of the environment, the studies of the production process and its main components determine the mathematical foundation of the Heuristic model for SMART management in the industrial enterprise that was studied and analysed. The most important limiting conditions are generated on the basis of the studies and analysis of the company and its production in the previous stages of the model:

- limitations arising from the volume of the natural production (number of the j-type products)

$$\sum_{j=1}^{n} X_j^* \geq \sum_{j=1}^{n} X_j \quad [1]$$

or

$$\sum_{j=1}^{n} \frac{OH_{PSS}^*}{IPT^*} \geq \sum_{j=1}^{n} \frac{OH_{PSS}}{IPT} \quad [2]$$

- limitations arising from the monetised losses of technological time for each j^{th} product by processes of the n^{th} j-type product

$$\sum_{j=1}^{n} TLTT_d^* \times X_{jd}^* \times P_{LTT} \quad \sum_{j=1}^{n} TLTT_d \times X_{jd} \; P_{LTT} \quad [3]$$

- limitations arising from the monetised costs of material resources for the production of each j^{th} product by processes per unit of the j-type product

$$\sum_{j=1}^{n} TCMR_{dg}^{*} \times X_{jd}^{*} \times P_{Mg} \leq \sum_{j=1}^{n} TCMR_{dg} \times X_{jd} \times P_{MG} \quad [4]$$

- limitations arising from the monetised costs of energy per unit of product that is used to achieve the production of each j^{th} product by processes

$$\sum_{j=1}^{n} TEC_{d}^{*} \times X_{jd}^{*} \times P_{E} \leq \sum_{j=1}^{n} TEC_{d} \times X_{jd} \times P_{E} \quad [5]$$

- limitations arising from the monetised costs of labour for the production of a j-type product by processes of the n^{th} j-type product

$$\sum_{j=1}^{n} TLC_{d}^{*} \times X_{jd}^{*} \times P_{T} \leq \sum_{j=1}^{n} TLC_{d} \times X_{jd} \times P_{T} \quad [6]$$

- limitations arising from the monetised costs of operating the machines and automated and robotic devices used in the production of a j-type product by processes of the n^{th} j-type product

$$\sum_{j=1}^{n} TCMAR_{d}^{*} \times X_{jd}^{*} \times P_{MAR} \leq \sum_{j=1}^{n} TCMAR_{d} \times X_{jd} \times P_{MAR} \quad [7]$$

The studies, analyses and assessments of the state of the company and its production naturally lead to the conclusion that economic efficiency should be considered as a target criterion in the Heuristic model for SMART management in the studied industrial enterprise:

$$E = \frac{TR}{CP} \quad [8]$$

or:

$$L = \frac{TR}{CP} \rightarrow \max/\text{compromise} \quad [9]$$

or

$$L = \frac{Xj \,.P_p}{\sum_{j=1}^{n} TLTT_{d} + \sum_{j=1}^{n} TCMR_{dg} + \sum_{j=1}^{n} TEC_{d} + \sum_{j=1}^{n} TLC_{d} + \sum_{j=1}^{n} TCMAR_{d}} \rightarrow \max/\text{compromise} \quad [10]$$

The search for maximum or compromise values for efficiency requires the integration of heuristic elements into the Heuristic Model for SMART management in the company in which the model is implemented. They appear in the Matrix-based model for the relations between production revenue and resource intensity. On that basis the Heuristic model for SMART management in the specific industrial enterprise relies on high revenues and low resource intensity. The tree of alternatives in the industrial enterprise subject of the testing selects, as a heuristic tool, the following options:

- increased production capacity;
- increase in production;
- concentration;
- integration;
- diversification.

The software information technology foundation in the Heuristic model for SMART management in «the specific industrial enterprise finds expression in a model-based programme that calculates the efficiency in different situations and manages the other parameters in it based on the optimality criterion (Figure 3.). The governing parameters in the optimality criterion in the Heuristic model for SMART management in the economic subject, object of the testing, are the cost and the total revenue.

$$TR = [TR_{1,} TR_{2,} \dots TR_{v}]^{T} \quad [11]$$

$$CP = [CP_{1,} CP_{2,} \dots CP_{v}]^{T} \quad [12]$$

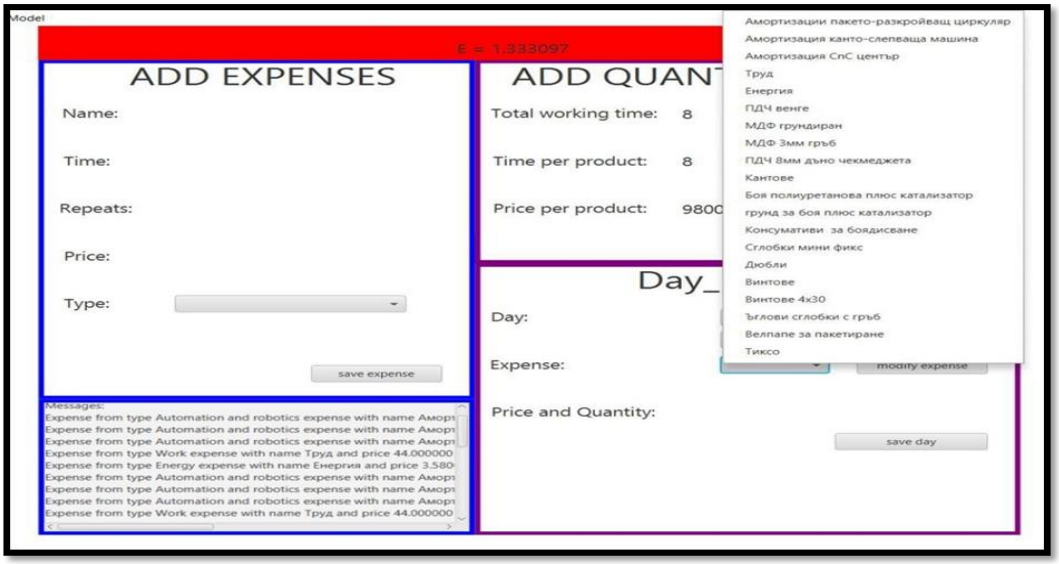

Figure 3. A software program of the Heuristic model for SMART management in a medium-sized industrial enterprise, tested in a specific economic entity – an operating window of the programme (developed by the authors)

Results and Discussion

The testing of the Heuristic Model for SMART management in the medium-sized industrial enterprise in a specific economic entity identifies certain changes within the entire production and financial life cycle. These changes are a kind of elastic chains that are connected and synchronized in the production programme of the particular company.

The implementation of the Heuristic model for SMART management in a medium-sized industrial enterprise determines the optimal management in the economic subjects applying it. The possibility of increasing the production capacity by 13% compared to 2021 and by 25% compared to 2020 was highlighted in the course of its testing in the specific industrial enterprise.

The application of the Heuristic Model for SMART management in a medium-sized industrial enterprise in the economic entity chosen for its testing creates real prerequisites for the development of the company in terms of the following strategic priorities:

- increase of personnel by 13%;
- cost reduction by 11% by:
- optimizing the storage and production capacity;
- optimizing the delivery and distribution channels and times;
- cutting technological resource losses by 8.1%;
- optimizing the technological equipment load by 35%;
- enhanced monitoring and control in the “bottlenecks” of the production process;
- reducing the production times by 8.7%;
- reducing the energy consumption by 9%;
- reducing material intensity by 20%;
- reducing time consumption by 17%;
- reducing the time for process management by 40%.

The significant changes provoked by the Heuristic model for SMART management in a medium-sized industrial enterprise in the company chosen for its testing caused qualitative changes in all value chains of the company and a quantitative change of the most important indicators of sustainability of the activities:

- productivity – it increased by 13% in that specific case;
- profitability – it increased from 0.26 to 0.30 after the testing of the model;
- efficiency – it increased from 1.32 to 1.67 after the testing of the model;

Conclusion

The application of the Heuristic Model for SMART management in a medium-sized industrial enterprise in a specific economic entity gives rise to the following more important conclusions assessing the results of the testing:

- The Heuristic model for SMART management in a medium-sized industrial enterprise is applicable to the industrial enterprises in all fields of production.
- The Heuristic model for SMART management in a medium-sized industrial enterprise can also be applied in the management of small industrial enterprises.
- The Heuristic model for SMART management in a medium-sized industrial enterprise provokes continuous organizational development in the industrial entities, as a result of which new organizational structures and new information reporting and information and communication systems are created.

The practical and applied usefulness of the Heuristic model for SMART management in a medium-sized industrial enterprise is based on the adaptation of familiar management approaches, technologies and tools to the qualitatively new requirements of the environment provoked by the development of Industry 4.0 (digitalization) and Industry 5.0 (heuristic practices and assessments). The management in the industrial enterprises that are subjects of the testing perceives the Heuristic model for SMART management in a medium-sized industrial enterprise as an opportunity to increase the efficiency and the added value of the activities in the industrial enterprises.

Maintaining efficiency in industrial enterprises requires continuous monitoring, analysis and assessment of their activities which means continuous application of the seven stages of the Heuristic Model for SMART management in a medium-sized industrial enterprise. Using its software-based model, this can be done automatically, with minimal labour and data entry time. Difficulties may arise when putting the model into operation due to the need for a large volume of production, technological, financial and other operational data.

Scientific Ethics Declaration

The authors declare that the scientific ethical and legal responsibility of this article published in EPSTEM journal belongs to the authors.

Acknowledgements or Notes

* This article was presented as an oral presentation at the International Conference on Technology, Engineering and Science (www.icontes.net) held in Antalya/Turkey on November 16-19, 2023.

References

European Union. (2020). *User guide to the SME definition.* https://op.europa.eu/en/publication-detail/-/publication/756d9260-ee54-11ea-991b-01aa75ed71a1

Portal Registery Agency. (n.d.). Retrieved from https://portal.registryagency.

Temelkova, M. (2010). *Controlling in the production organization.* Varna: Colour print.

Author Information

Miglena Temelkova
University of Telecommunications and Post
Sofia, Bulgaria.
Contact e-mail: *megitemelkova@abv.bg*

Iliyan Bakalov
Ministry of Innovation and Growth
Sofia, Bulgaria.

To cite this article:

Temelkova, M., & Bakalov, I. (2023). Validation pf the heuristic model for SMART management in a medium-sized industrial enterprise. *The Eurasia Proceedings of Science, Technology, Engineering & Mathematics (EPSTEM), 26*, 332-340.

The Eurasia Proceedings of Science, Technology, Engineering & Mathematics (EPSTEM)
ISSN: 2602-3199

The Eurasia Proceedings of Science, Technology, Engineering & Mathematics (EPSTEM), 2023

Volume 26, Pages 341-347

IConTES 2023: International Conference on Technology, Engineering and Science

Geophysical Techniques for Monitoring of Integrated Mine Waste Storage Facility: Case Study of Southeastern Bulgaria

Maya Tomova
University of Mining and Geology

Abstract: The extraction of mineral resources usually generates varying amounts of extractive waste, which require appropriate management. Extractive waste management is complicated and difficult process. It encompasses a lot of actions and many different competences. Here must be taken into account the mining excavation method, processing methods, beneficiation and overall mineral treatment. The results obtained from these study provide an important basis for the quantification and management of environmental impacts of the Integrated mine waste facility (IMWF) at the “Ada Tepa” gold mine. The aim of this research is to monitoring the process of internal water drainage into constructed cells of the facility. This task is performed using geophysical method based on electrical resistivity measurements made on the ground surface. Electrical resistivity tomography is commonly used to solve mining and engineering issues, because it is efficient and environmentally sound. This study demonstrates the efficiency of electrical resistivity tomography in detecting the saturated zones in the IMWF.

Keywords: Waste management, Electrical resistivity tomography, Water drainage, Monitoring.

Introduction

Bulgaria has old traditions in mining and processing of gold-bearing ores. Gold mining and processing in the Bulgarian territories has been practiced since ancient times. Currently, the main gold mining in Bulgaria is realized from copper and gold-bearing ores from the "Chelopech", "Elatsite" and "Asarel" deposits. Gold-bearing ores are available in "Khan Krum", "Chala", etc. deposits (Grigorova & Nishkov, 2016). The mining industry is witnessing an epochal revolution due to the metals growing demand (copper, iron, aluminum, nickel, gold), industrial minerals and energy resources (oil, uranium) all over the world and especially in the currently developing economies such as China, India and Brazil.

“Ada Tepe” gold mine is the oldest gold mine in Europe. It is located near Krumovgrad, on the summit of the Ada Tepe ridge and has operated from 1500 to about 600 BC. The region is part of the Eastern Rhodopes Massif, which hosts the eastern portion of a large metamorphic terrain. Gold and silver mineralisation in the Krumovgrad area is mostly identified within the Shavar Formation proximal to the unconformable fault contact or detachment with the underlying basement rocks of the Kessebir core complex. Base on the information from several drillings in the investigated area the following rocks are observed: clay, breccia conglomerate, breccia conglomerate with quartz inclusions and metamorphic clasts (Grigorova, 2020).

Open-pit method of mining is proposed for the “Ada Tepe” gold mine. It is used drilling and blasting works followed by loading by hydraulic excavators and haul trucks for the transportation of the extracted material. Conventional processing methods, including crushing, grinding, and flotation processing are employed for extracting gold at the “Ada Tepe” gold mine. Mineral processing generally is focused on extracting the most valuable components from the ore, while the rest of the material is disposed at the tailing ponds. Mining and ores beneficiation generate waste that have to be properly managed to reduce environmental risks. Plenty authors (Tayebi-Khorami et al., 2019; Yankova, 2020; Yankova, 2021), emphasize the key problems with

mining and processing waste along with particular tailings storage, mining waste amount reducing and safe storage. Effective waste management is the basis of sustainable development. Many experts contend the present stage of mineral-raw material industry evolution is describing by mineral deposits with complex mining-geological conditions, difficult for mining, low grade ores with complex processing, which leads to considerable waste quantities formation. Waste proper storage is critical to the planet and human health.

Extractive waste management is usually part of the overall ore extraction and the treatment of minerals. In the "Ada Tepa" gold mine for waste deposition is used Integrated Mine Waste Facility (IMWF). The idea behind the IMWF is to place thickened tailings into cells constructed from mine rock, because they provide strength required for overall stability and also internal drainage. It is known that tailings tend to have a lower vertical permeability than horizontal permeability and the IMWF exploits this characteristic fully by depositing the tailings into cells and the berms acting as dewatering pathways. The underdrain system collects and convey the rainfall and the excess pore water from the consolidation of the tailings. A two zone filter system will be placed to prevent tailings being carried through the outer rock berm (Diaz, 2014).

The aim of this research is to monitoring the effect of internal water drainage into constructed cells. For this purpose, is used popular non-destructive geophysical technique – electrical resistivity tomography. The investigation is performed in period of six months and has to evaluate the progress of water drainage into constructed cells during this period.

Description of the Technology

Generally speaking, mineral treatment consists of two main steps (Grewal, 2016; Kauppila et al., 2013). The first step, the comminution, is to reduce the size of the extracted materials and prepare the ore for the next step. Comminution consists of crushing, grinding, screening and classification steps. During that stage of the process, the ore is transformed into a granular material with a specific grain size depending on the mineral. The grain size is selected to allow the liberation of the targeted minerals during the beneficiation stage. The second step, the beneficiation, is to separate the valuable mineral resources from the rest of the ore, known as the gangue, in order to concentrate one or more targeted mineral resources in a product, also called concentrate. Beneficiation can be achieved using one or a combination of different types of processes - sorting, gravity concentration, magnetic separation, electrostatic separation, flotation processes, leaching processes and dewatering.

The gold ore is processed in dressing plant, involving a crushing and milling followed by froth flotation to produce gold and silver concentrates. Mineral processing waste, the gangue, are thickened to paste and disposed in Integrated Mine Waste Storage Facility, along with waste rocks (Grigorova, 2020). It is important to understand the stages in the process of ore preparation and processing at their basics, because the gangue and the non-valuable mine rocks are the core of the Integrated Mine Waste Facility. Their chemical composition and structure are important for the strength and stability of the facility and also are essential for the internal drainage.

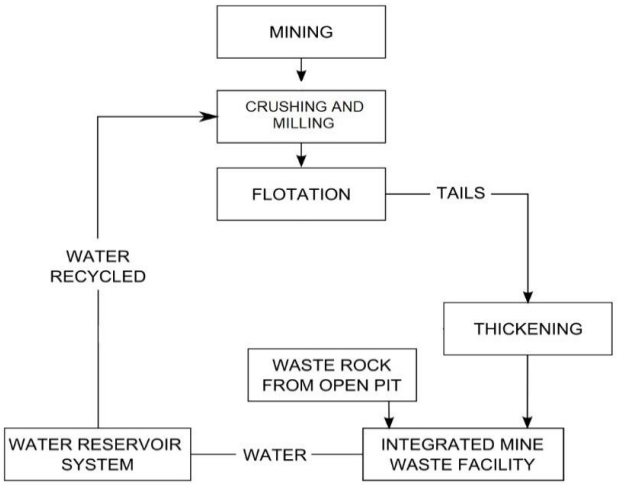

Figure 1. Overall flowsheet

The extraction of mineral resources may generate different amount of extractive waste, which require appropriate management. According to White et al. (2020) the mining method used at the Ada Tepe gold mine

is a conventional open pit, drill, blast, load and haul operation, using hydraulic excavators and haul trucks to mine the material. Ore is processed by crushing the mined ore in the primary jaw crushing circuit, grinding in a semi-autogenous grinding ("SAG") milling circuit followed by a further secondary grind in a vertimill circuit. Tailings and waste rock material from the mine are placed in an Integrated Mine Waste Facility ("IMWF") (White et al., 2020).

Mine waste rock and tailings are typically the two major waste types at mine sites. In the process of mining operation, the mine rock is trucked from the open pit to the IMWF, dumped and spread to construct containment cells for the tailings. Tailings are then thickened in the tailings thickening plant to the maximum practical amount (between 56-68% solids), and then conveyed by pump and pipeline to the containment cells. The IMWF is design to be a fully drained facility without a water pond during its operation. A system of underdrains is constructed along the axis of each small surface water channel in the footprint of the IMWF and these drains are prompted to discharge to one of two sumps located at the toe of the facility. Water reporting to the underdrain is pumped to the Raw and Process Water Reservoir ("RPWR") located southwest of the open pit. The underdrain system will collect and convey the rainfall and the excess pore water from the consolidation of the tailings. Water draining from or through the IMWF is collected and treated in the existing wastewater treatment plant (Diaz, 2014). The fast drainage of water is important for the faster consolidation of the tailings leading to better operational sequence as it is of crucial meaning (Eldridge et al., 2013). For this problem to be mitigated and to be better managed Aleksandrova et al. 2021 suggested that the critical path method (CPM) can be used.

Initial mine waste characterisation is essentials for any planning of the management of mine waste. It may be used for the classification of extractive waste, i.e. inert, non-inert non-hazardous or hazardous. Only if this background work is done properly appropriate management measures can be applied. Quality assessment and monitoring is performed using electrical resistivity tomography method. It is geophysical technique, which inject electrical current into the ground surface and couple of electrodes to measure the resistivity of the media. Electrical tomography method has the potential to provide fast and reliable information for observed area based on electrical resistivity (Dimovski et al., 2017).

Field Measurements and Results

The precise location of the geophysical surveying lines in the area of Integrated Mine Waste Facility is illustrated in Figure 2.

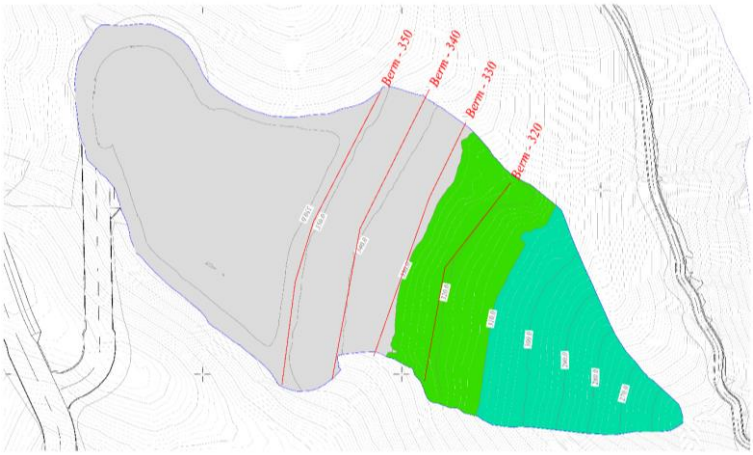

Figure 2. Field measurements situation plan

The ERT field measurements were performed along 4 lines. The total length of the measured profiles is 740m, and their exact location is presented in Figure 2. The aim of electrical resistivity survey is to measurethe resistivity distribution in the subsurface by conducting measurements along the ground surface. Apparent resistivity data were collected with a Wenner-Schlumberger array and distance of 10m between the electrodes (a total of 24 electrodes per arrangement). Electrical resistivity tomography data was process and analyzed using RES2DINV software. This computer program automatically determines the 2D resistivity model for the observed data (Griffiths, 1993). This study demonstrates the efficiency of application of electrical resistivity tomography (ERT) in detecting the saturated zones in the IMWF. This research will help in sustaining the berm stability via indicating the position of water saturated zones and water pathways.

Table 1. Total length of each line of integrated mine waste facility

Line	Berm - 350m	Berm - 340m	Berm - 330m	Berm - 320m
Length, m	210	210	170	150

The comparison of interpreted ERT sections is presented on Figure 3 to Figure 6.

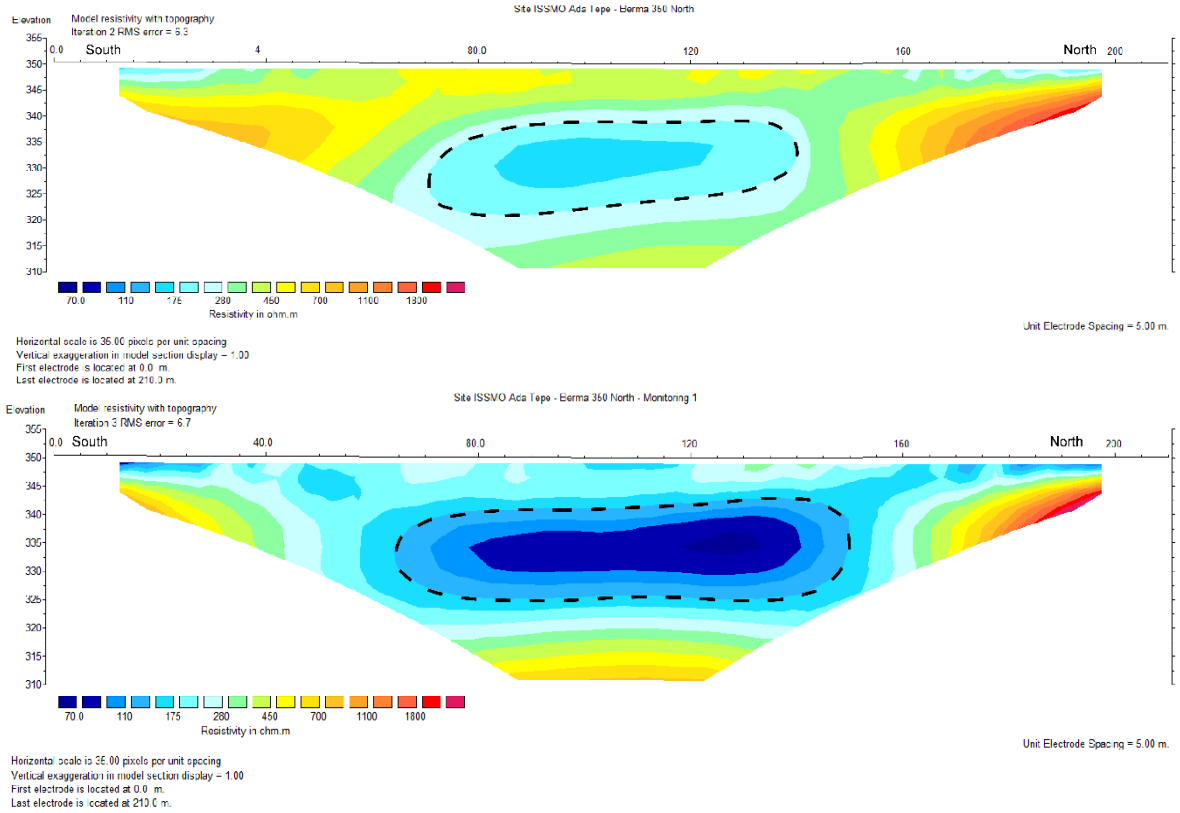

Figure 3. ERT section along Berm 350m measured in February 2020 and again in July 2020

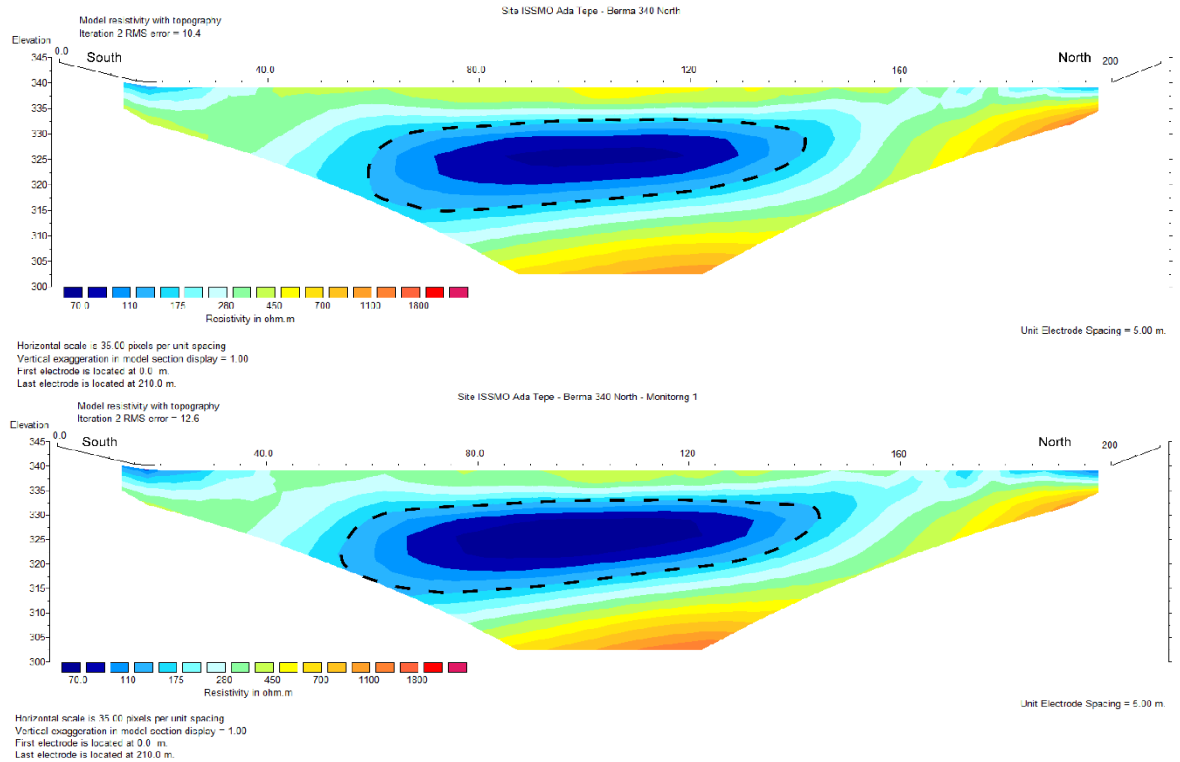

Figure 4. ERT section along Berm 340m measured in February 2020 and again in July 2020

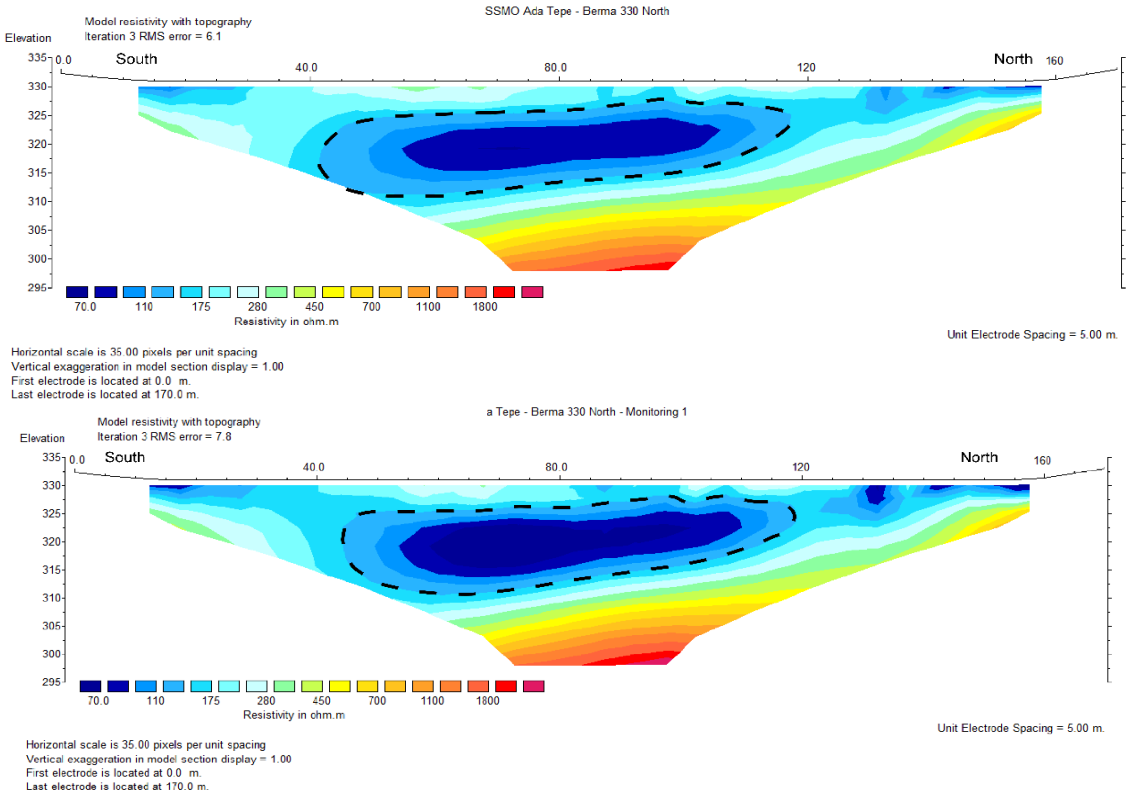

Figure 5. ERT section along Berm 330m measured in February 2020 and again in July 2020

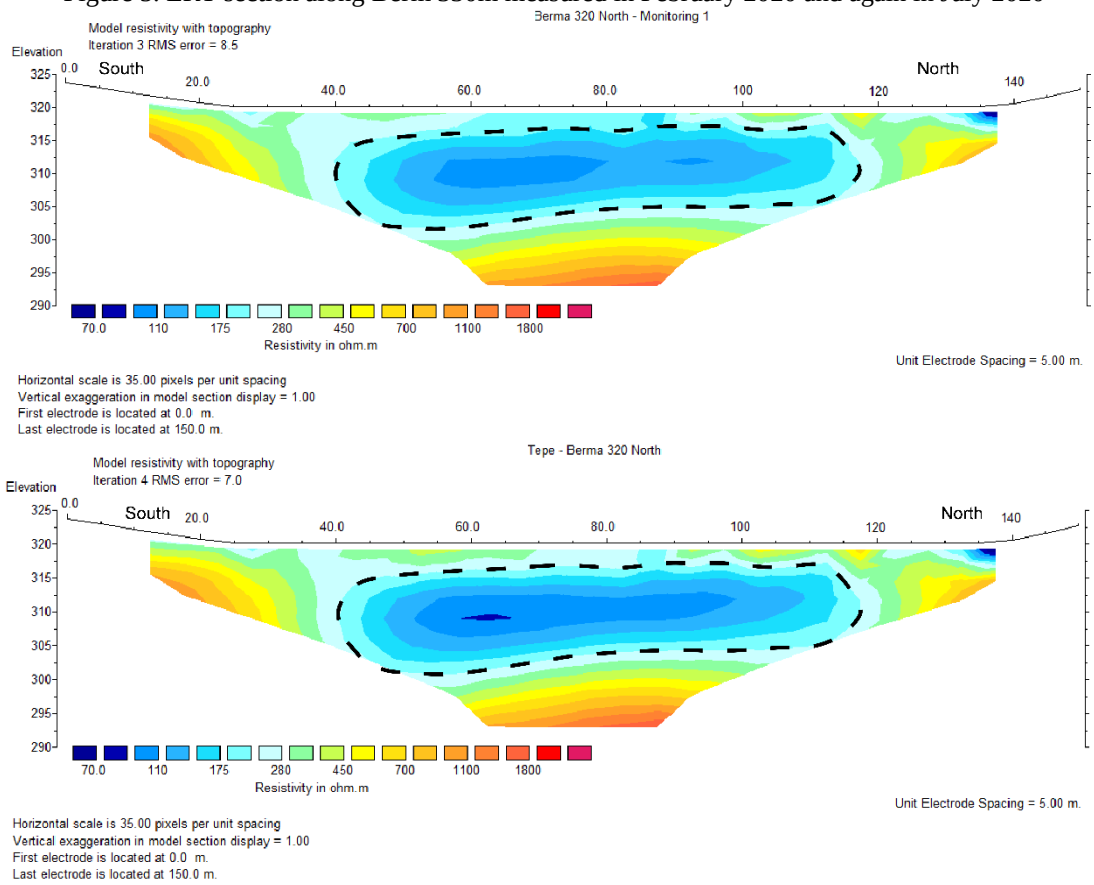

Figure 6. ERT section along Berm 320m measured in February 2020 and again in July 2020

From the comparison of the results between ERT measurements made in February and in July, can be drawn the following conclusions about the behavior of the zones that mark the spatial distribution of a zone with increased water saturation due to the incomplete drainage of the deposited material:

- The comparison of the electrical resistivity distribution on the ERT section along Berm 350m (Figure 3) shows that the area is currently much better defined with reduced resistance values. This is most likely due to the mining waste deposition during the period February - July in a cell with a design bottom of 340 m;
- The comparison of the electrical resistivity distribution on the ERT section along Berm 340m (Figure 4) shows that the area is currently similar in its electrical resistivity distribution, but with a slight increase in the southern direction, which corresponds to the slope of the natural terrain.
- The comparison of the electrical resistivity distribution on the ERT section along Berm 330m (Figure 5) shows that the area is currently similar in its appearance. There is a slight decrease in the electrical resistivity values, due to partial drainage of the deposited material.
- The comparison of the electrical resistivity distribution on the ERT section along Berm 320m (Figure 6) shows that the area is currently similar in its appearance. There is a very slight decrease in size, also suggesting slight drainage of the deposited material. This is also confirmed by the small increase in electrical resistivity values in the central part of the zone.

Conclusion

Mine waste treatment is a complex process. The effective and safe deposition of extractive wastes presents technical and environmental challenges. Each integrated mine waste facility is tailor-made and a sound approach is needed to ensure that the extractive waste management is safe and environmentally sound while also economically viable. Many efforts have been made in the last few decades by the extractive industries to prevent, reduce and minimise as far as possible the negative impacts as a result of the management of extractive waste and the extraction activities.

An integrated mine waste facility is considering to occupy a smaller footprint compared to a conventional slurry tailings impoundment due to an increased maximum stacking height and higher densities than can be achieved by conventional methods. The monitoring of the process of dewatering is essential to ensures the effectiveness and long-term stability of waste and tailings. The integrated waste mine facility in "Ada Tepe" gold mine deposit significantly reduces the mine footprint and also facilitates mine closure in the future. Construction and operation monitoring, management and quality assurance of the risks that tailings storage facilities pose to the environment and society is very important for the proper functioning of the mining sector at all. The question of how mine waste facilities can be effectively managed to avoid unwanted effects is essential for the long-term development of the industry.

Scientific Ethics Declaration

The author declares that the scientific ethical and legal responsibility of this article published in EPSTEM journal belongs to the author.

Acknowledgements or Notes

* This article was presented as an oral presentation at the International Conference on Technology, Engineering and Science (www.icontes.net) held in Antalya/Turkey on November 16-19, 2023.

References

Aleksandrova, E., Dimitrov, L., & Kaykov, D. (2021). Operational sequence for constructing a combined mine waste facility. *XVI International conference of the open and underwater mining of minerals* (pp. 7-13). Varna.

Diaz, M. (2014). Evaluation of liner requirement – Krumovgrad integrated mine waste facility (A150-14-R2243). Retrieved from https://s27.q4cdn.com/486073686/files/doc

Dimovski, S., Stoyanov, N., Tzankov Ch.,& Kisyov, A. (2017). Application of electrical resistivity tomography for studying fissure-karst water-bearing complexes, Proceedings of the *9th Congress of the Balkan Geophysical Society*, 1-5. Antalya, Turkey.

Eldridge, T., Kissiova, M., Wickland, B., Ahmed, I. B., & Laurin, J. F. (2013). Integrated mine waste storage facility, Krumovgrad gold project, Bulgaria. *XV Balkan Mineral Processing Congres*s. Sozopol.

Grewal I. (2016, Jun 1). *Mineral processing introduction*. Retrieved from http://met-solvelabs.com/library/articles/mineral-processing-introduction.

Grigorova, I., I. Nishkov. (2016) *Technogenic raw materials processing and recycling*. Annual of University of Mınıng and Geology. Sofia, Bulgaria: St. Ivan Rilski",,

Grigorova, M. (2020). Geophysical and mining technologies for increasing efficiency in Han Krum open pit mine, Bulgaria. *20th International Multidisciplinary Scientific GeoConference SGEM 2020, 20*(1.2), 111-118. Albena, Bulgaria

Kauppila P., Räisänen M. L. and Myllyola S. (2013). *Best environmental practices in metal ore mining.* Finnish Environment Institute

Tayebi-Khorami, M., Edraki, M., Corder, G., & Golev, A. (2019). Re-thinking mining waste through an integrative approach led by circular economy aspirations, *Minerals, 9*(286), 1-12.

White, G., Olden, K., Patrick, G., Kuzmanova, P., O'Connor, M. (2020). Technical report – mineral resource and mineral reserve update. *Ada Tepe mine (NI 43-101).*

Yankova, T. (2020). Mineral processing waste utilization. *XX International Multidisciplinary Scientific GeoConference SGEM, 20*(1-1), 219-226. Albena, Bulgaria.

Yankova, T. (2021). Mining damaged landscape reclamation study, *XXI International Multidisciplinary Scientific GeoConference SGEM, 2*(1-1), 383-390. Albena, Bulgaria.

Author Information

Maya Tomova
University of Mining and geology “St. Ivan Rilski”
Sofia, Studentski grad, prof. Boyan Kamenov", Sofia 1700
Sofia, Bulgaria
Contact e-mail: *maya.grigorova86@gmail.com*

To cite this article:

Tomova, M. (2023). Geophysical techniques for monitoring of integrated mine waste storage facility: Case study of Southeastern Bulgaria. *The Eurasia Proceedings of Science, Technology, Engineering & Mathematics (EPSTEM), 26*, 341-347.

The Eurasia Proceedings of Science, Technology, Engineering & Mathematics (EPSTEM)
ISSN: 2602-3199

The Eurasia Proceedings of Science, Technology, Engineering & Mathematics (EPSTEM), 2023

Volume 26, Pages 348-356

IConTES 2023: International Conference on Technology, Engineering and Science

Proposal for Generation of a Pseudo GPS Signal Used in Indoor Mode for Navigation Testing of Small Autonomous Flying Robot

Latroch Maamar
Hassiba Benbouali University of Chlef

Aissa Bokhtachte Aicha
Hassiba Benbouali University of Chlef

Toualbia Asma
Hassiba Benbouali University of Chlef

Abstract: In addition to the inertial navigation sensors embedded in an autonomous flying robot, Global Navigation Satellite Systems are most often used, in particular, the GPS (Global Positioning System). This offer information with an accuracy that depends on the arrangement of a constellation of satellites. It is very often that a measurement with errors of several meters is delivered by this system. With the need for agile decisions of the autonomous flying robot during its mission, especially in the case of rescuing people during disasters, it is not allowed for uncertainty to reign over the decision of the flying robot. In order to improve the estimators implemented experimentally, a secure laboratory test environment is more preferable. Here, we propose a way that helps researchers to conduct indoor experiments with a pseudo GPS that offers circumstances similar to outdoor navigation. The results that will be discussed are obtained with the Vicon motion tracker laboratory at Aalborg University, Denmark.

Keywords: Pseudo GPS, Outdoor navigation, UAV, Vicon motion tracker system

Introduction

Autonomous flying robots have the potential to revolutionize many industries and applications, such as delivery, logistics, search and rescue, and disaster relief. However, developing autonomous flying robots that are safe and reliable in real-world conditions is a challenging task. One of the main challenges is outdoor drone navigation, which is estimating the drone's position accurately in complex and dynamic environments.

Indoor autonomous flight tests of flying robots are only a preliminary step in developing controllers for real-world applications. In the real world, flying robots will not have access to the same navigation instruments that provide such accurate and convenient measurements of position and attitude. For example, GPS signals can be lost or unreliable in outdoor environments, and other sensors may also be inaccurate, especially in difficult environments such as urban areas, forests, and disaster zones.

To develop estimators or controllers for outdoor applications, it is important to perform continuous tests in real-world conditions. However, this can be dangerous and expensive, and it can be difficult to control all of the factors that can affect the performance of algorithms. Moreover, the main challenge to outdoor drone navigation is estimating the drone's position accurately. GPS signals can be lost or unreliable, and other sensors may also be inaccurate, especially in difficult environments. This can make it difficult for the drone to make decisions, especially in critical missions like disaster rescue (Ross, 2018). In these cases, human pilots often need to take over to assist the mission.

One way to address these challenges is to use simulated environments to test and develop autonomous flying robots. However, existing simulated environments do not fully capture the complexity and dynamism of real-world environments. Benjamin(2008) was an early temptation to simulate the GPS for outdoor simulations. The implementation of a simulated Global Positioning System receiver for the popular USARSim platform(Stefano, 2007; Shital, 2017) developed a simulator for autonomous flying robots by first implementing a quadrotor and then experimentally comparing the software components with real-world flights. The simulator is built on Unreal Engine and offers physically and visually realistic simulations. It includes a high-frequency physics engine for real-time hardware-in-the-loop (HITL) simulations with support for popular protocols such as MavLink. The simulator is designed to be extensible to accommodate new types of vehicles, hardware platforms, and software protocols.

An advanced novel hybrid architecture that uses an intermediate output from a fully trained attention DRL (Deep Reinforcement Learning) policy is proposed as a navigation cost map for outdoor navigation. This DRL network incorporates a robot-centric elevation map and IMU data to learn how to navigate in outdoor environments. In (Kasun, 2022), authors propose a new hybrid architecture that uses an intermediate output from a fully trained attention DRL policy as a navigation cost map for outdoor navigation. This DRL network incorporates a robot-centric elevation map and IMU data to learn how to navigate in outdoor environments.

These Simulating navigation perceptions are very powerful in virtual reality and simulators, but testing flying robots in real time requires deep study, control development, and real-time data processing. This is because the robot's controller must make decisions based on very uncertain and inaccurate measurements during some time lapses. To develop estimators or controllers for outdoor applications, it is important to perform continuous tests in real-world conditions. This is because outdoor environments are complex and dynamic, with many factors that can affect the performance of algorithms, such as wind, temperature, and electromagnetic noise (Lorenzo, 2021;Mozhou Gao1,2021). Many researchers believe that indoor tests are a valuable tool for developing and testing flying robot controllers. However, it is important to note that indoor experiments cannot fully prepare robots for the real world. One of the most successful indoor navigation methods is to use a constellation of cameras equipped with infrared sources, such as the Vicon MotionTracker system (VMTS). VMTS is commonly used to capture movement indoors for applications such as motion capture and virtual reality. Outdoor environments are more complex and challenging than indoor environments, with factors such as GPS outages, wind, and obstacles that can make it difficult for robots to navigate. Therefore, it is important to perform real-world testing of flying robots to ensure that their controllers can perform reliably in challenging environments. To develop algorithms that can reliably operate in the real world, it is important to first test them in controlled environments, such as indoors. However, GPS measurements are not available indoors, so alternative navigation methods are needed.

This paper proposes to modify a motion tracker system (VMTS) to generate simulated GPS measurements based on real Vicon motion tracking data. This simulated GPS can then be used to study the autonomy of flying robots in outdoor conditions without the need for real GPS signals. The modeling and performance of this simulated GPS will be discussed further in this paper.

The present paper is organized into five sections. The first section will briefly review satellite system positioning. The second section will describe the test bench used for the experiments, including the VMTS laboratory. The third section will describe the control scheme used during the experiments. The fourth section will present an approach to simulating the GPS signal. And, the fifth section will present the results of the experiments and conclude the paper.

GPS vs. Motion Tracker System

Accuracy of GPS Localization

GPS is a satellite-based navigation system that provides location, timing, and velocity information to users around the world. It can track the position of objects with an accuracy of up to 5 meters in most cases. GPS works by using a constellation of 30 satellites that transmit microwave signals to GPS receivers on Earth. The receiver calculates its distance from each satellite by measuring the time it takes for the signal to travel from the satellite to the receiver. By knowing its distance from three or more satellites, the receiver can calculate its position in three dimensions (Figure.1).

Figure1. GPS constellation

GPS accuracy can be affected by a number of factors, including atmospheric conditions, satellite geometry, signal blockage or interference, receiver quality, and the presence of buildings or natural obstacles. For civilian use, the US government intentionally degrades the accuracy of the GPS signal, but this was stopped in 2000. There are other global navigation satellite systems (GNSS), such as GLONASS, Galileo, and BeiDou, which can improve accuracy and reliability by using signals from multiple satellite constellations.

There are also differential GPS (DGPS) techniques that can further enhance accuracy by using additional reference stations to correct GPS measurements. In good conditions with a modern GPS receiver, we can expect accuracy within a few meters. However, the actual accuracy experienced in practice can vary depending on the factors mentioned earlier. The US Space Force is developing a new satellite constellation for localization, called the Next Generation GPS (NGGPS). The NGGPS is expected to provide more accurate and reliable positioning than the current constellation, and is expected to be fully operational by 2030. However, there is still much work to be done on developing controllers and estimators that can take advantage of the improved accuracy and reliability of the NGGPS.

Motion Tracker Accuracy

Analogous to a satellite constellation, but optic source, the motion tracking system typically consists of multiple cameras placed around the test area. These cameras are synchronized to capture the movement from different angles simultaneously. The cameras track the positions of reflective markers placed on the flying robot, allowing for accurate and detailed motion capture.

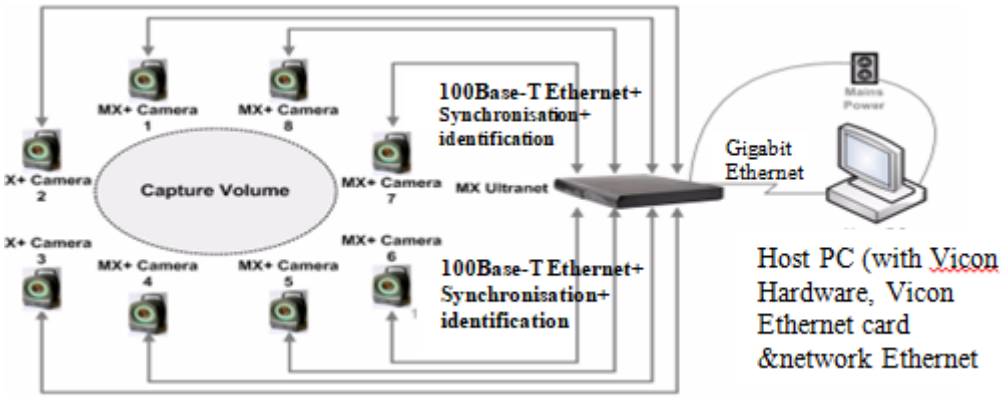

Figure 2. Basic Vicon MX architecture

ViconX motion trackers from Vicon were used in this study at the UAV Laboratory, Aalborg University, Denmark. VMTS accuracy depends on the number of cameras used, their placement, and the quality of the reflective markers. Nevertheless, VMTS is ultra-accurate compared to GPS, tracking 3D positions to 0.1 mm and rotations to 0.01 degrees.

GPS Simulator: Pseudo GPS

To simulate the real GPS signal in the laboratory, we will use the Motion Tracker Lab to track a quadrotor's position and inject a noise signal into the outputs of the Vicon MX system (see Figure 3).

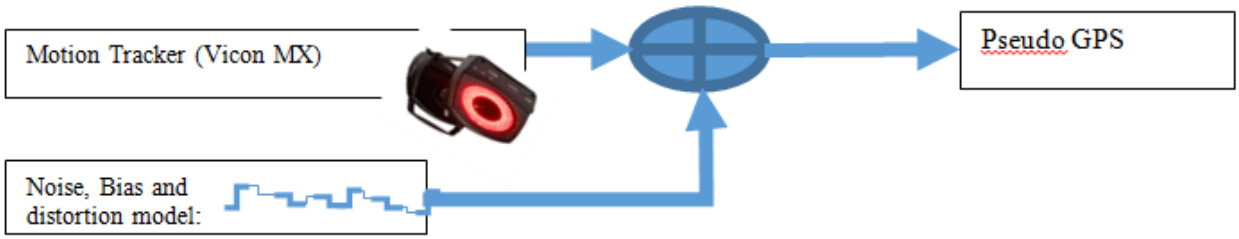

Figure 3. GPS simulator for indoor tests

Quadrotors are a good choice for indoor testing because they are versatile and well-suited for this purpose. They are relatively small and agile, making them easy to maneuver in confined spaces. They are also relatively quiet, making them less disruptive to people and activities in the vicinity. Quadrotors can also hover in place, making them easy to keep track of and control. The noise signal will have the same characteristics as the real GPS variance, but the limited space in the laboratory prevents us from running tests with an uncertainty cube greater than the size of the laboratory. We use a noise signal with a standard deviation of 30 cm, resulting in a positional uncertainty of less than 0.3 m in each direction. This space surrounding the quadrotor, known as the uncertainty cube, is shown in 3D in Figure.4. This means that the quadrotor will be able to fly freely within the laboratory, but it will not be able to experience the same level of uncertainty as it would in an outdoor environment. This is a limitation of the laboratory setup, but it is still possible to perform valuable tests and simulations of outdoor flight conditions.

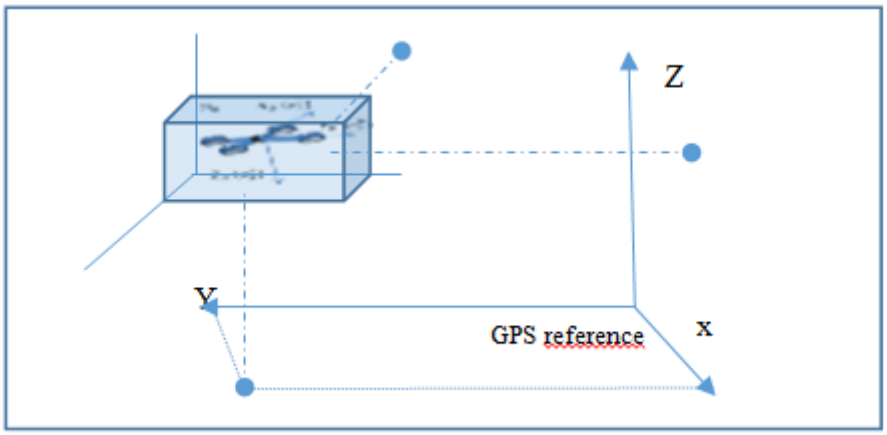

Figure 4. Cube of navigation uncertainty of the GPS

GPS Update Algorithm

To avoid malfunction or instability of the drone platform, a condition is necessary to proceed with a GPS update. This is the uncertainty cube that bounds the errors committed by the inertial measurement unit (IMU). The IMU is a collection of sensors that measure the drone's acceleration, rotation, and orientation. It is a critical component of the drone's control system, as it provides the drone with feedback on its current state. However, the IMU is susceptible to errors, which can accumulate over time.

The uncertainty cube is a mathematical representation of the possible errors in the IMU's measurements. It is a three-dimensional cube, with each axis representing a different error dimension (position, velocity, or orientation). The use of the uncertainty cube is a common technique used in drone control systems. It is a simple and effective way to improve the accuracy and reliability of the drone's navigation system. The size of the uncertainty cube represents the maximum possible error in each dimension. In summary, the uncertainty cube is a measure of the possible errors in the IMU's measurements. The drone's control system uses the uncertainty cube to determine when to trust the GPS measurement instead of the IMU's measurement.

A variety of algorithms to compare the GPS measurement to the estimated state and determine when to trust the GPS measurement has been developed in literature, (Aniket et al., 2022). The drone's control system uses the IMU's measurements to estimate the drone's current state. In time, the IMU's errors accumulate, and the estimated state may become inaccurate. The drone's control system can compare the GPS measurement to the

estimated state to detect when the IMU's errors have become too large. If the GPS measurement is outside of the uncertainty cube, then the control system can assume that the IMU's errors are significant and that the GPS measurement is more credible. Algorithm in figure.5 gives an overview of this procedure. Where the uncertainty cube is represented as limits of the tolerance of the estimate on the three Cartesian axis.

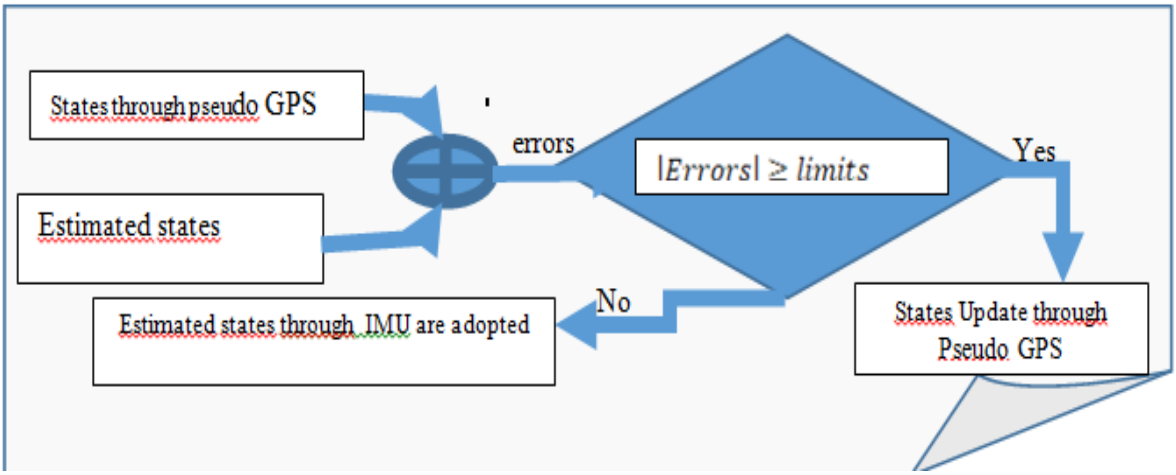

Figure 5. Quadrotor estimated states on cartisian axis update Algorithm

Indoor Experiments

The test bed consists of a laboratory equipped with a motion tracker system, a flying robot and a Matlab environment. The robot used in this study is a quadrotor X3D-BL from Ascending Technologies. It has the advantage of allowing access to its inertial sensor data for remote reading during flight. The radio remote control that links the ground pilot to this drone can also be accessed and manipulated by a URT communication. In a MATLAB environment, the position measurements from the inertial sensors are fused with the navigation data generated by ViconX. Thanks to the quadrotor model and the controller implemented by (Latroch,2019), commands are generated and sent autonomously to the robot's pilot.

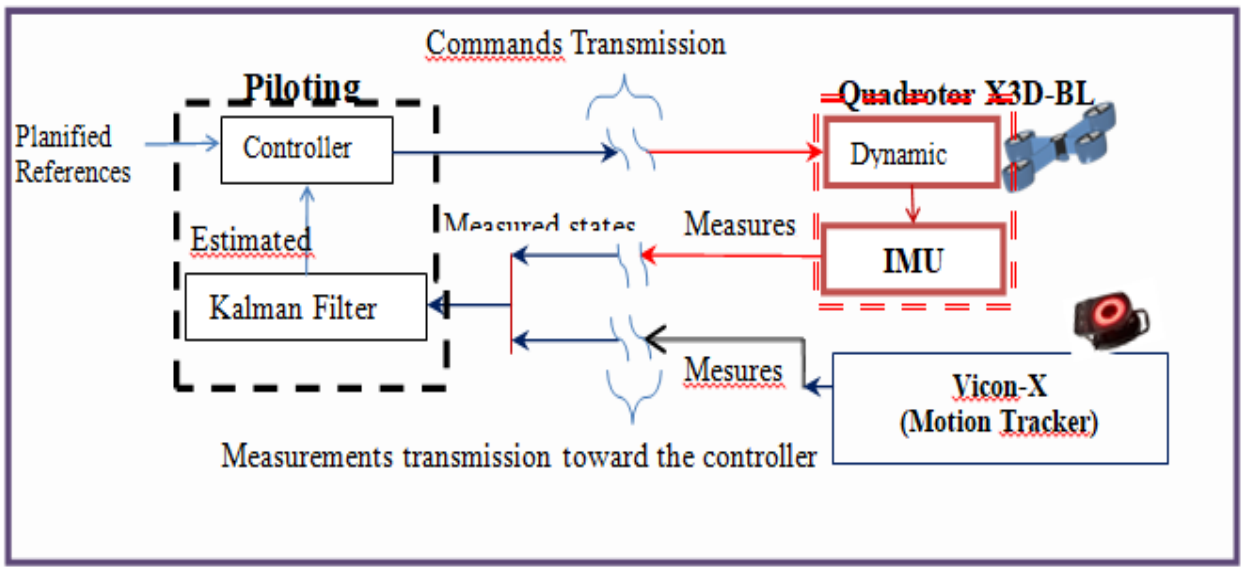

Figure 6. Closed Loop control of quadrotor X3D-BL scheme

The implemented controller is a linear-quadratic regulator (LQR). Due to noise and uncertainty in the measurements, it is always difficult to predict the integrated data from this model due to the accumulation of errors. Therefore, it is important to add an estimator filter capable of rejecting the terms induced by the noise process in order to obtain an output ready for use during closed-loop control. The diagram in Figure.6 illustrates the position of the controller in the closed-loop scheme of the quadrotor X3D-BL.

This controller is located on the pilot side with the extended Kalman filter. The IMU and motion tracker system measure the quadrotor's navigation states, which are sent to the controller via radio link. The Kalman filter then processes and fuses the data to generate an estimate of the quadrotor's navigation status as close as possible to its real position and attitude at the current moment. Based on this estimate, the controller can compare the quadrotor's actual state of navigation to the pre-planned trajectory. It can then send the appropriate control signals to the quadrotor's blades via radio link to autonomously follow the desired trajectory.

Tests of the Model and Controller

This same section describes indoor flight tests of a quadrotor assisted by a motion tracker. The quadrotor model was developed through identification and can be summarized as follows:

- The quadrotor is a nonlinear system with six degrees of freedom.
- The quadrotor's state is defined by its position, velocity, and attitude.
- The quadrotor's control inputs are the thrust and torque of the four propellers.
- The quadrotor's dynamics are described by a set of differential equations.

The controller is designed to stabilize the quadrotor and track a desired trajectory. It is implemented using a linear-quadratic regulator (LQR).

Results

Figure 7 shows the position of the quadrotor during a flight test, confirming the model's ability to describe the quadrotor's behavior successfully. The quadrotor is flying in a straight line, and the model's prediction of the quadrotor's position closely matches the actual position. This indicates that the model is accurately capturing the quadrotor's dynamics.

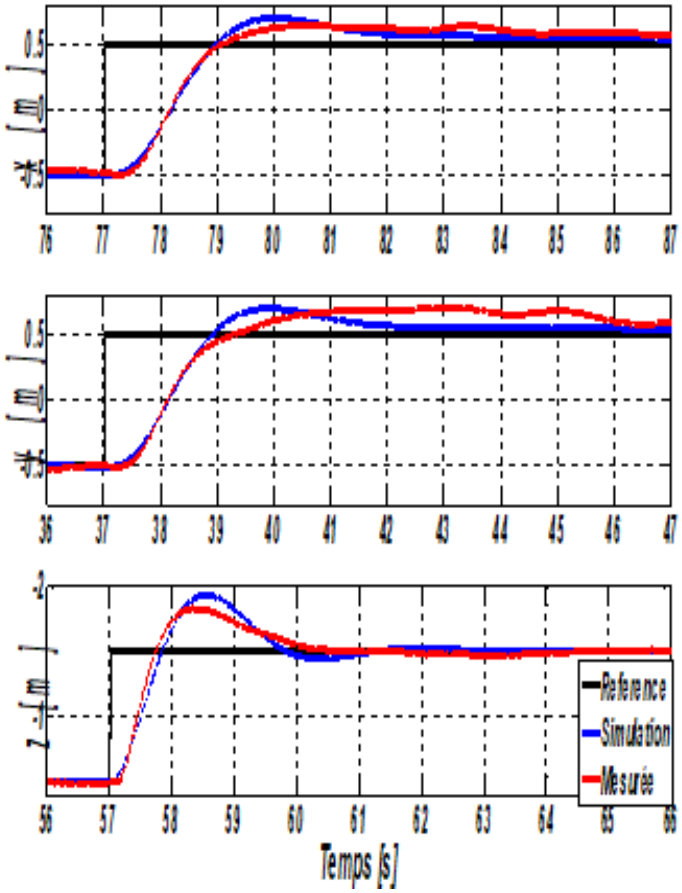

Figure 7. Comparison of step reference responses in cartesian positions: Simulation vs. Real X3-BL Quadrotor controlled by LQR in indoor flight test

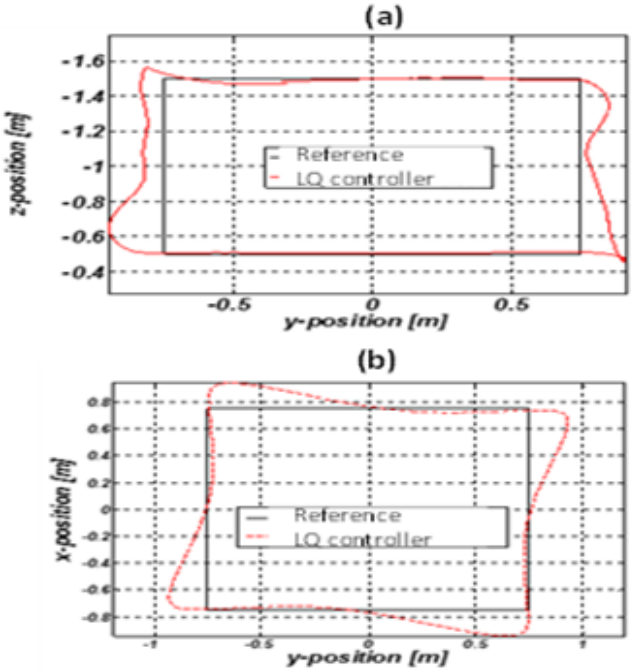

Figure 8. "Practical results of pre-planned trajectory tracking (Rectangle) of the quadrotor with LQ controller"
(a) Reference rectangle in [OY, OZ] (b) Reference rectangle in [OX, OY]

Figure 8 shows that the quadrotor can also track a pre-planned trajectory in the (x,y) plane with good accuracy. The quadrotor is following a square pattern, and the actual trajectory closely matches the desired trajectory. This indicates that the controller is able to effectively command the quadrotor to follow the desired path

The flight test results are encouraging and demonstrate the potential of the model and controller for real-world quadrotor applications. However, the controller can overshoot when changing direction, causing deviations from the trajectory near the corners of a rectangle. Despite this limitation, the model is still sufficient for testing purposes when the motion tracker is replaced with a GPS navigator. In the next section, we will perform the same flight tests, but with a simulated GPS signal generated through a modified motion tracker data sent to the controller.

Flight Test with Pseudo GPS Navigator

The following points will be considered during these tests. To wit that:

- The pure motion tracker (Vicon MX) will serve as a means of measuring the true position of the quadrotor without directly intervening in the correction.
- The drone will execute its flight using the pseudo GPS.
- Algorithm of figure.5 is considered for the generation of updates.
- The error tolerance limit, within the uncertainty cube between the estimate and the measurement by the pseudo GPS, is taken to be ± 0.3 meters on each Cartesian axis.

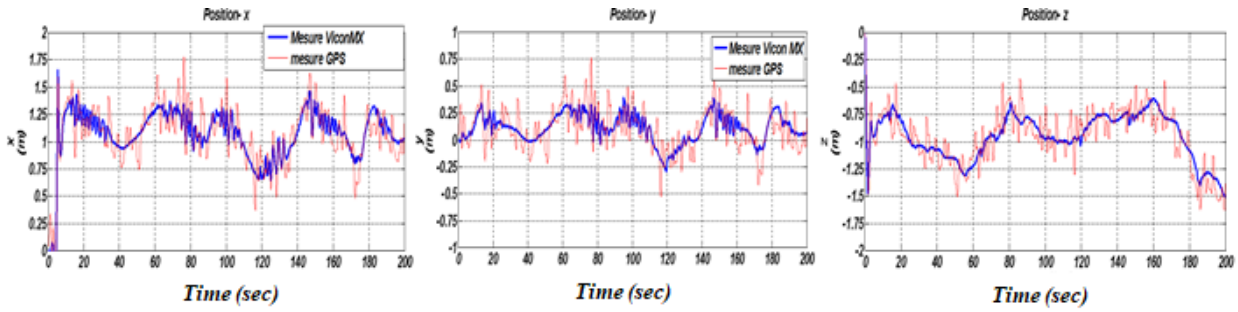

Figure 9. quadrotor xyz position during hovering flight around the cartisian position (1,0,-1) meseared by the Vicon MX and the pseudo GPS.

A hovering flight test of the quadrotor shows that the intrinsic errors of the inertial core induce, slowly, deviations of the quadrotor from the desired reference. Figure.9 shows the true position of this drone as seen by Vicon MX and Pseudo GPS. It is well noted from this figure that the drone performs a stationary flight with continuous displacement around the reference assigned to the controller. However, this displacement does not exceed the uncertainty band of the pseudo GPS in each direction. Updates are performed only when the estimate exceeds the error limits. This is the case during the time interval in seconds [10 30] and the time interval [140 160] where the controller start to relay on the pseudo GPS to control the quadrotor.

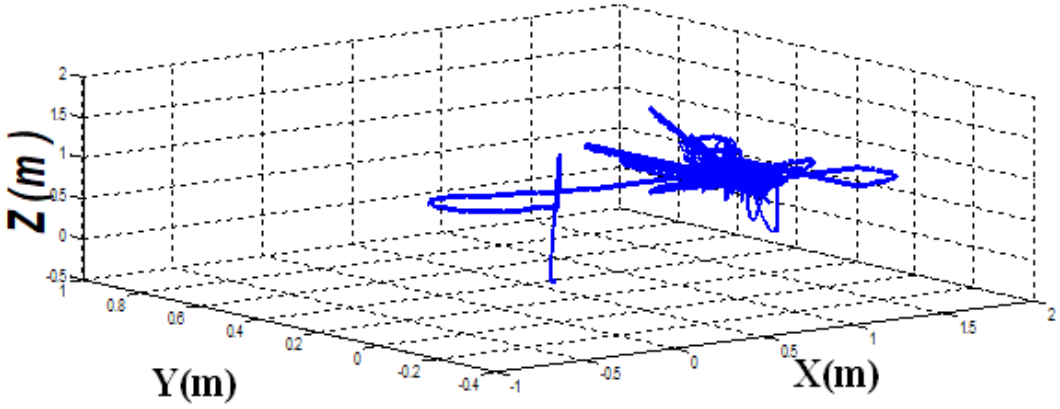

Figure .10 provides another three-dimensional overview of the pseudo GPS navigation from the hovering test.

As shown in this figure, the quadrotor is still flying inside the desired cube of uncertainty despite the distorted GPS signal. When these deviations exceed the estimation limit relative to the pseudo GPS measurement, an update is introduced. At this point, the controller becomes aware of its true position and begins to correct its errors.

Conclusion

To perform indoor tests of a flying robot that closely resemble real-world outdoor GPS navigation, we have developed and tested a new algorithm to substitute the GPS with a simulated GPS through a motion tracker. First, we confirmed the accuracy of the quadrotor model and the effectiveness of the controller using indoor tests. Then, we started injecting noise, biases, and distortions into the motion tracker data to simulate real-world GPS navigation.

A GPS simulator is a pseudo GPS that allows us to control the conditions in which the drone is being tested. This can be important for testing the performance of the drone in different environments, such as different levels of noise or interference. A GPS simulator can be used to troubleshoot problems with a drone's navigation system. By simulating different scenarios, one can identify the cause of the problem and develop a solution.

This pseudo GPS can be a cost-effective way to test drone navigation systems. Outdoor testing can be expensive, especially if one needs to travel to a remote location for safe tests. The results of this study show that the use of a motion tracker with this proposed algorithm is an efficient tool for outdoor conditions study simulation This algorithm provides a convenient tool for researchers to develop new models of GPS distortions and biases close to real GPS and perform tests in safe indoor environments without the influence of external.

Scientific Ethics Declaration

The authors declare that the scientific ethical and legal responsibility of this article published in EPSTEM journal belongs to the authors.

Acknowledgements or Notes

* This article was presented as an oral presentation at the International Conference on Technology, Engineering and Science (www.icontes.net) held in Antalya/Turkey on November 16-19, 2023.

*A part of this work has been established at the UAV LAB Aalborg University, Danemark. A special thank goes to Pr. Anders Lacour for the facilities provided during the tests.

References

Aniket, D., Kulkarni, Gaurav, G., Narkhede, Sumitra, N., Motade. (2022). Sensor fusion design by extended and unscented Kalman filter approaches for position and attitude estimation. *International Congress on Human-Computer Interaction, Optimization and Robotic Applications (HORA)*. IEEE.

Arnold, R. D., Yamaguchi, H., & Tanaka, T. (2018). Search and rescue with autonomous flying robots through behavior-based cooperative intelligence. *Journal of International Humanitarian Action 3*(1).

Balaguer, B., & Carpin, S.(2008). Where am I? A simulated GPS sensor for outdoor robotic applications. *International Conference on Simulation, Modeling, and Programming for Autonomous Robots SIMPAR: Simulation, Modeling, and Programming for Autonomous Robots*, 222–233.

Carpin, S., Lewis, M., Wang, J., & Balakirsky, S. (2007). USARSim: A robot simulator for research and education. Proceedings from *International Conference on Robotics and Automation*. IEEE

Gao, M., Hugenholtz, C. H., Fox, T. A., Kucharczyk, M., Barchyn, T., E., & Nesbit, P. (2021). Weather constraints on global drone fyability. *Nature Scientific Reports, 11*(1).

Kober, J., Bagnell, J.A., & Peters, J. (2013). Reinforcement learning in robotics: A survey. *International Journal of Robotics Research, 32*(11), 1238–1274.

Maamar, L., Ahmed, D., & Abdelhafid, O. (2019). A proposed use of Kalman gains behavior of navigation measurements for the sensor fault din quadcopter. *Instrumentation, Mesures, Métrologies I2M Journal, 18*(6), 567-575.

Palazzetti, L. (2021). Routing drones being aware of wind conditions: A case study. Proceedings from *: Wireless Sensors and Drones in Internet of Things Conference (Wi-DroIT).*

Shah, S., Dey, D., Lovett, C., & Kapoor, A. (2017). AirSim: High-fidelity visual and physical simulation for autonomous vehicles. *Field and Service Robotics Conference (FSR 2017).* Springer.

Weerakoon, K., Sathyamoorthy, A., & Manocha. D. (2022). Sim-to-real strategy for spatially aware robot navigation in uneven outdoor environments. *Robotics (cs.RO).*

Author Information

Latroch Maamar
Hassiba Benbouali University of Chlef,
(LGEER) laboratoy
BP 151 Hai Essalam 02000 Chlef, Algeria
Contact e-mail*: maamar.latroch@gmail.com*
m.latroch@univ-chlef.dz

Aissa Bokhtachte Aicha
Hassiba Benbouali University of Chlef,
(LGEER) laboratoy
BP 151 Hai Essalam 02000 Chlef, Algeria.

Toualbıa Asma
Hassiba Benbouali University of Chlef,
(LGEER) laboratoy
BP 151 Hai Essalam 02000 Chlef, Algeria

To cite this article:

Maamar, L., & Aicha, A. B., & Asma, T. (2023). Proposal for generation of a pseudo GPS signal used in indoor mode for navigation testing of small autonomous flying robot. *The Eurasia Proceedings of Science, Technology, Engineering & Mathematics (EPSTEM), 26*, 348-356.

The Eurasia Proceedings of Science, Technology, Engineering & Mathematics (EPSTEM)
ISSN: 2602-3199

The Eurasia Proceedings of Science, Technology, Engineering & Mathematics (EPSTEM), 2023

Volume 26, Pages 357-365

IConTES 2023: International Conference on Technology, Engineering and Science

Modeling Crashes Severity Using Ensemble Techniques

Taqwa Alhadidi
Al-Ahliyya Amman University

Mohammed Elhenawey
Queensland University of Science and Technology

Abstract: Traffic crashes are modelled using different techniques and contributing factors. In this work, several ensemble machine learning algorithms were used to model crash severity at urban roundabouts using data from 15 roundabouts in Jordan. The original dataset covers four years, from 2017 to 2021. A total of 15 variables were collected and used in this work. Results indicated that ten variables are important. The various models show their ability to classify traffic crash severity with a high overall accuracy range from 96% to 98%. Results indicated that driver fault and age are the most significant contributing factors for crash severity.

Keywords: Machine learning, K-nearest neighborhood, Support vector machine, Safety, Driver age, driver fault.

Introduction

The World Health Organization (WHO) aims to reduce traffic crash deaths and injuries by 2030 significantly. According to WHO, approximately 1.3 million people die yearly from traffic crashes; more than 93% are from low- and middle-income countries. Even though low- and middle-income countries have 60% of world vehicles. Non-fatal traffic crashes lead to suffering around 35 million people from different types of injuries, which may result in disability(WHO, 2022). According to Jordan Traffic Institute (JTI), in the last two years, Jordan witnessed 170,000 and 160,000 road crashes, with 562 and 589 fatalities in 2021 and 2022, respectively. Jordanian traffic crashes cost increases from $415 million in 2020to $454 million in 2022 (JTI, 2022). Come to crisp traffic crashes; several studies have been conducted to investigate the different contributing factors to crash occurrence in Jordan. According to JTI, about 97% of the total accidents that occurred in Jordan in 2021 happened due to various driver faults, including not taking proper pre-cautious actions (i.e., not using seatbelt, distracted drivers), going on wrong way direction, and violation of driving priorities (JTI, 2022). In recent years, researchers have paid close attention to traffic accident analysis to identify the elements that substantially impact traffic accidents. However, most research methodology is based on aggregated tabular data analysis using different statistical techniques including multiple linear regression, curve estimation, spatial analysis, or machine learning (Al-Mistarehi et al., 2022; Alomari et al., 2019; Edries & Alomari, 2022; Hazaymeh et al., 2022; R. Mujalli, 2018; R. O. Mujalli et al., 2017, 2023) Although the majority of traffic accidents occur in urban areas [1]; however, most of studies have been done at rural areas (Al-Rousan et al., 2021; R. Mujalli, 2018; Peng et al., 2019) . Several factors were identified as significant factors affecting crashes severity including lightning, roadway surface, holiday, driving speed, and roadway geometry (Almannaa et al., 2023; Yahaya et al., 2021) .Although roundabouts are a type of intersection that aims to improve traffic safety by converting the crossed movement to circular movement, traffic crashes at roundabouts still occur but with the least severity compared to other roadway elements (Hariri Asli, 2022; Mamlouk & Souliman, 2019; Polders et al., 2015; Qawasmeh et al., 2023). Yet, none of these studies consider driver age and driver gender in the severity of traffic crashes at roundabout. In this work, we focus on investigating and analyzing traffic crashes at several roundabouts. In this study we used several machine learning algorithms to identify the most important

factors that affect the occurrence of traffic crash occurrence. Subsequently, various machine learning algorithms were implemented and tested their performance to classify different crash severity types. The overall performance for each model was reported using different evaluation metrics discussed later in this paper. To sum up, the main contribution of this work is to identify and understand the contributing factors for traffic crashes at urban roundabouts in Jordan and to model traffic crashes severity at urban roundabouts considering driver age and gender.

Literature Review

Using different modelling techniques, machine learning has been done on various elements of transportation network including roadway, intersection and freeway segments. Modeling accident severity at freeways in Hebei, China was done using data from 2018. The gradient boosting algorithm was used to select the best feature for classifying traffic crashes severity based on 23 variables that were collected. After choosing the most important features, Bayesian network analysis was used to predict crash severity. Study results indicated that the gradient boosting is able to predict traffic crash severity with an accuracy of 89.05% (Yang et al., 2022). Using several machine learning algorithms to predict crash severity in Bangladesh was done in 2019, the researchers used Decision Tree, K-Nearest Neighbors (KNN), Naïve Bayes and AdaBoost these four supervised learning techniques, to classify the severity of accidents. Results indicated that the accuracy of model increases as the number of classes increase, also results indicated that the adaboost and Naïve Bayes have the highest accuracy (Labib et al., 2019). Also, a study on Saudi Arabia investigated that machine learning algorithm can be implemented to classify traffic accident severity at different types of network segment. Results indicated that the various used algorithms have different accuracy rate at different roadway type. Most importantly, their study showed that holidays affect the crash severity (Almannaa et al., 2023).Several works were conducted to model traffic crashes globally ((Almamlook et al., 2019; Almannaa et al., 2023; Al-Mistarehi et al., 2022; Al-Moqri et al., 2020; Alrumaidhi & Rakha, 2022; Anderson & Hernandez, 2017; Azhar et al., 2022) Most of these studies used machine learning algorithms including K-nearest neighborhoods (KNN), support vector machine, adaptive boosting tree or other machine learning algorithms (Ahmed et al., 2021; Almamlook et al., 2019; Almannaa et al., 2023a; Al-Mistarehi et al., 2022; Al-Moqri et al., 2020). Researchers indicated that providing driver sociodemographic attributes may improve the model prediction ((Almannaa et al., 2023; Jamal et al., 2021; R. O. Mujalli et al., 2017; Rahim & Hassan, 2021)

Settings

Data

In this research, crash data from the Jordanian traffic institute (JTI) is requested for the most critical roundabouts in the capital of Jordan, Amman. The dataset involves traffic accidents from 2017 to 2021, with 30,486 crashes from 15 roundabouts collected. The collected data have 23 variables describing roadway characteristics and conditions, weather condition, vehicle, driver, and crash type with the number of casualties. To avoid any misleading results, data was carefully screened and processed based on data completeness, irrelevant or redundant variables were disregarded. As such, in this study, the original dataset was reduced to 12,971 datapoints out of 30,486 were validated. This reduction was done according to previous stat-of-art, as following:

- Any missing value in driver age was removed as driver age is a significant attribute in crash severity prediction (Mujalli, 2018). The total missing values in driver age are 3,770 points.
- Only driver at fault records were included in this work and a total of 13,201 data points were deleted using this condition.
- Driver age an error in recording for instance it is not allowed to drive before 15 years old in Jordan nor the age can be a negative value a total of 922 data points were deleted.
- Drop any duplicate data point, following the previous steps were not keep any duplicate records.

Variable names, types and statistics are shown in Table 1. Table 1 shows that the collected data is imbalanced. This imbalance reduces the prediction model accuracy, for every new observation the prediction model tends to classify the new data point to the major class. Several researchers indicated that the traffic crash dataset suffers from an imbalance problem among all the studied factors (Jiang et al., 2020a, 2020b; Mohammadpour et al., 2023)

Balancing Techniques

The commonly used sampling technique was utilized to handle the imbalance problem, in the sampling technique a balance dataset is established from the imbalance data be either add more sample to the minor classes, in this case this process is called "over-sampling", or removing datapoints from the major class this process is called "under-sampling". Various balancing techniques were suggested to balance the data including Synthetic Minority Oversampling Technique (SMOTE) and ADASYN. SMOTE creates “synthesis” from the minor class by choosing k nearest neighbors without duplicates or replacements which effectively increases the overall accuracy and ability to generalize and saves the data from overfitting. Herein, the crash data was balanced before model development (Jiang et al., 2020a).

Machine Learning

In this section, a brief description of the used algorithm is presented, followed by evaluation metrics. It starts with KNN, Support Vector Machine and Adaptive Boosting Techniques. Then, a set of evaluation metrics was defined.

K-Nearest Neighborhood (KNN)

The k Nearest Neighbors (KNN) algorithm is one of the simplest methods of non-parametric modeling techniques (Zhang et al., 2017). The concept of the KNN is that similar data points that belong to the cluster have high probability. In essence, KNN starts by finding the K nearest neighborhood of training dataset them it predicts within the major class in the k nearest neighbors. Due to its simplicity and ability to predict with less time it has been selected as one of the top algorithms in data mining (Wu et al., 2008). KNN accuracy depends on choosing the best cluster size. The optimum K was selected based on the accuracy of prediction. Afterward, the response (i.e., accident severity in our problem) is classified by considering the majority vote of the K nearest points within the class as shown in equation 1.

$$y_j^{test} = \frac{1}{R}\sum_{X_j^{train}\in R_k} y_j^{train} \quad (1)$$

In equation 1, R is the number of assigned classes based on checking the model accuracy for each value. y_j^{test} is the test observation which is assigned to class R based on the majority of class R voting after train the model using X_j^{train} as input varaibles and y_j^{train} as the response variable (Friedman et al., 1975).

Support Vector Machines (SVMs)

The SVM algorithm is a supervised learning technique that classifies data based on the difference between classes. The algorithm, as shown in Equation 2, seeks the hyperplane (i.e., splitter) with the greatest minimum distance to the training data. The SVM seeks the weight (w) with the greatest margin around the hyperplane while satisfying the two constraints (see Equations (3) and (4)) (Hsu & Lin, 2002)

$$\min_{w,b,\xi}\left(\frac{1}{2}\, w^T\, w + \, c\, \sum_{n=1}^{N} \xi_n\right) \qquad (1)$$

subjected to:

$$y_n(w^T \phi(\, X_n) + b) \geq 1 - \xi_n \;\;, n = 1, \dots \dots, N \qquad (2)$$

$$\xi_n \geq 0\,, n = 1, \dots N \qquad (3)$$

Where: W is the set of parameters used to define class boundaries. C penalty parameter, ξ_n parameter to express the margin error. b intercept associated with the hyperplanes function to transform data from X space. ϕ(X_n) function to transform data from X space into Z space. y_n target value. The sum of the two terms in Equation 2 minimizes the objective function. Essentially, the first term seeks to define the gap between different classes.

Minimizing this term is equivalent to increasing the margin between classes. The second term seeks to reduce the error term multiplied by the penalty (regularization) parameter.

The penalty term is designed to deal with overfitting, while term C is designed to optimize the model's performance. Where n is the data observation's index, w is the decision boundary between classes, C is the regularization (or penalty) parameter, and jn is the margin violation error parameter. K is the number of observations x space that uses the $\phi(X_n)$ function to be converted to another space. In fact, the transformation is done to create a Z space which can be used to ease defining classes boundaries. In other hand, some functions can be used directly (i.e., Kernels) to create the transformation easier like the work in this paper. Meanwhile, equation 2 can be solved either by using the Kernels or using the $\phi(X_n)$ to transform data to Z plane. In fact, before constructing the model, the kernel type should be determined (e.g., linear, polynomial, Gaussian). One kernel may outperform the other depending on the problem. Based on data size, some practical considerations suggest using different kernels for different problems (Hsu & Lin, 2002).

Adaptive Boosting Algorithm

The adaptive boosting (AdaBoost) algorithm is a machine learning algorithm that is based on the incremental contribution concept. AdaBoost was created in response to the question of whether it was possible to combine a group of "weak" learner algorithms with low accuracy to create a learning algorithm with high accuracy. The traditional approach in machine learning prior to the introduction of AdaBoost was based on selecting the most discriminating class of features. In other words, algorithms must be thought of as a class. AdaBoost makes use of a collection of weak classifiers, each of which is trained using the same training dataset but with a different weight distribution. Each of the weak learners concentrates on the instances where the previous learner made a mistake. The output of AdaBoost is the weighted average of all weak learner outputs. AdaBoost is likely to have lower misclassification error than a sum of weak learners, and it also has a bound-on generalization error.

Evaluation Metrics

In classification problem, the output could classify the output in 4 possible values, true positive prediction (TP), true negative prediction (TN), false positive prediction (FP), and false negative prediction (FN). These different possible outcomes were used to compute the different evaluation metrics. The evaluation metrics are precision, recall, f1-score and support. These metrics are computes as following equations.

$$Precision = \frac{TP}{TP + NP}$$

$$Recall = \frac{TP}{TP + FN}$$

$$f1 - score = 2 * \frac{Precision * Recall}{Precision + Recall}$$

Results and Discussion

In this section, different modeling techniques results are presented and discussed.

Explanatory Data Analysis Results

After pre-processing the data according to section 3 and summarizing their values as in Table I. Results showed that more than 97.5% of the total accidents were property damage only, most of accidents occurred at a flat dry roadway surface during midday. Also, about 95% of the total accidents occurred in clear weather conditions. Interestingly, more than 75% of the accidents caused by male drivers with age less than 40 years old

Feature Engineering

This step was the first step in modeling data. It started with checking the data type, reporting the original data correlation matrix, and checking the most relevant variables in modeling the problem. The most relevant variables were selected based on using the P-value and the F-score. The selected features were chosen based on P-value and F-score greater than 0.05 and 5 respectively. According to this threshold, the most important variables were number of casualties for slight injuries, intermediate injuries, death and major injuries, number of vehicles, driver fault, lightening, hour, lanes, driver age and day of week.

Table 1.Explanatory Variable Descriptive statistics

Variable Name	Variable *Type*	*Categories*	*Mean*	*Standard Deviation*	*Percentage*
Crash type	Categorial	Collision Pedestrian Run Off Road	1.99	0.16	99.40 % 0.41% 0.19%
Day of week	Categorial	Weekday Weekend	0.23	0.48	76.98% 23.02%
Time of Day	Categorial	Morning Midday Evening Night	1.49	0.49	12.84% 39.09% 32.38% 15.69%
Season	Categorial	Summer Fall Winter Spring	1.59	1.18	26.10 % 24.71% 24.48% 24.71%
Holiday	Categorial	Yes No			2.86 % 97.14%
Driver gender	Categorial	Male Female	0.8	0.4	82% 18%
Driver Age	Continous	[13,76]	27	18	
Speed	Continous	[10,120]	48.4	9.8	
Direction and Location of Occurrence	Categorial	Divided two-lanes Undivided two-lanes One-way Inside a bus stop In the circular area	3.59	0.76	70.97 % 18.80 % 8.36 % 1.63 % 0.24 %
Alignments (Horizontal and Vertical)	Categorial	Uphill Curve Uphill Straight Downhill Curve Flat Curve Downhill	2.98	0.24	0.03% 2.35% 0.05% 96.82% 0.14% 0.61%
Vehicle Classification	Categorial	Passenger car Light truck Medium riding Heavy truck Bike	0.61	1.09	0.05% 96.82% 0.14% 0.61% 89.19%
Vehicle involved in the accident	Continous	1 2 3 ≥4	2.03	0.34	8.18% 1.87% 0.55% 0.16%
Surface Condition	Categorial	Dry Not dry	0.12	0.4	94.96% 5.04%
Lightening	Categorial	Day Night and road with sufficient lighting Insufficient night lighting	2.31	0.96	71.06% 22.59% 4.01%

		Sunset			2.17%
		Sunrise			0.12%
		Darkness			0.05%
Weather	Categorial	Clear	0.21	0.63	97.77%
		Not clear			2.23%
Severity	Categorial	Fatal	0.2	0.5	1.88%
		Non-Fatal			98.12%

Machine Learning Algorithms Results

This section discusses the results of the machine learning techniques used in this study, which were developed in Python.

KNN

In this study, KNN was used to identify the traffic severity. A 10-fold cross-validation was used to select the best model for each value of K, and the average highest accuracy among the 10 folds was chosen. After comparing different numbers of K to overall classification accuracy, the optimal K was determined.Table 2 presents the overall classification report of using the KNN method for different classes. In this table, 4 metrics are presented. Precision, recall, f1-score and support. While the confusion matrix is shown in Table 3.

Table 1. KNN Classification report

	Precision	Recall	F1-score	Support
Non-Fatal	0.97	1	0.98	4433
Fatal	1	0.96	0.98	4382

Table 2.KNN confusion Matrix

	Non-Fatal	Fatal
Non-Fatal	4420	13
Fatal	155	4227

According to Table 2 and 3, the accuracy of predicting fatal accidents was the highest and the precision for the non-fatal accidents was the lowest. The overall model accuracy was 98%.

SVM

In this study, SVM was used to identify the traffic accidents severity out of the four possible types. A 10-fold cross-validation was used to select the best model for each value of K, and the average highest accuracy among the 10 folds was chosen. Moreover, different kernels were used to train the model, the best kernel was rfb with gamma of 0.001. Table 4 presents the overall classification report of using the SVM method. In this table, 4 metrics are presented. Precision, recall, f1-score and support. While the confusion matrix is shown in Table 5.

Table 3. SVM Classification report

	Precision	Recall	F1-score	Support
Non-Fatal	1	0.99	0.99	4433
Fatal	0.99	1	0.99	4382

Table 4. SVM confusion Matrix

	Non-Fatal	Fatal
Non-Fatal	4386	47
Fatal	1	4382

According to Table 4 and 5, non-fatal accidents were the highest and the precision for the fatal accidents was the lowest. The overall model accuracy was 99%.

Adaboost

The AdaBoost classifier was used in this study to identify the crash severity of the wo possible types. Table 6 presents the overall classification report of using the Adaboost method. In this table, 4 metrics are presented. Precision, recall, f1-score and support. While the confusion matrix is shown in Table 7.

Table 5. Adaboost Classification report

	Precision	Recall	F1-score	Support
Non-Fatal	0.99	1	0.99	4433
Fatal	1	0.99	0.99	4382

Table 6. Adaboost confusion Matrix

	Non-Fatal	Fatal
Non-Fatal	4428	5
Fatal	57	4325

According to Table 6 and 7, the accuracy of predicting the fatal accident only was the highest. The variable importance in the adaboost is shown in Fig1.

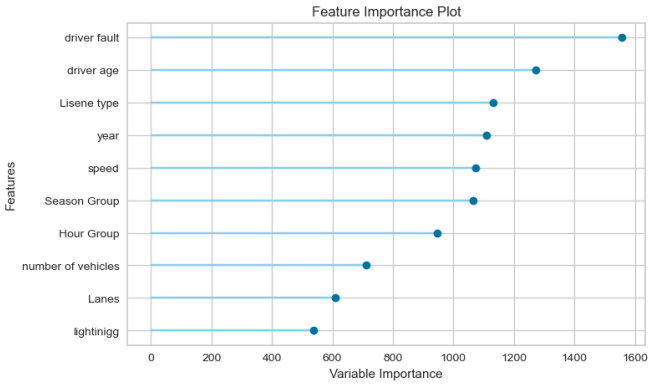

Figure 1. Adaboost variables importance.

The most relevent factors that significantly impact the crash severity prediction are (in order): driver fault, driver age, license type, year, speed, season, time of day, number of vehicles, lanes and lightning.

Conclusion

In this study, several machine learning algorithms were used to predict crashes severity at 15 urban roundabouts in Jordan. Given that roundabouts are created to improve traffic safety, yet in Jordan most of urban roundabouts are labeled as hotspots. Since 2014, traffic police central department has made several improvements in crash severity recording, they now collect several attributes including driver age, gender, spatial location characteristics even they use GPS to provide accident occurrence location exactly. In essence, the work in this study shows that there are ten significant variables to model crash severity including driver fault, driver age, license type, speed, year of occurrence, season, time of day, number of vehicles, geometric characteristics, and lightening. The study indicates that driver gender, holiday and roadway surface characteristics are not significant important features. The various machine learning algorithms were tested on balanced data after using SMOTE technique to balance the dataset. The various algorithms showed a consistent prediction precision for the different crash severity, while the overall accuracy for all of them are not identical, but there is not statistically significant difference between them as they are 98%, 99% and 99% for KNN, SVM and adaboost respectively. The results of this study help the various Jordanian agencies to create a long-term plan to improve

traffic safety by create new regulations to control driver behavior as it is the main reason behind the traffic accidents.

Recommendations

For future research, larger, more comprehensive, and reliable samples could be tested using the implemented models. Moreover, test different models and check variables effect on the models.

Scientific Ethics Declaration

The authors declare that the scientific ethical and legal responsibility of this article published in EPSTEM journal belongs to the authors.

Acknowledgements or Notes

* This article was presented as an oral presentation at the International Conference on Technology, Engineering and Science (www.icontes.net) held in Antalya/Turkey on November 16-19, 2023.

*Authors would like to thank the Jordanian traffic institute for providing the data used in this research. Also, first author would like to thank Al-Ahliyya Amman University for the financial support in joining the ICONTES conference.

References

Almamlook, R. E., Kwayu, K. M., Alkasisbeh, M. R., & Frefer, A. A. (2019). Comparison of machine learning algorithms for predicting traffic accident severity. *IEEE Jordan International Joint Conference on Electrical Engineering and Information Technology JEEIT 2019*, 272–276.

Almannaa, M., Zawad, M. N., Moshawah, M., & Alabduljabbar, H. (2023). Investigating the effect of road condition and vacation on crash severity using machine learning algorithms. *International Journal of Injury Control and Safety Promotion*, *30*(3), 392-402.

Al-Mistarehi, B. W., Alomari, A. H., Imam, R., & Mashaqba, M. (2022). Using machine learning models to forecast severity level of traffic crashes by R studio and ArcGIS. *Frontiers in Built Environment*, *8*.

Al-Moqri, T., Haijun, X., Pierre Namahoro, J., Naji Alfalahi, E., & Alwesabi, I. (2020). Exploiting machine learning algorithms for predicting crash injury severity in Yemen: Hospital case study. *Applied and Computational Mathematics*, *9*(5), 155.

Alomari, A. A., Khasawneh, M. A., Mohammad, P., & Ganam, B. (2019). Evaluation of traffic accidents in Jordan using accident hazard scale. *Jordan Journal of Civil Engineering*, *13*(1), 12-20.

Al-Rousan, T. M., Umar, A. A., & Al-Omari, A. A. (2021). Characteristics of crashes -caused by distracted driving on rural and suburban roadways in Jordan. *Infrastructures*, *6*(8), 107.

Alrumaidhi, M., & Rakha, H. A. (2022). Factors affecting crash severity among elderly drivers: A multilevel ordinal logistic regression approach. *Sustainability (Switzerland)*, *14*(18), 11543..

Anderson, J., & Hernandez, S. (2017). Roadway classifications and the accident injury severities of heavy-vehicle drivers. *Analytic Methods in Accident Research*, *15*, 17–28.

Azhar, A., Ariff, N. M., Bakar, M. A. A., & Roslan, A. (2022). Classification of driver injury severity for accidents involving heavy vehicles with decision tree and random forest. *Sustainability (Switzerland)*, *14*(7).

Edries, B., & Alomari, A. H. (2022). Forecasting the fatality rate of traffic accidents in Jordan: Applications of time-series, curve estimation, and multiple linear regression models. *Journal of Engineering Science and Technology Review*, *15*(6), 70–77.

Friedman, J. H., Baskett, F., & Shustek, L. J. (1975). An algorithm for finding nearest neighbors. *IEEE Transactions on Computers*, *100*(10), 1000–1006.

Hariri Asli, H. (2022). Investigation of the factors affecting pedestrian accidents in urban roundabouts. *Computatıonal Research Progress In Applıed Scıence & Engıneerıng*, *8*(1), 1–4.

Hazaymeh, K., Almagbile, A., & Alomari, A. H. (2022). Spatiotemporal analysis of traffic accidents Hotspots Based on Geospatial Techniques. *ISPRS International Journal of Geo-Information*, *11*(4), 260.

Hsu, C.-W., & Lin, C.-J. (2002). A comparison of methods for multiclass support vector machines. *IEEE Transactions on Neural Networks*, *13*(2), 415–425.

Jamal, A., Zahid, M., Tauhidur Rahman, M., Al-Ahmadi, H. M., Almoshaogeh, M., Farooq, D., & Ahmad, M. (2021). Injury severity prediction of traffic crashes with ensemble machine learning techniques: A comparative study. *International Journal of Injury Control and Safety Promotion*, *28*(4), 408–427.

Jiang, L., Xie, Y., Wen, X., & Ren, T. (2020a). Modeling highly imbalanced crash severity data by ensemble methods and global sensitivity analysis. *Journal of Transportation Safety and Security*, 1–23.

Jiang, L., Xie, Y., Wen, X., & Ren, T. (2020b). Modeling highly imbalanced crash severity data by ensemble methods and global sensitivity analysis. *Journal of Transportation Safety and Security*, 1–23.

JTI. (2022). *Annual accidents report.* Retrieved from https://www.jti.com/

Labib, M. F., Rifat, A. S., Hossain, M. M., Das, A. K., & Nawrine, F. (2019). Road accident analysis and prediction of accident severity by using machine learning in Bangladesh. *2019 7th International Conference on Smart Computing & Communications (ICSCC)*, 1–5.

Mamlouk, M., & Souliman, B. (2019). Effect of traffic roundabouts on accident rate and severity in Arizona. *Journal of Transportation Safety and Security*, *11*(4), 430–442.

Mohammadpour, S. I., Khedmati, M., & Zada, M. J. H. (2023). Classification of truck-involved crash severity: Dealing with missing, imbalanced, and high dimensional safety data. *PloS One*, *18*(3), e0281901.

Mujalli, R. (2018). Modeling risk of road crashes using aggregated data analysis of traffic accidents on two-lanes rural highways using data mining view project. *Jordan Journal of Civil Engineering*, *12*(1), 45-60.

Mujalli, R. O., Al-Masaeid, H., & Alamoush, S. (2023). Modeling traffic crashes on rural and suburban highways using ensemble machine learning methods. *KSCE Journal of Civil Engineering*, *27*(2), 814–825.

Mujalli, R. O., López, G., & Garach, L. (2017). Modeling injury severity of vehicular traffic crashes. *ACM International Conference Proceeding Series*, 51–55.

Peng, Y., Zhu, S., & Jiang, Y. (2019). Examining the crash severity on divided rural multilane highway segments using multilevel ordinal logistic models. *Advances in Mechanical Engineering*, *11*(4).

Polders, E., Daniels, S., Casters, W., & Brijs, T. (2015). Identifying crash patterns on roundabouts. *Traffic Injury Prevention*, *16*(2), 202–207.

Qawasmeh, B., Kwigizile, V., & Oh, J. S. (2023). Performance and safety effectiveness evaluation of mini-roundabouts in Michigan. *Journal of Engineering and Applied Science*, *70*(1), 36.

Rahim, M. A., & Hassan, H. M. (2021). A deep learning based traffic crash severity prediction framework. *Accident Analysis and Prevention*, *154*, 106090.

Wu, X., Kumar, V., Ross Quinlan, J., Ghosh, J., Yang, Q., Motoda, H., McLachlan, G. J., Ng, A., Liu, B., & Yu, P. S. (2008). Top 10 algorithms in data mining. *Knowledge and Information Systems*, *14*, 1–37.

Yahaya, M., Guo, R., Fan, W., Bashir, K., Fan, Y., Xu, S., & Jiang, X. (2021). Bayesian networks for imbalance data to investigate the contributing factors to fatal injury crashes on the Ghanaian highways. *Accident Analysis and Prevention*, *150*, 105936.

Yang, Y., Wang, K., Yuan, Z., & Liu, D. (2022). Predicting freeway traffic crash severity using XGBoost-Bayesian network model with consideration of features interaction. *Journal of Advanced Transportation*. Article ID 4257865. https://doi.org/10.1155/2022/4257865

Zhang, S., Li, X., Zong, M., Zhu, X., & Cheng, D. (2017). Learning k for knn classification. *ACM Transactions on Intelligent Systems and Technology (TIST)*, *8*(3), 1–19.

Author Information

Taqwa Alhadidi
Al-Ahliyya Amman University
Amman, Jordan
Contact e-mail: *t.alhadidi@ammanu.edu.jo*

Mohammed Elhenawey
Queensland University of Science and Technology
Queensland, Australia

To cite this article:

Alhadidi, T., & Elhenawey, M. (2023). Modeling crashes severity using ensemble techniques. *The Eurasia Proceedings of Science, Technology, Engineering & Mathematics (EPSTEM), 26*, 357-365.

TheEurasiaProceedings of Science, Technology, Engineering&Mathematics (EPSTEM)
ISSN: 2602-3199

The Eurasia Proceedings of Science, Technology, Engineering & Mathematics (EPSTEM), 2023

Volume 26, Pages 366-374

IConTES 2023: International Conference on Technology, Engineering and Science

Multi-Objective Optimization of the Inconel 718 Turning Parameters Using MARCOS–Based Taguchi S/N ratio

Septi Boucherit
8th May 1945 University

Mohamed Athmane Yallese
8th May 1945 University

Ilyes Kouahla
8th May 1945 University

Salim Belhadi
8th May 1945 University

Abdelkrim Haddad
8th May 1945 University

Abstract: Nickel-based alloys, such as Inconel 718, are widely used in space technology, rocket engines, nuclear reactors, petrochemicals, submarines, power plants, and other applications. It is classified as a challenging material to process due to its strong mechanical properties, low thermal conductivity, and other characteristics. The main objective of this work is to determine the optimal cutting parameters for turning Inconel 718 using a coated carbide tool, with the aim of reducing cutting tool vibration, minimizing surface roughness, and maximizing material removal rate. This is achieved by employing the Measurement of Alternatives and Ranking according to Compromise Solution technique (MARCOS) coupled with Taguchi's signal-to-noise ratio. The results have demonstrated that the configuration of the cutting parameters for achieving the aforementioned objectives is as follows: r = 0.8 mm, Vc = 70 mm/min, f = 0.08 mm/rev, and ap = 0.3 mm.

Keywords: MARCOS, Multi-objective optimization, Inconel 718, Taguchi

Introduction

In the machining process, optimization is considered a crucial activity that enables the selection of appropriate cutting conditions to enhance productivity, ensure product quality, and reduce production costs. Among the various optimization methods, multi-criteria decision-making (MCDM) methods are widely utilized due to their simplicity (Vats et al., 2022). These methods have been employed by numerous researchers in various machining processes, such as optimizing milling conditions (Arun Ramnath et al., 2019; Arun Ramnath & Thyla, 2022), drilling Ti-6Al-4V using the TOPSIS method (Samsedeensadham,2021), hard turning of medium carbon steel (Sristi, 2022), and grinding 9CrSi steel using CBN wheels (Thinh, & Trung,2022). Thirumalai et al. (2021) used the method (TOPSIS) to optimize the cutting parameters of Inconel 718 during turning. Sivalingam et al.(2021). used two MCDM approaches, ARAS and CODAS, to optimize the operating parameters for turning Inconel 718 alloy in dry cutting settings (ASCF). Several approaches have been proposed, combining multi-criteria decision-making methods with the Taguchi signal-to-noise ratio. Pawade and Joshi (2011) employed a coupled approach based on Taguchi's method and grey relational analysis (TGRA) to determine the optimal

process parameters for turning operations on Inconel 718 using a CNC lathe with cubic boron nitride (CBN) tools. B. Satyanarayana et al. (2013) also utilized TGRA to optimize cutting force, flank wear, and surface roughness during turning operations on Inconel 718 using a CNC lathe with CBN tools. Alsoruji et al. (2022) introduced the Taguchi analysis combined with the GRA approach for producing an ideal cutting regime that fulfills high (MRR), lower taper angle, and lowest roughness.The material used in this study is Inconel 718. This selection was based on the material's known challenges in machining, attributed to its high shear strength, tendency to work harden, and low thermal conductivity (Rajurkar & Chinchanikar, 2022;De Bartolomeis et al., 2021). Extensive research has been conducted to identify optimal machining conditions that ensure ease of machining, high surface quality, low energy consumption, and maximum productivity at a cost-effective level (Roy et al., 2018; Dudzinsk et al., 2004). Devillez et al. (2011) employed a coated carbide tool to conduct surface integrity tests on Inconel 718, both with and without lubrication. The results demonstrated that dry machining with a coated carbide tool produced an acceptable surface, exhibiting residual stresses and microhardness values equivalent to those achieved under the lubricated machining condition when using the optimized cutting speed value.

Deshpande et al. (2017) developed prediction models for surface roughness by considering cutting parameters, cutting force, sound emitted during machining, and vibrations during the turning of Inconel 718, using both cryogenically treated and untreated cutting tools. These models serve as a real-time control method for the turning process of Inconel 718. Tan et al. (2022) investigated the surface integrity of machined Inconel 718 using carbide and ceramic inserts. Surface roughness, residual stresses, and microhardness were studied in relation to the cutting parameters. Xu et al. (2022) conducted an experimental and numerical study on the machining of Inconel 718 using worn-out tools, examining chip formation, variations in cutting force, tool wear, heat distribution, and microstructure.

Numerous researchers have demonstrated the effectiveness of the signal-to-noise (SN) ratio when used in MCDM methods. Thus, this study distinguishes itself by applying the SN ratio-MARCOS, to optimize three objective functions: surface roughness, tangential vibrations of the cutting tool, and material removal rate during the turning of Inconel 718.

Theoretical Frameworks

Multi-Objective Optimization by MARCOS-Taguchi

Stevic et al.(2020) use equations the ideal solution "AI" and " the anti-ideal solution "AAI" to normalize the data set. In this work, the signal-to-noise ratio will be used.

Step 1: Data Normalization: using the following formulas:

Smaller-the-better $$\eta_i(j) = -10log_{10}\left[\frac{1}{n}x_i^2(j)\right] \quad (1)$$

Larger-the-better $$\eta_i(j) = -10log_{10}\left[\frac{1}{n.x_i^2(j)}\right] \quad (2)$$

Step 2: construct the Weighted Matrix

Generation of the weighted V matrix employing the criteria's weights:

$$V = \left[v_{ij}\right]_{m\times n} \quad (3)$$

Where $v_{ij} = \frac{\eta_{ij}}{Max(\eta_j)} \times w_j$ and $Max(\eta_j)$ is the maximum of column j.

Step 4: Perform the utility degrees for each alternative:

$$S_i = \sum v_{ij} \quad (4)$$

$$K_i^- = \frac{S_i}{\sum_{j=1}^{m} Max(\eta_j)} \quad (5)$$

$$K_i^+ = \frac{S_i}{\sum_{j=1}^{m} Min(\eta_j)} \quad (6)$$

Step 5: Construct the utility function

$$f(K_i^-) = \frac{K_i^+}{K_i^+ + K_i^-} \quad (7)$$

$$f(K_i^+) = \frac{K_i^-}{K_i^+ + K_i^-} \quad (8)$$

$$f(K_i) = \frac{K_i^- + K_i^+}{i + \frac{1-f(K_i^+)}{f(K_i^+)} + \frac{1-f(K_i^-)}{f(K_i^-)}} \quad (9)$$

Step 6: Ranking

Experimental Procedure

A cylindrical Inconel 718 bar with a diameter of 70 mm and a length of 350 mm was selected as the specimen. The turning tests were carried out on a conventional lathe (TOS TRENCIN) type SN40C (Pm=6.6 kW). The lathe is outfitted with an ABB series ACS355 variable speed drive with a speed sensor that allows the spindle speed to be controlled. SANDVIK metal carbide cutting inserts with a PVD coating of grade (GC1105) were used. The PVD coating is made up of a thin layer of TiAlN, which provides high tenacity, good adhesion, and even draft wear (Coromant & Catalogue, 2017). Fig. 1 shows the inserts mounted on a SANDVIK tool holder with the ISO designation PSBNR2525K12.

$$MRR = Vc.f.ap[cm^3/min] \quad (10)$$

Figure 1. Experimental equipments.

Figure 1 show the equipment used to measure the various output parameters. A roughness meter (2D) of the MITUTOYO type SJ-210 was used to measure roughness (Ra). It is made up of a 5 m diamond tip (feeler) that operates axially over a 4 mm distance on the machined surface. The measurements were obtained three times by

flipping the workpiece across a 120° angle and using the average of the three measurements. A vibrometer type VM-6360 and an accelerometer were used to measure the tool's vibrations in the tangential direction (atng). The measurements were collected using the software (data collection system). As a measure of productivity, the material removal rate (MRR) was chosen, and Eq. (10) was used to calculate it.

The experimental design was based on the conventional Taguchi L27 (3^4) orthogonal array. The first input component was allocated to the tool nose radius (r), the second to the cutting speed (Vc), the third to the feed rate per revolution (f), and the fourth to the depth of cut (ap). The range of variation for each factor is for r (0.8,1.2,1.6) mm, Vc (30,50,70) mm/min, f (0.08,0.12,0.16) mm/rev, and ap (0.1,0.2,0.3) mm. The cutting conditions are chosen in accordance with the manufacturer's instructions (SANDVIK). The Design of Experiments matrix, based on the Taguchi L27 design, provides various combinations of input factors, as illustrated in Table 1.

Table 1. Taguchi L27 experimental design

N° of test	Input parameters r (mm)	Vc (m/min)	f (mm/rev)	ap (mm)
1	1	1	1	1
2	1	1	2	2
3	1	1	3	3
4	1	2	1	2
5	1	2	2	3
6	1	2	3	1
7	1	3	1	3
8	1	3	2	1
9	1	3	3	2
10	2	1	1	1
11	2	1	2	2
12	2	1	3	3
13	2	2	1	2
14	2	2	2	3
15	2	2	3	1
16	2	3	1	3
17	2	3	2	1
18	2	3	3	2
19	3	1	1	1
20	3	1	2	2
21	3	1	3	3
22	3	2	1	2
23	3	2	2	3
24	3	2	3	1
25	2	3	1	3
26	3	3	2	1
27	3	3	3	2

Results and Discussions

ANOVA Signal to Noise Analysis

After machining operation, the performance characteristics of Ra, and atng were measured and they are summarized in Table 2. The responses were analyzed using lower is the better for Ra and atng using Taguchi's signal-to-noise ratio. The resulting response mean tables are shown in Tables 3, and 4. ANOVA is utilized to determine the significance and contribution of each process parameter to performance characteristics. Table 3 presents the ANOVA results for Ra.

The most influential factor affecting Ra is the feed rate (f), contributing 26.27% cont%. This is attributed to the fact that an increase in feed rate (f) leads to an expansion of grooves formed by the nose radius of the tool on the surfaces of Inconel 718, consequently resulting in surface quality deterioration. The results confirm previous findings in the literature (Amigo et al., 2023; Yin et al., 2020).

The interaction between radius (r) and feed rate (f) ranks as the second most significant contributor after f, accounting for 23.79%. This is supported by the interaction graph depicted in Figure 2 (c), where a clear interaction is observed. Specifically, for a tool radius of r = 1.6 mm, which generally yields good surface roughness, the feed rate has no substantial impact on Ra. However, for a radius of r = 0.8 mm, increasing the feed rate leads to a significant decrease in the Ra signal-to-noise ratio, indicating surface deterioration (Venkatesan et al.,2019).

The second factor that significantly contributes to surface roughness is cutting speed, with a contribution of 23.51%. This can be explained by the phenomenon of vibrations occurring in the cutting tool at high cutting speeds, primarily due to the increased hardness and resistance of Inconel 718. Consequently, the surface roughness of the machined part deteriorates (Fang et al., 2011; Thakur & Gangopadhyay, 2016). An effective approach to enhancing surface roughness involves increasing the tool radius. This approach is substantiated by the interaction graph depicted in Figure 2 (a), demonstrating a contribution percentage of 4.39% for the (r*Vc) interaction. Lastly, we observe the (r*ap) interaction, as well as the two factors (r and ap), contributing 3.20%, 1.94%, and 5.18%, respectively.

Table 2. Experimental result of performance parameters

N° of test	*Input parameters* r (mm)	Vc (m/min)	f (mm/rev)	ap (mm)	*Output parameters* Ra (μm)	a_{tng} (m/s^2)	MRR (cm^3/min)
1	0.8	30	0.08	0.1	0.401	2.077	0.240
2	0.8	30	0.12	0.2	0.571	2.247	0.720
3	0.8	30	0.16	0.3	0.672	2.691	1.440
4	0.8	50	0.08	0.2	0.328	1.334	0.800
5	0.8	50	0.12	0.3	0.349	2.142	1.800
6	0.8	50	0.16	0.1	0.787	1.603	0.800
7	0.8	70	0.08	0.3	0.280	1.828	1.680
8	0.8	70	0.12	0.1	0.338	1.484	0.840
9	0.8	70	0.16	0.2	0.435	2.106	2.240
10	1.2	30	0.08	0.1	0.457	2.870	0.240
11	1.2	30	0.12	0.2	0.431	3.537	0.720
12	1.2	30	0.16	0.3	0.582	3.728	1.440
13	1.2	50	0.08	0.2	0.386	2.865	0.800
14	1.2	50	0.12	0.3	0.433	2.673	1.800
15	1.2	50	0.16	0.1	0.649	2.037	0.800
16	1.2	70	0.08	0.3	0.428	2.428	1.680
17	1.2	70	0.12	0.1	0.282	2.012	0.840
18	1.2	70	0.16	0.2	0.476	2.440	2.240
19	1.6	30	0.08	0.1	0.394	3.393	0.240
20	1.6	30	0.12	0.2	0.390	3.683	0.720
21	1.6	30	0.16	0.3	0.464	3.535	1.440
22	1.6	50	0.08	0.2	0.434	2.157	0.800
23	1.6	50	0.12	0.3	0.445	2.839	1.800
24	1.6	50	0.16	0.1	0.457	2.400	0.800
25	1.6	70	0.08	0.3	0.433	2.579	1.680
26	1.6	70	0.12	0.1	0.357	2.383	0.840
27	1.6	70	0.16	0.2	0.284	2.588	2.240

Table 3. Analysis of variance for SN ratios (Ra).

Source	DF	Seq SS	Adj SS	Adj MS	F	P	Cont%
r	2	4.134	4.134	2.067	0.82	0.483	3.2082
Vc	2	30.304	30.304	15.152	6.04	0.036	23.5177
f	2	33.859	33.859	16.93	6.75	0.029	26.2766
ap	2	2.507	2.507	1.254	0.5	0.63	1.9456
*r*Vc*	4	5.664	5.664	1.416	0.56	0.698	4.3956
*r*f*	4	30.667	30.667	7.667	3.06	0.107	23.7994
*r*ap*	4	6.68	6.68	1.67	0.67	0.638	5.1841
ResidualError	6	15.042	15.042	2.507			11.6735
Total	26	128.856					100

Table 4 shows the ANOVA for the tangential vibrations (atng). The radius (r) has the most impact its contribution is 42.64%%, this can be explained by the fact that increasing the tool nose radius (r) leads to an increase in the contact length between the cutting edge and the workpiece, causing additional friction. Consequently, this causes an amplification of the tangential vibrations of the cutting tool. As for the cutting speed with a contribution of 35.35% , its increase when machining Inconel 718 is associated with excessive wear of the tool, poor surface quality, pressure of high cut and high vibration (Vats et al., 2022). Follow up factor. finally (ap) with a contribution of 9.42%.

Table 4. Analysis of variancefor SN ratios (a_{tnq}).

Source	DF	Seq SS	Adj SS	Adj MS	F	P	Cont%
r	2	59.852	59.852	29.9259	30.02	0.001	42.6436
Vc	2	49.629	49.629	24.8145	24.89	0.001	35.3599
f	2	2.16	2.16	1.0799	1.08	0.397	1.5390
ap	2	13.228	13.228	6.614	6.63	0.03	9.4247
*r*Vc*	4	1.84	1.84	0.46	0.46	0.763	1.3110
*r*f*	4	3.221	3.221	0.8053	0.81	0.563	2.2949
*r*ap*	4	4.442	4.442	1.1106	1.11	0.431	3.1649
ResidualError	6	5.982	5.982	0.9969			4.2621
Total	26	140.354					100

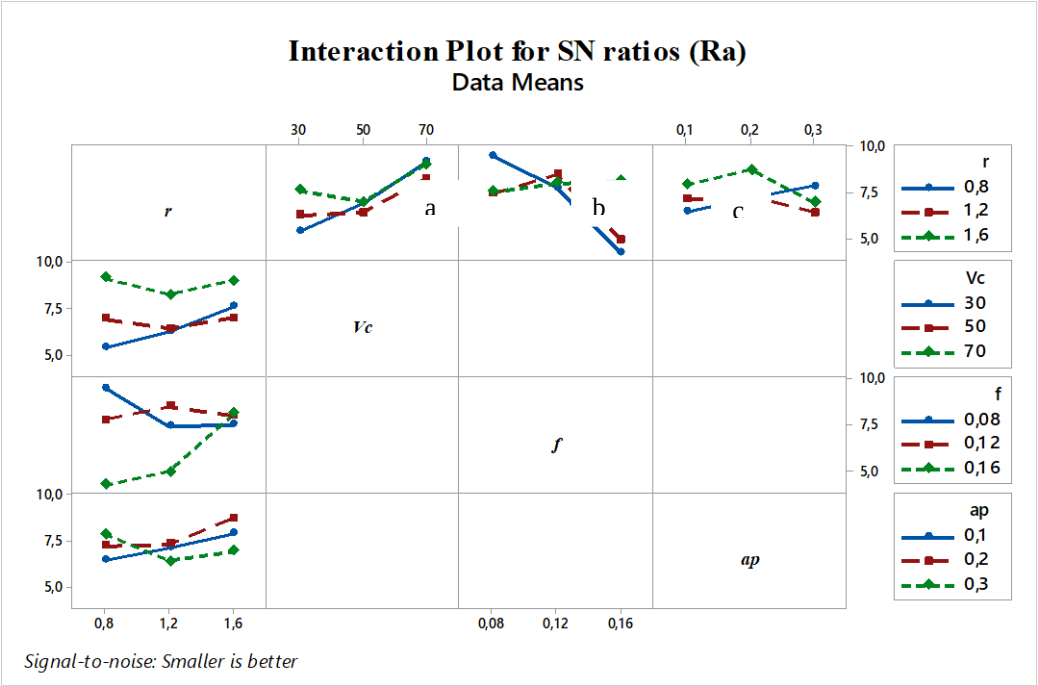

Figure 2. Interaction plot for SN (Ra)

Multi-Objective Optimization

The output parameters of table 2 are used for multi-objective optimization using The MARCOS-S/N ratio method. The normalization matrix for Ra, atng, and MRR is generated, considering Ra and atng as features to be minimized and MRR as a feature to be maximized. Table 5 the results of step 1 to 6 of the MARCOS-S/N ratio method.

Columns 2 to 4 contain the S/N ratio of step 1. Columns 5 to 7 form the element of weighting matrix. Here the weights are $\omega_1 = \omega_2 = \omega_3 = 0.33$ for all characteristics, but they can be modified by the maker according to the order of importance of each response. Columns 8 and 9 are the results of the calculation of the utility degree and the utility function.The utility function of the MARCOS using the Taguchi signal-to-noise ratio is ranked in descending order to determine the optimal solution. Finally, columns10 show the rank. The smallest values of the rank in table 6 correspond to optimum alternative. Table 6 highlights the optimization results provided by the strategies adopted.

Table 5. Results of the application of the MARCOS-S/N ratio.

Altern-atives N°:	Ra	S/N ration a_{tng}	MRR	Steps of MARCOS-S/N ration v_1	v_2	v_3	Si	f(k)	Rank
1	22.2508	7.9649	1.9179	0.2894	0.2225	0.0297	0.5417	0.0084	25
2	19.1809	7.2816	11.4603	0.2495	0.2035	0.1774	0.6303	0.0098	20
3	17.7663	5.7154	17.4809	0.2311	0.1597	0.2706	0.6614	0.0103	16
4	23.9962	11.8105	12.3754	0.3121	0.3300	0.1916	0.8337	0.0130	2
5	23.4571	7.6972	19.4191	0.3051	0.2151	0.3006	0.8208	0.0128	5
6	16.3941	10.2150	12.3754	0.2132	0.2854	0.1916	0.6902	0.0108	13
7	**25.3705**	**9.0741**	**18.8198**	**0.3300**	**0.2535**	**0.2913**	**0.8749**	**0.0136**	**1**
8	23.7353	10.8850	12.7992	0.3087	0.3041	0.1981	0.8110	0.0126	6
9	21.5439	7.8445	21.3186	0.2802	0.2192	0.3300	0.8294	0.0129	3
10	21.1153	5.1560	1.9179	0.2747	0.1441	0.0297	0.4484	0.0070	26
11	21.6241	3.3409	11.4603	0.2813	0.0933	0.1774	0.5520	0.0086	24
12	19.0152	2.8841	17.4809	0.2473	0.0806	0.2706	0.5985	0.0093	22
13	22.5819	5.1711	12.3754	0.2937	0.1445	0.1916	0.6298	0.0098	21
14	21.5839	5.7737	19.4191	0.2807	0.1613	0.3006	0.7427	0.0116	10
15	18.0687	8.1338	12.3754	0.2350	0.2273	0.1916	0.6539	0.0102	17
16	21.6848	6.6087	18.8198	0.2821	0.1847	0.2913	0.7580	0.0118	8
17	25.3087	8.2411	12.7992	0.3292	0.2303	0.1981	0.7576	0.0118	9
18	20.7615	6.5658	21.3186	0.2700	0.1835	0.3300	0.7835	0.0122	7
19	22.4037	3.7020	1.9179	0.2914	0.1034	0.0297	0.4245	0.0066	27
20	22.4923	2.9896	11.4603	0.2926	0.0835	0.1774	0.5535	0.0086	23
21	20.9833	3.3458	17.4809	0.2729	0.0935	0.2706	0.6370	0.0099	19
22	21.5638	7.6366	12.3754	0.2805	0.2134	0.1916	0.6854	0.0107	15
23	21.3464	5.2503	19.4191	0.2777	0.1467	0.3006	0.7250	0.0113	12
24	21.1153	6.7094	12.3754	0.2747	0.1875	0.1916	0.6537	0.0102	18
25	21.5839	6.0846	18.8198	0.2807	0.1700	0.2913	0.7421	0.0116	11
26	23.2603	6.7712	12.7992	0.3026	0.1892	0.1981	0.6899	0.0108	14
27	25.2473	6.0544	21.3186	0.3284	0.1692	0.3300	0.8276	0.0129	4

Table 6. Optimal results

Method	Altern-atives N°:	r	Vc	f	ap	Ra	a_{tng}	MRR
MARCOS-Taguchi	7	0.8	70	0.08	0.3	0.280	1.828	1.680

Conclusions

The present research proposes and implements the MARCOS-S/N ratio approach to address the challenge of multi-objective optimization during Inconel 718 dry turning. The research and analysis led to the following conclusions:

1. ANOVA analysis of Ra reveal that the most important factors that affect surface roughness is the feed rate (f), contributing 26.27%. The interaction between radius (r) and feed rate (f) ranks as the second most significant contributor after (f), accounting for 23.79%. The third factor that significantly contributes to surface roughness is cutting speed, with a contribution of 23.51%..
2. The radius (r) of cutting tools has the most impact on atng its contribution is 42.64%%, followed by the cutting speed with a contribution of 35.35%.Finally (ap) with a contribution of 9.42%.
3. Optimal cutting parameters for maximizing MRR while minimizing tangential vibration components and surface roughness are: r = 0.8 mm, Vc = 70 mm/min, f = 0.08 mm/rev, and ap = 0.3 mm.

Scientific Ethics Declaration

The authors declare that the scientific ethical and legal responsibility of this article published in EPSTEM journal belongs to the authors.

Acknowledgements

This article was presented at the International Conference on Technology, Engineering and Science (www.icontes.net) held in Antalya/Turkey on November 16-19, 2023.

References

Alsoruji, G., Muthuramalingam, T., Moustafa, E. B., & Elsheikh, A. (2022). Investigation and TGRA based optimization of laser beam drilling process during machining of Nickel Inconel 718 alloy. *Journal of Materials Research and Technology, 18*, 720–730.

Amigo, F.J., Urbikain, G., &de Lacalle, L.N.L. (2023).On the effects of cutting-edge angle on high-feed turning of Inconel 718© superalloy. *International Journal of Advanced Manufacturing Technology, 125*, 4237–4252.

Arunramnath, R.,Thyla, P. R., Mahendrakumar, N., Ramesh, M.,&Siddeshwaran, A. (2019).Multi-attribute optimization of end milling epoxy granite composites using TOPSIS. Journal of *Materials and Manufacturing Process, 34*(5), 530–543.

ArunRamnath, R., & Thyla, P. R. (2022). Measurement and optimization of multiattribute characteristics in milling epoxy granite composites using rsm and combined ahp-topsis. *Surface Topography: Metrology and Properties, 10*(2).

Coromant, S., & Catalogue, M. (2017). *The official website of Sandvik Coromant*. Retrieved from https://www.sandvik.coromant.com/

De Bartolomeis, A., Newman, S. T., Jawahir, I. S., Biermann, D., &Shokrani, A. (2021). Future research directions in the machining of Inconel 718, *Journal of Materials Processing Technology, 297*(10).

Devillez, A., Le Coz, G., Dominiak, S., & Dudzinski, D. (2011). Dry machining of Inconel 718, workpiece surface integrity. *Journal of Materials Processing Technology, 211*(10), 1590–1598.

Deshpande, Y., Andhare, A., & Sahu, N. K. (2017). Estimation of surface roughness using cutting parameters, force, sound, and vibration in turning of Inconel 718. *Journal of the Brazilian Society of Mechanical Sciences and Engineering, 39*(12), 5087–5096.

Dudzinski, D., Devillez, A., Moufki, A., Larrouquère, D., Zerrouki, V., & Vigneau, J. (2004). A review of developments towards dry and high speed machining of Inconel 718 alloy. *International Journal of Machine Tools and Manufacture, 44*(4), 439–456.

Fang, N., Pai, P.S.,& Mosquea, S.(2011). Effect of tool edge wear on the cutting forces and vibrations in high-speed finish machining of Inconel 718: An experimental study and wavelet transform analysis. *International Journal of Advanced Manufacturing Technology,52*(1), 65–77

Pawade, R.S., & Joshi, S.S. (2011). Multi-objective optimization of surface roughness and cutting forces in high-speed turning of Inconel 718 using Taguchi grey relational analysis (TGRA). *International Journal of Advanced Manufacturing Technoogy, 56*(1), 47–62.

Rajurkar, A.,& Chinchanikar, S. (2022) Experimental investigation on laser-processed micro-dimple and micro-channel textured tools during turning of Inconel 718 alloy. *Journal of Materials Engineering and Performance, 31*(10),4068-4083.

Roy, S., Kumar, R., Anurag, Panda, A., & Das, R. K. (2018). A brief review on machining of Inconel 718. *Materials Today: Proceedings, 5*(9), 18664–18673.

Satyanarayana, B.,Janardhana, R., &RaoD. H.(2013). Optimized high speed turning on Inconel 718 us ing Taguchi's method based grey relational analysis. *Indian Journal of Engineering & Material Sciences,20*(4),269-275.

Samsedeensadham,S., Mohan, A., ArunRamnath, R., & Keshav Thilak, R. (2021).*Optimization of machining parameters in drilling Ti-6Al-4V using user's preference rating based TOPSIS. In Materials, Design, and Manufacturing for Sustainable Environment: Select Proceedings of ICMDMSE 2020 (pp. 423-434).* Singapore: Springer.

Stević, Ž., Pamučar, D., Puška, A., & Chatterjee, P. (2020). Sustainable supplier selection in Healthcare Industries using a new MCDM method: Measurement of alternatives and ranking according to compromise solution (Marcos). *Computers & Industrial Engineering, 140*. 106231.

Sivalingam, V., Poogavanam, G., Natarajan, Y., & Sun, J. (2021). Optimization of atomized spray cutting fluid eco-friendly turning of Inconel 718 alloy using Aras and Codas methods. *The International Journal of Advanced Manufacturing Technology, 120*(7-8), 4551-4564

Sristi, N. A., Zaman, P., & Dhar, N. R. (2022). Multi-response optimization of hard turning parameters: A comparison between different hybrid Taguchi-based MCDM methods. *International Journal on Interactive Design and Manufacturing (IJIDeM), 16*(4), 1779–1795.

Tan, L., Yao, C., Li, X., Fan, Y., & Cui, M. (2022). Effects of machining parameters on surface integrity when turning Inconel 718. *Journal of Materials Engineering and Performance, 31*(5), 4176–4186.

Thakur, A., & Gangopadhyay, S. (2016). State-of-the-art in surface integrity in machining of nickel-based super alloys. *International Journal of Machine Tools and Manufacture, 100,* 25–54.

Thinh, H. X., & Trung, D. D. (2022). A research on application of the measurement of alternatives and ranking according to compromise solution method for multi-criteria decision making in the grinding process. *EUREKA: Physics and Engineering, (2),* 101–110.

Thirumalai, R., Seenivasan, M., & Panneerselvam, K. (2021). Experimental investigation and multi response optimization of turning process parameters for Inconel 718 using topsis approach. *Materials Today: Proceedings, 45*(1-3),467–472.

Vats, P., Singh, T., Dubey, V., &Sharma, A. K. (2022). Optimization of machining parameters in turning of AISI 1040 steel using hybrid MCDM technique. *Materials Today: Proceedings,50*(10),1758–1765.

Venkatesan, K., Manivannan, K., Devendiran, S., Mathew, A.T., Ghazaly, N. M., Aadhavan, S.M., Neha Benny, (2019). Study of forces, surface finish and chip morphology on machining of Inconel 825, *Procedia Manufacturing, 30,* 611-618.

Xu, D., Liu, Y., Ding, L., Zhou, J., M'Saoubi, R., & Liu, H. (2022). Experimental and numerical investigation of Inconel 718 machining with Worn tools. *Journal of Manufacturing Processes, 77*(1), 163–173.

Yin, Q., Liu, Z., Wang, B. (2020). Recent progress of machinability and surface integrity for mechanical machining Inconel 718: A review. *Inernational Journal of Advanced Manufacturing Technology,109*(1-2), 215–245.

Author Information

Septi Boucherit
LMS, 8th May 1945 University, Guelma-24000, Algeria
Contact e-mail: boucherit_sebti@yahoo.fr

Ilyes Kouahla
LMS, 8th May 1945 University, Guelma-24000, Algeria

Abdelkrim Haddad
LMS, 8th May 1945 University, Guelma-24000, Algeria

Mohamed Athmane Yallese
LMS, 8th May 1945 University, Guelma-24000, Algeria

Salim Belhadi
LMS, 8th May 1945 University, Guelma-24000, Algeria

To cite this article:

Boucherit, S., Yallese, M. A., Kouahla, I., Belhadi, S., & Haddad, A. (2023). Multi-objective optimization of the inconel 718 turning parameters using MARCOS –based Taguchi S/N ratio. *The Eurasia Proceedings of Science, Technology, Engineering & Mathematics (EPSTEM), 26,* 366-374.

The Eurasia Proceedings of Science, Technology, Engineering & Mathematics (EPSTEM)
ISSN: 2602-3199

The Eurasia Proceedings of Science, Technology, Engineering & Mathematics (EPSTEM), 2023

Volume 26, Pages 375-386

IConTES 2023: International Conference on Technology, Engineering and Science

Effect of Cuo-Water Nanofluid on the Thermal - Hydraulic Behavior of Triangular Corrugated Channel

Rahima Benchabi
University of Mentouri Brothers

Ahsene Lanani
University of Mentouri Brothers

Abstract: The aim of this study is to model and simulate laminar flow and heat transfer in a triangular-corrugated duct containing a CuO-water nanofluid. Note that a temperature is imposed on the walls, the considered Reynolds number (Re) and the nanoparticle volume fraction range from 100 to 800 and 0 to 5% respectively. The basic equations were discretized using the finite volume method. Dynamic and thermal fields were obtained, as well as the Nusselt number (Nu). In addition, the influence of certain parameters (Re, nanoparticle volume fraction) was taken into account. It can be observed that the mean Nu increases with increasing Re. Furthermore, raising the nanofluid volume fraction further enhances the heat transfer. For numerical resolution, we used the FLUENT code. Finally, we note that the results are in excellent accord with experimental ones published in the literature.

Keywords: Heat transfer, Nano-fluid, Corrugated channel, Numerical simulation, Fluent

Introduction

Heat transfer is an extremely important process in industry and technology. Although it manifests itself in different forms, namely radiation, conduction and convection, the latter is the most targeted in certain well-defined fields, such as the cooling of processors, electronic components, radiators and heat exchangers in industrial processes, etc... To this end, a large number of researchers have carried out a wide range of numerical and experimental studies on the phenomena governing convection, the effect of the systems in which it takes place (geometry in particular) and the properties of the fluids involved (physico-chemical properties). Over the last few decades, numerous studies have been conducted on heat transfer to improve the thermal performance of heat exchangers. Initially, researchers studied channels by considering simple fluids. Later, they considered fluids in which nanoparticles are dispersed in a base fluid, hence the term nanofluids (Choi & Eastman, 1995). For more than a century, several researchers have attempted to use suspended metal particles to perform the heat transfer of conventional cooling fluids. The base fluid is usually water, oil or ethylene glycol (EG). Nanofluids are colloidal solutions produced by dispersing nano-sized solid particles in a base fluid. A number of these solutions have shown themselves to be highly efficient in improving heat transfer under certain circumstances. Heat transfer in a nanofluid relies on the thermophysical characteristics of the solid and liquid phases.

In recent years, the study of nanofluids has attracted a great deal of interest in the field of heat transfer. The future of these new types of fluids looks very promising. Many researchers claim that this technology has the potential to become the cooling medium of choice in many fields of application. Numerous studies have shown that nanofluids (Al_2O_3, CuO, SiO_2, ZnO, etc...) have received a lot of interest because of their better heat transfer compared to conventional heat transfer fluids such as water, oil, ethylene glycol, etc..., especially since numerical and experimental studies on this type of problem are quite recent. A lot of numerical and experimental research has been carried out in this field to enhance the heat transfer in heat exchangers. A

numerical study is given by Ahmed et al, (2013a). This study concerns a laminar flow in forced convection based on the Al_2O_3-water nanofluid in a wavy triangular duct. The authors show that the Nu rises with Re and nanoparticle volume fraction. From this study, the authors conclude that the use of a nanofluid in a corrugated triangular channel is a good choice. Ahmed et al (2014a) numerically studied the heat transfer characteristics of the CuO-water nanofluid by considering a straight duct and then a corrugated channel. Also, the authors were interested in the effect of nanoparticle volume fraction and Re on temperature, velocity and Nu. The authors find that the average Nu rises with nanoparticle volume fraction and Re for the three examined corrugations (sinusoidal, triangular and trapezoidal). To improve heat transfer, Abed et al. (2015) considered a corrugated channel with various nanofluids, (Al_2O_3, CuO, SiO_2 and ZnO). The authors showed that of the four considered nanofluids, SiO_2 provides the best heat transfer enhancement. In numerical and experimental studies, Ahmed et al. (2015a) focused on improving heat transfer in a corrugated duct by utilizing SiO_2 as nanoparticles. In this study, the authors considered three corrugated channels (trapezoidal, sinusoidal and straight channel). Their results reveal that average Nu increases with nanoparticle volume fraction, and that the trapezoidal channel provides the greatest heat transfer, followed by the sinusoidal and straight channels. Ahmed et al, (2015b) conducted a numerical investigation involving turbulent forced convection flow. The used wavy channel is triangular and the flow considered contains nanoparticles (Al_2O_3, CuO, SiO_2 and ZnO). The authors showed that the best nanofluid was SiO_2, followed by Al_2O_3, ZnO and finally CuO. A numerical investigation concerning the influence of nanoparticles on the heat transfer of flow in a sinusoidal channel is carried out by Heidary & Kerman, (2010). The influence of Re, nanofluid volume fractions and amplitude on the local mean Nu and coefficient of friction has been investigated. The impact of various variables like amplitude, channel wavelength, volume fractions of the nanofluid under consideration and Re on velocity vectors, temperature contours, pressure drop and mean Nu are discussed and reported by Ahmed et al. (2013b). The results reveal an improvement in mean Nu as nanofluid volume fractions increase with channel amplitude, but this enhancement is associated with an increase in the pressure drop. Similarly, as pitch decreases, average Nu increases and pressure drop decreases. Numerical studies are given by Ahmed et al (2012). The authors investigated the effects of nanofluid volume fractions, channel amplitude, pitch and Re on mean and local Nusselt number, coefficient of friction, and heat transfer enhancement. The findings show that the coefficient of friction and the Nu increase with amplitude. In addition, as nanofluid volume fractions increase, the Nu rises with a slight increase in the friction coefficient.

The objective of this study is to evaluate the impact of CuO-water nanofluid on the thermal and hydraulic behavior of a triangular corrugated channel. The corrugated channel used is filled with CuO-water nanofluid. We are also trying to understand the influence of the nanofluid on the forced convection mechanism in this corrugated channel. In this context, we have used the Fluent computational code and carried out a parametric study of the thermomechanical and geometrical parameters. Numerical simulations are carried out for Re numbers ranging from 100 to 800 and for different volume fractions for the base fluid (water, $\varphi = 0$) and for CuO nanoparticles (φ ranging from 0.01 to 0.05).

Mathematical Modeling

Physical Model

Figure 1 illustrates the problem under study, which consists of a triangular corrugated channel. Our problem concerns the study of forced convection in a triangular corrugated duct. The height and total length of the triangular corrugated channel are H and L, respectively. The corrugated channel consists of ten corrugation units whose length, wavelength and corrugation amplitude are L_2, p and a, respectively. It is also assumed that the channel is charged with CuO-water nanofluid of uniform size and shape. The thermophysical characteristics of CuO nanoparticles and water are shown in Table 1.

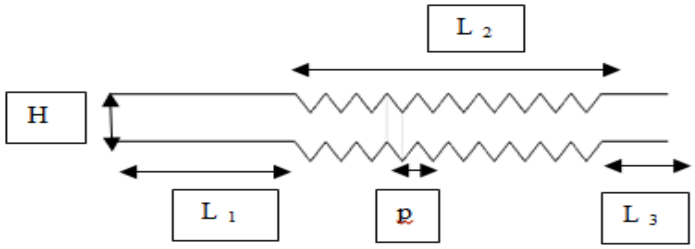

Figure 1. Studied configuration

Table 1. Thermo physical properties of nanoparticles and water

	ρ[Kg m^{-3}]	Cp[J Kg^{-1} K]	K[W m^{-1} K^{-1}]	□□□[Kg m^{-1}s^{-1}]
Water	996.5	4181	0.613	0.001
CuO	6500	533	17.65	_

Governing Equations

The governing equations are:

Continuity equation

$$\frac{\partial \mathrm{u}}{\partial \mathrm{x}} + \frac{\partial \mathrm{v}}{\partial y} = 0 \tag{1}$$

x - Momentum equation

$$\left(\mathrm{u}\frac{\partial u}{\partial x} + \mathrm{v}\frac{\partial u}{\partial y}\right) = \frac{1}{\rho_{nf}}\left[-\frac{\partial \mathrm{P}}{\partial \mathrm{x}} + \mu_{\mathrm{nf}}\left(\frac{\partial^2 \mathrm{u}}{\partial \mathrm{x}^2} + \frac{\partial^2 \mathrm{u}}{\partial \mathrm{y}^2}\right)\right] \tag{2}$$

y - Momentum equation

$$\left(\mathrm{u}\frac{\partial \mathrm{v}}{\partial x} + \mathrm{v}\frac{\partial \mathrm{v}}{\partial y}\right) = \frac{1}{\rho_{\mathrm{nf}}}\left[-\frac{\partial \mathrm{P}}{\partial \mathrm{y}} + \mu_{\mathrm{nf}}\left(\frac{\partial^2 \mathrm{v}}{\partial \mathrm{x}^2} + \frac{\partial^2 \mathrm{v}}{\partial \mathrm{y}^2}\right)\right]$$
(3)

Energy equation

$$\mathrm{u}\frac{\partial \mathrm{T}}{\partial \mathrm{x}} + \mathrm{v}\frac{\partial \mathrm{T}}{\partial \mathrm{y}} = \frac{\mathrm{K}}{\rho_{\mathrm{nf}} \mathrm{C}_{\mathrm{pnf}}}\left(\frac{\partial^2 \mathrm{T}}{\partial \mathrm{x}^2} + \frac{\partial^2 \mathrm{T}}{\partial \mathrm{x}^2}\right) \tag{4}$$

Boundary Conditions

Channel Inlet

The velocity component is obtained from Re based on the hydraulic diameter.

$$u_{nf} = \frac{\mu_{nf} \times R_e}{D_h \times \rho_{nf}} \tag{5a}$$

- Cold constant temperature is imposed.

Channel Outlet

$$\frac{\partial \mathrm{u}}{\partial \mathrm{x}} = 0, \frac{\partial \mathrm{v}}{\partial \mathrm{x}} = 0, \frac{\partial \mathrm{T}}{\partial \mathrm{x}} = 0 \tag{5b}$$

Walls of Corrugated Channel

$$u = v = 0$$
(5c)

Nanofluid Property

Density

$$\rho_{nf} = (1 - \varphi)\,\rho_f + \varphi \rho_P \tag{6}$$

Heat Capacity

Most studies done in the literature use one of the two models given by Pak & Cho, (1998) or Xuan & Roetzel, (2000). The later model is given by:

$$(\rho\ Cp)_{nf} = (1-\varphi)\ (\rho\ Cp)_f + \varphi(\rho\ Cp)p \tag{7}$$

Effective Dynamic Viscosity

Two models are proposed, Brinkman, (1952) and Corcione, (2010). The second is evaluated by the following correlation:

$$\frac{\mu_{nf}}{\mu_f} = \frac{1}{1-34{,}87\left(\frac{d_p}{d_f}\right)\varphi^{1.03}} \tag{8}$$

Where: dp is the diameter of the CuO particle and df that of the base liquid.

Effective Thermal Conductivity

Thermal conductivity plays a very important role in heat transfer (Choi & Eastman (1995); Eastman at al., (1996); Frouillat et al., (2011); Maxwell, (1881); Hamilton & Crosser, (1962). In this work, the used conductivity is that introduced by Maxwell (1881).

$$K_{nf} = \frac{(k_p+2k_f) - 2\varphi(k_f-k_p)}{(k_p+2k_f) + \varphi(k_f-k_p)}.K_f \tag{9}$$

Where: K_{nf} is the thermal conductivity of the nanofluid; k_f that of the base fluid; k_p that of solid particles and φ the volume fraction.

Numerical Method

The FLUENT code was applied to calculate the flow characteristics of the used fluid. For our study, the mesh chosen is based on quadratic cells. The accuracy and stability of our simulation results depend on the quality of the mesh, so a test of mesh independence on the solution was carried out for different numbers of nodes.

Results and Discussion

The numerical findings are derived for a two-dimensional flow of the CuO-water nanofluid They are presented in the form of velocity, pressure, temperature, velocity profile, variation of the Nu as a function of Re and nanoparticle volume fraction.

Independence Mesh

The influence of the mesh has been considered in order to obtain satisfactory solutions. To demonstrate the impact of the mesh size on the numerical findings, three mesh sizes (310131; 446825 and 607973) were tested in the flow regime and presented in the form of the local variation of the Nu, the heat transfer coefficient, the velocity profiles, the temperature at $Re = 500$ and a nanoparticle volume fraction, $\varphi = 0.05$.

Figures 2 and 3, show that the three meshes have an identical appearance and that the profiles are insensitive to the numbers of nodes. In order to minimize the computational burden, the considered mesh in this study is 446825 for Re varying from 100 to 800 and volume fractions between 0% and 5%. The grid independence test revealed that grid 446825 guarantees a satisfactory solution.

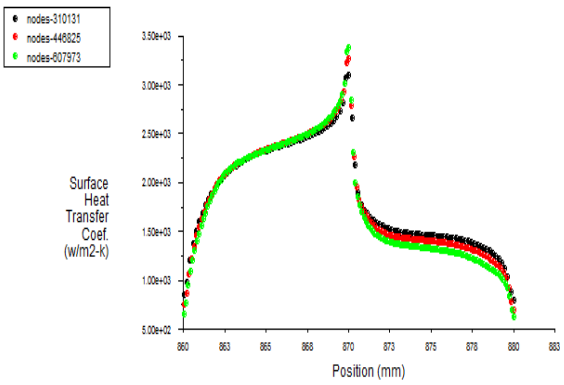

Figure 2. Variation of heat transfer coefficient with $Re = 500, \varphi = 0.05$ for different meshes

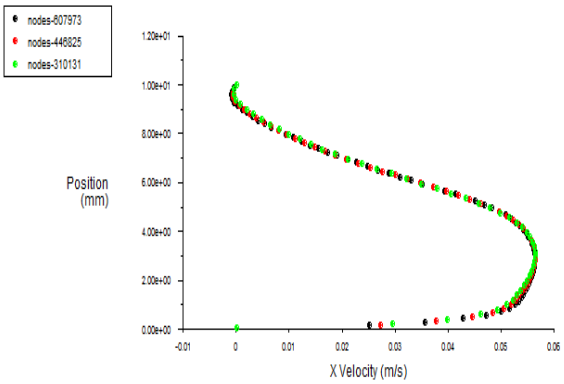

Figure 3. Profiles of the velocity horizontal component at $x = 0.860$ with $Re = 500, \varphi = 0.05$ for different meshes

Code Validation

Simulation validation is required to verify the precision of the findings obtained by the Fluent CFD code. A comparison of our results was made with the study by Ahmed et al, (2014a) which considered a triangular corrugated channel and a constant temperature imposed on the corrugated walls. Figure 4 shows the evolution of average Nu as a function of Re for a triangular corrugated channel using a volume fraction $\varphi = 0.05$. It can be seen that Nu is influenced by Re and that an increase in Re leads to a rise in Nu.

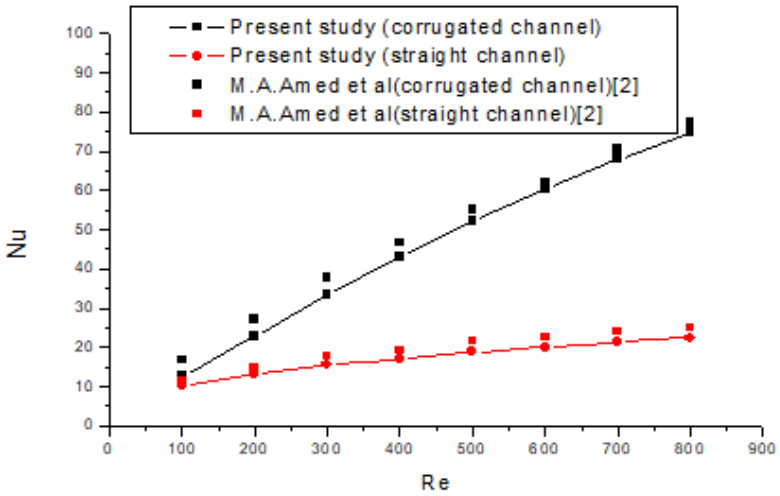

Figure 4. Variation of mean Nu versus Re at $\varphi = 0.05$

In addition, the Nu numbers for the triangular channel are much higher than those for the smooth channel. We also note that there is good accord with the findings of Ahmed et al. (2014a). Figure 5 shows the change in Nu versus various volume fractions at $Re = 300$. It can be seen that an increase in volume fraction leads to a rise in Nu. It is also observed that the Nu values are greater than those of the smooth channel. Moreover, there is good agreement between the numerical results obtained by this simulation and those of Ahmed et al. (2014a).

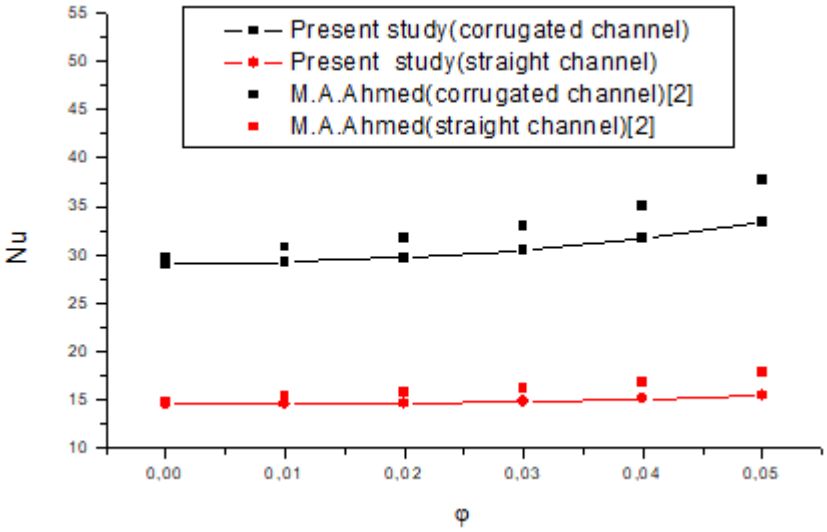

Figure 5. Variation of mean Nu versus volume fractions at $Re = 300$

Results and Discussion

The numerical findings are obtained for various Reynolds numbers which vary between 100 and 800 and different volume fractions, φ ranging from 0% to 5%. The effect of Re and volume fractions on flow and heat transfer will be analyzed in this numerical study.

Reynolds Number Effect

The dynamic and thermal fields are presented for various Reynolds numbers at a volume fraction $\varphi = 5\%$.

a- Dynamic Field

Figure 6 a, b, c illustrates the contours of the average velocity for various at a volume fraction $\varphi = 0.05$. We see a central flow with velocities more and more important as the Reynolds number increases. These velocities decrease to zero near solid walls, thus the non-slip condition is satisfied.

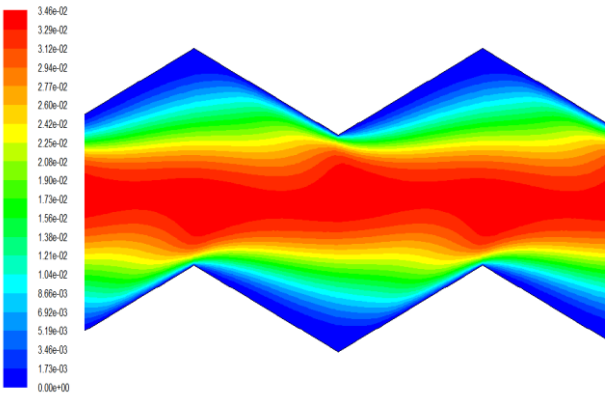

(a)

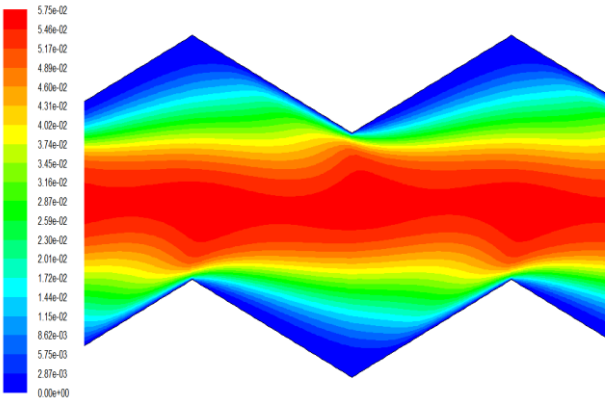

(b)

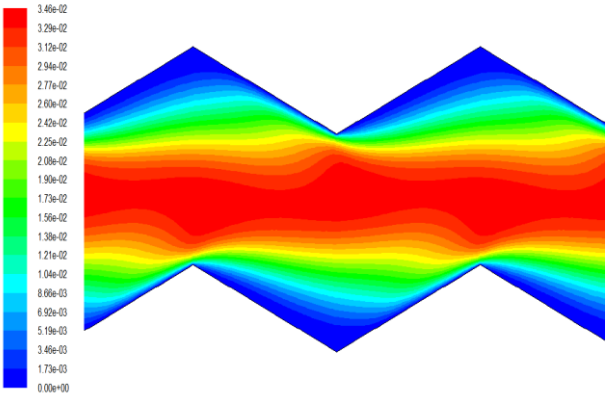

(c)

Figure 6. Velocity contours at $\varphi = 0.05$
$(a) Re = 300$ $(b)\ Re = 500$ $(c)\ Re = 800$

Thick dynamic boundary layers are seen along the upper wall corresponding to dunes, and along the lower wall in valleys where fluid velocities are low, and recirculation zones are present. We also note that the rate of thickening of the boundary layers becomes greater as the Re increases. Recirculation zones appear in the troughs of dunes and valleys. These zones grow in size as the Re increases.

The velocity profiles for various Re with $\varphi = 0.05$ at the stations $x = 0.860\,m$ and $x = 0.870\,m$ are represented by figure 7 a, b. We notice the appearance of negative velocities. This is due to the emergence of recirculation zones in the hollows of the dunes and valleys and that they are more and more important in increasing Reynolds number.

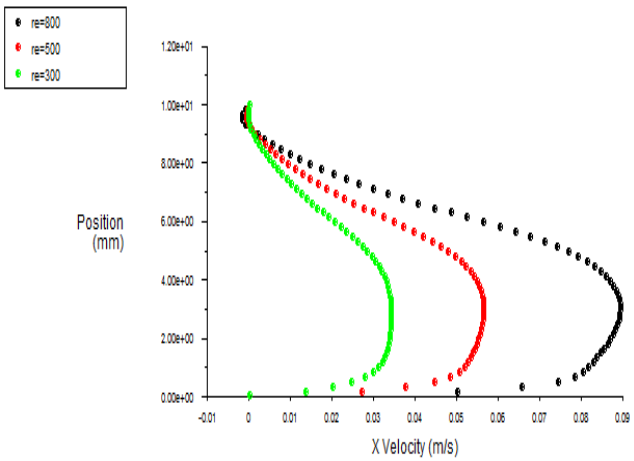

(a)

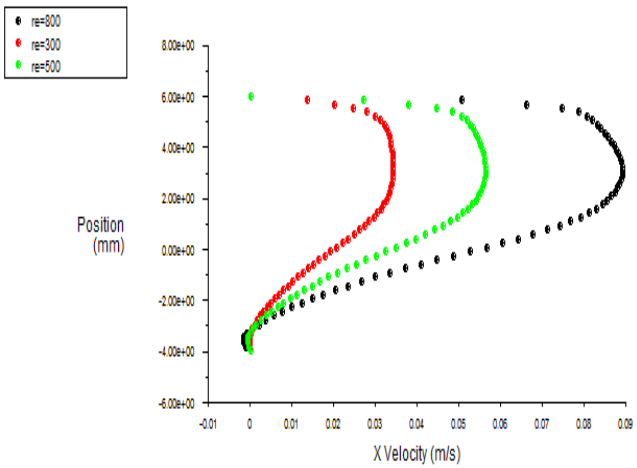

(b)

Figure 7. Profiles of the horizontal component of the velocity at $\varphi = 0.05$ for various Re
$(a)\ x = 0.860\ m$ $(b)\ x = 0.870\ m$

b- Thermal field

Figure 8 shows the change in mean Nu versus Re for the triangular wavy channel filled with CuO and water. We can see that the Nu is influenced by the Re. We also find that increasing Re leads to an increase in Nu, and that Nu values for CuO nanoparticles are greater than those for water.

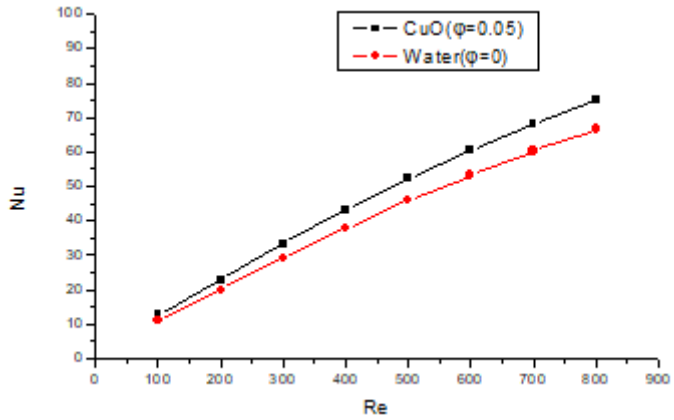

Figure 8. Change of the Mean Nu vs Re

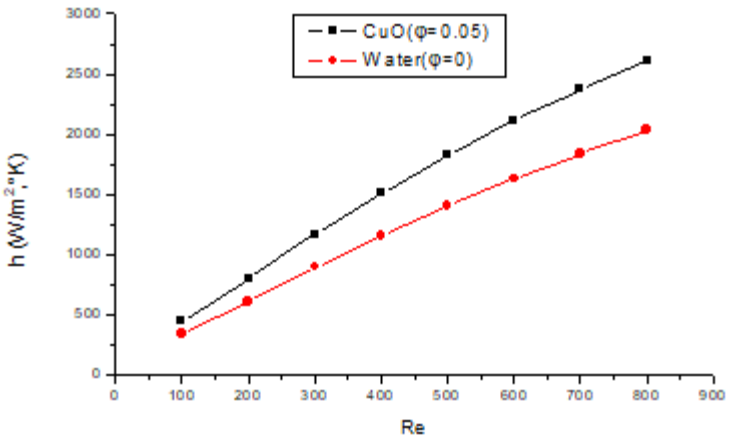

Figure 9. Change of the heat exchange coefficient vs Re

The evolution of the heat exchange coefficient versus Re for CuO and water is shown in Figure 9. The thermal coefficient h rises with increasing Re. The values of h for CuO are also large compared with those for water.

Volume Fraction Effect

Figure 10 a, b reveals the impact of volume fractions on average Nu at $Re = 300$ and $Re = 500$ for corrugated and smooth channels. It can be seen that an improvement in volume fractions causes an increase in Nu. This is explained by the improved thermal conductivity of the base fluid. It can also be observed that the Nu values of the wavy channel for the different volume fractions are much greater than those of the smooth one, due to the appearance of recirculation zones in the wavy channels, which improve heat transfer between the cold fluid in the channel and the hot fluid near the channel walls. It can also be seen that increasing the Reynolds number generates a very significant increase in Nu values. This is caused by the growing volume of recirculation zones.

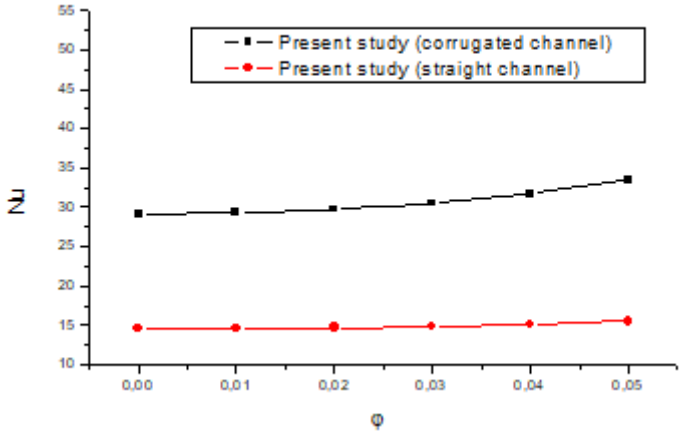

(a)

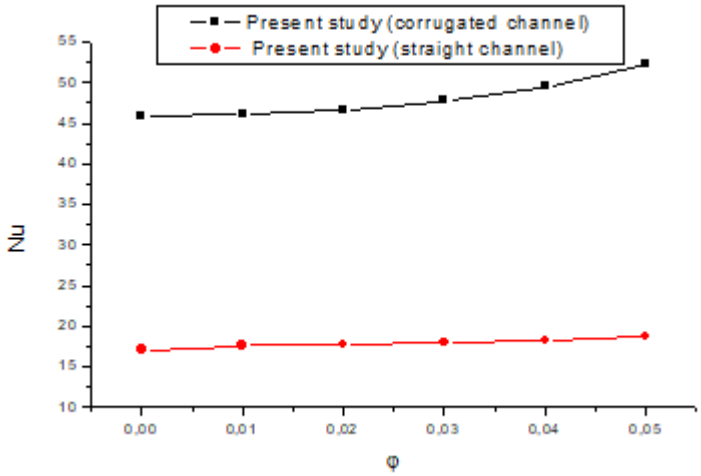

(b)

Figure 10. Variation of the mean Nu as a function of volume fractions
(a) $Re = 300$; (b) $Re = 500$

The impact of volume fractions on the heat exchange coefficient at $Re = 300$and $Re = 500$ is shown in Figure 11 a, b for the corrugated and smooth channels. We see an increase in the coefficient h with increasing volume fractions. This is due to the increase in the Nu and the improved thermal conductivity of the nanofluid. The values of the exchange coefficient are larger than those of the smooth channel, and are very significant as the Re increases. Figure 12 illustrates the change in mean Nu versus Re for various volume fractions. It can be seen that the improvement in heat transfer increases with increasing volume fractions and Reynolds number, as the addition of nanoparticles to the base fluid (water) improves the thermal conductivity of the fluid and hence the increase in heat transfer.

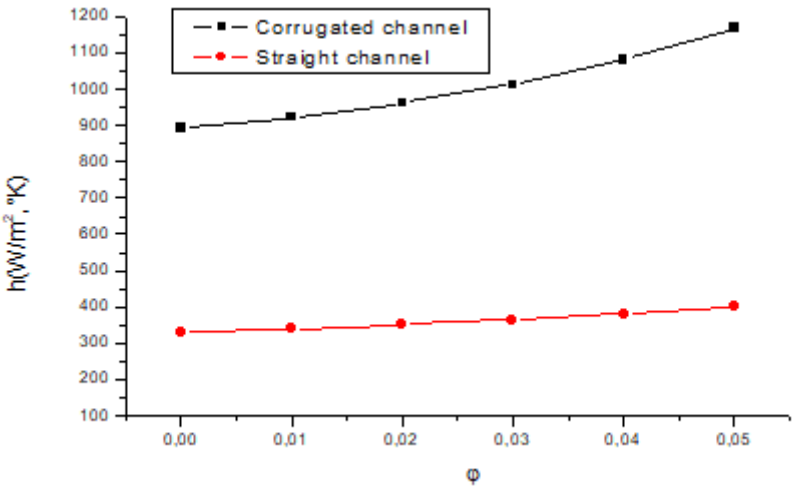

(a)

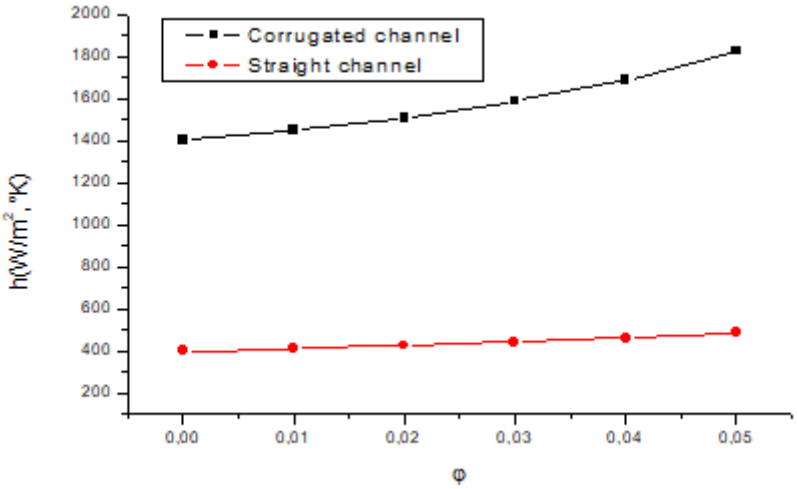

(b)

Figure 11. Variation of the heat exchange coefficient vs volume fractions (a) $Re = 300$; (b) $Re = 500$

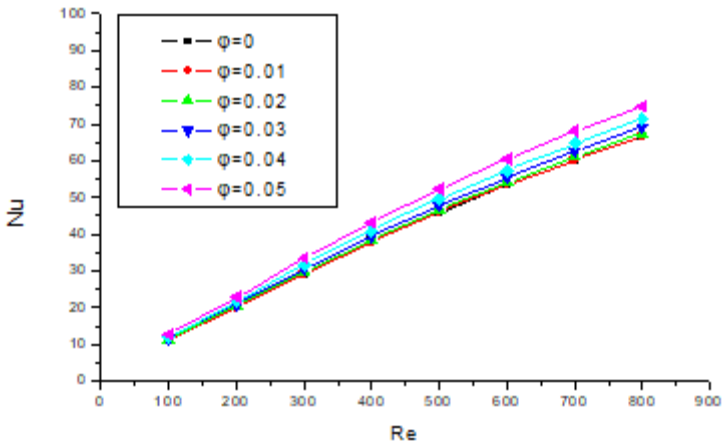

Figure 12. Change of the mean Nu vs Re for various volume fractions

The variation of the heat exchange coefficient for various volume fractions as a function of Re at $Re = 300$ and $Re = 500$ is illustrated in Fig. 13 a, b for the corrugated and smooth channels. An increase in the thermal coefficient h is noted with increasing volume fractions as well as Reynolds number, as fluid velocity is an important factor in heat transfer.

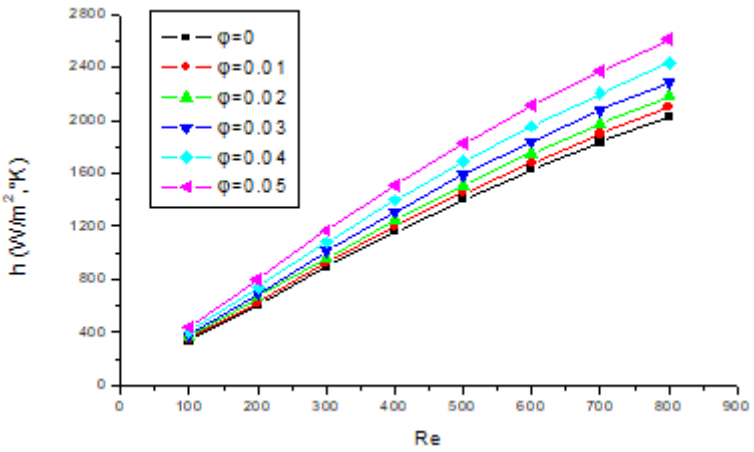

Figure 13. Variation of heat exchange factor as a function of Re for various volume fractions

Conclusions

In this work, a numerical investigation of convective heat transfer has been presented in a wavy channel filled with a mixture of water and nanofluids. The geometric configuration of the physical model is a triangular corrugated channel whose walls are subjected to an imposed temperature. Numerical simulations are also carried out for Re ranging from 100 to 800 and for various volume fractions for the base fluid (water, $\varphi = 0$) and for the CuO nanoparticle (φ ranging from 0.01 to 0.05). The basic equations are solved using the finite volume method and the numerical resolution is performed by the CFD code FLUENT. We noted that our numerical simulation procedure was confirmed by comparing our findings with those published in the literature, and good concordance was observed. The main outcomes are summarized below:

- Increasing the Reynolds number improves forced convection flow.
- Increasing the nanofluid volume fraction enhances heat transfer.

Scientific Ethics Declaration

The authors declare that the scientific ethical and legal responsibility of this article published in EPSTEM journal belongs to the authors.

Acknowledgements or Notes

* This article was presented as a poster presentation at the International Conference on Technology, Engineering and Science (www.icontes.net) held in Antalya/Turkey on November 16-19, 2023.

* This research was partially supported by the Algerian MESRS. Project research N°: A11N01UN250120200005.

References

Abed, A. M., Sopian, K., Mohammed, H. A., Alghoul, M. A., Ruslan, M. H., Mat, S., & Al-shamani, A.N. (2015). Enhance heat transfer in the channel with V-shaped wavy lower plate using liquid nanofluids. *Case studies in Thermal Engineering, 5*, 13-23.

Ahmed, M. A., Yusoff, M. Z., & Shuaib, N. H. (2012). Numerical investigations on the heat transfer enhancement in a wavy channel using nanofluid. *International journal of Heat and Mass Transfer, 55*, 5891-5898

Ahmed, M. A., Yusoff, M. Z., & Shuaib, N. H. (2013b). Effect of geometrical parameters on the flow and heat transfer characteristics in trapezoidal-corrugated channel using nanofluid. *International Communications in Heat and Mass Transfer, 42,* 69-74.

Ahmed, M. A., Yusoff, M. Z., Ng, K. C., & Shuaib, N. H. (2014a). Effect of corrugation profile on the thermal-hydraulic performance of corrugated channels using CuO-Water nanofluid. *Case studies in Thermal Engineering, 4,* 65-75.

Ahmed, M. A., Yusoff, M. Z., Ng, K. C., & Shuaib, N. H. (2014b). The effect of wavy-wall phase shift on thermal-hydraulic performance of Al_2O_3-Water nanofluid flow in sinusoidal-wavy channel. *Case studies in Thermal Engineering, 4,* 153-165.

Ahmed, M. A., Yusoff, M. Z., Ng, K. C., & Shuaib, N. H. (2015a). Numerical and experimental investigations on the heat transfer enhancement in corrugated channels using SiO2-Water nanofluid. *Case studies in Thermal Engineering, 6,* 77-92.

Ahmed, M. A., Yusoff, M. Z., Ng, K. C., & Shuaib, N. H. (2015b). Numerical investigations on the turbulent forced convection of nanofluids flow in a triangular-corrugated channel. *Case studies in Thermal Engineering, 6,* 212-225.

Ahmed, M. A., Yusoff, M. Z., Shuaib, N. H., & Ng, K. C. (2013a). A numerical study of laminar forced convection flow of Al_2O_3 - water nanofluid in triangular-corrugated channel. *ICEE.* Putrajaya, Malaysia

Brikman, H. C. (1952). The viscosity of concentrated suspensions and solutions. *The Journal of Chemical Physics, 20,* 571-581.

Choi, S.U.S., & Eastman, J. A. (1995). Enhancing thermal conductivity of fluids with nanoparticles. *ASME-Publ-Fed, 231,* 99-106.

Coorcione, M. (2010). Heat transfer features of buoyancy-driven nanofluids inside rectangular enclosures differentially heated at the sidewalls. *International Journal of Therm. Science, 45,* 1536-1546.

Eastman, J. A., Choi, S.U.S., Li, S., Thompson, L. J., & Lee, S. (1996). Enhanced thermal conductivity through the development of nanofluids. *MRS Proceeding, 457,* 3.

Frouillat, S., Bontemps, A., Ribeiro, J. P., Gruss, J. A., & Soriano, O. (2011). Hydraulic and heat transfer study of SiO_2 /Water nanofluids in horizontal tubes with imposed wall temperature boundary conditions. *International Journal of Heat and Fluid Flow, 32,* 424-439.

Hamilton, R. L., & Crosser, O. K. (1962). Thermal conductivity of heterogeneous two component systems. *Industrial and Engineering Chemistry Fundamentals, 1*(3), 187-191.

Heidary, H., & Kermani, M. J. (2010). Effect of nanoparticles on forced convection in sinusoidal-wall channel. *International Communications in Heat and Mass Transfer, 37,* 1520-1527.

Maxwell, J. A. (1881). *A treatise on electricity and magnetism* (2nd ed.). Oxford: Clarendon Press.

Pak, B. C., & Cho, Y. I. (1998). Hydrodynamic and heat transfer study of dispersed fluids with submicron metallic oxide particles. *Exp. Heat Transfer, 11,* 151-170.

Xuan, Y. M., & Roetzel, W. (2000). Conceptions for heat transfer correlation of nanofluids. *International Journal of Heat Mass Tranfer, 43*(19), 3701-3707.

Author Information

Rahima Benchabi
University of Mentouri Brothers
Constantine 1, 25000 Algeria
Contact e-mail: rbenchabi*@yahoo.fr*

Ahsene Lanani
University of Mentouri Brothers
Constantine 1, 25000 Algeria

To cite this article:

Benchabi, R., & Lanani, A. (2023). Effect of CuO-water nanofluid on the thermal - hydraulic behavior of triangular corrugated channel. *The Eurasia Proceedings of Science, Technology, Engineering & Mathematics (EPSTEM), 26,* 375-386.

The Eurasia Proceedings of Science, Technology, Engineering & Mathematics (EPSTEM)
ISSN: 2602-3199

The Eurasia Proceedings of Science, Technology, Engineering & Mathematics (EPSTEM), 2023

Volume 26, Pages 387-394

IConTES 2023: International Conference on Technology, Engineering and Science

Effect of Heat Treatment on Wear Behavior of Chromoly Steel

Soumaya Meddah
Research Center in Industrial Technologies (CRTI)

Mounira Bourebia
Research Center in Industrial Technologies (CRTI)

Latifa Kahloul
National Higher School of Technology and Engineering

Sihem Achouri
Research Center in Industrial Technologies (CRTI)

Amel Oulabbas
Research Center in Industrial Technologies (CRTI)

Samia Lemboub
National Higher School of Technology and Engineering

Ahlem Taleb
Research Center in Industrial Technologies (CRTI)

Wafa Boumacheta
National Higher School of Technology and Engineering

Abstract: Chromoly steel is a steel widely used in mechanical manufacturing, it finds many applications for oil and gas, aerospace, and automotive industries. In addition, its ductility, its resistance and its relatively low weight, and its malleability constitute one of the characteristics of choice for the manufacturers. In order to improve the use properties of this steel such as resistance to rupture, corrosion, wear and minimize the risks of fragility, heat treatments are considered in this study. Hence, the objective of this experimental work is to study the effect of heat treatment by quenching followed by tempering at different temperatures on the hardness, structural state, and wear resistance of chromoly steel. In addition, an investigation on the evolution of the rate of bearing surface after friction test was carried out. The results show on the structural level that the sample having undergone quenching followed by tempering at 700°C for 15min, presents a microstructure of globular pearlite with the coalescence of the complex carbides of Mo-Cr-Nb, and a hardness of 226HB. However, regarding the tribological behavior, the sample treated at 600°C recorded an improved wear rate of 49% compared to the sample treated at 550°C. For the wear mechanisms, the abrasive wear mechanism is observed for untreated sample, while the adhesive wear mechanism is dominant for the heat-treated samples. In addition, the rate of the lower bearing surface "Sr2" of this same sample was improved by 2.7% compared to that treated at 550°C.

Keywords: Chromoly steel production, Quenching and tempering treatment, Mechanical property, Structure, Wear resistance.

Introduction

In the mechanical engineering sector, to improve the mechanical properties of materials, quenching and tempering (Q&T) heat treatment is the standard treatment route used for commercial steels with medium carbon low alloy. The demand for these steels is gradually increasing in several sectors, due to their superior mechanical properties, their excellent fracture toughness and their high resistance to fatigue and wear (Hafeez, 2020; Sanij, 2012).These treatments offer the possibility of modifying the structural state and adjusting the mechanical properties of steels, such as hardness, resistance to wear, corrosion and fatigue (Bourebia, 2019; Mosayebi, 2021). By correctly selecting the tempering conditions, a wide range of mechanical properties, among others hardness and wear resistance can be obtained. These mechanical properties are an important aspect for medium carbon steels. However, several researchers have carried out investigations on the influence of quenching and tempering (Q&T) heat treatment, in order to elucidate the effect of this process on the microstructural evolution and the mechanical properties. These treatments provide an opportunity for the development of cost effective parts with improved properties. These research strategies are based on the development of microstructures consisting of ultrafine microconstituents formed in non-equilibrium conditions, such as martensite or bainite, in combination with Retained Austenite (RA) (de Diego-Calderón, 2015).

In this context, de Diego-Calderón et al.(2015) have studied the effect of Q&P with varying parameters (quenching temperature, partitioning temperature and time) on microstructure evolution and mechanical behaviour of Q&P steels with nominal composition of 0.25C–1.5Si– 3Mn–0.023Al (mass %). The results show that, a Multi-phase microstructure was obtained (different fractions of Tempered Martensite (TM), Untempered Martensite (UM) and Retained Austenite (RA)). The PT has a important effect on mechanical properties of the Q&P steel.

Qiangguo Li et al. (2020) studied the effects of bainite content on the mechanical properties of the triplex microstructure (bainite, martensite and retained austenite) in a quenched and partitioned medium-carbon bainitic steel, by controlling the temperature and holding time of the isothermal transformation. The results show that with the increase of the isothermal holding temperature from 320 to 400°C, the bainite changes from lower bainite to higher bainite and the ultimate yield strength and toughness decrease.

In the same context, in the work of Hafeez et al. (2020), the effect of cyclic heat treatment (SQT, DQT and TQT) on the mechanical and corrosion properties of medium carbon low alloy steel is studied. The results show the formation of fine ε-carbide ($Fe_{2.4}C$) after intermediate tempering at low temperature in DQT and TQT heat treatments. In addition, DQT and TQT heat treatments, improved the mechanical and corrosion properties of steel, in comparison to SQT heat treatment.

Hence, medium carbon low alloy steel (chromoly steel) was produced and cast at the URMM/CRTI laboratory in an induction furnace. This steel has been subjected to heat treatments including conventional quenching and tempering processes at different temperatures. Therefore, the objective of the present work is to validate the microstructure/mechanical properties, and Q&T parameters relationship. Dry friction tests were also performed to evaluate the wear resistance. In addition, an investigation on the evolution of the bearing surface rate after friction test was carried out.

Method

Samples of chromoly steel produced in an induction furnace under atmosphere controller(0.33C–0.55Mn–0.39Si–0.912Cr–0.188Mo–0.013Ni–0.045Cu-0.024Nb-0.079V-0.017P –0.007S, wt%) have undergone a heat treatment of quenching (austenization at 950°C for 15 min then quenched in oil). It should be noted that the temperature Ac3 was calculated according to formula 1 (http://micro.icaunais.free.fr/05_trait_therm.pdf). The quenched steel was tempered for a 15 min at various temperatures of 550°C, 600°C, and 700°C (Figure 1). The microstructural characterization and the wear mechanisms were revealed by scanning electron microscope type Quanta 250/FEI. A load of 187.5 kgf was used for Brinell hardness test.

Low alloy steels (C<0,6%) :

$$Ae1 \sim Ac1 = 723 - 10{,}7Mn - 16{,}9Ni + 29{,}1Si + 16{,}9Cr + 6{,}38W + 290As$$

$$Ae3 \sim Ac3 = 910 - 203\sqrt{C} - 15{,}2Ni + 44{,}7Si + 104V + 31{,}5Mo + 13{,}1W - 30Mn - 11Cr - 20Cu + 700P + 400Al + 120As + 400Ti\ldots \quad (1)$$

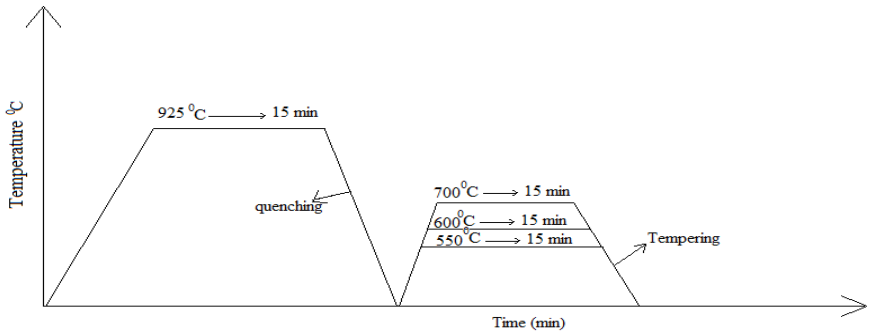

Figure 1. Schematic illustration of heat treatment (Quenching and Tempering).

For the friction tests, samples of size (1cmx1cmx1cm) were previously prepared by mechanical polishing. These friction tests were carried out using a typical tribometer ball/pin-on-disk, CSM Instrument according to ASTM G99-95 at ambient temperature using a 100C6 ball of 6 mm in diameter, under the following conditions: Load 8N, linear speed 2cm/s, distance traveled 50m. The friction coefficient was recorded automatically during the test using the Tribox 4.49 data acquisition software. The roughness parameters were measured (bearing surface) using a 3D laser source profiler of Cyber-Technology type, CT100 scan according to DIN ISO 25178. The wear rate is calculated according to the Archard (1961) formula (Eq.2), after calculating the worn surface.

$$Ws = V / PL \quad (2)$$

-W (mm3/N/m) is the wear rate;
-V (mm3) is the wear volume;
- P (N) the applied load;
- L (m) the sliding distance.

Results and Discussion

Microstructural Evolution

The microstructure of the different samples is shown in Figure 2. The sample produced has a Ferrito-pearlitic structure (0.33% C), after a normalization treatment at 900°C for 1 hour, and cooling in air. After austenization at 925°C and water quenching, the microstructure obtained is lower bainite, which is in the form of lath.

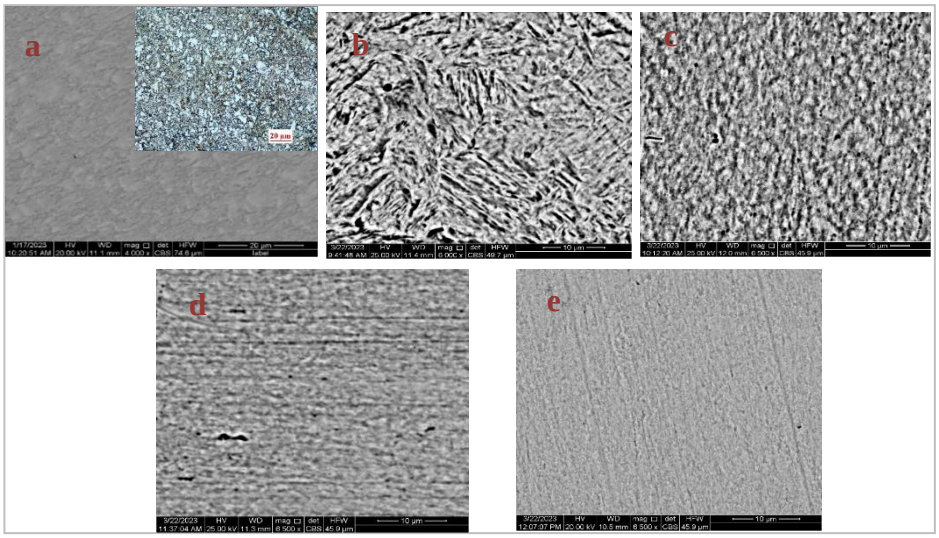

Figure 2. Microstructural evolution: a) Initial structure (B), b) Quenched, c) Tempering 550°C, d) Tempering 600°C, e) Tempering 700°C.

The carbon precipitates in the form of cementite which appears in the form of sticks of the same orientation within the bainitic ferrite supersaturated with carbon then in the austenite enriched with carbon (Élodie Boucard , 2014). The microstructure of the sample tempered at 550°C and 600°C - 15 min reveals the nucleation of fine carbides and the tendency for the bainitic morphology of lath to disappear. For the microstructure of the sample tempered at 700° C.-15 min, the microstructure obtained is globular pearlite including spheroidized carbide.

Hardness Evolution

Figure 3 displays the variation in hardness after the various quenching and tempering heat treatments. It can be seen that the hardness depends on the treatment temperature. However, the highest hardness is recorded for the sample quenched at 925°C which has a bainitic structure. Whereas, the decrease in hardness occurs at higher tempering temperatures. The same result is observed in the work of Mosayebi et al. (2021) and Hafeez et al. (2020). At 700°C, there is coalescence of the carbides (change in their morphology, globulization and a more homogeneous structure), which leads to a softening of the structure, and consequently a reduction in hardness.

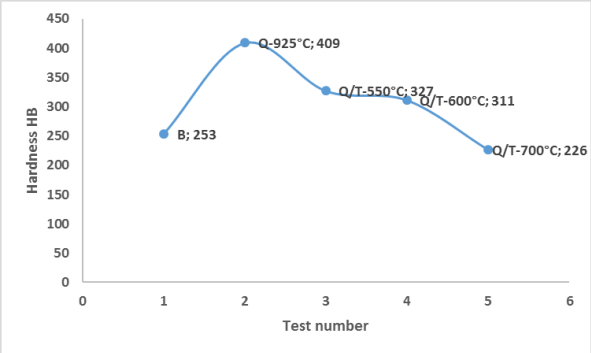

Figure 3. Hardness evolution during quenching and tempering.

Evolution of Friction Coefficient and Wear Rate

Analysis of the curves illustrated in Figure 4 show the variation of the friction coefficient for the tribological couple Chromoly steel (Q, Q/T)/100C6 as a function of the distance travelled. These curves clearly indicate the existence of three phases (Meddah, 2022). Friction begins with a break-in period during which the friction coefficient increases rapidly to reach a maximum value. This period is characterized by a plastic deformation of the surface asperities. The second phase is the transition phase, which is characterized by a slight decrease in the friction coefficient. This is due to the formation of the third body (wear debris), which acts as a solid lubricant. During the third period, the friction coefficient stabilizes and its value remains constant regardless the distance traveled. The friction coefficient reaches a maximum value of 0.567 for the quenched sample and a minimum value of 0.383 for the quenched sample and tempered at 700°C.

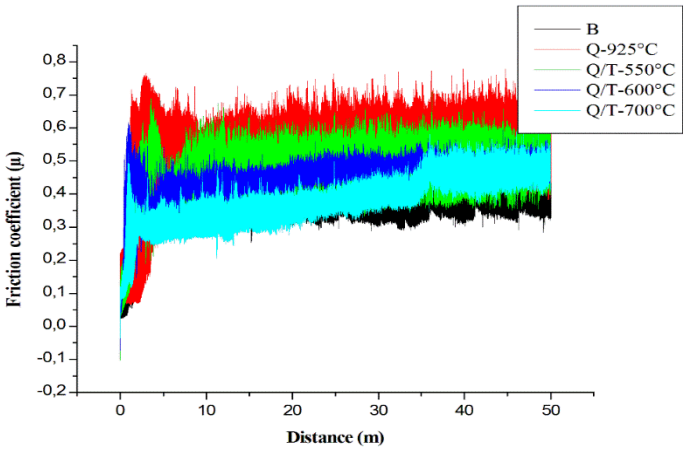

Figure 4. Evolution of friction coefficient as a function of heat treatment (Quenching/Tempering).

The evolution of the wear rate according to the heat treatment (quenching/tempering) is presented in the histogram of Figure 5. From this histogram, it is observed that the sample quenched at 925°C/water recorded the lowest wear rate equivalent to 1.192×10^{-5} $mm^3/N/m$. Whereas, the sample after normalization treatment recorded the highest wear rate equivalent to 3.864×10^{-5} $mm^3/N/m$. This result indicates that Archard's law is validated, where the volume of material lost is inversely proportional to the hardness value of the material (Meddah, 2020; Archard, 1953).

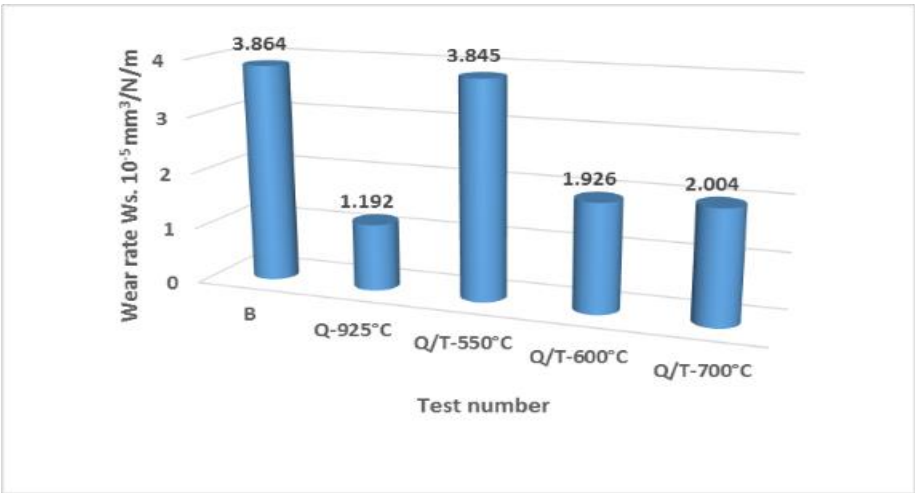

Figure 5. Evolution of wear rate as a function of heat treatment (Quenching/Tempering).

According to these results, it can be seen that the quenching and tempering treatment has provided an improvement in the wear resistance, which is manifested by the lower value of the wear rate. This behavior depends on the microstructure formed after treatment, the volumetric fraction, the morphologies, the size and the nature of the carbides formed. Moreover, the wear debris detached from the surface results in the formation of an adherent oxide film during the wear process which prevents the direct contact of the two rubbing bodies (Meddah, 2022).

Wear Track Morphology

Figure 6. show the SEM micrographs from the worn surfaces for tested samples . The micrograph for sample 1 (after normalization treatment) reveals the parallel grooves to the sliding direction, and the flakes confirming the presence of abrasive and adhesive wear mecanisms, with predominance of abrasive wear favoring the delamination of the rubbed surface. These observations are confirming by the highest wear rate. However for samples that have undergone the quenching and tempering treatment at different temperature, their micrographs reveals the parallel deep grooves to the sliding direction, signes of delamination, and wear debris resulting from the destruction of surface roughness. These observations confirm the abrasive and adhesive wear mechanisms with predominance of the adhesive mechanism. The latter is manifested by the lower wear rate recorded by the heat-treated samples, compared to the untreated one. This may be related to the structural state and to the adhesion of iron oxide to the contact surface. Hence, the good ductility of these iron oxides means that the non-abrasive particles promote wear by adhesion (Meddah, 2022).

Evolution of Bearing Surface

The evolution of the upper Sr1 and lower Sr2 bearing surface ratios for the friction test carried out after different heat treatments is illustrated in Figure 7. From witch, we note an improvement in the Sr1 parameter varying from 1.15% to 40.63%. This improvement shows the beneficial effect of heat treatment. It is explained by the distribution of the carbides formed, as well as their volume fractions, hence the homogenization of the microstructure which increases the bearing surface. On the other hand, the parameter Sr2 decreases, this phenomenon is explained by the detachment of the debris from the surface which causes a degradation of the latter; hence a reduction in the bearing surface.

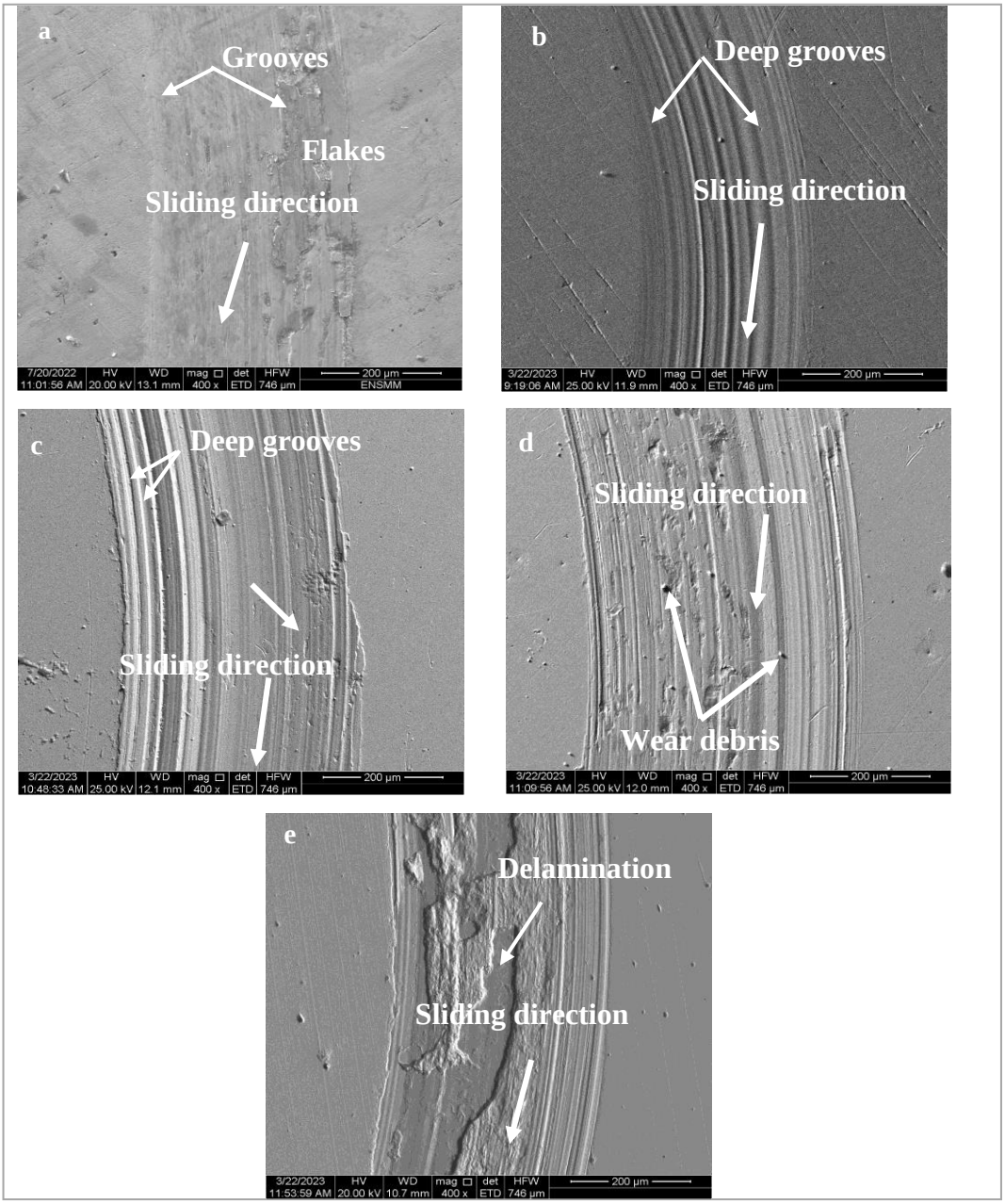

Figure 6. Wear mechanisms after friction test : a) Initial structure (B), b) Quenched, c) Tempering 550°C, d) Tempering 600°C, e) Tempering 700°C.

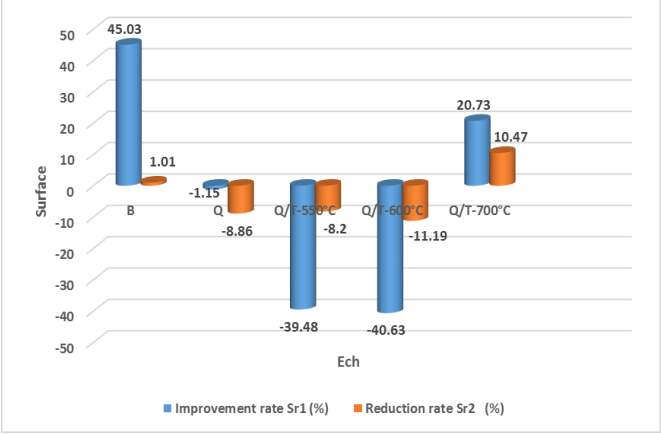

Figure 7. Evolution of improvement and reduction rate.

Conclusion

The effects of quenching and tempering heat treatment parameters on the microstructural evolution and the mechanical properties of a medium carbon steel have been studied. The main results can be summarized as follows:

Quenching resulted in the formation of lower bainite, while the microstructure after tempering at 700° C.-15 min is globular pearlite including spheroidized carbide. By increasing the tempering temperature, the hardness decreases to reach minimum values of 226HB. The highest friction coefficient is recorded for the quenched sample with a value of 0.567. The lowest wear rate is recorded for the quenched sample with a value 1.192×10^{-5} $mm^3/N/m$, indicating improved wear resistance. Predominance of the abrasive wear mechanism for untreated sample, while the adhesive wear mechanism is dominant for the heat-treated samples. An improvement in the rate of upper bearing surface Sr1with a rate varying from 1.15% to 40.63% during the running-in period. A reduction in the rate of the lower bearing surface Sr2 with a rate that varies between 8.2% and 11.19%.

Scientific Ethics Declaration

The authors declare that the scientific ethical and legal responsibility of this article published in EPSTEM journal belongs to the authors.

Acknowledgements or Notes

* This article was presented as an poster presentation at the International Conference on Technology, Engineering and Science (www.icontes.net) held in Antalya/Turkey on November 16-19, 2023.

* I would like to thank all the engineers of the PTSM/CRTI platform and the National Higher School of Technology and Engineering.

References

Archard, J. (1953). Contact and rubbing of flat surfaces. *Journal of Applied Physics*, *24*(8), 981-988.

Archard, J. F. (1961). Single contacts and multiple encounters. *Journal of Applied Physics*, *32*(8), 1420-1425.

Bourebia, M., Meddah, S., Hamadache, H., Taleb, A., Gharbi, A., & Laouar, L. (2019). Effect of heat treatment on surface hardness and tribological behavior of XC38 steel—approach by the experiments plans. *Materials Research Express*, *6*(7), 076568.

de Diego-Calderón, I., De Knijf, D., Molina-Aldareguia, J. M., Sabirov, I., Fojer, C., & Petrov, R. (2015). Effect of Q&P parameters on microstructure development and mechanical behaviour of Q&P steels. *Revista de Metalurgia*, *51*(1), 10-3989.

de Diego-Calderón, I., De Knijf, D., Molina-Aldareguia, J. M., Sabirov, I., Fojer, C., & Petrov, R. (2015). Effect of Q&P parameters on microstructure development and mechanical behaviour of Q&P steels. *Revista de Metalurgia*, *51*(1), 10-3989.

Élodie, B. les-Metz, F. (2014). *Étude de l'influence de l'état métallurgique de l'austénite sur la microstructure de transformation de phase dans les aciers bas carbone*. (Doctoral dissertation).

Hafeez, M. A., Inam, A., & Farooq, A. (2020). Mechanical and corrosion properties of medium carbon low alloy steel after cyclic quenching and tempering heat–treatments. *Materials Research Express*, *7*(1).

Micro icaunais free (n.d.). *Les traitements thermiques des aciers.* Retrieved from http://micro.icaunais.free.fr/05_trait_therm.pdf

Meddah, S., Bourebia, M., Gherfi, K., Lakhdar, L., Oulabbas, A., Achouri, S., & Kahloul, L. (2022). Influence of dry friction on the wear behavior of X52 steel—experimental study and simulation using response surfaces method. *The International Journal of Advanced Manufacturing Technology*, 1-11.

Meddah, S., Chadli, H., Bourebia, M., Montagne, A., Iost, A., Labaiz, M., & Taleb, A. (2020). Dry sliding wear performance of an annealed TiNi alloy with different nickel contents. *Materials Research Express*, *7*(3), 036508.

Mosayebi, A., Soleimani, M., Mirzadeh, H., & Dehghanian, C. (2021). Tempering kinetics and corrosion resistance of quenched and tempered AISI 4130 medium carbon steel. *Materials and Corrosion*, *72*(11), 1808-1812.

Sanij, M. K., Banadkouki, S. G., Mashreghi, A. R., & Moshrefifar, M. (2012). The effect of single and double quenching and tempering heat treatments on the microstructure and mechanical properties of AISI 4140 steel. *Materials & Design*, *42*, 339-346.

Author Information

Soumaya Meddah
Research Center in Industrial Technologies (CRTI), P.O.BOX 64, Cheraga 16014 Algiers, Algeria
Contact e-mail: *s.meddah@crti.dz*

Mounira Bourebia
Research Center in Industrial Technologies (CRTI), P.O.BOX 64, Cheraga 16014
Algiers, Algeria

Taleb Ahlem
Research Center in Industrial Technologies (CRTI), P.O.BOX 64, Cheraga 16014
Algiers, Algeria

Boumacheta Wafa
National Higher School of Technology and Engineering 2000 places pedagogic Sidi Amar, Annaba, Algeria

Latifa Kahloul
National Higher School of Technology and Engineering 2000 places pedagogic Sidi Amar, Annaba, Algeria

Sihem Achouri
Research Center in Industrial Technologies (CRTI), P.O.BOX 64, Cheraga 16014
Algiers, Algeria

Amel Oulabbas
Research Center in Industrial Technologies (CRTI), P.O.BOX 64, Cheraga 16014
Algiers, Algeria

Samia Lemboub
National Higher School of Technology and Engineering 2000 places pedagogic Sidi Amar, Annaba, Algeria

Ahlem Taleb
Research Center in Industrial Technologies (CRTI), P.O.BOX 64, Cheraga 16014
Algiers, Algeria

Wafa Boumacheta
National Higher School of Technology and Engineering 2000 places pedagogic Sidi Amar, Annaba, Algeria

To cite this article:

Meddah, S., Bourebia, M.**,** Kahloul , L., Achouri, S.**,** Oulabbas, A., Lemboub, S. , Taleb, A**.** & Boumacheta, W. (2023). Effect of heat treatment on wear behavior of chromoly steel. *The Eurasia Proceedings of Science, Technology, Engineering & Mathematics (EPSTEM), 26*, 387-394.

The Eurasia Proceedings of Science, Technology, Engineering & Mathematics (EPSTEM)
ISSN: 2602-3199

The Eurasia Proceedings of Science, Technology, Engineering & Mathematics (EPSTEM), 2023

Volume 26, Pages 395-403

IConTES 2023: International Conference on Technology, Engineering and Science

Comparison of the Effects of Vegetable Oils such as Castor and Canola Oil and Polyol Esters on the Metalworking Performance of Ti-6Al-4VAlloy by Tapping Torque Method

Kubra Kavut
Marmara University
Belgin Oil R&D Center

Hanife Gulen -Tom
Belgin Oil R&D Center

Tugce Ozpercin
Belgin Oil R&D Center

Abstract: Ti-6Al-4V material is an alloy of particular interest for engineering applications in a wide range of industries, especially aerospace and medicine, due to its outstanding corrosion resistance, favorable strength-to-weight ratio and biocompatibility properties. Due to the low thermal conductivity and high chemical reactivity of this alloy, its machinability is quite limited and is therefore referred to as the "difficult-to-cut" alloy. When the problems encountered in the processing of Ti-6Al-4V alloy are evaluated, the preparation of the appropriate cutting environment, ensuring optimum cutting parameters and the use of appropriate coolant are the priorities in overcoming these problems. Vegetable oil and polyol esters are biodegradable base fluids that can be used as a sustainable alternative to petroleum-derived oils in many lubricant applications. In this study, the effects of castor and canola oils and trimethylolpropane trioleate (TMPTO) and trimethylolpropane trioleate complex (TMPCX), neopentyl glycol (NPG) and pentaerythritol tetra-oleate (PE-TO) type polyol esters on the machining performance of Ti-6Al-4V alloy were investigated using the Tapping Torque test method. In the tests performed on Ti-6AL-4V, it was determined that the tapping performances of TMP-TO, TMP-CX, PE-TO and castor oil were close to each other and gave the best results. It has also been determined that the tapping performance of canola oil is lower than these oils. NPG-DO gave a striking result for Ti-6AL-4V and the tapping performance was found to be very low.

Keywords: Sustainability, Metalworking fluids, Tapping torque, Vegetable oils, Polyol ester, Ti-6Al-4V

Introduction

Titanium is considered to be one of the strongest metals. Its strength, heat, water and salt resistance, and its light weight make it the ideal metal for a variety of applications. Titanium alloys retain the same strength and corrosion resistance, but takes on the greater flexibility and malleability of the metal it is combined with. Titanium alloys, therefore, have more applications than pure titanium (Biesiekierski et al., 2021). Titanium alloys with low density, high specific strength, corrosion resistance, good process performance and biocompatible are of particular interest in engineering applications in a wide range of industries, such as aerospace engineering and medicine (Cui et al., 2011). Recently, the application ratio of CFRP (Carbon Fiber Reinforced Plastic) to airframes and engine parts has been growing to improve aircraft fuel consumption. Similarly, demand for titanium is also growing as it has excellent compatibility with CFRP with respect to corrosiveness and coefficient of thermal expansion issues (Inagaki et al., 2014). In addition to the advantages of

titanium alloys, they also have a major disadvantage such as difficult machinability. Titanium alloys are extremely difficult to machine due to their relatively high tensile strength, low ductile yield rate, 50% lower modulus of elasticity (104 GPa), and approximately 80% lower thermal conductivity than steel (Ahmed et al., 2012). Due to the low thermal conductivity of titanium, the heat generation during machining operation is very high which badly affects the machining performance and life of the tool. Due to heat generation at the machining zone, the surface quality of the workpiece gets hampered (Roy et al., 2018). Since the most important parameter in the machining of titanium is to ensure the removal of heat resulting from the friction between the tool and the material, it is extremely important to ensure cooling and lubrication balance during machining. In this regard, utilization of metal working fluids is crucial for effective machining of titanium alloys. Heat generated can be reduced in the cutting zone and excessive friction can be prevented by helping of metal working fluids. As a result, life of mechanical systems can be extended. When the problems encountered in the machining of titanium alloys are evaluated, the preparation of the appropriate cutting environment, ensuring optimum cutting parameters and the use of appropriate coolant are the first priorities in overcoming these problems.

The difficult machinability properties of titanium limit the use of traditional metalworking fluids in the processing of these alloys, and therefore special processing fluids need to be developed in the processing of these types of alloys. The use of metalworking fluids with flood lubrication operations is the most common use in the machining of light alloys (Priarone et al., 2014). However, conventional metalworking fluid formulations used in flood lubrication consist of toxic, non-biodegradable, unsustainable and environmentally harmful petroleum-derived products based on mineral oil as base oil. In line with the increasing demand for the use of light alloys in the aerospace, automotive and medical sectors, the environmental and health risks caused by flood lubrication, which is widely used in the processing of these alloys, and the demand for reducing the cost factor have increased the interest in research on the development of more economical and environmentally friendly production technologies. Another reason for the need to develop new products and technologies in the machining of light alloys is the need to produce alternative lubricants that can ensure sustainability due to the depletion of petroleum reserves (Kavut et al., 2022). There are various sustainable feedstocks to produce bio-lubricants. Highly unsaturated or high oleic vegetable oils (HOVOs), low viscosity polyalphaolefins (PAOs), polyalkylene glycols (PAGs), dibasic acid esters (DEs) and polyol esters (PEs) are categories of biodegradable base oils (Nagendramma & Kaul, 2012).

Vegetable oils which have large market share for biolubricants, are abundant and non-toxic feedstocks. They exhibit higher lubricity, higher flash point, lower volatility, and higher viscosity index than mineral oils. Presence of long chain fatty acid and polar groups in the structure of vegetable oil make them suitable for both boundary and hydrodynamic lubrications. Besides their advantages, they have low oxidation stability and their low temperature properties are poor. Thus, they can easily polymerize in the harsh working condition. This situation limits their industrial application (Wickramasinghe et al., 2021). Low viscosity biodegradable polyalphaolefins (PAOs) are another alternative for environmentally friendly lubricants and can be defined as low molecular dimers to tetramers. While low molecular weight causes undesirable high volatility for these fluids, it becomes an advantage at low temperatures where PAOs perform excellently. The absence of polarity of PAOs cause to problems of additive acceptability, but this results in excellent hydrolytic stability. Since PAOs have no double bonds or other reactive functional groups in their structure, oxidative stability of PAO with antioxidant additive is competitive to petroleum-based products. PAOs are finding increasing use as hydraulic and engine oils, especially in cold climate applications and where hydraulic pressures increase, as they are an attractive option for converting biodegradable lubricants to water in low temperature applications. PAOs are also used as gear lubricants because of their ability to provide lower operating temperatures and lower coefficients of friction, which helps reduce wear.

On the contrary of PAOs, polyalkylene glycols (PAGs) have high polarity as they have alternating ether linkages rather than essentially having a hydrocarbon backbone. However, they can be easily contaminated with moisture, resulting in increased solubility in water, which is detrimental for many lubricant applications. The solubility problem of organic additives in PAGs and the incompatibility of PAGs with conventional petroleum-based lubricants are often problematic for this species. For biodegradable PAGs usage, fire resistant fluids are often the best option. The high molecular weight of diesters makes volatility problems negligible and ester bonds provide high solubility power. Branching in alcohol fragments results in very good low temperature performance, but diesters score poorly in final biodegradability tests. For this species, ester linkages are not sterically hindered to restrict hydrolytic decomposition. Diesters find use in biodegradable hydraulic fluids with long drain intervals, compressor oils turbine oils, and are mixed with PAOs in some synthetic lubricants. Diester fluids have outstanding solubility and cleaning ability. Because of these properties, it can have a negative effect

on certain varnish or paint surfaces. This limits the use of dibasic acid esters. The most main area where dibasic acid esters find use is paint and coating applications.

At last, but not least, PEs are effective feedstocks. They consist of fatty acids attached to an alcohol and hydrogen atom on the β-carbon atom does not exist in their backbone. PEs are used as environmentally acceptable base fluids in high performance lubricants. PEs have found application in many lubricants due to its very good low temperature behavior, high thermo-oxidative stability of some types, very high viscosity index, good anti-wear and low evaporation properties. The physico-chemical characteristics of PEs indicate that the properties are matching with the conventional base stocks. The development of new synthetic-based base fluids to meet the needs of high-performance lubricants is increasing day by day. As a result, the use of synthetic esters as base fluids has gained great importance in various industrial and military applications. Examples of lubricant types using PEs are engine oils, gear oils, hydraulic oils, compressor oils, pump and turbine oils. Also, PEs are being evaluated for lubricity performance with a view for their application as metal working fluids (Kavut et al, 2022). In addition to the limited number of studies in the literature on comparing the metal processing behavior of these biodegradable base stocks, this study we will present can provide a very valuable perspective on the literature, considering the abundance of vegetable oils and the advantages of PEs.

There are various performance tests for metal working fluids. Lubricity behavior of metal working fluids can be investigated with Tapping Torque test method. It is a favorable method as bench scale test and combines qualitative and quantitative techniques. Tapping is a metal machining process to cut or form threads in a pre-drilled hole in a metal specimen which can be made of various metals while lubricating the contact zone between tap and hole wall by a metalworking fluid. Finally, a torque value to cut or form a thread is obtained. Smaller torque values indicate better metal working performance (Demmerling, & Söffker, 2020) In this study, metal working performance of vegetable oils and PEs were evaluated with Tapping Torque test method. Ti-6Al-4V alloy was selected as the metal sample to be machined.

In this study, machining performance of the castor and canola oils and trimethylolpropane trioleate (TMPTO) and trimethylolpropane trioleate complex (TMPCX), neopentyl glycol dioleate (NPGDO) and pentaerythritol tetra-oleate (PETO) type PEs on the Ti-6Al-4V alloy were investigated using the Tapping Torque test method.

Method

Materials

In the present study castor and canola oils and TMPTO, TMPCX, NPGDO and PETO type polyol esters were used and their technical properties were given in Table 1. Castor oil and canola oil were supplied from Kim-paş A.Ş and Oleo Kimya, respectively. NPGDO, TMPTO and PETO supplied by Oleon. TMPCX was supplied from Temix Oleo.

Table 1. Technical properties of used compounds in the study.

Test Parameter	Test Method	Castor Oil	Canola Oil	NPGDO	TMPTO	TMPCX	PETO
Kinematic Viscosity (40℃, cSt)	ASTM D 445	150	46	23	46	70	65
Kinematic Viscosity (100℃, cSt)	ASTM D 445	14.4	10	6	9.2	12.5	14
Viscosity Index	ASTM D 2270	93	212	228	187	180	225
Flash Point (℃)	ASTM D 92	172	≥ 190	≥ 250	≥ 270	300	≥ 280
Pour Point (℃)	ASTM D 97	≤-21	≤-18	≤-18	≤-42	-33	≤-25

Molecular Structure of Compounds

Molecular structure of used compounds in the study was shown in Table 2. Machining performance of castor and canola oils and TMPTO, TMPCX, NPGDO and PETO type polyol esters were investigated by Tapping Torque Test. In Tapping Torque Test, Ti-6Al-4V alloy were used and test was carried out with 5.0 mm depth and 800 rpm.

Table 2. Molecular structure of used compounds in the study.

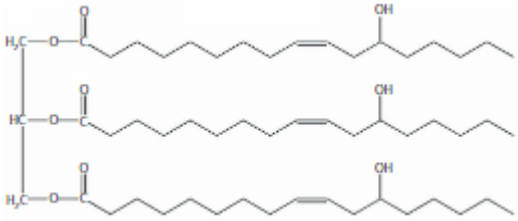 CASTOR OIL	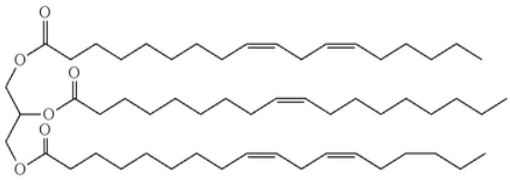 CANOLA OIL
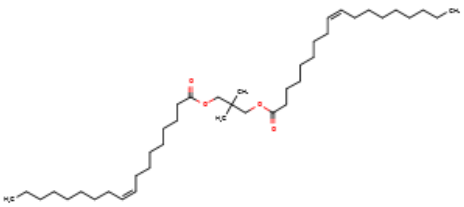 NPGDO	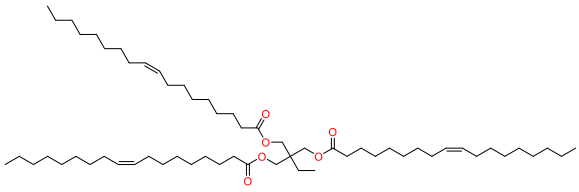 TMPTO
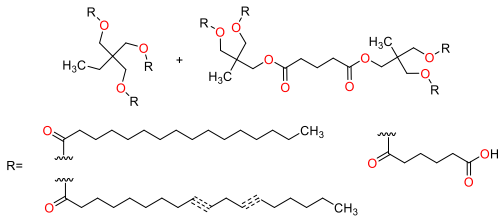 TMPCX	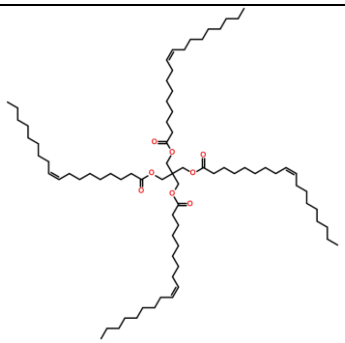 PETO

Tapping Torque Test

To understand of the machining performance of the neat fluids, a tapping torque test was conducted in Labtap G8 (Microtap, Munich, Germany). Comparison of vegetable oils and PEs using tapping torque testing machine was performed according to ASTM D8288. The material used for the machining was a Ti-6Al-4V alloy with pre-drilled holes as shown in Figure 1. A TTT-Ti6Al4V-M6C tool, size M6 with 69 helical channels per test plate was used for each fluid. Tapping Torque Test was performed using a Titanium Carbonitride (TiCN) coated tip suitable for the operation. The cutting fluid was poured in the holes to lubricate them during the tapping process at 300 rpm, with a 5.0 mm length of thread and each tapping process was repeated 3 times.

Figure 1. Tapping Torque Test System

Figure 2 shows the tapping process graphically where: (a) shows the beginning of the forming; (b) indicates the torque increasing and the tool penetrating the workpiece as a result of increasing contact surface between the workpiece and the tool; (c) implies the tool forming with all its chamber teeth until the length's thread is achieved and (d) indicates the beginning of the reversal of the forming tap to bring the tool to the initial position. Consequently, the forming performance results of the fluids were determined averaging the tapping torque values (N·cm) in the 0 to 14,4 mm range of form.

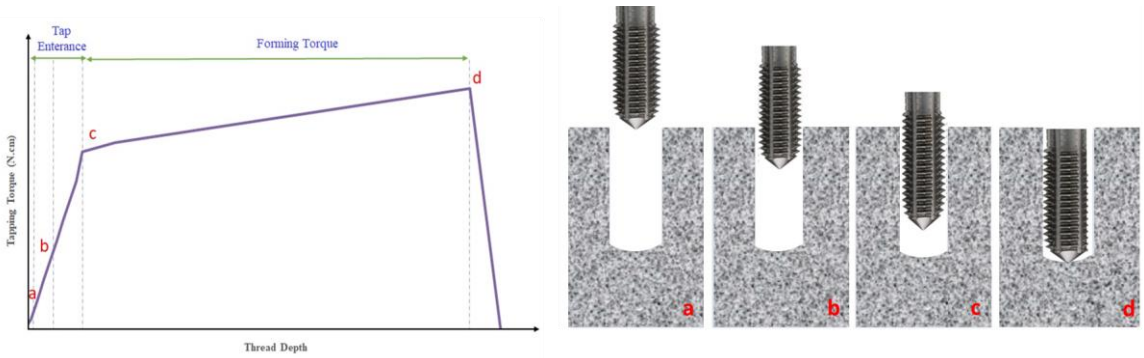

Figure 2. Graphical illustration of the tapping process and different positions of the tap during working. (a) beginning of the forming, (b) tool penetrating on workpiece, (c) teeth entering the chamber completely and (d) beginning of the reversal of the forming tap.

Results

Tapping torque test results of samples on Ti-6AL-4V series were shown in Table 3. In addition, torque graphs were obtained against the depth of cut applied to each sample, as shown in Figure 3 to Figure 8. Even a small difference observed in the torque value in the Ti-6AL-4V Tapping torque test is quite significant. It was determined that TMPTO exhibited the best machining performance on Ti-6Al-4V alloy, and the measured torque values of TMPCX and PETO were close to TMPTO. The measured torque value of castor oil was found to be close to TMPCX and PETO, but much worse than TMPTO. Canola oil was giving the most dramatic processing performance result.

Table 3. Tapping torque test results of neat fluids on Ti-6AL-4V alloy.

Test plate	Test Method	Castor Oil	Canola Oil	NPGDO	TMPTO	TMPCX	PETO
Ti-6Al-4V (300 rpm, d 5mm) (Nm)	ASTM D8288	149,9	152,8	187,1	146,5	147,4	148,2

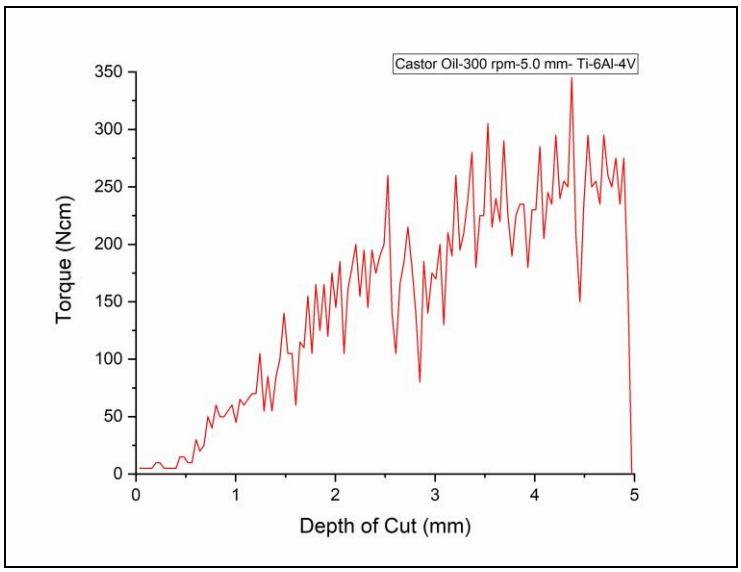

Figure 3. Tapping performance graphs of Castor Oil on Ti-6AL-4V.

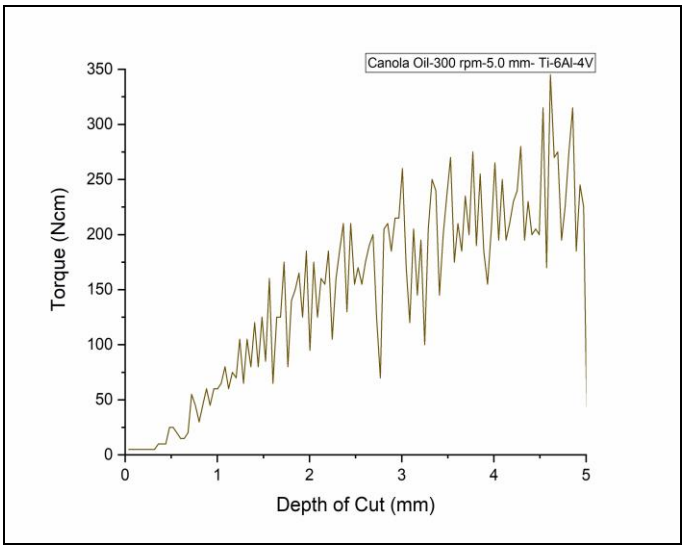

Figure 4. Tapping performance graphs of Canola Oil on Ti-6AL-4V.

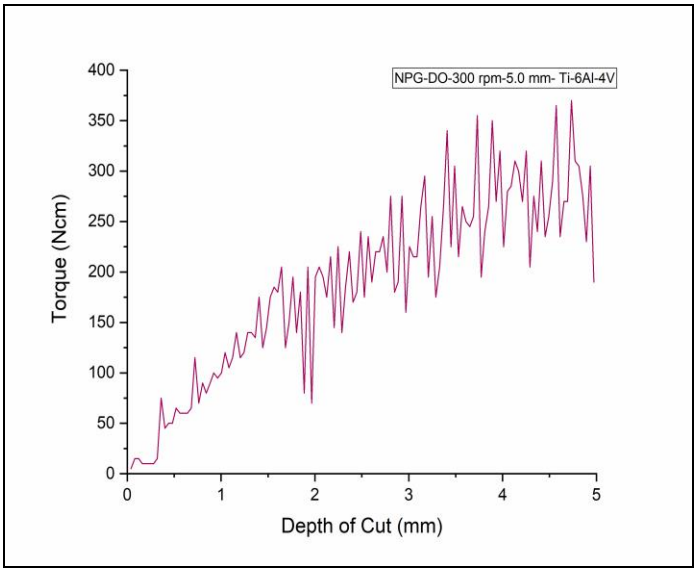

Figure 5. Tapping performance graphs of NPGDO on Ti-6AL-4V.

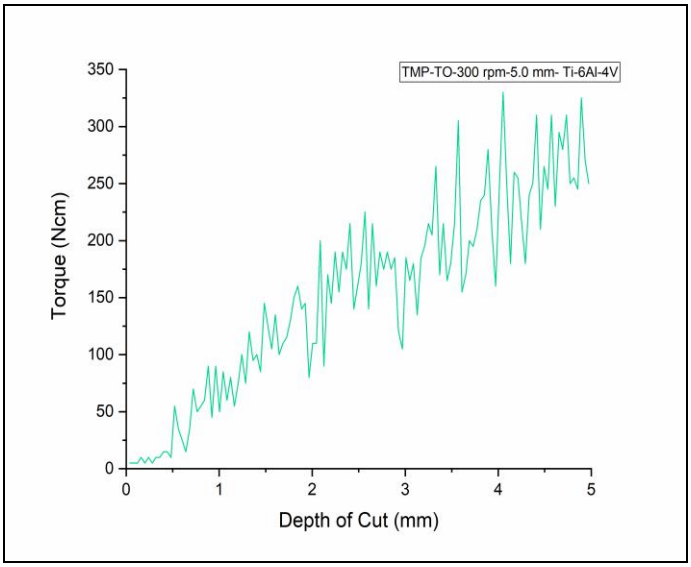

Figure 6. Tapping performance graphs of TMPTO on Ti-6AL-4V.

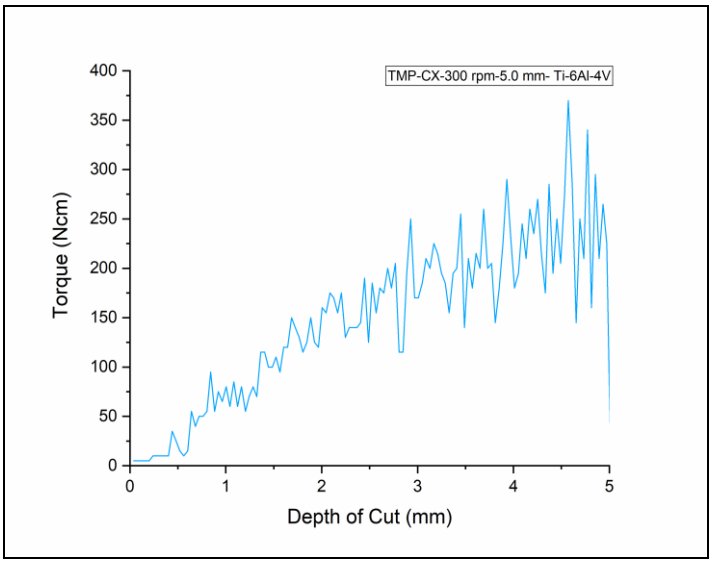

Figure 7. Tapping performance graphs of TMPCX on Ti-6AL-4V.

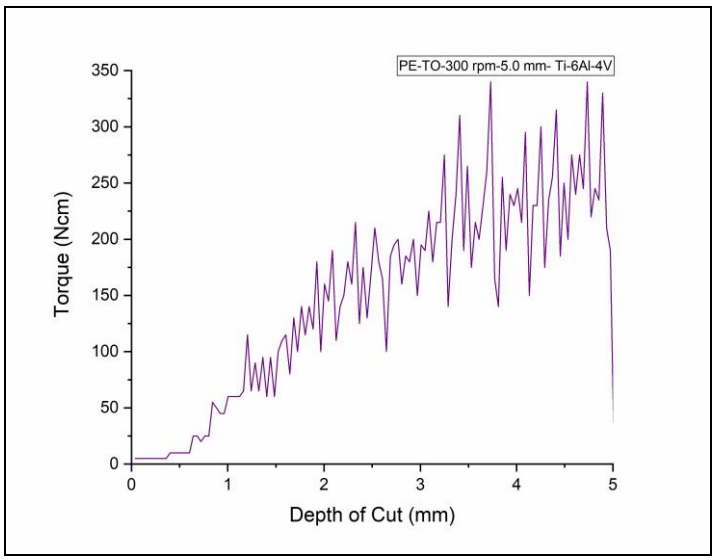

Figure 8. Tapping performance graphs of PETO on Ti-6AL-4V.

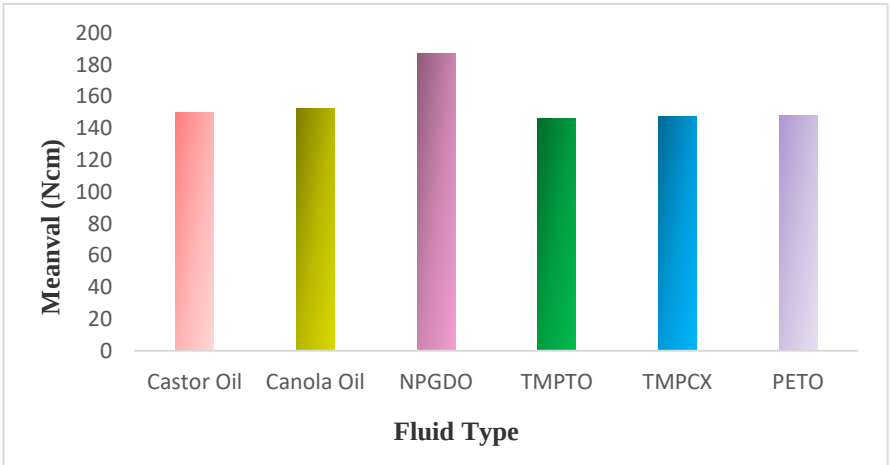

Figure 9. Tapping performance graphs of vegetable oils and esters on Ti-6Al-4V.

Conclusion

Machining performance of castor and canola oils and TMPTO and TMPCX, NPGDO and PETO type polyol esters were investigated by Tapping Torque Test on Ti-6Al-4V type titanium alloy. It was determined that TMPTO exhibited the best processing performance and NPGDO showed the worst performance machining performance on the Ti-6Al-4V. Samples was found as follows from best to worst:

TMPTO > TMPCX > PETO > Castor Oil > Canola oil > NPGDO.

Tapping torque test result graphs for neat liquids performed on the Ti-6Al-4V 1 are shown in Figure 9. Based on the above results, the following inferences can be drawn:

1. Since vegetable oils lack the oxidation stability, extreme pressure and anti-wear properties required to meet the demanding machining requirements of the Ti-6Al-4V alloy, as a result of the tests carried out on this alloy, the metal processing performance of both vegetable oils was determined to be quite low torque values compared to polyol esters.
2. The molecular structure of esters has a high impact on the conformation of the lubricant film, and increasing the ratio of esters in the lubricant film increases tribological performance. When the study was evaluated specifically for polyol esters, processing performance improved by increasing the ester parts on the molecule, resulting in stronger adsorption on the metal surface.
3. In the tests carried out on Ti-6Al-4V, TMPTO showed the best metal processing performance because it formed the highest lubricating film on the metal surface and therefore its lubricating effect was better than other polyol esters.
4. NPGDO exhibited the lowest adhesion ability to the Ti6Al4V surface among the tested vegetable oil and polyol esters, could not remove the heat generated on the tool and workpiece surface during operation, and exhibited the lowest metal processing performance with the highest torque value.
5. TMPCX and PETO similarly exhibited very good but relatively lower lubricity than TMPTO. This corresponds to a lower metal processing performance than TMPTO but very good compared to vegetable oils.
6. The results in this study indicate that oleate-type polyol esters, excluding NPGDO, have significant potential to be used as a sustainable and environmentally friendly alternative to mineral oil-based cutting fluids in machining operations of Ti-6Al-4V alloy.

Scientific Ethics Declaration

The authors declare that the scientific ethical and legal responsibility of this article published in EPSTEM journal belongs to the authors.

Acknowledgements or Notes

* This article was presented as an oral presentation at the International Conference on Technology, Engineering and Science (www.icontes.net) held in Antalya/Turkey on November 16-19, 2023.

* This study was carried out within the scope of the project labeled ARISEN, coded S0411 and financially supported by SMART Eureka.

References

Ahmed, W., Elhissi, A., & Jackson, M.J. (2012). The design and manufacture of medical devices. In *Precision Machining of Medical Devices* (pp. 59–113), Elsiever.

Biesiekierski, A., Munir, K., Li, Y., & Wen, C. (2021). Titanium alloys. In *Structural Biomaterials Properties, Characteristics and Selection* (pp.157-158). Woodhead Publishing Series in Biomaterials

Cui, C., Hu, B., Zhao, L., & Liu, S. (2011). Titanium alloy production technology, market prospects and industry development. *Materials and Design*, *32*(3), 1684–1691.

Demmerling, A., & Soffker, D. (2020). Improved examination and test procedure of tapping torque tests according to ASTM D5619 using coated forming taps and water-mixed metalworking fluids. *Tribology International, 145*. 106151.

Inagaki, I., Takechi, T., Shirai Y., & Ariyasu, N. (2014*) Application and features of titanium for the aerospace industry.* Nippon Steel & Sumitomo Metal Technical Report No. 106. Retrieved from https://www.nipponsteel.com/en/tech/report/nssmc/pdf/106-05.pdf

Kavut, K., Tom, H.G., & Ozpercin, T. (2022). Comparison of the effects of vegetable oils such as castor and canola oil and polyol esters on the metalworking performance of Al 6061 and Al 7075 metal alloys by Tapping Torque method. *The Eurasia Proceedings of Science Technology Engineering and Mathematics*, (21), 248 – 257.

Nagendramma, P., & Kaul, S. (2012). Development of ecofriendly/biodegradable lubricants: An overview. *Renewable and Sustainable Energy Reviews, 16*(1), 764-774.

Priarone, P. C., Robiglio, M., Settineri, L., & Tebaldo, V. (2014), Milling and turning of titanium aluminides by using minimum quantity lubrication, *Procedia CIRP, 24,* 62–67.

Roy,S., Kumar, R.A., Sahoo A.K., & Das, R. K. (2018). A brief review on machining of Ti-6Al-4V under different cooling environments. *IOP Conf. Series: Materials Science and Engineering, 455*(1).

Author Information

Kubra Kavut
Marmara University, Maltepe-Istanbul, Turkey,
Belgin Oil R&D Center Gebze-Kocaeli, Turkey
Contact e-mail: kubra.kavut@belginoil.com

Hanife Gulen -Tom
Belgin Oil R&D Center
Gebze -Kocaeli, Turkey

Tugçe Ozpercin
Belgin Oil R&D Center
Gebze-Kocaeli, Turkey

To cite this article:

Kavut, K., Gulen-Tom, H., & Ozpercin, T. (2023). Comparison of the effects of vegetable oils such as castor and canola oil and polyol esters on the metalworking performance of Ti-6Al-4V alloy by tapping torque method. *The Eurasia Proceedings of Science, Technology, Engineering & Mathematics (EPSTEM), 26*, 395-403.

The Eurasia Proceedings of Science, Technology, Engineering & Mathematics (EPSTEM)
ISSN: 2602-3199

The Eurasia Proceedings of Science, Technology, Engineering & Mathematics (EPSTEM), 2023

Volume 26, Pages 404-415

IConTES 2023: International Conference on Technology, Engineering and Science

Earthquakes in Kahramanmaras; Assessment of Affected Areas and Recommendations for Settlement Regeneration

Oktay Aksu
Istanbul Okan University

Agne Karlikanovaite-Balikci
Istanbul Okan University

Abstract: On February 6, 2023, two catastrophic earthquakes hit Turkey, causing significant damage and casualties. The main causes of these results are improper constructions and settlement placements. Regions where earthquake damage is typical are cities developed on fertile agricultural lands. Site selection for land suitability is one of the main application areas of the Geographical Information System (GIS). The Multi-Criteria Decision Approach (MCDA) has provided consistent and sufficient alternatives to decision-makers for land use planning activities for many years. This study focused on a large area covering five provinces with a total area of 36.409 km2 as the whole region represents 110.000 km2 and is challenging to manage in a single segment. Moreover, the heaviest damages were observed in the study area. Nine criteria were considered while using the weighted overlay function of the GIS via the Analytical Hierarchical Process (AHP). Agricultural and forest regions were excluded from the scope and the entire study area; 84.0% unsuitable, 0.4% low suitable, 1.5% moderately suitable, 11.3% suitable, and 3.2% highly suitable areas were identified for the post-disaster regeneration of settlements.

Keywords: Earthquake, Geographical Information System (GIS), Analytical Hierarchical Process (AHP), Site selection, Weighted overlay

Introduction

Turkey is situated in a very active tectonic area (Fig. 1) with the Northern Anatolian Fault (NAF) and Eastern Anatolian Fault (EAF) zones running through the entire country (KOERI, 2023). For a long time, these two zones have caused powerful earthquakes. There have been numerous casualties, particularly in the last 100 years. The 1936 Erzincan earthquake caused 32.968 deaths with a moment magnitude (Mw) of 7.9, and the 1999 Golcuk-Izmit (Marmara) and Duzce earthquakes caused 18.243 deaths with a moment magnitude of 7.4 (KOERI, 2023. The devastating Kahramanmaras earthquake, which hit on February 6, 2023, caused at least 50.500 deaths and caused the greatest damage in 11 provinces in Southern Turkey with moment magnitudes of 7.7 and 7.6 in a nine-hour interval. According to the Ministry of Interior Disaster and Emergency Management Presidency (AFAD), over 6,000 aftershocks have been recorded since the 7.7-magnitude earthquake hit Turkey and Syria (AFAD, 2023). Many people are still missing. According to the World Bank Disaster Assessment Report, 2023, the earthquake and aftershocks that hit southern Turkey on February 6 caused more than $34 billion in damage to the country. This amount equals 4 % of Turkey's 2021 gross domestic product (GDP).

Two primary reasons for the disaster's high number of deaths are a lack of building code enforcement and incorrect urbanization site selection. In the cities affected by the February 2023 earthquake, the widespread use of ready-mixed concrete was seen at a later date. As a result, it is a typical and expected circumstance that the concrete quality of structures built in the 1980s and 1990s, and even at the beginning of the 2000s, was below the project concrete class. At the same time, flat iron was used as rebar. Therefore, it is possible to say that

material weaknesses are one of the crucial factors in the collapse of the buildings built in these years or the heavy damage that they cannot be used (Turkiye Muhendislik Haberleri, 2023).

Regions where earthquake damage is typical are cities developed on fertile agricultural lands. Therefore, in weak ground conditions with deep bedrock and even on soils with liquefaction potential, 10-15 storey and flexible carrier system structures were severely damaged or collapsed entirely on February 6th. However, ground liquefaction may have occurred in some regions since structures that do not collapse but sink one storey or lean to the side have been recorded (Turkiye Muhendislik Haberleri, 2023).

Site selection for land suitability is one of the main application areas of the Geographical Information System (GIS). If adequate and proper criteria are defined, spatial analysis of GIS can provide viable options to decision-makers for optimal land use. Most of the studies in the literature focused on site selection problem for the landfilling area (Guler & Yomralioglu, 2017; Kamdar et al.,2019; Bilgilioglu et al., 2021; Dolui &Sarkar, 2021; Bilgilioglu, 2022;). However, there are few studies on landscape suitability for settlement, especially after an earthquake. Jena et al. (2019) used artificial neural networks and an analytical hierarchy process (AHP) to assess earthquake risk in Banda Aceh, Indonesia. They applied AHP to set criteria weights, grouped under susceptibility and hazard vulnerability. The aim was to evaluate potential hazards in Aceh City and provide technical recommendations to the urban planners. Dunford and Li (2011) evaluated the reconstruction activities in Wenchuan (China) after an earthquake of 8.0 on the Richter scale. Economic and social aspects of the recovery activities were considered, and areas suitable for reconstruction, appropriate suitable, and ecological reconstruction areas were classified, but GIS-based site selection was not included in their study.

Constructions of 405,000 new residences have been planned by the government in the Kahramanmaras earthquake area, according to the Post-Earthquake Assessment Report prepared by the Strategy and Budget Office (SBB, 2023). The location of new settlement sites will be critical in protecting people from future hazards and the environment from agricultural and forestry locations. This paper addresses a general review of the post-disaster area and recommendations on site selections using AHP and GIS for settlement regeneration, lacking in the scientific literature.

An Overview of the Disaster Area

The disaster area is located on and around the Eastern Anatolian Fault Zone (Fig. 1). Two consecutive earthquakes in Southeastern Turkey have affected eleven provinces (Adana, Adiyaman, Diyarbakir, Elazig, Gaziantep, Hatay, Kahramanmaras, Kilis, Malatya, Osmaniye, and Sanliurfa).

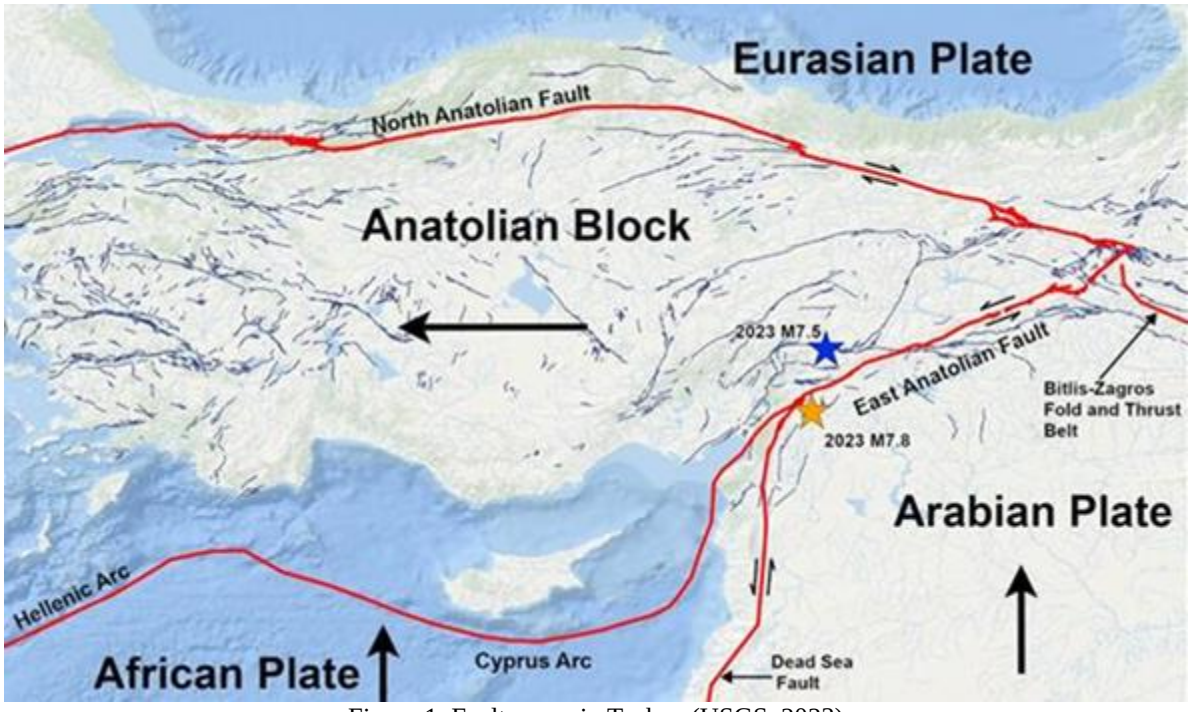

Figure 1. Fault zones in Turkey (USGS, 2023)

According to studies conducted by the Istanbul Technical University (ITU) and the Eurasia Institute of Earth Sciences, that fault zone is 550 km long and nearly 400 km long in section, causing 8-9 m positional shifts (ITU, 2023).

The first epicenter was at Yamacoba-Gaziantep, (06.02.2023 04:17), latitude 37º.1757- longitude 37º.0850, Mw=7.7, 5.4 km. depth and second epicentre is Ekinozu-Kahramanmaras, (06.02.2023 13:24, latitude 38º.0717- longitude 37º.2063), Mw=7.6, 5 km. depth (KOERI, 2023). Another third serious earthquake also happened at Samandag (Hatay) on February 20, 2023; Mw=6.4 and depth=13.4 km (36.0620 E, 36.1107 N).

Figure 2. The disaster area (General directorate of mapping, 2021)

96.7% of the population resides in cities and towns, 3.3% in villages, and 1.7 million immigrants (mainly from Syria) are in the area. According to SSB Report, 2023, with 637.222 independent units, the total number of destroyed, urgently needing to be demolished, and significantly damaged constructions was 227.027. In eleven provinces, 52% of all structures were built after 2001, 26.4% between 1981 and 2000, and 10% before 1980 (SBB, 2023).

There are no qualification requirements, including education level, to be a contractor. Quite recently, considerable attention has been paid to 797 individuals who are constructors or have official responsibility under legal issues. Another crucial issue is related to land use/planning. The entry flats of particular apartments have sunk into the ground as a result of inadequate attention for the soil research of settlements, particularly in Malatya and Hatay (Fig. 3).

Figure 3 Liquefaction-related building collapse (SSB Post-Earthquake Assessment Report, 2023)

As seen from Fig.4, most provinces in a disaster area are located on flat arable land with a 0-5^{o} slope. Hatay Province's airport and the highway between Hatay and Gaziantep have been significantly damaged, causing substantial harm in settlements.

Materials and Methods

Study Area

Kahramanmaras Earthquakes affected an area of over 110.000 km^2 in southeast Turkey (Fig. 2). Four 1:250.000 map sheets (Adana, Mersin, Gaziantep, and Kahramanmaras) covering a total area of 36.409 km^2 in the west with the most severe damages were utilized to choose the research region, as shown in Figs. 4.

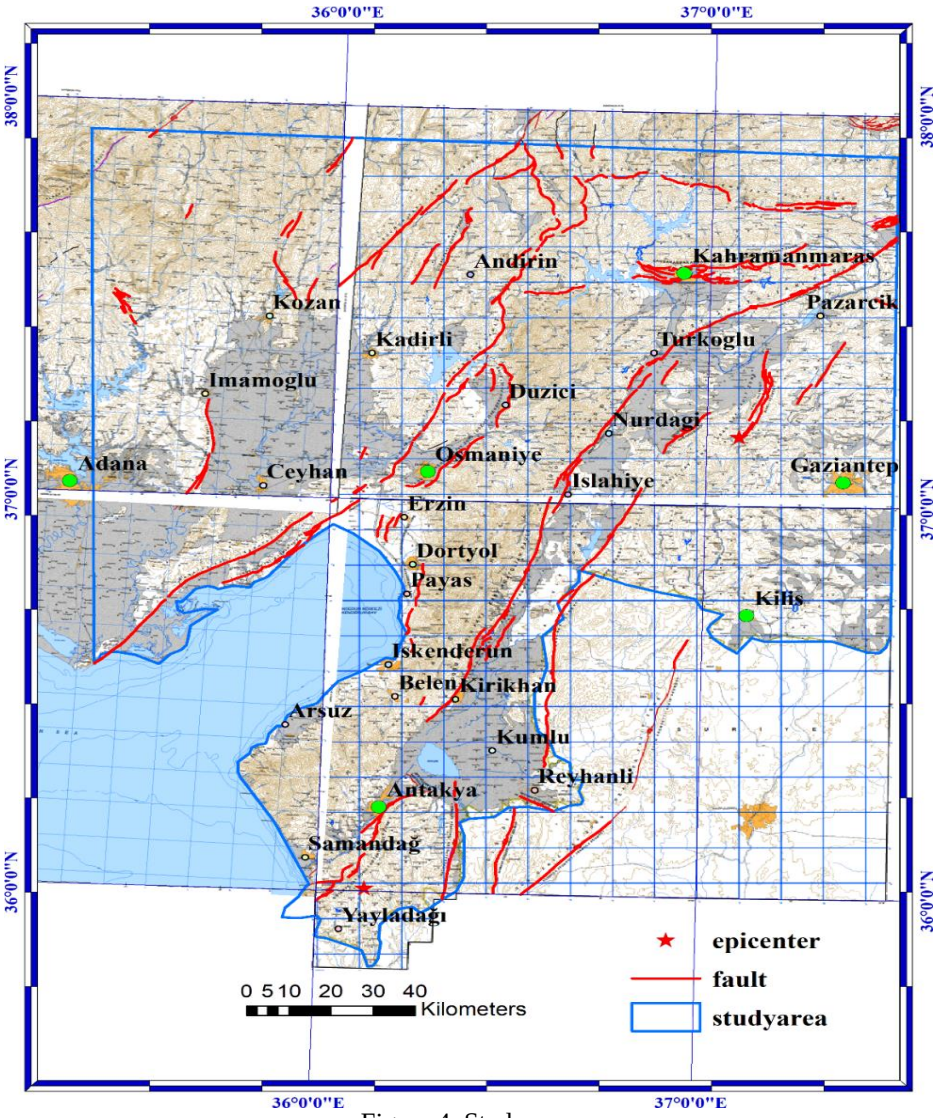

Figure 4. Study area

According to land use data (Corine, 2018), residential areas cover 610.9 km^2 and industrial areas cover 163.38 km^2 in the study region. The region's ground elevations vary between 0 to 2812 m. Nearly 60% of the land is hilly, while most settlements are on or near fault lines and flat areas.

Data Acquisition and Processing

This study intended to use the Multi-Criteria Decision Method (MCDM) in the Geographical Information System (GIS) by using AHP to assign weights to the specified criterion. Hence, data collection was

implemented according to the criteria. Lithology is one of the most important criteria, but since all municipalities in the study area experienced significant damage and personal loss, there was no chance to obtain the data. Active fault line maps on a 1:250.000 scale are accessible on the General Directorate of Mineral Exploration and Research's website (MTA, 2023). Using ArcGIS 10.4, four raster map sheets were georeferenced, and active fault lines digitized in vector format are depicted as red lines in Fig. 4.

12.5 m resolution Alos Palsar Digital Elevation Model (DEM) data (EarthData, 2023) was used to create an area slope map. Because all raster data utilized in the study had 10 m pixel size, DEM data were resampled by 10 m pixel size. Sentinel-2 10 m high-resolution terrain-corrected satellite images (ESA, 2023) have been used to construct a study area mosaic using ArcGIS. Agricultural areas, forests, water bodies and watercourses, residential and industrial areas, and roads have been extracted from Corine 2018 data and verified-edited on Sentinel 2 images. Four airports in the study area were manually digitized from Sentinel images.

Criteria

The 1999 Marmara and 2023 Karamanmaras earthquakes provided conclusive evidence that soil characteristics have a significant role in building destruction even far from epicenters. Hatay province's Antakya city center is 134 kilometers from the first epicenter (Sofalica-Gaziantep); most of the province's settlements are on alluvial agricultural land and had heavy damage. As a result, the Strategy and Budget Office (SBB, 2023) reported that the study area experienced significant damage, with 215.255 units collapsed or demolished. According to the authors, a similar situation occurred in the Yalova Hacimehmet Plate area, with a narrow stream and alluvial plains used for agricultural activities for many years. After the Marmara Earthquake in 1999, nearly all of the eight-story structures in this area collapsed.

Distance from Fault Lines

It is well-known that seismic intensity is strongest near fault lines and in their immediate vicinity. (Degerliyurt, 2014; Kalafat et al., 2021; USGS, 2023). Official governmental declarations specify that new settlement zones must be at least 500 meters from fault lines (SBB, 2023). Academicians from the ITU Eurasia Institute of Earth Science conducted an observatory study along fault lines, defining strike slips of 8-8.9 m and observing the heaviest damages at Nurdagi, Hatay, and Kirikhan centers located near fault lines (ITU, 2023). In the present study, a minimum distance of 1000 meters from fault lines was chosen: 0-1 km (1: unsuitable), 1-2 km (2: low suitable), 2-3 km (3: moderately suitable), 3-4 km (4: suitable), <5 km (high suitable).

Distance from Agricultural Areas

According to the Turkish Statistical Institute, agricultural regions in the seismic zone account for 16% of all agricultural areas in Turkey (TUIK, 2022). As indicated by Zeydan et al. (2018), fertile agriculture areas should be kept out of settlement enlargement zones. This has led the authors to choose 250 m—minimum distance to agricultural areas.

Distance from Water Bodies

Many dam reservoirs and ponds provide drinking water to settlements, agricultural watering, and hydroelectric energy production. In the study on landslide susceptibility evaluation, Ambarwulan et al. (2022) selected a 100 m minimum distance from rivers, whereas Wang et al.,2022 used a 100 m minimum distance from rivers. To protect drinking water sources, the Istanbul Municipality has enacted a regulation (ISKI, 2011) on basin protection, which states that settlement is prohibited between a radius of 0–1000 meters. Based on the law, the same value was applied in this study.

Slope

The most commonly accepted slope suitability in the literature or in various studies (Degerliyurt, 2014; Partigoc, 2018; Ambarwulan et al., 2022) is less than 5-8%. Nevertheless, 6°-10° high suitable and 0°-5° suitable approaches were applied in this study, as the flat areas are generally agricultural fields in the region.

Distance from Forests

Like agricultural areas, the minimum distance from forests was maintained at 250 m.

Distance from Industrial Areas

Considering the environmental conditions such as pollution, noise, and traffic jams, the minimum distance was considered as 2 km.

Distance from Airports

The precise approach radius for an airport runway is 1800 m, and the minimum distance should be greater than 3 km (Directorate General of Civil Aviation, 2016).

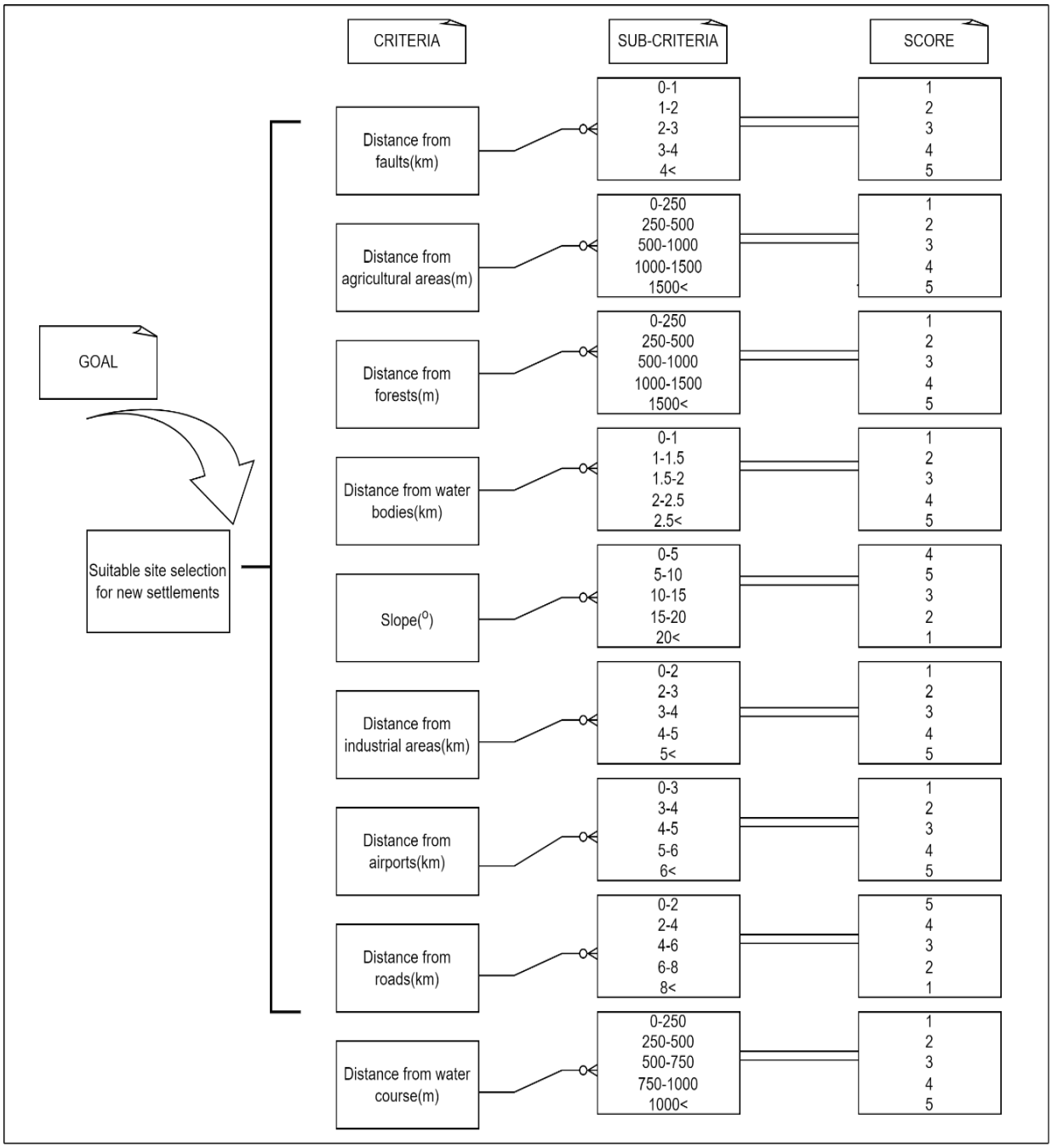

Figure 5. MCDM Conceptual design

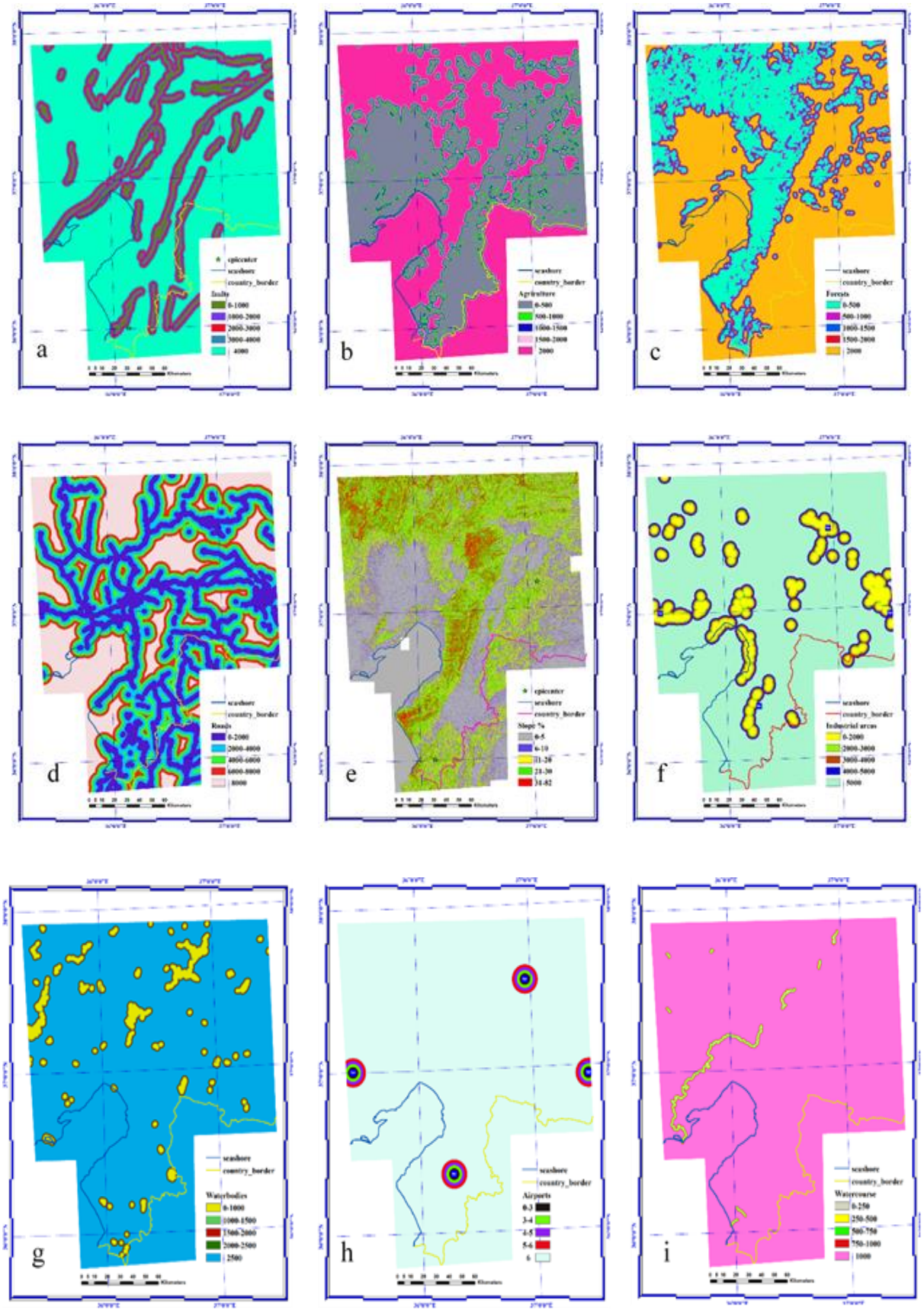

Figure 6. Thematic maps of criteria (a. Distance from fault lines, b. distance from agricultural areas, c. distance from forests, d. distance from water bodies, e. slope, f. distance from industrial areas, g. distance from airports, h. distance from roads, i. distance from the watercourse)

Distance from Roads

Access to major transportation routes is an essential economic consideration in developing a new settlement area. Therefore, a distance of 0 to 2 km is quite suitable.

Distance from Watercourse

In this study, 250 m was chosen as the minimal distance from watercourses. The conceptual design of the MCDM by GIS is shown in Fig. 5, considering nine criteria and sub-criteria ratings.

Weights by AHP

AHP is one of the most widely applied methods for assigning consistent weights to the criteria used in MCDM in order to provide options to decision-makers on land use planning activities (Ustaoglu et al., 2021; Liu., 2022; Kilicet al., 2023). According to Saaty (1980) AHP is a process that establishes a pair-wise comparison matrix of criteria. That step requires the researcher to conduct experiments on the subject under study so that it can be interpreted as a somewhat subjective component of the methodology. A fundamental scale with values ranging from 1 (equal importance) to 9 (great importance) was used to determine the priority score, as developed by Saaty et al. (1980). Table 1 shows the pairwise comparison matrix of this study.

Table 1. Pair-wise comparison matrix of criteria

CRITERIA	FL	AA	F	WB	S	IA	A	R	WT	W
FL	1	2	2	3	3	3	4	5	5	0.247
AA	1/2	1	2	2	3	3	3	4	5	0.190
F	1/2	1/2	1	2	3	3	3	4	4	0.160
WB	1/3	1/2	1/2	1	2	2	3	4	4	0.120
S	1/3	1/3	1/3	1/2	1	2	2	2	3	0.082
IA	1/3	1/3	1/3	1/2	1/2	1	2	3	3	0.075
A	1/3	1/3	1/3	1/3	1/2	1/2	1	2	3	0.057
R	1/5	1/4	1/4	1/4	1/2	1/3	1/2	1	2	0.039
WT	1/5	1/5	1/4	1/4	1/3	1/3	1/3	1/2	1	0.030
SUM	3.64	5.44	6.99	9.83	13.83	15.16	18.83	25.5	30	1

FL: Fault lines; AA: Agricultural areas; F: Forests; WB: Water bodies; S: Slope; IA: Industrial areas; A: Airports; R: Roads; WT: Watercourses; W: Weight

The eigenvector, which gives the criteria weights, is calculated by the solution of the normalized comparison matrix (Table 1). Eigenvalue (λ_{max}) was calculated to check consistency, the consistency index (CI) was calculated by CI= λ_{max}-n/n-1, where n represents the dimension of the matrix, and the consistency ratio (CR) was calculated as; CR=CI/RI, where RI is the random index shown in Table 2. If CR< 0.10, it is considered to be consistent. (Saaty, 1990). In this study, the following values: λmax = 9.3833, CI =0.048, and CR =0.033 have been calculated, and the weights in Table 1 were accepted as consistent.

Table 2. Random inconsistency indices for different values of n (Isalou et al.,2013)

n	1	2	3	4	5	6	7	8	9	10	11	12	13
RI	0	0	0.58	0.90	1.12	1.24	1.35	1.41	1.45	1.49	1.51	1.48	1.56

Thematic layers (Fig. 6) were produced using Euclidean distance and reclassified with ArcGIS 10.4. In the weighted overlay, all raster data had a resolution of 10 m and were classified into five categories: 1: not suitable, 2: low suitable, 3: moderately suitable, 4: suitable, and 5: highly suitable.

Results and Discussion

The land suitability map can be seen in Fig. 7 as a result of a weighted overlay, with weights assigned using an AHP method. 84% of the research area is unsuitable for settlement regeneration due to the presence of forests and agricultural areas (Table 3).

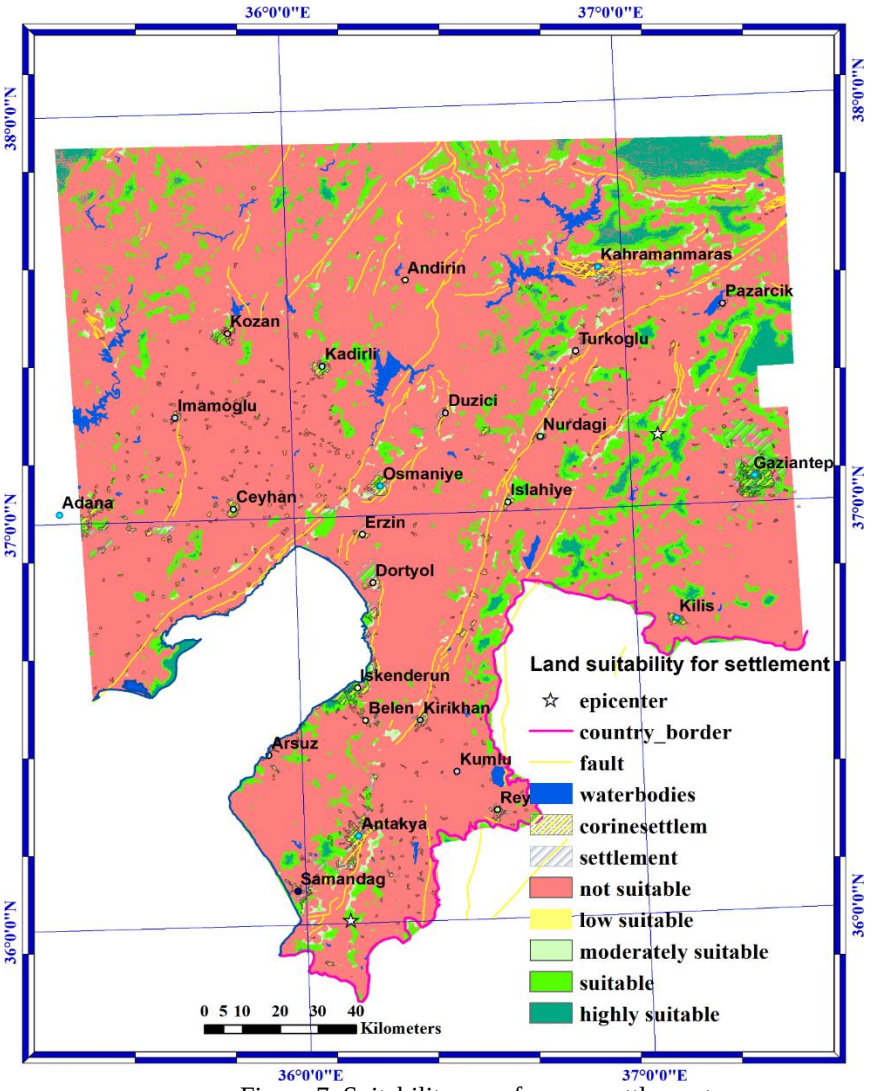

Figure 7. Suitability map for new settlements

Table 3. Suitability classes and area size

Class	Unsuitable	Low suitable	Moderately suitable	Suitable	Highly suitable
Area (ha)	2 406 395	20	24 128	367 474	76 285
%	84	0.4	1.5	11.3	3.2

However, it should be noted that data referring to geological ground characteristics are essential in such an application but were not applicable in our study due to the exceptional conditions in the municipalities. In addition to a suitable site selection process by GIS, geotechnical analysis must be completed at the optional locations before construction activities. The final map (Fig. 7) was superimposed on the Sentinel 2 satellite image of the study area and areas of existing locations of settlements measured by ArcMap 10.4. The following findings are evident;

- Kahramanmaras province covered 58.53 km^2 area (before the earthquake), and 0.09% of the city center was suitable, 8% was moderately suitable, and 91.1% was on the unsuitable area; the city center was on dense fault lines,
- The suitability map indicates that the city has to be relocated 5 kilometers to the North,
- Nurdagi, the closest settlement to the first epicenter, has a 7.58 km^2 area, of which 9.5% is appropriate, and 8.4% is moderately suitable,
- Hatay Province's City center, Antakya, has a 68.26 km^2 area, with 13% being moderately appropriate and 14% suitable.

In three provinces: Kahramanmaras 99.326 (Total: 481.362), Hatay 215.255 (Total: 847.380), and Gaziantep 29.155 (Total: 893.558), buildings have collapsed or have sustained significant damage. Even though Gaziantep is closer to the first epicenter (Yamacoba) than the other two provinces, buildings in that province have a significantly lower level of damage (SBB, 2023) than those with 3%, as it appears that most of them are in a suitable location. On the contrary, Hatay had the worst case in the region, constructed mainly on an alluvial area, as also indicated by ITU (2023).

Almost 58% of all settlements in Kadirli (in Osmaniye Province) are in suitable or moderately suitable locations but in Erzin (in Hatay Province) this rate is just 16.4% moderately suitable. As a result, low-rise structures and high-quality construction averted considerable damage in those regions.

Conclusions

There are many lessons to be learned from those two devastating earthquakes related to precautions, alleviating, and reviving activities before and after earthquakes. According to seismology experts such as Sengor, C. and Gorur, N., the NAF and EAF zones junctions at the North (Bingol-Karliova area) of the disaster area and potentially create destructive earthquakes in the near future. On the other hand, Turkey has already experienced two powerful earthquakes in the Marmara Region in 1999. and it is evident that individuals with management and decision-making responsibilities did not receive adequate training.

Most importantly, human life should be prioritized; governments must seek to improve the standard of living. Lithological characteristics, geotechnical analysis, and construction standards must never be overlooked; otherwise, terrible outcomes will be unavoidable. After an earthquake, a GIS-based disaster management system (also known as a disaster management information system) is a useful tool for organizing temporary settlements, suitable site selection for debris removal, logistic routes for aid materials, and site selection for permanent settlements.

Right after the Kahramanmaraş earthquake, there were many problems with first aid activities, a lack of coordination, delays in vital attempts, inappropriate tent locations (one near a river, another near the coast in Samandag city), and even wrong site selection for permanent settlements. Some of the temporary container houses were built on agricultural land, and domestic waste was transported to agricultural or nearby regions. Sanliurfa and Adiyaman provinces experienced massive flooding one month after the earthquake, and 18 people were killed. Sanliurfa province has experienced flooding on multiple occasions in the past, yet land use decisions have been made without considering topography, lithography, or other critical factors.

In conclusion, constructions can be performed in various soil conditions, but the soil should be improved to carry the superstructure loads safely. The right foundation system and superstructure carrier system should be selected according to the conditions, and it should not be forgotten that the design process should be carried out with a meticulous engineering approach, and expert engineers should supervise its design.

Scientific Ethics Declaration

The authors declare that the scientific, ethical, and legal responsibility of this article published in EPSTEM journal belongs to the authors.

Acknowledgments or Notes

* This article was presented as an oral presentation at the International Conference on Technology, Engineering and Science (www.icontes.net) held in Antalya/Turkey on November 16-19, 2023.

References

AFAD. (2018). *Turkiye deprem tehlike haritası*. Retrieved from https://www.afad.gov.tr/turkiye-deprem-tehlike-haritasi.

AFAD. (2022). *Disaster risk reduction plan of Turkey, 2022-2030*. Retrieved from https://www.afad.gov.tr/turkiye-afet-risk-azaltma-plani-tarap

AFAD. (2023). *Preliminary assessment report*. Retrieved, from https://deprem.afad.gov.tr

Alparslan, E., Ince, F., Erkan, B., Aydoner, C., Ozen, H., Donertas, A., Ergintav, S., Yagsan, F. S., Zaterogulları, A., Eroglu, I., Deger, M., Elalmıs, H., & Ozkan, M. (2008). A GIS model for settlement suitability regarding disaster mitigation, a case study in Bolu Turkey. *Engineering Geology, 96*, 126–140.

Aman, D. D. & Aytac, G. (2022). Multi-criteria decision making for the city-scale infrastructure of post-earthquake assembly areas: Case study of Istanbul. *International Journal of Disaster Risk Reduction, 67*.

Ambarwulan, W., Nahib, I. Widiatmaka, W., Dewi R. S., Munajati S. L., Suwarno, Y., Sutrisno, D., & Suprajaka, S. (2022). Delineating suitable site for settlement in potential earthquake vulnerable areas using spatial multi-criteria decision analysis in the Sukabumi regency, Indonesia. *Journal of Water And Land Development, 53* (4–6), 10–21.

ASF Data Search. (2023). Retrieved from https://search.asf.alaska.edu.

Bilgilioglu, S. S. (2022). Site selection for radioactive waste disposal facility by GIS-based multi-criteria decision making. *Annals of Nuclear Energy, 165*.

Bilgilioglu, S. S., & Gezgin, C., & Orhan, O. (2022). A GIS based multi-criteria decision making method for the selection of potential municipal solid waste disposal sites in Mersin, Turkey. *Environmental Science and Pollution Research, 29*, 5313–5329.

Bilgilioglu, S. S., Gezgin, C., Orhan, O., & Karakus, P. (2021). A GIS-based multi-criteria decision-making method for the selection of potential municipal solid waste disposal sites in Mersin, Turkey, *Environmental Science and Pollution Research, 29*(1), 5313–5329.

Bogazici University. (2023). *Kandilli observatory and earthquake research institute (KOERI).* Retrieved from http://www.koeri.boun.edu.tr/sismo/2/deprem-bilgileri/buyuk-depremler/

Corine, (2018). *Corine land cover 2018*. Retrieved from https://land.copernicus.eu/pan-european/corine-land-cover.

CSB. (2023). *Ministry of environment, urbanization and climate change*. Retrieved from https://csb.gov.tr/

Degerliyurt, M. (2014). Settlement suitability analysis of local ground characteristics in Iskenderun: A case study. *Procedia - Social and Behavioural Sciences, 120*, 637 – 644.

Directorate General of Civil Aviation (2016). *Runways.* https://web.shgm.gov.tr/documents/sivilhavacilik/files/pdf/kurumsal/yayinlar/Havaalani_Pistleri.pdf

Dolui, S., & Sarkar, S. (2021). Identifying potential landfill site using multicriteria evaluation modelling and GIS techniques for Kharagpur city, West Bengal, India, *Environmental Challenges, 5.* 100243

Dunford, M. & Li, L., (2011). Earthquake reconstruction in Wenchuan: Assessing the state overall plan and addressing the 'forgotten phase. *Applied Geography, 31* (3), 998-1009.

Earthdata, (2023). *Alaska*. Retrieved from https://search.asf.alaska.edu/#/

ESA. (2023). Retrieved from https://scihub.copernicus.eu/dhus/#/home

Guler, D., & Yomralioglu, T. (2017). Alternative suitable landfill site selection using analytic hierarchy process and geographic information systems: a case study in Istanbul. *Environmental Earth Science, 76*, 678.

Isalou, A.A., Zamani, V., Shahmoradi, B., & Alizadeh, H. (2013). Landfill site selection using integrated fuzzy logic and analytic network process (F-ANP). *Environmental Earth Sciences, 68,* 1745-1755.

ISKI. (2011). Basin protection regulation, ITU final report on Kahramanmaras earthquakes. Retrieved from https://haberler.itu.edu.tr/haberdetay/2023/03/24/itu-den-2023-nihai-deprem-raporu

Jena, R., Pradhan, B., Beydoun, G., Nizamuddin, Ardiansyah, Sofyan, H., & Affan, M. (2019). Integrated model for earthquake risk assessment using neural network and analytic hierarchy process: Aceh province, Indonesia. *Geoscience Frontiers, 11* (2020) 613–634.

Kalafat, D., Zulfikar, A. C., & Akcan, S. O. (2021). Seismicity of Turkey and real-time seismology applications in determining earthquake hazard, academic platform. *Journal of Natural Hazards and Disaster Management, 2*(2), 96-111.

Kamdar, I., Ali, S., Bennui, A., Techato, K., & Jutidamrongphan, W. (2019). Municipal solid waste landfill siting using an integrated GIS-AHP approach: A case study from Songkhla, Thailand. *Resources, Conservation and Recycling, 149*, 220-235.

Kilic, D., Yagci, C., & Iscan, F. (2023). A GIS-based multi-criteria decision analysis approach using AHP for rural settlement site selection and eco-village design in Erzincan. Turkey, *Socio-Economic Planning Sciences, 86.* 101478.

Liu, K. (2022). GIS-based MCDM framework combined with coupled multi-hazard assessment for site selection of post-earthquake emergency medical service facilities in Wenchuan, China. *International Journal of Disaster Risk Reduction, 73*, 102873.

MTA. (2023). *Active fault maps*. Retrieved from https://www.mta.gov.tr/v3.0/hizmetler/diri-fay-haritalari

Nappi, M. M. L., Nappi, V., & Souza, J. C. (2018). Multi-criteria decision model for the selection and location of temporary shelters in disaster management. *Journal of International Humanitarian Action*, *4*(1), 1-19.

Partigoc, N. S. (2018). GIS – based land suitability analysis in Cigli district. *Bilisim Teknolojileri Dergisi, 11*(1), 9-21.

Saaty, T.L. (1990). How to make a decision: The analytic hierarchy process? *European Journal of Operational Research*, *48*(1), 9-26.

Saaty, T.L. (1980). *The analytic hierarchy process: planning, priority setting, resource allocation*. McGraw-Hill International Book Company.

Strategy and Budget Office (SBB) (2023). *Post-earthquake assessment report*. Retrieved from https://www.sbb.gov.tr/wp-content/uploads/2023/03/2023-Kahramanmaras-and-Hatay-Earthquakes-Report.pdf

TBMM (2021). *Depreme karsı alınabilecek onlemlerin ve depremlerin zararlarının en aza indirilmesi icin alınması gereken tedbirlerin belirlenmesi amacıyla Kurulan Meclis Araştırması Komisyonu Raporu*, 278. Retrieved from https://www5.tbmm.gov.tr/sirasayi/donem27/yil01/ss278.pdf

TUIK. (2022). *Adrese dayalı nufus kayıt sistemi sonucları.* Retrieved from https://data.tuik.gov.tr/Bulten/Index?p=Adrese-Dayali-Nufus-Kayit-Sistemi-Sonuclari

Turkiye Muhendislik Haberleri. (2023) 6 subat Kahramanmaras Pazarcik ve Elbistan depremleri, *TMMOB İnsaat Muhendisleri Odasi, 68*(513).

USGS. (2023). *Earthquake magnitude, energy release and shaking intensity*. Retrieved from https://www.usgs.gov/programs/earthquake-hazards/earthquake-magnitude-energy-release-and-shaking-intensity

Ustaoglu, E., Sisman, S., & Aydinoglu, A. C. (2021). Determining agricultural suitable land in peri-urban geography using GIS and multi criteria decision analysis (MCDA) techniques. *Ecological Modelling*, 455, 109610.

Wang, X., Xinlong Zhang, X., Bi, J., Zhang, X., Deng, S., Liu, Z., Wang, L., & Guo, H. (2022). Landslide susceptibility evaluation based on potential disaster identification and ensemble learning. *International Journal of Environmental Research and Public Health, 19* (21), 14241.

World Bank (2023). *Disaster assessment report*, Retrieved from https://www.worldbank.org/en/news/press-release/2023/02/27/earthquake-damage-in-turkiye-

Xu, M. (n.d.). Resources, conservation and recycling. *149*, 220-235,

Zeydan M., Bostanci B., & Oralhan B. (2018). A new hybrid decision making approach for housing suitability mapping of an urban area. *Mathematical Problems in Engineering*, Article ID 7038643 https://doi.org/10.1155/2018/7038643

Author Information

Oktay Aksu
Istanbul Okan University
Istanbul Okan University, Faculty of Engineering and Natural Sciences, Akfirat Campus, 34959, Tuzla-Istanbul, Turkey
Contact e-mail: *oktay.aksu@okan.edu.tr*
ORCID: 0000-0001-5584-6079

Agne Karlikanovaite-Balikci
Istanbul Okan University
Istanbul Okan University, Faculty of Engineering and Natural Sciences, Akfirat Campus, 34959, Tuzla-Istanbul, Turkey
ORCID: 0000-0002-2290-5818

To cite this article:

Aksu, O. & Karlikanovaite-Balikci, A. (2023). Earthquakes in Kahramanmaras; Assessment of affected areas and recommendations for settlement regeneration. *The Eurasia Proceedings of Science, Technology, Engineering & Mathematics (EPSTEM), 26*, 404-415.

The Eurasia Proceedings of Science, Technology, Engineering & Mathematics (EPSTEM)
ISSN: 2602-3199

The Eurasia Proceedings of Science, Technology, Engineering & Mathematics (EPSTEM), 2023

Volume 26, Pages 416-419

IConTES 2023: International Conference on Technology, Engineering and Science

Glycine-Assisted Synthesis of High Surface Area $(FeMnCrCoZn)_3O_4$ Microsheets

Resat Can Ozden
Eskisehir Osmangazi University

Mustafa Anik
Eskisehir Osmangazi University

Abstract: To meet the current demands for energy storage and conversion, it is crucial to develop newly designed materials. Porous metal oxides with a high specific surface area and controllable porosity are promising electrode materials for electrochemical energy storage and conversion applications. Furthermore, porous materials offer a unique combination of structural, chemical and physical properties. In this study, porous high-entropy oxides $(FeMnCrCoZn)_3O_4$ were synthesized through soft chemistry route, employing glycine as a pore-forming agent, followed by calcination at various temperatures (500 °C, 600 °C and 700 °C) for 4h. The obtained samples were characterized by X-ray diffraction (XRD) and scanning electron microscopy (SEM) techniques. It was observed that the samples were successfully synthesized in porous microsheet morphology and as a single phase in the spinel crystal structure. Additionally, the effect of different calcination temperatures on the pore structure has been investigated.

Keywords: High-entropy oxides, Porous metal oxides, Template-free method

Introduction

Introducing porosity into metal oxides can significantly enhance their performance across various scientific applications, including catalysis (Adegoke &Maxakato, 2022), sensing (Chen et al., 2010), and energy conversion and storage technologies (Veerakumar et al., 2020; Hassan et al., 2021). Materials characterized by a high specific surface area, tunable pore size, and large pore volume play a crucial role in all the aforementioned applications. In fields like batteries and supercapacitors, key factors for effective reversible energy storage include energy density, rate capability, and cycle life. A hierarchically porous structure, featuring interconnected pores across different scales, shortens ion diffusion paths (Liu et al., 2019). This enables deeper electrochemical reactions, thereby maximizing electrode capacity and energy density. Moreover, it facilitates rapid and reversible ion de-intercalation, thereby enhancing rate performance (Liu et al., 2019).

Various chemical techniques (Suzuki et al., 2003; Wu et al., 2020) and physical-chemical methods (Chen et al., 2010) are available for synthesizing materials with hierarchically organized porous structures. Depending on the application of a template and the specific agents used, these approaches can be categorized into soft templating, hard templating, and template-free methods (Wu et al., 2020). Both soft and hard templating methods present challenges for large-scale production due to their high cost and labor-intensive preparation procedures. Ideally, methods devoid of templates are favored for producing hierarchically structured porous materials, featuring sizable pores and diverse shapes (Wu et al., 2020).

In this study, porous $(FeMnCrCoZn)_3O_4$ hierarchical structures were synthesized at different temperatures using the sol-gel based template-free method. The study also investigated how varying heat treatment temperatures affected the phase structure and porosity of the samples.

Method

The equimolar amounts of metal nitrates were dissolved in deionized water and stirred for 30 minutes. Subsequently, glycine (CH_2NH_2COOH) was introduced into the solution, serving as a fuel and chelating agent. Following 2 h of stirring, the solution was transferred onto a Teflon plate and dried overnight at 90°C. The resulting gel structure was subjected to heat treatment in an air atmosphere, with a heating rate of 5°C min^{-1} at 500 °C, 600 °C and 700 °C for 4h to obtain porous $(FeMnCrCoZn)_3O_4$ high-entropy oxide. The X-ray diffraction (XRD) analyses utilized a PANalytical Empyrean diffractometer equipped with Cu Kα radiation, employing a scanning rate of 2° min^{-1}. Sample morphologies were investigated using a ZEISS Ultraplus scanning electron microscope (SEM).

Results and Discussion

Figure 1 displays the XRD patterns for the obtained samples at various temperatures. The peak profiles signify well-crystallized samples in a cubic spinel structure within the Fd-3m space group (96-230-0280 reference card file). No impurities are found under all synthesis conditions. Hence, any significant impact of the synthesis temperature on the formation of the spinel phase is not observed. However, it was observed that the peak intensities increased slightly depending on the temperature, as seen in Figure 1. The lattice parameters of the samples were calculated as 8.3749 Å.

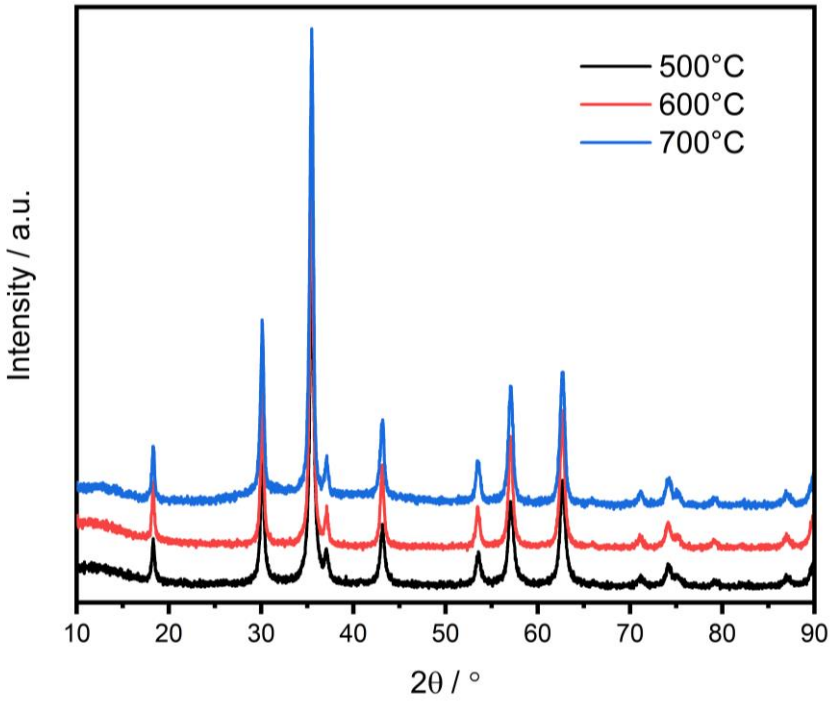

Figure 1. XRD patterns of the synthesized porous HEO samples.

The morphology of the synthesized samples was analyzed by SEM. As can be seen from the images in Figure 2, the samples exhibit a sheet-like and porous structure. This porosity arises from the release of substantial amounts of gas during the heat treatment. High-temperature decomposition of metal nitrate and glycine effectively yields foam-like materials (Yang et al., 2022). The chemical reactions occurring in this process can be expressed by the following equation:

$$M(NO_3)_x + CH_2NH_2COOH + \frac{35-18x}{12}O_2 \rightarrow \frac{1}{3}M_3O_4 + 2CO_2 + \frac{5}{2}H_2O + \frac{x+1}{2}N_2$$

As seen in Figure 2, it can be said that changing heat treatment temperatures has some effect on the porosity. The samples subjected to lower heat treatment temperatures exhibit relatively wider pore sizes. Clearly, this method enables the synthesis of HEO-based materials at low temperatures, tailored to the desired pore structure. In addition, upon revisiting the above equation, it becomes evident that this desired pore quantity can be attained

through careful control of various fuel (glycine) - oxidizer (metal nitrates) ratios. Similar investigations can be found in existing literature (Amirkhanyan et al., 2020; Shin et al., 2023). Nonetheless, adjusting the fuel quantity, whether increased or decreased, may lead to non-stoichiometry and the presence of residual carbon in the desired structure. Thus, these factors should be carefully considered in the synthesis of new porous materials.

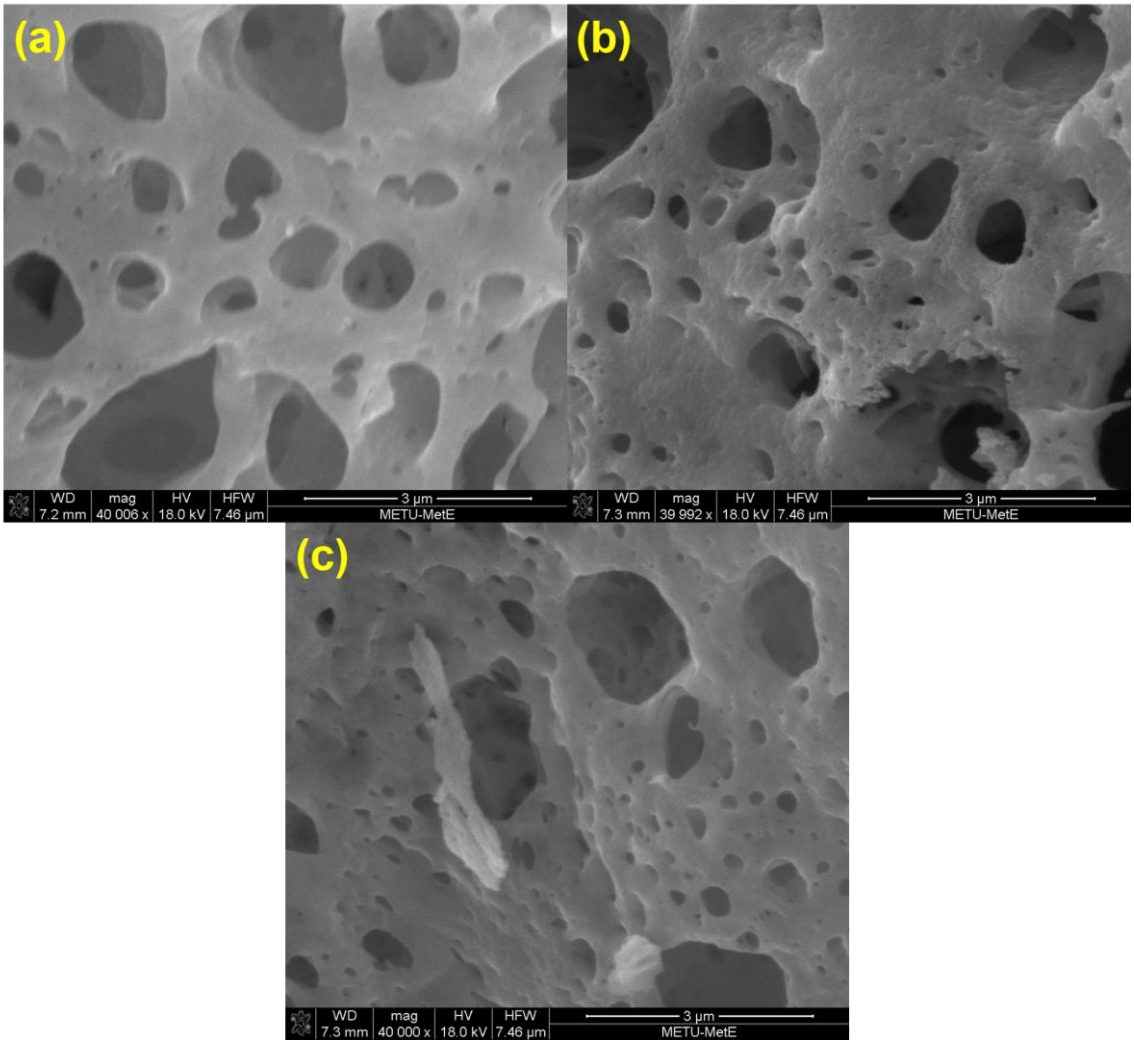

Figure 2. SEM images of the synthesized porous HEO samples at (a) 500 °C (b) 600 °C (c) 700 °C temperatures.

Conclusion

This research focused on creating porous $(FeMnCrCoZn)_3O_4$ high-entropy oxides. The synthesis process involved using glycine as a pore-forming agent through a soft chemistry method at various synthesis temperatures 500 °C, 600 °C and 700 °C. The structural and morphological analysis revealed that the samples were successfully produced with a porous microsheet structure and displayed a single-phase composition in the spinel crystal structure. The synthesis temperature was found to impact the sizes of the pores, as observed. This straightforward and easily scalable synthesis approach for HEO-based materials can also yield porous materials that cannot be prepared by conventional production methods.

Scientific Ethics Declaration

The authors declare that the scientific ethical and legal responsibility of this article published in EPSTEM journal belongs to the authors.

Acknowledgments or Notes

* This article was presented as an oral presentation at the International Conference on Technology, Engineering and Science (www.icontes.net) held in Antalya/Turkey on November 16-19, 2023.

References

Adegoke, K. A., & Maxakato, N. W. (2022). Porous metal oxide electrocatalytic nanomaterials for energy conversion: Oxygen defects and selection techniques. *Coordination Chemistry Reviews*, *457*, 214389.

Amirkhanyan, N., Kharatyan, S., Manukyan, K., & Aprahamian, A. (2020). Thermodynamics and kinetics of solution combustion synthesis: Ni(NO3)2 + fuels systems. *Combustion and Flame*, *221*, 110–119.

Chen, H., Zhao, Y., Yang, M., He, J., Chu, P. K., Zhang, J., & Wu, S. (2010). Glycine-assisted hydrothermal synthesis of peculiar porous α-Fe2O3 nanospheres with excellent gas-sensing properties. *Analytica Chimica Acta*, *659*(1–2), 266–273.

Hassan, I. U., Salim, H., Naikoo, G. A., Awan, T., Dar, R. A., Arshad, F., Tabidi, M. A., Das, R., Ahmed, W., Asiri, A. M., & Qurashi, A. H. (2021). A review on recent advances in hierarchically porous metal and metal oxide nanostructures as electrode materials for supercapacitors and non-enzymatic glucose sensors. *Journal of Saudi Chemical Society*, *25*(5), 101228.

Liu, Z., Yuan, X., Zhang, S., Wang, J., Huang, Q., Yu, N., Zhu, Y., Fu, L., Wang, F., Chen, Y., & Wu, Y. (2019). Three-dimensional ordered porous electrode materials for electrochemical energy storage. *NPG Asia Materials*, *11*(1), 12.

Shin, D., Chae, S., Park, S., Seo, B., & Choi, W. (2023). Rational engineering of high-entropy oxides for Li-ion battery anodes with finely tuned combustion syntheses. *NPG Asia Materials*, *15*(1), 54.

Suzuki, Y., Kondo, N., & Ohji, T. (2003). Reactive synthesis of a porous calcium zirconate/spinel composite with idiomorphic spinel grains. *Journal of the American Ceramic Society*, *86*(7), 1128–1131.

Veerakumar, P., Sangili, A., Manavalan, S., Thanasekaran, P., & Lin, K. C. (2020). Research progress on porous carbon supported metal/metal oxide nanomaterials for supercapacitor electrode applications. *Industrial and Engineering Chemistry Research*, *59*(14), 6347–6374.

Wu, L., Li, Y., Fu, Z., & Su, B. L. (2020). Hierarchically structured porous materials: Synthesis strategies and applications in energy storage. *National Science Review*, *7*(11), 1667–1701.

Yang, X., Wang, H., Song, Y., Liu, K., Huang, T., Wang, X., Zhang, C., & Li, J. (2022). Low-temperature synthesis of a porous high-entropy transition-metal oxide as an anode for high-performance lithium-ion batteries. *ACS Applied Materials and Interfaces*, *14*(23), 26873–26881.

Author Information

Resat Can Ozden
Eskisehir Osmangazi University
Buyukdere Meselik Yerleskesi, 26040 Odunpazarı/Eskisehir
Contact e-mail: *rcanozden@ogu.edu.tr*

Mustafa Anık
Eskisehir Osmangazi University
Buyukdere Meselik Yerleskesi, 26040 Odunpazarı/Eskisehir

To cite this article:

Ozden R.C. & Anik, M. (2023) Glycine-assisted synthesis of high surface area $(FeMnCrCoZn)_3O_4$ microsheets. *The Eurasia Proceedings of Science, Technology, Engineering & Mathematics (EPSTEM), 26,* 416-419.

The Eurasia Proceedings of Science, Technology, Engineering & Mathematics (EPSTEM)
ISSN: 2602-3199

The Eurasia Proceedings of Science, Technology, Engineering & Mathematics (EPSTEM), 2023

Volume 26, Pages 420-429

IConTES 2023: International Conference on Technology, Engineering and Science

Design and Analysis of LED-Based Artificial Plant-Growing Fixture for Vertical Indoor Farming Systems

Ismail Kiyak
Marmara University

Semih Asci
Moonlight Aydınlatma San. & Tic A.S.

Sercan Keskintas
Moonlight Aydınlatma San. & Tic A.S.

Ahmet Dibic
Moonlight Aydınlatma San. & Tic A.S.

Emre Kocak
Moonlight Aydınlatma San. & Tic A.S.

Abstract: The ability to perform photosynthesis with artificial lighting has eliminated the dependence on the sun in the agricultural industry. With the elimination of dependence on the sun, indoor plant production has been enabled by using artificial lighting in facilities such as vertical farming facilities. As a result of making soilless agriculture possible in vertical farming facilities, more organic and healthier plant production can be achieved as the plant is free from diseases and pests and therefore there is no need for pesticides. At the same time, thanks to the facilities to be established in city centers, the access process and cost of the plants grown will be reduced. In this study, the light needed for the growth of plants in the indoor vertical soilless agriculture facility was artificially designed using LED chips. In the luminaire(fixture) design, the wavelength and level of light can be adjusted according to the needs of plant growth periods. Comparative analyzes were made of the LED-based internal vertical luminaire design results carried out within the scope of the study and equivalent products used for the same purpose.

Keywords: Vertical farming, Plant-growing fixture, Indoor growth, LED-based fixture, Horticulture.

Introduction

The 21st century is an era where agricultural production methods change rapidly. As negative returns of the rapidly growing population, the decrease in the amount of land suitable for agriculture, the uncertainty and anomalies brought by climate changes as a result of global warming, the rapid depletion of natural resources as a result of the increase in production and consumption due to the increase in the world population, pose difficulties in food security and sustainability. The vertical farming industry is an innovative approach that can provide solutions to global problems such as food shortage by providing solutions to these challenges. This technology, which brings traditional horizontal agricultural fields to a vertical perspective, is a technology that has the potential to reshape the future of agriculture. (Bourget, 2008)

Effective use of technology is the key to the development of modern agriculture. One of the areas where technology is used most effectively in the agricultural sector is artificial lighting applications. By affecting the

photosynthesis processes of plants through artificial lighting applications, more efficient products can be produced and time can be used more efficiently. In this way, the efficiency of operations in food production facilities is increased. With the more effective use of lighting technologies in modern agriculture, sustainable and efficient agricultural practices can be developed. (Shareef & Hannan, 2011)

Nowadays, control can be achieved over the growth rate of the plant and the efficiency obtained from the plant by using LED lighting systems, one of the modern lighting technologies. This control is achieved by using targeted light spectrums in LED lights. In agricultural applications, LEDs are used in indoor agricultural facilities and vertical farming facilities to play the role of sun and enable the plant to develop by providing the light it needs for photosynthesis. The color of the light emitted by LEDs varies depending on the type of semiconductor material used. The wavelengths of light emitted by LEDs vary from 250 nm (Ultraviolet) to 1000 nm (Infrared). LEDs are generally not dangerous, but care should be taken when using them in the ultraviolet range because these wavelengths can be dangerous to the eyes and skin when sufficient power is provided. General standards for LEDs are a supply voltage of 3V, a current of 350 mA and a power consumption of 3W. (Birkby, 2016)

In agricultural applications, LEDs are used in indoor agricultural facilities and vertical farming facilities to play the role of sun and enable the plant to develop by providing the light it needs for photosynthesis. In this study, a fixture containing LED light sources was designed to be used as an artificial light source in a vertical farming facility. The designed luminaire(fixture) provides the light needed by the plants with an adjustable brightness level in the spectrum range of 400 nm-850 nm.

A Strategic Approach: Urban Soilless Agroecosystems

The concept of indoor soilless vertical farming is touted as a solution to the food crisis that is predicted to arise with the increasing population, especially in large metropolises. In this context, it can be thought that it should be addressed as a strategic issue. Vertical farming systems should be evaluated for the following five basic points;

- space saving,
- saving water,
- season independent production and optimum climate control,
- disease and pest control,
- high production capacity

Establishing vertical farming facilities in city centers allows the products obtained to be delivered to consumers in a short time. This not only significantly shortens the time spent during logistics activities, but also ensures that the shelf life of the plants is long, and also provides energy and cost savings by reducing transportation activities with trucks, ships and planes in the logistics process. In addition, vertical farming facilities located in city centers provide employment for people living in the city center. (Rouphael et al., 2016)

Vertical farming facilities provide significant water savings compared to traditional agriculture. The main reason for this is that vertical farming systems have the ability to use and reuse water more efficiently. The use of water in vertical farming facilities is provided by hydroponic, aeroponic and aquaponic systems. Hydroponic and aeroponic systems enable the cyclical use of water. If we give an example of water saving in vertical farming facilities; While 400 liters of water are consumed to grow 1 kilogram of tomatoes in traditional agricultural methods, 70 liters of water are consumed in hydroponic systems and 20 liters in aeroponic systems. (Zhang et al., 2021)

Since vertical farming facilities are designed to be as isolated as possible from external influences, the plants grown are not affected by climate changes. Production can continue without interruption by providing optimum climatic conditions for the plant grown within the facility. Additionally, production efficiency can be maximized by applying the desired amount of light for the desired period of time, regardless of the day and night cycle. (Perdahcı et al., 2018).

Diseases and harmful organisms are inevitable in traditional open field agriculture. Vertical farming, on the other hand, takes place in a closed and controlled environment. This prevents diseases and harmful organisms from entering the agricultural field. Therefore, the risk of spreading harmful organisms and diseases in vertical

farming facilities is much lower than in open field farming. Additionally, these closed systems also allow plants to be more resistant to diseases.

Due to the nature of vertical farming, the air circulation between plants has a positive effect on the development of the plant. This makes it harder for disease to spread between plants and improves the overall health of the plants. This air circulation between plants also contributes to faster plant growth and higher productivity. (Taiz et al., 2015)

In vertical farming, unlike traditional farming, the production per square meter is much higher as a result of placing and growing a series of plants on top of each other. Producing with vertical farming in the same area is much more efficient than producing with traditional agriculture. In addition, the fact that vertical farming facilities are closed and controlled areas makes it possible to optimize the growth conditions of plants. Providing light to the plant in the desired amount and for the desired duration, unlike sunlight, reduces the growing time of the plant. Thus, thanks to the space advantage and time advantage in vertical farming, the production capacity is much higher than in traditional agriculture. (Caglayan & Ertekin, 2018)

Plant-Growing LED Fixture Design

Within the scope of the study, the LED-based vertical farming luminaire was designed, the PID control card was designed to keep the operating temperature of the LED diodes under control, and the DALI master communication card was designed to control the luminaires within the facility.

Design Criteria and Materials

While designing the PCB, LEDs that can achieve intermediate wavelengths were selected. Placements were made on the luminaire where these selected LEDs could work with the best efficiency. While this settlement was being carried out, studies were carried out on online horticulture calculation tools. The output of the study is given in Figure 1.

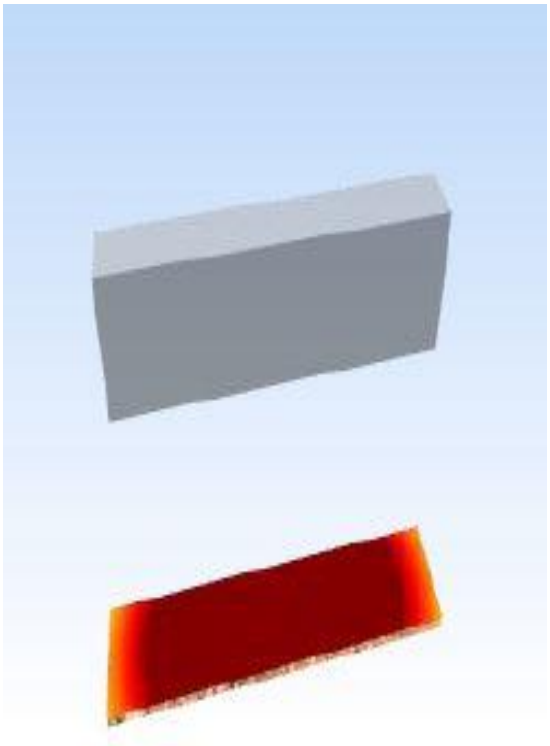

Figure 1. Horticulture calculation program image

A DALI luminaire driver suitable for separate luminaire power was used for each LED color on the PCB. Optical improvements have been made to the design and finish of the luminaire casing. Information about the LEDs used is given in Table 1.

Table 1. Features of the LEDs used

Variables	Wavelength (nm)	Forward Voltage(VF)	Forward Current(IF)	Color
LH351H Blue (Samsung)	450nm	2.86V	1000mA	Deep Blue
LH351H Red (Samsung)	730nm	1.9V	1000mA	Hyper Red
LH351 2W (Samsung)	660nm	2.07V	1000mA	Deep Red
LH351D (Samsung)	-	3.2V	3000mA	White

PID Control Card Design

A digital PID fan control circuit has been designed to keep the operating temperature of the LED luminaire at an ideal level and to ensure stabilization. PID control method is an automatic control system based on proportional, derivative and integral principles. By trying to keep the temperature value read from the NTC on the armature PCB at a constant value, when the PCB temperature rises, it increases the speed of our fans and contributes to cooling. When the temperature drops, the fan keeps the fan in balance by reducing the speed.

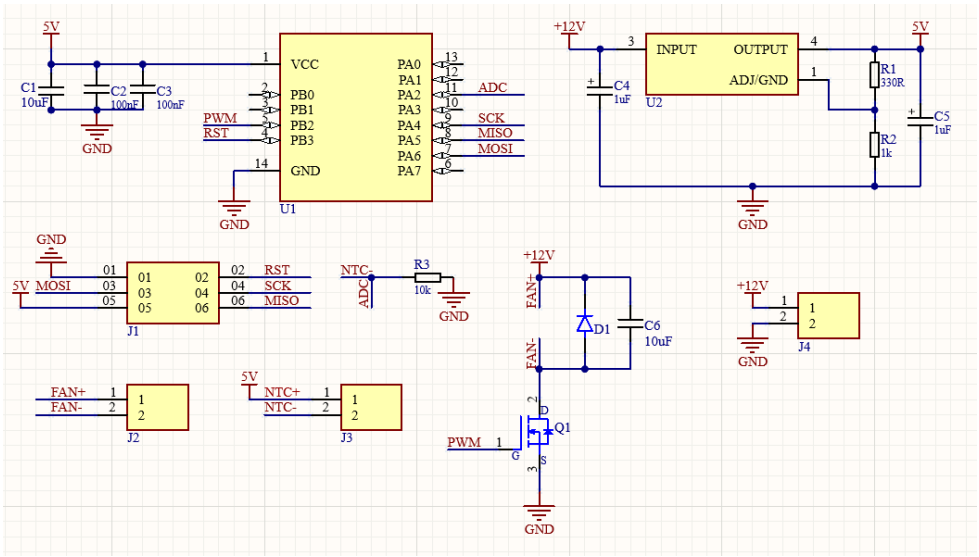

Figure 2. PCB schematic image

PCB schematic connections are given in Figure 2. The control card software is optimized to keep the temperature at a constant 40°.

DALI Master Communication Card Design

Within the scope of the project, DALI LED drivers were used to control the fixtures. DALI is a digital protocol that provides two-way data transmission for lighting systems. This protocol allows each LED driver to be controlled individually by giving an address, and 64 LED drivers can be connected to this system. Figure 3. shows the DALI Master PCB schematic connection.

In order to use this protocol, an intermediate converter circuit was designed and a communication protocol was written. According to the written software, the address and DIM value of each fixture is entered and controlled. Tested on 4 LED drivers. According to the results obtained, revision processes on the software continue.

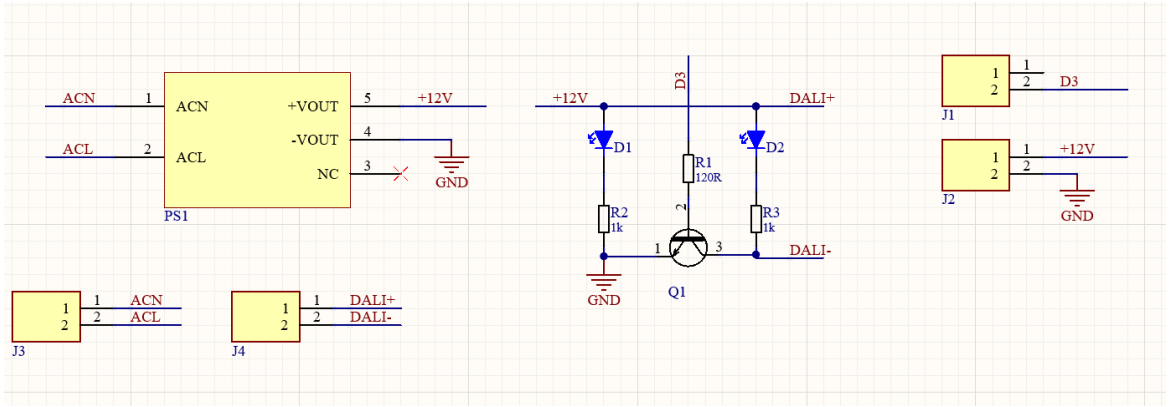

Figure 3. DALI master PCB schematic image

PCB Design

Separate PCB designs were made for the two different LED brands supplied. The number and sequence of LEDs to be used on a PCB were determined by performing various tests and applications. According to these studies, 20 of each LED were designed. These designed PCBs were typed and checked. The PCB design image is given in Figure 4.

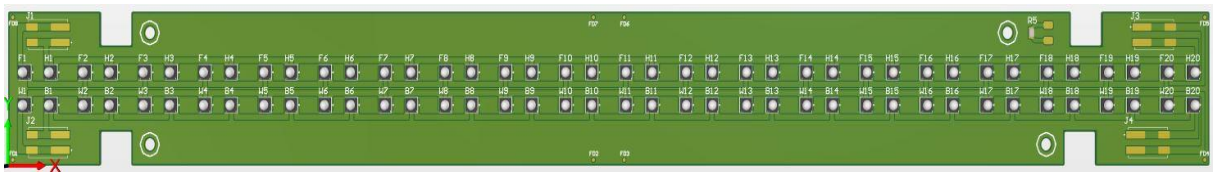

Figure 4. PCB image

Fixture External Body Design

The body design was made in accordance with the designed PCB. With the aim of passively distributing the heat of the designed body, prototype production was carried out on an aluminum block with dimensions of 40.6 mm x 406 mm on the cooling block. Figure 5. shows the luminaire body design components for which prototype production was carried out.

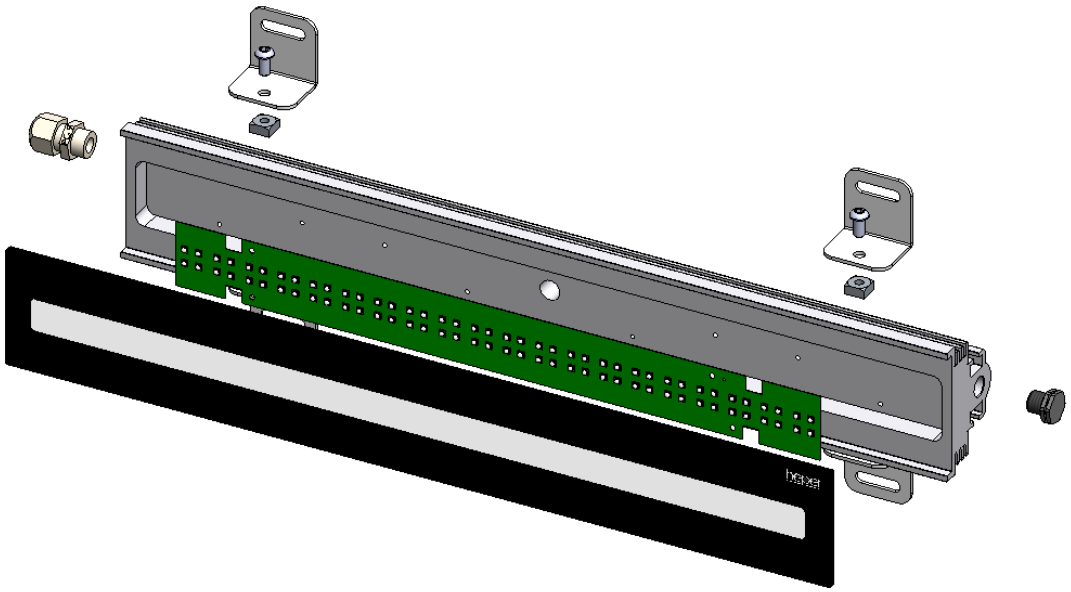

Figure 5. Luminaire body design components

The designed luminaire components were brought together and the product was brought to the prototype production point. The final version of the luminaire body design is seen in Figure 6. Thermal calculations were carried out to ensure that the designed luminaire could remain at optimum operating temperature. In this context, firstly the thermal resistance was calculated.

Figure 6. Luminaire body design image

When a voltage is applied to LED, current passes over semiconductor material and heat is created on LED under effect of this current. General formula of thermal resistance that will occur as a result of current passing is shown in Eq (1).

$$R_{a-b} = \frac{T_a - T_b}{P_{th}} \quad (1)$$

Thermal surface calculation formulas are calculated with the help of Equation 2-5 when heat sink channels are designed horizontally on ground:

$$P_d = P_{th} * (Verim) \quad (2)$$

$$T_{sp} = T_j - (R_{j-sp} * P_d) \quad (3)$$

$$T_{hs} = T_{sp} - (R_{sp-hs} * P_d) \quad (4)$$

$$R_{hs-a} = \frac{T_{hs} - T_a}{P_{th}} \quad (5)$$

P_d is amount of heat that must be cooled as a result of power consumed by LED. If an insulating material is used between LED and heat sink, value of R_{sp-hs} should be chosen between $0{,}2$ and $0{,}5$.

According to result obtained from eq. 5, required surface area for horizontal heat sink channels is calculated based on graphic in Figure 7. If heat sink channels are designed vertical to ground, horizontal surface wideness is calculated as follows (Sy):

$$S_y = \sqrt{P_d * 10} \quad (6)$$

In order to calculate required heat sink area per total watt of luminaire, surface areas calculated for both horizontal and vertical design must be collected. Material used as heat sink was chosen as aluminum because it is cheap and easy to process (Yuksel & Kıyak, 2020). Figure 7 is heat sink area-thermal conduction graph of aluminum (Antrak, 2023).

Solder point temperature (T_{sp}) value was taken as 76,82 °C, heat sink temperature (T_{hs}) 63,71°C, and ambient temperature (T_a) value as 26,27 °C in calculations conventional method calculations. Thickness value (R_{sp-hs}) between solder point and the heat sink was taken $0{,}2$ and the results were obtained. Resistance value of luminaire obtained as a result of resistance calculation by conventional method is 2,523 °C/W.

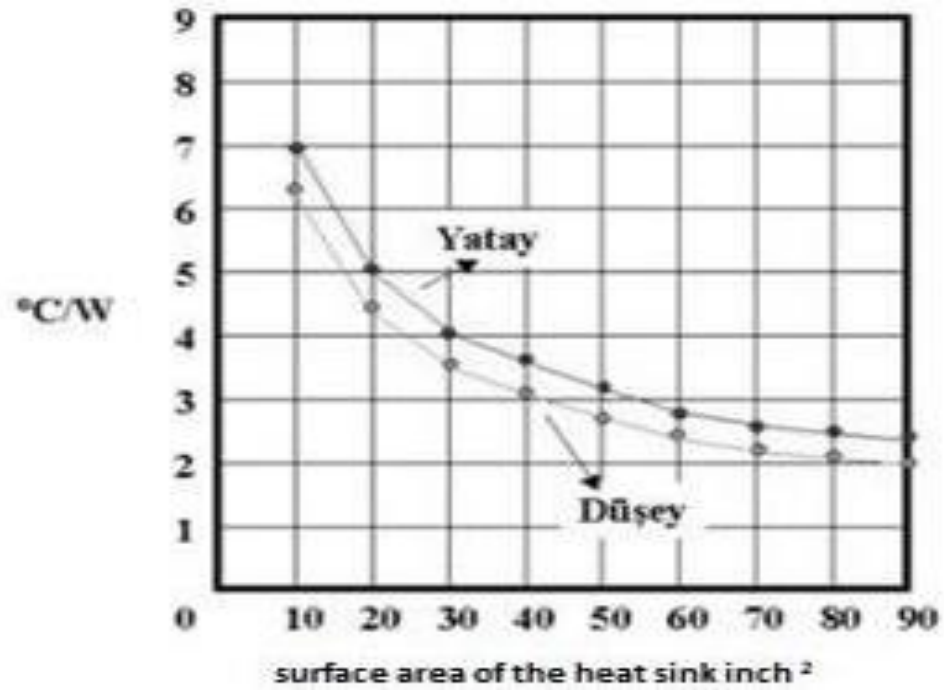

Figure 7. Heat sink area- thermal conduction

Design and Analysis Results

Testing and analysis of the body and PCB studies were carried out in a simulation environment and laboratory environment. Accordingly, analysis images of the designed armature are available below. The luminaire brightness analysis graph is seen in Figure 8.

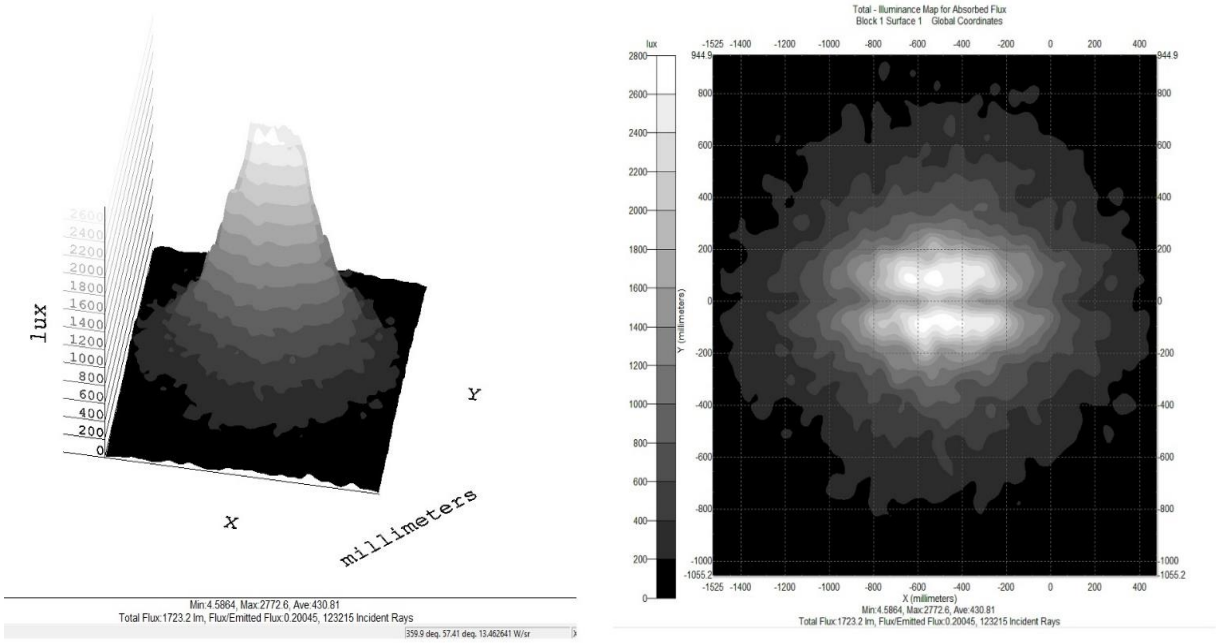

Figure 8. Luminaire(fixture) brightness analysis graph

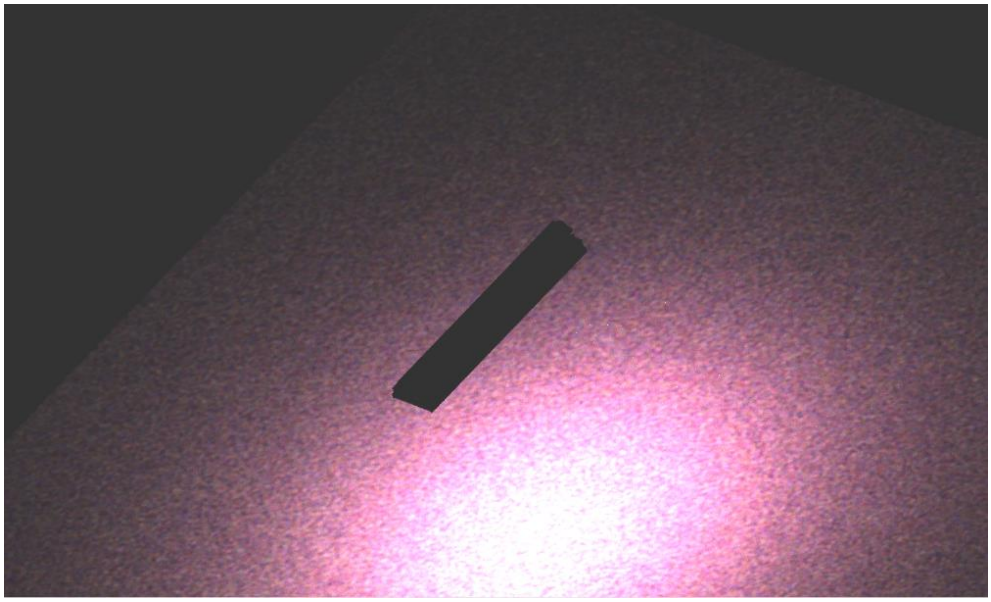

Figure 9. Real time rendered image of luminaire

The real-time rendered image of the designed luminaire is shown in Figure 9. The polar candela chart of the designed luminaire is shown in Figure 10.

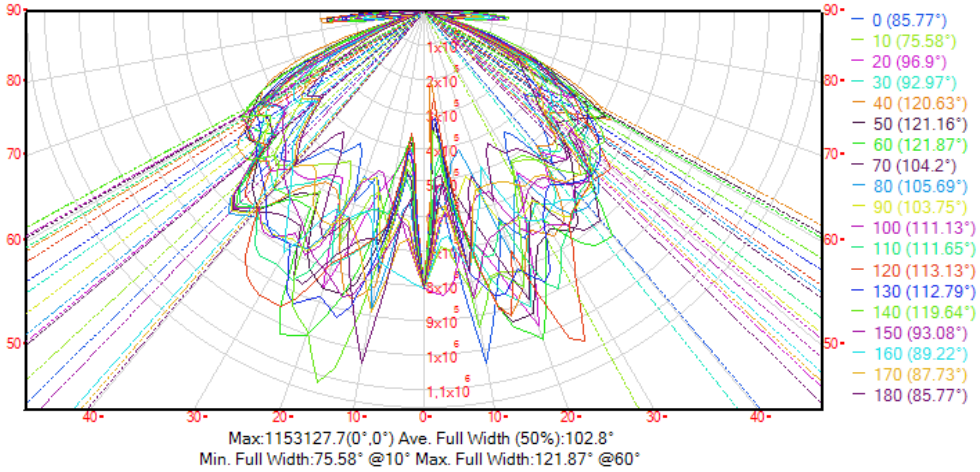

Figure 10. Polar candela chart.

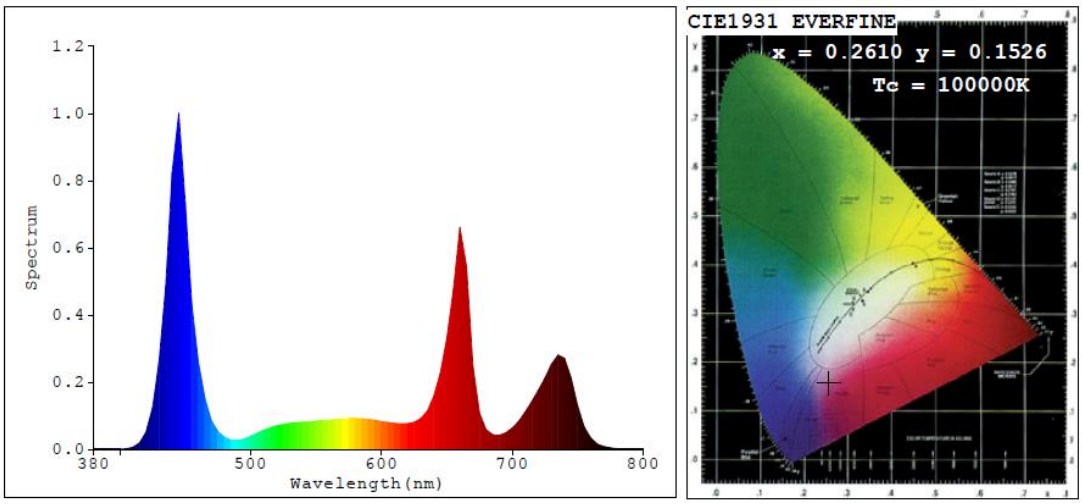

Figure 11. Spectrum analysis graph.

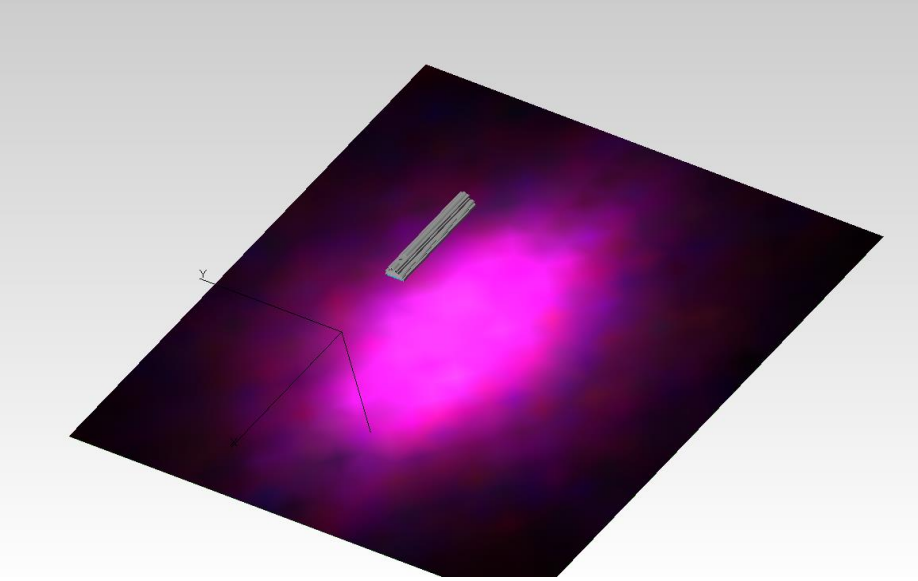

Figure 12. Simulation image.

Conclusion

The luminaire designed according to the data obtained as a result of the studies can provide illumination at the desired intermediate wavelengths. With the LED selection and driving technique, it can output any wavelength between 450nm and 780nm. A body design has been made that has passed thermal tests. Figure 11 shows the spectrum analysis obtained when all LEDs on the fixture are controlled with 350mA, and Figure 12 shows the analysis visual of this control data in the simulation environment.

Scientific Ethics Declaration

The authors declare that the scientific ethical and legal responsibility of this article published in EPSTEM journal belongs to the authors.

Acknowledgements or Notes

* This article was presented as an oral presentation at the International Conference on Technology, Engineering and Science (www.icontes.net) held in Antalya/Turkey on November 16-19, 2023.

References

ANTRAK (2023, August 7). Retrieved from (https://antrak.org.tr/genel/so%C4%9Futucular/)

Ares, G., Ha, B., & Jaeger, S. R. (2021). Consumer attitudes to vertical farming (indoor plant factory with artificial lighting) in China, Singapore, UK, and USA: A multi-method study. Food *Research International, 150*, 110811.

Belista, F. C. L., Go, M. P. C., Luceñara, L. L., Policarpio, C. J. G., Tan, X. J. M., & Baldovino, R. G. (2018). A smart aeroponic tailored for IoT vertical agriculture using network connected modular environmental chambers. In *2018 10th International Conference on Humanoid, Nanotechnology, Information Technology, Communication and Control, Environment and Management (HNICEM*) (pp. 1-4). IEEE.

Bennett, S. (2001). The past of PID controllers. *Annual Reviews in Control, 25*, 43-53.

Birkby, J. (2016). Vertical farming. *ATTRA Sustainable Agriculture, 2*, 1-12.

Bourget, M. C. (2008). *An introduction to light-emitting diodes*. America, USA: American Society for Horticultural Science.

Perdahcı, C., M., Akel, C., & Engec, S. (2018). *Ortualtı tarım uygulamaları için LED aydınlatma sistemleri ve ornek fizibilite calısması*. Turkey, Kocaeli TR: Elektrik Muhendisleri Odası (EMO)

Caglayan, N., & Ertekin, C. (2018). Farklı dalga boylu LED ısıklarının yesil yapraklı bitkilerin gelisimi uzerindeki etkileri. *Tarım Makinaları Bilimi Dergisi, 14*(2), 105-114.

Kalantari, F., Mohd Tahir, O., Mahmoudi Lahijani, A., & Kalantari, S. (2017). *A review of vertical farming technology: A guide for implementation of building integrated agriculture in cities.* In *Advanced engineering forum* (Vol. 24, pp. 76-91). Trans Tech Publications Ltd.

Kudryashov, A. V., Galishheva, E. S., & Kalinina, A. S. (2018, May). Lighting control using DALI interface. In 2018 *International Conference on Industrial Engineering, Applications and Manufacturing (ICIEAM*) (pp. 1-5). IEEE.

Kyriacou, M. C., Rouphael, Y., Di Gioia, F., Kyratzis, A., Serio, F., Renna, M., ... & Santamaria, P. (2016). Micro-scale vegetable production and the rise of microgreens. *Trends in Food Science & Technology, 57*, 103-115.

Liang, T. J., Huang, J. F., & Yadav, P. K. (2016). Design and implementation of dimmable LED control circuit with DALI protocol. In 2016 IEEE *International Conference on Power and Energy (PECon)* (pp. 121-126). IEEE.

OSRAM. (2023). *Horticulture tool*. Retrieved from https://apps.osram-os.com/horticulture/

Uddin, S., Shareef, H., Mohamed, A., & Hannan, M. A. (2011). LEDs as energy efficient lighting system: A detail review. *Malaysia: 2011 IEEE Student Conference on Research and Development*.

Škutová, J., & Šídlo, J. (2021, May). Design of fan model controlling system based on STM32. In *2021 22nd International Carpathian Control Conference (*ICCC) (pp. 1-5). IEEE.

Taiz, L., Zeiger, E., Møller, I. M., & Murphy, A. (2015). *Plant physiology and developmen*t (6 th ed.). Sinauer Associates Incorporated.

Wong, C. E., Teo, Z. W. N., Shen, L., & Yu, H. (2020). Seeing the lights for leafy greens in indoor vertical farming. *Trends in Food Science & Technology, 106*, 48-63.

Wu, W., Wu, M., & Liu, Y. (2006). A design of embedded DALI controller. In *2006 4th IEEE International Conference on Industrial Informatics* (pp. 1237-1240). IEEE.

Yuksel, L. B., & Kıyak, I. (2020). Thermal circuit calculation and real-time analysis of led light Source Luminaires. *European Journal of Technique (EJT), 10*(2), 252-263.

Zhang, Y., Xiao, Z., Ager, E., Kong, L., & Tan, L. (2021). Nutritional quality and health benefits of microgreens, a crop of modern agriculture. *Journal of Future Foods, 1*(1), 58-66.

Author Information

Ismail Kiyak
Marmara University
Istanbul, Turkey
Contact e-mail: *imkiyak@marmara.edu.tr*

Semih Asci
Moonlight Aydınlatma San. & Tic. A.S.
Ankara, Turkey

Sercan Keskintas
Moonlight Aydınlatma San. & Tic. A.S.
Ankara, Turkey

Emre Kocak
Moonlight Aydınlatma San. & Tic. A.S.
Ankara, Turkey

Ahmet Dibic
Moonlight Aydınlatma San. & Tic. A.S.
Ankara, Turkey
Contact e-mail: *adibic@hepergroup.com*

To cite this article:

Kiyak, I., Asci, S., Keskintas, S., Kocak, E., & Dibic, A. (2023). Design and analysis of LED-based artificial plant-growing fixture for vertical indoor farming systems. *The Eurasia Proceedings of Science, Technology, Engineering & Mathematics (EPSTEM), 26*, 420-429.

The Eurasia Proceedings of Science, Technology, Engineering & Mathematics (EPSTEM)
ISSN: 2602-3199

The Eurasia Proceedings of Science, Technology, Engineering & Mathematics (EPSTEM), 2023

Volume 26, Pages 430-438

IConTES 2023: International Conference on Technology, Engineering and Science

Management and Control of Hybrid System WIND-PV Systems Integrated to the VSC-HVDC Grid

Hamza Sahraoui
University of Chlef

Hacene Mellah
University of Bouira

Amar Maafa
University of Bouira

Abdelghani Yahiou
University of Bouira

Said Drid
Higher National School of Renewable Energies

L. Chrifi-Alaoui
University of Picardie

Abstract: The harvesting of natural resources that can be replenished is experiencing explosive growth not just in industrialized nations but also in some less developed nations. This study focuses on the control of a hybrid photovoltaic-wind energy system known as WIND-PV. This system is utilized to serve a load in a city that is not connected to the grid. The type of energy system that was investigated in this study is a hybrid one. It consists of two renewable energy sources—wind and photovoltaic—that are coupled with static converters for the purpose of adaptation and conversion of the forms of electrical energy that may be applied to an isolated metropolis. The modeling of a hybrid PV-WIND system is the most important component of the study that we are doing. We worked on a work plan, which was integrated into a Voltage Source Continuous High-Voltage Direct Current (VSC-HVDC), and this helped us a great deal to have well-determined signals.

Keywords: Wind energy, Renewable energy, Photovoltaic energy

Introduction

The use of renewable energies is not new. These have been exploited by man since the dawn of time. In the past, watermills, windmills, firewood, animal traction, sailing boats have largely contributed to the development of humanity. They constituted an economic activity in their own right, especially in rural areas where they were as important and as diversified as food production.

For this, renewable energies appear today and in the long term as the appropriate solution that covers this energy need by reducing the major inconvenience emitted by fossil fuels since a large part of the world's energy production is ensured from: coal, natural gas, oil and uraniu (Torkashvand et al.,2022). Because of these advantages and certain constraints that characterize them, particularly in terms of cost, the role assigned to

renewable energies, within the framework of the national energy policy, is to meet the energy demand on isolated sites far away. electricity networks. Solar electrification of villages in the deep south, etc.) than in other sectors of the national economy (road marking, water pumping, etc.).

To respond to these concerns, more and more countries are putting in place policies to encourage energy saving, but also the production of energy through other means often qualified as (clean) in reference to the fact that it does not generate carbon dioxide. These means of production are mainly derived from renewable energies, that is to say whose resources are inexhaustible by nature. Among these we can cite wind energy (from the wind), and energy (solar) (Sahraoui et al., 2016; Sahraoui et al., 2021). This entails a study of the sizing parameters of this type of application and their simulation will make it possible to highlight the available control strategies and to evaluate the optimization techniques. For this reason we present a method of optimal dimensioning of the size of the hybrid system of electricity production. To achieve this goal, we have our paper on the simulation of a PV-WIND hybrid system. Integrated in an HVDC Network We practiced on a work plan which helped us a lot to have well determined signals (Sahraoui et al., 2014; Sahraoui et al., 2015).

Photovoltaic-Wind Hybrid System

A hybrid system with renewable energy sources (HSRES) is an electrical system comprising more than one energy source, of which at least one is renewable. For example in this project is a hybrid system (photovoltaic – wind).The hybrid system may include a storage device. From a more global point of view, the energy system of a given country can be considered as a hybrid system. In the figure 1 represents diagram of a hybrid Photovoltaic-wind system.

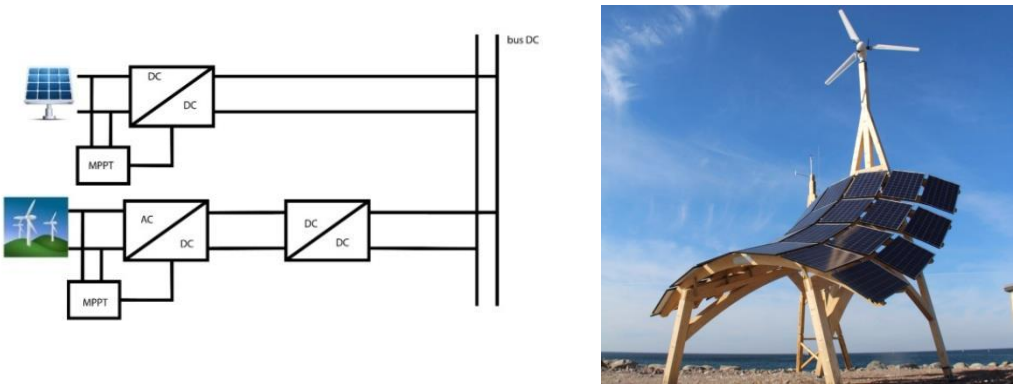

Figure 1. Diagram of a photovoltaic-wind hybrid system

Specifications of a Solar Panel

PV Panel specification

PV model	1STH-215-P
Short circuit current (Isc)	7.84 A
Open circuit voltage (Voc)	36.3 V
Maximum Voltage (Vmpp)	29 V
Maximum current (Impp)	7.35 A
Maximum power (Pmpp)	213.15 W
Number of cells in series (Ns)	60
Temperature coefficient of Isc	-0.36099%/°C
Temperature coefficient Voc	0.102%/°C
Diode ideality factor (A)	0.98117
Series resistance (Rs)	0.39383Ω
Shunt resistance (Rsh)	313.3991Ω

Figure 2. Electrical characteristics of the model solar panel (1Soltech 1STH-215-P Polycrystalline Module)

We will study in this work the model of a following panel: Soltech 1STH-215-P PV Panel
Features of this panel: The electrical characteristics of this photovoltaic panel are given by the Figure 2.

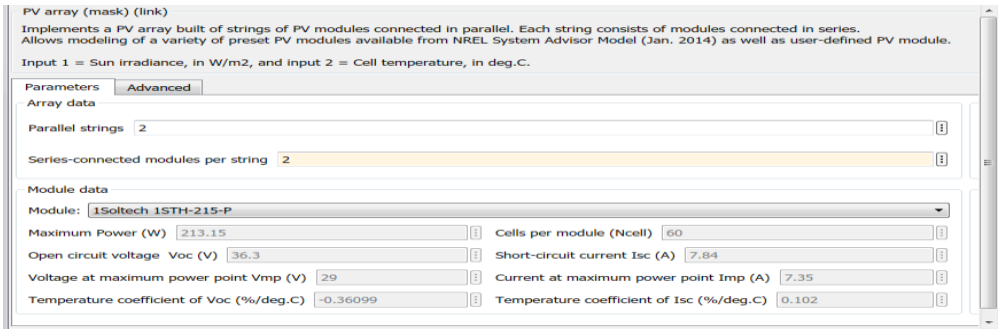

Figure 3. Electrical characteristics of solar panel

The representative diagram of the mathematical model of the photovoltaic module under Matlab-silink is given by (Figure.III.5):

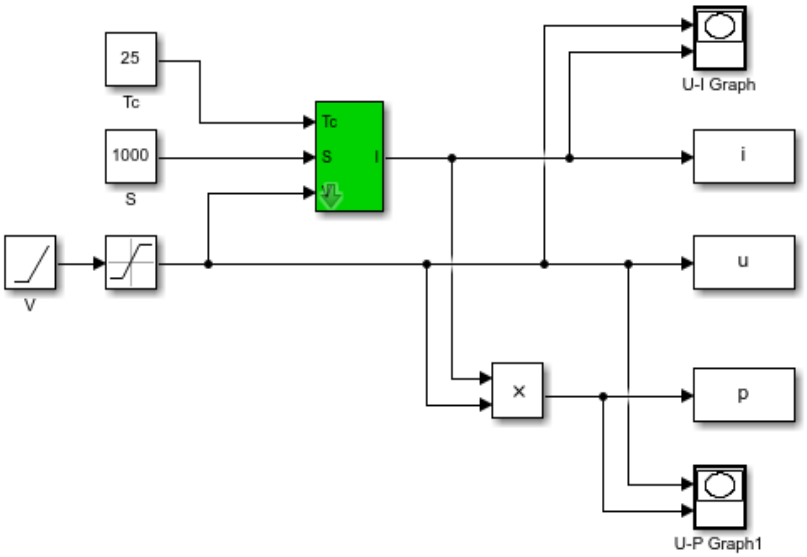

Figure 4. PV simulation diagram of PV

The simulation of a PV generator under standard conditions (E=1000 w/m² and T=25°), gave the curves presented in (figure 5). It is found that the set of characteristics P_PV and I_PV are strongly nonlinear and depends on the solar irradiation and the temperature of the photovoltaic panels.

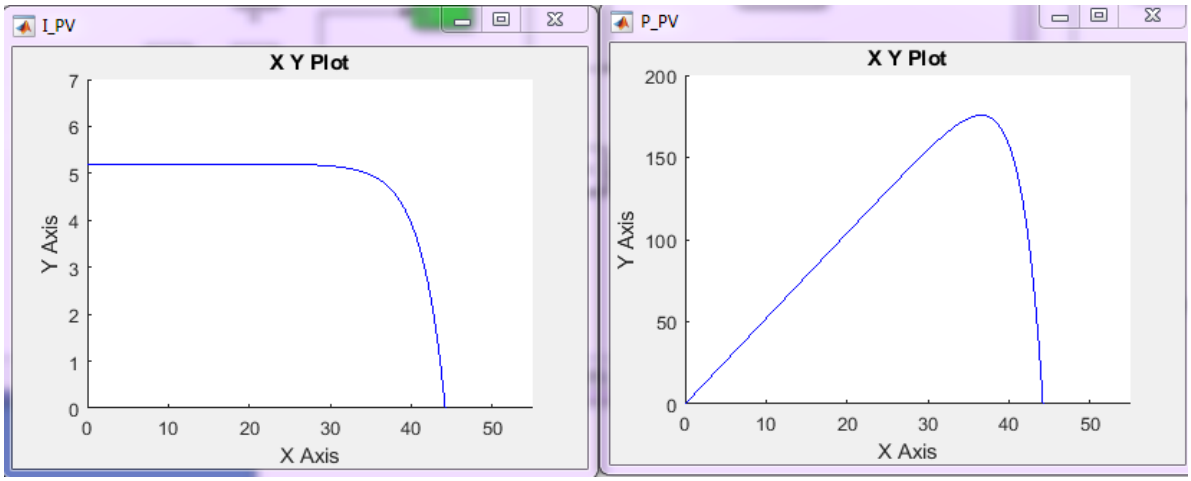

Figure 5. influence of radiation on the I_PV and P_PV characteristics (1000W/m² and 25°).

Simulation result of the generator (GPV) with variable illumination and temperature;
To observe the influence of external conditions of light and temperature

(E,T) on the characteristic (I-V) (P-V), we have adopted the following methods:
To visualize the influence of irradiation, the temperature a (T=25°) is fixed and the illumination is varied within a sufficient range.

We vary the irradiation (E) [1000 500 100] (W/m2), the characteristic (P=f(V)) and the characteristic (I=f(V)) are given by Figure 6 . According to these results, the current is directly proportional to the radiation, unlike the voltage which varies very little according to the illumination

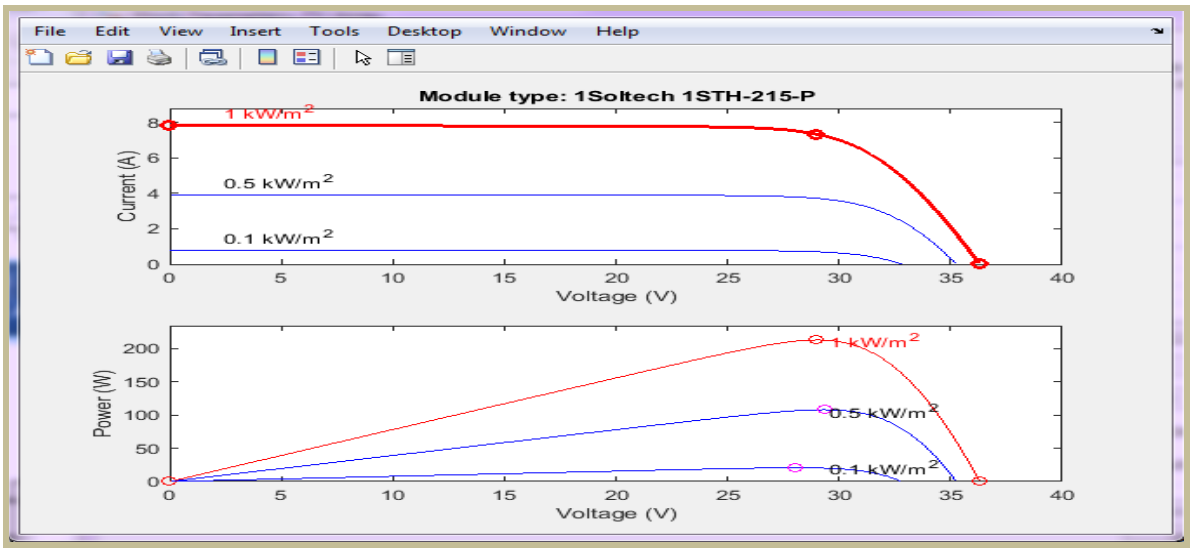

Figure 6. Influence of irradiation variation on characteristics (I-V) and (P_V)

Wind System Simulation with PMSG

Figure 7 represents the mechanical power as a function of the rotational frequency of the rotor for different wind speeds. Figure 8 represents Power coefficient as a function of specific speed. Figure 9 depicts the MPPT Block Figure 10 represents the final wind turbine simulation with MSG

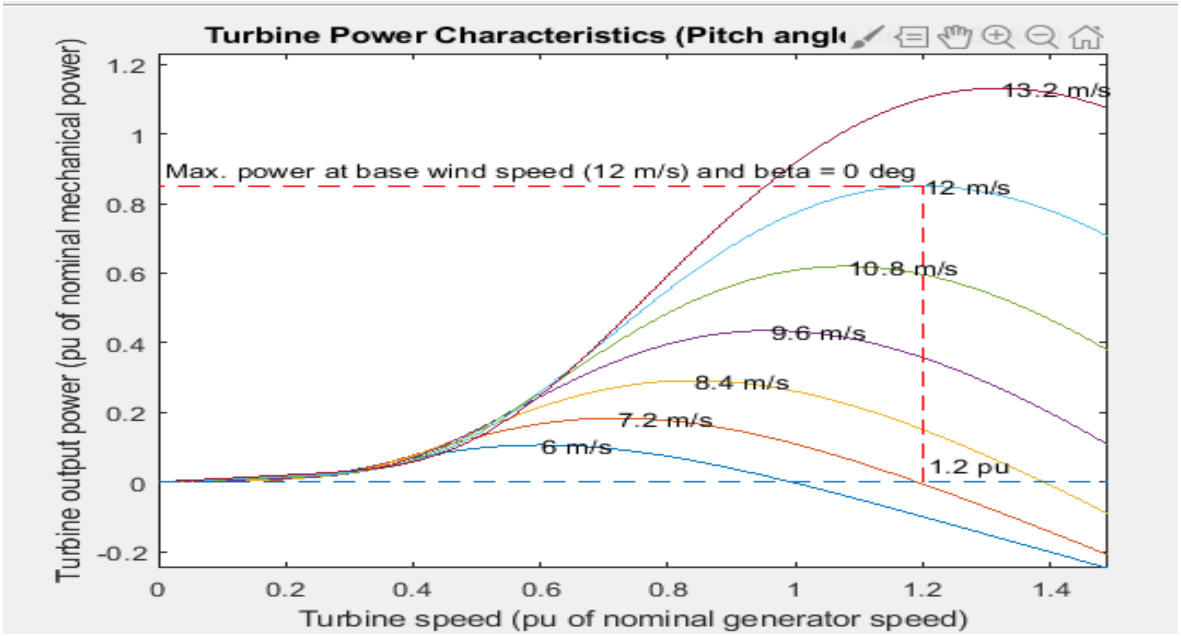

Figure 7. Power variation curves from speed.

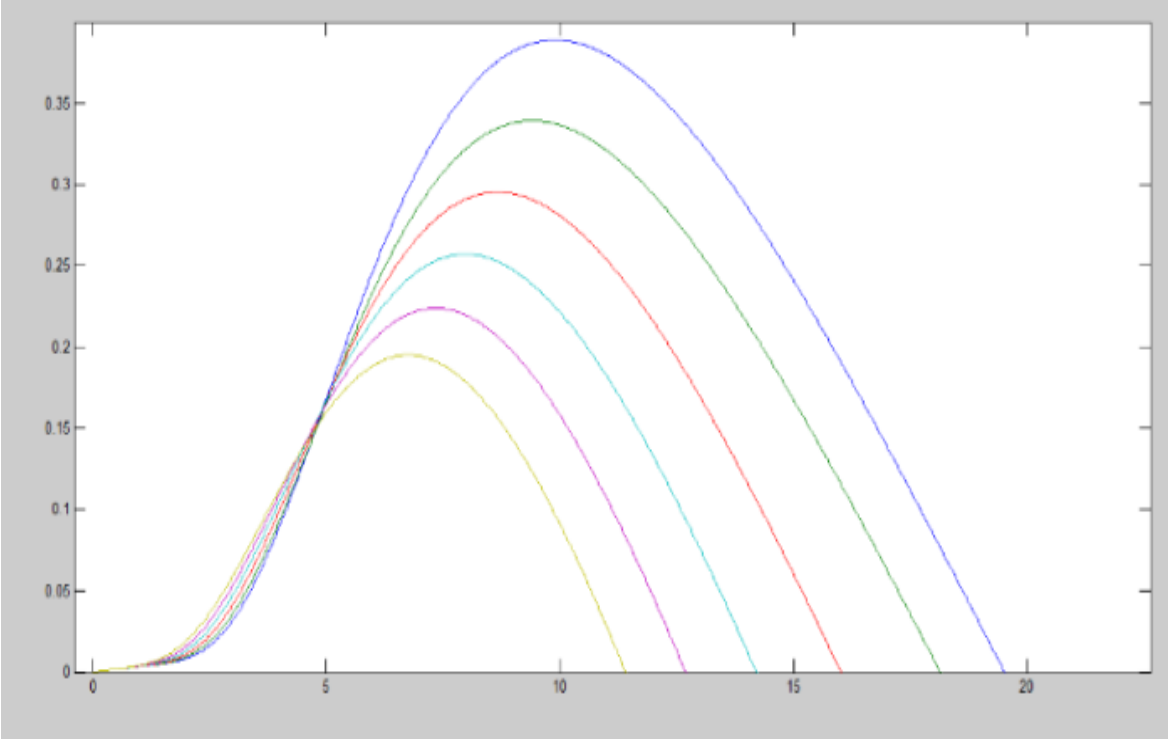

Figure 8. Curve of variation of Cp from lamda

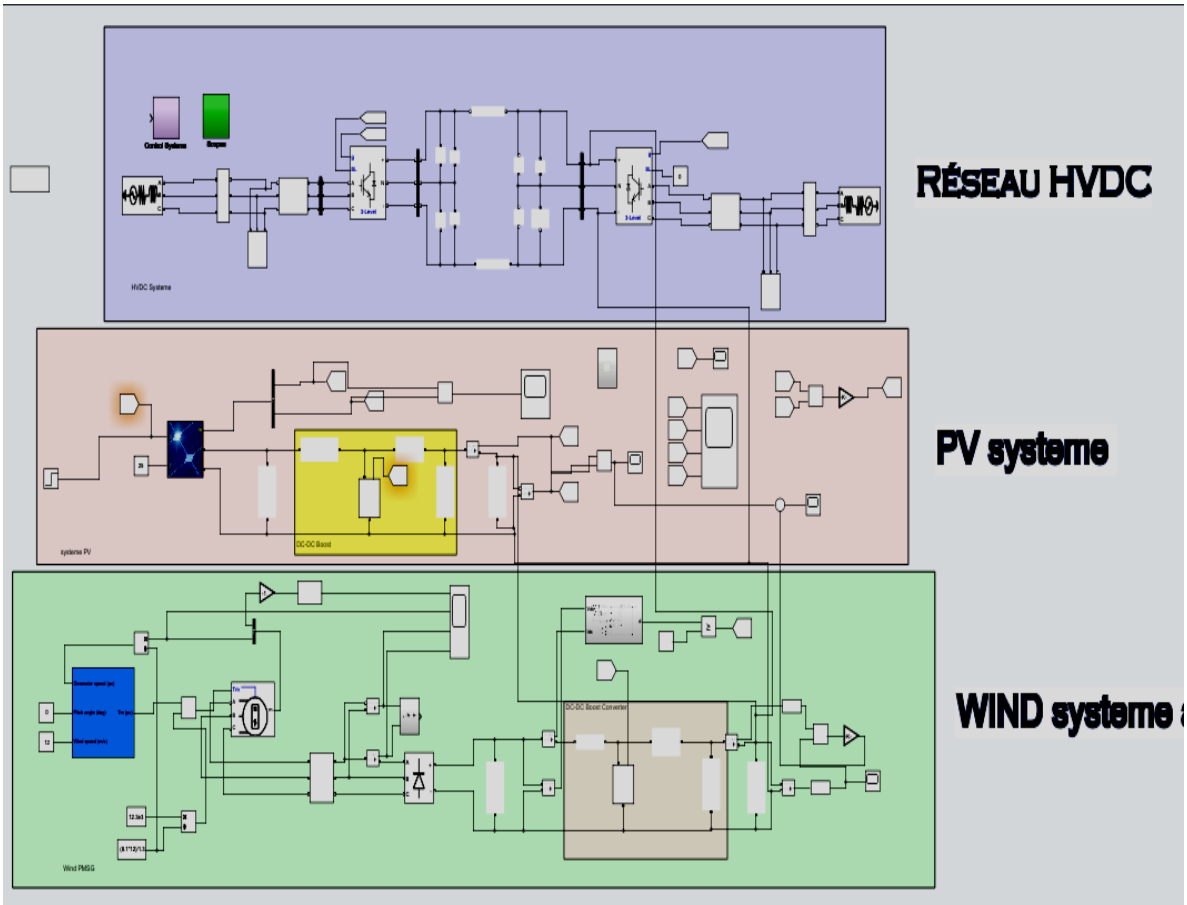

After having approached the simulation of solar system and wind system integrated in HVDC network, we obtain the following curves:

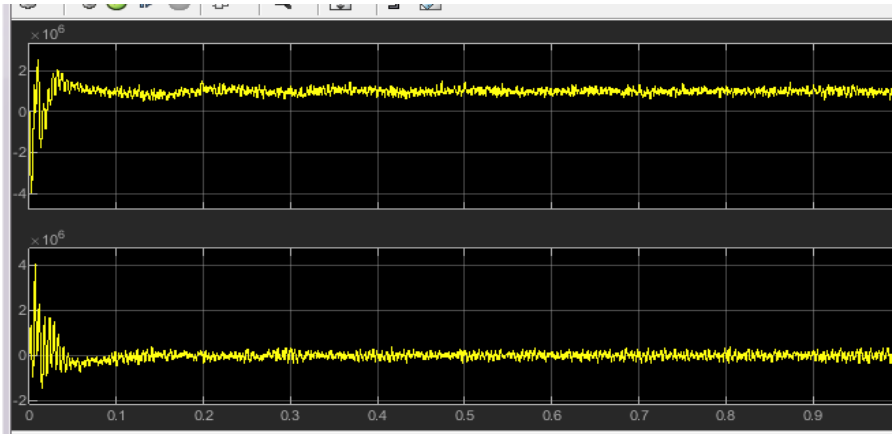

Figure 9. P and Q power curve at HVDC network output

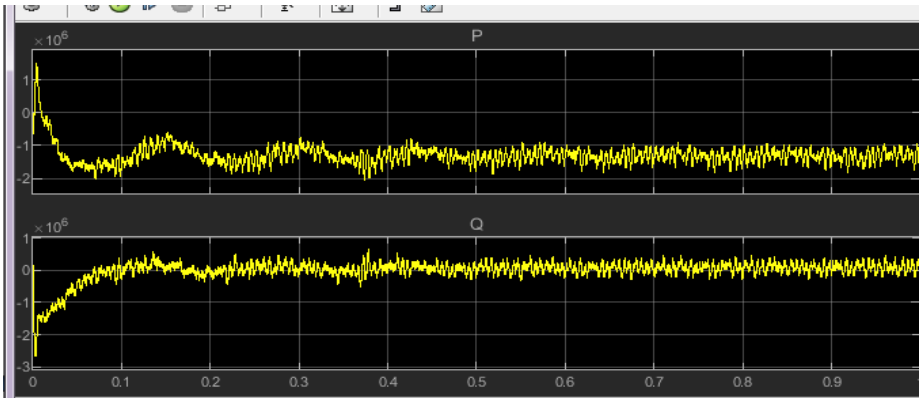

Figure 10. Curve of P and Q Grid

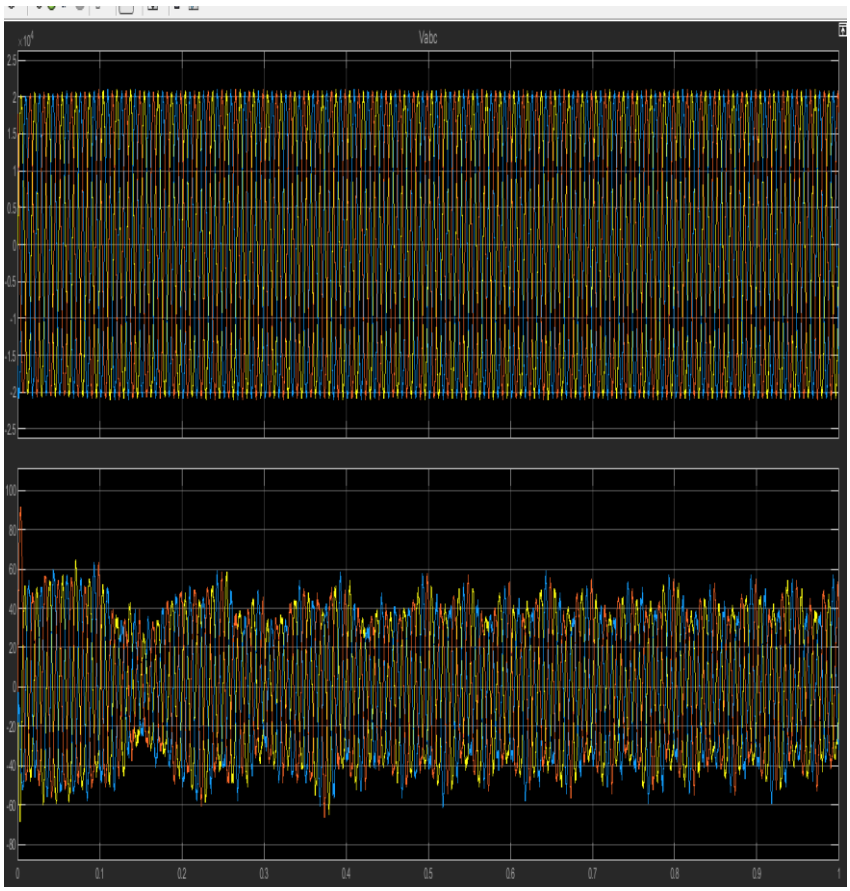

Figure 11. Vabc voltage curve

Voltage at the DC Bus of PV and Wind Power

After having approached the simulation of solar system and wind system integrated in HVDC network, we obtain the following curves of the DC BUS voltage Vout of PV and wind with PMSG:

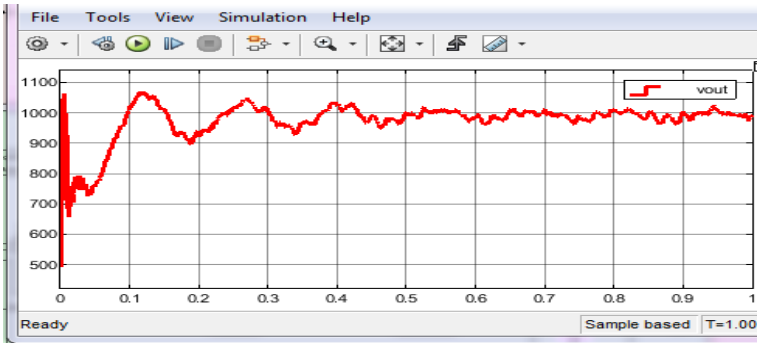

Figure 12.Courve of tension Bus DC of PV

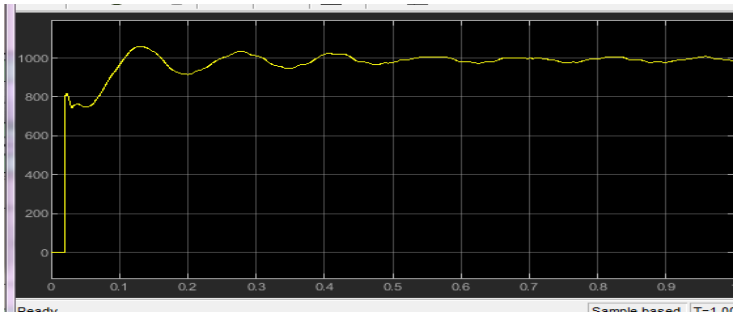

Figure 13. Courbe of tension Bus DC wind

After having approached the simulation of solar system and wind system integrated in HVDC network we obtain final curve of voltage of BUS DC Vdc:

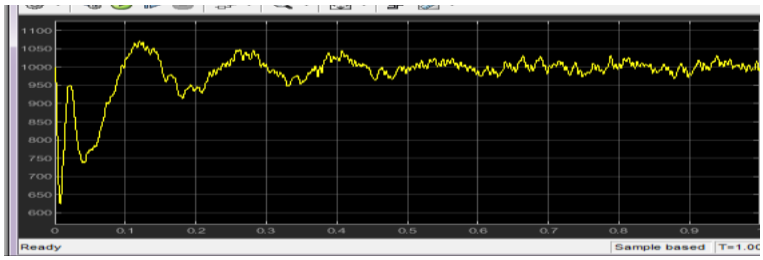

Figure 14.Courve of tension Bus DC HVDC

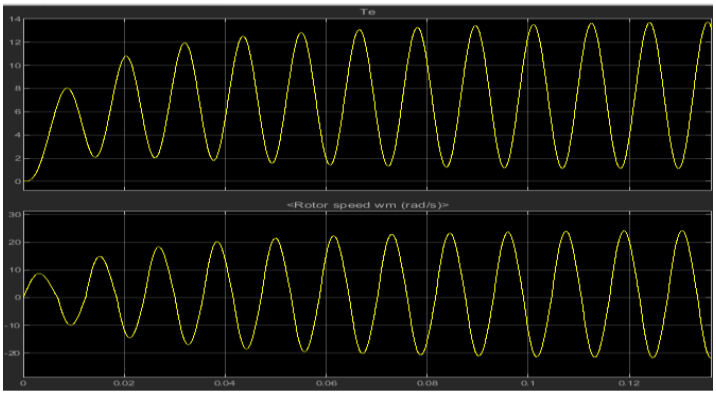

Figure 15. Courve electromagnetic Te avec Wm

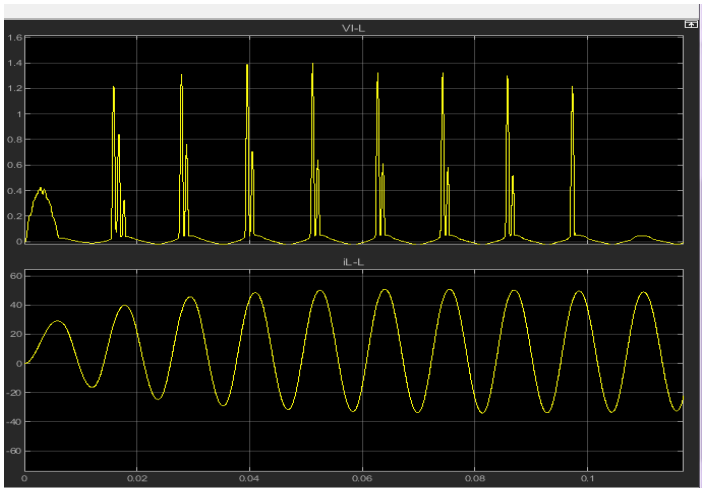

Figure 16. Courve of tension and courant of wind

Conclusion

In this paper, we have presented a study and a sizing of a hybrid PV / wind system with the method of the monthly energy produced by the system Per unit area for the purpose of having a good reliable configuration with a minimum cost, We will simulate a hybrid solar and wind system and notice the simulation results And the HVDC network simulation and we notice the results of this simulation In the end will integrate the solar and wind system into this network.

Scientific Ethics Declaration

The authors declare that the scientific ethical and legal responsibility of this article published in EPSTEM journal belongs to the authors.

Acknowledgements or Notes

* This article was presented as an oral presentation at the International Conference on Technology, Engineering and Science (www.icontes.net) held in Antalya/Turkey on November 16-19, 2023.

References

Alnejaili, T., Drid, S., Mehdi, D., Chrifi-Alaoui, L., & Sahraoui, H. (2015). Sliding mode control of a multi-source renewable power system. The *3rd International Conference Control, Engineering & Information Technology* (CEIT'2015). Tlemcen, Algeria. Retrieved from http://lat.univtlemcen.dz/ceit2015/index.php.

Boutabba, T., Sahraoui, H., Bechka, M. L., Drid, S., & Chrifi-Alaoui, L. (2020). A comparative study of MPPT techniques for standalone hybrid PV-wind with power management. *Lecture Notes in Electrical Engineering*, 93–108.

Sahraoui, H., Chrifi-Alaoui, L., Drid, S., & Bussy, P. (2016). Second order sliding mode control of DC-DC converter used in the photovoltaic system according an adaptive MPPT. *International Journal of Renewable Energy Research, 6*(2), 375-383.

Sahraoui H., Mellah H., Drid S., & Chrifi-Alaoui L. (2021). Adaptive maximum power point tracking using neural networks for a photovoltaic systems according grid. *Electrical Engineering & Electromechanics, 5*, 57-66.

Sahraoui, H., Drid, S., Chrifi-Alaoui, L., & Idriss, B. (2014). Modeling and control of the DC-DC converters. *International Conference on Industrial Engineering & Manufacturing ICIEM'14*, 11-13 Mai, Batna, Algeria. Retrieved from http://iciem2014.univbatna.dz/.

Sahraoui, H., Drid, S., Chrifi-Alaoui, L. (2014). Robust control of the second order sliding mode controller with dc boost converter improved for the photovoltaic Systems DC-DC. *15th International Conference on*

Sciences and Techniques of Automatic control & computer engineering. STA'2014.IEEE. Retrieved from www.sta-tn.com.

Sahraoui, H., Drid, S., Chrifi-Alaoui, L., & Hamzaoui, M. (2015). Voltage control of DC-DC buck converter using second order sliding mode control. The *3rd International Conference on Control, Engineering & Information Technology* (CEIT'2015). IEEE. Retrieved from http://lat.univtlemcen.dz/ceit2015/index.php.

Sahraoui, H., Chrifi-Alaoui, L., Ouriagli, M., Drid, S., & Mehdi, D. (2018). "he dynamic control and optimal management of the energy in the case of a territory isolated in Batna city. *7th International Conference on Systems and Control (ICSC*) . IEEE.

Torkashvand, M., Hasan-Zadeh, A., & Torkashvand, A. (2022). Mini review on importance, application, advantages and disadvantages of biofuels. *J. Mater. Environ. Sci., 13*(6), 612-630.

Author Information

Hamza Sahraoui
Electrical Engineering Department, Hassiba Benbouali University of Chlef, B.P 78C, Ouled Fares Chlef 02180, Chlef, Algeria, Research Laboratory LSPIE, Electrical Engineering Department, University of Batna 2
Contact e-mail: *hamzasahraoui@gmail.com*

Hacene Mellah
Electrical Engineering Department, University Akli Mouhand Oulhadj-Bouira, Rue Drissi Yahia Bouira, 10000, Algeria

Amar Maafa
Electrical Engineering Department, University Akli Mouhand Oulhadj-Bouira, Rue Drissi Yahia Bouira, 10000, Algeria

Abdelghani Yahiou
Electrical Engineering Department, University Akli Mouhand Oulhadj-Bouira, Rue Drissi Yahia Bouira, 10000, Algeria

Saïd Drid
Research Laboratory LSPIE, Electrical Engineering Department, University of Batna 2, 53, Route de Constantine, Fésdis, Batna 05078, Algeria

L. Chrifi-Alaoui
Laboratoire des Technologies Innovantes (LTI), University of Picardie Jules Verne, IUT de l'Aisne, 13 Avenue François Mitterrand 02880 Cuffies-Soissons, France

To cite this article:

Sahraoui, H., Mellah, H., Maafa, A., Yahiou, A., Drid, S., & Chrifi-Alaoui, L.(2023). Management and control of hybrid system WIND-PV systems integrated to the VSC-HVDC grid. *The Eurasia Proceedings of Science, Technology, Engineering & Mathematics (EPSTEM), 26*, 430-438.

The Eurasia Proceedings of Science, Technology, Engineering & Mathematics (EPSTEM)
ISSN: 2602-3199

The Eurasia Proceedings of Science, Technology, Engineering & Mathematics (EPSTEM), 2023

Volume 26, Pages 439-450

IConTES 2023: International Conference on Technology, Engineering and Science

Path Planning via Swarm Intelligence Algorithms in Unmanned Aerial Vehicle Population

Mustafa Cosar
Hitit University

Abstract: Unmanned Aerial Vehicle (UAV) is an autonomous aerial vehicle capable of operating autonomously or in swarm cooperation, performing various tasks in civilian and military domains that exceed human capabilities. These vehicles, which can be produced in different models with varying hardware and software features, include flight control systems, route tracking systems, sensors, and numerous additional components. UAVs have the ability to process data from themselves, the control center, and the external environment. Data processing enables functions such as flight management, swarm optimization, and target and route analysis. In this analysis process, optimization algorithms and especially swarm intelligence algorithms inspired by creatures that move in flocks in nature are used. In this study, the aim was to determine the optimal route and distance from 10 different coordinate points for collective task optimization within a UAV swarm. Artificial Bee Colony (ABC) Optimization and Particle Swarm Optimization (PSO) were used during the task optimization process. The application was coded in Python. As a result of the application, the optimal distance was calculated as 0.123 km for the ABC algorithm and 0.167 km for the PSO algorithm. In addition, both algorithms determined the best routes according to different start and end points in route planning task optimisation.

Keywords: UAV, Path planning, Swarm intelligence algorithms, ABC optimization, PSO

Introduction

Many risky and challenging tasks are carried out by a team consisting of multiple members. The success of the task relies on the collaboration and coordination exhibited by team members. Task optimization is defined as the interaction of team members with the goal of maximizing or minimizing an objective function. Task optimization aims to improve decision-making processes that involve numerous variables and constraints. This method is utilized to optimize one or more objective functions simultaneously, enabling the concurrent optimization of various objectives under the interaction of numerous variables.

Task optimization is applied in industrial design, engineering, manufacturing processes, finance, logistics, energy management and similar fields. This method often uses evolutionary algorithms, genetic algorithms, natural language processing, artificial neural networks, or various mathematical optimization techniques. Task optimization is an important tool for optimizing decision-making processes, reducing costs and using resources more effectively. Mission optimization in flying systems is especially used to optimize flight time, flight speed, energy consumption and path planning. Path planning refers to the process by which an autonomous system finds the safest and most appropriate path from a given starting point to a given destination point. During this process, multi-dimensional planning is made such as efficient use of resources, adaptation to environmental conditions and calculation of alternative routes. As output at the end of the plan, it calculates the optimum distance and route suitable for the mission objective function.

Task optimization in a UAV team exhibiting swarm behavior is defined as a metaheuristic optimization technique inspired by nature and social organizations. This technique typically involves members of a group

called "particles" or "agents" collaborating throughout the task process. Each member explores the potential solution space and shares knowledge through interaction with other members and works together to develop potential solutions. Herd optimization is especially effective in solving complex problems in disciplines such as engineering, fleet management, logistics and finance.

Many of the autonomous capabilities that swarms exhibit in task optimisation processes have traces of artificial intelligence (AI). This swarm AI is defined as the ability of a group of similar organisms or objects to interact while exhibiting complex collective behavior to achieve common goals based on local knowledge. Research on swarm intelligence aims to understand and improve collective behaviors by examining the internal interactions of the system, leadership structures, information sharing and coordination. Additionally, swarm intelligence is widely used to optimize objective functions such as communication, location verification and path planning in swarms of vehicles that exhibit autonomous behavior, such as UAVs.

In this study, a general introduction will be given to mission optimization techniques and swarm intelligence algorithms applied to UAV swarms. Then, an optimization application will be carried out to determine the best route in a mission scenario using some swarm intelligence algorithms. In this scenario, firstly, the flight parameters of the UAV swarm, mission boundaries and transit coordinates on the map were determined. Then, ABC and PSO algorithms, which are swarm intelligence algorithms suitable for the task objective function, were prepared. Finally, the scenario was coded in the Python programming language.

The architecture of the article is as follows. In Chapter Two, the conceptual framework of UAV mission optimization, swarm intelligence, and optimization algorithms is presented along with the literature review. Section 3 describes the architecture, scenario, and methodology of an example path planning task optimization. Additionally, this section introduces the parameters used in the path planning process, swarm intelligence algorithms, and the algorithm of the program developed in Python. In the fourth section, the values calculated for task optimization within the scenario and the visual outputs of these values when the Python program is run are presented. In the conclusion section, a general evaluation of the application is made. It is believed that this study will make significant contributions to future research on path planning task optimization in UAV swarms.

Conceptual Framework

This section contains information about the UAV's swarm structure, swarm intelligence, task optimization and AI algorithms used in swarm intelligence optimization.

UAV Swarm Structure

UAV, also called a drone, is a semi or fully autonomous aerial vehicle that utilizes electronic communication and control subsystems (Puente Castro et al., 2022). UAVs are autonomous aerial robotic systems capable of independently performing takeoff, flight, mission execution, and landing activities, and, in some cases, making autonomous decisions (Cosar, 2022). Although UAVs have different features and limitations in terms of software and hardware, they can exhibit complementary features when they come together to form a swarm. Such features are seen in many living populations in nature.

The successful completion of a common mission over vast geographical areas by multiple UAVs depends on the collective behaviors of all members, which involve cooperation, coordination, and communication. UAV swarms establish communication with ground stations, their own members, and other systems using wireless network technologies. The quality of this communication is expected to be flawless, uninterrupted and protected against attacks. This is crucial because a communication failure can lead to UAV collisions, deviations from the swarm, and mission failure.

For a UAV swarm to self-organize, it relies on network formation and the effective integration of local computing functions. This system, which behaves as two separate components, has complementary features. For example, the network formation system within the swarm can calculate new routes in real-time to prevent the swarm from suffering in adverse situations such as packet loss or cyberattacks during communication (Gupta et al., 2015). Cosar and Kıran (2021) proposed a blockchain-based collaborative network model between UAV swarms to increase their location accuracy against cyber-attacks.

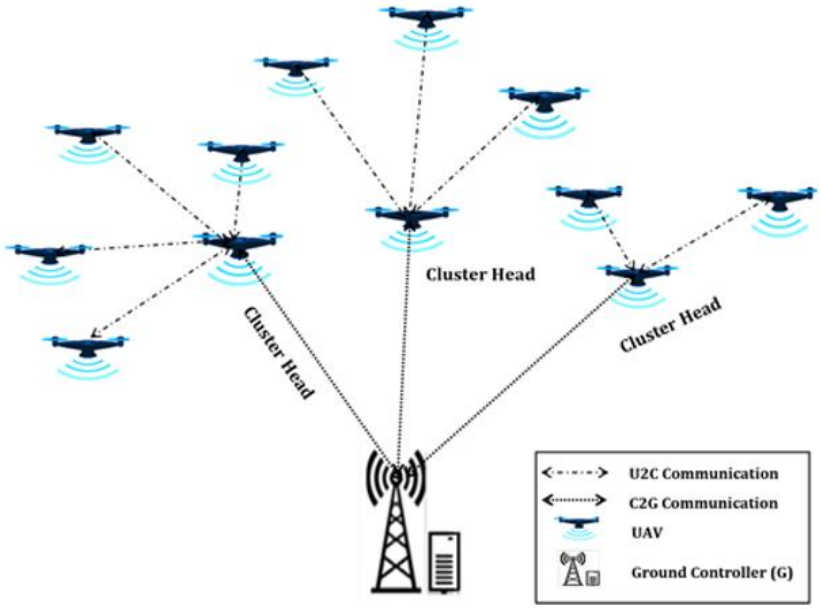

Figure 1. Communication architecture of UAV swarms (Asaamoning et al., 2021)

The proposed communication network model for UAV swarm cooperation and coordination during a wide-ranging mission is given in Figure 1. The computational system within the communication network of a UAV swarm is called a Networked Control System (NCS). The operating architecture of a general NCS consists of two basic systems. The first is a computational system that can collect data through sensors, make decisions and execute commands through actuators. The second is a network system that relies on network components, network standards and some basic protocols to communicate information (Asaamoning et al., 2021).

Swarm Intelligence

Swarm intelligence (SI) is the ability of a population of organisms, natural or artificial, to self-organize through collective behavior (Zhang et al., 2013). SI is the ability of a group of members to achieve a specific goal or task by exhibiting coordinated behavior based on simple rules. These rules regulate behaviors such as how swarm members interact with each other, the direction in which they move, and when they should stop. Each member can exhibit complex and organized behaviors, often sensitively responding only to nearby members, without explicit coordination. Often, these abilities observed in natural swarms can be reflected in various algorithms in computer science, AI, and engineering processes.

Throughout nature, different organisms often benefit from moving in swarms. Simple collective behavior models of group members demonstrate that they are sufficient to generate and provide group morphologies for uncomplicated partial interactions. Members collectively form groups capable of processing information and making decisions. Through shared information, a group can make better decisions than an individual member; this phenomenon is referred to as "collective intelligence" (Tang et al., 2021).

SI Algorithm

Rath et al (2020) emphasize that SI algorithms are used in many applications where real-time actions are processed efficiently, due to their dynamic properties. Idoko (2023) proposed a solution to the range anxiety experienced by electric car drivers with swarm intelligence algorithms. In this research, the author used PSO, a meta-heuristic optimization method, to optimize the travel path of electric vehicles between Bucharest and Cluj-Napoca.

During the mission of the UAV swarm, SI algorithms have been shown to be effective in some activities that require intelligence such as route planning, task allocation, obstacle avoidance, collision avoidance, target search, and communication (Bhagade & Puranik, 2012; Zhang & Duan, 2018). The algorithms used in the task optimization of UAV swarms involving intelligence are presented in Table 1.

Table 1. Algorithms for SI Problems

Algorithm Name	Type	Inspiration Source	Application Areas
Nearest Neighbor (NN)	Heuristic	Geometry	Logistics, Facility, Traveling Sales Problems (TSP)
Insertion Heuristic		Logistics	Production Planning, Location Selection
Swap Heuristic		Geometry, Sorting	Planning, Reversal
Clarke-Wright Savings		Logistics	Transportation, Distribution, Fleet Management
TSP Heuristics		Geometry	Travel Sales Problems, Logistics, Map Design
Genetic Algorithms (GA)	Meta-Heuristic	Genetic Evolution	Sorting, AI, Engineering, Optimization
Simulated Annealing		Statistical	Production Planning, Location Selection
Tabu Search (TS)		Local Search	Logistics, Sorting, Route Finding, Graph
ABC		Bee Behavior	Distributed Computing, Sorting, Logistics
Multi-Agent Systems (MAS)		Agent Systems	Game, Robotics, Distributed Systems
Firefly Swarm Algorithm		Insect Behavior	Distributed Computing, Sorting, AI
Artificial Fish Swarm Algorithm		Animal Behavior	
Cluster Search Algorithms		Clustering	Data Mining, Clustering, Grouping
Sparrow Search Algorithm		Bird Behavior	Optimization, Search
Ant Colony Optimization (ACO)	Optimization		Distributed Computing, Sorting, Logistics
PSO		Particle Behavior	Optimization, Production, Supply Chain
Cluster PSO (CPSO)		Based on PSO	Optimization, Clustering, Data Mining
A*		Geometry	Path Planning
Paxos Algorithm	Consensus		Load Balancing, Block chain
Raft Algorithm			

Table 1 shows the most widely used AI algorithms for improving SI. This table shows the names of the algorithms, their inspiration and the types of problems they are used to solve. SI algorithms are based on three approaches: heuristics, optimization and consensus, and aim to control the behavior of UAV swarms.

Path Planning via SI Algorithms in Task Optimization Process

Task Optimization is a concept that describes the process or method of an organization, an individual, or a system to perform specific objectives or tasks in the best possible way. The success of task optimization is determined by parameters such as the difficulty of the goal, environmental conditions, constraints, methods used, the number of members in the group, and coordination. Task optimization contributes to the efficient use of resources, process improvement, and minimizing losses. It has also become successful with the integration of next-generation information technologies such as machine learning, deep learning and AI to solve more complex problems. SI-based methods are commonly used in optimization problems. SI algorithms are often used in path planning processes.

Path planning involves determining the best route for an autonomous system from a starting point to one or more destination points. This process requires calculating the most efficient or safest route while taking into account factors such as environmental obstacles, system constraints, and objectives. SI algorithms can assist a group of autonomous entities, such as UAVs or autonomous vehicles, in coordinating their movements to find these routes.

While SI algorithms are used to ensure multiple autonomous systems work together simultaneously, path planning is used to ensure these autonomous systems move safely and effectively. When combined, SI algorithms and path planning can be applied in various fields, offering significant advantages. This approach is particularly beneficial in logistics, transportation, exploration, security, and more.

In their study, Akay and Karaboga (2012) introduced and applied a modified model of the ABC algorithm to effectively solve real parameter optimization problems. Lee et al. (2018) proposed the PSO algorithm for the target search task of a drone swarm. They demonstrated the practicality, accuracy, and robustness of their test simulation scenario. In Ekmen's study (2020), the task optimization of destroying a target with four drones was performed using ACO, PSO, and Krill Herd Optimization (KKO) algorithms. According to the research results, the objective function values for PSO, ACO, and KKO were 54.7, 73.83, and 69.41, respectively. Thus, the ranking of the best objective function value was PSO, KKO, and ACO. Saeed et al. (2022) obtained successful results in optimal road planning with 2D and 3D models of geographical environments with the ACO algorithm. They tried to optimize the ACO algorithm by measuring the estimated distances between the UAV and the obstacle to determine the new route during the flight. Especially in 2D environment, simulation results provided high efficiency.

The route planning and determination process is one of the most encountered problems in the task optimization process. Therefore, AI-supported search algorithms are often recommended (Giesbrecht, 2004). This problem needs to be handled with great care since it involves many static and dynamic factors such as distance, obstacles, error tolerance, and flight restrictions. Hoang et al. (2019) showed that by considering these factors and restructuring the PSO algorithm, the results of their application were more successful. In Wang et al.'s study (2023), the PSO algorithm was combined with the Enhanced SSA algorithm. In the application, they called PESSA method, under 10 basic functions, they achieved effective results in 3D route planning by comparing it with 12 other algorithms. In their TSP application, Wong et al. (2008) showed that the ABC algorithm outperformed GA, the Lin-Kernighan heuristic method, and other hybrid algorithms.

Method

In this study, swarm intelligence algorithms of the UAV swarm and ABC and PSO algorithms were used in path planning optimization. The task objective function of this path planning is to determine the best route and calculate the best distance. In this task, ten separate coordinate points and appropriate values for the parameters required for the algorithms to work were determined. The performances of the algorithms were compared by considering the objective function values obtained as a result of the application.

SI Algorithms

ABC Algorithm

This algorithm is a modelled approach inspired by the behavior of natural bee colonies during foraging in nature. Initially, the ABC algorithm was proposed as a SI approach to solve mathematical test function optimization problems using a unique neighborhood search mechanism (Choong et al., 2019). ABC is a computational process that starts by modelling a swarm of bees locating food sources in nature and communicating this to other swarm members. The model is a population-based algorithm in which the nectar quality, quantity and location of the source correspond to the optimum quality of the corresponding calculation.

In this algorithm, in the first step, the initial food source is determined. Bees start to move towards this food source, collecting information about the location of the food source, the amount of food available, and information about neighboring food sources, and then return to the hive. They then communicate the location and quantity of food to the other bees in the hive in a "dance" with a message. Each bee observes these dances and selects one of the food sources based on the information conveyed in the dances, then moves to that source. After selecting another neighboring source close to the food, they assess the amount of nectar. Food sources along the route are detected and replaced by other new locations discovered by the scout bees. At the end of this process, the best-found food source is recorded. The following Formula 1 is used to calculate the starting point of the foraging process of the bee swarm. In Formula 1, x_j^{min} and x_j^{max} are the initial values, in the mathematical model of the algorithm (Akay & Karaboga, 2012).

$$x_{ij} = x_j^{min} + rand(0,1) * (x_j^{max} - x_j^{min}) \quad (1)$$

$$v_{i,k} = x_{i,k} + \Phi_{i,k} * (x_{i,k} - x_{j,k}) \quad (2)$$

Each bee in the swarm produces a new position near its current position in Formula 2, where x_i is the initial position of the randomly selected bee and $\Phi_{i,k}$ is a randomly selected constant between (-1, 1). Then, the other bees evaluate the quantity information of nectar received from the scout bees and calculate the probability of nectar quantity according to Formula 3. Based on this calculation, they select a food source.

$$P_i = \frac{f_i}{\sum_j f_j} \quad (3)$$

At the end of each iteration, when a better source is calculated, the old source xi is discarded and replaced by this newly found food source. The scout bee then continues the calculation by discovering a new best food source with Formula 3 (Tsai et al., 2009; Akay & Karaboga, 2012).

PSO Algorithm

PSO is a method for optimizing nonlinear functions using particle swarm methodology (Kennedy & Eberhart, 1995). This method was put forward by observing that the movements of living creatures moving together for a purpose affect other individuals in the herd by communicating with other living creatures and the behaviors they determine in accordance with the purpose. PSO works to minimize a cost function. To model the swarm, each particle moves in a multidimensional space. In this algorithm, whose mathematical model for velocity and position calculations is given in Formulas 4 and 5, a particle is represented by the current position vector $x_n[t]$, the velocity vector $v_n[t]$, the desired position vector $x[t+1]$ and the next velocity vector $v_n[t+1]$. In the algorithm modelled with the help of these formulas, two vectors called the best local vector and the best global vector are calculated. The calculated size of these vectors depends on the size of the multidimensional space (Ekmen, 2020).

$$v_n\,[t+1] = wv_n[t] + c_1r_1(p(x) - x_n[t]) + c_2r_2(g(x) - x_n[t]) \tag{4}$$

$$x_n\,[t+1] = x_n[t] + v_n[t+1] \tag{5}$$

According to Formula 4, the velocity value of each particle is calculated for the next iteration (Hang et al., 2023). According to Formula 5, the positions of each particle are calculated for the next iteration. The main parameters of PSO are: size of the flock, number of iterations, acceleration coefficients and weight. In the process of each iteration, the new position of the particles in the swarm is tested with the objective function and its closeness to the solution is compared. The best state of the particle throughout the study is called 'pbest'. The position where the particles in the swarm are closest to the target throughout the study is called 'gbest'.

Scenario

It is assumed that the hardware and software characteristics of each UAV are the same. Variables such as inertia and torque values of the wing motors are added to the equation in the linear state space. It is assumed that the UAVs can communicate with each other within the swarm and are responsible for task distribution. Heuristic algorithms can give different results for each task definition and each re-route planning. The locations to be travelled in the algorithms may vary due to randomly selected parameter values. It is aimed to determine the shortest distance and optimum route starting from one unit and visiting other units once on the map formed by the units located at 10 coordinate points within the borders of the centre of Çorum province of Hitit University.

Coordinates of Academic Unit

The coordinate information of the names and addresses of the units of Hitit University located in Çorum Province are listed in Table 2. This information was obtained with Google Maps application.

Table 2. Coordinates of route points

Academic Units	Coordinates
Engineering Faculty (hitit_mf)	*(40.57044158989166, 34.982305542102566)*
Faculty of Theology (hitit_ilaf)	*(40.573342819527625, 34.984569326433615)*
Library (Hitit_lab)	*(40.57231599419518, 34.98657561872826)*
Rectorate (Hitit_rek)	*(40.57107726331548, 34.981071725847684)*
Faculty of Physical Education (hitit_besyo)	*(40.5688429641854, 34.98226248064795)*
Faculty of Arts and Sciences (hitit_fef)	*(40.56716352736973, 34.93347075523586)*
Hitit Research Laboratory (hitit_hb)	*(40.56845918300877, 34.9783109149586)*
Vocational School (hitit_myo)	*(40.55712101254516, 34.96893615751559)*
Health Sciences Faculty (hitit_sbf)	*(40.557292474174446, 34.9711289843594)*
Economics and Administrative Sciences (hitit_iibf)	*(40.53135121021779, 34.89877101655175)*

Hitit University units are marked on Google Maps and a sample route is shown in Figure 2. While these distances are measured in 10 meters within the campus, they reach kilometers with the addition of Hitit Fef and Hitit IIBF points. When these points are combined to form a route, its circumference is calculated as 18.81 km and its area is calculated as 12.15 km^2.

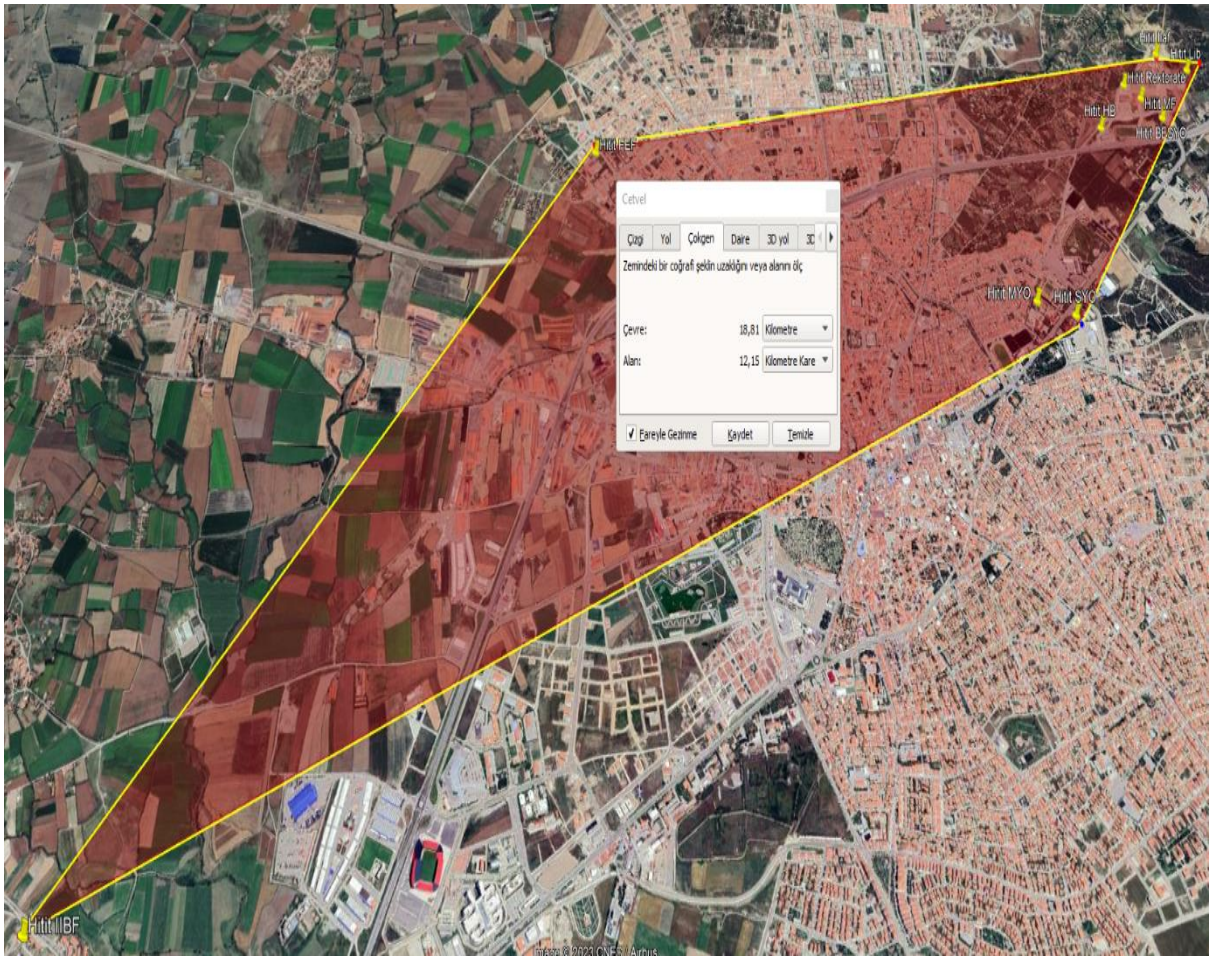

Figure 2. Representation of units on the map

Computational Parameters for the Algorithms

The computational parameters required for both algorithms are presented in Table 3. These values are set as standard and can be redefined according to criteria such as the number of elements in the swarm, UAV technical specifications, target distance and jump point.

Table 3. Parameters for the algorithms

Parameters for the ABC algorithm	Parameters for the PSO algorithm
number_of_bees = 100 # Swarm population	number_of_particles = 100 # Swarm population
n_iterations = 100 # Number of iterations	n_iterations = 100 # Number of iterations
flight_time = 40 # minutes	c1 = 0.5 # Personal best position weight
average_speed = 40 # km/h	c2 = 0.5 # Global best position weight
number_of_uavs = 20 # UAV population	w = 0.7 # Inertia weight
hop_node = 10 # Number of unit	hop_node = 10 # Number of unit

These parameters, coordinates of the units and mathematical models of the algorithms were taken from the scenario created within the scope of the application and coded in Python programming language. The codes are presented as computer algorithms in Algorithm 1 and Algorithm 2.

Python Pseudo Codes of the Scenario

Algorithm_1 shows the code steps that iteratively calculate the best path and distance within the scope of the application scenario with the ABC algorithm. The most important stage in this code is the stage where the ABC algorithm is applied in the light of the parameters.

Algorithm_1. Pseudo code of the ABC optimization algorithm.

1. Import necessary libraries:
   random, math and matplotlib libraries
2. Coordinates of academic units
   academic_units = {
   'hitit_mf': (34.982305542102566, 40.57044158989166),…
   }
3. Parameters for the ABC Algortihm:
   number_of_uavs, flight_time, average_speed, number_of_bees, num_of_iterations…
4. Calculate_distance
   def calculate_distance(…, …):
   x1, y1 = academic_units[…]
   x2, y2 = academic_units[…]
   return …
5. Calculate_total_distance.
   def calculate_total_distance(route, academic_units):
   total_distance = 0
   for i in range(len(route) - 1):
   total_distance += calculate_distance(route[i], route[i + 1])
   return total_distance.
6. Iteration for best_distace and best_route
   for _ in range(number_of_bees):
   bees_route
   route = list(academic_units.keys())
   random.shuffle(route)
   total_distance = calculate_total_distance(route, academic_units)
   bees_route.append((route, total_distance))
7. Sort bee tours by distance:
   bees_route.sort(key=lambda x: x[1])
8. Run the ABC algorithm
9. Print the best route and total distance
10. Display the plot using plt.show().
    Plot the route
    Plot academic units and the best route
    Plot the best distance/iteration graph

The pseudo code of the ABC optimisation of the scenario is shown in Algorithm_1. The algorithm is generally grouped in 10 stages. These stages, importing Python libraries, defining parameters. Calculating the distances, optimizing the result, implementing the ABC algorithm and displaying the outputs.

Algorithm_2. Pseudo code of the PSO optimization algorithm.

1. Import necessary libraries:
   random, numpy, math and matplotlib libraries
2. Coordinates of academic units
   academic_units = {
   'hitit_mf': (34.982305542102566, 40.57044158989166),…
   }
3. Parameters for the PSO Algortihm:
   number_of_uavs, flight_time, average_speed, number_of_particles, inertia_weight, p_best_position_weight, g_best_positions_weight, num_of_iterations…
4. Calculate distance
   total_distance = 0
   len(route) - 1):
   coord1 = coordinates[route[i]]
   coord2 = coordinates[route[i + 1]]
   distance = calculate_distance(particle, coordinates)
   total_distance += distance
   return total_distance
5. Calculate total distance.
   def calculate_total_distance(route, academic_units):
   total_distance = 0
   for i in range(len(route) - 1):
   total_distance += calculate_distance(route[i], route[i + 1])
   return total_distance.
6. Iteration for best_distace and best_route

normalized_distance = (global_best_distance - min_distance) / (max_distance - min_distance)
if global_best_distance < min_distance:
min_distance = global_best_distance
if global_best_distance > max_distance:
max_distance = global_best_distance

7. Sort particles tours by distance:
8. PSO initialization
   for iteration in range(n_iterations):
   for i in range(len(particles)):
   particle, distance = particles[i] …
9. Print the best route and total distance
10. Display the plot using plt.show().
    Plot the route
    Plot academic units and the best route
    Plot the best distance/iteration graph

The pseudo code of the PSO optimisation of the scenario is shown in Algorithm_2. The algorithm is generally grouped in 10 stages. These stages, importing Python libraries, Defining parameters. Calculating the distances, optimizing the result, implementing the PSO algorithm and displaying the outputs.

Results and Discussion

Firstly, in implementation, the positions of the UAV at the take-off point are created. The parameter values used in the PSO algorithm are; w=0.7 (usually chosen close to 1.), c_1=0.5 (a random value between 0 and 1), c_2=0.5 (a random value between 0 and 1). According to the ABC algorithm, the locations of the best nectar sources are initially randomized. The UAV check the nectar quantities of other UAVs and calculate which location they should go to for the next iteration. The proximity of each UAV to the target is determined according to the calculated new position objective function and it is decided whether it is suitable or not. This loop continues within itself until the determined iteration value. x_j^{min} (minimum value of initial coordinate) x_j^{max} (maximum value of initial coordinate).

```
---
ABC Alg_Best Route: ['hitit_hb', 'hitit_besyo', 'hitit_lib', 'hitit_ilaf', 'hitit_mf', 'hitit_rek', 'hitit_sbf', 'hitit_myo', 'hitit_fef', 'hitit_iibf']
ABC Alg_Best Total Distance: 0.12306030903721393 km
---
---
PSO Alg_Best Route: ['hitit_fef', 'hitit_iibf', 'hitit_myo', 'hitit_sbf', 'hitit_lib', 'hitit_mf', 'hitit_rek', 'hitit_hb', 'hitit_besyo', 'hitit_ilaf']
PSO Alg_Best Total Distance: 0.16771797460188603 km
---
```

Figure 3. Best route information and distance values of ABC and PSO algorithms

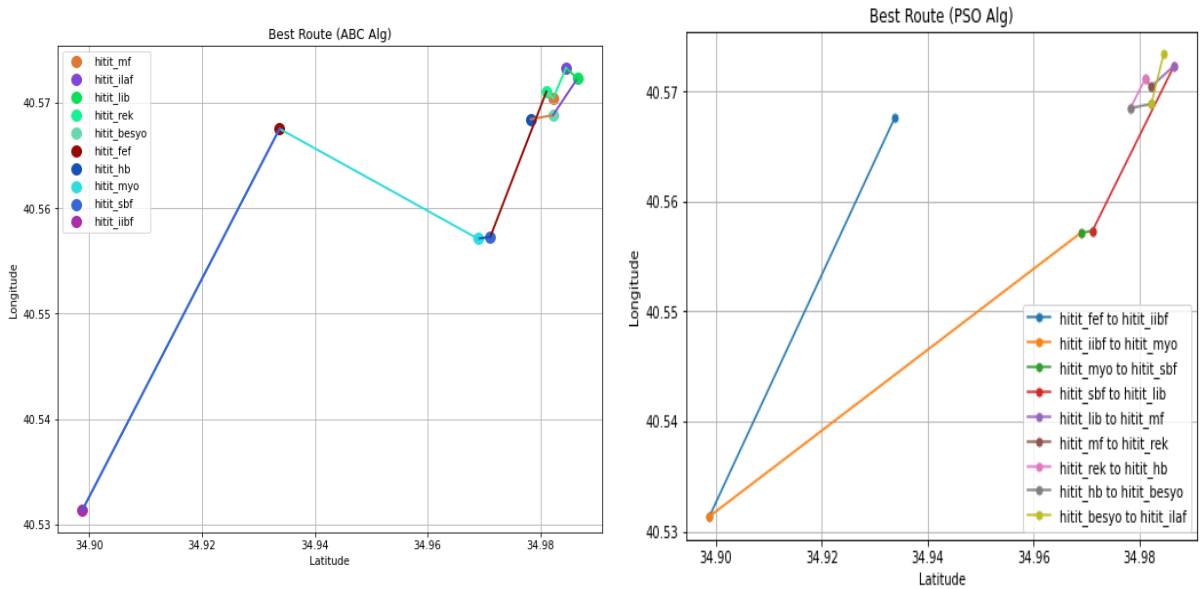

Figure 4. Best routes of ABC and PSO algorithms in route determination

When the Python codes were run, the results in Figure 3 were obtained. The best route estimation of the ABC algorithm started from Hitit Hubtuam (hitit_hb) and ended at Hitit Faculty of Economics and Administrative

Sciences (hitit_iibf). While the "Best Route Distance" value of the ABC algorithm was 0.123 km, the "Best Route Distance" value of the PSO algorithm was calculated as 0.167 km. The best route estimation of the PSO algorithm started from Hitit Faculty of Science and Literature (hitit_fef) and ended at Hitit Faculty of Theology (hitit_ilaf). These result values are the best values obtained at the end of the calculation by optimizing with the optimum number of iterations. The best path graph of the two algorithms calculated after each iteration is shown in Figure 4 and the best distance graph is shown in Figure 5.

Within the scope of task optimization and objective function, Figure 4 shows the best route determination of ABC and PSO algorithms. In this route determination process, the algorithms make calculations with the parameters given to them and determine this route by making a decision. Since the start and end points of the two algorithms are different, it is understood that they determine different routes.

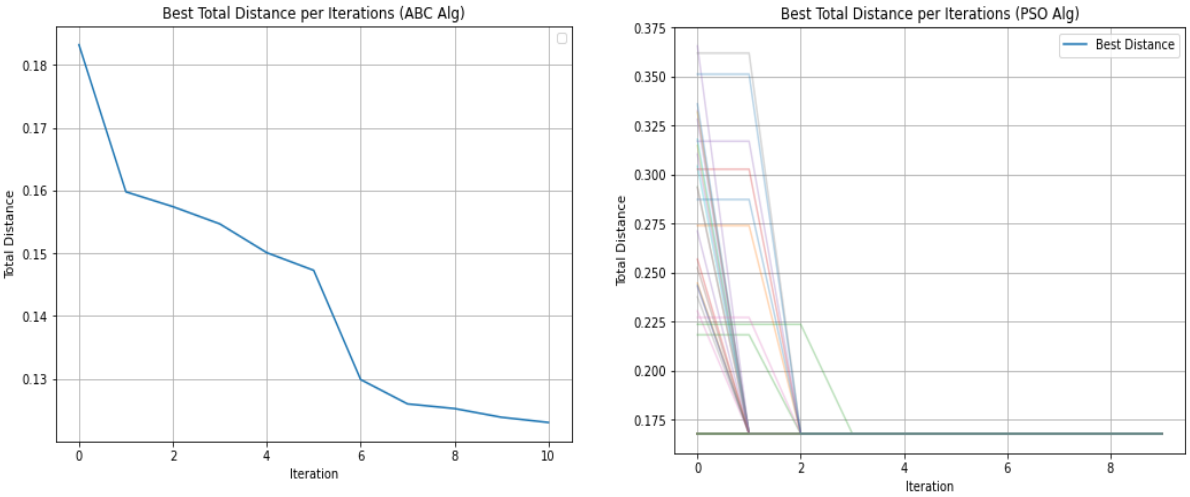

Figure 5. Best distance values with Iteration of ABC and PSO algorithms

The minimum distance calculation, which is the most important objective function of the task optimization, is shown in Figure 5. Both algorithms stabilized and calculated the distance after different iterations. Accordingly, the ABC algorithm determined the best distance as 0.123 km as a result of the 10th iteration. On the other hand, the PSO algorithm stabilized after the 3rd iteration and calculated the best distance as 0.167 km. It should be noted that these measurement values of the algorithms depend on the route determination, the swarm structure, the number of points and the distances between the units.

Conclusion

In this study, the objective functions of ABC and PSO algorithms, which are among the widely used SI algorithms for task optimization of UAV swarms, were calculated in a scenario developed over 10 different points. In the calculation of the best distance, which is one of the two important outputs of this scenario, the ABC algorithm produced approximately 25% more successful values than the PSO algorithm. In the determination of the optimal route, which is the other important output, the two algorithms determined different starting points. This difference is due to the parametric structures of the algorithms. In order to improve these values, both algorithms were subjected to iteration. As a result of different iterations, both algorithms became stable. This kind of research can be carried out with other swarm intelligence algorithms to reveal the similarities and differences between them. In addition, application results can be presented in a comparative manner to determine the most appropriate algorithm.

AI algorithms have become an important development tool for autonomous systems. In order for this tool to be used correctly and to provide successful results, it depends on the correct selection of the application-based algorithm, conditions and effective parameters. In addition, it should not be forgotten that constraints such as energy consumption, time, speed and information processing capacity, which are important for autonomous vehicles, should be included in the processes. In future studies, it is thought that new generation technologies such as blockchain will be effective in eliminating the constraints that prevent task optimization in UAV swarms.

Scientific Ethics Declaration

The author declares that the scientific ethical and legal responsibility of this article published in EPSTEM journal belongs to the author.

Acknowledgements or Notes

* This article is an updated and extended version of the abstract presented orally at the International Conference on Technology, Engineering and Science (www.icontes.net) held in Antalya/Turkey on November 16-19, 2023.

References

Akay, B., & Karaboga, D., (2012). A modified artificial bee colony algorithm for real-parameter optimization. *Information Sciences*, *192*, 120-142.

Asaamoning, G., Mendes P., Rosário, D., & Cerqueira, E. (2021). Drone swarms as networked control systems by integration of networking and computing. *Sensors*, *21*(8), 2642.

Bhagade, A. S., & Puranik, P. V. (2012). Artificial bee colony (abc) algorithm for vehicle routing optimization problem. *International Journal of Soft Computing and Engineering*, *2*(2), 329-333.

Chakraborty A., & Kar, A. K. (2017). Swarm intelligence: A review of algorithms. In *Nature-Inspired Computing and Optimization: Theory and Applications* (pp. 475-494). Cham, Germany: Springer.

Choong, S. S., Wong, L. P., & Lim, C. P. (2019). An artificial bee colony algorithm with a modified choice function for the traveling salesman problem. *Swarm and Evolutionary Computation*, *44*, 622-635.

Cosar, M., & Kiran, H. E. (2021). Verification of localization via blockchain technology on unmanned aerial vehicle Swarm. *Computing and Informatics*, *40*(2), 428–445.

Cosar, M. (2022). Cyber attacks on unmanned aerial vehicles and cyber security measures. *The Eurasia Proceedings of Science, Technology, Engineering & Mathematics (EPSTEM)*, *21*, 258-265.

Ekmen, M. I. (2020). Drone surusu ile hedef takip ve optmizasyonu. (Unpublised master's thesis) Konya Teknik University, Konya, Turkey.

Giesbrecht, J. (2004). *Global path planning for unmanned ground vehicles. Technical memorandum*, Defence Research and Development (DRDC) Suffield. Canada. Retrieved from https://apps.dtic.mil/sti/pdfs

Gupta, L., Jain, R., & Vaszkun, G. (2015). Survey of important issues in UAV communication networks. *IEEE Communications Surveys & Tutorials*, *18*(2).

Hoang, V.T., Phung, M. D., Dinh, T. H., Zhu, Q., & Ha, Q. P. (2019). Reconfigurable multi-UAV formation using angle-encoded PSO. *2019 IEEE 15th International Conference on Automation Science and Engineering (CASE)*, 1670-1675. Vancouver, BC, Canada.

Idoko, G. O. (2023). Drive path optimization for electric vehicles using particle swarm optimization. *13th International Symposium on Advanced Topics in Electrical Engineering (ATEE)*, 1-6, Bucharest, Romania.

Kennedy, J., & Eberhart, R. (1995). Particle swarm optimization. Proceedings of *ICNN'95 - International Conference on Neural Networks*, *4*, 1942-1948, Perth, WA, Australia.

Lee, K.B., Kim, Y. J., & Hong, Y.D. (2018). Real-time swarm search method for real-world quadcopter drones. *Applied Sciences*, *8*(7), 1169.

Puente Castro, A., Rivero, D., Pazos, A., & Fernandez Blanco, E. (2022). A review of artificial intelligence applied to path planning in UAV swarms. *Neural Computing and Applications*, *34*, 153-170.

Rath, M., Darwish, A., Pati, B., Pattanayak, B. K., & Panigrahi, C. R. (2020). Swarm intelligence as a solution for technological problems associated with internet of things. In *Swarm Intelligence for Resource Management in Internet of Thing* (pp. 21-45). Academic Press.

Saeed, R.A., Omri, M., Abdel-Khalek, S., Sayed, M., & Alotaibi, M.F. (2022). Optimal path planning for drones based on swarm intelligence algorithm. *Neural Computing and Applications*, *34*(12), 10133-10155.

Tang, J., Liu, G., & Pan, Q. (2021). A review on representative swarm intelligence algorithms for solving optimization problems: Applications and trends. *IEEE/CAA Journal of Automatica Sinica*, *8*(10), 1627-1643.

Tsai, P. W., Pan, J. S., Liao, B. Y., & Chu, S. C. (2009). Enhanced artificial bee colony optimization. International *Journal of Innovative Computing, Information and Control*, *5*(12), 5081-5092.

Wang, Z., Sun, G., Zhou, K., & Zhu, L. (2023). A parallel particle swarm optimization and enhanced sparrow search algorithm for unmanned aerial vehicle path planning. *Heliyon*, *9*(4).

Wong, L.P., Low, M.Y.H., & Chong, C.S. (2008). A bee colony optimization algorithm for traveling Salesman problem. *Second Asia International Conference on Modelling & Simulation (AMS*), 818-823. Kuala Lumpur, Malaysia.

Zhang, D., & Duan, H. (2018). Social-class pigeon-inspired optimization and time stamp segmentation for multi-UAV cooperative Path Planning. *Neurocomputing*, *313*,229-246.

Zhang, Y., Agarwal, P., Bhatnagar, V., Balochian, S., & Yan, J. (2013). Swarm intelligence and its applications. *The Scientific World Journal*, 3.

Author Information

Mustafa Cosar
Department of Computer Engineering, Hitit University
19030, Corum/Turkiye
Contact e-mail: *mustafacosar@gmail.com*

To cite this article:

Cosar, M. (2023). Path planning via swarm intelligence algorithms in unmanned aerial vehicle population. *The Eurasia Proceedings of Science, Technology, Engineering & Mathematics (EPSTEM), 26*, 439-450.

The Eurasia Proceedings of Science, Technology, Engineering & Mathematics (EPSTEM)
ISSN: 2602-3199

The Eurasia Proceedings of Science, Technology, Engineering & Mathematics (EPSTEM), 2023

Volume 26, Pages 451-457

IConTES 2023: International Conference on Technology, Engineering and Science

Generating and Evaluating City Building Facades Using Artificial Intelligence

Susa Dimitrova
University of Architecture

Abstract: The present study examines the various methods involved in the generation of city building facades. Elements of the entire process are explored – from obtaining the necessary information to using it to create a harmonious urban environment. The methods considered – the recognition and generation of facade elements, the generation of as-built Building Information Model (BIM) and Digital Twins of buildings (DT) – are evaluated against the needs of the generation, as well as what their place is in the foreseeable future development of architecture in the metaverse. The purpose of the study is to present the best practices in the field depending on the needs of the model and to show their practical application. An example is given of using drone imagery to assess the predominant coloration of facades with a view to generating examples harmonious with surrounding buildings. The example uses the scripting language python and different libraries to evaluate the image information and presents the results as a figure displaying the three predominant colors of the given image.

Keywords: Architecture, Artificial, Building, Facade, Metaverse

Introduction

The methods of implementation of artificial intelligence (AI) in architecture are increasing day by day with the development of these technologies – from the generation of floorplans (Inceoğlu et al., 2020; Rahbar et al., 2019), through generative volumetric-spatial models (As et al., 2018; Castro Pena et al., 2021), automation of the technical workflow (Daele et al., 2021). This paper concentrates on the application of AI in a narrower but potentially very important area of architectural models, namely the architectural building facade. Methods for generating facades from an existing model/drawing, as well as those for retrieving information from existing buildings, will be considered. The benefits of these methodologies are related to the processes that the architecture goes through to reach from CAD two-dimensional drawings, through a BIM model, to the creation of DT of buildings. In the research each of the already mentioned methods is going to be concerned as to establish and evaluate its advantages or disadvantages.

Study

There are four main sections in the study which allow to specify the examines. Beginning with the methods concerning facade generation in the early design stages, the study then pays attention on the recognition of particular elements on the facades. Continuing with the generation of facade elements as the third section of this very study, it is also essential to put a stress on the generation of as-built BIM and DT.

Facade Design

The generation of architectural design using the means of the computer software has taken over many of the young specialists in the field of architecture. The possibilities of creating many different options for design in as

little time and more complex forms are the main advantages of this approach. The potential of the software design possibilities could be seen as early as year 1991 (Roller, 1991). An example can be shown in the Grasshopper 3D environment with an experiment on different types of algorithmic approach. The parametric set of constraints of that time (using distance parameters for example) is replaced with an evolutionary optimization one (as BioMorpher generative design plug-in) in the present day. (Figure1)

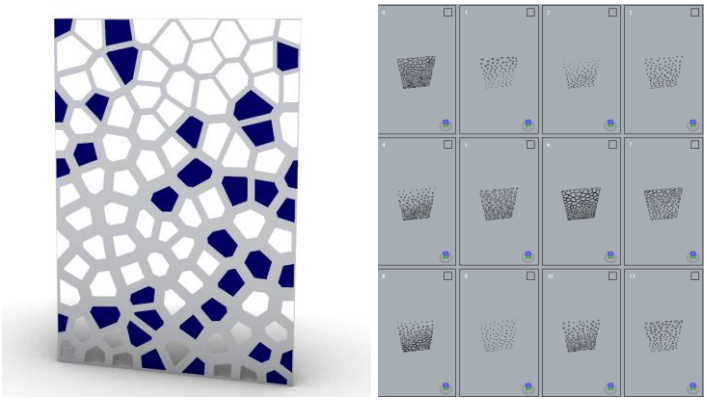

Figure 1. Facade conceptual design

The process, though, should be considered as part of the building design (Wang et al., 2022) – the connection between the building volume, style and other design characteristics is too close. In the early stages of the design is possible to integrate Machine Learning solutions for facade optimization such as solar radiation (El-Mowafy et al., 2022) and other energy simulations (Sebestyen & Tyc, 2020). However, the main goal is to connect all these methodologies in the context of the metaverse – the creation of DT of the buildings. This is possible through simulations already at the design level with smart buildings in mind and setting these goals in the design (Almusaed & Yitmen, 2023).

Facade Elements Recognition

There are many methods for facade recognition, depending on the needs of the specialist. Material recognition can help the possible reuse of the facade elements, pattern recognition can help the design of similar facades and the information gathered from the facades can be of use in the implementation of augmented reality tools.

The main elements of the facade used in these recognitions are the openings – windows, doors, empty openings as arcs etc. The second group of elements are the plinth and the cornice – the main elements which frame the facade at the bottom and the top. Using them, the main proportions of the facade are depicted and also with the pattern of the openings create a proportional mesh, which is unique for almost every city building facade. The third group of the elements which can be easily automated as recognition element are the alternating design elements.

The image recognition is very useful in the creation of city facades in multiple aspects. On one hand, after recognizing the surrounding urban environment one can design a corresponding building with harmonic volume and facades and on the other – a huge database can be created and used for multiple design tasks as combining different city designs and exploring many possible variations in as little time as allowed by the technology, for example.

The main means for this recognition are the use of Convolutional neural networks (CNNs) and Generative Adversarial Networks (GANs). This doesn't exclude the use of other methods, the use of machine learning, etc. A good example is the use of Markov chain Monte Carlo (MCMC) and its implementation in the window recognition (Tyleček & Šára, 2011).

The use of AI, however, has a promising future in the aspect of speed and accuracy. CNNs, for example, are recognized as a good method for multiple object recognition with relatively high efficiency and precision. (Figure2) They consist of three main types of layers – Convolutional layer, Pooling layer and Fully-connected (FC) layer. Each of these layers has its unique function contributing to the high functionality of the network. Namely, the main layer is the convolutional layer, which works as the feature detector which creates a map of characteristics which are then down sampled in the pooling layer and the FC layer then creates a classification

of the searched characteristics in the input of the CNN. That makes the CNNs easily recognizable as method and open to precision (Deng et al., 2023).

The other main NNs for image recognition are the GANs. (Figure2) These neural networks combine the basic CNN structure with logic based on so-called generator and discriminator algorithms which serve the following roles – the generator generates an image which is then used as an input along with a real-world example of the same image and the discriminator classifies the images as real or fake. The process continues until the generated image cannot be distinguished from a real one. The GANs are gaining more and more popularity due to their good results in the field. Their main advantage is the ability to "self-correct", which is why they generate similar to real data. Accordingly, they can, referring to real data, generate images indistinguishable from them. They combine well both image recognition and image generation and are becoming more and more sophisticated in the latter.

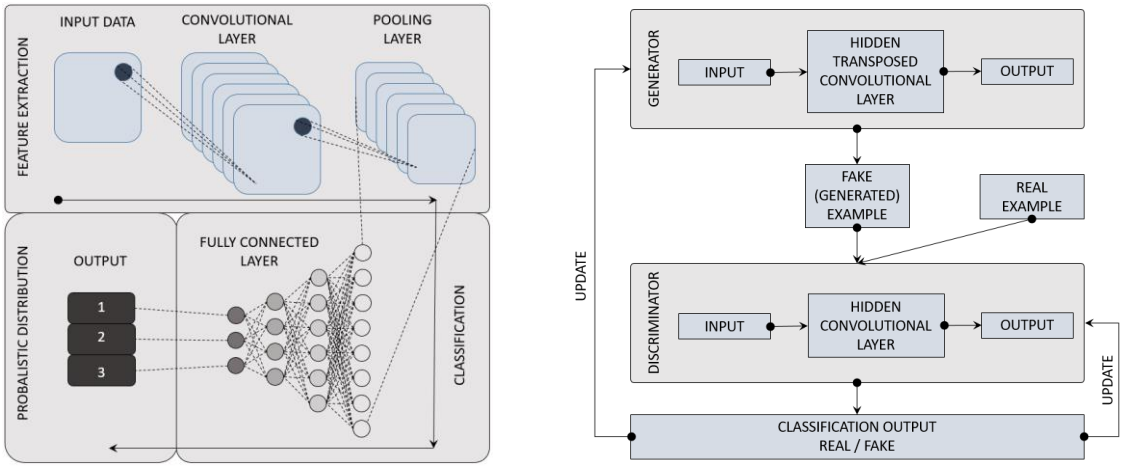

Figure 2. CNN architecture (left) and GANs workflow (right)

Facade Elements Generation

The generation of facade elements is very useful tool based on the NNs discussed in part B. In the given example (Figure3) a conditional GAN is being used. (*Image-to-Image Demo - Affine Layer*, n.d.) This pix2pix software generates an undistinguishable from real images based on an input from the user. The facade is created using modular input. The modules are represented as colorful fields in which the different color represents a different facade element. The output is not always a full image and has many disadvantages. Generating images in a certain architectural style, for example, as well as using a certain element design would be a field for future development, but could be achieved with a significantly larger input database for the neural network. However, this software example shows the base this NNs lay and the rich opportunities for development in the field. With the upgrade of this methods they can be used in the architectural profession, as well in other fields and also in the technical support of the urban environment (Zhang et al., 2022).

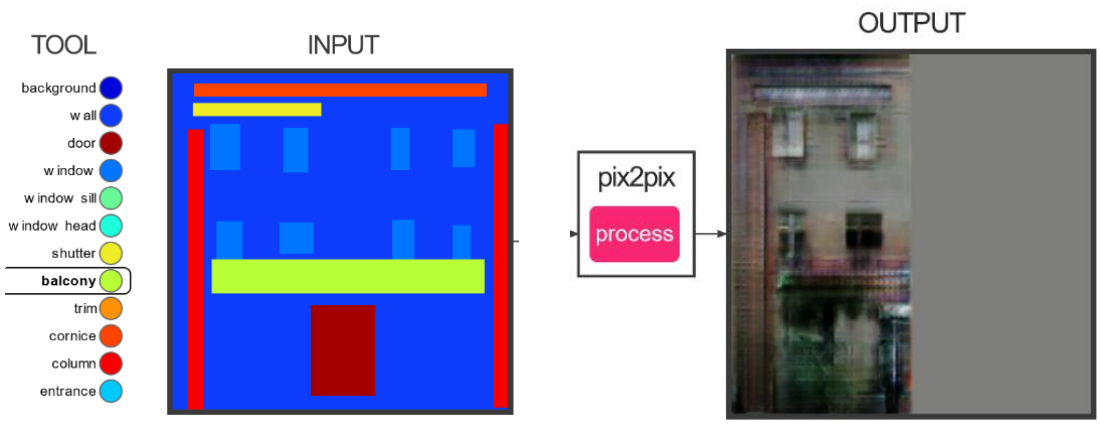

Figure 3. Facade creation based on elements

As-built BIM

The building information modelling (BIM) is developing at a rapid pace. This organization of the construction process supports both cost reduction during the design and construction of the buildings, as well as their long-term maintenance. It is far easier to create such an organization along with designing new buildings than for existing ones. This makes any technology aiding the process concerning the existing building stock very valuable. Such are the technologies that create as-built BIM based on laser scanning of the buildings.

The generation of an as-built BIM has many advantages. It can accompany the preservation of immovable cultural heritage (Jiang et al., 2022), can optimize the consumption of existing buildings and can be used as a basis for reconstruction and bonding with newly constructed buildings or parts of them. The information needed for the generation of a model like that can be used at the same time to detect particular details as facade materials, for example.

The models are created based on photogrammetry using laser and image databases collected from the existing buildings. The technology used creates point clouds which then can be imported into a BIM software (ArchiCAD or Revit, for example) and used to model a digital copy of the building. This method of digitalization of the buildings and their parameters is not yet fully developed so there is a good opportunity for new technological approaches – as the design of a parametric facade template which can be modified based on the collected data from the scans (Dore & Murphy, 2014).

As well as as-designed BIM, the as-built BIM can be used for the creation of DT of the buildings. The creation of DT is an important part of the information field linking the existing and future building stock through the internet of things (IoT). This technology allows the use of sensors monitoring various building parameters in real time and their digitization on a model of the building. Thanks to this, important decisions can be made in a short time and foresee future changes and timely overcoming of deepening problems invisible to the naked eye. This is important both for convenience and for optimizing building maintenance costs. Also, using the IoT, a stable connection between real buildings and the metaverse can be created. (Figure4)

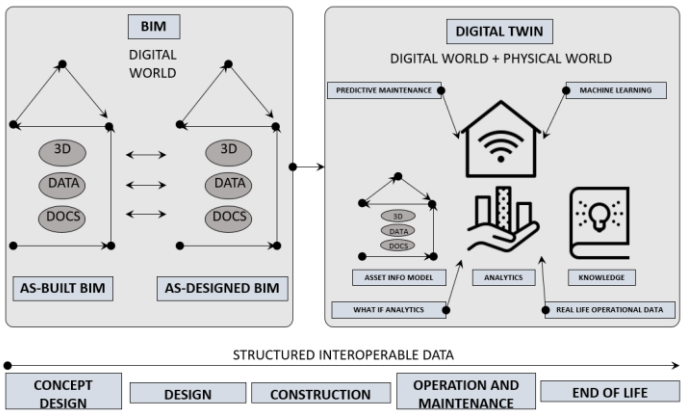

Figure 4. DT of buildings

The main advantage of this methodology and the full usage of the contemporary technologies is the use of structured data which allows the use of its full potential and its easy processing depending on the current needs.

Implementation

The design, recognition and model generation of building facades can be used in all levels of urban development. It can be a part of the foreseeable future processes regarding a block or a city as well as the optimization of the existing stock. The facade is the building element that determines the basic vision of the buildings and their perception by passers-by, which defines it as the main element in the construction of the architectural vision of the spaces. Modern technologies allow all kinds of problems that have arisen in the past, as well as should arise in the future, to be solved on a digital level.

One of these problems is the evaluation of the main colors on the facade. A study is made using image processing techniques. The following steps have been conducted:

1) High resolution drone photos of city facades have been captured. Main attention is paid to the uniform distribution of illumination on the facades in order to reflect correct color information. (Figure5)

Figure 5. Facade image example

2) The drone photos have been loaded into a programming environment (Python) with image processing library (OpenCV). The used libraries have been cv2, numpy, matplotlib.pyplot, os and KMeans from Scikit-Learn.
3) A region of interest (ROI) – specific sections of the facade or the whole building – can be defined. The ROI in the example is defined as the image.
4) The ROIs can be converted from RGB (red, green, blue) color space to HSV (hue, saturation, value), which separates color information (hue) from intensity (value) and saturation. In the example a RGB conversion has been used. A function to perform color analysis on a single image has been defined, which converts color information and reshapes the image into a list of RGB pixels.
5) Color histograms are calculated to represent the frequency of each color in the image. The histograms can be analyzed to obtain various statistics – dominant colors (the one used in the example), color distribution, color proportions, color trends. In the same function K-Means has been applied to identify dominant colors. The n_init parameter (the number of times the k-means algorithm is run with different centroid seeds) (*Sklearn.Cluster.KMeans*, n.d.).
6) The defined function is used for the processing of a single image. Therefore, a specific directory has been chosen and all images in the directory have been listed. A list has been initialized to store the results from the function used on these images. Each image has been analyzed.
7) The color information has been visualized for all of the images (Figure6).

Figure 6. Results visualization – dominant colors

Conclusion

The usage of AI in the field of architecture is rising and so is it in the field of city building facades. Facade generation methods contribute to the development of the architectural profession and the changing demands on

architects today. With the introduction of technologies, it is increasingly necessary for every specialist to be well-versed in the possibilities of AI and to make the most of the opportunities it provides. Each methodology has its advantages and disadvantages and, knowing them in greater detail, specialists will be able to develop together with the technologies, as well as create continuity between their environment and the metaverse.

Scientific Ethics Declaration

The author declares that the scientific ethical and legal responsibility of this article published in EPSTEM journal belongs to the author.

Acknowledgements

* This article was presented as an oral presentation at the International Conference on Technology, Engineering and Science (www.icontes.net) held in Antalya/Turkey on November 16-19, 2023.

* This article is conducted under the grant of the national program "Young scientists and postdoctoral students" 2022-2023, Ministry of Education and Science, Bulgaria.

References

Almusaed, A., & Yitmen, I. (2023). Architectural reply for smart building design concepts based on artificial intelligence simulation models and digital twins. *Sustainability*, *15*(6), 6, 4955.

As, I., Pal, S., & Basu, P. (2018). Artificial intelligence in architecture: Generating conceptual design via deep learning. *International Journal of Architectural Computing*, *16*(4), 306–327.

Castro Pena, M. L., Carballal, A., Rodríguez-Fernández, N., Santos, I., & Romero, J. (2021). Artificial intelligence applied to conceptual design. A review of its use in architecture. *Automation in Construction*, *124*, 103550.

Daele, D. V., Decleyre, N., Dubois, H., & Meert, W. (2021). An automated engineering assistant: Learning parsers for technical drawings. *Proceedings of the AAAI Conference on Artificial Intelligence*, *35*(17), 17.

Deng, Y., Xie, X., & Xing, C. (2023). CNN-based architecture recognition and contour standardization based on aerial images. *Neural Computing and Applications*, *35*(3), 2119–2127.

Dore, C., & Murphy, M. (2014). Semi-automatic generation of as-built BIM façade geometry from laser and image data. *Journal of Information Technology in Construction ITCON*, *19*, 20–46.

El-Mowafy, B. N., Elmokadem, A. A., & Waseef, A. A. (2022). Evaluating adaptive facade performance in early building design stage: An Integrated daylighting simulation and machine learning. In A. E. Hassanien, R. Y. Rizk, V. Snášel, & R. F. Abdel-Kader (Eds.), *The 8th International Conference on Advanced Machine Learning and Technologies and Applications (AMLTA2022)* (pp. 211–223). Springer International Publishing.

Image-to-Image Demo—Affine Layer. (n.d.). Retrieved from https://affinelayer.com/pixsrv/

Inceoglu, A., Uzun, C., & Colakoglu, M. B. (2020). GAN as a generative architectural plan layout tool: A case study for training DCGAN with Palladian Plans and evaluation of DCGAN outputs. *A|Z ITU Journal Of The Faculty Of Architecture*, *17*(2), 2. 185-198

Jiang, Y., Han, S., & Bai, Y. (2022). Scan4facade: Automated as-is facade modeling of historic high-rise buildings using drones and AI. *Journal of Architectural Engineering*, *28*(4). 04022031.

Rahbar, M., Mahdavinejad, M., Bemanian, M., Davaie Markazi, A. H., & Hovestadt, L. (2019). Generating synthetic space allocation probability layouts based on trained conditional-GANs. *Applied Artificial Intelligence*, *33*(8), 689–705.

Roller, D. (1991). An approach to computer-aided parametric. *Computer-Aided Design*, *23*(5), 385–391.

Sebestyen, A., & Tyc, J. (2020). *Machine learning methods in energy simulations for architects and designers—The implementation of supervised machine learning in the context of the computational design process*.

Sklearn.cluster.KMeans. (n.d.). Scikit-Learn. Retrieved from https://scikit-learn/stable/modules/generated/sklearn.cluster.

Tyleček, R., & Šára, R. (2011). A weak structure model for regular pattern recognition applied to facade images. In R. Kimmel, R. Klette, & A. Sugimoto (Eds.), *Computer vision – ACCV 2010* (pp. 450–463). Springer.

Wang, L., Zhang, H., Liu, X., & Ji, G. (2022). Exploring the synergy of building massing and façade design through evolutionary optimization. *Frontiers of Architectural Research*, *11*(4), 761-780.

Zhang, G., Pan, Y., & Zhang, L. (2022). Deep learning for detecting building façade elements from images considering prior knowledge. *Automation in Construction*, *133*. 104016.

Author Information

Susa Dimitrova
University of Architecture, Civil Engineering and Geodesy
(UACEG)
1 Hristo Smirnenski Blvd., 1164 Sofia, Bulgaria
Contact e-mail: *sdimitrova_far@uacg.bg*

To cite this article:

Dimitrova, S. (2023). Generating and evaluating city building facades using artificial intelligence. *The Eurasia Proceedings of Science, Technology, Engineering & Mathematics (EPSTEM), 26*, 451-457.

The Eurasia Proceedings of Science, Technology, Engineering & Mathematics (EPSTEM)
ISSN: 2602-3199

The Eurasia Proceedings of Science, Technology, Engineering & Mathematics (EPSTEM), 2023

Volume 26, Pages 458-461

IConTES 2023: International Conference on Technology, Engineering and Science

Numerical Study of the Mechanical Behavior of a Composite Material Plate

Abdelkader Kirad
Saad Dahlab University of Blida 1

Bassam Gamal Nasser Muthanna
Saad Dahlab University of Blida 1

Fateh Madani
Saad Dahlab University of Blida 1

Loukmane Zeddam
Saad Dahlab University of Blida 1

Abstract: Composite materials are playing an increasingly significant role in the field of mechanics, such as aeronautics, aerospace, ships, and modern cars. The objective of this work was to investigate the mechanical properties and behavior of a composite plate (carbon/epoxy) through various tests, including tension, compression, and bending, using numerical analysis. Additionally, static analysis of mechanical behavior was performed, as well as the natural vibration of undamped structures. This analysis aimed to determine stresses, displacements, natural frequencies, and modes of free vibration. The obtained results illustrated that the composite material has a significant impact on improving the quality of mechanical properties and increasing the lifetime of materials, making it a valuable option for design and repair techniques. Furthermore, the results obtained in this work align well with previous literature studies. By examining these parameters, this study aimed to enhance our understanding of how composite materials perform under different mechanical loads and dynamic conditions, thus contributing valuable data to advance the field of composite mechanics.

Keywords: Composite material, Vibration, Stress, Fiber, Mechanical tests.

Introduction

In response to the consistently high demands in the industrial sector, particularly in the areas of safety and energy consumption control, major aircraft manufacturers have been driven to develop lightweight structures that exhibit enhanced mechanical strength and rigidity. Composite materials, with their remarkable mechanical properties, low weight, chemical resistance, superior fatigue resistance, and adaptability in shaping, emerge as the optimal solution in the industrial landscape. These composite materials find wide-ranging applications across various industrial sectors, prominently in the construction of both civil and military aircraft. They are engineered through the fusion of two or more materials characterized by distinct appearances and compositions. This harmonious amalgamation of diverse components yields a product distinguished by specific high-performance properties and unique characteristics.

Composites offer the advantage of creating lightweight components with attributes like corrosion resistance and effective thermal and electrical insulation. However, composite materials are susceptible to specific dynamic forces, notably impact forces encountered during both service and operation. Unlike metallic materials, defects

resulting from these forces may remain partially hidden. Thus, the development of non-destructive methods for detecting these defects is of paramount importance.

One of the foremost challenges in the use of composite materials lies in the measurement of mechanical properties, including elastic moduli and ultimate strengths in all directions. These data serve as essential inputs for finite element calculations and failure criteria. In particular, determining mechanical properties in the fiber direction often governs the thickness of a component, as composite components are frequently designed with fibers aligned in the directions of maximum stress. Therefore, methods for precisely and reliably measuring these properties are imperative for efficient design. Understanding the phenomena associated with damage and the ability to identify the mechanisms governing the mechanical behavior of carbon fibers in conjunction with epoxy resin are crucial for the design and development of multifunctional composite structures exposed to various types of loading over their service life.

Laminates are composed of individual layers stacked together, each layer having a distinct orientation relative to a common reference frame for the entire laminate. This reference frame choice, particularly the layer stacking orientations, significantly influences the resulting mechanical properties. Laminates can be categorized into various types:

(i) Balanced: A laminate containing an equal number of layers oriented in the +θ and -θ directions.
(ii) Symmetric: A laminate with layers symmetrically arranged about a central plane.
(iii) Orthogonal: A laminate with an equal number of layers oriented at 0° and 90° angles.

In this work, the evaluation of stresses, displacements, and natural frequencies in a laminated composite material plate were numerically studied.

Numerical Simulation

The numerical simulation of a composite plate was specifically designed to investigate its mechanical behaviour. Simulation serves two primary purposes. Firstly, it aids in comprehending internal phenomena by providing access to the mechanisms governing them. Secondly, it enables us to apply structural knowledge to new configurations, reducing the cost of a study with an optimized number of tests. Simulation is a versatile tool that not only replaces experiments that could be slow and laborious on a physical test bench but also broadens the designer's capabilities by decoupling variables that are inherently interconnected in structures. Numerical simulations will be conducted on samples comprised of carbon fibre and an epoxy matrix. However, eight-ply laminated composite were conducted. Table 1 shows the different characteristics of composite material.

Table 1. Characteristics of composite material used in this work

Properties	Values	Properties	Values
Density	1632.9 kg/m^3	Poisson ratio YZ	0.4
Young's modulus X direction	2.3x10^{11} Pa	Poisson ratio XZ	0.2
Young's modulus Y direction	2.3x10^{10} Pa	Shear modulus XY	9x10^9 Pa
Young's modulus Z direction	2.3x10^{10} Pa	Shear modulus YZ	8.2143x10^9 Pa
Poisson ratio XY	0.2	Shear modulus XZ	9x10^9 Pa

Results and Discussion

Numerical software was used to meticulously determine the natural frequencies (Table 2) and mechanical characteristics. The modal analysis within the analysis software necessitates several crucial material properties, including Young's modulus, geometric characteristics, density, and Poisson's ratio. These properties play an integral role in defining the structural behaviour of the composite plates under investigation (Figure 1).

Young's modulus and Poisson's ratio are derived from elastic parameters and are fundamental in quantifying the material's stiffness and deformation characteristics. These parameters, in combination with the geometric properties, are vital for creating an accurate representation of the composite plate's geometry within the

simulation environment. The numerical results of tensile and bending tests are shown in Figures 2 and 3 respectively.

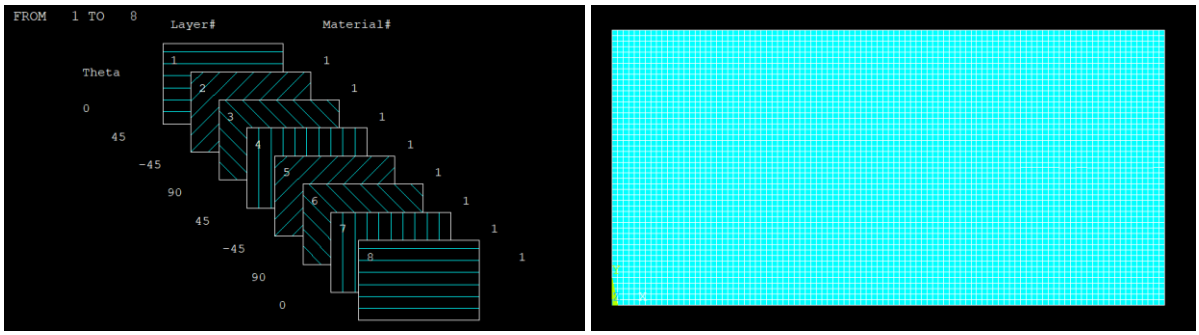

(a) (b)

Figure 1. (a) Distribution of layers and orientations**,** (b) meshing model

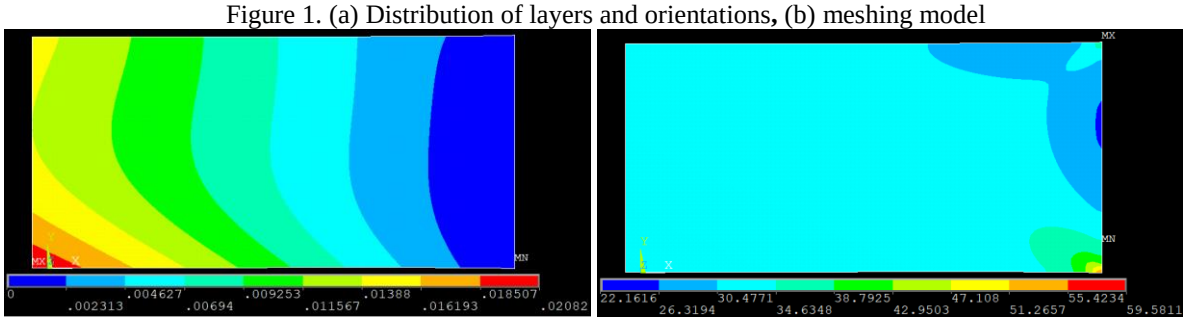

(a) (b)

Figure 2. Tensile test (a) displacement on axe X, and (b) stress on axe X

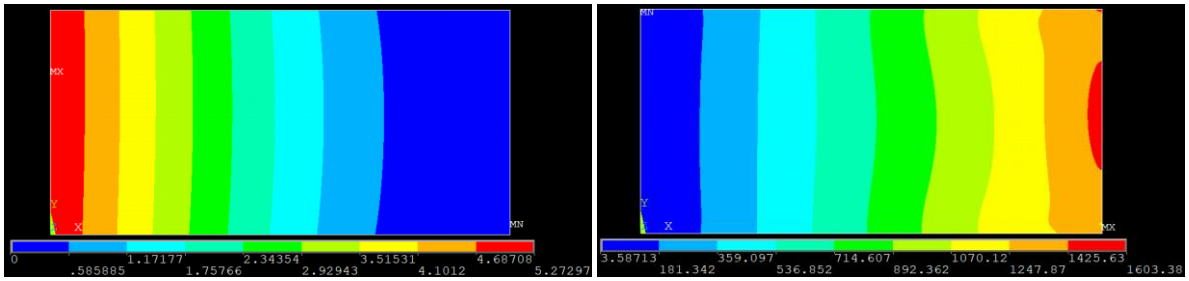

Figure 3. Bending test (a) displacement on axe Z, and (b) equivalent stress

Table 2. Natural frequency

Set	Frequency (Hz)
1	38.488
2	98.680
3	162.64
4	211.22
5	318.24
6	506.19
7	560.70
8	599.31
9	602.29
10	620.73

Conclusion

This study involved simulating the behavior of an aeronautical composite composed of carbon fiber and an epoxy matrix, with the goal of developing a strategy for replacing aging metallic structures with advanced

materials, such as epoxy/carbon composites. These results served as the foundation for conducting numerical simulations using commercial software.

The obtained findings have highlighted variations in the mechanical behavior of composite materials, particularly laminates, which provide insights into the possibility of using different types of reinforcement. The strength of these materials relies on the careful selection of components and the precise arrangement of fibers. As a result, we can tailor the degree of material anisotropy based on the specific composite used, taking into account factors such as the type of reinforcement and the orientation of fibers.

Scientific Ethics Declaration

The authors declare that the scientific ethical and legal responsibility of this article published in EPSTEM journal belongs to the authors.

Acknowledgements or Notes

* This article was presented as an oral presentation at the International Conference on Technology, Engineering and Science (www.icontes.net) held in Antalya/Turkey on November 16-19, 2023.

References

Ahmad, M. S., Farooq, U., & Subhani, T. (2015). Effect of multiwall carbon nanotubes on the ablative properties of carbon fiber-reinforced epoxy matrix composites. *Arabian Journal for Science and Engineering*, *40*, 1529-1538.

Goertzen, W. K., & Kessler, M. R. (2006). Creep behavior of carbon fiber/epoxy matrix composites. *Materials Science and Engineering:* A, *421*(1-2), 217-225.

Guo, H., Huang, Y., Liu, L., & Shi, X. (2010). Effect of epoxy coatings on carbon fibers during manufacture of carbon fiber reinforced resin matrix composites. *Materials & design*, *31*(3), 1186-1190.

Schultz, J., & Lavielle, L. (1989). Interfacial properties of carbon fiber—epoxy matrix composites. Chapter in *ACS Symposium Series*, *391*.

Zafar, A., Bertocco, F., Schjødt-Thomsen, J., & Rauhe, J. C. (2012). Investigation of the long term effects of moisture on carbon fibre and epoxy matrix composites. *Composites Science and Technology*, *72*(6), 656-666.

Author Information

Abdelkader Kirad
Department of Mechanics, Faculty of Technology, Saad Dahlab University of Blida 1, Algeria
Contact e-mail: *aek_kirad62@yahoo.com*

Bassam Gamal Nasser Muthanna
Department of Mechanics, Faculty of Technology, Saad Dahlab University of Blida 1, Algeria

Fateh Madani
Department of Mechanics, Faculty of Technology, Saad Dahlab University of Blida 1, Algeria

Loukmane Zeddam
Department of Mechanics, Faculty of Technology, Saad Dahlab University of Blida 1, Algeria

To cite this article:

Kirad, A. Muthanna, B.G.N. Madani, F. & Zeddam, L. (2023). Numerical study of the mechanical behavior of a composite material plate. *The Eurasia Proceedings of Science, Technology, Engineering & Mathematics (EPSTEM), 26*, 458-461.

The Eurasia Proceedings of Science, Technology, Engineering & Mathematics (EPSTEM)
ISSN: 2602-3199

The Eurasia Proceedings of Science, Technology, Engineering & Mathematics (EPSTEM), 2023

Volume 26, Pages 462-473

IConTES 2023: International Conference on Technology, Engineering and Science

Investigation of the Flow Performance of the Diverter Cover in the Dishwasher

Vasıf Can Yildiran
Haier Europe- Renta Elektrikli Ev Aletleri San. Tic. Ltd. Sti.

Fazıl Erinc Yavuz
Haier Europe- Renta Elektrikli Ev Aletleri San. Tic. Ltd. Sti.

Sebastian George Colleoni
Haier Europe

Abstract: Competition remains fierce within the dishwasher industry, mirroring the ongoing rivalry in all household appliance sectors. The influence of fresh regulations and advancements in technology has spurred a multitude of research endeavors. In the context of household dishwashers, it is widely recognized that the primary focal points are centered on washing efficiency, drying capabilities, water consumption, and energy efficiency. The effectiveness of the hydraulic system within the machine plays a pivotal role in determining its washing prowess, water usage, and energy performance. This research focuses on the examination of the geometry of the diverter element's cover within the hydraulic system of a dishwasher. The diverter and its associated cover, crucial components of the hydraulic circuit, underwent a comprehensive analysis utilizing Computational Fluid Dynamics (CFD) software. Subsequent to the analysis, efforts were made to enhance their performance, encompassing both experimental and numerical approaches. As a result of optimizing the diverter cover's geometry, a notable reduction of 26 ml in water volume within the reservoir was achieved, along with a substantial improvement in pressure loss, amounting to 20 mbar. Subsequent tests conducted with the improved design showcased a remarkable increase in flow rate, measuring 8.1% at 2400 pump revolutions per minute and 8.9% at 2800 pump revolutions per minute.

Keywords: Circulation pump, Computational fluid dynamics (CFD), Dishwasher, Hydraulic

Introduction

Dishwashers have become indispensable appliances in our homes, serving various purposes in both domestic and industrial settings. These machines, available in various types, are designed to efficiently wash and dry dirty dishes while minimizing water, energy, and noise consumption. The concept of dishwashers with continuous water spraying systems was first introduced with William Howard Livens' household-friendly dishwasher in 1924. The modern dishwasher, as we know it today, evolved towards the end of the 1970s (Livens, 1924). Since then, ongoing efforts have been dedicated to the development of more efficient dishwashers in response to resource constraints and evolving regulations.

The effectiveness of a dishwasher's performance hinges significantly on its hydraulic design. Enhancing this design directly translates to improved machine efficiency. It is imperative to minimize pressure losses within the hydraulic circuit components and throughout the circuit itself, as well as to conduct a comprehensive analysis of the flow within the hydraulic system.

The hydraulic system within a dishwasher is responsible for delivering pressurized water to the dishes with the least energy consumption and minimizing pressure loss. This system comprises critical components, including a circulation pump, diverter, sump, delivery tube, and spray arms. This particular study examined the diverter cover, an important component of the hydraulic system in the dishwasher. The investigations encompass not only diverter models, which are electromechanical components controlling the distribution of flow to the spray arms but also a study of a fixed model incorporated into the diverter cover. This region, referred to as the diverter cover, facilitates the distribution of water to both upper and lower spray arms in models without diverters. In models equipped with a diverter mechanism, the distribution of water to the spray arms operates based on the position of the diverter, which changes according to an algorithm. In both operating scenarios, the diverter region experiences high flow velocities and pressure losses.

The study encompasses both numerical and experimental methodologies. Computational Fluid Dynamics (CFD) analyses were conducted using Ansys Fluent software. Additionally, the experimental phase involved the assessment of finalized designs resulting from the CFD analysis in Haier Europe Washer R&D laboratories. Energy performance tests for dishwashers, on the other hand, were carried out in compliance with the EN 50242 standard at Haier Europe Energy Performance laboratories.

Hydraulic System of Dishwasher

The hydraulic system comprises several key components, including the circulation pump, sump, diverter, delivery tube, and spray arms. These components are strategically positioned within the dishwasher, as depicted in the CAD render below. It's important to note that the diverter location, a vital part of the hydraulic system, is not visible in this visual representation.

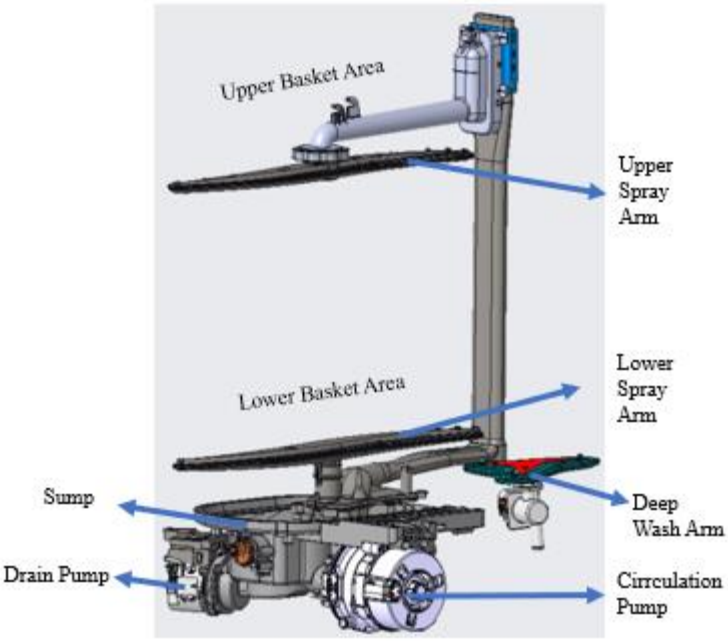

Figure 1. CAD render of hydraulic components

The hydraulic system's water cycle operates in the following sequence: Initially, water is pressurized by the circulation pump and subsequently directed to the diverter. Depending on the selected wash function, the diverter adjusts its position to guide the flow appropriately, or in models without diverters, all arms operate directly. The pressurized water then travels through connection points to reach the spray arms, from where it is expelled toward the dishes through nozzles on the spray arms.

Afterward, the water, having passed over the dishes, collects on the bottom surface of the machine and undergoes filtration before descending into the sump. From the sump, the water proceeds through the circulation pump channel, eventually reaching the impeller of the circulation pump. Here, it is primed to be pumped back to the spray arms, thereby continuing this cycle until the washing process is completed or until the dirty water is drained to make way for clean water replacement.

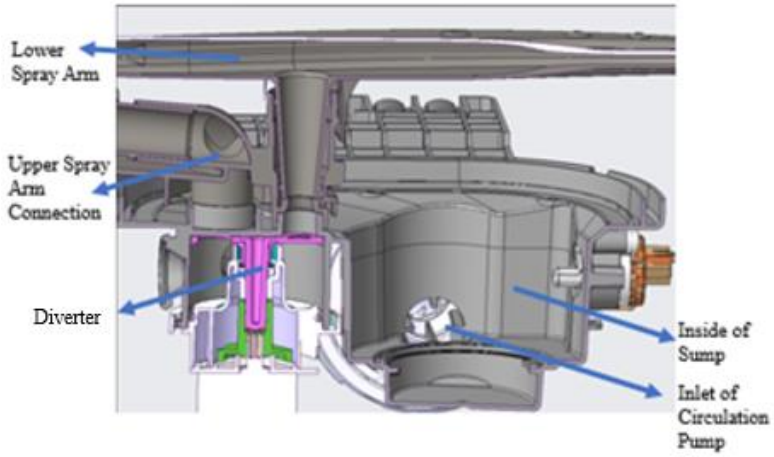

Figure 2. CAD rander of hydraulic components of sump area section

Aim of the Study for Diverter Cover

This study is related to the diverter region in the dishwasher, which follows the circulation pump and is responsible for distributing the flow to the spray arms. In this region, there is either an electromechanical component controlled by an algorithm that directs water to the spray arms based on the diverter's position, or there is a plastic geometry incorporated directly into the diverter cover, which distributes the flow to the spray arms. In the study, the aim was to minimize pressure losses in this region and analyze the flow rates going to the spray arms in non-diverter situations. Therefore, the analyses in the relevant area were examined, and appropriate geometry studies were conducted.

Method

Theory

Pipe Flow

Within a dishwasher's hydraulic system, the liquid follows a path through enclosed conduits before it ultimately reaches the tub. This particular flow, contingent on the cross-sectional shape of the conduits, is often classified as either pipe flow or duct flow (Munson et al., 2012). Figure 3 provides a visual representation of a standard pipe system, showcasing several of the typical components that constitute such a system.

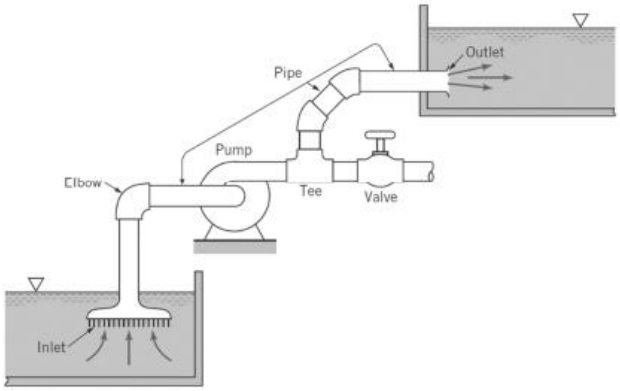

Figure 3. A pipe system and some hydraulics components flow (Munson et al., 2012)

Flow Regime in Pipe Flow

In the realm of fluid mechanics, this type of flow is categorized into two distinct regimes known as Laminar and Turbulent flow. These classifications were established based on experiments conducted by the British scientist

Osborne Reynolds (1842-1912). Laminar flow refers to the smooth movement of fluid in parallel layers, with no intermixing or interference between these layers (Batchelor, 1967). In contrast, turbulent flow is characterized by chaotic and irregular behavior, including significant lateral mixing of the fluid layers.

This classification primarily pertains to flows inside pipes, where both laminar and turbulent flows can manifest. Within the context of pipe flows, the Reynolds number holds immense significance as a crucial dimensionless quantity. For a pipe with a diameter represented as "D" and an average velocity denoted as "V," the Reynolds number can be expressed as follows:

$$Re = \frac{\rho V D}{\mu} \qquad (1)$$

In the context of the Reynolds number equation, where ρ represents fluid density and μ represents dynamic viscosity, it's important to note that the precise range at which the transition from laminar to turbulent pipe flows occurs cannot be precisely defined. This transition can take place at different Reynolds numbers, influenced by factors such as pipe vibrations and the roughness of the entrance region.

For practical engineering applications, the following values are commonly utilized: In a round pipe, flow is typically categorized as laminar if the Reynolds number is approximately below 2100 and as turbulent if it is approximately above 4000 (Munson et al., 2012). Within the intermediate range encompassed between these two thresholds, the flow is considered transitional and is highly susceptible to disturbances. Within a dishwasher's hydraulic system, the Reynolds number falls within the range of 3000 to 20000 for a pump speed of 1800 rpm and between 8000 to 30000 for a pump speed of 2800 rpm, predominantly resulting in turbulent flow. Therefore, for the purposes of this study, since the pump speeds are higher than 1800 rpm, the flow can be considered turbulent.

Energy Considerations in Pipe Flow

One of the fundamental principles in physics is the conservation of energy. Consequently, it is of paramount importance to analyze pipe flows from an energy perspective. When dealing with an incompressible fluid flowing inside a pipe, assuming steady flow along a streamline and neglecting the effects of friction (inviscid flow), the well-established Bernoulli equation can be applied.

$$\frac{p}{\rho} + \frac{V^2}{2} + gz = constant \qquad (2)$$

Indeed, the Bernoulli equation provides valuable insights into the factors that contribute to pressure changes in the case of inviscid flow along a streamline. It highlights how changes in certain parameters affect the pressure within the fluid. Specifically:

A decrease in the flow area (A) leads to an increase in fluid velocity (V), which is associated with a decrease in pressure (P). Conversely, if the flow area expands, or if the pipe slopes downward, the velocity of the fluid decreases, resulting in an increase in pressure.

This principle, elucidated by the Bernoulli equation, helps us understand how changes in flow velocity, pipe geometry, and elevation influence the pressure distribution within a fluid system (Pritchard & Mitchell, 2016).
Nevertheless, flows within pipes and ducts are subject to substantial friction and often exhibit turbulence, rendering the Bernoulli equation inapplicable. Essentially, the influence of friction results in a continuous decrease in the value of the Bernoulli constant as defined in Equation (2), leading to a dissipation of mechanical energy. Consequently, it becomes necessary to replace the Bernoulli equation with an energy equation that accounts for the effects of friction (Pritchard & Mitchell, 2016). In pursuit of this, we examine the energy equation for incompressible, steady flow between two points, as provided below.

$$\frac{p_1}{\rho g} + \alpha_1 \frac{V_1^2}{2g} + z_1 = \frac{p_2}{\rho g} + \alpha_2 \frac{V_2^2}{2g} + z_2 + h_{l_T} \qquad (3)$$

The coefficients α_1 and α_2 are used to account for kinetic energy losses due to non-uniform velocity profiles across the pipe. When dealing with a perfectly uniform velocity profile, α equals 1. However, for any non-uniform velocity profile, α is less than 1. In practice, for high Reynolds numbers, α is often very close to unity

because the change in kinetic energy is usually small compared to the dominant terms in the energy equation. Therefore, the approximation $\alpha \approx 1$ is commonly employed in calculations involving pipe flow (Pritchard & Mitchell, 2016).

The term h_{l_T} represents the head loss, which considers energy dissipation resulting from viscous effects present throughout the fluid in the pipe flow (Munson et al., 2012). This head loss accounts for the energy that is lost as the fluid flows through the pipe due to friction and other factors, contributing to a decrease in the overall energy of the fluid as it moves along the pipeline.

To calculate the pressure difference between any two points within a fluid system using Equation (3), it is crucial to accurately determine the head loss. The head loss accounts for energy dissipation due to various factors such as friction, non-uniform velocity profiles, and other influences that lead to a decrease in the total energy of the fluid as it traverses the system. Accurate estimation of the head loss is essential for understanding pressure changes and optimizing the performance of the fluid system. The head loss term, h_{l_T}, is often known as the total head loss, and it comprises two main components:

Major losses, denoted as h_l, which are primarily attributed to frictional effects occurring in fully developed flow within constant-area tubes. These losses are related to the resistance that the fluid encounters as it moves through the pipe due to friction with the pipe walls.

Minor losses, represented as h_{l_m}, which arise from various factors such as entrances, fittings, changes in area, and other elements within the fluid system. These minor losses are associated with deviations from ideal flow conditions, including abrupt changes in flow direction and the presence of components like valves and elbows (Pritchard & Mitchell, 2016). Both major and minor losses contribute to the overall head loss in a fluid system, and their accurate consideration is vital for understanding and managing pressure changes in the system.

CFD Methodology

Model Preparation

The initial phase of the CFD study involves model preparation. To begin, the specific region of interest is identified using the corresponding part code within a CAD program and then saved in .stp format onto the computer. Following this step, the file is imported into SpaceClaim software. Here, a thorough review of the geometric details on the part is conducted, and any elements found to be non-impactful on our CFD analysis results but potentially adding complexity to the solution mesh are systematically removed to optimize the model.

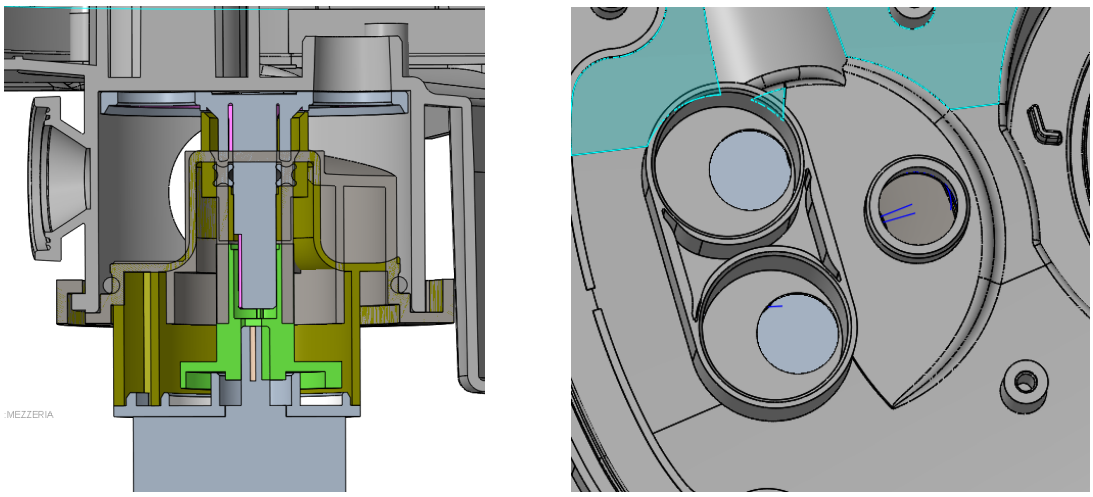

Figure 4. CAD model of diverter area section and top view of diverter spray arm connection

Diverter and non-diverter systems vary depending on the dishwasher model. In dishwashers with a diverter chamber, it is present to distribute water to the spray arms in models without diverters. In this study, the geometries of non-diverter systems in the diverter chamber have been examined.

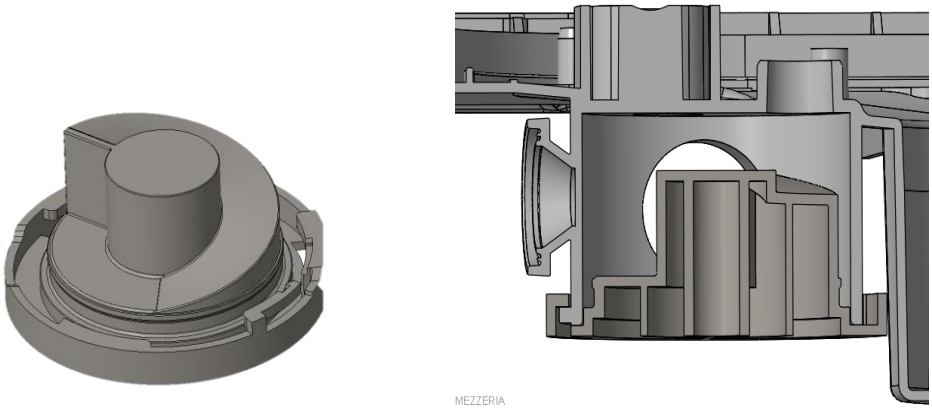

Figure 5. CAD model of current diverter cap and section of diverter area with current cap

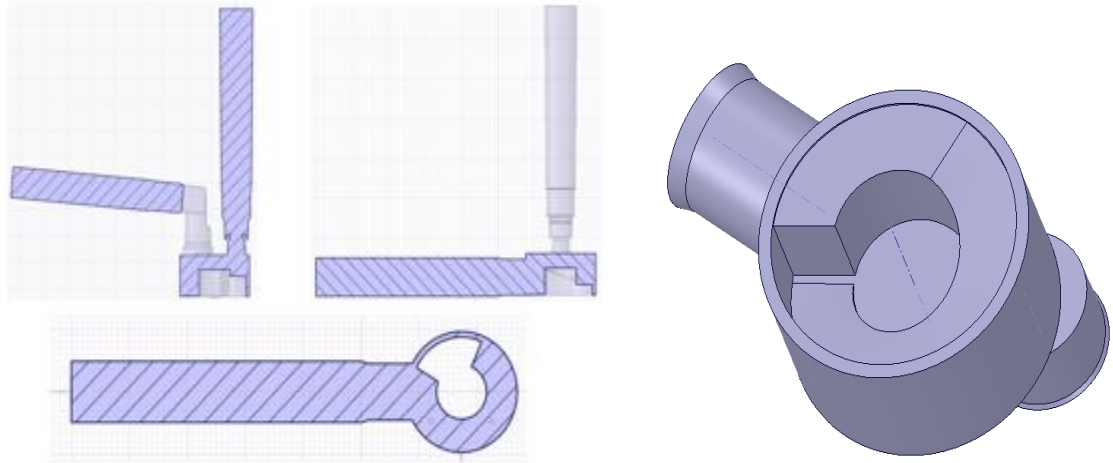

Figure 6. Some sections of full model fluid volume and bottom view of current cap diverter area

The necessary flow volume has been obtained for conducting fluid dynamics analysis. Inside this volume, a solution mesh will be created using Ansys Mesh software.

Mesh Preparation

Ansys Mesh software has been chosen for meshing the flow volumes. During the mesh creation process, finer elements have been implemented in areas where flow separation is anticipated. Additionally, a boundary layer mesh has been applied to solid surfaces to capture solid-liquid interactions. Before conducting CFD analyses, a mesh independence study has been carried out. The goal of this study is to ensure that the analyses are not influenced by the mesh cell count and sizes. The mesh independence study was conducted based on the variation of velocity values read from a specific of diverter inlet. At the end of the study, analyses were carried out with a mesh count of 1 million.

Table 1. Mesh independency

Study No	1	2	3	4	5
Mesh Number	510 k	820 k	1 M	1.2 M	1.4 M
Velocity for Control Point [m/s]	1,6	1,66	1,9	1,91	1,91
Skewness	0,87	0,86	0,85	0,85	0,83

The mesh count has been defined for the baseline, and a mesh independence study has been completed. The mesh count for each geometry varies according to geometric details, but there was no need to conduct another mesh independence study.

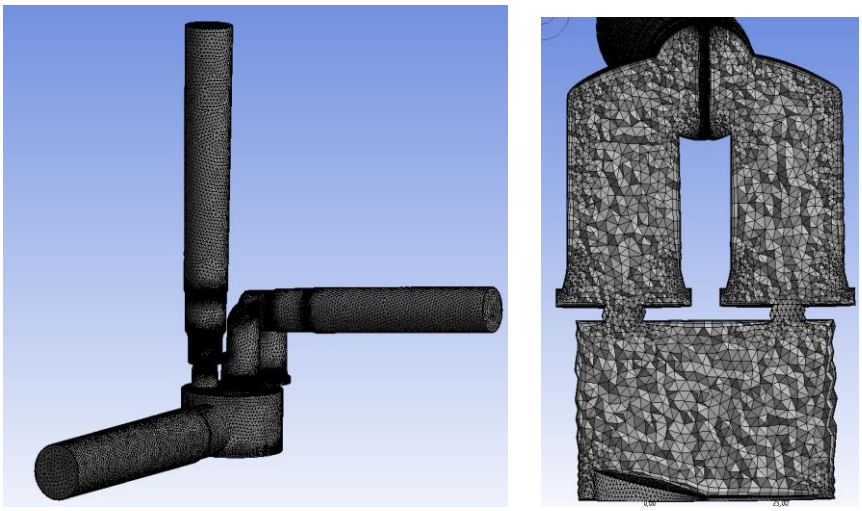

Figure 6. Mesh of full body and full body section

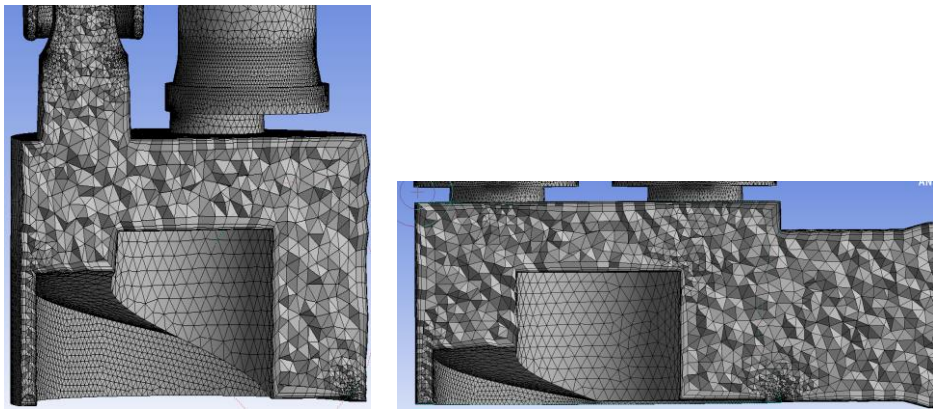

Figure 7. Mesh details for some sections

CFD Model and Studies

Design optimization studies (CFD) have become increasingly prevalent in numerous engineering projects. These studies help achieve cost savings in terms of prototypes and time, allowing for the testing of multiple designs within a short timeframe. In this study, Ansys Fluent software has been utilized for the CFD analyses. After creating the solution mesh using Ansys Mesh, boundary conditions for the CFD analysis were established using Fluent, as detailed in the Ansys User Guide.

The study focuses on determining the boundary conditions for the model in use. The numerical model has been adopted under the assumptions of incompressible, time-independent flow, and without energy equations. The fluid within the model is single-phase, using water as the working fluid. Atmospheric pressure has been set as the inlet condition for the diverter inlet channel, while the model's outlets are defined by the flow rate provided by the pump. The focus of this study is the pressure losses caused by the diverter models under investigation. Therefore, experimental data for the flow rates in the lower and upper spray arms have been used, and the same approach has been applied to all models. The boundary condition at the inlet of the flow is defined as the pressure input.

Table 2. Boundary conditions

Input Definition	Values
Pressure Inlet	101325 Pa
Volume Flow Rate Upper	28.5 lt/min
Volume Flow Rate Lower	26.5 lt/min
Density	992.2 kg/m^3
Dynamic Viscosity	0.0006533 Pa.s

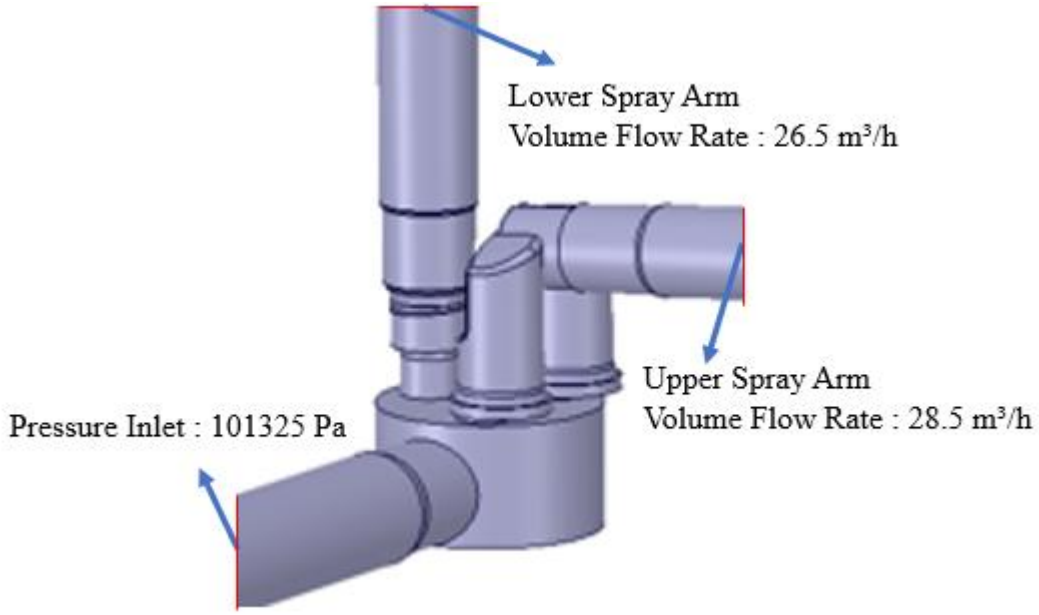

Figure 8. Boundary conditions on CFD model

At the outset of the research, the flow characteristics of the model were identified as turbulent using the Reynolds number relationship. The pressure-velocity coupling in the Navier-Stokes equations was resolved using the Coupled solution method (Wilcox, 1998). The equations for continuity and momentum employed in the solution are provided below.

$$\left(\frac{\partial v_x}{\partial x}+\frac{\partial v_y}{\partial y}+\frac{\partial v_z}{\partial z}\right)=0 \qquad (3)$$

$$\rho U\left(\frac{\partial U}{\partial x}+\frac{\partial V}{\partial x}+\frac{\partial W}{\partial x}\right)=-\frac{\partial P}{\partial x}+\mu\left(\frac{\partial^2 U}{\partial x^2}+\frac{\partial^2 U}{\partial y^2}+\frac{\partial^2 U}{\partial z^2}\right)-\mu\left(\frac{\partial \overline{u\prime^2}}{\partial x^2}+\frac{\partial \overline{u\prime v\prime}}{\partial x\partial y}+\frac{\partial \overline{u\prime w\prime}}{\partial x\partial z}\right) \qquad (5)$$

$$\rho V\left(\frac{\partial U}{\partial y}+\frac{\partial V}{\partial y}+\frac{\partial W}{\partial y}\right)=-\frac{\partial P}{\partial y}+\mu\left(\frac{\partial^2 V}{\partial x^2}+\frac{\partial^2 V}{\partial y^2}+\frac{\partial^2 V}{\partial z^2}\right)-\mu\left(\frac{\partial \overline{u\prime v\prime}}{\partial x\partial y}+\frac{\partial \overline{v\prime^2}}{\partial y^2}+\frac{\partial \overline{v\prime w\prime}}{\partial y\partial z}\right) \qquad (6)$$

$$\rho W\left(\frac{\partial U}{\partial z}+\frac{\partial V}{\partial z}+\frac{\partial W}{\partial z}\right)=-\frac{\partial P}{\partial z}+\mu\left(\frac{\partial^2 W}{\partial x^2}+\frac{\partial^2 W}{\partial y^2}+\frac{\partial^2 W}{\partial z^2}\right)-\mu\left(\frac{\partial \overline{u\prime w\prime}}{\partial x\partial z}+\frac{\partial \overline{v\prime w\prime}}{\partial y\partial z}+\frac{\partial \overline{w\prime^2}}{\partial z^2}\right) \qquad (7)$$

A range of turbulence methods and models are utilized for conducting Heat and Mass Diffusion (HAD) analyses. While Large Eddy Simulation (LES) and Direct Numerical Simulation (DNS) approaches are popular for fluid dynamics applications, this study has chosen the Reynolds-Averaged Navier-Stokes (RANS) approach, which is also widely recommended in engineering literature. The RANS approach is favored over other techniques more frequently due to its cost-effectiveness and applicability. Within the Ansys Fluent software used for HAD simulations, the k-ω SST (Shear Stress Transport) turbulence model has been selected from the available RANS options (Menter, 1994).

$$\rho\frac{\partial k}{\partial t}+\rho u_i\frac{\partial k}{\partial x_j}=P-\beta^*\rho k\omega+\frac{\partial}{\partial x_j}\left[(\mu+\sigma_k\mu_T)\frac{\partial_k}{\partial x_j}\right] \qquad (8)$$

$$\rho\frac{\partial \omega}{\partial t}+\rho u_i\frac{\partial \omega}{\partial x_j}=\frac{\gamma\rho}{\mu_T}P-\beta\rho\omega^2+\frac{\partial}{\partial x_j}\left[(\mu+\sigma_\omega\mu_T)\frac{\partial \omega}{\partial x_j}\right]+2\rho(1-F_1)\frac{\sigma_{\omega 2}}{\omega}\frac{\partial k}{\partial x_j}\frac{\partial \omega}{\partial x_j} \qquad (9)$$

Post Process

The CFD analyses were initially conducted for the diverter cap without any specific geometry. Subsequently, several models aimed at minimizing pressure losses were created. Analyses of CFD for all these models were completed, and pressure losses at the same control points were examined. Another topic is that volume reduction of diverter area to decrease water consumption.

The results of the currently employed model, Model A, have been examined. Other models have been developed to decrease pressure losses. The baseline model, on the other hand, was modeled solely to understand how results could be obtained when there is no figure on diverter cap. The baseline, Model A which is current production and other models are presented as shown in the following Figure 9.

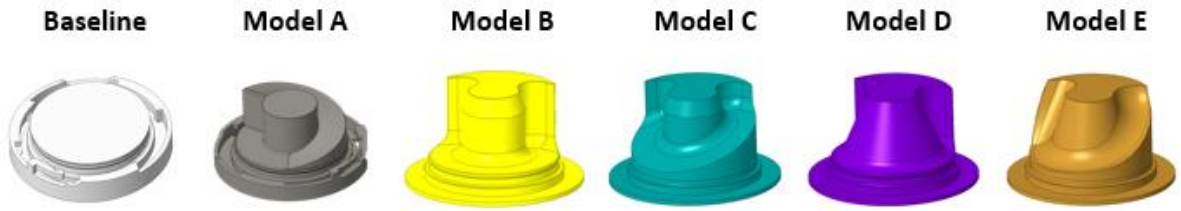

Figure 9. Diverter cap models

In order to examine the velocity distribution within the flow, velocity vectors, streamlines, and contours have been obtained from various cross-sections as shown in the following Figure 10 and 11.

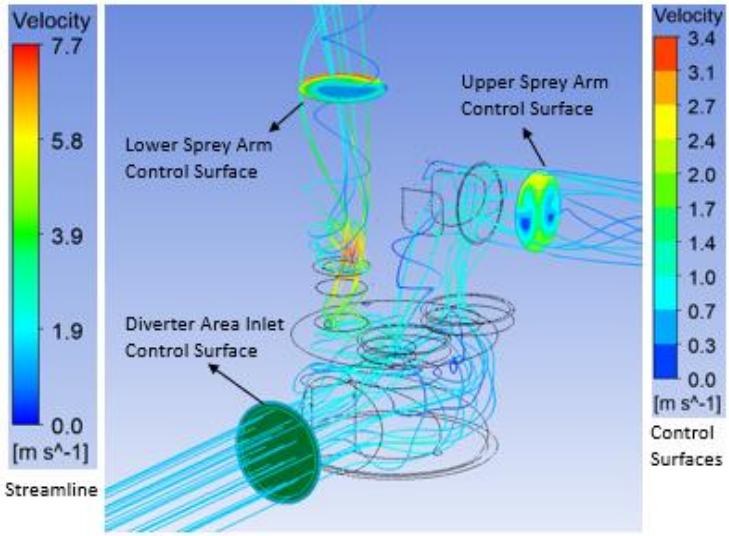

Figure 10. Streamlines and velocity distribution on control surfaces

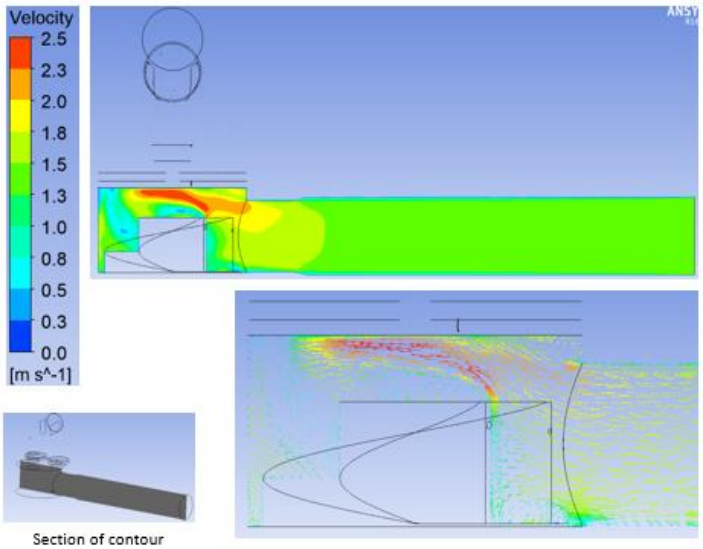

Figure 11. Velocity distribution on middle section

One of the main objectives of the study is to examine pressure losses. To understand pressure losses, pressures on the relevant control surfaces have been measured as shown in the following Figure 12.

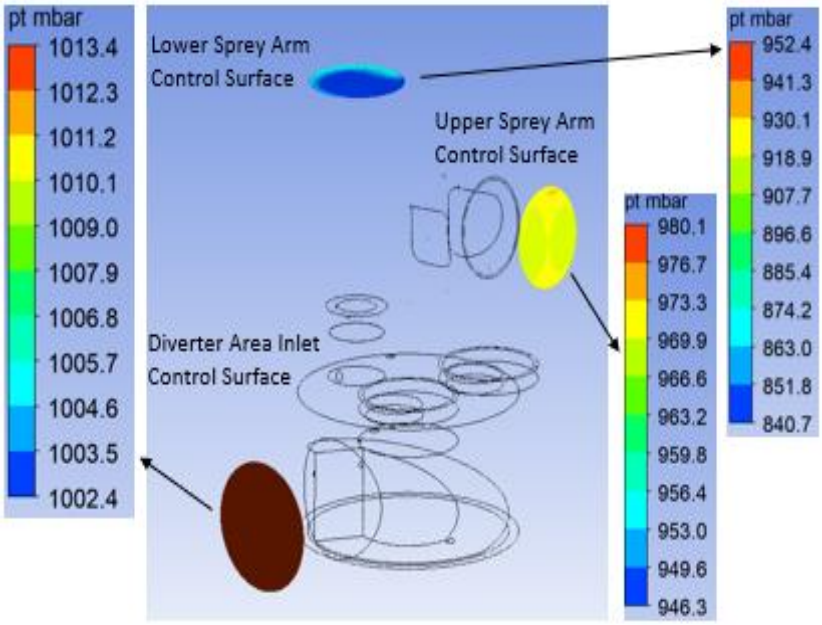

Figure 12. Total pressure value on control surfaces

The CFD results of Model A, which is currently used in the production, have been examined. Based on these results, it was observed that the relevant geometry induces a swirl motion in the flow, and it was determined that this swirl flow causes pressure losses. In the other models, the goal is to reduce these pressure losses and, at the same time, minimize the volume of the diverter chamber to decrease water consumption as much as possible. CFD analyses for all models have been completed. The results have been examined comparatively, and they are presented as shown in the following Table 3.

Table 3. CFD results of diverter cap models

Model Name	Baseline	Model A	Model B	Model C	Model D	Model E
Total Pressure Loss Upper (mbar)	52	55	39	41	38	44
Total Pressure Loss Upper (mbar)	143	167	145	146	151	146
Water Volume (ml)	154.9	131.8	126	114.8	117.9	111.4

Within the scope of this study, various designs of the diverter cap used in models without diverters have been examined. The design currently used in production, known as Model A, as well as the baseline where no specific geometry is present, and new models aimed at reducing pressure losses and water consumption have had their pressure and velocity distributions analyzed.

Results and Discussion

After analyzing the results, the outcomes of Model A, currently in use, have been compared with those of the other models. The comparison data consist of pressure losses between the connection points of the spray arms and the entry to the diverter chamber, as well as the water volume within the diverter chamber. The difference in results for the other models compared to Model A is provided in the table below which is Table 4.

Table 4. CFD results of diverter cap models

Model Name	Model A	Model B	Model C	Model D	Model E
Total Pressure Loss Upper (mbar)	55	-16	-14	-17	-11
Total Pressure Loss Upper (mbar)	167	-22	-21	-16	-21
Water Volume (ml)	131.8	-5.8	-17	-13.9	-20.4

The analyses have been reviewed and considering both the reduction in pressure losses and the decrease in chamber volume, it has been decided to proceed with Model 2C. Firstly, the prototyping process has been completed using a 3D printer. Subsequently, laboratory tests have been conducted. The reduction of pressure losses has allowed for a higher flow rate at the same pump speed.

After completing the laboratory tests, the design of the component was finalized. The mold output of the component is shown in Figure 13 below.

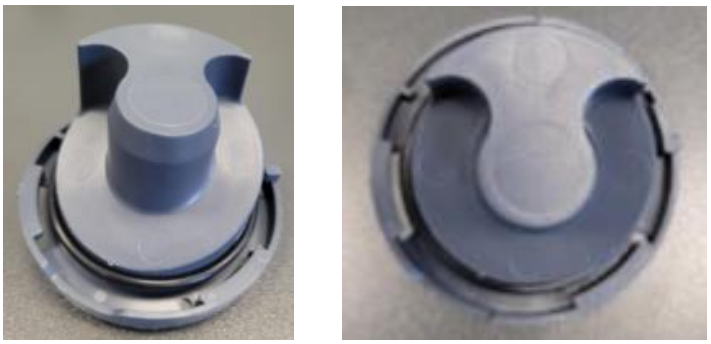

Figure 13. Output of the plastic injection mold after CFD study

Conclusion

With this study, a design change has been made for the diverter chamber. The design currently used in existing productions and other studies have been analyzed with CFD software at the same flow rates, and their results have been compared. The results have been examined to reduce pressure losses and minimize the empty volume of the chamber.

According to the analysis results, a part has been produced with 3D printers for the selected Model C. In tests conducted with this part, the total flow rate has increased from 38.2 l/min to 41.3 l/min at a pump speed of 2400 rpm, and from 52 l/min to 57 l/min at a pump speed of 2800 rpm. As a result of the change in the geometry of the diverter cap alone, there has been an approximate 8% increase in flow rate at 2400 pump speed and a 9% increase at 2800 pump speed.

Recommendations

Hydraulic circuit losses in hydraulic systems cause significant inefficiencies in the system. Hydraulic systems for dishwashers operating at high pump speeds should therefore be designed with this perspective in mind. HAD studies are very effective software tools to improve the design of relevant geometries. In our work, sometimes we need to examine a specific part of the system, and sometimes the entire system, through HAD analyses.

Scientific Ethics Declaration

The authors declare that the scientific ethical and legal responsibility of this article published in EPSTEM journal belongs to the authors.

Acknowledgements or Notes

* This article was presented as an oral presentation at the International Conference on Technology, Engineering and Science (www.icontes.net) held in Antalya/Turkey on November 16-19, 2023.

* For their contributions to this study, we extend our thanks to Renta Electric Home Appliances Industry and Foreign Trade Ltd. and our affiliated company, Haier Europe.

References

Ansys. (2010). *Ansys fluent user guide.* Conansburg: Ansys Inc
Batchelor, G. K. (1967). *An introduction to fluid dynamics*. Cambridge University Press.

DIN EN 50242/DIN EN 60436:2018-06. (2018) - *Electric dishwashers for household use - Methods for measuring the performance (IEC 60436:2004, modified + A1:2009, modified + A2:2012, modified*. VDE standarts

Livens, W. H. (1924). *Improvements in apparatus for washing household crockery and the like. FR579765*. UK : Intellectual Property Office.

Menter, F. R. (1994). Two-equation eddy-viscosity turbulence models for engineering applications. *AIAA Journal,32*(8), 1598-1605.

Munson, B. R., Rothmayer, A. P., Okiishi, T. H., & Huebsch, W. W. (2012). *Fundamentals of fluid mechanics*.(7th ed.). Wiley.

Pritchard, P. J., & Mitchell, J. W. (2016). *Fox and McDonald's introduction to fluid mechanics*. John Wiley & Sons.

Wilcox, D. C. (1998). *Turbulence modeling for CFD* (Vol. 2, pp. 103-217). La Canada, CA: DCW industries.

Author Information

Vasıf Can Yildiran
Haier Europe- Renta Elektrikli Ev Aletleri San. Tic. Ltd. Sti.
26110 Odunpazarı Eskisehir, Turkey
Contact e-mail:*vasifcan.yildiran@haier-europe.com*

Fazıl Erinc Yavuz
Haier Europe- Renta Elektrikli Ev Aletleri San. Tic. Ltd. Sti.
26110 Odunpazarı Eskisehir, Turkey

Sebastian George Colleoni
Haier Europe
Via Privata Eden Fumagalli 20861 Brugherio MB
Italy

To cite this article:

Yildiran, V.C., Yavuz, F.E., & Colleoni, S.G. (2023). Investigation of the flow performance of the diverter cover in the dishwasher. *The Eurasia Proceedings of Science, Technology, Engineering & Mathematics (EPSTEM), 26*, 462-473.

The Eurasia Proceedings of Science, Technology, Engineering & Mathematics (EPSTEM)
ISSN: 2602-3199

The Eurasia Proceedings of Science, Technology, Engineering & Mathematics (EPSTEM), 2023

Volume 26, Pages 474-480

IConTES 2023: International Conference on Technology, Engineering and Science

Small-Size Nanoparticles and Nanofluids Fabrication via Plasma Arc

David Gelenidze
E. Andronikashvili Institute of Physics

Gela Gelashvili
E. Andronikashvili Institute of Physics

Abstract: The main issue with nanotechnology is the rapidly expanding fields of application, which necessitate heavy investment in research and development, and complicated devices to produce (<10nm) nanoparticles. The article describes the method of plasma arc technology designed for the production of metal nanoparticles, which is related to "Vapor phase techniques" when the material is heated to its boiling point. It is common knowledge that the homogeneity of the plasma heating zone is affected by the varying amperage of electric current in the thermal plasma column caused by fluctuations in plasma column resistance. For the manufacture of small-size nanoparticles, it's also essential to create a sizable heating zone and give the feed materials plenty of time to vaporize completely. The suggested technique uses an electric arc, powered by a constant current power source, to produce a lengthy high-temperature plasma zone.

Keywords: Thermal plasma, Nanoparticles, Plasma reactor, Dispersion, Synthesis.

Introduction

Using their special qualities of high temperatures, thermal plasma has been employed as a heat source for a variety of material transformation processes such as melting, vaporization, Synthesis, and pyrolysis (Murphy et al., 2018). Using plasma can achieve high temperatures (4000^0C and above) so the production of nanoparticles in the gas phase has gained widespread acceptance. High-temperature plasma synthesis can produce particles with unique properties and morphology that are not possible with other methods. Currently, plasma technology is gaining great attention as a prominent “green” synthesis method for nanomaterials, due to its distinguishing properties when compared to solid, liquid, and gas phase synthesis approaches (Kaushik et al., 2019). Thermal plasma is an excellent way to prepare spherical metal powders with a stable composition, high sphericity, and good dispersion due to its advantages of high temperature, concentrated energy distribution, no electrode pollution, and flexible control (Yuming et al., 2013). Various types of plasma technology are used in the production of nanopowders of metals. The paper (Baskoro et al., 2019) examines a number of plasma processes for the production of metal powders.

Many assessments and tests found that the processing capabilities of current plasma technologies have some limitations and couldn’t satisfy the following critical requirement for low-cost nanoparticle production it's a long residence time for full vaporization of low-vapor-pressure materials. The Idaho National Laboratory developed two advanced hybrid plasma reactor concepts that produce a large uniform heating zone and a long residence time for the feed materials to achieve full vaporization. The concepts are modular AC/AC hybrid plasma and modular DC/DC hybrid plasma systems. The modular hybrid plasma concept means stacking plasma torches in sequence to form a long plasma system that produces a large uniform high-temperature heating zone and a very long residence time for feed materials vaporization (Kong, 2011). A three-stage AC/AC modular hybrid plasma reactor concept uses three arc discharges that form the cascading energy loading effect in the plasma reactor, which shows the overall increase in the plasma volume. The net plasma energy content cascading from the

modular unit above will increase by the superimposition of an arc discharge in the plasma gas and raise the total energy content.

We propose a technique for producing a long zone of high-temperature plasma with a single electric arc powered by a constant current power source when any variation in the resistance of the plasma column is compensated for by "just" changing the voltage. Thus, the stability of the current in the arc column ensures the homogeneity of the plasma zone as well as the ability to lengthen or shorten the length of the plasma arc during operation.

Method

The most essential component of plasma arc reactors for nanoparticle gaseous synthesis is a stable, uniform, high-temperature plasma arc column. Maintaining a stable current strength is critical to ensure uniformity of the heating zone when the material is fed into the plasma zone, as the plasma resistance begins to change dramatically. Non-uniformity has a negative impact on the efficiency of nanoparticle synthesis as well as their physicochemical properties.

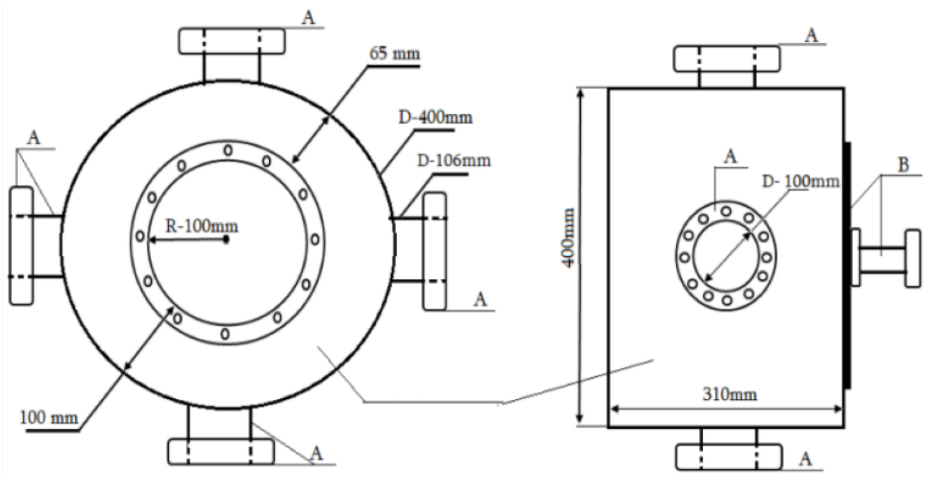

Figure 1. The reactor chamber's common scheme

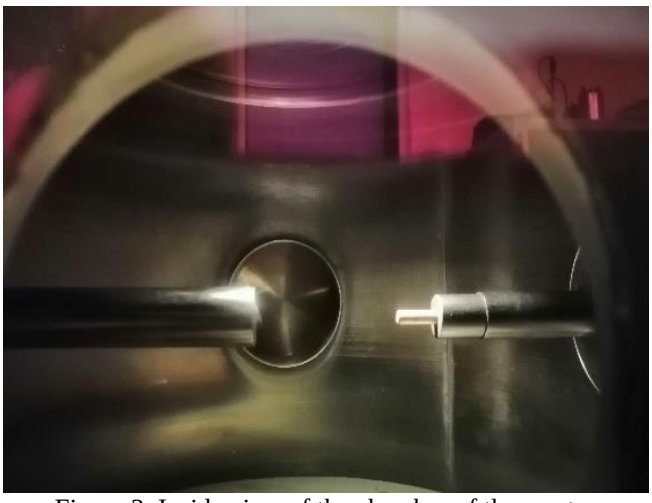

Figure 2. Inside view of the chamber of the reactor

From 2012 to 2016, E. Andronikashvili Institute of Physics in partnership with the Brookhaven National Laboratory led the US Department of Energy project "Gasification of Municipal Waste" (GIPP DOE, BNL-T2-0393). In order to ensure stable operation of the arc in the reactor, a plasma-arc reactor powered by a constant current power source with specific current-voltage characteristics was designed as part of this project. The power source with an almost rectangular volt-ampere characteristic was applied to ignite and continuously generate the plasma arc, ensuring the plasma zone's stability and homogeneity during operation. Experiments have shown that the plasma arc operates stably and its length can be adjusted (1–15 cm). The results of the

project allowed us to apply this approach to some applications. for example, we conducted research on burning low-quality coal (Gelashvili G. et al. 2018). Our team received a grant for applied research from the National Science Foundation of Georgia (AR-19-719. 2019-2024). The goal is to develop a plasma arc reactor in which the evaporated material passes through a long plasma heating zone. A laboratory prototype of a plasma-arc reactor with a power source of 30 kW has been developed (see Figures 1, and 2).

In the reactor chamber, a rod and one tubular graphite electrode are installed vertically. Step by step, a current conductive wire with an outer diameter equal to the inner diameter of the electrode is passed through the tubular electrode until it reaches the end of the graphite electrode rod, at which point the plasma arc ignites and vaporizes all the wire located between the electrodes. The distance between the two electrodes ranges from 1 to 12 cm. To ignite the plasma arc, a constant current power source with an almost rectangular volt-ampere characteristic is used, which ensures the stability and uniformity of the plasma zone during operation. Experiments were carried out to obtain copper and aluminum oxide nanoparticles (< 5nm). The materials used were wires with a cross-section of 0.8, 09, 1, ..., 5 mm. The voltage varied from 150 to 450V, and the amperage of the initial current from 120 to 250A depended on the wire's cross-section.

Results and Discussion

A high-resolution X-ray diffraction system (XRD), a transmission electron microscope (TEM), and a scanning electron microscope (SEM) were used to make measurements. The materials were copper and aluminum. The results of measurements including the Whole Powder Pattern Fitting (WPPF) analysis of obtained copper oxide and aluminum nanoparticles are shown in Figures 3,5, …,9.

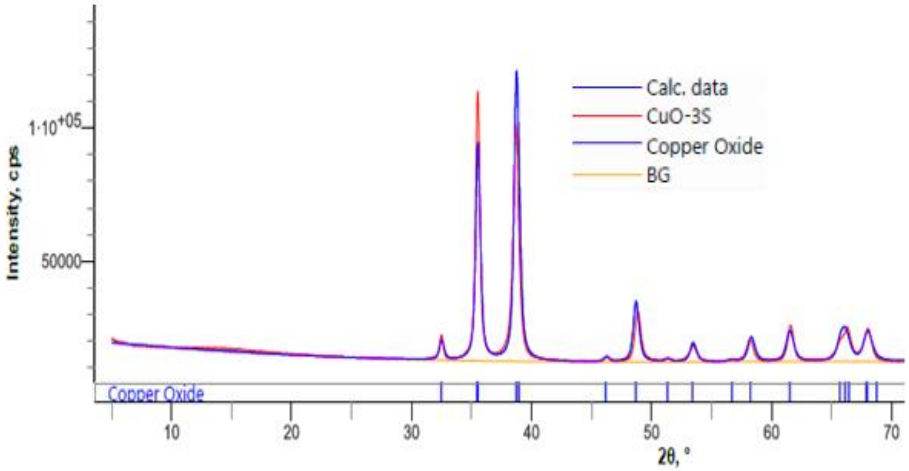

Figure 3. WWPF profile view of CuO nanoparticles. (XRD)

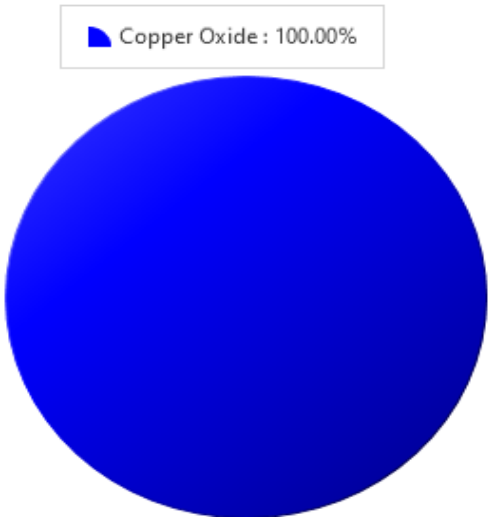

Figure 4. WPPF weight fraction of CuO nanoparticles. (XRD)

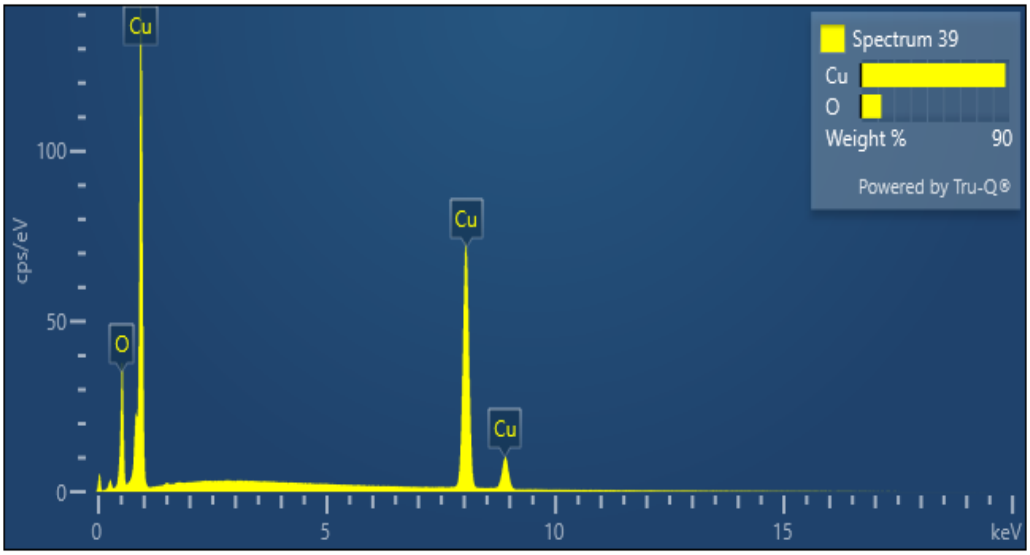

Figure 5. Spectrum of copper oxide nanoparticles. (SEM)

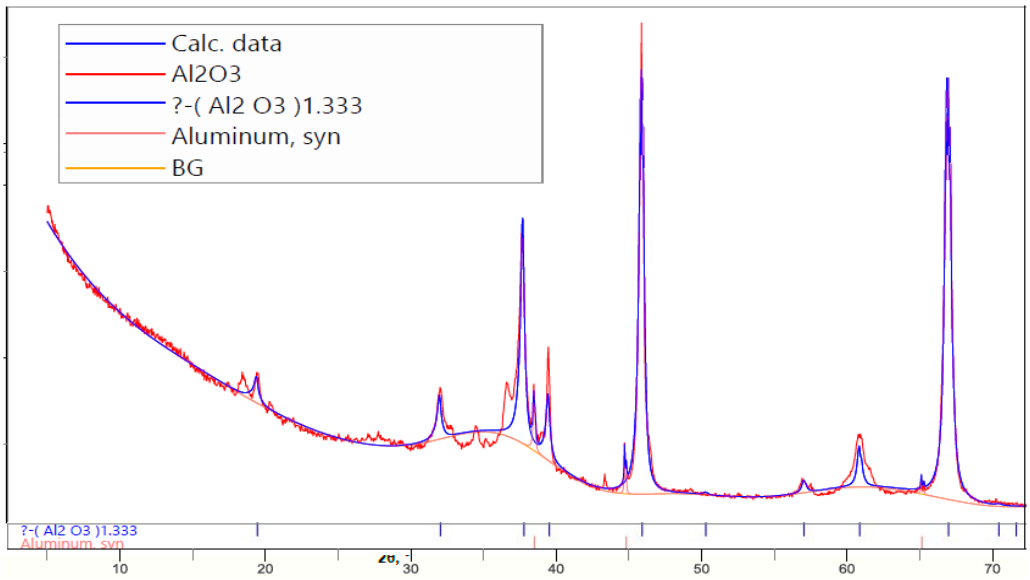

Figure 6. WWPF profile view of Al_2O_3 nanoparticles. (XRD)

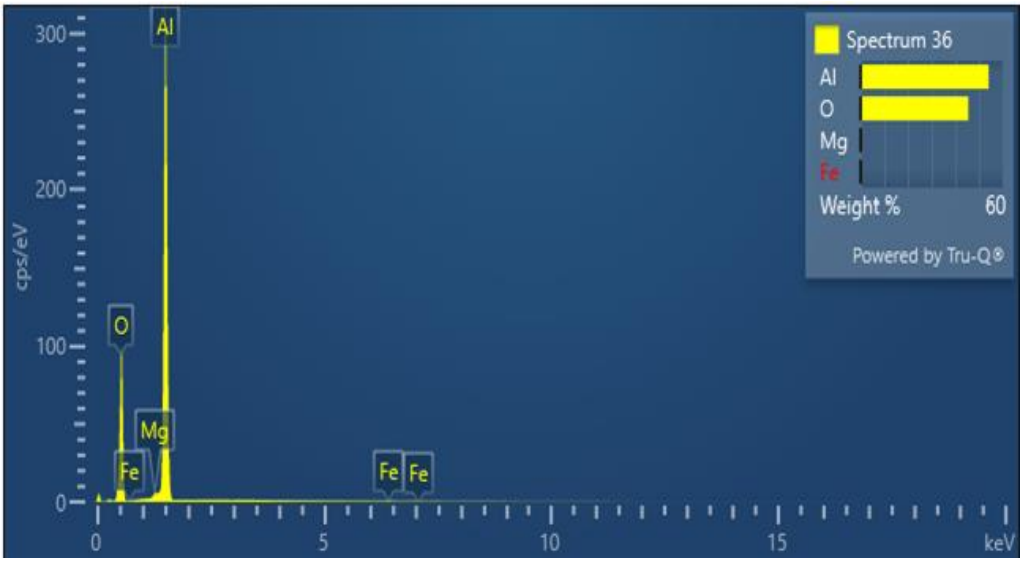

Figure 7. Spectrum of Al_2O_3 nanoparticles (SEM).

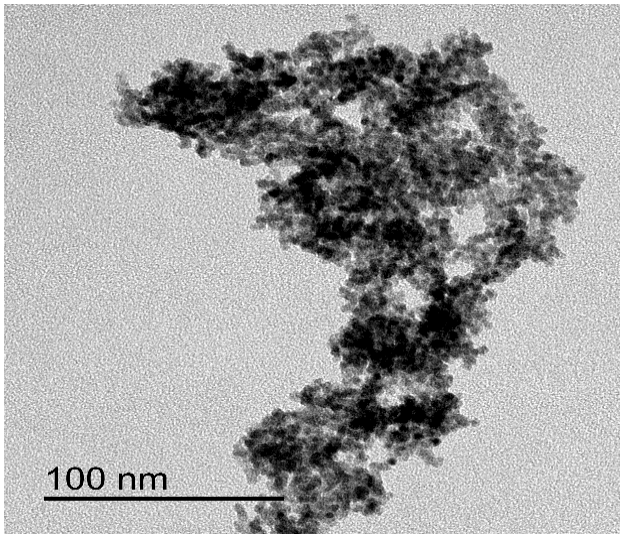

Figure 8. Al_2O_3 nanoparticles size (TEM).

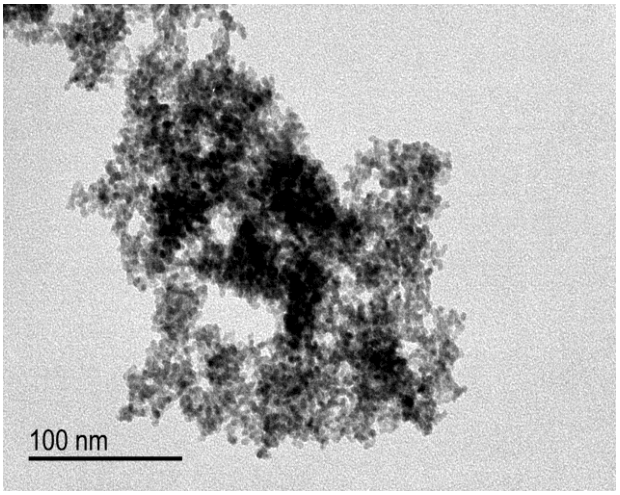

Figure 9. CuO nanoparticles size (TEM).

Nanofluids are used in many areas of industry: solar energy, heat transfer, microelectronics, fuel cells, pharmaceutical processes, hybrid engines, engine/vehicle cooling systems, nuclear reactor coolants, grinding, machining, space technology, defense, and shipbuilding, as well as in biomedical approaches in different fields.

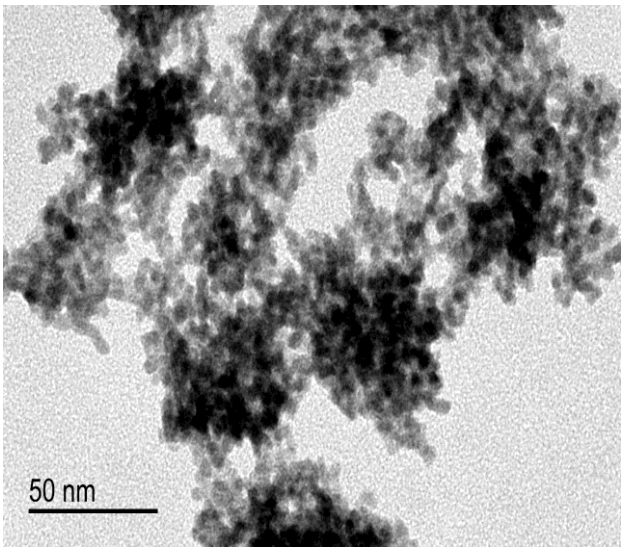

Figure 10. CuO nanoparticles dispersed in H_2O. (TEM)

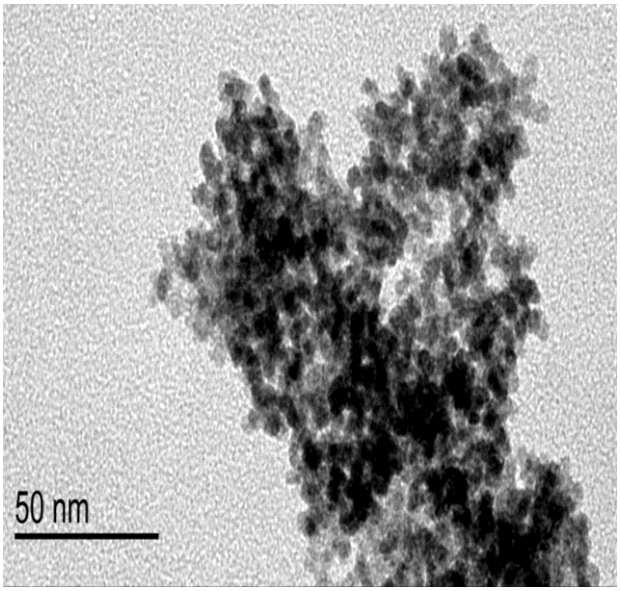

Figure 11. CuO nanoparticles dispersed in H_2O. (TEM)

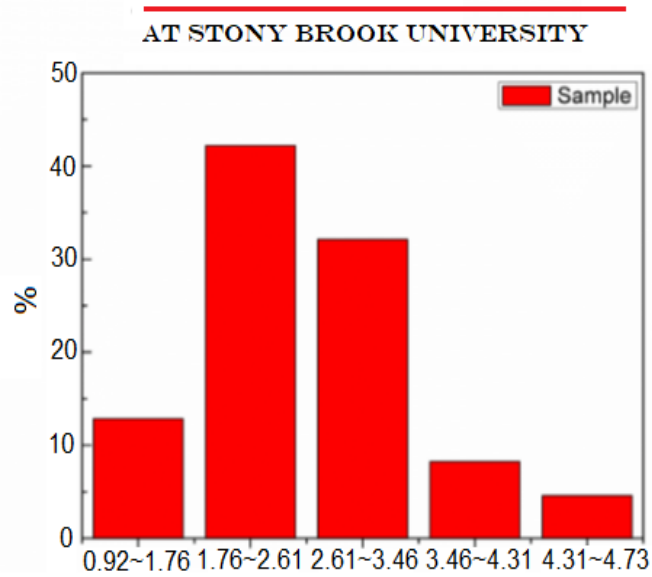

Figure 12. Size distribution of CuO nanoparticles dispersed in H_2O (TEM).

The goal of nanofluids is to achieve the highest possible thermal properties at the smallest possible concentrations (preferably < 1% by volume) by uniform dispersion and stable suspension of nanoparticles (preferably < 10 nm) in host fluids(Sawant et al., 2021). Using our approach, we also conducted some preliminary experiments to receive small-sized nanoparticles (<10nm) dispersed in deionized water. To obtain a dispersion of copper oxide in the liquid, plasma arcs were ignited in water using copper wire with various cross-sections. The results of the tests (shown in Figures 10, 11 and 12) are optimistic

Conclusion

When there are frequent sudden changes in the resistance of the plasma arc, its power is regulated solely by automatically changing the voltage. Consequently, a constant current passes through the arc column, which ensures homogeneity of the plasma medium, as well as precise adjustment of the length of the plasma arc during operation, and so complete evaporation of the loaded material. Nanofluids of various concentrations were obtained by a one-step method. There is no need to prepare dry nanoparticles in advance and then disperse them in water; both occur in a single discharge, simplifying the production of nanofluids. The sizes of the nanoparticles were almost uniform and ranged from 1 to 10 nm, with most of them being less than 3 nm.

Scientific Ethics Declaration

The authors declare that the scientific ethical and legal responsibility of this article published in EPSTEM journal belongs to the authors.

Acknowledgements or Notes

* This article was presented as a poster presentation at the International Conference on Technology, Engineering and Science (www.icontes.net) held in Antalya/Turkey on November 16-19, 2023.

* The authors would like to gratefully acknowledge the Shota Rustaveli National Science Foundation of Georgia for this work funding through the Applied Research Grant AR-19-719

References

Baskoro, A., Sugeng, S., & Dharmanto. (2019). Review on plasma atomizer technology for metal powder. Proceedings of the *MATEC Web Conference (IIW 2018), 269.*

Gelashvili, G., Gelenidze, D., Nanobashvili, S., Nanobashvili, I., Tavkhelidze, G., & Sitchinava, T.(2018). Plasma arc burner for pulverized coal combustion. *International Journal of Chemical and Molecular Engineering*, *12*, 278-281.

Kaushik K. N., Kaushik, N.,… & Choi H. E. (2019). *Plasma and nanomaterials: Fabrication and biomedical applications*. *Nanomaterials*, *9*(1), 98. https://doi.org/10.3390/nano9010098

Kong, P. (2011). *Modular hybrid plasma reactor for low-cost bulk production of nanomaterials. Technical report INL/EXT-11-24263*. Idaho National Lab.

Murphy, A. B., & Uhrlandt, D. (2018). Foundations of high-pressure thermal plasmas. *Plasma Sources Sci. Technology 27*.

Sawant, Y., Pathare, K., Patel, R., & Choughule, P. (2021). Nanofluids with recent application & future trends. *International Journal of Innovations in Engineering Research and Technology, 8* (6). 458–468.

Yuming, W., Junjie, H., & Yanwei, S. (2013). Spheroidization of Nd-Fe-B powders by RF in-duction plasma processing. *Materials Science, 42*, 1810-1813.

Author Information

David Gelenidze
E. Andronikashvili Institute of Physics
6, Tamarashvili St. 0186, Tbilisi, Georgia.
Contact e-mail: *david.gelenidze@tsu.ge*

Gela Gelashvili
E. Andronikashvili Institute of Physics
6, Tamarashvili St. 0186, Tbilisi, Georgia.

To cite this article:

Gelenidze, D. & Gelashvili, G. (2023). Small-size nanoparticles and nanofluids fabrication via plasma arc. *The Eurasia Proceedings of Science, Technology, Engineering & Mathematics (EPSTEM), 26*, 474-480.

The Eurasia Proceedings of Science, Technology, Engineering & Mathematics (EPSTEM)
ISSN: 2602-3199

The Eurasia Proceedings of Science, Technology, Engineering & Mathematics (EPSTEM), 2023

Volume 26, Pages 481-490

IConTES 2023: International Conference on Technology, Engineering and Science

Real-Time Structural Damage Detection Using EMI under Varying Load a and Temperature Conditions

Djemana Mohamed
National Higher School of Technology and Engineering

Meftah Hrairi
International Islamic University Malaysia

Abstract: Structural Health Monitoring (SHM) is a critical aspect of maintaining the safety and integrity of infrastructure. In recent years, there has been a significant shift towards adopting innovative techniques, and one of the most promising methods is Electromechanical Impedance (EMI). EMI involves the utilization of piezoelectric transducers to assess the health of structures in real-time by examining changes in their electrical characteristics. The presence of load causes a change in structural stiffness, which alters the resonant characteristics of the structure. Understanding how external factors like load and temperature influence the electrical impedance of these sensors is essential for its reliable application in damage detection. This article presents an experimental and numerical study to investigate the effects of load and temperature on the electrical impedance of a piezoelectric sensor used in the electromechanical impedance (EMI) technique. The experimental setup uses an impedance analyzer (Agilent 4294A model) to measure the in-situ EMI of piezoelectric wafer active sensors (PWAS) attached to the monitored structure. The numerical model uses ANSYS software to simulate an aluminum beam at varying temperatures. The results show that the load and temperature have a significant effect on the impedance of the transducer. However, it is shown that it is still possible to detect damage using EMI even under varying load and temperature conditions. The results also show that the accuracy of EMI-based damage detection can be improved by using temperature and load compensation techniques.

Keywords: Structural health monitoring, Electromechanical impedance, Piezoelectric sensor, Load detection, Temperature compensation.

Introduction

Structural health monitoring (SHM) is the process of assessing the structural integrity of a structure. SHM can be used to detect damage at an early stage, which can help to prevent catastrophic failure. Electromechanical impedance (EMI) is a promising SHM technique that uses piezoelectric transducers to measure the electrical impedance of a structure. EMI is based on the principle of electromechanical coupling, which is the conversion of electrical energy into mechanical energy and vice versa.

EMI SHM systems typically consist of a network of piezoelectric transducers bonded to the structure. The transducers are used to measure the impedance of the structure at various frequencies. Changes in the impedance of the structure can indicate damage. EMI SHM systems can be used to monitor a variety of structures, including bridges, buildings, and aircraft (Balouchi et al., 2019).

Electromechanical impedance (EMI) is a non-destructive evaluation (NDE) technique that can be used to detect damage in structures. EMI works by measuring the electrical impedance of a piezoelectric sensor bonded to the

structure. When damage is present, it changes the stiffness of the structure, which in turn changes the impedance of the sensor.

EMI is a particularly promising technique for structural health monitoring (SHM) because it is sensitive to small changes in damage and can be used to monitor structures in real time. However, EMI measurements can be affected by environmental factors such as load and temperature. Under varying load, the stiffness of a structure can changes, which can affect the EMI readings. This can make it difficult to distinguish between damage and load-induced changes. Similarly, temperature can also affect the stiffness of a structure and the EMI readings. Researchers are developing new techniques to compensate for the effects of load and temperature on EMI measurements. Furthermore, EMI technique has undergone continuous enhancement in recent decades, driven by its appealing characteristics. This method is known for its cost-effectiveness, lightweight nature, noninvasiveness, and its capacity to self-actuate and sense (Zou et al., 2021, 2023).

The effect of temperature and load on the fatigue behavior of steel was investigated by conducting fatigue tests on smooth and notched specimens at different temperatures and load levels. The results showed that the fatigue life of steel decreased with increasing temperature and load level. The fatigue crack growth rate increased with increasing temperature and load level. The fatigue failure mode changed from ductile to brittle with increasing temperature and load level (Wang et al., 2022). The effect of temperature and load on the fracture behavior of concrete was investigated by conducting fracture tests on concrete specimens at different temperatures and load levels. The results showed that the fracture toughness of concrete decreased with increasing temperature and load level. The fracture mode changed from ductile to brittle with increasing temperature and load level (Li et al., 2020). The effect of temperature and load on the creep behavior of polymers was investigated by conducting creep tests on polymer specimens at different temperatures and load levels. The results showed that the creep strain of polymers increased with increasing temperature and load level. The creep rate of polymers increased with increasing temperature and load level (Zhou et al., 2021). developed a damage detection system for aluminum plates using EMI signature monitoring under variable temperature conditions. They found that the EMI signature of a damaged plate is different from the EMI signature of an undamaged plate, even under variable temperature conditions. (Hu et al., 2022) investigated the temperature effect on EMI-based damage detection of aluminum plates with cracks. They found that the temperature effect on the EMI signature of a cracked plate is significant. (Liu et al., 2020) developed a temperature-compensated EMI-based damage detection system for aluminum plates with cracks. They found that their temperature-compensated EMI-based damage detection system was able to accurately detect cracks in aluminum plates under variable temperature conditions.

EMI-based SHM under varying load and temperature conditions is a challenging but promising area of research. By developing new compensation techniques, researchers are making it possible to use EMI to monitor a wide range of structures in real time and to detect damage early, before it leads to failure. This paper makes significant contributions to the field of structural engineering by addressing the intertwined challenges of temperature effects on structural materials and the early detection of small damages in aluminum beams. Our work not only advances the theoretical knowledge in this area but also offers practical solutions with real-world implications, ultimately promoting the safety and longevity of critical structures.

Principle of the Electromechanical Impedance Technique

Electromechanical impedance (EMI) is the measurement of the electrical impedance of a structure under dynamic loading. EMI is based on the principle of electromechanical coupling, which is the conversion of electrical energy into mechanical energy and vice versa. Piezoelectric transducers are used to measure EMI. Piezoelectric transducers are materials that generate an electric charge when they are subjected to mechanical stress.

EMI measurements can be used to monitor the structural health of a variety of structures, including bridges, buildings, and aircraft. EMI SHM systems typically consist of a network of piezoelectric transducers bonded to the structure. The transducers are used to measure the impedance of the structure at various frequencies. Changes in the impedance of the structure can indicate damage (Balouchi et al., 2019). The change is sensed electrically through changes in the apparent EMI of the piezoelectric transducer that is coupled to the host structure and is defined by

$$Z(\omega)=\left[i\omega C\left(1-k_{31}^{2}\frac{Z_{str}(\omega)}{Z_{PZT}(\omega)+Z_{str}(\omega)}\right)\right]^{-1}$$

Where Z(ω) is the equivalent electro-mechanical admittance as seen at the PZT transducer terminals, κ_{31} is the electro-mechanical cross coupling coefficient of the PZT transducer($\kappa_{31}=d_{13}/\sqrt{\bar{s}_{11}\bar{\varepsilon}_{33}}$), $_C$ is the zero-load capacity of the PZT transducer, Z_{str} is the impedance of the structure, and Z_{PZT} is the impedance of the PZT transducer (Giurgiutiu & Rogers,1998). The piezoelectric sensor-actuators (wafer transducers) are closely bonded to the structure, and their EMI variation is measured across a wide frequency spectrum located in the high kHz band of frequencies. The transducer frequency response, phase, and amplitude, the impedance response (both real and imaginary), and other significant physical parameters act as indicators of potential structure damage and reflect the level of structural integrity. The transducer approach has proven most effective in the ultrasonic range of frequencies, where changes in local dynamics due to the initiation of damage within the structure are captured. Changes at this nascent stage are very small and have minimal effect on the global dynamics of the structure, making them difficult to detect with traditional low frequency vibration techniques (Liu & Giurgiutiu,2007).

Methodology

Experimental Setup

In this section, a series of experiments were conducted using a structure made of aluminum alloy 1100, which had measurements of 500 mm in length, 30 mm in width, and 1 mm in thickness. Additionally, a PIC151 PZT patch, sized at 10 mm × 10 mm × 1 mm, was bonded 20 mm from the specimen's end. The electric impedance spectra of the sensor were examined employing the Agilent 4294A impedance analyzer. The frequency range of 18.5–20.5 kHz was determined based on the presence of piezoelectric resonance peaks observed in the impedance spectra. Figure 1 shows the experimental setup.

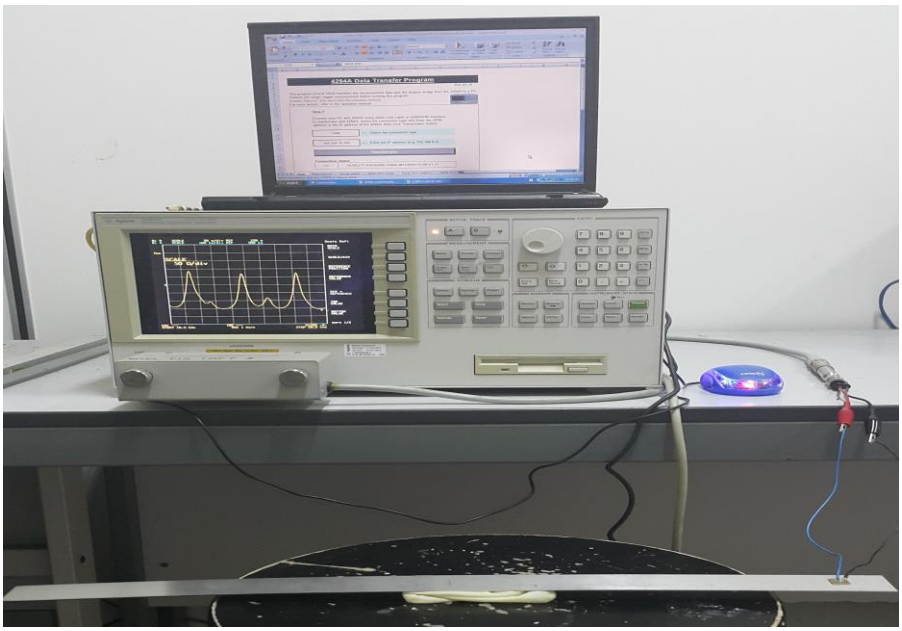

Figure 1. Experimental setup

Finite Element Analysis

Numerical simulation plays a pivotal role in understanding the intricate behavior of complex systems, and our approach involves harnessing the capabilities of ANSYS software to create a detailed model of a piezoelectric (PZT) patch bonded onto an aluminum beam. Within this simulation framework, we employed the versatile three-dimensional (3D) 20-node parabolic SOLID226 element to encapsulate the structural and piezoelectric properties of our system. SOLID226 stands out as an exceptional element within ANSYS due to its status as a coupled-field element. This element is not limited to just mechanical properties; it extends its influence across the domains of thermoelectric, piezoresistive, and piezoelectric phenomena. This unique combination of attributes within SOLID226 allows us to comprehensively capture the intricate interactions between the aluminum beam and the bonded PZT patch. Consequently, it empowers us to investigate a wide array of

complex responses, making it a valuable tool in our quest to understand and optimize the behavior of such systems. The model is presented in Figure 2.

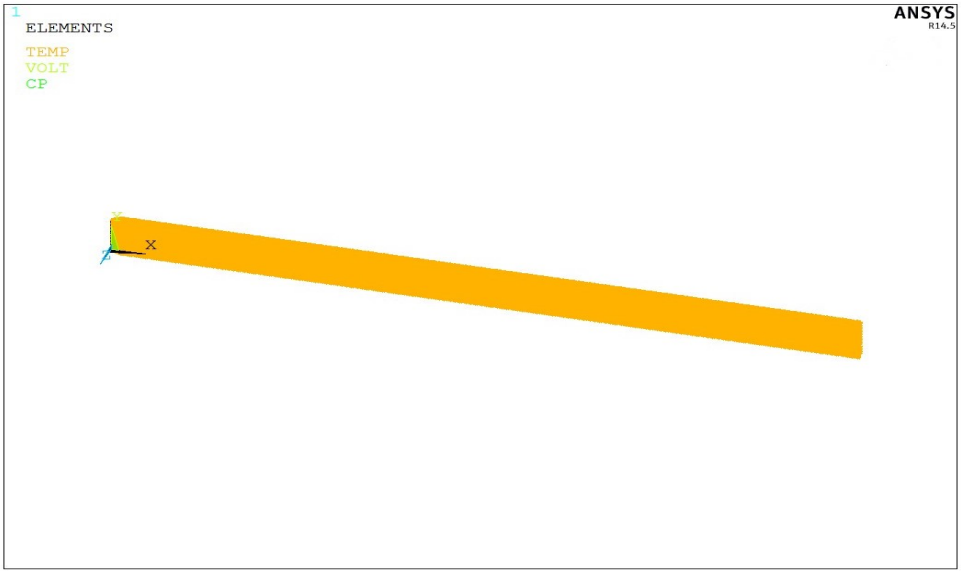

Figure 2. Aluminum beam with the PZT patch and the small steel nut

To generate frequency plots of electromechanical impedance, multiphysics harmonic analyses were performed on an elaborated finite element model with a 1V alternating voltage applied to one of the PZT electrodes. The simulation was extended to include a temperature effect, as temperature variation can affect the host structure properties, the PZT itself, and the bonding layer. This holistic approach allows us to explore the complex and interconnected interactions between electrical, mechanical, and thermal factors in the system, providing valuable insights into its behavior under different temperature conditions. To evaluate the reliability and precision of the finite element model proposed in this study, a validation process was conducted drawing upon experimental results for comparison. Figure 3 shows comparison of real part of impedance between the simulation and experimental results.

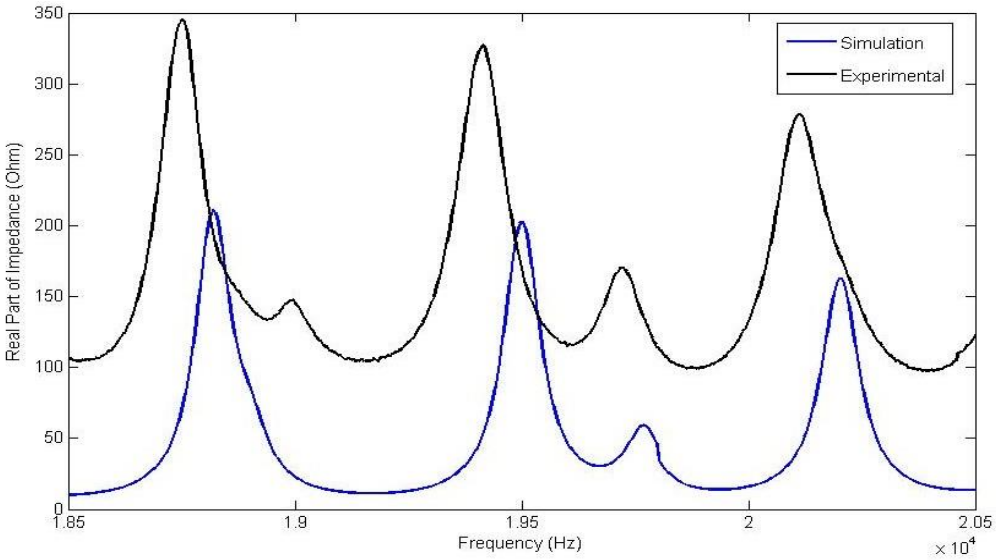

Figure 3. Aluminum beam with the PZT patch and the small steel nut

It is worth noting that the only noticeable deviation in the results was in the form of an upward shift in the experimental data, which can be attributed to the presence of a resistor, as previously documented by Djemana, et al. (2016) This validation procedure stands as a pivotal step in establishing the trustworthiness and appropriateness of the proposed finite element model for effectively simulating and analyzing the behavior of the studied system.

Results and Discussion

Temperature Effect

To thoroughly understand the effect of temperature on the electromechanical impedance (EMI) of aluminum beams, we conducted a systematic series of experiments, applying varying temperature conditions from 27 to 50°C. Figure 4 shows the real part of the EMI signatures for the aluminum beam at different temperatures, at frequencies from 18.5 to 20.5 kHz. This dataset provides a valuable resource for assessing the complex relationship between temperature variations and EMI characteristics of aluminum beams, shedding light on the material's behavior under a range of thermal conditions.

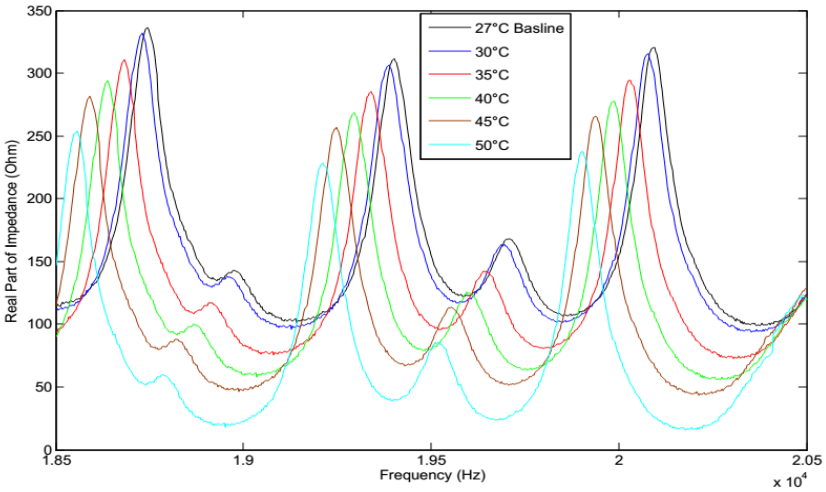

Figure 4. Aluminum beam with the PZT patch and the small steel nut

Figure 4 shows that temperature affects the EMI signature of the aluminum beam, shifting it to the left as temperature increases. This is due to the beam becoming less stiff at higher temperatures. The graph also shows some variation in electrical resistance and vertical shifts in the EMI signature.

Load Effects on EMI

Load is one of the problems occurring to moving components. When small metal particles get attached to the main rotating shaft of these sensitive structures, the changes of the modes of vibration or other negative effects on the working principles can seriously damage the total system. Structural load was induced in the structure by placing a small steel nut with dimensions of 8mm ×6mm×2mm and a mass of 0.6 g at different position from the sensor. The mass loadings of the monitored structure were approximately 14.56%. Figure 5 (a) shows the aluminum beam with the PZT patch and the small steel nut and (b) experimental result for real part of impedance for load attached to a structure. The mass loading produced variations in the mechanical impedance of the structure and could consequently be related to the structural load.

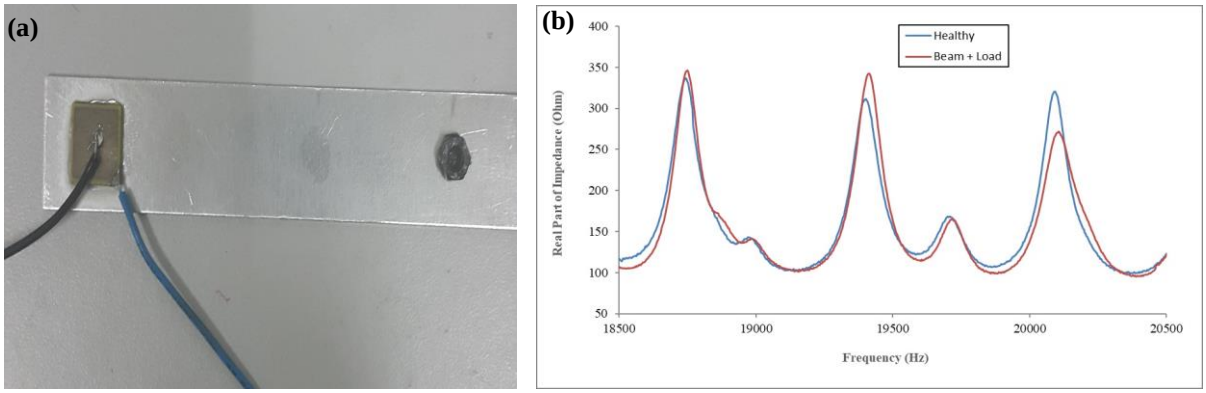

Figure 5. (a) Aluminum beam with the PZT patch and the small steel nut, (b) Real Part of impedance for Load attached to a structure.

Figure 5 (b) shows that the impedance signal amplitude increases with load positioning, but the resonance frequency remains unchanged. This suggests that the overall stiffness of the system is constant. This finding warrants further in-depth investigation.

Co-existence of Load and Temperature

During this part, in order to model more realistic cases and to prove that EMI systems can discover these problems, it was attempted to combine load and temperature damage at the same time. The model was then developed and compared. Apparently, it has the small nail-head with dimensions of 8 mm ×6 mm×2 mm and a mass of 0.6 g and it is then applied by bonding it at a distance of 100 mm from the sensor. The experimental results of real part of impedance can be seen in Figure 6. It depicts the different signals generated by the load and temperature attributed on the beam and the healthy beam.

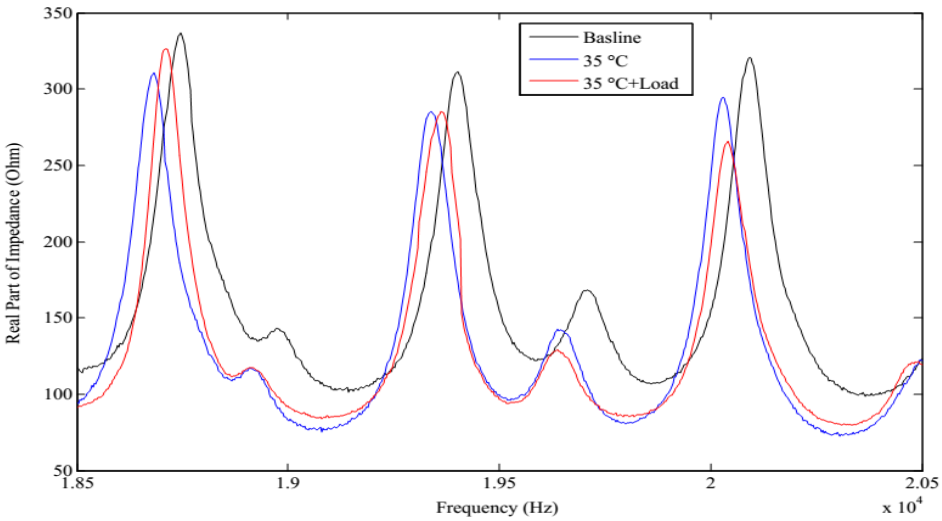

Figure 6. Real part of the electromechanical impedance resulting from temperature changes

Due to the beam signal with the load and temperature co-existence, the amplitudes increase in some frequencies for the electromechanical signature (as seen in Figure 2). However, it is also shifting to the left as the load influences the signal and it gets slightly eased compared to the data with temperature signal. Variations in the electrical resistance and some vertical shifts are also observed.

Compensation Technique

Detecting small damage within a structure becomes notably challenging when temperature variations are introduced into the equation. The reason behind this difficulty lies in the fact that temperature fluctuations can induce changes in the material's mechanical and electrical properties, often overshadowing the subtle signs of early damage. These variations can create a dynamic environment where distinguishing between the effects of temperature and actual structural damage becomes a formidable task. However, to overcome this challenge, a promising solution lies in the application of compensation techniques. These techniques are designed to account for the influence of temperature and isolate the genuine indicators of damage. By utilizing advanced algorithms and sensor networks, compensation techniques enable the identification of even minor structural changes with a high degree of accuracy, offering a practical and reliable means of damage detection within the presence of fluctuating thermal conditions. In doing so, they empower engineers and researchers to enhance the safety and longevity of critical structures and components.

Koo et al. (2009) improved on the Park & Kabeya (1999) method by creating an effective frequency shift (EFS) that countered temperature variations. (Sun et al.1995) compensated for the variations in signatures with a cross-correlation concept. Our approach is instead similar to a previous study (Sun et al.,1995) where similarities in two signals, the updated signatures and the baseline, are revealed to compensate for the frequency shifts. The compensation process involves the application of mathematical equations that can effectively neutralize or reduce the impact of temperature on the measured electromechanical impedance (EMI) signals.
The cross correlation R_{xy} of two signals x (t) and y (t) is defined by.

$$R_{xy}(\tau) = \lim_{T\to\infty} \frac{1}{T} \int_0^T f_x(t) f_y(t+\tau) dt$$

where $f_x(t)$ is the magnitude of the signal at point x, at time t, and $f_y(t+\tau)$ is the magnitude of the signal at a pointy at time $t+\tau$. By varying, the relationship between the signals at x and y as a function of time is obtained. The following definition applies for sampled signals:

$$R_{xy}(m) = \frac{1}{N} \sum_{n=1}^{N-m+1} x(n) y(n+m-1)$$

m=1, 2, 3,.., N+1

Figure 7 shows the results of the compensation technique for real part of impedance signatures.

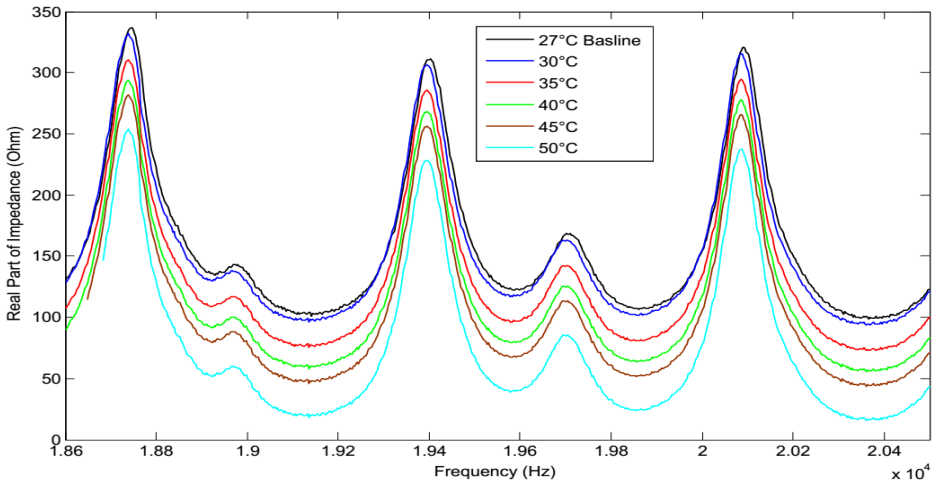

Figure 6. Experimental results for real part of impedance signatures with the proposed compensation method for the temperature effects

In Figure 7, the results of the compensation technique are vividly illustrated. When compared to Figure 4, which lacks the compensation, it is evident that this technique has effectively minimized the influence of temperature variations on the electromechanical impedance (EMI) signature. The primary objective of implementing the compensation method was to eliminate the occurrence of false positive damage detection in healthy structures. By essentially subtracting the temperature-induced variations, the EMI signature of the structure is rendered consistent across different temperature conditions, allowing for a more accurate assessment of structural damage.

The compensation technique was applied across a range of cases, each corresponding to temperatures within the previously mentioned range of 27 to 50°C, with a baseline acquired at 27°C. These results are instrumental in pinpointing the frequencies that exhibit variations due to structural damage rather than temperature effects. By isolating and emphasizing these frequencies, the compensation technique greatly enhances the precision and reliability of damage detection, even in environments where temperature fluctuations are inherent.
The correlation coefficient is the basis for the second index, CCDM, and is calculated by:

$$CCDM = 1 - C_C$$

Where CC is the correlation coefficient calculated using the real part of the electrical impedance signatures for the structure under healthy and damaged conditions, as defined before, in the same frequency range. It's calculated using the following equation

$$C_C = \frac{\sum_{k=\omega_1}^{\omega_F} \left[Z_{E,H}(k) - \bar{Z}_{E,H}\right]\left[Z_{E,D}(k) - \bar{Z}_{E,D}\right]}{\sqrt{\sum_{k=\omega_1}^{\omega_F} \left[Z_{E,H}(k) - \bar{Z}_{E,H}\right]^2} \sqrt{\sum_{k=\omega_1}^{\omega_F} \left[Z_{E,D}(k) - \bar{Z}_{E,D}\right]^2}}$$

Where the subscripts *D* and *H* indicate damaged and healthy conditions, respectively $(Z_{E,D}(k))$ and $R_E(Z_{E,H}(k))$ are the real parts of the electrical impedance signatures acquired by the measurement system of the structure's damaged and healthy states, respectively. The range of frequency *k* is measured between the initial and final frequencies. We use the real part of the impedance because it is known to be more reactive to damage or changes in the structure's integrity, and less sensitive to ambient temperature changes compared to the imaginary part (Djemana et al., 2022).

The shift profile derived from the compensation technique is a valuable tool for assessing the Cross-Correlation Damage Metric (CCDM) index, especially when it comes to distinguishing genuine load-induced variations from temperature effects. The CCDM index is chosen for this purpose due to its unique sensitivity to the shape of the electromechanical impedance (EMI) signature rather than variations in its electrical impedance amplitude.

The reason for selecting the CCDM index lies in its inherent insensitivity to changes in the electrical impedance amplitude. This attribute aligns perfectly with the objective of isolating and quantifying the influence of temperature-induced EMI variations. By focusing on the shape of the impedance signature, the CCDM index can effectively differentiate the alterations caused by changes in temperature conditions from those due to structural loads or damage.

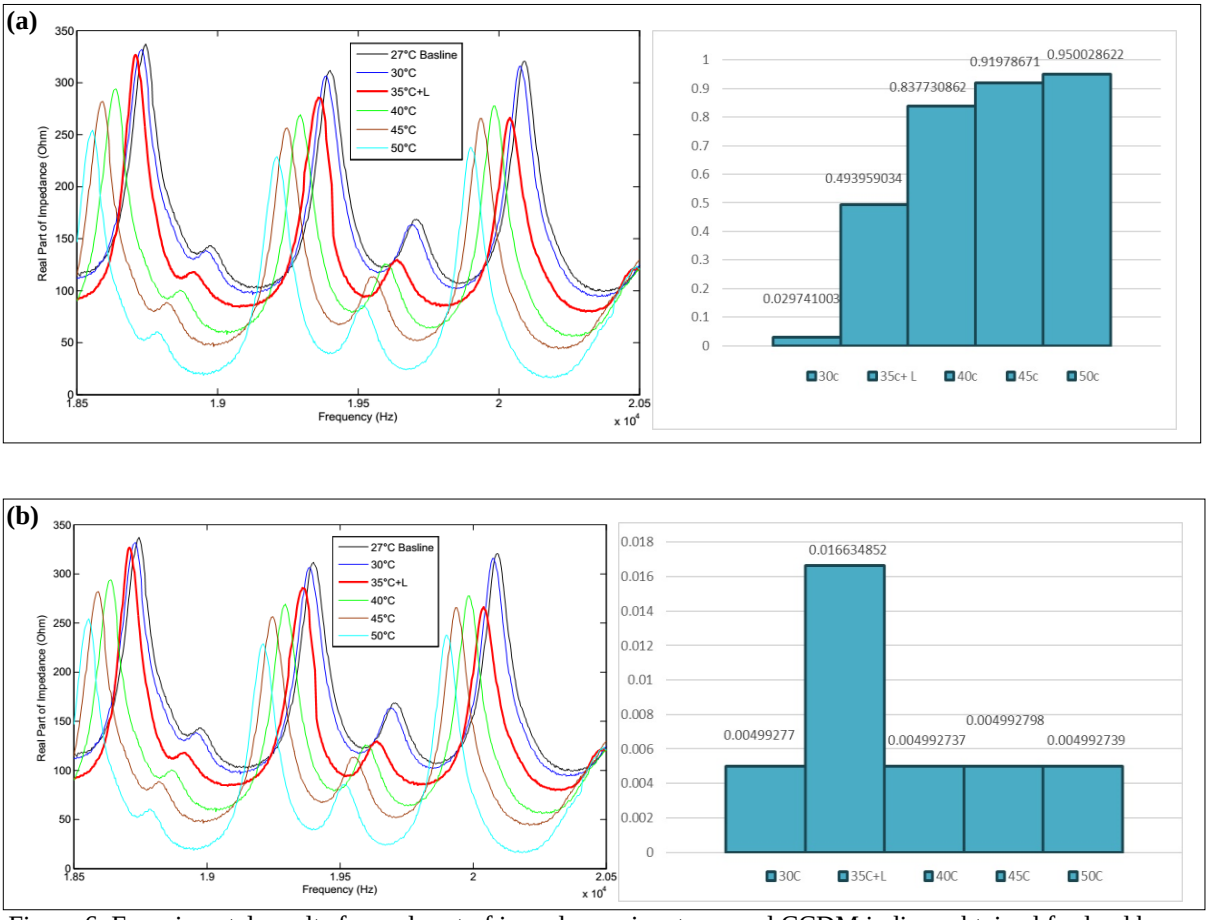

Figure 6. Experimental results for real part of impedance signatures and CCDM indices obtained for load beam (a) structure with load at 35°C without compensation and (b) with the proposed compensation method for the temperature effects.

Part (a) of the Figures vividly illustrates the challenge posed by temperature-induced ambiguities when it comes to diagnosing structural damage(load). At a temperature of 35°C, the electromechanical impedance (EMI) signatures for damaged and healthy specimens exhibit remarkable similarity, making it exceptionally difficult to discern and diagnose damage accurately under these conditions.

However, as depicted in part (b) of the Figures, the application of the compensation technique is transformative. This method substantially enhances the clarity of the results, effectively eliminating the shifts in the signatures induced by temperature fluctuations. The result is EMI signatures with peaks aligned perfectly with the baseline

reference. Additionally, the Cross-Correlation Damage Metric (CCDM) indices at 35°C register as notably low, suggesting the potential for detecting even smaller damage provided that the metric index threshold is appropriately set. Importantly, these positive outcomes are consistent across the entire temperature range, including the upper limit.

The introduction of a temperature compensation technique is pivotal in this context, as it serves to measure the precise impact of temperature variations and eliminates the inherent ambiguity in the results stemming from these thermal fluctuations. Such an approach is considered indispensable for enabling real-time health monitoring of structures operating in real-world conditions.

Temperature effects remain paramount concerns in the realm of electromechanical impedance (EMI) structural health monitoring, particularly when it comes to the detection of incipient or small damage. The development and implementation of effective compensation techniques emerge as key drivers for advancing the capabilities of EMI-based structural health monitoring systems. These techniques are instrumental in ensuring the reliability and accuracy of damage detection processes under varying thermal conditions, fostering the continued evolution of this field.

Conclusion

In our experimental model, we investigated the temperature sensitivity of electrical impedance signatures in a conventional PZT sensor used for Structural Health Monitoring (SHM). We focused on an aluminum beam subjected to a range of temperatures and found that the PZT sensor's dynamic response changed significantly. These temperature-induced variations were substantial enough to potentially lead to false positive damage detections, such as notches or applied loads, even when no damage was present. This raises concerns about the structural integrity of systems monitored using PZT sensors under variable temperature conditions.To address this challenge, we developed a temperature compensation technique that precisely measures and eliminates the ambiguity caused by temperature-induced effects. Such compensation techniques are essential for real-time SHM of structures operating in real-world conditions.

Temperature effects remain a critical concern in EMI-SHM, especially for early or subtle damage detection. Effective compensation techniques are linchpins for the ongoing development and refinement of EMI-SHM systems, ensuring accurate and reliable damage detection under variable thermal conditions. These techniques are pivotal in advancing the field of EMI-SHM.

Recommendations

Advanced Data Analytics: Suggest the use of advanced data analytics techniques, such as machine learning and artificial intelligence, to enhance real-time damage detection capabilities. Encourage researchers to explore these approaches. Load-Induced Damage Thresholds: Define load-induced damage thresholds specific to different structural materials and types of damage. These thresholds can serve as reference points for assessing structural health.

Scientific Ethics Declaration

The authors of this article, published in the EPSTEM journal, solemnly affirm our unwavering dedication to upholding the highest scientific, ethical, and legal standards in the conduct and dissemination of our research. We recognize our responsibilities as researchers, not only to advance knowledge but also to do so with integrity and in compliance with established ethical and legal guidelines.

Acknowledgements or Notes

* This article was presented as a poster presentation at the International Conference on Technology, Engineering and Science (www.icontes.net) held in Antalya/Turkey on November 16-19, 2023.

* This research was funded by a grant from International Islamic University Malaysia Research Management Grant [grant number/project id: RMCG20-032-0032].

* Laboratory of Energy Systems Technologies (LTSE). National Higher School of Technology and Engineering, Annaba, Algeria

References

Balouchi, S., Khaleghian, S., & Gholipour, A. (2019). Electromechanical impedance (EMI) technique for structural health monitoring: A review. *IEEE Access, 7*, 174392-174413.

Djemana, M., & Hrairi, M. (2016). Modelling and simulation of impedance-based damage monitoring of structures. *Int. J. Simul. Model, 15*(3), 395-408.

Djemana, M., Hrairi, M., & Yatim, N. H. M. (2022). Improving Electromechanical Impedance Damage Detection Under Varying Temperature. *Journal of Advanced Research in Fluid Mechanics and Thermal Sciences, 92(*1), 123-133.

Giurgiutiu, V., & Rogers, C. A. (1998). Recent advancements in the electromechanical (E/M) impedance method for structural health monitoring and NDE. In *Smart structures and materials 1998: Smart structures and integrated systems* (Vol. 3329, pp. 536-547). SPIE.

Hu, K., Lin, X., Chen, H., & Liu, Y. (2022). Temperature effect on electromechanical impedance-based damage detection of aluminum plates with cracks. *Mechanical Systems and Signal Processing, 173.*

Li, F., Wang, X., & Zhang, Q. (2020). *Effect of temperature and load on the creep behavior of polymers. Polymer Testing, 90*.

Liu, W., & Giurgiutiu, V. (2007). Finite element simulation of piezoelectric wafer active sensors for structural health monitoring with coupled-filed elements. *In sensors and smart structures technologies for civil, mechanical, and aerospace systems* (Vol. 6529, pp. 1144-1156). SPIE.

Liu, Z., Sun, Z., Wang, S., & Li, X. (2020). Temperature-compensated electromechanical impedance-based damage detection for aluminum plates with cracks. *IEEE Transactions on Instrumentation and Measurement, 70*, 1-10.

Wang, H., Yang, H., & Zhou, Y. (2022). Effect of temperature and load on the fracture behavior of concrete. *Journal of Materials Engineering and Performance, 31*(10), 8698-8711.

Zhang, Q., Chen, X., & Li, Y. (2023). Effect of temperature and load on the fatigue behavior of steel. *Engineering Fracture Mechanics, 270*.

Zhou, Y., Zhang, S., Wu, W., & Yan, Y. (2021). Damage detection for aluminum plate using electromechanical impedance method under variable temperature conditions. *Structural Health Monitoring, 20*(5), 1293-1312.

Zou, X., Li, B., & Dong, T. (2021). Structural damage detection using electromechanical impedance under varying load and temperature conditions: A state-of-the-art review. *Measurement Science and Technology, 32*(9).

Author Information

Djemana Mohamed
National Higher School of Technology and Engineering, 2000 pedagogical places Sidi Amar, Annaba, Algeria
Contact e-mail: *m.djemana@ensti-annaba.dz*

Meftah Hrairi
International Islamic University Malaysia
P.O. Box 10, 50728 Kuala Lumpur, Malaysia

To cite this article:

Mohamed, D., & Hrairi, M. (2023). Real-time structural damage detection using EMI under varying load and temperature conditions. *The Eurasia Proceedings of Science, Technology, Engineering & Mathematics (EPSTEM), 26*, 481-490.

The Eurasia Proceedings of Science, Technology, Engineering & Mathematics (EPSTEM)
ISSN: 2602-3199

The Eurasia Proceedings of Science, Technology, Engineering & Mathematics (EPSTEM), 2023

Volume 26, Pages 491-495

IConTES 2023: International Conference on Technology, Engineering and Science

Numerical Study of the Effect of the Ejection Angle on the Cooling Performance of a High-Pressure Gas Turbine

Aya Rehab-Bekouche
National Higher School of Technology and Engineering

Riyadh Belamadi
National Higher School of Technology and Engineering

Abstract: In modern gas turbines, the purge flow plays an important role in improving the performance of the gas turbine, as it is adapted against the problem of the ingestion of hot gases in the inter-disc cavity of the turbine. The performance of this purge flow is necessarily influenced by some geometrical and physical parameters. This paper presents a 3D numerical study on the influence of the ejection angle on the cooling performance in a high pressure transonic gas turbine with the presence of the cavity. Five inclination cavity angles are compared (ϕ = 30°, 45°,60°,75°and 90°) by using ANSYS Fluent, a steady flow Reynolds average Navier-Stokes equations are solved, and the turbulence model k-ω SST has been chosen based on comparison of the distribution of velocity and heat transfer convective coefficient with experimental results in a previous work. It was seen that that cooling is limited to the suction side because of the non-uniform pressure distribution of the main flow and the high pressure of the stagnation point. The optimal configuration was determined for an ejection angle of 30°.

Keywords: HP transonic gas turbine, 3D numerical study, Purge flow, Ejection angle, Cooling performance

Introduction

Today's gas turbines operate under extreme operating conditions to maximise efficiency, such that the temperature of the exhaust gases at the combustor outlet and turbine inlet exceeds 2000 K (Arts et al., 1997). Cooling air is extracted from the compressor to cool hot gas path components, such as end walls, blades and their tips using internal and film cooling, and other hot components such as the inter-disk cavity using purged air. In the turbine inter-disc cavity, a rim seal is installed between the stator and the adjacent rotor disc to prevent or at least dilute the ingress of hot main flow gases to a tolerable level which has two main causes: the pumping effect (rotationally-induced ingestion (RI)) and the non-axisymmetric pressure distribution in the annulus (externally-induced ingestion (EI)) (Gräf,., & Kleiser, 2014). The interaction between the channel flow (the purged flow) and the main flow produces an additional aerodynamic loss and a change in the thermal load distribution. This is why it seems necessary to analyse the interaction mechanisms of the flow from the inter-disc channel and to try to understand the origin of these significant losses. The article is carried out using ANSYS CFD software, it aims to clarify the effect of the ejection angle on the cooling performance in the high-pressure turbine rotor with the presence of a cavity, through analysis of the cooling efficiency contour and streamlines on different sections, and the maximum cooling efficiency values for different angles of inclination.

Computational Domain Mesh and Flow Conditions

The computational domain mesh is generated in Gambit using a multi-block topology and is illustrated in Figure 1. The domain is divided into 25 blocks and each block supports a structured mesh. The mesh resolution is very

fine and consists of 1.7×10^6 elements. The walls were resolved using structured boundary layers consisting of 15 elements normal to the passage surfaces and 7 elements normal to the cavity surfaces. The maximum y + value is on the order of 5.

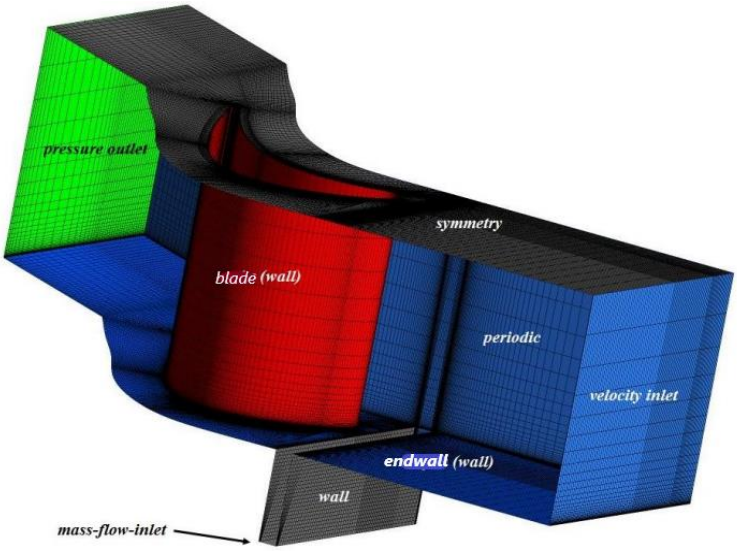

Figure 1. Calculation domain, boundary conditions and mesh

The boundary conditions are imposed as follows: at the main flow inlet, a velocity of 70 $m.\ s^{-1}$ is imposed with an angle of incidence of i = -5 °, a turbulence intensity of 5% and a warm static temperature of 1200 ° C. At the outlet, a relative static pressure of zero is imposed over the entire surface. For all walls, the non-slip and adiabatic condition is applied. At the entrance to the cavity, the mass-flow-inlet condition was imposed. At the same locations, a cooling temperature of 650°C was applied with a low turbulence intensity of 1%.

The Effect of Slot Inclination on Cooling Efficiency

In this section, we determine the influence of slot inclination on cooling efficiency (purge flow ejection angle $\boldsymbol{\phi}$) by setting slot width (E) to 4 mm and purge flow rate PF to 1%. Five ejection angles are studied $\boldsymbol{\phi}$ =30°, 45°,60°,75°,90° (Figure 2). Efficiency is analysed on the basis of the cooling efficiency parameter :

$$\boldsymbol{\theta} = (\boldsymbol{T_\infty} - \boldsymbol{T}) / (\boldsymbol{T_\infty} - \boldsymbol{T_p}) \quad (1)$$

Where $\boldsymbol{T_\infty}$ is the temperature of the main flow (hot flow), $\boldsymbol{T_p}$ is the temperature of the purge flow and $\boldsymbol{T}$ is the local temperature.

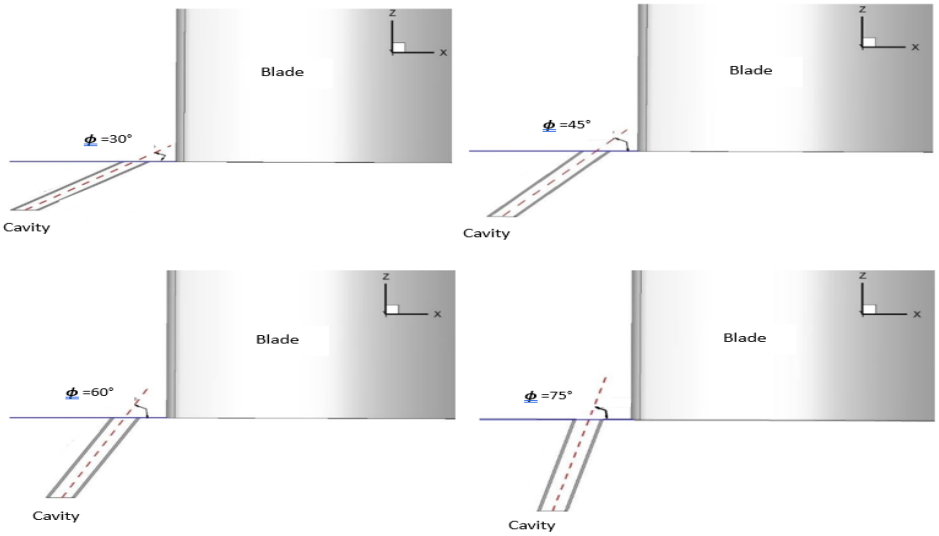

Figure 2. Geometry of the cavity

Results and Discussion

Figure 3 illustrates the cooling efficiency contours for all inclination angles, taking ϕ=90° a reference case. For all cases, film cooling is limited to the rotor's section side region, and approaches the leading edge slightly as the inclination angle becomes steeper, up to ϕ=30. All inclination angles provide superior cooling efficiency compared to the reference case. decreasing the inclination angle from 90° to 30° improves cooling efficiency by also increasing the area covered by the coolant as well as the uniformity of the coolant distribution particularly for ϕ=30°.

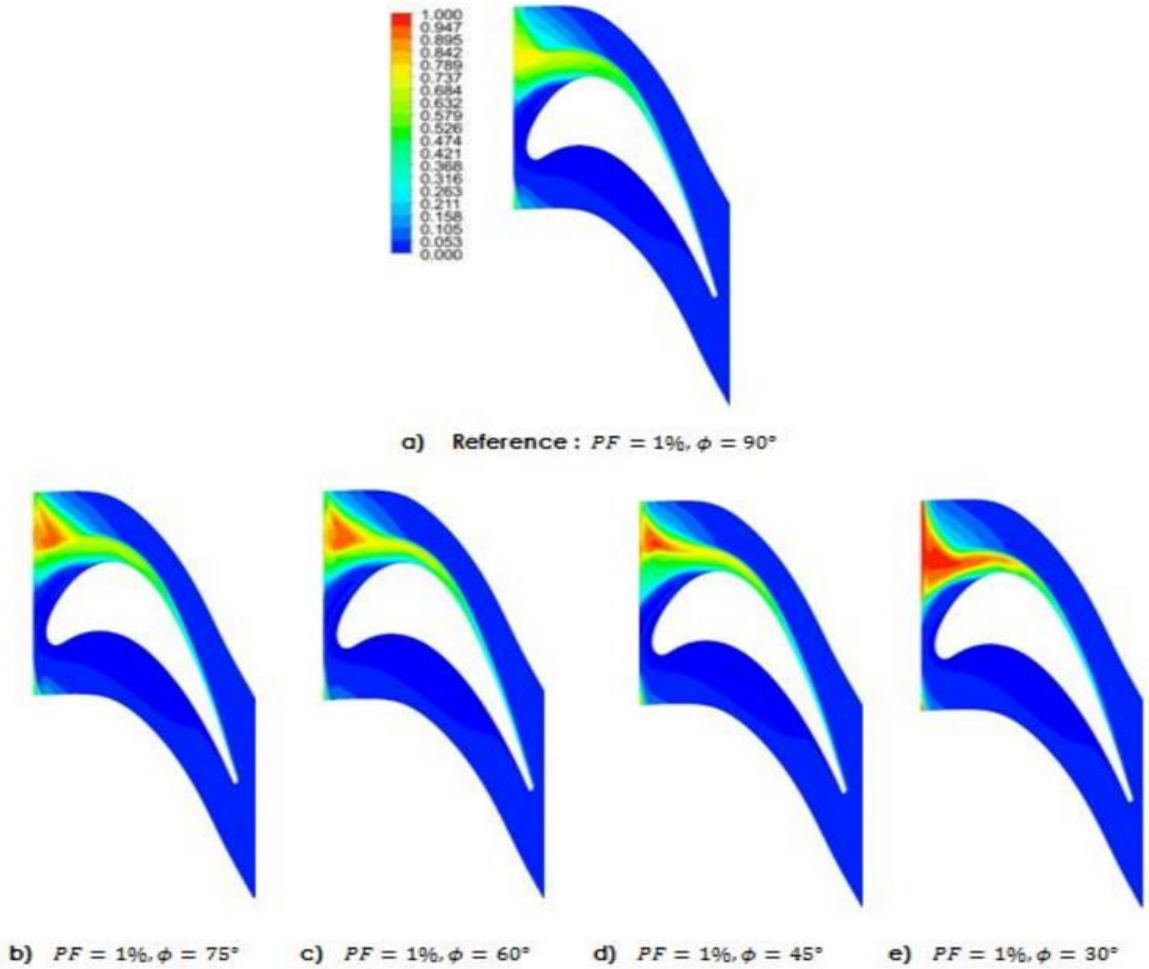

Figure 3. Contour of cooling efficiency

Figure 4 illustrates the cooling efficiency contour and streamlines on three sections for different angles of inclination. For all angles, significant differences can be found between the flow conditions of the three sections (plane 1, 2 and 3). This is due to the non-uniform pressure distribution of the main flow, as mentioned previously. For section 1 the phenomenon of main flow ingestion disappears for all angles of inclination, a more uniform distribution of film cooling efficiency is formed by decreasing the angle of inclination of the cooling fluid, and this phenomenon is particularly significant for ϕ = 45° et 30°. For section 3, the cooling efficiency is almost zero for all PF values. This is due to the high pressure of the main flow near the pressure side, where vortices are observed just downstream of the slot (return flow). The size of these vortices decreases as the angle of inclination becomes steeper.

In section 2, the main flow ingestion phenomenon can be observed, due to the high pressure at the stagnation point compared with other regions, which is responsible for the absence of a coolant ejection zone at the slot outlet shown in Figure 3. In addition, horseshoe vortices (HV) are observed downstream of the slot. Comparing the flow conditions in section 2 for the different angles of inclination, it is clear that the ingestion phenomenon is weakened and begins to disappear for ϕ = 45° et 30°.

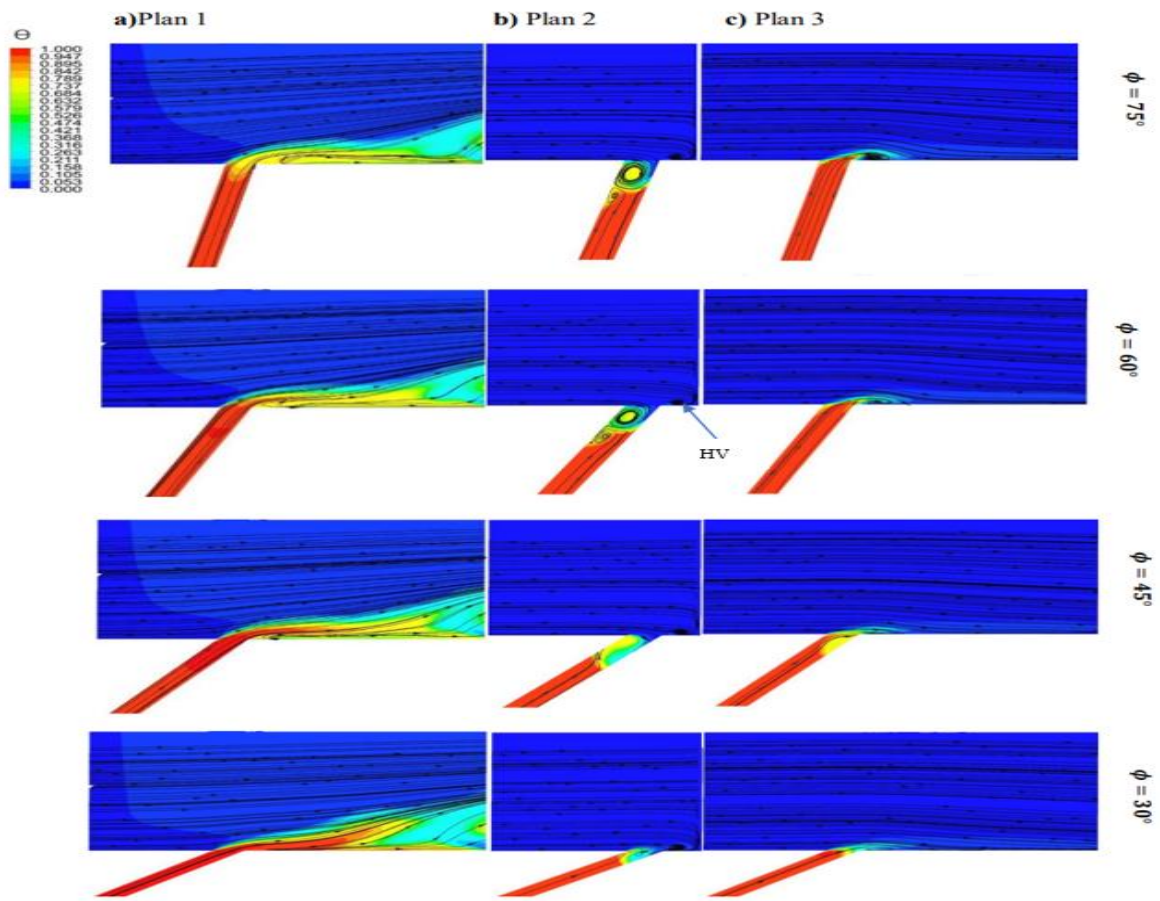

Figure 4. Cooling efficiency contour and streamlines on three sections

Figure 5 shows the maximum cooling efficiency values achieved for each angle of inclination. All the inclination cases studied give a higher cooling efficiency than the 90° reference case. The maximum θ obtained for each angle of inclination is 97.67% for an angle of 30°, 96.19% for 45°, 94.49% for 60°, 92.38% for 75° and 78.26% for 90°.The evolution of cooling efficiency is non-linear. It decreases from angle 30° to 90° with a relative difference of 1.51%, 1.76%, 2.23% and 15.28% respectively. In general, increasing the slot inclination angle has a negative effect on cooling efficiency. The best case inclination angle is 30°, with an improvement of 19.41% over the reference case.

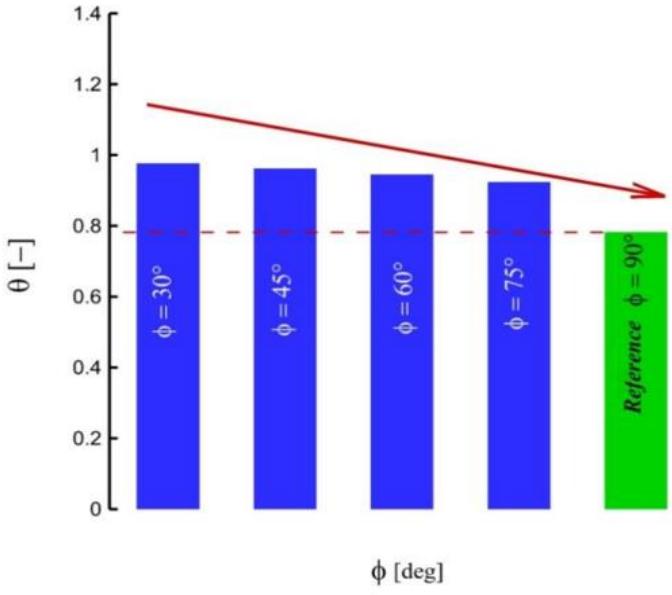

Figure 5. Maximum cooling efficiency at the hub

Conclusion

The study of the influence of the angle inclination of the cavity on the cooling efficiency is presented in this study. Five angles ($\boldsymbol{\phi}$ =30°, 45°,60°,75°,90°) were investigated with the coupled Navier-Stokes averaged equations for a stationary and incompressible 3-D flow using the k-ω SST turbulence model.
It was concluded that:

- Cooling is limited to the suction side because of the non-uniform pressure distribution of the main flow and the high pressure of the stagnation point.
- The influence of the angle of inclination is very important on the cooling performance around the blade and on the ingestion phenomenon near the zone facing the stagnation point, which is considerably weakened with the steepest angles of inclination.
- Cooling efficiency and uniformity of coolant distribution are improved by reducing the angle of inclination from 90° to 30°, such that the cooling efficiency increases by 19.41%. The optimum thermal design choice adopted for this study is 30°.

Scientific Ethics Declaration

The authors declare that the scientific ethical and legal responsibility of this article published in EPSTEM journal belongs to the authors.

Acknowledgements or Notes

* This article was presented as a poster presentation at the International Conference on Technology, Engineering and Science (www.icontes.net) held in Antalya/Turkey on November 16-19, 2023.

References

Arts, T., Duboue, J. M., & Rollin, G. (1997). Aero-thermal performance measurements and analysis of a two-dimensional high turning rotor blade. *American Society of Mechanical Engineers, 3. Vol. 78705, p. V003T09A013*

Gräf, L., & Kleiser, L. (2014). Film cooling using antikidney vortex pairs: effect of blowing conditions and yaw angle on cooling and losses. *Journal of Turbomachinery*, *136*(1), 011008.

Author Information

Aya Rehab-Bekouche
National Higher School of Technology and Engineering
Annaba- Algeria
Contact e-mail: *a.rehab-bekouche@ensti-annaba.dz*

Riyadh Belamadi
National Higher School of Technology and Engineering
Annaba- Algeria

To cite this article:

Rehab-Bekouche, A. & Belamadi, R. (2023). Numerical study of the effect of the ejection angle on the cooling performance of a high-pressure gas turbine. *The Eurasia Proceedings of Science, Technology, Engineering & Mathematics (EPSTEM), 26,* 491-495.

The Eurasia Proceedings of Science, Technology, Engineering & Mathematics (EPSTEM)
ISSN: 2602-3199

The Eurasia Proceedings of Science, Technology, Engineering & Mathematics (EPSTEM), 2023

Volume 26, Pages 496-506

IConTES 2023: International Conference on Technology, Engineering and Science

The Evaluation of the Impact of Road Width on Passenger Car Units (PCU) in Heterogeneous Traffic Conditions

Yasin Ahmed Addow
Near East University

Mustafa Alas
Near East University

Abstract: This study delves into the utilization of Passenger Car Units (PCU) as a pivotal metric for gauging the influence of diverse vehicle types on traffic flow. Focusing on the context of Mogadishu, data acquisition was conducted across eight key sections of major highways. Employing digital video recorders, the gathered data facilitated a comprehensive analysis of traffic dynamics, thereby enabling the computation of PCU values. The investigation unveiled a discernible trend wherein the traffic makeup, comprising bus, truck, light commercial vehicle (LCV), and car categories exhibited a positive correlation with carriageway width expansion. Nevertheless, the volume composition peaked notably in narrower carriageway widths. Concurrently, the speed of the aforementioned vehicle categories showcased a linear progression proportional to carriageway width augmentation. Intriguingly, PCU values assigned to motorcycles consistently undershot the figures stipulated in the Mogadishu Road Standards (MRS). Conversely, PCU values for bus, truck, and LCV categories consistently surpassed the MRS 2070 benchmarks. This scrutiny distinctly elucidated the intricate interplay between lane width and PCU values across distinct vehicle types, effectively underscoring the propensity of PCU values to escalate with escalating carriageway dimensions.

Keywords: Passenger car units, Road width, Traffic

Introduction

Mogadishu's road traffic is diverse, with cars, trucks, and other motorized vehicles of all shapes, sizes, weights, and horsepower using the same roadway. It is impossible to improve the condition of a road in very tiny steps, hence it is standard procedure to design and build new roads and upgrade projects to withstand the projected traffic in the future. This 20-year forward phase (perspective period) in Mogadishu requires that roads be built with the ability to handle the expected traffic flow by the time the project is finished (Hills, 2014).

Different vehicle classes have varying needs for road space, drive at varying speeds (for geometric design), and put various demands on the road's structure (for structural design). As a result, it's essential to construct a uniform traffic unit that can accommodate different vehicle kinds. The "Passenger Car Unit (PCU)" standard, which represents a typical car (passenger car), light van, or truck, is used to create the geometric layout of highways (Mohamed et al., 2023). Due to the fact that Mogadishu does not strictly adhere to the lane concept and cars frequently drive side-by-side, the purpose of the present study was to ascertain how road width affected traffic flow. In Mogadishu, the carriageway is the entire breadth of a road's paved surface, excluding its shoulders that can accommodate two lanes of traffic when there is mixed traffic (Nations, 2016).

This study acknowledges that real-life traffic situations are complicated and aims to provide results that are relevant to those situations. On this basis the current study attempted to fill the gap in the literature by

investigating how the width of the road, specifically the roadway width, affects traffic flow in a city with a diverse and mixed population like Mogadishu (Gani et al., 2014).

Method

Study Area

The study sites were chosen in order to meet the following criteria; (1) a segment of the road with variable width, traffic flow characteristics and all the types of vehicles needed for the investigation. (2) it's far from facilities like bus stations, which might slow down traffic. (3) the section is flat and straight. A total of 8 different sections illustrated in Figure 1 were studied within the above mentioned concept. These sections were namely; Bexani Karan, Ifkaxalane Xamarjadid, Bondhere Bondhere, Zoobe Wadajir, General Daud Sinay, Florenza Xariyale, Sayidka Howlwadaag and Jubba, Shibis.

Figure 1. Study area

Bexani, Karan road is 6.8 meters wide, it has a fine paved surface and both side shoulders are 3 meters wide. It is a section of the Bexani highway. There were no obstructions or encroachments. Ifkaxalane Xamarjadid is a 6.7 m wide section of the Ifkaxalane highway with a good asphalt surface. There were no obstructions or encroachments. Bondhere, Bondhere is a portion of the bondhere road with a paved surface and a width of 6.6 meters. There were no encroachments or impediments. Zoobe Wadajir is a piece of zoobe road with a paved surface and a width of 6.5 meters. General Daud Sinay is a portion of the general Daud Road with a 6.4 m road width and a nice paved surface. Florenza Xariyale is a portion of Florenza's road with a 6.1-meter road width and a decent paved surface. Sayidka Howlwadaag is a portion of the Sayidka road with a smooth paved surface and a road width of 5.8 meters. Jubba, Shibis is a road segment that runs from Jubba, Shibis, to Darjinka, Yaqshid, and has a 5.1 m road width with a decent paved surface. Details of the studies sections were given in Figures 2a-h respectively.

Data Collection and Extraction

The data collection method employed was video recording. On the road, a 20-meter-long longitudinal trap was constructed to monitor speed. A video camera was placed on the platform and raised high enough to capture the whole length of the trap with ample room on each side. During a typical workday, the camera was set to record for 4 to 5 hours. Additionally, specific measurements of the road width, shoulder width, and shoulder condition were taken.

Figure 2. Studied sections a) Bexani Karan b) Ifkaxalane Xamarjadid c) Bondhere Bondhere d) Zoobe Wadajir e) General Daud Sinay f) Florenza Xariyale g) Sayidka Howlwadaag h) Jubba Shibis

In the current study, the vehicles were split up into five separate groups which were bus, truck, LCV, cars and two wheelers. The dimensions of the vehicles observed in the video recordings were obtained from the supplier websites for each type of vehicles. According to AfDB (2016) typical dimensions of several categories were demonstrated in Table 1. With a precision of 0.1 s, the time shown on the video recording was used to calculate the average time it took for each kind of vehicle to complete the length of the trap. A minimum of 300 data points for each kind of vehicle were gathered at each site in order to establish the speed of a vehicle currently traversing the segment.

Table 1.The typical dimensions of several vehicle categories(AfDB, 2016)

Category	Vehicles included	Average dimension		Projected Area on Ground (m2)
		Length (m)	Width (m)	
Bus	Buses	11.12	2.49	27.74
Truck	Trucks	7.5	2.35	17.62
LCV	Minibus, mini truck, micro bus	6.10	2.10	12.81
Cars	Car, jeep, van	3.74	1.44	5.39
Two-wheeler	Scooters, motorcycles	1.87	0.64	1.2

Result and Discussion

Speed Distributions

The PCU factor is computed using the mean speed values of several vehicle types. In order to calculate this, the average speed of all other vehicle types were taken and subtracted from the average speed of passenger cars. In order to measure speed, a 20-meter-long longitudinal trap was constructed on the road. Following the recording

and viewing of the video on a large-screen television, data was gathered. A stopwatch was used to compute the average time each vehicle type took to complete the length of the trap, and the time was shown on the screen with an accuracy of 0.1 s. This time was used to calculate the speed at which a vehicle would pass through the segment. Table 2 below shows the average speed of various vehicles on various highway sections.

Table 2. Speed of different vehicles

Section Name	Speed of different vehicle (km/hr)				
	Bus	Truck	LCV	Car	Two-wheeler
Bexani	60.82	56.6	58.53	64.45	52.23
Ifkaxalane	60.18	55.77	57.87	63.48	51.97
Bondhere, Bondhere	60.29	58.79	56.34	61.9	50.7
Zoobe, Wadajir	57.95	54.46	55.94	60.90	50.30
General Daud, Sinay	57.66	53.49	55.19	59.62	49.56
Florenza, Xariyale	56.42	51.88	53.63	57.73	48.56
Howlwadaag	54.18	49.93	53.50	54.85	47.26
Jubba, Shibis	50.38	48.35	47.89	48.95	46.71

The analysis demonstrated that the vehicle speed across all categories rise linearly as road width increases. The investigation that was done to determine how carriageway width affected vehicle speed led to the formation of the following relationships:

For Bus

According to the study, bus speed increases linearly as carriageway width increases, as shown by the relationship Speed=5.958W + 21.30 with an R2 value of 0.986. The statically testing of regression shows the p-value below zero which proves the significance of derived relationship between speed and carriageway.

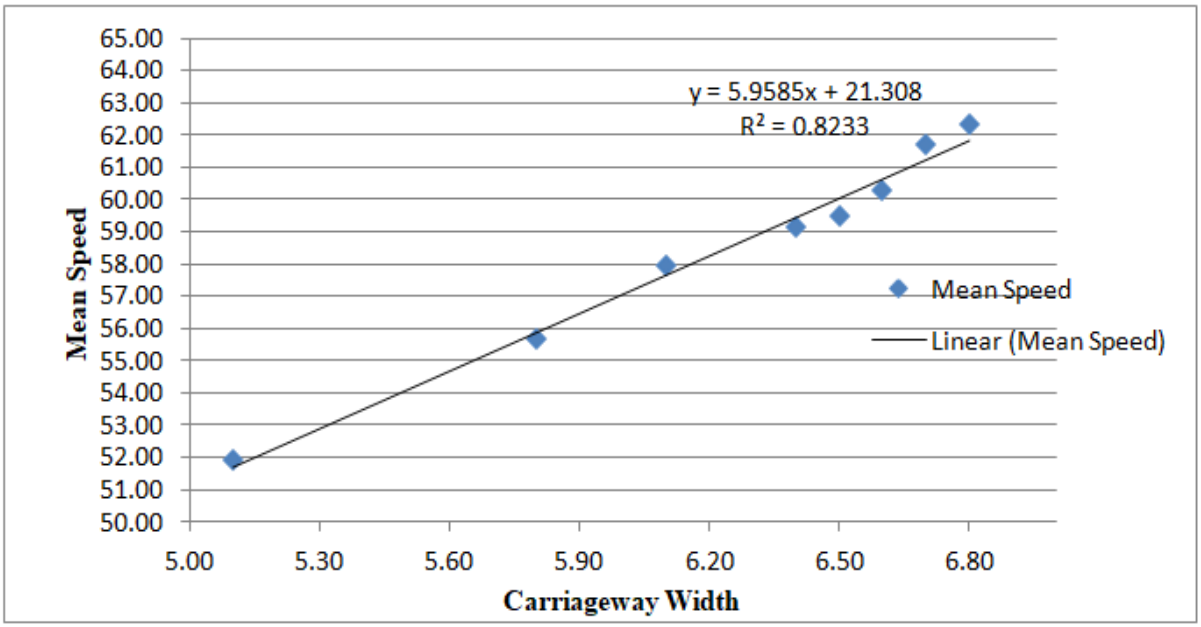

Figure 3. Bus; relationship of speed with carriageway width

For Truck

The study also demonstrated that the PCU values for the truck vehicle type have a linear connection and rely on the carriageway width, with Speed =5.012W+23.38 and an R2 value of 0.95. The statically testing of regression shows the P-value below zero which demonstrates the significance of derived relationship as presented in Figure 4.

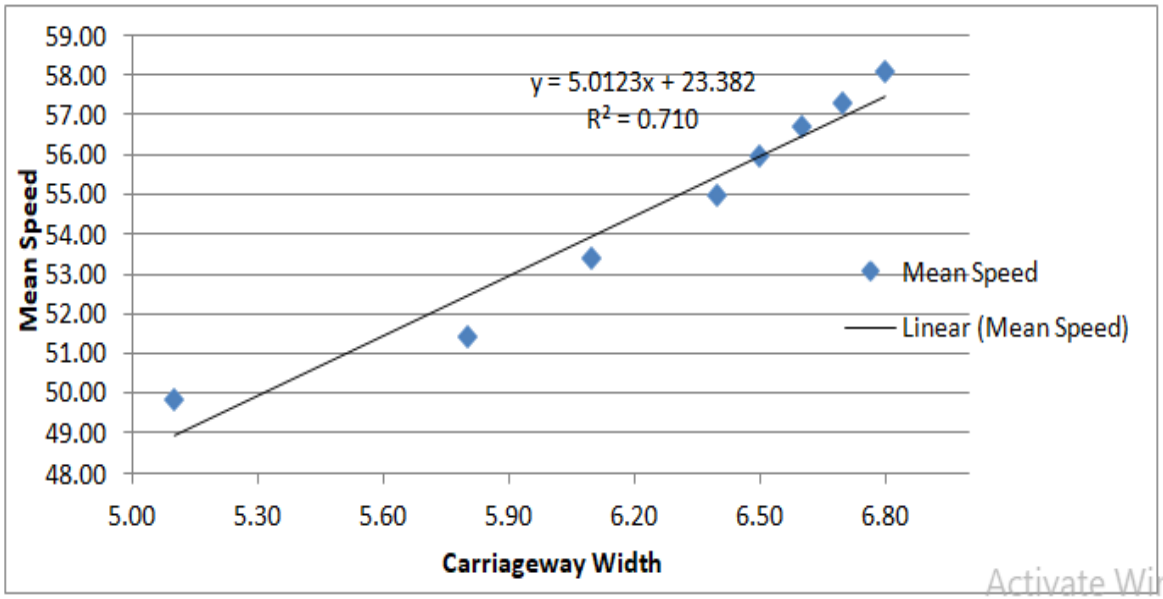

Figure 4. Truck; relationship of speed with carriageway width

For LCV

Similarly, the study showed that the Speed of LCV were dependent on carriageway width and also have linear relationship between them. The linear equation of Speed with Carriageway width is Speed =5.808W+20.09 with the R2 value of 0.966. The statically testing of regression shows the P-value below zero shows the significance of derived relationship

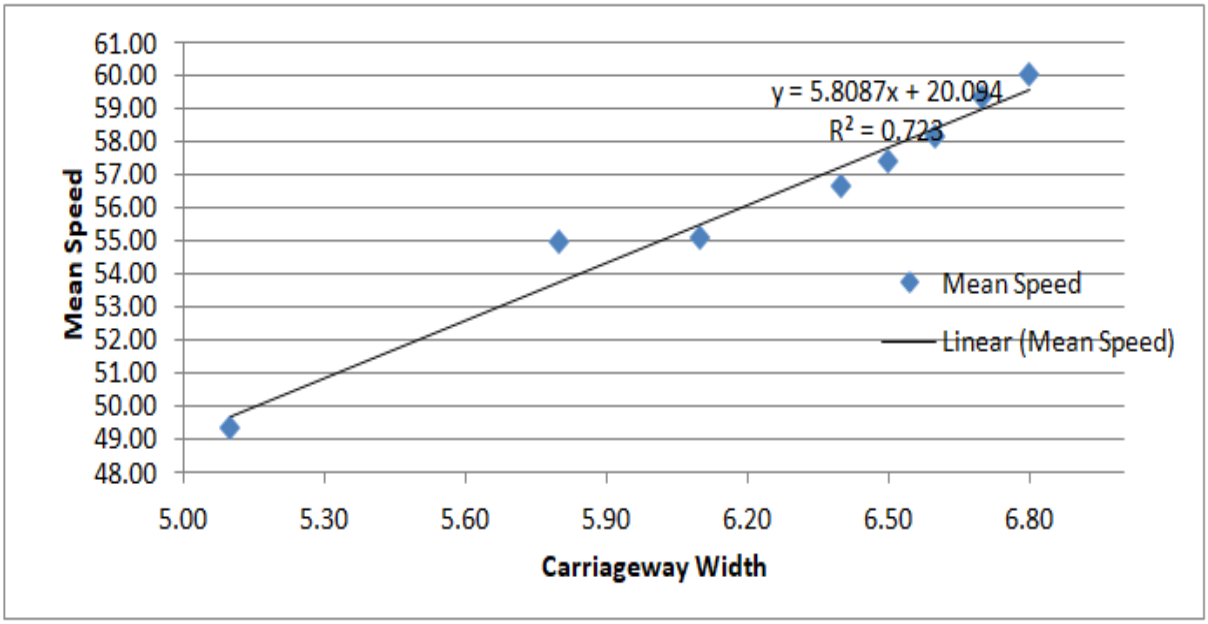

Figure 5. LCV; relationship of speed with carriageway width

For Two-Wheeler

The study showed that the Speed of Two-Wheeler are dependent on carriageway width and also have linear relationship between them. The linear equation of PCU values with Carriageway width is Speed =3.412W+29.87 with the R2 value of 0.881. The statically testing of regression shows the P-value below zero shows the significance of derived relationship.

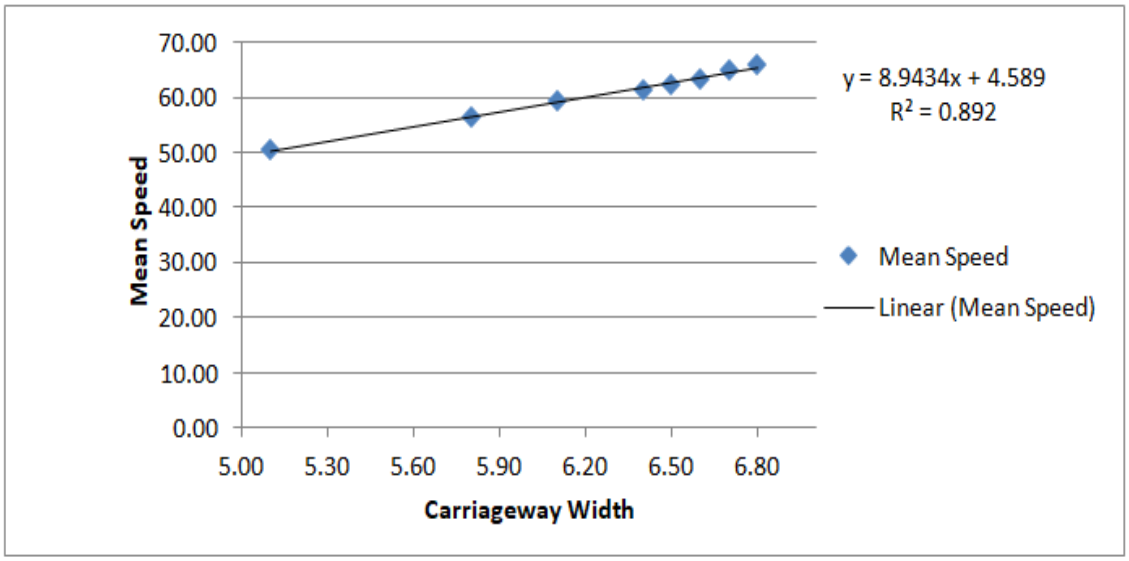

Figure 6: Two-wheeler; relationship of speed with carriageway width

For Car

Similarly, the study showed that the Speed of Car are dependent on carriageway width and also have linear relationship between them. The linear equation of PCU values with Carriageway width is Speed =8.943W+4.589 with the R2 value of 0.993. The statically testing of regression shows the P-value below zero shows the significance of derived relationship.

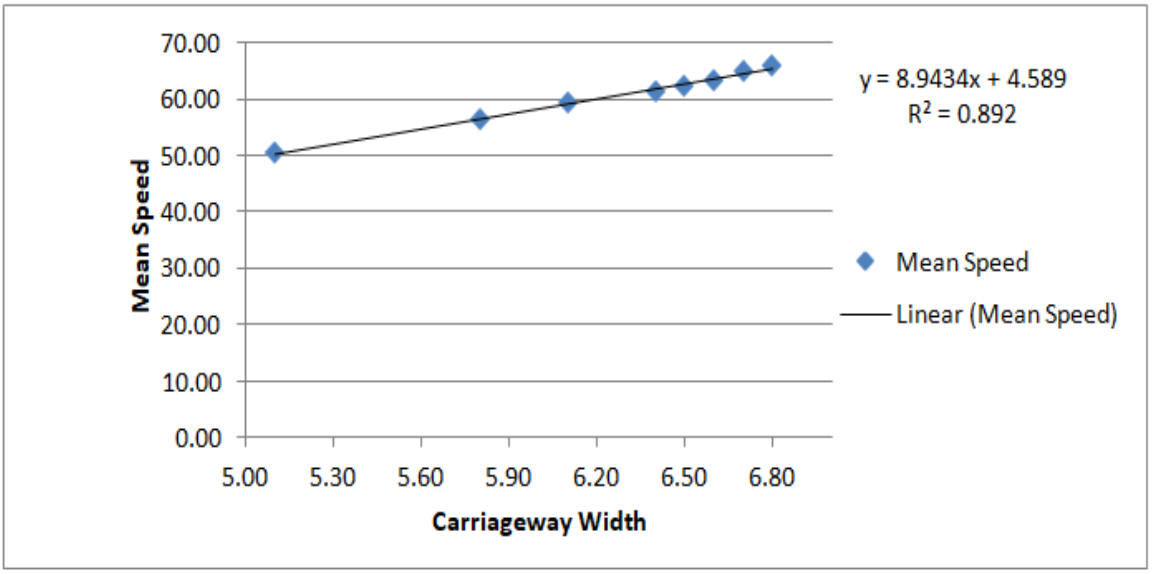

Figure 7. Car; Relationship of speed with carriageway width

Determination of PCU Values

The present study utilized (AfDB, 2016) relationship to calculate PCU values on highways. The PCU values are inversely related to the vehicle's space occupancy ratio when compared to the standard area of the vehicle, such as a car, and directly proportional to the vehicle's clearing speed ratio. The PCU for a certain type of vehicle is taken from the 2003 report by Chandra and Kumar. One crucial factor that distinguishes the speed approach from other PCU calculation techniques is the incorporation of both dynamic and static vehicle parameters, other headway techniques only take into account the dynamic characteristics of the vehicles.

PCU = (Vc/Vi)/(Ac/Ai)
PCU, or passenger car unit value, refers to this kind of vehicle.
The car's speed to the next vehicle is Vc/Vi.
The car's space to the next vehicle is Ac/Ai.
Vc is the vehicle's speed in kilometers per hour.
Vi=vehicle type I's speed (kilometers per hour).
Ai = static (projected rectangular) area of the vehicle type (m2).
AC = static (projected rectangular) area of an automobile.

Table 3 demonstrated the PCU values for the various vehicle categories that were determined at various road segments. This illustrates how PCU fluctuated based on the segment, vehicle type, and lane width. The PCU factor was computed by using the mean speed values of several vehicle types.

Table 3. PCU values for various vehicle categories calculated at various sections

Section Name	Carriageway width (m)	Bus	Truck	LCV	Two-Wheeler
Bexani,	6.8	5.454	3.722	2.617	0.275
Ifkaxalane	6.7	5.429	3.721	2.607	0.272
Bondhere, Bondhere	6.6	5.284	3.442	2.611	0.272
Zoobe, Wadajir	6.5	5.408	3.655	2.587	0.269
General Daud, Sinay	6.4	5.321	3.644	2.567	0.268
Florenza, Xariyale	6.1	5.266	3.638	2.558	0.265
Howlwadaag	5.8	5.210	3.591	2.436	0.258
Jubba, Shibis	5.1	5.000	3.309	2.429	0.233

Effect of Carriageway Width on PCU Values of Different Vehicles

The following relationships have been developed as a consequence of the investigation illustrating how carriageway width affects PCU values for various vehicles:

For Bus

The study shows that the PCU values of vehicle type Bus are dependent on carriageway width and have linear relationship between them. The linear equation of PCU values with Carriageway width is PCU=0.260W+3.681with the R2 value of 0.985.

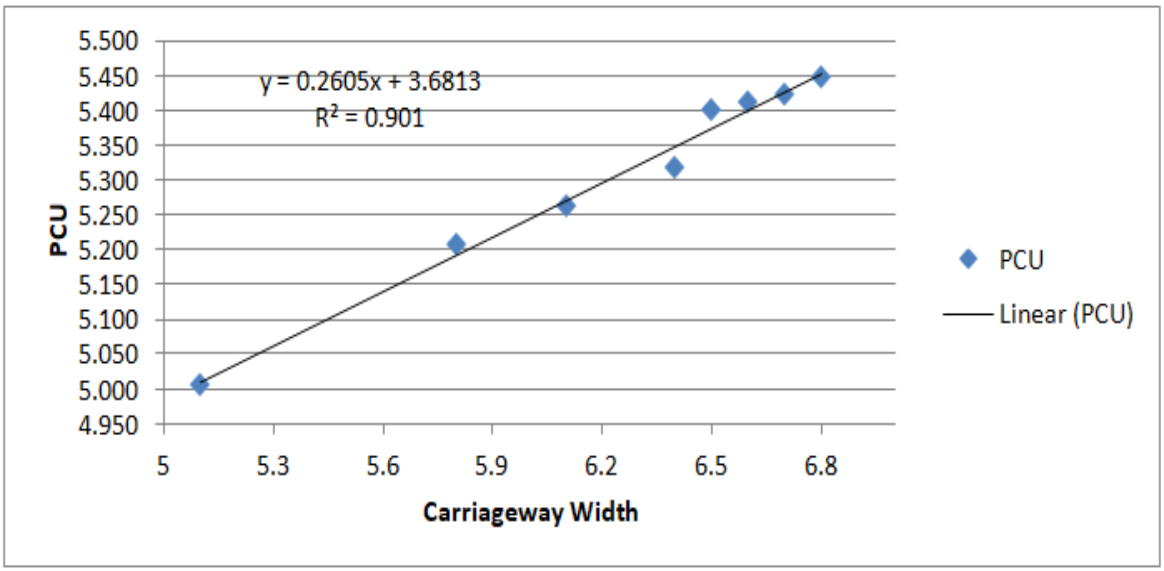

Figure 8. Bus; correlation chart of PCU with carriageway width

For Truck

Figure 9 illustrated the linear equation of PCU values with Carriageway width for vehicle Truck is PCU=0.214W+2.266 with the R2 value of 0.899 which shows the value of PCU is dependent on carriageway width.

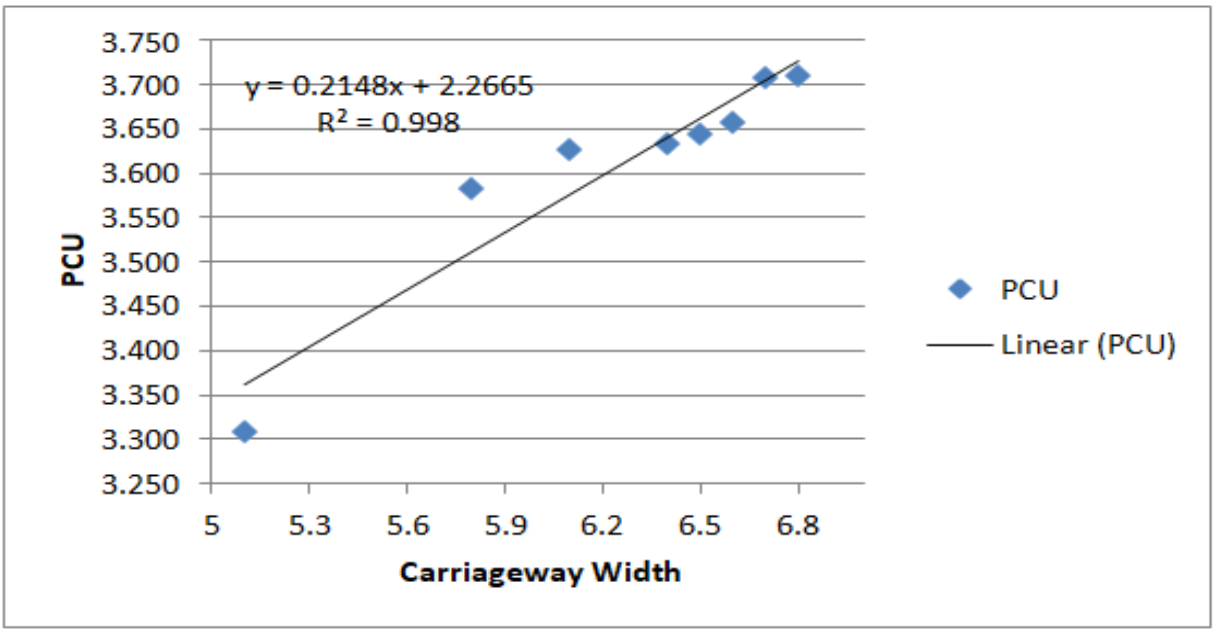

Figure 9. Truck; correlation chart of pcu with carriageway width

For LCV

The study also showed that the PCU values of vehicle type LCV are dependent on carriageway width and have linear relationship, where PCU =0.120W+1.790 with the R2 value of 0.883. The statically testing of regression shows the P-value below zero which demonstrates the significance of derived relationship as presented in Table 4.

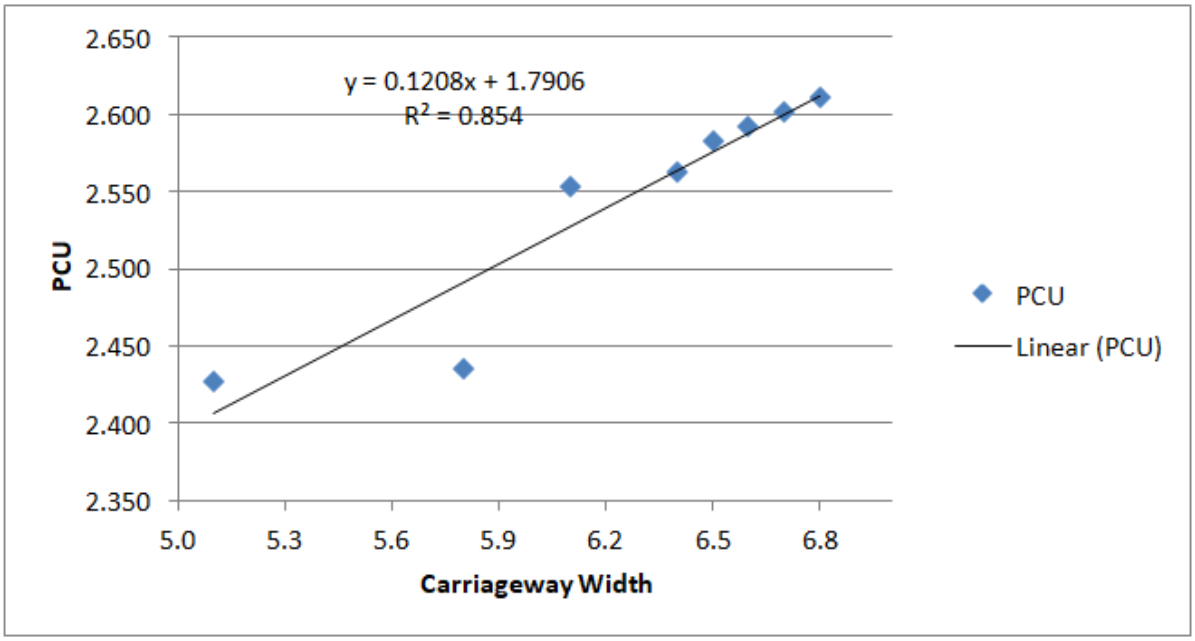

Figure 10. LCV; Correlation chart of PCU width carriageway width

For Two-Wheeler

Similarly, the study showed that the PCU values of Two-Wheeler are dependent on carriageway width and also have linear relationship between them. The linear equation of PCU values with Carriageway width is PCU =0.022W+0.124 with the R2 value of 0.944. The statically testing of regression shows the P-value below zero shows the significance of derived relationship.

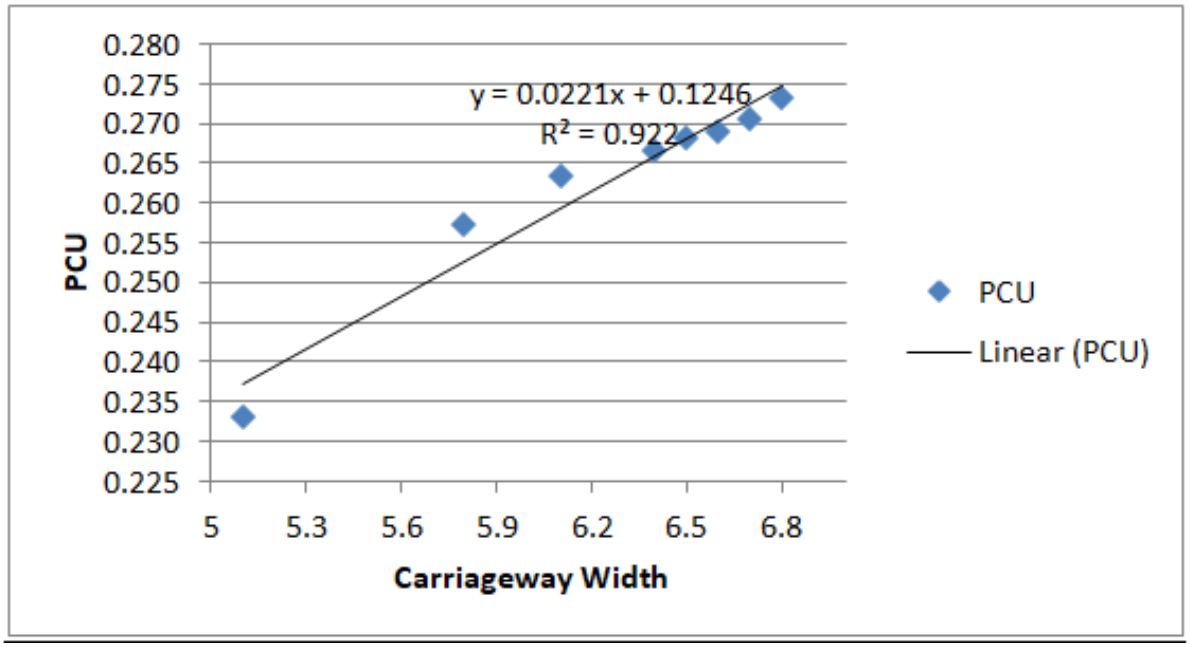

Figure 11. Two-wheeler; correlation chart of pcu with carriageway width

In Table 4. the general overview of the relationship between the PCU of various vehicle types and the carriageway width is given.

Table 4. Summary of the relationship between pcu of various vehicle types and roadway width

Vehicle Type	Relationship between roadway width (w) and passenger car unit	R^2 Value
Bus	PCU=0.260W+3.681	0.901
Truck	PCU =0.214W+2.266	0.998
LCV	PCU =0.120W+1.790	0.854
Two-Wheeler	PCU =0.022W+0.124	0.922

Conclusion

The study focused on four classes of vehicles that are frequently seen in Mogadishu: buses, trucks, light commercial vehicles (LCV), and two-wheelers. The field experiments were done at eight distinct places along the Mogadishu Highway. According to the survey, two-wheelers predominately make up the traffic composition almost at all sections. With broader carriageway widths, the volume of some vehicle types such as buses, trucks, light commercial vehicles, and cars increased linearly, but the volume of two-wheelers was the maximum on smaller lanes.

Wider road widths resulted in faster moving vehicles, proving a linear relationship. The Passenger Carrying Unit (PCU) values for each type of vehicle were influenced by the traffic composition, demonstrating a linear relationship between them. With carriageway widths ranging from 6.8 to 5.1, the PCU values for buses range from 5.454 to 5.000, trucks from 3.722 to 3.309, LCVs from 2.617 to 2.429, and two-wheelers from 0.275 to 0.233.

Lane width affected the PCU values, which typically rose with wider lanes. Lane width and PCU values possesed a substantial correlation, according to regression analysis. Highway lane width clearly had a linear

effect on PCU. It's interesting to note that the study's newly determined PCU values diverge significantly from those in the NRS standard. In comparison to MRS 2070, motorcycle PCU values were lower, whereas bus, truck, and LCV PCU values were higher.

In summary, the study examined vehicle composition, speed, and PCU values across different carriageway widths in Mogadishu. It has established a linear correlation between lane width and PCU, indicating that PCU values were influenced by lane width. The PCU values determined through this research differ from those in existing standards.

Recommendations

The recommendations provided in this article highlight the necessity for Mogadishu's urban planning and policymaking to place a high priority on infrastructure development that can support a variety of vehicle types. In order to do this, broader roads must be designed to accommodate buses, trucks, and LCVs. Additionally, safety measures must be put in place for two-wheelers, and systematic traffic monitoring must be established. Additionally, it is crucial to carry out public awareness programmed for safe driving, update outdated PCU standards to reflect the current traffic situation, and support continuous research in order to guarantee that the city's transportation infrastructure is effective and secure for all users of the roads. The overall goal of these suggestions is to improve Mogadishu's road network's adaptability, safety, and traffic management.

Scientific Ethics Declaration

The authors declare that the scientific ethical and legal responsibility of this article published in EPSTEM journal belongs to the authors.

Acknowledgements or Notes

* This article was presented as an oral presentation at the International Conference on Technology, Engineering and Science (www.icontes.net) held in Antalya/Turkey on November 16-19, 2023.

References

AfDB. (2016). Somalia transport sector needs assessment and investment programme. *AfDB*, *296*. Retrieved from https://www.afdb.org/en/topics-and-sectors/initiatives-partnerships/multi-partner-somalia-infrastructure

Al-Obaedi, J. T. S. (2016). Estimation of passenger car equivalents for basic freeway sections at different traffic conditions. *World Journal of Engineering and Technology*, *4*(2), 153–159.

Arasan, V. T., & Arkatkar, S. S. (2010). Microsimulation study of effect of volume and road width on PCU of vehicles under heterogeneous traffic. *Journal of Transportation Engineering*, *136*(12), 1110–1119.

Gani, F. A., Yoshii, T., & Kurauchi, S. (2014). The effect of heterogeneity of vehicle size on the fundamental diagram in mixed traffic. (Case study: Makassar traffic on Urip Sumoharjo street). *Proceeding of the International Conference of Transdiciplinary Research on Environmental Problem in Southeastern Asia*, 95–104.

Hills, A. (2014). Remembrance of things past: Somali roads to police development. *Stability*, *3*(1), 1–14.

Hordofa Tullu, H., & Tucay Quezon, E. (2021). Determination of passenger car unit for urban roads: A case study in Addis Ababa. *American Journal of Construction and Building Materials*, *5*(2), 57.

Khadka, A. (2017). *The study of effect of road width on passenger car units (PCU) of vehicles under Heterogeneous Traffic Conditions*. *11*(6), 451–459.

Khanorkar, A. R., Ghodmare, S. D., & Khode, B. V. (2014). Impact of lane width of road on passenger car unit capacity under mix traffic condition in cities on congested highways. *Journal of Engineering Research and Applicationswww.Ijera.Com*, *4*(5), 180–184

Khanorkar, A. R., Ghodmare, S. D., Khode, B. V, Patel, S. P., Karli, S., Story, W., Mankar, P. U., Khode, B. V, Chakravorty, S. K., Biswas, S., Singh, B., Saha, A., Babit, R., Sharma, V., Duggal, A. K., Li, J., Wang, X., Yu, R., Tremont, P. J., … Alam, R. Bin. (2016). Traffic volume survey analysis of the road connecting Career Point University. *Trends in Civil Engineering and Its Architecture*, *2*(3), 268–270.

Mbithi, P. (2016). *University of Nairobi: About the University of Nairobi*. Retrieved from https://uonbi.ac.ke/

Mohamed, J., Mohamed, A. I., Ali, D. A., & Gebremariam, T. T. (2023). Prevalence and factors associated with ever had road traffic accidents among drivers in Hargeisa city, Somaliland, 2022. *Heliyon*, *9*(8).

Nations, U. (2016). *R*oad infrastructure programme Somalia (Rıp-Somalıa) terms of reference for preliminary and detailed design of 82km section of Beledweyne-Galkayo road (LOT 1). *Lot 1*, 1–31.

Praveen, P. S., & Arasan, V. T. (2013). Influence of traffic mix on Pcu value of vehicles under heterogeneous traffic conditions. *International Journal for Traffic and Transport Engineering*, *3*(3), 302–330

Sharma, M., & Biswas, S. (2021). Estimation of passenger car unit on urban roads: A literature review. *International Journal of Transportation Science and Technology*, *10*(3), 283–298.

Author Information

Yasin Ahmed Addow
Near East University
faculty of Civil Engineering Department
Nicosia, North Cyprus
Contact e-mail: *Yaasiin517@email.com*

Mustafa Alas
Near East University
Faculty of Civil Engineering Department
Nicosia, North Cyprus

To cite this article:

Addow, Y.A., & Alas, M. (2023). The evaluation of the impact of road width on Passenger Car Units (PCU) in heterogeneous traffic conditions. *The Eurasia Proceedings of Science, Technology, Engineering & Mathematics (EPSTEM), 26*, 496-506.

The Eurasia Proceedings of Science, Technology, Engineering & Mathematics (EPSTEM)
ISSN: 2602-3199

The Eurasia Proceedings of Science, Technology, Engineering & Mathematics (EPSTEM), 2023

Volume 26, Pages 507-518

IConTES 2023: International Conference on Technology, Engineering and Science

Prediction of Conducted Disturbances Generated by a DC/DC Converter

Sara Ghalem
University Djilali Sidi Bel Abbes Liabes

Abdelber Bendaoud
University Djilali Sidi Bel Abbes Liabes

Houcine Miloudi
University Djilali Sidi Bel Abbes Liabes

Mohamed Hamza Bermaki
University Djilali Sidi Bel Abbes Liabes

Mohamed Miloudi
University Djilali Sidi Bel Abbes Liabes

Abdelhakim Zeghoudi
University Djilali Sidi Bel Abbes Liabes

Abstract: This paper introduces a detailed approach to model and simulate conducted electromagnetic interference (EMI) in the time domain using Lt-Spice software. The focus of the study is on the Buck converter, with the aim of identifying and characterizing electromagnetic disturbance sources arising from the power supply. The research also seeks to analyze their propagation paths and examine the impact of switch selection and control parameters on the electromagnetic compatibility (EMC) signature of the converter. The proposed methodology employs a comprehensive modeling strategy that accounts for the interactions between various converter components and their associated parasitic elements. By accurately representing the electrical and magnetic fields in the time domain, the simulation captures the dynamic behavior of the system, allowing for a realistic assessment of conducted disturbances. The research begins with a thorough examination of the power supply and its switching behavior. Key device characteristics, including switching frequency, voltage, and current waveforms, are carefully analyzed to understand their influence on conducted EMI. Additionally, the model integrates parasitic elements linked to the power device, such as inductive and capacitive components, to address their impact on electromagnetic emissions. Furthermore, the study delves into the propagation paths of conducted disturbances, considering the parasitic elements of the converter's layout, such as PCB traces, cables, and connectors. It evaluates the effects of these elements on electromagnetic emissions, providing insights into propagation mechanisms and potential coupling paths. Various switch types, such as MOSFET or IGBT, are examined, and their effects on conducted EMI are evaluated. Through comprehensive simulations and analysis, the paper offers valuable insights into the conducted disturbances generated by the DC/DC converter, contributing to a comprehensive understanding of the system's electromagnetic behavior. The findings presented in this study can inform the design and optimization of DC/DC converters, facilitating the development of more EMC-friendly solutions.

Keywords: EMC, DC/DC converter, Conducted disturbances, Common mode (CM), Differential mode (DM).

Introduction

Electromagnetic Compatibility (EMC) represents a significant limitation in the design of power electronics structures. Regrettably, it is often treated as a final phase of power converter development, representing the ultimate obstacle to their marketability (Benhadda, 2018).

The advancement of power electronic converters in various electric power sectors imposes new requirements, such as high-frequency switching operations, high power densities, elevated temperatures, and enhanced yields. All specifications must adhere to EMC regulations (Zeghoudi, 2021). The conventional method for EMC prediction involves simulation in the time domain and the use of Fourier transform (Eliana & Koyama, 2014). Despite its simplicity and efficacy, this approach has its limitations.

Our objective is to introduce a predictive model for conducted interference generated by a step-down chopper. This model aims to investigate and analyze the propagation mechanisms of these conducted disturbances, which propagate in both common mode (CM) and differential mode (DM). We seek to comprehend the various parameters that influence the spread and amplification of these disturbances and to quantify the noise level produced by the converter. This study will primarily focus on two specific areas:

1) Time-domain simulation for the analysis of propagation phenomena of conducted disturbances, including the simulation of the conduction and blocking behavior of the MOSFET.
2) Prediction of electromagnetic interference conducted in the Buck converter, with a particular emphasis on the impact of switch types and control parameters.

EMC Modeling of DC/DC Converter

The examined converter, as illustrated in Figure 1, constitutes a series-connected elementary cell of the chopper type linked to the Line Impedance Stabilization Network (LISN). It is supplied by a DC voltage source VDC, and the load converter is depicted by a perfect current source I. Additionally, the diagram includes a combination of resistive elements, inductive components, and capacitors assumed to account for the effects arising from the high-frequency structure's crosstalk.

The impedances Z_{line}, Z_f, and Z_{LP} represent the parasitic inductive coupling at the power level, while the impedances Z_{Load} and Z_{CP} respectively represent the stray coupling in the differential mode and in the common mode at the load. We can differentiate between the parasitic impedances Z_f and Z_{LP}, which are part of the switching cell and therefore closely associated with the cell's switching and the generation of disturbances. The Z_{line} impedance and Z_{Load}, Z_{CP}, are components of the external coupling that enables disturbances to propagate to the load and the power supply (Wu, 2019).

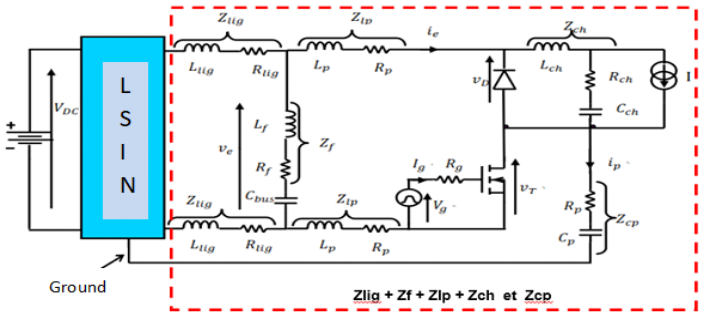

Figure 1. Illustration depicting the effects of crosstalk in a converter.

Simulation Results

The aim of the conducted simulations was to analyze the propagation phenomena of the conducted disturbances and to characterize their sources in the DC/DC converter, utilizing the Line Impedance Stabilization Network (LISN). The LTSpice software system facilitated time-domain simulations, enabling us to swiftly obtain a realistic assessment of the interference emitted by the converter in both the differential mode (DM) and common mode (CM). Figure 2 displays the simulation diagram, encompassing the numerical values of the various components, as well as the amplitude of the electrical quantities, set at a frequency of 10 kHz (with V_{DC} = 300 V and I = 5 A).

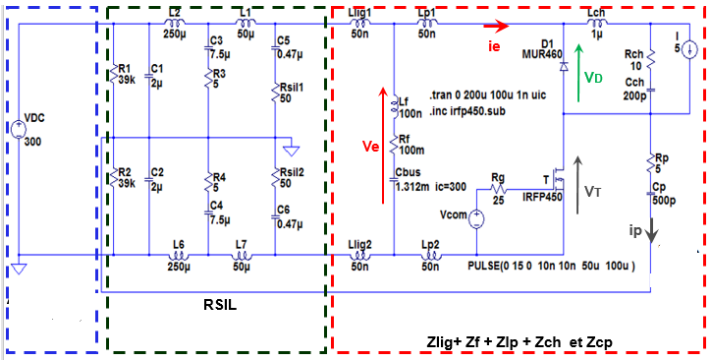

Figure 2. Simulation diagram of the series chopper supplied by a voltage source through the LISN.

MOSFET Conduction Switching

For the analysis of the phenomenon, one should focus on quantities at the input and output of the switching cell. The current i_e initiates an evolution until it reaches the maximum value determined by the diode during the reverse recovery phenomenon. Meanwhile, the voltage across the MOSFET V_t begins to decline due to the voltage drop induced by the parasitic inductances L_f and L_p of the switching cell. The switch terminates as the diode recovers its blocking capability following a substantial current variation (di_e/dt). This abrupt fluctuation in the current i_e at the cell's input results in an overvoltage across the DC bus (Figures 3 and 4).

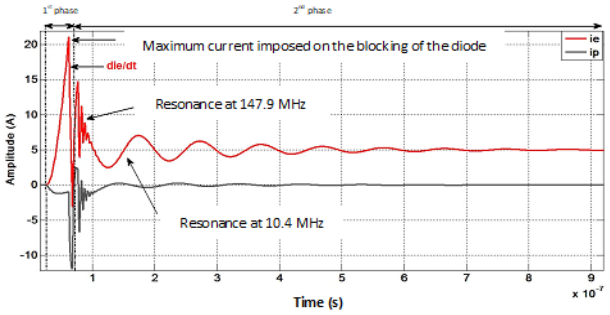

Figure 3. Currents I_e and I_p during MOSFET conduction switching in time domain.

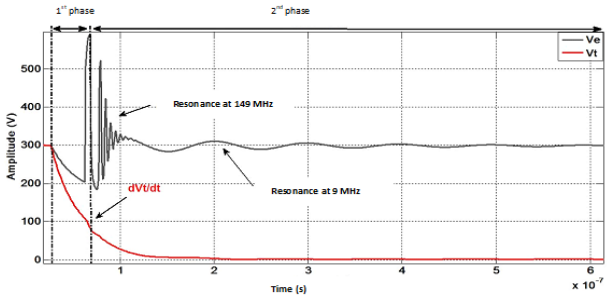

(a)

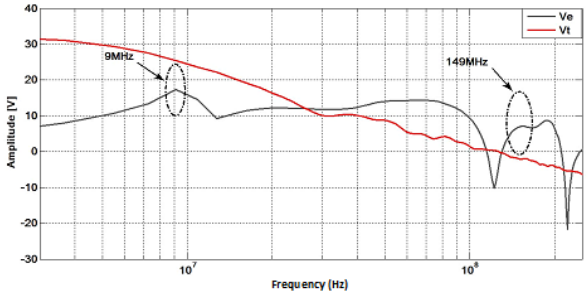

(b)

Figure 4. Voltages V_i and V_e during MOSFET conduction switching : (a) Time domain ; (b) Frequency domain.

The MOSFET conduction is considered rapid owing to the reverse recovery phenomenon in the blocking diode. The presence of highly variable quantities (current and voltage) implies that via crosstalk, oscillatory modes in the high frequency range could severely disrupt the environment outside the converter. The second phase corresponds to the propagation of CM and DM disturbances (Rezini, 2016).

MOSFET Blocking Switching

The first phase corresponds to the rise of the voltage V_t until it reaches the value of the DC bus. The initial phase, which involves the actual switching process, is completed. The charging of the common mode parasitic capacitor C_p and the discharging of the parasitic capacitor C_d of the diode until the voltage is zero. The diode then becomes conductive and the current in the latter can then evolve involving a variation of the current i_e at the input of the cell (Figure 5). The current variation in the switching mesh (di_e/dt) induces an overvoltage at the terminals of the DC bus followed by a highly damped oscillation phase at the frequency of 73 MHz. The second phase corresponds once again to the propagation of the disturbances of CM and DM (Figure 6).

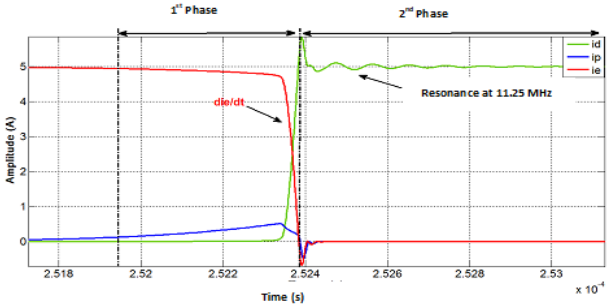

Figure 5. Current I_d, I_p, and I_e during MOSFET blocking switch.

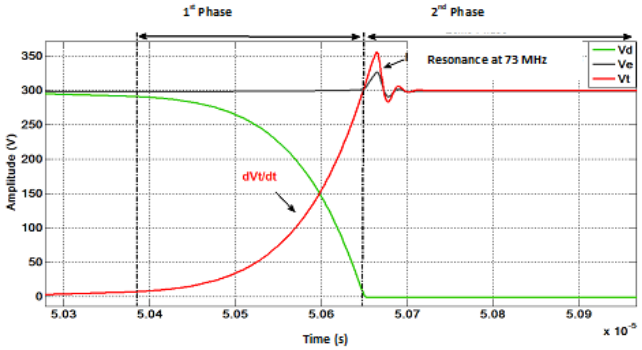

Figure 6. Voltages V_d, V_e, and V_t during MOSFET transition to the locked state.

The diagram in Figure 7 illustrates the various paths of disturbance propagation resulting from the interactions of the two signals, represented in blue and green for the differential mode, and in red for the common mode.

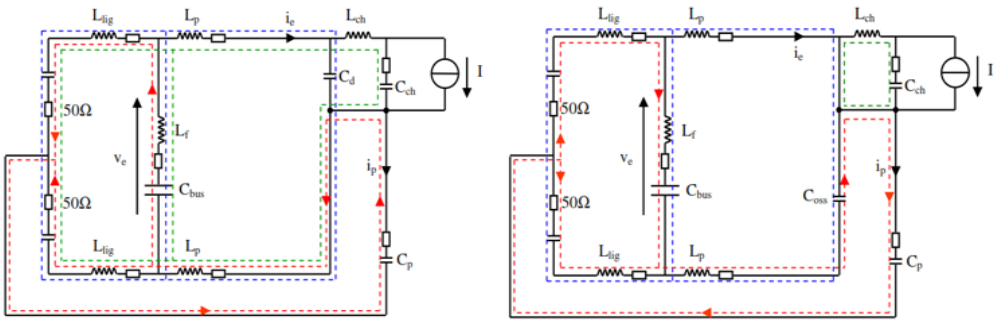

(a) (b)

Figure 7. Disturbance propagation paths of MOSFET: (a) conduction switching, (b) blocking switch

- ✓ On the conduction layout diagram:

The MOSFET is represented as a perfect conductor. The diode is represented by its parasitic capacitance C_d. The propagation of disturbances CM in this case corresponds to the discharge of the parasitic capacitance C_p due to the decrease in voltage V_t. The blue color indicates the interaction in the differential mode between the equivalent parasitic inductance of the entire circuit (L_{eq}) and the parasitic capacitance of the diode (C_d). The green clor indicates the interaction arising from the parasitic differential mode elements of the load (Z_{Load}).

- ✓ On the blocking scheme:

The diode is replaced by a perfect conductor. The MOSFET is represented by its C_{oss} output capacitance.
The propagation of disturbances CM in this case corresponds to the charging of the parasitic capacitance C_p due to the increase in voltage V_t.
The bleue color represents the interaction between the Coss output capacitance of the MOSFET and the equivalent parasitic inductance (L_{eq}).
The green color represents the interaction observed only by the diode and the load during the freewheeling phase.

Prediction of Driving Disturbances in the BUCK Converter

The simulation enabled us to anticipate and analyze the behavior of the Buck converter using two types of MOSFETs, specifically the IRFP450 and IRFP440, as provided by the LTspice software. Figures 8 and 9 illustrate the spectral profiles of the disturbance levels in DM and CM, respectively, in comparison with the standard conducted EN-55022 for both types of MOSFETs."

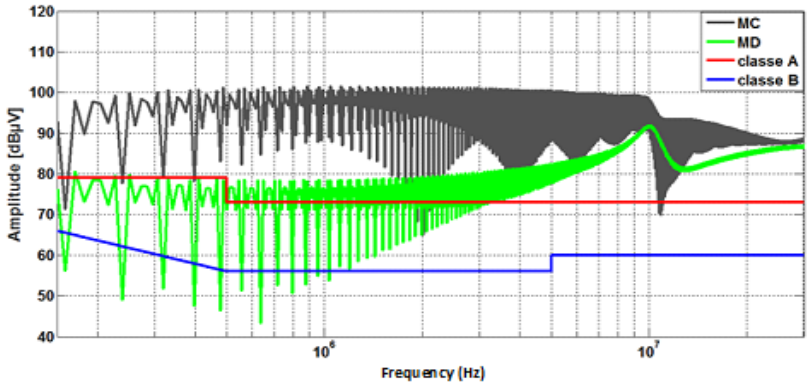

Figure 8. Simulation of the level of electromagnetic disturbances in CM and DM for IRFP 440

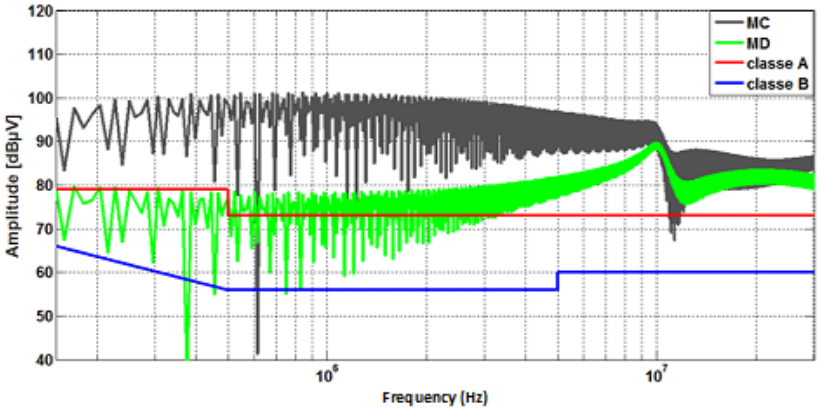

Figure 9. Simulation of the level of electromagnetic disturbances in CM and DM for IRFP 450.

The spectra of CM and DM from the two MOSFETs take on the same appearance with different amplitudes. The spectra are very disruptive because it greatly exceeds the standard templates. The common mode spectrum of the two MOSFETs is dominant over the entire frequency range while the DM gains amplitude in HF.

Comparison of the Voltage Simulations of CM and DM for the Two Types of MOSFETs.

The switching speed (dV/dt) for the IRFP440 MOSFET is higher than for the IRFP450 MOSFET, the levels of disturbances in CM become more important (Figures 10 and 11).

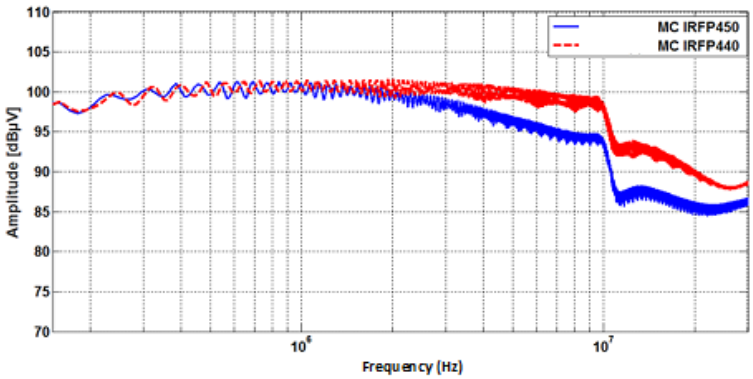

Figure 10. Comparison of the common mode (CM) spectra for IRFP440 and IRFP450.

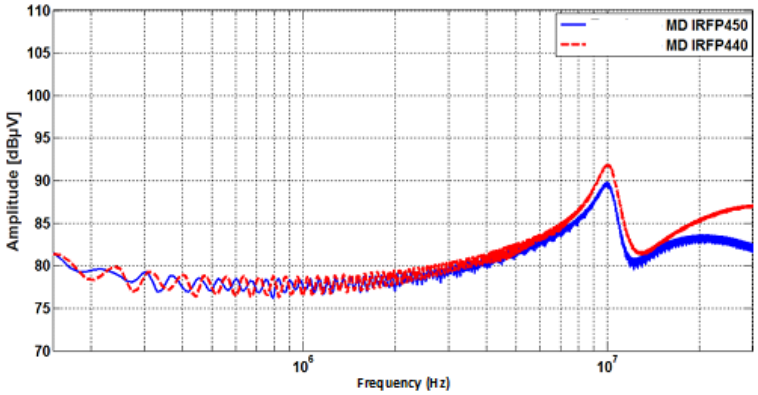

Figure 11. Comparison of the differential mode (DM) spectra for IRFP440 and IRFP450.

Since there are not many differences in the current response for the two components, consequently the voltage for DM is less variable.

Influence of the Gate Resistance

In this section, we examine the influence of the resistance of the gate of the MOSFET on the disturbing level generated by this component. For this purpose, we have varied this resistance from 25 Ω and 100 Ω for a fixed duty cycle equal to 50% and the switching frequency of 10 kHz. We took the converter with the IRFP450 MOSFET for the study and directly compared the interference generated in CM and DM for the two resistor values (Figures 12 and 13).

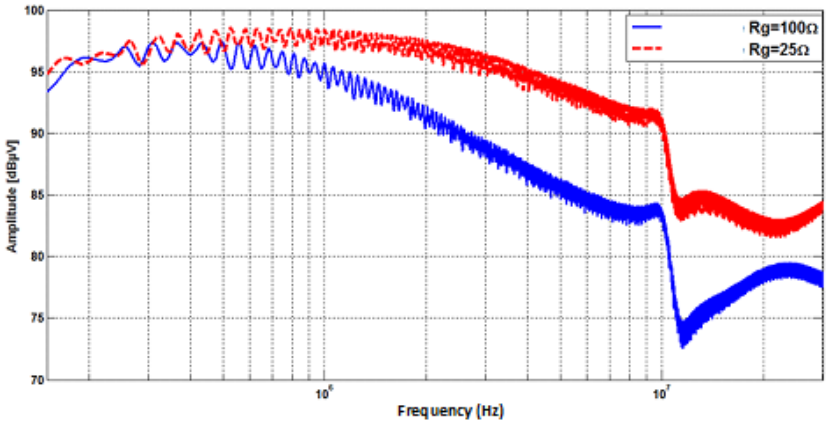

Figure 12. Comparison of the simulated CM disturbances for different resistances of the gate.

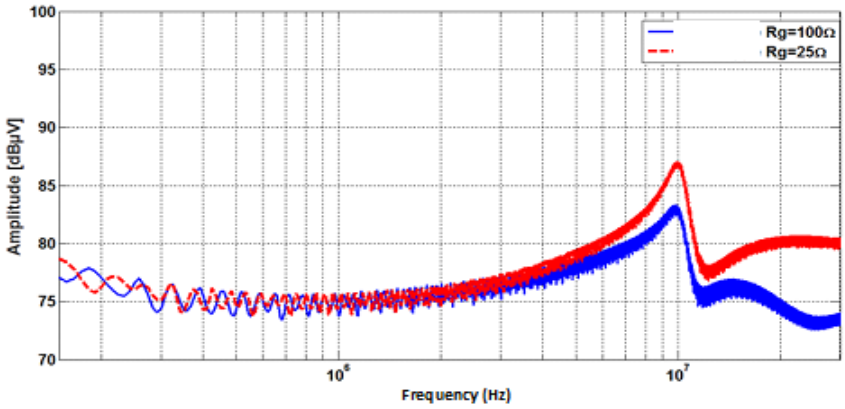

Figure 13. Comparison of the simulated DM disturbances for different resistances of the gate.

We note that the increase in the resistance of the gate allowed a clear decrease in the amplitude of the voltage in CM and DM. Due to the fact that the gate resistance value is inversely proportional to the switching speed, the results affirm that the disturbances in CM are directly related to the variations in dV/dt which change with the resistance of the gate. For the disturbances in DM, the impact of the switching speed is less significant at the spectrum level.

Influence of the Operating Point on the Conducted Electromagnetic Disturbances

With the same converter, and fixing the gate resistance at 25 Ω for a switching frequency of 10 kHz, we carried out comparisons in simulation of CM and DM voltages with a duty cycle of 25% and 90% (Figure 14).

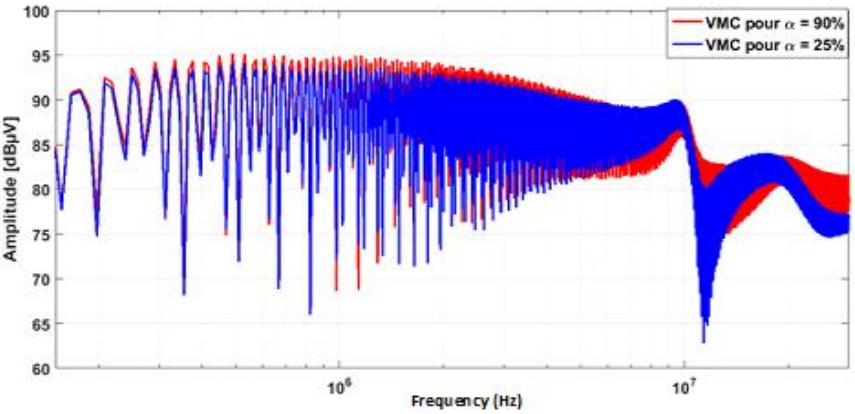

(a)

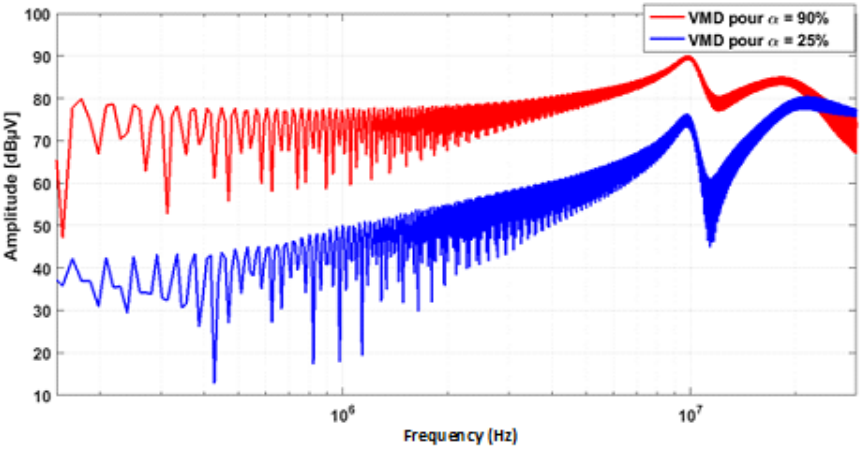

(b)

Figure 14. Comparison of the simulated voltage for different duty cycles : (a) CM, (b)DM.

The results show that the impact in the CM for different duty cycles is negligible. This is due to the fact that the switching speed (dv/dt) are not very different when the switched current varies. On the other hand, for the DM, the impact is significant. This can be explained by the fact that the switched current is directly proportional to the duty cycles. This analysis is consistent with the work (Zeghoudi, 2021) where the disturbances in CM are mainly due to variations in the voltage in the switching cell and the disturbances in DM are mainly due to variations in currents.

Influence of the Switching Frequency

In order to present the influence of the different times characterizing a voltage or current wave on the voltage spectrum. The following curves represent respectively the spectra of the CM and DM voltages at the level of the LISN and the spectra of the voltage or level of the load for different values of the following parameters: t_m, t_d and f_c.

Spectra Measured at the RSIL

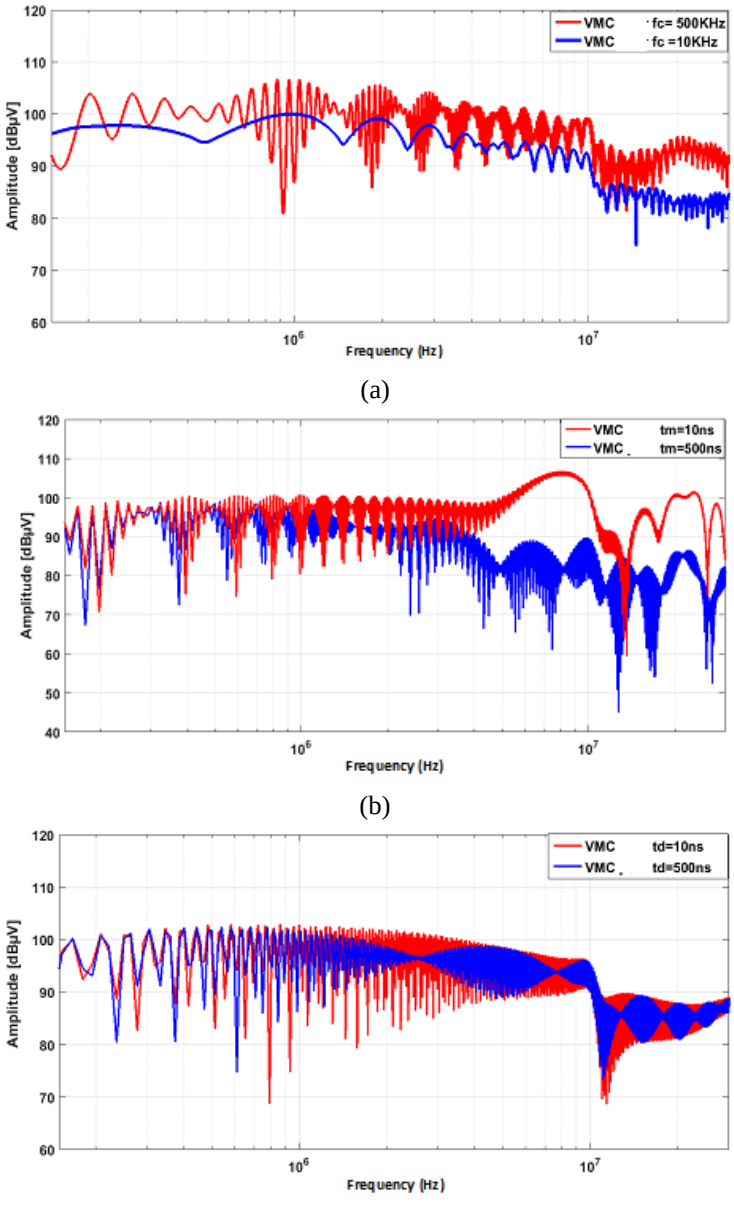

Figure 15. Influence of the switching frequency on the CM spectrum: (a) f_c, (b) t_m, (c), t_d.

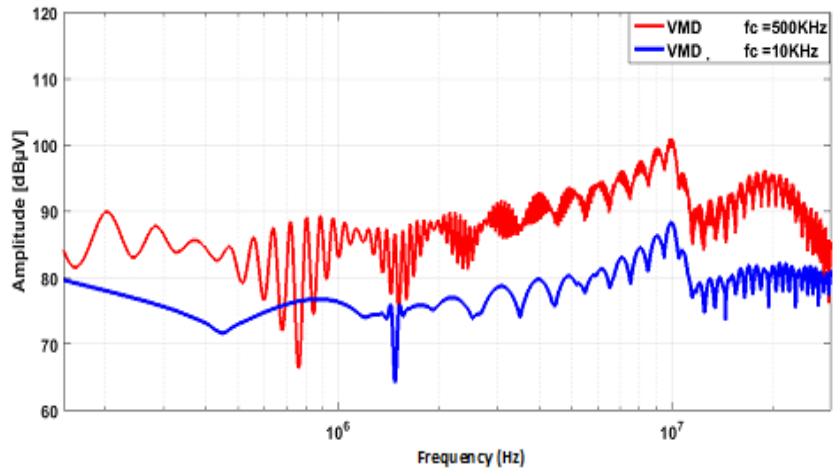

(a)

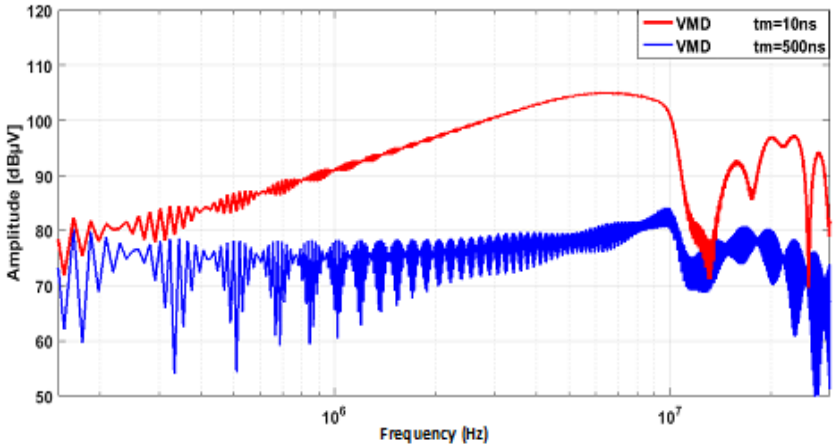

(b)

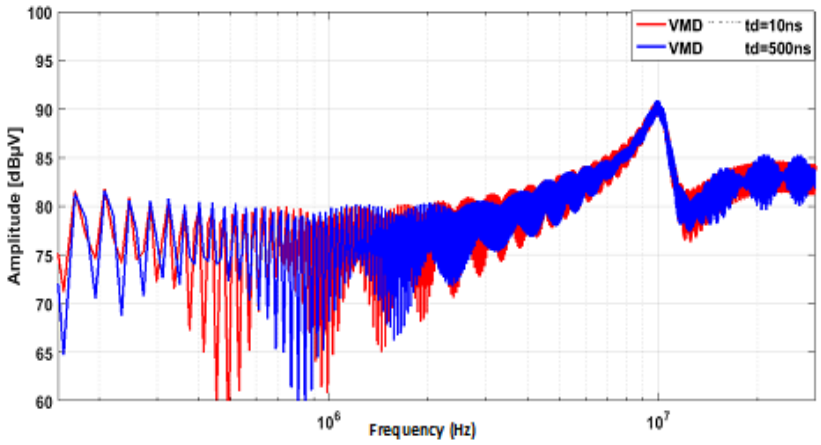

(c)

Figure 16. Influence of the switching frequency on the DM spectrum: (a) $f_{c,}$ (b) t_m, (c) t_d.

.

Spectra Measured at the Load

The analysis of the voltage spectra in CM and DM at the LISN, and the voltage at the load show that : The frequency spectrum of the voltage extends towards the HF as the rise time tm of the control signal of the switch considered (MOSFET) is low and it extends towards the LF when the rise time increases. The variation of the descent time t_d does not affect the frequency spectrum of the voltage. The increase in the switching frequency favors the spreading of the spectra towards the HF.

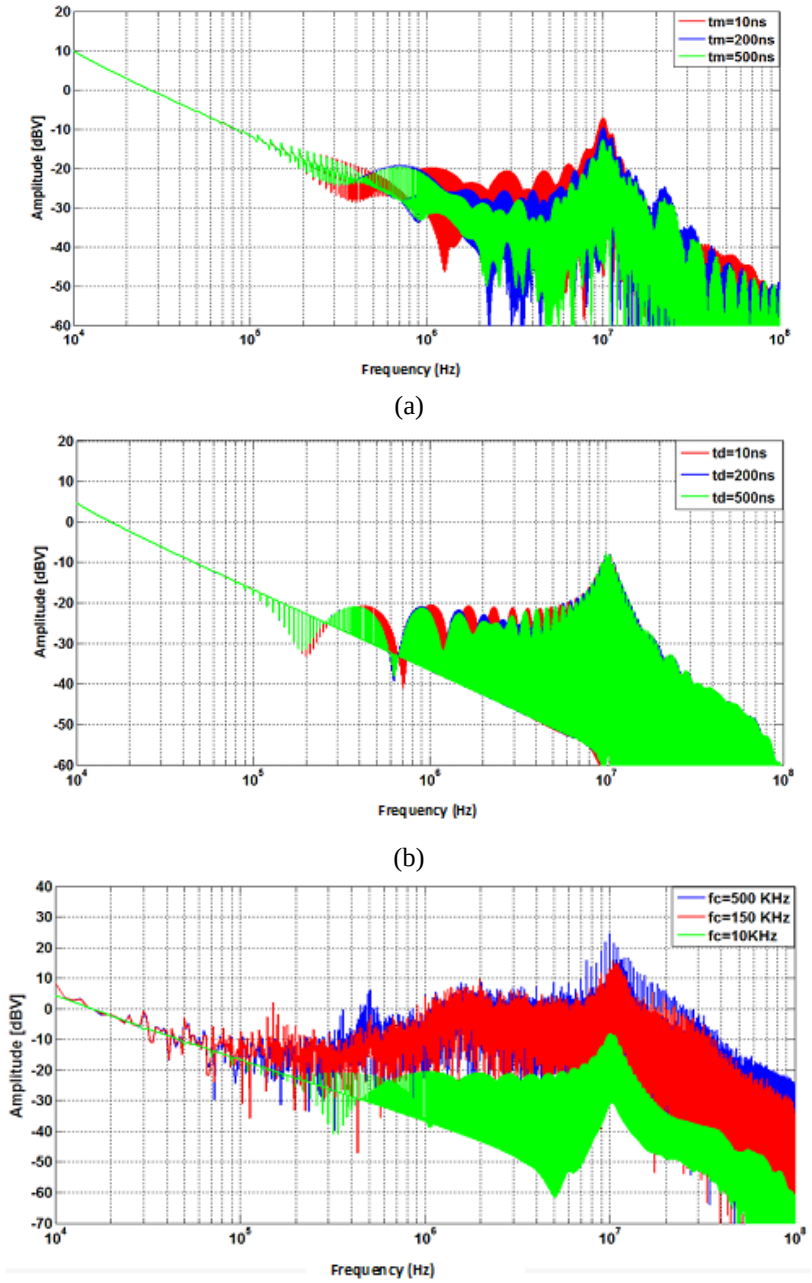

Figure 17. Influences of the switching frequency on the spectrum of the voltage at the load: (a) f_c, (b) t_m, (c) t_d.

Conclusion

In this work, a SPICE model for predicting disturbances conducted within a DC/DC step-down converter is presented. The levels of EMC disturbances are directly related to the switching speed of the active components, in particular in common mode, therefore, the judicious choice of the types of power switches can contribute to the reduction of these disturbances.

The more the spectrum of the signal extends towards the HF, the more the EM interferences are more important. By then decreasing the HF content of the spectrum, it will be possible to reduce the effectiveness of the EM interferences. From the EMC problem, it is therefore advantageous to avoid fast switching and high duty cycles. From this work, our perspective is to compare the simulation results with experimental measurements which will do in the future.

Scientific Ethics Declaration

The authors declare that the scientific ethical and legal responsibility of this article published in EPSTEM journal belongs to the authors.

Acknowledgement

* This article was presented as an oral presentation at the International Conference on Technology, Engineering and Science (www.icontes.net) held in Antalya/Turkey on November 16-19, 2023.

* The authors express their gratitude to the General Directorate of Scientific Research and Technological Development (DGRSDT) in Algeria for their valuable technical support and for providing the dedicated research budget for this program.

References

Benhadda N., Bendaoud A., & Chikhi N. (2018). A conducted EMI noise prediction in DC/DC converter using a frequency-domain approach. *Elektrotehniški Vestnik Journal 85*(3), 103-108.

Baudry, D., Arcambal, C., Louis, A., Mazari, B., & Eudeline, P. (2007). Applications of the near- field techniques in EMC investigations. *IEEE Transactions on Electromagnetic Compatibility, 49*(3). 485-493.

Costa, F., Voltaire, C., & Meuret, R. (2005). Modeling of conducted common mode disturbances in variable-speed drive systems. *Electromagnetic Compatibility, IEEE Transactions on, 47*(4), 1012-1021.

Rondon-Pinilla, E. (2014). *Design of electronic power converters with low electromagnetic impact incorporating new semiconductor switches technologies*. (Doctoral dissertation). Ecole Centrale de Lyon in

Koyama Y., Tanaka, & Akagi, H. (2010). Modeling and simulation for analysis of common mode noises produced by an inverter-driven air conditioner. *International Conference on Power Electronics (IPEC)*, 2877-2883.

Lai Y., Yao, J., Wang, S., luo, Z., & Li, Y. (2021). Electric near field emission from a 1Mhz power Converter for electric vehicles. *2021 IEEE Energy Conversion Congress and Exposition (ECCE)*. Vancouver, BC, Canada.

Maxime, M. (2009). *High frequency energy converters modeling. Application to the study of emission lines to the network* (Doctoral dissertation). Lille Central School.

Muttaqi M. K., & Haque E. (2008). Electromagnetic interference generated from fast switching power electronic devices. *International Journal of Innovations in Energy and Power Systems, 3*(1) 19-45.

Pei X., Xiong, J., Kang, Y., & Chen, J. (2003). Analysis and suppression of EMI Conducted Emission in PWM inverter. Int. Conf. IEMDC'03 we *Electric Machines and Drives, 3*, 1787- 1792,

Rezini, S. (2016). *Contribution to the study and characterization of EM disturbances caused by power electronic devices affecting an electrical network*. (Doctoral dissertation). University of Science and Technology of Oran Mohamed Boudiaf. Oran, Algeria

Rezini, S., Azzouz, Z., & Kouadri B. (n.d.) *Study of high frequency electromagnetic disturbances generated by grinding and chopper association*. University of Science and Technology of Oran Mohamed Boudiaf. Oran, Algeria

Saidi S., & Ben HadjSlama, J. (2014). A near-field technique based on PZMI, GA, and ANN: Application to power electronics systems. *IEEE Trans. Electromagn. Compat., 56*(4), 784–791.

Wu, X., Grassi, F., Pignari, S. A., Paoletti, U., & Hoda, I. (2020). Performance of electric near-field probes for immunity tests. *2020 XXXIIIrd General Assembly and Scientific Symposium of the International Union of Radio Science*. Rome, Italy.

Zeghoudi A., Bendaoud, A., Canale, L., Tilmatine, A., & Slimani, H. (2021). Common mode and differential mode noise of AC/DC LED driver. 20*21 IEEE International Conference on Environment and Electrical Engineering and 2021 IEEE Industrial and Commercial Power Systems Europe (EEEIC / I&CPS Europe)* (pp.1-6).

Zeghoudi A., Bendaoud, A., Tilmatine, A., Bechkir, S., Zissis, G., & Canale, L. (2022). Study of the impact of the power dimming and lighting modes of LED lamps on the near magnetic field", Optik, *271*,

Zeghoudi A., Bendaoud, A., Khalladi, S., Slimani, H., Miloudi, H., & Canale, L. (2022). Common and differential modes filter for the PFC boost AC/DC led driver. *22nd International Conference on Environment and Electrical Engineering, 6th Industrial and Commercial Power Systems*. Prague,

Czech Republic

Authors Information

Sara Ghalem
APELEC Laboratory, University Djilali Sidi Bel Abbes Liabes 22000, Algeria

Abdelber Bendaoud
APELEC Laboratory, University Djilali Sidi Bel Abbes Liabes 22000, Algeria
Contact e-mail: *babdelber@gmail.com*

Houcine Miloudi
APELEC Laboratory, University Djilali Sidi Bel Abbes Liabes 22000, Algeria

Mohamed Hamza Bermaki
APELEC Laboratory, University Djilali Sidi Bel Abbes Liabes 22000, Algeria

Mohamed Miloudi
APELEC Laboratory, University Djilali Sidi Bel Abbes Liabes 22000, Algeria

Abdelhakim Zeghoudi
APELEC Laboratory, University Djilali Sidi Bel Abbes Liabes 22000, Algeria

To cite this article:

Ghalem, S., Bendaoud, A., Miloudi, H., Bermaki, M. H., Miloudi, M., & Zeghoudi. A. (2023). Prediction of conducted disturbances generated by a DC/DC converter. *The Eurasia Proceedings of Science, Technology, Engineering & Mathematics (EPSTEM), 26,* 507-518.

The Eurasia Proceedings of Science, Technology, Engineering & Mathematics (EPSTEM)
ISSN: 2602-3199

The Eurasia Proceedings of Science, Technology, Engineering & Mathematics (EPSTEM), 2023

Volume 26, Pages 519-531

IConTES 2023: International Conference on Technology, Engineering and Science

Acceleration/Deceleration Detection System - Creation of Driving Behavior Profiles for Efficiency

Huseyin Karacali
TTTech Auto Turkey

Efecan Cebel
TTTech Auto Turkey

Nevzat Donum
TTTech Auto Turkey

Abstract: Driving behavior is a term used to describe deliberate or accidental activities while a driver drives a vehicle. Driving behavior data is useful for efficiency in the automotive domain, including insurance companies, aftermarkets, production planning, and vehicle servicing. Therefore, the aim of this study is to develop and investigate an Acceleration/Deceleration(A/D) detection system. A/D can be measured using a 3-axis accelerometer. The accelerometer on the vehicle cannot precisely reflect the driver's actual A/D behavior due to its undetermined orientation. Additionally, the accelerometer detects sudden movements. In order to prevent unexpected acceleration and deceleration changes and to achieve the desired driving behavior, a gyroscope has been incorporated into the system. Thus, a driving aid system was developed using the combined data from the gyroscope and accelerometer. Moreover, the A/D detection system reads and combines the vehicle's CAN messages to more stabilize the system. As a result, driving behavior data during vehicle trips is collected and recorded to inform the driver how to have a more efficient driving experience and as well as making the related companies aware of the trips that have been made. Furthermore, they can be combined with service feedback and support the manufacturer's production strategy to increase efficiency.

Keywords: Driving behavior, Acceleration, Deceleration, Driving efficiency

Introduction

The world's transition from a centralized to a decentralized structure is due to the increasing adoption of technologies such as blockchain, distributed ledger, and peer-to-peer networks. One of the most important factors enabling this transition is data. Data is essential for building decentralized systems as it allows for creating distributed databases and establishing consensus mechanisms that ensure the accuracy and validity of data records. This transition has affected the automotive domain as well as the whole sector. Blockchain technology has the potential to revolutionize the automotive industry. This technology offers a number of advantages, including data security, privacy, anonymity, traceability, accountability, integrity, robustness, transparency, reliability, and authentication (Fraga-Lamas et al., 2019, p. 17578). More vehicles are now equipped with sensors that collect and transmit data in real time, with the rise of connected cars and the Internet of Things (IoT). The integration of blockchain into IoT networks is becoming increasingly important in this context (Ahmad et al., 2019). Collecting and analyzing driving behavior data from vehicles provide valuable information for various processes in the automotive field, such as development and production. The driving behavior data is used during the development process to provide a safer and more efficient driving experience for the driver. More than 50% of serious road accidents caused by professional drivers of heavy vehicles are due to risky driving behavior. Quantitative estimation of driving performance and behavior is helpful in measuring the driving risk and internal driving style of professional drivers (He et al., 2022, p. 1). In addition, analyzing

data contributes to optimizing production performance and increasing productivity. This exemplifies the significance of driving behavior data in the automotive industry. The Acceleration/Deceleration(A/D) Detection System has been developed to create driving behavior profiles for efficiency. Acceleration and deceleration can be detected with a 3-axis accelerometer. However, with this detection method, A/D cannot be determined exactly to the uncertain orientation of the accelerometer. The real A/D behavior data of the driver cannot be collected since sudden movements are detected with this measurement method. The gyroscope is integrated into the A/D Detection System as a solution.

Unexpected acceleration and deceleration changes are prevented thanks to the gyroscope added to the system. In this way, desired driving behavior data was obtained. Data from the gyroscope and accelerometer were used in this study. The CAN messages of the vehicle were read in addition and the system was supported with messages from the CAN-BUS, to make the system more stable. A driving support system has been developed that collects driving behavior data in this way while the vehicle is in motion. Information is given to the driver to provide an efficient driving experience with these collected data, and the data is transmitted to the relevant companies.

Materials

Accelerometer

3-axis accelerometer is a type of micro-electromechanical system (MEMS) device that is capable of measuring acceleration along three perpendicular axes, typically denoted as x, y, and z. The device is composed of a proof mass that is suspended by a set of flexure springs and enclosed within a hermetically sealed package, which can be affixed onto a printed circuit board (“A beginner”, n.d.). Acceleration causes the proof mass to deflect, and this deflection is sensed by mechanisms that convert the mechanical motion into an electrical signal (“What is an accelerometer? (Fierce Electronics, 2023).

The implementation of 3-axis accelerometers in automotive applications has enabled the measurement of acceleration in vehicles, detection of impacts, and provision of feedback for electronic stability control, GPS positioning, and collision detection systems. Within the context of our study on A/D detection systems, the 3-axis accelerometer is utilized to gauge the acceleration and deceleration of the vehicle, as well as to detect changes in slope. Additionally, the device is utilized to determine the orientation of the platform within the vehicle, as the platform may not always be aligned with a consistent direction and may be subject to change based on the slope of the road.

Gyroscope

A gyroscope is an electronic sensor used to detect and measure rotational motion. These devices operate to determine the angular velocity of an object around a fixed axis. Essentially, a gyroscope detects the object's rotational motion by utilizing either the interferometer method or the Coriolis effect (Gill et al., p. 7405). The fundamental principle behind the operation of gyroscopes acknowledges that an object's rotational motion is governed by Newton's laws of conservation. An object maintains a certain angular momentum (angular velocity), and if the rotational speed changes, so does the angular momentum. This principle forms the foundation of how a gyroscope operates.

Modern electronic gyroscopes employ Micro-Electro-Mechanical Systems (MEMS) technology. A MEMS gyroscope typically consists of a microelectronic chip with an array of miniature capacitive plates or a small rotating mass. These components enable the device to detect rotational motion (Li et al., 2020, p. 4919). To detect rotational motion, the rotating mass of the gyroscope is connected to a reference or impact surface. During rotational motion, changes in the angular velocity of the rotating mass result in variations in the proximity of the capacitive plates. These changes are perceived as alterations in capacitance and are subsequently processed by electronic circuits.

In our A/D detection system work, the gyroscope is used to detect vehicles’ sharp turn motions and to calculate the magnitude of the turns. In acceleration and deceleration detection, parameters such as collision, no distortion, and bump cannot be detected with accelerometers. These undetectable parameters are detected with the gyroscope in the A/D detection system.

Microcontroller Unit (MCU)

Microcontroller Unit (MCU) is a specialized integrated circuit (IC) type responsible for the control and operation of electronic devices. Often referred to as a microcontroller or microcontroller unit, the MCU encompasses a central processing unit, memory units (including working memory and flash memory), input/output (I/O) ports, and an array of peripheral hardware components (HowStuffWorks, 2023). Microcontrollers are programmable by design and can be programmed by users to perform specific tasks. These programs are executed by the MCU's central processing unit. MCUs find widespread application in various electronic devices and systems, particularly in embedded systems, automotive control units, medical devices, and industrial automation systems. (, 2023). MCUs are renowned for their compact size, low power consumption, high processing capacity, and rapid response times. These characteristics make them an ideal choice for numerous applications that require energy efficiency, efficiency, and precise control. A/D detection system conducted utilizing the NXP S32K148 microcontroller platform. The NXP S32K148 is a 32-bit microcontroller operating on the ARM Cortex-M4 core, purpose-built for applications within the automotive industry. This microcontroller upholds the rigorous quality standards demanded by the automotive sector, ensuring dependable performance even in the demanding automotive electronics environment, and it adheres to the AEC-Q100 standards. Furthermore, it is fully compliant with the ISO 26262 functional safety requirements, rendering it a fitting choice for deployment in safety-critical systems (NXP, n.d.).

Controller Area Network (CAN)

The Controller Area Network (CAN-BUS) is a widely used communication protocol in various applications, particularly in automotive and industrial settings. It is a message-based protocol that enables different electronic control units (ECUs) within a system to communicate with one another efficiently (CAN in Automation (CiA), n). The fundamental principle behind the operation of the CAN-BUS protocol is to establish a reliable and robust means of data exchange.

CAN-BUS is based on the principles of message-oriented communication. It operates on a two-wire bus system, where one wire carries the high-level signal (dominant state), and the other carries the low-level signal (recessive state). In its working mechanism, CAN-BUS uses a differential signal pair, which provides noise immunity and reliability (Copper Hill Tech, n.d.). Each message transmitted on the CAN-BUS consists of an identifier, data, and a cyclic redundancy check (CRC) for error detection. ECUs on the network can both send and receive messages, and the protocol follows a priority-based arbitration system to handle concurrent message transmissions (Kvaser, 2023).

The CAN-BUS protocol is designed to be highly resilient and fault-tolerant. It employs a bit-wise arbitration process, allowing the node with the highest-priority message to gain access to the bus. This feature ensures that critical messages can be transmitted without interruption, making it ideal for real-time systems (Kvaser, 2023). In this study, messages containing vehicle speed and rpm data were read from the vehicle's CAN-BUS line.

Method

Acceleration deceleration detection system was developed to measure acceleration, deceleration, and sharp turn behaviors by harnessing data from a 3-axis accelerometer, gyroscope, and the vehicle's CAN-BUS messages. A block diagram illustrating the data sources and system output is presented in Figure 1.

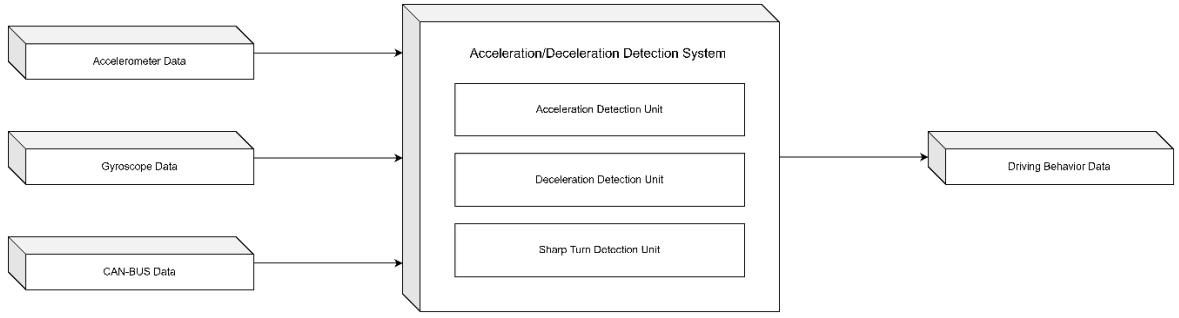

Figure 1. Acceleration deceleration detection system block diagram

The A/D detection system simultaneously detects acceleration, deceleration, and sharp turns. Each measurement is performed by independent software modules.

Acceleration Detection Software Unit

The accelerometer data, which includes the gravity component, should be processed in order to detect the vehicle's acceleration accurately. An acceleration detection software unit has been developed for this process. The raw data from the sensor represents the measured acceleration values along the X, Y, and Z axes. These values vary with the vehicle's motion and reflect the magnitude and direction of the detected motion as perceived by the accelerometer. However, directly summing up these values is insufficient for precise acceleration detection due to the inclusion of the gravity component. Hence, processing of the raw sensor data is required.

One of the processing steps involves calculating the magnitude of the acceleration values along the X, Y, and Z axes. The magnitude is computed by taking the square root of the sum of the squares of the three-dimensional acceleration values. This total value provides an accurate measure of the vehicle's acceleration magnitude by effectively eliminating the influence of the gravity component. Thus, the accelerometer data is filtered to focus solely on the components that indicate the vehicle's acceleration. Figure 2 illustrates the process for obtaining the acceleration magnitude representing the vehicle's acceleration.

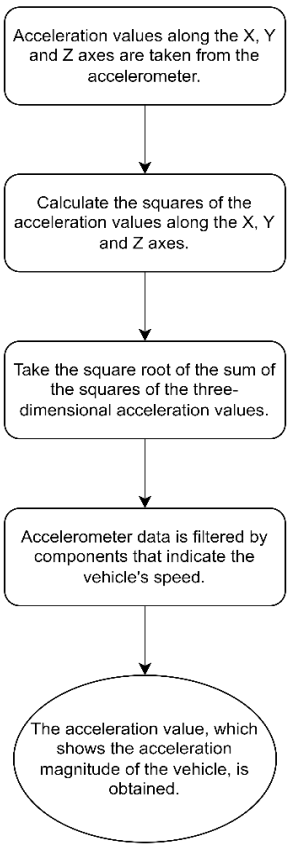

Figure 2. Vehicle acceleration magnitude calculation flow chart

It is necessary to apply filtering due to factors such as vehicle-induced motions and external influences like road inclination for the gyroscope. Undesirable noise and deviations may arise in the gyroscope data due to these factors. Therefore, processing steps are employed to enhance the accuracy of the gyroscope data and mitigate the unwanted effects.

The raw data from the gyroscope typically represent values for the three axes (X, Y, and Z) each. These values reflect the detected rotational velocity and direction. The values for all three axes are calculated from the raw data obtained from the sensor, yielding calibration data. The system ensures precision, resolution, and accuracy by collecting and processing idle state data from the vehicle. These values are utilized as offset values in the calibration settings of the sensors for subsequent measurements. Offset adjustment ensures the accuracy of the

sensor readings. In the context of this automotive system, crucial vehicular data, encompassing vehicle speed and Revolutions Per Minute (RPM), is meticulously gleaned from the CAN-BUS. This entails the extraction of raw data messages from the vehicle's onboard diagnostics system. Subsequently, an intricate parsing process is initiated to extract and isolate the precise values for vehicle speed and RPM.

The parsed data, encapsulating the vehicle speed and RPM, is subsequently subjected to a sophisticated comparative analysis alongside meticulously filtered acceleration data. This specific acceleration data is diligently obtained through a suite of advanced sensors, including accelerometers and gyroscopes, designed to detect and quantify changes in the vehicle's acceleration profile. The fundamental aim of this intricate comparison is to elevate the precision of acceleration detection within the system. By cross-referencing the acquired speed and RPM values with the carefully filtered accelerometer and gyroscope data, the system can discern and discriminate real-world accelerative events from other driving factors.

This approach enhances the accuracy and reliability of the system's acceleration detection capabilities, contributing to a more nuanced understanding of the vehicle's dynamic behavior. Various factors such as road conditions, braking, and acceleration, turning motions, vibrations, and shocks cause changes in the accelerometer and gyroscope data during vehicle motion. To accurately interpret these changes and detect acceleration, additional control mechanisms are implemented as described in this section. When the vehicle experiences acceleration, the accelerometer readings exhibit positive values. To ensure the reliability of this acceleration data, a threshold check is performed to determine if the accelerometer value exceeds a system-defined threshold. It's important to note that when the vehicle undergoes a turning motion, the accelerometer values also experience changes. Therefore, to specifically detect situations without turning motion, it is expected that the gyroscope value remains below the defined threshold.

In the event that these conditions are not met, the accelerometer value is reset, and the vehicle returns to an idle state. Subsequently, all calculations and checks are restarted to confirm the presence of acceleration. Once acceleration is verified, data related to speed, time, and location is collected for transmission to the server. This process ensures the accuracy of the acceleration detection mechanism while accounting for variations caused by turning motions.

The accelerometer value is continually monitored to detect if it surpasses a predefined threshold, serving as an indicator of the vehicle's acceleration. Once this check is successfully completed, the speed measured at that moment is considered the initial speed. Subsequently, at 3-second intervals, the initial speed is updated by comparing it with the current speed. The difference between the initial and current speeds is used to determine the magnitude of acceleration.

If this difference exceeds the predefined threshold, it indicates that the vehicle is undergoing continuous acceleration. In such a scenario, the current speed becomes the new instantaneous speed, and the comparative process continues. On the other hand, if the difference between the new instantaneous speed and the initial speed remains below the threshold, it suggests that the acceleration phase has concluded. Throughout this meticulous process, essential parameters are established, including the acceleration rate, initial speed, final speed, and the duration of the acceleration phase. These critical data points are subsequently communicated to the server for further analysis and utilization. This method ensures precise tracking of acceleration dynamics while accommodating potential fluctuations in the vehicle's speed. The inputs and outputs of the acceleration detection unit are depicted in Figure 3. The flowchart of the algorithm for acceleration detection is represented in Figure 4.

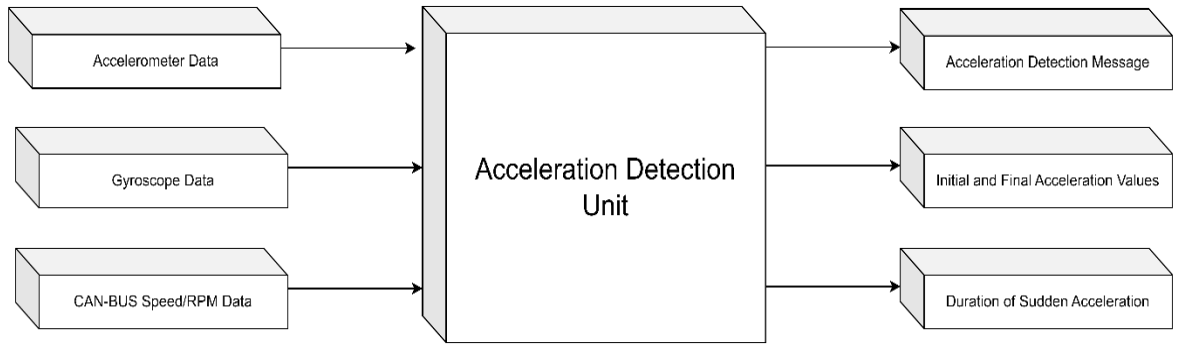

Figure 3. Acceleration detection unit inputs outputs block diagram

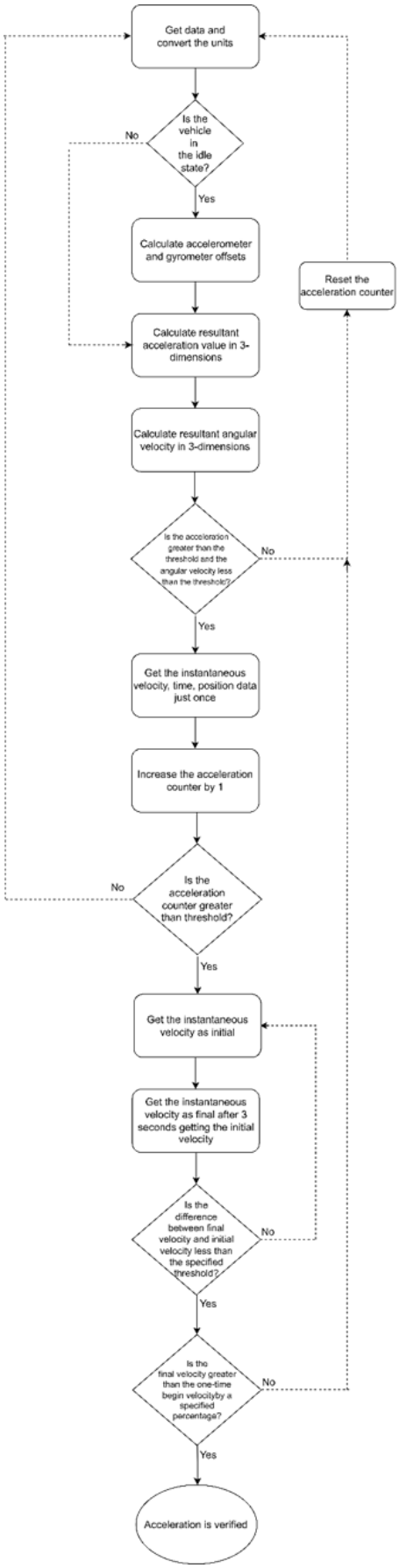

Figure 4. Acceleration detection algorithm flow chart

Deceleration Detection Software Unit

This algorithm was implemented in the developed deceleration detection software unit. As the first step of the deceleration detection algorithm, acceleration data in 3 axes (x, y, z) are taken from the accelerometer. The accelerometer returns a raw acceleration value. The following conversion process is performed in order to make sense of the raw data received. The raw data is converted into a meaningful acceleration value with the transformation.

$$R * \frac{F}{2^N} \tag{1}$$

Equation (1) shows the conversion from the raw sensor value to the acceleration value in mg. Where R represents the raw data read from the accelerometer, F is the range of the accelerometer module which is selected ±8 g in our study, and N refers the bit number which equals to 16. In the A/D detection system, the gyroscope is used together with the accelerometer for deceleration detection. Angular rotation data, which is raw data, in 3 axes (x, y, z) is read from the gyroscope. Dividing by resolution is used when converting this data into meaningful data as seen in (2).

$$\frac{R}{T} \tag{2}$$

Where R represent the raw data read from the gyroscope, and T is the resolution of the gyroscope module which equals to 14285 in our study. It is checked whether the vehicle is in motion by inserting it into the control cases determined by the acceleration and angular rotation data obtained from the accelerometer and gyroscope. If the vehicle is not in motion, the offset values of the accelerometer and gyroscope are set. If the vehicle is in motion other than idle, the acceleration values obtained are calculated in 3-dimension with the vector calculation as seen in (3). At the same time, angular rotation values taken from the gyroscope are calculated in 3-dimension, as well as the acceleration value calculated in the 3-dimension.

$$\sqrt{(x_{acc} - x_{off})^2 + (y_{acc} - y_{off})^2 + (z_{acc} - z_{off})^2} \tag{3}$$

The acceleration and angular rotation values calculated in 3-dimension are compared with the determined threshold values. If the value of the calculated data is less than the threshold values, instantaneous speed, time, and location data are taken. After the data is received, the counter holding the number of samples taken is increased to check that the slowdown is not instantaneous. These processes are repeated periodically to obtain the true deceleration value. The number of samples should be kept in a counter to filter the slowdown due to environmental factors such as bumps, ramps, and pits. It is checked whether the deceleration counter is greater than the specified threshold value. If this condition is met, the speed data is read from the CAN-BUS line of the vehicle and instantaneous speed data is obtained. In this way, the system is supported by CAN messages. After the instantaneous speed is read from the CAN line, the instantaneous speed is read again at the end of the specified time. A more stable deceleration is detected with the implementation of this process.

Finally, it is checked whether the final speed is less than the initial speed by the specified rate and percentage to ensure that the deceleration is stable. If the ratio is not less, the whole process repeats. Deceleration is only confirmed if the rate is slightly less than the initial speed at the final speed. With this last step, stable and real slowdown data are obtained. The inputs and outputs of the deceleration detection unit are depicted in Figure 5. The flowchart of the algorithm for deceleration detection is represented Figure 6.

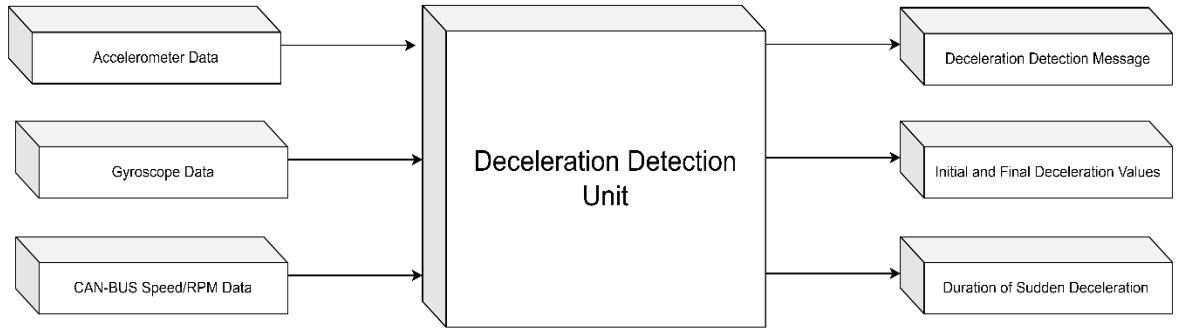

Figure 5. Deceleration detection unit inputs outputs block diagram

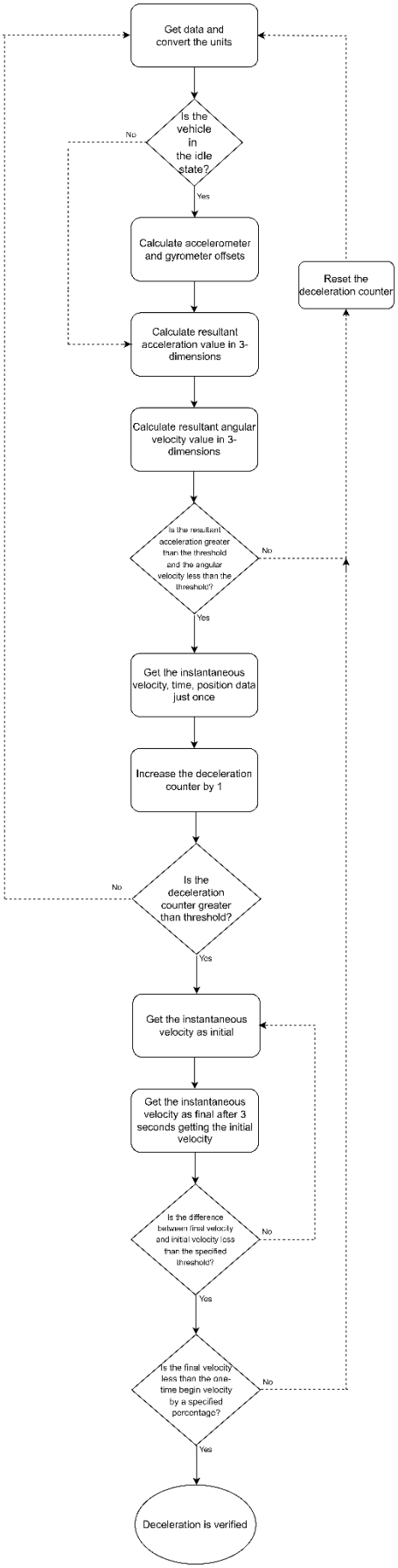

Figure 6. Deceleration detection algorithm flow chart

Sharp Turn Detection Software Unit

This algorithm was implemented in the developed sharp turn detection software unit. As the first step of the sharp turn detection algorithm, angular velocity data in 3 axes (x, y, z) are taken from the gyroscope. The gyroscope returns a raw angular velocity value. The following conversion process is performed to make sense of the raw data received. The raw data is converted into a meaningful angular velocity value with the transformation. In the A/D detection system, the accelerometer is not used for sharp turn detection. Angular velocity data in 3 axes (x, y, z) is enough for this operation. It is checked whether the vehicle is in motion by inserting it into the control cases determined by the angular velocity data obtained from the gyroscope. If the vehicle is not in motion, the offset values of the gyroscope are set. If the vehicle is in motion and not in an idle state, the values obtained from the gyroscope are calculated in 3-dimension with the addition of angular velocities in all dimensions. Thus, the resultant angular velocity is calculated. This resultant value is obtained for comparison with predetermined high and low threshold values. Crossing a high threshold indicates that the vehicle is in a sharp turn. The resultant angular velocity values below the low threshold value mean that there is no sharp turn or the sharp turn process has just terminated.

The A/D detection system expects this resultant angular velocity value to be higher than the high threshold value in the sharp turn algorithm. It calculates the angular velocity magnitude in degree per second (dps) when it first detects this situation and increments the rotation counter by one. Then, it waits for new data to be read from the gyroscope. After reading a value above the high threshold value the first time, the system waits for the resultant angular velocity value to be high 9 more times in a row, which corresponds to about half a second. If at least 10 consecutive values do not exceed the high threshold value, it determines that this process is not a sharp turn, resets the counters, and the angular velocity magnitudes it calculates. On the other hand, if the A/D detection system reads a higher value 10 or more times in a row, it now waits for a value less than the low threshold value to be read, which indicates that the sharp turn is starting to be completed, other higher data to come will not affect any situation until that lower value is read. In this case, it is certain that the vehicle has made a sharp turn, but it waits for the turn to be completed before sending information about the sharp turn to the server.

When the low value indicating that the sharp turn process has started to be completed for the first time comes, the counter that counts this stable state is increased by one and new data is awaited. Just like the high threshold value, this low value is expected to come 10 times in a row, confirming that the turning operation is definitely over. In this case, the sharp turn is confirmed and the process is completely reset. While waiting for 10 consecutive values, if a value above the threshold value comes, the counter controlling this lower threshold value is reset, because this shows that there is still a sharp turn. The inputs and outputs of the sharp turn detection unit are depicted in Figure 7. The flowchart of the algorithm for sharp turn detection is represented Figure 8.

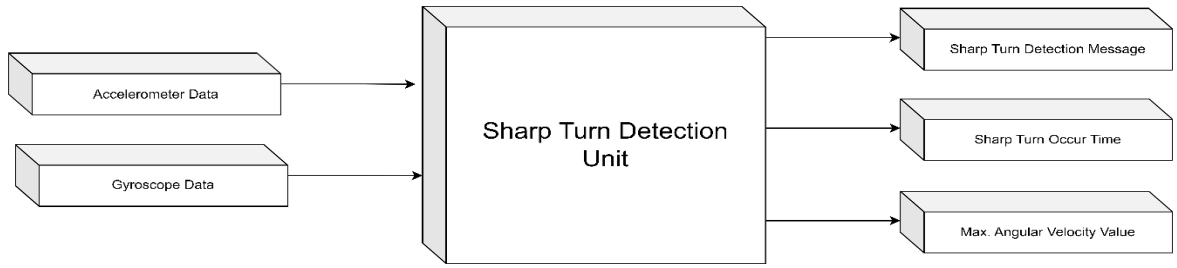

Figure 7. Sharp turn detection unit inputs outputs block diagram

Results and Discussion

Most traffic accidents are primarily attributed to poor driving habits. Monitoring drivers' abnormal driving behaviors online can significantly contribute to the reduction of traffic accidents. In an effort to enhance the accuracy and robustness of driving behavior recognition, algorithms based on Soft Thresholding and Temporal Convolutional Networks (S-TCN) have been developed (Zhao et al., 2022). Traffic accidents predominantly result from drivers' unsafe driving behaviors during their journeys. Studies aimed at addressing low safety issues through real-time driver alerts are underway. Research endeavors have combined Pose Estimation to identify various driving behaviors during the driving process and have concurrently developed a scoring model to assess drivers' driving behaviors (Dai et al., 2022).

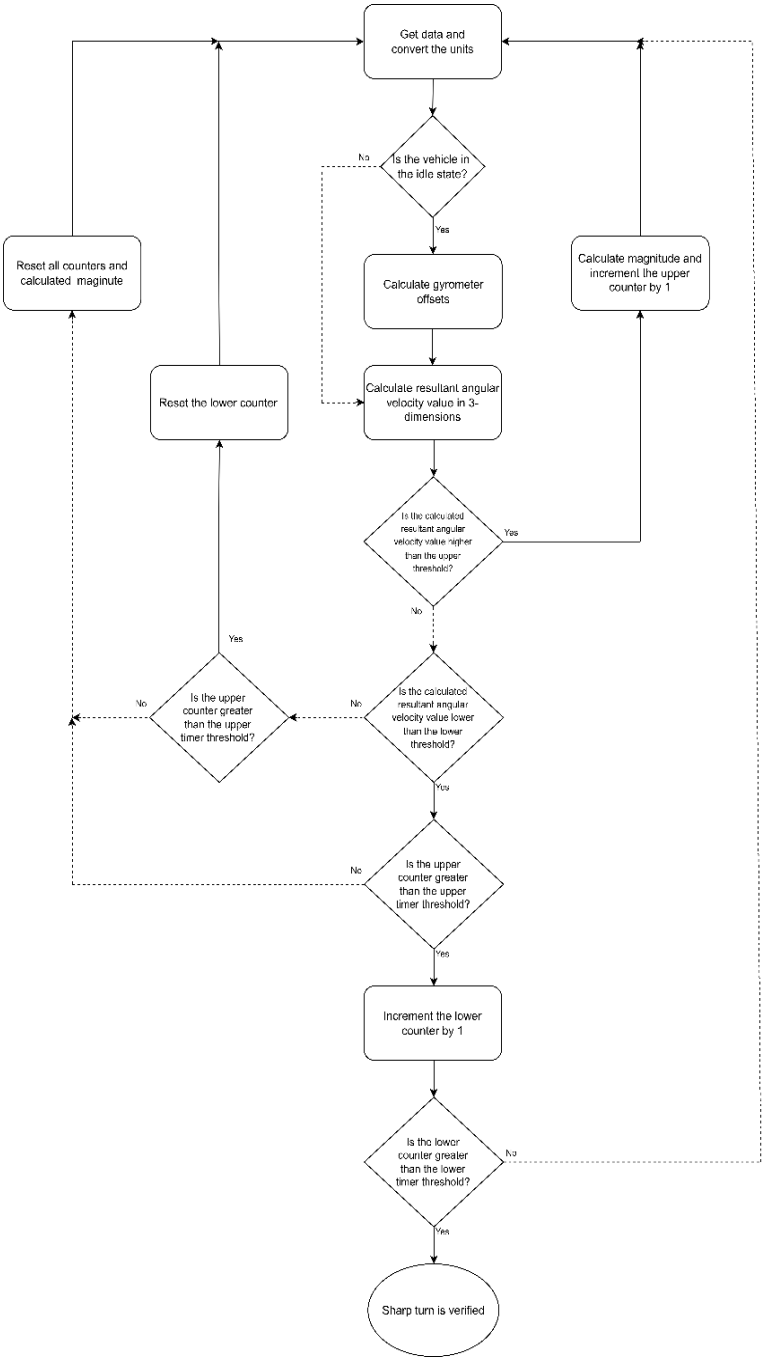

Figure 4. Sharp turn detection algorithm flow chart

The importance of driving data for the development of Advanced Driver Assistance Systems (ADAS) and the enhancement of traffic safety is increasing. Many predictive models may overlook the potential heterogeneity in driving behavior by not taking into account individual driver characteristics. A Finite Mixture of Hidden Markov Model (MHMM) is employed to segment driving behavior into different semantic segments. Approaches based on driving behavior analysis and machine learning methods are being developed (Zou et al., 2022). Our system for detecting driving behaviors, in comparison to existing systems, stands out in terms of ease of application and integration in this field. To characterize driving behaviors, this system was brought to life by employing the tools outlined in the materials section and applying the methods specified in the methods section. As a result, it has become possible to identify sudden acceleration, abrupt deceleration, and sharp turning movements in vehicles. These detections contribute to the acquisition of driving behavior data that can be meaningfully interpreted. The intention is to share this data with entities such as automotive companies, insurance firms, production planning, and vehicle service providers, with the aim of enhancing driving efficiency. The potential benefits arising from the utilization of this data are listed below.

Benefits for Insurance Companies

Driving behavior data is a valuable asset for insurance companies as it enables precise risk assessment for vehicle owners. These data are collected through sensors and telematics devices, capturing driving patterns, including sudden acceleration, abrupt deceleration, and sharp turning movements. By analyzing the output of the A/D detection system and making it interpretable, insurance companies can establish exact risk profiles for each policyholder. This affords the opportunity for a more detailed and equitable pricing structure; safer and lower-risk drivers are rewarded with lower premiums, while high-risk drivers incur higher premiums. This approach aims to optimize the profitability of insurance companies by aligning premiums with actual risk, reducing adverse selection, and enhancing the overall sustainability of the insurance industry. Furthermore, it seeks to encourage customers to adopt safe driving practices by providing opportunities for premium savings.

Benefits for Spare Parts and Aftermarket Services

Driving behavior data plays a pivotal role in gaining a better understanding of the maintenance needs of vehicles. Service providers can predict when specific components, including brakes, tires, and engine parts, should be replaced by monitoring wear and tear patterns. This predictive maintenance approach ensures cost-effective and efficient maintenance. Vehicle owners benefit from having a longer-lasting and more reliable vehicle, as maintenance is based on actual usage and wear, rather than traditional fixed schedules. Furthermore, this data can be leveraged to optimize spare parts inventory management and improve the aftermarket service supply chain. Manufacturers and service providers can ensure they have the correct parts available when needed, reducing unexpected maintenance costs and downtime for vehicle owners.

Benefits for Production Planning

Driving behavior data provides automotive manufacturers with the profound ability to understand how vehicles are used and the conditions under which they operate. This information can significantly influence production planning and processes. By aligning production processes with the real-world usage and wear patterns of vehicles, manufacturers can enhance the durability and reliability of their products. Moreover, this data can be utilized for more precise demand forecasting, leading to more efficient production planning. As a result, manufacturers can reduce overproduction, minimize inventory carrying costs, and respond more effectively to fluctuations in market demand. This not only enhances operational efficiency but also improves the sustainability and profitability of manufacturing operations.

Benefits for Vehicle Services

Driving behavior data enables automotive service technicians to proactively predict vehicle service requirements. By analyzing the output of the A/D detection system and making it interpretable, technicians can identify how specific faults and maintenance needs can be determined before they escalate into critical issues. This proactive approach reduces vehicle downtime and results in faster and more efficient servicing. Customers experience less inconvenience due to quicker turnaround times for repairs and maintenance, leading to increased customer satisfaction. Furthermore, vehicle service providers can optimize their service schedules, allocate resources more effectively, and reduce operational costs, ultimately enhancing profitability and competitiveness in the market.

Benefits for Efficient Driving Experience

Driving behavior data offers feedback to drivers to provide a more efficient driving experience. Drivers can reduce fuel consumption by improving their acceleration and braking habits, thereby reducing fuel costs and minimizing environmental impact.

Benefits for Production Strategy

Manufacturers can utilize driving behavior data to make strategic decisions for vehicle design and production. By comprehending how vehicles are used in real-world conditions, they can devise strategies to make their

products more efficient and durable. This data-driven approach enables manufacturers to enhance their competitive advantage, surpassing customer expectations in terms of reliability, fuel efficiency, and overall performance. As a result, manufacturers can stimulate innovation by capitalizing on the insights provided by driving behavior data, continuously improving their products.

Accelerometer was used for acceleration and deceleration detections. At the same time, the A/D detection system, which is designed in real time, calculates by considering all environmental factors that the vehicle may encounter while on the road. A gyroscope is also included in the project for filtering false data in acceleration, deceleration, and sharp turn detection. The raw values read from the accelerometer and gyroscope were converted into real acceleration and angular rotation units and evaluated within the framework of the mathematical model. In addition to these, the A/D detection system is open to development both in terms of content and technique. In this system, which is expected to increase efficiency and control by sharing the obtained data with insurance companies, new features can be added by examining the data that can be obtained with the accelerometer and gyroscope in the light of different subjects. One of these features is the accident status of the vehicle, which will also be of interest to insurance companies. With the sudden change in both acceleration and angular rotation angle, serious vibration or accident in the vehicle can be detected and the user or related companies can be informed about the subject if necessary.

Scientific Ethics Declaration

The authors declare that the scientific ethical and legal responsibility of this article published in EPSTEM journal belongs to the authors.

Acknowledgements or Notes

* This article was presented as an oral presentation at the International Conference on Technology, Engineering and Science (www.icontes.net) held in Antalya/Turkey on November 16-19, 2023.

* We extend our gratitude to Huseyin Karacali, the Software Architect, for his skilled mentorship and motivating influence. Additionally, we would like to acknowledge the valuable assistance provided by TTTech Auto Turkey throughout the project's development.

References

Ahmad, F., Ahmad, Z., Kerrache, C. A., Kurugollu, F., Adnane, A., & Barka, E. (2019). Blockchain in internet-of-things: Architecture, applications and research directions. *2019 International Conference on Computer and Information Sciences (ICCIS).*

CAN in Automation (CiA). (2023).*History of the CAN technology*. Retrieved from https://www.can-cia.org/can-knowledge/can/can-history/

Copper Hill Tech (n.d.). *A brief introduction to controller area network*.Retrieved from https://copperhilltech.com/a-brief-introduction-to-controller-area-network/

Dai, S., Zhong, Y., Xu, C., Liu, H., Yuan, J., & Wang, P. (2022). An intelligent security classification model of driver's driving behavior based on V2X in IoT networks. *Security and Communication Networks*, 1–12.

Dimension Engineering. (2023). *A beginner.* Retrieved from https://www.dimensionengineering.com/info/accelerometers

Farnell. (2023). *Sensor technology*. Retrieved from September 19, 2023. https://tr.farnell.com/sensor-technology.

Fierce Electronics. (2023). What is an accelerometer Retrieved fromhttps://www.fierceelectronics.com/sensors/what-accelerometer?

Fraga-Lamas, P., & Fernandez-Carames, T. M. (2019). A review on blockchain technologies for an advanced and cyber-resilient automotive industry. *IEEE Access, 7,* 17578-17598.

Gill, W. A., Howard, I., Mazhar, I., & McKee, K. (2022). A review of MEMS vibrating gyroscopes and their reliability issues in harsh environments. *Sensors, 22*(19).

He, Y., Yang, S., Zhou, X., & Lu, X.-Y. (2022). An individual driving behavior portrait approach for professional driver of HDVs with naturalistic driving data. *Computational Intelligence and Neuroscience,* 1-14.

HowStuffWorks. (2023). *What is a microcontroller?* Retrieved fromhttps://electronics.howstuffworks.com/microcontroller1.htm.

Kvaser. (2023). *Can bus protocol tutorial*. Retrieved from https://www.kvaser.com/can-protocol-tutorial/

Li, C., Yang, B., Guo, X., & Chen, X. (2020). Design, analysis and simulation of a MEMS-based gyroscope with differential tunneling magnetoresistance sensing structure. *Sensors, 20*(17), 4919.

NXP. (n.d.). *Automotive general-purpose evaluation board.* Retrieved from https://www.nxp.com/design/development-boards/automotive-development-platforms/s32k-mcu-platforms/s32k148-q176-evaluation-board-for-automotive-general-purpose:S32K148EVB

Tutorials Point. (2023) *Microprocessor microcontrollers overview.* Retrieved from https://www.tutorialspoint.com/microprocessor/microcontrollers_overview.htm.

Zhao, Y., Jia, H., Luo, H., Zhao, F., Qin, Y., & Wang, Y. (2022). An abnormal driving behavior recognition algorithm based on the temporal convolutional network and soft thresholding. *International Journal of Intelligent Systems, 37*(9), 6244–6261.

Zou, Y., Ding, L., Zhang, H., Zhu, T., & Wu, L. (2022). Vehicle acceleration prediction based on machine learning models and driving behavior analysis. *Applied Sciences, 12*(10), 5259.

Author Information

Huseyin Karacali
TTTech Auto, Turkey

Efecan Cebel
TTTech Auto Turkey
Contact e-mail: *efecan.cebel@tttech-auto.com*

Nevzat Donum
TTTech Auto Turkey

To cite this article:

Karacali, H., Cebel, E., & Donum, N. (2023). Acceleration/deceleration detection system - creation of driving behavior profiles for efficiency. *The Eurasia Proceedings of Science, Technology, Engineering & Mathematics (EPSTEM), 26*, 519-531.

The Eurasia Proceedings of Science, Technology, Engineering & Mathematics (EPSTEM)
ISSN: 2602-3199

The Eurasia Proceedings of Science, Technology, Engineering & Mathematics (EPSTEM), 2023

Volume 26, Pages 532-540

IConTES 2023: International Conference on Technology, Engineering and Science

The Classification of Asphalt Pavement Crack Images Based on Beamlet Transform

Hassan Idow Mohamed
Near East University

Mustafa Alas
Near East University

Abstract: Pavement cracking is a common road infrastructure issue which significantly affects road performance, safety and longevity. This article employed a Beamlet Transform algorithm to detect and classify different types of flexible asphalt concrete pavement cracks. Additionally, a dedicated crack segmentation network was employed for precise segmentation of pavement crack. This approach incorporates advancements that has improve precision in crack classification and segmentation. Based on the results of the beamlet transform, significant improvements in the gray scale representation of crack, enhanced crack detection, reduced noise in crack images and a more precise measurement of cracks length were achieved. Computations were performed to determine the length of linear cracks and the area of block cracks. A total of 1000 pavement images were used for training and testing the accuracy of asphalt pavement crack detection and classification models. The research results showed that block cracking, alligator cracking, transverse cracking, and longitudinal cracking can all be recognized with a remarkable accuracy. Alligator cracks and block cracks achieved detection rates more than 90%, while detection rates for the longitudinal and transverse cracks reached more than 95% accuracy.

Keywords: Pavement crack detection, Crack classification, Longitudinal crack, Alligator crack, Block crack, Transverse crack, Beamlet transform.

Introduction

Pavement cracks pose a significant challenge in road maintenance, as they have a profound impact on the structural integrity, functional performance and lifespan of roads. These cracks, which are frequently a sign of several pavement problems, can cause structural damage if ignored, highlighting the significance of early diagnosis and timely repair (Ying & Salari, 2010).

The investigation of enhanced means of crack detection is necessary. Although, the traditional methods for crack detection have proven to be somewhat effective, they are labor intensive, include lengthy procedures, and provide limited accuracy (Safaei et al., 2021). In response to this need, recent years have seen a proliferation of scientific research aimed at leveraging modern technological advancements to achieve accurate and efficient extraction of crack information from images (Zhang et al., 2017). The valley bottom boundary extraction methodology (Safaei et al., 2022) and the Prim minimum spanning tree-based crack connection algorithm (Yang et al., 2022) were the two major methods for identifying pavement cracks that have been described in the literature. These traditional procedures, which were initially designed for particular databases or scenarios, might not produce satisfactory results under changing circumstances.

Deep learning algorithms have become more popular in pavement crack identification after the development of artificial intelligence (Hu et al., 2021). Despite the fact that these methods have significantly improved detection

accuracy (Zhang et al., 2017), a number of problems still existed. For example, current models were unable to directly access road conditions due to their reliance on complicated feature extraction techniques and their limited adaptability to a variety of image sources and road segments (Alayat & Omar, 2023). To overcome these constraints, the current study offered a novel methodology that combines the deep learning and Beamlet algorithms for classification of asphalt pavement deterioration. The simultaneous crack detection and segmentation provided by this approach was a special benefit that boosted the model effectiveness.

The significance of developing complex image processing algorithms for pavement crack assessment becomes clear in light of the growing issues regarding pavement distresses. This study further explored the earlier work, such as the application of histogram projection (Zhao & Wang, 2010), the use of moment invariants and neural networks (Zhao & Wang, 2010), and the use of neural networks for crack detection and classification (Safaei et al., 2022), adding to the overall understanding of this field.

Beamlet Transform Algorithm

The implementation of the beamlet transform occurs within image sections that are dynamically divided into squares. Visual representations of images occur within the continuous square $[0, 1]^2$, in this scenario, pixels are arranged in a grid of 1/n by 1/n squares throughout the $[0, 1]^2$ area. The compilation of beamlets constitutes a diverse range of line segments, encompassing a broad spectrum of orientations, positions, and scales. This variation is visually portrayed in Figure 1. (Ouyang et al., 2014)

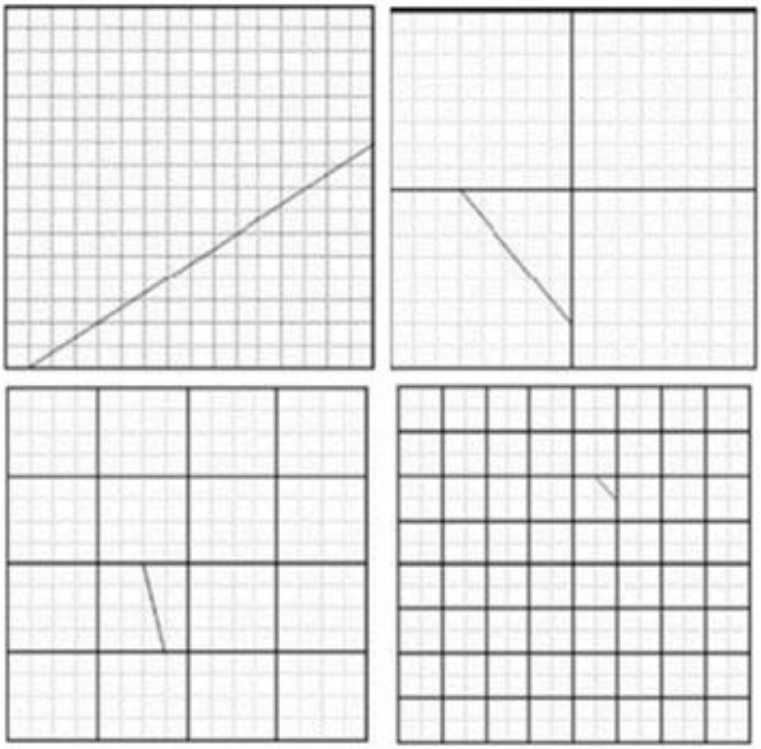

Figure 1. Different in size, location, and orientation, four beamlets

The beamlet transform is characterized as the summation of line integrals calculated across the entirety of the beamlet set. Consider f (x_1, x_2) to be perceived as a continuous function within a two-dimensional space, where x_1 and x_2 denote coordinates (Ouyang et al., 2014). The beamlet transform Tf of the function f is outlined as follows equation 1:

$$T_f(b) = \int_b f(x(l))dl, b \in B_E \qquad (1)$$

Here, B_E represents the total collection of beamlets.

In the context of digital images, the beamlet transform evaluates the line integral within the discrete domain. As depicted in Figure 2, the depiction of the beamlet transform for all points along beamlet b is articulated in the following equation 2 manner: (Ouyang et al., 2014)

$$f(x_1,x_2) = \sum_{i_1,i_2} f_{i_1,i_2} \Phi_{i_1,i_2}(x_1,x_2) \qquad (2)$$

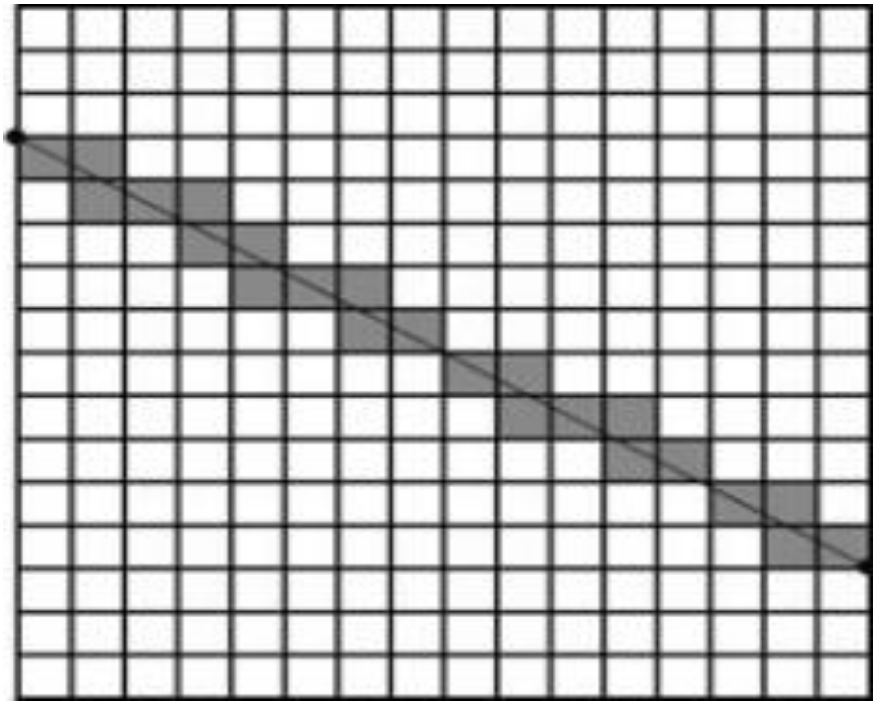

Figure 2. A weighted sum of pixel values along the lines' direction represents the beamlet transform.

Where f_{i_1,i_2} refers to the gray level value of the pixel located at (i_1, i_2) and $\Phi_{i_1,i_2}(x_1,x_2)$ stands for the pixel's related weight function. Multiple options are available for the selection of. $\Phi_{i_1,i_2}(x_1,x_2)$, and In this study, the average interpolation function is the one we choose. (Ouyang et al., 2014)

If $p(x_1,x_2)$ represent $[i_1/n, (i_1+1)/n] \times [i_2/n, (i_2+1)/n]$, choose function Φ_{i_1,i_2} fulfill the equation 3:

$$n^2 \int_{P(x_1,x_2)} \Phi_{i_1,i_2}(x_1,x_2) dx_1 dx_2 = \delta_{i_1,i_2} \qquad (3)$$

Methods

The data-set of the images used in the current study were procured from asphalt concrete pavement roads which is available at the https://github.com/cuilimeng/CrackForest-dataset. A total of 1000 images for four different types of cracks as presented in Table 1 were used in the testing processes.

Table 1. Four main types of cracks

Crack Types	Number of images	**Crack angle Ω**	Branches
Block	250	$\Omega \geq 60°$	NO
Longitudinal	250	$\Omega \leq 30°$	NO
Transverse	250	$60° > \Omega > 30°$	NO
Alligator	250	-	YES

Generally, images of pavement cracks display linear attributes and are often discontinuous due to considerable environmental interference, making it challenging for traditional pixel-based methods to effectively detect and categorize these cracks. On the other hand, the Beamlet algorithm as utilized in the current study proves robust in its line detection capabilities, making it suitable for asphalt pavement crack detection and classification tasks. The outline of the procedures followed for developing the crack detection and classification models by using beamlet algorithm was illustrated in Figure 3.

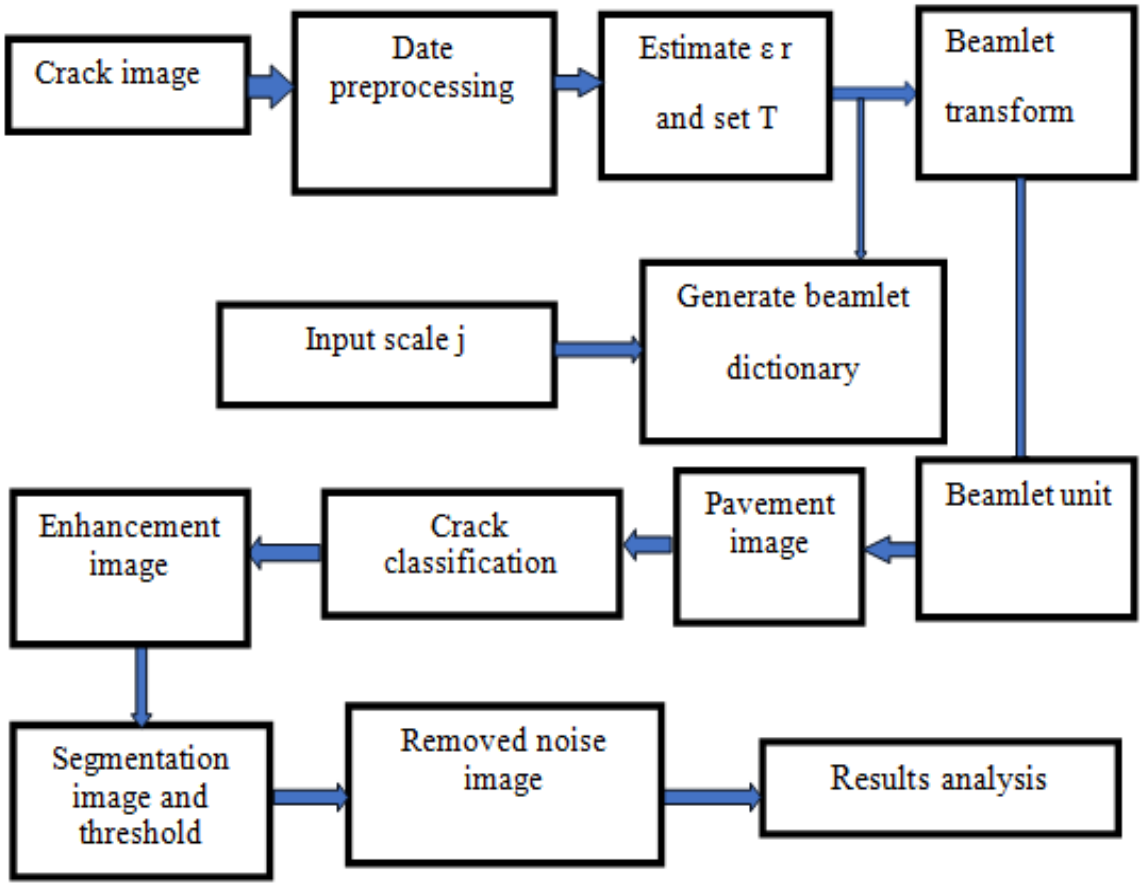

Figure 3. Processing steps Beamlet Transform Algorithm flowchart

Result and Discussion

Asphalt pavement crack detection was performed by using the steps outlined in Figure 1. Primarily the original images were converted to grey scale and then an image enhancement technique was utilized in order to enhance the crack visibility. Image segmentation by using a thresholding technique, and denoising were further applied in order to improve crack visuals and highlight crack features in the images. These procedures were conducted for all 1000 images which included longitudinal, transverse, alligator and block cracking features. Figures 4-7 illustrated the procedures followed during the crack detection and classification for each type of crack; longitudinal, transverse, alligator and block cracking respectively.

A single longitudinal crack was initially detected in Figure 4. The longitudinal crack was classified with a length of 0.7504 m and a crack angle of 66°. Figure 5 contained both transverse and lengthy cracks. Segmentation with a threshold value of 0.85m isolated the transverse crack. The transverse crack was classified with a length of 0.98556m and a crack angle of 11° using the classification of asphalt pavement crack detection based on Beamlet transform algorithm. The first crack image shown in Figure 6 displayed an alligator crack with four branches. Segmentation with a threshold value of 0.93 m isolated the alligator crack. The alligator crack was classified with a length of 0.53137 m and a crack angle of 14°. Finally, the block crack as shown in Figure 7 was detected with a threshold value of 0.84m and crack area of 0.72035m2.

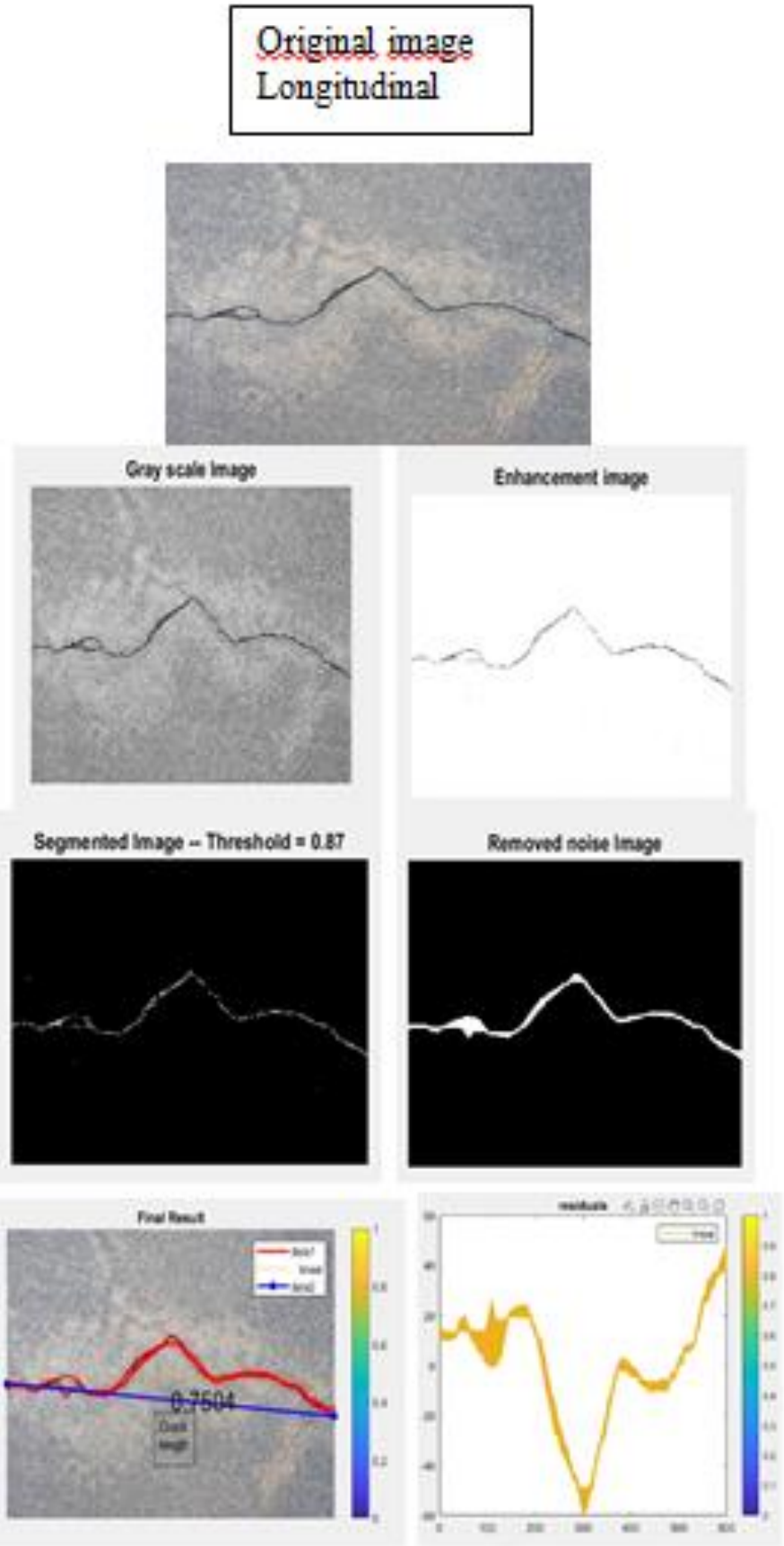

Figure 4. Longitudinal crack detection and classification

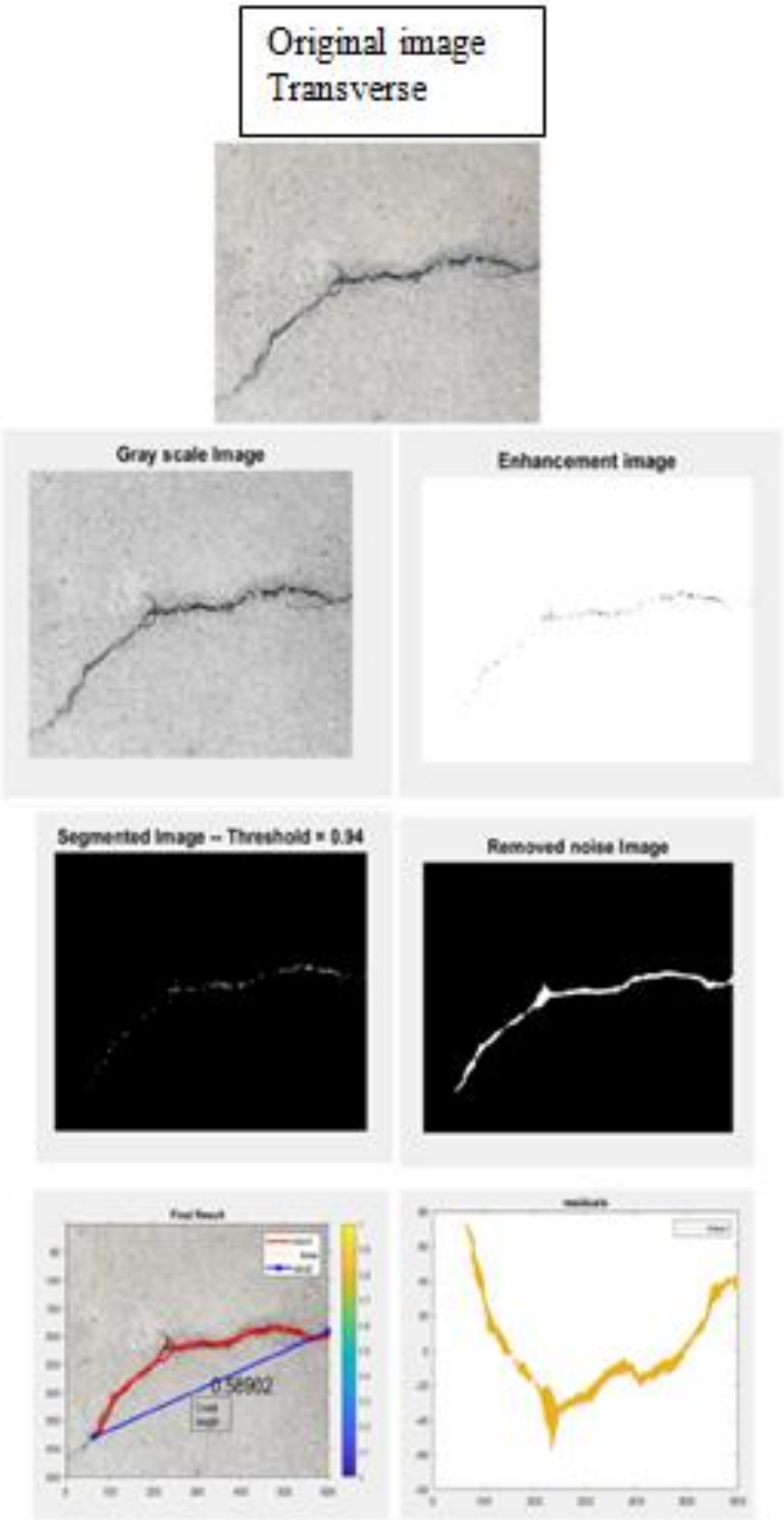

Figure 5. Transverse crack detection and classificatio

The outcomes of the complete analysis were summarized by using the crack angle, crack length, branches and threshold values and the analysis results were tabulated in Table 2

Table 2. Pavement crack detection and classification results

Crack angle Ω	Crack length	Branches	Threshold	Crack types
11°	0.98556 m	YES	0.85 m	Transverse
66°	0.7504 m	YES	0.87 m	Longitudinal
14°	0.53137 m	YES	0.93 m	Alligator
-	Area= 0.72035 m^2	YES	0.84 m	Block

The results showed that the Beamlet algorithm can accurately identify pavement crack images into longitudinal, Transverse block, and Alligator. As in table 3 the result of success rate percentage was identified by Using the percentage change formula: dividing the success rate number by the total crack tested number and then multiplying by 100.

Table 3. The classification of success rate

Types of Cracks	Number	Longitudinal	Transverse	Alligator	Block
Alligator	250		5	226	6
Block	250			2	234
Longitudinal	250	238			
Transverse	250	8	243	13	
Success rate		95.2%	97.2%	90.4%	93.6%

Conclusion

In this research, an improved model for detecting and classifying asphalt pavement cracks was developed by utilizing the beamlet transform algorithm. The suggested model showed a high degree of accuracy in accurately identifying and classifying various types of pavement cracks. These included block cracks, alligator cracks, transverse cracks, and longitudinal cracks. The models were able to observe crack information, enhance crack visibility, and provide precise crack measurements by utilizing the beamlet transform algorithm. The abilities of beamlet transform algorithm to efficiently detect and classify asphalt concrete pavement cracks may be constrained and outside influences like lighting conditions can affect the model's performance. To determine the model's applicability to various road conditions and environmental variables, further research is required.

Recommendations

The recommended that the use of the Beamlet Transform Algorithm for detecting and classifying pavement cracks. To make it really useful, also, need to test it on a wider range of real-world crack situations and see how well it works with noisy conditions and different road situations. The algorithm has done well in classifying cracks, even when there is noise, but we can make it even better. try different ways of processing images, and test it with different datasets. This will make it more accurate and useful for taking care of roads and making them safer. Also, recommended to make the width of the crack.

Scientific Ethics Declaration

The authors declare that the scientific ethical and legal responsibility of this article published in EPSTEM journal belongs to the authors.

Acknowledgements or Notes

* This article was presented as an oral presentation at the International Conference on Technology, Engineering and Science (www.icontes.net) held in Antalya/Turkey on November 16-19, 2023.

References

Alayat, A. B., & Omar, H. A. (2023). Pavement surface distress detection using digital image processing. *Techniques*, *35*(1), 247-256.

Deng, L., Zhang, A., Guo, J., & Liu, Y. (2023). An integrated method for road crack segmentation and surface feature quantification under complex backgrounds.*Remote Sensing*, *15*(6).

Du, Y., Pan, N., Xu, Z., Deng, F., Shen, Y., & Kang, H. (2020). Pavement distress detection and classification based on YOLO network. *International Journal of Pavement Engineering*, *22*(1), 1–14.

Duc, N., Quoc, H., & Nguyen, L. (2018). A novel method for asphalt pavement crack classification based on image processing and machine learning. *Engineering with Computers*, *35*, 487-495.

Feng, X., Xiao, L., Li, W., Pei, L., Sun, Z., Ma, Z., Shen, H., & Ju, H. (2020). Pavement crack detection and segmentation method based on improved deep learning fusion model. *Mathematical Problems in Engineering*, 1-22.

Fereidoon, H. Z., Nejad, M., & Fahimifar, A. (2017). Image based techniques for crack detection , classification and quantification in asphalt pavement : A review. *Archives of Computational Methods in Engineering*, *24*(4), 935–977.

Guo, K., He, C., Yang, M., & Wang, S. (2022). Open A pavement distresses identification method optimized for YOLOv5s. *Scientific Reports*, 1–15.

Hong, N., Nguyen, T., Perry, S., Bone, D., Thanh, H., & Thi, T. (2021). Two-stage convolutional neural network for road crack detection and segmentation. *Expert Systems With Applications*, *186*. 115718.

Hu, G. X., Hu, B. L., Yang, Z., Huang, L., & Li, P. (2021). Pavement crack detection method based on deep learning models. *Wireless Communications and Mobile Computing, 2021,* 1-13.

Huang, Z., Chen, W., Al-tabbaa, A., & Brilakis, I. (2022). NHA12D : A new pavement crack dataset and a comparison study of crack detectıon algorithms.*2022 European Conference on Computing in Construction.* Rhodes, Greece

Majidifard, H., Adu- Gyamfi, Y., & Buttlar, W. (2020).Pavement image datasets : A new benchmark dataset to classify and densify pavement distresses. *Journal of the Transportation Research Board, 2674*(2). 328-339.

Mandal, V., Uong, L., & Adu-Gyamfi, Y. (2018). Automated road crack detection using deep convolutional neural networks. *2018 IEEE International Conference on Big Data (Big Data)*, 5212–5215.

Mei, Q., & Gul, M. (2020). A cost effective solution for pavement crack inspection using cameras and deep neural networks. *Construction and Building Materials*, *256*. 119397.

Mohan, A., & Poobal, S. (2017). Crack detection using image processing : A critical review and analysis. *Alexandria Engineering Journal*, *57*(2), 787-798.

Nguyen, T. H., Perry, S., Ngyuen, T., & Le, H. (2018). *Pa*vement crack detection using convolutional neural network. *The Nint International Symposium*, 16–21.

Ouyang, A., Dong, Q., Wang, Y., & Liu, Y. (2014). The classification of pavement crack image based on beamlet algorithm. *International Conference on Computer and Computing Technologies in Agriculture* (pp.129–137).

Safaei, N., Smadi, O., Masoud, A., & Safaei, B. (2022). An automatic image processing algorithm based on crack pixel density for pavement crack detection and classification. *International Journal of Pavement Research and Technology*, *15*(1), 159–172.

Salman, M., Mathavan, S., Kamal, K., & Rahman, M. (2013). Pavement crack detection using the Gabor filter. *ITSC 2013*, 2039–2044.

Song, W., Jia, G., Jia, D. I., & Zhu, H. (2019). Automatic pavement crack detection and classification using multiscale feature attention network. *IEEE Access*, *7*, 171001-171012.

Tsai, Y., Kaul, V., & Mersereau, R. M. (2010). Critical assessment of pavement distress segmentation methods. *Journal of Transportation Engineering, 136*(1) , 11–19.

Yang, J., Fu, Q., & Nie, M. (2019). Deep convolution neural network for crack detection on asphalt pavement Deep convolution neural network for crack detection on asphalt pavement. In *Journal of Physics: Conference Series* (Vol. 1349, No. 1, p. 012020). IOP Publishing.

Yang, Z., Ni, C., Li, L., Luo, W., & Qin, Y. (2022). Three-stage pavement crack localization and segmentation. *Sensors*, *22*(21), 8459.

Ying, L., & Salari, E. (2010). Beamlet transform-based technique for pavement crack detection and classification. *Computer- Aided Civil and Infrastructure Engineering*, *25*(8), 572–580.

Zalama, E., Jaime, G., & Medina, R. (2014). Road crack detection using visual features extracted by Gabor *Filters*. *29*, 342–358.

Zhang, A., Wang, K. C. P., Fei, Y., Liu, Y., Li, J. Q., & Chen, C. (2017). Automated pixel-level pavement crack

detection on 3D asphalt surfaces using a deep-learning network. *Computer-Aided Civil Engineering, 34*(5) 1–15.

Zhang, D. Y., Yang, F., Zhu, J. Y., & Zhang, L.(2016.). Road crack detection using deep convolutional neural network. *International Conference on Image Processing*. IEEE

Zhao, H., & Wang, X. (2010). Improvement of canny algorithm based on pavement edge detection. 3*rd International Congress on Image and Signal Processing*, 964–967. Yantai, China.

Author Information

Hassan Idow Mohamed
Near East University
Faculty of Civil Engineering Department
Nicosia, North Cyprus
Contact e-mail: hassanidka@email.com

Mustafa Alas
Near East University
Faculty of Civil Engineering Department
Nicosia, North Cyprus

To cite this article:

Mohamed, H. I., & Alas, M. (2023). The classification of asphalt pavement crack images based on beamlet transform. *The Eurasia Proceedings of Science, Technology, Engineering & Mathematics (EPSTEM), 26*, 532-540.

The Eurasia Proceedings of Science, Technology, Engineering & Mathematics (EPSTEM)
ISSN: 2602-3199

The Eurasia Proceedings of Science, Technology, Engineering & Mathematics (EPSTEM), 2023

Volume 26, Pages 541-547

IConTES 2023: International Conference on Technology, Engineering and Science

Human Resources Analytics Usage in Turkish Organizations

M. Cagri Budak
Istanbul Technical University
Dokuz Eylul University

Ayberk Soyer
Istanbul Technical University

Abstract: Since the early 2000s, the use of analytics in Human Resources (HR) has become increasingly widespread. With the spread of analytical applications, it is thought that the Human Resources Department will contribute more to making effective decisions in organizations. This study investigates the fundamental differences between organizations that use and do not use Human Resources Analytics (HRA). The research was carried out by collecting data from organizations operating in different sectors in Turkey. The organizations participating in the survey were compared in terms of the organization's total age, turnover (2022) and number of employees, and it was investigated whether these variables had an impact on the use of HRA. In addition, in organizations that stated that they used HRA, it was also investigated how long these practices have been carried out and by which function they were carried out. The results have been analyzed in the context of descriptive statistics and finalized according to the responses received from a total of 175 organizations, and it was observed that the main difference in the use of HRA emerged in the context of the number of employees and organizational turnover. Moreover, by conducting a t-test for organizational age, it was concluded that the age of organizational age creates a difference in the use of HRA. Additionally, it has been determined that more than half of the organizations that apply analytics have been using HRA for less than 5 years and analytics applications are not carried out by a separate analytics team.

Keywords: HR analytics, Big data, Organizational management, Technology usage

Introduction

Data-driven decision making is becoming increasingly important in Human Resources Management (HRM) due to the realization of the potential contributions of the insights that it provides in the areas where it is applied. However, applying data-based approaches to HRM is quite complex (Shet et al., 2021). It has been on the agenda for a long time to use analytics for HR applications, which highlights the nature of this complexity. This is because the concept of measurement in HRM can be traced back to the 1980s (Marler & Boudreau, 2017). Although it is referred to by different names and definitions, HRA applications which determine the measurement, decisions and actions in HRM with an evidence-based approach using human-oriented data are carried out with HRA applications (Margherita, 2022).

Van den Heuvel and Bondarouk (2017) have suggested that HRA would have a major impact on the decision-making mechanisms of organizations. To be able to influence the decision-making mechanism, HRA must first be used. In this study, the general structures of organizations that use and do not use HRA were revealed and the differences between these organizations were tried to be determined.

The rest of the study is organized as follows: Section 2 summarizes the general literature and definitions related to HRA, Section 3 explains the purpose and methodology of the study, Section 4 presents the findings of the

analysis. The last section includes the conclusions of the study, managerial implications and suggestions for future work.

Literature Review

The term HRA has been studied in the literature under many different keywords such as "Human Capital Analytics", Human Resources Analytics", "Talent Analytics", "Workforce Analytics", "Collaboration Analytics", "Labor Analytics", "Relationships Analytics", "People Analytics" (Tursunbayeva et al., 2018). Although it has been referred to under many names in the literature, it basically refers to the use of analytics in HRM. Particularly with the ease of access to data after the acceleration of digital transformation, HRA has become more visible within organizations. For instance, data collection methods such as emails, calendars and even wearable technologies make it possible to understand employee behavior and thereby improve performance (Fernandez and Gallardo-Gallardo, 2021).

Ever since the emergence of the HR function in organizations, the main evaluation criterion has been the activities performed by the HR function in general. For instance, indicators such as how many employees have been hired and fired/left in the previous period, which trainings have been organized, etc. have been used to evaluate the HR function. These indicators are relatively easy to assess numerically, however, more important is the quality of the activities associated with these indicators. For instance, instead of determining how many people participated in the training provided in the previous activity period, it is necessary to have an advanced understanding of how the training increases customer satisfaction and how increased customer satisfaction impacts sales in an analytical way (McIver et al., 2018). Such measurements would be possible with the widespread use of HRA within the organization.

In order to use HRA in organizations, it is required to have data. Data are raw and unorganized facts. Data should be processed and organized to obtain information, and information should be transformed into meaningful knowledge according to the problem that needs to be solved. Organizations usually have huge amount of data and information can be provided through operational reports. On the other hand, HRA is the systematic identification and measurement of human factors affecting the business results and contributing to competitive advantage by transforming them into meaningful knowledge (Minbaeva, 2017). In other words, having data or information does not mean improving the performance of the organization by having HRA. HRA is a more systematic application throughout the organization. Shet et al. (2021) have examined the reasons why organizations cannot implement HRA and why organizations that use HRA cannot generate business value from HRA in the following categories: technological reasons, organizational reasons, environmental reasons, data management reasons and individual reasons. In this context, organizations which use and do not use HRA have been compared in terms of age, turnover and number of employees in this study.

Methodology

By contacting HR professionals working in different organizations via the LinkedIn social media platform in order to evaluate the differences between organizations that use HRA and do not, a survey has been sent to the relevant HR professionals to measure the concept of HRA. The survey has been prepared on the Google Forms platform and sent to 1378 HR professionals working in different organizations with different titles. The survey has been completed by 175 HR professionals in the period May 2023 - October 2023 with a return rate of 12.69%. The sectoral distribution of the 175 responses covers a wide range of sectors, including Information Technology; Glass, Cement and Soil; Education; Electricity and Electronics; Energy; Finance; Food; Holding; Construction; Chemistry; Mining; Machinery; Media; Metal; Automotive; Health; Insurance; Technology; Textile; Telecommunications; Trade (Sales and Marketing) ; Tourism; and Consumer Goods. For this reason, it can be said that the answers given represent different sectors in Turkey. Furthermore, 86 out of 175 participants who responded to the survey (i.e., 49.14%) have stated that HRA is used in their organizations.

The 175 respondent organizations have been evaluated in terms of their age, total number of employees (1-50 employees, 51-250 employees, 251-500 employees, 501-1000 employees, 1001-2500 employees, 2501-5000 employees and 5001 and above employees) and their turnover in 2022 (less than 1 million TL, between 1 million TL and 50 million TL, between 50 million TL and 100 million TL, between 100 million TL and 500 million TL, between 500 million TL and 1 billion TL and above 1 billion TL). In terms of the variables mentioned, organizations using and not using HRA have been compared using descriptive statistics. Besides this comparison, the 86 organizations which indicate that they use HRA have been examined in terms of how long

they have been using HRA, which department performs HRA applications and which tools/software are used for HRA applications.

Results

The main purpose of this study is to compare organizations that use and do not use HRA in terms of the age of the organization, number of employees and the turnover generated by the organization. The number of employees of the organization has been considered in a total range of 7 levels. Table 1 shows an overview of HRA usage by number of employees. According to Table 1, as the number of employees increases, the percentage of organizations that use HRA surpasses the percentage of organizations that do not use HRA. Figure 1 shows the general pattern of HRA usage percentage compared to the number of employees. As the number of employees within the organization is above 1,000, it is seen that, as a percentage, the organizations that use HRA are more than the organizations that do not. It can be said that as the number of employees increases, the number of people to be monitored increases and it is more difficult to achieve this monitoring through non-systematic means. According to this result, it is not surprising that organizations with more employees perform analytical applications more than organizations with fewer employees.

Table 1. HRA usage by number of employees

Number of Employees	Number of Organizations	Number of Organizations Using HRA	Percentage	Number of Organizations not Using HRA	Percentage
1-50 employees	23	8	9.30%	15	16.85%
51-250 employees	50	17	19.77%	33	37.08%
251-500 employees	23	8	9.30%	15	16.85%
501-1000 employees	20	8	9.30%	12	13.48%
1,001-2,500 employees	18	14	16.28%	4	4.49%
2,501-5,000 employees	12	10	11.63%	2	2.25%
5,001 and more employees	29	21	24.42%	8	8.99%
Total	175	86		89	

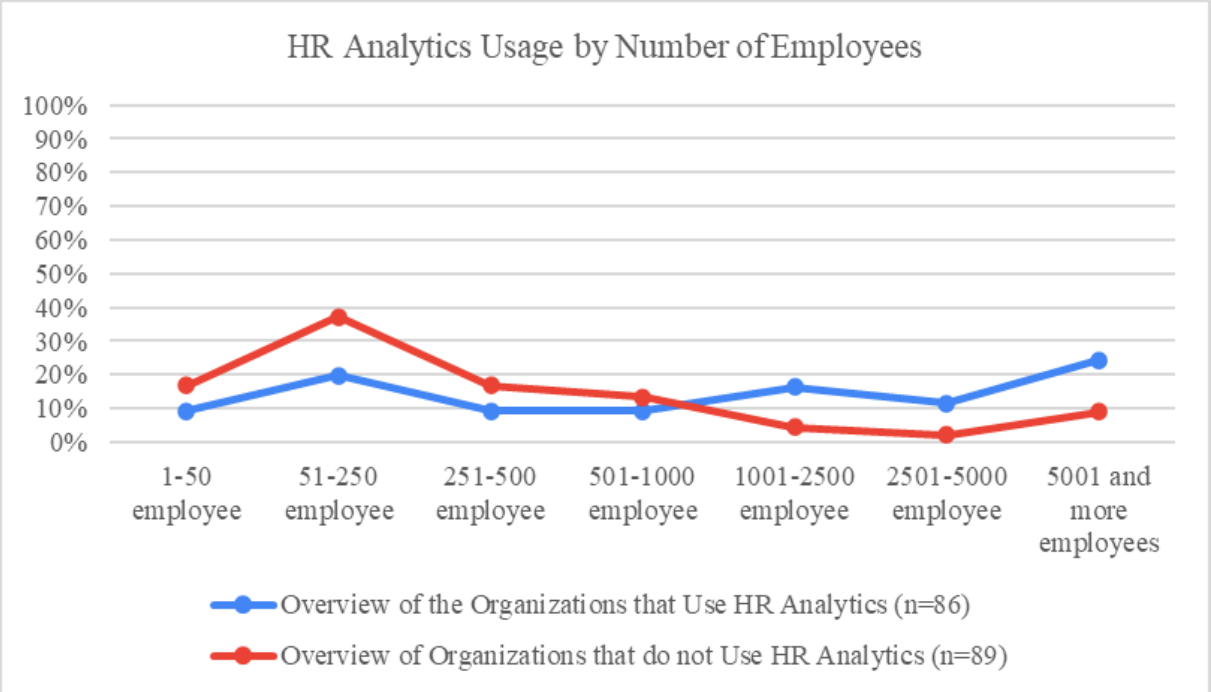

Figure 1. HRA usage by number of employees

The turnover generated by the organizations in this study has been divided into 6 levels. Table 2 shows the number and percentages of HRA usage by organizations according to their turnover range in 2022. According to Table 2, for organizations that have 100 million TL turnover or less, the rate of not using HRA is higher than the

rate of using HRA at every turnover level. However, if the turnover of the organization exceeds 100 million TL, the rate of using HRA in organizations surpasses the rate of non-users. At each level, the gap becomes larger. For organizations with turnover between 100 million TL and 500 million TL, the percentage of using HRA (10.47%) is almost equal to the percentage of non-users (10.11%), while for organizations with a total turnover more than 1 billion TL, the percentage of using HRA (43.02%) is much higher than the percentage of non-users (16.85%). In other words, it has been observed that after a certain turnover level, the usage of HRA keeps increasing. Figure 2 illustrates the percentages of HRA utilization by turnover in a similar way and visually demonstrates the aforementioned difference.

Table 2. HRA Usage by turnover in 2022

Turnover in 2022	Number Organizations	Number ofOrganizations Using HRA	Percentage	Number of Organizations not Using HRA	Percentage
Less than 1 million TL	9	2	2.33%	7	7.87%
1 million TL to 50 million TL	49	15	17.44%	34	38.20%
50 million TL to 100 million TL	28	10	11.63%	17	19.10%
100 million TL to 500 million TL	18	9	10.47%	9	10.11%
500 million TL to 1 billion TL	19	13	15.12%	6	6.74%
More than 1 billion TL	52	37	43.02%	15	16.85%
Total	175	86		89	

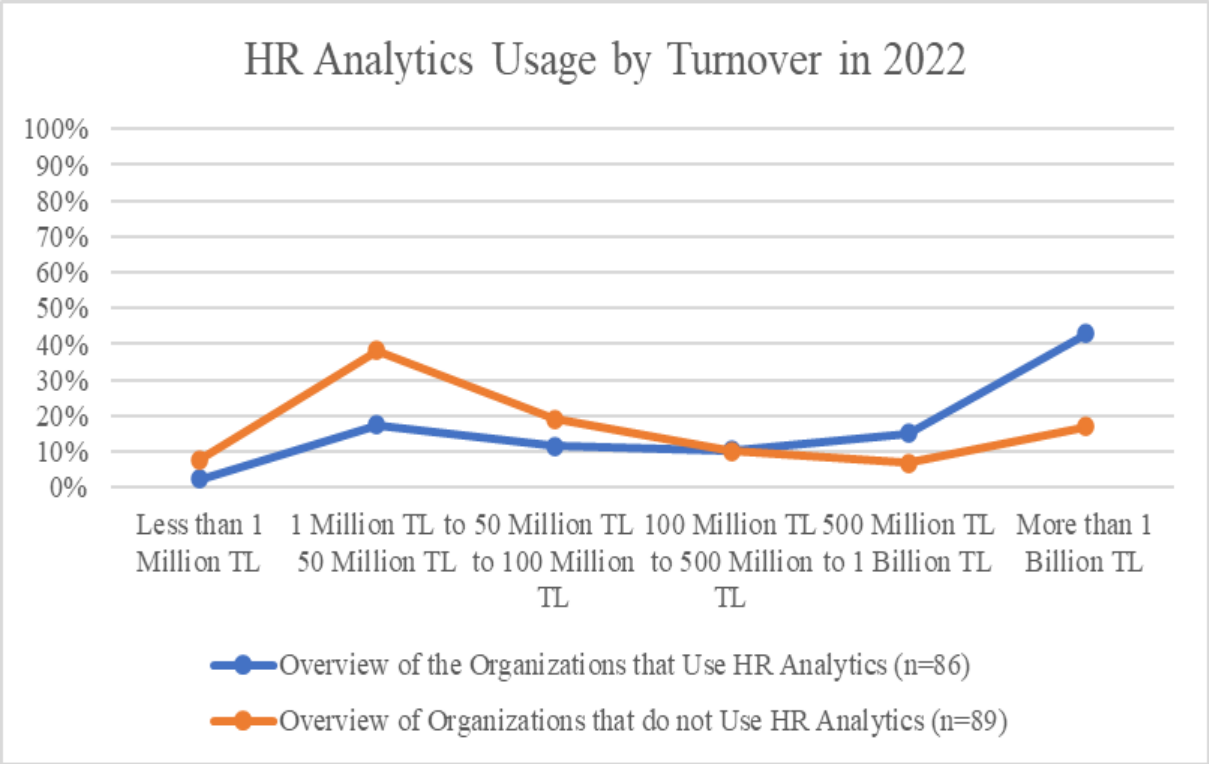

Figure 2. HRA usage by turnover in 2022

Following the observation of whether there is a relationship between the organization's turnover and number of employees and HRA, it has been also investigated that whether there is a relationship between the age of the organization and the organization's use of HRA. Figure 3 demonstrates the usage of HRA according to the age of the organization. As can be seen in Figure 3, the average age of organizations that use HRA is 38.38 years with a median of 30, while the average age of organizations that do not use HRA is 22.34 years with a median of 15.5. In order to determine whether there is statistically significant difference in terms of the usage of HRA, an independent sample t-test has been conducted using the IBM SPSS program (Version 28.0.0.0.0). Table 3 summarizes the results of the independent sample t-test results at 95% confidence interval. According to the result of the test, there is a statistically significant difference between the age of the organization and the

organization's use of HRA. In other terms, organizations with a higher average age have a higher usage of HRA than the organizations with a lower average age.

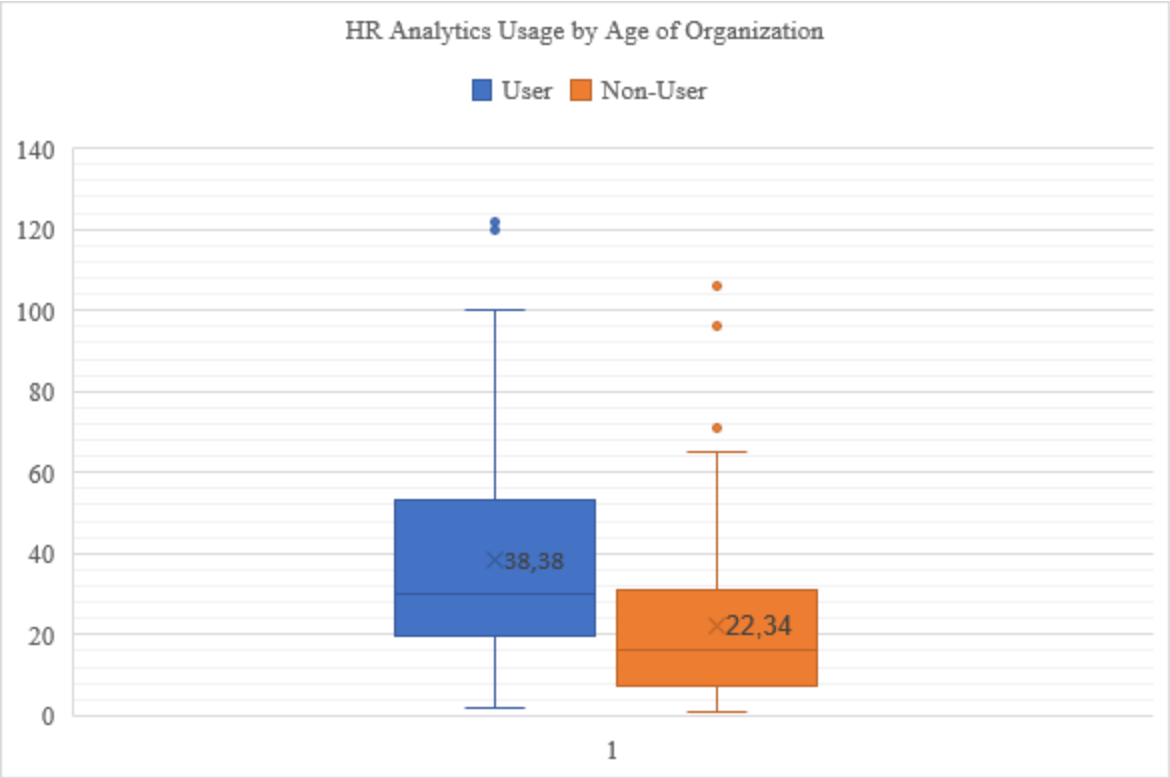

Figure 3. HRA usage by age of organization

Table 3. Independent sample t-test results

						Significance	
						One-Sided	Two-Sided
		F	Sig.	t	df	p	p
Age of Organization	Equal variances assumed	9,342	,003	-4,424	173	<,001	<,001
	Equal variances not assumed			-4,402	156,533	<,001	<,001

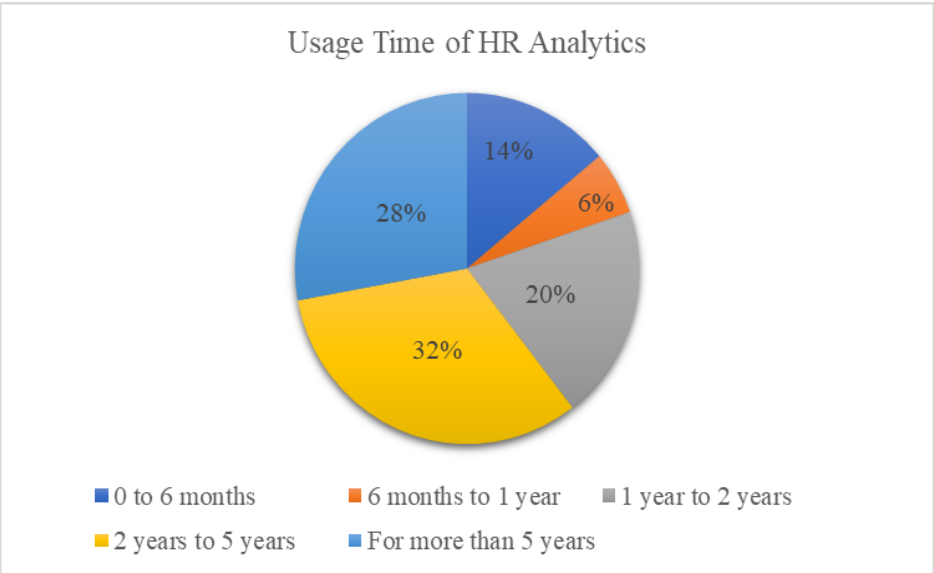

Figure 5. Usage time of HRA

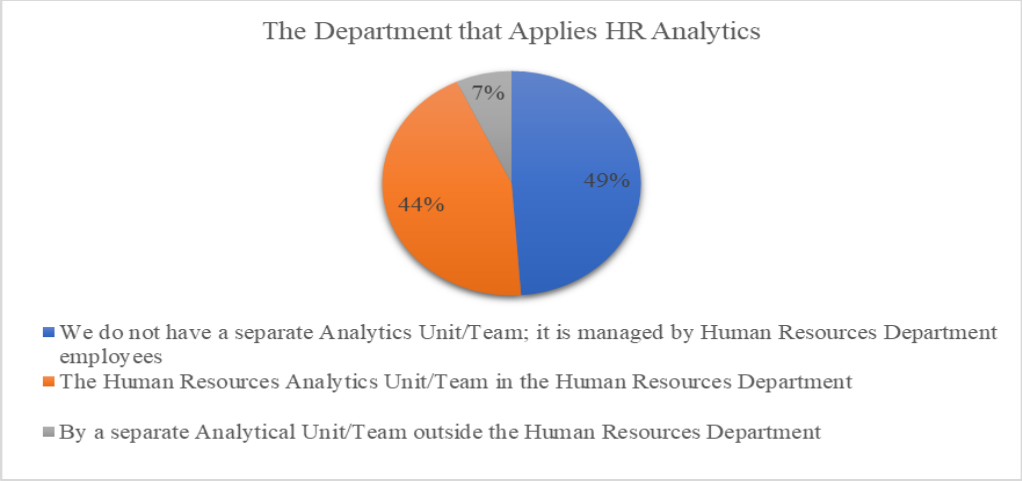

Figure 6. The department that applies HRA

Out of 175 organizations that responded, 86 of them use HRA. These organizations have also been investigated in terms of how long HRA has been used and how HRA activities have been carried out. Figure 4 displays how long organizations that use HRA have been using it. According to the results, 60% of the organizations have used HRA for more than 2 years and 28% for more than 5 years. In addition, it has been found that 20% of the organizations have used HRA for less than 1 year. Figure 5 illustrates the department that HRA applications are carried out under in organizations. It can be seen that almost half of the organizations that use HRA do not have a separate analytics team, and HRA applications are carried out by HR employees. Only 7% of all organizations have established an external analytical department apart from the HR function and this unit conducts HRA activities.

Conclusions and Managerial Implications

This study aims to explore the main differences between organizations that use and do not use HRA. In order to address the aforementioned objective, a survey has been designed and evaluations have been made based on the data collected from this survey. The usage of HRA within the organization has been evaluated in the context of the age of the organization, the number of employees and the turnover of the organization. According to the results, there is a statistically significant difference between the age of the organization and the usage of HRA by the organization. Levenson & Fink (2017) have mentioned the importance of continuous learning for the usage of HRA. Considering that organizations provide a continuity of learning from past to present, along with the corporate culture that is established along with the age of the organization, it can be said that organizations have become more ready for the use of HRA over the time since their establishment. Fernandez and Gallardo-Gallardo (2021) have stated that one of the key drivers for adopting HRA is financial readiness. According to the results of this study, the percentage of HRA usage increases when the turnover exceeds a certain level. Consistent with Fernandez and Gallardo-Gallardo (2021), the organization is required to be financially ready to adopt HRA. It is observed that when the number of employees in the organization exceeds a certain threshold similar to the turnover of the organization, the percentage of HRA usage surpasses the percentage of non-usage. As the number of employees increases, the organizational structure expands, in other words, the number of employees that need to be managed increases, therefore it is not surprising that above a certain threshold, the percentage of organizations that use HRA is greater than the non-user organizations.

Among the 86 organizations that participated in the study and used HRA, it has been observed that 20% of them have used HRA for less than 1 year. This rate has been found as 28% for HRA usage for more than 5 years. According to these results, it can be concluded that the use of HRA in Turkey is generally spread over the short and medium term and there are fewer organizations that have been using HRA for a long time. From this point of view, it can be stated that the usage of HRA applications among organizations in Turkey is relatively new. However, considering that the emergence of HRA after the 2000s and its development together with the digital structure (Tursunbayeva et al., 2018), it can be said that it is not too late for organizations to implement HRA. In addition, it has been observed that organizations that use HRA largely implement HRA applications within the HR function. It is observed that 49% of the organizations conduct HRA applications by HR department employees, not by a separate analytics team. Investigating whether the requirement of analytical competence of the implementing team for HRA applications, put forward by McCartney and Fu (2022) and Minbaeva (2018),

is met for organizations using HRA in Turkey may open an area for future studies. One of the major limitations of this study is that while investigating on the usage of HRA by organizations, the comparison between organizations is based on a limited number of variables, namely the age of the organization, the number of employees and the turnover of the organization. Especially in the context of organizational turnover, a single period has been taken as a basis and a comparison has been made over a single period. In future studies, inferences regarding HRA can be made by observing turnover over a wider period of time.

Scientific Ethics Declaration

The authors declare that the scientific ethical and legal responsibility of this article published in EPSTEM journal belongs to the authors.

Acknowledgements or Notes

* This article was presented as an oral presentation at the International Conference on Technology, Engineering and Science (www.icontes.net) held in Antalya/Turkey on November 16-19, 2023.

References

Fernandez, V., & Gallardo-Gallardo, E. (2021). Tackling the HR digitalization challenge: Key factors and barriers to HR analytics adoption. *Competitiveness Review: An International Business Journal, 31*(1), 162–187.

Levenson, A., & Fink, A. (2017). Human capital analytics: Too much data and analysis, not enough models and business insights. *Journal of Organizational Effectiveness: People and Performance*, *4*(2), 145–156.

Margherita, A. (2022). Human resources analytics: A systematization of research topics and directions for future research. *Human Resource Management Review*, *32*(2), 100795.

Marler, J. H., & Boudreau, J. W. (2017). An evidence-based review of HR Analytics. T*he International Journal of Human Resource Management*, *28*(1), 3–26.

McCartney, S., & Fu, N. (2022). Bridging the gap: Why, how and when HR analytics can impact organizational performance. *Management Decision*, *60*(13), 25–47.

McIver, D., Lengnick-Hall, M. L., & Lengnick-Hall, C. A. (2018). A strategic approach to workforce analytics: Integrating science and agility. *Business Horizons*, *6*1(3), 397–407.

Minbaeva, D. (2017). Human capital analytics: Why aren't we there? Introduction to the special issue. *Journal of Organizational Effectiveness: People and Performance*, *4*(2), 110–118.

Minbaeva, D. B. (2018). Building credible human capital analytics for organizational competitive advantage: Building credible human capital analytics. *Human Resource Management*, *57*(3), 701–713.

Shet, Sateesh. V., Poddar, T., Wamba Samuel, F., & Dwivedi, Y. K. (2021). Examining the determinants of successful adoption of data analytics in human resource management – A framework for implications. *Journal of Business Research*, *131*, 311–326.

Tursunbayeva, A., Di Lauro, S., & Pagliari, C. (2018). People analytics—A scoping review of conceptual boundaries and value propositions. *International Journal of Information Management*, *43*, 224–247.

van den Heuvel, S., & Bondarouk, T. (2017). The rise (and fall?) of HR analytics: A study into the future application, value, structure, and system support. *Journal of Organizational Effectiveness: People and Performance*, *4*(2), 157–178.

Author Information

M. Cagri Budak
Istanbul Technical University, Istanbul/Turkey
Dokuz Eylul University, Izmir/Turkey
Contact e-mail: *budakm17@itu.edu.tr*
muhammedcagri.budak@deu.edu.tr

Ayberk Soyer
Istanbul Technical University
Istanbul/Turkey
Contact e-mail: ayberk@itu.edu.tr

To cite this article:

Budak, M. C., & Soyer, A. (2023). Human resources analytics usage in Turkish organizations. *The Eurasia Proceedings of Science, Technology, Engineering & Mathematics (EPSTEM), 26*, 541-547.

The Eurasia Proceedings of Science, Technology, Engineering & Mathematics (EPSTEM)
ISSN: 2602-3199

The Eurasia Proceedings of Science, Technology, Engineering & Mathematics (EPSTEM), 2023

Volume 26, Pages 548-553

IConTES 2023: International Conference on Technology, Engineering and Science

Probabilistic Seismic Damage for Existing RC Buildings Used for Educational Purposes

Sabeur Bendehiba
University Abdelhamid Ibn Badis

Sidi Mohammed El-Amine Bourdim
University Center of Maghnia Algeria.

Hugo Rodrigues
University of Aveiro

Abstract: The objective of this research is to evaluate the seismic vulnerability of a collection of 55 reinforced concrete educational establishments, comprising approximately 516 buildings, located within the urban area of Mostaganem. Among them, 328 constructions were built in compliance with Algerian seismic regulations (Date > 1980 = 328 constructions), while 188 constructions were constructed prior to the implementation of seismic design codes (Date < 1980 = 188 constructions). This classification corresponds to the introduction and enforcement of the regulations following a significant earthquake in Chlef (El Asnam) in 1980.Using the RISK-UE lm1 method, the vulnerability index was determined through visual inspections of each building. An on-site inventory form was utilized to identify the main sources of seismic vulnerability, considering factors such as building typology, structural system, code adherence, maintenance condition, number of floors, plan and elevation irregularities, soil characteristics, and more. This approach allowed for the prioritization of buildings based on their specific vulnerabilities. The results obtained from this methodology were integrated into a Geographic Information System (GIS) environment, enabling a comprehensive understanding of the seismic behavior of the structures and facilitating the estimation of seismic risk levels. This integration also supports simulations and efforts to implement concrete preventive measures aimed at strengthening existing educational buildings, thereby reducing the potential negative consequences of future earthquakes.

Keywords: Seismic scenarios, Vulnerability, RISK-UE, Damage, Reinforced concrete buildings

Introduction

Mostaganem, a significant city in Northwestern Algeria, has undergone distinct phases of urban development throughout its history, including antiquity, Arab-Turkish influence, colonial era, and post-independence (Belhamissi, 1982). This historical context has resulted in a diverse range of building typologies within the city. The objective of this article is to present the outcomes of a comprehensive preliminary study focused on evaluating the seismic vulnerability and anticipated damage (seismic scenario analysis) of 45 reinforced concrete educational facilities, encompassing a total of 516 buildings situated within the urban boundaries of Mostaganem. This research is executed in two main stages:

1) Field investigations involved visual inspections of the school buildings to identify general sources of seismic vulnerability for the 516 existing reinforced concrete school structures (Giovinazzi & Lagomarsino, 2002). A diagnostic record was created for each building, containing information on building typology, technical design, topographical conditions, construction type, age of the building, number of floors, number of basements, history of structural damage and repairs, expansion projects, and other relevant data (Giovinazzi, 2005).

2) The estimation of the average damage index for each structure was achieved using a semi-empirical relationship that correlates seismic hazard data with the estimated seismic vulnerability analysis. This research is grounded in the RISK-UE methodology and results in the definition of eight seismic scenarios representing the potential damage to buildings based on the European Macroseismic Scale EMS-98 (Grunthal, 1998).

With the aim of preserving the educational infrastructure in Mostaganem, this study focuses on assessing seismic risk by estimating the seismic vulnerability of reinforced concrete buildings. In this context, the RISK-UE method offers significant advantages, particularly concerning the expected functional damage. These findings should undoubtedly raise concerns among local authorities and prompt the initiation of rehabilitation and strengthening efforts for school buildings (Sabeur et al., 2023). The results obtained through this approach form a database detailing the potential damages to school structures, which are presented and integrated within a GIS environment.

Methodology for Estimating Vulnerability 'APPROCHE RISK-UE'

The RISK-UE lm1 method, also referred to as the macroseismic approach at level 1, is centered on the evaluation of a vulnerability index for a specific building. This index takes into consideration the building's construction type and various factors that can influence its behavior (CETE Méditerranée, 2008). Utilizing this index, vulnerability curves can be established based on the macroseismic intensity in accordance with EMS-98 (European Macroseismic Scale). This, in turn, allows for the assessment of the probability distribution of damage for the building. This method involves the identification of various states of deterioration for the structure and the evaluation of the likelihood of the structure being in different damage states at a given level of seismic ground motion (Mouroux & Le Brun, 2006; Mouroux et al., 2004).

Study Area

Our research is centered within the urban boundaries of Mostaganem and encompasses two distinct urban zones. One of these areas is the historic core, which includes historical structures, while the other area represents the city's expansion post-independence. The study area encompasses a total surface area of 20 square kilometers and extends with an average radius of 2.50 kilometers, as depicted in Figure 2.

The current study specifically focuses on 55 reinforced concrete educational facilities, which are part of a larger total of 516 buildings situated in the urban fabric of Mostaganem. This diverse area comprises buildings with various purposes, including 30 primary schools, 11 middle schools, 8 high schools, 3 universities, 2 vocational training centers, and 1 paramedical center.

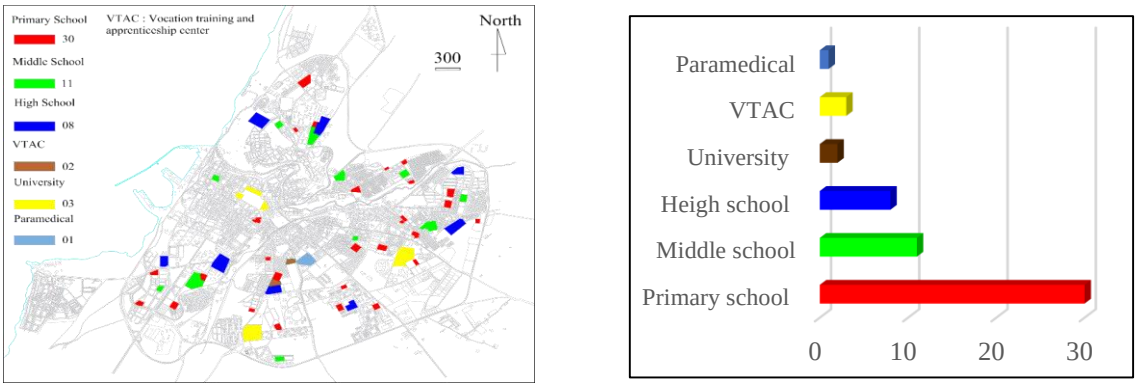

Figure 2. Spatial distributions/uses of educational buildings: (a) Localization of reinforced concrete (RC) existing buildings in the study area, (b) Categories of existing RC School Buildings.

The distribution of buildings in the study area, categorized by type, is visualized in Figure 2, revealing a notably high percentage of primary schools compared to other categories. These identified buildings span the entirety of the urban area within the city of Mostaganem. As a result, a comprehensive database has been constructed from this spatial distribution, addressing the educational requirements in the province of Mostaganem.

Results and Discussion

Estimation of Vulnerability Index

Based on visual assessment, the vulnerability index is calculated by considering 11 modifying factors of the studied buildings (Giovinazzi and Lagomarsino, 2004):

$$\overline{V_I} = V_I^* + \Delta V_R + \Delta V_m \quad (1)$$

The vulnerability index is associated with the building class (as shown in Table 4). ΔVR is a factor utilized to consider the characteristics of specific typologies at the regional level and is considered negligible in this study. ΔVm represents modifiers that depict how various typological parameters influence the seismic behavior of the building. Through visual assessment, four vulnerability typologies were examined for the reinforced concrete buildings in the study area (RC3.1, RC3.2, RC4, and RC5), with RC3.1 being the predominant category at 93.60%. This assessment of construction vulnerability (as presented in Table 1) can now be employed to evaluate and map the vulnerability of these structures using the RISK-UE methodology.

Table 1 presents the typology of RC buildings according to RISK-UE (Giovinazzi 2005).

RISK-UE type		Description	Number	(%)	∑(%)
RC Buildings	RC3.1	Regularly infilled walls	483	93,60	
	RC3.2	Irregular frames	14	2,71	
	RC4	RC Dual systems (RC frame and wall)	4	0,78	100
	RC5	Precast Concrete Tilt-Up Walls	15	2,91	
Total			516	100,00	

For a single building, the overall vulnerability index can now be obtained by summing up all the scores of modifying factors.

$$\Delta V_m = \sum V_m \quad (2)$$

Furthermore, surveys conducted in the study area in accordance with the requirements of the RISK-UE approach (Milutinovic and Trendafiloski (2003)) affect 52.13% of buildings with a vulnerability index of 0.30 < VI < 0.54 to vulnerability class D, 16.09% of buildings belonging to vulnerability class C (0.46 < VI < 0.70), and 40.70% of constructions are assigned to vulnerability class B (0.46 < VI < 0.70). Figure 3 shows the spatial distribution of the vulnerability index for pre-diagnosed educational buildings.

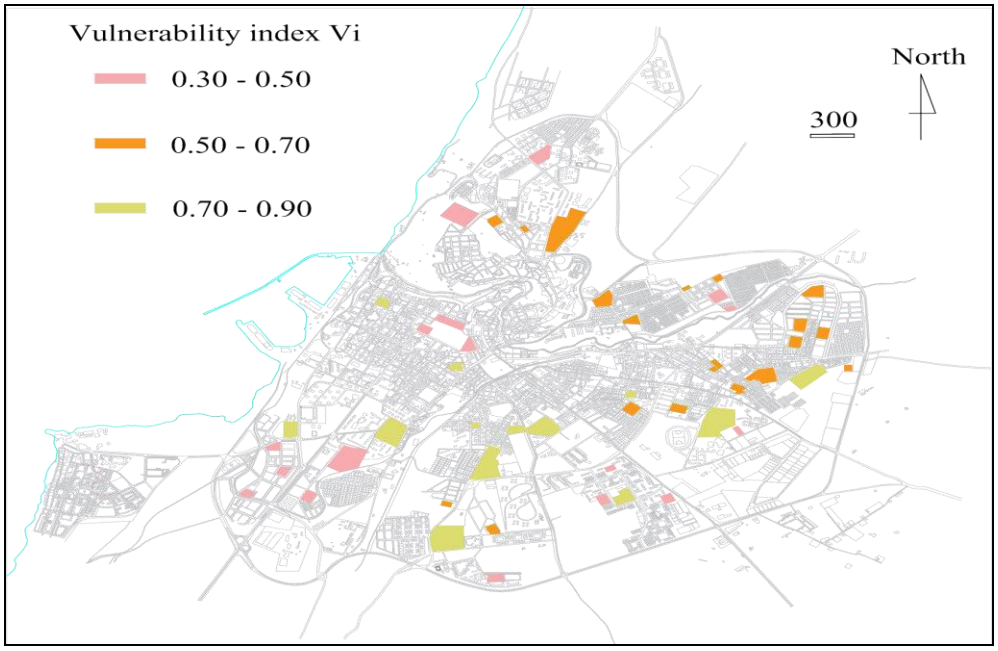

Figure 3. Spatial distribution of the vulnerability index using the RISK-UE method.

Estimation of average damage to educational buildings

The corresponding average damages, denoted as μD, are subsequently calculated by considering the macroseismic intensity I according to the EMS-98 scale and the vulnerability index V (as per Equation 3). μD falls within a range from 1 to 5, following the EMS-98 scale, which is divided into five classes (Giovinazzi 2005).

$$\mu_D = 2.5\left[1 + tanh\left(\frac{I+6.25V_I-13.1}{2.3}\right)\right] \quad (3)$$

The fragility curves depicted in Figure 04 are produced using Equation N03, which correlates seismic hazard data (seismic intensity I) with the results obtained from the seismic vulnerability analysis (V).

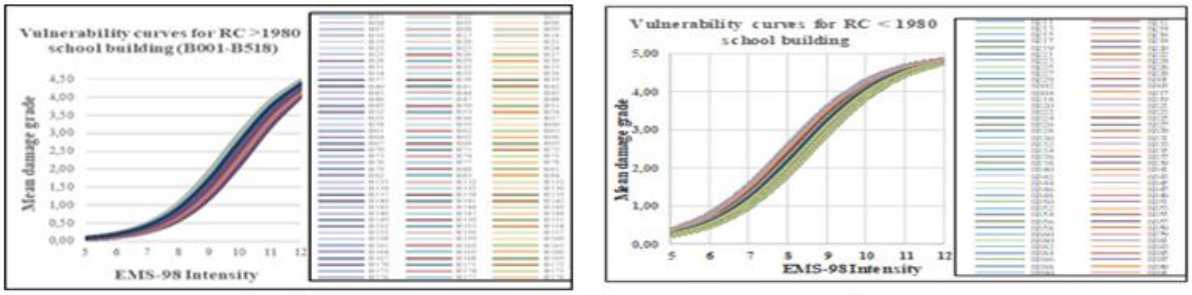

(a) (b)

Figure 4. Mean Damage Grade Estimation School Building, (a) μD index for RC >1980, (c) μD index for RC<1980

Seismic Scenario Study

Seismic scenarios should be calculated using the beta distribution for each vulnerability class. This damage distribution function is defined as follows (basic equation of the beta distribution): The damage distribution is calculated using a beta distribution.
Probability density:

$$P_\beta(x) = \frac{\Gamma(t)}{\Gamma(t)\Gamma(t-q)} \frac{(x-a)^{q-1}(b-x)}{(b-a)^{t-1}} \qquad a \le x \le b \quad (4)$$

Cumulative distribution function:

$$P_\beta(x) = \int_a^x p_\beta(\varepsilon)d(\varepsilon) \quad (5)$$

Where: the beta distribution is parameterized by a, b, t, and q, and x represents the continuous random variable ranging between a and b. Γ is the gamma function. With the parameters: a = 0, b = 6, t = 8

$$q = t(0.007\,\mu_D{}^3 - 0.052\mu_D{}^2 + 0.28\mu_D) \quad (6)$$

Discrete probabilities: The probability pk associated with each damage degree k is expressed in the following form:

$$p_k = P_\beta(k+1) - P_\beta(k) \quad (7)$$

Fragility curve:
The fragility curve, which defines the probability of reaching or exceeding a damage level k, is directly obtained from the cumulative distribution function.

$$p(D \ge D_k) = 1 - P_k(k) \quad (8)$$

Seismic Scenarios for RC building

Analyzing Figure 5 for reinforced concrete structures built before 1980 reveals multiple seismic scenarios. In the first scenario, corresponding to an IEMS-98 intensity of 5.6, no significant damage is reported, and all structures remain intact at a D0 level of 100%. Subsequently, for an IEMS-98 intensity of 7, minor to light damage is expected, with 63.57% of constructions classified as D0 and 36.43% as D1. The seismic scenario resulting from an IEMS-98 intensity of 8 shows probable damage distributed across D0 (54.46%), D1 (9.11%), D2 (26.74%), and D3 (9.69%). The expected damage in this case ranges from negligible to moderate. As the seismic intensity reaches IEMS-98=9, moderate damage is predicted on the structural side, and heavy damage on the non-structural side, with 46.32% of the buildings classified as D1, 17.25% as D2, 13.57% as D3, and 22.87% as D4. The scenario assessed for an IEMS-98 intensity of 10 foresees heavy structural damage and very heavy non-structural damage, with a distribution of 21.71% in D2, 41.86% in D3, 10.85% in D4, and 25.58% in D5. As for the final scenario, which corresponds to an IEMS-98 intensity of 11, it is characterized by severe to total building damage, with 17.63% of structures classified as D3, 45.93% as D4, and 36.43% as D5. In the last scenario, corresponding to IEMS-98=12, all buildings experience total destruction (collapse), with 15.12% in D4 and 84.88% in D5.

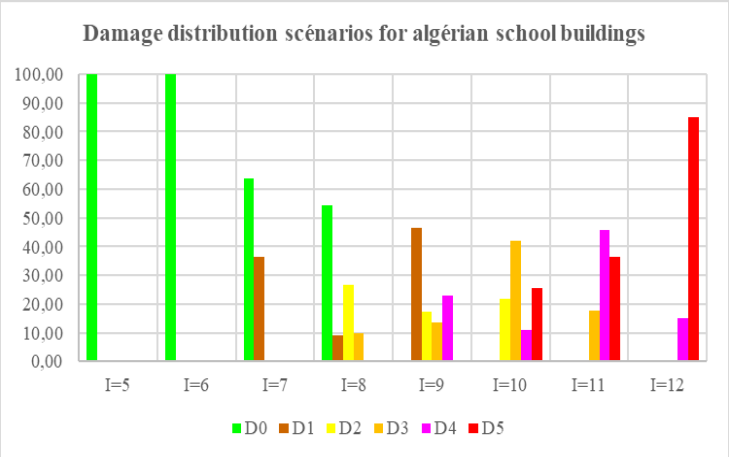

Figure 5. Synthesis of global damage scenarios for different EMS-98 Intensity

The key insight gleaned from the Geographic Information System, as depicted in Figure 5, is the significant variation in estimated damages across various intensities for all educational facilities.

Conclusion

The seismic scenarios obtained through the application of the RISK-UE method have been integrated and compared using a Geographic Information System (GIS). These scenarios will guide decision-makers in assessing the severity and extent of seismic risk for various types of existing buildings in Mostaganem or other cities in the country. This is aimed at implementing preventive measures and naturally reducing disaster risks by lowering vulnerability. Recommendations can be proposed to Algerian authorities to simulate and facilitate efforts aimed at taking concrete, specific prevention measures to enhance existing educational buildings, thus mitigating the adverse impact of future disasters.

Recommendations

At this juncture, we have arrived at the conclusion that it is of utmost importance for research to delve into how school buildings should function to ensure the safety of students in the aftermath of an earthquake. This research project represents just the initial phase and should be succeeded by further analysis, as we have pinpointed a substantial research avenue to explore based on the foundational findings from this initial phase of the work.

Scientific Ethics Declaration

The authors declare that the scientific ethical and legal responsibility of this article published in EPSTEM journal belongs to the authors.

Acknowledgements or Notes

* This article was presented as an oral presentation at the International Conference on Technology, Engineering and Science (www.icontes.net) held in Antalya/Turkey on November 16-19, 2023.

References

Belhamissi, M. (1976). *Histoire de mostaganem (des origines à l'occupation française)*. Alger : S.N.E.D

CETE Méditerranée. (2008). *Centre d'Etude technique de l'equipement Méditerranée, Comparaison de méthodes qualitatives d'évaluation de la vulnérabilité des constructions aux séismes*. Plan séisme - action 2.4.7. Guide des méthodes de diagnostics de la résistance des bâtiments aux séismes

Giovinazzi S (2005) *Vulnerability assessment and the damage scenario in seismic risk analysis* (Doctoral dissertation). University of Florence, Italy

Giovinazzi, S. (2005) *Vulnerability assessment and the damage scenario in seismic risk analysis* (Doctoral dissertation). University of Florence, Italy

Giovinazzi, S., & Lagomarsino, S. (2004). A macroseismic method for the vulnerability assessment of buildings, In: Proceedings from*13th World Conference on Earthquake Engineering, 896.* Vancouver, B.C., Canada

Giovinazzi, S., & Lagomarsino, S.(2002) *WP04: Guidelines for the implementation of the I level methodology for the vulnerability assessment of current buildings: RISK-UE project.* University of Genoa

Grunthal, G. (1998). *L'Echelle macrosismique Européenn*e (EMS98) (Vol.15). Conseil de l'Europe, Cahiers du Centre Européen de Géodynamique et de Séismologie

Meslem, A. (2006) *Seismic vulnerability evaluation of existing Algerian school buildings.* ProVention Consortium Applied Grants for DisasterRisk Reduction II.

Milutinovic, Z., & Trendafiloski, G. (2003) WP04: *Vulnerability of current buildings. RISK-UE project: An advanced approach to earthquake risk scenarios with applications to different European towns*(pp.479-508).Skopje

Mouroux, P, Le Brun, B., Depinois S, Bertrand, E, & Masure, P. (2004) *Europeen project RISK-UE: application to Nice City.* France: BRGM Report

Mouroux, P., & Brun, B. (2006) Presentation of RISK-UE project. *Bull Earthquake Engineering, 4,*323–339

Sabeur, B., Sidi Mohammed El-Amine Bourdim, S. M E.A., & Hugo Rodrigues, H. (2023). Seismic damage scenarios for existing Masonry buildings for educational use in the Mostaganem City, KSCE. *Journal of Civil Engineering, 27*(1), 1-15

Author Information

Sabeur Bendehiba
Materials and Construction Processes Laboratory, Civil Engineering Department, University Abdelhamid Ibn Badis, Mostaganem 27000, Algeria.
Contact e-mail : *bendehiba.sabeur@univ-mosta.dz*

Sidi Mohammed El-Amine Bourdim
Senior lecturer, Department of Hydraulic and Civil Engineering, University Center of Maghnia, Tlemcen 13300, Algeria.

Hugo Rodrigues
Associate Professor, University of Aveiro - Civil Engineering Department Campus Universitário de Santiago 3810-193 Aveiro, Portugal.

To cite this article:

Bendehiba, S., El-Amine Bourdim, S. M., & Rodrigues, H. (2023). Probabilistic seismic damage for existing RC buildings used for educational purposes. *The Eurasia Proceedings of Science, Technology, Engineering & Mathematics (EPSTEM), 26,* 548-553.

The Eurasia Proceedings of Science, Technology, Engineering & Mathematics (EPSTEM)
ISSN: 2602-3199

The Eurasia Proceedings of Science, Technology, Engineering & Mathematics (EPSTEM), 2023

Volume 26, Pages 554-577

IConTES 2023: International Conference on Technology, Engineering and Science

Some 3D-Determinant Properties for Calculating of Cubic-Matrix of Order 2 and Order 3

Armend Salihu
Universum International College

Orgest Zaka
Agricultural University of Tirana

Abstract: In this paper, as a continuation of our work on the determinant of cubic matrices, we have studied some properties of calculation of the determinant of cubic matrices for the cubic matrix of the order 2×2, as well as the order 3×3. Like properties of square determinants, these properties are analogous to some properties for determinants of the square matrix we have proved and noted that these properties also are applicable (or not in some details) to this concept for the determinant of the cubic matrix of orders 2×2 and order 3×3. All properties that have been proved in this paper, are proved for each case for orders 2×2 and order 3×3, by including all elements of the matrix, as well as all horizontal plans, horizontal layers, and vertical layers. All results in this paper, are presented in detail during the theorem proofs.

Keywords: Cubic-matrix, Determinant of cubic-matrix, Determinant properties.

Introduction and Preliminaries

In this paper we prove some properties for determinant of cubic-matrix of order 2 and order 3. In the paper Salihu et.al. (2023a), we have defined the concept of determinant for cubic-matrix of order 2 and order 3, and we have prove some basic properties for calculating this determinants. This idea for developing this concept, it came simply from the determinant of 2D square matrices (Salihu et.al., 2021; Salihu et al., 2019b; Salihu, 2018; Artin, 1991; Bretscher 2005, Schneide et.al. 1973), as well as determinant of rectangular matrices (Salihu et al., 2022a, Salihu et al., 2023b, Salihu et al., 2022b, Salihu et al., 2022c; Salihu et al., 2019a; Amiri et al., 2010; Radic, 1966; Radic, 2005; Makarewicz et al., 2014).

In paper Zaka et al. (2023) we have prove that the Laplace expansion method is valid for calculating the determinant of cubic-matrix for orders 2 and 3. Encouraged by geometric intuition, in this paper we are trying to give an idea and visualize the meaning of the determinants for the cubic-matrix. Our early research mainly lies between geometry, algebra, matrix theory, etc., (see Peters et al., 2023; Zaka 2019a; Zaka et al., 2016, Filipi et al., 2019; Zaka, 2018a, 2018b, Zaka 2016b, Zaka et al., 2019b, 2019c, Zaka et al., 2020a, 2020b).

This paper is continuation of the ideas that arise based on previous researches of 3D matrix ring with element from any whatever field F see Zaka (2019d), but here we study the case when the field F is the field of real numbers $\mathbb{R}$ also is continuation of our research Salihu et al. (2023a) and Zaka et.al (2023) related to the study of the properties of determinants for cubic-matrix of order 2 and 3. In this paper we follow a different method from method which is studied in Zaka (2017).

Results for More Properties of Determinants of Cubic-Matrix of Order 2 and Order 3

In this section, all proofs of our theorems are based on the definition of determinant for cubic-matrix of orders 2 and 3, presented in the papers Salihu et al. (2023a) and Zaka et al. (2023), and results obtained in these papers. The proofs of the following Theorems are too loaded with indices to calculate, and we are trying to make them a little simpler by separating them case by case, to avoid the difficulty of calculations!

Theorem 1:

Let's be A and B 3D-cubic matrix with same order (second and third order matrices), then we have that:

$$\det(A+B) = \det(A) + \det(B).$$

Proof:

Case 1: The cubic-matrix A of order 2, (and B has order 2), we will proof the case 1 for each "horizontal layer", "vertical page" and "vertical layer", as following:

1. For plan $i = 1$: Let A and B be cubic-matrix of order 2, where all elements on the plan $i = 1$ are identical in both matrices, then based on definition of determinant of cubic-matrix presented in Salihu et.al (2023a) and Zaka et.al (2023) we have:

$$det(A_{[2\times2\times2]}) + \det(B_{[2\times2\times2]}) = det\left(\begin{matrix} a_{111} & a_{121} \\ a_{211} & a_{221} \end{matrix}\middle|\begin{matrix} a_{112} & a_{122} \\ a_{212} & a_{222} \end{matrix}\right) + det\left(\begin{matrix} a_{111} & a_{121} \\ b_{211} & b_{221} \end{matrix}\middle|\begin{matrix} a_{112} & a_{122} \\ b_{212} & b_{222} \end{matrix}\right)$$
$$= a_{111}\cdot a_{222} - a_{112}\cdot a_{221} - a_{121}\cdot a_{212} + a_{122}\cdot a_{211} + a_{111}\cdot b_{222} - a_{112}\cdot b_{221} - a_{121}\cdot b_{212} + a_{122}\cdot b_{211},$$

while,

$$det(A_{[2\times2\times2]} + B_{[2\times2\times2]}) = det\left(\begin{matrix} a_{111} & a_{121} \\ a_{211}+b_{211} & a_{221}+b_{221} \end{matrix}\middle|\begin{matrix} a_{112} & a_{122} \\ a_{212}+b_{212} & a_{222}+b_{222} \end{matrix}\right)$$
$$= a_{111}\cdot(a_{222}+b_{222}) - a_{112}\cdot(a_{221}+b_{221}) - a_{121}\cdot(a_{212}+b_{212}) + a_{122}\cdot(a_{211}+b_{211})$$
$$= a_{111}\cdot a_{222} + a_{111}\cdot b_{222} - a_{112}\cdot a_{221} - a_{112}\cdot b_{221} - a_{121}\cdot a_{212} - a_{121}\cdot b_{212} + a_{122}\cdot a_{211} + a_{122}\cdot b_{211}.$$

If we compare results of above equations, we can see that we have the same result in both cases. Similarly, we will proof for all other cases.

2. For plan $i = 2$: Let A and B be cubic-matries of order 2, where all elements on the plan $i = 2$ are identical in both matrices, then we have:

$$det(A_{[2\times2\times2]}) + det(B_{[2\times2\times2]}) = det\left(\begin{matrix} a_{111} & a_{121} \\ a_{211} & a_{221} \end{matrix}\middle|\begin{matrix} a_{112} & a_{122} \\ a_{212} & a_{222} \end{matrix}\right) + det\left(\begin{matrix} b_{111} & b_{121} \\ a_{211} & a_{221} \end{matrix}\middle|\begin{matrix} b_{112} & b_{122} \\ a_{212} & a_{222} \end{matrix}\right)$$
$$= a_{111}\cdot a_{222} - a_{112}\cdot a_{221} - a_{121}\cdot a_{212} + a_{122}\cdot a_{211} + b_{111}\cdot a_{222} - b_{112}\cdot a_{221} - b_{121}\cdot a_{212} + b_{122}\cdot a_{211},$$

while,

$$det(A_{[2\times2\times2]} + B_{[2\times2\times2]}) = det\left(\begin{matrix} a_{111}+b_{111} & a_{121}+b_{121} \\ a_{211} & a_{221} \end{matrix}\middle|\begin{matrix} a_{112}+b_{112} & a_{122}+b_{122} \\ a_{212} & a_{222} \end{matrix}\right)$$
$$= (a_{111}+b_{111})\cdot a_{222} - (a_{112}+b_{112})\cdot a_{221} - (a_{121}+b_{121})\cdot a_{212} + (a_{122}+b_{122})\cdot a_{211}$$
$$= a_{111}\cdot a_{222} + b_{111}\cdot a_{222} - a_{112}\cdot a_{221} - b_{112}\cdot a_{221} - a_{121}\cdot a_{212} - b_{121}\cdot a_{212} + a_{122}\cdot a_{211} + b_{122}\cdot a_{211}.$$

If we compare results of above equations, we can see that we have the same result in both cases.

3. For plan $j = 1$: Let A and B be cubic-matries of order 2, where all elements on the plan $j = 1$ are identical in both matrices, then we have:

$$det(A_{[2\times2\times2]}) + det(B_{[2\times2\times2]}) = det\left(\begin{matrix} a_{111} & a_{121} \\ a_{211} & a_{221} \end{matrix}\middle|\begin{matrix} a_{112} & a_{122} \\ a_{212} & a_{222} \end{matrix}\right) + det\left(\begin{matrix} a_{111} & b_{121} \\ a_{211} & b_{221} \end{matrix}\middle|\begin{matrix} a_{112} & b_{122} \\ a_{212} & b_{222} \end{matrix}\right)$$
$$= a_{111}\cdot a_{222} - a_{112}\cdot a_{221} - a_{121}\cdot a_{212} + a_{122}\cdot a_{211} + a_{111}\cdot b_{222} - a_{112}\cdot b_{221} - b_{121}\cdot a_{212} + b_{122}\cdot a_{211},$$

while,

$$det\left(A_{[2\times2\times2]}+B_{[2\times2\times2]}\right)=det\left(\begin{matrix}a_{111} & a_{121}+b_{121}\\ a_{211} & a_{221}+b_{221}\end{matrix}\middle|\begin{matrix}a_{112} & a_{122}+b_{122}\\ a_{212} & a_{222}+b_{222}\end{matrix}\right)$$
$$=a_{111}\cdot(a_{222}+b_{222})-a_{112}\cdot(a_{221}+b_{221})-(a_{121}+b_{121})\cdot a_{212}+(a_{122}+b_{122})\cdot a_{211}$$
$$=a_{111}\cdot a_{222}+a_{111}\cdot b_{222}-a_{112}\cdot a_{221}-a_{112}\cdot b_{221}-a_{121}\cdot a_{212}-b_{121}\cdot a_{212}+a_{122}\cdot a_{211}+b_{122}\cdot a_{211}.$$

If we compare results of above equations, we can see that we have the same result in both cases.

4. For plan $j=2$: Let A and B be cubic-matries of order 2, where all elements on the plan $j=2$ are identical in both matrices, then we have:

$$det\left(A_{[2\times2\times2]}\right)+det\left(B_{[2\times2\times2]}\right)=det\left(\begin{matrix}a_{111} & a_{121}\\ a_{211} & a_{221}\end{matrix}\middle|\begin{matrix}a_{112} & a_{122}\\ a_{212} & a_{222}\end{matrix}\right)+det\left(\begin{matrix}b_{111} & a_{121}\\ b_{211} & a_{221}\end{matrix}\middle|\begin{matrix}b_{112} & a_{122}\\ b_{212} & a_{222}\end{matrix}\right)$$
$$=a_{111}\cdot a_{222}-a_{112}\cdot a_{221}-a_{121}\cdot a_{212}+a_{122}\cdot a_{211}+b_{111}\cdot a_{222}-b_{112}\cdot a_{221}-a_{121}\cdot b_{212}+a_{122}\cdot b_{211},$$

while,

$$det\left(A_{[2\times2\times2]}+B_{[2\times2\times2]}\right)=det\left(\begin{matrix}a_{111}+b_{111} & a_{121}\\ a_{211}+b_{211} & a_{221}\end{matrix}\middle|\begin{matrix}a_{112}+b_{112} & a_{122}\\ a_{212}+b_{212} & a_{222}\end{matrix}\right)$$
$$=(a_{111}+b_{111})\cdot a_{222}-(a_{112}+b_{112})\cdot a_{221}-a_{121}\cdot(a_{212}+b_{212})+a_{122}\cdot(a_{211}+b_{211})$$
$$=a_{111}\cdot a_{222}+b_{111}\cdot a_{222}-a_{112}\cdot a_{221}-b_{112}\cdot a_{221}-a_{121}\cdot a_{212}-a_{121}\cdot b_{212}+a_{122}\cdot a_{211}+a_{122}\cdot b_{211}.$$

If we compare results of above equations, we can see that we have the same result in both cases.

5. For plan $k=1$: Let A and B be cubic-matries of order 2, where all elements on the plan $k=1$ are identical in both matrices, then we have:

$$det\left(A_{[2\times2\times2]}\right)+det\left(B_{[2\times2\times2]}\right)=det\left(\begin{matrix}a_{111} & a_{121}\\ a_{211} & a_{221}\end{matrix}\middle|\begin{matrix}a_{112} & a_{122}\\ a_{212} & a_{222}\end{matrix}\right)+det\left(\begin{matrix}a_{111} & a_{121}\\ a_{211} & a_{221}\end{matrix}\middle|\begin{matrix}b_{112} & b_{122}\\ b_{212} & b_{222}\end{matrix}\right)$$
$$=a_{111}\cdot a_{222}-a_{112}\cdot a_{221}-a_{121}\cdot a_{212}+a_{122}\cdot a_{211}+a_{111}\cdot b_{222}-b_{112}\cdot a_{221}-a_{121}\cdot b_{212}+b_{122}\cdot a_{211},$$

while,

$$det\left(A_{[2\times2\times2]}+B_{[2\times2\times2]}\right)=det\left(\begin{matrix}a_{111} & a_{121}\\ a_{211} & a_{221}\end{matrix}\middle|\begin{matrix}a_{112}+b_{112} & a_{122}+b_{122}\\ a_{212}+b_{212} & a_{222}+b_{222}\end{matrix}\right)$$
$$=a_{111}\cdot(a_{222}+b_{222})-(a_{112}+b_{112})\cdot a_{221}-a_{121}\cdot(a_{212}+b_{212})+(a_{122}+b_{122})\cdot a_{211}$$
$$=a_{111}\cdot a_{222}+a_{111}\cdot b_{222}-a_{112}\cdot a_{221}-b_{112}\cdot a_{221}-a_{121}\cdot a_{212}-a_{121}\cdot b_{212}+a_{122}\cdot a_{211}+b_{122}\cdot a_{211}.$$

If we compare results of above equations, we can see that we have the same result in both cases.

6. For plan $k=2$: Let A and B be cubic-matries of order 2, where all elements on the plan $k=2$ are identical in both matrices, then we have:

$$det\left(A_{[2\times2\times2]}\right)+det\left(B_{[2\times2\times2]}\right)=det\left(\begin{matrix}a_{111} & a_{121}\\ a_{211} & a_{221}\end{matrix}\middle|\begin{matrix}a_{112} & a_{122}\\ a_{212} & a_{222}\end{matrix}\right)+det\left(\begin{matrix}b_{111} & b_{121}\\ b_{211} & b_{221}\end{matrix}\middle|\begin{matrix}a_{112} & a_{122}\\ a_{212} & a_{222}\end{matrix}\right)$$
$$=a_{111}\cdot a_{222}-a_{112}\cdot a_{221}-a_{121}\cdot a_{212}+a_{122}\cdot a_{211}+b_{111}\cdot a_{222}-a_{112}\cdot b_{221}-b_{121}\cdot a_{212}+a_{122}\cdot b_{211},$$

while,

$$det\left(A_{[2\times2\times2]}+B_{[2\times2\times2]}\right)=det\left(\begin{matrix}a_{111}+b_{111} & a_{121}+b_{121}\\ a_{211}+b_{211} & a_{221}+b_{221}\end{matrix}\middle|\begin{matrix}a_{112} & a_{122}\\ a_{212} & a_{222}\end{matrix}\right)$$
$$=(a_{111}+b_{111})\cdot a_{222}-(a_{112}+b_{112})\cdot a_{221}-(a_{121}+b_{121})\cdot a_{212}+(a_{122}+b_{122})\cdot a_{211}$$
$$=a_{111}\cdot a_{222}+b_{111}\cdot a_{222}-a_{112}\cdot a_{221}-b_{112}\cdot a_{221}-a_{121}\cdot a_{212}-b_{121}\cdot a_{212}+a_{122}\cdot a_{211}+b_{122}\cdot a_{211}.$$

If we compare results of above equations, we can see that we have the same result in both cases.

Case 2: The cubic-matrix A of order 3, (and B has order 3), we will proof the case 1 for each "horizontal layer", "vertical page" and "vertical layer", as following:

1. For plan $i = 1$: Let A and B be cubic-matries of order 3, where all elements on the plan $i = 1$ and $i = 2$ are identical in both matrices, then we have:

$$det\left(A_{[3\times3\times3]}\right) + det\left(B_{[3\times3\times3]}\right) = det\left(\begin{array}{ccc|ccc|ccc} a_{111} & a_{121} & a_{131} & a_{112} & a_{122} & a_{132} & a_{113} & a_{123} & a_{133} \\ a_{211} & a_{221} & a_{231} & a_{212} & a_{222} & a_{232} & a_{213} & a_{223} & a_{233} \\ a_{311} & a_{321} & a_{331} & a_{312} & a_{322} & a_{332} & a_{313} & a_{323} & a_{333} \end{array}\right)$$

$$+det\left(\begin{array}{ccc|ccc|ccc} a_{111} & a_{121} & a_{131} & a_{112} & a_{122} & a_{132} & a_{113} & a_{123} & a_{133} \\ a_{211} & a_{221} & a_{231} & a_{212} & a_{222} & a_{232} & a_{213} & a_{223} & a_{233} \\ b_{311} & b_{321} & b_{331} & b_{312} & b_{322} & b_{332} & b_{313} & b_{323} & b_{333} \end{array}\right)$$

$$\begin{aligned} &= \{a_{111}\cdot a_{222}\cdot a_{333} - a_{111}\cdot a_{232}\cdot a_{323} - a_{111}\cdot a_{223}\cdot a_{332} + a_{111}\cdot a_{233}\cdot a_{322} - a_{112}\cdot a_{221}\cdot a_{333} \\ &+a_{112}\cdot a_{223}\cdot a_{331} + a_{112}\cdot a_{231}\cdot a_{323} - a_{112}\cdot a_{233}\cdot a_{321} + a_{113}\cdot a_{221}\cdot a_{332} - a_{113}\cdot a_{222}\cdot a_{331} \\ &-a_{113}\cdot a_{231}\cdot a_{322} + a_{113}\cdot a_{232}\cdot a_{321} - a_{121}\cdot a_{212}\cdot a_{333} + a_{121}\cdot a_{213}\cdot a_{332} + a_{121}\cdot a_{232}\cdot a_{313} \\ &-a_{121}\cdot a_{233}\cdot a_{312} + a_{122}\cdot a_{211}\cdot a_{333} - a_{122}\cdot a_{213}\cdot a_{331} - a_{122}\cdot a_{231}\cdot a_{313} + a_{122}\cdot a_{233}\cdot a_{311} \\ &-a_{123}\cdot a_{211}\cdot a_{332} + a_{123}\cdot a_{212}\cdot a_{331} + a_{123}\cdot a_{231}\cdot a_{312} - a_{123}\cdot a_{232}\cdot a_{311} + a_{131}\cdot a_{212}\cdot a_{323} \\ &-a_{131}\cdot a_{213}\cdot a_{322} - a_{131}\cdot a_{222}\cdot a_{313} + a_{131}\cdot a_{223}\cdot a_{312} - a_{132}\cdot a_{211}\cdot a_{323} + a_{132}\cdot a_{213}\cdot a_{321} \\ &+a_{132}\cdot a_{221}\cdot a_{313} - a_{132}\cdot a_{223}\cdot a_{311} + a_{133}\cdot a_{211}\cdot a_{322} - a_{133}\cdot a_{212}\cdot a_{321} - a_{133}\cdot a_{221}\cdot a_{312} \\ &+a_{133}\cdot a_{222}\cdot a_{311}\} + \{a_{111}\cdot a_{222}\cdot b_{333} - a_{111}\cdot a_{232}\cdot b_{323} - a_{111}\cdot a_{223}\cdot b_{332} + a_{111}\cdot a_{233}\cdot b_{322} \\ &-a_{112}\cdot a_{221}\cdot b_{333} + a_{112}\cdot a_{223}\cdot b_{331} + a_{112}\cdot a_{231}\cdot b_{323} - a_{112}\cdot a_{233}\cdot b_{321} + a_{113}\cdot a_{221}\cdot b_{332} \\ &-a_{113}\cdot a_{222}\cdot b_{331} - a_{113}\cdot a_{231}\cdot b_{322} + a_{113}\cdot a_{232}\cdot b_{321} - a_{121}\cdot a_{212}\cdot b_{333} + a_{121}\cdot a_{213}\cdot b_{332} \\ &+a_{121}\cdot a_{232}\cdot b_{313} - a_{121}\cdot a_{233}\cdot b_{312} + a_{122}\cdot a_{211}\cdot b_{333} - a_{122}\cdot a_{213}\cdot b_{331} - a_{122}\cdot a_{231}\cdot b_{313} \\ &+a_{122}\cdot a_{233}\cdot b_{311} - a_{123}\cdot a_{211}\cdot b_{332} + a_{123}\cdot a_{212}\cdot b_{331} + a_{123}\cdot a_{231}\cdot b_{312} - a_{123}\cdot a_{232}\cdot b_{311} \\ &+a_{131}\cdot a_{212}\cdot b_{323} - a_{131}\cdot a_{213}\cdot b_{322} - a_{131}\cdot a_{222}\cdot b_{313} + a_{131}\cdot a_{223}\cdot b_{312} - a_{132}\cdot a_{211}\cdot b_{323} \\ &+a_{132}\cdot a_{213}\cdot b_{321} + a_{132}\cdot a_{221}\cdot b_{313} - a_{132}\cdot a_{223}\cdot b_{311} + a_{133}\cdot a_{211}\cdot b_{322} - a_{133}\cdot a_{212}\cdot b_{321} \\ &-a_{133}\cdot a_{221}\cdot b_{312} + a_{133}\cdot a_{222}\cdot b_{311}\}, \end{aligned}$$

while,

$$det\left(A_{[3\times3\times3]}\right) + det\left(B_{[3\times3\times3]}\right) = det\left(\begin{array}{ccc|ccc} a_{111} & a_{121} & a_{131} & a_{113} & a_{123} & a_{133} \\ a_{211} & a_{221} & a_{231} & a_{213} & a_{223} & a_{233} \\ a_{311}+b_{311} & a_{321}+b_{321} & a_{331}+b_{331} & a_{313}+b_{313} & a_{323}+b_{323} & a_{333}+b_{333} \\ a_{112} & a_{122} & a_{132} & a_{113} & a_{123} & a_{133} \\ a_{212} & a_{222} & a_{232} & a_{213} & a_{223} & a_{233} \\ a_{312}+b_{312} & a_{322}+b_{322} & a_{332}+b_{332} & a_{313}+b_{313} & a_{323}+b_{323} & a_{333}+b_{333} \end{array}\right)$$

$$\begin{aligned} &= a_{111}\cdot a_{222}\cdot(a_{333}+b_{333}) - a_{111}\cdot a_{232}\cdot(a_{323}+b_{323}) - a_{111}\cdot a_{223}\cdot(a_{332}+b_{332}) \\ &+a_{111}\cdot a_{233}\cdot(a_{322}+b_{322}) - a_{112}\cdot a_{221}\cdot(a_{333}+b_{333}) + a_{112}\cdot a_{223}\cdot(a_{331}+b_{331}) \\ &+a_{112}\cdot a_{231}\cdot(a_{323}+b_{323}) - a_{112}\cdot a_{233}\cdot(a_{321}+b_{321}) + a_{113}\cdot a_{221}\cdot(a_{332}+b_{332}) \\ &-a_{113}\cdot a_{222}\cdot(a_{331}+b_{331}) - a_{113}\cdot a_{231}\cdot(a_{322}+b_{322}) + a_{113}\cdot a_{232}\cdot(a_{321}+b_{321}) \\ &-a_{121}\cdot a_{212}\cdot(a_{333}+b_{333}) + a_{121}\cdot a_{213}\cdot(a_{332}+b_{332}) + a_{121}\cdot a_{232}\cdot(a_{313}+b_{313}) \\ &-a_{121}\cdot a_{233}\cdot(a_{312}+b_{312}) + a_{122}\cdot a_{211}\cdot(a_{333}+b_{333}) - a_{122}\cdot a_{213}\cdot(a_{331}+b_{331}) \\ &-a_{122}\cdot a_{231}\cdot(a_{313}+b_{313}) + a_{122}\cdot a_{233}\cdot(a_{311}+b_{311}) - a_{123}\cdot a_{211}\cdot(a_{332}+b_{332}) \\ &+a_{123}\cdot a_{212}\cdot(a_{331}+b_{331}) + a_{123}\cdot a_{231}\cdot(a_{312}+b_{312}) - a_{123}\cdot a_{232}\cdot(a_{311}+b_{311}) \\ &+a_{131}\cdot a_{212}\cdot(a_{323}+b_{323}) - a_{131}\cdot a_{213}\cdot(a_{322}+b_{322}) - a_{131}\cdot a_{222}\cdot(a_{313}+b_{313}) \\ &+a_{131}\cdot a_{223}\cdot(a_{312}+b_{312}) - a_{132}\cdot a_{211}\cdot(a_{323}+b_{323}) + a_{132}\cdot a_{213}\cdot(a_{321}+b_{321}) \\ &+a_{132}\cdot a_{221}\cdot(a_{313}+b_{313}) - a_{132}\cdot a_{223}\cdot(a_{311}+b_{311}) + a_{133}\cdot a_{211}\cdot(a_{322}+b_{322}) \\ &-a_{133}\cdot a_{212}\cdot(a_{321}+b_{321}) - a_{133}\cdot a_{221}\cdot(a_{312}+b_{312}) + a_{133}\cdot a_{222}\cdot(a_{311}+b_{311}). \end{aligned}$$

Hence,

$$det\left(A_{[3\times3\times3]}\right) + det\left(B_{[3\times3\times3]}\right) = a_{111}\cdot a_{222}\cdot a_{333} + a_{111}\cdot a_{222}\cdot b_{333}$$
$$-a_{111}\cdot a_{232}\cdot a_{323} - a_{111}\cdot a_{232}\cdot b_{323} - a_{111}\cdot a_{223}\cdot a_{332} - a_{111}\cdot a_{223}\cdot b_{332} + a_{111}\cdot a_{233}\cdot a_{322}$$
$$+a_{111}\cdot a_{233}\cdot b_{322} - a_{112}\cdot a_{221}\cdot a_{333} - a_{112}\cdot a_{221}\cdot b_{333} + a_{112}\cdot a_{223}\cdot a_{331} + a_{112}\cdot a_{223}\cdot b_{331}$$
$$+a_{112}\cdot a_{231}\cdot a_{323} + a_{112}\cdot a_{231}\cdot b_{323} - a_{112}\cdot a_{233}\cdot a_{321} - a_{112}\cdot a_{233}\cdot b_{321} + a_{113}\cdot a_{221}\cdot a_{332}$$
$$+a_{113}\cdot a_{221}\cdot b_{332} - a_{113}\cdot a_{222}\cdot a_{331} - a_{113}\cdot a_{222}\cdot b_{331} - a_{113}\cdot a_{231}\cdot a_{322} - a_{113}\cdot a_{231}\cdot b_{322}$$
$$+a_{113}\cdot a_{232}\cdot a_{321} + a_{113}\cdot a_{232}\cdot b_{321} - a_{121}\cdot a_{212}\cdot a_{333} - a_{121}\cdot a_{212}\cdot b_{333} + a_{121}\cdot a_{213}\cdot a_{332}$$
$$+a_{121}\cdot a_{213}\cdot b_{332} + a_{121}\cdot a_{232}\cdot a_{313} + a_{121}\cdot a_{232}\cdot b_{313} - a_{121}\cdot a_{233}\cdot a_{312} - a_{121}\cdot a_{233}\cdot b_{312}$$
$$+a_{122}\cdot a_{211}\cdot a_{333} + a_{122}\cdot a_{211}\cdot b_{333} - a_{122}\cdot a_{213}\cdot a_{331} - a_{122}\cdot a_{213}\cdot b_{331} - a_{122}\cdot a_{231}\cdot a_{313}$$
$$-a_{122}\cdot a_{231}\cdot b_{313} + a_{122}\cdot a_{233}\cdot a_{311} + a_{122}\cdot a_{233}\cdot b_{311} - a_{123}\cdot a_{211}\cdot a_{332} - a_{123}\cdot a_{211}\cdot b_{332}$$
$$+a_{123}\cdot a_{212}\cdot a_{331} + a_{123}\cdot a_{212}\cdot b_{331} + a_{123}\cdot a_{231}\cdot a_{312} + a_{123}\cdot a_{231}\cdot b_{312} - a_{123}\cdot a_{232}\cdot a_{311}$$
$$-a_{123}\cdot a_{232}\cdot b_{311} + a_{131}\cdot a_{212}\cdot a_{323} + a_{131}\cdot a_{212}\cdot b_{323} - a_{131}\cdot a_{213}\cdot a_{322} - a_{131}\cdot a_{213}\cdot b_{322}$$
$$-a_{131}\cdot a_{222}\cdot a_{313} - a_{131}\cdot a_{222}\cdot b_{313} + a_{131}\cdot a_{223}\cdot a_{312} + a_{131}\cdot a_{223}\cdot b_{312} - a_{132}\cdot a_{211}\cdot a_{323}$$
$$-a_{132}\cdot a_{211}\cdot b_{323} + a_{132}\cdot a_{213}\cdot a_{321} + a_{132}\cdot a_{213}\cdot b_{321} + a_{132}\cdot a_{221}\cdot a_{313} + a_{132}\cdot a_{221}\cdot b_{313}$$
$$-a_{132}\cdot a_{223}\cdot a_{311} - a_{132}\cdot a_{223}\cdot b_{311} + a_{133}\cdot a_{211}\cdot a_{322} + a_{133}\cdot a_{211}\cdot b_{322} - a_{133}\cdot a_{212}\cdot a_{321}$$
$$-a_{133}\cdot a_{212}\cdot b_{321} - a_{133}\cdot a_{221}\cdot a_{312} - a_{133}\cdot a_{221}\cdot b_{312} + a_{133}\cdot a_{222}\cdot a_{311} + a_{133}\cdot a_{222}\cdot b_{311}.$$

If we compare results of above equations, we can see that we have the same result in both cases.

2. For plan $i = 2$: Let A and B be cubic-matries of order 3, where all elements on the plan $i = 1$ and $i = 3$ are identical in both matrices, then we have:

$$det\left(A_{[3\times3\times3]}\right) + det\left(B_{[3\times3\times3]}\right) = det\left(\begin{array}{ccc|ccc|ccc} a_{111} & a_{121} & a_{131} & a_{112} & a_{122} & a_{132} & a_{113} & a_{123} & a_{133} \\ a_{211} & a_{221} & a_{231} & a_{212} & a_{222} & a_{232} & a_{213} & a_{223} & a_{233} \\ a_{311} & a_{321} & a_{331} & a_{312} & a_{322} & a_{332} & a_{313} & a_{323} & a_{333} \end{array}\right)$$
$$+det\left(\begin{array}{ccc|ccc|ccc} a_{111} & a_{121} & a_{131} & a_{112} & a_{122} & a_{132} & a_{113} & a_{123} & a_{133} \\ b_{211} & b_{221} & b_{231} & b_{212} & b_{222} & b_{232} & b_{213} & b_{223} & b_{233} \\ a_{311} & a_{321} & a_{331} & a_{312} & a_{322} & a_{332} & a_{313} & a_{323} & a_{333} \end{array}\right)$$
$$= \{a_{111}\cdot a_{222}\cdot a_{333} - a_{111}\cdot a_{232}\cdot a_{323} - a_{111}\cdot a_{223}\cdot a_{332} + a_{111}\cdot a_{233}\cdot a_{322} - a_{112}\cdot a_{221}\cdot a_{333}$$
$$+a_{112}\cdot a_{223}\cdot a_{331} + a_{112}\cdot a_{231}\cdot a_{323} - a_{112}\cdot a_{233}\cdot a_{321} + a_{113}\cdot a_{221}\cdot a_{332} - a_{113}\cdot a_{222}\cdot a_{331}$$
$$-a_{113}\cdot a_{231}\cdot a_{322} + a_{113}\cdot a_{232}\cdot a_{321} - a_{121}\cdot a_{212}\cdot a_{333} + a_{121}\cdot a_{213}\cdot a_{332} + a_{121}\cdot a_{232}\cdot a_{313}$$
$$-a_{121}\cdot a_{233}\cdot a_{312} + a_{122}\cdot a_{211}\cdot a_{333} - a_{122}\cdot a_{213}\cdot a_{331} - a_{122}\cdot a_{231}\cdot a_{313} + a_{122}\cdot a_{233}\cdot a_{311}$$
$$-a_{123}\cdot a_{211}\cdot a_{332} + a_{123}\cdot a_{212}\cdot a_{331} + a_{123}\cdot a_{231}\cdot a_{312} - a_{123}\cdot a_{232}\cdot a_{311} + a_{131}\cdot a_{212}\cdot a_{323}$$
$$-a_{131}\cdot a_{213}\cdot a_{322} - a_{131}\cdot a_{222}\cdot a_{313} + a_{131}\cdot a_{223}\cdot a_{312} - a_{132}\cdot a_{211}\cdot a_{323} + a_{132}\cdot a_{213}\cdot a_{321}$$
$$+a_{132}\cdot a_{221}\cdot a_{313} - a_{132}\cdot a_{223}\cdot a_{311} + a_{133}\cdot a_{211}\cdot a_{322} - a_{133}\cdot a_{212}\cdot a_{321} - a_{133}\cdot a_{221}\cdot a_{312}$$
$$+a_{133}\cdot a_{222}\cdot a_{311}\} + \{a_{111}\cdot b_{222}\cdot a_{333} - a_{111}\cdot b_{232}\cdot a_{323} - a_{111}\cdot b_{223}\cdot a_{332} + a_{111}\cdot b_{233}\cdot a_{322}$$
$$-a_{112}\cdot b_{221}\cdot a_{333} + a_{112}\cdot b_{223}\cdot a_{331} + a_{112}\cdot b_{231}\cdot a_{323} - a_{112}\cdot b_{233}\cdot a_{321} + a_{113}\cdot b_{221}\cdot a_{332}$$
$$-a_{113}\cdot b_{222}\cdot a_{331} - a_{113}\cdot b_{231}\cdot a_{322} + a_{113}\cdot b_{232}\cdot a_{321} - a_{121}\cdot b_{212}\cdot a_{333} + a_{121}\cdot b_{213}\cdot a_{332}$$
$$+a_{121}\cdot b_{232}\cdot a_{313} - a_{121}\cdot b_{233}\cdot a_{312} + a_{122}\cdot b_{211}\cdot a_{333} - a_{122}\cdot b_{213}\cdot a_{331} - a_{122}\cdot b_{231}\cdot a_{313}$$
$$+a_{122}\cdot b_{233}\cdot a_{311} - a_{123}\cdot b_{211}\cdot a_{332} + a_{123}\cdot b_{212}\cdot a_{331} + a_{123}\cdot b_{231}\cdot a_{312} - a_{123}\cdot b_{232}\cdot a_{311}$$
$$+a_{131}\cdot b_{212}\cdot a_{323} - a_{131}\cdot b_{213}\cdot a_{322} - a_{131}\cdot b_{222}\cdot a_{313} + a_{131}\cdot b_{223}\cdot a_{312} - a_{132}\cdot b_{211}\cdot a_{323}$$
$$+a_{132}\cdot b_{213}\cdot a_{321} + a_{132}\cdot b_{221}\cdot a_{313} - a_{132}\cdot b_{223}\cdot a_{311} + a_{133}\cdot b_{211}\cdot a_{322} - a_{133}\cdot b_{212}\cdot a_{321}$$
$$-a_{133}\cdot b_{221}\cdot a_{312} + a_{133}\cdot b_{222}\cdot a_{311}\},$$

while,

$$det\left(A_{[3\times3\times3]}\right) + det\left(B_{[3\times3\times3]}\right) = det\left(\begin{array}{ccc} a_{111} & a_{121} & a_{131} \\ a_{211}+b_{211} & a_{221}+b_{221} & a_{231}+b_{231} \\ a_{311} & a_{321} & a_{331} \end{array}\right|$$

$$\begin{pmatrix} a_{112} & a_{122} & a_{132} \\ a_{212}+b_{212} & a_{222}+b_{222} & a_{232}+b_{232} \\ a_{312} & a_{322} & a_{332} \end{vmatrix} \begin{matrix} a_{113} & a_{123} & a_{133} \\ a_{213}+b_{213} & a_{223}+b_{223} & a_{233}+b_{233} \\ a_{313} & a_{323} & a_{333} \end{pmatrix}$$

$$= a_{111}\cdot(a_{222}+b_{222})\cdot a_{333} - a_{111}\cdot(a_{232}+b_{232})\cdot a_{323} - a_{111}\cdot(a_{223}+b_{223})\cdot a_{332}$$
$$+a_{111}\cdot(a_{233}+b_{233})\cdot a_{322} - a_{112}\cdot(a_{221}+b_{221})\cdot a_{333} + a_{112}\cdot(a_{223}+b_{223})\cdot a_{331}$$
$$+a_{112}\cdot(a_{231}+b_{231})\cdot a_{323} - a_{112}\cdot(a_{233}+b_{233})\cdot a_{321} + a_{113}\cdot(a_{221}+b_{221})\cdot a_{332}$$
$$-a_{113}\cdot(a_{222}+b_{222})\cdot a_{331} - a_{113}\cdot(a_{231}+b_{231})\cdot a_{322} + a_{113}\cdot(a_{232}+b_{232})\cdot a_{321}$$
$$-a_{121}\cdot(a_{212}+b_{212})\cdot a_{333} + a_{121}\cdot(a_{213}+b_{213})\cdot a_{332} + a_{121}\cdot(a_{232}+b_{232})\cdot a_{313}$$
$$-a_{121}\cdot(a_{233}+b_{233})\cdot a_{312} + a_{122}\cdot(a_{211}+b_{211})\cdot a_{333} - a_{122}\cdot(a_{213}+b_{213})\cdot a_{331}$$
$$-a_{122}\cdot(a_{231}+b_{231})\cdot a_{313} + a_{122}\cdot(a_{233}+b_{233})\cdot a_{311} - a_{123}\cdot(a_{211}+b_{211})\cdot a_{332}$$
$$+a_{123}\cdot(a_{212}+b_{212})\cdot a_{331} + a_{123}\cdot(a_{231}+b_{231})\cdot a_{312} - a_{123}\cdot(a_{232}+b_{232})\cdot a_{311}$$
$$+a_{131}\cdot(a_{212}+b_{212})\cdot a_{323} - a_{131}\cdot(a_{213}+b_{213})\cdot a_{322} - a_{131}\cdot(a_{222}+b_{222})\cdot a_{313}$$
$$+a_{131}\cdot(a_{223}+b_{223})\cdot a_{312} - a_{132}\cdot(a_{211}+b_{211})\cdot a_{323} + a_{132}\cdot(a_{213}+b_{213})\cdot a_{321}$$
$$+a_{132}\cdot(a_{221}+b_{221})\cdot a_{313} - a_{132}\cdot(a_{223}+b_{223})\cdot a_{311} + a_{133}\cdot(a_{211}+b_{211})\cdot a_{322}$$
$$-a_{133}\cdot(a_{212}+b_{212})\cdot a_{321} - a_{133}\cdot(a_{221}+b_{221})\cdot a_{312} + a_{133}\cdot(a_{222}+b_{222})\cdot a_{311}.$$

Hence,

$$det\left(A_{[3\times3\times3]}\right) + det\left(B_{[3\times3\times3]}\right) = a_{111}\cdot a_{222}\cdot a_{333} + a_{111}\cdot b_{222}\cdot a_{333}$$
$$-a_{111}\cdot a_{232}\cdot a_{323} - a_{111}\cdot b_{232}\cdot a_{323} - a_{111}\cdot a_{223}\cdot a_{332} - a_{111}\cdot b_{223}\cdot a_{332} + a_{111}\cdot a_{233}\cdot a_{322}$$
$$+a_{111}\cdot b_{233}\cdot a_{322} - a_{112}\cdot a_{221}\cdot a_{333} - a_{112}\cdot b_{221}\cdot a_{333} + a_{112}\cdot a_{223}\cdot a_{331} + a_{112}\cdot b_{223}\cdot a_{331}$$
$$+a_{112}\cdot a_{231}\cdot a_{323} + a_{112}\cdot b_{231}\cdot a_{323} - a_{112}\cdot a_{233}\cdot a_{321} - a_{112}\cdot b_{233}\cdot a_{321} + a_{113}\cdot a_{221}\cdot a_{332}$$
$$+a_{113}\cdot b_{221}\cdot a_{332} - a_{113}\cdot a_{222}\cdot a_{331} - a_{113}\cdot b_{222}\cdot a_{331} - a_{113}\cdot a_{231}\cdot a_{322} - a_{113}\cdot b_{231}\cdot a_{322}$$
$$+a_{113}\cdot a_{232}\cdot a_{321} + a_{113}\cdot b_{232}\cdot a_{321} - a_{121}\cdot a_{212}\cdot a_{333} - a_{121}\cdot b_{212}\cdot a_{333} + a_{121}\cdot a_{213}\cdot a_{332}$$
$$+a_{121}\cdot b_{213}\cdot a_{332} + a_{121}\cdot a_{232}\cdot a_{313} + a_{121}\cdot b_{232}\cdot a_{313} - a_{121}\cdot a_{233}\cdot a_{312} - a_{121}\cdot b_{233}\cdot a_{312}$$
$$+a_{122}\cdot a_{211}\cdot a_{333} + a_{122}\cdot b_{211}\cdot a_{333} - a_{122}\cdot a_{213}\cdot a_{331} - a_{122}\cdot b_{213}\cdot a_{331} - a_{122}\cdot a_{231}\cdot a_{313}$$
$$-a_{122}\cdot b_{231}\cdot a_{313} + a_{122}\cdot a_{233}\cdot a_{311} + a_{122}\cdot b_{233}\cdot a_{311} - a_{123}\cdot a_{211}\cdot a_{332} - a_{123}\cdot b_{211}\cdot a_{332}$$
$$+a_{123}\cdot a_{212}\cdot a_{331} + a_{123}\cdot b_{212}\cdot a_{331} + a_{123}\cdot a_{231}\cdot a_{312} + a_{123}\cdot b_{231}\cdot a_{312} - a_{123}\cdot a_{232}\cdot a_{311}$$
$$-a_{123}\cdot b_{232}\cdot a_{311} + a_{131}\cdot a_{212}\cdot a_{323} + a_{131}\cdot b_{212}\cdot a_{323} - a_{131}\cdot a_{213}\cdot a_{322} - a_{131}\cdot b_{213}\cdot a_{322}$$
$$-a_{131}\cdot a_{222}\cdot a_{313} - a_{131}\cdot b_{222}\cdot a_{313} + a_{131}\cdot a_{223}\cdot a_{312} + a_{131}\cdot b_{223}\cdot a_{312} - a_{132}\cdot a_{211}\cdot a_{323}$$
$$-a_{132}\cdot b_{211}\cdot a_{323} + a_{132}\cdot a_{213}\cdot a_{321} + a_{132}\cdot b_{213}\cdot a_{321} + a_{132}\cdot a_{221}\cdot a_{313} + a_{132}\cdot b_{221}\cdot a_{313}$$
$$-a_{132}\cdot a_{223}\cdot a_{311} - a_{132}\cdot b_{223}\cdot a_{311} + a_{133}\cdot a_{211}\cdot a_{322} + a_{133}\cdot b_{211}\cdot a_{322} - a_{133}\cdot a_{212}\cdot a_{321}$$
$$-a_{133}\cdot b_{212}\cdot a_{321} - a_{133}\cdot a_{221}\cdot a_{312} - a_{133}\cdot b_{221}\cdot a_{312} + a_{133}\cdot a_{222}\cdot a_{311} + a_{133}\cdot b_{222}\cdot a_{311}.$$

If we compare results of above equations, we can see that we have the same result in both cases.

3. For plan $i = 3$: Let A and B be cubic-matries of order 3, where all elements on the plan $i = 2$ and $i = 3$ are identical in both matrices, then we have:

$$det\left(A_{[3\times3\times3]}\right) + det\left(B_{[3\times3\times3]}\right) = det\begin{pmatrix} a_{111} & a_{121} & a_{131} \\ a_{211} & a_{221} & a_{231} \\ a_{311} & a_{321} & a_{331} \end{vmatrix} \begin{matrix} a_{112} & a_{122} & a_{132} \\ a_{212} & a_{222} & a_{232} \\ a_{312} & a_{322} & a_{332} \end{vmatrix} \begin{matrix} a_{113} & a_{123} & a_{133} \\ a_{213} & a_{223} & a_{233} \\ a_{313} & a_{323} & a_{333} \end{pmatrix}$$
$$+det\begin{pmatrix} b_{111} & b_{121} & b_{131} \\ a_{211} & a_{221} & a_{231} \\ a_{311} & a_{321} & a_{331} \end{vmatrix} \begin{matrix} b_{112} & b_{122} & b_{132} \\ a_{212} & a_{222} & a_{232} \\ a_{312} & a_{322} & a_{332} \end{vmatrix} \begin{matrix} b_{113} & b_{123} & b_{133} \\ a_{213} & a_{223} & a_{233} \\ a_{313} & a_{323} & a_{333} \end{pmatrix}$$

$$= \{a_{111}\cdot a_{222}\cdot a_{333} - a_{111}\cdot a_{232}\cdot a_{323} - a_{111}\cdot a_{223}\cdot a_{332} + a_{111}\cdot a_{233}\cdot a_{322} - a_{112}\cdot a_{221}\cdot a_{333}$$
$$+a_{112}\cdot a_{223}\cdot a_{331} + a_{112}\cdot a_{231}\cdot a_{323} - a_{112}\cdot a_{233}\cdot a_{321} + a_{113}\cdot a_{221}\cdot a_{332} - a_{113}\cdot a_{222}\cdot a_{331}$$
$$-a_{113}\cdot a_{231}\cdot a_{322} + a_{113}\cdot a_{232}\cdot a_{321} - a_{121}\cdot a_{212}\cdot a_{333} + a_{121}\cdot a_{213}\cdot a_{332} + a_{121}\cdot a_{232}\cdot a_{313}$$

$$-a_{121}\cdot a_{233}\cdot a_{312}+a_{122}\cdot a_{211}\cdot a_{333}-a_{122}\cdot a_{213}\cdot a_{331}-a_{122}\cdot a_{231}\cdot a_{313}+a_{122}\cdot a_{233}\cdot a_{311}$$
$$-a_{123}\cdot a_{211}\cdot a_{332}+a_{123}\cdot a_{212}\cdot a_{331}+a_{123}\cdot a_{231}\cdot a_{312}-a_{123}\cdot a_{232}\cdot a_{311}+a_{131}\cdot a_{212}\cdot a_{323}$$
$$-a_{131}\cdot a_{213}\cdot a_{322}-a_{131}\cdot a_{222}\cdot a_{313}+a_{131}\cdot a_{223}\cdot a_{312}-a_{132}\cdot a_{211}\cdot a_{323}+a_{132}\cdot a_{213}\cdot a_{321}$$
$$+a_{132}\cdot a_{221}\cdot a_{313}-a_{132}\cdot a_{223}\cdot a_{311}+a_{133}\cdot a_{211}\cdot a_{322}-a_{133}\cdot a_{212}\cdot a_{321}-a_{133}\cdot a_{221}\cdot a_{312}$$
$$+a_{133}\cdot a_{222}\cdot a_{311}\}+\{b_{111}\cdot a_{222}\cdot a_{333}-b_{111}\cdot a_{232}\cdot a_{323}-b_{111}\cdot a_{223}\cdot a_{332}+b_{111}\cdot a_{233}\cdot a_{322}$$
$$-b_{112}\cdot a_{221}\cdot a_{333}+b_{112}\cdot a_{223}\cdot a_{331}+b_{112}\cdot a_{231}\cdot a_{323}-b_{112}\cdot a_{233}\cdot a_{321}+b_{113}\cdot a_{221}\cdot a_{332}$$
$$-b_{113}\cdot a_{222}\cdot a_{331}-b_{113}\cdot a_{231}\cdot a_{322}+b_{113}\cdot a_{232}\cdot a_{321}-b_{121}\cdot a_{212}\cdot a_{333}+b_{121}\cdot a_{213}\cdot a_{332}$$
$$+b_{121}\cdot a_{232}\cdot a_{313}-b_{121}\cdot a_{233}\cdot a_{312}+b_{122}\cdot a_{211}\cdot a_{333}-b_{122}\cdot a_{213}\cdot a_{331}-b_{122}\cdot a_{231}\cdot a_{313}$$
$$+b_{122}\cdot a_{233}\cdot a_{311}-b_{123}\cdot a_{211}\cdot a_{332}+b_{123}\cdot a_{212}\cdot a_{331}+b_{123}\cdot a_{231}\cdot a_{312}-b_{123}\cdot a_{232}\cdot a_{311}$$
$$+b_{131}\cdot a_{212}\cdot a_{323}-b_{131}\cdot a_{213}\cdot a_{322}-b_{131}\cdot a_{222}\cdot a_{313}+b_{131}\cdot a_{223}\cdot a_{312}-b_{132}\cdot a_{211}\cdot a_{323}$$
$$+b_{132}\cdot a_{213}\cdot a_{321}+b_{132}\cdot a_{221}\cdot a_{313}-b_{132}\cdot a_{223}\cdot a_{311}+b_{133}\cdot a_{211}\cdot a_{322}-b_{133}\cdot a_{212}\cdot a_{321}$$
$$-b_{133}\cdot a_{221}\cdot a_{312}+b_{133}\cdot a_{222}\cdot a_{311},$$

while,

$$det\left(A_{[3\times3\times3]}\right)+det\left(B_{[3\times3\times3]}\right)=det\begin{pmatrix}a_{111}+b_{111} & a_{121}+b_{121} & a_{131}+b_{131}\\ a_{211} & a_{221} & a_{231}\\ a_{311} & a_{321} & a_{331}\end{vmatrix}\begin{matrix}a_{112}+b_{112} & a_{122}+b_{122} & a_{132}+b_{132}\\ a_{212} & a_{222} & a_{232}\\ a_{312} & a_{322} & a_{332}\end{vmatrix}\begin{matrix}a_{113}+b_{113} & a_{123}+b_{123} & a_{133}+b_{133}\\ a_{213} & a_{223} & a_{233}\\ a_{313} & a_{323} & a_{333}\end{matrix}\end{pmatrix}$$
$$=(a_{111}+b_{111})\cdot a_{222}\cdot a_{333}-(a_{111}+b_{111})\cdot a_{232}\cdot a_{323}-(a_{111}+b_{111})\cdot a_{223}\cdot a_{332}$$
$$+(a_{111}+b_{111})\cdot a_{233}\cdot a_{322}-(a_{112}+b_{112})\cdot a_{221}\cdot a_{333}+(a_{112}+b_{112})\cdot a_{223}\cdot a_{331}$$
$$+(a_{112}+b_{112})\cdot a_{231}\cdot a_{323}-(a_{112}+b_{112})\cdot a_{233}\cdot a_{321}+(a_{113}+b_{113})\cdot a_{221}\cdot a_{332}$$
$$-(a_{113}+b_{113})\cdot a_{222}\cdot a_{331}-(a_{113}+b_{113})\cdot a_{231}\cdot a_{322}+(a_{113}+b_{113})\cdot a_{232}\cdot a_{321}$$
$$-(a_{121}+b_{121})\cdot a_{212}\cdot a_{333}+(a_{121}+b_{121})\cdot a_{213}\cdot a_{332}+(a_{121}+b_{121})\cdot a_{232}\cdot a_{313}$$
$$-(a_{121}+b_{121})\cdot a_{233}\cdot a_{312}+(a_{122}+b_{122})\cdot a_{211}\cdot a_{333}-(a_{122}+b_{122})\cdot a_{213}\cdot a_{331}$$
$$-(a_{122}+b_{122})\cdot a_{231}\cdot a_{313}+(a_{122}+b_{122})\cdot a_{233}\cdot a_{311}-(a_{123}+b_{123})\cdot a_{211}\cdot a_{332}$$
$$+(a_{123}+b_{123})\cdot a_{212}\cdot a_{331}+(a_{123}+b_{123})\cdot a_{231}\cdot a_{312}-(a_{123}+b_{123})\cdot a_{232}\cdot a_{311}$$
$$+(a_{131}+b_{131})\cdot a_{212}\cdot a_{323}-(a_{131}+b_{131})\cdot a_{213}\cdot a_{322}-(a_{131}+b_{131})\cdot a_{222}\cdot a_{313}$$
$$+(a_{131}+b_{131})\cdot a_{223}\cdot a_{312}-(a_{132}+b_{132})\cdot a_{211}\cdot a_{323}+(a_{132}+b_{132})\cdot a_{213}\cdot a_{321}$$
$$+(a_{132}+b_{132})\cdot a_{221}\cdot a_{313}-(a_{132}+b_{132})\cdot a_{223}\cdot a_{311}+(a_{133}+b_{133})\cdot a_{211}\cdot a_{322}$$
$$-(a_{133}+b_{133})\cdot a_{212}\cdot a_{321}-(a_{133}+b_{133})\cdot a_{221}\cdot a_{312}+(a_{133}+b_{133})\cdot a_{222}\cdot a_{311}.$$

Hence,

$$det\left(A_{[3\times3\times3]}\right)+det\left(B_{[3\times3\times3]}\right)=a_{111}\cdot a_{222}\cdot a_{333}+b_{111}\cdot a_{222}\cdot a_{333}$$
$$-a_{111}\cdot a_{232}\cdot a_{323}-b_{111}\cdot a_{232}\cdot a_{323}-a_{111}\cdot a_{223}\cdot a_{332}-b_{111}\cdot a_{223}\cdot a_{332}+a_{111}\cdot a_{233}\cdot a_{322}$$
$$+b_{111}\cdot a_{233}\cdot a_{322}-a_{112}\cdot a_{221}\cdot a_{333}-b_{112}\cdot a_{221}\cdot a_{333}+a_{112}\cdot a_{223}\cdot a_{331}+b_{112}\cdot a_{223}\cdot a_{331}$$
$$+a_{112}\cdot a_{231}\cdot a_{323}+b_{112}\cdot a_{231}\cdot a_{323}-a_{112}\cdot a_{233}\cdot a_{321}-b_{112}\cdot a_{233}\cdot a_{321}+a_{113}\cdot a_{221}\cdot a_{332}$$
$$+b_{113}\cdot a_{221}\cdot a_{332}-a_{113}\cdot a_{222}\cdot a_{331}-b_{113}\cdot a_{222}\cdot a_{331}-a_{113}\cdot a_{231}\cdot a_{322}-b_{113}\cdot a_{231}\cdot a_{322}$$
$$+a_{113}\cdot a_{232}\cdot a_{321}+b_{113}\cdot a_{232}\cdot a_{321}-a_{121}\cdot a_{212}\cdot a_{333}-b_{121}\cdot a_{212}\cdot a_{333}+a_{121}\cdot a_{213}\cdot a_{332}$$
$$+b_{121}\cdot a_{213}\cdot a_{332}+a_{121}\cdot a_{232}\cdot a_{313}+b_{121}\cdot a_{232}\cdot a_{313}-a_{121}\cdot a_{233}\cdot a_{312}-b_{121}\cdot a_{233}\cdot a_{312}$$
$$+a_{122}\cdot a_{211}\cdot a_{333}+b_{122}\cdot a_{211}\cdot a_{333}-a_{122}\cdot a_{213}\cdot a_{331}-b_{122}\cdot a_{213}\cdot a_{331}-a_{122}\cdot a_{231}\cdot a_{313}$$
$$-b_{122}\cdot a_{231}\cdot a_{313}+a_{122}\cdot a_{233}\cdot a_{311}+b_{122}\cdot a_{233}\cdot a_{311}-a_{123}\cdot a_{211}\cdot a_{332}-b_{123}\cdot a_{211}\cdot a_{332}$$
$$+a_{123}\cdot a_{212}\cdot a_{331}+b_{123}\cdot a_{212}\cdot a_{331}+a_{123}\cdot a_{231}\cdot a_{312}+b_{123}\cdot a_{231}\cdot a_{312}-a_{123}\cdot a_{232}\cdot a_{311}$$

$$-b_{123}\cdot a_{232}\cdot a_{311}+a_{131}\cdot a_{212}\cdot a_{323}+b_{131}\cdot a_{212}\cdot a_{323}-a_{131}\cdot a_{213}\cdot a_{322}-b_{131}\cdot a_{213}\cdot a_{322}$$
$$-a_{131}\cdot a_{222}\cdot a_{313}-b_{131}\cdot a_{222}\cdot a_{313}+a_{131}\cdot a_{223}\cdot a_{312}+b_{131}\cdot a_{223}\cdot a_{312}-a_{132}\cdot a_{211}\cdot a_{323}$$
$$-b_{132}\cdot a_{211}\cdot a_{323}+a_{132}\cdot a_{213}\cdot a_{321}+b_{132}\cdot a_{213}\cdot a_{321}+a_{132}\cdot a_{221}\cdot a_{313}+b_{132}\cdot a_{221}\cdot a_{313}$$
$$-a_{132}\cdot a_{223}\cdot a_{311}-b_{132}\cdot a_{223}\cdot a_{311}+a_{133}\cdot a_{211}\cdot a_{322}+b_{133}\cdot a_{211}\cdot a_{322}-a_{133}\cdot a_{212}\cdot a_{321}$$
$$-b_{133}\cdot a_{212}\cdot a_{321}-a_{133}\cdot a_{221}\cdot a_{312}-b_{133}\cdot a_{221}\cdot a_{312}+a_{133}\cdot a_{222}\cdot a_{311}+b_{133}\cdot a_{222}\cdot a_{311}.$$

If we compare results of above equations, we can see that we have the same result in both cases.

4. For plan $j=1$: Let A and B be cubic-matries of order 3, where all elements on the plan $j=1$ and $j=2$ are identical in both matrices, then we have:

$$det\left(A_{[3\times3\times3]}\right)+det\left(B_{[3\times3\times3]}\right)=det\left(\begin{array}{ccc|ccc|ccc}a_{111}&a_{121}&a_{131}&a_{112}&a_{122}&a_{132}&a_{113}&a_{123}&a_{133}\\a_{211}&a_{221}&a_{231}&a_{212}&a_{222}&a_{232}&a_{213}&a_{223}&a_{233}\\a_{311}&a_{321}&a_{331}&a_{312}&a_{322}&a_{332}&a_{313}&a_{323}&a_{333}\end{array}\right)$$
$$+det\left(\begin{array}{ccc|ccc|ccc}a_{111}&a_{121}&b_{131}&a_{112}&a_{122}&b_{132}&a_{113}&a_{123}&b_{133}\\a_{211}&a_{221}&b_{231}&a_{212}&a_{222}&b_{232}&a_{213}&a_{223}&b_{233}\\a_{311}&a_{321}&b_{331}&a_{312}&a_{322}&b_{332}&a_{313}&a_{323}&b_{333}\end{array}\right)$$
$$=\{a_{111}\cdot a_{222}\cdot a_{333}-a_{111}\cdot a_{232}\cdot a_{323}-a_{111}\cdot a_{223}\cdot a_{332}+a_{111}\cdot a_{233}\cdot a_{322}-a_{112}\cdot a_{221}\cdot a_{333}$$
$$+a_{112}\cdot a_{223}\cdot a_{331}+a_{112}\cdot a_{231}\cdot a_{323}-a_{112}\cdot a_{233}\cdot a_{321}+a_{113}\cdot a_{221}\cdot a_{332}-a_{113}\cdot a_{222}\cdot a_{331}$$
$$-a_{113}\cdot a_{231}\cdot a_{322}+a_{113}\cdot a_{232}\cdot a_{321}-a_{121}\cdot a_{212}\cdot a_{333}+a_{121}\cdot a_{213}\cdot a_{332}+a_{121}\cdot a_{232}\cdot a_{313}$$
$$-a_{121}\cdot a_{233}\cdot a_{312}+a_{122}\cdot a_{211}\cdot a_{333}-a_{122}\cdot a_{213}\cdot a_{331}-a_{122}\cdot a_{231}\cdot a_{313}+a_{122}\cdot a_{233}\cdot a_{311}$$
$$-a_{123}\cdot a_{211}\cdot a_{332}+a_{123}\cdot a_{212}\cdot a_{331}+a_{123}\cdot a_{231}\cdot a_{312}-a_{123}\cdot a_{232}\cdot a_{311}+a_{131}\cdot a_{212}\cdot a_{323}$$
$$-a_{131}\cdot a_{213}\cdot a_{322}-a_{131}\cdot a_{222}\cdot a_{313}+a_{131}\cdot a_{223}\cdot a_{312}-a_{132}\cdot a_{211}\cdot a_{323}+a_{132}\cdot a_{213}\cdot a_{321}$$
$$+a_{132}\cdot a_{221}\cdot a_{313}-a_{132}\cdot a_{223}\cdot a_{311}+a_{133}\cdot a_{211}\cdot a_{322}-a_{133}\cdot a_{212}\cdot a_{321}-a_{133}\cdot a_{221}\cdot a_{312}$$
$$+a_{133}\cdot a_{222}\cdot a_{311}\}+\{a_{111}\cdot a_{222}\cdot b_{333}-a_{111}\cdot b_{232}\cdot a_{323}-a_{111}\cdot a_{223}\cdot b_{332}+a_{111}\cdot b_{233}\cdot a_{322}$$
$$-a_{112}\cdot a_{221}\cdot b_{333}+a_{112}\cdot a_{223}\cdot b_{331}+a_{112}\cdot b_{231}\cdot a_{323}-a_{112}\cdot b_{233}\cdot a_{321}+a_{113}\cdot a_{221}\cdot b_{332}$$
$$-a_{113}\cdot a_{222}\cdot b_{331}-a_{113}\cdot b_{231}\cdot a_{322}+a_{113}\cdot b_{232}\cdot a_{321}-a_{121}\cdot a_{212}\cdot b_{333}+a_{121}\cdot a_{213}\cdot b_{332}$$
$$+a_{121}\cdot b_{232}\cdot a_{313}-a_{121}\cdot b_{233}\cdot a_{312}+a_{122}\cdot a_{211}\cdot b_{333}-a_{122}\cdot a_{213}\cdot b_{331}-a_{122}\cdot b_{231}\cdot a_{313}$$
$$+a_{122}\cdot b_{233}\cdot a_{311}-a_{123}\cdot a_{211}\cdot b_{332}+a_{123}\cdot a_{212}\cdot b_{331}+a_{123}\cdot b_{231}\cdot a_{312}-a_{123}\cdot b_{232}\cdot a_{311}$$
$$+b_{131}\cdot a_{212}\cdot a_{323}-b_{131}\cdot a_{213}\cdot a_{322}-b_{131}\cdot a_{222}\cdot a_{313}+b_{131}\cdot a_{223}\cdot a_{312}-b_{132}\cdot a_{211}\cdot a_{323}$$
$$+b_{132}\cdot a_{213}\cdot a_{321}+b_{132}\cdot a_{221}\cdot a_{313}-b_{132}\cdot a_{223}\cdot a_{311}+b_{133}\cdot a_{211}\cdot a_{322}-b_{133}\cdot a_{212}\cdot a_{321}$$
$$-b_{133}\cdot a_{221}\cdot a_{312}+b_{133}\cdot a_{222}\cdot a_{311}\},$$

while,

$$\det\left(A_{[3\times3\times3]}\right)+det\left(B_{[3\times3\times3]}\right)$$
$$=\det\left(\begin{array}{ccc|ccc|ccc}a_{111}&a_{121}&a_{131}+b_{131}&a_{112}&a_{122}&a_{132}+b_{132}&a_{113}&a_{123}&a_{133}+b_{133}\\a_{211}&a_{221}&a_{231}+b_{231}&a_{212}&a_{222}&a_{232}+b_{232}&a_{213}&a_{223}&a_{233}+b_{233}\\a_{311}&a_{321}&a_{331}+b_{331}&a_{312}&a_{322}&a_{332}+b_{332}&a_{313}&a_{323}&a_{333}+b_{333}\end{array}\right)$$
$$=a_{111}\cdot a_{222}\cdot(a_{333}+b_{333})-a_{111}\cdot(a_{232}+b_{232})\cdot a_{323}-a_{111}\cdot a_{223}\cdot(a_{332}+b_{332})$$
$$+a_{111}\cdot(a_{233}+b_{233})\cdot a_{322}-a_{112}\cdot a_{221}\cdot(a_{333}+b_{333})+a_{112}\cdot a_{223}\cdot(a_{331}+b_{331})$$
$$+a_{112}\cdot(a_{231}+b_{231})\cdot a_{323}-a_{112}\cdot(a_{233}+b_{233})\cdot a_{321}+a_{113}\cdot a_{221}\cdot(a_{332}+b_{332})$$
$$-a_{113}\cdot a_{222}\cdot(a_{331}+b_{331})-a_{113}\cdot(a_{231}+b_{231})\cdot a_{322}+a_{113}\cdot(a_{232}+b_{232})\cdot a_{321}$$
$$-a_{121}\cdot a_{212}\cdot(a_{333}+b_{333})+a_{121}\cdot a_{213}\cdot(a_{332}+b_{332})+a_{121}\cdot(a_{232}+b_{232})\cdot a_{313}$$
$$-a_{121}\cdot(a_{233}+b_{233})\cdot a_{312}+a_{122}\cdot a_{211}\cdot(a_{333}+b_{333})-a_{122}\cdot a_{213}\cdot(a_{331}+b_{331})$$
$$-a_{122}\cdot(a_{231}+b_{231})\cdot a_{313}+a_{122}\cdot(a_{233}+b_{233})\cdot a_{311}-a_{123}\cdot a_{211}\cdot(a_{332}+b_{332})$$
$$+a_{123}\cdot a_{212}\cdot(a_{331}+b_{331})+a_{123}\cdot(a_{231}+b_{231})\cdot a_{312}-a_{123}\cdot(a_{232}+b_{232})\cdot a_{311}$$

$$+(a_{131}+b_{131})\cdot a_{212}\cdot a_{323}-(a_{131}+b_{131})\cdot a_{213}\cdot a_{322}-(a_{131}+b_{131})\cdot a_{222}\cdot a_{313}$$
$$+(a_{131}+b_{131})\cdot a_{223}\cdot a_{312}-(a_{132}+b_{132})\cdot a_{211}\cdot a_{323}+(a_{132}+b_{132})\cdot a_{213}\cdot a_{321}$$
$$+(a_{132}+b_{132})\cdot a_{221}\cdot a_{313}-(a_{132}+b_{132})\cdot a_{223}\cdot a_{311}+(a_{133}+b_{133})\cdot a_{211}\cdot a_{322}$$
$$-(a_{133}+b_{133})\cdot a_{212}\cdot a_{321}-(a_{133}+b_{133})\cdot a_{221}\cdot a_{312}+(a_{133}+b_{133})\cdot a_{222}\cdot a_{311}$$
$$=a_{111}\cdot a_{222}\cdot a_{333}+a_{111}\cdot a_{222}\cdot b_{333}-a_{111}\cdot a_{232}\cdot a_{323}-a_{111}\cdot b_{232}\cdot a_{323}-a_{111}\cdot a_{223}\cdot a_{332}$$
$$-a_{111}\cdot a_{223}\cdot b_{332}+a_{111}\cdot a_{233}\cdot a_{322}+a_{111}\cdot b_{233}\cdot a_{322}-a_{112}\cdot a_{221}\cdot a_{333}-a_{112}\cdot a_{221}\cdot b_{333}$$
$$+a_{112}\cdot a_{223}\cdot a_{331}+a_{112}\cdot b_{223}\cdot a_{331}+a_{112}\cdot a_{231}\cdot a_{323}+a_{112}\cdot b_{231}\cdot a_{323}-a_{112}\cdot a_{233}\cdot a_{321}$$
$$-a_{112}\cdot b_{233}\cdot a_{321}+a_{113}\cdot a_{221}\cdot a_{332}+a_{113}\cdot a_{221}\cdot b_{332}-a_{113}\cdot a_{222}\cdot a_{331}-a_{113}\cdot a_{222}\cdot b_{331}$$
$$-a_{113}\cdot a_{231}\cdot a_{322}-a_{113}\cdot b_{231}\cdot a_{322}+a_{113}\cdot a_{232}\cdot a_{321}+a_{113}\cdot b_{232}\cdot a_{321}-a_{121}\cdot a_{212}\cdot a_{333}$$
$$-a_{121}\cdot a_{212}\cdot b_{333}+a_{121}\cdot a_{213}\cdot a_{332}+a_{121}\cdot a_{213}\cdot b_{332}+a_{121}\cdot a_{232}\cdot a_{313}+a_{121}\cdot b_{232}\cdot a_{313}$$
$$-a_{121}\cdot a_{233}\cdot a_{312}-a_{121}\cdot b_{233}\cdot a_{312}+a_{122}\cdot a_{211}\cdot a_{333}+a_{122}\cdot a_{211}\cdot b_{333}-a_{122}\cdot a_{213}\cdot a_{331}$$
$$-a_{122}\cdot a_{213}\cdot b_{331}-a_{122}\cdot a_{231}\cdot a_{313}-a_{122}\cdot b_{231}\cdot a_{313}+a_{122}\cdot a_{233}\cdot a_{311}+a_{122}\cdot b_{233}\cdot a_{311}$$
$$-a_{123}\cdot a_{211}\cdot a_{332}-a_{123}\cdot a_{211}\cdot b_{332}+a_{123}\cdot a_{212}\cdot a_{331}+a_{123}\cdot a_{212}\cdot b_{331}+a_{123}\cdot a_{231}\cdot a_{312}$$
$$+a_{123}\cdot b_{231}\cdot a_{312}-a_{123}\cdot a_{232}\cdot a_{311}-a_{123}\cdot b_{232}\cdot a_{311}+a_{131}\cdot a_{212}\cdot a_{323}+b_{131}\cdot a_{212}\cdot a_{323}$$
$$-a_{131}\cdot a_{213}\cdot a_{322}-b_{131}\cdot a_{213}\cdot a_{322}-a_{131}\cdot a_{222}\cdot a_{313}-b_{131}\cdot a_{222}\cdot a_{313}+a_{131}\cdot a_{223}\cdot a_{312}$$
$$+b_{131}\cdot a_{223}\cdot a_{312}-a_{132}\cdot a_{211}\cdot a_{323}-b_{132}\cdot a_{211}\cdot a_{323}+a_{132}\cdot a_{213}\cdot a_{321}+b_{132}\cdot a_{213}\cdot a_{321}$$
$$+a_{132}\cdot a_{221}\cdot a_{313}+b_{132}\cdot a_{221}\cdot a_{313}-a_{132}\cdot a_{223}\cdot a_{311}-b_{132}\cdot a_{223}\cdot a_{311}+a_{133}\cdot a_{211}\cdot a_{322}$$
$$+b_{133}\cdot a_{211}\cdot a_{322}-a_{133}\cdot a_{212}\cdot a_{321}-b_{133}\cdot a_{212}\cdot a_{321}-a_{133}\cdot a_{221}\cdot a_{312}-b_{133}\cdot a_{221}\cdot a_{312}$$
$$+a_{133}\cdot a_{222}\cdot a_{311}+b_{133}\cdot a_{222}\cdot a_{311}.$$

If we compare results of above equations, we can see that we have the same result in both cases.

5. For plan $j=2$: Let A and B be cubic-matries of order 3, where all elements on the plan $j=1$ and $j=3$ are identical in both matrices, then we have:

$$det\left(A_{[3\times3\times3]}\right)+det\left(B_{[3\times3\times3]}\right)=det\left(\begin{array}{ccc|ccc|ccc}a_{111}&a_{121}&a_{131}&a_{112}&a_{122}&a_{132}&a_{113}&a_{123}&a_{133}\\a_{211}&a_{221}&a_{231}&a_{212}&a_{222}&a_{232}&a_{213}&a_{223}&a_{233}\\a_{311}&a_{321}&a_{331}&a_{312}&a_{322}&a_{332}&a_{313}&a_{323}&a_{333}\end{array}\right)$$
$$+det\left(\begin{array}{ccc|ccc|ccc}a_{111}&b_{121}&a_{131}&a_{112}&b_{122}&a_{132}&a_{113}&b_{123}&a_{133}\\a_{211}&b_{221}&a_{231}&a_{212}&b_{222}&a_{232}&a_{213}&b_{223}&a_{233}\\a_{311}&b_{321}&a_{331}&a_{312}&b_{322}&a_{332}&a_{313}&b_{323}&a_{333}\end{array}\right)$$
$$=\{a_{111}\cdot a_{222}\cdot a_{333}-a_{111}\cdot a_{232}\cdot a_{323}-a_{111}\cdot a_{223}\cdot a_{332}+a_{111}\cdot a_{233}\cdot a_{322}-a_{112}\cdot a_{221}\cdot a_{333}$$
$$+a_{112}\cdot a_{223}\cdot a_{331}+a_{112}\cdot a_{231}\cdot a_{323}-a_{112}\cdot a_{233}\cdot a_{321}+a_{113}\cdot a_{221}\cdot a_{332}-a_{113}\cdot a_{222}\cdot a_{331}$$
$$-a_{113}\cdot a_{231}\cdot a_{322}+a_{113}\cdot a_{232}\cdot a_{321}-a_{121}\cdot a_{212}\cdot a_{333}+a_{121}\cdot a_{213}\cdot a_{332}+a_{121}\cdot a_{232}\cdot a_{313}$$
$$-a_{121}\cdot a_{233}\cdot a_{312}+a_{122}\cdot a_{211}\cdot a_{333}-a_{122}\cdot a_{213}\cdot a_{331}-a_{122}\cdot a_{231}\cdot a_{313}+a_{122}\cdot a_{233}\cdot a_{311}$$
$$-a_{123}\cdot a_{211}\cdot a_{332}+a_{123}\cdot a_{212}\cdot a_{331}+a_{123}\cdot a_{231}\cdot a_{312}-a_{123}\cdot a_{232}\cdot a_{311}+a_{131}\cdot a_{212}\cdot a_{323}$$
$$-a_{131}\cdot a_{213}\cdot a_{322}-a_{131}\cdot a_{222}\cdot a_{313}+a_{131}\cdot a_{223}\cdot a_{312}-a_{132}\cdot a_{211}\cdot a_{323}+a_{132}\cdot a_{213}\cdot a_{321}$$
$$+a_{132}\cdot a_{221}\cdot a_{313}-a_{132}\cdot a_{223}\cdot a_{311}+a_{133}\cdot a_{211}\cdot a_{322}-a_{133}\cdot a_{212}\cdot a_{321}-a_{133}\cdot a_{221}\cdot a_{312}$$
$$+a_{133}\cdot a_{222}\cdot a_{311}\}+\{a_{111}\cdot b_{222}\cdot a_{333}-a_{111}\cdot a_{232}\cdot b_{323}-a_{111}\cdot b_{223}\cdot a_{332}+a_{111}\cdot a_{233}\cdot b_{322}$$
$$-a_{112}\cdot b_{221}\cdot a_{333}+a_{112}\cdot b_{223}\cdot a_{331}+a_{112}\cdot a_{231}\cdot b_{323}-a_{112}\cdot a_{233}\cdot b_{321}+a_{113}\cdot b_{221}\cdot a_{332}$$
$$-a_{113}\cdot b_{222}\cdot a_{331}-a_{113}\cdot a_{231}\cdot b_{322}+a_{113}\cdot a_{232}\cdot b_{321}-b_{121}\cdot a_{212}\cdot a_{333}+b_{121}\cdot a_{213}\cdot a_{332}$$
$$+b_{121}\cdot a_{232}\cdot a_{313}-b_{121}\cdot a_{233}\cdot a_{312}+b_{122}\cdot a_{211}\cdot a_{333}-b_{122}\cdot a_{213}\cdot a_{331}-b_{122}\cdot a_{231}\cdot a_{313}$$
$$+b_{122}\cdot a_{233}\cdot a_{311}-b_{123}\cdot a_{211}\cdot a_{332}+b_{123}\cdot a_{212}\cdot a_{331}+b_{123}\cdot a_{231}\cdot a_{312}-b_{123}\cdot a_{232}\cdot a_{311}$$
$$+a_{131}\cdot a_{212}\cdot b_{323}-a_{131}\cdot a_{213}\cdot b_{322}-a_{131}\cdot b_{222}\cdot a_{313}+a_{131}\cdot b_{223}\cdot a_{312}-a_{132}\cdot a_{211}\cdot b_{323}$$
$$+a_{132}\cdot a_{213}\cdot b_{321}+a_{132}\cdot b_{221}\cdot a_{313}-a_{132}\cdot b_{223}\cdot a_{311}+a_{133}\cdot a_{211}\cdot b_{322}-a_{133}\cdot a_{212}\cdot a_{321}$$
$$-a_{133}\cdot b_{221}\cdot a_{312}+a_{133}\cdot b_{222}\cdot a_{311}\},$$

while,

$$\det\left(A_{[3\times3\times3]}\right) + det\left(B_{[3\times3\times3]}\right)$$

$$= \det\left(\begin{array}{ccc|ccc|ccc} a_{111} & a_{121}+b_{121} & a_{131} & a_{112} & a_{122}+b_{122} & a_{132} & a_{113} & a_{123}+b_{123} & a_{133} \\ a_{211} & a_{221}+b_{221} & a_{231} & a_{212} & a_{222}+b_{222} & a_{232} & a_{213} & a_{223}+b_{223} & a_{233} \\ a_{311} & a_{321}+b_{321} & a_{331} & a_{312} & a_{322}+b_{322} & a_{332} & a_{313} & a_{323}+b_{323} & a_{333} \end{array}\right)$$

$$= a_{111}\cdot(a_{222}+b_{222})\cdot a_{333} - a_{111}\cdot a_{232}\cdot(a_{323}+b_{323}) - a_{111}\cdot(a_{223}+b_{223})\cdot a_{332}$$
$$+a_{111}\cdot a_{233}\cdot(a_{322}+b_{322}) - a_{112}\cdot(a_{221}+b_{221})\cdot a_{333} + a_{112}\cdot(a_{223}+b_{223})\cdot a_{331}$$
$$+a_{112}\cdot a_{231}\cdot(a_{323}+b_{323}) - a_{112}\cdot a_{233}\cdot(a_{321}+b_{321}) + a_{113}\cdot(a_{221}+b_{221})\cdot a_{332}$$
$$-a_{113}\cdot(a_{222}+b_{222})\cdot a_{331} - a_{113}\cdot a_{231}\cdot(a_{322}+b_{322}) + a_{113}\cdot a_{232}\cdot(a_{321}+b_{321})$$
$$-(a_{121}+b_{121})\cdot a_{212}\cdot a_{333} + (a_{121}+b_{121})\cdot a_{213}\cdot a_{332} + (a_{121}+b_{121})\cdot a_{232}\cdot a_{313}$$
$$-(a_{121}+b_{121})\cdot a_{233}\cdot a_{312} + (a_{122}+b_{122})\cdot a_{211}\cdot a_{333} - (a_{122}+b_{122})\cdot a_{213}\cdot a_{331}$$
$$-(a_{122}+b_{122})\cdot a_{231}\cdot a_{313} + (a_{122}+b_{122})\cdot a_{233}\cdot a_{311} - (a_{123}+b_{123})\cdot a_{211}\cdot a_{332}$$
$$+(a_{123}+b_{123})\cdot a_{212}\cdot a_{331} + (a_{123}+b_{123})\cdot a_{231}\cdot a_{312} - (a_{123}+b_{123})\cdot a_{232}\cdot a_{311}$$
$$+a_{131}\cdot a_{212}\cdot(a_{323}+b_{323}) - a_{131}\cdot a_{213}\cdot(a_{322}+b_{322}) - a_{131}\cdot(a_{222}+b_{222})\cdot a_{313}$$
$$+a_{131}\cdot(a_{223}+b_{223})\cdot a_{312} - a_{132}\cdot a_{211}\cdot(a_{323}+b_{323}) + a_{132}\cdot a_{213}\cdot(a_{321}+b_{321})$$
$$+a_{132}\cdot(a_{221}+b_{221})\cdot a_{313} - a_{132}\cdot(a_{223}+b_{223})\cdot a_{311} + a_{133}\cdot a_{211}\cdot(a_{322}+b_{322})$$
$$-a_{133}\cdot a_{212}\cdot(a_{321}+b_{321}) - a_{133}\cdot(a_{221}+b_{221})\cdot a_{312} + a_{133}\cdot(a_{222}+b_{222})\cdot a_{311}$$
$$= a_{111}\cdot a_{222}\cdot a_{333} + a_{111}\cdot b_{222}\cdot a_{333} - a_{111}\cdot a_{232}\cdot a_{323} - a_{111}\cdot a_{232}\cdot b_{323} - a_{111}\cdot a_{223}\cdot a_{332}$$
$$-a_{111}\cdot b_{223}\cdot a_{332} + a_{111}\cdot a_{233}\cdot a_{322} + a_{111}\cdot a_{233}\cdot b_{322} - a_{112}\cdot a_{221}\cdot a_{333} - a_{112}\cdot b_{221}\cdot a_{333}$$
$$+a_{112}\cdot a_{223}\cdot a_{331} + a_{112}\cdot b_{223}\cdot a_{331} + a_{112}\cdot a_{231}\cdot a_{323} + a_{112}\cdot a_{231}\cdot b_{323} - a_{112}\cdot a_{233}\cdot a_{321}$$
$$-a_{112}\cdot a_{233}\cdot b_{321} + a_{113}\cdot a_{221}\cdot a_{332} + a_{113}\cdot b_{221}\cdot a_{332} - a_{113}\cdot a_{222}\cdot a_{331} - a_{113}\cdot b_{222}\cdot a_{331}$$
$$-a_{113}\cdot a_{231}\cdot a_{322} - a_{113}\cdot a_{231}\cdot b_{322} + a_{113}\cdot a_{232}\cdot a_{321} + a_{113}\cdot a_{232}\cdot b_{321} - a_{121}\cdot a_{212}\cdot a_{333}$$
$$-b_{121}\cdot a_{212}\cdot a_{333} + a_{121}\cdot a_{213}\cdot a_{332} + b_{121}\cdot a_{213}\cdot a_{332} + a_{121}\cdot a_{232}\cdot a_{313} + b_{121}\cdot a_{232}\cdot a_{313}$$
$$-a_{121}\cdot a_{233}\cdot a_{312} - b_{121}\cdot a_{233}\cdot a_{312} + a_{122}\cdot a_{211}\cdot a_{333} + b_{122}\cdot a_{211}\cdot a_{333} - a_{122}\cdot a_{213}\cdot a_{331}$$
$$-b_{122}\cdot a_{213}\cdot a_{331} - a_{122}\cdot a_{231}\cdot a_{313} - b_{122}\cdot a_{231}\cdot a_{313} + a_{122}\cdot a_{233}\cdot a_{311} + b_{122}\cdot a_{233}\cdot a_{311}$$
$$-a_{123}\cdot a_{211}\cdot a_{332} - b_{123}\cdot a_{211}\cdot a_{332} + a_{123}\cdot a_{212}\cdot a_{331} + b_{123}\cdot a_{212}\cdot a_{331} + a_{123}\cdot a_{231}\cdot a_{312}$$
$$+b_{123}\cdot a_{231}\cdot a_{312} - a_{123}\cdot a_{232}\cdot a_{311} - b_{123}\cdot a_{232}\cdot a_{311} + a_{131}\cdot a_{212}\cdot a_{323} + a_{131}\cdot a_{212}\cdot b_{323}$$
$$-a_{131}\cdot a_{213}\cdot a_{322} - a_{131}\cdot a_{213}\cdot b_{322} - a_{131}\cdot a_{222}\cdot a_{313} - a_{131}\cdot b_{222}\cdot a_{313} + a_{131}\cdot a_{223}\cdot a_{312}$$
$$+a_{131}\cdot b_{223}\cdot a_{312} - a_{132}\cdot a_{211}\cdot a_{323} - a_{132}\cdot a_{211}\cdot b_{323} + a_{132}\cdot a_{213}\cdot a_{321} + a_{132}\cdot a_{213}\cdot b_{321}$$
$$+a_{132}\cdot a_{221}\cdot a_{313} + a_{132}\cdot b_{221}\cdot a_{313} - a_{132}\cdot a_{223}\cdot a_{311} - a_{132}\cdot b_{223}\cdot a_{311} + a_{133}\cdot a_{211}\cdot a_{322}$$
$$+a_{133}\cdot a_{211}\cdot b_{322} - a_{133}\cdot a_{212}\cdot a_{321} - a_{133}\cdot a_{212}\cdot b_{321} - a_{133}\cdot a_{221}\cdot a_{312} - a_{133}\cdot b_{221}\cdot a_{312}$$
$$+a_{133}\cdot a_{222}\cdot a_{311} + a_{133}\cdot b_{222}\cdot a_{311}.$$

If we compare results of above equations, we can see that we have the same result in both cases.

6. For plan $j = 3$: Let A and B be cubic-matries of order 3, where all elements on the plan $j = 2$ and $j = 3$ are identical in both matrices, then we have:

$$det\left(A_{[3\times3\times3]}\right) + det\left(B_{[3\times3\times3]}\right) = det\left(\begin{array}{ccc|ccc|ccc} a_{111} & a_{121} & a_{131} & a_{112} & a_{122} & a_{132} & a_{113} & a_{123} & a_{133} \\ a_{211} & a_{221} & a_{231} & a_{212} & a_{222} & a_{232} & a_{213} & a_{223} & a_{233} \\ a_{311} & a_{321} & a_{331} & a_{312} & a_{322} & a_{332} & a_{313} & a_{323} & a_{333} \end{array}\right)$$
$$+det\left(\begin{array}{ccc|ccc|ccc} b_{111} & a_{121} & a_{131} & b_{112} & a_{122} & a_{132} & b_{113} & a_{123} & a_{133} \\ b_{211} & a_{221} & a_{231} & b_{212} & a_{222} & a_{232} & b_{213} & a_{223} & a_{233} \\ b_{311} & a_{321} & a_{331} & b_{312} & a_{322} & a_{332} & b_{313} & a_{323} & a_{333} \end{array}\right)$$
$$= \{a_{111}\cdot a_{222}\cdot a_{333} - a_{111}\cdot a_{232}\cdot a_{323} - a_{111}\cdot a_{223}\cdot a_{332} + a_{111}\cdot a_{233}\cdot a_{322} - a_{112}\cdot a_{221}\cdot a_{333}$$
$$+a_{112}\cdot a_{223}\cdot a_{331} + a_{112}\cdot a_{231}\cdot a_{323} - a_{112}\cdot a_{233}\cdot a_{321} + a_{113}\cdot a_{221}\cdot a_{332} - a_{113}\cdot a_{222}\cdot a_{331}$$
$$-a_{113}\cdot a_{231}\cdot a_{322} + a_{113}\cdot a_{232}\cdot a_{321} - a_{121}\cdot a_{212}\cdot a_{333} + a_{121}\cdot a_{213}\cdot a_{332} + a_{121}\cdot a_{232}\cdot a_{313}$$

$$-a_{121}\cdot a_{233}\cdot a_{312}+a_{122}\cdot a_{211}\cdot a_{333}-a_{122}\cdot a_{213}\cdot a_{331}-a_{122}\cdot a_{231}\cdot a_{313}+a_{122}\cdot a_{233}\cdot a_{311}$$
$$-a_{123}\cdot a_{211}\cdot a_{332}+a_{123}\cdot a_{212}\cdot a_{331}+a_{123}\cdot a_{231}\cdot a_{312}-a_{123}\cdot a_{232}\cdot a_{311}+a_{131}\cdot a_{212}\cdot a_{323}$$
$$-a_{131}\cdot a_{213}\cdot a_{322}-a_{131}\cdot a_{222}\cdot a_{313}+a_{131}\cdot a_{223}\cdot a_{312}-a_{132}\cdot a_{211}\cdot a_{323}+a_{132}\cdot a_{213}\cdot a_{321}$$
$$+a_{132}\cdot a_{221}\cdot a_{313}-a_{132}\cdot a_{223}\cdot a_{311}+a_{133}\cdot a_{211}\cdot a_{322}-a_{133}\cdot a_{212}\cdot a_{321}-a_{133}\cdot a_{221}\cdot a_{312}$$
$$+a_{133}\cdot a_{222}\cdot a_{311}\}+\{b_{111}\cdot a_{222}\cdot a_{333}-b_{111}\cdot a_{232}\cdot a_{323}-b_{111}\cdot a_{223}\cdot a_{332}+b_{111}\cdot a_{233}\cdot a_{322}$$
$$-b_{112}\cdot a_{221}\cdot a_{333}+b_{112}\cdot a_{223}\cdot a_{331}+b_{112}\cdot a_{231}\cdot a_{323}-b_{112}\cdot a_{233}\cdot a_{321}+b_{113}\cdot a_{221}\cdot a_{332}$$
$$-b_{113}\cdot a_{222}\cdot a_{331}-b_{113}\cdot a_{231}\cdot a_{322}+b_{113}\cdot a_{232}\cdot a_{321}-a_{121}\cdot b_{212}\cdot a_{333}+a_{121}\cdot b_{213}\cdot a_{332}$$
$$+a_{121}\cdot a_{232}\cdot b_{313}-a_{121}\cdot a_{233}\cdot b_{312}+a_{122}\cdot b_{211}\cdot a_{333}-a_{122}\cdot b_{213}\cdot a_{331}-a_{122}\cdot a_{231}\cdot b_{313}$$
$$+a_{122}\cdot a_{233}\cdot b_{311}-a_{123}\cdot b_{211}\cdot a_{332}+a_{123}\cdot b_{212}\cdot a_{331}+a_{123}\cdot a_{231}\cdot b_{312}-a_{123}\cdot a_{232}\cdot b_{311}$$
$$+a_{131}\cdot b_{212}\cdot a_{323}-a_{131}\cdot b_{213}\cdot a_{322}-a_{131}\cdot a_{222}\cdot b_{313}+a_{131}\cdot a_{223}\cdot b_{312}-a_{132}\cdot b_{211}\cdot a_{323}$$
$$+a_{132}\cdot b_{213}\cdot a_{321}+a_{132}\cdot a_{221}\cdot b_{313}-a_{132}\cdot a_{223}\cdot b_{311}+a_{133}\cdot b_{211}\cdot a_{322}-a_{133}\cdot b_{212}\cdot a_{321}$$
$$-a_{133}\cdot a_{221}\cdot b_{312}+a_{133}\cdot a_{222}\cdot b_{311}\},$$

while,

$$\det\left(A_{[3\times3\times3]}\right)+det\left(B_{[3\times3\times3]}\right)$$
$$=\det\left(\begin{array}{ccc|ccc|ccc} a_{111}+b_{111} & a_{121} & a_{131} & a_{112}+b_{112} & a_{122} & a_{132} & a_{113}+b_{113} & a_{123} & a_{133} \\ a_{211}+b_{211} & a_{221} & a_{231} & a_{212}+b_{212} & a_{222} & a_{232} & a_{213}+b_{213} & a_{223} & a_{233} \\ a_{311}+b_{311} & a_{321} & a_{331} & a_{312}+b_{312} & a_{322} & a_{332} & a_{313}+b_{313} & a_{323} & a_{333} \end{array}\right)$$
$$=(a_{111}+b_{111})\cdot a_{222}\cdot a_{333}-(a_{111}+b_{111})\cdot a_{232}\cdot a_{323}-(a_{111}+b_{111})\cdot a_{223}\cdot a_{332}$$
$$+(a_{111}+b_{111})\cdot a_{233}\cdot a_{322}-(a_{112}+b_{112})\cdot a_{221}\cdot a_{333}+(a_{112}+b_{112})\cdot a_{223}\cdot a_{331}$$
$$+(a_{112}+b_{112})\cdot a_{231}\cdot a_{323}-(a_{112}+b_{112})\cdot a_{233}\cdot a_{321}+(a_{113}+b_{113})\cdot a_{221}\cdot a_{332}$$
$$-(a_{113}+b_{113})\cdot a_{222}\cdot a_{331}-(a_{113}+b_{113})\cdot a_{231}\cdot a_{322}+(a_{113}+b_{113})\cdot a_{232}\cdot a_{321}$$
$$-a_{121}\cdot(a_{212}+b_{212})\cdot a_{333}+a_{121}\cdot(a_{213}+b_{213})\cdot a_{332}+a_{121}\cdot a_{232}\cdot(a_{313}+b_{313})$$
$$-a_{121}\cdot a_{233}\cdot(a_{312}+b_{312})+a_{122}\cdot(a_{211}+b_{211})\cdot a_{333}-a_{122}\cdot(a_{213}+b_{213})\cdot a_{331}$$
$$-a_{122}\cdot a_{231}\cdot(a_{313}+b_{313})+a_{122}\cdot a_{233}\cdot(a_{311}+b_{311})-a_{123}\cdot(a_{211}+b_{211})\cdot a_{332}$$
$$+a_{123}\cdot(a_{212}+b_{212})\cdot a_{331}+a_{123}\cdot a_{231}\cdot(a_{312}+b_{312})-a_{123}\cdot a_{232}\cdot(a_{311}+b_{311})$$
$$+a_{131}\cdot(a_{212}+b_{212})\cdot a_{323}-a_{131}\cdot(a_{213}+b_{213})\cdot a_{322}-a_{131}\cdot a_{222}\cdot(a_{313}+b_{313})$$
$$+a_{131}\cdot a_{223}\cdot(a_{312}+b_{312})-a_{132}\cdot(a_{211}+b_{211})\cdot a_{323}+a_{132}\cdot(a_{213}+b_{213})\cdot a_{321}$$
$$+a_{132}\cdot a_{221}\cdot(a_{313}+b_{313})-a_{132}\cdot a_{223}\cdot(a_{311}+b_{311})+a_{133}\cdot(a_{211}+b_{211})\cdot a_{322}$$
$$-a_{133}\cdot(a_{212}+b_{212})\cdot a_{321}-a_{133}\cdot a_{221}\cdot(a_{312}+b_{312})+a_{133}\cdot a_{222}\cdot(a_{311}+b_{311})$$
$$=a_{111}\cdot a_{222}\cdot a_{333}+b_{111}\cdot a_{222}\cdot a_{333}-a_{111}\cdot a_{232}\cdot a_{323}-b_{111}\cdot a_{232}\cdot a_{323}-a_{111}\cdot a_{223}\cdot a_{332}$$
$$-b_{111}\cdot a_{223}\cdot a_{332}+a_{111}\cdot a_{233}\cdot a_{322}+b_{111}\cdot a_{233}\cdot a_{322}-a_{112}\cdot a_{221}\cdot a_{333}-b_{112}\cdot a_{221}\cdot a_{333}$$
$$+a_{112}\cdot a_{223}\cdot a_{331}+b_{112}\cdot a_{223}\cdot a_{331}+a_{112}\cdot a_{231}\cdot a_{323}+b_{112}\cdot a_{231}\cdot a_{323}-a_{112}\cdot a_{233}\cdot a_{321}$$
$$-b_{112}\cdot a_{233}\cdot a_{321}+a_{113}\cdot a_{221}\cdot a_{332}+b_{113}\cdot a_{221}\cdot a_{332}-a_{113}\cdot a_{222}\cdot a_{331}-b_{113}\cdot a_{222}\cdot a_{331}$$
$$-a_{113}\cdot a_{231}\cdot a_{322}-b_{113}\cdot a_{231}\cdot a_{322}+a_{113}\cdot a_{232}\cdot a_{321}+b_{113}\cdot a_{232}\cdot a_{321}-a_{121}\cdot a_{212}\cdot a_{333}$$
$$-a_{121}\cdot b_{212}\cdot a_{333}+a_{121}\cdot a_{213}\cdot a_{332}+a_{121}\cdot b_{213}\cdot a_{332}+a_{121}\cdot a_{232}\cdot a_{313}+a_{121}\cdot a_{232}\cdot b_{313}$$
$$-a_{121}\cdot a_{233}\cdot a_{312}-a_{121}\cdot a_{233}\cdot b_{312}+a_{122}\cdot a_{211}\cdot a_{333}+a_{122}\cdot b_{211}\cdot a_{333}-a_{122}\cdot a_{213}\cdot a_{331}$$
$$-a_{122}\cdot b_{213}\cdot a_{331}-a_{122}\cdot a_{231}\cdot a_{313}-a_{122}\cdot a_{231}\cdot b_{313}+a_{122}\cdot a_{233}\cdot a_{311}+a_{122}\cdot a_{233}\cdot b_{311}$$
$$-a_{123}\cdot a_{211}\cdot a_{332}-a_{123}\cdot b_{211}\cdot a_{332}+a_{123}\cdot a_{212}\cdot a_{331}+a_{123}\cdot b_{212}\cdot a_{331}+a_{123}\cdot a_{231}\cdot a_{312}$$
$$+a_{123}\cdot a_{231}\cdot b_{312}-a_{123}\cdot a_{232}\cdot a_{311}-a_{123}\cdot a_{232}\cdot b_{311}+a_{131}\cdot a_{212}\cdot a_{323}+a_{131}\cdot b_{212}\cdot a_{323}$$
$$-a_{131}\cdot a_{213}\cdot a_{322}-a_{131}\cdot b_{213}\cdot a_{322}-a_{131}\cdot a_{222}\cdot a_{313}-a_{131}\cdot a_{222}\cdot b_{313}+a_{131}\cdot a_{223}\cdot a_{312}$$
$$+a_{131}\cdot a_{223}\cdot b_{312}-a_{132}\cdot a_{211}\cdot a_{323}-a_{132}\cdot b_{211}\cdot a_{323}+a_{132}\cdot a_{213}\cdot a_{321}+a_{132}\cdot b_{213}\cdot a_{321}$$
$$+a_{132}\cdot a_{221}\cdot a_{313}+a_{132}\cdot a_{221}\cdot b_{313}-a_{132}\cdot a_{223}\cdot a_{311}-a_{132}\cdot a_{223}\cdot b_{311}+a_{133}\cdot a_{211}\cdot a_{322}$$
$$+a_{133}\cdot b_{211}\cdot a_{322}-a_{133}\cdot a_{212}\cdot a_{321}-a_{133}\cdot b_{212}\cdot a_{321}-a_{133}\cdot a_{221}\cdot a_{312}-a_{133}\cdot a_{221}\cdot b_{312}$$

$$+a_{133}\cdot a_{222}\cdot a_{311}+a_{133}\cdot a_{222}\cdot b_{311}.$$

If we compare results of above equations, we can see that we have the same result in both cases.

7. For plan $k=1$: Let A and B be cubic-matries of order 3, where all elements on the plan $k=1$ and $k=2$ are identical in both matrices, then we have:

$$det\left(A_{[3\times3\times3]}\right)+det\left(B_{[3\times3\times3]}\right)=det\left(\begin{array}{ccc|ccc|ccc}a_{111}&a_{121}&a_{131}&a_{112}&a_{122}&a_{132}&a_{113}&a_{123}&a_{133}\\a_{211}&a_{221}&a_{231}&a_{212}&a_{222}&a_{232}&a_{213}&a_{223}&a_{233}\\a_{311}&a_{321}&a_{331}&a_{312}&a_{322}&a_{332}&a_{313}&a_{323}&a_{333}\end{array}\right)$$
$$+det\left(\begin{array}{ccc|ccc|ccc}a_{111}&a_{121}&a_{131}&a_{112}&a_{122}&a_{132}&b_{113}&b_{123}&b_{133}\\a_{211}&a_{221}&a_{231}&a_{212}&a_{222}&a_{232}&b_{213}&b_{223}&b_{233}\\a_{311}&a_{321}&a_{331}&a_{312}&a_{322}&a_{332}&b_{313}&b_{323}&b_{333}\end{array}\right)$$
$$=\{a_{111}\cdot a_{222}\cdot a_{333}-a_{111}\cdot a_{232}\cdot a_{323}-a_{111}\cdot a_{223}\cdot a_{332}+a_{111}\cdot a_{233}\cdot a_{322}-a_{112}\cdot a_{221}\cdot a_{333}$$
$$+a_{112}\cdot a_{223}\cdot a_{331}+a_{112}\cdot a_{231}\cdot a_{323}-a_{112}\cdot a_{233}\cdot a_{321}+a_{113}\cdot a_{221}\cdot a_{332}-a_{113}\cdot a_{222}\cdot a_{331}$$
$$-a_{113}\cdot a_{231}\cdot a_{322}+a_{113}\cdot a_{232}\cdot a_{321}-a_{121}\cdot a_{212}\cdot a_{333}+a_{121}\cdot a_{213}\cdot a_{332}+a_{121}\cdot a_{232}\cdot a_{313}$$
$$-a_{121}\cdot a_{233}\cdot a_{312}+a_{122}\cdot a_{211}\cdot a_{333}-a_{122}\cdot a_{213}\cdot a_{331}-a_{122}\cdot a_{231}\cdot a_{313}+a_{122}\cdot a_{233}\cdot a_{311}$$
$$-a_{123}\cdot a_{211}\cdot a_{332}+a_{123}\cdot a_{212}\cdot a_{331}+a_{123}\cdot a_{231}\cdot a_{312}-a_{123}\cdot a_{232}\cdot a_{311}+a_{131}\cdot a_{212}\cdot a_{323}$$
$$-a_{131}\cdot a_{213}\cdot a_{322}-a_{131}\cdot a_{222}\cdot a_{313}+a_{131}\cdot a_{223}\cdot a_{312}-a_{132}\cdot a_{211}\cdot a_{323}+a_{132}\cdot a_{213}\cdot a_{321}$$
$$+a_{132}\cdot a_{221}\cdot a_{313}-a_{132}\cdot a_{223}\cdot a_{311}+a_{133}\cdot a_{211}\cdot a_{322}-a_{133}\cdot a_{212}\cdot a_{321}-a_{133}\cdot a_{221}\cdot a_{312}$$
$$+a_{133}\cdot a_{222}\cdot a_{311}\}+\{a_{111}\cdot a_{222}\cdot b_{333}-a_{111}\cdot a_{232}\cdot b_{323}-a_{111}\cdot b_{223}\cdot a_{332}+a_{111}\cdot b_{233}\cdot a_{322}$$
$$-a_{112}\cdot a_{221}\cdot b_{333}+a_{112}\cdot b_{223}\cdot a_{331}+a_{112}\cdot a_{231}\cdot b_{323}-a_{112}\cdot b_{233}\cdot a_{321}+b_{113}\cdot a_{221}\cdot a_{332}$$
$$-b_{113}\cdot a_{222}\cdot a_{331}-b_{113}\cdot a_{231}\cdot a_{322}+b_{113}\cdot a_{232}\cdot a_{321}-a_{121}\cdot a_{212}\cdot b_{333}+a_{121}\cdot b_{213}\cdot a_{332}$$
$$+a_{121}\cdot a_{232}\cdot b_{313}-a_{121}\cdot b_{233}\cdot a_{312}+a_{122}\cdot a_{211}\cdot b_{333}-a_{122}\cdot b_{213}\cdot a_{331}-a_{122}\cdot a_{231}\cdot b_{313}$$
$$+a_{122}\cdot b_{233}\cdot a_{311}-b_{123}\cdot a_{211}\cdot a_{332}+b_{123}\cdot a_{212}\cdot a_{331}+b_{123}\cdot a_{231}\cdot a_{312}-b_{123}\cdot a_{232}\cdot a_{311}$$
$$+a_{131}\cdot a_{212}\cdot b_{323}-a_{131}\cdot b_{213}\cdot a_{322}-a_{131}\cdot a_{222}\cdot b_{313}+a_{131}\cdot b_{223}\cdot a_{312}-a_{132}\cdot a_{211}\cdot b_{323}$$
$$+a_{132}\cdot b_{213}\cdot a_{321}+a_{132}\cdot a_{221}\cdot b_{313}-a_{132}\cdot b_{223}\cdot a_{311}+b_{133}\cdot a_{211}\cdot a_{322}-b_{133}\cdot a_{212}\cdot a_{321}$$
$$-b_{133}\cdot a_{221}\cdot a_{312}+b_{133}\cdot a_{222}\cdot a_{311}\},$$

while,

$$\det\left(A_{[3\times3\times3]}\right)+det\left(B_{[3\times3\times3]}\right)$$
$$=\det\left(\begin{array}{ccc|ccc|ccc}a_{111}&a_{121}&a_{131}&a_{112}&a_{122}&a_{132}&a_{113}+b_{113}&a_{123}+b_{123}&a_{133}+b_{133}\\a_{211}&a_{221}&a_{231}&a_{212}&a_{222}&a_{232}&a_{213}+b_{213}&a_{223}+b_{223}&a_{233}+b_{233}\\a_{311}&a_{321}&a_{331}&a_{312}&a_{322}&a_{332}&a_{313}+b_{313}&a_{323}+b_{323}&a_{333}+b_{333}\end{array}\right)$$
$$=a_{111}\cdot a_{222}\cdot(a_{333}+b_{333})-a_{111}\cdot a_{232}\cdot(a_{323}+b_{323})-a_{111}\cdot(a_{223}+b_{223})\cdot a_{332}$$
$$+a_{111}\cdot(a_{233}+b_{233})\cdot a_{322}-a_{112}\cdot a_{221}\cdot(a_{333}+b_{333})+a_{112}\cdot(a_{223}+b_{223})\cdot a_{331}$$
$$+a_{112}\cdot a_{231}\cdot(a_{323}+b_{323})-a_{112}\cdot(a_{233}+b_{233})\cdot a_{321}+(a_{113}+b_{113})\cdot a_{221}\cdot a_{332}$$
$$-(a_{113}+b_{113})\cdot a_{222}\cdot a_{331}-(a_{113}+b_{113})\cdot a_{231}\cdot a_{322}+(a_{113}+b_{113})\cdot a_{232}\cdot a_{321}$$
$$-a_{121}\cdot a_{212}\cdot(a_{333}+b_{333})+a_{121}\cdot(a_{213}+b_{213})\cdot a_{332}+a_{121}\cdot a_{232}\cdot(a_{313}+b_{313})$$
$$-a_{121}\cdot(a_{233}+b_{233})\cdot a_{312}+a_{122}\cdot a_{211}\cdot(a_{333}+b_{333})-a_{122}\cdot(a_{213}+b_{213})\cdot a_{331}$$
$$-a_{122}\cdot a_{231}\cdot(a_{313}+b_{313})+a_{122}\cdot(a_{233}+b_{233})\cdot a_{311}-(a_{123}+b_{123})\cdot a_{211}\cdot a_{332}$$
$$+(a_{123}+b_{123})\cdot a_{212}\cdot a_{331}+(a_{123}+b_{123})\cdot a_{231}\cdot a_{312}-(a_{123}+b_{123})\cdot a_{232}\cdot a_{311}$$
$$+a_{131}\cdot a_{212}\cdot(a_{323}+b_{323})-a_{131}\cdot(a_{213}+b_{213})\cdot a_{322}-a_{131}\cdot a_{222}\cdot(a_{313}+b_{313})$$
$$+a_{131}\cdot(a_{223}+b_{223})\cdot a_{312}-a_{132}\cdot a_{211}\cdot(a_{323}+b_{323})+a_{132}\cdot(a_{213}+b_{213})\cdot a_{321}$$
$$+a_{132}\cdot a_{221}\cdot(a_{313}+b_{313})-a_{132}\cdot(a_{223}+b_{223})\cdot a_{311}+(a_{133}+b_{133})\cdot a_{211}\cdot a_{322}$$
$$-(a_{133}+b_{133})\cdot a_{212}\cdot a_{321}-(a_{133}+b_{133})\cdot a_{221}\cdot a_{312}+(a_{133}+b_{133})\cdot a_{222}\cdot a_{311}$$
$$=a_{111}\cdot a_{222}\cdot a_{333}+a_{111}\cdot a_{222}\cdot b_{333}-a_{111}\cdot a_{232}\cdot a_{323}-a_{111}\cdot a_{232}\cdot b_{323}-a_{111}\cdot a_{223}\cdot a_{332}$$

$$-a_{111}\cdot b_{223}\cdot a_{332}+a_{111}\cdot a_{233}\cdot a_{322}+a_{111}\cdot b_{233}\cdot a_{322}-a_{112}\cdot a_{221}\cdot a_{333}-a_{112}\cdot a_{221}\cdot b_{333}$$
$$+a_{112}\cdot a_{223}\cdot a_{331}+a_{112}\cdot b_{223}\cdot a_{331}+a_{112}\cdot a_{231}\cdot a_{323}+a_{112}\cdot a_{231}\cdot b_{323}-a_{112}\cdot a_{233}\cdot a_{321}$$
$$-a_{112}\cdot b_{233}\cdot a_{321}+a_{113}\cdot a_{221}\cdot a_{332}+b_{113}\cdot a_{221}\cdot a_{332}-a_{113}\cdot a_{222}\cdot a_{331}-b_{113}\cdot a_{222}\cdot a_{331}$$
$$-a_{113}\cdot a_{231}\cdot a_{322}-b_{113}\cdot a_{231}\cdot a_{322}+a_{113}\cdot a_{232}\cdot a_{321}+b_{113}\cdot a_{232}\cdot a_{321}-a_{121}\cdot a_{212}\cdot a_{333}$$
$$-a_{121}\cdot a_{212}\cdot b_{333}+a_{121}\cdot a_{213}\cdot a_{332}+a_{121}\cdot b_{213}\cdot a_{332}+a_{121}\cdot a_{232}\cdot a_{313}+a_{121}\cdot a_{232}\cdot b_{313}$$
$$-a_{121}\cdot a_{233}\cdot a_{312}-a_{121}\cdot b_{233}\cdot a_{312}+a_{122}\cdot a_{211}\cdot a_{333}+a_{122}\cdot a_{211}\cdot b_{333}-a_{122}\cdot a_{213}\cdot a_{331}$$
$$-a_{122}\cdot b_{213}\cdot a_{331}-a_{122}\cdot a_{231}\cdot a_{313}-a_{122}\cdot a_{231}\cdot b_{313}+a_{122}\cdot a_{233}\cdot a_{311}+a_{122}\cdot b_{233}\cdot a_{311}$$
$$-a_{123}\cdot a_{211}\cdot a_{332}-b_{123}\cdot a_{211}\cdot a_{332}+a_{123}\cdot a_{212}\cdot a_{331}+b_{123}\cdot a_{212}\cdot a_{331}+a_{123}\cdot a_{231}\cdot a_{312}$$
$$+b_{123}\cdot a_{231}\cdot a_{312}-a_{123}\cdot a_{232}\cdot a_{311}-b_{123}\cdot a_{232}\cdot a_{311}+a_{131}\cdot a_{212}\cdot a_{323}+a_{131}\cdot a_{212}\cdot b_{323}$$
$$-a_{131}\cdot a_{213}\cdot a_{322}-a_{131}\cdot b_{213}\cdot a_{322}-a_{131}\cdot a_{222}\cdot a_{313}-a_{131}\cdot a_{222}\cdot b_{313}+a_{131}\cdot a_{223}\cdot a_{312}$$
$$+a_{131}\cdot b_{223}\cdot a_{312}-a_{132}\cdot a_{211}\cdot a_{323}-a_{132}\cdot a_{211}\cdot b_{323}+a_{132}\cdot a_{213}\cdot a_{321}+a_{132}\cdot b_{213}\cdot a_{321}$$
$$+a_{132}\cdot a_{221}\cdot a_{313}+a_{132}\cdot a_{221}\cdot b_{313}-a_{132}\cdot a_{223}\cdot a_{311}-a_{132}\cdot b_{223}\cdot a_{311}+a_{133}\cdot a_{211}\cdot a_{322}$$
$$+b_{133}\cdot a_{211}\cdot a_{322}-a_{133}\cdot a_{212}\cdot a_{321}-b_{133}\cdot a_{212}\cdot a_{321}-a_{133}\cdot a_{221}\cdot a_{312}-b_{133}\cdot a_{221}\cdot a_{312}$$
$$+a_{133}\cdot a_{222}\cdot a_{311}+b_{133}\cdot a_{222}\cdot a_{311}.$$

If we compare results of above equations, we can see that we have the same result in both cases.

8. For plan $k=2$: Let A and B be cubic-matries of order 3, where all elements on the plan $k=1$ and $k=3$ are identical in both matrices, then we have:

$$det\left(A_{[3\times3\times3]}\right)+det\left(B_{[3\times3\times3]}\right)=det\left(\begin{array}{ccc|ccc|ccc}a_{111}&a_{121}&a_{131}&a_{112}&a_{122}&a_{132}&a_{113}&a_{123}&a_{133}\\a_{211}&a_{221}&a_{231}&a_{212}&a_{222}&a_{232}&a_{213}&a_{223}&a_{233}\\a_{311}&a_{321}&a_{331}&a_{312}&a_{322}&a_{332}&a_{313}&a_{323}&a_{333}\end{array}\right)$$
$$+det\left(\begin{array}{ccc|ccc|ccc}a_{111}&a_{121}&a_{131}&b_{112}&b_{122}&b_{132}&a_{113}&a_{123}&a_{133}\\a_{211}&a_{221}&a_{231}&b_{212}&b_{222}&b_{232}&a_{213}&a_{223}&a_{233}\\a_{311}&a_{321}&a_{331}&b_{312}&b_{322}&b_{332}&a_{313}&a_{323}&a_{333}\end{array}\right)$$
$$=\{a_{111}\cdot a_{222}\cdot a_{333}-a_{111}\cdot a_{232}\cdot a_{323}-a_{111}\cdot a_{223}\cdot a_{332}+a_{111}\cdot a_{233}\cdot a_{322}-a_{112}\cdot a_{221}\cdot a_{333}$$
$$+a_{112}\cdot a_{223}\cdot a_{331}+a_{112}\cdot a_{231}\cdot a_{323}-a_{112}\cdot a_{233}\cdot a_{321}+a_{113}\cdot a_{221}\cdot a_{332}-a_{113}\cdot a_{222}\cdot a_{331}$$
$$-a_{113}\cdot a_{231}\cdot a_{322}+a_{113}\cdot a_{232}\cdot a_{321}-a_{121}\cdot a_{212}\cdot a_{333}+a_{121}\cdot a_{213}\cdot a_{332}+a_{121}\cdot a_{232}\cdot a_{313}$$
$$-a_{121}\cdot a_{233}\cdot a_{312}+a_{122}\cdot a_{211}\cdot a_{333}-a_{122}\cdot a_{213}\cdot a_{331}-a_{122}\cdot a_{231}\cdot a_{313}+a_{122}\cdot a_{233}\cdot a_{311}$$
$$-a_{123}\cdot a_{211}\cdot a_{332}+a_{123}\cdot a_{212}\cdot a_{331}+a_{123}\cdot a_{231}\cdot a_{312}-a_{123}\cdot a_{232}\cdot a_{311}+a_{131}\cdot a_{212}\cdot a_{323}$$
$$-a_{131}\cdot a_{213}\cdot a_{322}-a_{131}\cdot a_{222}\cdot a_{313}+a_{131}\cdot a_{223}\cdot a_{312}-a_{132}\cdot a_{211}\cdot a_{323}+a_{132}\cdot a_{213}\cdot a_{321}$$
$$+a_{132}\cdot a_{221}\cdot a_{313}-a_{132}\cdot a_{223}\cdot a_{311}+a_{133}\cdot a_{211}\cdot a_{322}-a_{133}\cdot a_{212}\cdot a_{321}-a_{133}\cdot a_{221}\cdot a_{312}$$
$$+a_{133}\cdot a_{222}\cdot a_{311}\}+\{a_{111}\cdot b_{222}\cdot a_{333}-a_{111}\cdot b_{232}\cdot a_{323}-a_{111}\cdot a_{223}\cdot b_{332}+a_{111}\cdot a_{233}\cdot b_{322}$$
$$-b_{112}\cdot a_{221}\cdot a_{333}+b_{112}\cdot a_{223}\cdot a_{331}+b_{112}\cdot a_{231}\cdot a_{323}-b_{112}\cdot a_{233}\cdot a_{321}+a_{113}\cdot a_{221}\cdot b_{332}$$
$$-a_{113}\cdot b_{222}\cdot a_{331}-a_{113}\cdot a_{231}\cdot b_{322}+a_{113}\cdot b_{232}\cdot a_{321}-a_{121}\cdot b_{212}\cdot a_{333}+a_{121}\cdot a_{213}\cdot b_{332}$$
$$+a_{121}\cdot b_{232}\cdot a_{313}-a_{121}\cdot a_{233}\cdot b_{312}+b_{122}\cdot a_{211}\cdot a_{333}-b_{122}\cdot a_{213}\cdot a_{331}-b_{122}\cdot a_{231}\cdot a_{313}$$
$$+b_{122}\cdot a_{233}\cdot a_{311}-a_{123}\cdot a_{211}\cdot b_{332}+a_{123}\cdot b_{212}\cdot a_{331}+a_{123}\cdot a_{231}\cdot b_{312}-a_{123}\cdot b_{232}\cdot a_{311}$$
$$+a_{131}\cdot b_{212}\cdot a_{323}-a_{131}\cdot a_{213}\cdot b_{322}-a_{131}\cdot b_{222}\cdot a_{313}+a_{131}\cdot a_{223}\cdot b_{312}-b_{132}\cdot a_{211}\cdot a_{323}$$
$$+b_{132}\cdot a_{213}\cdot a_{321}+b_{132}\cdot a_{221}\cdot a_{313}-b_{132}\cdot a_{223}\cdot a_{311}+a_{133}\cdot a_{211}\cdot b_{322}-a_{133}\cdot b_{212}\cdot a_{321}$$
$$-a_{133}\cdot a_{221}\cdot b_{312}+a_{133}\cdot b_{222}\cdot a_{311}\},$$

while,

$$\det\left(A_{[3\times3\times3]}\right)+det\left(B_{[3\times3\times3]}\right)$$
$$=\det\left(\begin{array}{ccc|ccc|ccc}a_{111}&a_{121}&a_{131}&a_{112}+b_{112}&a_{122}+b_{122}&a_{132}+b_{132}&a_{113}&a_{123}&a_{133}\\a_{211}&a_{221}&a_{231}&a_{212}+b_{212}&a_{222}+b_{222}&a_{232}+b_{232}&a_{213}&a_{223}&a_{233}\\a_{311}&a_{321}&a_{331}&a_{312}+b_{312}&a_{322}+b_{322}&a_{332}+b_{332}&a_{313}&a_{323}&a_{333}\end{array}\right)$$

$$= a_{111}\cdot(a_{222}+b_{222})\cdot a_{333} - a_{111}\cdot(a_{232}+b_{232})\cdot a_{323} - a_{111}\cdot a_{223}\cdot(a_{332}+b_{332})$$
$$+a_{111}\cdot a_{233}\cdot(a_{322}+b_{322}) - (a_{112}+b_{112})\cdot a_{221}\cdot a_{333} + (a_{112}+b_{112})\cdot a_{223}\cdot a_{331}$$
$$+(a_{112}+b_{112})\cdot a_{231}\cdot a_{323} - (a_{112}+b_{112})\cdot a_{233}\cdot a_{321} + a_{113}\cdot a_{221}\cdot(a_{332}+b_{332})$$
$$-a_{113}\cdot(a_{222}+b_{222})\cdot a_{331} - a_{113}\cdot a_{231}\cdot(a_{322}+b_{322}) + a_{113}\cdot(a_{232}+b_{232})\cdot a_{321}$$
$$-a_{121}\cdot(a_{212}+b_{212})\cdot a_{333} + a_{121}\cdot a_{213}\cdot(a_{332}+b_{332}) + a_{121}\cdot(a_{232}+b_{232})\cdot a_{313}$$
$$-a_{121}\cdot a_{233}\cdot(a_{312}+b_{312}) + (a_{122}+b_{122})\cdot a_{211}\cdot a_{333} - (a_{122}+b_{122})\cdot a_{213}\cdot a_{331}$$
$$-(a_{122}+b_{122})\cdot a_{231}\cdot a_{313} + (a_{122}+b_{122})\cdot a_{233}\cdot a_{311} - a_{123}\cdot a_{211}\cdot(a_{332}+b_{332})$$
$$+a_{123}\cdot(a_{212}+b_{212})\cdot a_{331} + a_{123}\cdot a_{231}\cdot(a_{312}+b_{312}) - a_{123}\cdot(a_{232}+b_{232})\cdot a_{311}$$
$$+a_{131}\cdot(a_{212}+b_{212})\cdot a_{323} - a_{131}\cdot a_{213}\cdot(a_{322}+b_{322}) - a_{131}\cdot(a_{222}+b_{222})\cdot a_{313}$$
$$+a_{131}\cdot a_{223}\cdot(a_{312}+b_{312}) - (a_{132}+b_{132})\cdot a_{211}\cdot a_{323} + (a_{132}+b_{132})\cdot a_{213}\cdot a_{321}$$
$$+(a_{132}+b_{132})\cdot a_{221}\cdot a_{313} - (a_{132}+b_{132})\cdot a_{223}\cdot a_{311} + a_{133}\cdot a_{211}\cdot(a_{322}+b_{322})$$
$$-a_{133}\cdot(a_{212}+b_{212})\cdot a_{321} - a_{133}\cdot a_{221}\cdot(a_{312}+b_{312}) + a_{133}\cdot(a_{222}+b_{222})\cdot a_{311}$$
$$= a_{111}\cdot a_{222}\cdot a_{333} + a_{111}\cdot b_{222}\cdot a_{333} - a_{111}\cdot a_{232}\cdot a_{323} - a_{111}\cdot b_{232}\cdot a_{323} - a_{111}\cdot a_{223}\cdot a_{332}$$
$$-a_{111}\cdot a_{223}\cdot b_{332} + a_{111}\cdot a_{233}\cdot a_{322} + a_{111}\cdot a_{233}\cdot b_{322} - a_{112}\cdot a_{221}\cdot a_{333} - b_{112}\cdot a_{221}\cdot a_{333}$$
$$+a_{112}\cdot a_{223}\cdot a_{331} + b_{112}\cdot a_{223}\cdot a_{331} + a_{112}\cdot a_{231}\cdot a_{323} + b_{112}\cdot a_{231}\cdot a_{323} - a_{112}\cdot a_{233}\cdot a_{321}$$
$$-b_{112}\cdot a_{233}\cdot a_{321} + a_{113}\cdot a_{221}\cdot a_{332} + a_{113}\cdot a_{221}\cdot b_{332} - a_{113}\cdot a_{222}\cdot a_{331} - a_{113}\cdot b_{222}\cdot a_{331}$$
$$-a_{113}\cdot a_{231}\cdot a_{322} - a_{113}\cdot a_{231}\cdot b_{322} + a_{113}\cdot a_{232}\cdot a_{321} + a_{113}\cdot b_{232}\cdot a_{321} - a_{121}\cdot a_{212}\cdot a_{333}$$
$$-a_{121}\cdot b_{212}\cdot a_{333} + a_{121}\cdot a_{213}\cdot a_{332} + a_{121}\cdot a_{213}\cdot b_{332} + a_{121}\cdot a_{232}\cdot a_{313} + a_{121}\cdot b_{232}\cdot a_{313}$$
$$-a_{121}\cdot a_{233}\cdot a_{312} - a_{121}\cdot a_{233}\cdot b_{312} + a_{122}\cdot a_{211}\cdot a_{333} + b_{122}\cdot a_{211}\cdot a_{333} - a_{122}\cdot a_{213}\cdot a_{331}$$
$$-b_{122}\cdot a_{213}\cdot a_{331} - a_{122}\cdot a_{231}\cdot a_{313} - b_{122}\cdot a_{231}\cdot a_{313} + a_{122}\cdot a_{233}\cdot a_{311} + b_{122}\cdot a_{233}\cdot a_{311}$$
$$-a_{123}\cdot a_{211}\cdot a_{332} - a_{123}\cdot a_{211}\cdot b_{332} + a_{123}\cdot a_{212}\cdot a_{331} + a_{123}\cdot b_{212}\cdot a_{331} + a_{123}\cdot a_{231}\cdot a_{312}$$
$$+a_{123}\cdot a_{231}\cdot b_{312} - a_{123}\cdot a_{232}\cdot a_{311} - a_{123}\cdot b_{232}\cdot a_{311} + a_{131}\cdot a_{212}\cdot a_{323} + a_{131}\cdot b_{212}\cdot a_{323}$$
$$-a_{131}\cdot a_{213}\cdot a_{322} - a_{131}\cdot a_{213}\cdot b_{322} - a_{131}\cdot a_{222}\cdot a_{313} - a_{131}\cdot b_{222}\cdot a_{313} + a_{131}\cdot a_{223}\cdot a_{312}$$
$$+a_{131}\cdot a_{223}\cdot b_{312} - a_{132}\cdot a_{211}\cdot a_{323} - b_{132}\cdot a_{211}\cdot a_{323} + a_{132}\cdot a_{213}\cdot a_{321} + b_{132}\cdot a_{213}\cdot a_{321}$$
$$+a_{132}\cdot a_{221}\cdot a_{313} + b_{132}\cdot a_{221}\cdot a_{313} - a_{132}\cdot a_{223}\cdot a_{311} - b_{132}\cdot a_{223}\cdot a_{311} + a_{133}\cdot a_{211}\cdot a_{322}$$
$$+a_{133}\cdot a_{211}\cdot b_{322} - a_{133}\cdot a_{212}\cdot a_{321} - a_{133}\cdot b_{212}\cdot a_{321} - a_{133}\cdot a_{221}\cdot a_{312} - a_{133}\cdot a_{221}\cdot b_{312}$$
$$+a_{133}\cdot a_{222}\cdot a_{311} + a_{133}\cdot b_{222}\cdot a_{311}.$$

If we compare results of above equations, we can see that we have the same result in both cases.

9. For plan $k = 3$: Let A and B be cubic-matries of order 3, where all elements on the plan $k = 2$ and $k = 3$ are identical in both matrices, then we have:

$$det\left(A_{[3\times3\times3]}\right) + det\left(B_{[3\times3\times3]}\right) = det\left(\begin{array}{ccc|ccc|ccc} a_{111} & a_{121} & a_{131} & a_{112} & a_{122} & a_{132} & a_{113} & a_{123} & a_{133} \\ a_{211} & a_{221} & a_{231} & a_{212} & a_{222} & a_{232} & a_{213} & a_{223} & a_{233} \\ a_{311} & a_{321} & a_{331} & a_{312} & a_{322} & a_{332} & a_{313} & a_{323} & a_{333} \end{array}\right)$$
$$+det\left(\begin{array}{ccc|ccc|ccc} b_{111} & b_{121} & b_{131} & a_{112} & a_{122} & a_{132} & a_{113} & a_{123} & a_{133} \\ b_{211} & b_{221} & b_{231} & a_{212} & a_{222} & a_{232} & a_{213} & a_{223} & a_{233} \\ b_{311} & b_{321} & b_{331} & a_{312} & a_{322} & a_{332} & a_{313} & a_{323} & a_{333} \end{array}\right)$$
$$= \{a_{111}\cdot a_{222}\cdot a_{333} - a_{111}\cdot a_{232}\cdot a_{323} - a_{111}\cdot a_{223}\cdot a_{332} + a_{111}\cdot a_{233}\cdot a_{322} - a_{112}\cdot a_{221}\cdot a_{333}$$
$$+a_{112}\cdot a_{223}\cdot a_{331} + a_{112}\cdot a_{231}\cdot a_{323} - a_{112}\cdot a_{233}\cdot a_{321} + a_{113}\cdot a_{221}\cdot a_{332} - a_{113}\cdot a_{222}\cdot a_{331}$$
$$-a_{113}\cdot a_{231}\cdot a_{322} + a_{113}\cdot a_{232}\cdot a_{321} - a_{121}\cdot a_{212}\cdot a_{333} + a_{121}\cdot a_{213}\cdot a_{332} + a_{121}\cdot a_{232}\cdot a_{313}$$
$$-a_{121}\cdot a_{233}\cdot a_{312} + a_{122}\cdot a_{211}\cdot a_{333} - a_{122}\cdot a_{213}\cdot a_{331} - a_{122}\cdot a_{231}\cdot a_{313} + a_{122}\cdot a_{233}\cdot a_{311}$$
$$-a_{123}\cdot a_{211}\cdot a_{332} + a_{123}\cdot a_{212}\cdot a_{331} + a_{123}\cdot a_{231}\cdot a_{312} - a_{123}\cdot a_{232}\cdot a_{311} + a_{131}\cdot a_{212}\cdot a_{323}$$
$$-a_{131}\cdot a_{213}\cdot a_{322} - a_{131}\cdot a_{222}\cdot a_{313} + a_{131}\cdot a_{223}\cdot a_{312} - a_{132}\cdot a_{211}\cdot a_{323} + a_{132}\cdot a_{213}\cdot a_{321}$$
$$+a_{132}\cdot a_{221}\cdot a_{313} - a_{132}\cdot a_{223}\cdot a_{311} + a_{133}\cdot a_{211}\cdot a_{322} - a_{133}\cdot a_{212}\cdot a_{321} - a_{133}\cdot a_{221}\cdot a_{312}$$
$$+a_{133}\cdot a_{222}\cdot a_{311}\} + \{b_{111}\cdot a_{222}\cdot a_{333} - b_{111}\cdot a_{232}\cdot a_{323} - b_{111}\cdot a_{223}\cdot a_{332} + b_{111}\cdot a_{233}\cdot a_{322}$$

$$-a_{112}\cdot b_{221}\cdot a_{333}+a_{112}\cdot a_{223}\cdot b_{331}+a_{112}\cdot b_{231}\cdot a_{323}-a_{112}\cdot a_{233}\cdot b_{321}+a_{113}\cdot b_{221}\cdot a_{332}$$
$$-a_{113}\cdot a_{222}\cdot b_{331}-a_{113}\cdot b_{231}\cdot a_{322}+a_{113}\cdot a_{232}\cdot b_{321}-b_{121}\cdot a_{212}\cdot a_{333}+b_{121}\cdot a_{213}\cdot a_{332}$$
$$+b_{121}\cdot a_{232}\cdot a_{313}-b_{121}\cdot a_{233}\cdot a_{312}+a_{122}\cdot b_{211}\cdot a_{333}-a_{122}\cdot a_{213}\cdot b_{331}-a_{122}\cdot b_{231}\cdot a_{313}$$
$$+a_{122}\cdot a_{233}\cdot b_{311}-a_{123}\cdot b_{211}\cdot a_{332}+a_{123}\cdot a_{212}\cdot b_{331}+a_{123}\cdot b_{231}\cdot a_{312}-a_{123}\cdot a_{232}\cdot b_{311}$$
$$+b_{131}\cdot a_{212}\cdot a_{323}-b_{131}\cdot a_{213}\cdot a_{322}-b_{131}\cdot a_{222}\cdot a_{313}+b_{131}\cdot a_{223}\cdot a_{312}-a_{132}\cdot b_{211}\cdot a_{323}$$
$$+a_{132}\cdot a_{213}\cdot b_{321}+a_{132}\cdot b_{221}\cdot a_{313}-a_{132}\cdot a_{223}\cdot b_{311}+a_{133}\cdot b_{211}\cdot a_{322}-a_{133}\cdot a_{212}\cdot b_{321}$$
$$-a_{133}\cdot b_{221}\cdot a_{312}+a_{133}\cdot a_{222}\cdot b_{311}\},$$

while,

$$\det\left(A_{[3\times3\times3]}\right)+det\left(B_{[3\times3\times3]}\right)$$
$$=\det\left(\begin{array}{ccc|ccc|ccc}a_{111}+b_{111} & a_{121}+b_{121} & a_{131}+b_{131} & a_{112} & a_{122} & a_{132} & a_{113} & a_{123} & a_{133}\\ a_{211}+b_{211} & a_{221}+b_{221} & a_{231}+b_{231} & a_{212} & a_{222} & a_{232} & a_{213} & a_{223} & a_{233}\\ a_{311}+b_{311} & a_{321}+b_{321} & a_{331}+b_{331} & a_{312} & a_{322} & a_{332} & a_{313} & a_{323} & a_{333}\end{array}\right)$$
$$=(a_{111}+b_{111})\cdot a_{222}\cdot a_{333}-(a_{111}+b_{111})\cdot a_{232}\cdot a_{323}-(a_{111}+b_{111})\cdot a_{223}\cdot a_{332}$$
$$+(a_{111}+b_{111})\cdot a_{233}\cdot a_{322}-a_{112}\cdot(a_{221}+b_{221})\cdot a_{333}+a_{112}\cdot a_{223}\cdot(a_{331}+b_{331})$$
$$+a_{112}\cdot(a_{231}+b_{231})\cdot a_{323}-a_{112}\cdot a_{233}\cdot(a_{321}+b_{321})+a_{113}\cdot(a_{221}+b_{221})\cdot a_{332}$$
$$-a_{113}\cdot a_{222}\cdot(a_{331}+b_{331})-a_{113}\cdot(a_{231}+b_{231})\cdot a_{322}+a_{113}\cdot a_{232}\cdot(a_{321}+b_{321})$$
$$-(a_{121}+b_{121})\cdot a_{212}\cdot a_{333}+(a_{121}+b_{121})\cdot a_{213}\cdot a_{332}+(a_{121}+b_{121})\cdot a_{232}\cdot a_{313}$$
$$-(a_{121}+b_{121})\cdot a_{233}\cdot a_{312}+a_{122}\cdot(a_{211}+b_{211})\cdot a_{333}-a_{122}\cdot a_{213}\cdot(a_{331}+b_{331})$$
$$-a_{122}\cdot(a_{231}+b_{231})\cdot a_{313}+a_{122}\cdot a_{233}\cdot(a_{311}+b_{311})-a_{123}\cdot(a_{211}+b_{211})\cdot a_{332}$$
$$+a_{123}\cdot a_{212}\cdot(a_{331}+b_{331})+a_{123}\cdot(a_{231}+b_{231})\cdot a_{312}-a_{123}\cdot a_{232}\cdot(a_{311}+b_{311})$$
$$+(a_{131}+b_{131})\cdot a_{212}\cdot a_{323}-(a_{131}+b_{131})\cdot a_{213}\cdot a_{322}-(a_{131}+b_{131})\cdot a_{222}\cdot a_{313}$$
$$+(a_{131}+b_{131})\cdot a_{223}\cdot a_{312}-a_{132}\cdot(a_{211}+b_{211})\cdot a_{323}+a_{132}\cdot a_{213}\cdot(a_{321}+b_{321})$$
$$+a_{132}\cdot(a_{221}+b_{221})\cdot a_{313}-a_{132}\cdot a_{223}\cdot(a_{311}+b_{311})+a_{133}\cdot(a_{211}+b_{211})\cdot a_{322}$$
$$-a_{133}\cdot a_{212}\cdot(a_{321}+b_{321})-a_{133}\cdot(a_{221}+b_{221})\cdot a_{312}+a_{133}\cdot a_{222}\cdot(a_{311}+b_{311})$$
$$=a_{111}\cdot a_{222}\cdot a_{333}+b_{111}\cdot a_{222}\cdot a_{333}-a_{111}\cdot a_{232}\cdot a_{323}-b_{111}\cdot a_{232}\cdot a_{323}-a_{111}\cdot a_{223}\cdot a_{332}$$
$$-b_{111}\cdot a_{223}\cdot a_{332}+a_{111}\cdot a_{233}\cdot a_{322}+b_{111}\cdot a_{233}\cdot a_{322}-a_{112}\cdot a_{221}\cdot a_{333}-a_{112}\cdot b_{221}\cdot a_{333}$$
$$+a_{112}\cdot a_{223}\cdot a_{331}+a_{112}\cdot a_{223}\cdot b_{331}+a_{112}\cdot a_{231}\cdot a_{323}+a_{112}\cdot b_{231}\cdot a_{323}-a_{112}\cdot a_{233}\cdot a_{321}$$
$$-a_{112}\cdot a_{233}\cdot b_{321}+a_{113}\cdot a_{221}\cdot a_{332}+a_{113}\cdot b_{221}\cdot a_{332}-a_{113}\cdot a_{222}\cdot a_{331}-a_{113}\cdot a_{222}\cdot b_{331}$$
$$-a_{113}\cdot a_{231}\cdot a_{322}-a_{113}\cdot a_{231}\cdot a_{322}+a_{113}\cdot a_{232}\cdot a_{321}+a_{113}\cdot a_{232}\cdot b_{321}-a_{121}\cdot a_{212}\cdot a_{333}$$
$$-b_{121}\cdot a_{212}\cdot a_{333}+a_{121}\cdot a_{213}\cdot a_{332}+b_{121}\cdot a_{213}\cdot a_{332}+a_{121}\cdot a_{232}\cdot a_{313}+b_{121}\cdot a_{232}\cdot a_{313}$$
$$-a_{121}\cdot a_{233}\cdot a_{312}-b_{121}\cdot a_{233}\cdot a_{312}+a_{122}\cdot a_{211}\cdot a_{333}+a_{122}\cdot b_{211}\cdot a_{333}-a_{122}\cdot a_{213}\cdot a_{331}$$
$$-a_{122}\cdot a_{213}\cdot b_{331}-a_{122}\cdot a_{231}\cdot a_{313}-a_{122}\cdot b_{231}\cdot a_{313}+a_{122}\cdot a_{233}\cdot a_{311}+a_{122}\cdot a_{233}\cdot b_{311}$$
$$-a_{123}\cdot a_{211}\cdot a_{332}-a_{123}\cdot b_{211}\cdot a_{332}+a_{123}\cdot a_{212}\cdot a_{331}+a_{123}\cdot a_{212}\cdot b_{331}+a_{123}\cdot a_{231}\cdot a_{312}$$
$$+a_{123}\cdot b_{231}\cdot a_{312}-a_{123}\cdot a_{232}\cdot a_{311}-a_{123}\cdot a_{232}\cdot b_{311}+a_{131}\cdot a_{212}\cdot a_{323}+b_{131}\cdot a_{212}\cdot a_{323}$$
$$-a_{131}\cdot a_{213}\cdot a_{322}-b_{131}\cdot a_{213}\cdot a_{322}-a_{131}\cdot a_{222}\cdot a_{313}-b_{131}\cdot a_{222}\cdot a_{313}+a_{131}\cdot a_{223}\cdot a_{312}$$
$$+b_{131}\cdot a_{223}\cdot a_{312}-a_{132}\cdot a_{211}\cdot a_{323}-a_{132}\cdot b_{211}\cdot a_{323}+a_{132}\cdot a_{213}\cdot a_{321}+a_{132}\cdot a_{213}\cdot b_{321}$$
$$+a_{132}\cdot a_{221}\cdot a_{313}+a_{132}\cdot b_{221}\cdot a_{313}-a_{132}\cdot a_{223}\cdot a_{311}-a_{132}\cdot a_{223}\cdot b_{311}+a_{133}\cdot a_{211}\cdot a_{322}$$
$$+a_{133}\cdot b_{211}\cdot a_{322}-a_{133}\cdot a_{212}\cdot a_{321}-a_{133}\cdot a_{212}\cdot b_{321}-a_{133}\cdot a_{221}\cdot a_{312}-a_{133}\cdot b_{221}\cdot a_{312}$$
$$+a_{133}\cdot a_{222}\cdot a_{311}+a_{133}\cdot a_{222}\cdot b_{311}.$$

If we compare results of above equations, we can see that we have the same result in both cases.
The proof is complete.

Theorem 2:

Let it be the cubic matrix B, which is formed by multiplying a plane (in the indices j and k, it does not work in the index i) of the matrix A by a scalar α, and addition another plane, then we have:

$$det(A) = det(B)$$

Proof:

Case 1: The cubic-matrix A of order 2, (and B has order 2), we will proof the case 1 for each "vertical page" and "vertical layer", as following:

$$det\left(A_{[2\times2\times2]}\right) = \left(\begin{matrix} a_{111} & a_{121} \\ a_{211} & a_{221} \end{matrix}\middle|\begin{matrix} a_{112} & a_{122} \\ a_{212} & a_{222} \end{matrix}\right) = a_{111}\cdot a_{222} - a_{112}\cdot a_{221} - a_{121}\cdot a_{212} + a_{122}\cdot a_{211}.$$

1. For plan $j = 1$: Let us add first vertical page to second vertical page while multiplying by a scalar α.

$$det\left(B_{[2\times2\times2]}\right) = \left(\begin{matrix} a_{111} & a_{121}+\alpha\cdot a_{111} \\ a_{211} & a_{221}+\alpha\cdot a_{211} \end{matrix}\middle|\begin{matrix} a_{112} & a_{122}+\alpha\cdot a_{112} \\ a_{212} & a_{222}+\alpha\cdot a_{212} \end{matrix}\right) = a_{111}\cdot(a_{222}+\alpha\cdot a_{212})$$
$$-(a_{122}+\alpha\cdot a_{112})\cdot a_{221} - (a_{121}+\alpha\cdot a_{111})\cdot a_{212} + a_{122}\cdot(a_{221}+\alpha\cdot a_{211}).$$

After expanding further, we get the following result:

$$det\left(B_{[2\times2\times2]}\right) = a_{111}\cdot a_{222} - a_{112}\cdot a_{221} - a_{121}\cdot a_{212} + a_{122}\cdot a_{211}$$

If we compare results of above equations, we can see that we have the same result in both cases.

2. For plan $j = 2$: Let us add first vertical page to first vertical page while multiplying by a scalar α.

$$det\left(B_{[2\times2\times2]}\right) = \left(\begin{matrix} a_{111}+\alpha\cdot a_{121} & a_{121} \\ a_{211}+\alpha\cdot a_{211} & a_{221} \end{matrix}\middle|\begin{matrix} a_{112}+\alpha\cdot a_{122} & a_{122} \\ a_{212}+\alpha\cdot a_{222} & a_{222} \end{matrix}\right) = (a_{111}+\alpha\cdot a_{121})\cdot a_{222}$$
$$-(a_{112}+\alpha\cdot a_{122})\cdot a_{221} - a_{121}\cdot(a_{212}+\alpha\cdot a_{222}) + a_{122}\cdot(a_{211}+\alpha\cdot a_{221})$$

After expanding further, we get the following result:

$$det\left(B_{[2\times2\times2]}\right) = a_{111}\cdot a_{222} - a_{112}\cdot a_{221} - a_{121}\cdot a_{212} + a_{122}\cdot a_{211}$$

If we compare results of above equations, we can see that we have the same result in both cases.

3. For plan $k = 1$: Let us add first vertical page to second vertical layer while multiplying by a scalar α.

$$det\left(B_{[2\times2\times2]}\right) = \left(\begin{matrix} a_{111} & a_{121} \\ a_{211} & a_{221} \end{matrix}\middle|\begin{matrix} a_{112}+\alpha\cdot a_{111} & a_{122}+\alpha\cdot a_{121} \\ a_{212}+\alpha\cdot a_{211} & a_{222}+\alpha\cdot a_{221} \end{matrix}\right) = a_{111}\cdot(a_{222}+\alpha\cdot a_{221})$$
$$-(a_{112}+\alpha\cdot a_{111})\cdot a_{221} - a_{121}\cdot(a_{212}+\alpha\cdot a_{211}) + (a_{122}+\alpha\cdot a_{121})\cdot a_{211}$$

After expanding further, we get the following result:

$$det\left(B_{[2\times2\times2]}\right) = a_{111}\cdot a_{222} - a_{112}\cdot a_{221} - a_{121}\cdot a_{212} + a_{122}\cdot a_{211}$$

If we compare results of above equations, we can see that we have the same result in both cases.

4. For plan $k = 2$: Let us add first vertical page to first vertical layer while multiplying by a scalar α.

$$det\left(B_{[2\times2\times2]}\right) = \left(\begin{matrix} a_{111}+\alpha\cdot a_{112} & a_{121}+\alpha\cdot a_{122} \\ a_{211}+\alpha\cdot a_{212} & a_{221}+\alpha\cdot a_{222} \end{matrix}\middle|\begin{matrix} a_{112} & a_{122} \\ a_{212} & a_{222} \end{matrix}\right) = (a_{111}+\alpha\cdot a_{112})\cdot a_{222}$$
$$-a_{112}\cdot(a_{221}+\alpha\cdot a_{222}) - (a_{121}+\alpha\cdot a_{122})\cdot a_{212} + a_{122}\cdot(a_{211}+\alpha\cdot a_{212})$$

After expanding further, we get the following result:

$$det\left(B_{[2\times2\times2]}\right) = a_{111}\cdot a_{222} - a_{112}\cdot a_{221} - a_{121}\cdot a_{212} + a_{122}\cdot a_{211}$$

If we compare results of above equations, we can see that we have the same result in both cases.

Case 2: The cubic-matrix A of order 3, (and B has order 3), we will proof the case 1 for each "vertical page" and "vertical layer", as following:

$$det\left(A_{[3\times3\times3]}\right) = det\left(\begin{array}{ccc|ccc|ccc} a_{111} & a_{121} & a_{131} & a_{112} & a_{122} & a_{132} & a_{113} & a_{123} & a_{133} \\ a_{211} & a_{221} & a_{231} & a_{212} & a_{222} & a_{232} & a_{213} & a_{223} & a_{233} \\ a_{311} & a_{321} & a_{331} & a_{312} & a_{322} & a_{332} & a_{313} & a_{323} & a_{333} \end{array}\right)$$

$$= a_{111}\cdot a_{222}\cdot a_{333} - a_{111}\cdot a_{232}\cdot a_{323} - a_{111}\cdot a_{223}\cdot a_{332} + a_{111}\cdot a_{233}\cdot a_{322} - a_{112}\cdot a_{221}\cdot a_{333}$$
$$+a_{112}\cdot a_{223}\cdot a_{331} + a_{112}\cdot a_{231}\cdot a_{323} - a_{112}\cdot a_{233}\cdot a_{321} + a_{113}\cdot a_{221}\cdot a_{332} - a_{113}\cdot a_{222}\cdot a_{331}$$
$$-a_{113}\cdot a_{231}\cdot a_{322} + a_{113}\cdot a_{232}\cdot a_{321} - a_{121}\cdot a_{212}\cdot a_{333} + a_{121}\cdot a_{213}\cdot a_{332} + a_{121}\cdot a_{232}\cdot a_{313}$$
$$-a_{121}\cdot a_{233}\cdot a_{312} + a_{122}\cdot a_{211}\cdot a_{333} - a_{122}\cdot a_{213}\cdot a_{331} - a_{122}\cdot a_{231}\cdot a_{313} + a_{122}\cdot a_{233}\cdot a_{311}$$
$$-a_{123}\cdot a_{211}\cdot a_{332} + a_{123}\cdot a_{212}\cdot a_{331} + a_{123}\cdot a_{231}\cdot a_{312} - a_{123}\cdot a_{232}\cdot a_{311} + a_{131}\cdot a_{212}\cdot a_{323}$$
$$-a_{131}\cdot a_{213}\cdot a_{322} - a_{131}\cdot a_{222}\cdot a_{313} + a_{131}\cdot a_{223}\cdot a_{312} - a_{132}\cdot a_{211}\cdot a_{323} + a_{132}\cdot a_{213}\cdot a_{321}$$
$$+a_{132}\cdot a_{221}\cdot a_{313} - a_{132}\cdot a_{223}\cdot a_{311} + a_{133}\cdot a_{211}\cdot a_{322} - a_{133}\cdot a_{212}\cdot a_{321} - a_{133}\cdot a_{221}\cdot a_{312}$$
$$+a_{133}\cdot a_{222}\cdot a_{311}$$

1. For plan $j = 1$: Let us add first vertical page to second vertical page while multiplying by a scalar α.

$$det\left(B_{[3\times3\times3]}\right)$$
$$= det\left(\begin{array}{ccc|ccc|ccc} a_{111} & a_{121}+\alpha\cdot a_{111} & a_{131} & a_{112} & a_{122}+\alpha\cdot a_{112} & a_{132} & a_{113} & a_{123}+\alpha\cdot a_{113} & a_{133} \\ a_{211} & a_{221}+\alpha\cdot a_{211} & a_{231} & a_{212} & a_{222}+\alpha\cdot a_{212} & a_{232} & a_{213} & a_{223}+\alpha\cdot a_{213} & a_{233} \\ a_{311} & a_{321}+\alpha\cdot a_{311} & a_{331} & a_{312} & a_{322}+\alpha\cdot a_{312} & a_{332} & a_{313} & a_{323}+\alpha\cdot a_{313} & a_{333} \end{array}\right)$$
$$= a_{111}\cdot(a_{222}+\alpha\cdot a_{212})\cdot a_{333} - a_{111}\cdot a_{232}\cdot(a_{323}+\alpha\cdot a_{313}) - a_{111}\cdot(a_{223}+\alpha\cdot a_{213})\cdot a_{332}$$
$$+a_{111}\cdot a_{233}\cdot(a_{322}+\alpha\cdot a_{312}) - a_{112}\cdot(a_{221}+\alpha\cdot a_{211})\cdot a_{333} + a_{112}\cdot(a_{223}+\alpha\cdot a_{213})\cdot a_{331}$$
$$+a_{112}\cdot a_{231}\cdot(a_{323}+\alpha\cdot a_{313}) - a_{112}\cdot a_{233}\cdot(a_{321}+\alpha\cdot a_{311}) + a_{113}\cdot(a_{221}+\alpha\cdot a_{211})\cdot a_{332}$$
$$-a_{113}\cdot(a_{222}+\alpha\cdot a_{212})\cdot a_{331} - a_{113}\cdot a_{231}\cdot(a_{322}+\alpha\cdot a_{312}) + a_{113}\cdot a_{232}\cdot(a_{321}+\alpha\cdot a_{311})$$
$$-(a_{121}+\alpha\cdot a_{111})\cdot a_{212}\cdot a_{333} + (a_{121}+\alpha\cdot a_{111})\cdot a_{213}\cdot a_{332} + (a_{121}+\alpha\cdot a_{111})\cdot a_{232}\cdot a_{313}$$
$$-(a_{121}+\alpha\cdot a_{111})\cdot a_{233}\cdot a_{312} + (a_{122}+\alpha\cdot a_{112})\cdot a_{211}\cdot a_{333} - (a_{122}+\alpha\cdot a_{112})\cdot a_{213}\cdot a_{331}$$
$$-(a_{122}+\alpha\cdot a_{112})\cdot a_{231}\cdot a_{313} + (a_{122}+\alpha\cdot a_{112})\cdot a_{233}\cdot a_{311} - (a_{123}+\alpha\cdot a_{113})\cdot a_{211}\cdot a_{332}$$
$$+(a_{123}+\alpha\cdot a_{113})\cdot a_{212}\cdot a_{331} + (a_{123}+\alpha\cdot a_{113})\cdot a_{231}\cdot a_{312} - (a_{123}+\alpha\cdot a_{113})\cdot a_{232}\cdot a_{311}$$
$$+a_{131}\cdot a_{212}\cdot(a_{323}+\alpha\cdot a_{313}) - a_{131}\cdot a_{213}\cdot(a_{322}+\alpha\cdot a_{312}) - a_{131}\cdot(a_{222}+\alpha\cdot a_{212})\cdot a_{313}$$
$$+a_{131}\cdot(a_{223}+\alpha\cdot a_{213})\cdot a_{312} - a_{132}\cdot a_{211}\cdot(a_{323}+\alpha\cdot a_{313}) + a_{132}\cdot a_{213}\cdot(a_{321}+\alpha\cdot a_{311})$$
$$+a_{132}\cdot(a_{221}+\alpha\cdot a_{211})\cdot a_{313} - a_{132}\cdot(a_{223}+\alpha\cdot a_{213})\cdot a_{311} + a_{133}\cdot a_{211}\cdot(a_{322}+\alpha\cdot a_{312})$$
$$-a_{133}\cdot a_{212}\cdot(a_{321}+\alpha\cdot a_{311}) - a_{133}\cdot(a_{221}+\alpha\cdot a_{211})\cdot a_{312} + a_{133}\cdot(a_{222}+\alpha\cdot a_{212})\cdot a_{311}.$$

After expanding further, we get the following result:

$$det\left(B_{[3\times3\times3]}\right) = a_{111}\cdot a_{222}\cdot a_{333} - a_{111}\cdot a_{232}\cdot a_{323} - a_{111}\cdot a_{223}\cdot a_{332} + a_{111}\cdot a_{233}\cdot a_{322}$$
$$-a_{112}\cdot a_{221}\cdot a_{333} + a_{112}\cdot a_{223}\cdot a_{331} + a_{112}\cdot a_{231}\cdot a_{323} - a_{112}\cdot a_{233}\cdot a_{321} + a_{113}\cdot a_{221}\cdot a_{332}$$
$$-a_{113}\cdot a_{222}\cdot a_{331} - a_{113}\cdot a_{231}\cdot a_{322} + a_{113}\cdot a_{232}\cdot a_{321} - a_{121}\cdot a_{212}\cdot a_{333} + a_{121}\cdot a_{213}\cdot a_{332}$$
$$+a_{121}\cdot a_{232}\cdot a_{313} - a_{121}\cdot a_{233}\cdot a_{312} + a_{122}\cdot a_{211}\cdot a_{333} - a_{122}\cdot a_{213}\cdot a_{331} - a_{122}\cdot a_{231}\cdot a_{313}$$
$$+a_{122}\cdot a_{233}\cdot a_{311} - a_{123}\cdot a_{211}\cdot a_{332} + a_{123}\cdot a_{212}\cdot a_{331} + a_{123}\cdot a_{231}\cdot a_{312} - a_{123}\cdot a_{232}\cdot a_{311}$$
$$+a_{131}\cdot a_{212}\cdot a_{323} - a_{131}\cdot a_{213}\cdot a_{322} - a_{131}\cdot a_{222}\cdot a_{313} + a_{131}\cdot a_{223}\cdot a_{312} - a_{132}\cdot a_{211}\cdot a_{323}$$
$$+a_{132}\cdot a_{213}\cdot a_{321} + a_{132}\cdot a_{221}\cdot a_{313} - a_{132}\cdot a_{223}\cdot a_{311} + a_{133}\cdot a_{211}\cdot a_{322} - a_{133}\cdot a_{212}\cdot a_{321}$$
$$-a_{133}\cdot a_{221}\cdot a_{312} + a_{133}\cdot a_{222}\cdot a_{311}.$$

If we compare results of above equations, we can see that we have the same result in both cases.

2. For plan $j = 2$: Let us add first vertical page to third vertical page while multiplying by a scalar α.

$$det\left(B_{[3\times3\times3]}\right)$$
$$= det\left(\begin{array}{ccc|ccc|ccc} a_{111} & a_{121} & a_{131}+\alpha\cdot a_{111} & a_{112} & a_{122} & a_{132}+\alpha\cdot a_{112} & a_{113} & a_{123} & a_{133}+\alpha\cdot a_{113} \\ a_{211} & a_{221} & a_{231}+\alpha\cdot a_{211} & a_{212} & a_{222} & a_{232}+\alpha\cdot a_{212} & a_{213} & a_{223} & a_{233}+\alpha\cdot a_{213} \\ a_{311} & a_{321} & a_{331}+\alpha\cdot a_{311} & a_{312} & a_{322} & a_{332}+\alpha\cdot a_{312} & a_{313} & a_{323} & a_{333}+\alpha\cdot a_{313} \end{array}\right)$$
$$= a_{111}\cdot a_{222}\cdot(a_{333}+\alpha\cdot a_{313}) - a_{111}\cdot(a_{232}+\alpha\cdot a_{212})\cdot a_{323} - a_{111}\cdot a_{223}\cdot(a_{332}+\alpha\cdot a_{312})$$
$$+a_{111}\cdot(a_{233}+\alpha\cdot a_{213})\cdot a_{322} - a_{112}\cdot a_{221}\cdot(a_{333}+\alpha\cdot a_{313}) + a_{112}\cdot a_{223}\cdot(a_{331}+\alpha\cdot a_{311})$$
$$+a_{112}\cdot(a_{231}+\alpha\cdot a_{211})\cdot a_{323} - a_{112}\cdot(a_{233}+\alpha\cdot a_{213})\cdot a_{321} + a_{113}\cdot a_{221}\cdot(a_{332}+\alpha\cdot a_{312})$$
$$-a_{113}\cdot a_{222}\cdot(a_{331}+\alpha\cdot a_{311}) - a_{113}\cdot(a_{231}+\alpha\cdot a_{211})\cdot a_{322} + a_{113}\cdot(a_{232}+\alpha\cdot a_{212})\cdot a_{321}$$
$$-a_{121}\cdot a_{212}\cdot(a_{333}+\alpha\cdot a_{313}) + a_{121}\cdot a_{213}\cdot(a_{332}+\alpha\cdot a_{312}) + a_{121}\cdot(a_{232}+\alpha\cdot a_{212})\cdot a_{313}$$
$$-a_{121}\cdot(a_{233}+\alpha\cdot a_{213})\cdot a_{312} + a_{122}\cdot a_{211}\cdot(a_{333}+\alpha\cdot a_{313}) - a_{122}\cdot a_{213}\cdot(a_{331}+\alpha\cdot a_{311})$$
$$-a_{122}\cdot(a_{231}+\alpha\cdot a_{211})\cdot a_{313} + a_{122}\cdot(a_{233}+\alpha\cdot a_{213})\cdot a_{311} - a_{123}\cdot a_{211}\cdot(a_{332}+\alpha\cdot a_{312})$$
$$+a_{123}\cdot a_{212}\cdot(a_{331}+\alpha\cdot a_{311}) + a_{123}\cdot(a_{231}+\alpha\cdot a_{211})\cdot a_{312} - a_{123}\cdot(a_{232}+\alpha\cdot a_{212})\cdot a_{311}$$
$$+(a_{131}+\alpha\cdot a_{111})\cdot a_{212}\cdot a_{323} - (a_{131}+\alpha\cdot a_{111})\cdot a_{213}\cdot a_{322} - (a_{131}+\alpha\cdot a_{111})\cdot a_{222}\cdot a_{313}$$
$$+(a_{131}+\alpha\cdot a_{111})\cdot a_{223}\cdot a_{312} - (a_{132}+\alpha\cdot a_{112})\cdot a_{211}\cdot a_{323} + (a_{132}+\alpha\cdot a_{112})\cdot a_{213}\cdot a_{321}$$
$$+(a_{132}+\alpha\cdot a_{112})\cdot a_{221}\cdot a_{313} - (a_{132}+\alpha\cdot a_{112})\cdot a_{223}\cdot a_{311} + (a_{133}+\alpha\cdot a_{113})\cdot a_{211}\cdot a_{322}$$
$$-(a_{133}+\alpha\cdot a_{113})\cdot a_{212}\cdot a_{321} - (a_{133}+\alpha\cdot a_{113})\cdot a_{221}\cdot a_{312} + (a_{133}+\alpha\cdot a_{113})\cdot a_{222}\cdot a_{311}.$$

After expanding further, we get the following result:

$$det\left(B_{[3\times3\times3]}\right) = a_{111}\cdot a_{222}\cdot a_{333} - a_{111}\cdot a_{232}\cdot a_{323} - a_{111}\cdot a_{223}\cdot a_{332} + a_{111}\cdot a_{233}\cdot a_{322}$$
$$-a_{112}\cdot a_{221}\cdot a_{333} + a_{112}\cdot a_{223}\cdot a_{331} + a_{112}\cdot a_{231}\cdot a_{323} - a_{112}\cdot a_{233}\cdot a_{321} + a_{113}\cdot a_{221}\cdot a_{332}$$
$$-a_{113}\cdot a_{222}\cdot a_{331} - a_{113}\cdot a_{231}\cdot a_{322} + a_{113}\cdot a_{232}\cdot a_{321} - a_{121}\cdot a_{212}\cdot a_{333} + a_{121}\cdot a_{213}\cdot a_{332}$$
$$+a_{121}\cdot a_{232}\cdot a_{313} - a_{121}\cdot a_{233}\cdot a_{312} + a_{122}\cdot a_{211}\cdot a_{333} - a_{122}\cdot a_{213}\cdot a_{331} - a_{122}\cdot a_{231}\cdot a_{313}$$
$$+a_{122}\cdot a_{233}\cdot a_{311} - a_{123}\cdot a_{211}\cdot a_{332} + a_{123}\cdot a_{212}\cdot a_{331} + a_{123}\cdot a_{231}\cdot a_{312} - a_{123}\cdot a_{232}\cdot a_{311}$$
$$+a_{131}\cdot a_{212}\cdot a_{323} - a_{131}\cdot a_{213}\cdot a_{322} - a_{131}\cdot a_{222}\cdot a_{313} + a_{131}\cdot a_{223}\cdot a_{312} - a_{132}\cdot a_{211}\cdot a_{323}$$
$$+a_{132}\cdot a_{213}\cdot a_{321} + a_{132}\cdot a_{221}\cdot a_{313} - a_{132}\cdot a_{223}\cdot a_{311} + a_{133}\cdot a_{211}\cdot a_{322} - a_{133}\cdot a_{212}\cdot a_{321}$$
$$-a_{133}\cdot a_{221}\cdot a_{312} + a_{133}\cdot a_{222}\cdot a_{311}.$$

3. For plan $j = 3$: Let us add second vertical page to third vertical page while multiplying by a scalar α.

$$det\left(B_{[3\times3\times3]}\right)$$
$$= det\left(\begin{array}{ccc|ccc|ccc} a_{111} & a_{121} & a_{131}+\alpha\cdot a_{121} & a_{112} & a_{122} & a_{132}+\alpha\cdot a_{122} & a_{113} & a_{123} & a_{133}+\alpha\cdot a_{123} \\ a_{211} & a_{221} & a_{231}+\alpha\cdot a_{221} & a_{212} & a_{222} & a_{232}+\alpha\cdot a_{222} & a_{213} & a_{223} & a_{233}+\alpha\cdot a_{223} \\ a_{311} & a_{321} & a_{331}+\alpha\cdot a_{321} & a_{312} & a_{322} & a_{332}+\alpha\cdot a_{322} & a_{313} & a_{323} & a_{333}+\alpha\cdot a_{323} \end{array}\right)$$
$$= a_{111}\cdot a_{222}\cdot(a_{333}+\alpha\cdot a_{323}) - a_{111}\cdot(a_{232}+\alpha\cdot a_{222})\cdot a_{323} - a_{111}\cdot a_{223}\cdot(a_{332}+\alpha\cdot a_{312})$$
$$+a_{111}\cdot(a_{233}+\alpha\cdot a_{223})\cdot a_{322} - a_{112}\cdot a_{221}\cdot(a_{333}+\alpha\cdot a_{323}) + a_{112}\cdot a_{223}\cdot(a_{331}+\alpha\cdot a_{321})$$
$$+a_{112}\cdot(a_{231}+\alpha\cdot a_{211})\cdot a_{323} - a_{112}\cdot(a_{233}+\alpha\cdot a_{223})\cdot a_{321} + a_{113}\cdot a_{221}\cdot(a_{332}+\alpha\cdot a_{322})$$
$$-a_{113}\cdot a_{222}\cdot(a_{331}+\alpha\cdot a_{321}) - a_{113}\cdot(a_{231}+\alpha\cdot a_{211})\cdot a_{322} + a_{113}\cdot(a_{232}+\alpha\cdot a_{222})\cdot a_{321}$$
$$-a_{121}\cdot a_{212}\cdot(a_{333}+\alpha\cdot a_{323}) + a_{121}\cdot a_{213}\cdot(a_{332}+\alpha\cdot a_{322}) + a_{121}\cdot(a_{232}+\alpha\cdot a_{212})\cdot a_{313}$$
$$-a_{121}\cdot(a_{233}+\alpha\cdot a_{223})\cdot a_{312} + a_{122}\cdot a_{211}\cdot(a_{333}+\alpha\cdot a_{323}) - a_{122}\cdot a_{213}\cdot(a_{331}+\alpha\cdot a_{321})$$
$$-a_{122}\cdot(a_{231}+\alpha\cdot a_{211})\cdot a_{313} + a_{122}\cdot(a_{233}+\alpha\cdot a_{223})\cdot a_{311} - a_{123}\cdot a_{211}\cdot(a_{332}+\alpha\cdot a_{322})$$
$$+a_{123}\cdot a_{212}\cdot(a_{331}+\alpha\cdot a_{321}) + a_{123}\cdot(a_{231}+\alpha\cdot a_{211})\cdot a_{312} - a_{123}\cdot(a_{232}+\alpha\cdot a_{222})\cdot a_{311}$$
$$+(a_{131}+\alpha\cdot a_{121})\cdot a_{212}\cdot a_{323} - (a_{131}+\alpha\cdot a_{121})\cdot a_{213}\cdot a_{322} - (a_{131}+\alpha\cdot a_{121})\cdot a_{222}\cdot a_{313}$$
$$+(a_{131}+\alpha\cdot a_{121})\cdot a_{223}\cdot a_{312} - (a_{132}+\alpha\cdot a_{122})\cdot a_{211}\cdot a_{323} + (a_{132}+\alpha\cdot a_{122})\cdot a_{213}\cdot a_{321}$$

$$+(a_{132}+\alpha\cdot a_{122})\cdot a_{221}\cdot a_{313}-(a_{132}+\alpha\cdot a_{122})\cdot a_{223}\cdot a_{311}+(a_{133}+\alpha\cdot a_{123})\cdot a_{211}\cdot a_{322}$$
$$-(a_{133}+\alpha\cdot a_{123})\cdot a_{212}\cdot a_{321}-(a_{133}+\alpha\cdot a_{123})\cdot a_{221}\cdot a_{312}+(a_{133}+\alpha\cdot a_{123})\cdot a_{222}\cdot a_{311}.$$

After expanding further, we get the following result:

$$det\left(B_{[3\times3\times3]}\right)=a_{111}\cdot a_{222}\cdot a_{333}-a_{111}\cdot a_{232}\cdot a_{323}-a_{111}\cdot a_{223}\cdot a_{332}+a_{111}\cdot a_{233}\cdot a_{322}$$
$$-a_{112}\cdot a_{221}\cdot a_{333}+a_{112}\cdot a_{223}\cdot a_{331}+a_{112}\cdot a_{231}\cdot a_{323}-a_{112}\cdot a_{233}\cdot a_{321}+a_{113}\cdot a_{221}\cdot a_{332}$$
$$-a_{113}\cdot a_{222}\cdot a_{331}-a_{113}\cdot a_{231}\cdot a_{322}+a_{113}\cdot a_{232}\cdot a_{321}-a_{121}\cdot a_{212}\cdot a_{333}+a_{121}\cdot a_{213}\cdot a_{332}$$
$$+a_{121}\cdot a_{232}\cdot a_{313}-a_{121}\cdot a_{233}\cdot a_{312}+a_{122}\cdot a_{211}\cdot a_{333}-a_{122}\cdot a_{213}\cdot a_{331}-a_{122}\cdot a_{231}\cdot a_{313}$$
$$+a_{122}\cdot a_{233}\cdot a_{311}-a_{123}\cdot a_{211}\cdot a_{332}+a_{123}\cdot a_{212}\cdot a_{331}+a_{123}\cdot a_{231}\cdot a_{312}-a_{123}\cdot a_{232}\cdot a_{311}$$
$$+a_{131}\cdot a_{212}\cdot a_{323}-a_{131}\cdot a_{213}\cdot a_{322}-a_{131}\cdot a_{222}\cdot a_{313}+a_{131}\cdot a_{223}\cdot a_{312}-a_{132}\cdot a_{211}\cdot a_{323}$$
$$+a_{132}\cdot a_{213}\cdot a_{321}+a_{132}\cdot a_{221}\cdot a_{313}-a_{132}\cdot a_{223}\cdot a_{311}+a_{133}\cdot a_{211}\cdot a_{322}-a_{133}\cdot a_{212}\cdot a_{321}$$
$$-a_{133}\cdot a_{221}\cdot a_{312}+a_{133}\cdot a_{222}\cdot a_{311}.$$

If we compare results of above equations, we can see that we have the same result in both cases.

4. For plan $k=1$: Let us add first vertical layer to second vertical layer while multiplying by a scalar α.

$$det\left(B_{[3\times3\times3]}\right)$$
$$=det\left(\begin{array}{ccc|ccc|ccc}a_{111}&a_{121}&a_{131}&a_{112}+\alpha\cdot a_{111}&a_{122}+\alpha\cdot a_{121}&a_{132}+\alpha\cdot a_{131}&a_{113}&a_{123}&a_{133}\\a_{211}&a_{221}&a_{231}&a_{212}+\alpha\cdot a_{211}&a_{222}+\alpha\cdot a_{221}&a_{232}+\alpha\cdot a_{231}&a_{213}&a_{223}&a_{233}\\a_{311}&a_{321}&a_{331}&a_{312}+\alpha\cdot a_{311}&a_{322}+\alpha\cdot a_{321}&a_{332}+\alpha\cdot a_{331}&a_{313}&a_{323}&a_{333}\end{array}\right)$$
$$=a_{111}\cdot(a_{222}+\alpha\cdot a_{221})\cdot a_{333}-a_{111}\cdot(a_{232}+\alpha\cdot a_{231})\cdot a_{323}-a_{111}\cdot a_{223}\cdot(a_{332}+\alpha\cdot a_{331})$$
$$+a_{111}\cdot a_{233}\cdot(a_{322}+\alpha\cdot a_{321})-(a_{112}+\alpha\cdot a_{111})\cdot a_{221}\cdot a_{333}+(a_{112}+\alpha\cdot a_{111})\cdot a_{223}\cdot a_{331}$$
$$+(a_{112}+\alpha\cdot a_{111})\cdot a_{231}\cdot a_{323}-(a_{112}+\alpha\cdot a_{111})\cdot a_{233}\cdot a_{321}+a_{113}\cdot a_{221}\cdot(a_{332}+\alpha\cdot a_{331})$$
$$-a_{113}\cdot(a_{222}+\alpha\cdot a_{221})\cdot a_{331}-a_{113}\cdot a_{231}\cdot(a_{322}+\alpha\cdot a_{321})+a_{113}\cdot(a_{232}+\alpha\cdot a_{231})\cdot a_{321}$$
$$-a_{121}\cdot(a_{212}+\alpha\cdot a_{211})\cdot a_{333}+a_{121}\cdot a_{213}\cdot(a_{332}+\alpha\cdot a_{331})+a_{121}\cdot(a_{232}+\alpha\cdot a_{231})\cdot a_{313}$$
$$-a_{121}\cdot a_{233}\cdot(a_{312}+\alpha\cdot a_{311})+(a_{122}+\alpha\cdot a_{121})\cdot a_{211}\cdot a_{333}-(a_{122}+\alpha\cdot a_{121})\cdot a_{213}\cdot a_{331}$$
$$-(a_{122}+\alpha\cdot a_{121})\cdot a_{231}\cdot a_{313}+(a_{122}+\alpha\cdot a_{121})\cdot a_{233}\cdot a_{311}-a_{123}\cdot a_{211}\cdot(a_{332}+\alpha\cdot a_{331})$$
$$+a_{123}\cdot(a_{212}+\alpha\cdot a_{211})\cdot a_{331}+a_{123}\cdot a_{231}\cdot(a_{312}+\alpha\cdot a_{311})-a_{123}\cdot(a_{232}+\alpha\cdot a_{231})\cdot a_{311}$$
$$+a_{131}\cdot(a_{212}+\alpha\cdot a_{211})\cdot a_{323}-a_{131}\cdot a_{213}\cdot(a_{322}+\alpha\cdot a_{321})-a_{131}\cdot(a_{222}+\alpha\cdot a_{221})\cdot a_{313}$$
$$+a_{131}\cdot a_{223}\cdot(a_{312}+\alpha\cdot a_{311})-(a_{132}+\alpha\cdot a_{131})\cdot a_{211}\cdot a_{323}+(a_{132}+\alpha\cdot a_{131})\cdot a_{213}\cdot a_{321}$$
$$+(a_{132}+\alpha\cdot a_{131})\cdot a_{221}\cdot a_{313}-(a_{132}+\alpha\cdot a_{131})\cdot a_{223}\cdot a_{311}+a_{133}\cdot a_{211}\cdot(a_{322}+\alpha\cdot a_{321})$$
$$-a_{133}\cdot(a_{212}+\alpha\cdot a_{211})\cdot a_{321}-a_{133}\cdot a_{221}\cdot(a_{312}+\alpha\cdot a_{311})+a_{133}\cdot(a_{222}+\alpha\cdot a_{221})\cdot a_{311}.$$

After expanding further, we get the following result:

$$det\left(B_{[3\times3\times3]}\right)=a_{111}\cdot a_{222}\cdot a_{333}-a_{111}\cdot a_{232}\cdot a_{323}-a_{111}\cdot a_{223}\cdot a_{332}+a_{111}\cdot a_{233}\cdot a_{322}$$
$$-a_{112}\cdot a_{221}\cdot a_{333}+a_{112}\cdot a_{223}\cdot a_{331}+a_{112}\cdot a_{231}\cdot a_{323}-a_{112}\cdot a_{233}\cdot a_{321}+a_{113}\cdot a_{221}\cdot a_{332}$$
$$-a_{113}\cdot a_{222}\cdot a_{331}-a_{113}\cdot a_{231}\cdot a_{322}+a_{113}\cdot a_{232}\cdot a_{321}-a_{121}\cdot a_{212}\cdot a_{333}+a_{121}\cdot a_{213}\cdot a_{332}$$
$$+a_{121}\cdot a_{232}\cdot a_{313}-a_{121}\cdot a_{233}\cdot a_{312}+a_{122}\cdot a_{211}\cdot a_{333}-a_{122}\cdot a_{213}\cdot a_{331}-a_{122}\cdot a_{231}\cdot a_{313}$$
$$+a_{122}\cdot a_{233}\cdot a_{311}-a_{123}\cdot a_{211}\cdot a_{332}+a_{123}\cdot a_{212}\cdot a_{331}+a_{123}\cdot a_{231}\cdot a_{312}-a_{123}\cdot a_{232}\cdot a_{311}$$
$$+a_{131}\cdot a_{212}\cdot a_{323}-a_{131}\cdot a_{213}\cdot a_{322}-a_{131}\cdot a_{222}\cdot a_{313}+a_{131}\cdot a_{223}\cdot a_{312}-a_{132}\cdot a_{211}\cdot a_{323}$$
$$+a_{132}\cdot a_{213}\cdot a_{321}+a_{132}\cdot a_{221}\cdot a_{313}-a_{132}\cdot a_{223}\cdot a_{311}+a_{133}\cdot a_{211}\cdot a_{322}-a_{133}\cdot a_{212}\cdot a_{321}$$
$$-a_{133}\cdot a_{221}\cdot a_{312}+a_{133}\cdot a_{222}\cdot a_{311}.$$

If we compare results of above equations, we can see that we have the same result in both cases.

5. For plan $k = 2$: Let us add first vertical layer to third vertical layer while multiplying by a scalar α.

$$det\left(B_{[3\times3\times3]}\right)$$
$$= det\left(\begin{array}{ccc|ccc|ccc} a_{111} & a_{121} & a_{131} & a_{112} & a_{122} & a_{132} & a_{113}+\alpha\cdot a_{111} & a_{123}+\alpha\cdot a_{121} & a_{133}+\alpha\cdot a_{131} \\ a_{211} & a_{221} & a_{231} & a_{212} & a_{222} & a_{232} & a_{213}+\alpha\cdot a_{211} & a_{223}+\alpha\cdot a_{221} & a_{233}+\alpha\cdot a_{231} \\ a_{311} & a_{321} & a_{331} & a_{312} & a_{322} & a_{332} & a_{313}+\alpha\cdot a_{311} & a_{323}+\alpha\cdot a_{321} & a_{333}+\alpha\cdot a_{331} \end{array}\right)$$
$$= a_{111}\cdot a_{222}\cdot(a_{333}+\alpha\cdot a_{331}) - a_{111}\cdot a_{232}\cdot(a_{323}+\alpha\cdot a_{321}) - a_{111}\cdot(a_{223}+\alpha\cdot a_{221})\cdot a_{332}$$
$$+a_{111}\cdot(a_{233}+\alpha\cdot a_{231})\cdot a_{322} - a_{112}\cdot a_{221}\cdot(a_{333}+\alpha\cdot a_{331}) + a_{112}\cdot(a_{223}+\alpha\cdot a_{221})\cdot a_{331}$$
$$+a_{112}\cdot a_{231}\cdot(a_{323}+\alpha\cdot a_{321}) - a_{112}\cdot(a_{233}+\alpha\cdot a_{231})\cdot a_{321} + (a_{113}+\alpha\cdot a_{111})\cdot a_{221}\cdot a_{332}$$
$$-(a_{113}+\alpha\cdot a_{111})\cdot a_{222}\cdot a_{331} - (a_{113}+\alpha\cdot a_{111})\cdot a_{231}\cdot a_{322} + (a_{113}+\alpha\cdot a_{111})\cdot a_{232}\cdot a_{321}$$
$$-a_{121}\cdot a_{212}\cdot(a_{333}+\alpha\cdot a_{331}) + a_{121}\cdot(a_{213}+\alpha\cdot a_{211})\cdot a_{332} + a_{121}\cdot a_{232}\cdot(a_{313}+\alpha\cdot a_{311})$$
$$-a_{121}\cdot(a_{233}+\alpha\cdot a_{231})\cdot a_{312} + a_{122}\cdot a_{211}\cdot(a_{333}+\alpha\cdot a_{331}) - a_{122}\cdot(a_{213}+\alpha\cdot a_{211})\cdot a_{331}$$
$$-a_{122}\cdot a_{231}\cdot(a_{313}+\alpha\cdot a_{311}) + a_{122}\cdot(a_{233}+\alpha\cdot a_{231})\cdot a_{311} - (a_{123}+\alpha\cdot a_{121})\cdot a_{211}\cdot a_{332}$$
$$+(a_{123}+\alpha\cdot a_{121})\cdot a_{212}\cdot a_{331} + (a_{123}+\alpha\cdot a_{121})\cdot a_{231}\cdot a_{312} - (a_{123}+\alpha\cdot a_{121})\cdot a_{232}\cdot a_{311}$$
$$+a_{131}\cdot a_{212}\cdot(a_{323}+\alpha\cdot a_{321}) - a_{131}\cdot(a_{213}+\alpha\cdot a_{211})\cdot a_{322} - a_{131}\cdot a_{222}\cdot(a_{313}+\alpha\cdot a_{311})$$
$$+a_{131}\cdot(a_{223}+\alpha\cdot a_{221})\cdot a_{312} - a_{132}\cdot a_{211}\cdot(a_{323}+\alpha\cdot a_{321}) + a_{132}\cdot(a_{213}+\alpha\cdot a_{211})\cdot a_{321}$$
$$+a_{132}\cdot a_{221}\cdot(a_{313}+\alpha\cdot a_{311}) - a_{132}\cdot(a_{223}+\alpha\cdot a_{221})\cdot a_{311} + (a_{133}+\alpha\cdot a_{131})\cdot a_{211}\cdot a_{322}$$
$$-(a_{133}+\alpha\cdot a_{131})\cdot a_{212}\cdot a_{321} - (a_{133}+\alpha\cdot a_{131})\cdot a_{221}\cdot a_{312} + (a_{133}+\alpha\cdot a_{131})\cdot a_{222}\cdot a_{311}.$$

After expanding further, we get the following result:

$$det\left(B_{[3\times3\times3]}\right) = a_{111}\cdot a_{222}\cdot a_{333} - a_{111}\cdot a_{232}\cdot a_{323} - a_{111}\cdot a_{223}\cdot a_{332} + a_{111}\cdot a_{233}\cdot a_{322}$$
$$-a_{112}\cdot a_{221}\cdot a_{333} + a_{112}\cdot a_{223}\cdot a_{331} + a_{112}\cdot a_{231}\cdot a_{323} - a_{112}\cdot a_{233}\cdot a_{321} + a_{113}\cdot a_{221}\cdot a_{332}$$
$$-a_{113}\cdot a_{222}\cdot a_{331} - a_{113}\cdot a_{231}\cdot a_{322} + a_{113}\cdot a_{232}\cdot a_{321} - a_{121}\cdot a_{212}\cdot a_{333} + a_{121}\cdot a_{213}\cdot a_{332}$$
$$+a_{121}\cdot a_{232}\cdot a_{313} - a_{121}\cdot a_{233}\cdot a_{312} + a_{122}\cdot a_{211}\cdot a_{333} - a_{122}\cdot a_{213}\cdot a_{331} - a_{122}\cdot a_{231}\cdot a_{313}$$
$$+a_{122}\cdot a_{233}\cdot a_{311} - a_{123}\cdot a_{211}\cdot a_{332} + a_{123}\cdot a_{212}\cdot a_{331} + a_{123}\cdot a_{231}\cdot a_{312} - a_{123}\cdot a_{232}\cdot a_{311}$$
$$+a_{131}\cdot a_{212}\cdot a_{323} - a_{131}\cdot a_{213}\cdot a_{322} - a_{131}\cdot a_{222}\cdot a_{313} + a_{131}\cdot a_{223}\cdot a_{312} - a_{132}\cdot a_{211}\cdot a_{323}$$
$$+a_{132}\cdot a_{213}\cdot a_{321} + a_{132}\cdot a_{221}\cdot a_{313} - a_{132}\cdot a_{223}\cdot a_{311} + a_{133}\cdot a_{211}\cdot a_{322} - a_{133}\cdot a_{212}\cdot a_{321}$$
$$-a_{133}\cdot a_{221}\cdot a_{312} + a_{133}\cdot a_{222}\cdot a_{311}.$$

If we compare results of above equations, we can see that we have the same result in both cases.

6. For plan $k = 3$: Let us add first vertical layer to third vertical layer while multiplying by a scalar α.

$$det\left(B_{[3\times3\times3]}\right)$$
$$= det\left(\begin{array}{ccc|ccc|ccc} a_{111} & a_{121} & a_{131} & a_{112} & a_{122} & a_{132} & a_{113}+\alpha\cdot a_{112} & a_{123}+\alpha\cdot a_{122} & a_{133}+\alpha\cdot a_{132} \\ a_{211} & a_{221} & a_{231} & a_{212} & a_{222} & a_{232} & a_{213}+\alpha\cdot a_{212} & a_{223}+\alpha\cdot a_{222} & a_{233}+\alpha\cdot a_{232} \\ a_{311} & a_{321} & a_{331} & a_{312} & a_{322} & a_{332} & a_{313}+\alpha\cdot a_{312} & a_{323}+\alpha\cdot a_{322} & a_{333}+\alpha\cdot a_{332} \end{array}\right)$$
$$= a_{111}\cdot a_{222}\cdot(a_{333}+\alpha\cdot a_{332}) - a_{111}\cdot a_{232}\cdot(a_{323}+\alpha\cdot a_{322}) - a_{111}\cdot(a_{223}+\alpha\cdot a_{222})\cdot a_{332}$$
$$+a_{111}\cdot(a_{233}+\alpha\cdot a_{232})\cdot a_{322} - a_{112}\cdot a_{221}\cdot(a_{333}+\alpha\cdot a_{332}) + a_{112}\cdot(a_{223}+\alpha\cdot a_{222})\cdot a_{331}$$
$$+a_{112}\cdot a_{231}\cdot(a_{323}+\alpha\cdot a_{322}) - a_{112}\cdot(a_{233}+\alpha\cdot a_{232})\cdot a_{321} + (a_{113}+\alpha\cdot a_{112})\cdot a_{221}\cdot a_{332}$$
$$-(a_{113}+\alpha\cdot a_{112})\cdot a_{222}\cdot a_{331} - (a_{113}+\alpha\cdot a_{112})\cdot a_{231}\cdot a_{322} + (a_{113}+\alpha\cdot a_{112})\cdot a_{232}\cdot a_{321}$$
$$-a_{121}\cdot a_{212}\cdot(a_{333}+\alpha\cdot a_{332}) + a_{121}\cdot(a_{213}+\alpha\cdot a_{212})\cdot a_{332} + a_{121}\cdot a_{232}\cdot(a_{313}+\alpha\cdot a_{312})$$
$$-a_{121}\cdot(a_{233}+\alpha\cdot a_{232})\cdot a_{312} + a_{122}\cdot a_{211}\cdot(a_{333}+\alpha\cdot a_{332}) - a_{122}\cdot(a_{213}+\alpha\cdot a_{212})\cdot a_{331}$$
$$-a_{122}\cdot a_{231}\cdot(a_{313}+\alpha\cdot a_{312}) + a_{122}\cdot(a_{233}+\alpha\cdot a_{232})\cdot a_{311} - (a_{123}+\alpha\cdot a_{122})\cdot a_{211}\cdot a_{332}$$
$$+(a_{123}+\alpha\cdot a_{122})\cdot a_{212}\cdot a_{331} + (a_{123}+\alpha\cdot a_{122})\cdot a_{231}\cdot a_{312} - (a_{123}+\alpha\cdot a_{122})\cdot a_{232}\cdot a_{311}$$

$$+a_{131}\cdot a_{212}\cdot(a_{323}+\alpha\cdot a_{322})-a_{131}\cdot(a_{213}+\alpha\cdot a_{212})\cdot a_{322}-a_{131}\cdot a_{222}\cdot(a_{313}+\alpha\cdot a_{312})\backslash$$
$$+a_{131}\cdot(a_{223}+\alpha\cdot a_{222})\cdot a_{312}-a_{132}\cdot a_{211}\cdot(a_{323}+\alpha\cdot a_{322})+a_{132}\cdot(a_{213}+\alpha\cdot a_{212})\cdot a_{321}$$
$$+a_{132}\cdot a_{221}\cdot(a_{313}+\alpha\cdot a_{312})-a_{132}\cdot(a_{223}+\alpha\cdot a_{222})\cdot a_{311}+(a_{133}+\alpha\cdot a_{132})\cdot a_{211}\cdot a_{322}$$
$$-(a_{133}+\alpha\cdot a_{132})\cdot a_{212}\cdot a_{321}-(a_{133}+\alpha\cdot a_{132})\cdot a_{221}\cdot a_{312}+(a_{133}+\alpha\cdot a_{132})\cdot a_{222}\cdot a_{311}.$$

After expanding further, we get the following result:

$$det(B_{[3\times3\times3]})=a_{111}\cdot a_{222}\cdot a_{333}-a_{111}\cdot a_{232}\cdot a_{323}-a_{111}\cdot a_{223}\cdot a_{332}+a_{111}\cdot a_{233}\cdot a_{322}$$
$$-a_{112}\cdot a_{221}\cdot a_{333}+a_{112}\cdot a_{223}\cdot a_{331}+a_{112}\cdot a_{231}\cdot a_{323}-a_{112}\cdot a_{233}\cdot a_{321}+a_{113}\cdot a_{221}\cdot a_{332}$$
$$-a_{113}\cdot a_{222}\cdot a_{331}-a_{113}\cdot a_{231}\cdot a_{322}+a_{113}\cdot a_{232}\cdot a_{321}-a_{121}\cdot a_{212}\cdot a_{333}+a_{121}\cdot a_{213}\cdot a_{332}$$
$$+a_{121}\cdot a_{232}\cdot a_{313}-a_{121}\cdot a_{233}\cdot a_{312}+a_{122}\cdot a_{211}\cdot a_{333}-a_{122}\cdot a_{213}\cdot a_{331}-a_{122}\cdot a_{231}\cdot a_{313}$$
$$+a_{122}\cdot a_{233}\cdot a_{311}-a_{123}\cdot a_{211}\cdot a_{332}+a_{123}\cdot a_{212}\cdot a_{331}+a_{123}\cdot a_{231}\cdot a_{312}-a_{123}\cdot a_{232}\cdot a_{311}$$
$$+a_{131}\cdot a_{212}\cdot a_{323}-a_{131}\cdot a_{213}\cdot a_{322}-a_{131}\cdot a_{222}\cdot a_{313}+a_{131}\cdot a_{223}\cdot a_{312}-a_{132}\cdot a_{211}\cdot a_{323}$$
$$+a_{132}\cdot a_{213}\cdot a_{321}+a_{132}\cdot a_{221}\cdot a_{313}-a_{132}\cdot a_{223}\cdot a_{311}+a_{133}\cdot a_{211}\cdot a_{322}-a_{133}\cdot a_{212}\cdot a_{321}$$
$$-a_{133}\cdot a_{221}\cdot a_{312}+a_{133}\cdot a_{222}\cdot a_{311}.$$

If we compare results of above equations, we can see that we have the same result in both cases.

Remark: This theorem does not hold for plan "Horizontal Layers".

Theorem 3:
Suppose that A is 3D Determinant with two identical "Vertical Pages" or two identical "Vertical Layers".

Then $|A|=0$.

Proof:

Case 1: The cubic-matrix A of order 2 with two identical "Vertical Pages" or two identical "Vertical Layers", we will proof the case 1, as following:
1. For two identical "Vertical Pages":

$$det(A_{[2\times2\times2]})=\begin{pmatrix}a_{111} & a_{111}|a_{112} & a_{112}\\ a_{211} & a_{211}|a_{212} & a_{212}\end{pmatrix}=a_{111}\cdot a_{212}-a_{112}\cdot a_{211}-a_{111}\cdot a_{212}+a_{112}\cdot a_{211}=0.$$

2. For two identical "Vertical Layers":

$$det(A_{[2\times2\times2]})=\begin{pmatrix}a_{111} & a_{121}|a_{111} & a_{121}\\ a_{211} & a_{221}|a_{211} & a_{221}\end{pmatrix}=a_{111}\cdot a_{221}-a_{111}\cdot a_{221}-a_{121}\cdot a_{211}+a_{121}\cdot a_{211}=0.$$

Case 2: The cubic-matrix A of order 3 with two identical "Vertical Pages" or two identical "Vertical Layers", we will proof the case 1, as following:

1. For two identical "Vertical Pages", first "Vertical Page" identical to second "Vertical Page":

$$det(A_{[3\times3\times3]})=det\begin{pmatrix}a_{111} & a_{111} & a_{131}|a_{112} & a_{112} & a_{132}|a_{113} & a_{113} & a_{133}\\ a_{211} & a_{211} & a_{231}|a_{212} & a_{212} & a_{232}|a_{213} & a_{213} & a_{233}\\ a_{311} & a_{311} & a_{331}|a_{312} & a_{312} & a_{332}|a_{313} & a_{313} & a_{333}\end{pmatrix}$$
$$=a_{111}\cdot a_{212}\cdot a_{333}-a_{111}\cdot a_{232}\cdot a_{313}-a_{111}\cdot a_{213}\cdot a_{332}+a_{111}\cdot a_{233}\cdot a_{312}-a_{112}\cdot a_{211}\cdot a_{333}$$
$$+a_{112}\cdot a_{213}\cdot a_{331}+a_{112}\cdot a_{231}\cdot a_{313}-a_{112}\cdot a_{233}\cdot a_{311}+a_{113}\cdot a_{211}\cdot a_{332}-a_{113}\cdot a_{212}\cdot a_{331}$$
$$-a_{113}\cdot a_{231}\cdot a_{312}+a_{113}\cdot a_{232}\cdot a_{311}-a_{111}\cdot a_{212}\cdot a_{333}+a_{111}\cdot a_{213}\cdot a_{332}+a_{111}\cdot a_{232}\cdot a_{313}$$
$$-a_{111}\cdot a_{233}\cdot a_{312}+a_{112}\cdot a_{211}\cdot a_{333}-a_{112}\cdot a_{213}\cdot a_{331}-a_{112}\cdot a_{231}\cdot a_{313}+a_{112}\cdot a_{233}\cdot a_{311}$$
$$-a_{113}\cdot a_{211}\cdot a_{332}+a_{113}\cdot a_{212}\cdot a_{331}+a_{113}\cdot a_{231}\cdot a_{312}-a_{113}\cdot a_{232}\cdot a_{311}+a_{131}\cdot a_{212}\cdot a_{313}$$
$$-a_{131}\cdot a_{213}\cdot a_{312}-a_{131}\cdot a_{212}\cdot a_{313}+a_{131}\cdot a_{213}\cdot a_{312}-a_{132}\cdot a_{211}\cdot a_{313}+a_{132}\cdot a_{213}\cdot a_{311}$$

$$+a_{132}\cdot a_{211}\cdot a_{313}-a_{132}\cdot a_{213}\cdot a_{311}+a_{133}\cdot a_{211}\cdot a_{312}-a_{133}\cdot a_{212}\cdot a_{311}-a_{133}\cdot a_{211}\cdot a_{312}$$
$$+a_{133}\cdot a_{212}\cdot a_{311}=0.$$

2. For two identical "Vertical Pages", first "Vertical Page" identical to third "Vertical Page":

$$det\left(A_{[3\times3\times3]}\right)=det\left(\begin{array}{ccc|ccc|ccc}a_{111}&a_{121}&a_{111}&a_{112}&a_{122}&a_{112}&a_{113}&a_{123}&a_{113}\\a_{211}&a_{221}&a_{211}&a_{212}&a_{222}&a_{212}&a_{213}&a_{223}&a_{213}\\a_{311}&a_{321}&a_{311}&a_{312}&a_{322}&a_{312}&a_{313}&a_{323}&a_{313}\end{array}\right)$$
$$=a_{111}\cdot a_{222}\cdot a_{313}-a_{111}\cdot a_{212}\cdot a_{323}-a_{111}\cdot a_{223}\cdot a_{312}+a_{111}\cdot a_{213}\cdot a_{322}-a_{112}\cdot a_{221}\cdot a_{313}$$
$$+a_{112}\cdot a_{223}\cdot a_{311}+a_{112}\cdot a_{211}\cdot a_{323}-a_{112}\cdot a_{213}\cdot a_{321}+a_{113}\cdot a_{221}\cdot a_{312}-a_{113}\cdot a_{222}\cdot a_{311}$$
$$-a_{113}\cdot a_{231}\cdot a_{322}+a_{113}\cdot a_{212}\cdot a_{321}-a_{121}\cdot a_{212}\cdot a_{313}+a_{121}\cdot a_{213}\cdot a_{312}+a_{121}\cdot a_{212}\cdot a_{313}$$
$$-a_{121}\cdot a_{213}\cdot a_{312}+a_{122}\cdot a_{211}\cdot a_{313}-a_{122}\cdot a_{213}\cdot a_{311}-a_{122}\cdot a_{211}\cdot a_{313}+a_{122}\cdot a_{213}\cdot a_{311}$$
$$-a_{123}\cdot a_{211}\cdot a_{312}+a_{123}\cdot a_{212}\cdot a_{311}+a_{123}\cdot a_{211}\cdot a_{312}-a_{123}\cdot a_{212}\cdot a_{311}+a_{111}\cdot a_{212}\cdot a_{323}$$
$$-a_{111}\cdot a_{213}\cdot a_{322}-a_{111}\cdot a_{222}\cdot a_{313}+a_{111}\cdot a_{223}\cdot a_{312}-a_{112}\cdot a_{211}\cdot a_{323}+a_{112}\cdot a_{213}\cdot a_{321}$$
$$+a_{112}\cdot a_{221}\cdot a_{313}-a_{112}\cdot a_{223}\cdot a_{311}+a_{113}\cdot a_{211}\cdot a_{322}-a_{113}\cdot a_{212}\cdot a_{321}-a_{113}\cdot a_{221}\cdot a_{312}$$
$$+a_{113}\cdot a_{222}\cdot a_{311}=0.$$

3. For two identical "Vertical Pages", second "Vertical Page" identical to third "Vertical Page":

$$det\left(A_{[3\times3\times3]}\right)=det\left(\begin{array}{ccc|ccc|ccc}a_{111}&a_{121}&a_{121}&a_{112}&a_{122}&a_{122}&a_{113}&a_{123}&a_{123}\\a_{211}&a_{221}&a_{221}&a_{212}&a_{222}&a_{222}&a_{213}&a_{223}&a_{223}\\a_{311}&a_{321}&a_{321}&a_{312}&a_{322}&a_{322}&a_{313}&a_{323}&a_{323}\end{array}\right)$$
$$=a_{111}\cdot a_{222}\cdot a_{323}-a_{111}\cdot a_{222}\cdot a_{323}-a_{111}\cdot a_{223}\cdot a_{322}+a_{111}\cdot a_{223}\cdot a_{322}-a_{112}\cdot a_{221}\cdot a_{323}$$
$$+a_{112}\cdot a_{223}\cdot a_{321}+a_{112}\cdot a_{221}\cdot a_{323}-a_{112}\cdot a_{223}\cdot a_{321}+a_{113}\cdot a_{221}\cdot a_{322}-a_{113}\cdot a_{222}\cdot a_{321}$$
$$-a_{113}\cdot a_{221}\cdot a_{322}+a_{113}\cdot a_{222}\cdot a_{321}-a_{121}\cdot a_{212}\cdot a_{323}+a_{121}\cdot a_{213}\cdot a_{322}+a_{121}\cdot a_{222}\cdot a_{313}$$
$$-a_{121}\cdot a_{223}\cdot a_{312}+a_{122}\cdot a_{211}\cdot a_{323}-a_{122}\cdot a_{213}\cdot a_{321}-a_{122}\cdot a_{221}\cdot a_{313}+a_{122}\cdot a_{223}\cdot a_{311}$$
$$-a_{123}\cdot a_{211}\cdot a_{322}+a_{123}\cdot a_{212}\cdot a_{321}+a_{123}\cdot a_{221}\cdot a_{312}-a_{123}\cdot a_{222}\cdot a_{311}+a_{121}\cdot a_{212}\cdot a_{323}$$
$$-a_{121}\cdot a_{213}\cdot a_{322}-a_{121}\cdot a_{222}\cdot a_{313}+a_{121}\cdot a_{223}\cdot a_{312}-a_{122}\cdot a_{211}\cdot a_{323}+a_{122}\cdot a_{213}\cdot a_{321}$$
$$+a_{122}\cdot a_{221}\cdot a_{313}-a_{122}\cdot a_{223}\cdot a_{311}+a_{123}\cdot a_{211}\cdot a_{322}-a_{123}\cdot a_{212}\cdot a_{321}-a_{123}\cdot a_{221}\cdot a_{312}$$
$$+a_{123}\cdot a_{222}\cdot a_{311}=0.$$

4. For two identical "Vertical Layers", first "Vertical Layer" identical to second "Vertical Layer":

$$det\left(A_{[3\times3\times3]}\right)=det\left(\begin{array}{ccc|ccc|ccc}a_{111}&a_{121}&a_{131}&a_{111}&a_{121}&a_{131}&a_{113}&a_{123}&a_{133}\\a_{211}&a_{221}&a_{231}&a_{211}&a_{221}&a_{231}&a_{213}&a_{223}&a_{233}\\a_{311}&a_{321}&a_{331}&a_{311}&a_{321}&a_{331}&a_{313}&a_{323}&a_{333}\end{array}\right)$$
$$=a_{111}\cdot a_{221}\cdot a_{333}-a_{111}\cdot a_{231}\cdot a_{323}-a_{111}\cdot a_{223}\cdot a_{331}+a_{111}\cdot a_{233}\cdot a_{321}-a_{111}\cdot a_{221}\cdot a_{333}$$
$$+a_{111}\cdot a_{223}\cdot a_{331}+a_{111}\cdot a_{231}\cdot a_{323}-a_{111}\cdot a_{233}\cdot a_{321}+a_{113}\cdot a_{221}\cdot a_{331}-a_{113}\cdot a_{221}\cdot a_{331}$$
$$-a_{113}\cdot a_{231}\cdot a_{321}+a_{113}\cdot a_{231}\cdot a_{321}-a_{121}\cdot a_{211}\cdot a_{333}+a_{121}\cdot a_{213}\cdot a_{331}+a_{121}\cdot a_{231}\cdot a_{313}$$
$$-a_{121}\cdot a_{233}\cdot a_{311}+a_{121}\cdot a_{211}\cdot a_{333}-a_{121}\cdot a_{213}\cdot a_{331}-a_{121}\cdot a_{231}\cdot a_{313}+a_{121}\cdot a_{233}\cdot a_{311}$$
$$-a_{123}\cdot a_{211}\cdot a_{331}+a_{123}\cdot a_{211}\cdot a_{331}+a_{123}\cdot a_{231}\cdot a_{311}-a_{123}\cdot a_{231}\cdot a_{311}+a_{131}\cdot a_{211}\cdot a_{323}$$
$$-a_{131}\cdot a_{213}\cdot a_{321}-a_{131}\cdot a_{221}\cdot a_{313}+a_{131}\cdot a_{223}\cdot a_{311}-a_{131}\cdot a_{211}\cdot a_{323}+a_{131}\cdot a_{213}\cdot a_{321}$$
$$+a_{131}\cdot a_{221}\cdot a_{313}-a_{131}\cdot a_{223}\cdot a_{311}+a_{133}\cdot a_{211}\cdot a_{321}-a_{133}\cdot a_{211}\cdot a_{321}-a_{133}\cdot a_{221}\cdot a_{311}$$
$$+a_{133}\cdot a_{221}\cdot a_{311}=0.$$

5. For two identical "Vertical Layers", first "Vertical Layer" identical to third "Vertical Layer":

$$det\left(A_{[3\times3\times3]}\right)=det\left(\begin{array}{ccc|ccc|ccc}a_{111}&a_{121}&a_{131}&a_{112}&a_{122}&a_{132}&a_{111}&a_{121}&a_{131}\\a_{211}&a_{221}&a_{231}&a_{212}&a_{222}&a_{232}&a_{211}&a_{221}&a_{231}\\a_{311}&a_{321}&a_{331}&a_{312}&a_{322}&a_{332}&a_{311}&a_{321}&a_{331}\end{array}\right)$$
$$=a_{111}\cdot a_{222}\cdot a_{331}-a_{111}\cdot a_{232}\cdot a_{321}-a_{111}\cdot a_{221}\cdot a_{332}+a_{111}\cdot a_{231}\cdot a_{322}-a_{112}\cdot a_{221}\cdot a_{331}$$

$$+a_{112}\cdot a_{221}\cdot a_{331}+a_{112}\cdot a_{231}\cdot a_{321}-a_{112}\cdot a_{231}\cdot a_{321}+a_{111}\cdot a_{221}\cdot a_{332}-a_{111}\cdot a_{222}\cdot a_{331}$$
$$-a_{111}\cdot a_{231}\cdot a_{322}+a_{111}\cdot a_{232}\cdot a_{321}-a_{121}\cdot a_{212}\cdot a_{331}+a_{121}\cdot a_{211}\cdot a_{332}+a_{121}\cdot a_{232}\cdot a_{311}$$
$$-a_{121}\cdot a_{231}\cdot a_{312}+a_{122}\cdot a_{211}\cdot a_{331}-a_{122}\cdot a_{211}\cdot a_{331}-a_{122}\cdot a_{231}\cdot a_{311}+a_{122}\cdot a_{231}\cdot a_{311}$$
$$-a_{121}\cdot a_{211}\cdot a_{332}+a_{121}\cdot a_{212}\cdot a_{331}+a_{121}\cdot a_{231}\cdot a_{312}-a_{121}\cdot a_{232}\cdot a_{311}+a_{131}\cdot a_{212}\cdot a_{321}$$
$$-a_{131}\cdot a_{211}\cdot a_{322}-a_{131}\cdot a_{222}\cdot a_{311}+a_{131}\cdot a_{221}\cdot a_{312}-a_{132}\cdot a_{211}\cdot a_{321}+a_{132}\cdot a_{211}\cdot a_{321}$$
$$+a_{132}\cdot a_{221}\cdot a_{311}-a_{132}\cdot a_{221}\cdot a_{311}+a_{131}\cdot a_{211}\cdot a_{322}-a_{131}\cdot a_{212}\cdot a_{321}-a_{131}\cdot a_{221}\cdot a_{312}$$
$$+a_{131}\cdot a_{222}\cdot a_{311}=0.$$

6. For two identical "Vertical Layers", second "Vertical Layer" identical to third "Vertical Layer":

$$det\left(A_{[3\times3\times3]}\right)=det\left(\begin{array}{ccc|ccc|ccc}a_{111}&a_{121}&a_{131}&a_{112}&a_{122}&a_{132}&a_{112}&a_{122}&a_{132}\\a_{211}&a_{221}&a_{231}&a_{212}&a_{222}&a_{232}&a_{212}&a_{222}&a_{232}\\a_{311}&a_{321}&a_{331}&a_{312}&a_{322}&a_{332}&a_{312}&a_{322}&a_{332}\end{array}\right)$$
$$=a_{111}\cdot a_{222}\cdot a_{332}-a_{111}\cdot a_{232}\cdot a_{322}-a_{111}\cdot a_{222}\cdot a_{332}+a_{111}\cdot a_{232}\cdot a_{322}-a_{112}\cdot a_{221}\cdot a_{332}$$
$$+a_{112}\cdot a_{222}\cdot a_{331}+a_{112}\cdot a_{231}\cdot a_{322}-a_{112}\cdot a_{232}\cdot a_{321}+a_{112}\cdot a_{221}\cdot a_{332}-a_{112}\cdot a_{222}\cdot a_{331}$$
$$-a_{112}\cdot a_{231}\cdot a_{322}+a_{112}\cdot a_{232}\cdot a_{321}-a_{121}\cdot a_{212}\cdot a_{332}+a_{121}\cdot a_{212}\cdot a_{332}+a_{121}\cdot a_{232}\cdot a_{312}$$
$$-a_{121}\cdot a_{232}\cdot a_{312}+a_{122}\cdot a_{211}\cdot a_{332}-a_{122}\cdot a_{212}\cdot a_{331}-a_{122}\cdot a_{231}\cdot a_{312}+a_{122}\cdot a_{232}\cdot a_{311}$$
$$-a_{122}\cdot a_{211}\cdot a_{332}+a_{122}\cdot a_{212}\cdot a_{331}+a_{122}\cdot a_{231}\cdot a_{312}-a_{122}\cdot a_{232}\cdot a_{311}+a_{131}\cdot a_{212}\cdot a_{322}$$
$$-a_{131}\cdot a_{212}\cdot a_{322}-a_{131}\cdot a_{222}\cdot a_{312}+a_{131}\cdot a_{222}\cdot a_{312}-a_{132}\cdot a_{211}\cdot a_{322}+a_{132}\cdot a_{212}\cdot a_{321}$$
$$+a_{132}\cdot a_{221}\cdot a_{312}-a_{132}\cdot a_{222}\cdot a_{311}+a_{132}\cdot a_{211}\cdot a_{322}-a_{132}\cdot a_{212}\cdot a_{321}-a_{132}\cdot a_{221}\cdot a_{312}$$
$$+a_{132}\cdot a_{222}\cdot a_{311}=0.$$

Scientific Ethics Declaration

The authors declare that the scientific ethical and legal responsibility of this article published in EPSTEM journal belongs to the authors.

Acknowledgements or Notes

* This article was presented as an oral presentation at the International Conference on Technology, Engineering and Science (www.icontes.net) held in Antalya/Turkey on November 16-19, 2023.

References

Amiri, A., Fathy, M., & Bayat, M. (2010). Generalization of some determinantal identities for non-square matrices based on Radic's definition. *TWMS J. Pure Appl. Math, 1*(2), 163-175.

Artin, M. (1991). *Algebra*. Upper Saddle River: Prentice Hall

Bretscher, O. (2005) *Linear algebra with applications* (3rd ed.). Upper Saddle River: Prentice Hall,

Filipi, K., Zaka, O., & Jusufi, A. (2019). The construction of a corp in the set of points in a line of desargues affine plane. *Matematicki Bilten, 43*(1), 27-46.

Lang, S. (1987) *Linear algebra*. Springer.

Makarewicz, A., Pikuta, P., & Szałkowski, D. (2014). Properties of the determinant of a rectangular matrix. Annales Universitatis *Mariae Curie-Skłodowska, sectio A–Mathematica, 68(*1), 31-41.

Milne-Thomson, L. M. (1941). Determinant expansions. *The Mathematical Gazette, 25*(265), 130-135.

Peters, J. F., & Zaka, O. (2023). Dyck fundamental group on Arcwise-connected polygon cycles. *Afrika Matematika, 34*(2), 31.

Poole, D. (2005) *Linear algebra. A modern introduction* (4th ed. ,pp. 265–267). Cengage Learning.

Radic, M. (1966). A definition of the determinant of a rectangular matrix. *Glas. Mat, 1*(21), 17-22.

Radić, M. (2005). About a determinant of rectangular matrix and its geometric interpretation. *Beiträge zur Algebra und Geometrie, 46*(2), 321-349.

Rose, E. H. (2002) *Linear algebra. A pure mathematical approach* (pp. 57-60). Springer

Salihu, A. (2018). A modern modification of Gjonbalaj-Salihu cornice determinant, transformation to semi-diagonal determinant. *International Journal of Mathematics and Computer Science, 13,* 133-138.

Salihu, A., & Marevci, F. (2019a). Determinants order decrease/increase for k orders, interpretation with computer algorithms and comparison. *Computer Science, 9*(2), 501-518.

Salihu, A., & Marevci, F. (2021). Chio's-like method for calculating the rectangular (non-square) determinants: Computer algorithm interpretation and comparison. *European Journal of Pure and Applied Mathematics, 14*(2), 431-450.

Salihu, A., & Zaka, O. (2023a). Some 3D-determinant properties for calculating of cubic-matrix of order 2 and order 3. *Preprints*

Salihu, A., Jusufi, A., & Salihu, F. (2019b). Comparison of computer execution time of cornice determinant calculation. *International Journal of Mathematics and Computer Science, 14,* 9-16.

Salihu, A., Snopçe, H., Ajdari, J., & Luma, A. (2022b). Generalization of Dodgson's condensation method for calculating determinant of rectangular matrices. In *2022 International Conference on Electrical, Computer and Energy Technologies (ICECET)* (pp. 1-6). IEEE.

Salihu, A., Snopce, H., Luma, A., & Ajdari, J. (2022a). Optimization of Dodgson's condensation method for rectangular determinant calculations. *Advanced Mathematical Models & Applications, 7*(3), 264-274.

Salihu, A., Snopce, H., Luma, A., & Ajdari, J. (2022c). Time complexity analysis for Cullis. Radic and Dodgson's generalized/modified method for rectangular determinants calculations. *International Jwenal of Computers and Their Applications, 29*(4), 245-254.

Salihu, A., Snopce, H., Luma, A., & Ajdari, J. (2023b). Comparison of time complexity growth for different methods/algorithms for rectangular determinant calculations. In *2023 International Conference on Recent Trends in Electronics and Communication (ICRTEC)* (pp. 1-6). IEEE.

Schneide, H., & Barker, G.P. (1973) *Matrices and linear algebra* (2nd.ed.). Dover Books on Mathematics

Zaka, O. (2016b). *Contribution to reports of some algebraic structures with affine plane geometry and applications.* Polytechnic University of Tirana, Tirana, Albania.

Zaka, O. (2017). 3D matrix ring with a "common" multiplication. *Open Access Library Journal, 4(*5), 1-11.

Zaka, O. (2018a). A description of collineations-groups of an affine plane. *Libertas Mathematica (new series), 37*(2), 81-96.

Zaka, O. (2018b). Three vertex and parallelograms in the affine plane: Similarity and addition abelian groups of similarly n-vertexes in the Desargues affine plane. *Mathematical Modelling and Applications, 3(*1), 9-15.

Zaka, O. (2019a). Dilations of line in itself as the automorphism of the skew-field constructed over in the same line in Desargues affine plane. *Applied Mathematical Sciences, 13*(5), 231-237.

Zaka, O. (2019d). The general linear group of degree n for 3D matrices GL(n; n; p; F). *Libertas Mathematica, New Series. 39*(1), 13–30.

Zaka, O., & Filipi, K. (2016a). The transform of a line of Desargues affine plane in an additive group of its points. *Journal of Current Research, 8*(7), 34983-34990.

Zaka, O., & Mohammed, M. A. (2020a). Skew-field of trace-preserving endomorphisms, of translation group in affine plane. *Proyecciones (Antofagasta), 39*(4), 835-850.

Zaka, O., & Mohammed, M. A. (2020b). The endomorphisms algebra of translations group and associative unitary ring of trace-preserving endomorphisms in affine plane. *Proyecciones (Antofagasta), 39*(4), 821-834.

Zaka, O., & Peters, J. F. (2019b). Isomorphic-dilations of the skew-fields constructed over parallel lines in the desargues affine plane. *Balkan Journal of Geom. Applications, 25,* 141-157.

Zaka, O., & Peters, J. F. (2019c). Ordered line and skew-fields in the Desargues affine plane. *Balkan Journal of Geom. Appl.. 26,* 141-156.

Zaka, O., & Salihu, A. (2023). Laplace method for calculate the determinant of cubic-matrix of order 2 and order 3. *Preprints*

Author Information

Armend Salihu
Universum International College
Prishtine, Kosovo
Contact e-mail: *ar.salihu@gmail.com*

Orgest Zaka
Agricultural University of Tirana
Tirana, Albania

To cite this article:

Salihu, A. & Zaka, O. (2023). Some 3D-determinant properties for calculating of cubic-matrix of order 2 and order 3. *The Eurasia Proceedings of Science, Technology, Engineering & Mathematics (EPSTEM), 26,* 554-577.

The Eurasia Proceedings of Science, Technology, Engineering & Mathematics (EPSTEM)
ISSN: 2602-3199

The Eurasia Proceedings of Science, Technology, Engineering & Mathematics (EPSTEM), 2023

Volume 26, Pages 578-588

IConTES 2023: International Conference on Technology, Engineering and Science

Point on Wave Energization Strategy and Sequential Phase Shifting for Sympathetic Inrush Current Mitigation in Three-Phase Transformer - Measurement

Abdelghani Yahiou
University of Bouira

Amar Maafa
University of Bouira

Hacene Mellah
University of Bouira

Hamza Sahraoui
University of Chlef

Abdelhafid Bayadi
University of Setif -1-

Xose. M. Lopez-Fernandez
Universidade de Vigo

César M. A. Vasques
Universidade de Aveiro

Abstract: Inrush currents generated when an electrical transformer is energized can achieve great values and cause abnormal difficulties in the power grid. The sympathetic inrush current phenomenon is resulted in the power system when a transformer is energized with the existence of other transformer already energized. The main objective of this article is the attenuation of sympathetic inrush current in a three-phase transformer. The control technique is carried out by the consideration of the residual flux value when de-energizing the transformer as well as respecting the three-phase shifting. Moreover, an experimental setup to measure the inrush current will be presented. Furthermore, a technique for controlling the circuit breaker to energize a 2 kVA three-phase transformer which allows the sympathetic inrush current to be attenuated was also applied and tested in the experimental. The contribution of this paper is that this technique is applied in measurements with an in-depth estimation of the residual flux. The proposed technique made it possible to completely eliminate the sympathetic inrush current.

Keywords: Three-phase transformer, Sympathetic inrush current, Acquisition, Measurements, Control switching.

Introduction

The sympathetic inrush current is a transient phenomenon, in a power system, resulting from the interaction between transformers, i.e. this current appears when a transformer is energized in an electrical system, the latter

containing one or more transformers, but are not put into transient mode (already powered). Figure 1 shows the relationship between flux and inrush current, also how an inrush current is generated in a transformer, therefore, the existence of a residual flux in a transformer core at the time of energizing the latter results in a considerable magnetizing current, which can in some cases reach a value ten times higher than the rated transformer current. from results said that the amplitude of this transient current, called inrush current, can reach the transformer short-circuit current (Steurer & Frohlich, 2002), a good analysis of this phenomenon in several circumstances is mandatory and necessary to make a good design and planning of the protection system. Following this necessity, several analytical and numerical methods have been developed in the literature (Bertagnolli, 1996; Specht, 1951; Holcomb, 1961).

Furthermore, to reduce and mitigate the inrush currents produced when energizing transformers, several methods are developed and proposed. Like that proposed by Cano-González et al. in (Cano-González et al., 2017) where they made a detailed comparison between four strategies, the authors here identified that these strategies are a result of a combination between the possibility of taking into consideration the residual flux in the core of the transformer and the possibility of using circuit breakers with independent poles. It found also Brunke et al. in (Brunke et al., 2001, 2001b), they suggested a strategy to mitigate the inrush current of three-phase and single-phase transformers, they are considered among the first in this field. Therefore, the proposed technique is validated theoretically and by measurement. In addition, this strategy is based on three techniques: Delayed, Rapid and that of taking into consideration the residual flux for a simultaneous closing. To increase the transient inductance and subsequently reduce the inrush current, Cheng et al. (2004) based on the technique of modifying the distribution of the coils of the winding. This technique is considered new in this field. There is also a simple technique based on the integration of a resistance in the neutral of the three-phase transformer, this technique is proposed in (Arand, 2013; Abdulsalam et al., 2017; Abdelsalam et al., 2015; Cui et al. , 2005). This is not enough but the authors exploit the phase shift of the three phases to create a sequential excitation. A method proposed by the authors in (Xu et al., 2005) which uses a photovoltaic source for the elimination of the inrush current; the authors applied an opposing magnetic flux, taking into account the moment of the maneuver. In (Cano-González et al., 2015), the authors used a controllable circuit breaker to isolate the neutral of the transformer, here the residual flow and the sequential one are taken into account. In (Cano-González et al., 2015), a method for isolating the neutral of the three-phase transformer by controlled switching is presented, taking into account the sequential and residual flow of the phases.

There are different paths to limit the interaction of daily transformer energization with load protection and relays. This is what the authors address in (Schramm et al., 2011), They also demonstrated the technique of using resistors connected in parallel with the circuit breakers during transformer energization. First, the circuit breaker is opened so that current inevitably passes through the resistance, and after a short time, the circuit breaker is closed, eliminating the resistance effect. In the article (Rudez et al., 2016), in order to extract the equivalent circuit, the authors used state equations resulting from the resolution of differential equations. This method is modal and is based on a systematic study of the derivation of vectors and eigenvalues. In addition, the authors studied the consequences and impacts of the transient regime on transformers already energized by a transformer energized at full load. In the article we also find a comparison of the measurements results taken using the Wide Area Monitoring System (WAMS) with the simulation results. The authors in (Pontt et al., 2007) have used the technique of reducing the transient current by increasing the impedance of the coil. The technique was implemented to reduce the inrush current and its effects, relying on the tap changer of the connected transformer.

In this study, for measuring the sympathetic inrush current using a dSPACE data acquisition system, an experimental setup with a three-phase transformer will be presented. Then, the residual flux is extracted while the circuit breaker is opened through a strategic technique to estimate the flux waveform. This extracted value is used to erase the instantaneous flux value in the next energization to reduce the sympathetic inrush current in three-phase transformer. Using Faraday's laws, the flux wave is estimated from the voltage wave, and through it the residual flux is induced when the circuit breaker is opened. To reduce the values of the currents resulting from the influence of a transformer under the transient regime on already energized transformers, or the so-called sympathetic inrush current, the method that was proposed by the authors in (Yahiou et al., 2019) was exploited in this work. It is sufficient to calculate the value of the residual flux for only one phase U, and use it as a value to calculate the optimal time to close the circuit breaker without the appearance of the sympathetic calling current, without calculating the optimal time for the other phases V and W. Therefore, by exploiting the time of the phase U, the time of the V and W phases is calculated by adding the value of the phase shift $2*\pi/3$ and $2*\pi/3$ respectively. The technique proposed here is applied to real-time measurements.

Relationship between Inrush Current and Magnetic Flux

When energizing of any unloaded transformer, it will result in the presence of an unloaded current in the steady state and the inrush current in the transient regime. This current has a direct relationship with the magnetic flux waveform of the transformer core, and this is what Figure 1 shows. As shown in the figure, one of the most important reasons that leads to the appearance of an inrush current at the instant of transformer energization is the presence of residual flux in the core (it can reach values that exceed ten times the nominal current of the transformer). In the normal case (no residual flux), there is only the magnetizing current to the transformer at the operating moment.

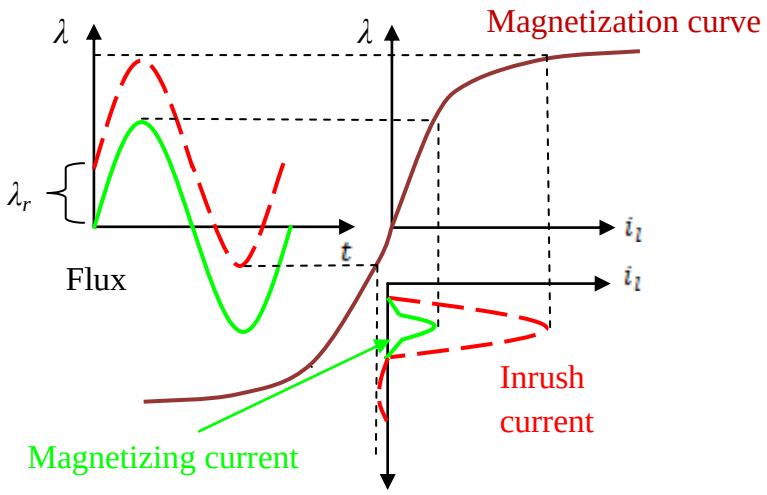

Figure 1. Relationship between inrush current and magnetic flux

Test Proceedings and Measurement Setup

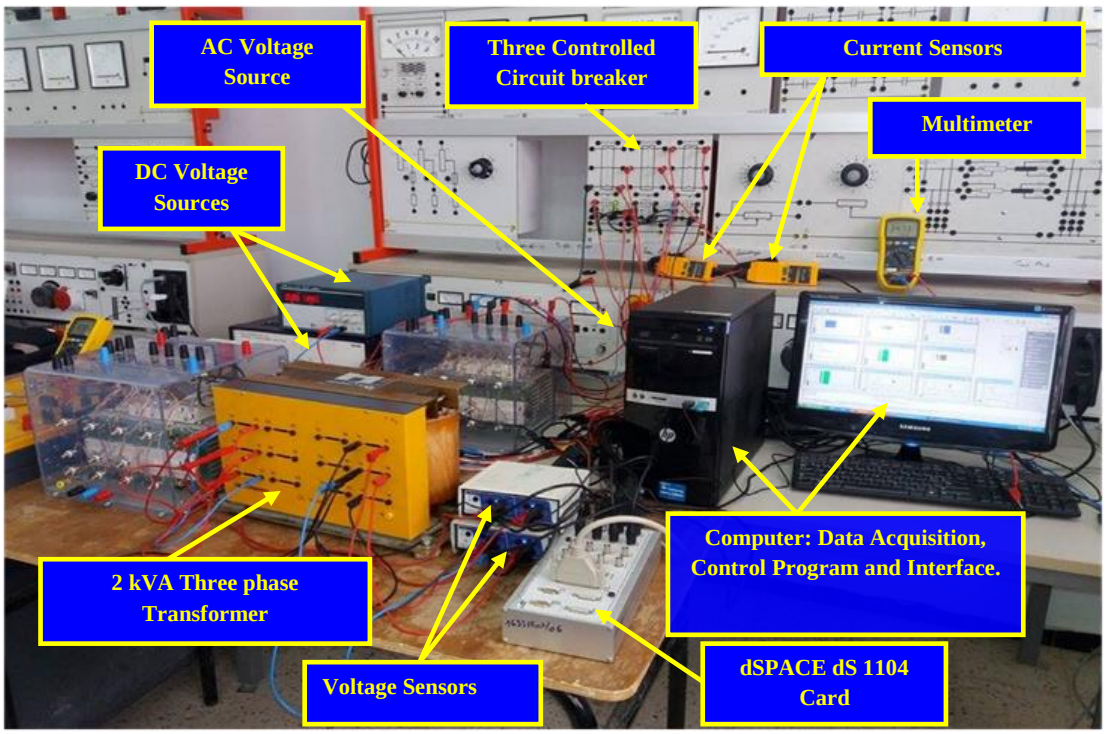

Figure 2. Laboratory setup for inrush current measurement.

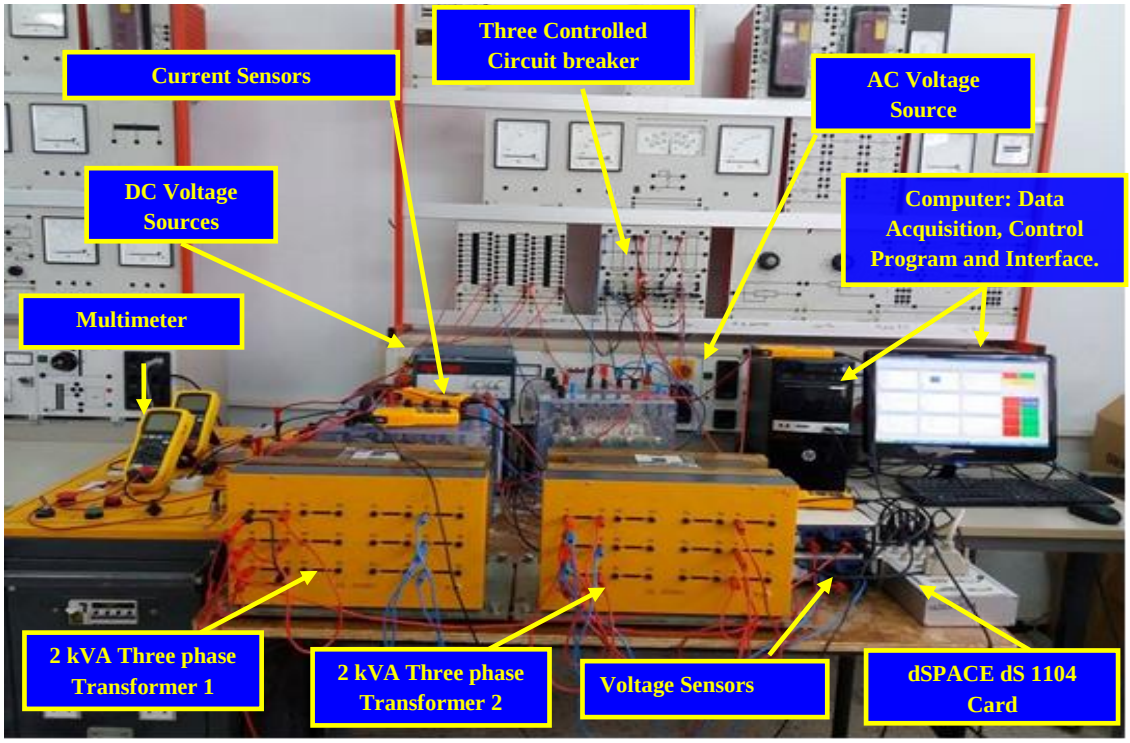

Figure 3. Sympathetic inrush current measurement setup.

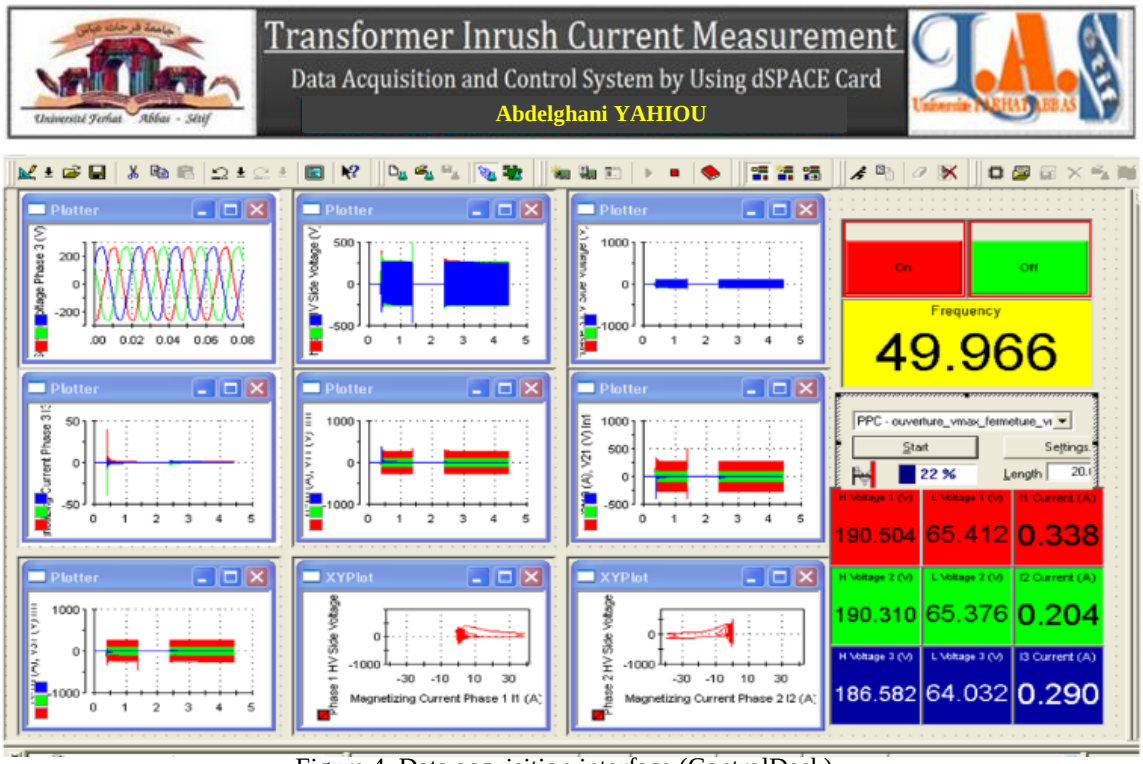

Figure 4. Data acquisition interface (ControlDesk).

Figures 2 and 3 respectively show a setup picture of the inrush current measurement and a setup picture of the sympathetic inrush current measuring for a three-phase transformer, with the label of each part used. The 2kVA transformer is supplied by three-phase power source through a voltage of 220 volts. The applied voltage and magnetizing current are measured using a voltage probe and a current sensor respectively. Using the ControlDesk program installed in the computer with the data acquisition system (dSPACE 1104 card), we can obtain waveforms for various quantities (voltage and current). We obtain the same waves using a digital

oscilloscope to confirm those of computer. Figure 4 is the ControlDesk interface, through which all data are obtained and stored in the MATLAB program

Random sympathetic Inrush current

For the random energization, Figure 5 represents the measurement waveforms of the sympathetic inrush current in the second transformer T2 (already energinzed) resulted by the interaction with transformer T1 (under inrush current).

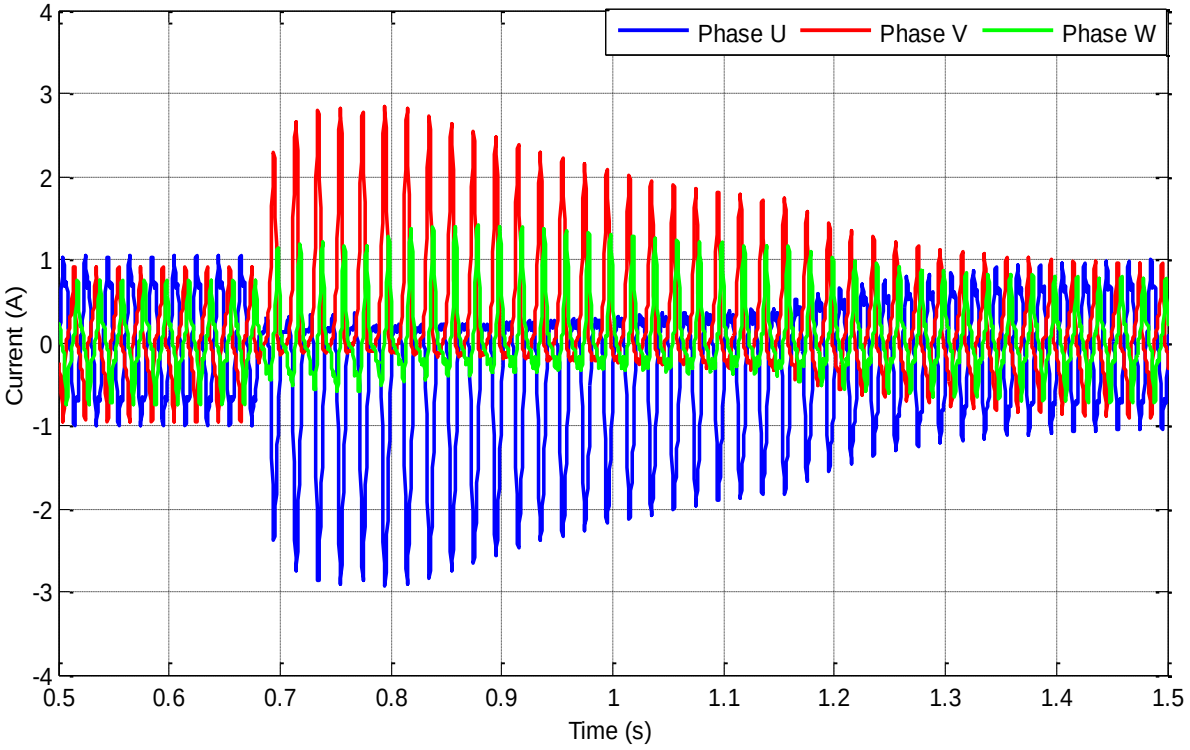

Figure 5. Sympathetic inrush current of transformer T2.

Sympathetic Inrush Current Mitigation

This part of the article is devoted to presenting the proposed sympathetic current reduction technique. MATLAB was used as program with dSPACE to apply the proposed technique on three-phase transformer, and the laboratory measurement results showed the extent of its effectiveness in mitigation of this transient current. Calculating the optimal closing moment is the basis of the technique applied to the transformer T1 under the inrush current. This calculation is done by taking into account the point on the voltage wave and the appropriate value of the residual flux, of course for phase U only, and also acquiring the value of the residual flux for the next process. Regarding the two phases (V and W), the optimal timing is calculated by adding the phase shifting with the U phase

Control Process

Here in this part, the method of closing and opening the circuit breaker is presented, whether using the proposed control technique or the random state. The first energization of transformer T1 is random. After a short closing period, there is also a random opening of the circuit breaker. Then there is a second energization of the same transformer with the application of the proposed technique. Here, the information stored when the breaker is opened is taken and matched to the appropriate point on the voltage wave, and used as data to calculate the ideal time to close the breaker for turn U without appearance of the sympathetic current. Transformer 2 is already supplied and is not concerned with any opening or closing of the breaker. In order to ensure the effectiveness of

this technique, its similar and good results in the field of sympathetic current mitigation, the previous operations are repeated five times before the results can be judged (Figure 6).

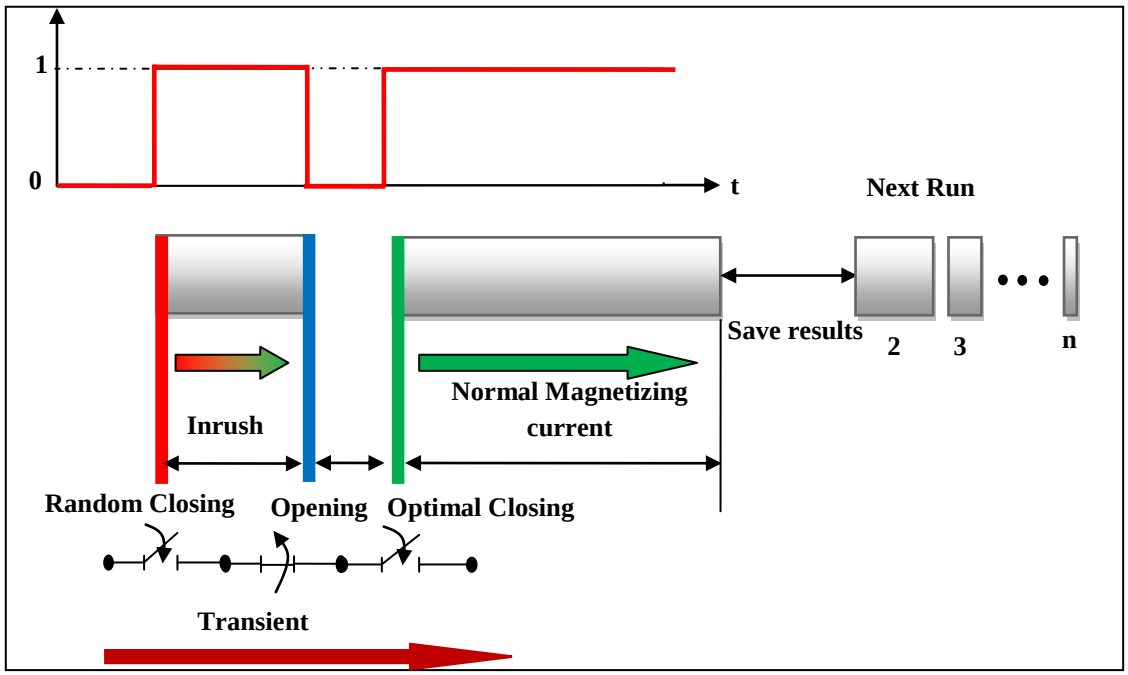

Figure 6. Process of opening and closing the circuit breaker

Principle of Controlled Switching

As is the case with magnetic circuits (here, the case of a coiled transformer core), considering that the electric voltage wave is completely sinusoidal, applying the laws of magnetization there is a proportionality and relationship between the electrical voltage *v* applied to the coil and the magnetic flux in the core. The method for calculating the optimal closing time, for phase U, of the circuit breaker is the same as that used in the article (Yahiou et al., 2019)

Figure 7 is a graphical illustration of the various stages of opening and closing the breaker using the control technique, it illustrate the relationship between the two waveforms of the applied voltage *v* and the magnetic flux λ. In addition, in order to avoid a decrease or change in the value of the residual flux, the time between opening and closing is not large. The various stages in the proposed technique are explained in the flow chart of Figure 8.

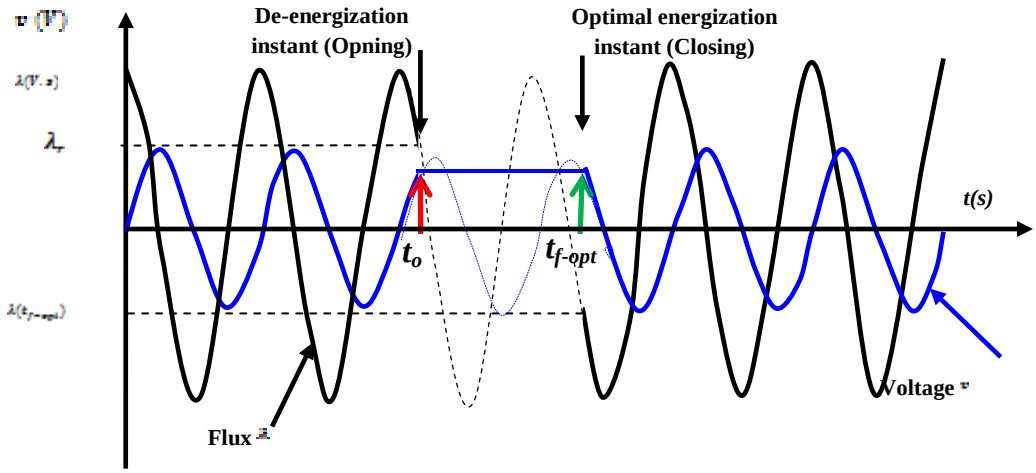

Figure 7. Optimal switching time and relationship between flux and votage.

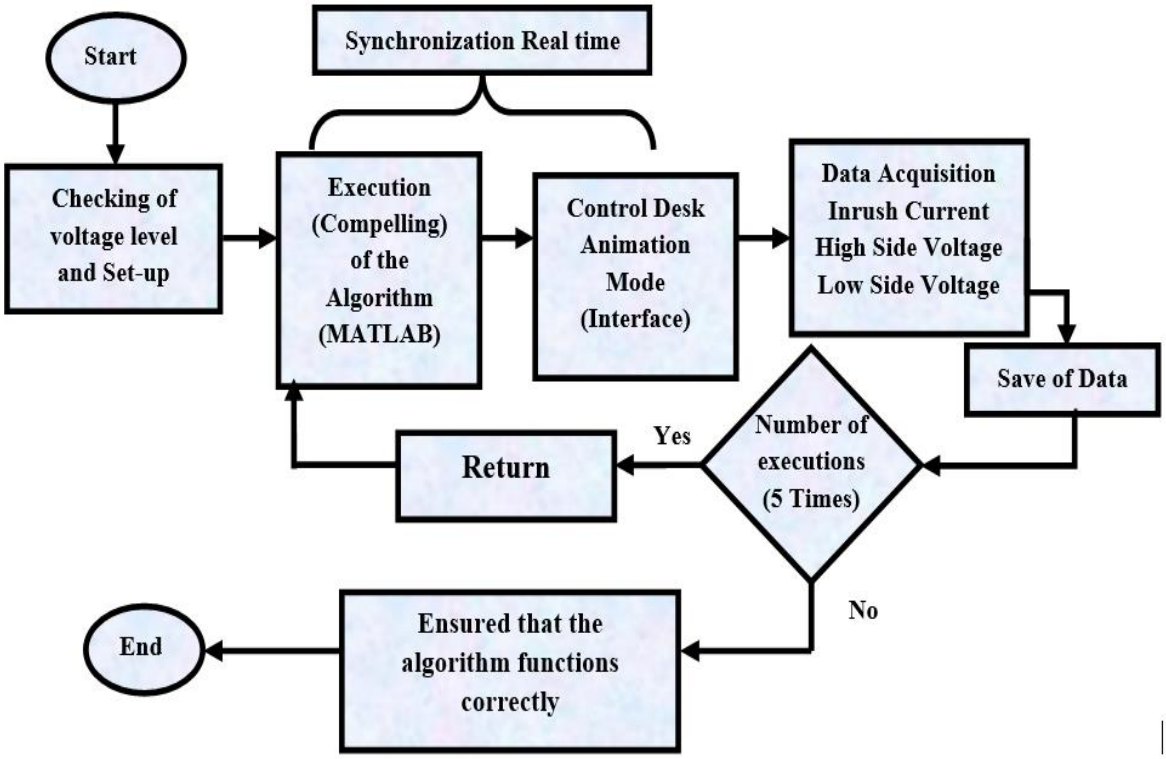

Figure 8. Flow chart of the proposed technique stages.

Control Technology and its Application in Real Time

The technique for calculating the flux values to be used to control the breaker is shown in Figure 6. The following stages explain the steps of this technique and the measurement in real time:7

1- The identical three-phase transformers T1 and T2 are connected in parallel, and the high-voltage side is supplied by source with a voltage value of 220 volts, which is the nominal value. Measurement signals are obtained through measuring instruments.
2- To be able to achieve synchronization between the sinusoidal signal of the simulation program (MATLAB) and the pressure signal used in the measurement, a Phase-Locked Loop (PLL) was used. The goal of this synchronization is to detect the crossing point of the voltage signal through the zero point. Here an order is given to the three breakers to close, regardless of the value of the residual flux.
3- The magnetic flux signal of the same phase is estimated by integrating the voltage signal U.
4- Estimate the residual flux value at the opening instant of the circuit breaker via ControlDesk interface.
5- After calculating the optimal time for closing the circuit breaker on phase U, the ControlDesk interface is used in synchronous with executing the MATLAB program.
6- For the two phases U and W, the circuit breaker is closed after the phase U with a small time difference estimated as the phase shifting.
7- In all previous steps, the three-phase transformer T2 is always supplied.

Figure 9 and Figure 10 display respectively a flow chart of the steps for estimating the optimal time for closing the breakers, as well as an illustrative diagram of the alternation of the three phases when the breakers are closed.

The advantage of the technique proposed in this article is that the optimal time for closing the breaker is calculated for only one phase U. This calculation is used to estimate the optimal time for closing the breaker for the two other phases V and W, by adding the phase shifting, respectively, of 2*π/3 and 4*π. /3.

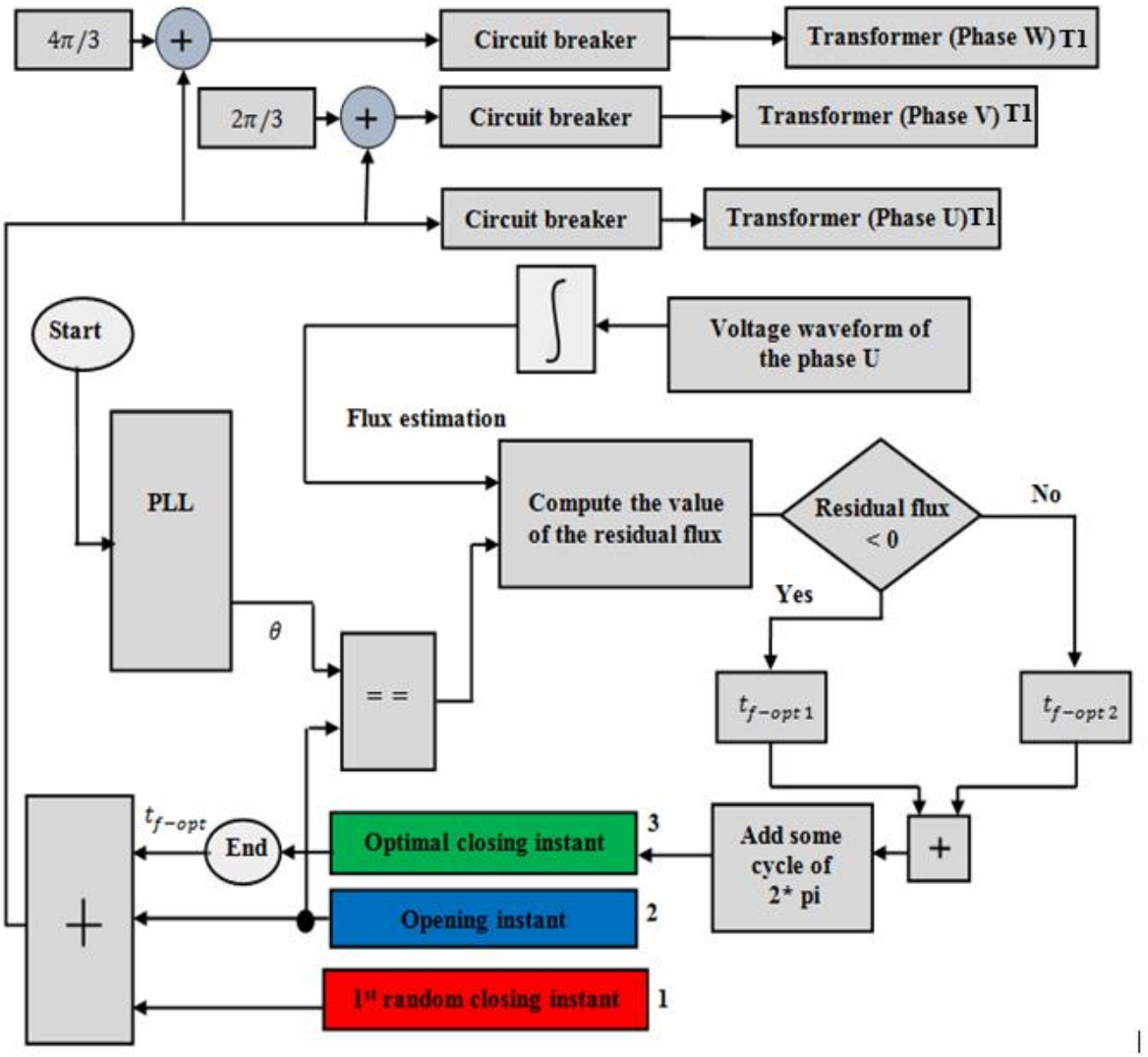

Figure 9. Diagram of the time and flux estimation steps

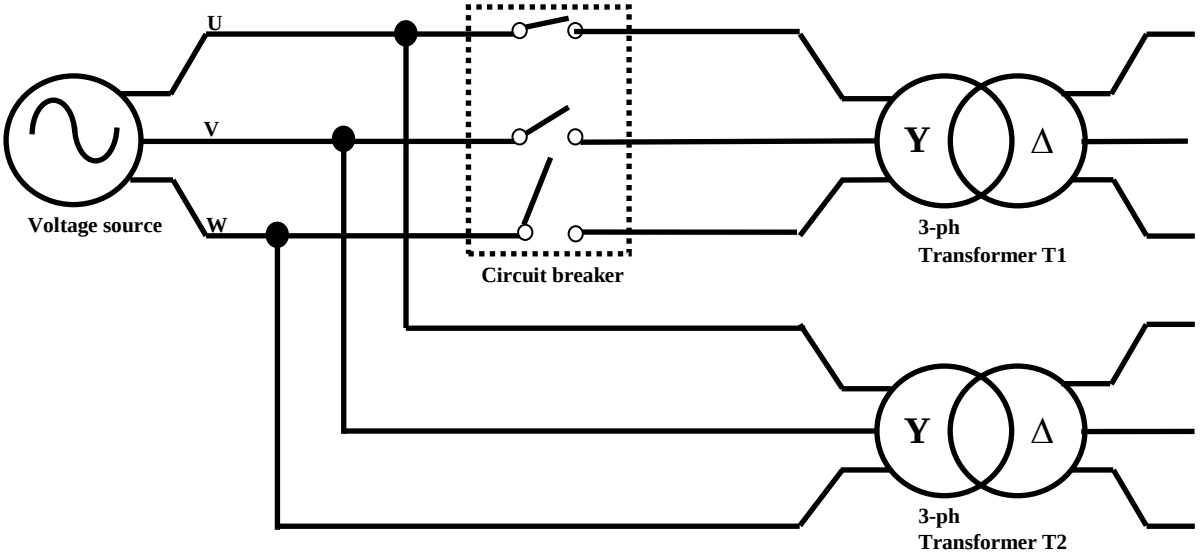

Figure 10. Illustrative diagram of the phase shifting energization

Results

Figures 11 and 12 are the obtained results for applying the proposed technique for sympathetic inrush current reduction in real-time measurements. When the circuit breaker is opened, the value of the residual magnetic flux in the core is estimated. This quantity is taken into account in calculating the optimal time to close the circuit in a controlled and not random manner. So we do not find any presence of the sympathetic inrush current for transformer T2.

As can be observed from Figure 11 and Figure 12, it is clear that from the experimental results there is reduction of the sympathetic inrush current in three-phase transformer T2. The sympathetic inrush is decrease to the no-load current value regardless of the residual flux pattern. A significant attenuation of sympathetic current has been reached since the de-excitation and excitation are controlled, the open and close of the circuit-breaker is made at the same point on voltage wave. The effectiveness of the proposed controlled switching was confirmed and has a direct influence on the re-energization of the transformer.

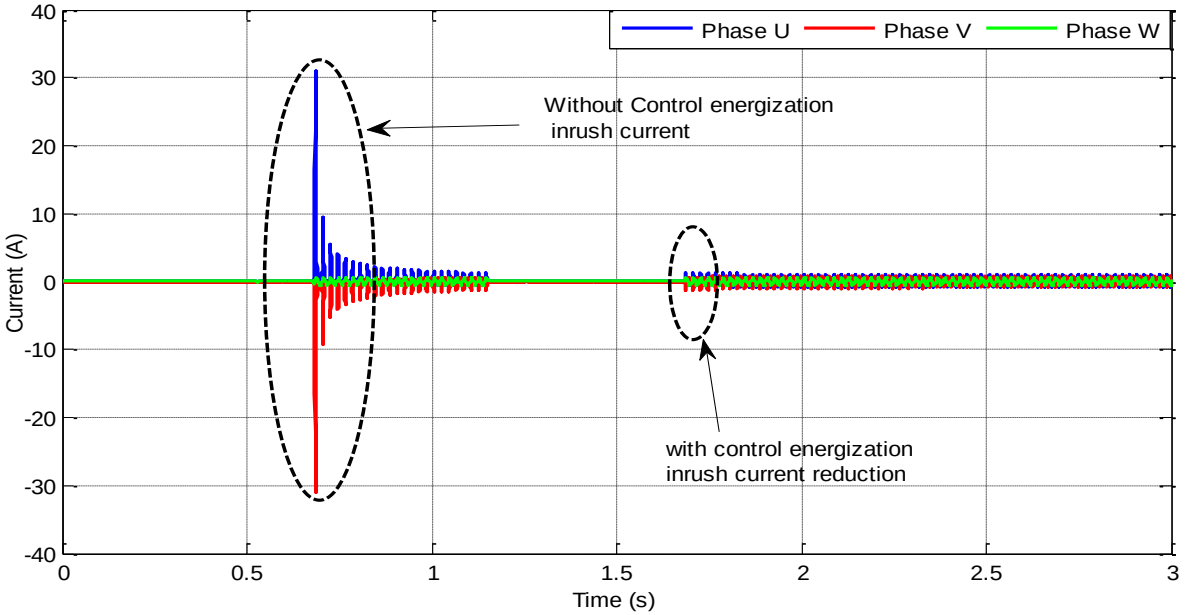

Figure 11. Inrush current mitigation by controlled switching of transformer T1.

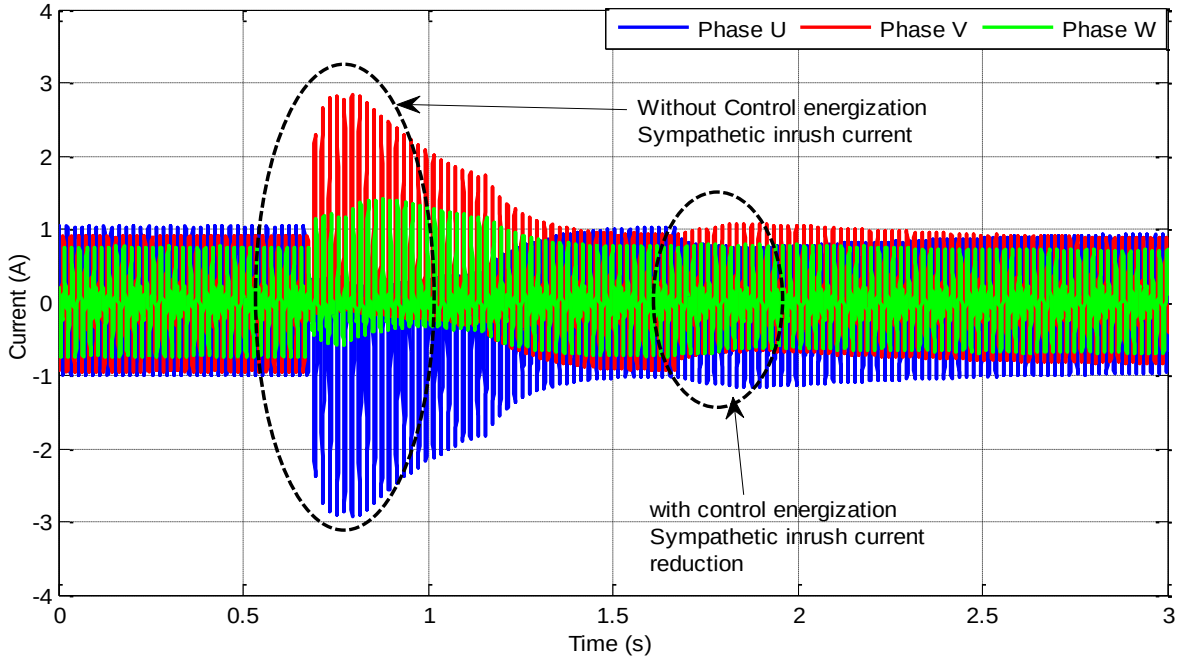

Figure 12. Sympathetic inrush current mitigation by controlled switching of transformer T2.

Conclusion

The work proposed in this article summarizes a set of software experiments carried out with the aim of measuring the inrush current and the sympathetic current resulting from the influence of a transformer situated under the transient regime on a transformer connected to the electrical network and already energized. The main goal of this completed work is to propose a technique that enables us to reduce, or rather eliminate, this sympathetic current in three-phase transformers. The proposed technique depends mainly on finding a point on wave of the electric voltage, and thus the magnetic flux is proportional to the value of the residual flux in the core of the first transformer, from which the sum of the two values equals zero. The proposed technique was demonstrated practically through experiments in the laboratory using the data acquisition system (dSPACE card).

The results obtained proved the accuracy of the technique in eliminating the sympathetic current. The advantage of the technique proposed in this article is that the optimal time for closing the breaker is calculated for only one phase U. This calculation is used to estimate the optimal time for closing the breaker for the two other phases V and W, by adding the phase shifting. The proposed technique resulted in complete attenuation of sympathetic outflow. The technique applied here is in the experiment with a good study of the residual flux. Deletion of the inrush current in the first transformer inevitably leads to the deletion of the sympathetic inrush current in the second transformer

Scientific Ethics Declaration

The authors declare that the scientific ethical and legal responsibility of this article published in EPSTEM journal belongs to the authors.

Acknowledgements or Notes

* This article was presented as an oral presentation at the International Conference on Technology, Engineering and Science (www.icontes.net) held in Antalya/Turkey on November 16-19, 2023.

References

Abdelsalam, H. A., & Abdelaziz, A. Y. (2015). A new strategy for selection of switching instant to reduce transformer inrush current in a single-phase grid-connected photovoltaic system. *Electric Power Components and Systems*, *43*(11), 1297–1306.

Abdulsalam, S. G., & Xu, W. (2007). A sequential phase Energization method for Transformer inrush current reduction& Amp; mdash: Transient performance and practical considerations. *IEEE Transactions on Power Delivery*, *22*(1), 208–216.

Arand, S. J. (2013). Transformer inrush current mitigation using controlled switching and magnetic flux shunts. *International Journal of Energy and Power Engineering*, *2*(2), 46–53.

Bertagnolli, G. (1996). *Short-circuit duty of Power Transformers: The ABB approach*. Golinelli.

Brunke, J. H., & Frohlich, K. J. (2001b). Elimination of transformer inrush currents by controlled switching. II. application and performance considerations. *IEEE Transactions on Power Delivery*, *16*(2), 281–285.

Cano-González, R., Bachiller-Soler, A., Rosendo-Macías, J. A., & Álvarez-Cordero, G. (2017). Controlled switching strategies for transformer inrush current reduction: A comparative study. *Electric Power Systems Research*, *145*, 12–18. Brunke, J. H., & Frohlich, K. J. (2001). Elimination of transformer inrush currents by controlled switching. I. Theoretical Considerations. *IEEE Transactions on Power Delivery*, *16*(2), 276–280.

Cano-González, R., Bachiller-Soler, A., Rosendo-Macías, J. A., & Álvarez-Cordero, G. (2015). Inrush current mitigation in three-phase transformers with isolated neutral. *Electric Power Systems Research*, *121*, 14–19.

Cheng, C.-K., Liang, T.-J., Chen, J.-F., Chen, S.-D., & Yang, W.-H. (2004). Novel approach to reducing the inrush current of a power transformer. *IEE Proceedings - Electric Power Applications*, *151*(3), 289–295.

Cui, Y., Abdulsalam, S. G., Chen, S., & Xu, W. (2005). A sequential phase Energization technique for transformer inrush current reduction— part I: Simulation and experimental results. *IEEE Transactions on Power Delivery*, *20*(2), 943–949.

Holcomb, J. E. (1961). Distribution transformer magnetizing inrush current. *Transactions of the American Institute of Electrical Engineers. Part III: Power Apparatus and Systems*, *80*(3), 697–702.

Pontt, J., Rodriguez, J., San Martin, J., & Aguilera, R. (2007). Mitigation of sympathetic interaction between power transformers fed by long overhead lines caused by inrush transient currents. *2007 IEEE Industry Applications Annual Meeting*.

Rudez, U., & Mihalic, R. (2016). Sympathetic inrush current phenomenon with loaded transformers. *Electric Power Systems Research*, *138*, 3–10.

Schramm, S., Sihler, C., & Rosado S., (2011). Limiting sympathetic interaction between transformers caused by inrush transients. *International Conference on Power Systems Transients IPST*, Netherlands, 11IPST053. Retrieved from https://www.ipstconf.org

Specht, T. R. (1951). Transformer magnetizing inrush current. *Transactions of the American Institute of Electrical Engineers*, *70*(1), 323–328.

Steurer, M., & Frohlich, K. (2002). The impact of inrush currents on the mechanical stress of high voltage power transformer coils. *IEEE Transactions on Power Delivery*, *17*(1), 155–160.

Xu, W., Abdulsalam, S. G., Cui, Y., & Liu, X. (2005). A sequential phase Energization technique for transformer inrush current reduction—part II: Theoretical Analysis and design guide. *IEEE Transactions on Power Delivery*, *20*(2), 950–957.

Yahiou, A., Bayadi, A., & Babes, B. (2019). Modified method for transformer magnetizing characteristic computation and point-on-wave control switching for inrush current mitigation. *International Journal of Circuit Theory and Applications*, *47*(10), 1664–1679.

Author Information

Abdelghani Yahiou
Department of Electrical Engineering, University of Bouira, Algeria.
Automatic Laboratory of Setif (LAS), University of Setif-1-, Algeria.
Contact e-mail: *abdelghani.yahiou@univ-bouira.dz*

Amar Maafa
Department of Electrical Engineering, University of Bouira, Algeria.

Hacene Mellah
Department of Electrical Engineering, University of Bouira, Algeria.
Automatic Laboratory of Setif (LAS), University of Setif-1-, Algeria.

Hamza Sahraoui
Department of Electrical Engineering, University of Chlef, Algeria.

Abdelhafid Bayadi
Automatic Laboratory of Setif (LAS), University of Setif-1-, Algeria.

Xose. M. Lopez-Fernandez
Department of Electrical Engineering, E. E. Industriales, Universidade de Vigo, Spain

César M. A. Vasques
Department of Mechanical Engineering, Universidade de Aveiro, Aveiro, Portugal

To cite this article:

Yahiou, A., Maafa, A., Mellah, H., Sahraoui H., Bayadi, A., Lopez-Fernandez, X., M., & Vasques, C., V., A., (2023). Point on wave energization strategy and sequential phase shifting for sympathetic inrush current mitigation in three-phase transformer - measurement. *The Eurasia Proceedings of Science, Technology, Engineering & Mathematics (EPSTEM), 26*, 578-588.

The Eurasia Proceedings of Science, Technology, Engineering & Mathematics (EPSTEM)
ISSN: 2602-3199

The Eurasia Proceedings of Science, Technology, Engineering & Mathematics (EPSTEM), 2023

Volume 26, Pages 589-595

IConTES 2023: International Conference on Technology, Engineering and Science

Information Technology Essence of the Heuristic Model for SMART Management in a Medium-Sized Industrial Enterprise

Nikola Bakalov
University of Telecommunications and Post

Iliyan Bakalov
Ministry of Innovation and Growth

Abstract: This article presents the information and technological essence of a qualitatively new generated Heuristic model for SMART management in medium-sized industrial enterprises. A summary is made of the features of heuristics in the modern reality and of the prerequisites necessitating the implementation of heuristic and smart-based tools in a single and comprehensive software programme. The general framework of the mathematical model on which its architecture is based is also defined in order to make a comprehensive description of the structure and information and technological features of the software-based programme. The criterion for optimality, which is targeted in the Heuristic model for SMART management in a medium-sized industrial enterprise and its constituent engineering-technological, financial and production parameters, is presented. The main relationships, tools and approaches in the software programme itself are described. The main characteristics and connections of the software-based program of the Heuristic model for SMART management in the medium-sized industrial enterprise are presented.

Keywords: Information technology, Heuristic model, SMART management, Medium-sized industrial enterprise

Introduction

Today, the concept of heuristics has been repeatedly transformed in view of the challenges and requirements of information technology and artificial intelligence. The heuristic model in modern literature is understood in the context of logical thinking. In it, through heuristic methods, the reasoning process is observed or recreated by posing questions, drawing schemes and diagrams, building assumptions, examining the problem from different points of view. It is a kind of examination of directions however based on a specific logical framework. In this line of thought, a heuristic model is a study having its own structure and a defined space for discovering a solution to specific problems.

In modern smart information systems, heuristic models are not driven by psychology. They have a specific problem area, the solution to which requires the application of precisely defined heuristic methods and tools. The purpose of SMART heuristic models is to improve certain indicators, to provide information on the favourable elaboration of the problem embedded in the model.

Heuristic models are most often objectified when there is no precise and comprehensive algorithm for solving a specific case. In some situations, however, it is possible to apply heuristic techniques and models to a completely unknown problem, and their application often leads to reaching a solution based on an algorithm. Therefore, many authors (Michalewicz &Fogel, 2010; Polya &Conway, 2014; Pólya et al., 1995) consider that the terms «algorithm» and «heuristics» are different categories of concepts and that algorithms are not applicable in the study of new problems as the new cases are subject to examination by heuristics. An algorithm appears only when a successful solution to a particular task has been reached for the first time and the path to its

achievement is analysed. The term «heuristic search» is often used in the literature (Barr et al., 1981; Ernst & Newell, 1966; Noyes,1992; Winston, 1975) on intelligent systems – an attempt to formulate something that seems common to programmes integrating artificial intelligence. Therefore, heuristic search contributes to the construction of a unified approach leading to solving tasks based on a common paradigm (methodology and modelling) for solving problems.

In artificial intelligence programmes, based on clear rules for generating objects, heuristic search matches objects and rules for their generation, resulting in either a new object or an indication of non-matching. The generation of new objects, however, leads to the definition of a tree of objects, in which the heuristic search, defined by the initial situation and aimed at finding a way to the desired situation, should be implemented. The heuristic search is also about finding a solution „in the dark" in parallel with the search for a relevant outcome from a specific case study using a tree of objects. This is a search within a specific space in AI-based programmes based on a certain state of the object, based on heuristic decision-making processes.

Heuristic search within a tree of objects, as well as its algorithmic basis, lead to the introduction of plausible, but not always correct, procedures that are an integral part of computer programmes. On this basis, programming can be defined as a process of designing programmes based on a certain algorithm, in which procedures based on both partially verified and on absolutely valid, formal and informal reasoning rules are implanted. They may be the result of practical applied research or experiment, or they may derive from certain theories, concepts and laws. Some authors (Raphael, 1976) define them as carriers of "a certain degree of foreboding". In all cases, however, heuristic programming leads to a reduction in the amount of work required to arrive at the solution to a particular case study.

Information and Technological Features of the Heuristic Model for SMART Management in a Medium-Sized Industrial Enterprise

Preconditions

SMART programmes use two main methods to reach a solution to a problem:

- an algorithmic method – procedures that guarantee a solution to a defined case;
- a heuristic method – a set of empirical rules or strategies that operate in practice as a rule. (Solso, 1979)

The SMART based programme is a kind of performance improvement strategy. According to some scientists (Sampson, 1976), the heuristic programming approach to artificial intelligence is one of the most popular and productive approaches today. According to these researchers, however, this is in contrast to another major approach – the simulation of human thought, where the goal is to apply the characteristics of human intelligence.

A SMART-based programme is not a cyber-physical production system because it is not a "robotized model that is able, through a precisely described and machine-simulated algorithm, to analyse and evaluate the environment and to take actions that increase the possibility of achieving certain goals" (Temelkova, 2022). According to some authors, the cyber-physical production system is "an innovative type of human-machine-cyber device ecosystem" that has its real physical manifestation, but also its virtual duplicate corresponding to the real production system in terms of its structure, organization, resources, goal setting and strategy" (Temelkova, 2022).

The heuristic model for SMART management in the medium-sized industrial enterprise presented in this articles operates with several types of heuristics:

- practical – it is different from the theoretical assumption and derives from application;
- region-specific – it is characteristic of a precisely defined scientific field and is related to its characteristic features;
- ad hoc – it arose spontaneously or for a specific case;
- empirical – it establishes the presence of certain facts and trends through experience and practice.

The heuristic model for SMART management in the medium-sized industrial enterprise is based on analogies. It is a set of simplified representations that allow for differentiation of the more important aspects of intelligent management and the specifics of the medium-sized industrial entity. A complex, succinct presentation of the

main elements of the case study is achieved through the analogies. Thus, they appear as partial insights that could evoke new insights that give greater breadth to the studied problem.

The heuristic model for SMART management in a medium-sized industrial enterprise is a combination of theoretical and practical knowledge facilitating the performance of selection and evaluation. The modelling based on criteria, methods, principles, tools seeks to find a solution to a specific production-technical, financial, logistic or other case in the medium-sized industrial enterprise.

The heuristic model for SMART management in the medium-sized industrial enterprise is a complex compilation of procedures and has a hierarchical structure. It is composed of a set of rules for the applicable search strategies and functions regarding the selection and evaluation in the search process. Rules rank higher hierarchically than functions, and the model can also be defined as a strategy for retrospective selection of rules. At the same time, the heuristic model for SMART management in the medium-sized industrial enterprise handles multiple data, process principles, management functions, organizational and structural maps.

The synthesis of the main components serving as basis of the heuristic model for SMART management in the medium-sized industrial enterprise indicates that four fundamental elements should be its invariable part:

- heuristic search;
- algorithm based on artificial intelligence;
- heuristic programming;
- SMART based programme.

General Presentation of the Mathematical Model of the Heuristic Model for SMART Management in the Medium-Sized Industrial Enterprise

The heuristic model for SMART management in the medium-sized industrial enterprise seeks to solve the problems and cases in the industrial unit based on the achievement of optimality or a balanced compromise. This means that criteria that guarantee optimality or a combined compromise should be integrated as objective functions in the mathematical model of the Heuristic model for SMART management in the medium-sized industrial enterprise.

On the basis of the conducted research and the practical and applied developments, a conclusion has been reached that economic efficiency should be set as a target criterion in the Heuristic model for SMART management in the medium-sized industrial enterprise; economic efficiency is a relationship between the value of the utility achieved in the course of an economic activity and the value of the necessary production resources and all other costs incurred in the production and sale of a specific product of the j type. [11] In this respect efficiency is most clearly highlighted through the economic category of production costs per unit of manufactured product that is also used to estimate the economic effect. It is this category that forms the cost.

Therefore:

$$\text{E} = \frac{\text{полезност}}{\text{себестойност}} \quad [1]$$

or:

$$\text{E} = \frac{TR}{CP} \quad [2]$$

where:
TR – total revenue
CP – cost price

Therefore:

$$L = \frac{TR}{CP} \rightarrow \max/\text{compromise} \quad [3]$$

However, the constituent elements of the specified quotient can be expressed as follows:

$$TR = X_j \times P_p \quad [4]$$

$$X_j = \sum_{j=1}^{n} \frac{OH_{PSS}}{IPT} \quad [5]$$

$$CP = \sum_{j=1}^{n} \mathrm{TLTT_d} + \sum_{j=1}^{n} \mathrm{TCMR_{dg}} + \sum_{j=1}^{n} \mathrm{TEC_d} + \sum_{j=1}^{n} \mathrm{TLC_d} + \sum_{j=1}^{n} \mathrm{TCMAR_d} \quad [6]$$

where:

P_p – commodity price of the product formed in a previous production cycle

Therefore, the target criterion has the following mathematical expression:

$$L = \frac{\mathrm{Xj}.P_p}{\sum_{j=1}^{n} \mathrm{TLTT_d} + \sum_{j=1}^{n} \mathrm{TCMR_{dg}} + \sum_{j=1}^{n} \mathrm{TEC_d} + \sum_{j=1}^{n} \mathrm{TLC_d} + \sum_{j=1}^{n} \mathrm{TCMAR_d}} \rightarrow \max/\mathrm{compromise} \quad [7]$$

Information technology software-based programme of the Heuristic model for SMART management in the medium-sized industrial enterprise

The heuristic model for SMART management in the medium-sized industrial enterprise is based on a mathematical model in which multiple limiting conditions are described with limiting target values of certain production-technical and engineering-technological indicators, which derive from the initially set limits. They, in turn, are logical consequences of the limitations set at the stage of input. This facilitates the generation of a hypothesis about the unknown parameters which helps to increase the strength of the limitations and to synthesize new limiting conditions.When a contradiction is reached, the process loops back again to search for a new value of the unknown parameter or to reach a target state based on a sufficiently strong realization of the limiting conditions and satisfying the criterion for evaluation. The rules by which the limitations are distributed and the rules by which the hypotheses are made depend on the specifics of the medium-sized industrial enterprise and on the limiting conditions and evaluation criteria set in the assignment.

The variables subject to optimization or a combined compromise between them are of essential importance in the Heuristic model for SMART management in the medium-sized industrial enterprise. These are, on the one hand, the costs forming the dynamic variable cost of production, and on the other hand, the ratio between the hours of operation of the production system and the ideal production time, determining the quantity produced in terms of in-kind value, which is a dynamic variable in the calculation of the total revenue. On this basis and based on the fact that the limiting conditions are related precisely to these dynamic variables, the information technology model emphasizes precisely on their description, integration and possibilities for implementing various options.

```
public abstract class BaseExpense implements Expense{
    private String name;
    private double time;
    private int reps;
    private double price;

    public BaseExpense(String name, double time, int reps, double price){
        setName(name);
        setTime(time);
        setReps(reps);
        setPrice(price);
    }

    private void setName(String name){
        if (name==null || name.trim().equals("")){
            throw new NullPointerException("Name cannot be empty.");
        }
        this.name = name;
    }

    private void setTime(double time){
        if(time<0){
            throw new IllegalArgumentException("Time cannot be negative number");
        }
        this.time = time;
    }

    private void setReps(int reps){
```

Figure 1. A software programme of the Heuristic Model for SMART Management in the medium-sized industrial enterprise (author's work)

For the purposes of conceptual modelling, the information technologies for the Heuristic Model for SMART management in the medium-sized industrial enterprise are provided on the basis of classes and objects. Thus, the digital counterpart of each expense in the medium-sized industrial enterprise in the model for SMART management based on information technology and heuristics is determined by the abstract class (Base expance). The logic for calculating the cash outlay by types is implemented in the class. All other expense types inherit Base expance – accordingly $TLTT_d$ (total losses of technological time), $TCMR_{dg}$ (total cost of material resources), TEC_d* (total energy costs), TLC_d (total labor costs), $TCMAR_d$ (total costs for machines, automata, robots), CP (cost price). Each of these expenses uses the constructor from Base expance, and the constructor expects a name, the time wjen the expense occurred, the recurrence of the expense, and its value (Figure 1.).

The expanceRepository class has a collection of the expance type as attributes. It does not accept information but initializes the collected data as a list. This class makes it possible to add, remove, find by name, and retrieve (use) all input data on a case-by-case basis. The other part of the efficiency formula – TR (total revenue) – is determined by the Quantity class. The constructor takes the total operating time of the production subsystem and the ideal production time and makes them part of the object of the programming.

The digital counterpart of the price is the Price class. Its constructor accepts a floating point number that represents the cost of the manufactured product. The interaction between the user and the application takes place through a graphical user interface developed on the basis of the Java fx library. The user interacts with the SceneBuilder class and interacts with the programme when entering data. After entering data and pressing a command button, the data is transferred to the Controller class. It has a repository of the expanceRepository type as attributes. In the Controller class all commands are executed, e.g. “save cost” – adds a cost to the cost repository, “delete cost” – removes a cost from the cost repository, “find by name” – finds a cost by keyword name, names are accepted as unique.

The information technology programme, integrating conceptual and heuristic modelling, meets the needs of the Heuristic Model for SMART management in the medium-sized industrial enterprise as it solves the set management tasks by providing an option to enter data by days. This makes possible the recording of trends and expands the possibilities of achieving an optimal solution or a combined compromise solution while at the same time it serves as a possible basis for the strategies for development of the studied economic entity.

```
public class CreateEfficiencyScreen {

    public static void createEfficiencyScreen(Group root, String efficiencyCalculated){
        Rectangle blueRectangle = new Rectangle();
        blueRectangle.setFill(Color.RED);
        blueRectangle.setX(50);
        blueRectangle.setY(0);
        blueRectangle.setWidth(900);
        blueRectangle.setHeight(50);
        root.getChildren().add(blueRectangle);
        Label efficiencyLabel = new Label(String.format("%s", efficiencyCalculated));
        efficiencyLabel.setScaleX(1.5);
        efficiencyLabel.setScaleY(1.5);
        efficiencyLabel.setTranslateY(25);
        efficiencyLabel.setTranslateX(450);
        root.getChildren().add(efficiencyLabel);
```

Figure 2. A software programme of the Heuristic Model for SMART Management in the average industrial enterprise (author’s work)

Results and Discussion

The heuristic model for SMART management in the medium-sized industrial enterprise, and hence its software image, integrates four main features:

- uncertainty;
- incomplete knowledge;

- improved performance;
- decision making guidelines.

The heuristic model for SMART management in the medium-sized industrial enterprise is a unique compilation of:

- subjective uncertainty regarding the success in solving a particular problem arising from the problem's heuristic nature;
- objective security based on the algorithms in the model.

The uncertainty in the model is related to a real practical case that needs to be solved while the algorithms are applied to abstract and theoretical tasks. They provide safe, reliable and good solutions based on the mechanical application of certain logical postulates. However, the search for a solution to a practical assignment cannot be achieved only on a theoretical basis. This is not inherently a heuristic strategy.

The model for SMART management in the medium-sized industrial enterprise is heuristic because there is no guarantee that it is practically optimal for finding optimal options within a space of states. However, the fact that every task finds its optimal solution in the long run should not be overlooked. Therefore, the heuristics in the software-based model for SMART management in the medium-sized industrial enterprise is only possible if it is based on practical problems and integrates practical algorithms on this basis.

When a case is property set the algorithm in the information technology software model offers an exact step-by-step procedure that leads to a solution to the task, using a certain set and amount of resources, or points to the impossibility to solve the task. However, finding a solution to any problem is always related to scarcity of resources – the limitation of the required resources compared to the growing needs for them. Time, space and technological limitations are among the most important resources, but also among the most variable factors for providing a certain solution. It is this uncertainty, influenced by the dynamics of the environment, that introduces uncertainty into every process in the medium-sized industrial enterprise. This also means that there is a need for a heuristic model for its SMART management, because in the conditions of dynamic external and internal organizational factors, guaranteeing a secure, reliable, efficient and optimal solution seems illogical. In reality, the uncertainty in the case of strong variability of the environment factors does not even guarantee a correct solution of the constituent problems of the decomposed case that is the object of solution. This justifies the conclusion that in the heuristic model, and consequently in its software-based programme, the rules that condition the combined compromise decision have an essential place.

Conclusion

The information technology features of the Heuristic Model for SMART management in the medium-sized industrial enterprise are integrated into a software-based programme, in which the following fundamental elements also stand out:

- presence of an unsolved problem, case or assignment;
- a SMART based programme integrating:
  - an algorithm based on artificial intelligence;
  - heuristics based on practice, specificity, empiricism, expertise, or spontaneity;
  - heuristic programming (code);
- an optimal or combined compromise solution, conclusion or inference.

In the software-based programme algorithms and heuristics are integrated by means of code into a single system, and the relations between them are semantically adjusted. They are used to achieve optimality or a combined compromise of the problems, cases or assignments initially defined.

The algorithms in the software programme of the Heuristic Model for SMART Management in the medium-sized industrial enterprise represent a sequence of commands that are performed in order to solve a given task. They are based on:

- artificial intelligence in the form of conditionals;
- cloud servers performing the calculations submitted by the equipment and returning them to the investigated fundamental plane;
- a filter and analysis of large data sets;

- The Internet of Things, interactively connecting every physical element with its digital counterpart;
- additive manufacturing obtained on the basis of a created digital counterpart and a method set for the production of a given physical object.

Scientific Ethics Declaration

The authors declare that the scientific ethical and legal responsibility of this article published in EPSTEM journal belongs to the authors.

Acknowledgements or Notes

* This article was presented as an oral presentation at the International Conference on Technology, Engineering and Science (www.icontes.net) held in Antalya/Turkey on November 16-19, 2023.

References

Barr, A., Feigenbaum, E. A., & Cohen, P. R. (1981). *The handbook of artificial intelligence*. USA: William Kaufmann.

Ernst, G. W., & Newell, A. (1966). *Generality and generality and problem solving.* Carnegie Institute of Technology.

Michalewicz, Z., & Fogel, D. B. (2010). *How to solve it: Modern heuristics*. Berlin – Heidelberg: Springer

Мирчев, А. (1996). *Производствен мениджмънт.* Princeps.

Noyes, J. (1992). *Artificial intelligence with common lisp: Fundamentals of symbolic and numeric processing*. USA: Heath and Company

Polya, G., & Conway, J. H. (2014). *How to solve it: A new aspect of mathematical method*. Princeton University Press.

Pólya, G., Roquette, P., & Behnke, E. (1995). *Schule des denkens: Vom losen mathematischer probleme*. Bern, Francke, A.

Raphael, B. (1976). *The thinking computer: Mind inside matter*. W. H. Freeman.

Sampson, J. R. (1976). *Adaptive information processing*. New York, NY: Springer.

Solso, R. L. (1979). *Cognitive psychology*. NewYork, NY: Harcourt Brace Jovanovich

Temelkova, M. (2022). Model for the organization of a cyber-physical production system. *Intelligent Sustainable Systems - Selected Papers of WorldS42022,* (Vol. 1, pp 703–718).

Temelkova, M. (2022). Model for the organization of a cyber-physical production system. *Intelligent Sustainable Systems - Selected Papers of WorldS42022,* (Vol. 1, pp 785–794).

Winston, P. (1975). *The psychology of computer vision*. NewYork, NY: McGraw-Hill.

Author Information

Nikola Bakalov
University of Telecommunications and Post
Bulgaria, Sofia
Contact e-mail: *nikola_bakalov@abv.bg*

Iliyan Bakalov
Ministry of Innovation and Growth
Bulgaria, Sofia

To cite this article:

Bakalov, N. & Bakalov, I. (2023). Information technology essence of the heuristic model for smart management in a medium-sized industrial enterprise. *The Eurasia Proceedings of Science, Technology, Engineering & Mathematics (EPSTEM), 26,* 589-595.

The Eurasia Proceedings of Science, Technology, Engineering & Mathematics (EPSTEM)
ISSN: 2602-3199

The Eurasia Proceedings of Science, Technology, Engineering & Mathematics (EPSTEM), 2023

Volume 26, Pages 596-603

IConTES 2023: International Conference on Technology, Engineering and Science

Analysing and Evaluation of Routing Protocols in VANET

Bilal Saoud
University of Bouira

Tahar Zireg
University of Bouira

Idir Bouaoud
University of Bouira

Smail Medjedoub
University of Bouira

Abstract: Among the application of Ad Hoc network we have Vehicular Ad Hoc Network (VANET), which is an important data research domain today. VANET can improve the traffic road efficiency in order to overcome many problems and offer more services to customer. For instance, VANET can lead to reduce traffic jam or improve road safety by minimizing vehicles' accident. Like any wireless network without infrastructure, the routing task is the most difficult task especially when nodes are mobile. The mobility of nodes, which are vehicles in VANET, causes a rapid change of network topology and leads to bread connection between source and destination nodes. In this paper, we will analyze some routing protocols in order to evaluate their performances. In this study we have proposed some scenarios of VANET routing protocols. The simulation has been done on NS3 simulator and SUMO. Simulation proves that routing protocols have a huge impact on VANET network performances.

Keywords: VANET, NS3, SUMO, AODV, DSDV, GPSR, OLSR

Introduction

Today wireless communication is very important and it can be used in different areas. Wireless communication has the ability to solve many problems and overcome different issues because of its flexibility and mobility. MaNet (Mobile Ad Hoc Network) (Hui et al., 2022) is an example of wiles communication without exiting of infrastructure. Many studies have been done around Ad Hoc networks. Among application of Ad Hoc networks we can find Vehicular Ad Hoc Network (VANET) (Babu & Raj Kumar, 2022). VANET has been gained a lot of attention by scientists in the last decades. VANET can allow communication and data transmission between vehicles, which allow sharing different kind of information about the state of vehicles, roads, traffic, etc**.**

VANET could be seen as a set of mobile nodes, which are vehicles, and some fixed unites (like roadside). These mobile nodes cooperate together in order to ensure communication and data transmission between source node and destination node. Among the areas of VANET communications we have Vehicle to Vehicle (V2V) communication, Vehicle-to-Infrastructure (V2I) communication, Intra-Infrastructure communication (I2I), Vehicle-to-Sensor communication (V2S), Vehicle-to-Personal Device communication (V2PD), Vehicle-to-Cellular Network infrastructure communication (V2CN). In addition, we can find also Vehicle to Everything communications (V2X) based on emergence of cellular networks. VANET has been used to ensure different services such as infotainment applications, driver assistance, video on demand, etc. Furthermore, VANET

improves significantly safety by warning messages in order to avoid accident. Figure 1 shows the communication between nodes in VANET network.

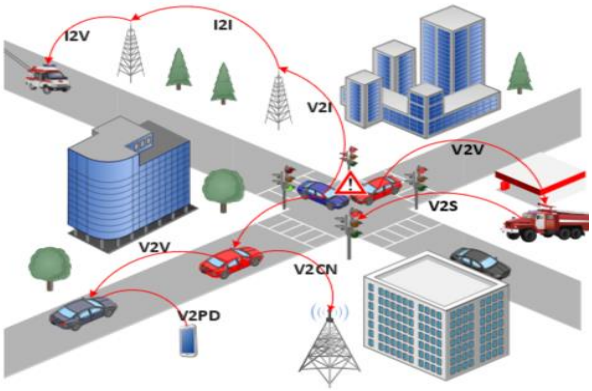

Figure 1. Communication between nodes in VANET network

Routing is a difficult task and is very important to ensure the transmission of data. Data can be sent from node source to destination nodes through many intermediate nodes. The establishment of roads between source node and destination nodes has huge impact on VANET performances such as packet received, errors, link breaks, etc. In this study, some routing protocols for VANET has been studied, analyzed and evaluated in different VANET scenarios. We organize the rest of the paper as follows. Section 2 the architecture of VANET. Section 3 discusses VANET routing protocols. Section 4 discusses simulation and results. Finally, section 5 concludes our paper.

VANET Architecture

VANET offers a wireless communication between mobile vehicles. Communication can be assured based on different standards such as Dedicated Short Range Communication (DSRC), Wireless Access in Vehicular Environments (WAVE). Furthermore, in VANET we have three basic units, which are AU: application unit, OBU: on board unit and RSU: Road side unit. AU unit is a device,which is integrated to vehicle (it can be separated). AU runs applications that communicate with OBU. In generally, AU and OBU are connected through wired or wireless connection. OBU receives, processes and manages data generated from vehicle. OBU unit of each vehicle communicates between each other. Communication between these units is assured by employing a standard of communication like IEEE 802.11 (Szott et al., 2022). RSU is fixed unit, which sends and receives data from OBU units. RSU communicates also with a central center, which is managed generally by government. It is worth to mention that RSU units are fixed in order to provide reliable coverage of network. The VANET architecture is briefly described in Figure 2.

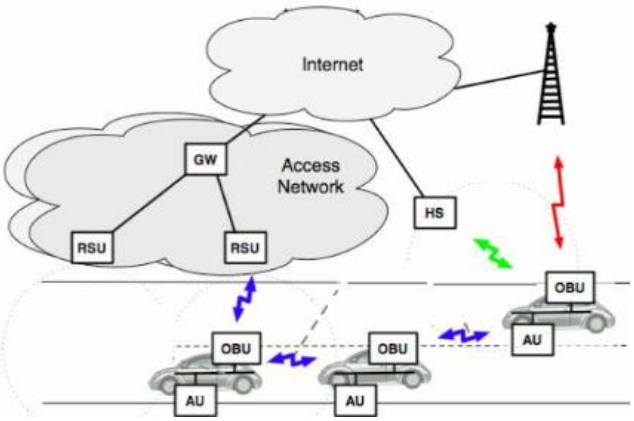

Figure 2. VANET architecture

Routing Protocols in Vanet

Data communication between nodes in VANET is assured based on routing protocols, which means that routing is very important and essential (Poonia, 2017). Among the features of VANET, we find the mobility of nodes.

This feature leads to frequently change of topology. By changing network topology link disruption can appears and keeping communication between nodes becomes a challenge task. VANET routing protocols are classified into topology, position, cluster, broadcast and geocast protocols (Babu & Raj Kumar, 2022). Figure 3 presents the classification of routing protocols in VANET.

Distance-to-Destination Dynamic Dequenced Vector (DSDV)

DSDV is a proactive routing protocol, node periodically transmit its routing tables to its neighbors. A node also transmits their routing table if there is any significant change occurred in their routing table from the last update sent (He, 2002). So each node has a route for any destination node in the network at all-time even the path unused currently.

Optimized Link State Routing Protocol (OLSR)

OLSR is a link state routing protocol (Clausen & Jacquet, 2003). It uses a multi-point relays (MPR) concept. MPR reduces network load when broadcasting the same messages through different nodes.

Routing with Distance-to-Demand Vector (AEDV)

AODV () (Perkins & Royer, 1999), is a reactive protocol. It has been proposed based distance vector strategy. AODV is designed by taking in consideration DSDV and DSR protocol. AODV has two procedures to discovery and maintenance routes ”Route Discovery” and ”Route Maintenance” like the protocol DSR. Routes between nodes update based on sequence numbers. This protocol is very used due to all its characteristics. It is one of the main protocols within the MANET research group.

Greedy Perimeter Stateless Routing (GPSR)

GPSR is a position-based routing protocol, which uses the geographic position of nodes to make the routing decisions(Karp & Kung, 2000). Nodes know their own geographical locations by using global positioning systems (GPS).

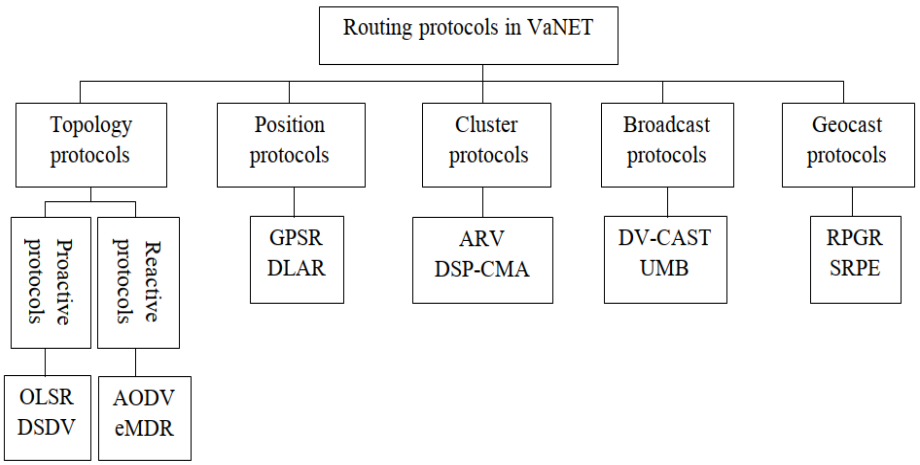

Figure 3. Routing protocols in VANET classification

Simulation and Results

In this section, we present the simulation setup and results. Our simulations were conducted using the NS3 simulator in conjunction with SUMO. We designed a scenario representing Bouira city in Algeria using SUMO. To evaluate the performance, we compared four routing protocols: AODV, DSDV, OLSR, and GPSR. The simulation parameters are detailed in Table 1.

In order to compare these routing protocols we have used some test metrics. Basic safety message packet delivery ratio (BSM_PDR) has been used. BSM_PDR is estimated based on(Pak & Kumar, 2018):

$$\text{BSM\_PDR} = \frac{\text{BSM packet reveived}}{\text{BSM packet transmitted}} \qquad (1)$$

In our simulation each node transmits 10 basics safety message of 200 KB every second. If BSM_PDR is high, this means that communication in the network is reliable. MAC/PHY overhead has been used also to compare routing protocols. It is defined as follows(Pak & Kumar, 2018):

$$\text{MAC/PHY} = \frac{\text{PHY bytes} - \text{App bytes}}{\text{PHY bytes}} \qquad (2)$$

Average Goodput is used, which is calculated based on useful data transmitted from source to destination node per time unit.

Table 1. Simulation parameters

Parameter	Value
Simulation tool	NS3
Path loss model	Friis model
Trasmission power	10 dBm
MAC layer	802.11p
Channel	Wifi (5.9 GHZ)
Trasmission mas delay	10 ms
Routing protocol	AODV, DSDV,OLSR, GPSR
Simulation area	1000 x 1050 m2
Number of vehicles	30, 50
Vehicle speed	10 m/s
Simulation time	30 s

Scenario 1

In the first scenario, vehicle speed was set at 10 m/s, and a total of 30 vehicles were deployed. Figure 4 displays the results of BSM_PDR for all protocols. It is evident from this figure that GPSR achieved a notably high BSM_PDR value.

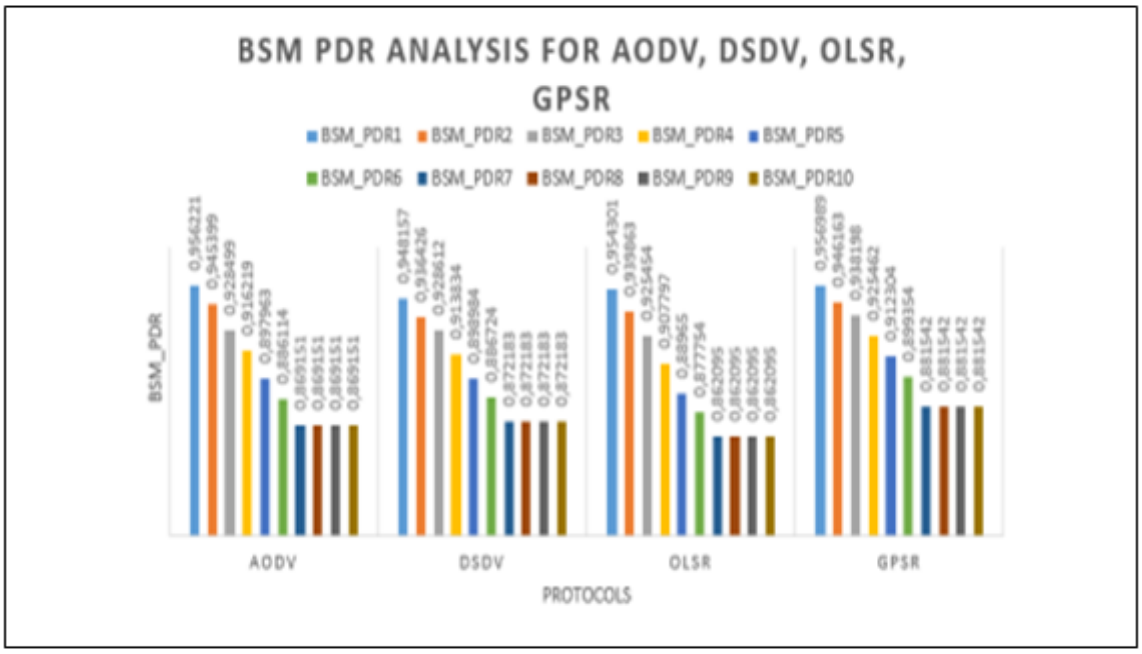

Figure 4. BSM_PDR analysis with 30 vehicles andspeed= 10m/s

Figure 5 presents an analysis of MAC/PHY Overhead. In this context, a lower value of this metric indicates greater network efficiency. As observed in Figure 5, GPSR achieves the lowest value after 15 seconds of simulation, indicating its efficiency. In contrast, AODV records the highest value, primarily due to its periodic use of hello message.

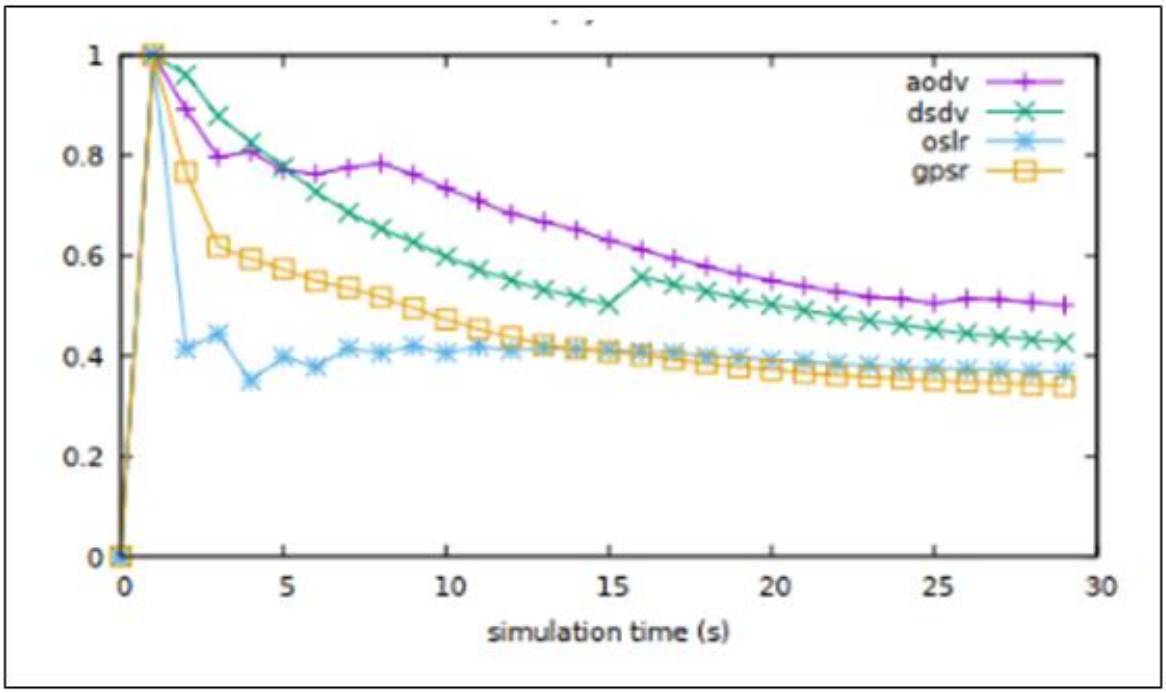

Figure 5. MAC/PHY overhead for 30 vehicles and speed = 10m/s

Regarding to goodput analysis, AODV stands out with the highest value among the compared protocols. This superior performance can be linked to AODV's frequent utilization of 'Hello' messages, which provides a detailed insight into the network topology. Conversely, GPSR registers the lowest goodput value. Figure 6 vividly illustrates these observations. However, both DSDV and OLSR exhibit similar goodput performance results.

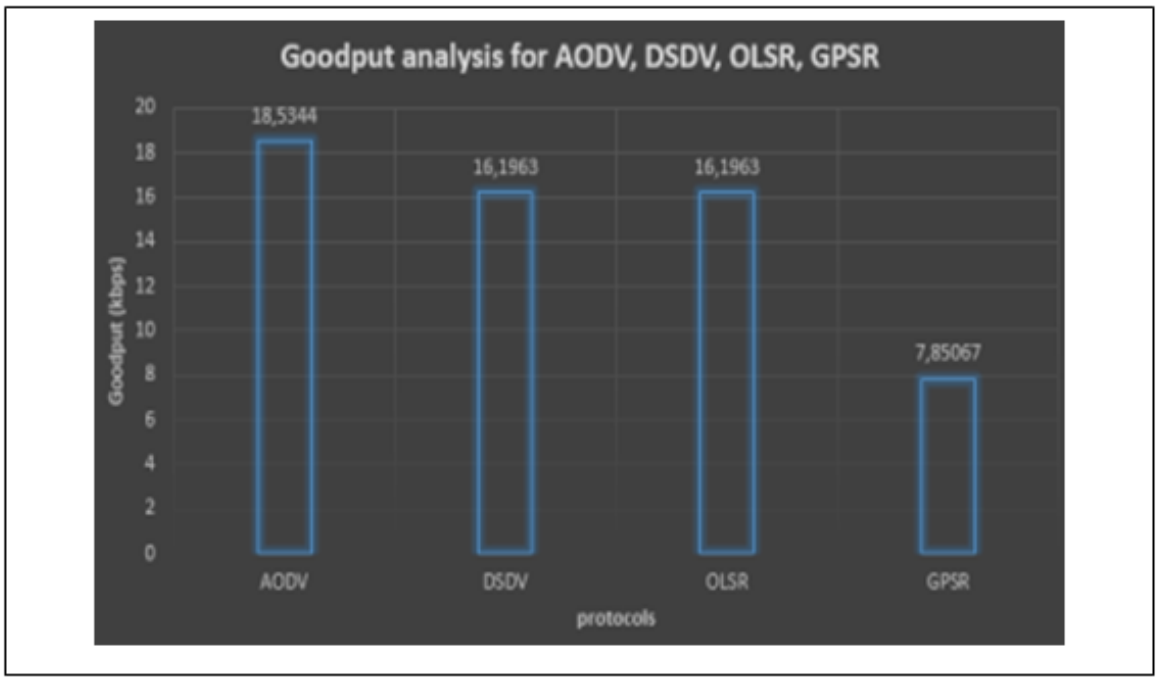

Figure 6. Goodput analysis for 30 vehicles and speed = 10m/s

Scenario 2

In our second simulation, we increased the number of nodes (50 vehicles) and we kept the same speed of vehicles (10 m/s) and the same simulation time (30 seconds). For the analysis of BSM_PDR in the case of 50 vehicles it was noted that OLSR gave the best results compared to other protocols. Because OLSR protocol uses MRP, which is a good strategy to find best routes between source and destination nodes. However, AODV is the protocol that gave the lowest values in this scenario. Figure 7 illustrates this result.

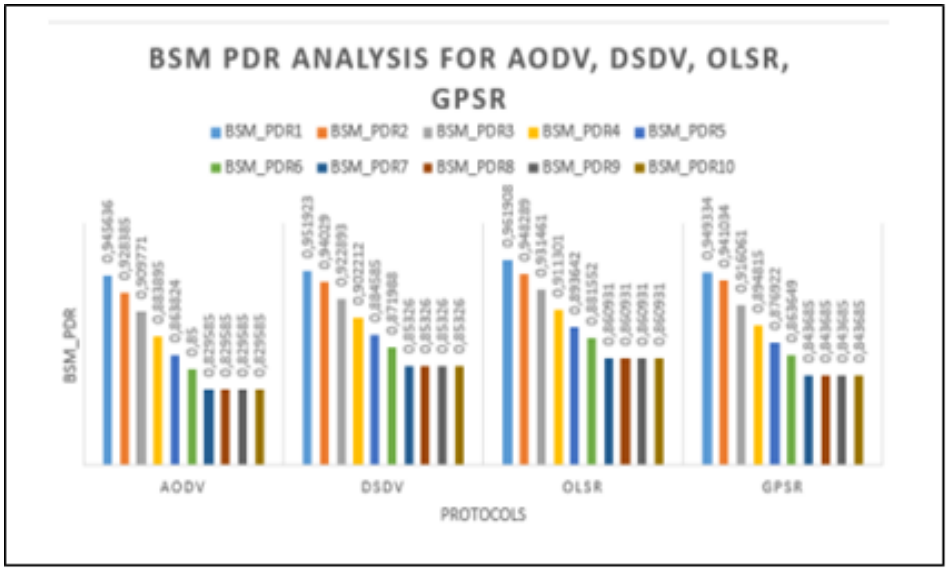

Figure 7. BSM_PDR Analysis with 50 vehicles and speed= 10m/s

In Figure 8, the MAC/PHY Overhead is graphically presented. Similar to the previous results, GPSR stands out as the most efficient protocol when evaluating the MAC/PHY overhead metric, outperforming all other protocols. GPSR excels in terms of both BSM_PDR and MAC/PHY Overhead metrics. However, it's worth noting that it yields the lowest MAC/PHY Overhead performance among the protocols examined.

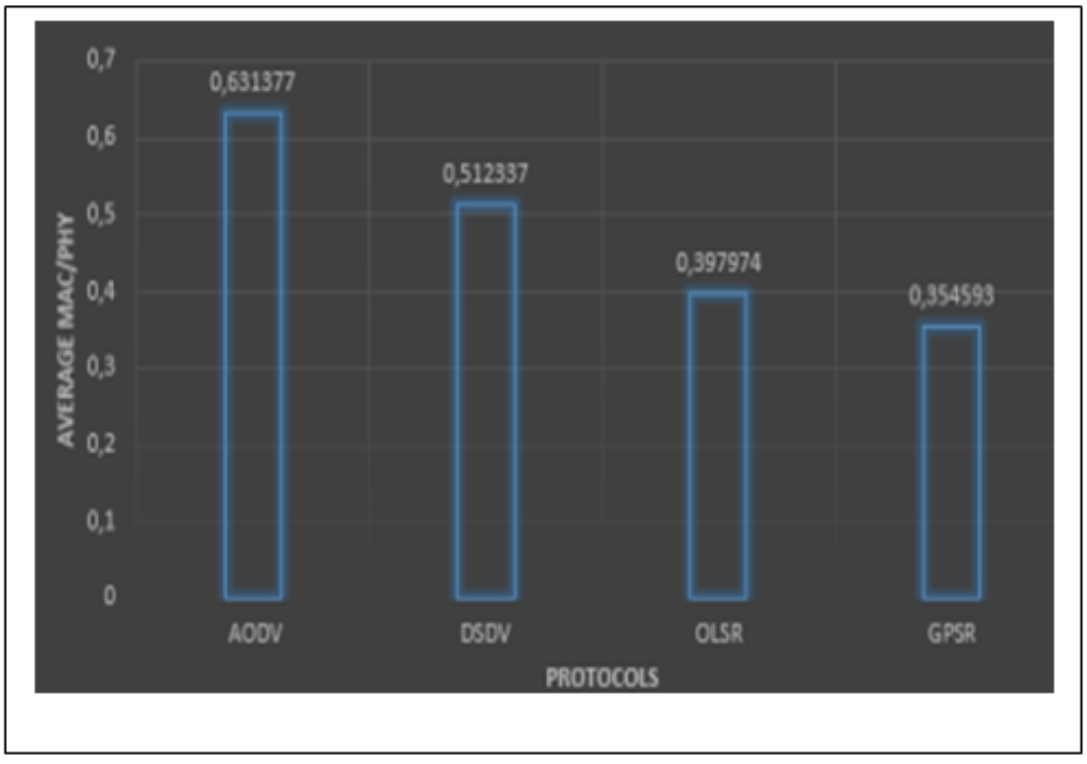

Figure 8. MAC/PHY overhead for 50 vehicles and speed = 10m/s

Figure 9 illustrates a graph depicting the goodput metric calculated for different routing protocols. The graph highlights that, at a vehicle density of 50, DSDV outperforms the other protocols. However, it's worth noting that DSDV exhibits lower goodput compared to AODV in scenarios with lower vehicle density (30 vehicles). However, OLSR demonstrates consistent goodput performance, closely resembling that of the best-performing protocol, across both high and low vehicle density scenarios. Notably, GPSR stands out as it consistently exhibits the lowest goodput performance among all the examined protocols, irrespective of the vehicle density.

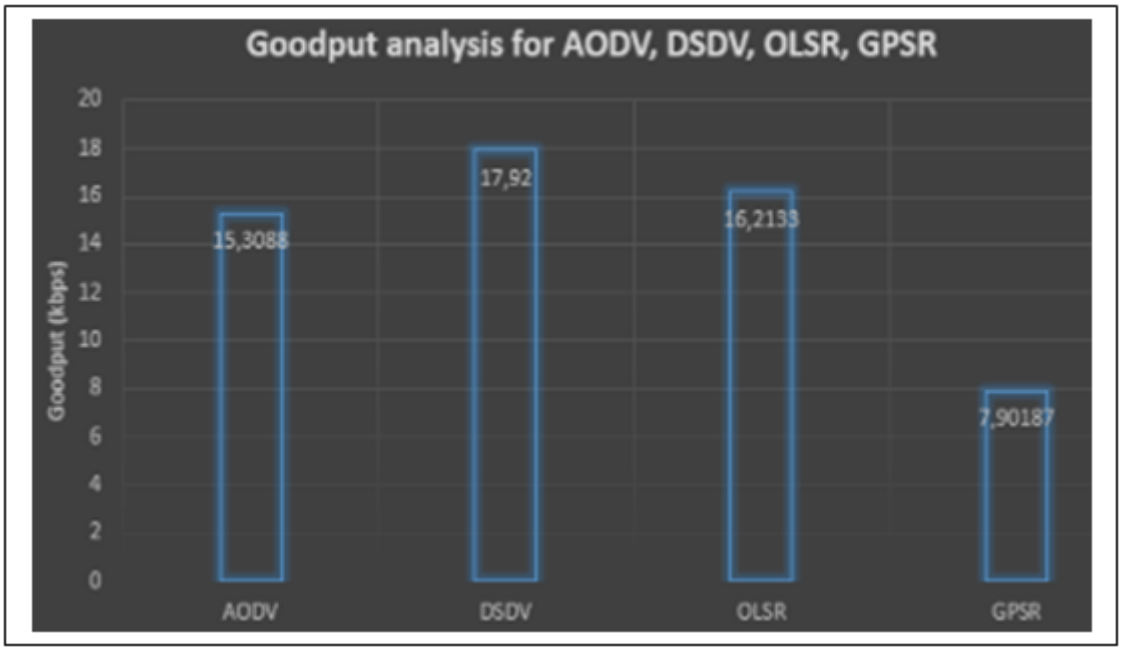

Figure 9. Goodput analysis for 50 vehicles and speed = 10m/s

Conclusion

In VANET networks, vehicles are mobile and can enter or leave the network at any moment, leading to frequent topology changes. Therefore, routing protocols must carefully consider this aspect and establish stable routes between source and destination nodes. This paper has investigated various routing protocols in VANET and proposed two simulation scenarios using NS3 and SUMO simulators. Several metrics were selected to evaluate and compare these routing protocols. The simulation results demonstrate that routing protocols significantly influence VANET performance, making it challenging to identify the best one. While compromise solutions can be proposed to improve the performance of the VANET network.

Scientific Ethics Declaration

The authors declare that the scientific ethical and legal responsibility of this article published in EPSTEM journal belongs to the authors.

Acknowledgements or Notes

* This article was presented as an oral presentation at the International Conference on Technology, Engineering and Science (www.icontes.net) held in Antalya/Turkey on November 16-19, 2023.

* This research article is conducted as part of the academic research project PRFU - Projet de recherche formation universitaire intitulé: Transmission de l'information dans un environnement sans-fil: Propagation, Accès au canal et Routage.

References

Clausen, T., & Jacquet, P. (2003). Optimized link state routing protocol (OLSR). *HAL*

Babu, S., & Raj Kumar P, A. (2022). A comprehensive survey on simulators, emulators, and testbeds for VANETs. *International Journal of Communication Systems*, *35*(8), e5123.

Brendha, R., & Prakash, V. S. (2017). A survey on routing protocols for vehicular ad hoc networks. *2017 4th International Conference on Advanced Computing and Communication Systems (ICACCS)*.

Deepak, & Rajkumar. (2018). Performance comparison of routing protocols in VANETs using network simulator-NS3. *Internatıonal Journal of Research in Electronıcs and Computer Engıneering*, *6*(2), 2098–2104.

He, G. (2002). Destination-sequenced distance vector (DSDV) protocol. *Networking Laboratory, Helsinki University of Technology*, (pp.1-9).

Hui, Z., Lingli, Z., Yonghang, Y., & Linlin, C. (2022). A survey of multipath load balancing based on network stochastic model in Manet. *2022 24th International Conference on Advanced Communication Technology (ICACT)*, 243-254.

Karp, B., & Kung, H. T. (2000). GPSR. *Proceedings of the 6th Annual International Conference on Mobile Computing and Networking*.

Perkins, C., Belding-Royer, E., & Das, S. (2003). *Ad hoc on-demand distance vector (AODV) routing* (pp.90-100).

Poonia, R. C. (2017). A performance evaluation of routing protocols for vehicular ad hoc networks with swarm intelligence. *International Journal of System Assurance Engineering and Management*, *9*(4), 830–835.

Szott, S., Kosek-Szott, K., Gawlowicz, P., Gomez, J. T., Bellalta, B., Zubow, A., & Dressler, F. (2022). Wi-fi meets ML: A survey on improving IEEE 802.11 performance with machine learning. *IEEE Communications Surveys & Tutorials*, *24*(3), 1843–1893.

Author Information

Bilal Saoud
Department of Electrical Engineering, Sciences and Applied Sciences Faculty, University of Bouira, Bouira 1000, Algeria
Contact e-mail: *bilal340@gmail.com*

Tahar Zireg
Department of Electrical Engineering, Sciences and Applied Sciences Faculty, University of Bouira, Bouira 1000, Algeria

Idir Bouaoud
Department of Electrical Engineering, Sciences and Applied Sciences Faculty, University of Bouira, Bouira 1000, Algeria

Smail Medjedoub
Department of Electrical Engineering, Sciences and Applied Sciences Faculty, University of Bouira, Bouira 1000, Algeria

To cite this article:

Saoud, B., Zireg, T., Bouaoud, I., & Medjedoub, S. (2023). Analysing and evaluation of routing protocols in VANET. *The Eurasia Proceedings of Science, Technology, Engineering & Mathematics (EPSTEM), 26*, 596-603.

The Eurasia Proceedings of Science, Technology, Engineering & Mathematics (EPSTEM)
ISSN: 2602-3199

The Eurasia Proceedings of Science, Technology, Engineering & Mathematics (EPSTEM), 2023

Volume 26, Pages 604-623

IConTES 2023: International Conference on Technology, Engineering and Science

Numerical Modeling and Simulation of a Poroelastic Journal Bearing Lubricated By Nanofluids with Couple-Stresses

Mustapha Lahmar
University 8th may 1945 Guelma

Ammar Athmania
University 8th may 1945 Guelma

Benyebka Bou-Said
University of Lyon

Abstract: In this paper we present a numerical simulation of a porous journal bearing considering the fluid film – poroelastic matrix interaction and the non-Newtonian rheological behavior of nanolubricant consisting of base fluid and nanoparticles (NPs). The flow of nanolubricant in the bearing clearance space is described by the Vijay Kumar Stokes micro-continuum theory which considers the characteristic size of nanoparticles such as fullerenes dispersed in a base oil. The flow of the nanolubricant in the porous medium is modeled by the modified Darcy's law where the Beavers–Joseph slip conditions are applied at the fluid film-porous matrix interface. The deformation of the fluid-film porous matrix interface due to hydrodynamic pressure is calculated by using a simplified analytical thin elastic liner model. The hydrodynamic behavior of lubricating film is governed by the modified Reynolds equation obtained from the momentum, moment of momentum, and mass conservation laws using the classical Reynolds derivation process. The bearing porosity is introduced into the governing modified Reynolds equation by means of the Morgan-Cameron approximation. The steady-state analysis shows that for an imposed operating eccentricity, the load capacity increases with the characteristic size and the concentration of NPs while the attitude angle, the leakage flow rate, and the coefficient of friction decrease. On the other hand, the permeability decreases the hydrodynamic pressure, the load capacity, and the leakage flow rate, and increases the attitude angle and the coefficient of friction.

Keywords: Poro-elasto-hydrodynamic lubrication, Porous bearings, Nanoparticle, Non-Newtonian fluid.

Introduction

The plain journal bearings are widely used as machine elements in both rotating and reciprocating machinery. The porous journal bearing is a specific cost-efficient and eco-friendly type of plain journal bearing which comprises a pervious bush that is filled with lubricant giving it self-lubricating properties. Thus, no additional lubrication circuit is necessary to supply the bearing because the saturated porous matrix plays the role of lubricant reservoir.

As in any fluid bearing, the shaft axis is eccentric with respect to the bearing axis under the effect of the applied load, thereby creating a convergent-divergent film geometry. The rotation of the shaft causes an increase of pressure in the convergent region, and a decrease in the divergent part, up to a limit value of cavitation or saturation vapor pressure (Figure 1).

Increasingly, the use of porous bearings is extended to severe operating conditions such as higher applied loads often with changing direction, and higher rotor speeds. Instead of numerous steady-state analyses that are often

proposed in technical literature, accurate static and dynamical models are required to investigate the bearing's behavior under such operating conditions. They are widely used in different areas: computers, electric motors, automobiles (motor starters), and so on. Porous or self-lubricating bearings have been the subject of numerous research works since the early work from (Morgan & Cameron, 1957). Given the huge number of theoretical and experimental investigations carried out on both liquid and gas-lubricated porous bearings, we can cite the recent non exhaustive list of papers Morgan and Cameron (1957), Rouleau et al. (1974), Krieger and Dougherty (1959), Elsharkawy et al. (2001), Naduvinamani et al. (2002), Kaneko et al. (1994), Prakash et al. (1974).

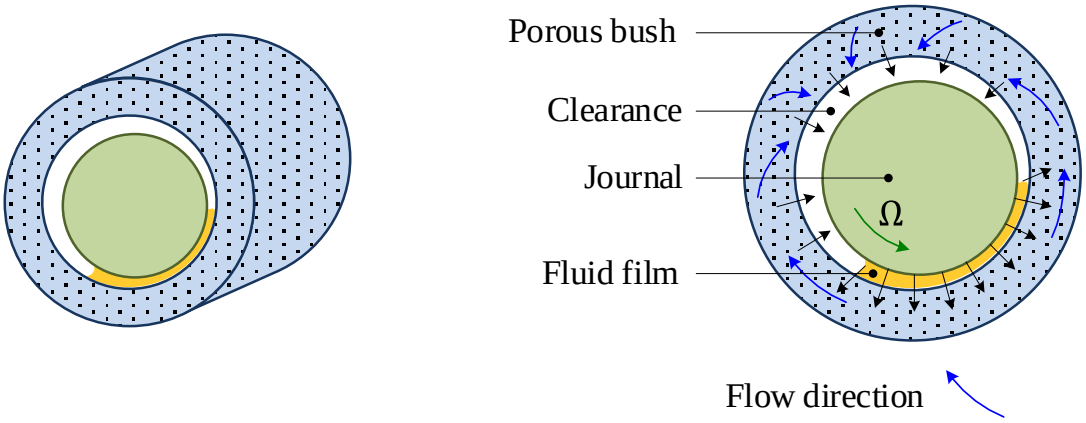

Figure 1 Schematic representation of a porous plain bearing with visualization of the streamlines of the lubricant flow.

Many theoretical studies have used the traditional Darcy's model (Darcy, 1856; Mokhtar et al., 1984) to describe the linear viscous (Newtonian) fluid flow in the porous bearing. The fluid model used does not consider the effects of the viscous forces of the lubricant infiltrating through the porous layer, which are at the origin of the generation of boundary layers. (Beavers and Joseph, 1967) experimentally showed that fluid slip can occur at the fluid film-porous layer interface (figure 2). They suggested replacing the boundary layer effect with appropriate slip conditions. According to the technical literature, several authors have applied such conditions to study non-deformable porous bearings lubricated by fluids with Newtonian rheological behavior (Lin, 1993,1994; Trachsel, 2017).

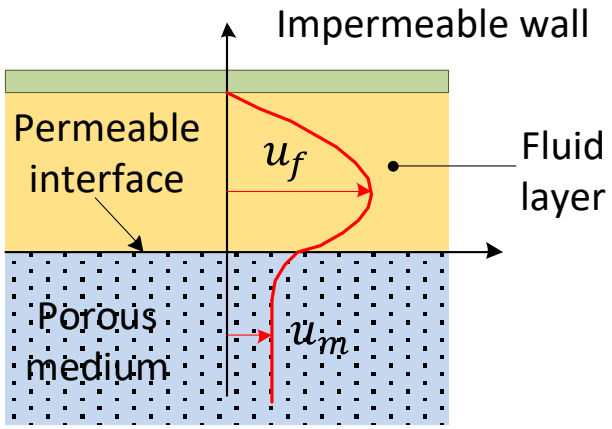

Figure 2. Typical velocity profiles of a unidirectional flow in the fluid film and the saturated porous medium.

Nowadays, with the progress of modern industry, the use of a non-Newtonian lubricant is becoming more and more interesting. Experimental studies Oliver (1988) and Scott et al. (1995) have shown that a base oil mixed with molecular additives or nanoparticles significantly improves the lubrication properties and thus reduces friction and wear, especially during the start-up and shutdown phases of machines.

Accordingly, the flow cannot be described by the classical continuum theory based on the classical Newtonian Navier-Stokes equations which neglects the size of the particles present in the doped oils. Several theoretical models to describe the flow of such complex fluids include the Vijay Kumar Stokes model Stokes (1965), Stokes (1984), Ariman et al. (1974) based on the micro-polar theory have been proposed in literature. The Vijay

Kumar Stokes fluid model, inspired from the theoretical work of Cosserat brothers (Cosserat E. & Cosserat F., (1909) for polar elastic media, considers polar effects in the form of couple stresses and body couples in addition to the surface and body forces. So, the flow of fluids with surface forces and couple-stresses is described by the theory of polar media which considers the effects of micrometric or nanometric size of the nano-additives or the agglomerates of nano-particles suspended in the base lubricant. In addition to the non-Newtonian rheological behavior of the fluid film, it is necessary to consider the deformation of the porous material, due to the high pressures generated in the film. Studies have already been carried out on rigid porous bearings lubricated by non-Newtonian couple stress fluid with a porous bearing containing a Newtonian fluid Bujurke et al. (1991), Naduvinamani (2001), and on deformable porous bearings lubricated by Newtonian fluid (Mak, 1977), Lin et al. (1996), (Elsharkawy, 2001).

The thrust of this paper is to investigate the combined effects of the characteristic size and concentration of nanoparticles or their aggregates such as inorganic fullerene (IF-WS2 NPs) or (IF-MoS2 NPs) on the steady-state performance characteristics of a porous journal bearing using nanofluids as lubricants. It is assumed that the journal (crankshaft) currently made of a forged steel is rigid and the bearing consists of a thin poro-elastic liner fixed in a stiff housing. The simplified thin elastic liner model (TELM), derived from an analytical elastic approach based on the use of complex Kolosov and Muskhelishvili potentials and Fourier series expansions (Lahmar, 1991, Lahmar, 2005).

The Reynolds' equation is derived in transient conditions and modified to account for the size of nanoparticles dispersed in the base lubricant, and the bearing-liner permeability property. This material property is introduced by means of the Morgan-Cameron approximation. In the proposed PEHD model, the normalized steady-state Reynolds equation is spatially discretized by the finite differences method using a nine point calculation molecule.

Bearing Description

Figure 3 shows the cross section of a porous plain bearing with the geometrical details. The plain bearing consists of two mechanical elements: the shaft and the bearing. The surfaces are assumed to be smooth. The shaft of radius R rotates around its axis with a peripheral or tangential constant speed $U=\Omega R$ with respect to the poroelastic matrix of thickness H, permeability k, Young's elasticity modulus E and Poisson's ratio υ. The shaft and the porous bearing are assumed to be aligned and separated by a non-Newtonian fluid film of thickness h.

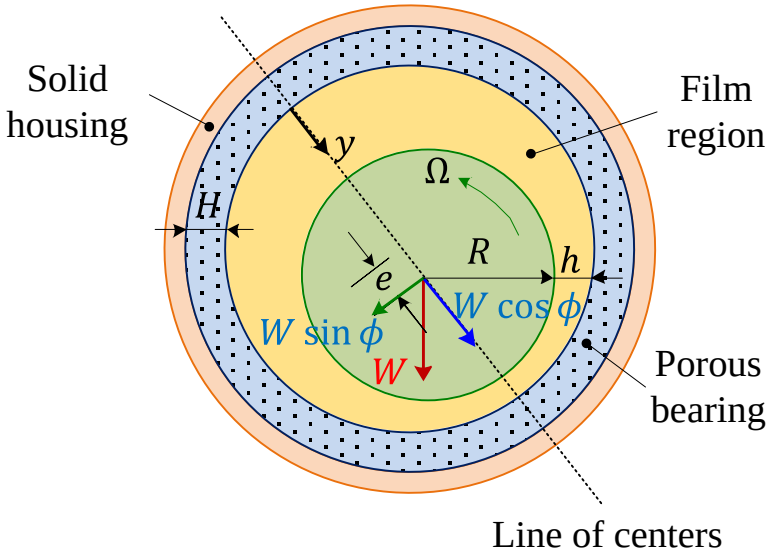

Figure 3. Geometric configuration of a porous journal bearing.

Basic Equations

The nanolubricant is modeled as a non-Newtonian couple stress fluid. In the absence of body couples and body forces, the V. K. Stokes couple stress fluid motion equation is written as follows:

$$\frac{1}{\nu}\left(\frac{\partial\vec{v}}{\partial t}+\vec{v}\,\overline{\overline{\text{grad}}}\,\vec{v}\right)=-\frac{1}{\mu}\vec{\nabla}p+\vec{\nabla}^2\vec{v}-\ell^2\vec{\nabla}^4\vec{v} \tag{1}$$

where $\ell=\sqrt{\eta/\mu}$ is a characteristic size of nanoparticles or agglomerates of NPs.

The dimensional analysis of the above equation (1) in the context of the viscous thin films theory significantly simplifies this equation which becomes:

$$\frac{\partial p}{\partial x}=\mu\frac{\partial^2 u}{\partial y^2}-\eta\frac{\partial^4 u}{\partial y^4} \tag{2}$$

$$\frac{\partial p}{\partial y}=0\rightarrow p=p(x,z) \tag{3}$$

$$\frac{\partial p}{\partial z}=\mu\frac{\partial^2 w}{\partial y^2}-\eta\frac{\partial^4 w}{\partial y^4} \tag{4}$$

We use the following kinematic boundary conditions:

• On the surface of the shaft $y=h$

$$u(x,h,z)=U(x,z)=\Omega R \tag{5-a}$$

$$v(x,h,z)=\frac{dh}{dt}=\frac{\partial h}{\partial t}+U\frac{\partial h}{\partial x}+W\frac{\partial h}{\partial z} \tag{5-b}$$

$$w(x,h,z)=W=0 \tag{5-c}$$

$$\left.\frac{\partial^2 u}{\partial y^2}\right|_{x,y=h,z}=0 \tag{5-d}$$

$$\left.\frac{\partial^2 w}{\partial y^2}\right|_{x,y=h,z}=0 \tag{5-e}$$

The conditions (5-d) and (5-e) express the nullity of the couple stresses on the surface of the shaft; i. e.

$$-2\eta\left.\frac{\partial^2 u}{\partial y^2}\right|_{x,y=h,z}=-2\eta\left.\frac{\partial^2 w}{\partial y^2}\right|_{x,y=h,z}=0$$

• At the bush fluid film-porous interface $y=0$

$$u(x,0,z)=U_b(x,z) \tag{6-a}$$

$$\left.\frac{\partial u}{\partial y}\right|_{x,y=0,z}=\frac{\alpha_b}{\sqrt{k}}(U_b-u^*) \tag{6-b}$$

$$v(x,0,z)=v^*(x,z) \tag{6-c}$$

$$w(x,0,z) = W_b(x,z) \tag{6-d}$$

$$\left.\frac{\partial w}{\partial y}\right|_{x,y=0,z} = \frac{\alpha_b}{\sqrt{k}}(W_b - w^*) \tag{6-e}$$

$$\left.\frac{\partial^2 u}{\partial y^2}\right|_{x,y=0,z} = 0 \tag{6-f}$$

$$\left.\frac{\partial^2 w}{\partial y^2}\right|_{x,y=0,z} = 0 \tag{6-g}$$

where U_b and W_b are respectively the Beavers-Joseph sliding velocities at the fluid film-porous interface along the x and z directions.

α_b is the dimensionless Beavers slip coefficient and k being the permeability of the isotropic porous layer's material in (m^2).

The conditions (6-f) and (6-g) reflect the nullity of the couple stresses at the interface due to the absence of rotation of the particles at the solid wall level, i.e.

$$-2\eta \left.\frac{\partial^2 u}{\partial y^2}\right|_{x,y=0,z} = -2\eta \left.\frac{\partial^2 w}{\partial y^2}\right|_{x,y=0,z} = 0$$

Equations (6-a), (6-b), (6-d), and (6-e) represent the Beavers-Joseph slip conditions and equation (6-c) explain the condition of continuity of the velocity along the normal to the fluid film-porous layer interface. u^*, v^*, w^* are respectively the components of the velocity vector of the fluid with particles along the x, y, and z directions at the interface. These velocities are calculated by the following modified Darcy's law:

$$u^* = -\frac{k}{\mu(1-\beta)}\frac{\partial p^*}{\partial x} \tag{7-a}$$

$$v^* = -\frac{k}{\mu(1-\beta)}\frac{\partial p^*}{\partial y} \tag{7-b}$$

$$w^* = -\frac{k}{\mu(1-\beta)}\frac{\partial p^*}{\partial z} \tag{7-c}$$

or in more condensed form: $\vec{v}^* = -\frac{k}{\mu(1-\beta)}\vec{\nabla}p^*$

where $\beta = \ell^2/k$ is the percolation (or penetration) parameter of the particles in the porous matrix and p^* is the pressure in the porous medium obtained from the solution of Laplace's equation (8) :

$$\vec{\nabla}^2 p^*(x,y,z) = \frac{\partial^2 p^*}{\partial x^2} + \frac{\partial^2 p^*}{\partial y^2} + \frac{\partial^2 p^*}{\partial z^2} = 0 \tag{8}$$

with: $0 \le x \le 2\pi R$; $-H \le y \le 0$; $-\frac{L}{2} \le z \le \frac{L}{2}$.

The boundary conditions associated to the Laplace equation (8) are:

In the middle section of the bearing assumed to be aligned ($z = 0$), the pressure is maximum (axial symmetry of the pressure profile) :

$$\left.\frac{\partial p^*}{\partial z}\right|_{x,y,z=0} = 0 \tag{9-a}$$

On the edges (ends) of the porous bearing ($z = \pm L/2$), the absolute pressure of the fluid in the porous matrix is taken equal to the atmospheric pressure:

$$p^*|_{x,y,z=L/2} = 0 \tag{9-b}$$

In the case where the edges of the bearing are sealed, condition (9-b) will be replaced by the following condition:

$$\left.\frac{\partial p^*}{\partial z}\right|_{x,y,z=\pm L/2} = 0 \tag{9-c}$$

Pressure periodicity condition:

$$p^*(\theta, y, z) = p^*(\theta + 2\pi, y, z) \tag{9-d}$$

$\theta = x/R$ being the circumferential coordinate of the bearing ($0 \leq \theta \leq 2\pi$).

On the outer surface of the porous coating, $y = -H$, the impermeability condition is written:

$$\left.\frac{\partial p^*}{\partial y}\right|_{x,y=-H,z} = 0$$

At the fluid film-porous layer interface, $y = 0$, the pressure continuity condition is applied:

$$p^*|_{x,y=0,z} = p|_{x,z} \tag{9-e}$$

Given the appropriate boundary conditions (5), (6) one can obtain:

$$u(x,y,z) = \frac{U}{h}y + U_b(x,z)\left(1 - \frac{y}{h}\right) + \frac{1}{2\mu}\frac{\partial p}{\partial x}\left\{y(y-h) + 2\ell^2\left[1 - \frac{\cosh\left(\frac{h-2y}{2\ell}\right)}{\cosh\left(\frac{h}{2\ell}\right)}\right]\right\} \tag{10}$$

$$w(x,y,z) = W_b(x,z)\left(1 - \frac{y}{h}\right) + \frac{1}{2\mu}\frac{\partial p}{\partial z}\left\{y(y-h) + 2\ell^2\left[1 - \frac{\cosh\left(\frac{h-2y}{2\ell}\right)}{\cosh\left(\frac{h}{2\ell}\right)}\right]\right\} \tag{11}$$

The Beavers-Joseph slip velocities U_b and W_b are obtained by inserting the analytical expressions of u and w (Eq. 10) and (Eq. 11) respectively in the equations (6-b) and (6-e) :

$$U_b(x,z) = \frac{1}{\alpha_b\sigma + 1}\left\{U + \alpha_b\sigma\, u^*(x,0,z) + \frac{1}{2\mu}\frac{\partial p}{\partial x}\left[-h^2 + 2h\ell\tanh\left(\frac{h}{2\ell}\right)\right]\right\} \tag{12-a}$$

$$W_b(x,z) = \frac{1}{\alpha_b\sigma + 1}\left\{\alpha_b\sigma\, w^*(x,0,z) + \frac{1}{2\mu}\frac{\partial p}{\partial z}\left[-h^2 + 2h\ell\tanh\left(\frac{h}{2\ell}\right)\right]\right\} \tag{12-b}$$

with $\sigma = \frac{h}{\sqrt{k}}$, $u^*(x,0,z) = -\frac{k}{\mu(1-\beta)}\frac{\partial p}{\partial x}$, $w^*(x,0,z) = -\frac{k}{\mu(1-\beta)}\frac{\partial p}{\partial z}$.

The velocities u and w of the flow can also be expressed in the following form:

$$u(x,y,z) = \frac{U}{h}[y(1-\xi_0) + h\xi_0] + \frac{1}{2\mu}\frac{\partial p}{\partial x}\left\{(y-h)\left[y + \frac{h}{3}\xi_1 - 2\ell\xi_0\tanh\left(\frac{h}{2\ell}\right)\right] + 2\ell^2\left[1 - \frac{\cosh\left(\frac{2y-h}{2\ell}\right)}{\cosh\left(\frac{h}{2\ell}\right)}\right]\right\} \tag{13}$$

and

$$w(x,y,z) = \frac{1}{2\mu}\frac{\partial p}{\partial z}\left\{(y-h)\left[y + \frac{h}{3}\xi_1 - 2\ell\xi_0\tanh\left(\frac{h}{2\ell}\right)\right] + 2\ell^2\left[1 - \frac{\cosh\left(\frac{2y-h}{2\ell}\right)}{\cosh\left(\frac{h}{2\ell}\right)}\right]\right\} \tag{14}$$

With $\xi_0 = \frac{1}{\alpha_b\sigma+1} = \frac{\sqrt{k}/\alpha_b}{h+\sqrt{k}/\alpha_b}$ and $\xi_1 = \frac{3\left(\frac{2k}{1-\beta}+h\frac{\sqrt{k}}{\alpha_b}\right)}{h\left(\frac{\sqrt{k}}{\alpha_b}+h\right)}$

Substituting the analytical expressions of $u(x,y,z)$ and $w(x,y,z)$ in the continuity equation then integrating across the film thickness gives:

$$\frac{\partial}{\partial x}\left[f(h,\ell,k)\frac{\partial p}{\partial x}\right] + \frac{\partial}{\partial z}\left[f(h,\ell,k)\frac{\partial p}{\partial z}\right] = 6\mu U\frac{\partial}{\partial x}[h(1+\xi_0)] + 12\frac{k}{1-\beta}\frac{\partial p^*}{\partial y}\bigg|_{x,y=0,z} + 12\mu\frac{\partial h}{\partial t} \tag{15}$$

with $f(h,\ell,k) = h^3(1+\xi_1) - 6h^2\ell\,\xi_0\tanh\left(\frac{h}{2\ell}\right) - 12\ell^2\left[h - 2\ell\tanh\left(\frac{h}{2\ell}\right)\right]$

From the Morgan-Cameron approximation for a very thin, porous layer $(H/R \ll 1)$ we can express $\partial p^*/\partial y$ at the fluid film-porous layer interface $(y=0)$ as follows:

$$\frac{\partial p^*}{\partial y}\bigg|_{x,y=0,z} = -H\left(\frac{\partial^2 p}{\partial x^2} + \frac{\partial^2 p}{\partial z^2}\right) \tag{16}$$

Finally, we obtain the following modified Reynolds equation :

$$\begin{aligned}\frac{\partial}{\partial x}\left\{\left[h^3(1+\xi_1) - 6h^2\ell\,\xi_0\tanh\left(\frac{h}{2\ell}\right) - 12\,\ell^2\left(h - 2\ell\tanh\left(\frac{h}{2\ell}\right)\right) + \frac{12kH}{(1-\beta)}\right]\frac{\partial p}{\partial x}\right\} \\ + \frac{\partial}{\partial z}\left\{\left[h^3(1+\xi_1) - 6h^2\ell\,\xi_0\tanh\left(\frac{h}{2\ell}\right) - 12\ell^2\left(h - 2\ell\tanh\left(\frac{h}{2\ell}\right)\right) + \frac{12kH}{(1-\beta)}\right]\frac{\partial p}{\partial z}\right\} \\ = 6\mu U\frac{\partial}{\partial x}[h(1+\xi_0)] + 12\mu\frac{\partial h}{\partial t}\end{aligned} \tag{17}$$

The modified Reynolds equation (17) is a nonlinear partial differential equation whose the main unknown is the hydrodynamic pressure p. This equation is coupled to the film geometric equation:

$$h(\theta,z,t) = C(1+\varepsilon\cos\theta) + \mathcal{L}\,p \tag{18}$$

where $C = R_b - R$ is the bearing radial clearance, $\varepsilon = e/C$ is the relative operating eccentricity, $\theta = \frac{x}{R}$ is the bearing angle, and $\mathcal{L} = \frac{(1+\upsilon)(1-2\upsilon)}{1-\upsilon}\frac{H}{E}$ is the compliance operator. The parameters appearing in the expression of $\mathcal{L}$ are the Young's elasticity modulus E, the Poisson's ratio υ, and the thickness of the poroelastic layer H.

Boundary Conditions

The pressure field in the lubricating film must satisfy the modified Reynolds equation (17) and the following boundary conditions:

In the middle section of the aligned bearing $(z = 0)$, the pressure being maximum, i.e.: $\left.\frac{\partial p}{\partial z}\right|_{x,z=0,t} = 0$

On the two free edges of the bearing $(z = \pm L/2)$, the absolute pressure in the fluid film is assumed to be equal to atmospheric pressure, i. e. : $p(x, z = \pm L/2, t) = 0$

The pressure field is assumed to be periodic in the circumferential direction, i.e.: $p(2\pi R, z, t) = p(0, z, t)$
In addition to the aforementioned conditions, the Swift-Stieber conditions related to the flow of the fluid in the bearing are considered:

$$p(x_c,z,t) = \left.\frac{\partial p}{\partial x}\right|_{x_c,z,t} = \left.\frac{\partial p}{\partial z}\right|_{x_c,z,t} = 0$$

where x_c is the break abscissa of the film (cavitation) which is an additional unknown of the problem.

Equation (17) can be rewritten in dimensionless form for the numerical treatment. For this, we use for the spatial coordinates : $\theta = x/R$, $\bar{z} = z/L$; for the velocity components : $\bar{u} = u/U$, $\bar{v} = Lv/(UC)$, $\bar{w} = w/U$; for the the fluid film pressure: $\bar{p} = C^2p/(\mu_0 UR)$; for the film thickness : $\bar{h} = h/C$; for the fluid dynamic viscosity : $\bar{\mu} = \mu/\mu_0$ with μ_0 the reference viscosity, and finally for the characteristic size of the nanoparticles $\bar{\ell} = \ell/C$.

This change of variables leads to the normalized stationary modified Reynolds equation (19):

$$\frac{\partial}{\partial\theta}\left[\bar{G}(\bar{h},\bar{\ell},K)\frac{\partial\bar{p}}{\partial\theta}\right] + \left(\frac{R}{L}\right)^2\frac{\partial}{\partial\bar{z}}\left[\bar{G}(\bar{h},\bar{l},K)\frac{\partial\bar{p}}{\partial\bar{z}}\right] = 6\bar{\mu}\frac{\partial}{\partial\theta}[\bar{h}(1+\xi_0)] \tag{19}$$

where $\bar{\mu} = \left(1-\frac{\phi}{\phi_m}\right)^{-[\eta]\phi_m}$ is the relative viscosity of the nanolubricant considered as a suspension according to the Krieger-Dougherty model, and

$$\bar{G}(\bar{h},\bar{\ell},K) = \bar{h}^3(1+\xi_1) - 12\bar{\ell}^2\left[\bar{h} - 2\bar{\ell}\tanh\left(\frac{\bar{h}}{2\bar{\ell}}\right)\right] - 6\bar{h}^2\bar{\ell}\,\xi_0\tanh\left(\frac{\bar{h}}{2\bar{\ell}}\right) + \frac{12\,K\bar{H}}{(1-\beta)}$$

$K = kR/C^3$ and $\bar{H} = H/R$ are the dimensionless permeability and the relative thickness of the porous coating, respectively. Equation (18) can be written in its normalized form as

$$\bar{h}(\theta,z,t) = 1 + \varepsilon\cos\theta + \bar{\mathcal{L}}\,\bar{p} \quad \text{where} \quad \bar{\mathcal{L}} = \frac{(1-2\upsilon)(1+\upsilon)}{1-\upsilon}\,\frac{\mu_0\omega_J\left(\frac{R}{C}\right)^3}{E}\,\bar{H} \tag{20}$$

Figure 4 shows a typical variation of the relative viscosity $\bar{\mu} = \mu/\mu_0$ as a function of the volume fraction ϕ calculated by the Krieger-Dougherty viscosity model.

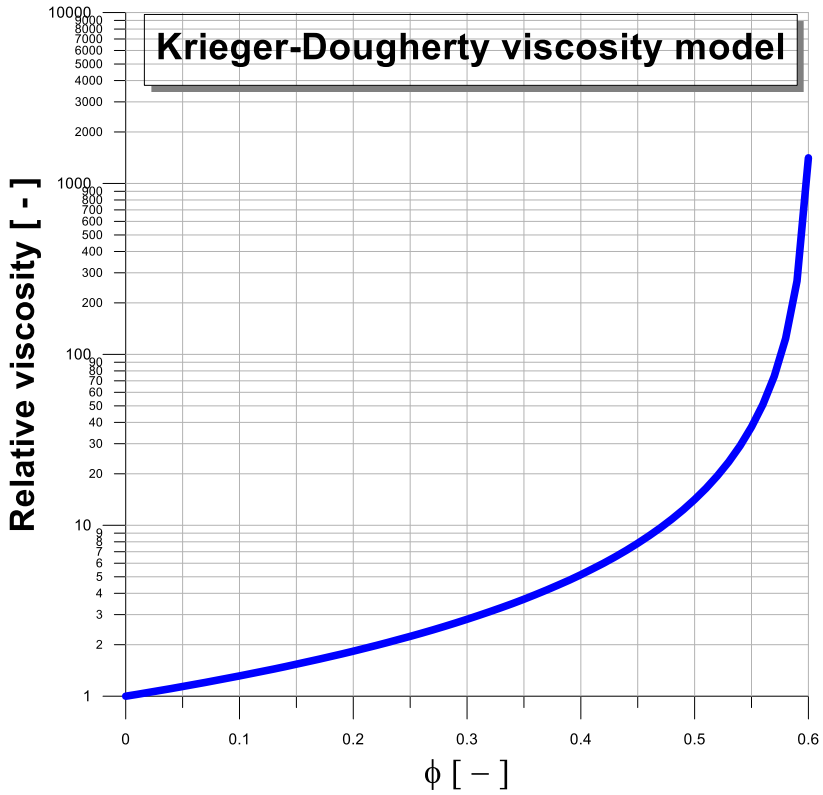

Figure 4. Graphical representation of the Krieger-Dougherty viscosity model for a range of volume fraction and $\phi_m = 0.605$

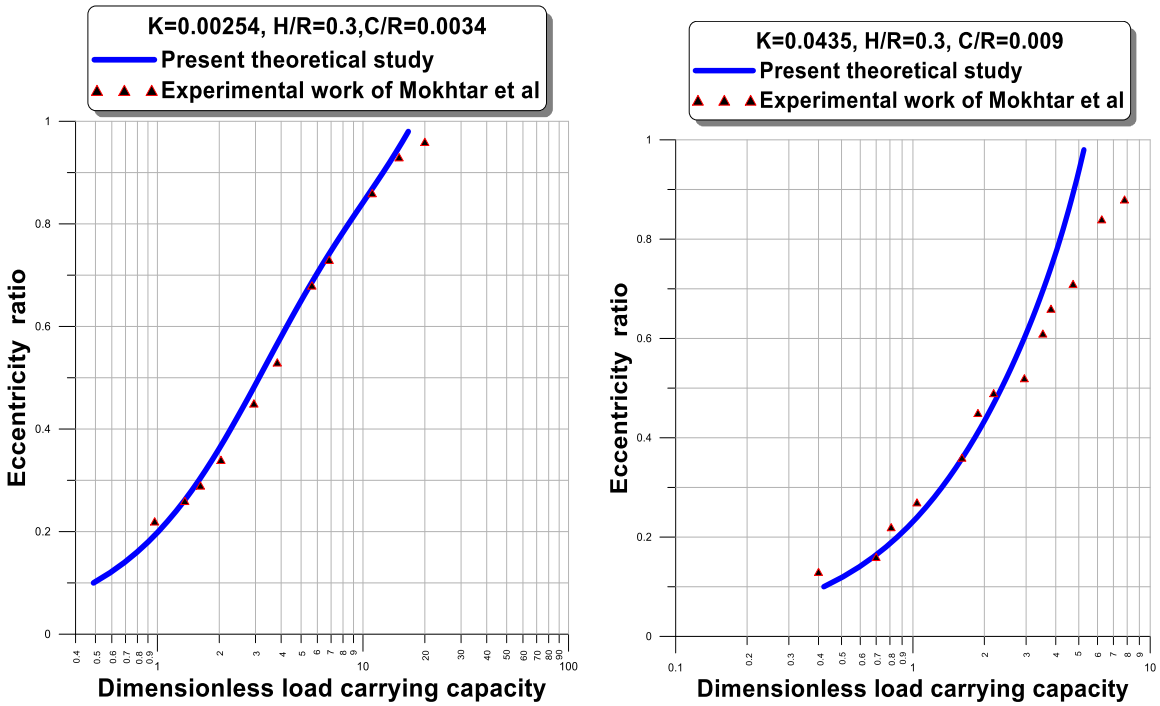

Figure 5. Comparison of dimensionless load capacity with experimental data for two values of K and $\frac{C}{R}$.

Validation

The coupled equations (19) and (20) with the associated boundary conditions are solved numerically using finite differences method and a numerical iterative scheme with under-relaxation coefficient. To validate the model, we compare the obtained results with the experimental data of Mokhtar et al. For this, the following data were considered:

$R = 9.5 \times 10^{-3}\ m$, $L = 0.033\ m$, $C = 32$ and $85.5\ \mu m$, $H = 3.0225 \times 10^{-3}\ m$, $k = 8.76 \times 10^{-15}$ and $2.86 \times 10^{-12}\ m^2$.

Figure 5 depicts the evolution of the dimensionless carrying capacity against eccentricity ratio $\varepsilon = \frac{e}{C}$.

This figure shows that the numerical predictions are in perfect agreement with the experimental data. However, a deviation can be observed for large relative eccentricities especially in the case of high permeability. This discrepancy can be attributed to thermal effects which are neglected in the present study. To further validate the model, we compare, in Table 1, our obtained results with those published by Rouleau et al. for different values of the operating eccentricity ratios and the dimensionless permeability of the porous layer.

Calculations are performed for the case of a finite length bearing with a longitudinal feeding groove using the Morgan-Cameron approximation as well as cavitation Reynolds boundary conditions. On the other hand, the slip phenomenon occurring at the interface is not considered in these calculations. According to the results presented in this table, we can conclude that the Morgan-Cameron approximation used in the proposed numerical model gives good results especially for a thin porous layer and this for the different simulated cases. We recall:

$\bar{F} = \frac{W}{\frac{\mu_0 U R^2 L}{C^2}} = \sqrt{\bar{F}_X^2 + \bar{F}_Y^2}$ where $\bar{F}_X, \bar{F}_Y$ are the load components along the direction of the applied load (X −axis) and the normal to the latter (Y −axis)

$\bar{F}_X = 2\int_{\bar{z}=0}^{\bar{z}=1/2}\int_{\theta=0}^{\theta=\theta_c} \bar{p}\cos\theta d\theta\, d\bar{z}$ and $\bar{F}_Y = 2\int_{\bar{z}=0}^{\bar{z}=1/2}\int_{\theta=0}^{\theta=\theta_c} \bar{p}\sin\theta d\theta\, d\bar{z}$ .The attitude angle is given by :

$\varphi = \tan^{-1}\left(\frac{\bar{F}_Y}{\bar{F}_X}\right)$. The friction force is: $\bar{F}_f = \frac{F_f}{\frac{\mu_0 U R L}{C}}$ with $F_f = \|\vec{F_f}\| = \sqrt{{F_f}_1^2 + {F_f}_2^2}$

${F_f}_1 = 2\int_0^{L/2}\int_0^{2\pi} \tau_{xy}\big|_{x,y=h,z} R d\theta dz$ and ${F_f}_2 = 2\int_0^{L/2}\int_0^{2\pi} \tau_{zy}\big|_{x,y=h,z} R d\theta dz$ are the friction force components of $\vec{F_f}$ in θ and z-axis direction, respectively. In these relationships, the wall shear stresses express as

$\tau_{xy}\big|_{y=h} = \mu\frac{\partial u}{\partial y}\Big|_{y=h} = \mu\frac{U}{h}(1-\xi_0) + \frac{h}{2}\frac{\partial p}{\partial x}\left(1+\frac{\xi_1}{3}\right)$ and $\tau_{zy}\big|_{y=h} = \mu\frac{\partial w}{\partial y}\Big|_{y=h} = \frac{h}{2}\frac{\partial p}{\partial z}\left(1+\frac{\xi_1}{3}\right)$

The friction coefficient and friction number are given by the following relationships:

$C_f = \frac{C}{R}\frac{\bar{F}_f}{\bar{F}}$ and $f = \frac{R}{C}C_f = \frac{\bar{F}_f}{\bar{F}}$

Table 1. Comparison of the theoretical results obtained by the developed computer code with those published by Rouleau et al. for : $R/L = 0.5$; $H/R = 0.2$; $C/R = 0.001$

ε	K	$\overline{F}$	$f\left(\frac{R}{C}\right)$	$\Phi\ (degrees)$	Note
0.80	0.001	**6.9215**	**1.7465**	**35.7342**	**Rouleau et al.**
		6.7472	**1.7337**	**37.1612**	**Present study**
		0.0251	**0.0073**	**0.0399**	**Relative discrepancy (%)**
	1.000	**0.5296**	**20.1582**	**73.4712**	**Rouleau et al.**
		0.5536	**19.3003**	**73.1705**	**Present study**
		0.0453	**0.0426**	**0.0041**	**Relative discrepancy (%)**
	10.000	**0.0658**	**---**	**84.4858**	**1**
		0.0794	**132.3135**	**82.8903**	**Present study**
		0.2066	**---**	**0.0188**	**Relative discrepancy (%)**
0.60	0.001	**2.6126**	**3.2355**	**49.8640**	**Rouleau et al.**
		2.6041	**3.2482**	**50.7268**	**Present study**
		0.0032	**0.0039**	**0.0173**	**Relative discrepancy (%)**
	1.000	**0.4080**	**19.5417**	**75.8843**	**Rouleau et al.**
		0.4271	**18.6807**	**75.5757**	**Present study**
		0.0468	**0.0441**	**0.0041**	**Relative discrepancy (%)**
	10.000	**0.0499**	**---**	**84.9922**	**Rouleau et al.**
		0.0602	**130.7896**	**83.4594**	**Present study**
		0.2064	**---**	**0.0180**	**Relative discrepancy (%)**
0.20	0.001	**0.4984**	**12.9634**	**73.5610**	**Rouleau et al.**
		0.5025	**12.8589**	**73.8830**	**Present study**
		0.0082	**0.0080**	**0.0043**	**Relative discrepancy (%)**
	1.000	**0.1395**	**46.0617**	**81.8352**	**1**
		0.1464	**43.9127**	**81.5428**	**2**
		0.0501	**0.0467**	**0.0035**	**Relative discrepancy (%)**
	10.000	**0.0168**	**---**	**85.8865**	**1**
		0.0203	**315.8283**	**84.4840**	**2**
		0.2083	**---**	**0.0118**	**Relative discrepancy (%)**

Parametric Study

In the following, the relevant calculation results are obtained using the geometric data and the operating conditions reported in Table 2 below. We analyze the effects of key design parameters on the steady-state performance characteristics of a finite length porous journal bearing, namely: the hydrodynamic pressure profile in the middle section of the bearing $\bar{p}$, the load capacity $\bar{F}$, the leakage flow rate $\bar{Q}$, the coefficient of friction $f\left(\frac{R}{C}\right)$, and the attitude angle φ. These key parameters are: the size of NPs (or agglomerates of NPs) characterized by the normalized couple stress parameter $\bar{\ell} = \ell/C$, the non-dimensional parameters of permeability and elasticity $K = kR/C^3$ and $\bar{\mathcal{L}}$ of the poroelastic matrix, the concentration of NPs in the base fluid ϕ, and the Joseph-Beavers slip coefficient α_b .

Effects of the Characteristic Size of NPs or Agglomerates of NPs

Figure 6 represents the circumferential variation of the dimensionless pressure $\bar{p}$ calculated in the middle section of the bearing, $\bar{z} = 0$, for different values of the characteristic diameter $\bar{\ell}$ of the NPs (fullerenes IF WS2 or IF MoS2) dispersed in the base lubricant, $\varepsilon = 0.8$, $K = 2.54 \times 10^{-3}$, $\phi = 0.$, and $\bar{\mathcal{L}} = 1.15 \times 10^{-4}$. It is observed that the use of a nano-lubricant (base fluid + nano-additives) whose behavior is naturally non-Newtonian leads to a greater increase in the pressure peak compared to the case of the lubricant without additives. Nano-additives or agglomerates of NPs, mixed with the lubricant, oppose the movement of the fluid and thus further improve the pressure in the fluid film.

Table 2. Bearing geometric characteristics and operating conditions.

Bearing length, (m)	L	33×10^{-3}
Shaft radius, (m)	R	9.5×10^{-3}
Radial clearance, (m)	C	85.5×10^{-6}
Shaft rotation velocity, (rpm)	Ω	870.
Porous thickness coating, (m)	H	3×10^{-3}
Porous coating permeability, (m^2)	k	0., 2.86×10^{-12}
Sliding parameter (dimensionless)	α_b	0.1
Penetration (percolation) coefficient	β	0.0
Young's modulus, (GPa) Bronze porous (Hamrock, 2004)	E	60.
Poisson's ratio (-) Bronze porous (Hamrock, 2004)	υ	0.22
Kinematic viscosity of the base oil $(SAE\ 30)\ at$ 40 °C, (cSt or mm^2/s)	ν_0	106.6
Lubricant density $(SAE\ 30)\ at$ 20 °C, (kg/m^3)	ρ_0	888.
Relative characteristic diameter of NPs (-)	ℓ/C	0., 0.1, 0.4
Volume fraction of NPs, (-)	ϕ	0., 25 %

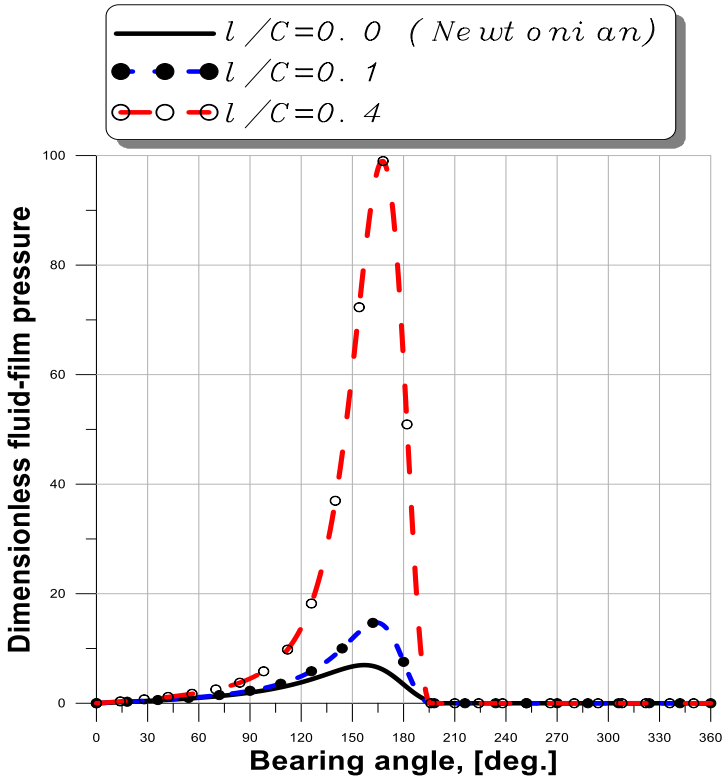

Figure 6. Calculated pressure profiles in the mid-section $(\bar{z} = 0)$ for different values of the characteristic diameter of NPs, $\varepsilon = 0.8$; $K = 2.54 \times 10^{-3}$; $= 0.$; $\bar{\mathcal{L}} = 1.15 \times 10^{-4}$ *and* $\alpha_b = 0.$

Figure 7 depicts the evolution of the dimensionless load capacity $\bar{F}$ as a function of the eccentricity ratio for different values of the characteristic diameter of the NPs $\bar{\ell}$ *for* $K = 2.54 \times 10^{-3}$, $\phi = 0.$, *and* $\bar{\mathcal{L}} = 1.15 \times 10^{-4}$. As in the case of the hydrodynamic pressure, the size of the NPs increases significantly the hydrodynamic lift, $\bar{F}$, of the journal bearing system. This is due to the flow resistance generated by the additives mixed into the lubricant. As expected, a large increase in $\bar{F}$ is observed for high values of the operating eccentricity ratio ε.

Figure 8 shows the variation of the bearing attitude angle, φ, versus the operating eccentricity ratio ε for different values of the characteristic diameter of the NPs $\bar{\ell}$, $K = 2.54 \times 10^{-3}$, $\phi = 0.$, *and* $\bar{\mathcal{L}} = 1.15 \times 10^{-4}$.

For a same value of eccentricity ratio, the increase in $\bar{\ell}$ leads to a significant decrease in the attitude angle, especially when the nano-lubricant contains large NPs or agglomerates of NPs. It can be concluded that the presence of large NPs plays a positive role with respect to the dynamic stability of the bearing. This can be confirmed through a more complete linear dynamic study based on the calculation of the stiffness and damping coefficients of the bearing.

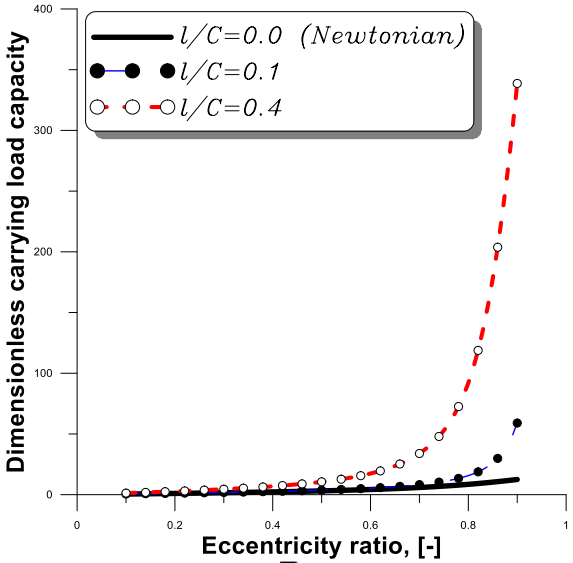

Figure 7. Evolution of the dimensionless load capacity $\bar{F}$ as a function of the eccentricity for different values of the characteristic size of the NPs, $K = 2.54 \times 10^{-3}$; $\phi = 0.$; $\bar{\mathcal{L}} = 1.15 \times 10^{-4}$ *and* $\alpha_b = 0.$

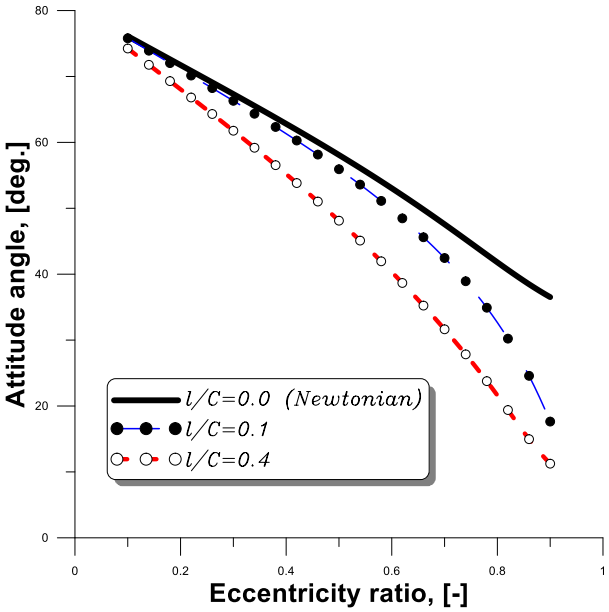

Figure 8. Variation of the attitude angle as a function of the eccentricity for different values of the characteristic size of the NPs, $\mathbf{K = 2.54 \times 10^{-3}}$; $\phi = 0.$; $\bar{\mathcal{L}} = 1.15 \times 10^{-4}$ *and* $\alpha_b = 0.$

Figure 9 gives the variation of the coefficient of friction, as a function of the eccentricity for different values of the characteristic diameter of the NPs $\bar{\ell}$ *for* $K = 2.54 \times 10^{-3}$, $\phi = 0.$,*and* $\bar{\mathcal{L}} = 1.15 \times 10^{-4}$. It is shown that the coefficient of friction decreases with the operating eccentricity. For a given value of eccentricity, the coefficient of friction calculated in the case of large NPs is clearly lower than that obtained in the case of NPs of small relative size. It should be noted that the frictional force acting on the surface of the shaft is calculated in excess assuming that the entire bearing surface is drained with lubricant.

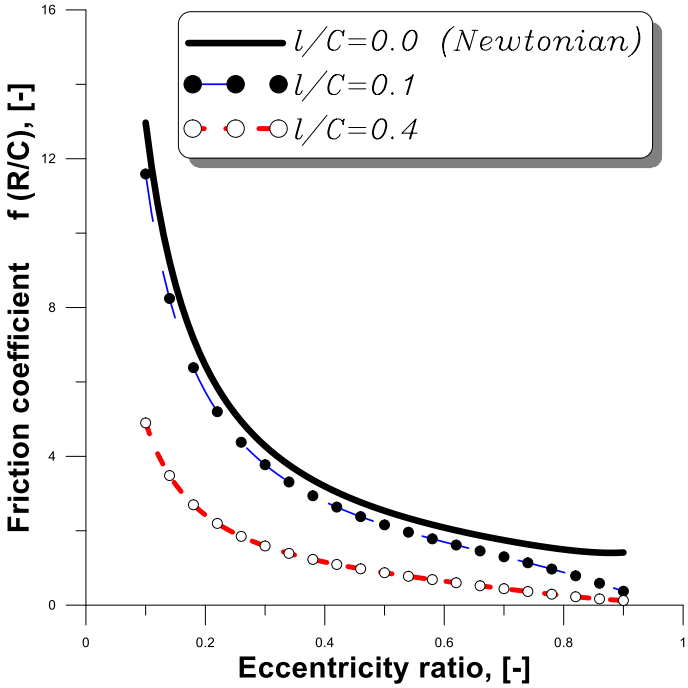

Figure 9. Evolution of the coefficient of friction $\boldsymbol{f(R/C)}$ for different values of the characteristic size of NPs, $\boldsymbol{K = 2.54 \times 10^{-3}}$; $\boldsymbol{\phi = 0.}$; $\boldsymbol{\bar{\mathcal{L}} = 1.15 \times 10^{-4}}$; $\boldsymbol{\alpha_b = 0.}$

Figure 10 shows the variation of the calculated dimensionless leakage flow at the free edges of the bearing, $\bar{Q}$, as a function of the eccentricity ratio ε for different values of the characteristic diameter of the NPs $\bar{\ell}$ *for* $K = 2.54 \times 10^{-3}$, $\phi = 0.$, *and* $\bar{\mathcal{L}} = 1.15 \times 10^{-4}$. The flow is calculated by integrating the average velocities $\bar{w}(x,z) = \frac{1}{h}\int_0^h w(x,y,z)dy$ of the flow at the two ends of the bearing $z = \pm L/2$. This figure clearly shows that the more the size of the NPs, $\bar{\ell}$, increases, the more the leakage rate decreases, especially for high operating eccentricities, i.e. when the bearing is moderately or heavily loaded.

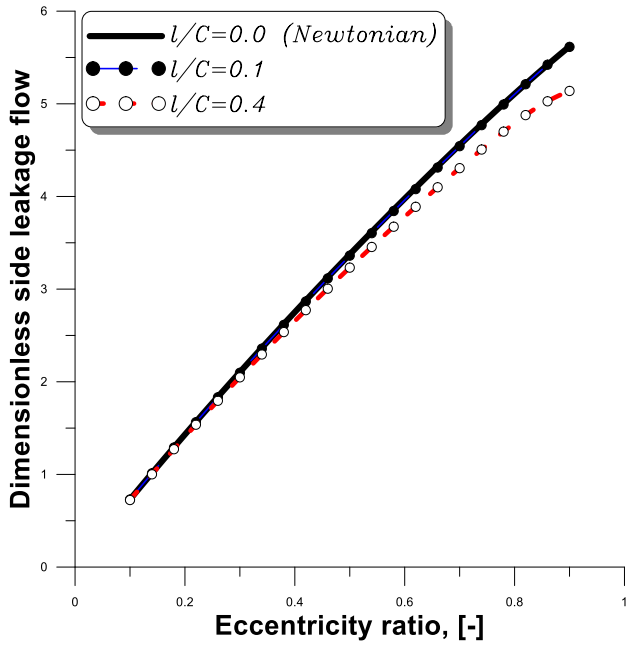

Figure 10. Variation of the leakage flow rate for different values of the characteristic size of the NPs, $\boldsymbol{K = 2.54 \times 10^{-3}}$; $\boldsymbol{\phi = 0}$; $\boldsymbol{\bar{\mathcal{L}} = 1.15 \times 10^{-4}}$; *and* $\boldsymbol{\alpha_b = 0.}$

Effects of Porous Layer Permeability

The calculated circumferential pressure distribution for different dimensionless permeability parameters K of the porous matrix, $\varepsilon = 0.6$, $\bar{\ell} = 0.1$, $\phi = 0.$, and $\bar{\mathcal{L}} = 1.15 \times 10^{-4}$ is shown in Figure 11. The pressure in the fluid film decreases significantly with the permeability parameter. This is explained by the fact that for large values of K i.e. for a larger number of pores, part of the lubricating fluid infiltrates more easily inside the porous matrix through the fluid-bearing film interface. Thus, the amount of fluid in the space between the shaft and bearing surfaces decreases which causes the pressure drop and hence the load capacity of the bearing $\bar{F}$ which corresponds to the area delimited by the pressure curve.

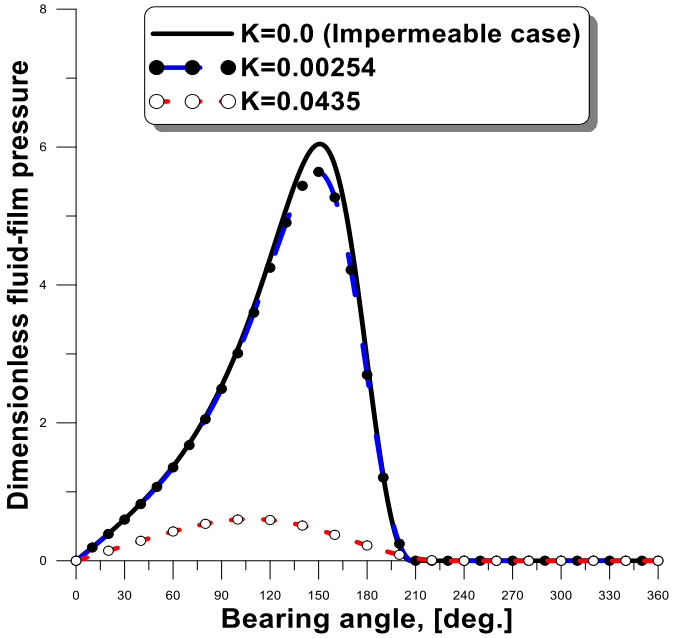

Figure 11. Pressure profile calculated at $\bar{z} = 0$ for different permeability parameters K, $\varepsilon = 0.6$; $\bar{\ell} = 0.1$; $\phi = 0.$; $\bar{\mathcal{L}} = 1.15 \times 10^{-4}$ *and* $\alpha_b = 0.$

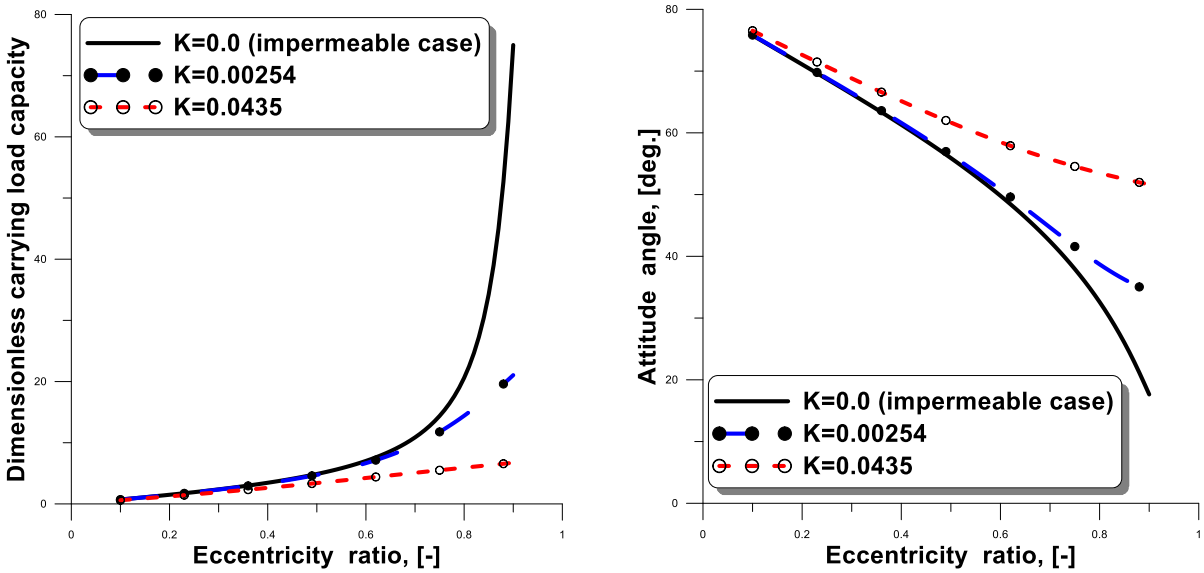

Figure 12. Effects of the permeability K of the porous layer on the hydrodynamic performance of the bearing (carrying load capacity and attitude angle) for $\beta = 0.0$; $\bar{\ell} = 0.1$; $\phi = 10\ \%$; $\bar{\mathcal{L}} = 1.15 \times 10^{-4}$; *and* $\alpha_b = 0.$

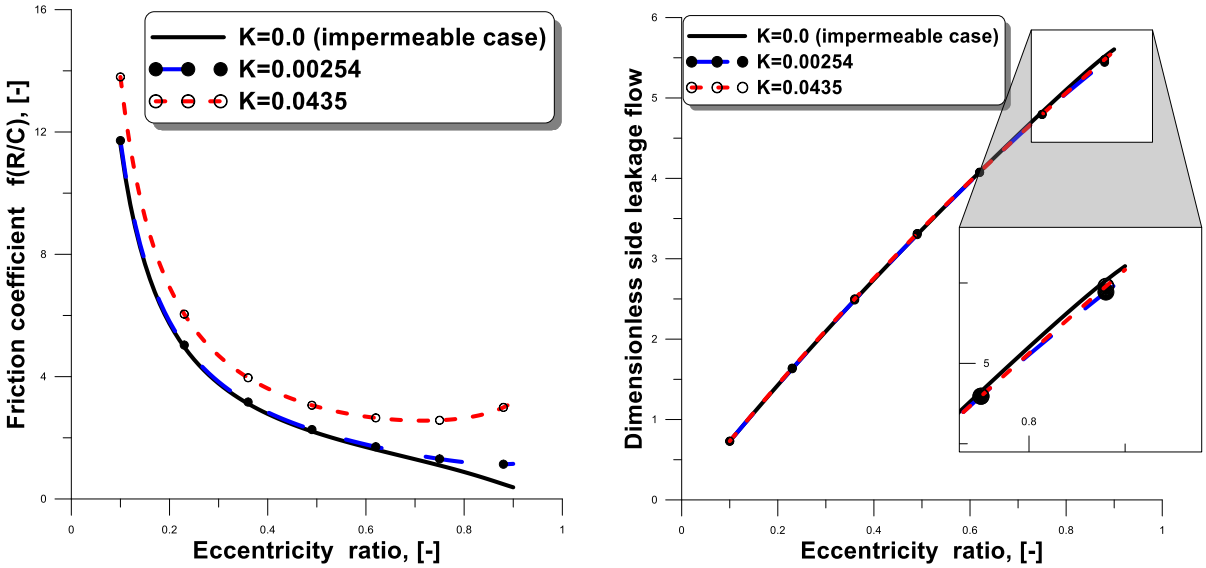

Figure 13. Effects of the layer's permeability $\boldsymbol{K}$ on the hydrodynamic performance of the bearing (friction coefficient and side leakage flow) for $\boldsymbol{\beta = 0.0}$; $\boldsymbol{\bar{\ell} = 0.1}$; $\boldsymbol{\phi = 10\ \%}$; $\boldsymbol{\bar{\mathcal{L}} = 1.15 \times 10^{-4}}$; *and* $\boldsymbol{\alpha_b = 0.}$

Figures 12 and 13 give the effects of the permeability K of the porous matrix on the hydrodynamic performance of the porous journal bearing for eccentricity ratios varying from 0.1 to 0.90. For the same operating eccentricity ε, we observe: an increase in the attitude angle φ and the coefficient of friction $f(R/C)$ with K; a decrease in bearing load capacity with K. On the other hand, the leakage flow rate is not significantly affected by the permeability even for high eccentricities.

Effects of the volume fraction $\boldsymbol{\phi}$ *of the NPs, the elasticity factor* $\boldsymbol{\bar{\mathcal{L}}}$*, the slip coefficient* $\boldsymbol{\alpha_b}$ *and the penetration coefficient* $\boldsymbol{\beta}$ *on the pressure*

Figures 14 to 16 represent the hydrodynamic pressure profiles determined for different values of the volume fraction ϕ, of the elasticity factor $\bar{\mathcal{L}}$, and the Beavers-Joseph slip coefficient α_b.

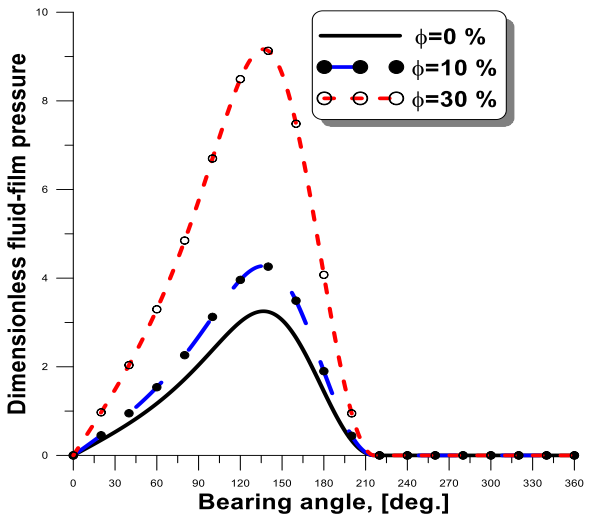

Figure 14. Pressure profiles calculated at $\boldsymbol{\bar{z} = 0}$ for different volume fractions $\boldsymbol{\phi}$, $\boldsymbol{\varepsilon = 0.6}$; $\boldsymbol{\bar{\ell} = 0.1}$; $\boldsymbol{\bar{\mathcal{L}} = 1.15 \times 10^{-4}}$; $\boldsymbol{\alpha_b = 0.}$; $\boldsymbol{K = 4.35 \times 10^{-2}}$; *and* $\boldsymbol{\beta = 0.}$

The influence of these parameters on the pressure can be summarized as follows:

- The pressure in the film increases with the volume fraction of the NPs since the viscosity of the nanolubricant is an increasing function of the concentration according to the Krieger-Dougherty viscosity model as depicted in Figure 14.
- Consideration of the elasticity of the fluid film-porous layer interface leads to a substantial drop in pressure due to an increase in film thickness accompanied by an extension of the active area of the bearing as shown in Figure 15.
- The effect of the slip velocity at the fluid film-porous layer interface on the pressure cannot be neglected, especially for low values of the Beavers-Joseph slip coefficient α_b (Figure 16).

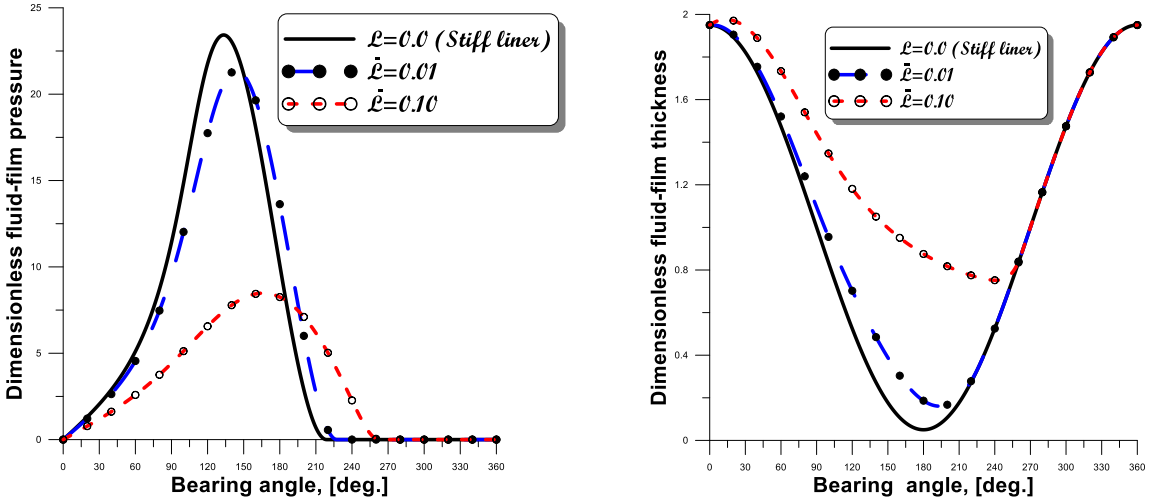

Figure 15. Pressure profiles of and thickness of the film calculated at $\bar{z} = 0$ for different values of the elasticity factor $\bar{\mathcal{L}}$, $\phi = 30\%$; $\varepsilon = 0.95$; $\bar{\ell} = 0.4, \alpha_b = 0.$; $K = 4.35 \times 10^{-2}$; *and* $\beta = 0$.

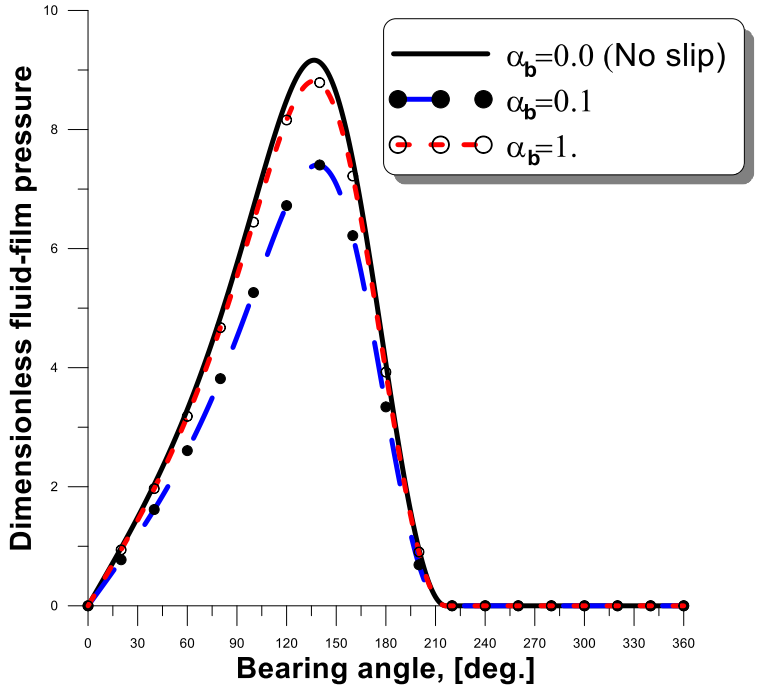

Figure 16. Pressure profiles calculated at $\bar{z} = 0$ for different values of the Beavers-Joseph slip coefficient α_b, $\bar{\mathcal{L}} = 6 \times 10^{-6}$; $\phi = 30\%$; $\varepsilon = 0.60$; $\bar{\ell} = 0.1$; $K = 4.35 \times 10^{-2}$; *and* $\beta = 0$.

Conclusions

The main objective of this research work was to rigorously analyze the elastohydrodynamic behavior of finite length porous journal bearings operating in isothermal regime and involving laminar flows of rheologically complex nanolubricants modeled as non-Newtonian polar fluids with couple-stresses effects. The aim was to set up efficient numerical simulation codes to aid in the design of porous bearings. The choice of this fluid model makes possible to take into consideration the characteristic size of the nanoparticles (NPs) added to the base lubricant. In this paper, we have studied the influence of some key parameters, namely: the characteristic size and the concentration of NPs on the steady-state performance characteristics of a finite length compliant porous plain bearing by solving the direct PEHD lubrication problem; i.e. the case of the bearing operating at an imposed eccentricity ratio ε. The non-Newtonian behavior of the nanolubricant was considered by adopting the V. K. Stokes micro-continuum theory. The modified Reynolds equation, considering the elastic deformation of the porous bearing and the Beavers–Joseph slip conditions at the fluid film–poroelastic bearing interface was derived within the context of thin fluid films lubrication theory.

The permeability of the porous medium was successfully introduced into the modified Reynolds equation using the Morgan-Cameron approximation in the case of a very thin porous layer ($H/R \ll 1$). This further simplified the numerical solution of the direct PEHD problem and thus avoided making the coupling between the modified Reynolds equation and the modified Darcy's equation governing the flow of the polar nanolubricant in the porous medium using an iterative procedure.

The elastic deformation of the fluid film-porous layer interface was predicted by the simplified analytical thin elastic layer model. The modified Reynolds equation was normalized then discretized and solved by the finite difference technique using a nine point calculation stencil (molecule).

The developed model based on the Cameron-Morgan approximation was successfully validated by comparing the theoretical results with the experimental measurements carried out by Mokhtar et al. in the case of a Newtonian lubricant and a porous bearing (89% copper, 10% Tin, 1% Graphite) obtained by sintering (powder technology). A second validation was made by comparing the results obtained by the developed computer code with the theoretical results published by Rouleau et al.(1974).

The parametric study highlighted the non-negligible effects of certain key parameters related to the formulation of modern nanolubricants, namely the characteristic size and the concentration of NPs (fullerenes) or agglomerates of NPs. The results from the various numerical simulations carried out are summarized as follows:

- For an imposed operating eccentricity, the size and concentration of NPs increase the pressure and therefore the load capacity of the journal bearing system, while the attitude angle, the leakage flow rate, and the coefficient of friction decrease. The combined effects of the size and the concentration of the NPs are more significant as the operating eccentricity is high.
- The pressure in the fluid film, the carrying capacity, and the leakage rate decrease with the permeability of the porous layer. However, the attitude angle and the coefficient of friction increase.
- The deformation of the porous layer due to pressure significantly affects the pressure distribution and the geometry of the film, especially for large operating eccentricities and low values of Young's elasticity modulus.
-

The results obtained provide interesting information for the designers of porous bearings as well as the manufacturers of lubricants.

Scientific Ethics Declaration

The authors declare that the scientific ethical and legal responsibility of this article published in EPSTEM journal belongs to the authors.

Acknowledgements or Notes

* This article was presented as a poster presentation at the International Conference on Technology, Engineering and Science (www.icontes.net) held in Antalya/Turkey on November 16-19, 2023.

References

Ariman, T., Turk, M. A., & Sylvester, N. D. (1974). Applications of micro-continuum fluid mechanics. *International Journal of Engineering Science*, *12*(4), 273–293.

Bujurke N. M., &Naduvinamani, N. B. (1991). On the performance of narrow porous journal bearing lubricated with couple stress fluid. *Acta mechanica*, *86*(1), 179–191.

Beavers, G. S., & Joseph, D. D. (1967). Boundary conditions at a naturally permeable wall. *Journal of Fluid Mechanics*, *30*(1), 197–207.

Cosserat, E., & Cosserat, F. (1909). *Théorie des corps déformables.* Librairie

Darcy, H. (1856). *Les fontaines publiques de la ville de Dijon*. In V. Dalmont (Ed.). Paris.

Elsharkawy, A. A., & Guedouar, L. H. (2001). Direct and inverse solutions for elastohydrodynamic lubrication of finite porous journal bearings. *Journal of Tribology*, *123*(2), 276–282.

Elsharkawy, A. A., & Guedouar, L. H. (2001). Hydrodynamic lubrication of porous journal bearings using a modified Brinkman-extended Darcy model. *Tribology International*, *34*(11), 767–777.

Hamrock, B. J., Schmid, S. R., & Jacobson Bo, O. (2004). *Fundamentals of fluid film lubrication* (2nd ed.). Marcel Dekker, Inc.

Krieger, I. M., & Dougherty, T. J. (1959). A mechanism for nonnewtonian flow in suspensions of rigid spheres. *Transactions of the Society of Rheology*, *3*(1), 137-152.

Kaneko, S., Inoue, H., & Ushio, K. (1994). Experimental study on mechanism of Lubrication in Porous Journal Bearings: Oil film formed in bearing clearance. *JSME International Journal. Ser. C, Dynamics, Control, Robotics, Design and Manufacturing*, *37*(1), 185–192.

Lahmar, M., (1991).*Modélisation du comportement élastohydrodynamique des revêtements de surface dans les paliers hydrodynamiques.* (Doctoral dissertation).Poitiers University.

Lahmar, M. (2005). Elastohydrodynamic analysis of double-layered journal bearings lubricated with couple stress fluids. *Proceedings of the Institution of Mechanical Engineers, Part J: Journal of Engineering Tribology*, *219*(2), 145-165.

Lin, J. R., Hwang, C. C., & Yang, R. F. (1996). Hydrodynamic lubrication of long, flexible, porous journal bearings using the Brinkman model. *Wear*, *198*(1), 156–164.

Lin, J. R. & Hwang, C.C. (1993). Lubrication of short porous journal bearings–use of the Brinkman-extended Darcy model. *Wear*, *161*(1–2), 93–104.

Lin, J. R., & Hwang, C. C. (1994). Hydrodynamic lubrication of finite porous journal bearings–use of the Brinkman-extended Darcy model. *International Journal of Mechanical Sciences*, *36*(7), 631–644.

Mak, W. C., & Conwy, H. D. (1977). The lubrication of a long, porous, flexible journal bearing. *Journal of Lubrication Technology*, *99*(4), 449–454.

Morgan, V. T., &Cameron, A. (1957). Mechanism of lubrication in porous metal bearings. In Proceedings of the *Conference on Lubrication and Wear* (Vol. 89,151-157). London

Mokhtar, M. O. A., Rafaat, M., & Shawki, G. S .A (1984). *Experimental investigations into the performance of porous journal bearings (*No.840097). SAE Technical Paper

Naduvinamani, N. B., Hiremath, P. S., & Fathim, S. T. (2002). Lubrication of a narrow porous journal bearing with a couple stress fluid. *Lubrication Science*, *14*(4), 393–413.

Prakash, J., & Vij, S. K. (1974). Analysis of narrow porous journal bearing using Beavers-Joseph criterion of velocity slip. *Journal of Applied Mechanics*, *41*(2), 348–354.

Naduvinamani, N. B., Hiremath, P. S., & Gurubasavaraj,, G. (2001). Static and dynamic behaviour of squeeze-film lubrication of narrow porous journal bearings with coupled stress fluid. *Proceedings of the Institution of Mechanical Engineers, Part J: Journal of Engineering Tribology*, *215*(1), 45–62.

Oliver, D. R. (1988). Load enhancement effects due to polymer thickening in a short model journal bearing. *Journal of Non-Newtonian Fluid Mechanics*, *30*(2–3), 185–196.

Rouleau, W. T., & Steiner, L. I. (1974). Hydrodynamic porous journal bearings. part i—finite full bearings. *Journal of Lubrication Technology*, *96*(3), 346–353.

Scott, W., &Suntiwattana, P. (1995). Effect of oil additives on the performance of a wet friction clutch material. *Wear*, *181*, 850–855.

Stokes, V. K. (1966). Couple stresses in fluids. The Physics of Fluids, *9*(9), 1709–1715.

Stokes, V. K. (1984). *Theories of fluids with microstructures: An introduction*, Springer Science & Business Media.

Trachsel, M., Pittini, R., & Dual, J. (2017). A combined approach to study and model the effect of viscous heating in small porous, self-lubricating journal bearings. *Tribology International, 116,* 199–207.

Author Information

Mustapha Lahmar
University 8th may 1945 Guelma
BP 401, Guelma University, Guelma (24000)
Contact e-mail: *lahmar.mustapha@univ-guelma.dz*

Ammar Athmania
University 8th may 1945 Guelma
BP 401, Guelma University, Guelma (24000)

Benyebka Bou-Said
Université de Lyon, LaMCoS, INSA Lyon
Bâtiment Sophie Germain
27bis, Avenue Jean Capelle
F69621 Villeurbanne cedex
France

To cite this article:

Lahmar, M., Athmania, A., & Bou-Said, B. (2023). Numerical modeling and simulation of a poroelastic journal bearing lubricated by nanofluids with couple-stresses. *The Eurasia Proceedings of Science, Technology, Engineering & Mathematics (EPSTEM), 26,* 604-623.

The Eurasia Proceedings of Science, Technology, Engineering & Mathematics (EPSTEM)
ISSN: 2602-3199

The Eurasia Proceedings of Science, Technology, Engineering & Mathematics (EPSTEM), 2023

Volume 26, Pages 624-632

IConTES 2023: International Conference on Technology, Engineering and Science

Roadmap for Simulating Quantum Circuits Utilising IBM's Qiskit Library: Programming Approach

Yousef Jaradat
Al-Zaytoonah University of Jordan

Mohammad Alia
Al-Zaytoonah University of Jordan

Mohammad Masoud
Al-Zaytoonah University of Jordan

Ahmad Mansrah
Al-Zaytoonah University of Jordan

Ismael Jannoud
Al-Zaytoonah University of Jordan

Omar Alheyasat
AlBalqa' Applied University

Abstract: This paper explains the roadmap for running quantum circuit programs based on the Qiskit library in quantum simulators as well as real cloud-based IBM quantum computers. Qiskit is a free and open-source software development platform based on the Python programming language that is used in quantum programming. Qiskit acts as a link between quantum computing's theoretical foundations and the practical aspects of programming and experimentation. It also allows users to experiment with and develop quantum algorithms, as well as simulate and execute them on simulators and real-world cloud-based quantum devices. It also simplifies the quantum programming process and allows a diverse range of people to participate in the exciting world of quantum computing. The paper, on the other hand, provides the mathematical foundation for analyzing quantum circuits and algorithms using linear algebra principles, as they provide the tools needed to describe and manipulate quantum states and operations. Furthermore, the paper shows quantum circuit design and implementation using real Qiskit codes.

Keywords: Qiskit, Quantum circuit, Quantum algorithm, Entanglement, IBM

Introduction

Quantum computing is a type of computer that processes information using quantum mechanics principles. Quantum computers are substantially quicker than conventional computers at solving specific sorts of problems, such as breaking encryption, simulating physical systems, and discovering novel pharmaceuticals (Gill et al., 2023). Information is processed in classical computing using bits that can represent either as 0 or a 1. Quantum computing, on the other hand, employs quantum bits, or qubits, which can exist in a state of superposition, expressing both 0 and 1 at the same time (Preskill, 2021; Hidary & Hidary, 2019). Some of the key ideas in quantum computing (Nielsen & Chuang, 2010; Gyongyosi & Imre, 2019):

- Superposition: Unlike classical bits, which can only exist in one of two states (0 or 1) at any time, qubits can exist in a superposition of both states at the same time. This enables quantum computers to do several calculations at the same time, potentially speeding up certain algorithms.
- Entanglement occurs when the state of one qubit becomes intertwined with the state of another, regardless of their physical distance. This phenomenon allows quantum computers to process information in a highly correlated and interconnected manner, which can be used to perform specialized computations.

The most prevalent types of quantum computers being developed are gate-based quantum computers and adiabatic quantum computers (Bruzewicz et al., 2019; Albash & Lidar, 2018). Gate-based quantum computers operate qubits using a series of quantum gates, whereas adiabatic quantum computers find the ground state of a quantum system via a process known as adiabatic evolution. Quantum computing is still in its early stages of research and development, but it has the potential to transform many sectors. The following are some of the potential uses of quantum computing (Hassija et al., 2020):

- Breaking encryption: Quantum computers have the potential to break the encryption employed in many modern security systems, such as credit card and online banking systems.
- Physical system simulation: Quantum computers could be used to simulate the behavior of physical systems like molecules and materials. This might be used to develop novel treatments and materials, as well as to investigate the effects of climate change.
- Finding new pharmaceuticals: By simulating the interactions of molecules, quantum computers could be utilized to find novel drugs. This might significantly speed up the drug discovery process.
- Optimization: Quantum computers could be used to address optimization problems like finding the shortest path between two points or determining the best method to allocate resources. This could be applied to transportation, logistics, and manufacturing.

Qiskit is a free and open-source software development (SDK) platform for programming, simulation, or and performing quantum computations on real-world quantum hardware (Wille et al., 2019; Fingerhuth et al., 2018). It is one of the most prominent frameworks for working with quantum computers, invented by IBM. Qiskit is a suite of tools and components (Python libraries) that allows researchers, developers, and programmers to work with quantum computing algorithms and experiments. Qiskit is made up broadly of four core modules:

- *Qiskit Terra*: is the foundation of the Qiskit framework. It serves as the foundation for quantum circuits, gates, and operators. Users can create quantum circuits with numerous gate types and apply operations on qubits. Terra also provides circuit visualization and optimization tools.
- *Qiskit Aer*: This is a quantum circuit simulator. It can be used to test and debug quantum programs before they are executed on actual hardware. Aer also offers tools for modelling noise's impact on quantum circuits.
- *Qiskit Ignis*: This is a set of error-mitigation tools. It can be used to increase the accuracy of quantum programs by compensating for noise errors.
- *Qiskit Aqua*: is a quantum algorithm development framework. It contains libraries for many different quantum algorithms, as well as tools for optimizing and benchmarking these algorithms.

Qiskit is an elegant tool for building and testing quantum computing algorithms. Researchers and developers from all over the world use it to investigate the potential of quantum computing for a wide range of applications. The rest of the paper is organized as follows. Section II provides an overview of the quantum circuits. Quantum circuits programming details for both simulators and real quantum computers are provided in section III. Section IV concludes the paper.

Quantum Circuits

Basic Concepts

A quantum circuit is a set of quantum gates that are applied to a group of qubits (Cervera-Lierta et al., 2019; Fisher et al., 2023). In quantum computing, qubit is the fundamental computational unit. Quantum circuits are used to create quantum algorithms that can only be run on a quantum computer. Depending on the quantum algorithm used, quantum gates in any quantum circuit can be connected in series or parallel or both. Quantum circuits have the following basic components:

- Qubits: In quantum computing, qubits are the fundamental unit of information. They can be in a state that is a superposition of two states, 0 and 1.
- Quantum gates are the fundamental operations that can be done on qubits. They can be employed to spin a qubit's state or to entangle two qubits.
- Measurements are used to determine the state of a qubit. When a qubit is measured, it collapses into one of two states: 0 or 1.

Quantum circuits are depicted graphically, with qubits denoted by lines and quantum gates denoted by boxes. The sequence of the gates in the circuit is critical because it dictates how the gates are applied to the qubits. Fig. 1 shows a sample of quantum circuits that is used throughout this paper. This circuit is produced using the IBM's quantum composer platform.

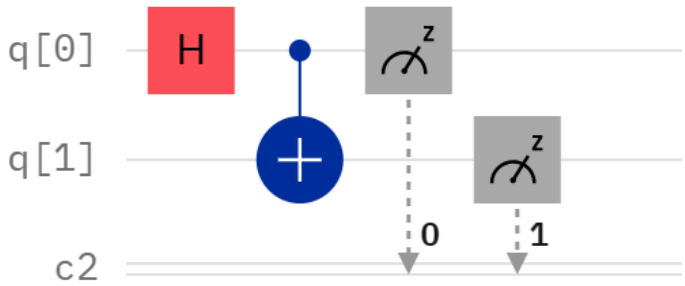

Figure 1. Entangled quantum circuit using IBM's composer platform

Quantum circuits can be used to construct a wide range of quantum algorithms, including Shor's algorithm for integer factoring, Grover's algorithm for searching an unsorted database, and quantum simulation of physical systems. Quantum circuits have the following essential properties:

- Quantum circuits are acyclic: This signifies that the circuit has no loops. A loop is a gate sequence that begins and ends at the same qubit. Loops are not permitted in quantum circuits because they can induce computing errors.
- Fan-in and fan-out are not permitted in quantum circuits. The number of qubits that can be acted on by a single gate is known as fan-in, and the number of qubits that can be influenced by a single gate is known as fan-out. Fan-in and fan-out in quantum circuits are normally limited to 1.
- Quantum circuits are reversible: Quantum circuit reversibility is a fundamental characteristic of quantum physics. It is critical for the development of quantum computing and offers a wide range of possible applications. Quantum reversibility requires that the number of inputs for any quantum circuits is equal to the number of outputs. The reason for quantum circuit reversibility is that the wavefunction that represents the state of he quantum system obeys the Schrodinger equation, which is a reversible equation. This means that it is possible to go from any state of the system to any other state. In addition, quantum gate is a unitary operator, which means it retains the wavefunction's norm. This means that the quantum gate is reversible.
- quantum measurement is irreversible: This is because measuring a qubit causes its wavefunction to collapse into a fixed state. This means that the knowledge about the qubit's other potential states is lost.

Mathematical Analysis

Qubits can be represented using vectors in Hilbert space. Dirac notation is used to represents qubits [3]. Unitary matrices can be used to study quantum circuits (Cruz-Lemus et al., 2021). A unitary matrix is one that maintains the inner product of vectors. This means that multiplying a vector by a unitary matrix has no effect on its length. The unitary matrix for a quantum circuit is the product of the unitary matrices for the individual gates in the circuit. The direction of the product is from right to left. Tensor product is utilized to multiply two or more parallel gates. The final state ($|\psi_f\rangle$) of the circuit shown in Figure 1 is given by:

$$|\psi_f\rangle = CNOT(H \otimes I)(q[0] \otimes q[1]) \quad (1)$$

if $q[0]$ and $q[1]$ are both initialized to $|0\rangle$, then the equation will be:

$$|\psi_f\rangle = CNOT(H \otimes I)|00\rangle \quad (2)$$

CNOT, Hadamard, and identity gates are given by the following unitary matrices.

$$CNOT = \begin{bmatrix} 1 & 0 & 0 & 0 \\ 0 & 1 & 0 & 0 \\ 0 & 0 & 0 & 1 \\ 0 & 0 & 1 & 0 \end{bmatrix}, \; H = 1/\sqrt{(2)} \begin{bmatrix} 1 & 1 \\ 1 & -1 \end{bmatrix}, \; I = \begin{bmatrix} 1 & 0 \\ 0 & 1 \end{bmatrix}$$

Then, equation 2 is given by:

$$|\psi_f\rangle = 1/2 \begin{bmatrix} 1 & 0 & 0 & 0 \\ 0 & 1 & 0 & 0 \\ 0 & 0 & 0 & 1 \\ 0 & 0 & 1 & 0 \end{bmatrix} \begin{bmatrix} 1 & 0 & 1 & 0 \\ 0 & 1 & 0 & 1 \\ 1 & 0 & -1 & 0 \\ 0 & 1 & 0 & -1 \end{bmatrix} \begin{bmatrix} 1 \\ 0 \\ 0 \\ 0 \end{bmatrix}$$

after reduction, the equation above is given by:

$$|\psi_f\rangle = 1/2 \begin{bmatrix} 1 \\ 0 \\ 0 \\ 1 \end{bmatrix} = 1/2(|00\rangle + |11\rangle)$$

which is a perfect entangled state, usually referred to as a Bells state. Bell states are an essential component of quantum ´ information science. Many quantum algorithms, such as quantum teleportation and quantum cryptography, make use of them.

Qiskit Programming Roadmap

This section describes how to run Qiskit-based quantum circuit programs on both a quantum simulator and IBM's real cloud-based quantum computer.

1) To begin, run the following command in a *Jupyter* notebook terminal to quickly install the library. This will install the most recent stable version of the library. It is recommended to install Qiskit with the extra visualization if you intend to use visualization functionality or *Jupyter* notebooks. The Qiskit library was install on August 20th, 2023.

```
pip install qiskit[visualization]
```

2) To check the version of Qiskit and its components in the Notebook by running the following command:

```
import qiskit
qiskit.__qiskit_version__
```

3) To implement the quantum circuit shown in Figure 1, execute the following code:

```
from qiskit import
QuantumCircuit
qc = QuantumCircuit(2,2)
qc.barrier()
qc.h(0)
qc.barrier()
qc.cx(0,1)
qc.measure([0,1],[0,1])
qc.draw(output='mpl')
```

The code utilizes the *matplotlib* library to produce much better circuit visualization as shown in Figure 2.

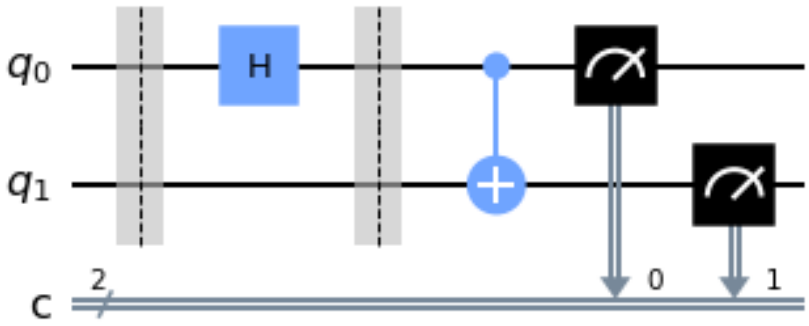

Figure 2. Entangled quantum circuit using Qiskit library

4) To confirm the entanglement of the two qubits, the code must be performed on either a quantum simulator or a real quantum computer platform. Quantum simulator can run quantum circuit programs on your local machine or on the cloud. Qiskit *Aer* is the simulator used to run and debug quantum programs before executing them on real quantum computers. First, let us run the given code on Aer simulator installed on a local machine. To get a list of the available simulators, the following statement should be executed.

```
from qiskit import Aer
Aer.backends()
```

The above statement should produce something similar to the following list, as illustrated in Figure 3.

```
[AerSimulator('aer_simulator'),
 AerSimulator('aer_simulator_statevector'),
 AerSimulator('aer_simulator_density_matrix'),
 AerSimulator('aer_simulator_stabilizer'),
 AerSimulator('aer_simulator_matrix_product_state'),
 AerSimulator('aer_simulator_extended_stabilizer'),
 AerSimulator('aer_simulator_unitary'),
 AerSimulator('aer_simulator_superop'),
 QasmSimulator('qasm_simulator'),
 StatevectorSimulator('statevector_simulator'),
 UnitarySimulator('unitary_simulator'),
 PulseSimulator('pulse_simulator')]
```

Figure 3. List of local Aer quantum simulators

Then we choose one of these simulators, *transpile* the quantum circuit to match the constraints and characteristics of the target quantum simulator/device and produce the results of the entangled quantum circuit as shown in the following code:

```
sim = Aer.get_backend('qasm_simulator')
from qiskit import transpile
qc_trans = transpile(qc, sim)
result = sim.run(qc_trans).result()
state_counts = result.get_counts(qc_trans)
from qiskit.visualization import plot_histogram
plot_histogram(state_counts,title='Bell-State counts')
```

Figure 4 shows the result of the above code, and it is compatible with equations above, with a probability of almost 0.5 for each of the entangled state.

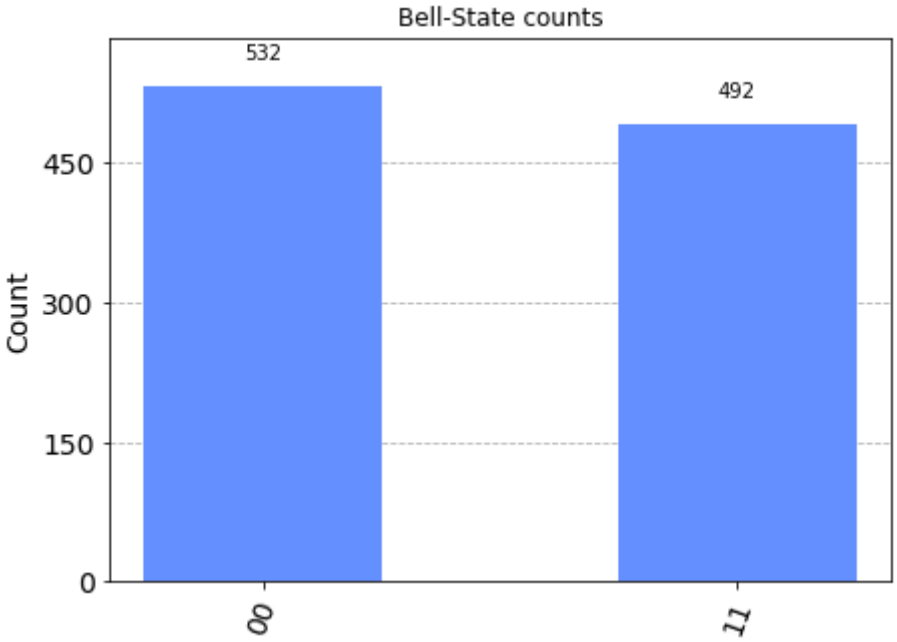

Figure 4. Histogram of entangled states (counts)

To get the probability of each quantum state, Qiskit introduced primitives which are the smallest processing instruction for a given abstraction level. *Sampler* is a Qiskit primitive that calculates probabilities or quasi-probabilities of quantum states. Quasi-probabilities are similar to regular probabilities except they may include negative values, which can occur when using certain error mitigation techniques. The code below shows how to calculate the quasi-probabilities of the Bell circuit. Figure 5 shows the corresponding probability distribution of the quantum states.

```
from qiskit_aer.primitives import Sampler
sampler = Sampler()
job = sampler.run(qc_trans)
plot_histogram(job.result().quasi_dists, title='Bell-State prob.')
```

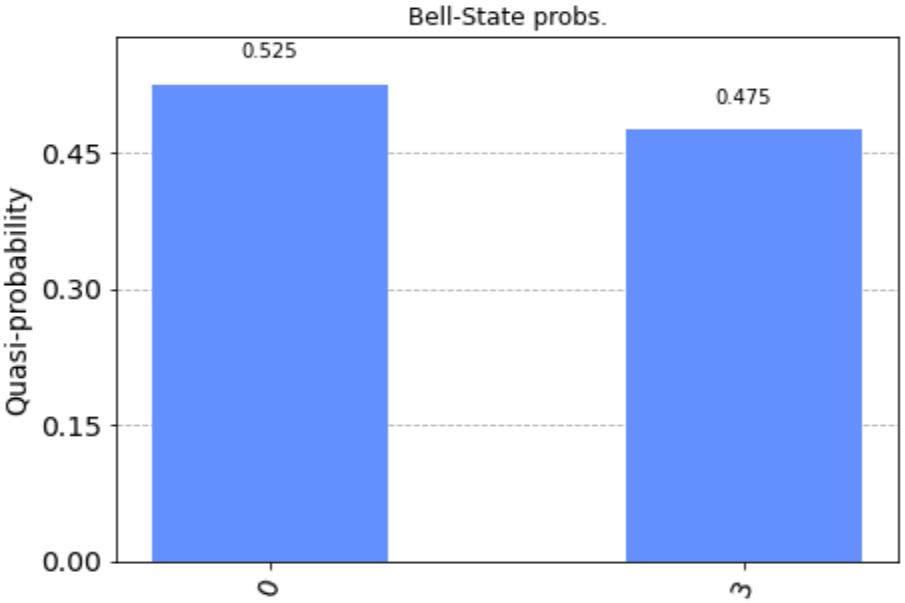

Figure 5. Histogram of entangled states probabilities

5) To run the quantum circuit code on IBM's online quantum computer systems, the following code should be run:

```
from qiskit_ibm_runtime import QiskitRuntimeService, Sampler
IBMTOKEN = "********" # IBM API Token
service = QiskitRuntimeService( channel='ibm_quantum', token=IBMTOKEN)
```

The code above will import the *QiskitRuntimeService* class and use it to connect the IBM cloud-based quantum computer through your IBM API token. The circuit code then can be run on a simulator or real quantum system. To get a list of real operational quantum computers, the following code is used.

```
service_real = QiskitRuntimeService( channel='ibm_quantum', token=tkn)
be_real = service_real.backends(simulator=False, operational=True)
```

Figure 6 shows a list of the operational real quantum systems.

```
[<IBMBackend('ibmq_quito')>,
 <IBMBackend('ibmq_lima')>,
 <IBMBackend('ibmq_belem')>,
 <IBMBackend('ibm_lagos')>,
 <IBMBackend('ibm_perth')>,
 <IBMBackend('ibmq_jakarta')>,
 <IBMBackend('ibmq_manila')>,
 <IBMBackend('ibm_nairobi')>]
```

Figure 6. Real quantum computers backends

To check the queue of pending jobs, number of qubits of the quantum computer backends, the following code is used.

```
for i in range(len(be_real)):
    be_name = be_real[i].name
    be_qb = be_real[i].num_qubits
    be_pj = be_real[i].status(). to_dict()['pending_jobs']
   print(f'{be_name :<15}: {be_pj :<5}, num_qubits: {be_qb}')
```

The output of the above code is shown in Figure 7.

```
ibmq_quito      :  542  , num_qubits:  5
ibmq_lima       :  364  , num_qubits:  5
ibmq_belem      :  305  , num_qubits:  5
ibm_lagos       :  148  , num_qubits:  7
ibm_perth       :  123  , num_qubits:  7
ibmq_jakarta    :  313  , num_qubits:  7
ibmq_manila     :  4111 , num_qubits:  5
ibm_nairobi     :  204  , num_qubits:  7
```

Figure 7. Pending jobs and number of qubits on the backends

To selected the least busy real quantum computer to run your quantum circuit, the following code is used.

```
backend_r = service_real.least_busy (simulator=False,operational=True)
print(backend_r.name)
```

In our case, the least busy computer to run the quantum circuit is the *ibmq perth* quantum computer. The quantum circuit program is then executed on the real quantum computer backend. Most of the time, the result is not as immediate as it is on the simulator backend. Normally, the program is queued before being executed. So, checking the program status is necessary as it may take a long time before it is executed. The following code provides the necessary steps for executing and monitoring the program.

```
sampler_r = Sampler(backend_r) job_r = sampler_r.run(qc, shots=4000)
job_r.status()
plot_histogram(job_r.result().quasi_dists,title='Bell-State prob.')
```

It is important to run the program many times as real quantum computers suffer from noise. In the code above the program was run 4000 times before getting the results as shown in Figure 8. Noise has its own effect on the entangled states. Negative low probabilities are noticed on the |01⟩ and |10⟩ quantum states.

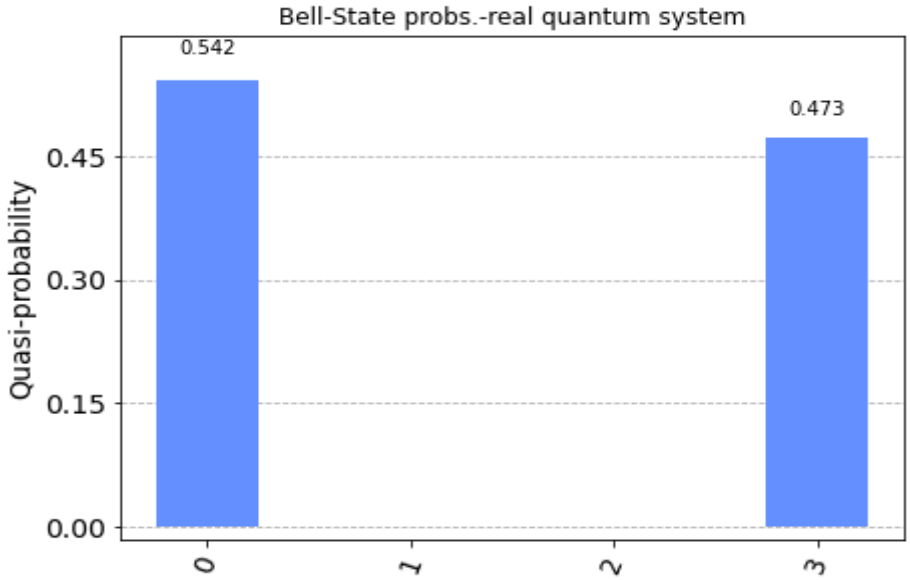

Figure 8. Quasi-probabilities of different quantum states

Conclusion

The paper includes programming details for building quantum applications using the IBM's Qiskit toolkit. It demonstrates the programming steps required to build quantum gates, quantum circuits, and quantum algorithms. It additionally illustrates how to simulate quantum circuits in quantum simulator backends. Moreover, it describes how to execute quantum circuits in a real cloud-based IBM quantum computer. Furthermore, it demonstrates how to choose the least busy real quantum computer to run the circuit program.

Scientific Ethics Declaration

The authors declare that the scientific ethical and legal responsibility of this article published in EPSTEM journal belongs to the authors.

Acknowledgements or Notes

* This article was presented as an oral presentation at the International Conference on Technology, Engineering and Science (www.icontes.net) held in Antalya/Turkey on November 16-19, 2023.

* The authors would like to thank the Deanship of scientific research and Innovation at Al-Zaytoonah University of Jordan (ZUJ) for Funding this work through ZUJ research fund No. (41/17/2022-2023)

References

Albash, T., & Lidar, D. A. (2018). Adiabatic quantum computation. *Reviews of Modern Physics*, *90*(1), 015002.

Bruzewicz, C. D., Chiaverini, J., McConnell, R., & Sage, J. M. (2019). Trapped-ion quantum computing: Progress and challenges. *Applied Physics Reviews*, *6*(2).

Cervera-Lierta, A., Latorre, J. I., & Goyeneche, D. (2019). Quantum circuits for maximally entangled states. *Physical Review A*, *100*(2), 022342.

Cruz-Lemus, J. A., Marcelo, L. A., & Piattini, M. (2021). Towards a set of metrics for quantum circuits understandability. In *International Conference on the Quality of Information and Communications Technology* (pp. 239-249). Cham: Springer International Publishing.

Fingerhuth, M., Babej, T., & Wittek, P. (2018). Open source software in quantum computing. *PloS one*, *13*(12), e0208561.

Fisher, M. P., Khemani, V., Nahum, A., & Vijay, S. (2023). Random quantum circuits. *Annual Review of Condensed Matter Physics*, *14*, 335-379.

Gill, S. S., Kumar, A., Singh, H., Singh, M., Kaur, K., Usman, M., & Buyya, R. (2022). Quantum computing: A taxonomy, systematic review and future directions. *Software: Practice and Experience*, *52*(1), 66-114.

Gyongyosi, L., & Imre, S. (2019). A survey on quantum computing technology. *Computer Science Review*, *31*, 51-71.

Hassija, V., Chamola, V., Saxena, V., Chanana, V., Parashari, P., Mumtaz, S., & Guizani, M. (2020). Present landscape of quantum computing. *IET Quantum Communication*, *1*(2), 42-48.

Hassija, V., Chamola, V., Goyal, A., Kanhere, S. S., & Guizani, N. (2020). Forthcoming applications of quantum computing: peeking into the future. *IET Quantum Communication*, *1*(2), 35-41.

Hidary, J. D., & Hidary, J. D. (2019). *Quantum computing: an applied approach* (Vol. 1). Cham: Springer.

Nielsen, M. A., & Chuang, I. L. (2010). *Quantum computation and quantum information*. Cambridge university press.

Preskill, J. (2021). Quantum computing 40 years later. In *Feynman lecturures on* computation (pp. 193-244). CRC Press.

Wille, R., Van Meter, R., & Naveh, Y. (2019). IBM's Qiskit tool chain: Working with and developing for real quantum computers. In 2019 *Design, Automation & Test in Europe Conference & Exhibition (DATE)* (pp. 1234-1240). IEEE.

Author Information

Yousef Jaradat
Al-Zaytoonah University of Jordan
Amman - Jordan
Contact e-mail: *y.jaradat@zuj.edu.jo*

Mohammad Alia
Al-Zaytoonah University of Jordan
Amman - Jordan

Mohammad Masoud
Al-Zaytoonah University of Jordan
Amman - Jordan

Ahmad Mansrah
Al-Zaytoonah University of Jordan
Amman - Jordan

Ismael Janooud
Al-Zaytoonah University of Jordan
Amman - Jordan

Omar Alheyasat
AlBalqa' Applied University
Salt-Jordan

To cite this article:

Jaradat, Y., Mohammad, A., Masoud, M., Mansrah, A., Jannoud, I., & Alheyasat, O. (2023). Roadmap for simulating quantum circuits utilising ibm's qiskit library: programming approach. *The Eurasia Proceedings of Science, Technology, Engineering & Mathematics (EPSTEM), 26*, 624-632.

The Eurasia Proceedings of Science, Technology, Engineering & Mathematics (EPSTEM)
ISSN: 2602-3199

The Eurasia Proceedings of Science, Technology, Engineering & Mathematics (EPSTEM), 2023

Volume 26, Pages 633-640

IConTES 2023: International Conference on Technology, Engineering and Science

Using RDF Models to Create Knowledge Bases in the Kazakh Language: Comparison with Other Methods

Assel Mukanova
Astana International University

Gulnazym Abdikalyk
Astana International University

Aizhan Nazyrova
Astana International University

Assem Dauletkaliyeva
Astana International University

Abstract: Currently, there is a rapid development of information technologies, the amount of information on the Internet is growing very fast and it is becoming increasingly difficult to find the necessary information. A search using keywords does not give results adequate to the meaning of the information sought. Therefore, the creation of a technology for designing intelligent question answering systems in the Kazakh language based on the presentation, processing and extraction of knowledge is a very actual problem, since it is in such a system that the linguistic and semantic relationships between the texts of the request and the answer can be taken into account. This research paper focuses on the integration of the Resource Description Framework (RDF) model, a semantic web technology, and provides a detailed evaluation of data mining techniques in Kazakh. The paper examines many Kazakh language data collection methods such as online scraping, community collaboration and translation. It also explores the function of RDF models in organizing knowledge, connecting data points and adding semantic richness to datasets. The paper discusses linguistic features and challenges unique to the Kazakh language and emphasizes the need to address these challenges with domain-specific data. The need for thorough cleaning, annotation and data quality assurance is emphasized to guarantee the reliability and use of the collected datasets. Within global communications and technology, the study emphasizes the importance of languages other than English and examines how semantic web technologies can improve data representation and knowledge retrieval. The study lays the groundwork for future initiatives to address the shortage of datasets in languages with fewer resources and to create semantic web technologies for language diversity.

Keywords: Resource description framework (RDF) model, Question-Answering system, Ontology model, Knowledge base

Introduction

Recent advances in machine learning and deep learning have led to significant progress in natural language processing, or NLP. The availability of high-quality datasets that serve as the basis for training and evaluating language models and applications is essential for the development of natural language processing (NLP) (Tang et al., 2021). Underrepresented languages such as Kazakh often face a lack of data, while dominant languages such as English, Chinese, and Spanish benefit from huge databases and linguistic resources (Zhubanov, 2018).

In order to shed light on the opportunities and challenges faced when collecting Kazakh language data sets, this study aims to explore the different approaches used in this process. In particular, it is about integrating structured data representation and semantic enrichment using the Resource Description Framework (RDF) paradigm, a semantic web technology (Rubiera et al., 2012). A variety of datasets are needed in linguistic research, machine learning, and NLP applications for model training, language understanding, and cross-linguistic research. However, due to data limitations, lack of digital material, and specific linguistic features, underrepresented languages such as Kazakh face particular challenges.

This study reviews the methods currently used to collect Kazakh datasets, such as online scraping, community collaboration and translation, and critically analyzes the function of RDF models in providing semantic enrichment and interconnectivity of data points. A more efficient knowledge organization is made possible by the structured representation of data in RDF, which also enables linking data points and sophisticated information retrieval (Decker et al., 2000).

To address the problem of data scarcity in under-represented languages such as Kazakh, this paper explores the use of representational density models (RDF). This paper emphasizes the importance of linguistic diversity and language representations beyond English in communication and technology. It lays the groundwork for future NLP research that will focus on structured and semantically enriched datasets. As NLP research develops, it will also contribute to linguistic diversity.

Research Methods

Modeling the Semantic Web Using RDF

In the field of semantic web, the Resource Description Framework (RDF) is a fundamental technology. Its ability to simplify the representation of structured data has had a great impact on many different areas, such as the development of structured databases for underrepresented languages such as Kazakh. In this part, we will look at the features, principles and applications of RDF, highlighting how important this technology is for data organization and language diversity.

RDF: A Framework for Representing Structured Data

At its core, RDF is an adaptable and extensible framework for structuring and semantically meaningful expression of information on the Web. RDF, unlike conventional databases, allows data to be represented as linked triples, each consisting of three elements: object, predicate and subject. By establishing associations between things, these triples allow data to be conceptualized semantically (Heath & Bizer, 2022). A resource is represented by the subject, its relation or attribute is labeled by the predicate, and its value or target resource is identified by the object. RDF is an effective tool for encoding, connecting and analyzing data in a way that conveys not only the information itself, but also its meaning and context because it is based on this triple structure, which serves as the basis for the semantic representation of RDF (Prud'hommeaux & Seaborne, 2008).

Interoperability and Semantic Structure

The strength of RDF lies in its ability to provide semantic context to data. RDF builds a semantic network in which things are connected by clear links by storing information in the form of trills. This semantic structure provides several advantages for data representation.

- Interoperability: RDF allows easy integration of data from different sources. The overall structure of RDF allows the integration and searching of different datasets, each represented within it. Since interoperability offers some structure for data integration, it is particularly useful when dealing with multilingual datasets (Bizer et al., 2023).
- Semantic enrichment: RDF allows the addition of meanings to data. RDF data can be enriched with meaning through the use of ontologies and controlled vocabularies, allowing for more precise and context-aware searches. Semantic enrichment can be used to reflect the subtleties and cultural features of the Kazakh language in the context of Kazakh datasets.

• Structured representation: RDF offers a structured data representation that allows semantic analysis and cross-lingual comparisons, making it useful for Kazakh datasets in Natural Language Processing (NLP) tasks due to its ability to provide a semantically meaningful representation.

RDF Regarding Kazakh Datasets

RDF models greatly facilitate NLP research using Kazakh language datasets. These models reflect the subtle cultural and linguistic aspects of the Kazakh language, improving data quality and facilitating interaction with other resources. By allowing NLP applications to access structured data, RDF models promote linguistic diversity. RDF preserves the semantic richness of data through the use of controlled vocabularies and domain-specific ontologies, allowing for more accurate and context-aware processing. The semantic web-based RDF model is a powerful tool that can be used to create structured datasets in Kazakh, to provide context-rich and structured data representation, and to promote linguistic diversity in NLP applications and research.

The Value of Non-English QA Datasets

High quality datasets play an important role in the development of Natural Language Processing (NLP) technology, which has advanced significantly in recent years. However, linguistic diversity and representation is becoming increasingly important for the development and relevance of this field. One language that is still underrepresented in the global digital arena is Kazakh, which is the official language of Kazakhstan and spoken by millions of people throughout Central Asia. Due to the lack of high-quality datasets, the Kazakh language is still neglected by NLP researchers, despite its importance to the region and its cultural heritage.

Beyond English: Kazakh QA Data is Needed

The importance of non-English QA data, like Kazakh, is in highlighting the world's linguistic diversity. Millions of people speak Kazakh, a Turkic language that is widely spoken and the official language of Kazakhstan. Kazakh language datasets are created with consideration for the language's variety as well as its distinct cultural, historical, and contextual elements. The development of Kazakh QA datasets contributes to a more comprehensive, inclusive and integrated natural language processing (NLP) ecosystem by acting as a model for the development of comparable resources in other non-English languages. The NLP community's dedication to fairly serve people worldwide is demonstrated by the development of multilingual QA datasets, particularly in Kazakh. These databases foster inclusion and creativity in addition to maintaining language.

Lack of Up-To-Date Data: A Major Challenge

While it is a laudable goal to create excellent Kazakh-language question answering (QA) datasets, there are a number of difficulties. The lack of available data in Kazakh language is one of the main obstacles faced by researchers in this field (Hao & Agichtein, 2012). Kazakh language does not have a data corpus similar to English, which is rich in textual data including QA pairs, making it unsuitable for creating QA data. The importance of this issue cannot be overemphasized, as the process of creating reliable Kazakh QA data is complicated by the lack of available data.

Another major challenge in creating Kazakh QA datasets is the translation of existing English-language QA datasets into Kazakh. Although translation is a common method of extending QA sets into non-English languages, it is not without drawbacks. In the process of translating English QA pairs into Kazakh, linguistic nuances, cultural context and contextual variations present in the original language may be inadvertently excluded, reducing the overall quality and efficiency of the dataset (Diab & Resnik, 2002).

Overview of Data Collection Methods

This section reviews various methods of data collection in Kazakh language, in particular web scraping, manual translation, crowdsourcing and innovative methods. It presents an in-depth analysis of the advantages and limitations of each method, emphasizing the importance of linguistic diversity and supporting research and applications in the field of natural language processing (NLP) in Kazakh.

Inclusivity

One of the frequently used methods for data collection in Kazakh language is web scraping. With this method, text and information are automatically extracted from various internet sources such as blogs, news portals, forums and social networks. Considering Kazakh data sets, some advantages and disadvantages of online scraping should be noted (Finkel et al., 2005).

Advantages
• Rich and up-to-date material: Web scraping provides access to a large amount of relevant and diverse material, which keeps datasets up-to-date. This is particularly useful for applications such as sentiment analysis and event monitoring that need up-to-date data (Callison-Burch et al., 2011).
• Large scale data collection: Automated web scraping allows for the rapid collection of huge amounts of data, making it a useful tool for creating the huge data sets needed to train large NLP models (Bird et al., 2006).

Limitations
• Legal and ethical issues: When it comes to copyrighted or proprietary material, both legal and ethical issues can arise in web scraping. Respecting the rights and limitations of sources, the terms of service and intellectual property rights must be carefully considered (Spalka, 2015).
• Data Quality: Due to unstable formatting and unstructured content, raw data obtained through web scraping often needs careful cleaning and preparation. It is not easy to ensure the accuracy and high quality of the collected data (Baeza-Yates & Ribeiro-Neto, 2011).

Manual Translation

Manual translation involves the use of human translators to create new data entirely in Kazakh or to translate existing information into that language. When it comes to Kazakh data sets, manual translation has a unique combination of advantages and disadvantages (Lewis, 1992).

Advantages
• Accuracy and quality: The use of human translators ensures accurate translations that convey the subtleties and unique cultural characteristics of the Kazakh language. This is particularly useful for initiatives that need to be culturally sensitive and accurate in wording (Bird, 2006).

Limitations
• Time and resource costs: Manual text translation can be laborious and resource intensive, especially when dealing with large data sets. It increases the cost and duration of data collection as it requires skilled translators who are fluent in both the source and target language (Snow et al., 2008).

Online Auctions

Crowdsourcing is a method of creating or translating materials that utilizes the collaborative efforts of many people, sometimes with different language backgrounds. There are some advantages and disadvantages of using crowdsourcing when dealing with Kazakh datasets (Ipeirotis, 2010).

Advantages
• Scalability: Crowdsourcing is a very scalable technology that allows for the rapid creation of large datasets. This is especially effective for initiatives where large amounts of data need to be collected in a short period of time.

Limitations
• Semantic Correctness: The semantic correctness of crowd-sourced translations may be inferior to translations produced by expert translators. Ensuring that crowd-sourced translations adequately convey the desired meaning is an ongoing challenge that requires careful supervision and quality control procedures (Callison-Burch et al., 2011).

Other Innovative Techniques

To overcome the limitations of the lack of linguistic resources, new approaches including data augmentation, transfer learning and parallel corpora are being used to collect Kazakh language data. Data augmentation is the process of adding new data to existing datasets through transformations such as data synthesis, text expansion and paraphrasing (Wei et al., 2017). Transfer learning improves NLP tasks in underrepresented languages, such as Kazakh, by utilizing already existing models and information from well-resourced languages (Peters et al., 2018). Parallel corpora in similar languages such as Turkish or Uzbek can be used to improve Kazakh datasets (Bekarystankyzy et al., 2023). This would allow cross-lingual analysis and adaptation of NLP models to the Kazakh language.

Related Works

Interest in collecting data sets in the Kazakh language is growing, and researchers are considering a number of strategies to overcome the difficulties associated with resource creation and data collection. The authors of the article are engaged in the field of text processing in the Kazakh language. In (Mukanova et al., 2014) (Yergesh et al., 2014) a semantic hypergraph was used to describe ontological models of morphological rules of the Kazakh language. In (Yelibayeva et al., 2020) describes the metalanguage of morphological concepts of the Turkic languages for the creation of knowledge bases. In articles (Sharipbay et al., 2019) (Yelibayeva et al., 2020) (Yelibayeva et al., 2022) describes the methods of syntactic analysis of the text in the Kazakh language based on the ontological model.

Other related publications provide insights into the various approaches, challenges and uses associated with data collection in the Kazakh language. One of them builds on a BERT-like concept to create an extractive question-answer system using Google Cloud Translation API and a Kazakh question-answer dataset (KazQA). The ability of the system to generate Kazakh language question-answer systems with few resources is demonstrated using ALBERT and multilingual BERT as base models (Shymbayev & Alimzhanov, 2023). The following paper proposes a modular approach to question analysis using rule-based methods and Hidden Markov Models (HMM) to generate a question-answering (QA) system in Kazakh language. Using dependency relations between words, the method integrates question classifiers, focus extraction and system classification (Rakhimova et al., 2021).

There are methods using seq2seq approach to collect 60,000 corpora in Kazakh language (Rakhimova et al., 2022). There is a large number of works devoted to the creation of QA data in Kazakh language. But despite this, the Kazakh language with its rich history and multiple uses is widely spoken and studied, which makes it an invaluable resource for scholars and specialists.

Results and Discussion

One of the main parameters of text analysis for understanding the meaning of a sentence is to determine the properties of words in the text and the relationships between them. In our project, ontology was used to represent domain knowledge. It reflects the concepts of the subject area and the semantic relations between them. The semantic relation is binary.

The OWL language is used to describe ontological knowledge. This language is designed not only to represent domain knowledge, but also for applications that allow you to process this knowledge. This language uses RDF resources as its main elements. An RDF resource can be expressed as a triplet: subject – predicate - object." Then if we take the vertices of the ontology as subject and object, the relationship or property between them will be predicates.

In the Kazakh language, phrases have 4 types of communication (Kiysu (Kiysu), Mengeru (MengEt), Matasu (MatEs), Kabysu (KabEs)).These structures are created by combining two or more words. Phrases can have a head word (head) and a dependent word (dep). Words in a phrase can be a concept of a subject area, a relation or a property between them. Therefore, using formal rules (Yelibayeva . et al., 2019) constructing phrases in the Kazakh language, consider the fragment rules for converting words in the text into concepts and knowledge base relationships in the form of RDF (Table1). Using the SPARQL language to query in our knowledge base, it is possible to extract answers to questions and analyze data in Kazakh through these rules.

Table 1. Fragment rules for converting words in the text into concepts and knowledge base relationships in the form of RDF

Types of communication	Dependent word dep	Head word head	Subject S	Predicate P	Object O
KabEs	Adj	Dom	dom	? (hasType)	dep
KabEs	Adj	Dom	dom	? (hasClass)	dep
KabEs	Adj	Dom	dom	? (hasProperty)	dep
KabEs	Num	Dom	dom	? (hasNuber)	dep
KabEs	Num	dom	dom	? (hasOrder)	dep
MatEs	dep	dom	dep	dom	?
Kiysu	dep	dom	dep	?	dom
Kiysu	dep	V	dep	dom	?
MengEt	dep	V	dep	dom	?

Conclusion

This study examines different approaches to the collection of Kazakh datasets with a focus on the use of RDF models. The article discusses the methods of applying semantic models of RDF triplets depending on the type of phrases in the sentence, developed formal rules. Based on this, the question and answer are compared in accordance with the knowledge available in the knowledge base. The study sheds light on the evolution of linguistic diversity and highlights the revolutionary potential of structured data in Natural Language Processing (NLP) research and applications. Linked Data principles and the implementation of the RDF model pave the way for a more diverse and international NLP community. The study also emphasizes the need to promote underrepresented languages to guarantee their participation in the digital age. This study reminds us that language diversity is a critical resource as NLP technologies evolve. We must work together to protect and preserve these multiple language ecosystems so that no language is lost in the digital age. The findings of the study and the structured data it collects contribute to the goal of making NLP a truly inclusive and global field. We hope that this study will serve as a springboard for further research, partnerships and projects to support linguistic diversity and the inclusion of all languages in the global semantic network of the future.

Future Recommendations

The study focuses on RDF models in exploring different approaches to collecting Kazakh language datasets. It emphasizes the need for further recommendations and makes suggestions for future approaches to maintain the sustainability of structured data in underrepresented languages such as Kazakh and improve linguistic diversity. Domain-specific Kazakh language ontologies are needed to organize data in specialized industries such as healthcare, banking, and law. Creating strong ontologies requires the collaborative efforts of experts, linguists and engineers. Modeling RDF in Kazakh requires standardization at the community level to ensure that data representations conform to common practices and rigorous data standards.

Adding Kazakh datasets to the global Linked Data ecosystem can foster the development of multilingual applications, facilitate cross-language information retrieval, and increase the availability of Kazakh-language material on the Semantic Web. Crowdsourcing methods can be used to accelerate the collection and enrichment of Kazakh data, especially in areas where specialized knowledge is required. In addition to solving the problem of data scarcity, this can facilitate community engagement. The burden of human quality control can be reduced by using machine learning and artificial intelligence to clean and validate data. The goal of this effort is to improve the visibility of Kazakh language information in the Semantic Web and to create a more complete, connected knowledge network.

Scientific Ethics Declaration

The authors declare that the scientific ethical and legal responsibility of this article published in EPSTEM journal belongs to the authors.

Acknowledgements

* This article was presented as an oral presentation at the International Conference on Technology, Engineering and Science (www.icontes.net) held in Antalya/Turkey on November 16-19, 2023.

* This research has been funded by the Science Committee of the Ministry of Science and Higher Education of the Republic of Kazakhstan (Grant No. AP19577922)

References

Baeza-Yates, R., & Ribeiro-Neto, B. (1999). *Modern information retrieval* (Vol. 463, No. 1999). New York, NY: ACM Press.

Bekarystankyzy, A., Mamyrbayev, O., Mendes, M., Oralbekova, D., Zhumazhanov, B., & Fazylzhanova, A. (2023). Automatic speech recognition improvement for Kazakh language with enhanced language model. In *Asian Conference on Intelligent Information and Database Systems* (pp. 538-545). Cham: Springer Nature.

Bird, S. (2006). NLTK.: The natural language toolkit. In *Proceedings of the COLING/ACL on Interactive Presentation Sessions*, 69-72.

Bird, S., Loper, E., & Klein, E. (2009). *Natural language processing with Python.* Sebastopol, USA: O'Reilly Media Inc

Bizer, C., Heath, T., & Berners-Lee, T. (2023). Linked data-the story so *far. In Linking the World's Information: Essays on Tim Berners-Lee's Invention of the World Wide Web,* 115-143.

Callison-Burch, C., Koehn, P., Monz, C., & Schroeder, J. (2011). Findings of the 2011 workshop on statistical machine translation. In *Proceedings of the Sixth Workshop on Statistical Machine Translation* (WMT *'11)* (pp.22-64).

Callison-Burch, C., Koehn, P., Monz, C., & Schroeder, J. (2011). Findings of the 2011 workshop on statistical machine translation. In *Proceedings of the Sixth Workshop on Statistical Machine Translation* (WMT *'11)* (pp.22-64).

Decker, S., Mitra, P., & Melnik, S. (2000). Framework for the semantic Web: An RDF tutorial. *IEEE Internet Computing*, *4*(6), pp. 68-73.

Diab, M., & Resnik, P. (2002). An unsupervised method for word sense tagging using parallel corpora. In Proceedings of *the 40th Annual Meeting of the Association for Computational Linguistics* (pp. 255-262).

Finkel, J. R., Grenager, T., & Manning, C. D. (2005, June). Incorporating non-local information into information extraction systems by gibbs sampling. *In Proceedings of the 43rd annual meeting of the association for computational linguistics (ACL'05)* (pp. 363-370).

Hao, T., & Agichtein, E. (2012). Finding similar questions in collaborative question answering archives: toward bootstrapping-based equivalent pattern learning. *Information Retrieval*, *15*, 332-353.

Heath, T., & Bizer, C. (2022). *Linked data: Evolving the web into a global data space* (pp.1-136). Springer Nature.

Ipeirotis, P. G. (2010). Analyzing the amazon mechanical Turk marketplace. *XRDS: Crossroads, The ACM magazine for students*, *17*(2), 16-21.

Lewis, D. D. (1992, June). An evaluation of phrasal and clustered representations on a text categorization task. In *Proceedings of the 15th annual international ACM SIGIR conference on Research and development in information retrieval* (pp. 37-50).

Mukanova, A., Yergesh, B., Bekmanova, G., Razakhova, B., & Sharipbay, A. (2014). Formal models of nouns in the Kazakh language. *Leonardo Electronic Journal of Practices and Technologies*, *13*(25), 264-273.

Peters, M. E., Neumann, M., Iyyer, M., Gardner, M., Clark, C., Lee, K., & Zettlemoyer, L. (2018). Deep contextualized word representations. In Proceedings of the 2018 Conference of the North American *Chapter of the Association for Computational Linguistics: Human Language Technologies (NAACL-HLT)* (pp. 2227-2237).

Prud'hommeaux, E., & Seaborne, A. (2008). SPARQL query language for RDF. *W3C Recommendation*.

Rakhimova D., Suleimenov Y. and Akhmet G. (2022). The task of synthesizing the Kazakh language based on the seq2seq approach for a question-answer system. *7th International Conference on Computer Science and Engineering (UBMK)* (pp. 289-293). IEEE.

Rakhimova, D., Khairova, N., Kassymova, D., & Janibekovich, K. (2021). Development of a system of questions and answers for the Kazakh language based on rule-based and HMM: development of a system of questions and answers for the kazakh language based on rule-based and HMM. *Advanced Technologies and Computer Science,* (2), 34–44.

Rubiera, E., Polo, L., Berrueta, D., & El Ghali, A. (2012, May). TELIX: An RDF-based model for linguistic annotation. *In Extended Semantic Web Conference* (pp. 195-209). Berlin, Heidelberg: Springer.

Sharipbay, A., Yergesh, B., Razakhova, B., Yelibayeva, G., & Mukanova A. (2019). Syntax parsing model of Kazakh simple sentences. *ACM International Conference on Data Science, E- Learning and Information Systems* (pp.1-5).

Shymbayev M., & Alimzhanov Y (2023). Extractive question answering for Kazakh language. *IEEE International Conference on Smart Information Systems and Technologies* (SIST) (pp. 401-405).

Snow, R., O'connor, B., Jurafsky, D., & Ng, A. Y. (2008, October). Cheap and fast–but is it good? evaluating non-expert annotations for natural language tasks. In *Proceedings of the 2008 conference on empirical methods in natural language processing* (pp. 254-263).

Spalka, A. (2015). Challenges of Web Scraping. Strohmaier, R., Schuetz, M., & Vannuccini, S. (2019). A systemic perspective on socioeconomic transformation in the digital age. *Journal of Industrial and Business Economics*, *46*(3), 361-378.

Tang, S. X., Kriz, R., Cho, S., Park, S. J., Harowitz, J., Gur, R. E., ... & Liberman, M. Y. (2021). Natural language processing methods are sensitive to sub-clinical linguistic differences in schizophrenia spectrum disorders. *NPJ Schizophrenia*, *7*(1), 25.

Wei, J., Zhao, Y., & Li, M. (2017). Neural machine translation with external phrase memory. In *Proceedings of* the *55th Annual Meeting of the Association for Computational Linguistics* (Vol.1, pp. 2181-2190).

Yelibayeva G., Mukanova A., Zhulkhazhav A, Razakhova B., & Sharipbay A. (2019). Combined morphological analyzer of the Kazakh language based on ontological modeling. *Human Language Technologies as a Challenge for Computer Science and Linguistics*, 241-244.

Yelibayeva, G., Mukanova, A., Sharipbay, A., Zulkhazhav, A., Yergesh, B., & Bekmanova G. (2019). Metalanguage and knowledgebase for Kazakh morphology. In *Computational Science and Its Applications- ICCSA 2019: 19 th International Conference, Saint Petersburg, Russia* (pp. 693-706). Springer International Publishing.

Yelibayeva, G., Razakhova, B., Yergesh, B., Sharipbay, A., Bekmanova, G., & Mukanova, A. (2022) Modeling of verb phrases of the Kazakh language. In *2022 International Conference on Engineering and MIS, ICEMIS 2022*. (pp.1-3). IEEE.

Yelibayeva, G., Sharipbay, A., Mukanova, A., & Razakhova, B. (2020). Applied ontology for the automatic classification of simple sentences of the Kazakh language *5th International Conference on Computer Science and Engineering (UBMK)* (pp.13-18). IEEE

Yergesh, B., Mukanova, A., Sharipbay A., Bekmanova G., Razakhova B. (2014). Semantic hyper-graph based representation of nouns in the Kazakh language. *Computacion y Sistemas, 18*(3), 627-635.

Zhubanov A.K. (2018). For digital Kazakhstan creation of the speaker corps of the Kazakh language is a topical problem. *Tiltanym, (4),* 45-50.

Author Information

Assel Mukanova
Astana International University
Kabanbay Batyra Avenue 8, Astana, Kazakhstan
Contact e-mail: *asiserikovna@gmail.com*

Gulnazym Abdikalyk
Astana International University
Kabanbay Batyra Avenue 8, Astana, Kazakhstan

Aizhan Nazyrova
Astana International University
Kabanbay Batyra Avenue 8, Astana, Kazakhstan

Assem Dauletkaliyeva
Astana International University
Kabanbay Batyra Avenue 8, Astana, Kazakhstan

To cite this article:

Mukanova, A., Abdikalyk, G., Nazyrova, A., & Dauletkaliyeva, A. (2023). Using RDF models to create knowledge bases in the kazakh language: comparison with other methods. *The Eurasia Proceedings of Science, Technology, Engineering & Mathematics (EPSTEM), 26*, 633-640.

The Eurasia Proceedings of Science, Technology, Engineering & Mathematics (EPSTEM)
ISSN: 2602-3199

The Eurasia Proceedings of Science, Technology, Engineering & Mathematics (EPSTEM), 2023

Volume 26, Pages 641-647

IConTES 2023: International Conference on Technology, Engineering and Science

Plastic Fiber Low Light Measurement Method

Brindus Comanescu
Optoelectronica 2001 S.A.

Paul Schiopu
University Politechnica of Bucharest

Marian Vladescu
University Politechnica of Bucharest

Melu Vlad
Optoelectronica 2001 S.A.

Abstract: Paper describe researches performed to develop a method for checking the light transmission through plastic scintillating fiber. Such fibers are used in different industrial or research application but for our purpose are main components of a flexible detector. Such detector use photon scintillating signals read by higly sensitive detectors and special measures taken to get such sensitivity. We present in paper a method and algorithm developed for measurement of light transmission through plastic fiber when signals are at level of nW. We develop a stand to implement and verify this method. We use fibers with connectors at each fiber end. Fibers are previously polished at each end in order to allows to pass the signal through surface with low losses. Using the stand we perform measurements to analyse the feasibility of method. We present the results that demonstrate the feasibility of method. We succeed to measure signals at level of nW using special measures. Our results shows that method and stand can be used to measure low level signals through fibers. Using this method, it is possible to check the quality of plastic fiber polishing. A fiber with end surface well-polished allows to pass the signal at such low level (nW)..

Keywords: Low light optical signal transmission, Plastic fiber testing, Fiber optic

Introduction

The purpose of the paper is to present research aspects in the field of fiber optic. Domain of flexible detector is relative new in photonic. Such flexible detectors appear because of special need, for special application were a flat detector do not offer enough information. There are situations in the domain of industry, medical, research, border control, smuggling monitoring, were this type of detector can be used as supplementary detector to offer more date and information. One of such flexible detector is presented in figure 1. In figure 1 we see fiber matrix. There is a zone, active area were stimuli can interact with fibers and following this interaction photon are emitted. At both ends of plastic fibers there are silicon photomultiplier - SiPMs. Fibers are fill in with scintillating material specially that allows to emit photons when are excited. Matrix of fiber are immersed in a resin. Resins used to build matrix are made from silicon or epoxy with purpose to became flexible after construction. We implement the method and we measure the signal transmitted through fiber.

We use for experiments plastic scintillating fiber from Kuraray (Kuraray, n.d.) with 1 mm diameter made from polymer. Fiber has core and clad. Fiber core is made from polystyrene material and clad is made from polymethyl methacrylat - PMMA. We present our concept for developing a method for testing light transmission through plastic scintillating fiber. Fibers are manual polished at both ends. All tests and

measurements are performed in a special conditions to eliminate environment light influence on fiber sensitivity wavelength range. Due to low level of scintillating signal even a reduced level of influence is important and can modify the results.

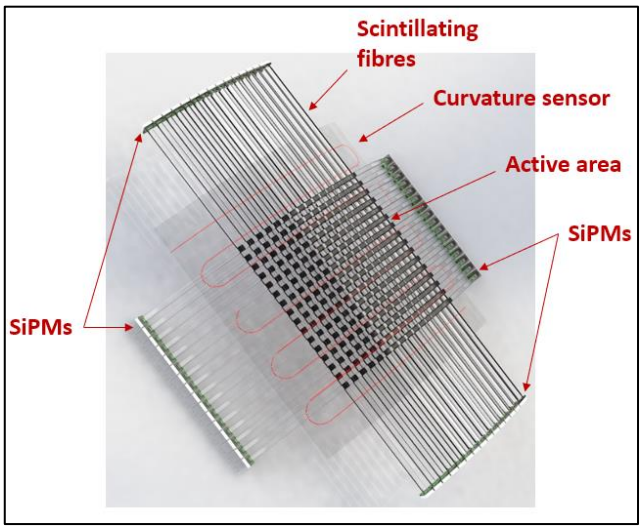

Figure 1. Flexible detector (Wibur et al.,2021)

Method

To define the method for testing the quality of signal transmission through plastic scintillating fiber it is need to start from light propagation through fiber. On same type of the plastic scintillating fiber, depending of the polishing quality, the light propagates on same way through the fiber because other influence factors can be controlled in order to minimize or eliminate their influence. We start our method design from definition of fundamental constant of speed of light. Speed of light (c) definition represents "the speed at which light waves propagate through different materials (Oxford Reference, n.d.). In our case is the speed at which light at known wavelength pass through fiber. Wavelength represents wavelength on which fiber is sensitive and this is a parameter set by manufacturer .

Speed of light in vacuum, "c" is defined by formula (1)

$$c = 299{,}792{,}458\ m * s^{-1} \quad (1)$$

Wavelength - frequency equation is defined by formula (2)

$$c = \lambda * \nu \quad (2)$$

were
λ - wavelength of light, [nm]
ν - frequency , [Hz]
According with formula (2) , when frequency increase, the wavelength decrease because speed of light" ***c*** **"** is a fundamental constant.
In our case the scintillating fiber is dedicated to transmit photons on blue domains of light spectra, especially on 440 nm. For example, a photon of light has a frequency " ν" = 638 THz (terahertz) and will have wavelength " λ ".
Based on formula (2) we can wrote the formula of wavelength function of speed of light and frequency

$$\lambda = c / \nu \quad (3)$$

We introduce values in formula (3) and we obtained the value of wavelength:

$$\lambda = 3*10^{8} m*s^{-1} / 638*10^{12} *m*s^{-1} = 460\ nm \quad (4)$$

We know that the energy of a photon can be obtained by multiplying Planck constant by frequency, as is expressed by formula (5) :

$$E = h * \nu \quad (5)$$

Were

h - Planck constant, $h = 6{,}626 * 10^{-34}$ J*s

ν - vibration frequency

We fill in values in formula (5) and we obtain the value of energy:

$$E = h * c / \lambda = (6{,}626 * 10^{-34} \text{ J*s}) * (3 * 10^{8} \text{ m*s}^{-1}) / 4{,}6 * 10^{-7} \text{ m} \quad (6)$$

For a photon with wavelength λ = 460nm, placed in blue region of optical spectrum, the energy value is

$$E = 4{,}32 \times 10^{-19} \text{ J} \quad (7)$$

Of course this results need corrections because in real situation there is more photons that pass through fiber not just a single photon. From this reason the result (7) should be multiplied by the number of photons. Scintillating photons appeared in plastic fiber are transmitted from one end to the other end were is a Multi-Pixel Photon Counter (MPPC), that convert optical photons in electrons. An electronic PCB receive electronic signal converted from photons, amplify signal using an amplifier integrated in PCB and send it further. For our researches we use a MPPC from Hamamatsu, type S13360 with a gain 4×10^{6} or a Silicon Photomultiplier (SiPM) from ONSEMI with gain 3×10^{6}.

With such high gain we are able to measure energy of photons in the range of pJ:

$$E = 4{,}32 * 10^{-19} * 4 * 10^{6} = 1{,}632 * 10^{-12} \text{ J} = 1{,}632 \text{ pJ} \quad (8)$$

Experiments

In the Figure 2 is a scintillating plastic fiber polished with metallic ferule at both ends. In the figure we have a fiber support made from plastic used for fixing fiber and metallic ferule. We have a plastic scintillating fiber with metallic ferule at both ends.

Figure 2. Plastic fiber polished

We design a method of testing the transmission of photons through plastic scintillating fiber using a special developed stand. his surface is manufactured by polishing. This method can be used to check the quality of fiber end surface because of this surface quality depend the signal send it. In order to investigate our assumption, it is need to implement a method into a stand. Developed stand (figure 3,4) is composed by following components:

- LED :
  - producer Wurth Electronik
  - wavelength λ = 460 nm
  - maximum illumination 25 Lm for 350 mA

- Regulated Power Supply :

  - model DC QJ 3003 C
  - DC tension is variable from 0 - to 30 Vcc
  - DC current is also variable from 0 - to 3 Vcc

- Rezistance :

- 100 Ohms
- max. 0.1A
- accuracy class 0.01

- Digital multimeter:

- producer UNI-T
- model UT 70A
- DC tension from 0.2 to 1000 V
- DC current 20 μA - 10A

- Plastic scintillating fiber:

- model Kuraray SCSF - 78
- 1 mm diameter
- wavelength peak 450 nm
- fiber is polished at both ends

- Detector

- model Ophir PD300R
- sensitivity spectre 200 - 1100 nm
- power range
  - 20 pW - 3mW
  - 2μW - 300 mW
- error ±2% for 420 nm - 980 nm
- noise ±1%

Detector meter:
- Laserstar

capable to measure: power, energy, pulse power, pulse energy
- command screen
- detect automatic the detector head

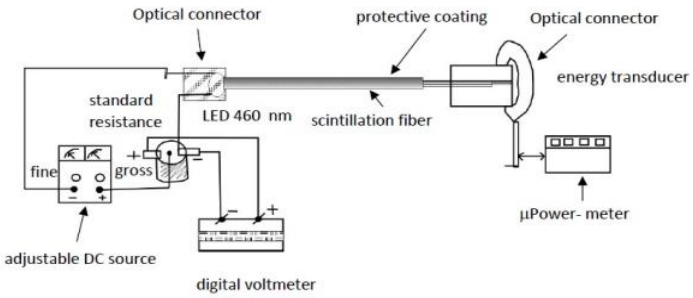

Figure 3. Measurement scheme

In Figure 3 is the schema of measurement stand. This schema is implemented by Figure 4. Implementation of method from Figure 3 is presented in Figure 4. In figure can be identified all parts of the measurement stand:

- output detector
- plastic fiber
- DC current measurement device
- power supply unit
- tools
- resistance

Fiber is inserted in tube for mechanical protection and and to avoid influence of environment. We increase slowly the input voltage applied at entrance of LED using coarse and fine knob from power supply. When on display it is indicated 2,2 V, we noticed that LED has emission on 460 nm wavelength. We increase slowly tension at LED entrance in small steps and we read the indication on multi meter display. The light emitted by LED is transmitted in fiber and is read with detector at output fiber. Fiber has both ends polished. Radiation pass

through plastic fiber and reach a photosensitive detector, PD300UV from OPHIR. Such detector is very sensitive and was chosen from this reason. Each value of input and output is written and a graphics is prepared and shown bellow. Influence of environment is eliminated using few methods:

- protect fiber with a plastic jacket as in Figure 4
- coat fiber with protective paint
- perform measurements inside of a protective box.

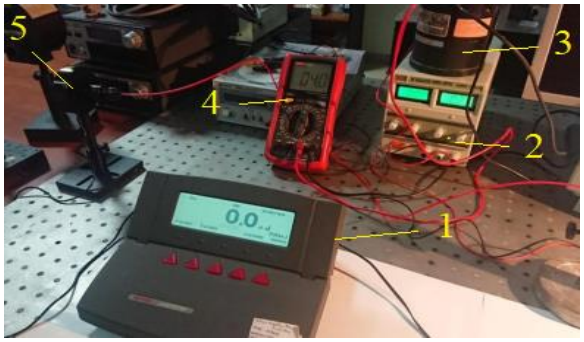

Figure 4. Measurement stand

1 -Laserstar; 2 - power supply; 3 - precision resistance; 4 - multimeter; 5 detector

In the Figure 4 are presented all components of stand used for testing measurement method:

- computing unit - Laserstar - position 1
- power supply - position 2
- precision resistance - position 3
- multimeter - position 4
- detector - position 5
- plastic scintillating fiber - red tube

In experiment we prefer to coat plastic scintillating fiber by black paint. Fiber is painted in black color to avoid external bad influence and perform measurements in a black box as in Figure 5. The box is a standard box painted with black paint. During measurements plastic scintillating fiber are inside of black box with LED and detector. Such protection avoid possible fake input stimulation's and possible error.
Possible errors on the results appear because of:

- mounting fiber and detector in supports,
- detector errors.

We do not consider errors appeared due to external influence because we consider that we take needed measures to eliminate them.

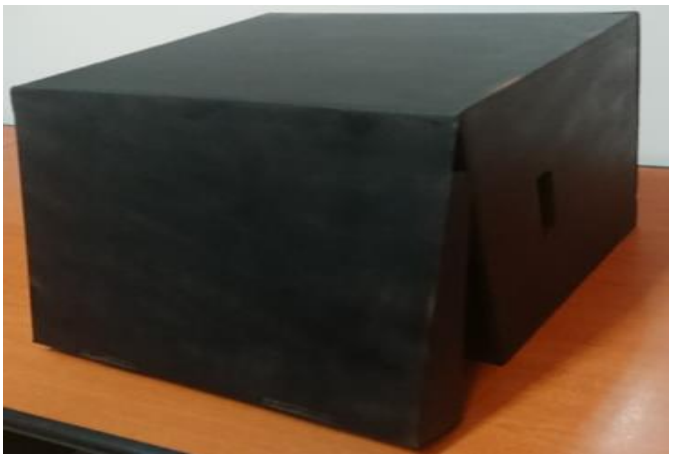

Figure 5. Black box

In Figure 5 is presented black box for protection against environment influence.

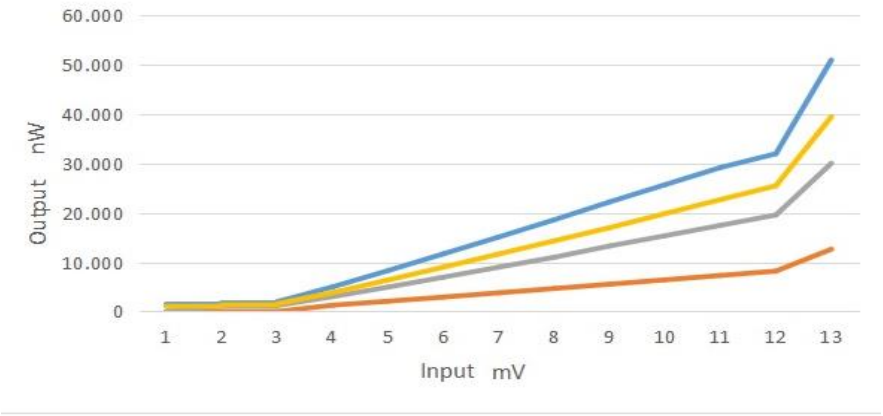

Figure 6. Measurements using method

Measurements are performed as were described earlier. After we obtain from LED output light, the value from multimeter and laserstar are written in a table. We measure 5 fibers and we obtain the graphic from Figure 6. We notice that if the fiber is well polished the output value increase with increase of input. We can claim that fiber is well polished using another method, an video microscope with 100x magnification from Edmund Optics. We noticed that for low input values, the output is not increasing. It is not plotted this situation in graphic because we do not considered. This is normal situation because for low level of measurements, we are in the range of errors given by tools and instruments used. When we increase the input value the output value increase also, there is a direct correlation between input and output. In conclusion method and stand associated are feasible to use them for testing plastic scintillating fiber polishing quality. Method and stand are is easy to implement and use it.

Abbreviations and Acronyms

PMMA - polymethyl methacrylat
MPPC - Multi-Pixel Photon Counter
SiPM - Silicon photomultiplier

Scientific Ethics Declaration

The authors declare that the scientific ethical and legal responsibility of this article published in EPSTEM journal belongs to the authors.

Acknowledgments

* This article was presented as an oral presentation at the International Conference on Technology, Engineering and Science (www.icontes.net) held in Antalya/Turkey on November 16-19, 2023.

* We develop our experiments under the project " *Flex-Ray - Inherently Flexible X-Ray Imaging Detector using Single Photon Avalanche Photodiodes and Scintillating Fibres*", project funded from the European Union's Horizon 2020 research and innovation programme under grant agreement No 899634.

References

Kuraray(n.d.). *Plastic scintillating fibers*. Retrieved from https://www.kuraray.com/products.
Oxford Reference (n.d.). *Oxford reference*. Retrieved from https://www.oxfordreference.com

Wilbur, S., Anastopoulos, C., Angelmahr, M., Asfis, G., Koch, J., M. Lindblom, M., K. Lohwasser, K.,& Margulis, W. (2021). Flexible X-ray imaging detectors using scintillating fibers. *Journal of Instrumentation, 17*(10), C10013.

Author Information

Brindus Comanescu
Optoelectronica 2001 S.A.
35 Lacului st., 077125 Măgurele, Ilfov county, Romania
Contact e-mail: *brindus_comanescu@yahoo*.com

Paul Schiopu
Science and Technology National University Politehnica Bucharest
313 Splaiul Independenţei st., 060042 Bucharest, sector 6, Romania

Marian Vladescu
Science and Technology National University Politehnica Bucharest
313 Splaiul Independenţei st., 060042 Bucharest, sector 6, Romania

Melu Vlad
Optoelectronica 2001 S.A.
35 Lacului st., 077125 Măgurele, Ilfov county, Romania

To cite this article:

Comanescu, B.., Schiopu, P., Vladescu, M., & Vlad, M. (2023).Plastic fiber low light measurement method. *The Eurasia Proceedings of Science, Technology, Engineering & Mathematics (EPSTEM), 26,* 641-647.

The Eurasia Proceedings of Science, Technology, Engineering & Mathematics (EPSTEM)
ISSN: 2602-3199

The Eurasia Proceedings of Science, Technology, Engineering & Mathematics (EPSTEM), 2023

Volume 26, Pages 648-658

IConTES 2023: International Conference on Technology, Engineering and Science

Flexural Torsional Buckling of a Beam from the Dee Bridge of 1846 - Analytical and Finite Element Analyses

Krasimir Petrov
Terna AD - Bulgaria

Abstract: The Industrial Revolution in Victorian England was a period marked by rapid development of the machine industry, accompanied by new technologies in metallurgy and a need for transport between economic areas that was fast, cheap and convenient. This is a period when the railway transport arose and in a short time acquired an image familiar to us to this day. Passage of train sets across rivers and hard-to-reach areas requires transport facilities. In this period, an extremely large number of bridges and aqueducts were built, which have different constructive solutions, different technologies are applied and they are made of different materials, depending on the preference of their creator. This paper examines the collapse of one of the beams of the Dee Bridge on 24 May 1847. The analysis carried out shows the irrationality of the cross-sectional dimensions and types of girder supports witch generate large compressive forces in the beam, leading to flexural torsional buckling.

Keywords: Beam, Off-center supported beam, Flexural torsional buckling, Critical force, Finite element method

Introduction

The Industrial Revolution in Victorian England created the conditions for rapid development of railway transport and its accompanying facilities. At this stage in the development of engineering sciences, there is still a lack of knowledge regarding structures, materials, dynamic effects (Walley, 2020). An extraordinary number of bridges and aqueducts was built during this period (Petrov, 2020; Sutherland, 2009; Bill, 2014). Often used design solutions are innovative and without the necessary calculations. They have been verify, with experimental tests that often did not account for all the factors that could compromise the structures. Minor accidents in the structural elements were commonplace at the time. Investigations into the causes of destruction are a leading factor in the accumulation of experience by their creators. In some cases, however, knowledge has not yet reached that level to provide a logical and indisputable explanation of events. Some accidents continue to arouse interest and specialists seek an explication through new knowledge and technology in structural studies. One such modern computer analysis in Martin and MacLeod (1995) of wind loading on the Tay Rail Bridge explains the reasons for its collapse in 1879. In Martin and MacLeod (2004), the suggestion that the collapse of the same bridge resulted from material fatigue failure caused by dynamic load it was rejected. The paper shows that the evidence to support this is weak.

In the 1840s and 1850s, cast iron replaced stone, brick and wood as a building material. It is cheaper than wrought iron, which is the other alternative to the known old materials, and makes it possible to bridge relatively large openings – up to about 20 meters at the time. Detailed technical information and illustrations, of modern materials, presented against the background of one of the great catastrophes of the mid-19th century - the fall of the Dee Bridge in May 1847 was been made in Lewis (2007). We read about the accumulated knowledge about the materials, the mechanical response of the beams, experimental studies of the dynamic properties of the materials in Walley (2020) and Mylius (2005).

The cast iron and wrought iron facilities preserved to this day are reconstructed after the assessment of their dynamic load and familiarization with the construction materials from which they are made (Pękalski & Rabiega, 2011; Parke et al., 2005; Taylor et al., 2009).

Statement of the Problem Under Consideration

In November 1846, the Dee Bridge was open on the London-Holyhead (Wales) line, just outside the city of Chester (Petroski, 1994; Clark, 2009; Thorpe, 2015). The project's chief engineer, Robert Stephenson, chose a cast iron girder design. One of the girders is damage and the bridge is close until a new one is cast. After its reopening, about six months later, on 24 May 1847, a local train was crossing the final span when one of the girders failed suddenly, sending most of the train crashing into the river below. Five lives were lost. The accident cause a national furore, and Stephenson came close to being accuse of manslaughter for the design. An unprecedented investigation began, accompanied by a lengthy process of gathering eyewitness accounts and additional "expert" testimony from military and civilian engineers.

The Dee Bridge consists of three 98-foot spans set between masonry piers. Each section is made up of four cast iron beams (two for each line in both directions) and each is made by bolting together three shorter lengths of iron I-sections. Each beam is reinforce with wrought iron trusses (Figure 1). The rails was been laid on wooden sleepers supported by oak beams resting on the lower flanges of the beams (Figure 2). The bridge is located in a horizontal curve with a radius of 7000ft = 2133.60m (Figure 3).

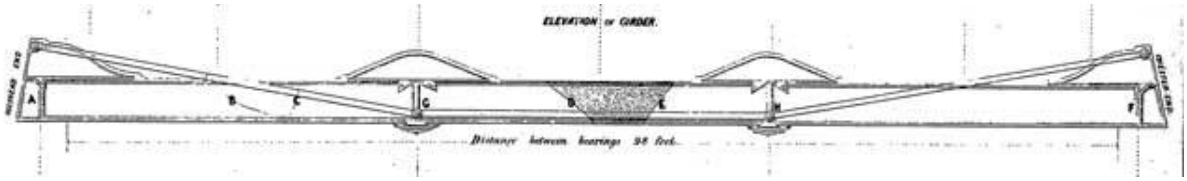

Figure 1. Elevation of one of the girders over the river dee (Taylor, 2013)

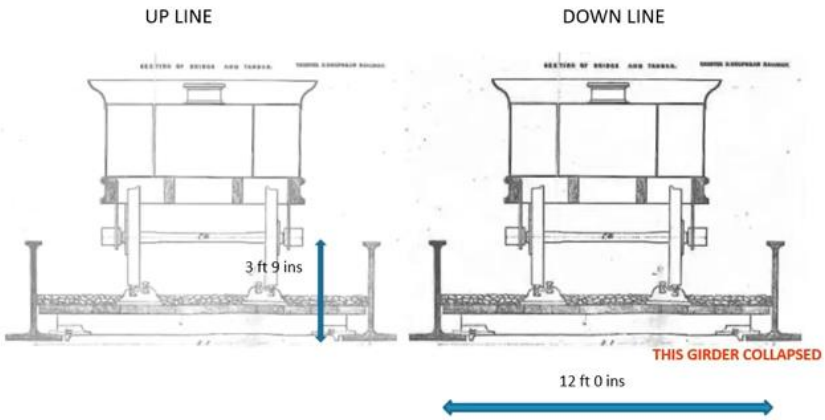

Figure 2. Section of failed bridge (Hayward, 2022)

The River Dee Bridge was first open to local freight traffic on 4 November 1846, but a small fracture was discover near the joint between two girders. Stevenson concluded that this was the result of a casting defect. Next comes strengthening of the bridge, casting and replacement of the damaged part. Painters working on the structure at the time noticed large deformations of several to two inches (5 cm) on both tracks. On faster moving, the deflection on the train is 3 1/2 (9cm) to 4 inches (10cm). However, neither Stevenson nor his team is been informed for this discovery (Lewis & Gagg, 2004; Taylor, 2013). At the time of innovative ideas, contracts could be based on wrong assumptions and prove difficult to enforce. Once a project has gained momentum, those working on it may fear that any attempt to draw attention to risks or defects will be perceive as disloyal (Hawker, 2007).

On the morning of the disaster, six trains passed the bridge without incident, and Stevenson inspected the facility that day (Taylor, 2013). The danger of sparks and cinders from passing trains falling on the oak sleepers and setting them on fire is real. Stevenson subsequently ordered five inches (12.5cm) of ash ballast to be place over the timber. The ash promises fire protection, but the material adds to each of the three spans an additional

static (or "dead") load estimated at eighteen tons. The additional dead load of one beam would be about nine tons (Lewis & Gagg, 2004). The ballast was been laid just before the ill-fated train left the Chester station at 6:15 p.m. The train weigh was about sixty tons, and was traveling at about thirty miles an hour (30 mph = 48,28 km/h) toward the bridge (Lewis & Gagg, 2004). The train left Chester station 10 minutes late (Hayward, 2022).

Figure 3. The old bridge is on the left. On the right is the newly built bridge (Hayward, 2022)

Eyewitnesses described a crash for two or three seconds before the four carriages tumbled down into the river "in a row". Others speak of a tremendous crash and a large piece of the beam falling from the middle support. Still others claim that when the train reached the furthest section, they saw an open crack in the middle of the beam. “It opened from the bottom of the beam". The machinist testified that as the 60-ton locomotive crossed the third span of the bridge, part of the structure, began to collapse and he felt the bridge give way beneath him.

Captain Simmons from the Royal Engineers and James Walker are investigating the incident. They check the accuracy of Stevenson's original design and calculations. They perform tests on the surviving beams and measure their deformation under static and dynamic loads. They use a 48-ton locomotive who is moving along the beams at about 20 miles per hour (20 mph = 32,19 km/h). The train according to Lewis and Gagg, 2004 gives a distributed load of twenty-four tons on each beam. According to Hayward, 2014; Hayward, 2011, initially the load on the bridges, at that time, was taken as the average weight per unit length, ignoring the axle concentration and using large safety factors to compensate for the lack of any dynamic tolerance. Here, however, Stevenson has bet on a strangely low safety factor - 1,5. Simmons measured the sag of the joists, and it was 2.36 inches (6cm) at their center. The upper flange moved inward about half an inch (1.27cm), the lower flange moved outward due to the asymmetric load on the beam (Figure 4) (Taylor, 2013). Also from Lewis & Gagg, 2004 we learn that in their joint paper Walker and Simmons report that wrought iron chain gives little or no reinforcement to cast iron beams because the ends of the chain is connected to the cast iron itself (Figure 1). The beam was test in the foundry for deformation under a static load of twenty-five tons and two and a half inches (6,35cm) of sag was measure. However, the foundry test does not replicate the working conditions of the beam because the load is not on the flange. Walker and Simmons examined both types of ironwork, and reported that the cast iron was sound and contained no voids or holes (especially in the fracture surfaces). Likewise, wrought iron was of good quality. However, they believe that the vibrations caused by the trains can weaken the materials.

At that time, it was already clear that dynamic impact affects wear ability, but knowledge was still lacking. Until the end of the nineteenth century, there is no way to study this problem, and this gave reason to explain incomprehensible processes at the time with the unstudied dynamic influence (Walley, 2020). According to Stevenson's theory, the dynamic interaction of materials and machinery played a role in the collapse. He negates a manufacturing defect in a cast iron beam or an inherent brittleness of the metal. Simmons and Walker describe a "general" condition, where the breaking weight of any cast iron beam may be reduce by repetitive vibration, thus opening up a realm of possibilities.

The term "breaking weight" comes from the research of Eaton Hodgkinson, a British engineer. In 1830, the Manchester Literary and Philosophical Society published his Optimized Sections, which greatly influenced engineering practice in the 19th century. Hodgkinson derived an empirical formula for the maximum concentrated force F that a simple beam of span L, sectional height d, and bottom girdle area "A" can support, namely:

$$F = \frac{26Ad}{L} \tag{1}$$

For our beam, this means force: $F = 60,65\,t$

Results and Discussion - Modern Analysis

The beam is $L = 98\,ft = 29,87m$ long and $h = 45in = 114,3cm$ high.

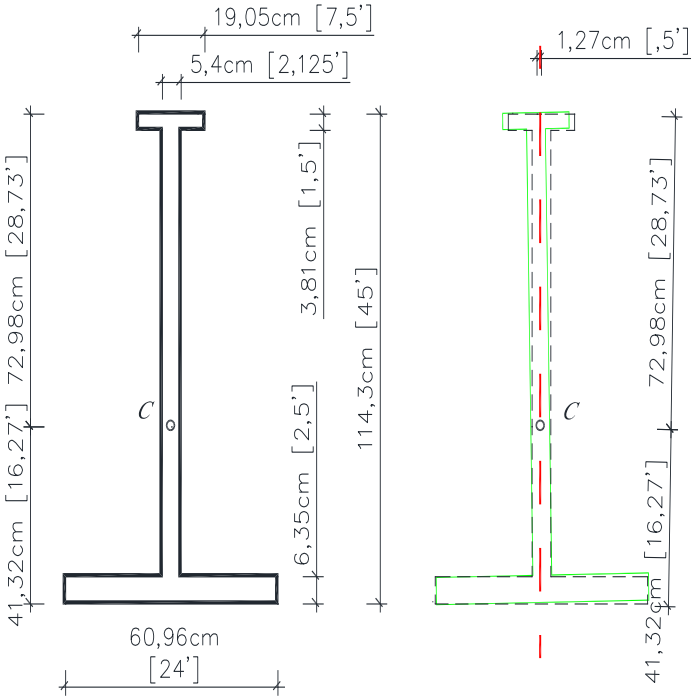

Figure 4. Cross section of the beam (Clark, 2009)

The reasons for the failure of the beam are three main underestimated factors:

1. Off-center supports and the larger normal stresses.
2. The inertial force arising when the train moves in a curve.
3. Flexural torsional buckling.

Off-Center Supports

The beam is support along its bottom edge, not at the center of gravity of the end sections. Such off-center support leads to a particularly stressed and deformed state of the beam (Doicheva & Mladenov, 2009; Doicheva, 2011). The center-supported beam, loaded with vertical loads, only will not generate axial internal force, while off-center supported beam, such are available (Figure 5). Often they are large, even in some cases exceeding the vertical loads that caused them (Mladenov et al., 2012; Mladenov & Doicheva, 2011). Depending on the position of the supports along the height of the end section, the axial forces are either tensile or compressive. Supports located along the bottom edge of the beam lead to the occurrence of compressive horizontal support reactions, and accordingly, compressive axial forces, who can endanger the stability of the beam.

The example below will show how the internal forces vary depending on the different locations of the support in a beam. The load is taken as a distributed load q=30kN/m'. The geometric characteristics of cross section of the beam, were determined with AutoCAD 2022 and they are: area of the cross section $A = 1021,77cm^2$ and moments of inertia $I_y = 1603643,62cm^4$; $I_z = 123434,25cm^4$. Calculations were perform in the MATLAB R2017b environment, with a finite element (FEM) program, for off-center supports, reported in Doicheva, 2022.

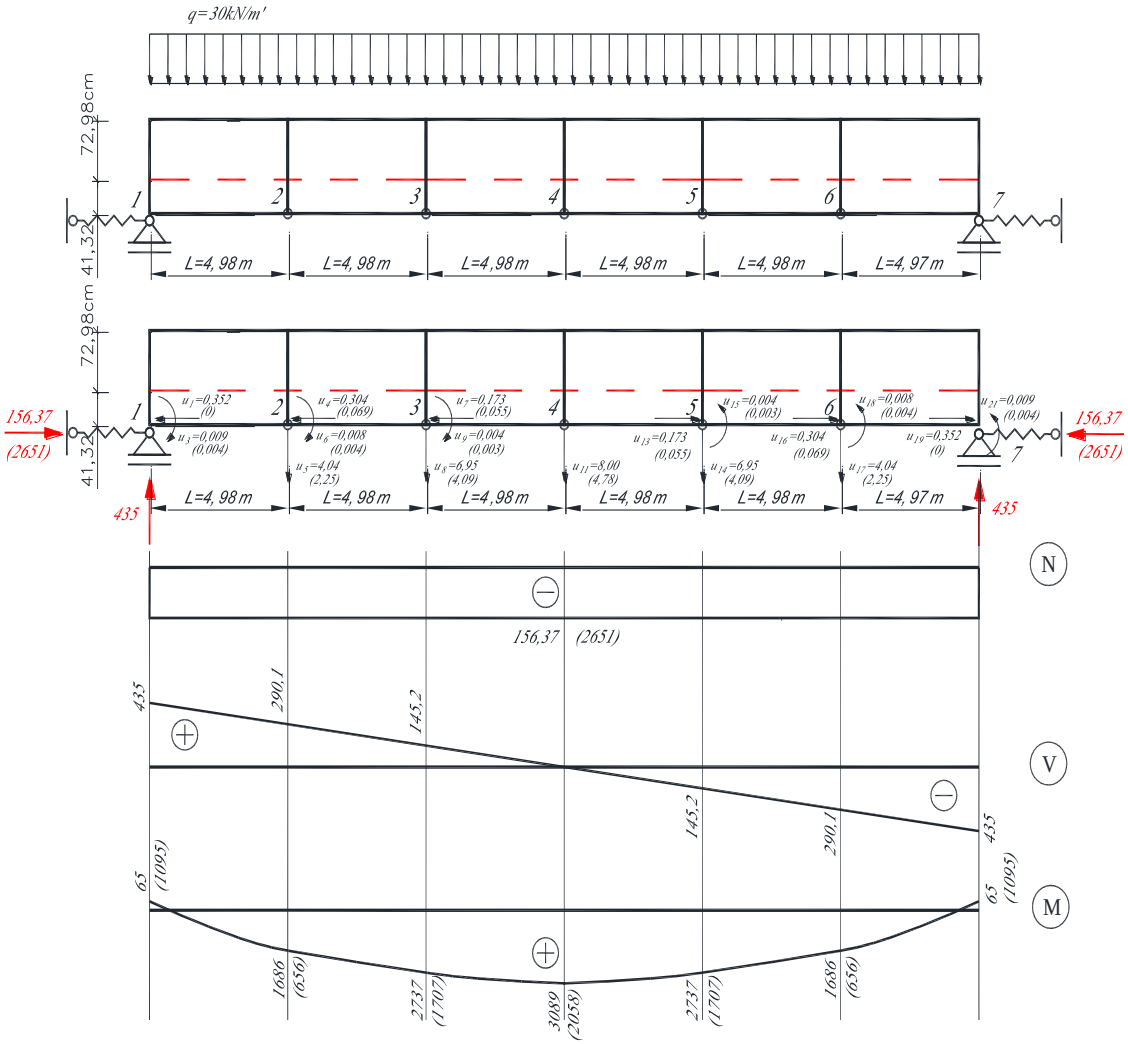

Figure 5. Off-center supported beam

Limiting the movement of the bottom support, i.e. increasing the stiffness of a linear spring, leads to an increase in the horizontal support reaction in it and an increase in the axial force. The values in parentheses in Figure 5 show the internal forces at fixed supports. How will it affect the tense state, the controversial reinforcing chain – Figure 6. The following two things may be noted.

The Reduced Magnitudes of the Vertical Displacements

The reduced magnitudes of the vertical displacements, for the node in the middle u=8cm, and when applying the chain u=5.39cm, which is about 33% less, but the reduced displacements come at the expense of greatly increased axial forces.

The Growth of Axial Forces

They will grow even faster, because the bending of the beam leads to tension in the lower threads of the beam and pressure in the upper ones (Figure 7). The points along the bottom edge of the beam where the chain is

attached move down faster than the attachment points along the upper edge of the beam. Therefore, the chain will stretch and put additional load on the upper strands in a direction coinciding with the direction of pressure. This will accelerate the deformations and displacements of the chain attachment nodes at points A and B, and the axial compressive forces will increase. Also if in the case without chain Nmax= 156.37kN, then when applying the chain Nmax= 1942.9kN, which is 12.5 times greater compressive axial force. The correction in the normal stresses is:

$$\sigma_x = \frac{N}{A} = \frac{1942,9}{1021,77} = 1,90 kN / cm^2 \text{ (compression)} \tag{2}$$

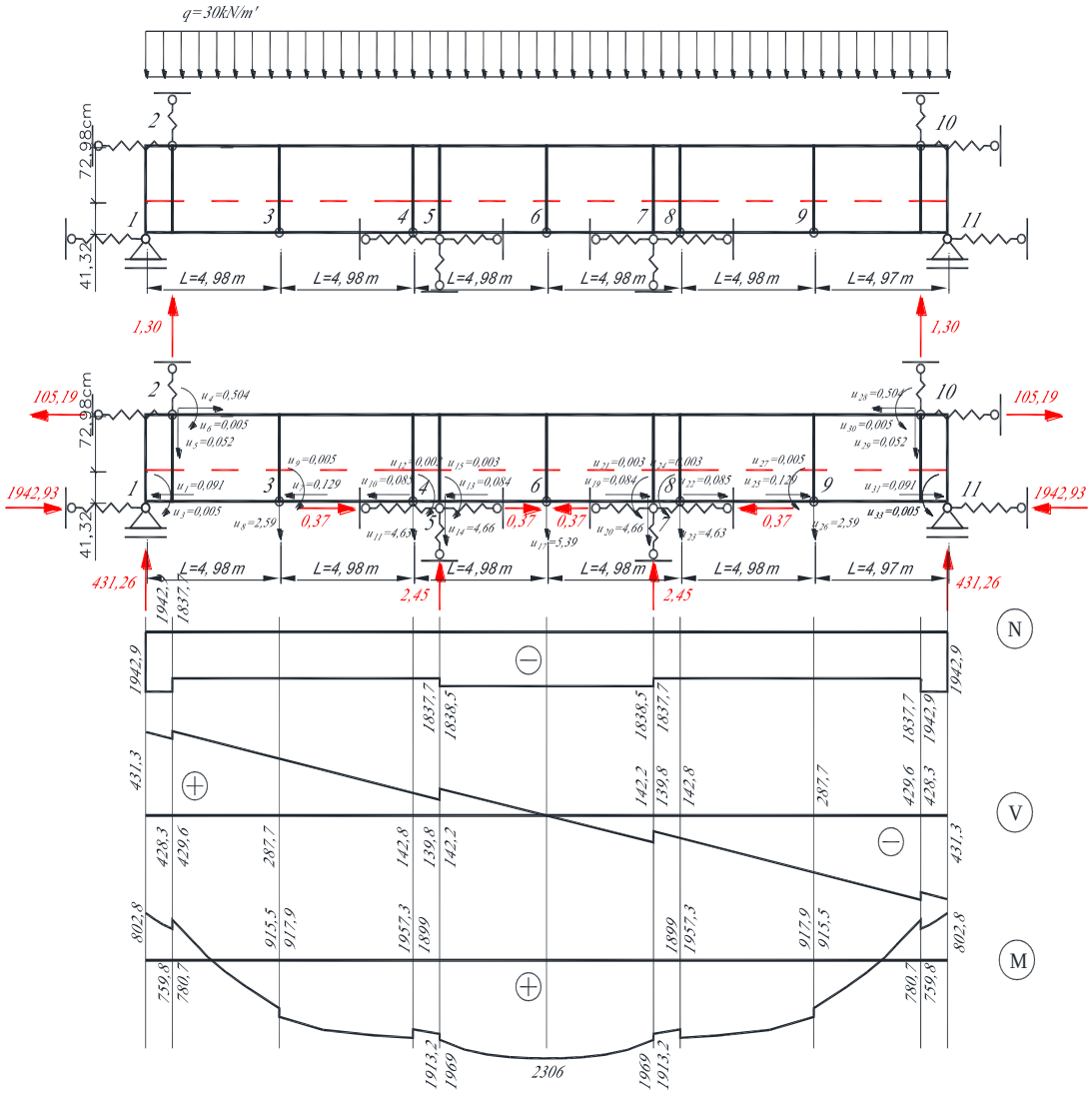

Figure 6. Off-center supported beam with reinforcing chain

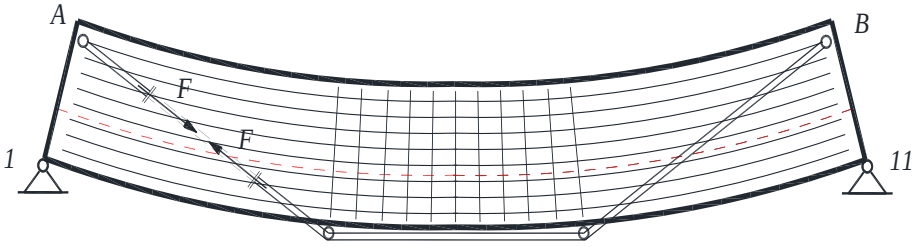

Figure 7. Beam bending

The conclusion that has to be drawn is that, the chain is completely unacceptable with the designed support, on the beam itself. This conclusion was also reach by Simmons and Walker, and it is report in their paper, that wrought iron chain provides little or no reinforcement to cast iron beams, because the ends of the chain are tie to the beam itself (Lewis & Gagg 2004). We can only guess, but it is logical to assume that Robert Stephenson sought to reduce the displacement values of the beam deflection. The displacements are easy to see, but he was hardly aware of the large axial compressive forces occurring. How the internal forces change with the additional slag load is shown in a Figure 8.

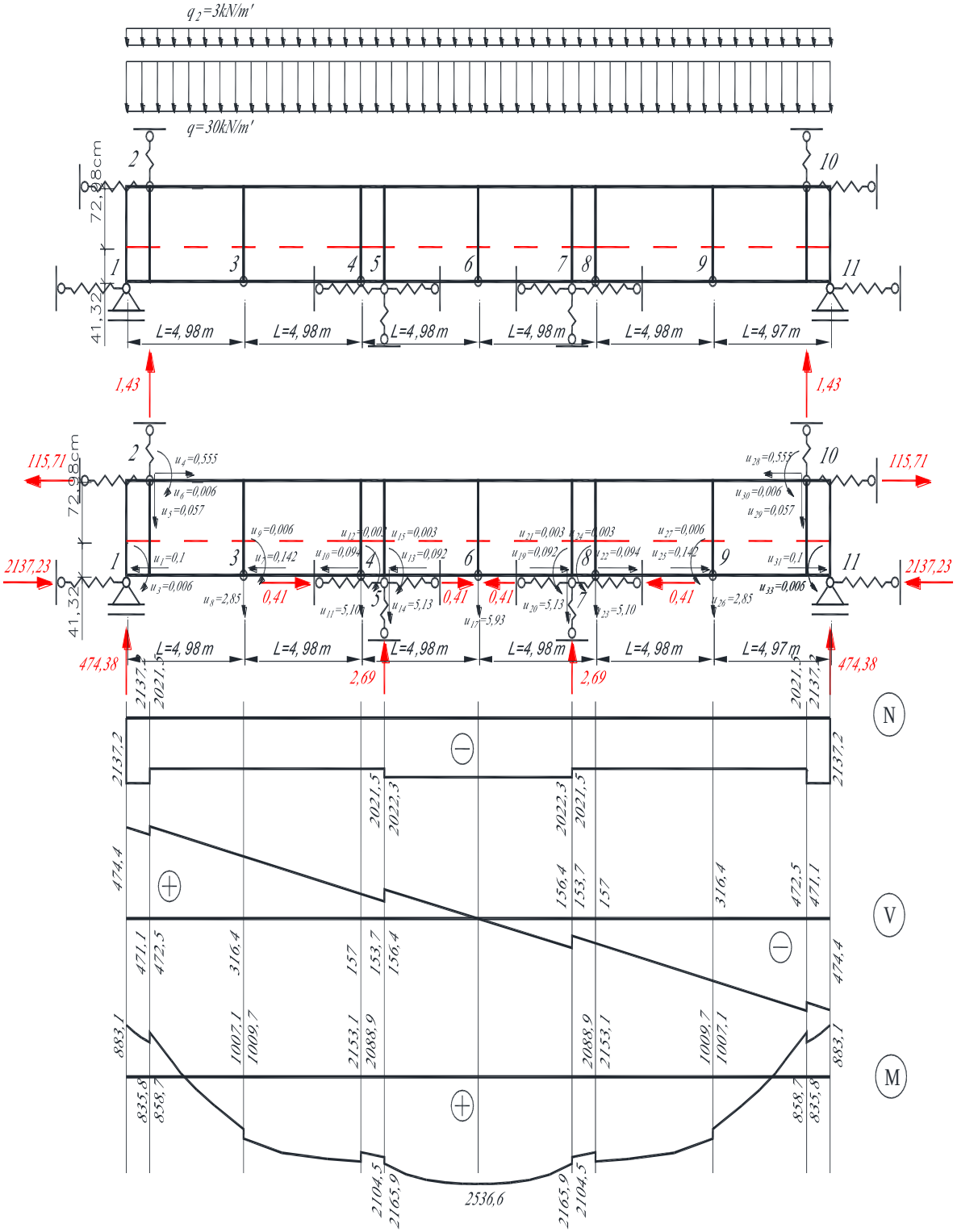

Figure 8. Off-center supported beam with reinforcing chain and additional dead load

The Inertial Force Arising When the Train Moves in a Curve

The bridge is on a curve of radius 7000ft = 2133.60m and the train is moving at 30 mph = 48.28 km/h. It causes the normal acceleration, $a_n = \frac{v^2}{R} = \frac{48280^2}{(60.60)^2 .2133,6} = 0,0843 m/s^2$ and the inertial force for a locomotive weighing 60 tons is $\Phi = M.a_n = 60000.0,0843 = 5057,9N = 5,1kN$.

Flexural Torsional Buckling

The displacement of the load from the vertical axis of symmetry of the beam cross-section was not been taken into account in the calculations. The presence of such a large axial force raises questions about Euler buckling load, just by bending about the vertical z-axis. For the failed beam, F_{cr}^{Euler} will be:

$$F_{cr}^{Euler} = \frac{\pi^2 EI_z}{L^2} = 1911,6kN \tag{3}$$

where:

modulus of elasticity - $E = 1,4.10^4 kN/cm^2$; moments of inertia - $I_z = 123434,25cm^4$, beam length - $L = 29,87m$

In Mladenov & Doicheva 2009 and Mladenov & Doicheva 2008, the flexural-torsional buckling of an off-center supported beam was consider (Figure 9). It was establish that, it is significantly influence by the position of the support devices, along the height of the beam and by the level of load action.

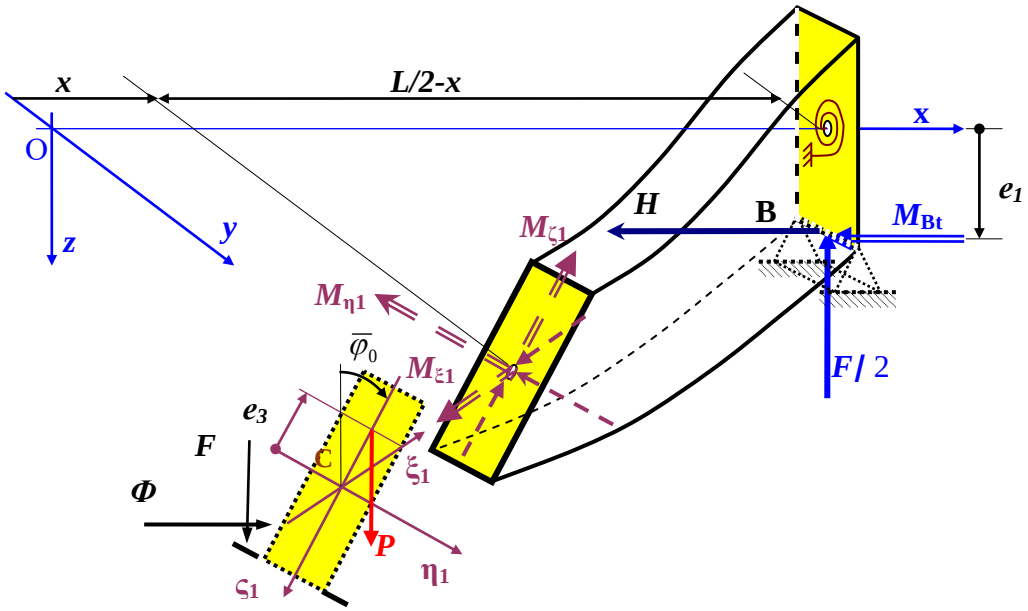

Figure 9. Part of the beam after loss of stability

Supports in the axis of the beam and force acting on the axis of the beam (Mladenov & Doicheva 2009):

$$F_{cr} = \frac{16,97\sqrt{GI_t EI_z}}{L^2} = 557,904kN \tag{4}$$

where:

modulus of elasticity - $E = 1,4.10^4 kN/cm^2$; modulus of angular deformation – $G = 0,441.10^4 kN/cm^2$; torsional moment of inertia - $I_t = 11290cm^4$, calculated by SSRC 1998; moments of inertia -

$I_z = 123434,25cm^4$, beam length - $L = 29,87m$, eccentricity of supports - $e_1 = 0cm$; eccentricity of force - $e_3 = 0cm$.

Comparing the critical force for off-center support with that of Euler, we have:

$$\frac{F_{cr}^{Euler}}{F_{cr}} = \frac{1911,6}{557,904} = 3,426 \tag{5}$$

Supports are along the bottom edge of the beam and force acting on the axis of the beam (Mladenov & Doicheva 2009):

$$F_{cr} = \frac{10,5938\sqrt{GI_t EI_z}}{L^2} = 348,282kN \tag{6}$$

where:

eccentricity of supports - $e_1 = 41,32cm$; eccentricity of force - $e_3 = 0cm$.

Supports are along the bottom edge of the beam and force acting on the bottom edge of the beam (Mladenov & Doicheva 2009):

$$F_{cr} = \frac{10,772842\sqrt{GI_t EI_z}}{L^2} = 354,167kN \tag{7}$$

where:

eccentricity of supports - $e_1 = 41,32cm$; eccentricity of force - $e_3 = -41,32cm$.

Studies of flexural torsional buckling show, that the critical forces for the beam, under consideration are small and easily achievable from the applied loads. The location of the force at the lower edge of the beam has a stabilizing effect (Rossia et al., 2020; Ranjithkumar & Punitha Kumar, 2022; Mladenov & Doicheva, 2009). This is also evident from the result of formula (7). The critical force is greater than the case of force on the axis of the beam - formula (6). If the load is off the vertical axis of the beam, on the inside of the curve (Figure 9), as it is with our beam, then this will cause an additional torsional effect of the beam.

There is a complex 3D stressed and deformed state of an off-center supported beam, in a horizontal curve with forces acting on the bottom flange of the beam, and horizontal inertial forces acting at the base of the profile stem, which is made of cast iron. The load bends the beam. An inappropriately chosen construction of a beam "reinforced" with a chain and supported on the bottom edge, lead to the appearance of significant compressive horizontal forces. The tall but thin stem of the beam is compress by the axial forces. The stem of the cross-section to try to bend about the z-axis, and to rotate about the x-axis, however, here the inertial forces appear, and the non-centric load located on the flange of the beam intervenes. A load displaced from the vertical axis of the cross-section leads to additional torsion of the beam. Inertial force presses the slender stem, which is under compressional stress and breaking it. We have conditions for a local stability loss. Cast iron is a brittle material, with no plastic deformations, and this accounts for its instantaneous destruction.

The destruction of the girder of the Dee Bridge is of interest with the interweaving of many factors, each of which bears blame for the fatal end. Analyzes of the causes of structure failures can help develop knowledge about equipment. This is how research on off-center supporting and flexural torsional buckling has developed over the past few decades. Engineers must become familiar with the causes of accidents that occur, in order to train and prevent the observed errors.

Conclusion

The search for answers to a major accident that occurred on the Dee River Bridge continues to this day. However, a mechanical analysis shows that, the adopted constructive solution is doomed to failure. The large axial forces caused by the improper support of the beam, with wrought iron chains, led to a tragic accident. The

application of additional fire protection material only accelerated the collapse of one of the beams. This analysis would not be possible without the modern knowledge of off-center supports and flexural torsional buckling.

Recommendations

A survey was made of the girder of the bridge over the River Dee, which collapsed on 24 May 1847. The large axial forces occurring in the beam, as a result of the off-center supports are shown. The critical forces were calculated for the different positions of the supports, and the load on the beam. The critical force is small and achievable for the load under consideration.

Scientific Ethics Declaration

The authors declare that the scientific ethical and legal responsibility of this article published in EPSTEM journal belongs to the authors.

Acknowledgements or Notes

* This article was presented as an oral presentation at the International Conference on Technology, Engineering and Science (www.icontes.net) held in Antalya/Turkey on November 16-19, 2023.

References

AutoCAD. (2022). *Autodesk*. San Francisco, California, USA.

Bill, N. (2014) The safety record of timber railway bridges in the UK: 1840–1870. *Proceedings of the Institution of Civil Engineers - Engineering History and Heritage*, *167* (1), 34-46.

Clark, N. S. (2009) *The dee railway bridge disaster of 1847*. Retrieved from http://anengineersaspect.blogspot.com/2009/07/the-dee-railway-bridge-disaster-of-1847.html

Doicheva, A. (2022). Finite element method for analysis of off-center connected continuous beams. *The Eurasia Proceedings of Science, Technology, Engineering & Mathematics (EPSTEM), 18*, 37-45.

Doicheva, A. (2011) Exact solution for a beam on off-center spring supports. *Journal of Theoretical and Applied Mechanics*, *2*, 69-82.

Doicheva, A. & Mladenov, (2009). A problem of an off-centre supported beam with an elastic link. *Third Symposium on bridges "Design and construction of bridges* (p.165). UACEG

SofiaHawker, A. (2007). Cast iron promises. *Inform Prim Care*, *15*(3),137-141.

Hayward, A. (2022). *The Dee bridge collapse of 1847: The institution of structural engineers* [Video] Youtube. Retrieved from https://www.youtube.com/@theinstitutionofstructural2470/videos

Hayward, A. C. G. (2014). Train loading on bridges since Stephenson's rocket. *Proceedings of the Institution of Civil Engineers - Bridge Engineering*, *167*(4), 326-337.

Hayward, A. C. G. (2011). Train loads on bridges 1825 to 2010. *The International Journal for the History of Engineering & Technology, 81*(2), 159-191.

Lewis, P. R. (2007). *Disaster on the Dee: Robert Stephenson's nemesis of* 1847. Tempus.

Lewis, P. R., & Gagg, C. (2004) Aesthetics versus function: the fall of the Dee bridge, 1847, *Interdisciplinary Science Reviews, 29* (2), 177-191.

Martin, T., & MacLeod, I. A. (1995). The Tay bridge disaster—A reappraisal based on modern analysis methods. In *Proceedings of the Institution of Civil Engineers*, *108*(2), 77–83. London: Published for the Institution of Civil Engineerings by Thomas Telford Services.

Martin, T., & MacLeod, I.A. (2004) The Tay Rail Bridge disaster revisited. In Proceedings *of the Institution of Civil Engineers - Bridge Engineering*, *157* (4), 187-192.

MATLAB (b). (2017). *Image acquisition toolbox user's guide*. Natick, USA: The MathWorks *Inc*.

Mladenov, K., Doicheva, A. & Kochev P. (2012). Development of finite beam element for off-center transfer of forces. *Annual of the University of Arhitecture, Civil Engineering and Geodezy*, *14*(8), 213-227.

Mladenov, K. & Doicheva, A. (2011). A study of off-center supported beams with large deflections, *Civil Engineering - Bulgaria*, *1*, 10-22.

Mladenov, K., & Doicheva, A. (2009) Flexural-torsional buckling of an off-centre supported beam. *International Conference UACEG2009: Science and Practice*, *44*(5),103-114.

Mladenov, K., & Doicheva, A. (2008). Bending-torsional buckling of a beam on elastic rotational springs, *Civil Engineeing - Bulgaria*, (6), 2-7.

Mylius, A. (2005). *Cast iron excuse*. Semantic Scholar.

Parke, G. A., Disney P., Bamgbade, C. A., Coxon S., & Cole, G. (2005). *Old wey bridge refurbishment. Surrey*, UK: Surrey County Council

Pękalski, G. & Rabiega, J. (2011) Grey cast iron as construction material of bridges from the 18 th and 19 th century. *Arch Foundry Eng., 11* (2), 175–179.

Petroski, H. (1994). Success syndrome: The collapse of the dee bridge. *Civil Engineering, 64*(4), 52.

Petrov, K. D. (2020) *Bridges after wood and stone and before steel and concrete* (p.279). Retrieved from izdavam.com

Ranjithkumar, M., & Punitha Kumar, A. (2022) Numerical study on lateral torsional buckling of coped beams. *Journal of Build Rehabilitation, 7*(1), *48.*

Rossia, A., Ferreiraa, F. P. V., Martinsa, C. H., & Júnior, E. C. M. (2020) Assessment of lateral distortional buckling resistance in welded I-beams, *Journal of Constructional Steel Research, 166*,105924.

SSRC. (1998). Guide to Stability Design Criteria for Metal Structures T.V. Galambos (Ed.), *Structural Stability Research Council* (5th ed.). Newyork, NY: John Wiley & Sons

Sutherland, J. (2009) The birth of prestressing? Iron bridges for railways 1830 to 1850. *The International Journal for the History of Engineering & Technology*, *79* (1), 113-130.

Taylor, A., Plant, C., & Dickerson, J. (2009) Wellington street swing Bridge, Hull, UK, *Proceedings of the Institution of Civil Engineers - Engineering History and Heritage*, *162*(2), 67-79.

Taylor, W (2013) Iron, engineering and architectural history in crisis: Following the case of the river dee bridge. *Architectural Histories, 1*(1), 1-13.

Thorpe, P. (2015). An early railway disaster in the parliamentary papers. Retrieved from https://blog.railwaymuseum.org.uk/early-railway-disaster-parliamentary-papers/

Walley, S. M. (2020) Highways and byways in the history of high rate mechanical testing. *Journal of Dynamic Behavior of Materials 6*, 113–158,

Author Information

Krasimir Petrov
Terna AD - Bulgaria
Sofia, Bulgaria
Contact e-mail: *krasimir_petrov_s@abv.bg*

To cite this article:

Petrov, K. (2023). Flexural torsional buckling of a beam from the Dee bridge of 1846 - analytical and finite element analyses. *The Eurasia Proceedings of Science, Technology, Engineering & Mathematics (EPSTEM), 26*, 648-658.

The Eurasia Proceedings of Science, Technology, Engineering & Mathematics (EPSTEM)
ISSN: 2602-3199

The Eurasia Proceedings of Science, Technology, Engineering & Mathematics (EPSTEM), 2023

Volume 26, Pages 659-663

IConTES 2023: International Conference on Technology, Engineering and Science

Relationship between Nusselt and Rayleigh Numbers in Natural Convection

Ahsene Lanani
University of Mentouri Brothers

Rahima Benchabi
University of Mentouri Brothers

Abstract: When studying heat transfer in laminar or turbulent flow, the aim is to maximize heat transfer, using for example corrugated channels; nanofluids or hybrid nanofluids, etc.; to determine the factors that influence the thermal and hydraulic performance of the used equipment and to determine the relationships that may exist between heat transfer efficiency and these various variables; hence the study of the relationships between these various factors. The findings can be analyzed by using tables, graphs or correlations. The objective of the current paper is focused on the last approach. In addition, we are attempting to determine the influence of the physical parameter Rayleigh number (Ra) on thermal and hydraulic behavior, using the FLUENT calculation code, on the one hand, and to validate the correlation obtained, based on a statistical model, on the other hand. We have also validated that our findings are in excellent accord with those of prior work involving this statistical method.

Keywords: Correlations, Convection, Nusselt (Nu), Rayleigh (Ra), Statistical model

Introduction

In industrial companies, heat exchangers are an important element in energy management, since a large proportion of thermal energy passes through a heat exchanger. These heat exchangers find their application in the food industry, HVAC engineering, petrochemicals, etc. Many heat exchangers in a wide variety of processes are equipped with exchange surfaces specially designed to offer high heat exchange coefficients, notably higher than those of smooth surfaces. Among the techniques used in exchanger design, the use of corrugations increases turbulence and therefore heat transfer. Many researchers have been motived in recent years to study the heat transfer by natural convection in different enclosures and the correlations between the Nu and the Ra.

A numerical study of the natural convection of air (a compressible, Newtonian fluid) in a square enclosure was conducted by Prasopchingchana et al. (2009). The left and right walls of the enclosure were heated and cooled respectively, while the top and bottom sides were adiabatic. In addition, the equations governing the flow of the fluid under consideration were discretized using the finite volume method. The angles of inclination of the square cavity yielding the mean Nu are 110° for $Ra = 10^3$ and 130° for $Ra = 3.10^3$ and $Ra = 10^4$.

Simulations of natural convection flow in a square cavity were undertaken by Barakos et al. (1994). The control volume method was used to solve the governing equations for Ra up to 10^{10}. The k-ϵ model was used to model turbulence. Numerous correlations of Nusselt and Rayleigh numbers with experimental results have been given in this study.

In (Fusegi et al., 1991), transient three-dimensional calculations are performed for Ra of 10^6 and for $Pr = 0.71$. The numerical resolution used in this work is compared with the maximum precisions that have been reached in two-dimensional steady-state situations. The equations governing the flow are solved using the finite difference method. In addition, the current investigation is a natural continuation of the three-dimensional steady-state analysis. The authors have studied the flow properties and proposed a correlation between Nu and Ra.

A computational method used to obtain an analytical solution of the flow equations for two-dimensional natural convection in an air-filled square enclosure is given by De Vahl Davis (1983). The mean Nu are given for Ra varying from 10^3 to 10^6. A numerical study concerning two-dimensional laminar natural convection for rectangular enclosures filled with differentially heated air is carried out by Chang (2014). The author studied the cavity tilt angle, which varies from 0° to 180°, and the effect of tilt on heat transfer and flow field in the range $10^3 \leq Ra \leq 10^6$. Mean Nusselt correlations are also reported. Marcatos and Pericleous, (1984) investigated turbulent and laminar flows numerically. A turbulence model was used for Ra higher than 10^6. The findings are presented in the form of tables, graphs and correlations between Nu and Ra. These results are also compared with those of (De Vahl Davis, 1983).

In the present work, we are attempting to determine the influence of the physical parameter Rayleigh number (Ra) on thermal and hydraulic behavior, using the FLUENT calculation code, on the one hand; and examine a possible relationship between Nu and Ra, in the other hand. Findings can be presented in tables, graphs or correlations. The objective of the current study is to use the correlation method (Draper & Smith, 1981; D'agostino et al., 1986; Chang et al., 2008; Yoshitsugu et al., 2015). The equations of these correlations are used to predict the average Nu. We have also established that our findings are in excellent accord with those of prior work involving a statistical method.

Physical and Mathematical Model Formulation

Geometric Configuration

The used geometry (figure.1) is a square, differentially-heated enclosure. It consists of two active vertical sides, held at temperatures T_h and T_c with $T_h > T_c$, while the other sides are assumed to be adiabatic. The zone under study is long in both x and y directions.

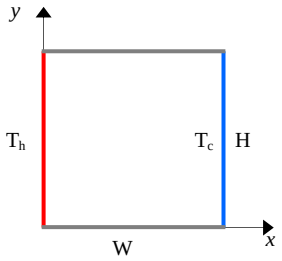

Figure 1. The studied configuration

Governing Equations

The equations governing the flow are:
Continuity equation:

$$\frac{\partial u}{\partial x} + \frac{\partial v}{\partial y} = 0 \tag{1}$$

x – Momentum:

$$u\frac{\partial u}{\partial x} + v\frac{\partial u}{\partial y} = -\frac{1}{\rho}\frac{\partial p}{\partial x} + \vartheta\left[\frac{\partial^2 u}{\partial x^2} + \frac{\partial^2 u}{\partial y^2}\right] \tag{2}$$

y – Momentum:

$$u\frac{\partial v}{\partial x}+v\frac{\partial v}{\partial y}=-\frac{1}{\rho}\frac{\partial p}{\partial y}+\vartheta\left[\frac{\partial^2 v}{\partial x^2}+\frac{\partial^2 v}{\partial y^2}\right]-g\beta(T-T_0) \quad (3)$$

Energy equation:

$$u\frac{\partial T}{\partial x}+v\frac{\partial T}{\partial y}=\alpha\left[\frac{\partial^2 T}{\partial x^2}+\frac{\partial^2 T}{\partial y^2}\right] \quad (4)$$

Solution Procedure

In our previous work, a numerical study of laminar natural convection inside an air-filled, differentially heated square enclosure, on horizontal walls subjected to zero flow, was carried out using the CFD program FLUENT. Numerical computations were conducted on a fine square mesh near the walls. The finite volume approach was used to discretize the equations governing natural convection flow. The calculation validation code was run and good agreement was observed between numerical and experimental results. Figure 2 illustrates the increase in mean Nu numbers with increasing Raleigh numbers.

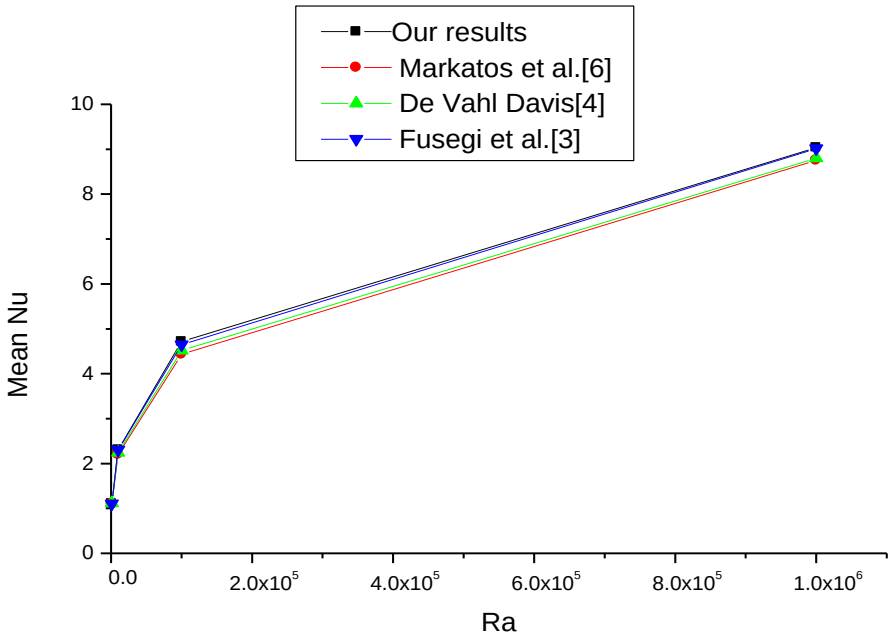

Figure 2. Change of the mean Nu vs Ra

Statistical Method

This approach uses a statistical model. The employed approach is a power function. This method allows us to predict the average Nusselt number as a function of the Rayleigh number. It also provides us the relationship between these numbers. To adjust the various data and calculate the correlation between the average Nu and the Ra number, we use the following equation:

$$\overline{N_u}=B(Ra)^a \quad (5)$$

B and a: constants to be calculated.
The correlation coefficient is a very significant factor, used to determine the relationship between the mean Nusselt and the Rayleigh.

Results Discussion

Experimental Results and Simulation

Table1 shows the findings of a prior investigation. Table 1 illustrates that our findings are in excellent accord with those of the cited authors.The findings of the current research are summarized in Table 2.

Table1. A comparison of average Nu

Mean Nu numbers	Current results	Markatos & pericleous Davis	De Vahl	Fusegie et al.
$Ra = 10^3$	1.1073	1.108	1.118	1.105
$Ra = 10^4$	2.3057	2.201	2.243	2.302
$Ra = 10^5$	4.7175	4.430	4.519	4.646
$Ra = 10^6$	9.0339	8.754	8.799	9.012

Statistical Method

Using equation (5), we found the different values of B and those of parameter (a) applying the linear regression method. In addition, the correlation coefficient (ρ) between mean Nu and Ra is calculated.

Table 2. B value; (a) and the coefficient of correlation (ρ)

	B	a	ρ
Present work	0.136	0.306	0.997
Markos & Pericleous	0.141	0.299	0.997
DeVahl Davis	0.141	0.298	0.997
Fusegie et al.	0.139	0.303	0.992

Table 2 shows that the correlations obtained in our study and those of previous authors demonstrates the appropriateness of the used power model, on the one hand and that, our findings are in excellent accord with those obtained by the authors cited in Table 1, on the other hand.

Conclusions

In this study, we first took a series of Nusselt and Rayleigh numbers ranging from 10^3 to 10^6 corresponding to laminar natural convection; after studying these data, we deduced the following results:

1- We have validated the association between mean Nu and Ra. There is a strong correlation between these numbers. In addition, there is an increasing Nu as the Ra rises.
2- We found our results to be in good accord with those of the previous mentioned authors using a statistical approach.

Scientific Ethics Declaration

The authors declare that the scientific ethical and legal responsibility of this article published in EPSTEM journal belongs to the authors.

Acknowledgements or Notes

* This article was presented as an poster presentation at the International Conference on Technology, Engineering and Science (www.icontes.net) held in Antalya/Turkey on November 16-19, 2023.

* This research was partially supported by the Algerian MESRS. Project research N°: A11N01UN250120200005.

References

Barakos, G., Mitsoulis, E., & Assimacopoulos, D. (1994). Natural convection flow in a square cavity revisited: laminar and turbulent models with wall functions. *International Journal of Numerical Methods in Fluids, 18,* 695-719.

Chang Yvonne, S. H., Ganesan, T., & Lau, K. K. (2008). Comparison between empirical correlation and computational fluid dynamics Simulation for the pressure gradient of multiphase flow. *Proceedings of the World Congress on Engineering* (Vol.III), WCE. London, UK.

Chang, B. H. (2014). Numerical study of flow and heat transfer in differentially heated enclosures. *Thermal Science, 18*(2), 451-463.

D'agostino, R. B. & Sephens, M. A. (1986). *Goodness - of - fit techniques*. New York, NY: Marcel Deker.

De Vahl Davis, G. (1983). Natural convection of air in a square cavity: A benchmark numerical solution. *International Journal of Numerical Methods in Fluids, 1*(3), 249-264.

Draper, N. R. & Smith, H. (1981). *Applied regression analysis*. New York, NY: Wiley.

Fusegi, T., Hyun, J. M., & Kuwahara, K. (1991). Transient three-dimensional natural convection in a differentially heated cubical enclosure. *International Journal of Heat and Mass Transfer, 34*(6), 1543-1557.

Markatos, N. C., & Pericleous, K. A. (1984). Laminar and turbulent natural convection in an enclosed cavity. *International Journal of Heat and Mass Transfer, 27*(5), 755-771.

Prasopchingchana, U., Pirompugd, W., Laipradit, P., & Boonlong, K. (2013). Numerical study of natural convection of air in an inclined square enclosure. *International Journal of Materials, Mechanics and Manufacturing, 1*(2), 131-135.

Yoshitsugu, N., Stanislas, M., Foucaut, J-M & Coudert**,** S. (2015). Space-time pressure-velocity correlations in a turbulent boundary layer. *Journal of Fluid Mechanics 771,* 624-675.

Author Information

Ahsene Lanani
University of Mentouri Brothers
Constantine 1, 25000, Algeria
Contact e-mail: *lanani.ahsene@umc.edu.dz*

Rahima Benchabi
University of Mentouri Brothers
Constantine 1, 25000, Algeria

To cite this article:

Lanani, A., & Benchabi, R. (2023). Relationship between Nusselt and Rayleigh numbers in natural convection. *The Eurasia Proceedings of Science, Technology, Engineering & Mathematics (EPSTEM), 26,* 659-663.

The Eurasia Proceedings of Science, Technology, Engineering & Mathematics (EPSTEM)
ISSN: 2602-3199

The Eurasia Proceedings of Science, Technology, Engineering & Mathematics (EPSTEM), 2023

Volume 26, Pages 664-671

IConTES 2023: International Conference on Technology, Engineering and Science

Exploring the Opportunities for Sustainable Management of Critical Raw Materials in the Circular Economy

Vessela Petrova
University of Mining and Geology

Abstract: Critical raw materials are essential for various industries due to their importance, significance, and various applications. They are classified into various types, such as rare earth elements and strategic minerals, and have key characteristics such as scarcity, high economic importance, and geopolitical implications. Factors influencing the availability of critical raw materials include geological factors, environmental challenges, regulations, trade, and geopolitical factors. Global demand and supply of critical raw materials are also analyzed, with a focus on recycling and sustainable practices. Potential risks and challenges associated with critical raw materials include environmental and social impacts, dependence on these raw materials, and dependence on foreign countries. Understanding these factors is crucial for ensuring the continued success of critical metals in various industries. The research paper discusses the importance of critical metals in the circular economy, their definition, and the research's objectives. It also discusses the circular economy concept and its relevance to resource management, identifying critical metals and their specific roles, and discussing challenges and opportunities related to their use. The article focuses on the potential for critical raw material management within the circular economy. The study's goal is to investigate and analyse the various tactics and methodologies that can be used to successfully utilise, recycle, and reintroduce key metals into the economy. The circular economy is viewed as a method of improving sustainable resource management by closing the material flow and encouraging renewability and recycling. The circular economy is currently understudied in the context of critical metals - a set of raw materials that are vital for modern technology but are limited in supply and cause significant environmental damage.

Keywords: Critical raw materials, Critical metals, Circular economy, Engineering economics, Industrial engineering

Introduction

Critical raw materials represent an important part of the modern economy and industry. Essential to various sectors, including electronics, automotive, and green energy, these raw materials play a key role in our daily lifestyles and economic activity. (Hool et al., 2023) Despite their importance, access to some of these raw materials is limited, and their stocks are subject to various risks. This topic is essential because it requires learning how to sustainably manage critical raw materials, search for alternatives, and optimise their use in an increasingly developing global economy. The circular economy and critical raw materials are linked through an approach that promotes the sustainable use, recycling, and optimisation of raw materials, including those considered critical for various industries. (Hristova, 2022) This cyclical model of economic activity aims to reduce dependence on new extraction of raw materials, extend the life of materials, and encourage innovation that reduces the use of critical raw materials in products and production, supports sustainability, and reduces negative environmental impacts. (Piotrowski, 2023)

The Impact of the Circular Economy in the Context of Critical Raw Materials

Within conventional linear business models, the process often involves the extraction of key materials, subsequent use in the manufacturing of a product, and eventual disposal. Nevertheless, these approaches are no longer compatible with the present supply chains, increasing demand, current and future sustainability targets and regulatory requirements. The critical raw mineral supply chain is faced with several main difficulties, which encompass:

- The rapid acceleration of the energy transition poses challenges to supply chains, which are currently strained and potentially unable to promptly adjust to meet the increasing demand. According to Deloitte, it is projected that by the year 2035, a total of 74 additional lithium mines and 97 additional graphite mines will be required. However, it is important to note that the process of transitioning a mineral deposit from its initial discovery to full-scale production typically entails a time frame of approximately 10 to 12 years. (Deloitte, 2023)
- The security of supply pertaining to the mining and processing of essential minerals is subject to significant concentration and vulnerability due to geopolitical conflicts and fluctuations in prices. For instance, a mere three nations currently dominate almost 75% of the worldwide production of cobalt, lithium, and rare earth elements.
- There are several environmental, social, and governance issues associated with the mineral extraction process. These encompass elevated carbon emissions, degradation of land, loss of biodiversity, water scarcity, and more extensive concerns regarding safety and human rights.

A circular strategy decreases exposure to these difficulties by lowering the need to mine essential minerals.
The progression towards achieving net zero emissions will persistently gain momentum, hence intensifying our dependence on essential minerals. The implementation of a circular economy has the potential to decrease dependence, enhance the adaptability and durability of organisations, and present novel avenues for commercial ventures. Companies that utilise key minerals in their goods must modify their approach to product manufacturing and utilisation, and embrace novel business models and digital technologies that facilitate circularity.

Identification of Critical Raw Materials

The European Commission defines critical raw materials as raw materials of great importance to the EU economy and with a high risk associated with their supply. (European Commission, 2023). Critical raw materials form a strong industrial base and serve as the basic material basis for the development of modern society. (Ruan et al., 2023).

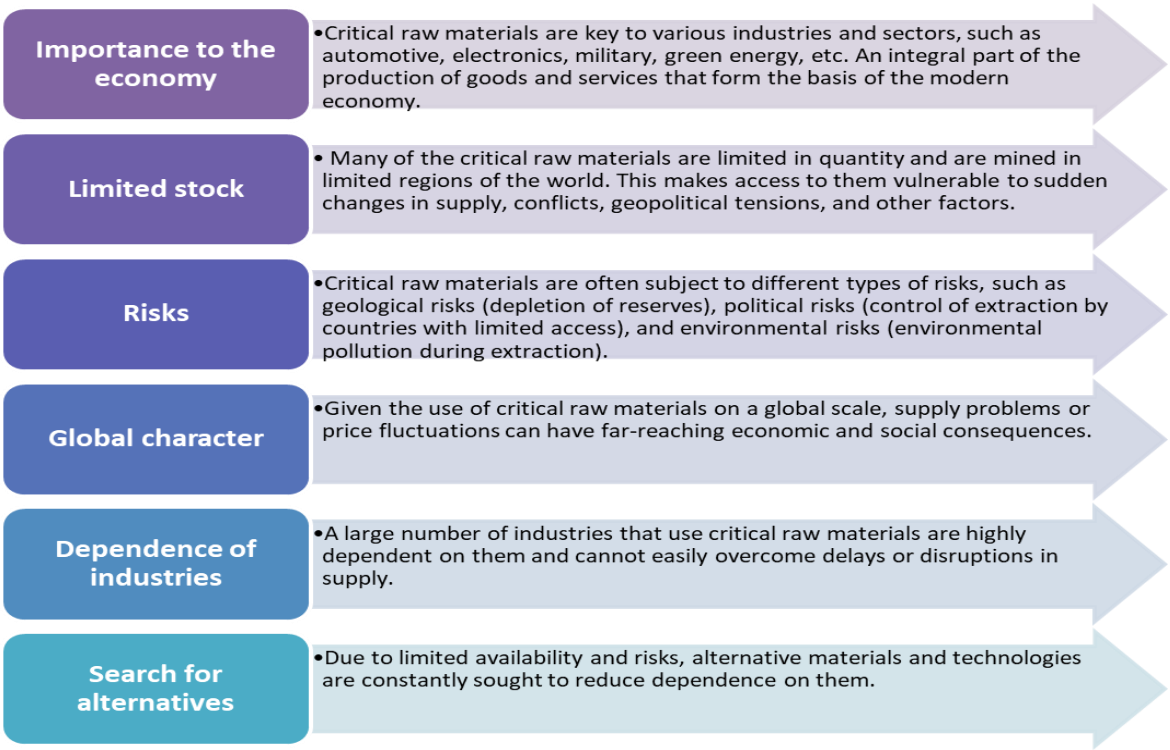

Figure 1. Basic characteristics of critical raw materials (Author's research)

They are a major building block, an element of growth and competitiveness, and crucial for Europe's economy. In this regard, reliable and unhindered access to certain raw materials is an increasing commitment, both for Europe and the whole world. Fig. 1 marks the main characteristics of critical raw materials. All these features highlight the need for sustainable management of critical raw materials. It is essential for the economic stability and sustainability of countries and the global economy as a whole. The importance of critical raw materials is determined by their strong link with industry—non-energy raw materials are linked to all industries at all stages of supply—but also by modern technology. On the threshold of the next industrial revolution, technological progress and quality of life rely on access to an increasing number of raw materials. The role of the environment is no less important; raw materials are closely related to clean, green technologies, and it is believed that the next industrial revolution will be dedicated to them. Critical metals such as copper, aluminium, nickel, and titanium are widely used and indispensable in solar panels, wind turbines, electric vehicles, energy-efficient lighting, and high-tech industries such as semiconductors, healthcare, defence, and aerospace. (Watari et al., 2020).

Critical raw minerals are important not only for industrial and technological needs but also for sustainable development and ecological balance. As the consumption of these resources increases, so do the challenges of sustainable management and supply. To address these challenges, the European Commission has created a list of critical raw materials for the EU, which is subject to review and updating every three years. Table 1 presents the critical raw materials included in the five EU lists

Table 1 Critical raw materials lists 2011 - 2023

Critical raw material	2011	2014	2017	2020	2023
Aluminium/Bauxite				■	■
Antimony	■	■	■	■	■
Arsenic					■
Baryte			■	■	■
Beryllium	■	■	■	■	■
Bismuth			■	■	■
Boron/Borate		■	■	■	■
Chromium		■			
Cobalt	■	■	■	■	■
Cocking Coal		■	■	■	
Copper					■
Feldspar					■
Fluorspar	■	■	■	■	■
Gallium	■	■	■	■	■
Germanium	■	■	■	■	■
Hafnium			■	■	■
Heavy rare earth elements		■	■	■	■
Helium			■		
Indium	■	■	■	■	
Light rare earth elements		■	■	■	■
Lithium				■	■
Magnesium	■	■	■	■	■
Manganese					■
Natural graphite	■	■	■	■	■
Natural rubber			■	■	
Nickel					■
Niobium	■	■	■	■	■
Phosphate Rock		■	■	■	■
Phosphorus			■	■	■
Platinum group metals	■	■	■	■	■
Rare Earths	■				
Scandium			■	■	■
Silicon metal (Silicium)		■	■	■	■
Strontium				■	■
Tantalum	■		■	■	■
Titanium metal				■	■
Tungsten (Wolframium)	■	■	■	■	■
Vanadium			■		■

Impressive are copper and nickel, which do not cross the threshold of critical raw materials but are included in the fifth list from 2023 as strategic raw materials, in accordance with the Law on Critical Raw Materials. Their role in bringing about a green transformation is key, especially copper, which is involved in every single low-carbon green technology. It is believed that the list of critical raw materials would support the development of recycling policies and the transition to a more circular and sustainable economy, as well as more efficient use of resources and strengthening the competitiveness of the continent. (Blengini et al., 2019). Europe is relatively poor in critical raw materials, also due to the fact that the natural reserves of these raw materials are concentrated mainly in China, Russia, South Africa, Brazil, and the USA. (Massari, Ruberti, 2013) However, critical raw materials are not only the focus of Europe and the European Commission. They are the subject of study by researchers and institutions around the world.

Classification of Critical Raw Materials

The classification of critical raw materials is a key element in understanding and managing this type of mineral resource. It is carried out depending on a number of criteria, such as geographical spread, degree of dependence on imports, importance for different industrial sectors, and potential risks in relation to their supply. Critical raw materials can also be classified according to their degree of availability and digestibility. This kind of classification not only helps in prioritizing economic strategies and innovations but also in formulating policies for sustainable management and recycling of critical raw materials. At the same time, it emphasizes the importance of diversity and sustainability in the energy and raw materials sectors, striving to reduce dependence on limited resources and promote alternative technologies and materials. It is important to emphasize that the classification of critical raw materials changes over time, as new technologies and innovations may change the importance of certain metals or cause new critical elements to appear. For this reason, continuous monitoring and analysis of the supply of critical raw materials is essential for the economy and the scientific community.

This publication examines some of the critical raw materials relevant to modern technology and provides an analysis of their availability and substitutability (Table 2). The classification of critical raw materials represents an important tool for understanding and managing the supply of these key resources, promoting the sustainability, innovation, and efficient use of raw materials required for the modern world.

Table 2 Classification of a part of critical raw materials (Author's research)

Critical Raw Material	Key Use	Geographical Distribution	Comments
Cobalt	In the manufacture of lithium-ion batteries, electronics, automobile batteries, and other products.	Specifically, the Democratic Republic of the Congo.	Cobalt mining in the Democratic Republic of the Congo is linked to human rights violations, child labour, and hazardous working conditions. The environmental impact of cobalt mining is a source of contention.
Lithium	In the production of lithium-ion batteries for mobile devices, electric vehicles, and batteries for the storage of energy from renewable sources.	Chile (major global producer), Australia, Argentina, and China	Lithium mining can be affected by restrictions related to environmental protection, regulations, and social issues.
Niobium	In the production of superconductors, light industry, and military equipment	Brazil (the main global producer), Canada, and Australia	Political and economic instability in the mining regions is one of many factors that can affect niobium mining and production. The niobium processing process is complex and requires specialised technologies. Processing restrictions may limit the availability of finished products. Despite these challenges, there are currently no widespread, economically viable alternatives to replace niobium. Instead, efforts are focused on

			optimising production and making efficient use of available resources.
Platinum group metals (platinum, palladium, rhodium, iridium, ruthenium, and osmium)	In the production of catalysts and in the automotive industry.	South Africa, Russia, Zimbabwe, the USA, and Canada have limited supply and high prices.	Supply is considered risky. Replacing PGMs is challenging due to their unique combination of properties that are difficult to replace with other materials. However, research and the development of new technologies are focused on the development of alternative materials and methods to use less platinum-group metals or even completely without them. Some of the options for substitution include the use of other metals, such as nickel, copper, gold, or silver; the development of new catalysts and materials with similar properties; and the transition to more efficient and sustainable production processes.
Rare Earth Elements (neodymium, praseodymium, dysprosium, etc.)	In the production of magnets for electric motors, magnetic materials, and catalysts	China, Australia, the USA, Brazil, and Russia	The elements are not literally rare in the earth's crust but are scattered in very small concentrations and are difficult to extract and process. There are geopolitical challenges and risks associated with the supply of raw materials.
Tantalum	In the production of capacitors, mobile phones, computers, aerospace, and other high-tech systems.	Australia, Brazil, and Canada	The process of processing tantalum ore into the final product is complex and requires specialised technologies. Processing limitations and low efficiency can limit the availability of finished products. Despite these challenges, research is being conducted, and alternative materials and technologies are being developed to reduce dependence on tantalum. Some of the replacement options include the use of other materials such as ceramics, polymers, or other metals with similar electrical and physical properties. In addition, the recycling of tantalum from used products is becoming increasingly important for the recovery of available resources. However, currently, tantalum remains an important and indispensable element in high-tech devices, and efforts are being made to ensure a stable supply and sustainable use of this metal.

Methods and Technologies for Recycling Critical Raw Materials and Evaluating Their Efficiency and Environmental Impact

Recycling critical raw materials, including metals and rare elements, is an important process aimed at optimizing the use of limited resources and reducing dependence on new mining. It enables the recovery of valuable materials from waste products and waste, including metals such as gold, silver, platinum, palladium, and other critical metals that can be reused in various industrial and technological applications. Recycling reduces the need for new extraction of raw materials, which has a positive effect on the environment. The extraction of raw materials is often associated with significant environmental impacts, including water pollution, ecosystem destruction, and greenhouse gas emissions. Recycling raw materials requires less energy and resources compared to the process of extracting and processing new raw materials. This helps to reduce energy consumption and optimize the use of limited resources. Recycling critical raw materials creates economic opportunities in the form of new business models and jobs. This can encourage the development of a recycling industry and innovation in recycling technology.

Despite these benefits, recycling of critical raw materials still faces some challenges, including technological and economic limitations, a lack of efficient collection and recycling infrastructure, and complex waste collection systems. The continuous improvement of recycling technologies and the development of sustainable and innovative raw material management models are essential to achieving sustainable use of critical raw

materials in the future. There are various methods and technologies for recycling critical metals, and their efficiency and environmental impact can vary depending on the process and application. Some of the main methods of recycling critical metals include:

1. Physical separation and sorting - physical separation and sorting of waste, separating valuable materials from other components. It may involve the use of various methods, such as magnetic separation, size sorting, or gravity methods.
2. Pyrometallurgy – these processes use high temperatures and chemical reactions to extract the metals from the waste. It can involve melting the materials and passing them through various phases of extraction, purification, and recycling of the metals.
3. Hydrometallurgy - use solvents and chemical reactions to dissolve metals from waste and extract them. This may involve various steps such as leaching, extraction, and electrodeposition of the metals.
4. Biotechnologies - use microorganisms or biological processes to degrade or extract metals from waste. It may involve the use of bacteria, fungi, or other biological agents capable of degrading or accumulating the metals.

Assessing the effectiveness and environmental impact of these methods and technologies can be complex and depends on many factors, including waste types, process conditions, energy requirements, emissions of harmful substances, and waste management. It is important to carry out a comprehensive assessment of the entire life cycle of the recycling process, from waste extraction to the final product or material.

The continued development of new technologies, innovations in recycling processes, and strict adherence to environmental standards and norms are essential to reducing the adverse impact on the environment and achieving a sustainable recycling industry.

Technological Innovations for the Recovery of Critical Metals

Technological innovations for the recovery of critical metals are being developed to efficiently use limited resources and reduce dependence on new mining. (Patil et al., 2022) Here are some of the main innovations in this area:

1. Use of high-efficiency chemical processes. New methods and processes are being developed to efficiently extract critical metals from various sources. This may include the use of chemical solvents and extraction techniques that allow for more efficient separation and extraction of the metals from the waste.
2. Nanotechnology. Nanomaterials and nanotechnology play an important role in the recovery of critical metals. Nanoparticles can be used to efficiently extract metals from waste or to facilitate metal separation and purification processes.
3. Biotechnologies. The use of microorganisms and biological processes can be an innovative method to recover critical metals. Some microorganisms are able to accumulate metals or extract metal ions from waste, which can facilitate the recycling process.
4. Development of new materials and alternatives. Options for replacing critical metals are being explored extensively. New materials and technologies are being developed to reduce or eliminate the use of critical metals in various applications. For example, alternative materials for lithium-ion batteries are being investigated to reduce or eliminate the use of critical metals such as cobalt.

These technological innovations have the potential to change the landscape of critical metal recovery by reducing reliance on new mining and optimising the use of limited resources. (Song et al., 2022) However, many of these innovations are still in their early stages of development and require further research and development before they can be widely implemented on an industrial scale.

Results and Discussion

The present study will contribute to the understanding and development of strategies and practices that can help achieve sustainable use and management of critical raw materials within a circular economy. Critical metals are a group of raw materials that are of strategic importance to modern technology but are limited in availability and are found in geographically concentrated areas. They are used in various industries, such as electronics, power systems, automotive, military, and others. Replacement of critical raw materials can be accomplished by

developing alternative materials, changing product design, increasing use efficiency, recycling, and improving extraction methods. Investments in research and development projects are essential to finding sustainable solutions for the use of critical raw materials. (Dimov, et al., 2020). To achieve more sustainable management of critical raw materials and metals, the following improvements can be made and certain guidelines followed:

1. Changing production processes: Manufacturers can use more sustainable methods and technologies to extract, process, and manufacture critical metals. This may include the use of energy-efficient processes, the reduction of waste disposal and emissions of harmful substances, as well as the use of renewable energy sources.
2. Convert to closed supply chains: For critical metals, closed supply chains are a viable way to implement the circular economy principle. This means increasing the efficiency of recycling, recovery, and secondary use of critical metals, as well as reducing dependence on new mining.
3. Develop standards and certifications: Establishing standards and certifications for the responsible management of critical metals can help track and ensure ethical, environmental, and socially responsible behaviour throughout the supply chain. Such standards and certifications can be applied both in the mining industry and in the production and consumption of critical metals.
4. Investment in research and innovation: Funding research projects and innovation in the field of critical metals can lead to the development of new technologies and processes for the efficient recovery, recycling, and replacement of these materials.
5. Cooperation and knowledge sharing: It is important to support cooperation between governments, industry, academia, and civil society to exchange knowledge and experience in the field of critical metals management. This may include organising forums, working groups, and projects to share good practices and research.

The implementation of these improvements and guidelines can contribute to achieving more sustainable management of critical metals, reducing environmental burden and independence from mining, as well as creating more sustainable and innovative business models in this area.

Scientific Ethics Declaration

The author declares that the scientific ethical and legal responsibility of this article published in EPSTEM journal belongs to the author.

Acknowledgements or Notes

* This article was presented as an oral presentation at the International Conference on Technology, Engineering and Science (www.icontes.net) held in Antalya/Turkey on November 16-19, 2023.

References

Blengini, G., Mathieux, F., Mancini, L., Nyberg, M., Viegas, H.M., Salminen, J., Garbarino, E., Orveillon, G., Saveyn, H., Aquilino, V. Llorens, T., Polonio, F., Horckmans, L., d'Hugues, P., Balomenos, E., Dino, G., Feld, M., Madai, F., Janos, F., & Calleja, I.. (2019). *Recovery of critical and other raw materials from mining waste and landfills state of play on existing practices*. Joınt Research Centre (JRC).

Dimov, E., Bakyrdjieva, R., & Stratiev. N. (2020). The mining industry and the recycling of raw materials as an important element of the Bulgarian economy. *Journal of Mining and Geological Sciences, 63*, 289-292.

European Commission (2023). Directorate-general for internal market, industry, entrepreneurship and SMEs, *Study on the critical raw materials for the EU 2023 – Final report.* Office of the European Union

Hool, A., Christoph, H., & Gijsbert. W. (2023). Challenges and opportunities of the European critical raw materials act. *Mineral Economics,* 1-8.

Hristova, T. (2022). The place of the blockchain in the recycling of raw materials. In *2022 8th International Conference on Energy Efficiency and Agricultural Engineering (EE&AE)* (pp. 1-4). IEEE.

Massari, S., & Ruberti, M. (2013). Rare earth elements as critical raw Mümaterials: Focus on international markets and future Strategies. *Resources Policy, 38*, 36-43.

Patil, A., Rudolf, S., & Christian. L. (2022). Opportunities in critical rare earth metal recycling value chains for economic growth with sustainable technological innovations. *Circular Economy and Sustainability.* 3, 1127-1140.

Piotrowski, S. (2023). Critical raw materials in the semiconductor industry: Current challenges and perspectives. *The Third International Scientific Conference: Studies in Changing Bussiness Environment.* Vilnius.

Ruan, S., Song, Y., Cheng, J., & Zhan, C. (2023). Green eco-innovation and supply of critical metals: Evidence from China. *Sustainability*, *15*(17), 12730.

Song, Y., Zhouyi, Z., Yijun, Z., & Jinhua. C. (2022). Technological innovation and supply of critical metals: A perspective of industrial chains. *Resources Policy, 79,* 103144.

Watari, T., Nansai, K., & Nakajima, K. (2020). Review of critical metal dynamics to 2050 for 48 elements, resources. *Conservation and Recycling, 155*. 104669.

Author Information

Vessela Petrova
University of Mining and Geology "St. Ivan Rilski"
Sofia, Bulgaria
Contact e-mail: *vessela.petrova@mgu.bg*

To cite this article:

Petrova, V. (2023). Exploring the opportunities for sustainable management of critical raw materials in the circular economy. *The Eurasia Proceedings of Science, Technology, Engineering & Mathematics (EPSTEM), 26,* 664-671.

The Eurasia Proceedings of Science, Technology, Engineering & Mathematics (EPSTEM)
ISSN: 2602-3199

The Eurasia Proceedings of Science, Technology, Engineering & Mathematics (EPSTEM), 2023

Volume 26, Pages 672-676

IConTES 2023: International Conference on Technology, Engineering and Science

Investigation of the Efficiency of Reversible Radial-Shear Rolling to Obtain a Gradient Ultrafine-Grained Structure in 5KHV2S Steel

Abdrakhman Naizabekov
Rudny Industrial Institute

Vladislav Pishchikov
Rudny Industrial Institute

Yevgeniy Panin
Karaganda Industrial University

Alexandr Arbuz
Nazarbayev University

Sergey Lezhnev
Rudny Industrial Institute

Abstract: It has long been proven that radial-shear rolling has a number of advantages over other methods of pressure treatment, which allows obtaining an ultrafine-grained structure, including gradient, in various ferrous and non-ferrous metals and alloys. Therefore, radial-shear rolling plays an important role in the production of high-quality bars with an increased level of properties. This work, carried out within the framework of grant № AP14869135, funded by the Committee of Science of the Ministry of Science and Higher Education of the Republic of Kazakhstan, is devoted to the study of reversible radial-shear rolling of 5KHV2C steel and the identification of its influence on the possible gradient modification of the microstructure of this steel grade. In the course of experimental studies, it was proved that during the deformation of a bar made of 5KHV2C steel with an initial diameter of 36 mm, a gradient microstructure is formed along the cross section of the bar on a radial-shear rolling mill with an extraction equal to 4, i.e. up to a diameter of 18 mm. The cross-section structure of the bar varies from an elongated rolling texture in the central part of the bar to an equiaxed ultrafine-grained microstructure in the peripheral layers of the bar. The gradient character of the microstructure is also confirmed by the distribution of microhardness over the cross section of the bar: microhardness in the peripheral layers of the bar is on average 1.7 times higher than in the central part of the bar.

Keywords: Radial-Shear rolling, Gradient Ultrafine-Grained structure, Microhardness, Alloy steel, Rod

Introduction

One of the main methods of gradient modification of long products made of ferrous and non-ferrous metals and alloys is their deformation on radial-shear rolling mills (Galkin et al., 2021). The widespread development of such a method of deformation as radial shear rolling (Galkin et al., 2014) began in the early 90s of the last century under the leadership of S.P. Galkin and represents to some extent a previously known process, namely transverse-helical rolling according to a three-roll scheme (Galkin, 2014). The main difference of proposed schemes from the previously known scheme are an increased feed angle $\alpha = 18\text{-}20°$ (with a normal rolling angle $\beta = 5\text{-}7°$), which, firstly, contributes to the development of the strongest vortex deformation from the surface to the center, and secondly reduces the likelihood of tensile stresses in the axial part of the workpiece. Based on the

- Selection and peer-review under responsibility of the Organizing Committee of the Conference

proposed deformation scheme, a number of rolling mills for radial shear rolling of solid round blanks were developed and put into small-scale production by the research team under the leadership of S.P. Galkin.

Currently, a number of studies have been carried out to identify the influence of radial-shear rolling on the microstructure evolution and changes in the mechanical properties of bars made of various ferrous and non-ferrous metals and alloys. For example, the study of the influence of radial-shear rolling on the microstructure evolution and the change in the mechanical properties of technical titanium was presented (Nayzabekov et al., 2020). Also the influence of radial-shear rolling on changes in the structure and properties of aluminum was studied (Gamin et al., 2020; Stefanik et al., 2015). In a number of scientific papers the results of a study on the effect of radial-shear rolling on grain size changes and mechanical properties of austenitic stainless steel are presented (Naizabekov et al., 2021; Naizabekov et al., 2021).

It should be noted that radial-shear rolling can be used not only to produce ultrafine-grained long-length products from various ferrous and non-ferrous metals and alloys, but also to produce such products from various composite materials. The effect of radial-shear rolling on the formation of the structure and mechanical properties of aluminum matrix composite alloys of the eutectic type Al-Ni and Al-Ca was investigated (Akopyan et al., 2021).

The main purpose of this work, carried out within the framework of grant № AP14869135, funded by the Committee of Science of the Ministry of Science and Higher Education of the Republic of Kazakhstan, is to study the process of radial shear rolling of alloy steel 5KHV2S and to identify the influence of this deformation process on the possible gradient modification of the microstructure of this steel grade.

Method

To achieve this goal, a laboratory experiment using a radial shear rolling mill SVP-08 was conducted (Figure 1).

Figure 1. SVP-08 radial-shear rolling mill

The technical characteristics of SVP-08 radial-shear rolling mill are presented in Table 1. This mill is equipped with 3 rolls, the shape of which is shown in Figure 2. This form of rolls allows for the deformation of rods on the SVP-08 radial-shear rolling mill to ensure the reversible nature of the rotation of the rolls and to change the direction of metal movement in the rolling stand. This mill has two replaceable roll groups with different roll diameters, which ensure rolling of the initial billet up to a diameter of 8 mm. The material for the study was

5KHV2S steel after homogenizing annealing. For the experiment, blanks with a diameter of 36 mm and a length of 200 mm were prepared, which were heated to 1100°C in a Nabertherm R120/1000/13 tubular furnace with an exposure time of 36 minutes to equalize the temperature along the cross section.

Table 1. Technical characteristics of SVP-08 radial-shear rolling mill

Characteristic	Value
Rolling speed, mm/s	70
Rolls rotation speed, rpm	56
Torque on one roll, N·m	890
Force per roll, kN	100
Rolling angle, deg	7
Feed angle, deg	20
Taper gauge of roll groups, deg	8-12
Extraction coefficient	1,1-4,5
Workpiece length, mm	100-2000
Product length, mm	till 6000
Product diameter, mm	8-35
Product accuracy, %	till 1
Deviation from straightness (curvature), %	till 1
Productivity, t/h	0,1-2,0

The technology of rolling blanks made of 5KHV2S steel on a radial-shear rolling mill was as follows. The preheated workpieces are fed into the working cage of the rolling mill, in which it is compressed with an absolute compression step of 3.0 mm in diameter. After the workpiece has completely exited the cage, the rolls are arched and the direction of their rotation is switched. The workpiece is fed into the rolls in accordance with the scheme shown in Figure 2, in which it is compressed again with an absolute compression step of 3.0 mm in diameter. According to this deformation scheme, rods with a diameter of 18 mm and a length of about 800 mm were obtained from the initial blanks with a diameter of 36 mm and a length of 200 mm in 6 passes. The temperature of the workpieces during deformation was monitored using a CEM DT-9897 thermal imager. After the 6th rolling pass, the temperature of the workpieces lay in the range of 830-850°C.

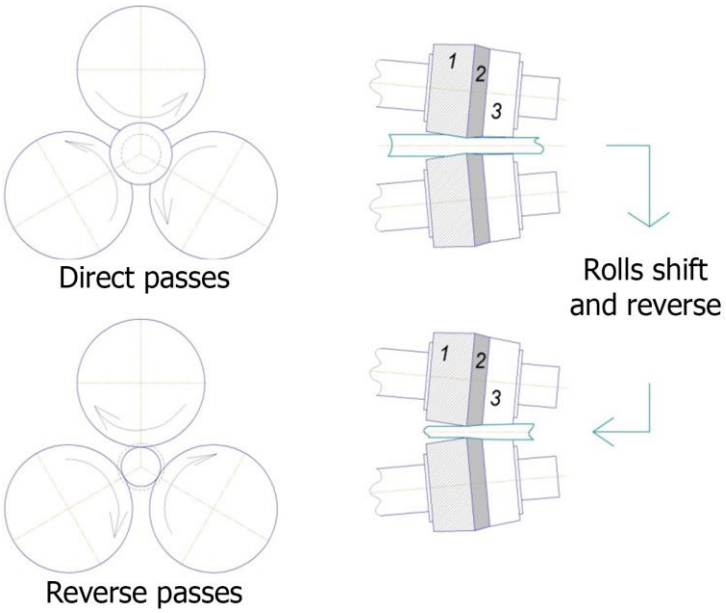

Figure 2. Radial-shear rolling scheme: 1 – crimping section for straight passes; 2 – calibration section for all passes; 3 - crimping section for reverse passes

Results and Discussion

Samples were cut from the initial bars and the bars obtained after rolling with a diameter of 18 mm and slots were made for metallographic studies and microhardness measurements. Microstructural analysis was carried out using a scanning electron microscope JSM-5610 LV, and the determination of the values of microhardness

was carried out on a Duramin microhardness meter (Struers, Denmark) by the Vickers method with a load on the indenter of 10-2000 g, exposure time of 10 s. This analysis showed that the microstructure of the initial bars made of 5KHV2S steel, subjected to homogenizing annealing, represents a distribution of perlite about 63% and ferrite about 47% (Figure 3a).

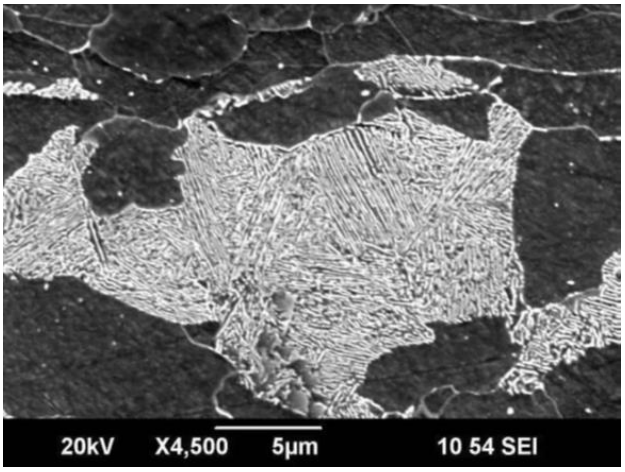

a

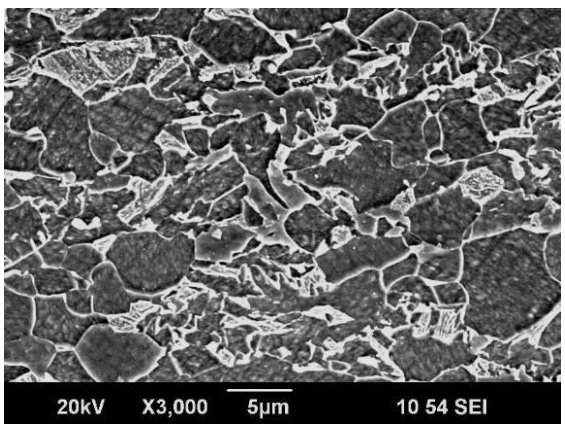

b

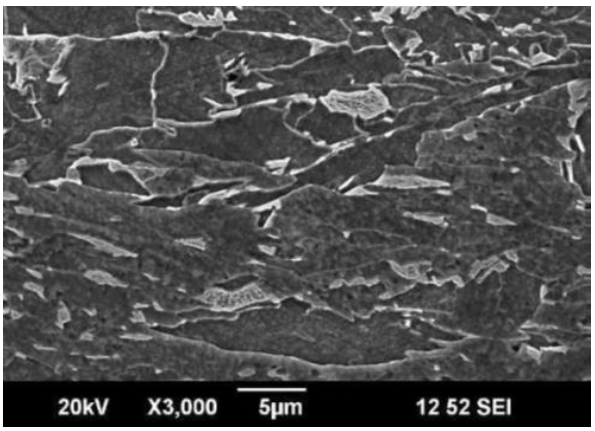

c

Figure 3 - Microstructure of 5KHV2S steel after radial-shear rolling up to a diameter of 18 mm: a - initial, b – surface zone, c – central zone

The microstructural analysis of the diameter bars obtained at the radial-shear rolling mill showed that the initial grain size of steel 5KHV2S after rolling significantly decreased. At the same time, the microstructure of the peripheral zone of the bars formed at the radial-shear rolling mill has a predominantly equiaxial ultrafine-grained character with grain sizes of about 1.8-3.2 microns. In the central zone of the bars being formed, grains elongated in the direction of rolling are observed with dimensions lying in the range of 6÷10.5×1.1÷1.9 microns. Also, in order to confirm the gradient nature of the microstructure evolution along the cross-section of radial shear rods made of 5KHV2S steel formed on the mill, microhardness measurements were carried out along the cross-section of the rods. Analysis of the results of the study showed that the difference in microhardness values between the peripheral and central zone after the 6th pass showed that the microhardness in the peripheral layers of the bar is on average 1.17 times higher than the central part of the bar. At the same time, the highest value of microhardness was 265 HV (a point at a distance of 1 mm from the edge of the rod), and the minimum value was 224 HV at one of the points in the central zone of the rod.

Conclusion

In the course of the conducted research, the process of reversible radial-shear rolling of alloy steel 5KHV2S was studied and the possibility of obtaining a gradient ultra-fine-grained structure in alloy steel 5KHV2S during deformation at the SVP-08 radial-shear rolling mill was proved.

Scientific Ethics Declaration

The authors declare that the scientific ethical and legal responsibility of this article published in EPSTEM journal belongs to the authors.

Acknowledgements or Notes

* This article was presented as an poster presentation at the International Conference on Technology, Engineering and Science (www.icontes.net) held in Antalya/Turkey on November 16-19, 2023.

* This research was funded by the Science Committee of the Ministry of Science and Higher Education of the Republic of Kazakhstan (Grant № AP14869135).

References

Akopyan, T. K., Aleshchenko, A. S., Belov, N. A. & Galkin, S. P. (2018). Effect of radial–shear rolling on the formation of structure and mechanical properties of Al–Ni and Al–Ca aluminum–matrix composite alloys of eutectic type. *Physics of Metals and Metallography, 119*(3), 241-250.

Galkin S. P. (2014). Radial shear rolling as an optimal technology for lean production. *Steel in Translation, 44*(1), 61-64.

Galkin, S. P., Gamin, Yu. V., Aleshchenko, A. S., & Romantsev, B. A. (2021). Modern development of elements of theory, technology and mini-mills of radial-shear rolling. *Chernye Metally, 12*, 51-58.

Galkin, S. P., Romantsev, B. A., & Kharitonov, E. A. (2014). Putting into practice innovative potential in the universal radial-shear rolling process. *CIS Iron and Steel Review, 9*(9), 35-39.

Gamin, Y. V., Akopyan, T. K., Koshmin, A. N., Dolbachev, A. P., & Goncharuk, A. V. (2020). Microstructure evolution and property analysis of commercial pure Al alloy processed by radial-shear rolling. *Archives of Civil and Mechanical Engineering, 20*(4), 143.

Naizabekov, A. B., Lezhnev, S. N. & Panin, E. A. (2021). Formation of a gradient structure in austenitic stainless steel AISI 321 by radial-shear rolling. *Solid State Phenomena, 316*, 246-251.

Naizabekov, A., Lezhnev, S., Panin, E., Volokitina, I., & Kasperovich, A. (2021). Realization of the innovative potential of radial-shear rolling for forming the structure and mechanical properties of AISI-321 austenitic stainless steel. *Revista Matéria, 26*(3). https://doi.org/10.1590/S1517-707620210003.13018

Nayzabekov, A., Lezhnev, S., & Arbuz, A. (2020). The effect of radial-shear rolling on the microstructure and mechanical properties of technical titanium. *Solid State Phenomena, 299*, 565-570.

Stefanik, A., Szota, P., Mróz, S. & Dyja, H. (2015). Analysis of the aluminum bars in three-high skew rolling mill rolling process. *Solid State Phenomena, 220-221*, 892-897.

Author Information

Abdrakhman Naizabekov
Rudny Industrial Institute
38 50 let Oktyabrya str., Rudny, Kazakhstan

Vladislav Pishchikov
Rudny Industrial Institute
38 50 let Oktyabrya str., Rudny, Kazakhstan

Yevgeniy Panin
Karaganda Industrial University
30 Republic av., Temirtau, Kazakhstan

Alexandr Arbuz
Nazarbayev University
53 Kabanbay Batyr av., Astana, Kazakhstan

Sergey Lezhnev
Rudny Industrial Institute
38 50 let Oktyabrya str., Rudny, Kazakhstan
Contact e-mail: *sergey_legnev@mail.ru*

To cite this article:

Naizabekov, A., Pishchikov V., Panin, Y., Arbuz A., & Lezhnev, S. (2023). Investigation of the efficiency of reversible radial-shear rolling to obtain a gradient ultrafine-grained structure in 5KHV2S steel. *The Eurasia Proceedings of Science, Technology, Engineering & Mathematics (EPSTEM), 26*, 672-676.

The Eurasia Proceedings of Science, Technology, Engineering & Mathematics (EPSTEM)
ISSN: 2602-3199

The Eurasia Proceedings of Science, Technology, Engineering & Mathematics (EPSTEM), 2023

Volume 26, Pages 677-684

IConTES 2023: International Conference on Technology, Engineering and Science

Influence of the Behaviour Coefficient on the Damage Level of an RC Elevated Tank under Seismic Loading

Ourdia Ider
Mouloud Mammeri University

Hocine Hammoum
Mouloud Mammeri University

Karima Bouzelha
Mouloud Mammeri University

Amar Aliche
Mouloud Mammeri University

Abstract: In Algeria, the seismic design of elevated concrete storage tanks is carried out in accordance with seismic standard, involving a behavior coefficient of the structure. This behaviour coefficient is used to determine the internal forces and to estimate the inelastic deformations undergone by the structure. For the elevated water tank, considered as reverse pendulum structure, this coefficient assumes a constant value (R=2) in the Algerian seismic code. Taking into account a single value, whatever the seismic zone, the site of implantation and the geometric characteristics of the structure, can lead to design errors leading to oversizing, hence an additional cost of the structure. Thus, faced with the need to design resistant structures while minimizing construction costs, it is important to precisely determine the value of this behaviour coefficient to introduce into the evaluation of the structure's response. In this research, the seismic performance of an RC elevated tank is analyzed, using a nonlinear approach based on the Pushover method, initially using the behavior coefficient prescribed by the Algerian seismic code, then secondly using the behavior coefficient approximated by a power-type law, taking into account the seismic zone, the type of soil, the height of the structure and the storage capacity. The results of this study highlight the influence of the value of the behavior coefficient on the seismic performance and the level of damage to an elevated tank.

Keywords: Behavior coefficient, Pushover method, Nonlinear approach, Elevated tank.

Introduction

In civil engineering, structures damage after strong seismic action is an indisputable result that depends on many factors, including the value of the adopted seismic behaviour coefficient. Thus, if the latter is underestimated, the structure is likely to suffer extreme deformation and major damage. On the other hand, if the behaviour coefficient is overestimated, the structure may be over-designed, without significantly reducing the risk of damage it will face during a devastating earthquake. Given the need to design resistant structures while minimising construction costs, it is important to determine precisely the value of the behaviour coefficient to introduce into the calculation of the structure's performance point.

In this research, the influence of the value of the seismic behaviour coefficient on damage is studied, in order to assess the effect of this parameter on the structure performance. The behaviour coefficient is calculated by a power relation proposed in section 1 as a function of the seismic zone and the height of the pedestal, performed

by a nonlinear approach. The methodology for evaluating the performance point is defined in procedure B of ATC-40. The spectral displacement S_d of the performance point defined by the intersection between the effective demand spectrum, defining the earthquake, and the capacity curve of the structure gives the value of the maximum displacement of the structure. This is considered to be the major factor conditioning structural damage (Mekki, 2015). Once this displacement S_d is defined, we proceed to classify the RC elevated tank in a damage domain that we propose as a function of the ultimate displacement δ_u extracted from the capacity curve (defined by the passage of the structure from the plastic phase to ruin) and the elastic displacement δ_e (obtained by the bilinear curve).

Evaluation of the Behaviour Coefficient Using a Non-Linear Approach

The evaluation of the behaviour coefficient, noted R, using a non-linear approach was carried out as part of the preparation of Ider's doctoral thesis (Ider, 2023). The results of this research showed that the behaviour coefficient is a function of the height of the pedestal H (Figure 1) and obeys to a power law as follows :

$$R = aH^b$$

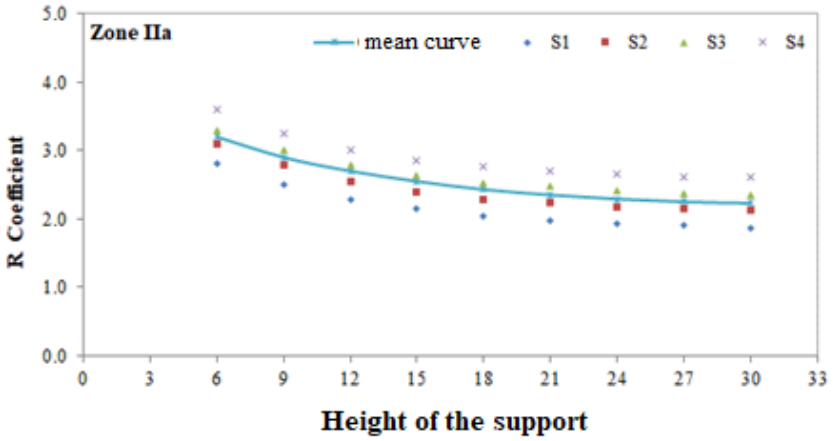

Figure 1. Behaviour coefficient as a function of pedestal height H.

The values of parameters (a) and (b) are obtained as a function of the seismic zone and the the site type. An summary of the results for the behavior coefficient is presented in table 1 for the seismic zone IIa. The results show that the behaviour coefficient takes different values for each height and each site (table 1), contrary to the Algerian Seismic Regulations (RPA,2003) which consider a single value of the behavior coefficient (R=2) whatever the study parameters.

Table 1. Value of the behavior coefficient R as a function of the height of the pedestal H, and site type, in medium seismic zone (IIa)

H(m)	6	9	12	15	18	21	24	27	30
S1 site	2.8	2.5	2.28	2.14	2.05	1.98	1.94	1.9	1.87
S2 site	3.1	2.78	2.55	2.4	2.29	2.23	2.18	2.15	2.12
S3 site	3.3	3	2.78	**2.63**	2.53	2.47	2.42	2.38	2.35
S4 site	3.6	3.25	3.00	2.85	2.76	2.7	2.65	2.62	2.6

Evaluation of Damage Level

In the field of earthquake engineering, the assessment of seismic risk is linked to both the demand (seismic hazard) and the capacity of the structure (performance) (Desprez, 2005; Mekki, 2015). For this, and in order to carry out an assessment of the seismic performance of a structure, through a mechanical analysis, recourse to the concept of damage indicator, which provides information on the extent of degradation that may occur in a structure, is necessary. Several methods for damage evaluation to civil engineering structures have been developed, such as the RISK-UE method, which is a qualitative method widely used in Europe to assess the effects of earthquakes on structures (RISK-UE, 2001). This method links the concept of visual observation of damage to displacements measured at the top of the structure. The RISK-UE method provides a range of criteria

for observing and describing damage, classified according to a rating scale from 0 (no damage) to 5 (very significant damage). Based on this classification, we propose six damage domains for RC elevated tanks, as illustrated in Table 2.

Table 2. Proposed damage domains for RC elevated tanks.

Degrees and damage domains	Relations for differents limits spectrals displacements
Green 1 Domain (Negligible Damages)	$Sd < 0.4\ \delta e$
Green 2 Domain (Minor Damages)	$0.4\ \delta e \leq Sd < 0.8\ \delta e$
Orange 1 Domain (Moderate Damages)	$0.8\ \delta e \leq Sd < \delta e + 0.25\ (\delta u - \delta e)$
Orange 2 Domain (Significant Damages)	$\delta e + 0.25\ (\delta u - \delta e) \leq Sd < 0.75\ \delta u$
Orange 3Domain (Severe Damages)	$0.75\ \delta u \leq Sd < \delta u$
Red Domain (Complete Structural Collapse)	$Sd \geq \delta u$
δe :Elastic limit displacement	
δu : Ultimate limit diplacement	

The ultimate displacement δu is extracted from the capacity curve (Figure 2), and is defined by the passage of the structure from the plastic phase to ruin, while the elastic displacement δe is obtained by the bilinear curve.

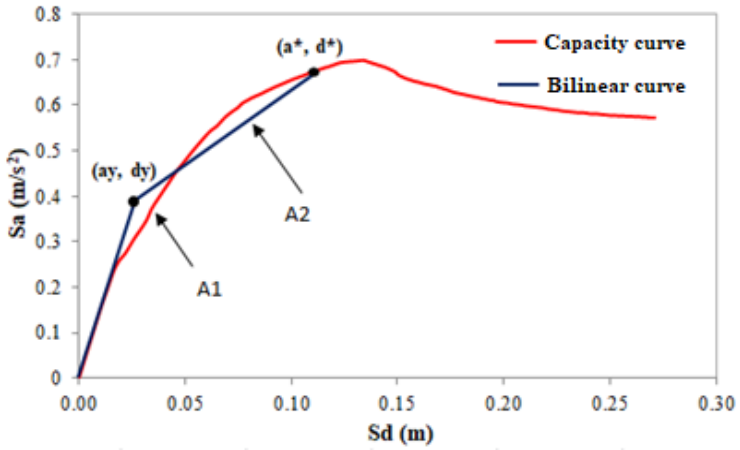

Figure 2. Capacity curve.

Application to the Case Study

To apply the methodology presented above, we consider an RC elevated tank with a capacity of 200 m3, with pedestal height of H=15m. The tank is located in Zone IIa on a soft site (S3). The behaviour coefficient given by the power law is (R = 2.63). A three-dimensional finite element model was developed to simulate the behaviour of the tank under lateral loading of the progressive thrust type, using the ETABS© software.

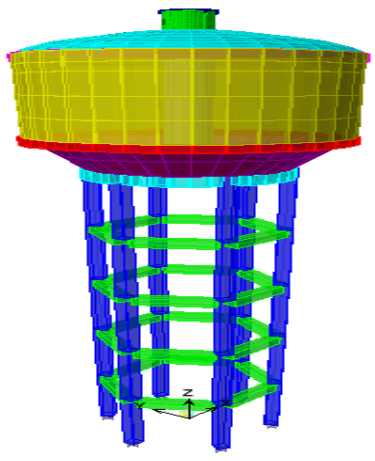

Figure 3. Finite element modeling of the elevated tank.

Evaluation of the Performance Point

Estimation of the Effective Damping of the Structure

To evaluate the right damping of the structure, a series of reduced spectra is developed, varying the damping factor ξ by 5%, 10%, 15%, ..., 29% (Figure 4), as stipulated in ATC40 for type B structures.

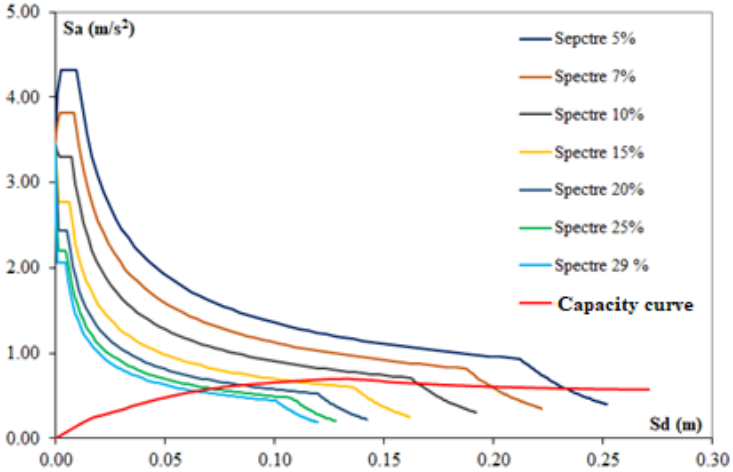

Figure 4. Representation of the family of reduced spectra

In the vicinity of the point with coordinates (a*; d*), defined by the bilinear curve (Figure 2), we choose three points one step apart on either side whose coordinates are defined by (api,dpi).
For each value of (api , dpi), the effective damping ξeff is determined by the following relation according to ATC 40.

$$\xi_{eff} = 5 + \kappa.\xi_0$$

ξ o represents the viscous damping which is a function of the coordinates of the points (api ; dpi) and (ay ; dy)

$$\xi_0 = \frac{63.7(a_y d_{pi} - d_y a_{pi})}{a_{pi} d_{pi}}$$

For an elevated tank, classified as type B (public works of national interest or of certain socio-cultural and economic importance), the k factor is taken equal to 0.67 (see ATC 40). For each value of dpi in the series under consideration, we deduce pairs (dpi , ξeff), recorded in the table below (Table 3):

Table 3. Selected displacement values and corresponding damping.

d_{pi}	a_{pi}	ξ_o	k	ξ_{eff}
0.061	0.54	18.970	0.670	17.710
0.069	0.575	18.880	0.670	17.650
0.077	0.605	18.730	0.670	17.549
0.088	0.631	18.540	0.670	17.422
0.101	0.658	18.140	0.670	17.154
0.112	0.677	17.700	0.670	16.859
0.123	0.694	16.820	0.670	16.269

Different spectra are generated from the values of ξeff (Figure 5). The intersection of generated spectra with the vertical projections of the corresponding dpi , gives a set of points with coordinates (dpi , ξeff). By interconnecting these resulting points, we obtain a curve whose intersection with the capacity spectrum defines the structure's performance point, corresponding to the maximum displacement. This performance point represents the intersection of the capacity curve with the actual seismic demand corresponding to the effective damping of the structure ξeff =17.30% obtained by interpolation (Figure 5). The coordinates of the performance point are given in Table 4 and illustrated in Figure 6.

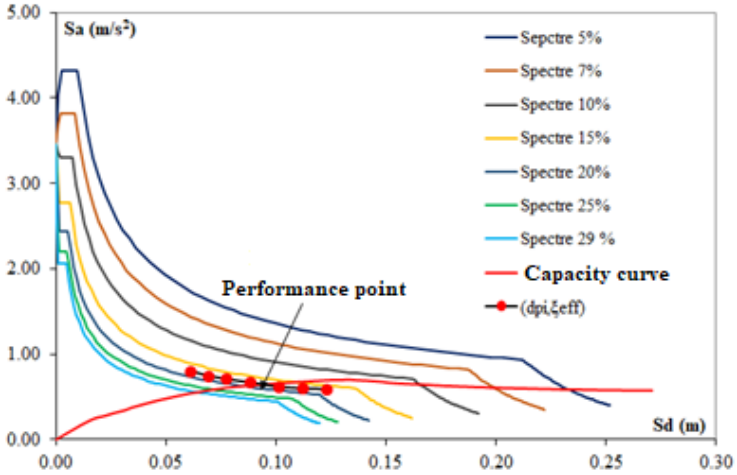

Figure 5. Evaluation of the performance point

Table 4. Coordinates of the performance point

S_d spectral displacement of the performance point	0.099	m
S_a spectral acceleration of the performance point	0.654	m/s^2
Effective damping ξ_{eff}	17.30	%

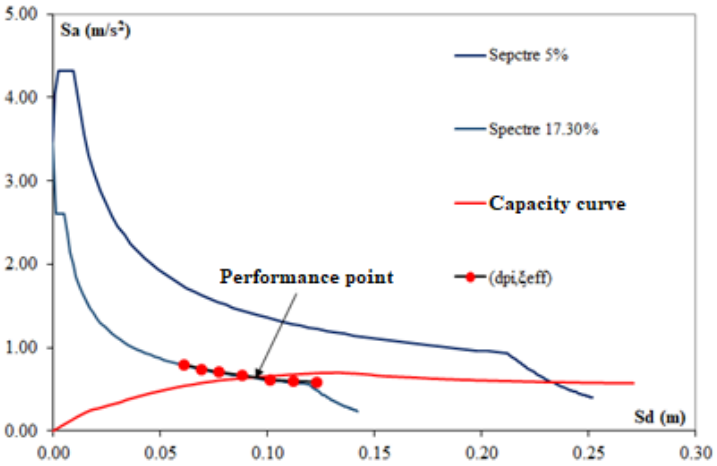

Figure 6. Coordinates of the performance point

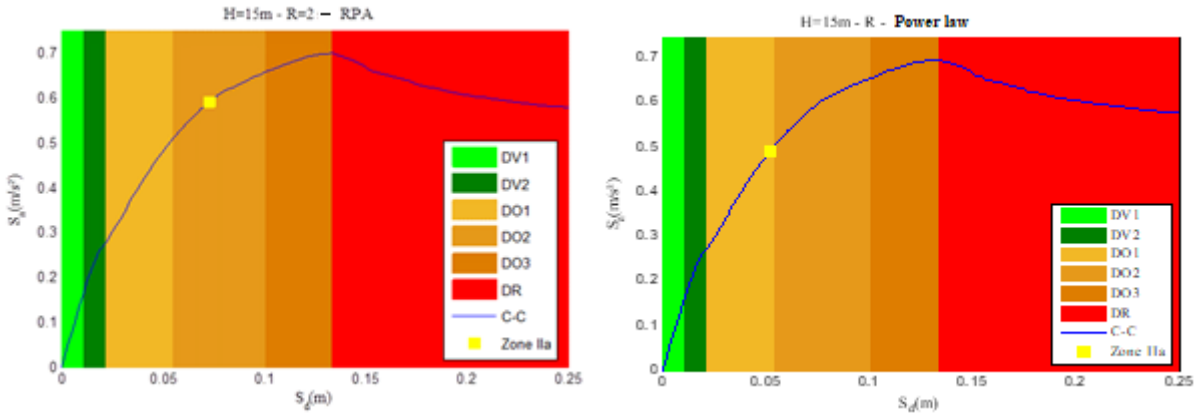

(a) (b)

Figure 7. Position of the performance point in the damage domain.

The position of the performance point in the damage domain defined in Table 2 is shown in Figure 7(a) for R=2 (RPA, 2003) and Figure 7(b) for R=2.63from the power law. It should be noted that this performance point is

located in the orange 2 domain for R =2 and at the limit of the orange 1 domain for R=2.63. In this case, it can be seen that the RPA overestimates the damage. However, by considering the R power law coefficient, the structure becomes more ductile and works more in the plastic domain, which enables it to reduce the maximum displacement and consequently the damage.

Influence of the Behaviour Coefficient and the Seismic Zone

To assess the influence of the behaviour coefficient R on tank performance, we carried out a two-stage analysis. In the first case, we considered the behaviour coefficient R recommended by the RPA, varying the seismic zone, and in the second case, we considered the behaviour coefficient R evaluated from the proposed power law, also varying the seismic zone. The results are shown in Figures 8 (a) and (b).

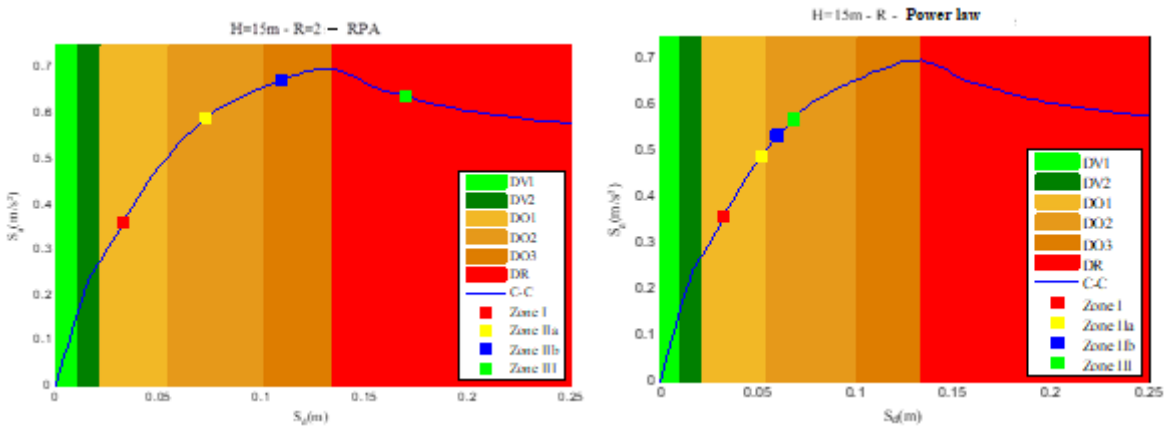

(a) (b)

Figure 8. Position of the performance point for different seismic zones

The comparison of the results of the performance point shows that when the behaviour coefficient (R=2) recommended by the Algerian seismic regulations (RPA, 2003) is considered, the structure rapidly penetrates the red domain. Conversely, the results of the value from the of thepower law of the behaviour coefficient R show a significant reduction in the penetration of the elevated tank into the red zone, which is reflected in the correct consideration of the force-displacement pair to which the structure is subjected. In fact, the use of a coefficient R>2 has a direct influence on the ductility of the elevated tank by reducing the range of values of the estimated performance points compared with those resulting from the use of R of the RPA, thus leading to an economical design.

Influence of Pedestal System Height

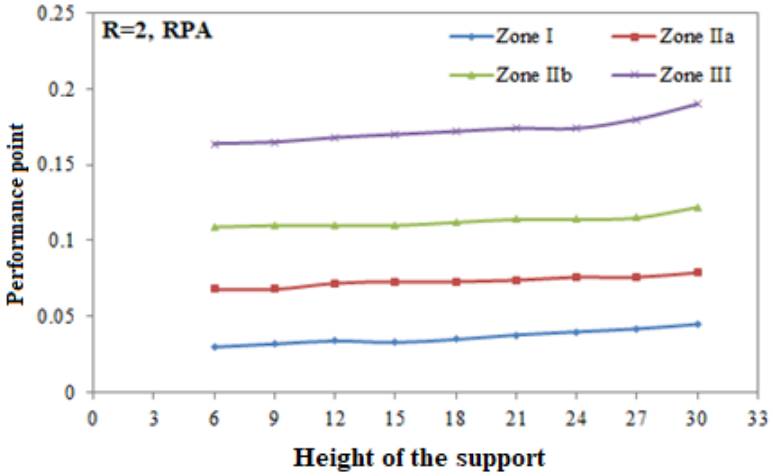

Figure 9. Evolution of the performance point as a function of the height of the pedestal H, for R=2 (RPA)

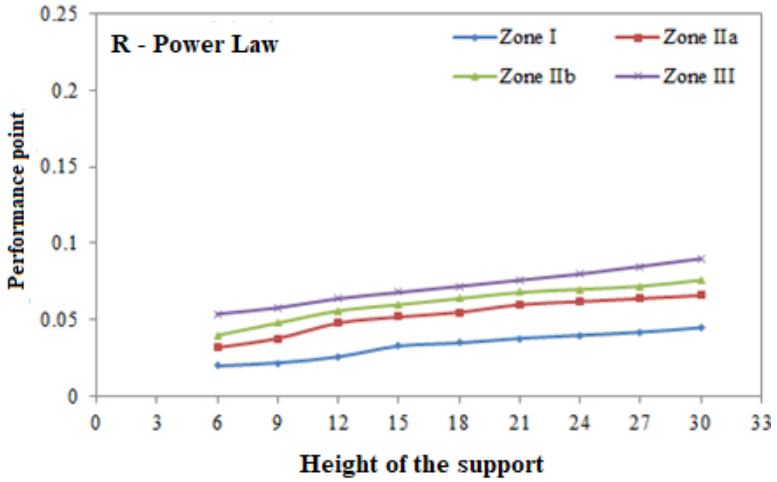

Figure 10. Evolution of the performance point as a function of different pedestal heights H, for R obtained from the power law

A summary of the results obtained for the evolution of the performance point for different seismic zones and different heights of the pedestal is presented in Figures 9 and 10 for the behaviour coefficient R recommended by the RPA (R=2) and the values of the behaviour coefficient R obtained by the power law apraoch, respectively.

It can be seen that whatever the value of the behaviour coefficient R, the spectral displacement of the performance point increases with the height of the tank pedestal sytem. However, we note that this increase is more pronounced for the value of R recommended by the RPA (R=2), and this is very visible in zones of very high seismicity (zone III); this reduces the performance of the tank and causes the structure to enter the failure domain more quickly, moving from zone I to zone III. On the other hand, considering the values of the behaviour coefficient R, obtained from the power law , the structure gains in performance.

The behaviour coefficient R recommended by the RPA has the effect of overestimating the spectral displacement Sd of the performance point and is very easily positioned in safety, given that it adopts the same value whatever the height and whatever the seismic zone. It should also be noted that the various spectral shifts Sd of the performance point obtained for the behaviour coefficient R from the power law are less than those given by the value of (R=2), recommended by the RPA.

Conclusion

The non-linear analysis of the seismic behaviour of an elevated tankis carried out in this study using the "Pushover" method, varying the seismic zone, the location and the height of the pedestal. To calculate the seismic response of the tank, we focused on the value of the behaviour coefficient R. We adopted the value of the R coefficient recommended by Algerian seismic code (R=2) and the R value obtained from the power law.
The results of the spectral displacement of the performance point showed that by considering the value of R=2, the tank rapidly enters the red domain, depending on the seismic zone and the height of the tank pedestal, contrary to the case of the R coefficient obtained from the power law. The latter has a direct influence on the ductility of the tank by reducing the range of performance point values. Using more realistic values of R, its reflects a better performance of the structure, which translates into greater penetration into the plastic zone and therefore better damping of seismic stresses and more controlled displacements, resulting in an economical design.

Scientific Ethics Declaration

The authors declare that the scientific ethical and legal responsibility of this article published in EPSTEM journal belongs to the authors.

Acknowledgements or Notes

* This article was presented as a poster presentation at the International Conference on Technology, Engineering and Science (www.icontes.net) held in Antalya/Turkey on November 16-19, 2023.

References

ATC-40. (1996). *Seismic evaluation and retrofit of concrete buildings* (Volume 1). Applied Technology Council. Retrieved from https://www.atcouncil.org/pdfs/atc40toc.pdf

Desprez, C., Mazars, J., Kotronis, P., & Paultre, P. (2013). Damage model for FRP-confined concrete columns under cyclic loading. *Engineering Structures, 48*, 519–531.

DTR/B-C 2–48. (2003) .National seismic code for building design and construction (R.P.A 99/ version 2003).

Ider, O. (2023). *Evaluation of the global behavior coefficient R for elevated tanks*. (Doctoral dissertation). Mouloud Mammeri University of Tizi-Ouzou. Algeria.

Mekki, M. (2015). *Approche probabiliste dans la détermination des courbes de vulnérabilité des structures en génie civil* (Doctoral dissertation). Université de Bordeaux; Université des Sciences et de la Technologie d'Oran. Mohamed Boudiaf (Algérie).

RISK-UE. (2003). An advanced approache to earthquake risk scenarios with applications to different European towns.

Author Information

Ider Ourdia
Mouloud Mammeri University
Civil Engineering Department, Mouloud Mammeri University, 15 000 Tizi-Ouzou, Algeria

Hocine Hammoum
Civil Engineering Department, Mouloud Mammeri University, 15 000 Tizi-Ouzou, Algeria

Bouzelha Karima
Civil Engineering Department, Mouloud Mammeri University, 15 000 Tizi-Ouzou, Algeria

Amar Aliche
Mouloud Mammeri University
Civil Engineering Department, Mouloud Mammeri University, 15 000 Tizi-Ouzou, Algeria
Contact e-mail: *amar.aliche@ummto.dz*

To cite this article:

Ider, O., Hammoum, H., Bouzelha, K., & Aliche, A. (2023). Influence of the behavior coefficient on the damage level of an RC elevated tank under seismic loading. *The Eurasia Proceedings of Science, Technology, Engineering & Mathematics (EPSTEM), 26*, 677-684.

The Eurasia Proceedings of Science, Technology, Engineering & Mathematics (EPSTEM)
ISSN: 2602-3199

The Eurasia Proceedings of Science, Technology, Engineering & Mathematics (EPSTEM), 2023

Volume 26, Pages 685-692

IConTES 2023: International Conference on Technology, Engineering and Science

Effect of Fiber Stacking Sequence on Mechanical Property of Polymeric Composite through VARTIM Method and Metallographic Examination

Yusuf Sahin
OSTIM Technical University
Nisantası University

Abstract: Because of higher specific modulus/strength, lower weight, good corrosion resistance with design flexibility and easy production, carbon fiber reinforced epoxy composites are widely used for many structural applications. Glass woven (plain) and carbon fabric (plain) were studied. Thus, glass fabric-reinforced epoxy composites (GFRCs) and carbon fabric-reinforced composites (CFRCs) were fabricated throughVacuum Assisted Resin Transfer moulding (VARTM) methodology. Firstly, manufacturing unit/control system, preparation stages and some elements used in manufacturing the epoxy based composites are reviewed. Then, effects of stacking sequence of fibers on mechanical properties were investigated and a comparison was made on two types of fabrics on hardness/deformation depth through Stereo Microscope (SM). The experimental results exhibited that the hardnesses measured were around 40.6 HB and 52.4 HRB for GFRP and CFRP, respectively. Improvements in carbon fiber were about 29% in comparison to glass fiber. Further, both hybrid composites made from glass and carbon fiber, the hardnesses values were reduced. In case of C2/G2/C2 hybrid composites, reduction rate was about 9.3% in comparison to C6 fiber reinforced laminate composite. Moreover, it is clearly revealed that there were extensive deformation regions reflecting the white areas because top layer was in G2/C2/G2 samples, but there was no such a white area in C2/G2/C2 composite.

Keywords: Carbon fiber, Epoxy, VARTM, Hardness, Deformation region

Introduction

Carbon fibers are commonly preferred reinforcement elements because they have higher strength/modulus associated with lower weight and good flame resistance. This makes carbon fibers to be increased usage in automobile, aircraft, ships, construction, and sport industries (Paiva et al.,2009;Taketa et al.,2010). Whereas they have some disadvantages like lower strain to failure, poor impact resistance, very high electrical conductivity and costly produced (Rosa Garcia et al.2013). In order to improve the weakness of CFRP composite is to design and fabricate the hybrid composites, which are produced by combining two or more different fibers in common matrix (Dong et al., 2012). In this way, new materials are created by improvement of mechanical and physical properties associated with lower cost. This can be ductile fibers/fabrics like glass, basalt or kevlar by forming various layers.

Basalt/carbon fibers, glass/carbon fiber or glass/kevlar fiber are used to provide excellent mechanical behaviour in the fiber axis direction. Therefore, it is possible to incorporate high elongation fibers (glass) into low elongation fibers (carbon) for increasing the failure strain. There are many parametres affecting on mechanical property of epoxy composites including matrix/fiber types and fracture mechanics (Hashim et al., 2017; Zhang et al.,2019; Ma et al.,2017; Ma et al.,2016; Agarwal et al.,2014), nano addition (Xu & Hoa, 2008; Sanchez et al., 2013; Phong et al., 2013; Bora & Kirtania, 2020), interface bonding (Liu et al., 2014; Li et al., 2013), applied methods (Sahin et al., 2021; Bodaghi et al.,2016), stacking sequence effect on hybrid including carbon/glass, carbon/basalt, glass/carbon (Turla et al., 2014; Ary Subagia et al., 2014; Zhang et al., 2012), carbon epoxy,

- Selection and peer-review under responsibility of the Organizing Committee of the Conference

carbon/kenaf and carbon/basalt/epoxy (Artemenko&Kadykova, 2008; Yusuff et al.2021; Reis et al.2012); characterization (Çecen & Sarıkanat, 2008; Ozsoy et al., 2015; Shokriech & Omidi, 2009; Pandya et al., 2011) and effect of orientation (Yokozeki et al.2005; Rahmani et al.2014; Mohamed Kaleemulla& Sideswarappa, 2010; Agrawal&Bhattacharya, 2021; GuruRaja&HariRao,2013) for manufacturing the composites. The purpose of this study is to see the effects of stacking sequence of fibers on mechanical properties of composites and a comparison was made on two types of fabrics on hardness/deformation depth through Stereo Microscope (SM).

Materials/Composite Preparation

GFRP & CFRC epoxy composites were manufactured through Vacuum Assisted Resin Infusion Transfer Molding (VARTIM) method. Carbon and glass fibers with plain-weave type, which are supplied from Kompozitsan Inc. İzmir/Turkey. Thermosetting bisphenol-A epoxy resin (F-1564) and its hardener like F-3487 were mixed in 100:35 ratio. Areal weights for both fibers wemulla as 200 g/m^2, selected as reinforcement, average diameter is about 10/20 µm, respectively. The properties of carbon fabrics used for VARTIM approach were indicated in Table 1. In production of composites, total of three plies of plain carbon fabrics were stacked on release film of aluminum mold. VARTIM is commonly adopted to manufacture large and high quality components. VARTIM production unit is shown in Fig.1, compose of aluminum alloy as a main table, temperature and vacuum are provided through this table, electrical heating system to heat up the table, close-loop temperature control and thermo couple fixed under the table, PLC controller and touch screen unit, temperature can be controlled to 200 ^{o}C, A vacuum pomp, which can be open loop control.

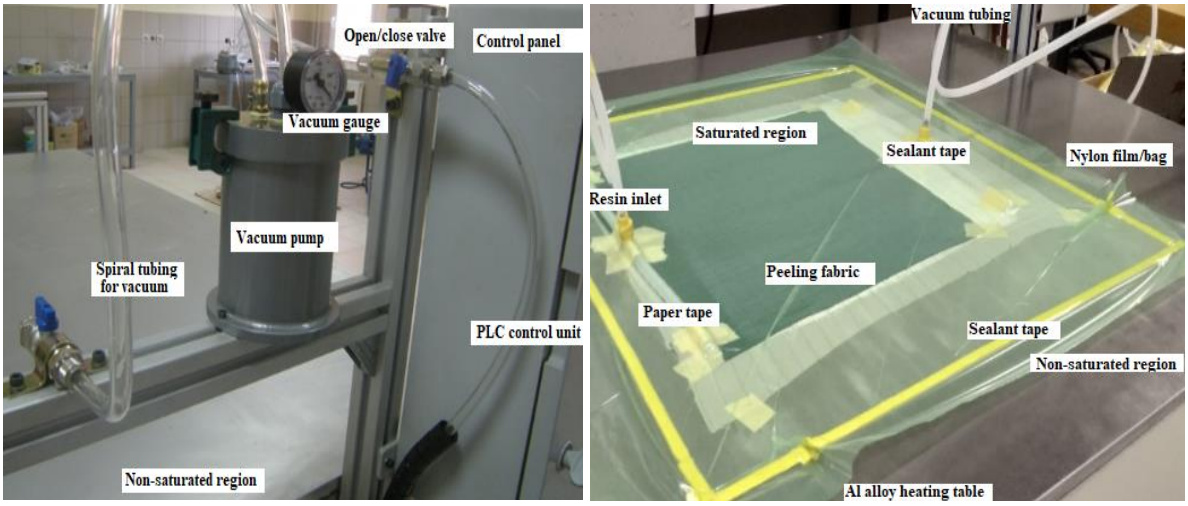

Figure 1. VARTIM unit and preparation stages of VARTIM with some basic elements

The machine can be set up using control panel for three temperatures for curing cycle of the composites. In first step, machine set at ambient temperature to 95°C for 50 min, then moved to second step, materials are cured and fibers started to get fixed with each other. It is kept at 95°C for 45 min to absorb the epoxy resin. At last step, the temperature downs to 50°C for 45 min duration. Then, the machine will be automatically stopped to return back about room temperature. The laminate composites produced by VARTIM was a dimension of 500 x 500 x 2.5 mm.

Hardness

Table 1. The properties of glass/carbon fabrics, epoxy used for VARTIM [43].

Materials	Plain Carbon Fabric (CF)	Glass fiber (GF)	Epoxy resin (EP)
Fabric weight (g/m^2)	200	220	-
Fabric thickness (mm)	0.32	0.15	-
Warp construction/fill	12/13	22/26	-
Monofilament diameter (µm)	7-10	10-18	-
Density (g/cm^3)	1.78	2.60	1.15
Modulus of elasticity (GPa)	230	80-90	30-50
Tensile strength (MPa)	4900	1380-3200	73

Hardness's were measured with Rockwell B hardness method by applying 60 Kgf load, and at least, the mean of five readings was taken.

Stereo Microscopy

After hardness testing results, samples were photographed and failure modes were analyzed by Stereo microscope (SM).

Results & Discussion

Hardness Results

Table 3 exhibites the hardness values obtained for epoxy reinforced with carbon and glass fibers. The hardnesses measured were about 40.6 HB and 52.4 HRB for glass and carbon fiber reinforced composite, respectively. This is due to used reinforcement effect. The hardness increased from 40.6 to 52.4 HRB, as shown in Fig. 3. The improvements in carbon in comparison to glass were about 29%. In other words, the hardness increased more significantly with increasing the carbon fibers.

In the case of hybrid composites, lower hardnesses were obtained. For G2/C2/G2 epoxy laminate composites, the hardness was meassured as 37.6 HRB, the reductions in hybrid composites was about 5% in comparison to G6 composites. The strengthening effect was not achieved by forming an enough interface bonding between the matrix and fibers, especially for the G2/C2/G2 hybrid composites. As for the case of C2/G2/C2 hybrid composites, reduction rate was around 9.3% in comparison to C6 fiber reinforced laminate composites because its measured value was about 47.5 HRB. During hardness testing, the indentation on the specimen's surface under the effect of load resulted in localised plastic deformation of the material. For the hybrid composite samples, the indenter caused a slightly higher degree of localised plastic deformation because of containing G2 fiber in the matrix. However, during hardness testing of C6 composites, there was decreases in localised plastic deformations due to presence of hard C6 fibers on the top layer. Further, for a given plain composite, the increase in hardness values was observed with using G6 or C6 reinforced composite. On the other hand, for hardness testing, compressive force allows the material to flow in a vertical direction. This vertical flow of material causes the reinforced material to concentrate beneath the indenter. The pattern of plastic deformation in the G6/C6 is more uniform. The changes in fibers below the indenter leads to transfer of load from matrix to reinforcement.

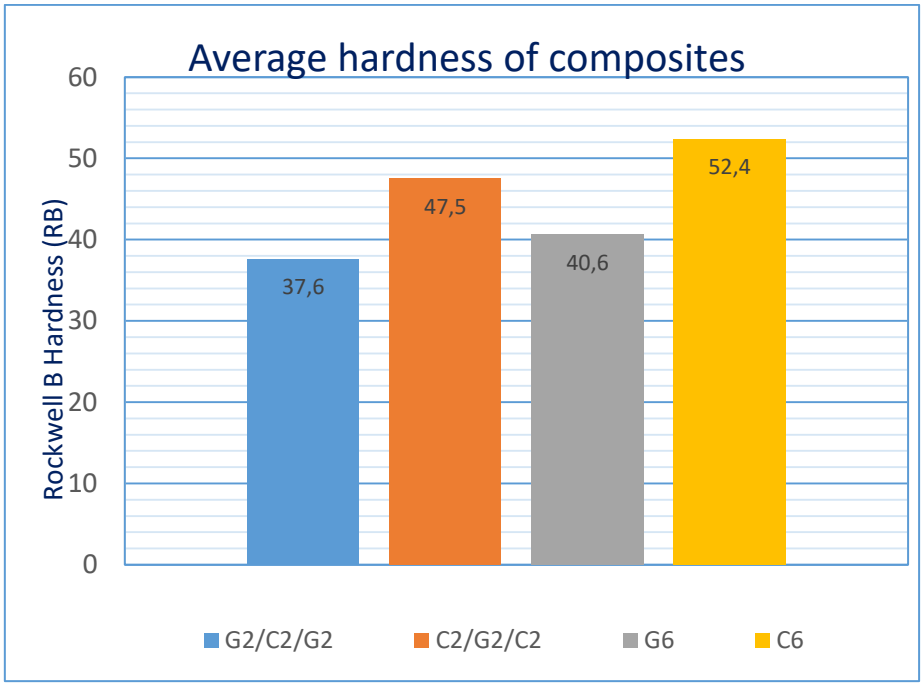

Figure 3. Hardness of the laminate composites.

Also, plastic deformation of epoxy matrix increases with decrease in hardness of fibers. Thus, hardness of normal composites rose with the type of reinforcements. For that reason, at given reinforcement types, C6 fiber reinforced composites showed higher hardness than G6 fiber reinforced composites. The lowest hardness was achieved for the G2/C2/G2 type hybrid composites, followed by C2/G2/C2 type hybrid composites.

Deformation Region/Depth

Stereo microscope was used the measure and determine the deformation region/size after the hardness testing of the composites. The micrographs in these figures show compressive damages. These can be in the forms fiber micro-buckling, kinking, shear, fiber fracturing/splitting or kinking-splitting mode. Fig. 4 shows the depth and deformation regions of G6 composites by stereo micoscope. Green color represents the glass reinforcement material in polymeric matrix. It is taken from two different local areas,showing the low distortion and localized buckling area at the left side reached to about 500 µm, but not heavily deformation formed in Fig.4a because the hardness measured was around 40.6 HB for these samples while similar case was observed at the left-upper side of the sample in Fig.4b even indicating slightly less amount of edge distortion. Evidence of microbuckling at the compressive side is the predominant features found in shear failure (Sudarisman & Davies, 2009). Fig. 5a indicates the compressive failure regions at three locations for C6 composites. It is taken with SM from different regions again. It is oberved that fiber fracturing/splitting and size of the splitted region was about 430 µm due to hardness of these composite reached at 52.4HB. Other sample shown in Fig.5b measured from two localizations and indicated more clear deformation like a hole. When you compared to these two samples in Figs. 4 and 5, improvements in carbon fiber reinforced composites were about 29% compared to glass fiber reinforced composites based on the hardnesses values and micro-scale size.

Let's see the hybrid composites that are made using glass and carbon fibers in epoxy matrix. Fig. 6 shows the deformation regions for G2/C2/G2 hybrid composites. Top/bottom layers consists of glasses while medium one is carbon fiber in composites. White area in these SM views reflects the localized kinking types of failure regions, as shown in Fig.6a. It is clearly revealed that there were extensive distortion regions were observed which is reached to 800 µm size for both samples because top layer was glass. Similar observation was also shown in Fig.6b for other samples tested at two different locations and in terms of the deformation area, which is close to other one. On the other hand, hardness of the composites measured at about 37.6HB. The reduction in hardness was found to be estimated as 7.3% in comparison to G6 reinforced epoxy composites. The compressive damage in the form of fibre buckling-modes was reported (Chen et al., 1993). However, delamination occurred at the carbon–glass interface work carried out with the previous study (Davies & Hamada, 2001). In another words, the hybrid composite increased the toughness of these samples. Moreover, Fig.7a,b exhibites the deformation/fracture regions for C2/G2/C2 hybrid composites. It is exhibited clear deformed region due to top layer carbon fibers, whereas, there are no white areas in these micrographs. Size of the deformations for these samples which is lower than 500 µm reduced significantly designing carbon layers and their brittleness, as indicated in Fig.7b. Other reason might be due to changing from kinking to splitting failure mode for these samples. The reduction in hardness was calculated 9.35% in comparison to C6 reinforced epoxy composites due to using 2 glass layers at the medium interface.

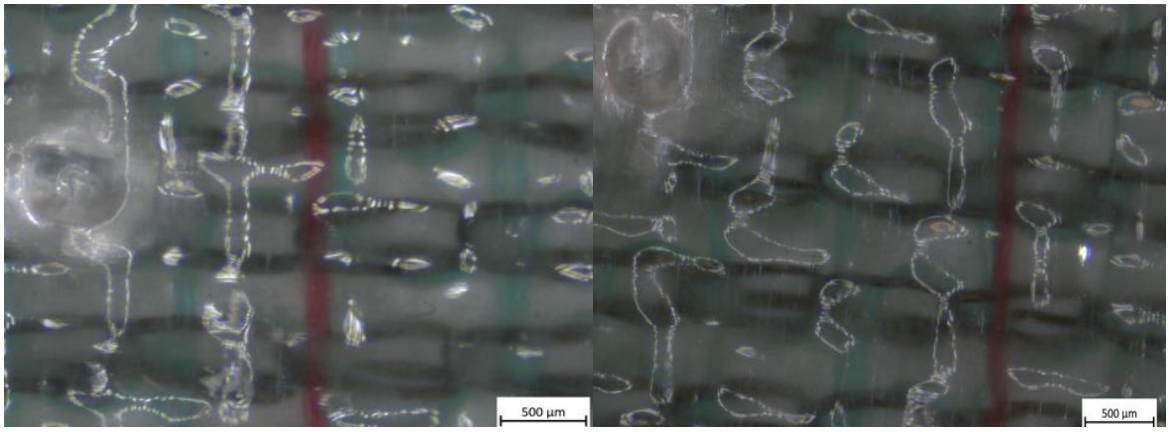

Figure 4. Depth and deformation regions for G6 composites (40.6 HB), indicating very slight distortion and not clear.

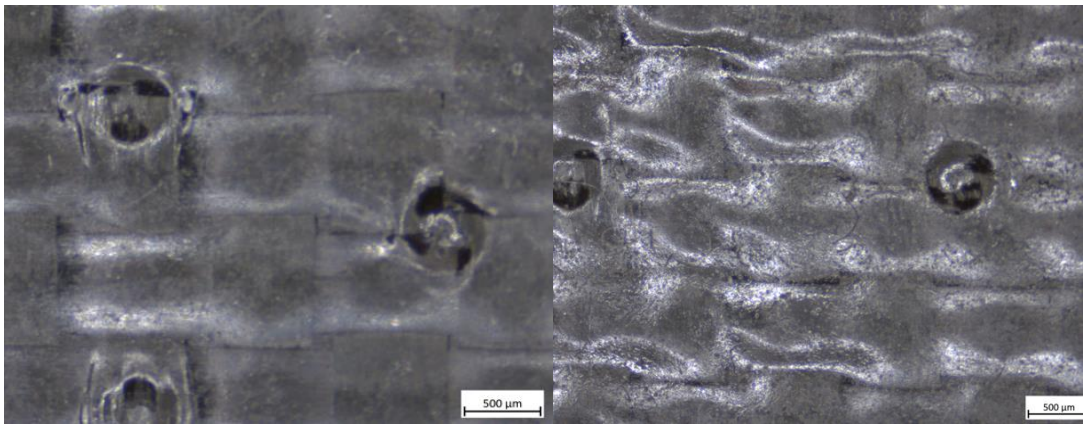

Figure 5. Depth and deformation regions for C6 composites (52.4HB), showing the deformed zone and like a hole.

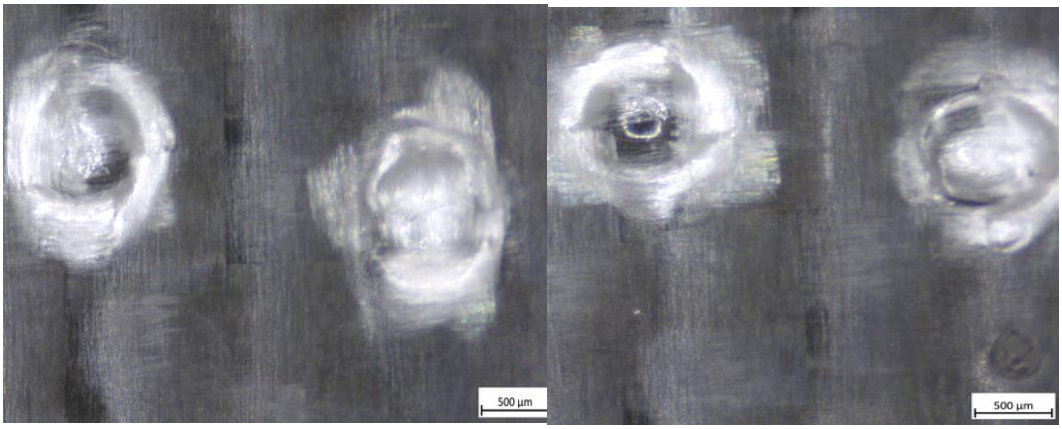

Figure 6. Depth and deformation regions for G2/C2/G2 hybrid composites (37.6HB), revealing kinking regions from all applied depth.

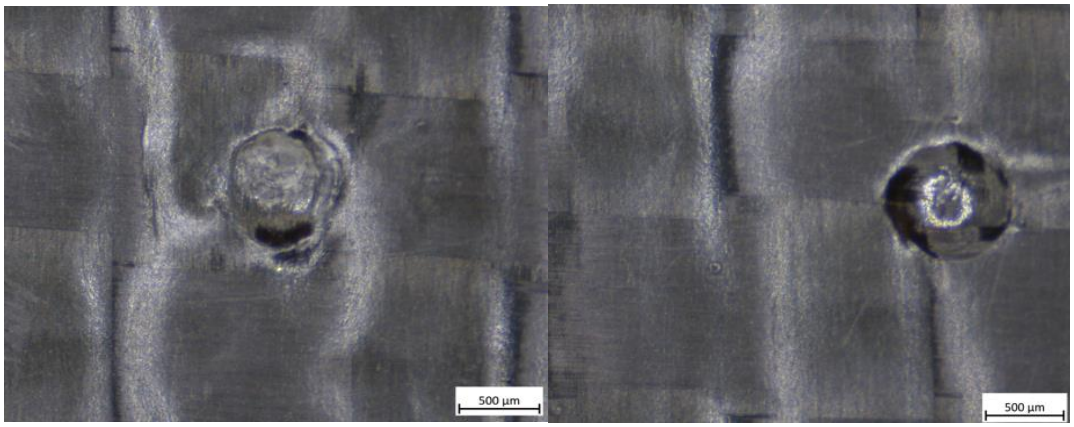

Figure 7. Depth and deformation region for C2/G2/C2 hybrid composites (47.5HB), exhibiting clear deformed and fractured region due to brittleness of top layer of carbon fibers.

Conclusions

The following conclusions were drawn from the current study on carbon reinforced epoxy composites (CFRCs) and its hybrid composites produced by glass fibers using VARTIM method. Mechanical properties such as hardness, depth of deformatin zone were investigated with Streeo microscope (SM), comparison was made for both composites.

1. Experimentally obtained results indicated that hardness of the composites changed with fabric types. The hardness increased from 40.6 to 52.4 HRB and improvements in carbon in comparison to glass fibers were about 29%.

2. In the case of hybrid composites, lower hardness was obtained. The hardness of G2/C2/G2 epoxy laminate composites was meassured as 37.6 HRB, the reductions in hybrid composites was about 5% in comparison to G6 composites. For the case of C2/G2/C2 hybrid composites, reduction rate was around 9.3% in comparison to C6 fiber reinforced laminate composites because for the hybrid composite samples indicating split-mode, the indenter caused a slightly high degree of localised plastic deformation because of containing G2 fiber in the matrix for dominating kink-mode.

3. For G6 composites, the size of deformation areas reached to about 500 µm while the deformed region was about 430 µm for C6 composites due to increased the hardness of these composites.

4. There were extensive deformation regions for hybrid composites. Their deformation depth were reached to around 800 µm for both samples when the top layer was glass fibers. Whereas, the plastic deformations for C2/G2/C2 samples reduced considerably due to using carbon layer on the top.

Scientific Ethics Declaration

The author declares that the scientific ethical and legal responsibility of this article published in EPSTEM journal belongs to the authors.

Acknowledgements

* This article was presented as an oral presentation at the International Conference on Technology, Engineering and Science (www.icontes.net) held in Antalya/Turkey on November 16-19, 2023.

* This study has financially supported by “The Scientific Research Coordination Unit of İstanbul Nişantaşı University”, Turkey (Grant No. BAP 2020/10).

References

Agarwal, G., Patnaik, A.,& Sharma, R.K.(2014). Mechanical and thermo–mechanical properties of bi-directional and short carbon fiber reinforced epoxy composites. *Journal of Engineering Science and Technology Taylor’s University, 9*(5), 590-604.

Agrawal, S.A., & Bhattacharya, S.(2021). Mechanical performance of woven carbon reinforced epoxy composites with varied orientation angle. *Journal of Metals Materials and Minerals., 31*(1), 82-87.

Ary Subagia, I.D.G., Kim,Y., Tijing,L.D., Kim,C.S., & Shon, H. K.(2014). Effect of stacking sequence on the flexural properties of hybrid composites reinforced with carbon and basalt. *Compos. Part B*, *58*(1), 251-258.

Artemenko, S.E. & Kadykova, Y.A.(2008). Polymer composite materials based on carbon, basalt, and glass fibers. *Fiber Chemistry*, *40*(1), 37-39.

Bora, J., & Kirtania, S. (2020). Comparative study of elastic properties and mode I fracture energy of carbon nanotube/epoxy and carbon fiber/epoxy laminated composites. *Micro- Nano Syst. Lett., 8* (19), 2-10.

Bodaghi, M., Cristóvão, C., Gomes R, &Correia, N.C. (2016). Experimental characterization of voids in high fiber volume fraction composites processed by high injection pressure RTM. *Compos Part A: Appl. Sci. Manuf.*,*82*(1), 88-99.

Chen F et al. (1993). Flexural failure mechanisms in unidirectional glass-fibre reinforced thermoplastics. *Composites*, *25*(1), 11–20.

Cecen, V., & Sarıkanat, M.(2008). Experimental characterization of traditional composites manufactured by vacuum assisted resin transfer molding. *Journal of Applied Polymer Science*, *107*(3), 1822-1830.

Davies I. J, & Hamada, H. (2001). Flexural properties of a hybrid polymer matrix composite containing carbon and silicon carbide fibres. Adv Compos Mater, *10*(1), 77–96.

Dong, C., Heshan A. Ranaweera-Jayawardena, Davies,I. J. (2012).Flexural properties of hybrid composites reinforced by S-2 glass and T700S carbon fibres. *Composites: Part B* ,43, 573–581

Hashim, N., Majid, D. L., Uda,N., Zahari,R.,& Yidris, N. (2017). Vacuum infusion method for woven carbon/Kevlar reinforced hybrid composite. *IOP Conference Series: Materials Science and Engineering, 270.*

GuruRaja, M. .N., &HariRao, A. N.(2013). Influence of angle ply orientation on tensile properties carbon/glass hybrid composites. *J. Miner. Mater. Charac. Eng.,1*(5), 231-235.

Kaleemulla, K. M. & Siddeswarappa, B. (2010). Influence of fiber orientation on the in-plane mechanical properties of laminated hybrid polymer composites. *Jorunal of Reinforced Plastics and Composites, 29*(12), 1900-1914.

Liu, W. B., Zhang, S., Li, B., Yang, F., Jiao, W.C., Hao, L.F., & Wang, R. G. (2014). Improvement in interfacial shear strength and fracture toughness for carbon fiber reinforced epoxy composite by fiber sizing. *Poly. Composition, 35*(3), 482-488.

Li, M., Gu,Y., Liu,Y., Li,Y.,& Zhang, Z. (2013). Interfacial improvement of carbon fiber/epoxy composites using a simple process for depositing commercially functionalized carbon nanotubes on the fibers. *Carbon, 52,*109-121.

Ma,Y., Yang, Y., Sugahara, T., & Hamada, H. (2016). A Study on the failure behavior and mechanical properties of unidirectional fiber reinforced thermosetting and thermoplastic composites. *Composites Part B: Engineering, 99* (1),162-172.

Ma, Y., Jin, S., Yokozeki, T., Ueda,M., Yang, Y., Elbadry, E., & Hamada, H. (2017). A comparative study of the mechanical properties and failure behavior of carbon fiber/epoxy and carbon fiber/polyamide 6 unidirectional composites. *Composite Structures,160* (1), 89-99.

Taketa, I., Ustarroz, J., Gorbatikh, L., Lomov, S.V., & Verpoest, I. (2010). Interply hybrid composites with carbon fiber reinforced polypropylene and self-reinforced polypropylene. *Composites Part A:Applied Science and Manufacturing, 41*(8), 927–932.

Turla, P., Kumar,S.S., Reddy,P.H., & Chandra Shekar, K. (2014). Processing and flexural strength of carbon fiber and glass fiber reinforced epoxy-matrix hybrid composite. *Internationational Journal of Engineering Research & Technology, (IJERT), 3*(4), 394-398.

Ozsoy, N., Mimaroglu, A. & Ozsoy, M. (2015). Comparison of mechanical behavior of carbon and glass fiber reinforced epoxy composites. *Acta Physic A Polonic A,127,* 1032-1034.

Pandya, K. S., Veerraju, Ch.,& Naik, N. K. (2011). Hybrid composites made of carbon and glass woven fabrics under quasi-static loading. *Materials & Design, 32*(7), 4094-4099.

Paivaa, J. M. F., dos Santos, A.D.N., & Rezendec, M.C. (2009). Mechanical and morphological characterizations of carbon fiber fabric reinforced epoxy composites used in aeronautical field. *Journal of Materials Research, 12*(3), 367–374.

Phong, N.T., Gabr, M.H., Okubo, K., Chuong, B., & Fujii, T. (2013). Improvement in the mechanical performances of carbon fiber/epoxy composite with addition of nano-(polyvinyl alcohol) fibers. *Composite Structures, 99,* 80-387.

Rahmani, H., Najafi, S. H. M., Saffarzadeh-Matin, S., & Ashori, A. (2014). Mechanical properties of carbon fiber/epoxy composites; effects of number of plies, fiber contents and, angle-ply layers. *Polymer Engineering & Science, 54*(11), 2461-2476.

Reis, J. M. L., Coelho, J. L.V., Monteiro, A. H., & da Costa Mattos, H.S. (2012). Tensile behavior of glass/epoxy laminates at varying strain rates and temperatures. *Compos. Part B, 43*(4), 2041-2047.

Rosa García P., Escamilla, A.C., & Nieves González García, M.(2013). Bending reinforcement of timber beams with composite carbon fiber and basalt fiber materials. *Compos Part B-Engineering, 55*, 528–36.

Sudarisman, Davies I. J. (2008). Flexural failure of unidirectional hybrid fibre-reinforced polymer (FRP) composites containing different grades of glass fibre. *Advanced Materials Research, 41–42,* 357–362.

Sanchez,M., Campo,M., Jimenez-Suarez, A., & Urena, A. (2013). Effect of the carbon nanotube functionalization on flexural properties of multiscale carbon fiber/epoxy composites manufactured by VARIM. *Compos. Part B: Engineering, 45*(1), 1613-1619.

Sahin, Y., Alsayed, M., & Nur Gunturk, M.M. (2021). Production processing of fabric reinforced composites by vacuum-assisted resin transfer molding. Y. Sahin & S. Yalcınkaya (Eds.), *International innovative approaches in engineering & technology* (pp.115-128). Istanbul,Turkey :Guven Plus Grup Publishing.

Shokrieh, M.M., & Omidi, M.J.(2009). Tension behavior of unidirectional glass/epoxy composites under different strain rates. *Composite Structures, 88*(4), 595-601.

Xu,Y., & Hoa S.V. (2008). Mechanical properties of carbon fiber reinforced epoxy/clay nanocomposites. *Composite Science and Technology, 68*(3-4), 854-861.

Yokozeki, T., Aoki, T., Ogasawara,T., & Ishikawa,T. (2005). Effects of layup angle and ply thickness on matrix crack interaction in continuous plies of composite laminates. *Compos. Part A: Applied Science and Manufacturing, 36*(9), 1229-1235.

Yusuff, I., Sarifuddin, N., Norbahiyah,S., Ali, A.M., & Ismail, H. (2021). Tensile and flexural properties of woven carbon-kenaf fiber reinforced epoxy matrix hybrid composite: Effect of hybridization and stacking sequences. *AIP Conference Proceeding*, 2267(1).

Zhang, S., Hao, A., Nguyen, N., Oluwalowo, A., Liu, Z., Dessureault, Y., Park, J.G., & Liang, R. (2019). Carbon nanotube/ carbon composite fiber with improved strength and electrical conductivity via interface engineering. *Carbon, 142*, 628-638.

Zhang, J., Chaisombat, K., He, S., & Wang, C. H. (2012). Hybrid composite laminates reinforced with glass/carbon woven fabrics for lightweight load bearing structures. *Materials & Design, 36*(1), 75-80.

Author Information

Yusuf Sahin
Department of Mechanical Engineering, Faculty of Engineering, OSTIM Technical University, 100 Yıl Blv.55/F, Ostim, Yeni Mahalle, Ankara, Turkey
Contact e-mail: *yusuf.sahin@ostimteknik.edu.tr*

Department of Mechanical Engineering Faculty of Engineering&Architecture of Nişantaşı University1453 Neotech Kampus, Maslak, Sarıyer, İstanbul, Turkey

To cite this article:

Sahin, Y. (2023). Effect of fiber stacking sequence on mechanical property of polymeric composite through VARTIM method and metallographic examination. *The Eurasia Proceedings of Science, Technology, Engineering & Mathematics (EPSTEM), 26*, 685-692.

The Eurasia Proceedings of Science, Technology, Engineering & Mathematics (EPSTEM)
ISSN: 2602-3199

The Eurasia Proceedings of Science, Technology, Engineering & Mathematics (EPSTEM), 2023

Volume 26, Pages 693-699

IConTES 2023: International Conference on Technology, Engineering and Science

Interaction of Polycarboxylate-Based Water-Reducing Admixture Molecular Structure with Fly Ash Substituted Cementitious Systems: Marsh-Funnel and Mini-Slump Performance

Veysel Kobya
Bursa Uludag University

Ali Mardani
Bursa Uludag University

Abstract: Polycarboxylate ether-based high-range water-reducing admixtures (PCE) play a crucial role in enhancing the workability of fly ash-substituted cementitious systems. Alterations to the chemical structures of both the main and side chains can particularly enhance the electrostatic repulsion and steric hindrance effects of PCEs. As a consequence, this results in improved performance within cementitious systems containing fly ash substitutions. This study investigated the compatibility of the altered molecular structure of polycarboxylate ether (PCE) with cementitious systems containing fly ash substitutions. To achieve this, five polymers were synthesized, varying the side chain length, molecular weight, main chain length, and main chain lengths of PCEs while maintaining other properties constant. Cement pastes were then prepared using the synthesized PCEs with fly ash replacements at three different rates. Marsh-funnel flow time and mini-slump values were measured in the prepared mixtures. The study revealed that in mixtures without fly ash, PCEs with a long main chain (40k) and short side chain length (1000 g/mole) exhibited the lowest Marsh-funnel flow and mini-slump performance among PCEs with diverse molecular structures. For the other PCEs in these mixtures, the change in molecular structure did not significantly affect their performance. However, as the fly ash replacement rate increased, PCE having a medium main chain (21k) and side chain (2400 g/mole) length outperformed other PCEs in terms of Marsh-funnel flow and mini-slump performance.

Keywords: Fly ash replacement rate, Polycarboxylate-based water-reducing admixture (PCE), change in PCE side chain length, change in PCE main and side chain length.

Introduction

Fly ash, a waste material released in production industries that use coal as fuel, is substituted in certain proportions instead of cement to enhance the long-term strength and durability of concrete mixtures (Yao et al., 2015). The spherical shape and smooth surface of fly ash generally enhance fluidity, reducing the demand for water-reducing admixtures in mixes. However, it has been emphasized that the water need of mixes increases with the use of some fly ash types in certain proportions (Toledano-Prodos et al., 2013; Mardani-Aghabaglou et al., 2014; Karakuzu et al., 2021). Additionally, substitution of fly ashes with different particle size distributions (PSD) instead of cement causes the PSD of the fly ash-cement mixture to change. This affects the need for water / water-reducing additives, causing the fluidity properties of the mixtures to change (Karakuzu et al., 2021). Since fly ash particles are negatively charged, the adsorption amount of polycarboxylate-based water reducing additive (PCE) on the fly ash surface is lower compared to cement. According to Ng and Justnes (2016), at lower substitution rates, fly ash acted as a filler and did not exert a substantial impact on the efficiency of PCE. However, it was stated that PCEs showed poor performance with replacement of fly ash above 40%. It has been reported that increasing the fly ash replacement rate in mortar mixtures up to a certain point (30% by cement

weight) reduces the need for additives for target spreading (Toledano-Prodos et al., 2013; Altun et al. 2021). In fly ash substituted systems, it has been observed that the molecular structure of PCE also affects workability (Ozen et al., 2022; Altun et al., 2023). Özen et al. (2022), in their study where they investigated the impact of PCEs with varying chain lengths on the properties of fly ash substituted systems, reported that among the synthesized PCEs, the one with medium main and side chain length exhibited the best flow performance. As a result, it has been observed that the impact of fly ash on the fluidity properties of cementitious systems may vary depending on the substitution rate, fineness and morphological properties of fly ash, as well as the structural characteristics of PCEs used in fly ash substituted mixtures.

In this study, the effect of PCE chain lengths on Marsh-funnel flow time and mini-spread performance in paste mixtures with different fly ash replacement ratios was examined. In this context, five different PCEs were synthesized by changing their chain lengths. A grand total of 20 paste mixtures were meticulously concocted with synthesized PCEs and fly ash substituted cements at three different rates (15, 30 and 45%).

Material and Methods

Materials

In this study, CEMI 42.5R Portland cement, which complies with the EN 197-1 Standard, and class F fly ash, meeting the EN 450-2 Standard, were employed. Detailed information about the properties of these binders is provided in Table 1.

Table 1. The physical, chemical, and mechanical characteristics of the binders

Oxides (%)	SiO_2	Al_2O_3	Fe_2O_3	CaO	MgO	SO_3	Cl^-	*Free CaO*	*LOI*	Specific gravity	Specific surface (cm^2/g)
Cement	18.9	4,.3	5.5	61.7	1.6	2,8	0.04	0.75	3.33	3.21	3786
Fly Ash	59.2	22.9	6.3	3.1	1.3	0.2	0.001	-	3.2	2.31	4300

Throughout the synthesis process, a consistent free non-ionic content and an anionic/non-ionic group ratio of 2.78 moles and 3 moles per mole, respectively, were maintained for all PCEs. The primary chain lengths of the PCEs were determined based on the number of non-ionic groups they contained, while the anionic/non-ionic group ratio remained constant for each polymer. The nomenclature for each PCE was derived from their respective primary and side chain lengths. As an example, a PCE having 21 non-ionic groups, a main chain length of 21k, and a side chain length of 1000 g/mole would be denoted as MC21k-SC1000. Table 2 contains the characteristics of the synthesized PCEs.

Table 2. Some characteristics of PCEs

PCE	Density (g/cm^3)	Mw (g/mole)	PDI (Mw/Mn)	Main chain length	Side chain length (g/mole)
MC21k-SC1000	1.09	26,000	2.3	21k	1000
MC21k-SC2400	1.10	56,000	2.1	21k	2400
MC21k-SC3000	1.08	69,000	2.0	21k	3000
MC17k-SC3000	1.08	57,000	2.1	17k	3000
MC40k-SC1000	1.09	56,000	2.3	40k	1000

To assess Marsh-funnel flow times, paste mixes were formulated using a water-to-binder (W/B) ratio of 0.35. This methodology is in accordance with the protocols described in the following references: Mardani-Aghabaglou, 2016; Altun et al., 2021; Özen et al., 2022; Kobya et al., 2022; Kobya et al., 2023.a). The mixture formulated for the Marsh funnel test was also utilized for the mini-flow test, with procedures in line with the guidelines presented in references (Aïtcin, 2004; Kantro, 1980). The nomenclature for the paste mixtures was established based on both the fly ash replacement rate and the specific PCE utilized. For instance, a mixture

created using the additive MC21k-SC1000 and having no fly ash replacement (0% fly ash) is designated as FA0-MC21k-SC1000.

Results and Discussion

Table 3 contains the Marsh-funnel flow times, while Table 4 displays the mini-slump values for all paste mixes. It is observed that the Marsh-funnel flow times of all mixtures increased as the fly ash replacement ratio increased. Within cementitious systems that incorporate fly ash as a substitute, various mechanisms influence workability, either positively or negatively, depending on the properties of the fly ash. Since fly ash particles are typically finer than the cement particles they replace, this results in increased surface area, potentially causing agglomeration and an elevated demand for PCE and/or water, as indicated by studies like Ozen et al. (2022), and Sha et al., (2018). These conditions tend to have an adverse impact on workability. Conversely, the spherical shape of fly ash particles can introduce a lubricating effect, leading to increased workability, as suggested by Tkaczewska et al. (2014) and Wang et al. (2021). However, this beneficial effect may be somewhat limited, possibly due to the prevailing presence of irregular fly ash particles in comparison to spherical ones. It is worth noting that the factors negatively influencing workability appeared to be predominant in all paste mixes used in the Marsh-funnel experiment. In mixtures without fly ash, the side chain length of the PCE molecule did not cause a notable change in the saturation point flow time. However, the saturation point flow time of mixtures containing MC21k-SC1000 with 15, 30, and 45% fly ash substitution was increased by 19%, 13%, and 28% in comparison to those that contain MC21k-SC2400. PCE might create a bridging effect by adsorbing to multiple fly ash particles simultaneously (Wang et al., 2021).

In the absence of fly ash, the flow time at the saturation point of the mixture containing PCE with a moderate main and side chain length (MC21k-SC2400) was 12% and 8% shorter compared to PCEs with longer main chain and shorter side chain length (MC40k-SC1000) and PCEs with shorter main chain and longer side chain length (MC17k-SC3000), respectively. In fly ash substituted mixtures, the saturation point flow times of MC21k-SC2400 decreased by 28-37% and 3-9%, respectively, in comparison to MC40k-SC1000 and MC17k-SC3000. As the fly ash substitution ratio increased, the performance degradation of MC40k-SC1000 with long main and short side chains became more significant. The worst performance of the aforementioned PCE was associated with the inability of maintaining its stretched structure (Zhang et al., 2020), weak dispersion effect due to short side chains (Kobya et al., 2023.a- 2023.b). Regardless of the PCE variety, an increment in the saturation point flow times was observed with the increment in the substitution ratio. With 15%, 30% and 45% fly ash replacement, flow times increased by an average of 31%, 63%, and 89% compared to mixtures without fly ash prepared with the same PCEs.

Table 3. Marsh-funnel flow times of mixes

	PCE dosage (%)						
Mixes	0.5	0.75	1	1.25	1.5	1.75	2
FA0-MC21k-SC1000	85.1	69.3	62.4	57.7[a]	55.6	54.8	55.2
FA0-MC21k-SC2400	81.9	65.2	60.9	55.7	55.2	53.7	54
FA0-MC21k-SC3000	98.4	70.4	61.2	56.7	53.5	50.8	51.1
FA0-MC17k-SC3000	102.1	74.4	64.1	59.9	57.9	57.6	57.2
FA0-MC40k-SC1000	82	69.7	65.3	62.5	60.5	60.4	60.2
FA15-MC21k-SC1000	136.5	98.4	88.1	82.9	80.3	76.7	76.6
FA15-MC21k-SC2400	115.3	85.8	75.3	69.7	67.3	66.3	64.6
FA15-MC21k-SC3000	121.9	90.1	75.3	70.9	68.6	68.5	68.1
FA15-MC17k-SC3000	148.1	100.9	83.8	74.1	73.2	72.4	72.1
FA15-MC40k-SC1000	122.3	101.2	93.2	89.3	87.4	87.1	88.3
FA30-MC21k-SC1000	171.1	120.4	105.3	98.4	95.4	93.6	92.1
FA30-MC21k-SC2400	147	105.5	92.7	87.3	84.8	82.2	81.8
FA30-MC21k-SC3000	162.8	111.7	93.7	91.9	91.6	91.8	92.4
FA30-MC17k-SC3000	172.5	119.8	103.1	90.1	88.3	85.6	84.7
FA30-MC40k-SC1000	157.2	128.8	118.1	114.3	112.7	112.1	113
FA45-MC21k-SC1000	214.8	147.6	130.8	124.1	121.9	121.3	123
FA45-MC21k-SC2400	193.8	151.2	104.7	97.2	94.3	92.8	93.1
FA45-MC21k-SC3000	188.9	124.5	107.7	99.3	93.8	91.3	91.1
FA45-MC17k-SC3000	194.7	130.4	114.7	105.5	104	104	107
FA45-MC40k-SC1000	187.6	151.2	138.9	133.2	132.9	132.1	135

a. The saturation point flow time is highlighted with the bolt.

Table 4. Mini- slump values of mixes

Mixes	0,5	0,75	1	1,25	1,5	1,75	2
FA0-MC21k-SC1000	17,3	19,3	19,2	**19,9**	20,5	21,0	20,3
FA0-MC21k-SC2400	17,6	18,9	20,2	**20,1**	20,3	20,3	19,1
FA0-MC21k-SC3000	17,1	18,5	18,6	**18,5**	18,8	19,2	18,2
FA0-MC17k-SC3000	19,0	20,0	21,5	**22,5**	22,6	22,4	22,2
FA0-MC40k-SC1000	18,0	18,8	19,0	**20,2**	20,6	19,8	19,9
FA15-MC21k-SC1000	16,1	18,0	18,7	**20,0**	20,5	21,5	21,8
FA15-MC21k-SC2400	17,8	18,2	18,5	**19,3**	19,4	19,6	19,2
FA15-MC21k-SC3000	18,8	19,5	19,6	**20,0**	21,4	21,6	21,5
FA15-MC17k-SC3000	19,2	20,8	21,0	**21,1**	21,5	21,5	22,0
FA15-MC40k-SC1000	19,9	21,9	21,0	**21,2**	21,0	21,3	21,6
FA30-MC21k-SC1000	17,3	18,0	19,1	**19,6**	20,2	21,7	21,8
FA30-MC21k-SC2400	17,6	18,0	18,2	**18,1**	18,5	18,7	18,2
FA30-MC21k-SC3000	18,4	19,0	19,2	**19,4**	20,1	20,8	21,4
FA30-MC17k-SC3000	18,5	20,9	21,5	**21,0**	21,2	21,4	21,8
FA30-MC40k-SC1000	18,8	19,7	19,2	**19,7**	20,0	20,1	19,3
FA45-MC21k-SC1000	16,3	18,1	19,0	**19,4**	19,7	19,8	20,4
FA45-MC21k-SC2400	16,9	17,6	18,2	**19,0**	18,8	19,1	18,7
FA45-MC21k-SC3000	18,5	19,6	19,5	**19,9**	20,1	20,7	21,2
FA45-MC17k-SC3000	16,6	17,1	17,6	**18,1**	19,0	19,2	18,3
FA45-MC40k-SC1000	16,0	16,7	16,8	**17,0**	17,2	17,4	16,3

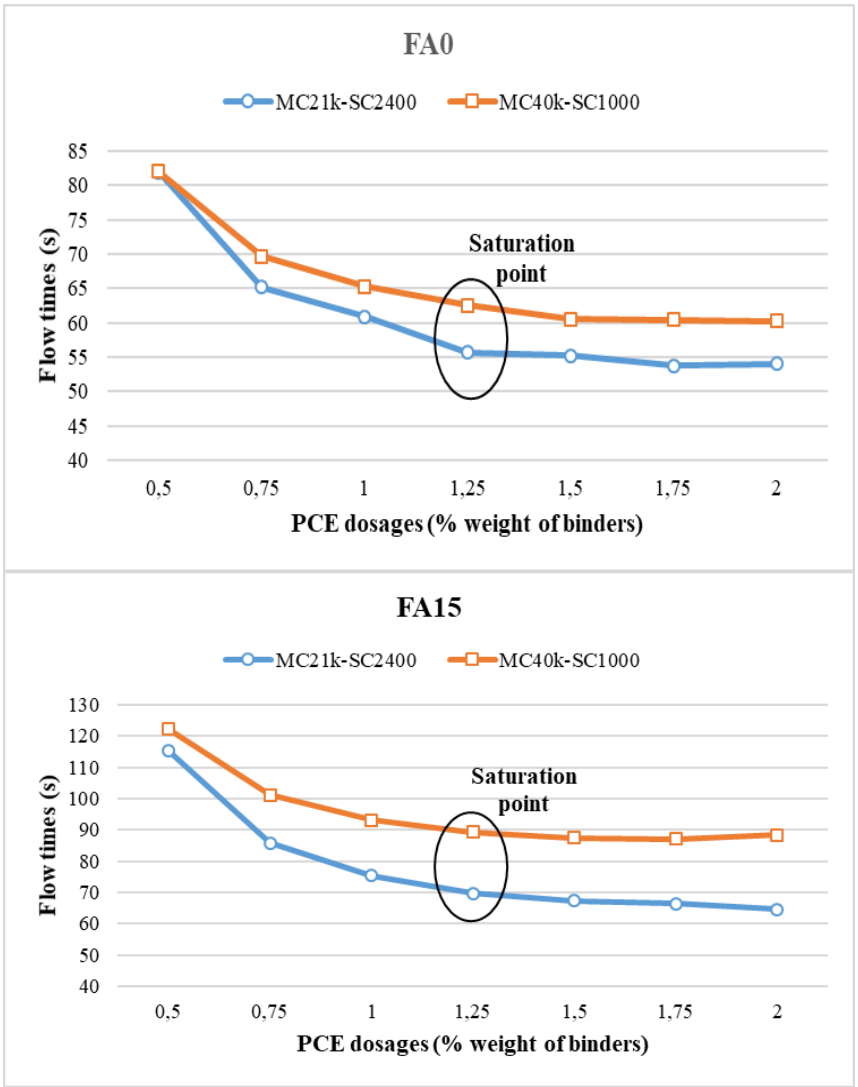

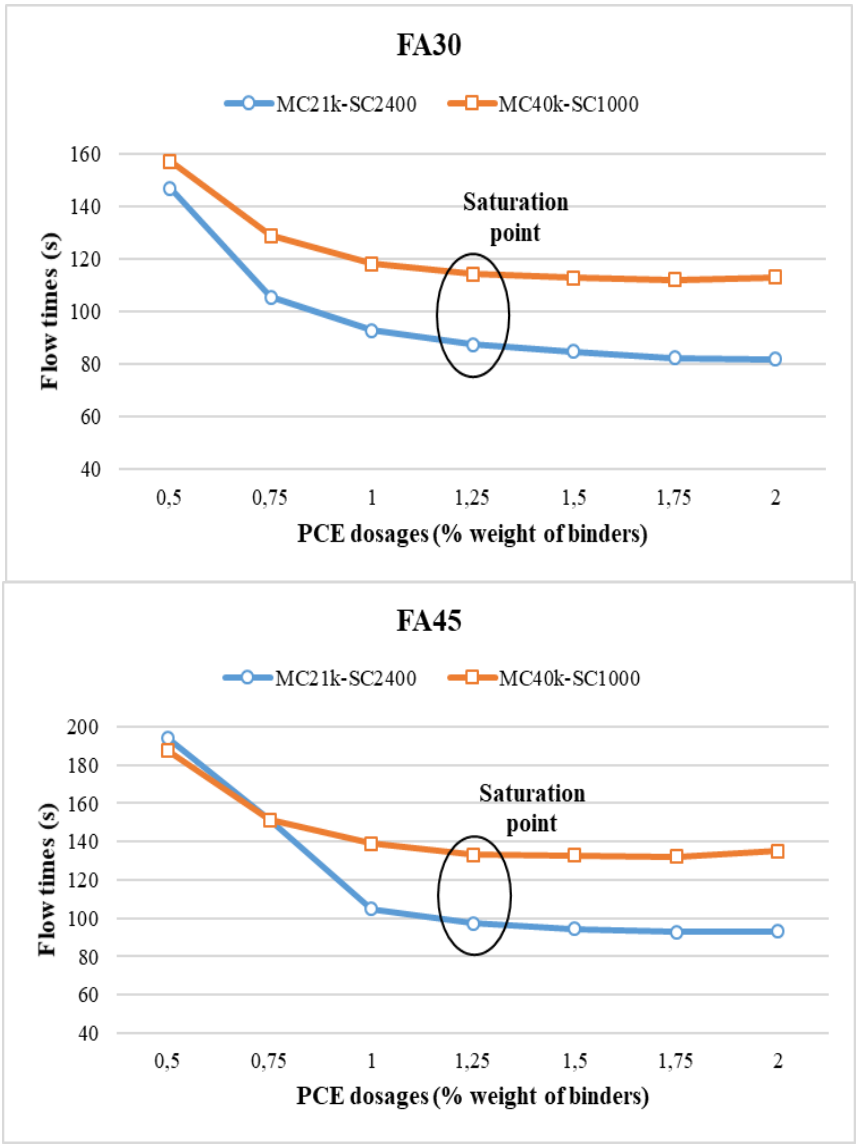

Figure 1. Marsh-funnel flow times of mixes prepared with MC21k-SC2400 and MC40k-SC1000

Figure 1 displays the graph of Marsh-funnel flow time against PCE dosage (expressed as a percentage of binder's weight) for the mixtures prepared with the MC21k-SC2400 and MC40k-SC1000. These additives represent the best and worst performing cases for each fly ash replacement rate. The flow performance at the saturation point of mixes prepared with MC21k-SC2400 exhibited a notable increase, ranging from 12% to 37%, in comparison to those prepared with MC40k-SC1000. Furthermore, this performance improvement became more pronounced as the fly ash replacement rate increased (Figure 1). When assessing the mini-slump values, it was noted that there was no substantial alteration in the mini-slump values at the saturation point, regardless of the PCE variety or the extent of fly ash replacement.

Conclusion

This study focused on assessing the compatibility between the modified molecular structure of polycarboxylate ether (PCE) and cementitious systems that incorporate fly ash substitutions. The results obtained from the experiments are summarized below:

- The Marsh-funnel flow times increased with the increment in fly ash replacement ratio.
- Mini-slump values at the saturation point remained fairly consistent across all tested mixtures, showing no significant changes irrespective of the PCE type or the extent of fly ash replacement.

- Flow performance at the saturation point was substantially improved in mixtures prepared with MC21k-SC2400 compared to those with MC40k-SC1000. This performance increase was more pronounced with higher fly ash replacement rates.

Recommendations

It is advisable to explore the compatibility of polycarboxylate ether (PCE) with cementitious systems containing fly ash substitutions by introducing variations in the molecular composition of PCE. This may include altering side chain density and adjusting the anionic/nonionic ratio. This approach allows for a comprehensive examination of how PCE interacts with different fly ash substitution scenarios.

Furthermore, it is worthwhile to investigate how PCE interacts with fly ashes of varying types and levels of fineness. This extensive investigation will contribute to a deeper understanding of the interplay between PCE and the diverse characteristics of fly ash, ultimately leading to the potential optimization of cementitious mixtures.

Scientific Ethics Declaration

The authors declare that the scientific ethical and legal responsibility of this article published in EPSTEM journal belongs to the authors.

Acknowledgements or Notes

* This article was presented as an oral presentation at the International Conference on Technology, Engineering and Science (www.icontes.net) held in Antalya/Turkey on November 16-19, 2023.

References

Aïtcin, P.C., (2004). *High performance concrete*. New York, NY: E&FN SPON

Altun, M. G., Ozen, S., & Mardani-Aghabaglou, A. (2021). Effect of side chain length change of polycarboxylate-ether–based high-range water–reducing admixture on properties of cementitious systems containing fly ash. *Journal of Materials in Civil Engineering, 33*(4), 04021015.

Altun, M. G., Ozen, S., Karakuzu, K., Mardani, A., & Ramyar, K. (2023). Single and multi-effects of polycarboxylate main and side chain lengths on setting time, viscosity, and yield stress of cementitious mixtures containing fly ash. *Journal of Materials in Civil Engineering, 35*(7). 04023204.

Kantro, D. L. (1980). Influence of water-reducing admixtures on properties of cement paste—a miniature slump test. *Cement, Concrete, and Aggregates, 2*(2), 95-102.

Karakuzu, K., Kobya, V., Mardani-Aghabaglou, A., Felekoglu, B., & Ramyar, K. (2021). Adsorption properties of polycarboxylate ether-based high range water reducing admixture on cementitious systems: A review. *Construction and Building Materials, 312*. 125366.

Kobya, V., Karakuzu, K., Mardani, A., Felekoglu, B., & Ramyar, K. (2023a). Effect of polycarboxylate-based water-reducing admixture chains length on portland cement-admixture compatibility. *Journal of Sustainable Cement-Based Materials*, 1-18.

Kobya, V., Karakuzu, K., Mardani, A., Felekoğlu, B., & Ramyar, K. (2023b). Combined interaction of PCE chains lengths, C_3A and water content in cementitious systems. *Construction and Building Materials, 378*. 131178.

Kobya, V., Kaya, Y., & Mardani-Aghabaglou, A. (2022). Effect of amine and glycol-based grinding aids utilization rate on grinding efficiency and rheological properties of cementitious systems. *Journal of Building Engineering, 47*. 103917.

Mardani-Aghabaglou, A. (2016). *Investigation of cement-superplasticizer admixture compatibility* (Doctoral dissertation). Ege University, Izmir, Turkey

Mardani-Aghabaglou, A., Sezer, G. I., & Ramyar, K. (2014). Comparison of fly ash, silica fume and metakaolin from mechanical properties and durability performance of mortar mixtures view point. *Construction and Building Materials, 70*, 17-25.

Ng, S., & Justnes, H. (2016). Influence of plasticizers on the rheology and early heat of hydration of blended cements with high content of fly ash. *Cement and Concrete Composites, 65*, 41-54.

Ozen, S., Altun, M. G., Mardani-Aghabaglou, A., & Ramyar, K. (2022). Multi-effect of superplasticisers main and side-chain length on cementitious systems with fly ash. *Magazine of Concrete Research, 74(*14), 727-739.

Sha, F., Li, S., Liu, R., Li, Z., & Zhang, Q. (2018). Experimental study on performance of cement-based grouts admixed with fly ash, bentonite, superplasticizer and water glass. *Construction and Building Materials, 161*, 282-291.

Tkaczewska, E. (2014). Effect of the superplasticizer type on the properties of the fly ash blended cement. *Construction and Building Materials, 70*, 388-393.

Toledano-Prados, M., Lorenzo-Pesqueira, M., González-Fonteboa, B., & Seara-Paz, S. (2013). Effect of polycarboxylate superplasticizers on large amounts of fly ash cements. *Construction and Building Materials, 48*, 628-635.

Wang, C., Kayali, O., & Liow, J. L. (2021). The effectiveness and mechanisms of superplasticisers in dispersing class F fly ash pastes. *Powder Technology, 392*, 81-92.

Yao, Z. T., Ji, X. S., Sarker, P. K., Tang, J. H., Ge, L. Q., Xia, M. S., & Xi, Y. Q. (2015). A comprehensive review on the applications of coal fly ash. *Earth-Science Reviews, 141*, 105-121.

Zhang, Q., Shu, X., Yu, X., Yang, Y., & Ran, Q. (2020). Toward the viscosity reducing of cement paste: Optimization of the molecular weight of polycarboxylate superplasticizers. *Construction and Building Materials, 242*. 117984.

Author Information

Veysel Kobya
Department of Civil Engineering, Bursa Uludag University, Bursa, Turkey-Turkiye

Ali Mardani
Department of Civil Engineering, Bursa Uludag University, Bursa, Turkey-Turkiye
Contact e- mail:*alimardani@uludag.edu.tr*

To cite this article:

Kobya, V. & Mardani, A. (2023). Interaction of polycarboxylate-based water-reducing admixture molecular structure with fly ash substituted cementitious systems: Marsh-funnel and mini-slump performance. *The Eurasia Proceedings of Science, Technology, Engineering & Mathematics (EPSTEM), 26*, 693-699.

The Eurasia Proceedings of Science, Technology, Engineering & Mathematics (EPSTEM)
ISSN: 2602-3199

The Eurasia Proceedings of Science, Technology, Engineering & Mathematics (EPSTEM), 2023

Volume 26, Pages 700-709

IConTES 2023: International Conference on Technology, Engineering and Science

Optimization of the Powers Exchanged between a Cascaded Doubly Fed Induction Generator and the Grid with a Matrix Converter

Amar Maafa
Akli Mohand Oulhadj University Bouira

Yahiou Abdelghani
Akli Mohand Oulhadj University Bouira

Hacene Mellah
Akli Mohand Oulhadj University Bouira

Houria Smail
Akli Mohand Oulhadj University Bouira

Hamza Sahraoui
Hassiba Ben Bouali University Chlef

Abstract: The use of an electromagnetic converter of great reliability in wind energy, like the cascaded doubly fed induction generator (CDFIG), can solve several problems compared to the doubly fed induction generator (DFIG), among them the elimination of the brushes and copper rings. The work consists of studying the performance of a CDFIG-based wind system using a matrix converter and a variable pitch control system. The traditional PI is able to successfully solve a number of linear control problems. The fuzzy logic controller used can dramatically improve the system's performance. The active and reactive energy transferred between the CDFIG and the grid can be controlled by adjusting the machine inverter. The DC bus voltage has been kept stable by controlling the grid inverter. The pitch controller's objective is to maximise aerodynamic power while staying within the converter's power limits. Numerical simulation results implemented in the MATLAB/Simulink package will be provided in this study to show that the suggested control strategy is both possible and effective.

Keywords: Variable speed wind turbine, Cascaded doubly fed induction generator, Fuzzy logic controller, Matrix converter

Introduction

The penetration rate of renewable energies in many countries continues to increase because the geopolitical context in the world. Wind energy is one of the promising energies among these renewable energies. Wind turbines are installed all over the world whether in the offshore or onshore. The structure described in this study includes the utilization of a cascaded doubly-fed induction generator with variable speed, which is interconnected with the grid by a matrix converter using variable pitch control system. The cascaded doubly fed induction generator (CDFIG) is made up of two induction generators with p1 and p2 pole-pairs that are mechanically and electrically connected in cascade via their rotors to eliminate the brushes and copper rings observed in typical doubly fed induction machines. (DFIM). (Maafa et al., 2022 ; Admowicz et al. 2008 ; Maafa, et al. 2016 ;Achkar et al. 2017 ;Moazen et al., 2016 ; Zahedi Abdolhadi et al., 2021 ;Yan & Cheng, 2019). The increasing costs associated with maintaining conventional doubly-fed induction generator

- Selection and peer-review under responsibility of the Organizing Committee of the Conference

(DFIG) resulted in a need to explore alternate generator systems. Because they behave similarly, the CDFIG is a good choice to replace the DFIG. (Poitiers et al., 2009 ; Aouzellag et al., 2009 ; Adjoudj et al., 2011 ; Ghedamsi et al., 2008 ;Kerboua & Abid, 2012).

The three-phase matrix converter (MC) is one of the most recent types of direct-power AC-AC converters. There are a total of nine bidirectional switches. The capacity to invert the direction of power transmission through the MC is one of the many advantages of the MC over typical AC-AC converter topologies (Alesina & Venturini, 1989). The effect of the nonlinearities has been minimized successfully when applying the fuzzy logic controller (Tokachichu & Gaddam, 2022 ;Kerboua & Abid, 2012). The superiority of the studied control strategy over the traditional PI regulator has also been proved through a number of numerical simulation results.

A wind turbine with variable pitch control was designed. The wind turbine's rotating speed can be kept constant by adjusting the variable pitch angle of the blade, allowing rated electric power to be produced even when the wind speed exceeds the rated wind speed.

CDFIG Modeling

In this research, we focus on a cascaded doubly fed induction machine, which comprises of two induction machines, IM 1 and IM 2, with identically-pole wound rotor poles. The rotors of the two DFIMs can be connected in two different ways. Connecting the identical phases produces a direct connection, while connecting the phases in the opposite order produces an inverse connection (Maafa, et al., 2022 ;Maafa, et al., 2016 ;Taka & Shibata, 1992). The second configuration is the focus of our study. Two wound rotors are mechanically and electrically coupled in Figure. 1.

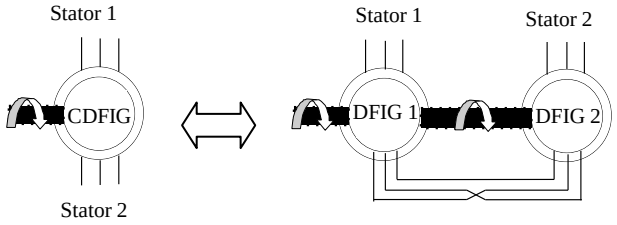

Figure 1. Two DFIGs connected mechanically and electrically to make the CDFIG

The method of analysis employs the Park transformation. Here are the voltage and flow equations for the two DFIGs:

- The machine 1:

$$\begin{cases} v_{ds1} = R_{s1} i_{ds1} + \dfrac{d}{dt}\varphi_{ds1} - \omega_s \varphi_{qs1} \\ v_{qs1} = R_{s1} i_{qs1} + \dfrac{d}{dt}\varphi_{qs1} + \omega_s \varphi_{ds1} \\ v_{dr1} = R_{r1} i_{dr1} + \dfrac{d}{dt}\varphi_{dr1} - (\omega_s - \omega_{r1})\varphi_{qr1} \\ v_{qr1} = R_{r1} i_{qr1} + \dfrac{d}{dt}\varphi_{qr1} + (\omega_s - \omega_{r1})\varphi_{dr1} \end{cases} \quad (1)$$

- The second machine:

$$\begin{cases} v_{dr2} = R_{r2} i_{dr2} + \dfrac{d}{dt}\varphi_{dr2} - (\omega_s - \omega_{r1})\varphi_{qr2} \\ v_{qr2} = R_{r2} i_{qr2} + \dfrac{d}{dt}\varphi_{qr2} + (\omega_s - \omega_{r1})\varphi_{dr2} \\ v_{ds2} = R_{s2} i_{ds2} + \dfrac{d}{dt}\varphi_{ds2} - (\omega_s - \omega_{r1} - \gamma\omega_{r2})\varphi_{qs2} \\ v_{qs2} = R_{s2} i_{qs2} + \dfrac{d}{dt}\varphi_{qs2} + (\omega_s - \omega_{r1} - \gamma\omega_{r2})\varphi_{ds2} \end{cases} \quad (2)$$

The CDFID stators and rotors flux can be written as:

$$\begin{cases} \varphi_{ds1} = L_{s1} i_{ds1} + L_{m1} i_{dr} \\ \varphi_{qs1} = L_{s1} i_{qs1} + L_{m1} i_{qr} \\ \varphi_{dr1} = L_{r1} i_{dr} + L_{m1} i_{ds1} \\ \varphi_{qr1} = L_{r1} i_{qr} + L_{m1} i_{qs1} \end{cases} \quad (3)$$

$$\begin{cases} \varphi_{ds2} = L_{s2} i_{ds2} - L_{m2} i_{dr} \\ \varphi_{qs2} = L_{s2} i_{qs2} - L_{m2} i_{qr} \\ \varphi_{dr2} = -L_{r2} i_{dr} + L_{m2} i_{ds2} \\ \varphi_{qr2} = -L_{r2} i_{qr} + L_{m2} i_{qs2} \end{cases} \quad (4)$$

The modeling of the electric coupling of the two rotors will be in the following way:

$$\begin{cases} v_{dr1} = \gamma\ v_{dr2} = v_{dr} \\ v_{qr1} = \gamma\ v_{qr2} = v_{qr} \end{cases} \quad (5) \qquad \begin{cases} i_{dr1} = -\gamma\, i_{dr2} = i_{dr} \\ i_{qr1} = -\gamma\, i_{qr2} = i_{qr} \end{cases} \quad (6)$$

Powers Control of CDFIG

Matrix Converter

The direct matrix converter consists of a total of nine bidirectional switches, facilitating the interconnection of the input phases (a, b, and c) with the output phases (a, b, and c) in a flexible manner. Figure 2 shows that each output phase is connected to three input phases by three switches. The input voltages with fixed amplitude and frequency must be converted into frequency and/or variable amplitude sinusoidal output voltages (Casadei, et al. 1993 ;Huber & Borojevic, 1995).

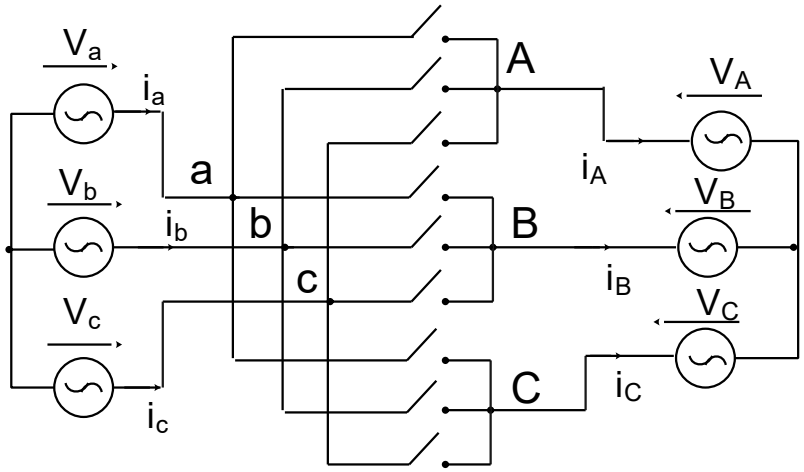

Figure 2. Topology of a matrix converter

The switching function of switch S_{ij} in Figure 1 is formally defined as.

$$S_{ij} = \begin{cases} 1 & Sw_{ij}\ is\ closed \\ 0 & Sw_{ij}\ is\ open \end{cases} \qquad i \in \{A, B, C\},\ j \in \{a, b, c\}, \quad (7)$$

The preceding restrictions can be expressed as

$$Sw_{Aj} + Sw_{Bj} + Sw_{Cj} = 1 \qquad j \in \{a, b, c\}, \quad (8)$$

In order to effectively manage the active and reactive power exchange between the machine and the grid, we propose a control for the machine inverter. The wind energy conversion system incorporates reactive power regulation to achieve a power factor of unity between the stator 1 and the grid. Meanwhile, the active power output is adjusted in response to variations in wind speed.

SVM for the Rectifier Stage

Using a transformation like this, the present input current space vector I_{in} is expressed as a space vector:

$$I_{in} = \frac{2}{3}(I_a + I_b e^{j\frac{2\pi}{3}} + I_c e^{-j\frac{2\pi}{3}}) \quad (9)$$

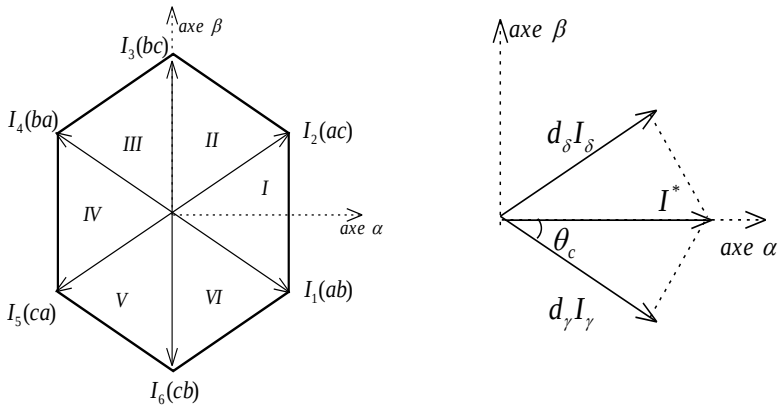

Figure 3. Reference current vector synthesis

The group of discrete seven-dimensional vectors can be organized in a hexagonal structure within the complex plane, as depicted in Fig 4.

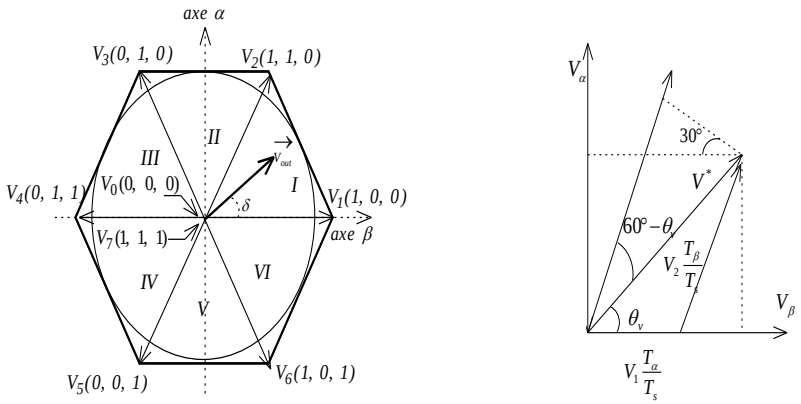

Figure 4. Output voltage modulation for rectification stage

Two adjacent switching vectors v_α and v_β with the duty cycles d_α and d_β, respectively, generate the reference output voltage space vector.

$$V^* = d_\alpha v_\alpha + d_\beta I_\beta \tag{13}$$

The duty cycle of the active vectors is calculated by:

$$\begin{cases} d_\alpha = \dfrac{T_\alpha}{T_s} = m_v \sin(\dfrac{\pi}{3} - \theta_v) \\ d_\beta = \dfrac{T_\beta}{T_s} = m_v \sin(\theta_v) \\ d_0 = \dfrac{T_0}{T_s} = 1 - (d_\alpha + d_\beta) \end{cases} \tag{14}$$

where θ_v is the angle of the reference voltage vector within the hexagon sector itself. The voltage modulation index, m_V, specifies the desired voltage transfer ratio, such as

SVM for the Entire Matrix Converter

For the nine bidirectional switched matrix converter, the two independent space vector modulations need to be combined into a single modulation technique.

$$\begin{cases} d_{\alpha\gamma} = d_{\alpha}.d_{\gamma} = m_v \sin\left(\frac{\pi}{3}-\theta_i\right).\sin\left(\frac{\pi}{3}-\theta_v\right) \\ d_{\alpha\delta} = d_{\alpha}.d_{\delta} = m_v \sin\left(\theta_i\right).\sin\left(\frac{\pi}{3}-\theta_v\right) \\ d_{\beta\delta} = d_{\beta}.d_{\delta} = m_v \sin\left(\frac{\pi}{3}-\theta_i\right).\sin\left(\theta_v\right) \\ d_{\beta\delta} = d_{\beta}.d_{\delta} = m_v \sin\left(\theta_i\right).\sin\left(\theta_v\right) \end{cases} \quad (15)$$

Zero vector is applied throughout the remainder of the switching period (TS).

$$d_0 = 1-(d_{\alpha\gamma}+d_{\alpha\delta}+d_{\beta\gamma}+d_{\beta\gamma\delta}) \quad (16)$$

We select a d-q reference frame that is synchronised with the flux of stator 1.

$$\begin{cases} \varphi_{ds1} = \varphi_{s1} \\ \varphi_{qs1} = 0 \end{cases} \quad (17)$$

We can write: ignoring the stator 1 resistance Rs1:

$$\begin{cases} v_{ds1} = 0 \\ v_{qs1} = V_s = \omega_s.\varphi_{s1} \end{cases} \quad (18)$$

For slip values relatively weak according to the stator 2 currents, the rotor and stator 1 currents, the stator 2 voltages expressions as the active and reactive powers of stator 1 and grid are presented in (19) – (22) respectively:

$$\begin{cases} i_{dr} = C.i_{ds2} - C.\dfrac{L_{m1}.V_s}{\omega_s.L_{s1}.L_{m2}} \\ i_{qr} = C.i_{qs2} \end{cases} \quad (19)$$

$$\begin{cases} i_{ds1} = \dfrac{V_s}{\omega_s.L_{s1}}\left(1+\dfrac{C.L_{m1}^2}{L_{s1}.L_{m2}}\right) - C.\dfrac{L_{m1}}{L_{s1}}i_{ds2} \\ i_{qs1} = -C.\dfrac{L_{m1}}{L_{s1}}i_{qs2} \end{cases} \quad (20)$$

$$\begin{cases} v_{ds2} = R_{s2}i_{ds2} + \left(L_{s2}-C.L_{m2}\right)\dfrac{di_{ds2}}{dt} - s.\omega_s\left(L_{s2}-C.L_{m2}\right).i_{qs2} \\ v_{qs2} = R_{s2}i_{qs2} + \left(L_{s2}-C.L_{m2}\right)\dfrac{di_{qs2}}{dt} + s.\omega_s\left(L_{s2}-C.L_{m2}\right).i_{ds2} + s.\dfrac{L_{m1}V_s}{L_{s1}} \end{cases} \quad (21)$$

$$\begin{cases} P_{s1} = -C.V_s\dfrac{L_{m1}}{L_{s1}}i_{qs2} \\ Q_{s1} = \dfrac{V_s^2}{\omega_s.L_{s1}}\left(1+\dfrac{C.L_{m1}^2}{L_{s1}.L_{m2}}\right) - C.V_s\dfrac{L_{m1}}{L_{s1}}i_{ds2} \end{cases} \quad (22)$$

With: $s = s_1.s_2 = \frac{\omega_s - \omega_{r1} - \omega_{r2}}{\omega_s} = \frac{\omega_s - (p_1 + p_2)\Omega_r}{\omega_s}$, $s_1 = \frac{\omega_s - p_1.\Omega_r}{\omega_s}$, $s_2 = \frac{s_1.\omega_s - p_2.\Omega_r}{s_1.\omega_s}$

and $C = \frac{L_{m2}}{L_{r1} + L_{r2} - \frac{L_{m1}^2}{L_{s1}}}$

Fuzzy Logic Controller

Fuzzification, an inference engine, and defuzzification are the three processes that are utilised throughout the FLC strategy. Each of these procedures is necessary for the implementation of FLC. The inputs of the our fuzzy controllers receive the currents and their variations to synthesise the CDFIG reference voltages.

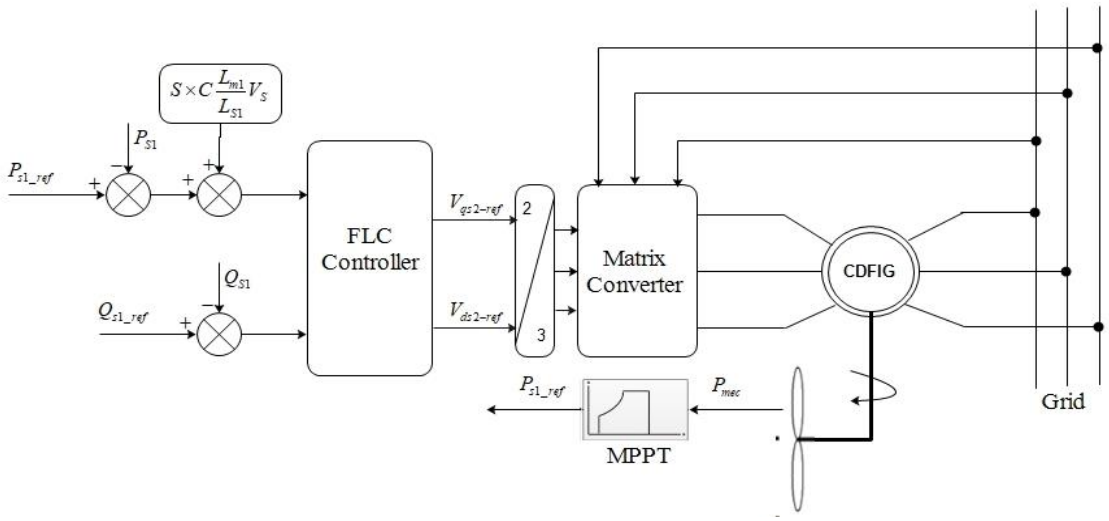

Figure 5. Whole system control

Results and Discussions

The suggested wind system was implemented in Matlab/Simulink as shown in Figure 5. This section presents a simulation of an AC/AC direct converter-controlled direct grid connection of CDFIG. The system under consideration is regulated to produce the most energy possible.

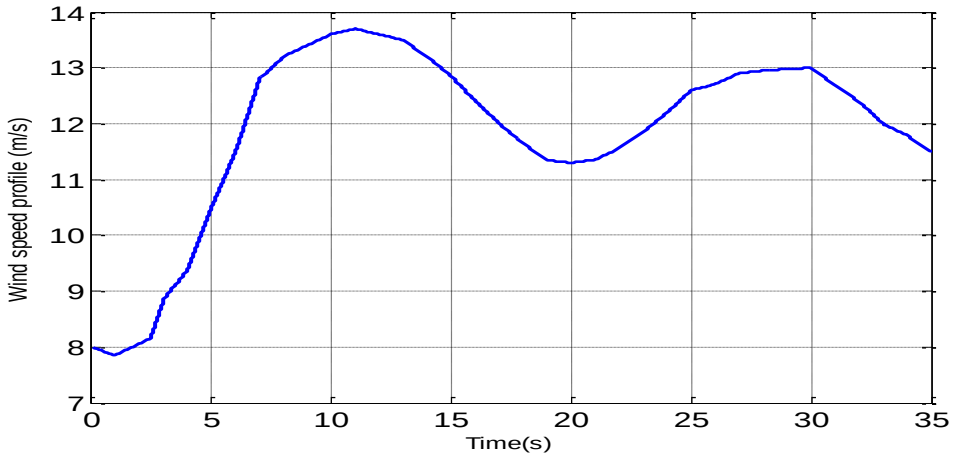

Figure 6. Wind speed profile

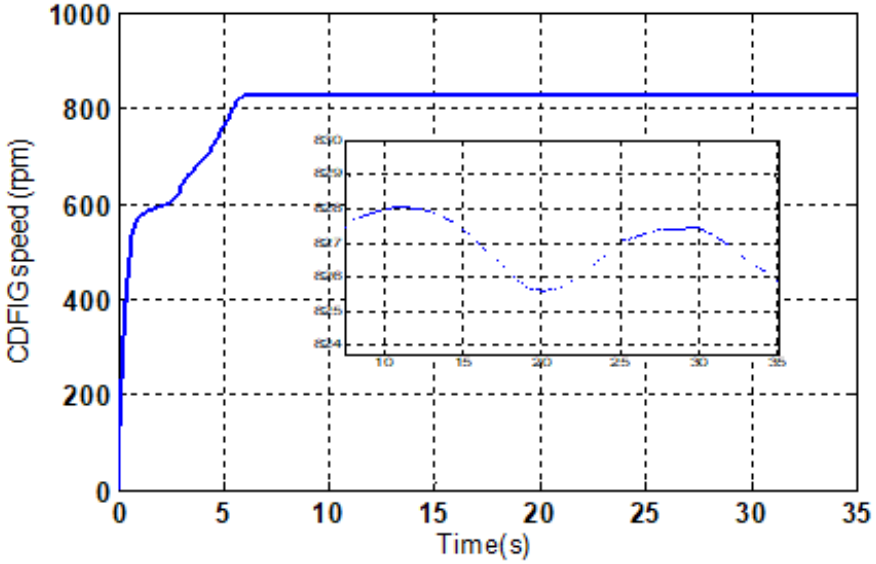

Figure 7. CDFIG speed

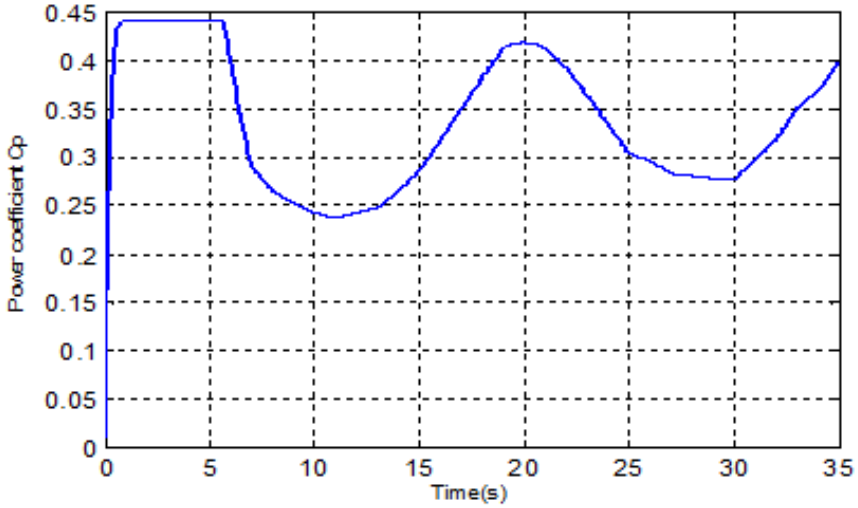

Figure 8. Power coefficient

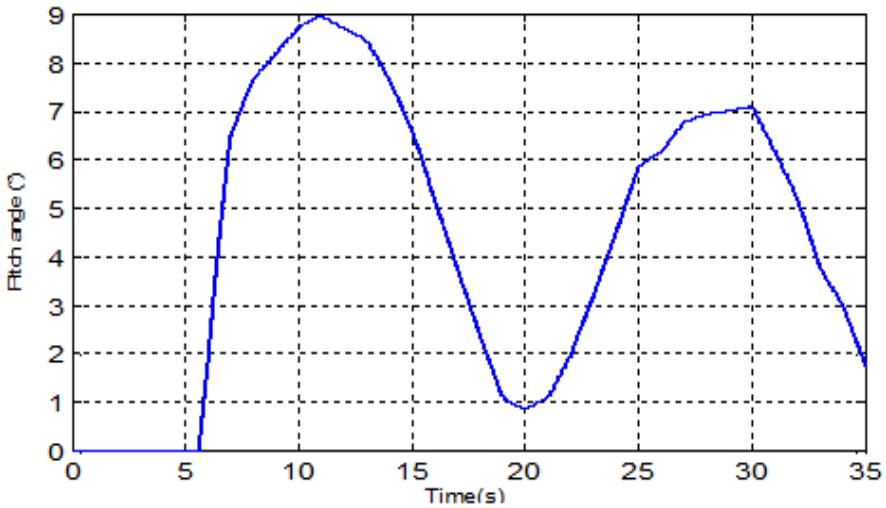

Figure 9. Pitch angle

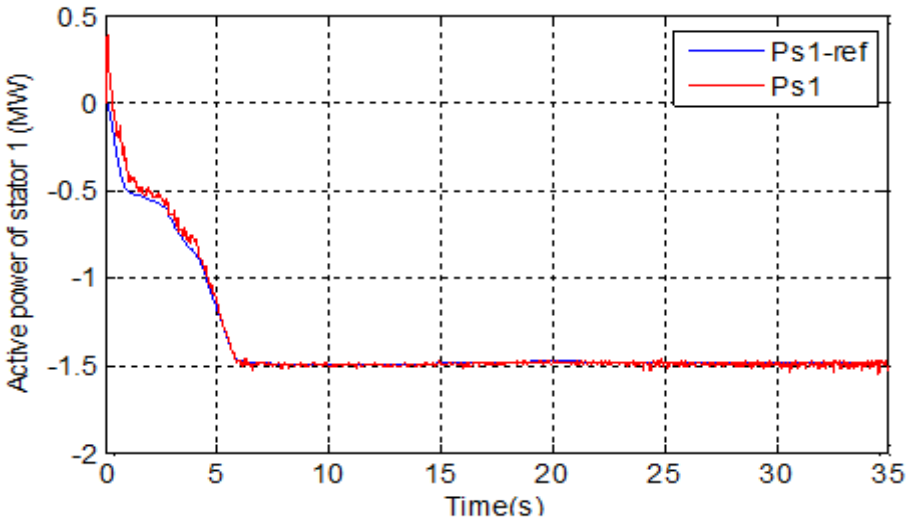

Figure 10. Stator one's active power

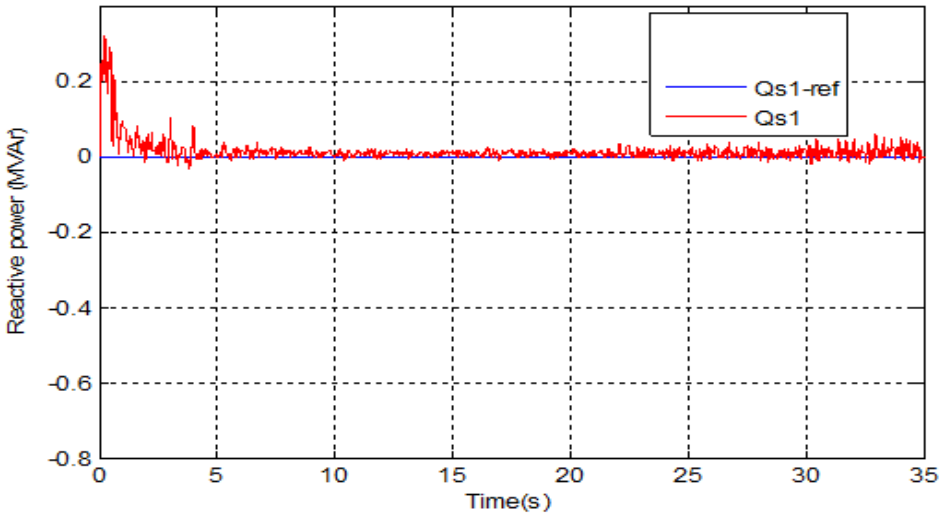

Figure 11.Stator one's reactive power

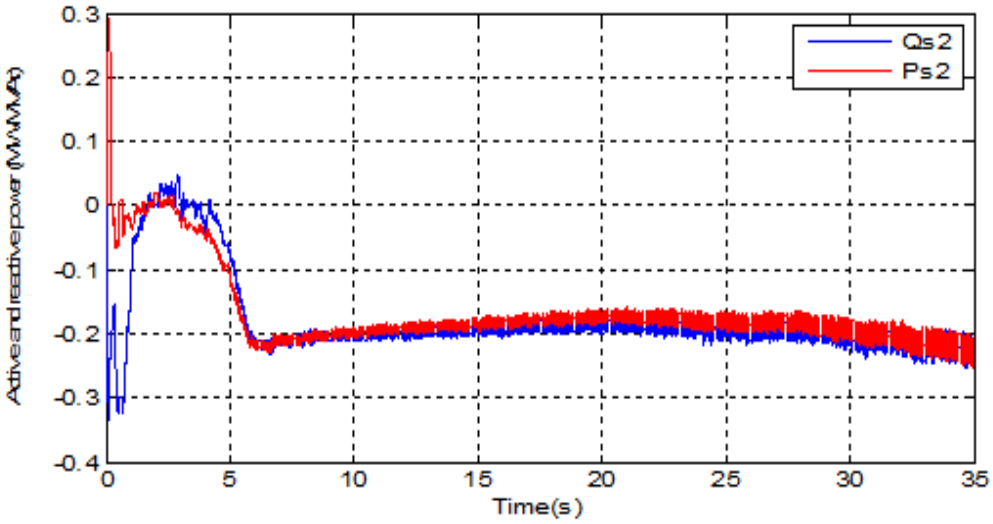

Figure 12. Stator Two's active and reactive

Wind speed is shown in figure 6. The speed and zoom of a CDFIG are presented in figure 7. The power coefficient is displayed in figure 8. In Figure 9, the pitch angle is shown. The wind turbine's pitch angle is managed to achieve the highest C_{Pmax}. Stator 1's active power is shown in Figure 10. The stator one powers properly adhere to their references. Figure 11 represents the reactive power of stator 1. It is kept constant at zero. Figure 12 shows the active and reactive powers of stator two. It is evident that in a hyper-synchronous operation mode, a portion of the active power exceeding 1.5 MW is transferred from the stator 2 side of the CDFIG.

Conclusion

This study focuses on the analysis of a wind energy system that utilizes a CDFIG and is connected to the electrical grid via a matrix converter using logic fuzzy controllers. All of the results can be observed using a DFIG or CDFIG instead; the distinction is that the CDFIG eliminates brushes-ring electrical connectors, resulting in a more reliable and robust structure. The pitch controller's objective is to maximise aerodynamic power while staying within the converter's power limits. Results from the simulation demonstrated that the active and reactive powers were quite similar to their reference values. The proposed structure is preserved and has a longer lifespan because the matrix converter contains no energy storage component. The effectiveness and reliability of the suggested method are demonstrated by the simulation results.

Scientific Ethics Declaration

The authors declare that the scientific ethical and legal responsibility of this article published in EPSTEM journal belongs to the authors.

Acknowledgements or Notes

* This article was presented as an oral presentation at the International Conference on Technology, Engineering and Science (www.icontes.net) held in Antalya/Turkey on November 16-19, 2023.

References

Achkar, M., Mbayed, R., Salloum, G., & Le Ballois, S. (2017). Generic study of the power capability of a cascaded doubly fed induction machine. *International Journal of Electrical Power & Energy Systems, 86*, 61-70.

Adjoudj, M., Abid, M., Aissaoui, A., Ramdani, Y., & Bounoua, H. (2011). Sliding mode control of a doubly fed induction generator for wind turbines. *Rev. Roum. Sci. Techn. – Électrotechn. et Énerg, 56*(1), 15–24.

Admowicz, M., & Strzeleki, R. (2008). Cascaded doubly fed induction generator for mini and micro power plants connected to grid. *IEEE Power Electronics Motion Control. Conference*, 1729 – 1733.

Alesina, A., & Venturini, M. (1989). Analysis and design of optimumamplitude nine-switch direct AC-AC converters. *IEEE Transactions on Power Electronics*, *4*(1), 101–112.

Aouzellag, D., Ghedamsi, K., & Berkouk, E. (2009). Network power flux control of a wind generator. *Renewable Energy*, *34*, 615–622 .

Casadei, D., Grandi, G., Serra, G., & Tani, A. (1993). Space vector control of matrix converters with unity input power factor and sinusoidal input/output waveforms. *Fifth European Conference on Power Electronics and Applications*, 170-175.

Ghedamsi, K., Aouzellag, D., & Berkouk, E. (2008). Control of wind generator associated to a flywheel energy storage system. *Renewable Energy*, *33*, 2145–2156.

Huber, L., & Borojevic, D. (1995). Space vector modulated three-phase to three-phase matrix converter with input power factor correction. *IEEE Transactions on Industry Applications*, *31*(6), 1234–1246.

Kerboua, A., & Abid, M. (2012). Hybrid fuzzy sliding mode control of a doubly-fed induction generator in wind turbines. *Rev. Roum. Sci. Techn. – Électrotechn. et Énerg, 57*(4), 412–421.

Maafa, A., Aouzellag, D., Ghedamsi, K., & Abdessemed, R. (2016). Cascaded doubly fed induction generator with variable pitch control system. *Revue Roumaine des Sciences Techniques, 61*(4), 361–366.

Maafa, A., Mellah, H., Ghedamsi, K., & Aouzelag, D. (2022). Improvement of sliding mode control strategy founded on cascaded doubly fed induction generator powered by a Matrix converter. *Engineering, Technology & Applied Science Research, 12*(5), 9217-9223.

Moazen, M., Kazemzadeh, R., & Azizian, M. R. (2016). Mathematical modeling and analysis of brushless doubly fed reluctance generator under unbalanced grid voltage condition. *International Journal of Electrical Power & Energy Systems, 83*, 547–559.

Poitiers, F., Bouaouiche, T., & Machmoum, M. (2009). Advanced control of a doubly-fed induction generator for wind energy conversion. *Electric Power Systems Research, 79*, 1085–1096.

Taka, K., & Shibata, F. (1992). A self-cascaded induction generator system with DC chopper, PWM inverter and LPF. *IEEE Xplore*, 31-31.

Tokachichu, J., & Gaddam, T. (2022). Performance analysis of a transmission line connected with Upfc designed with three level cascaded H bridge inverter with generalized SVM technique using PI, LOGIC, ANN and ANFIS controllers. *Materials Today: Proceedings, 51*, 1243-1251.

Yan, X., & Cheng, M. (2019). A robust rid synchronization method for cascaded brushless doubly fed Induction generator. *International Conference on Electrical Machines and Systems*, 1-6.

Zahedi Abdolhadi, H., Arab Markadeh, G., & Tagh, S. (2021). Sliding mode and terminal sliding mode control of cascaded doubly fed induction generator. *Iranian Journal of Electrical and Electronic Engineering, 17*(3), 1955–1955.

Author Information

Amar Maafa
Department of Electrical Engineering
Akli Mohand Oulhadj University
Bouira, Algeria
Contact e-mail*: omaafa@univ-bouira.dz*

Yahiou Abdelghani
Name of Institution or University
Address of Institution or University
Bouira, Algeria

Mellah Hacene
Department of Electrical Engineering
Akli Mohand Oulhadj University
Bouira, Algeria

Houria Smail
Department of Electrical Engineering
Akli Mohand Oulhadj University
Bouira, Algeria

Hamza Sahraoui
Department of Electrical Engineering
Hassiba Ben Bouali University
Chlef, Algeria

To cite this article:

Maafa, A. Abdelghani**,** Y**.,** Hacene, M**.,** Smail, H., & Sahraoui, H. (2023). Optimization of the powers exchanged between a cascaded doubly fed induction generator and the grid with a matrix converter. *The Eurasia Proceedings of Science, Technology, Engineering & Mathematics (EPSTEM), 26*, 700-709.

The Eurasia Proceedings of Science, Technology, Engineering & Mathematics (EPSTEM)
ISSN: 2602-3199

The Eurasia Proceedings of Science, Technology, Engineering & Mathematics (EPSTEM), 2023

Volume 26, 710-717

IConTES 2023: International Conference on Technology, Engineering and Science

Decoupled Control of a Multi-Machines System Fed by a Single Multilevel Inverter Six-Phase

Taieb Bessaad
Hassiba Benbouali University of Chlef

Khelifa Khelifi Otmane
Blida University

Rachid Taleb
Hassiba Benbouali University of Chlef

Aderrahmen Benbouali
Hassiba Benbouali University of Chlef

Abstract: The use of multiphase motors offers an additional possibility of independent control of a set of series-connected motors that are supplied from a single inverter.This paper presents independent vector control of six-phase two-motor drive machine series-connected fed by a seven-level six-phase inverter. Via appropriate phase transposition during the series connection of the stator windings, the fully decoupled control of the two machines is possible. The control system multi-machines classic based on vector control with conventional inverters comprise various problems are related to low power quality, pressure on motor bearing, etc. However, decoupling control of a series six-phase two-motor drive machine by a seven-level six-phase inverter is developed. A simulations result clearly shows the possibility of independent vector control of the two machines, although a single seven-level six-phase inverter is used as the supply.

Keywords: Multiphase machines, Six-phase, Vector control, Seven-level six-phase inverter

Introduction

Recently, researchers are interested in machines with a number of phases greater than three. These machines are often called «multiphase machines». Multi-phase machines have following advantages over three-phase machines: The application of these machines is an effective solution to the problem of high power under supply voltage restriction circumstances. Power segmentation, reducing torque ripple and increasing ripple frequency, significantly improving low-speed performance; by reducing vibration and noise, the reliability of the drive system is greatly improved with increased number of phases. A lot of works have been presented with diverse control diagrams of multi–phase machines is independent control of a group of series-connected machines.

These control diagrams are usually based on vector control notion with conventional two-level voltage source inverter. with the conventional inverters comprise various problems are related to low power quality, immense voltage stresses, common mode noise, pressure on motor bearing, etc. These problems are overcome by increasing the number phases and levels instead of conventional inverters, called as multi-level inverters.

Multilevel power conversion was rest introduced more than two decades ago. The general concept involves utilizing a higher number of active semiconductor switches to perform the power conversion in small voltage steps. Multilevel inverters are promising; they have nearly sinusoidal outputvoltage waveforms, output current

with better harmonic pro le, less stressing of electronic components owing to decreased voltages, switching losses that are lower than those of conventional two-level inverters, a smaller size, and lower EMI, all of which make them cheaper, lighter, and more compact. This paper studies the seven levels inverter NPC structure applied in multi-machines system, we focus in particular on the modeling and the decoupling control of a series-connected two six-phase and three-phase machines supplied by a seven-level six-phase Voltage source inverter.

Seven Lever Six-Phase NPC Inverter Scheme

Multilevel inverters are increasingly being used in high-power medium-voltage applications due to their superior performance compared to two-level inverters. Different types of multilevel inverter topologies were presented. The seven-level hexaphase inverter studies and consists of six arms and four sources of voltage contained. Each arm has eight switches, six in series and the other two in parallel, plus two diodes. The structure chosen in this study is that of the five-level NPC-structured six-phase voltage inverter, represented by the figure 1:

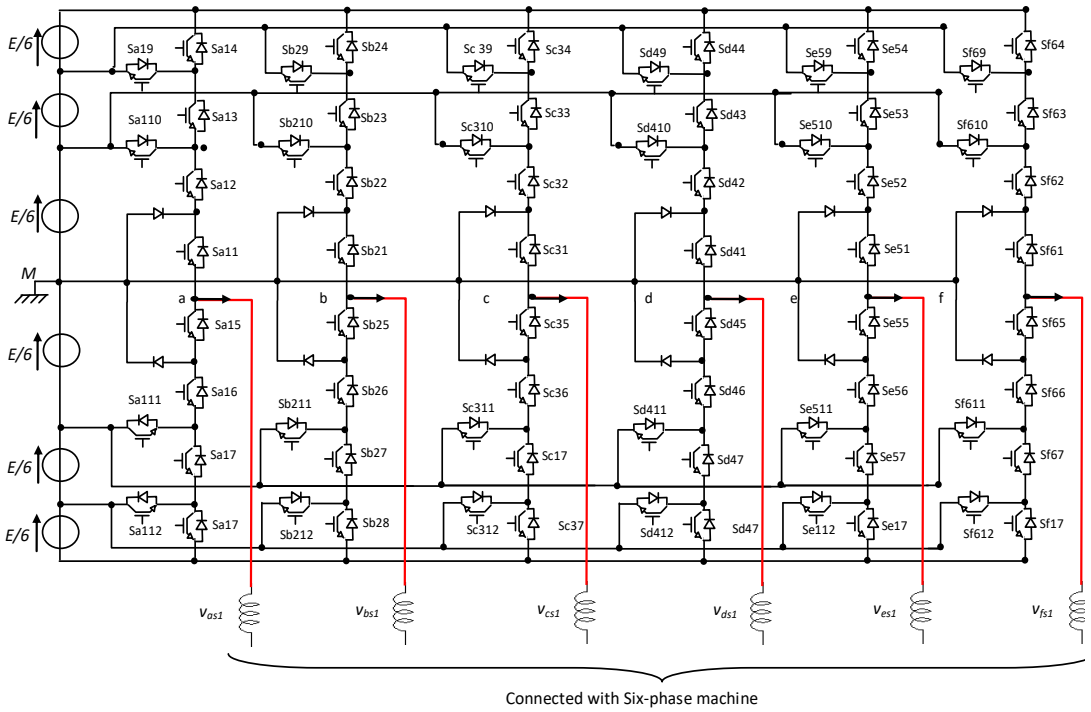

Figure 1. Seven level six-phase NPC-inverter

The switching states of the proposed seven-level SC-based inverter current flowing paths in different output voltage levels are presented in Table 1.

Table 1. Switching States of the proposed 7-level inverter

Switching states of the converter												Level of V_{ao}
S_{a1}	S_{a2}	S_{a3}	S_{a4}	S_{a5}	S_{a6}	S_{a7}	S_{a8}	S_{a9}	S_{a10}	S_{a11}	S_{a12}	
1	1	1	1	1	1	0	0	0	0	0	0	E/2
0	1	1	1	1	1	1	0	0	0	0	0	E/3
0	0	1	1	1	1	1	1	0	0	0	0	E/6
0	0	0	1	1	1	1	1	1	0	0	0	0
0	0	0	0	1	1	1	1	1	1	0	1	-E/2
0	0	0	0	0	1	1	1	1	1	1	0	-E/3
0	0	0	0	0	0	1	1	1	1	1	1	-E/6

Modeling of the Series-Connected Six-Phase -Two-Motor

The drive system is composed by two induction machines. The first one is a symmetrical six-phase induction motor I.M1 which its windings are series connected with that of a second three-phase induction motor I.M2. The

two motors are supplied by a single power converter which is a 7-level six-phase Voltage Source Inverter (VSI). Figure 2. presents the connecting and suppling schematic of the two motors and the converter. The six-phase machine has the spatial displacement between any two consecutive stator phases equal to 60° (i.e. $\alpha = 2\pi/6$).Only phases 1, 3 and 5 are used by the second machine I.M2, this phases are electrically displaced to each other by and angle of $2\pi/3$.

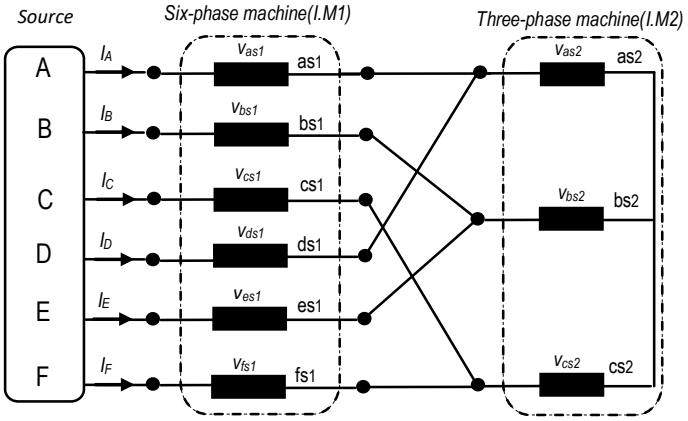

Figure 2. Diagram of connection of a tow-machine in series

According to Figure 2, the stator and rotor voltages of the two machines can be written as follows:

$$[v_s] = \begin{bmatrix} V_A \\ V_B \\ V_C \\ V_D \\ V_E \\ V_F \end{bmatrix} = \begin{bmatrix} v_{as1} + v_{as2} \\ v_{bs1} + v_{bs2} \\ v_{cs1} + v_{cs2} \\ v_{ds1} + v_{as2} \\ v_{es1} + v_{bs2} \\ v_{fs1} + v_{cs2} \end{bmatrix} \tag{1}$$

The relationship between the current source and the stator currents of each machine are given as follows:

$$\begin{aligned} [i_s] &= [I_A \quad I_B \quad I_C \quad I_D \quad I_E \quad I_F] \\ &= [i_{as1} \quad i_{bs1} \quad i_{cs1} \quad i_{ds1} \quad i_{es1} \quad i_{fs1}] \\ &= [i_{s1}] \end{aligned} \tag{2}$$

$$[i_{s2}] = \begin{bmatrix} i_{as2} \\ i_{bs2} \\ i_{cs2} \end{bmatrix} = \begin{bmatrix} I_A + I_D \\ I_B + I_E \\ I_C + I_F \end{bmatrix} \tag{3}$$

The electrical equations:

$$\begin{cases} [V_{sk}] = [R_{sk}][i_{sk}] + \dfrac{d}{dt}[\varphi_{sk}] \\ [0] = [R_{rk}][i_{rk}] + \dfrac{d}{dt}[\varphi_{rk}] \end{cases} \tag{4}$$

where :

$$\begin{cases} [\varphi_{sk}] = [L_{ssk}][i_{sk}] + [M_{srk}][i_{rk}] \\ [\varphi_{rk}] = [L_{rrk}][i_{rk}] + [M_{rsk}][i_{sk}] \end{cases} \tag{5}$$

Knowing that k = 1 for the I.M1 and k = 2 for the I.M2

with:

$$\left[R_{seq}\right]=\left[R_{s1}\right]+\begin{bmatrix}\left[R_{s2}\right] & \left[R_{s2}\right]\\ \left[R_{s2}\right] & \left[R_{s2}\right]\end{bmatrix} \quad ; \quad \left[L_{seq}\right]=\left[L_{s1}\right]+\begin{bmatrix}\left[L_{s2}\right] & \left[L_{s2}\right]\\ \left[L_{s2}\right] & \left[L_{s2}\right]\end{bmatrix}$$

Modeling of Multi-Machine System (MSCS) into Three Subspaces (α,β), (X,Y), (O+,O-)

The original six dimensional systems of the SMMC can be decomposed into three orthogonal subspaces, (α, β), (x, y) and (o+, o-), using the following transformation $X_{\alpha\beta o}= [T_6(\alpha)]^{-1}.X_{abc}$ and $X_{dqo} = [T_6(\alpha)]^{-1} X_{\alpha\beta o}$
Where: X represents stator currents, stator flux, stator voltages in MSCS. The matrix $[T_6(\alpha)]$ is given by:

$$\left[T_6(\alpha)\right]=\frac{1}{\sqrt{3}}\begin{bmatrix}1 & \cos(\alpha) & \cos(2\alpha) & \cos(3\alpha) & \cos(4\alpha) & \cos(5\alpha)\\ 0 & \sin(\alpha) & \sin(2\alpha) & \sin(3\alpha) & \sin(4\alpha) & \sin(5\alpha)\\ 1 & \cos(2\alpha) & \cos(4\alpha) & \cos(6\alpha) & \cos(8\alpha) & \cos(10\alpha)\\ 0 & \sin(2\alpha) & \sin(4\alpha) & \sin(6\alpha) & \sin(8\alpha) & \sin(10\alpha)\\ 1/\sqrt{2} & 1/\sqrt{2} & 1/\sqrt{2} & 1/\sqrt{2} & 1/\sqrt{2} & 1/\sqrt{2}\\ 1/\sqrt{2} & -1/\sqrt{2} & 1/\sqrt{2} & -1/\sqrt{2} & 1/\sqrt{2} & -1/\sqrt{2}\end{bmatrix} \quad (6)$$

$$\left[T_3(\alpha)\right]=\sqrt{\frac{2}{3}}\begin{bmatrix}1 & \cos2\alpha & \cos4\alpha\\ 0 & \sin2\alpha & \sin4\alpha\\ 1/\sqrt{2} & 1/\sqrt{2} & 1/\sqrt{2}\end{bmatrix} \quad (7)$$

$$\left[\rho(\theta)\right]=\begin{bmatrix}\begin{bmatrix}\cos(\theta o & -\sin(\theta i\\ -\sin(\theta i & \cos(\theta o\end{bmatrix} & \left[0\right]_{2\times4}\\ \left[0\right]_{4\times2} & \left[I\right]_{4\times4}\end{bmatrix} \quad (8)$$

where:

$$\begin{cases}\left[T_6\right]^{-1}\left[\varphi_{s,abcdef}\right]=\left[\varphi_{s\alpha} \quad \varphi_{s\beta} \quad \varphi_{sx} \quad \varphi_{sy} \quad \varphi_{so+} \quad \varphi_{so-}\right]T\\ \left[T_6\right]^{-1}\left[i_{s,abcdef}\right]=\left[i_{s\alpha} \quad i_{s\beta} \quad i_{sx} \quad i_{sy} \quad i_{so+} \quad i_{so-}\right]T\end{cases} \quad (9)$$

$$\begin{cases}\left[T_6\right]^{-1}\left[\varphi_r\right]=\left[0 \quad 0 \quad 0\right]T\\ \left[T_6\right]^{-1}\left[i_r\right]=\left[i_{r\alpha} \quad i_{r\beta} \quad i_{o+}\right]T\end{cases}$$

Application of the transformations matrix (6) and (7) in conjunction with the first row of (4) lead to the decoupled model of the six-phase two-motor drive system. Source voltage equations that include equations of the two stator windings connected in series can be given as:

Sub-system (α, β):

$$\begin{cases}V_{s\alpha}=R_{s1}i_{s\alpha1}+L_{s1}\dfrac{di_{s\alpha1}}{dt}+M_1\dfrac{di_{r\alpha1}}{dt}\\ V_{s\beta}=R_{s1}i_{s\beta1}+L_{s1}\dfrac{di_{s\beta1}}{dt}+M_1\dfrac{di_{r\beta1}}{dt}\end{cases} \quad (10)$$

Sub-system (x, y):

$$\begin{cases}V_{sx}=R_{eq}i_{sx1}+(l_{s1}+2L_{s2})\dfrac{di_{sx1}}{dt}+\sqrt{2}M_2\dfrac{di_{r\alpha2}}{dt}\\ V_{sy}=R_{eq}i_{sy1}+(l_{s1}+2L_{s2})\dfrac{di_{sy1}}{dt}+\sqrt{2}M_2\dfrac{di_{r\beta2}}{dt}\end{cases} \quad (11)$$

Sub-system (O^+, O^-):

$$\begin{cases} V_{so+} = R_{eq} i_{so+1} + (l_{s1} + 2L_{s2}) \dfrac{di_{so+1}}{dt} \\ V_{so-} = R_{eq} i_{so-1} + l_{s1} \dfrac{di_{so-1}}{dt} \end{cases} \quad (12)$$

Rotor voltage equations of six-phase machine and three-phase machine are:

$$\begin{cases} 0 = R_{r1} i_{r\alpha 1} + L_{m1} \dfrac{di_{s\alpha 1}}{dt} + L_{r1} \dfrac{di_{r\alpha 1}}{dt} + \omega_{r1} (L_{m1} i_{s\beta 1} + L_{r1} i_{r\beta 1}) \\ 0 = R_{r1} i_{r\beta 1} + L_{m1} \dfrac{di_{s\beta 1}}{dt} + L_{r1} \dfrac{di_{r\beta 1}}{dt} + \omega_{r1} (L_{m1} i_{s\alpha 1} + L_{r1} i_{r\alpha 1}) \end{cases} \quad (13)$$

$$\begin{cases} 0 = R_{r2} i_{r\alpha 2} + \sqrt{2} L_{m2} \dfrac{di_{sx1}}{dt} + L_{r2} \dfrac{di_{r\alpha 2}}{dt} + \omega_{r2} (\sqrt{2} L_{m2} i_{sy1} + L_{r2} i_{r\beta 2}) \\ 0 = R_{r2} i_{r\beta 2} + \sqrt{2} L_{m2} \dfrac{di_{sy1}}{dt} + L_{r2} \dfrac{di_{r\beta 2}}{dt} - \omega_{r2} (\sqrt{2} L_{m2} i_{sx1} + L_{r2} i_{r\alpha 2}) \end{cases} \quad (14)$$

with:

$$\begin{cases} L_{s1} = l_{s1} + \dfrac{3}{2} L_{ms1} \\ M_1 = \dfrac{3}{\sqrt{2}} L_{sr1} \\ L_{r1} = l_{r1} + \dfrac{3}{2} L_{mr1} \end{cases} \quad \begin{cases} L_{s2} = l_{s2} + \dfrac{3}{2} L_{ms2} \\ M_2 = \dfrac{3}{\sqrt{2}} M_{sr2} \\ L_{r2} = l_{r2} + \dfrac{3}{2} L_{mr2} \end{cases} \quad (15)$$

Application of (6) in conjunction with (1) yields:

$$\begin{bmatrix} v_{s\alpha} \\ v_{s\beta} \\ v_{sx} \\ v_{sy} \\ v_{so+} \\ v_{so-} \end{bmatrix} = [T_6] \begin{bmatrix} v_{sa1} + v_{sa2} \\ v_{sb1} + v_{sb2} \\ v_{sc1} + v_{sc2} \\ v_{sd1} + v_{sa2} \\ v_{se1} + v_{sb2} \\ v_{sf1} + v_{sc2} \end{bmatrix} = \begin{bmatrix} v_{s\alpha} \\ v_{s\beta} \\ v_{sx1} + \sqrt{2} v_{s\alpha 2} \\ v_{sy1} + \sqrt{2} v_{s\beta 2} \\ v_{so+} \\ v_{so-} \end{bmatrix} \quad (16)$$

and

$$\begin{cases} i_{s\alpha} = i_{s\alpha 1} \\ i_{s\beta} = i_{s\beta 1} \end{cases} ; \quad \begin{cases} i_x = i_{sx1} = \dfrac{i_{s\alpha 2}}{\sqrt{2}} \\ i_y = i_{sy1} = \dfrac{i_{s\beta 2}}{\sqrt{2}} \end{cases} ; \begin{cases} i_{o+} = i_{so+1} \\ i_{o-} = i_{so-1} \end{cases} \quad (17)$$

Torque equations of the two machines are:

$$\begin{cases} T_{em1} = P_1 M_1 (i_{rd} 1_{isq1} - i_{sd} i_{rq1}) \\ T_{em2} = P_2 M_2 (i_{rd2} i_{sy1} - i_{sx} i_{rq2}) \end{cases} \quad (18)$$

As can be seen to equations (10)-(14) and (18), that flux/torque producing stator currents of the six-phase machine are the source (α, β) current components, while the flux/torque producing stator currents of the three-phase machine are the source (x, y) current components. This indicates the possibility of independent vector control of two machines. It therefore follows that independent vector control of the two machines can be realized with a single six-phase inverter.

Vector Control of the Two-Motor Drive

With the transformation (8), the components of the plane (α, β) to equations (10)-(14) can be expressed in the (d, q) plane. The two series-connected machines can be controlled independently using rotor-flux oriented control principles (Figure 3).

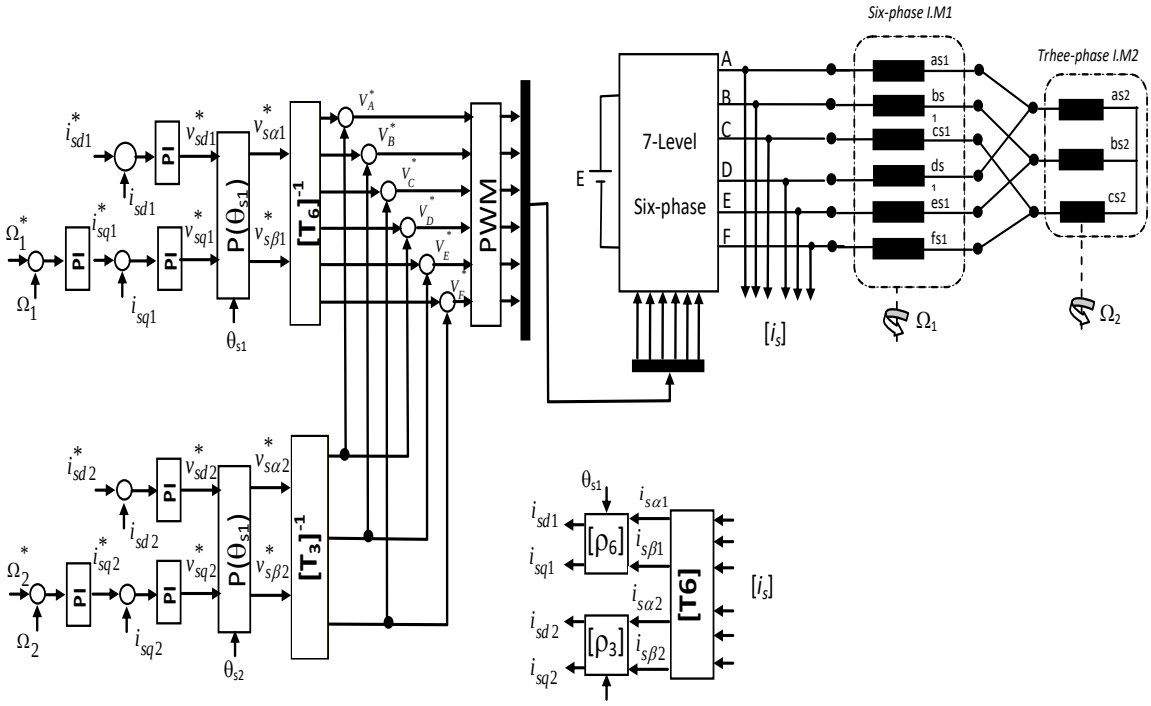

Figure 3. Indirect rotor flux oriented controller for the two-motor drive

Simulation Results

The simulation results of vector speed control of the two series connected machines in (MSCS) is developed in the MATLAB, different simulation results demonstrating the decoupling and independent control of the two machines connected in series are shown in figures 4 and 5. The following simulations are performed using two machines. Many simulation tests are performed in order to verify the independence of the control of the two machines. Fig. 4 shows the operation of the two-machine drive system for many different speeds references with no load at starting up phase. At steady state condition, the two machines are loaded simultaneously or not by their nominal loads. At the beginning, the first machine is running at 20 rad/s; at t=0.5 s, it is accelerated to 50 rad/s, after that, its direction of rotation is reversed to -50 rad/s at t=2s and then stopped at t=3.5s. For the second machine the speed reference is set at 40 rad/s, 100 rad/s,-60 rad/s , and -40 rad/s at t=0 s, 1 s, 2.5 s, 3.5 s, respectively.It is clear too that the start of six phase machine (I.M1) did not have an impact on the speed or on the electromagnetic torque of the three phase machine (I.M2).

As shown from figure 5, the starting and reversing transients of one machine do not have any tangible consequence on the operation of the second machine. The decoupled control is preserved and the characteristics of both machines are unaffected. In the stating phase, the first machine is rotating at 50 rad/s; the other is running at the opposite speed. After that Ω1 is kept at standstill, while the second machine, the speed reference is set at -100 rad/s, 0 rad/s and 100 rad/s at t = 0s, 1s and 2s respectively. It can be seen in Fig. 5 that initiation of a speed transient for the three-phase machine has no impact on the behavior of the six-phase machine since neither the speed nor the stator-axis.

Conclusion

The paper examines a six-phase series-connected two-motor drive system, powered by a five-level six-phase inverter. Modeling and simulation of the two machine-drives and independent vector control of the two machines has been considered. The transposition of two machines has al lowed us to have more degree of freedom on the axes of currents and so ordered two machines independently.The control system multi-machines classic based on vector control with conventional inverters comprise various problems. These problems are overcome by increasing the number of level instead of conventional two-level six-phase inverter.The independent vector control two machines gave good results and helped to decouple control flow and torque for both machines.

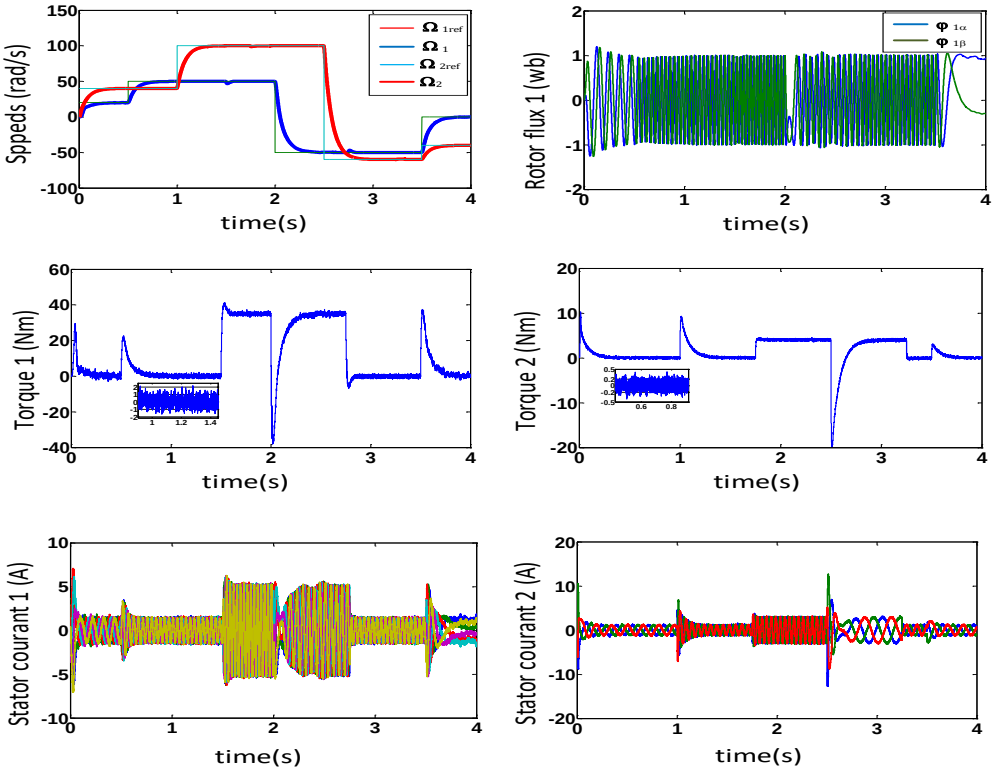

Figure 4. Dynamic responses of series-connected two six-phase system fed by a 7-level six-phase inverter at different reference speeds values.

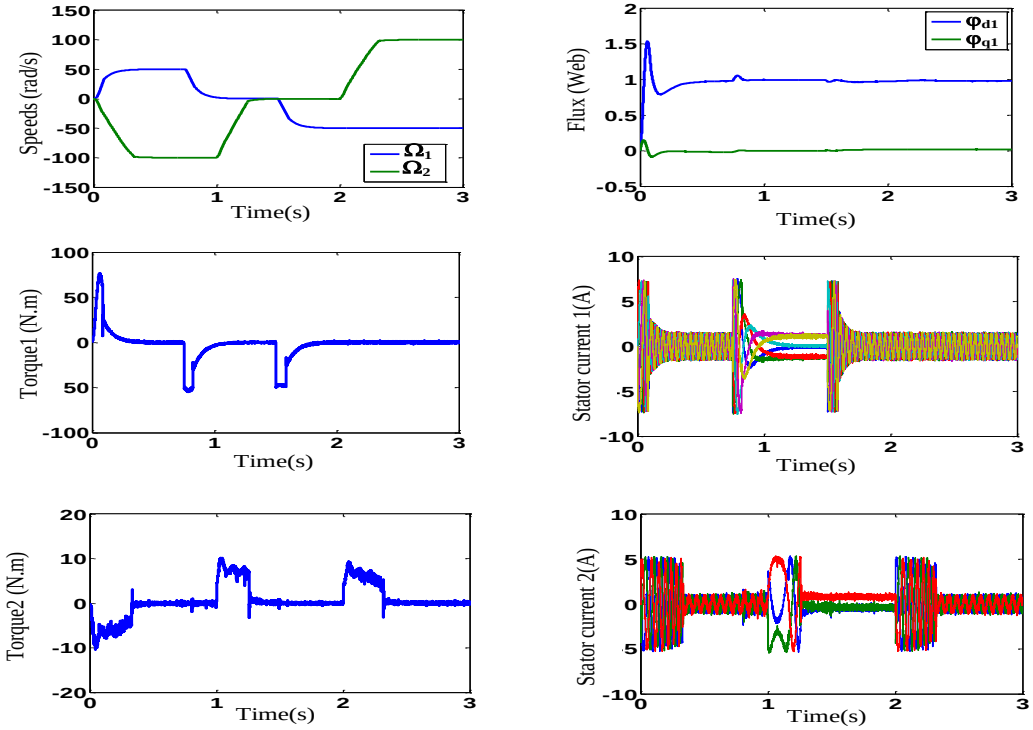

Figure 5. Dynamic responses of series-connected two six-phase system fed by a 7-level six-phase inverter: when the two motors are operating in the opposite directions.

Scientific Ethics Declaration

The authors declare that the scientific ethical and legal responsibility of this article published in EPSTEM Journal belongs to the authors.

Acknowledgements or Notes

* This article was presented as an poster presentation at the International Conference on Technology, Engineering and Science (www.icontes.net) held in Antalya/Turkey on November 16-19, 2023.

References

Bessaad, T., Taleb, R., Bachir, B. & Mellakhi, A. (2015). Modélisation et commande d'un système Multi machines alimentées par un seul convertisseur. *Revue des Energies Renouvelables*, *19*(1), 127 – 136.

Cui, Y., & Kavasseri, R. (2015). A particle filter for dynamic state estimation in multi-machine systems with detailed models. *IEEE Transactions on Power Systems*, *30*(6), 1-9.

Gheraia H., Berkouk E.M., & Manesse G. (2001). Modelling and control of a seven level NPC voltage source inverter, application to high power induction machine drive. *The European Physical Journal*, *15*, 105-115.

Iqbal, A., & Levi, E. (2004). Modeling of a six-phase series-connected two motor drive system. *in Proc. Int. Conf. on Electrical Machines ICEM*. Krakow, Poland

Jyothi1, B. & Rao, M.V.G. (2017). Performance analysis of 3-level 5-phase multilevel inverter topologies. *International Journal of Electrical and Computer Engineering*, *7*(4), 1696 – 1705.

Kim, H., Shin, K., Englebretson, S., Frankand, N., & Arshad, W. (2013). Application areasof Multiphase Machines. *IEEE Conference on Electric Machines & Drives, Chicago, IL, USA*, 172 – 179.

Levi, E. (2008). Multiphase electric machines for variable-speed applications. *IEEE Conference on Industrial Electronics*, *55*(5), 1893 - 1909.

Levi, E., Jones, M., & Vukosavic, S.N. (2004). A novel concept of a multiphase, multi-motor vector controlled drive system supplied from a single voltage source inverter. *IEEE Trans. on Power Electronics*, 19(2), 320-335.

Levi, E., Jones, M., Vukosavic, S.N. (2005). A six-phase series-connected two-motor drive with decoupled dynamic control. *IEEE Trans. on Industry Applications*, *41*(4), 1056-1066.

Mohapatra, K. K., Baiju, M. R., & Gopakumar, K. (2004). Independent speed control of two six-phase induction motors using a single six-phase inverter. *EPE J.*, *14*(3) 49–62.

Odeh, C. I., Obeand, E. S., & Ojo, O. (2016). Topology for cascaded multilevel inverter', *IET Power Electronics*, *9(*5), 921 - 929,

Poh Chiang, L., Donald, G. H., Yusuke, F., & Thomas Lipo, A. (2004). A reduced common mode hysteresis current regulation strategy for multilevel inverters. *IEEE Transactions on Power Electronics*, *19*(1), pp. 192-200.

Ranjan, A., Bhatnagar, P., Sahu, L.K., & Jain, S.(2016). Multilevel inverter topologies with Reduced Device Count: A Review. *IEEE Power Electronics Society*, *31*(1), 135-151,

Saleh, M.A. (2013). *Development of control techniques for direct AC/AC matrix converter fed multiphase multi-motor drive system*. (Doctoral dissertation). Victoria University, Melbourne, Australia,

Author Information

Taieb Bessaad
Hassiba Benbouali University of Chlef
Hssania Chlef, Algeria
Contact e-mail: *t.bessaad@univ-chlef.dz*

Khelifa Khelifi Otmane
Department of Automatic and Electrotechnic, Blida University 1, Algeria

Rachid Taleb
Hassiba Benbouali University of Chlef
Hssania Chlef, Algeria

Aderrahmen Benbouali
Hassiba Benbouali University of Chlef
Hssania Chlef, Algeria

To cite this article:

Bessaad, T., Khelifi Otmane, K., Taleb, R., & Benbouali, A. (2023). Decoupled control of a multi-machines system fed by a single multilevel inverter six-phase. *The Eurasia Proceedings of Science, Technology, Engineering & Mathematics (EPSTEM), 26*, 710-717.

The Eurasia Proceedings of Science, Technology, Engineering & Mathematics (EPSTEM)
ISSN: 2602-3199

The Eurasia Proceedings of Science, Technology, Engineering & Mathematics (EPSTEM), 2023

Volume 26, Pages 718-722

IConTES 2023: International Conference on Technology, Engineering and Science

Effect of H_2/Ar Ratio on the Photoanodic Currents of Graphene/MoS_2 Films

Resat Can Ozden
Eskisehir Osmangazi University

Mustafa Anik
Eskişehir Osmangazi University

Abstract: Enhancing advanced solar energy storage in rechargeable batteries is one of the most critical challenges in clean energy technology aimed at reducing air pollution and dependence on fossil fuels. It has been demonstrated that dye-sensitized electrodes, silicon electrodes, and transition metal-based photoelectrodes can be applied in solar-charged rechargeable batteries to effectively capture visible light. However, potential pollution and cost issues limit their large-scale applications. This study aims to reduce the increased charging potential, caused by the high overvoltage due to the dissolution of compounds such as lithium peroxide and lithium carbonate, through photo-assisted charging. To achieve this goal, efficient graphene/MoS_2 composites are synthesized with chemical vapor deposition (CVD), and their photoelectrochemical properties are characterized to facilitate efficient photocharging. In this context, by positively altering the carrier gas ratio towards H_2 (from 30% to 60%), samples are synthesized at different H_2/Ar ratios to investigate the varying ratio's impact on photoanodic currents.

Keywords: Graphene, Transition metal dichalcogenides, Chemical vapor deposition

Introduction

The MoS_2 material intended to be produced on graphene using CVD is a single-layer transition metal dichalcogenide. It exhibits a range of novel physical properties, including a direct optical bandgap within the visible spectrum and a strong exciton binding energy (Eb), along with distinctive circular dichroism. These characteristics makes MoS2 an appealing semiconductor for use in electronic devices. What's even more fascinating is the recent increase in scientific interest in layer-by-layer stacking of single-layer MX_2 and graphene. This stacking approach has led to the discovery of various captivating physical properties such as superconductivity. Furthermore, it has paved the way for the development of new devices with exceptional performance, such as transistors and light-emitting diodes (Shi et al., 2015).

Chemical vapor deposition (CVD) offers promising opportunities for the synthesis of high-quality graphene films as well as single-layer MoS2 on various substrates, ranging from insulators to metal foils (Shi et al., 2012). In a MoS2/graphene structure with all components produced through the CVD method, graphene offers advantages such as high transparency, high conductivity, and an adjustable work function, while MoS2 provides an advantage with its bandgap (Cai et al., 2018).

The optical absorption of 2D transition metal dichalcogenides is greater than $10^7 m^{-1}$ in the visible range, which means that a 300 nm film will absorb 95% of visible light. However, their conductivity is low, limiting their use in photovoltaic (PV) solar cells. On the other hand, graphene exhibits excellent electrical transport behavior, good transparency, and high carrier mobility, making it a potential candidate for PV solar cells. However, the lack of a bandgap in graphene limits its applicability in PV solar cells. Heterostructures of graphene and 2D

transition metal dichalcogenides can effectively be used in photovoltaics, with graphene serving as a good transparent electrode and transition metal dichalcogenides acting as the photoactive component (Azadmanjiri et al., 2020).

In this study, Ar and H_2 gases were used as carrier gases during CVD synthesis. During the nucleation stage, the density of MoS_2 areas on graphene shows a positive correlation with the Ar flow rate, while extending the growth time can increase the average size of MoS_2 areas. Hydrogen, on the other hand, ensures the survival of graphene at the high temperatures required for MoS_2 crystallization. In this context, the effect of carrier gases on photoanodic currents was investigated by using different H_2/Ar ratios.

Method

Methane was used as the carbon source in graphene production. Graphene is produced on copper substrates and transferred onto Si/SiO_2 wafer. The flowchart for CVD graphene production is provided in Figure 1.

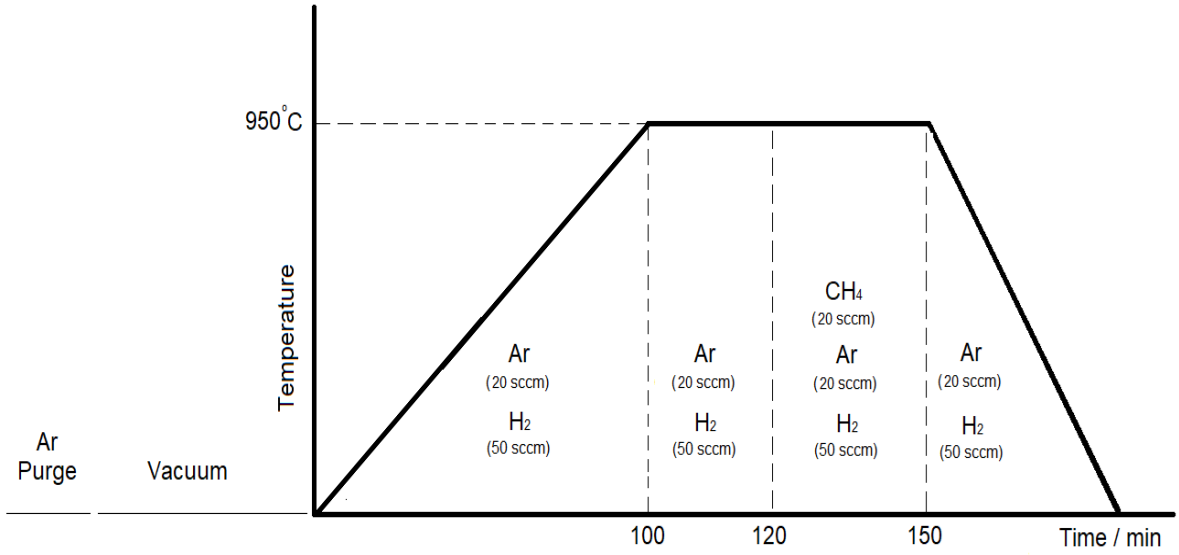

Figure 1. Production flow chart of graphene

Following synthesis of graphene, MoS_2 was performed on a Graphene/Si substrate located inside CVD furnace at 770°C, with various flow rates and the delivery of H_2 (30-40-50-60%), Ar (70-60-50-40%) as carrier gases. The quantities of the solid precursors MoO_3 and S used were 2 mg and 150 mg, respectively. Figure 2 schematically illustrates the positions of the precursors and the substrate inside the CVD furnace.

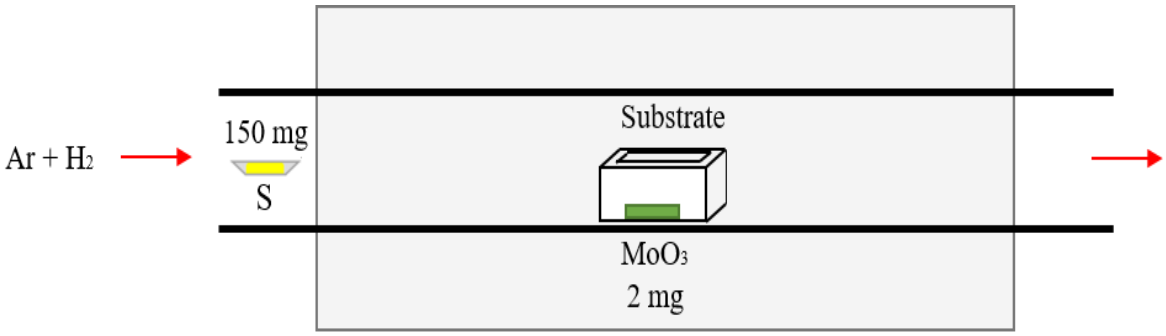

Figure 2. Schematic illustration of the CVD furnace setup for MoS_2 synthesis.

The samples prepared for photo-current experiments were coated on indium tin oxide (ITO) glass and dried in a vacuum-controlled atmosphere at 100°C for 12 hours. Linear Sweep Voltammetry experiments conducted with a GAMRY Reference 3000 potentiostat in a 0.1 M KCl / 0.1 M H2PO4 solution (pH 7), light from a solar simulator (Type A 150 W, 1-3 SUN, Xenon lamp, 1.5 AM Filter) was directed onto the ITO surface (wavelength range of 400 nm - 700 nm). Raman spectroscopy was performed using a RENISHAW inVia Microscope Raman Spectroscopy system, and measurements were carried out at a wavelength of 532 nm.

Results and Discussion

In the Raman spectrum of graphene, you can observe two distinct Raman features known as the G and 2D bands, which are typical characteristics in almost all sp2 materials. The G band, situated at 1583 cm^{-1}, is a first-order scattering phenomenon resulting from the stretching of bonds between all sp2 atom pairs. In contrast, the 2D band, located at 2670 cm^{-1}, is a second-order scattering effect, and the D band is a specific peak at 1350cm^{-1}. Regarding the 2D mode, it connects two zone-boundary phonons, while the D mode links a single phonon and a defect. Consequently, in high-quality, pristine graphene, D band is absent (Childres et al., 2013). In the Raman spectrum of MoS_2, you can observe two characteristic Raman peaks, one at about 405.7 cm^{-1} (A_{1g}) corresponding to the out-of-plane vibration of sulfur atoms and another at around 385.5 cm^{-1} (E^1_{2g}) corresponding to the in-plane vibration of both molybdenum and sulfur atoms (Shi et al., 2015).

The frequency gap (Dk) between the E^1_{2g} and A_{1g} modes in MoS_2 is related to the number of layers. As the thickness of MoS_2 decreases, the difference between the E^1_{2g} and A_{1g} modes also decreases. It was noted that for a single layer MoS_2, the Dk for E^1_{2g} and A_{1g} modes is less than 21 cm^{-1}, around 21-22 cm^{-1} for a double layer, and greater than 25 cm^{-1} for bulk MoS_2. The intensity ratios for E^1_{2g} and A_{1g} are roughly 0.31 for a single-layer MoS_2 and about 0.45 for bulk MoS_2 (Shi et al., 2012).

The Raman spectrum in Figure 3 corresponds to the sample labeled as 30-70, which contains the highest Ar content at 70%. The peaks at 520 and 964 cm-1 are attributed to the Si substrate. The intensity ratio for the E^1_{2g} and A_{1g} modes is 0.45, and the frequency difference (Δk) between these modes is 25 cm^{-1}. These features indicate that the sample exhibits bulk characteristics.

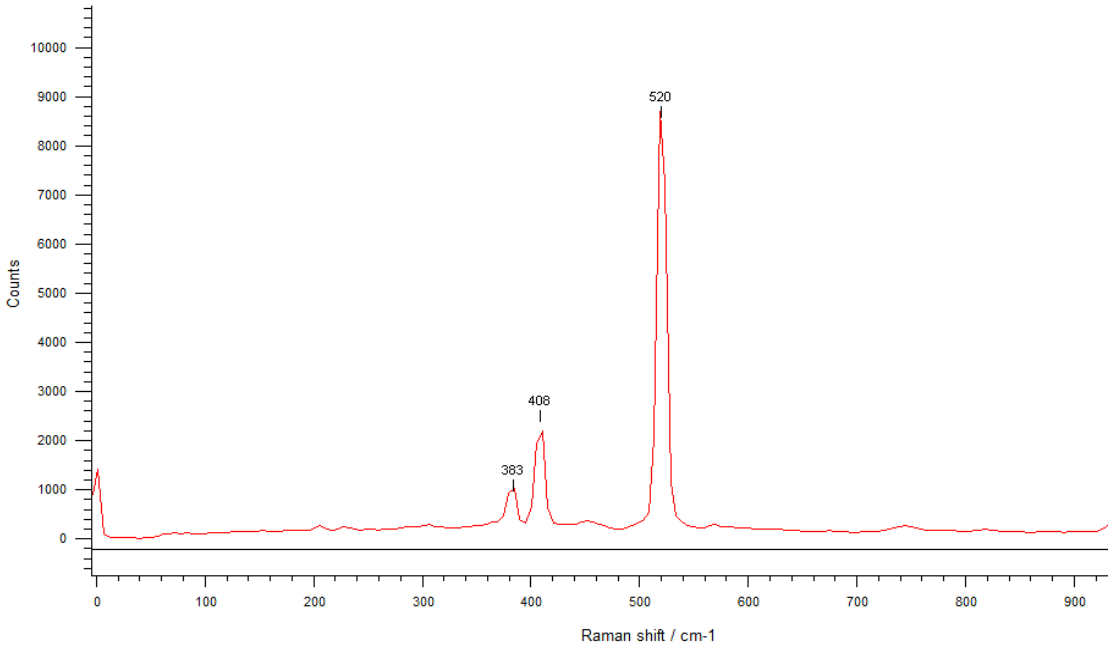

Figure 3. Raman spectrum of %30 H_2 – %70 Ar (30-70) sample

With the increasing H_2 density (60%), the frequency difference between the Raman modes has decreased. In the 60-40 sample, the frequency difference has reached the empirically defined limit of 21 for a single-layer structure. The Raman spectrum for this sample is presented in Figure 4.

The photoanodic currents of the samples were measured using the linear sweep voltammetry method, and the results of these experiments are presented in Figure 5. As can be seen from the figure, in experiments conducted with intermittent potential changes (20 seconds of polarization under light followed by 20 seconds of polarization in dark). The photoanodic currents generated by the samples were clearly detectable. It was observed that the current values of the samples increased as the hydrogen ratios were raised, and it was determined that the samples with the highest hydrogen content (50-50 and 60-40) were capable of producing significantly higher photoanodic currents compared to the other two samples.

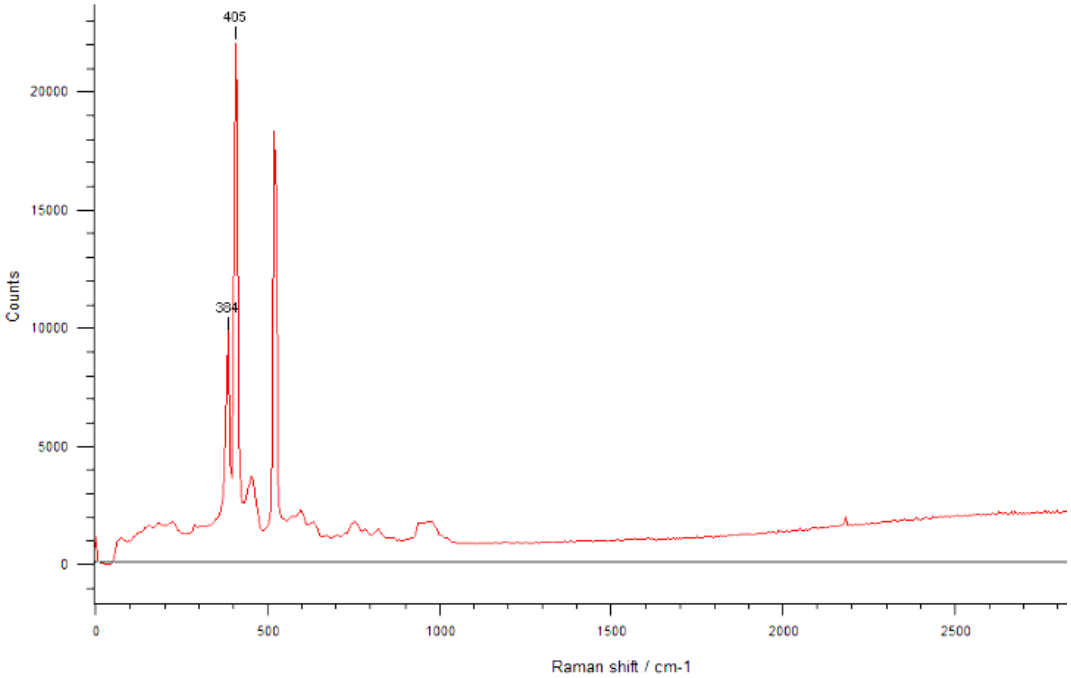

Figure 4. Raman spectrum of %60 H_2 – %40 Ar (60-40) sample

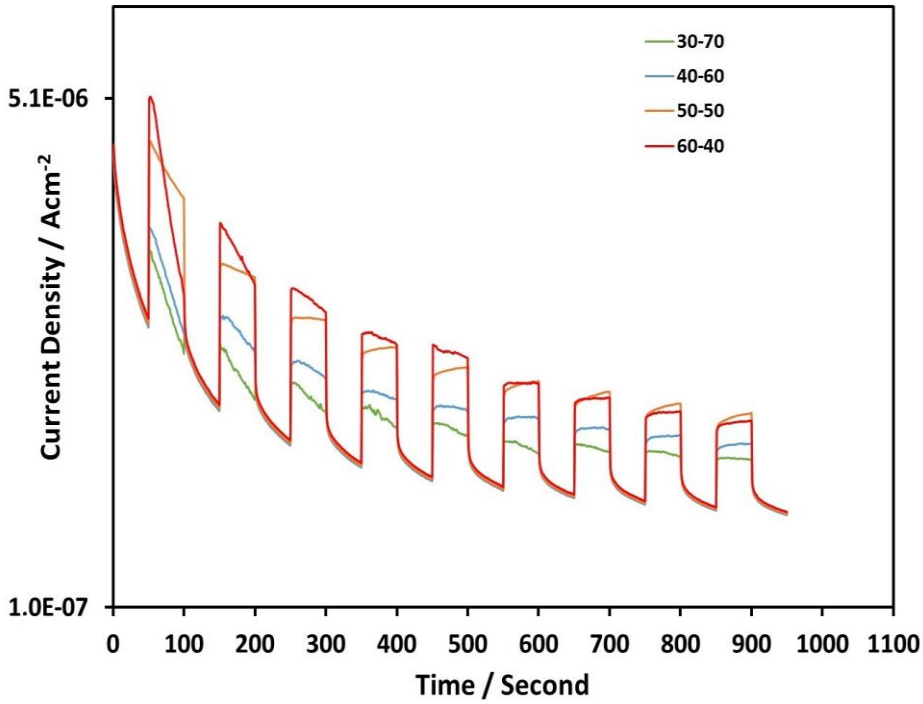

Figure 5. The photoanodic currents of the samples

Conclusion

In this study, graphene/MoS_2 films were produced using the CVD method, and the photoanodic characteristics of the films produced with varying H_2/Ar ratios were determined. According to the results:

1) When the hydrogen content fell below a certain level (50%), the structure was found to be multilayered.

2) Significantly higher photoanodic currents were observed in single-layer or bi-layer coatings. This indicates that single-layer structures offer a distinct advantage in terms of photoanodic performance.

Scientific Ethics Declaration

The authors declare that the scientific ethical and legal responsibility of this article published in EPSTEM journal belongs to the authors.

Acknowledgments or Notes

* This article was presented as an oral presentation at the International Conference on Technology, Engineering and Science (www.icontes.net) held in Antalya/Turkey on November 16-19, 2023.

*Financial assistance from Eskisehir Osmangazi University Research Fund is gratefully acknowledged (Project No: FOA-2022-2332).

References

Azadmanjiri, J., Srivastava, V. K., Kumar, P., Sofer, Z., Min, J., & Gong, J. (2020). Graphene-supported 2D transition metal dichalcogenide van der waals heterostructures. *Applied Materials Today*, *19*, 100600.

Cai, Z., Liu, B., Zou, X., & Cheng, H. M. (2018). Chemical vapor deposition growth and applications of two-dimensional materials and their heterostructures (Review-article). *Chemical Reviews*, *118*(13), 6091–6133.

Childres, I., Jauregui, L. A., Park, W., Caoa, H., & Chena, Y. P. (2013). Raman spectroscopy of graphene and related materials. *New Developments in Photon and Materials Research*, 403–418.

Shi, J., Liu, M., Wen, J., Ren, X., Zhou, X., Ji, Q., Ma, D., Zhang, Y., Jin, C., Chen, H., Deng, S., Xu, N., Liu, Z., & Zhang, Y. (2015). All chemical vapor deposition synthesis and intrinsic Bandgap observation of MoS2/graphene heterostructures. *Advanced Materials*, *27*(44), 7086–7092.

Shi, Y., Zhou, W., Lu, A. Y., Fang, W., Lee, Y. H., Hsu, A. L., Kim, S. M., Kim, K. K., Yang, H. Y., Li, L. J., Idrobo, J. C., & Kong, J. (2012). Van der Waals epitaxy of MoS 2 layers using graphene as growth templates. *Nano Letters*, *12*(6), 2784–2791.

Author Information

Resat Can Ozden
Eskisehir Osmangazi University
Buyukdere Meselik Yerleskesi, 26040 Odunpazarı/Eskisehir
Contact e-mail: *rcanozden@ogu.edu.tr*

Mustafa Anık
Eskisehir Osmangazi University
Buyukdere Meselik Yerleskesi, 26040 Odunpazarı/Eskisehir

To cite this article:

Ozden R.C. & Anik, M. (2023). Effect of H2/Ar ratio on the photoanodic currents of graphene/MoS2 films. *The Eurasia Proceedings of Science, Technology, Engineering & Mathematics (EPSTEM), 26,* 718-722.

The Eurasia Proceedings of Science, Technology, Engineering & Mathematics (EPSTEM)
ISSN: 2602-3199

The Eurasia Proceedings of Science, Technology, Engineering & Mathematics (EPSTEM), 2023

Volume 26, Pages 723-732

IConTES 2023: International Conference on Technology, Engineering and Science

Numerical and Statistical Analysis of the Influence of Damage and Temperature on EMI for Structural Health Monitoring

Bouzitouna Abdallah
Badji Mokhtar Annaba University

Djemana Mohamed
National Higher School of Technology and Engineering

Abstract: Structural health monitoring (SHM) is a process of implementing a system to monitor the structural condition of a structure and assess the structural health. SHM is used to detect damage, predict future performance, and monitor the overall structural health of a structure. Electromechanical impedance (EMI)-based SHM is a non-destructive evaluation (NDE) technique that can be used to detect damage in structures by measuring the changes in the electrical impedance of a piezoelectric transducer that is bonded to the structure. EMI has several advantages over other NDE techniques, including being a passive, local, and relatively inexpensive technique. However, one of the challenges of using EMI for structural health monitoring (SHM) is the effect of damage and temperature on the impedance of the piezoelectric transducer. As the damage and temperature changes, the impedance of the transducer will also change. This can make it difficult to detect small damage if the damage and temperature co-exist on the same structure (aluminum plate). This research presents a numerical and statistical study to investigate the effects of damage and temperature on EMI-based SHM. The numerical model uses ANSYS software to simulate an aluminum plate at different temperatures. The findings have shown that both damage and temperature have a significant effect on the impedance of the transducer. However, the study has also demonstrated that it is still possible to detect structural damage using EMI even under varying damage and temperature conditions. This underscores the robustness of EMI-based damage detection methodologies in practical applications.

Keywords: Statistical analysis, Finite element modeling, Structural health monitoring (SHM), Damage detection, Electromechanical impedance (EMI).

Introduction

Structural Health Monitoring (SHM) has emerged as a critical field within structural engineering and materials science, aiming to enhance the safety, reliability, and longevity of various civil, mechanical, and aerospace structures. Central to SHM is the utilization of advanced techniques for non-destructive evaluation, and one such powerful approach is Electromechanical Impedance (EMI).

EMI is a technique that employs piezoelectric transducers to monitor the structural integrity of systems by analyzing the impedance signatures of materials and structures. It has gained increasing attention due to its capability to provide real-time data and early damage detection, making it a valuable tool in predicting and preventing structural failures. The performance and reliability of engineering structures are intimately linked to the material properties, operational conditions, and the ability to detect potential issues promptly.

Two crucial aspects in this context are the understanding of temperature effects on structural materials and the early detection of small damages, particularly in aluminum plates. The influence of temperature variations on the behavior of materials is a topic of significant importance in fields ranging from aerospace to civil

engineering. The mechanical, thermal, and even electrical properties of materials can change in response to temperature fluctuations, which, in turn, can impact the structural integrity and safety of components. Concurrently, the early detection of small damages in aluminum plates is a fundamental concern for ensuring the continued reliable performance of structures.

Recently, there has been a growing focus on addressing the impacts of temperature in scientific experiments. This challenge has been particularly significant in the context of various practical models, some of which include: Tian et al. (2017) investigated the electromechanical impedance (EMI) signature of aluminum plates with small damages under temperature variation. They found that the EMI signature of a damaged plate is shifted to the left as the temperature increases. Zhou et al. (2021) developed a damage detection system for aluminum plates using EMI signature monitoring under variable temperature conditions. They found that the EMI signature of a damaged plate is different from the EMI signature of an undamaged plate, even under variable temperature conditions. Hu et al. (2022) investigated the temperature effect on EMI-based damage detection of aluminum plates with cracks. They found that the temperature effect on the EMI signature of a cracked plate is significant. Liu et al. (2020) developed a temperature-compensated EMI-based damage detection system for aluminum plates with cracks. They found that their temperature-compensated EMI-based damage detection system was able to accurately detect cracks in aluminum plates under variable temperature conditions. Chen et al. (2019) developed a modified whale optimization algorithm for temperature compensation in EMI-based damage detection of aluminum plates with cracks. They found that their modified whale optimization algorithm was able to accurately compensate for temperature effects in EMI-based damage detection systems.

Detecting and addressing small damages before they escalate into critical issues is vital in preventing costly repairs or, worse yet, catastrophic failures. This paper serves as a comprehensive exploration of the dual concerns related to temperature effects on structural materials and the early detection of small damages in aluminum plates. We outline the objectives and methodology, which aim to shed light on the complex interplay between temperature and structural materials while offering practical insights into damage detection techniques and mitigation strategies.

Structural Health Monitoring Based on Electromechanical Impedance (EMI)

Principal structural health monitoring based on electromechanical impedance (EMI) is a non-destructive testing (NDT) method that uses piezoelectric transducers to monitor the health of structures. The principle is based on the fact that the electrical impedance of a piezoelectric transducer changes when it is bonded to a structure and the structure undergoes mechanical damage.

EMI-based structural health monitoring systems typically consist of a network of piezoelectric transducers that are bonded to the structure to be monitored. The transducers are excited with an alternating electric field and the electrical impedance of each transducer is measured. The electrical impedance measurements are then compared to a baseline set of measurements taken when the structure is known to be in good condition. If there is a significant change in the electrical impedance of any of the transducers, it indicates that there may be damage in the structure. EMI-based structural health monitoring systems have a number of advantages over other NDT methods. They are non-destructive, relatively inexpensive, and easy to implement. They are also very sensitive to small or incipient damage, making them ideal for detecting damage early on.

Finite Element Model for Aluminum Plate

Finite element (FE) analysis was performed deterministically to model a circular AL2024 aluminum plate in free suspension with PZT transducers bonded to its surface by a thin adhesive layer. The adhesive was factored into the model. The geometry of the thin plate with bonded piezoelectric wafer active sensors (PWAS) was $r = 50.08\,mm, h = 0.835\,mm, r_a = 4\,mm$, and $r_b = 1\,mm$ (Figure 01). The thickness of the adhesive layer was $100\ \mu m$. The PZT was made of PZT-5A. A SOLID186 20-node parabolic element was used to build the structure, and a SOLID226 element was used for the PZT models. The SOLID226 element is a coupled-field element with thermoelectric, piezoresistive, and piezoelectric capabilities, making it an excellent choice for modeling complex problems. A SOLID95 element was used to model the adhesive layer, which also includes the same full electromagnetic (EM) coupling as piezoelectric materials. The finite element model of the thin plate with bonded PWAS is shown in the Figure 02.

To assess the accuracy of the proposed FE model, it was subjected to a validation test benchmarked from Rugina et al. (2014) (Figure 03). Validation was accepted based on the approximation of curve trend and magnitude, creating a close reproduction of the experimental results.

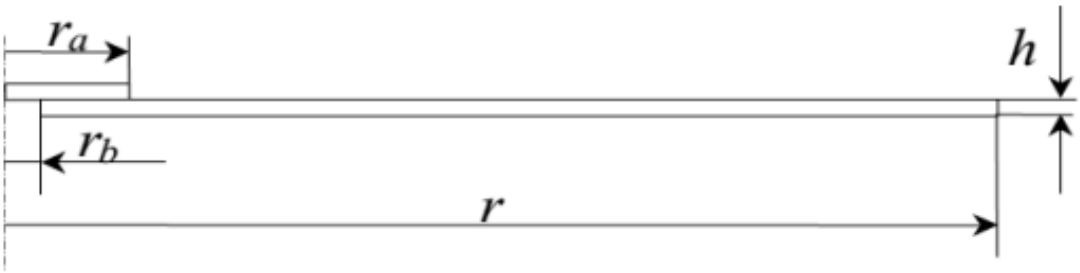

Figure 1. The geometry of the thin plate with bonded piezoelectric wafer active sensors (PWAS)

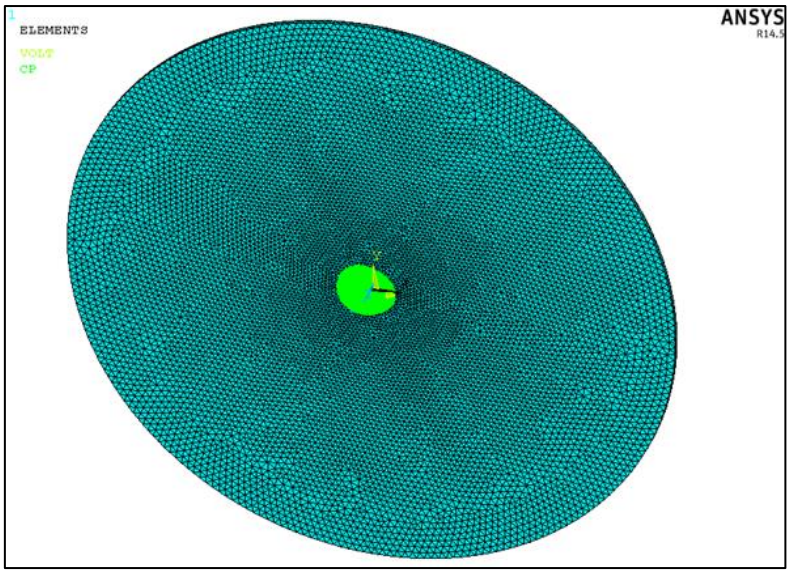

Figure 2. FE model of the thin plate with bonded piezoelectric PWAS

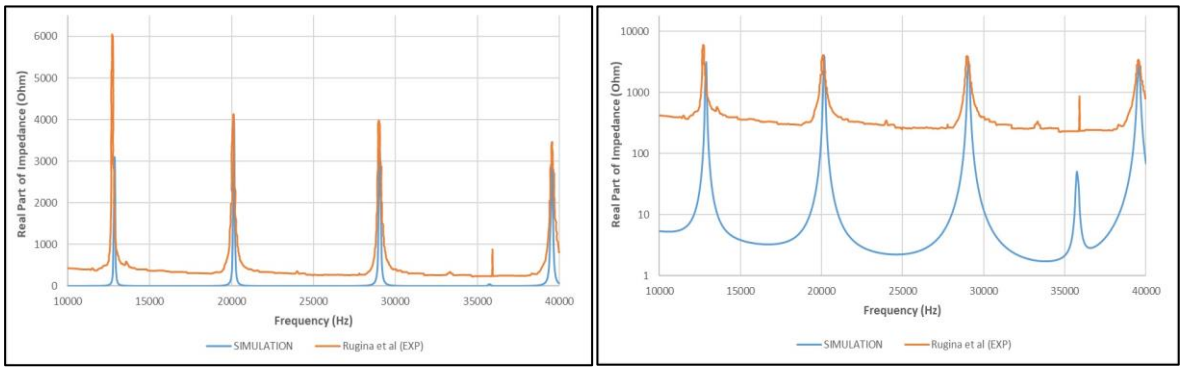

Figure 3. Comparison between the simulation and experimental results (Rugina et al.,2014) for the circular aluminum plate

In order to evaluate the reliability and accuracy of the finite element model proposed in this study, it underwent a validation process, which was based on a benchmark test drawn from the research conducted by Rugina et al. (2014) The validation was deemed successful when the model demonstrated a close approximation of the experimental results, both in terms of reproducing the trend of the data and closely matching the magnitudes observed in the original experiments. The noticeable difference is only observed in terms of the upward shifting of the experimental results due to the usage of a resistor (Djemana et al., 2016) This validation process serves as a critical step in affirming the credibility and suitability of the proposed finite element model for simulating and analyzing the behavior of the studied system.

Effect of Temperature on Aluminum Plate

In the pursuit of a comprehensive understanding of the temperature effects on the electromechanical impedance (EMI) of aluminum plates, a series of experiments was conducted, applying varying temperature conditions to the material between 25 and $70°C$. Figure 04 shows the real part of the electromechanical impedance signatures for aluminum plate with different temperature for frequencies from 10 to 40 kHz.

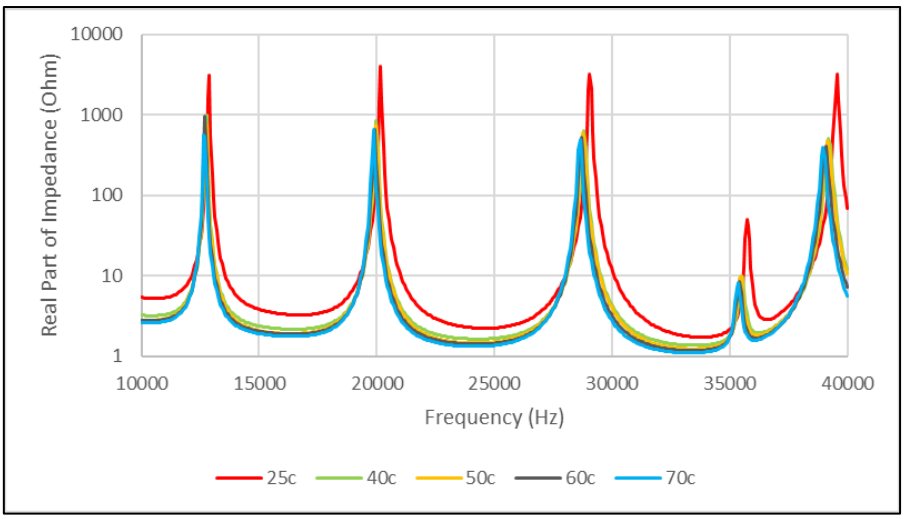

Figure 4. Real part of the electromechanical impedances resulting from temperature changes

In Figure 4, a notable frequency shift can be observed in the electromechanical signature as the temperature is change. Specifically, an increase in temperature leads to a leftward shift in the signature. These shifts are indicative of significant alterations in the material's behavior, which can be attributed to the changing thermal conditions. Additionally, alongside these frequency shifts, variations in electrical resistance are evident, further underscoring the intricate relationship between temperature and the material's impedance characteristics. The presence of vertical shifts in the signature further emphasizes the dynamic nature of the material's response to changing temperature conditions, offering valuable insights into the nuanced effects of thermal fluctuations on its electromechanical behavior.

Co-Existence of Crack Damage and Temperature on Aluminum Plate

The impact of additional types of damage delved into examining, specifically, both structural damage and temperature variations. As part of this exploration, we conducted experiments where we simultaneously introduced crack damage and controlled temperature change with $40°C$. In this sub section, structural damage was simulated. Two different sizes of the cracks took with the form of a $0.3mm$ wide, $20mm$ long (**crack 1**) and $0.15mm$ wide,$10mm$ long (**crack 2**) is the following (Figure 05).

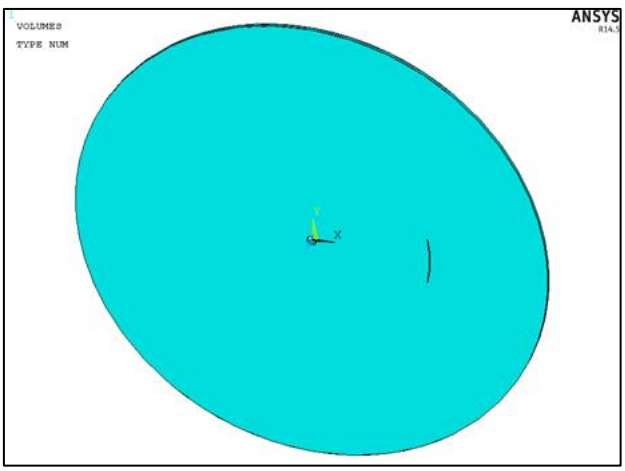

Figure 5. FE model of aluminum thin plate with crack

This approach aimed to simulate more realistic scenarios, mirroring real-world conditions where multiple factors can influence the behavior of structural components. By combining these forms of damage and temperature fluctuations, we sought to demonstrate the capabilities of EMI systems in detecting and characterizing such complex issues. Figure 06 shows the real part of the electromechanical impedance signatures for aluminum plate with different crack damage at $40°C$ for frequencies from 10 to 40 kHz.

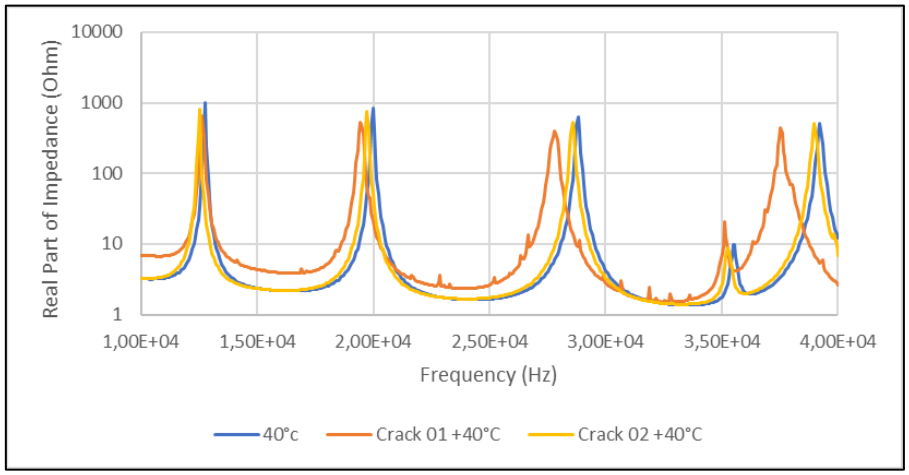

Figure 6. Real part of the electromechanical impedances with different crack damage at 40°C

Observing the data, it becomes apparent that the electromechanical signature associated with the presence of temperature on the cracked plate exhibits a decrease when compared to the signature corresponding solely to temperature variations. Furthermore, this signature undergoes a discernible shift towards the left side. This phenomenon can be attributed to the decreasing stiffness of the structure when subjected to temperature fluctuations. The decrease in stiffness influences the structural response, resulting in alterations in the impedance signature and its leftward shift. This observation underscores the sensitivity of the electromechanical impedance technique in detecting structural changes induced by varying temperature conditions, ultimately contributing to a deeper understanding of the system's behavior and mechanical integrity.

Mathematics and Statistical Analysis

The parameters of clearance factor, crest factor, and impulse factor for three different signals: 40°C and two cracks. This is an interesting observation, as it suggests that these three signals may have a common underlying cause. One possible explanation for this observation is that the three signals are all generated by the same physical process, but under different conditions. For example, the cracks may be caused by the same type of stress, but at different levels of severity. Another possibility is that the three signals are all generated by different physical processes, but that these processes have similar statistical properties. This could be the case, for example, if the three signals are all generated by random noise.

Further research is needed to determine the exact cause of the identical signal parameters in these three signals. However, the observation itself is intriguing and suggests that there may be a deeper connection between these signals than is currently understood. Other signal parameters, such as peak amplitude, mean value, standard deviation, skewness, kurtosis, spectral distribution, autocorrelation function, and power spectral density, may also be identical in the three signals. These parameters can all be used to characterize the shape and frequency content of a signal. By comparing these parameters for the three signals, we may be able to identify additional similarities or differences between them. If the other signal parameters are also identical in the three signals, this would further support the hypothesis that they have a common underlying cause. It would also suggest that the identical signal parameters could be used to develop new methods for crack detection or other diagnostic tasks.

Statistical Analysis

Statistical analysis of impedance signals can be used to detect cracks in materials by identifying changes in the mean, range, standard deviation, skewness, and kurtosis of the impedance signals. These changes are caused by the presence of a crack disrupting the flow of current through the material. By comparing the statistical parameters of the impedance signals for the cracked material to those for a reference material, it is possible to

identify the presence of cracks and even estimate their size and severity. This method is non-destructive, relatively inexpensive, and can be used to inspect a wide variety of materials.

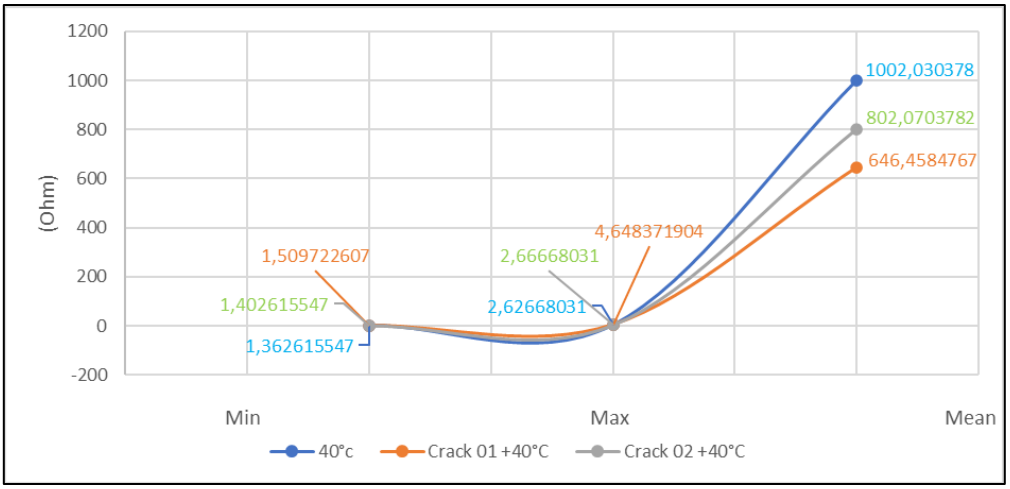

Figure 7. Max, min and mean of signal 40°C, Crack 1 & 2

The graph shows that the mean value of the real part of impedance increases with increasing size of the crack. This is because the presence of a crack reduces the cross-sectional area of the plate, which increases the resistance of the plate. It also shows that the range of the real part of impedance (i.e., the difference between the maximum and minimum values) increases with decreasing size of the crack. This is because the presence of a crack introduces a non-uniformity in the distribution of current, which leads to a wider range of impedance values. An increase in the mean value of the real part of impedance and a decrease in the range of the real part of impedance are both indicative of the presence of a crack. The size of the crack can be estimated by comparing the mean and range values to those for a plate with no crack. This information could be useful for developing non-destructive testing (NDT) methods for detecting cracks in materials. By measuring the impedance of the material at different frequencies and temperatures, it may be possible to identify the presence of cracks and even estimate their size and severity.

Mathematical Analysis

Detecting crack damage in aluminum plates with temperature is a challenging task, as temperature can have a significant impact on the properties of aluminum and the propagation of waves through the material. However, there are a number of methods that can be used to detect crack damage in aluminum plates, even in the presence of temperature variations. Detecting crack damage in aluminum plates with temperature is a challenging task, as temperature can have a significant impact on the properties of aluminum and the propagation of waves through the material. However, there are a number of methods that can be used to detect crack damage in aluminum plates, even in the presence of temperature variations. However, it is important to note that the accuracy and reliability of each method will depend on a number of factors, such as the type of crack damage, the temperature of the plate, and the specific testing method used, alignment technique for the effects of temperature variation can be accomplished through a variety of methods. (Park et al.1999) modified the RMSD index to compensate for shifts in both frequency and amplitude. Our approach is instead similar to a previous study (Park et al.1999).

The root mean square deviation (RMSD) index is a statistical measure of the similarity between two or more sets of data. It is calculated by taking the square root of the average squared difference between the two sets of data. The lower the RMSD index, the more similar the two sets of data are. The RMSD index can be used to compare two signals in a number of different ways. For example, it can be used to compare the waveforms of two signals, the amplitudes of two signals, or the frequencies of two signals. The specific way in which the RMSD index is used depends on the specific application. Here is an equation for the RMSD index:

$$RMSD = \sqrt{\frac{1}{N}\sum_{i=1}^{N}(x_i - y_i)^2}$$

where:

RMSD is the root mean square deviation
$\boldsymbol{N}$ is the number of samples in the two signals
$\boldsymbol{x_i}$ is the *i*-th sample of the first signal
$\boldsymbol{y_i}$ is the *i*-th sample of the second signal

Figure 08 shows the impedance of the PZT transducer for a healthy beam condition at a regulated temperature of 40°C with the proposed alignment method for the temperature effects.

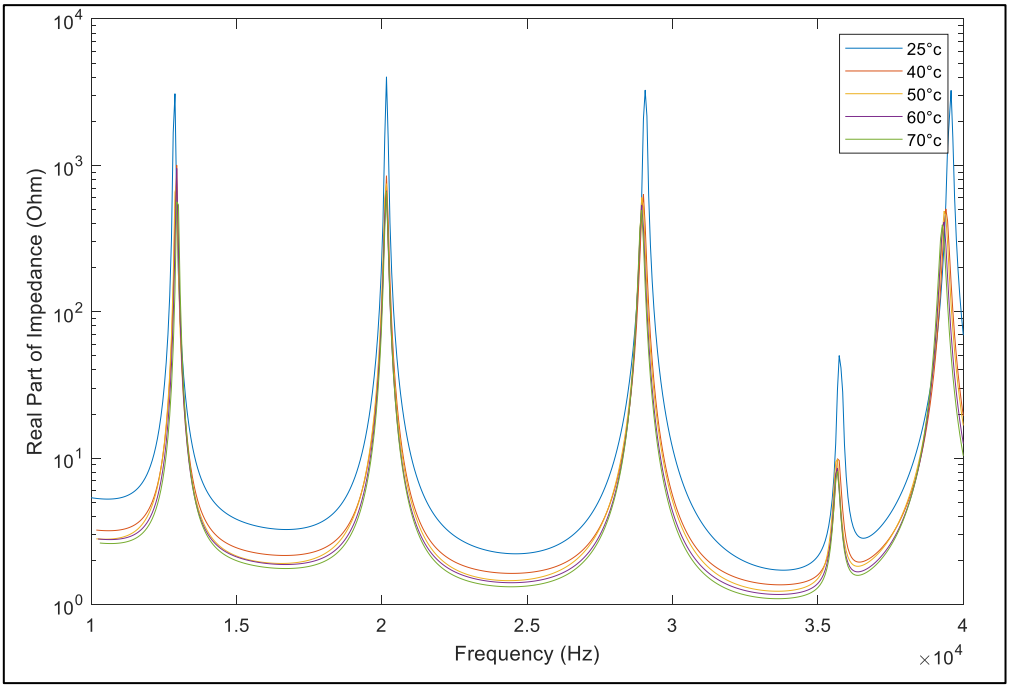

Figure 8. Alignment method for real part of the electromechanical impedances under temperatures varying

The figure shows the impedance of a PZT transducer for a healthy beam condition at a regulated temperature of 40°C, with the proposed alignment method for the temperature effects. This suggests that the proposed alignment method is effective at compensating for the effects of temperature variations on the electromechanical impedance (EMI) signature. Alignment method can be very effective in reducing or eliminating the effects of temperature on EMI signatures. This is important for crack detection in aluminum plates, as it allows crack damage to be detected even in the presence of temperature variations.

The proposed alignment method could be used to develop non-destructive testing (NDT) methods by measuring the impedance of a material at different frequencies and temperatures, and then aligning the impedance spectra using the proposed method, it may be possible to identify the presence of cracks and even estimate their size and severity. The RMSD index is a powerful tool for comparing two signals. It is a simple and robust measure of similarity that can be used in a variety of applications. Its index is selected for this purpose because it is uniquely sensitive to the shape of the electromechanical impedance (EMI) signature, rather than to variations in its electrical impedance amplitude. In other words, the RMSD index is insensitive to changes in the overall strength of the EMI signal, but it is sensitive to changes in the pattern of the signal. This makes it ideal for isolating and quantifying the influence of temperature-induced EMI variations. By focusing on the shape of the impedance signature, the RMSD index can effectively distinguish between the changes caused by changes in temperature conditions and those caused by structural loads or damage.

Figure 09 shows that the EMI signatures of damaged and healthy aluminum plates at 40°C were similar enough to make damage difficult to diagnose at that temperature. According to Figure 11 of Figures, the compensation technique made the results significantly easier to interpret. The shifts in the signatures were eliminated and the peaks were perfectly aligned with the baseline result. Additionally, the RMSD indices at 40°C (Figure 12) were very low, suggesting that smaller damage could be detected with an appropriately set threshold. The results were acceptable across the entire temperature range, even at the upper end. Temperature effects remain a critical issue in EMI structural health monitoring, especially for detecting nascent or small damage. Effective compensation techniques are essential for the continued development of this field.

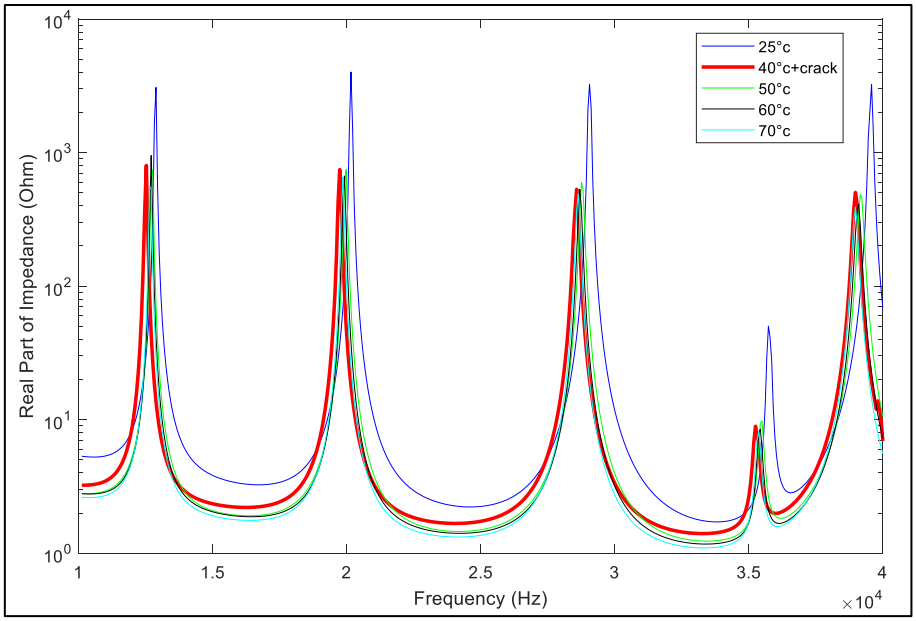

Figure 9. Real part of the electromechanical impedances with crack

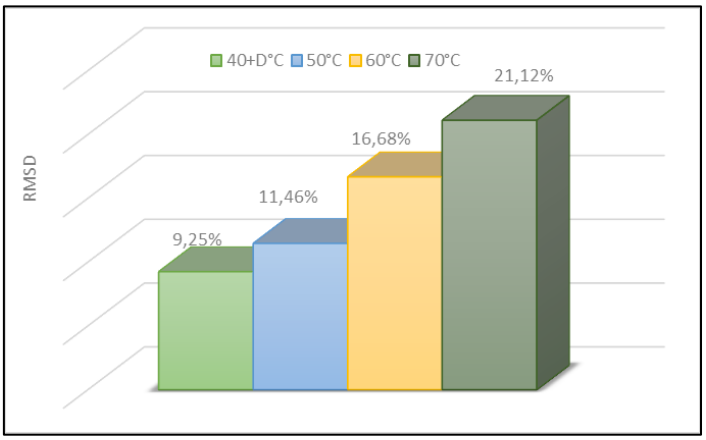

Figure 10. RMSD before alignment under temperatures varying

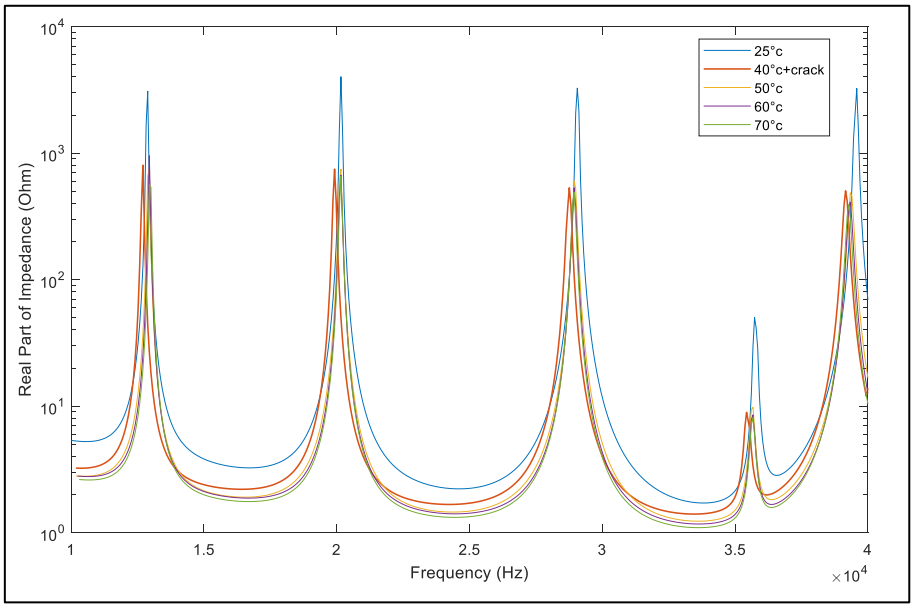

Figure 11. Alignment method for real part of the electromechanical impedances with crack

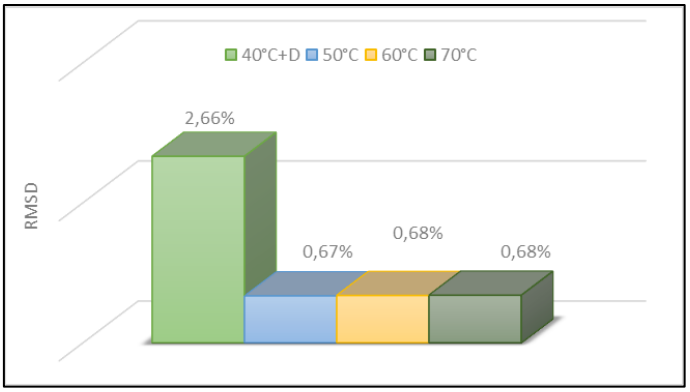

Figure 12. RMSD after alignment with crack

Conclusion

In conclusion, our study has provided valuable insights into the complex interplay between temperature variations and the presence of small cracks in aluminum plates. Through a combination of mathematical and statistical analyses, we have investigated the effects of temperature and damage coexisting in the same structural element, with a particular focus on the early detection of small cracks in the presence of thermal fluctuations. These investigations sought to unravel the intricate interplay between temperature and EMI, recognizing that temperature fluctuations can induce notable changes in the mechanical and electrical properties of structural materials.

By systematically subjecting aluminum plates to different temperature regimes, we aimed to scrutinize how alterations in temperature impact the impedance signatures of the plates. This rigorous approach allowed us to discern the shifts in resonance frequencies, impedance magnitude, and phase characteristics under changing thermal conditions. Furthermore, the study explored the sensitivity of EMI as a non-destructive evaluation technique to temperature variations. The results not only contribute to the fundamental understanding of the temperature-EMI relationship but also have practical implications for the assessment of structural health in real-world applications exposed to varying environmental conditions.

Recommendations

Recommendations for future work on EMI-based SHM and mathematical analysis:

- Develop signal processing and data analysis techniques to extract features from impedance signals that are more correlated with the presence of cracks. This would improve the accuracy and reliability of EMI-based SHM systems.
- Develop theoretical models to predict the impedance of a cracked material in more complex geometries. This would allow EMI-based SHM systems to be used to inspect a wider range of structures and components.

Scientific Ethics Declaration

The authors of this article, published in the EPSTEM journal, solemnly affirm our unwavering dedication to upholding the highest scientific, ethical, and legal standards in the conduct and dissemination of our research. We recognize our responsibilities as researchers, not only to advance knowledge but also to do so with integrity and in compliance with established ethical and legal guidelines.

Acknowledgements or Notes

* This article was presented as a poster presentation at the International Conference on Technology, Engineering and Science (www.icontes.net) held in Antalya/Turkey on November 16-19, 2023.

References

Chen, C., Huang, S., & Wu, F. (2019). Temperature compensation for electromechanical impedance-based damage detection of aluminum plates with cracks using a modified whale optimization algorithm. *Journal of Intelligent Manufacturing*, *30*(8), 2993-3005.

Djemana, M., & Hrairi, M. (2016). Modelling and simulation of impedance-ased damage monitoring of structures. *International Journal of Simulation Model, 15*(3), 395-408.

Hu, K., Lin, X., Chen, H., & Liu, Y. (2022). Temperature effect on electromechanical impedance-based damage detection of aluminum plates with cracks. *Mechanical Systems and Signal Processing*, *173*.

Liu, Z., Sun, Z., Wang, S., & Li, X. (2020). Temperature-compensated electromechanical impedance-based damage detection for aluminum plates with cracks. *IEEE Transactions on Instrumentation and Measurement*, *70*, 1-10.

Park, G., Kabeya, K., Cudney, H. H., & Inman, D. J. (1999). Impedance-based structural health monitoring for temperature varying applications. *JSME International Journal Series a Solid Mechanics and Material Engineering*, *42(*2), 249-258.

Rugina, C., Toader, A., Giurgiutiu, V., & Ursu, I. (2014). The electromechanical impedance method for structural health monitoring of thin circular plates. *Proceedings of the Romanian Academy*, *Series A, Mathematics, Physics, Technical Sciences, Information Sciences 15*(3), 272-282.

Tian, Z., Yu, L., & Bicanic, N. (2017). Electromechanical impedance-based structural health monitoring of plates under temperature variation. *Journal of Sound and Vibration*, *398*, 28-39.

Zhou, Y., Zhang, S., Wu, W., & Yan, Y. (2021). Damage detection for aluminum plate using electromechanical impedance method under variable temperature conditions. *Structural Health Monitoring*, *20*(5), 1293-1312.

Author Information

Bouzitouna Abdallah
National Higher School of Technology and Engineering, Annaba, Algeria
2000 pedagogical seats Sidi Amar, Annaba, Algeria
Contact e-mail: *a.bouzitouna@ensti-annaba.dz*

Djemana Mohamed
National Higher School of Technology and Engineering, Annaba, Algeria
2000 pedagogical seats Sidi Amar, Annaba, Algeria

To cite this article:

Abdallah, B.., & Mohamed, D.. (2023). Numerical and statistical analysis of the influence of damage and temperature on EMI for structural health monitoring. *The Eurasia Proceedings of Science, Technology, Engineering & Mathematics (EPSTEM), 26*, 723-732.

The Eurasia Proceedings of Science, Technology, Engineering & Mathematics (EPSTEM)
ISSN: 2602-3199

The Eurasia Proceedings of Science, Technology, Engineering & Mathematics (EPSTEM), 2023

Volume 26, Pages 733-740

IConTES 2023: International Conference on Technology, Engineering and Science

Modern Control of a Power Supply Based on a Matrix Converter for Water Disinfection by UVC Radiation

Aissa Bokhtachte Aicha
Hassiba Benbouali University of Chlef

Latroch Maamar
Hassiba Benbouali University of Chlef

Toualbia Asma
Hassiba Benbouali University of Chlef

Djafer Lemya
Hassiba Benbouali University of Chlef

Benallou Maamar
Hassiba Benbouali University of Chlef

Abstract: Water, an essential resource, has been facing gradual deterioration in quality over an extended period. Water treatment has emerged as a critical concern, with a long-standing acknowledgment of the importance of preserving and appreciating this precious resource. UV-C technology has proven to be an ideal solution that effectively addresses these twin needs. The core principle of UV bactericidal treatment revolves around generating ultraviolet rays within a treatment chamber filled with water. Consequently, ensuring a dependable power source for low-pressure mercury-argon discharge lamps has become imperative to guarantee the efficiency of UV-C disinfection.The primary goal of this study is to supply our discharge lamp with a current source that produces a sinusoidal current at its output, featuring a frequency of 50 kHz and an effective value of 0.65 A. Electronic ballasts enable lamps to enhance radiation quality by operating at high frequencies, and the selection of a power supply is a response to this specific challenge.The aim of this research centers on the utilization of a single-phase matrix converter. The bidirectional switching cells within this converter offer frequency-related advantages. To achieve the desired magnitude and frequency, we employed a PWM control strategy. Subsequently, we implemented a linear current adjustment approach using two controllers: a Proportional-Integral (PI) controller and a Generalized Predictive Control (GPC) in the RST polynomial form. This was done to ensure a high-quality current source with the desired waveform and low Total Harmonic Distortion (THD).The research outcomes have led to environmental simulations conducted using Matlab/Simpower system and Matlab/Simulink.

Keywords: Disinfection, UV-C Lamp, Electronic ballast, Matrix converter, Predictive control (GPC).

Introduction

Ultraviolet radiation at a wavelength between 100 and 400 nm has germicidal properties highlighted from the end of the 19th century. These properties specific to UV-C (200-280 nm), result from an action on the nucleic acids of micro-organisms which show variable sensitivity to this radiation depending on their composition. UV radiation is produced by generators: UV lamps, discharge lamps, made up of rare gas (argon, galium, etc.) and mercury vapor (Costache, 2000). These lamps, intended for the purification and sterilization of air and water and

- Selection and peer-review under responsibility of the Organizing Committee of the Conference

for the disinfection of small surfaces, have an electrical operating point, characterized by a voltage/current couple, which depends on their geometry and the gases used, but also of the electrical source that supplies them. Each operating point is therefore linked to the couplings between the power supply and the electrical discharge. Power supplies are studied in electronics and electrical engineering laboratories in order to characterize their electrical behavior and carry out their design. These power supplies are well modeled and their development relies heavily on simulation (Aissa Bokhtache et al., 2016), (Aissa Bokhtache et al., 2015). The models used make it possible to simulate the electrical behavior (on the basis of voltage and current quantities). We have endeavored to tackle the problem of the study of a "discharge lamp intended for sterilization, powered by electronic ballast" system. We contented ourselves with studying the modeling and control of the electronic ballast supplying the low-pressure mercury-argon discharge lamp under the best conditions in order to generate the maximum UV radiation at 253.7 nm with high germicidal power (Toumi et al., 2013). The main objective of the use of the matrix converter, in this work, is the replacement of conventional converters with DC intermediate circuits, for the power supply of the lamp, by a converter carrying out the direct AC/AC conversion. The article is therefore organized in such a way as to deal successively with the different points of the problem. it develops two axes: modeling and control. In order to study the behavior of the lamp-converter association, we simulate and visualize the current and the arc voltage of the lamp as well as their harmonic spectra for the desired frequency which is 50KHz (by increasing the frequency of power supply, a better luminous efficiency is obtained) The effective value of the arcing current will be 650 mA, a value which will later constitute the reference in the regulation loop. The switch control signals are obtained by the PWM control. We will simulate the "converter-lamp" system in open loop, first in order to study the dynamic behavior of the system, and then in closed loop for the regulation of the lamp current. In this context, this article is the subject of a comparison of the results of simulation in particular on the plan "rate of harmonic distortion (THD)" with a traditional regulator (PI) and a GPC regulator in the polynomial form RST, in the purpose of improving the performance of the converter.

Discharge Lamp-Electronic Ballast Description and Modeling of the System

The electric circuit model of the discharge lamp consists of two main components: the arc resistor "Rarc" and the filament resistors "*rf*" for each cathode. In the model, the arc resistor "*Rarc*" represents the electrical characteristics of the lamp's arc, which depend on the arc power and temperature. This resistor is used to simulate the behavior of the discharge within the lamp (Aissa Bokhtache et al. , 2021) .

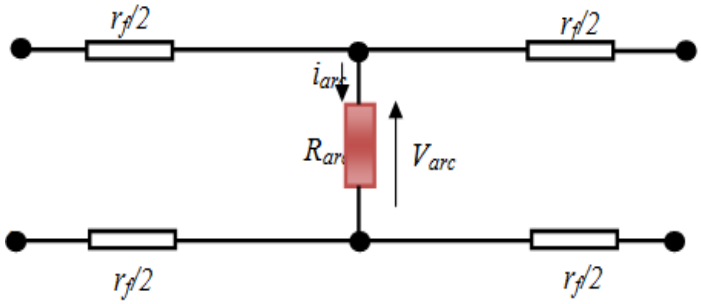

Figure1**.** Model of the electric circuit of the gas-discharge lamp.

Figure 2 summarizes the system studied: Discharge lamp-electronic ballast powered by a converter.

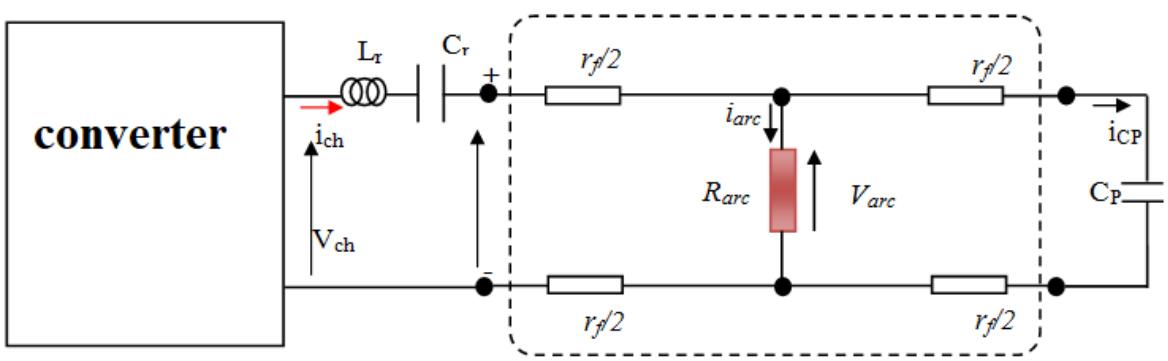

Figure 2. Equivalent circuit of electronic ballast-discharge lamp with converter.

Characteristics of the Load Used

The load used in the simulation is a specific discharge lamp described in references (Aissa Bokhtache et al. , 2017). The table below presents the main characteristics of the lamp:

Table 1. Characterıstıcs of the dıscharge lamp-electronıc ballast assembly (Aissa Bokhtache et al., 2021)

Variables	values
C_r	147 nF/ 250 V
C_p	8.2 nF/ 600 V
L_r	1.08 mH
P_{Lamp}	65 W
f	50 KHz
R_{arc}	170.769 Ω
r_f	5 Ω
L_{tube}	150 cm
I_{arcrms}	0.65 A

With : r_f: filament resistor, R_{arc}: arc resistance, Z_{cp} : starter impedance,i_{arc}: arc current, V_{arc} :arc voltage, i_r: load current, i_{cp}: starter current, and V_{lamp} :lamp voltage, L_r , C_r: resonant circuit parameters, C_p: starter capacitor. Transfer function of the system Discharge lamp-Electronic ballast(Aissa Bokhtache et al., 2017). The total impedance of the discharge lamp-electronic ballast system is given by:

$$Z(s)=\frac{(R_{arc}+r_f)L_r\,C_r\,C_pS^3+\left[\left(2R_{arc}+r_f\right)L_r\,C_r\,C_p+L_r\,C_r\right]S^2+(R_{arc}+r_f)(C_r+C_p)\,S+1}{\left[(R_{arc}+r_f)C_p\,S+1\right]C_rS} \quad (1)$$

Where "*s* " is the Laplace operator. As a result, the transfer function of the open loop system is:

$$\frac{I_{arc}}{V_{ch}}=\frac{r_fC_rC_pS^2+C_rS}{(R_{arc}+r_f)L_r\,C_r\,C_pS^3+\left[\left(2R_{arc}+r_f\right)L_r\,C_r\,C_p+L_r\,C_r\right]S^2+(R_{arc}+r_f)(C_r+C_p)\,S+1} \quad (2)$$

The Structure of the Electronic Ballast Based on Matrix Converter

The single-phase matrix converter is characterized by a matrix topology of four bidirectional power switches connecting the input voltage to the load. The schematic diagram of the SPMC (Single-Phase Matrix Converter) is shown in Figure 4. The power switches (supposedly ideal) of the matrix S1, S2, S3, S4 are bidirectional, they allow the current to be conducted in both directions, as well as to block the voltages of two polarities (Bouhani, 2012; Hanafi et al.,2006).

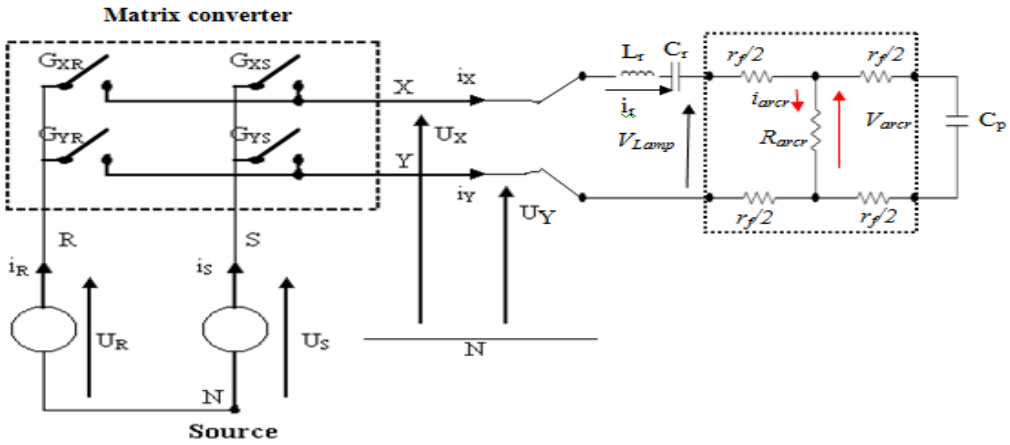

Figure 3. System representation discharge lamp-electronic ballast powered by a matrix converte.

Figure 4. SPMC Structure, bidirectional switch module (Abrous, 2008)

Method

The switches are controlled by natural PWM with a modulation ratio r = 0.86 and a modulation index m = 21, which makes it possible to obtain the rms current value of the desired (I_{arcrms} = 0.65A).

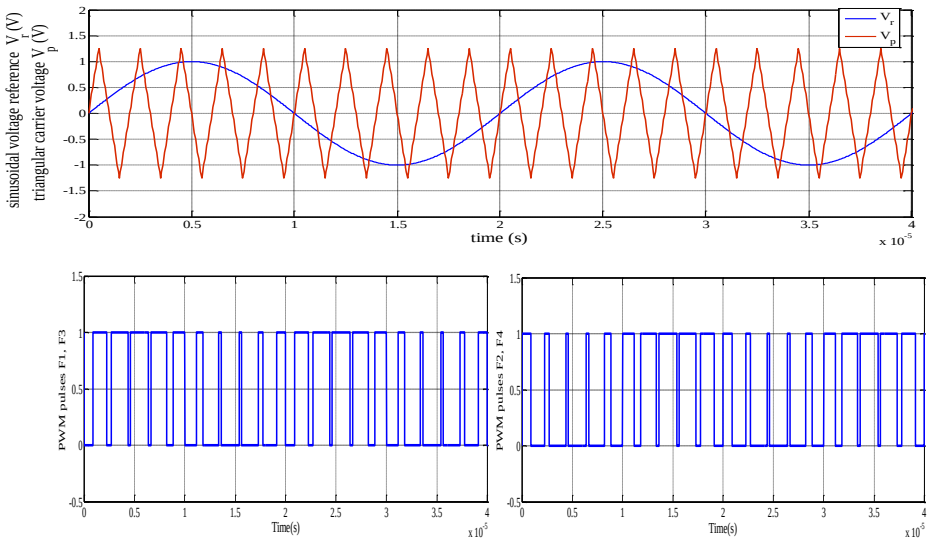

Figure 5. Control sequence of the switches made by the natural PWM.

Simulation in Open Loop

The simulation results of the system matrix converter - electronic Ballast- discharge lamp in open loop are given by the following figures:

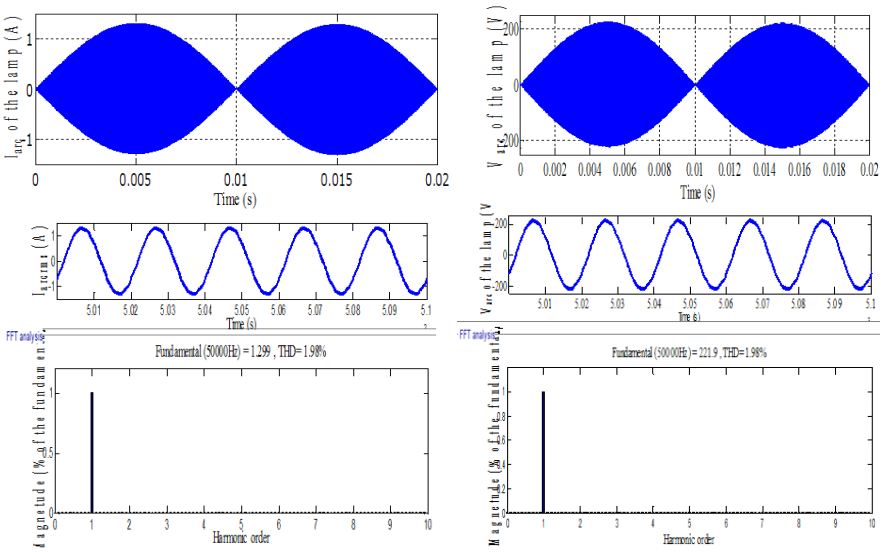

Figure 6.Current and arc voltage of the lamp and their harmonic spectra in open loop

Figure. 6 shows the waveforms of the current and arc voltage of the lamp. Note that the envelope of the voltage and the arc current oscillate at a frequency of 100 Hz. It shows that the current and the arc voltage oscillate at the desired frequency which is 50 kHz with a rate of 1.98% distortion for current and arc voltage. We find that the current and the voltage are totally in phase with the same THD. This is explained by the fact that the electric arc of the lamp is characterized by a resistance Rarc. The waveforms of voltage and current are perfectly sinusoidal in steady state of operation. Figure 7 shows that the effective arc current is stabilized at 0.65A (the desired value) after a transient regime of about 0.0195s.

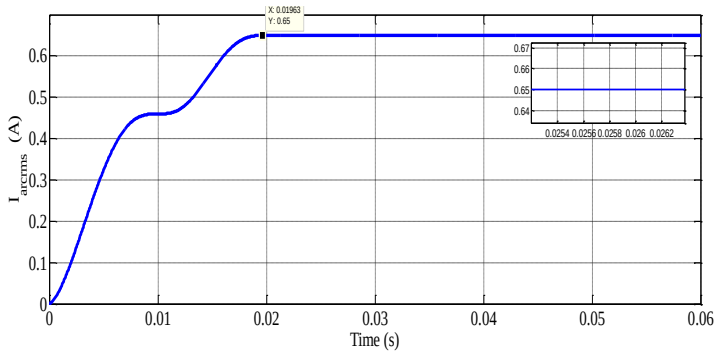

Figure 7**.** RMS arc current of the lamp in open loop

Simulation in Close Loop

To ensure good performance of the discharge lamp in terms of radiation, i.e. maximum UV radiation at 253.7 nm (a good germicidal effect), we must keep the arc current of the lamp strictly stable around a constant value close to 0.65A we must therefore impose regulation of the arc current with a reference of 0.65A. The difference will be transformed into the switching frequency of the switches.

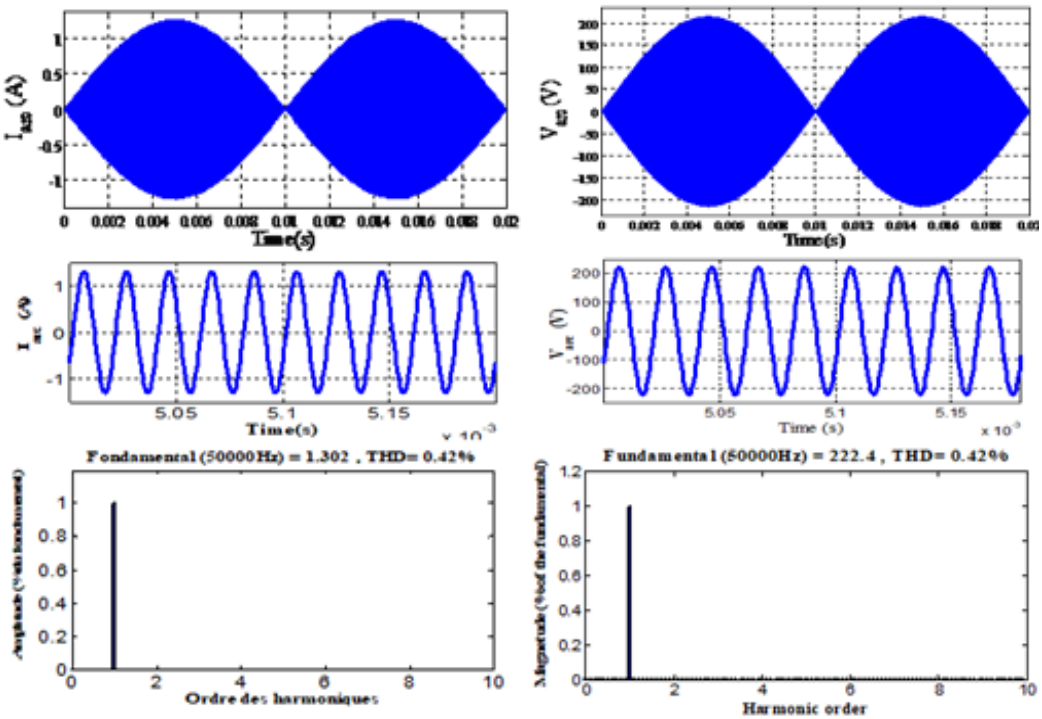

Figure 8**.** Current and arc voltage of the lamp and their harmonic spectra in close loop

We see from Figure 8 that the arc current and voltage are completely in phase with the same THD. The voltage and current waveforms are perfectly sinusoidal in steady state with a frequency of 50 KHz. The THD is improved (0.42% with introduction of PI in the regulation loop compared to 1.98% in open loop). From Figure 9 the effective value of the regulated arc current stabilizes at 0.65 A after a transient regime which lasts 0.0095 s compared to 0.0195 s in open loop, we therefore notice a considerable improvement.

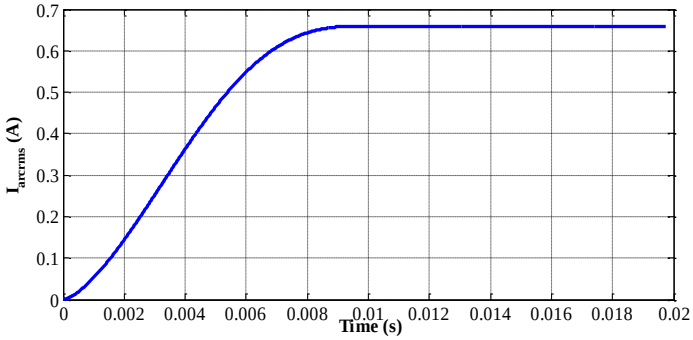

Figure 9**.** RMS arc current of the lamp in close loop

Summary of the GPC Regulator for the ARC Current Loop

Starting from the transfer function of the lamp model given by equation 2, take a sampling period Te = 10^{-7}, we obtain the discretized transfer function of the model 3 (Khati et al. , 2020):

$$\frac{I_{arc}}{V_L} = \frac{6.554e-006q^{-2} - 4.312e-006q^{-1} - 2.242e-006}{q^{-3} - 2.883q^{-2} + 2.768q^{-1} - 0.8849} \tag{3}$$

According to 3, we obtain the following polynomials $A_i q^{-1}$ and $B_i q^{-1}$ of the CARIMA model:

$$\begin{aligned} A_i q^{-1} &= q^{-3} - 2.883q^{-2} + 2.768q^{-1} - 0.8849 \\ B_i q^{-1} &= 6.554e-006q^{-2} - 4.312e-006q^{-1} - 2.242e-006 \end{aligned} \tag{4}$$

The current regulator is synthesized for the following setting: N1=1; N2=10; Nu=1 and λ = trace ($G^T G$). RST polynomials are calculated by the general program (Benallou , 2009)

Results and Discussion

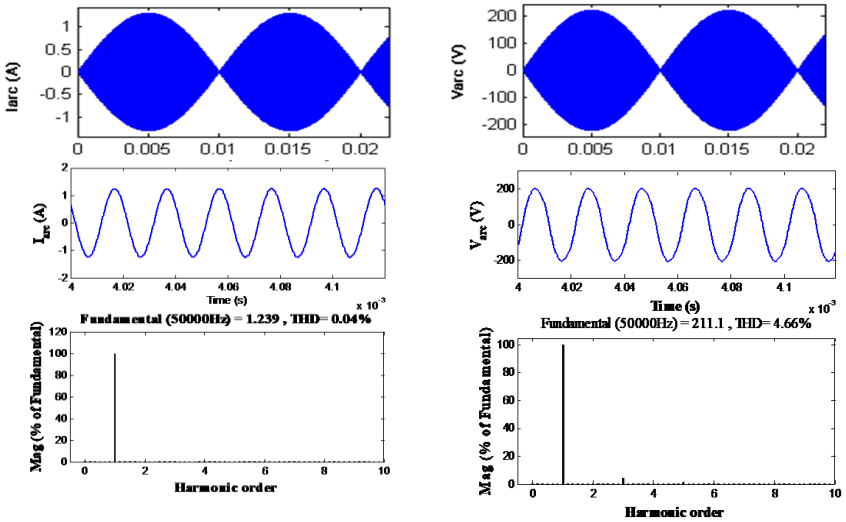

Figure 10**.** Current and arc voltage of the lamp and their harmonic spectra for GPC regulator.

The GPC regulator provided very good performance to the lamp. A remarkable reduction in terms of THD (0.04%) compared to that obtained with PI regulator (0.42%). The current and voltage waveforms are sinusoidal.

Conclusion

The implementation of discharge lamps for most industrial oriented applications (processing of finished products), makes use of diverse knowledge: electrical engineering, optics, plasma physics, and chemistry. We have put in place the foundations of the study of the power of our discharge lamp (electronic ballast). The first part was devoted to the presentation of the general structure of an electronic ballast (using a half-bridge inverter and direct matrix converter), choice of switches and their characteristics, the model of the electrical circuit of the discharge lamp as well highlighting the relative influences of the various parameters of the electronic components constituting the electronic ballast. The electrical behavior of the fluorescent lamp powered by an electronic ballast with HF can be modeled by a power dependent resistor and the temperature. The second part of this article was devoted to the MATLAB simulation of the electronic ballast circuit, two regulators were separately used to regulate the arc current: the classic PI regulator and the GPC regulator in polynomial RST form. These two control techniques made it possible both to control the effective value of Iarc and to improve the waveform of currents and voltages since the THD was reduced to 0.42% with PI and to 0.04% with GPC against 1.98% open loop.

Scientific Ethics Declaration

The authors declare that the scientific ethical and legal responsibility of this article published in EPSTEM journal belongs to the authors.

Acknowledgements or Notes

* This article was presented as a poster presentation at the International Conference on Technology, Engineering and Science (www.icontes.net) held in Antalya/Turkey on November 16-19, 2023.

References

Abrous, A. (2008). *Modélisation, commande et réalisation d'un convertisseur matriciel.* (Master'sThesis). ENP.

Aissa Bokhtache, A., Zegaoui, A., Kellal, M., Boucherit, M.S., Belmadani, B., & Aillerie, M. (2016). Optimization based on fuzzy logic control of discharge lamp-electronic ballast system for water purification. *Electric Power Components and Systems*, *44*, 1981–1990.

Aissa Bokhtache, A., Zegaoui, A., Belmadani, B., & Bouchrit, M.S. (2015). Water purification by a lamp discharge-electronic ballast system using a full bridge inverter. *Energy Procedia*, *74*, 446–452.

Aissa Bokhtache, A., Zegaoui, A., Aillerie, M., Djahbar, A., Allouache, H., Hemici, K., Kessassia, F.Z, & Bouchrit, M. S. (2017). Power supply improvements for ballasts-low pressure mercury/argon discharge lamp for water purification. *AIP Conference Proceedings 1814*. American Institute of Physic.

Aissa Bokhtache, A., Zegaouia, A., Taleb, R., & Aillerie, M. (2021). Control of an electronic ballast-discharge lamp system supplied by a multicellular converter dedicated to water purification. *Desalination and Water Treatment, 228*, 176–186.

Benallou, M. (2009). *Commande d'un système convertisseur matriciel-lampe'' destinée a la stérilisation des eaux* . (Master's Thesis). Hassiba Ben BOUALI University, Chlef.

Bouhani, B. (2012).*Étude et réalisation d'un convertisseurmatricielmonophasé.* (Master's Thesis). Hassiba Ben BOUALI University, Chlef.

Costache, M. C., Damelincourt, J.J., & Zissis, G. (2000). Optimisation of an ultraviolet source working in a consumer water reactor. *UVX 2000 Colloque sur les sources cohérentes et incohérentes UV, VUV, et X – Applications et développements récents, 87*(5), 65–66, France.

Hanafi, M., Idris, H., Hamzah, Z., & Azilah Saparon, M. K.(2006). Modelling and simulation of single-phase matrix converter as a frequency changer with sinusoidal pulse width modulation using MATLAB/simulink. *First International Power and Energy CoferencePECon 2006*, 482. Putrajaya, Malaysia.

Khati, A., Kansab, A., Taleb, R. & Khouidmi, H.(2020). Current predictive controller for high frequency resonant inverter in induction heating. *International Journal of Electrical and Computer Engineering (IJECE)*, (1), 255-264.

Toumi, A., Chhun, L., Bhosle, S., Zissis, G., Maussion, P. & Hirsch, J. (2013). Acoustic resonance characterization and numerical model including acoustic streaming in an HPS lamp. *IEEE Industry Applications Society Annual Meeting*, *49*, 1154-1160. Orlando, FL, USA: IEEE

Author Information

Aissa Bokhtachte Aicha
Hassiba Benbouali University of Chlef,
(LGEER) laboratoy
BP 151 Hai Essalam 02000 Chlef, Algeria.
Contact e-mail: *a.aissabokhtache@univ-chlef.dz*

Latroche Maamar
Hassiba Benbouali University of Chlef,
(LGEER) laboratoy
BP 151 Hai Essalam 02000 Chlef, Algeria

Toualbia Asma
Hassiba Benbouali University of Chlef,
(LGEER) laboratoy
BP 151 Hai Essalam 02000 Chlef, Algeria

Djafer Lemya
Hassiba Benbouali University of Chlef,
(LGEER) laboratoy
BP 151 Hai Essalam 02000 Chlef, Algeria

Benallou Maamar
Hassiba Benbouali University of Chlef
(LGEER) laboratoy
BP 151 Hai Essalam 02000 Chlef, Algeria

To cite this article:

Aicha, A. B., Maamar, L., Asma, T., Lemya, D. & Maamar, B. (2023). Modern control of a power supply based on a matrix converter for water disinfection by UVC radiation. The Eurasia Proceedings of Science, Technology, Engineering & Mathematics (EPSTEM), 26, 733-740.

The Eurasia Proceedings of Science, Technology, Engineering & Mathematics (EPSTEM)
ISSN: 2602-3199

The Eurasia Proceedings of Science, Technology, Engineering & Mathematics (EPSTEM), 2023

Volume 26, Pages 741-751

IConTES 2023: International Conference on Technology, Engineering and Science

Algorithm of the Heuristic Model for SMART Management in a Medium-Sized Industrial Enterprise

Miglena Temelkova
University of Telecommunications and Post

Iliyan Bakalov
Ministry of Innovation and Growth

Abstract: The present article synthesizes and describes a 9-step algorithm of a heuristic model for SMART management in a medium-sized industrial enterprise. The need for such a model is related both to the unpredictability of an industrial entity, and to the increasing competition on the basis of innovations, speed and efficiency of manufacturing between the industrial enterprises. This requires the generation, on the basis of research and analysis, of an algorithm of a model integrating a heuristic, as well as a mathematical, management and information-and-technological toolset. The architecture of the algorithm is based on some core fundaments, which determine the activities and development of a medium-sized industrial enterprise, and goes through the following nine stages: researching a medium-sized industrial enterprise and its productiom process, content-related description, containing the dependencies and the properties of the elements of the relation «production – management» in an medium-sized industrial enterprise, decomposition of a medium-sized industrial enterprise to subsystems, and of production to subprocesess and operations, forming a mathematical model through mathematical ratios expressing the links between the parameters of the production process and the borderline and initial conditions, forming an algorithmic model of data base code, creating strict procedures, determining the relations between the parameters of the production process and the borderline and initial conditions, forming an heuristic model of empirical rules and procedures, standards, analogies, expert examinations providing information about the potential development of the correlations between the parameters of the production process and the borderline and initial conditions, forming an information-and-technological model on the basis of connected into a network devices (computers, machines, sensors, etc.), determining a relational system of data exchanged between the parameters of the production process and the borderline and initial conditions, choosing manageable parameters, which should be representative, related to the target function, and also sensitive, meaningful, measurable, related to the bottlenecks in the production process and easily described, and the last stage – specifying the model.

Keywords: Heuristic model, SMART management, Medium-sized industrial enterprise

Introduction

The present day conditions ever more insistently require the implementation of automated and smart-based management systems in the industrial enterprises. A major difficulty, however, is the integration of a SMART-model for management in a medium-sized industrial enterprise due to several reasons:

- a medium-sized industrial enterprise is not a large economic entity, and the smart-based management systems would burden its financial stability, since they are quite expensive in respect to manufacturing, introduction and maintenance;

- the processes in a medium-sized industrial enterprise are not so much in parallel in respect to their components, or similar, as it is in the large economic entities, since a medium-sized industrial enterprise does not manufactire only mass production, but quite often fulfills individual client's orders;
- in a medium-sized industrial enterprise, the production situations are often unpredictable and unique in their nature, origin, functional scope, consequences, which requires an individual approach based on previous experience when resolving certain problems.

The reasons mentioned above necessitate the integration in a medium-sized industrial enterprise of a new type of a model for SMART management, which alongside the automation of the management and engineering-and-production processes, and the financial indicators of the production process, also cumulates heuristic methods and tools for using the knowledge, practice and conclusions obtained during the activities of the economic entity.

Taking into account the stated reasons, the present research generates a new and still difficult to recognize management model, allowing for the cumulative merging of traditional and innovative socio-economic and management doctrines, of elements providing a software and digitally based management system with the heuristic approaches and methodologies typical for the human activities. The generated Heuristic model for SMART management in a medium-sized industrial enterprise integrates the well-known and traditional mathematical, software, economic and management concepts, approaches and methods, as well as the already established in the practice management-and-analytical and controlling-and-evaluation toolset with the challenges and requirements of digitalization and the high innovative technological solutions. The combination of SMART management and heuristics is in its nature a novelty in the theoretical doctrine, as well as in the practice of the industrial entities. That is exactly why the Heuristic model for SMART management in a medium-sized industrial enterprise is a specific production-and-management innovation, which has its surplus value, proven by approbation, for the activities of a medium-sized industrial unit.

Only the fundamental and most important characteristics of SMART management in a medium-sized industrial entity are interpreted in the Heuristic model for SMART management in a medium-sized industrial enterprise. The relevance of the model in respect to the basic features of the entity – original, depends on the purpose of modeling – achieving heuristic-based SMART management in a medium-sized industrial enterprise. Since the main activity in a medium-sized industrial enterprise is the engineering-and-production one, and since it adds the highest value to it, then the study of the relationship between production and management logically determines also the closest approximation of the model to the original image (the management process in a medium-sized industrial enterprise). On this basis, in view of achieving management efficiency, the main characteristics of the theoretical and empirical research model should be cumulatively added to the Heuristic model for SMART management in a medium-sized industrial enterprise. Thus, the operational-and-process theoretical methods, such as analysis, synthesis, comparison, abstraction, induction, deduction, generalizing, specifying, formalizing, summarizing are logically preceded by the operational-and-process empirical methods of observation, measurement, expert evaluation, trialing, testing, interviewing, and the theoretical-and-cognitive methods, such as identification, resolving contradictions, setting of a problem, generating a hypothesis, analogy, modeling are complemented by intellectually based methods, such as monitoring, exploring, retrospection, forecasting, experimenting, summarizing experience.

The integration of the two core models of knowledge, of the elements of conceptual and heursitic modeling and of conventional and smart-based management with the particular characteristics of a medium-sized industrial enterprise and the uncertainty of its environment, specify in a structural and functional respect the goal of the model on the basis of searching two main types of solution – optimal or a combined compromise one. (Temelkova, 2017), (Temelkova, 2010) Thus, goal setting in the Heuristic model for SMART management in a medium-sized industrial enterprise is refracted through those specific characteristics and the goal is upgraded to the following: achieving optimal or rational (combining optimal and compromise values of some of the satisfaction indicators) heuristic-based SMART management in a medium-sized industrial enterprise. This exactly requires the accumulation in the model of mathematical, heuristic and information-and-technological models, which, complying with the goal of the model, should meet equal criteria for the efficency of SMART management in a medium-sized industrial enterprise.

The deductive approach requires the deduction from the goal of the model - achieving heuristic-based SMART management in a medium-sized industrial enterprise, of the fundamental informational, morphological and fucntional descriptions of each of its consecutive stages. Thus, formalization, as a theoretical research model, leads not only to formal objectivizing of the raod map of the model, but also to a possibility for forcasting major events, phenomena or behavioural reactions of the medium-sized industrial enterprise itself.

The setting of the task for generating a Heuristic model for SMART management in a medium-sized industrial enterprise requires the definition of a designable medium industrial enterprise - MIE, which should function within a particular temporal aspect with a finite number of designable parameters – P, and under the conditions of the heuristic-based SMART management in it, in line with:

- defined restrictive conditions - RC RC><=0;
- evaluation criteria - EC;
- design goal – Q_D;
- conceptual modeling goal – Q_A (automated goal);
- local task goal – Q_{LT}.

For the purposes of modeling, the medium-sized industrial enterprise shall be defined as a system, which is decomposed into its consituent subsytems. They are interrelated and determined by the other subsystems from the system of the medium-sized industrial enterprise, however, they are modeled independently, as an integral part of the general model. That is why, exactly, as well as on the basis of adapting various models and applying the principles of deduction, the Heuristic model for SMART management in a medium-sized industrial enterprise has a complex architecture, and its realization follows a complex algorithm, demonstrated on Figure 1. and described in the present article.

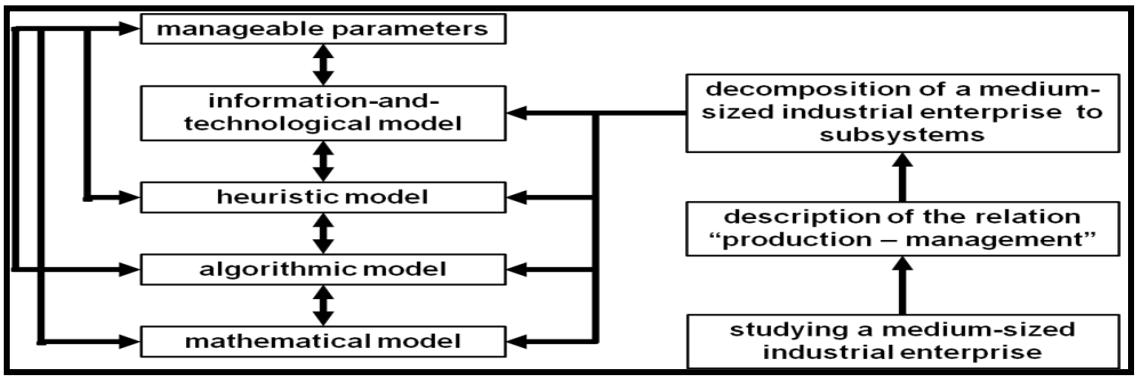

Figure 1. Algorithm of the Heuristic model for SMART management in a medium-sized industrial enterprise (author's elaboration)

Steps in the Algorithm of the Heuristic Model for SMART Management in a Medium-Sized Industrial Enterprise

Studying a Medium-Sized Industrial Enterprise and Its Production Process

Studying a medium-sized industrial enterprise and its production process, and on this basis, outlining the specific characteristics of the relation between production and management therein, requires, for the modeling purposes, carrying out an analysis and assessment of the external and internal environment. The dynamics and the uncertainty of the external environment are major factoirs, which largely determine the overall development of a medium-sized industrial entity. That makes necessary studying the external environment factors. The summarization of numerous literary sources (Христов, 2000), (Bovée, 1993), (Freeman, 2010), (Porter, 1979), (Shrivastava, 1994), (Subramanian, IsHak, 1998), leads to the conclusion that this study will be realized through:

- Political, Economic, Social, Technological Analysis, which reviews the main factors of the external environment determining management in the industrial enterprise and the effects of that impact on its strategic development;
- Industry Analysis, which studies, analyzes and evaluates the parameters of the sector where the medium-sized industrial enterprise operates;
- Strategic analysis of the strengths of the competition, which is realized by:
  - Competitive Analysis, determining the factors driving the competition, the strength and intensity of competitive rivalry;

  - Michael Porter's analysis, which is carried out on the basis of five forces important for competitiveness: threat of new entrants, bargaining power of suppliers, bargaining power of customers, threat of substitutes and competitive rivalry;
  - Competitor Profiling, which gathers and summarizes the complete information about the competitor, and, on this basis enables the evaluation of its strong and weak competitive qualities;

- Pressure Analysis, which classifies the communities in a medium-sized industrial enterprise and studies and analyzes their interests;
- Key Success Factors Analysis, which takes into account, analyzes and evaluates the most important factors, leading the medium-sized industrial enterprise to success in the external environment.

Forming alternative options for solution in a medium-sized industrial enterprise requires the observation and analysis of its internal environment. Studying numerous scientific sources (Котлър, 2005), (Boston Consulting Group, 1974), (David, 1989), (Hatten, Hatten, 1988), (Hurd, 1977), (Porter, 1979), (Various Authors, 2022) provides grounds to make a justified conclusion that important for the Heuristic model for SMART management in a medium-sized industrial enterprise are the evaluations made from the following analyses:

- Strategic analysis of the products, determined by:
  - Strategic Product Analysis, which analyzes the products as a prerequisite for achieving set as a goal results in a medium-sized industrial enterprise;
  - Analysis of Boston Consulting Group, which determines the strategic position of each product on the basis of its relative market share and market growth rate;
- Value - Chain Analysis, which analyzes the value created in a medium-sized industrial enterprise, and identifies the activities contributing to its increase;
- Strategic analysis of the activity - Ratio Analysis, which studies and evaluates the production activity in a medium-sized industrial enterprise;
- Strategic Position Analysis, which evaluates the positioning of a medium-sized industrial enterprise on the basis of financial indicators;
- Vulnerability Analysis, which takes into account the weaknesses of a medium-sized industrial enterprise;
- Critical Success Factors Analysis, which is focused on the specific factors preventing the achievement of the strategic goals of a medium-sized industrial enterprise.

Description of the Relation "Production – Management" in a Medium-Sized Industrial Enterprise

Some aditional analytical activities could be carried out on the basis of the analytical research of a medium-sized industrial enterprise, which would faciliate drawing the content-related and functional description of the link between management and production process therein. The toolset of some strategic and operational tools is adapted for the purpose of the Heuristic model for SMART management in a medium-sized industrial enterprise for more in-depth understanding of this relation:

- A balanced system of indicators (Темелкова, 2010), which is a strategic approach integrating financial and non-financial indicators, revealing the actual correlation between production and management in a medium-sized industrial entity on the basis of measuring the targeted satisfaction;
- Brown's framework of process assessment (Браун, 1996), (Нийли, 2001), which analyzes the processes on operational level in respect to their financial resource consumption, evaluates production organization and management down to its smallest component – the operations, and determines the importance and sustainability of the final result – the manufactured production volume.

Using and adapting the Balanced system of indicators and Brown's framework for measuring the processes for the purposes of the Heuristic Model for SMART management in a medium-sized industrial enterprise enables also to outline the components of the "management" and "production" and the location of their intersection points. (Table 1.)

Table 1. Intersection points between the «production» and «management» subsystems in a medium-sized industrial enterprise adapted by the author (Темелкова, 2010)

Medium-Sized Industrial Enterprise		
Subsystem	Elements	Intersectıon Poınts
Management	Strategıc Management	planning organizing coordinating motivating reporting control
	Work Processes	information flows processing and transfer of information communication intersection points
	Investments	return optimality profit profitability
	Productivity	production result gross income
	Marketing	customers/buyers quality price market share servicing trade and distribution network
	Innovation	research work development and implementation activities digitalization robotization
	Human Resources	physiology mentality qualities qualification needs
	Operating Management	planning organizing coordinating reporting control
Production	Production Process	functions power capacity work principles operations time
	Logistics	supplies procurement transportation stock availability forwarding
	Technologies	materials information energy productivity/time
	Human Resources	physiology mentality qualities needs

Decomposition of a Medium-Sized Industrial Enterprise to Subsystems, and of Production to Processes and Operations

The clarified relationship between the two main subsystems in a medium-sized industrial enterprise enables also its decompistion into its constituent subsystems. It can be summarized from the analysis of the literary sources that a medium-sized industrial enterprise is formed by two major subsytems – management and production one. The production process has the strongest impact on its organizational-and-management structure, and it determines the nature and tasks of management. The management process in a medium-sized industrial enterprise, in its turn, strives to achieve the strategic targets, set as goals, by applying rational methods and tools.

The analyses drawn for the purposes of the present research provide grounds to synthesize the following main factors, which originate from production but determine management in a medium-sized industrial enterprise: nature of operations, type of technological processes, level of production technological effectiveness, level of digitalization of production, level of robotization of production, production volume, production capacity, production range, structural complexity of the production process, production life cycle, type of resource flows, specific characteristics of the production process, spatial location of the production sites, permanent nature degree of the production parameters, hierarchical levels of the organizational-and-management structure, complexity and dynamics of the operational production goals.

The decomposition of production down to processes (Figure 2.) allows for coordination and control of all incoming resources and planned tasks in every business process, of the results going out from it and their compliance with the plan, and of the activities on transforming the resources into particular products or templates – at the output. When decomposing the production process down to operations, the specific organizational-and-production conditions should be observed (Темелкова, 2010), such as: way of combining the operations – consecutive, parallel or parallel-and-consecutive, time consumption for each operation, the way of movement of the details and templates, time consumption for the movement of the details and templates, time for setting the machines, type of technological routes, time for producing a product unit.

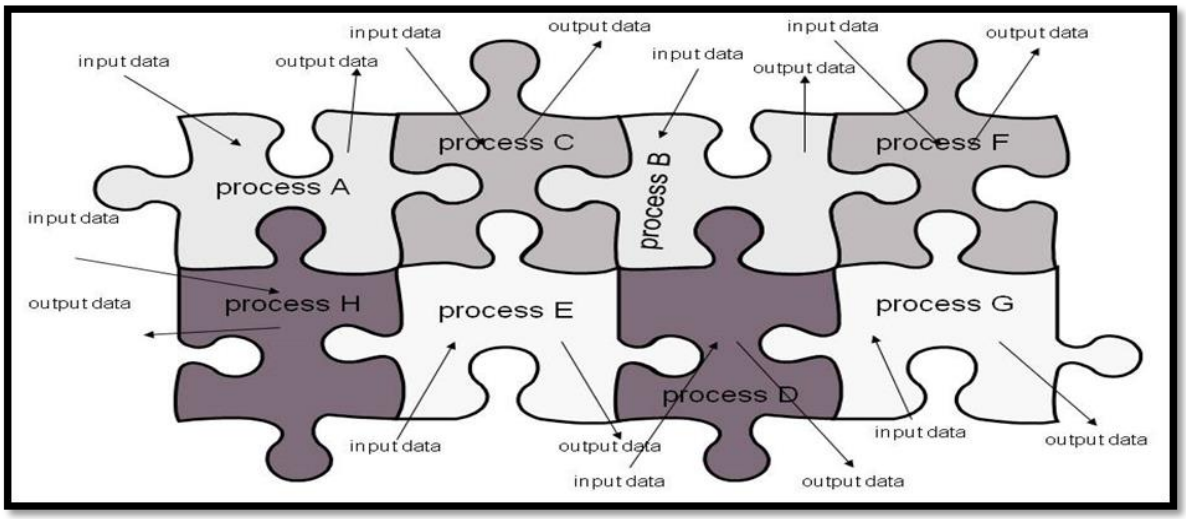

Figure 2. Decomposition of production to processes in a medium-sized industrial enterprise adapted by the author (Темелкова, М. 2010)

Mathematical Fundament of the Heuristic Model for SMART Management in a Medium-Sized Industrial Enterprise

The mathematical basis of the Heuristic Model for SMART management in a medium-sized industrial enterprise requires the goal setting in respect to the main elements of the general task for designing a medium-sized industrial enterprise, integrating heuristically based SMART management. The conditions and restrictions under which a solution should be searched in the Heuristic Model for SMART management in a medium-sized industrial enterprise, are:

- restrictions resulting from the volume of the production in kind (number of products of the j-th type)

- restrictions resulting from the determined in cash losses of technological time for each j–th product (the number of products is within the limit j=1÷n) under processes varying from 1 to d (X_{jn}=1÷d) of the n-th product of the j–th type (X_{jn})
- restrictions resulting from the cost in money for material resources (varying from 1 to g – M=1÷g), ensuring the production of each j–th product (the number of products is within the limit j=1÷n) under processes varying from 1 to d (X_{jn}=1÷d) of a product unit of the j–th type (X_{jn})
- restrictions resulting from the cost in money for energy per product unit (X_{jn}), whereby the production is reached of each j–th product (the number of products is within the limit j=1÷n) under processes varying from 1 to d (X_{jn}=1÷d)
- restrictions resulting from the cost in money for labour ensuring the production of a product of the j–th type (the number of products is within the limit j=1÷n) under processes varying from 1 to d (X_{jn}=1÷d) of the n-th product of the j–th type (X_{jn})
- restrictions resulting from the cost in money for the exploitation of the machines, and of the automated and robotized equipment, ensuring the production of a product of the j–th type (the number of products is within the limit j=1÷n) under processes varying from 1 to d (X_{jn}=1÷d) of the n-th product of the j–th type (X_{jn})

An optimal or a compromise combined solution should be searched under the conditions of the Heuristic Model for SMART management in a medium-sized industrial enterprise. This requires also setting certain criteira guaranteeing optimality or a compromise. The target criterion in the Heuristic Model for SMART management in a medium-sized industrial enterprise represents a target function and is designated with L. A target criterion in the Heuristic Model for SMART management in a medium-sized industrial enterprise should be the economic efficiency, which is a relation between the value expression of the utility achieved during the economic activity and the value of the necessary production resources, and all the other costs made for the production and realization of a certain product of the j-th type. (Мирчев, 1996)

In view of the specific characteristics of the selected target criterion (the presence of numerous integrated parameters in it), the Heuristic Model for SMART management in a medium-sized industrial enterprise is reduced to searching a multi-criteria solution. Provided that one of the searched alternatives is optimality, then the application of the Pareto method for multi-criteria optimization is a suitable strategy, which to some extent balances the optimization task through “scalarization of the multiple criteria vector” (Stoyanov, Stoyanova, 2019).

Heuristic Elements in the Heuristic Model for SMART Management in a Medium-Sized Industrial Enterprise

The heuristic elements in the Heuristic Model for SMART management in a medium-sized industrial enterprise are rules, which can save efforts, provide satisfactory solutions and do not guarantee that they are optimal. They, however, offer smart variants, selectivity and directions in the decision making process, and, therefore, lead to plausible options for final conclusions and summarization in respect to a particluar problematic situation.

The heuristics in the Heuristic Model for SMART management in a medium-sized industrial enterprise are represented in a various way in the form of maxims, proposals, principles, production and management rules, criteria, programmes, procedures, methods, strategies, option “filters”, goal transformers. Thus, the use of heuristic elements provides certainty concenring the existence of a decision making mechanism.

The heuristic elements in the Heuristic Model for SMART management in a medium-sized industrial enterprise result from the specific features of the relation “production – management” in a medium-sized industrial enterprise, and from decomposing it into subsystems. At the same time, the heuristic elements should be adjusted also to the mathematical and algorithmic aparatus in the Heuristic Model for SMART management in a medium-sized industrial enterprise. The observation of those requirements and the specific frameworks of the model determine further the instrumental borderlines of the heuristics. Its toolset should ensure the analysis of the strategic alternatives in the search for the efficiency already set in the mathematical model as a target criterion, and the tree of alternative objects, where the heuristic search should take place.

The expert systems are good sources for finding effects as a result of applying heuristics. They are a set of characteristics of a particular entity – alternative, and facilitate with arguments, judgments, analogies, experience reaching a decision or outcome of a certain case study. In the Heuristic Model for SMART management in a medium-sized industrial enterprise they are a computer system, which imitates the human

ability to make decisions, and which integrates heuristic elements (tools, methods, strategies) with established hypotheses, rules, facts in view of achieving a satisfactory, interactive and reliable solution of complex assignments.

The expert systems in the Heuristic Model for SMART management in a medium-sized industrial enterprise are provided with the option to maintain reasoning. This is possible since their structure includes two subsystems – data bases – certain specific knowledge, facts, experience and algorithm for conclusion – a set of rules relevant to the data base and the specificity of one particular situation. There are not integrated by a code in conceptual modeling, but through the rule "If-Then".

Informational-and-Technological Fundaments of the Heuristic Model for SMART Management in a Medium-Sized Industrial Enterprise

For the purposes of conceptual modeling, the informational-and-technological provision of the Heuristic Model for SMART management in a medium-sized industrial enterprise is ensured on the basis of classes and objects. Thus, the digital counterpart of each cost in a medium-sized industrial enterprise in the model for SMART management based on information technology and heuristics is determined by the abstract class (Base expance). The logic for calculating the cash outlay by types is implemented in the class. All other cost types inherit Base expance – accordingly $TLTT_d$ (total losses of technological time), $TCMR_{dg}$ (total cost of material resources), $TEC_d{}^*$ (total energy costs), TLC_d (total labor costs), $TCMAR_d$ (total costs for machines, automata, robots), CP (cost price). Each of these costs uses the constructor from Base expance, where the constructor expects a name, the time when the cost was incurred, the recurrence of the cost, and its value (Figure 3.).

```
public abstract class BaseExpense implements Expense{
    private String name;
    private double time;
    private int reps;
    private double price;

    public BaseExpense(String name, double time, int reps, double price){
        setName(name);
        setTime(time);
        setReps(reps);
        setPrice(price);
    }

    private void setName(String name){
        if (name==null || name.trim().equals("")){
            throw new NullPointerException("Name cannot be empty.");
        }
        this.name = name;
    }

    private void setTime(double time){
        if(time<0){
            throw new IllegalArgumentException("Time cannot be negative number");
        }
        this.time = time;
    }

    private void setReps(int reps){
```

Figure 3. A software programme of the Heuristic Model for SMART management in a medium-sized industrial enterprise (author's elaboration)

Governing Parameters in the Heuristic Model for SMART Management in a Medium-Sized Industrial Enterprise

The governing parameters in the Heuristic Model for SMART management in a medium-sized industrial enterprise are parameters, which change independently from each other. Their variation according to a selected approach (heuristic, Pareto method, the Gauss-Seidel method, etc.), is a prerequisite for navigating and managing the qualitative characteristics of the designable new medium-sized industrial enterprise. The optimization methods require the presence of at least one governing parameter in the optimization task. There are two governing parameters in the Heuristic Model for SMART management in a medium-sized industrial enterprise – cost price (CP) and total revenue (TR).

The cost price has five constituent elements, and, in that sense, it could be claimed that they are governing vectors (parameters) in the setting of the general task of programming the Heuristic Model for SMART management in a medium-sized industrial enterprise. These are the measurable in money for the production per

product unit: total losses of technological time ($TLTT_d$), total cost of material resources - $TCMR_{dg}$, total energy costs - TEC_d, total labor costs - TLC_d, total costs for machines, automata, robots - $TCMAR_d$.

The change in the elements of the governing parameters (v in number) leads to generating various options of the object to be optimized. That is a prerequisite for an effcient choice of the best possible option under the evaluation criterion. The variations of the governing parameters in the Heuristic Model for SMART management in a medium-sized industrial enterprise determine the level of freedom of the task therein, where generaing numerous changes will increase substantially the options for reaching a higher quality solution.

Results and Discussion

The Heuristic Model for SMART management in a medium-sized industrial enterprise, generated in the present article, is based on:

- modeling, implementing the principles of conceptual modeling and of business modeling, which is outlined as a major architectural element of the Concept for application of the heuristic models for SMART management in a medium-sized industrial enterprise;
- the description, research and analysis of the content-related, functional, quantitative, qualitative and structural characteristics of the constituent elements of the conceptual and business modeling in a medium-sized industrial enterprise;
- the synthesis of the algorithm of the Heuristic Model for SMART management in a medium-sized industrial enterprise;
- the definition of the general task of designing the Heuristic Model for SMART management in a medium-sized industrial enterprise and the specification of its structural algorithm;
- the research and analysis of the elements from the structure of the Heuristic Model for SMART management in a medium-sized industrial enterprise, such as:

    - studying the relation “production – management” in a medium-sized industrial enterprise;
    - decomposing the architectural unity of a medium-sized industrial enterprise down to subsystems, processes and operations following the deduction method;
    - synthesis of the mathematical justification of the Heuristic Model for SMART management in a medium-sized industrial enterprise;
    - description of the heuristic system integrated in the Heuristic Model for SMART management in a medium-sized industrial enterprise;
    - summarizing the main characteristics of the informational-and-technological fundament of the Heuristic Model for SMART management in a medium-sized industrial enterprise;
    - bringing forward the governing parameters in the model together with their correlations with other parameters.

Conclusion

The Heuristic Model for SMART management in a medium-sized industrial enterprise is generated via the methods of the systematic analysis, dialectics, induction and deduction, and it should lead to efficiency in the object of designing (a medium-sized industrial unit). It comprises not only scientific, heuristic and informational-and-technological flows, but also the essential specific features of a medium-sized industrial enterprise as an economic entity. On this background, it leads to synthesizing the following main conclusions:

- the specific characteristics of the Heuristic Model for SMART management in a medium-sized industrial enterprise are related to the implemented in it essential, process-related and functional specific features of conceptual modeling and of business modeling, suggesting in architectural aspect the interrelation of algorithms and heuristics in a single system;
- in the course of the observation of the practical application of the algorithms and heuristics in management, as well as while studying and analyzing their specific features, a hypothesis is reached concerning the outcome (solution) of the task for designing the Heuristic Model for SMART management in a medium-sized industrial enterprise – optimization or achieving a combined compromise solution;
- the specificity of a medium-sized industrial enterprise as an economic entity in the commercial turnover is integrated in the Heuristic Model for SMART management in a medium-sized industrial

enterprise by outlining in its structure the relation "production – management", whereby a justified conclusion could be drawn not only about the main subject of activity of the industrial unit (production), but also about the point adding the highest value to it (the production process), as well as about the size and complexity of the structural development of the production process itself;

- the conducted informational study provides substantial research basis for synthesizing the mathematical model in the Heuristic Model for SMART management in a medium-sized industrial enterprise with specific evaluation criteria (efficiency), restrictive conditions (the expenses forming the cost price and the volume of the manufactured production), as well as indicators for achieved effect (cost price and revenue);
- the relationship "restrictive conditions – evaluation criterion" requires the introduction into the Heuristic Model for SMART management in a medium-sized industrial enterprise of cost price and productivity as governing parameters;
- observation, monitoring, research, interpretation, specification, experimentation with synthesizing the essential specific features of heuristics suggest carrying out a deliberated, structured process of intellectual reasoning of the various consequences in respect to the actually manifested factors and realized development scenarios, which is fundamental for the implicit integration of the heuristic toolset in the Heuristic Model for SMART management in a medium-sized industrial enterprise;
- the organizational principles in a medium-sized industrial enterprise, and the nature of the relationship between production and management adjust the toolset of the informational-and-technological programming to the specificity of a medium-sized industrial entity and the creation of a smart-based software program managing from efficiency perspective the entire production process.

Scientific Ethics Declaration

The authors declare that the scientific ethical and legal responsibility of this article published in EPSTEM journal belongs to the authors.

Acknowledgements or Notes

* This article was presented as an oral presentation at the International Conference on Technology, Engineering and Science (www.icontes.net) held in Antalya/Turkey on November 16-19, 2023.

References

Boston Consulting Group. (1974). *Perspectives on experience*. Boston.

Bovée, C. L. (1993). *Management*. Mc Graw Hill.

David, F. (1989). *Concepts of strategic management* (2nd ed.,pp.104-105).Columbus, Ohio: Merrill Publishing

Hatten, K., Hatten, M. (1988). *Effective strategic management*. Englewood Cliffs.

Hurd, D. (1977). *Vulnerability analysis in business planning*. SRI International Research Report.

Jauch, L., Glueck, W. (1988). *Business, policy and strategic management*. McGraw-Hill

Porter, M. (1979). How competitive forces shape strategy. *Harvard Business Review, 57(2)*. 137–145.

Shrivastava, P. (1994). Castrated environment. *Greening Organizational Studies, 15*(5). 705-726.

Stoyanov, S., Stoyanova, S. (2019). Strategies for optimal decisions making. *Информатика и иновативни технологии, 1*.

Subramanian, R., & IsHak, S. T. (1998). Competitor analysis practices of US companies: An empirical investigation. *Management International Review, 38*(1), 7-23.

Temelkova, M. (2010). Scheme of Braun for processes measurement – an instrument for operative controlling in checking stability of the micro-level. *KSI Transactions on Knowledge Society, 3.*

Temelkova, M. (2017). Development of controlling in the organizations from the service sector under the conditions of the fourth industrial revolution. *International Journal of Advanced Research in Management and Social Sciences*, *6(*3), 28-43.

Various Authors. (2022). *Routledge library editions: Small business* (Vol. 17). Routledge.

Браун, М. (1996). *Проследяване на резултатите: Използване на правилни метрични начини за подобряване на световните стандарти за дейността.* Куолити Ресорсиз.

Котлър, Ф. (2005). *Управление на маркетинга*. Класика и стил. София.

Мирчев, А. (1996). *Производствен мениджмънт.* Princeps.

Нийли, А. (2001). *Перспективи за развитие на бизнеса.* Класика и Стил. София.

Темелкова, М. (2010). *Контролинг в производствената организация.* Колор принт. Варна.
Темелкова, М. (2010). *Оптимизация на производствената организация в условията на криза*. Черноризец Храбър. Варна.
Христов, С. (2000). *Стратегически мениджмънт*. Стопанство. София.

Author Information

Miglena Temelkova
University of Telecommunications and Post
Bulgaria, Sofia
Contact e-mail: *megitemelkova@abv.bg*

Iliyan Bakalov
Ministry of Innovation and Growth
Bulgaria, Sofia

To cite this article:

Temelkova, M. & Bakalov, I. (2023). Algorithm of the heuristic model for smart management in a medium-sized industrial enterprise. *The Eurasia Proceedings of Science, Technology, Engineering & Mathematics (EPSTEM), 26,* 741-751.

The Eurasia Proceedings of Science, Technology, Engineering & Mathematics (EPSTEM)
ISSN: 2602-3199

The Eurasia Proceedings of Science, Technology, Engineering & Mathematics (EPSTEM), 2023

Volume 26, Pages 752-759

IConTES 2023: International Conference on Technology, Engineering and Science

Multilayered Semi-Elliptical Arch Structures: A Damping Analysis

Victor Rizov
University of Architecture

Abstract: Arch structures are used in various load-bearing applications in up-to-date engineering. In some cases these structures are made of multilayered materials with elastic-plastic behaviour. In many applications, the arch structures are subjected to cyclic external loading. This circumstance necessitates developing analyses of damping energy. Such analyses can be very useful for evaluating the effects of a variety of factors and parameters on the damping energy. The present paper is concerned with analyzing of damping energy in a semi-elliptical multilayered arch structure under cyclic bending. The left foot of the arch is clamped. Besides, the arch right foot is restrained by a rotational spring. An approach for determining of the changes in curvature and the coordinates of neutral axis in the portions of the arch is developed. Then damping energy in the arch is derived by integrating the damping energy density in the layers and summation for the arch portions. A parametric investigation of effects of the strength of the rotational spring, ratio of the ellipse semi axes and loading on damping energy is carried-out.

Keywords: Damping energy, Semi-elliptical arch, Elastic-plastic behaviour, Bending, Parametric investigation

Introduction

The application of arch structural members in various load-bearing structures is closely connected with search of new constructive solutions, usage of efficient engineering materials and creation of new methods for analyzing their mechanical response to various loads and external influences. One of the important directions for modernization of arch structures and enhancement of their safety, reliability and efficiency is the usage of multilayered materials.

In fact, the modern multilayered materials are advanced engineering materials capable of withstanding heavy loadings in extreme environment (Kim et al., 1999; Rzhanitsyn, 1986; Tokova et al., 2016). Application of layers of different materials in a multilayered system allows for design of efficient load-bearing multilayered structures and equipments distinguished for relatively low deadweight, high strength and stiffness, perfect response to various influences (temperature, humidity, etc.) and excellent mechanical behaviour (Kaul, 2014; Lloyd & Molina-Aldareguia, 2003; Rizov, 2018; Yu et al., 2003). Thus, the usage of multilayered materials in various areas of up-to-date engineering has intensified in recent decades (Rizov, 2021; Sy-Ngoc Nguyen et al., 2015; Sy-Ngoc Nguyen et al., 2020). The progress in the usage of multilayered materials in modern arch structures requires more theoretical knowledge elucidating the mechanical behaviour of these structures under various loading conditions.

In the present paper, the energy damping in multilayered arch structures of elastic-plastic behaviour under cyclic bending is analyzed theoretically by applying the apparatus of engineering mechanics (it should be underlined that the previous damping analyses usually consider beam structural members (Dowling, 2007; Rizov, 2021). In particular, an arch whose left foot is rigidly fixed while the right foot is restrained by a rotational spring is considered here. The arch has a semi-elliptical shape of small initial curvature. The damping energy in the arch is derived. A parametric investigation that elucidates the influence of the strength of the rotational spring, ratio of the ellipse semi axes and load magnitude on the damping energy is performed.

Deriving of Damping Energy

The load-bearing structure, Q_1Q_3, shown in Fig. 1 represents a semi-elliptical arch. The arch is built-up by n longitudinal layers (the cross-section of the arch is shown in Fig. 2).

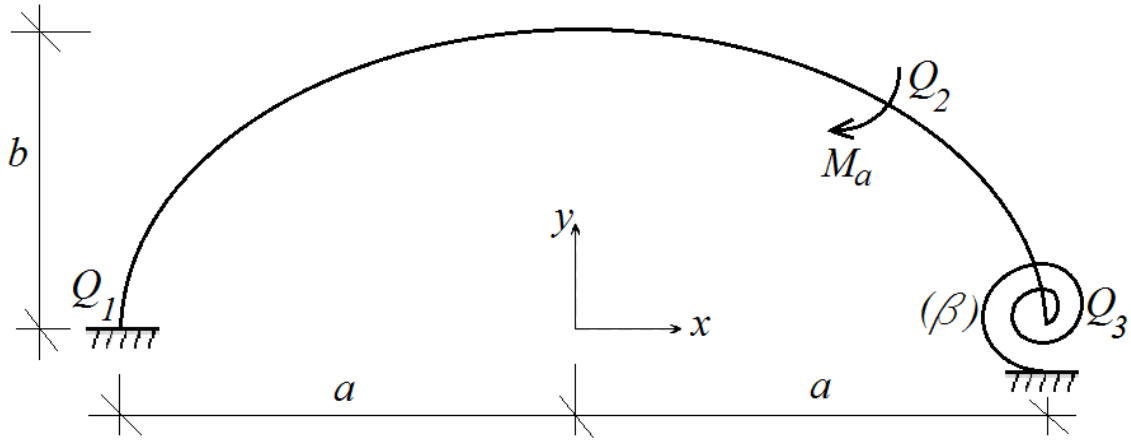

Figure 1. Semi-elliptical arch structure.

The left foot of the arch is clamped (Fig. 1). The arch is restrained also by a rotational spring in the right foot. The strength of the rotational spring is denoted by β. The arch is under a cyclic bending moment, M_a, about zero mean applied in section, Q_2, as shown in Fig. 1. The arch geometry is given by (Fig. 1)

$$\frac{x^2}{a^2}+\frac{y^2}{b^2}=1, \tag{1}$$

where

$$-a \le x \le a, \tag{2}$$

$$0 \le y \le b. \tag{3}$$

In formulas (1), (2) and (3), a and b are the horizontal and vertical semi axes of the ellipse, respectively.

The arch has elastic-plastic mechanical behaviour treated by the following constitutive law (Dowling, 2007):

$$\varepsilon_a=\frac{\sigma_{ai}}{E_i}+\left(\frac{\sigma_{ai}}{H_i}\right)^{\frac{1}{m_i}}, \tag{4}$$

where the subscript, i, refers to the *i*-th layer of the arch, ε_a and σ_{ai} are the half ranges of the strain and stress, respectively, E_i is the modulus of elasticity, H_i and m_i are material parameters. Deriving of the damping energy, ΔU, in the arch is given by

$$\Delta U=\Delta U_{Q1Q2}+\Delta U_{Q2Q3}, \tag{5}$$

where ΔU_{Q1Q2} and ΔU_{Q2Q3} are the damping energies in arch portions, Q_1Q_2 and Q_2Q_3, respectively (Fig. 1).

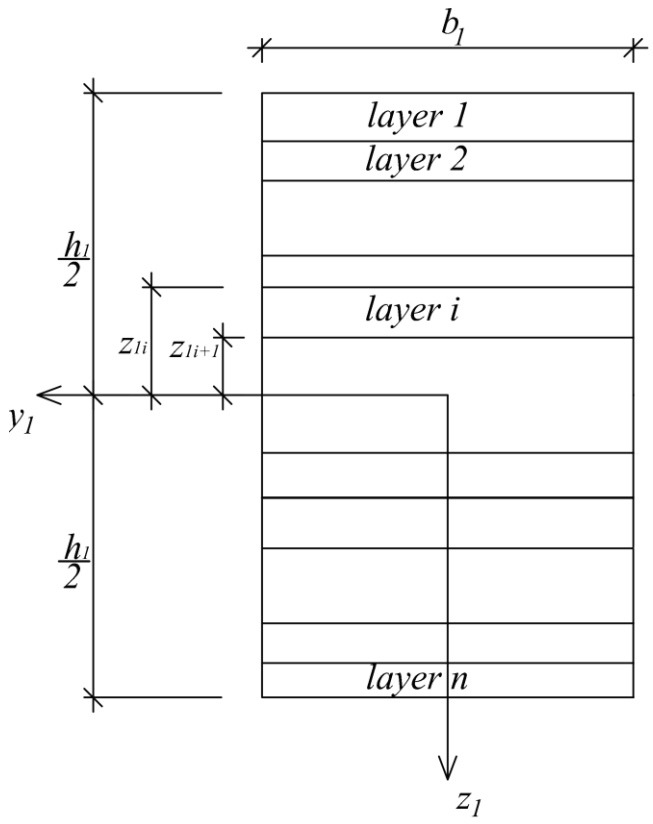

Figure 2. Cross-section of the arch structure

Formula (6) is applied for obtaining of ΔU_{Q1Q2} , i.e.

$$\Delta U_{Q1Q2} = s_{Q1Q2} b_1 \sum_{i=1}^{i=n} \int_{z_{1i}}^{z_{1i+1}} \Delta u_{Q1Q2i} dz_1 , \tag{6}$$

where s_{Q1Q2} is the length of portion, Q_1Q_2 , of the arch, b_1 is the width (Fig. 2), z_{1i} and z_{1i+1} are the coordinates of the upper and lower surface of the *i*-th layer (Fig. 2), Δu_{Q2Q3i} is the damping energy density, z_1 is the vertical centric axis. Formula (7) is used for calculating of Δu_{Q2Q3i} (Dowling, 2007).

$$\Delta u_{Q1Q2i} = \frac{4(1-m_i)\sigma_{ai}^{1+\frac{1}{m_i}}}{(1+m_i)(H_i)^{\frac{1}{m_i}}} , \tag{7}$$

where

$$i = 1, 2, \ ..., n . \tag{8}$$

In order to calculate s_{Q1Q2} , we apply formula (9), i.e.

$$s_{Q1Q2} = \int_{-a}^{x_{Q2}} \sqrt{1+y'^2}\, dx , \tag{9}$$

where x_{Q2} is abscissa of Q_2 . The quantities, y and y' , can be derived from (1).

The distribution of ε_a along the arch thickness portion, Q_1Q_2 , is defined by (10), i.e.

$$\varepsilon_a = \kappa\left(z_1 - z_{1nn}\right), \tag{10}$$

where

$$-\frac{h_1}{2} \le z_1 \le \frac{h_1}{2}. \tag{11}$$

In formulas (10) and (11), κ is the change in curvature, z_{1nn} is the neutral axis coordinate, h_1 is the thickness. The changes in curvatures and neutral axis coordinates in portions, Q_1Q_2 and Q_2Q_3 , of the arch are determined from equations (12) – (16).

$$\varphi_{Q3} = \kappa\, s_{Q1Q2} + \kappa_{Q2Q3} s_{Q2Q3}, \tag{12}$$

$$N_{aQ1Q2} = b_1 \sum_{i=1}^{i=n} \int_{z_{1i}}^{z_{1i+1}} \sigma_a dz_1, \tag{13}$$

$$M_{aQ1Q2} = b_1 \sum_{i=1}^{i=n} \int_{z_{1i}}^{z_{1i+1}} \sigma_a z_1 dz_1, \tag{14}$$

$$N_{aQ2Q3} = b_1 \sum_{i=1}^{i=n} \int_{z_{1i}}^{z_{1i+1}} \sigma_{aQ2Q3} dz_1, \tag{15}$$

$$M_{aQ2Q3} = b_1 \sum_{i=1}^{i=n} \int_{z_{1i}}^{z_{1i+1}} \sigma_{aQ2Q3} z_1 dz_1, \tag{16}$$

where

$$s_{Q2Q3} = \int_{x_{Q2}}^{a} \sqrt{1 + y'^2}\, dx, \tag{17}$$

$$N_{aQ1Q2} = 0, \tag{18}$$

$$N_{aQ2Q3} = 0, \tag{19}$$

$$M_{aQ1Q2} = M_{aQ3} - M_a, \tag{20}$$

$$M_{aQ3} = \varphi_{Q3}\beta, \tag{21}$$

$$M_{aQ2Q3} = M_{aQ3}. \tag{22}$$

In formulas (12) – (22), φ_{Q3} is the angle of rotation of section, Q_3, of the arch (actually, formula (12) is obtained by using the integrals of Maxwell-Mohr), κ_{Q2Q3} and s_{Q2Q3} are the change in the curvature and the length of portion, Q_2Q_3 , of the arch, N_{aQ1Q2} and N_{aQ2Q3} are the axial forces in the two portions of the arch (here, $N_{aQ1Q2} = 0$ and $N_{aQ2Q3} = 0$), M_{aQ1Q2} and M_{aQ2Q3} are the bending moments in the two arch

portions, M_{aQ3} is the bending moment in section, Q_3, of the arch. The MatLab is applied for solving equations (12) – (16). The damping energy in arch portion, Q_2Q_3 , is given by (23)

$$\Delta U_{Q2Q3}= s_{Q2Q3} b_1 \sum_{i=1}^{i=n} \int_{z_{1i}}^{z_{1i+1}} \Delta u_{Q2Q3i} dz_1 , \tag{23}$$

where

$$\Delta u_{Q2Q3i} = \frac{4(1-m_i)\sigma_{aQ2Q3i}^{1+\frac{1}{m_i}}}{(1+m_i)(H_i)^{\frac{1}{m_i}}} . \tag{24}$$

Here, σ_{aQ2Q3i} is the stress in the *i*-th layer.

Formulas (6) and (23) are substituted in (5) to obtain the damping energy in the arch structure (the integrals are solved by the MatLab).

Numerical Results

Numerical results indicating the effects of various parameters (strength of the rotational spring, ratio of the ellipse semi axes, load magnitude, etc.) on the damping energy in the multilayered semi-elliptical arch structure are derived by using the following data: $a = 0.450$ m, $b = 0.300$ m, $b_1 = 0.005$ m, $h_1 = 0.008$ m, $n = 5$ and $M_a = 4$ Nm.

First, the influence of the strength of the rotational spring, β, on the damping energy is analyzed. Figure 3 shows the damping energy variation with increasing of the value of β. One can see that the damping energy reduces when β increases (Fig. 3). The increase of E_2 / E_1 ratio (here, subscripts, 1 and 2, refer to layers 1 and 2 of the arch structure, respectively) also causes a reduction of the damping energy as illustrated in Fig. 3.

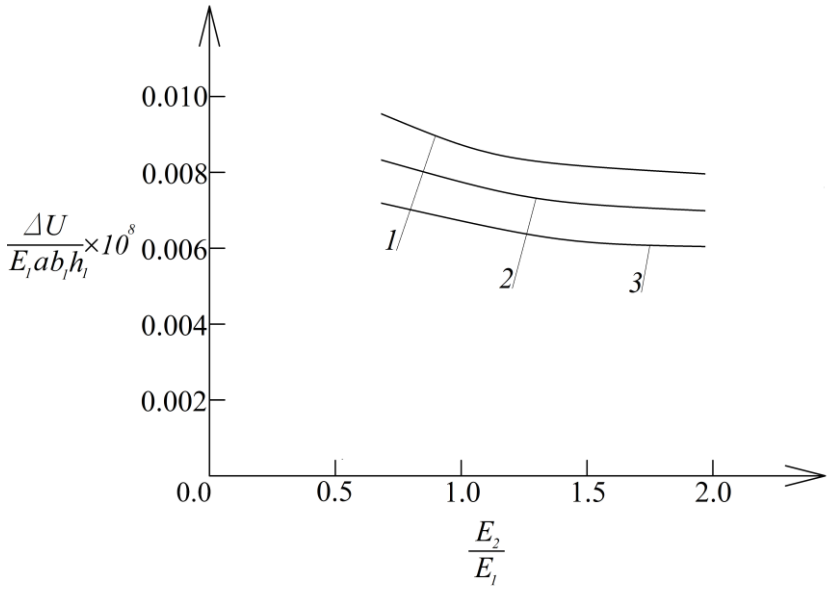

Figure 3. The damping energy versus E_1 / E_2 ratio (curve 1 – at $\beta = 800$ Nm, curve 2 – at $\beta = 1600$ Nm and curve 3 – at $\beta = 2400$ Nm).

The influence of the geometry of the arch structure on the damping energy is analyzed too. The geometry is presented by the ratio of the ellipse semi axes, a/b. The influence of a/b and H_2/H_1 ratios is shown in Fig. 4. It can be observed that increase of the ratio of the ellipse semi axes leads to growth of the damping energy (Fig. 4). The increase of H_2/H_1 ratio causes a substantial reduction of the damping energy as indicated by the curves in Fig. 4. Besides, comparison of Fig. 3 and Fig. 4 reveals that the reduction of the damping energy due to increase of H_2/H_1 ratio is stronger than this caused by increase of E_2/E_1 ratio. Finally, the effects of the bending moment value, M_a, and the ratio of the thickness and width of the arch cross-section, h_1/b_1, on the damping energy are evaluated.

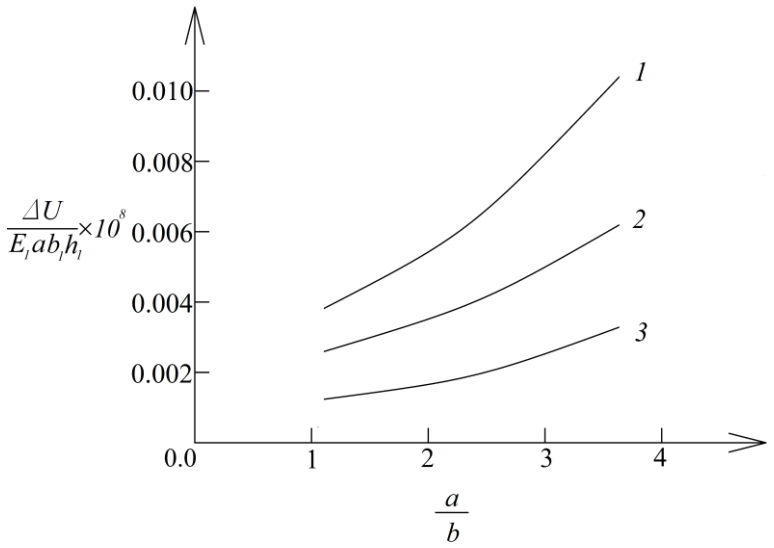

Figure 4. The damping energy versus a/b ratio (curve 1 – at $H_1/H_2 = 0.5$, curve 2 – at $H_1/H_2 = 1.0$ and curve 3 – at $H_1/H_2 = 2.0$).

These effects are illustrated by the curves shown in Fig. 5

.

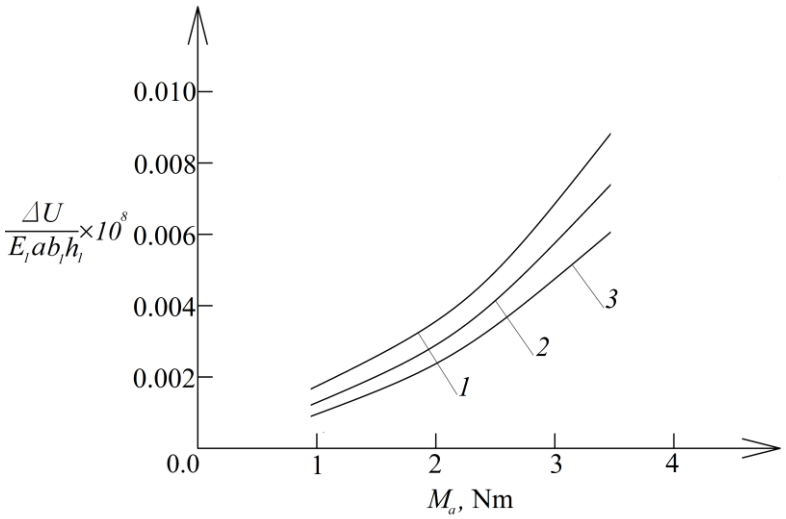

Figure 5. The damping energy versus M_a (curve 1 – at $h_1/b_1 = 1.4$, curve 2 – at $h_1/b_1 = 1.6$ and curve 3 – at $h_1/b_1 = 1.8$).

It can be seen in Fig. 5 that when M_a increases, the behaviour of the damping energy is characterized by a quick growth. The increase of h_1 / b_1 ratio leads to reduction of the damping energy (Fig. 5).

Conclusion

A theoretical investigation of the damping energy in a multilayered semi-elliptical arch structure is performed. The investigation yielded the following findings:

1) the damping energy reduces when the strength of the rotational spring increases;

2) increase of E_2 / E_1 ratio causes a reduction of the damping energy;

3) increase of the ratio of the ellipse semi axes leads to growth of the damping energy;

4) increase of H_2 / H_1 ratio causes a substantial reduction of the damping energy;

5) increase of h_1 / b_1 ratio leads also to reduction of the damping energy.

Recommendations

The analysis developed in the present paper can be recommended for application in engineering practice as a tool for investigation of the damping energy in multilayered semi-elliptical arch structures.

Scientific Ethics Declaration

The author declares that the scientific ethical and legal responsibility of this article published in EPSTEM journal belongs to the author.

Acknowledgements or Notes

* This article was presented as an oral presentation at the International Conference on Technology, Engineering and Science (www.icontes.net) held in Antalya/Turkey on November 16-19, 2023.

References

Dowling, N. E.(2007). Engineering methods for deformation, fracture and fatigue. *Mechanical behavior of materials*. Pearson.

Kaul, A. B. (2014). Two-dimensional layered materials: Structure, properties, and prospects for device application. *Journal of Materials Research, 29*(3), 348-361.

Kim, J. S., Paik, K.W., & Oh, S. H. (1999). The multilayer-modified Stoney's formula for laminated polymer composites on a silicon substrate. *Journal of Applied Physics, 86*(10), 5474–5479.

Lloyd, S.J., & Molina-Aldareguia, J. M. (2003), Multilayered materials: a palette for the materials artist. *Phil. Transactions of the Royal Society of London. Series A, 361*(1813), 2931-2949.

Rizov, V.I. (2018). Analysis of cylindrical delamination cracks in multilayered functionally graded non-linear elastic circular shafts under combined loads. *Frattura ed Integrità Strutturale, 12*(46), 158-170.

Rizov, V. I. (2021). Delamination analysis of multilayered beams exhibiting creep under torsion. *Coupled Systems Mechanics, 10*(4), *317-331*.

Rizov, V. I. (2021). On the analysis of damping in elastic-plastic inhomogeneous beams. In *Materials Science Forum*. (Vol 1046, pp.59-64).

Rzhanitsyn, A.R. (1986). *Built-up bars and plates*. Moscow: Stroyizdat

Nguyen, S., Lee, J., & Cho, M. (2015). Efficient higher-order zig-zag theory for viscoelastic laminated composite plates. *International Journal of Solids and Structures, 62*, 174-185.

Nguyen, S., Lee, J., & Cho, M. (2020). A coupled hygrothermo-mechanical viscoelastic analysis of multilayered composite plates for long-term creep behaviors. *Composite Structures, 242*, 112030.

Tokova, L., Yasinskyy, A., & Ma, C.-C. (2016). Effect of the layer inhomogeneity on the distribution of stresses and displacements in an elastic multilayer cylinder. *Acta Mechanica, 228*(8), 2865-2877.

Yu, J. H, Guo, S., & Gillard, D.A. (2003). Bimaterial curvature measurements for CTE of adhesives: optimization and modelling. *Journal of Adhesion Science and Technology, 17*(2), 149-164.

Author Information

Victor Rizov
Department of Technical Mechanics
University of Architecture, Civil Engineering and Geodesy
1 Chr. Smirnensky blvd.
1046 – Sofia
Bulgaria
Contact e-mail: *V_RIZOV_FHE@UACG.BG*

To cite this article:

Rizov, V. (2023). Multilayered semi-elliptical arch structures: A damping analysis. *The Eurasia Proceedings of Science, Technology, Engineering & Mathematics (EPSTEM), 26*, 752-759.

The Eurasia Proceedings of Science, Technology, Engineering & Mathematics (EPSTEM)
ISSN: 2602-3199

The Eurasia Proceedings of Science, Technology, Engineering & Mathematics (EPSTEM), 2023

Volume 26, Pages 760-769

IConTES 2023: International Conference on Technology, Engineering and Science

A Framework for Implementation Public-Private Partnership in Roads' Maintenance and Operating Projects in Jordan

Taqwa Alhadidi
Al-Ahliyya Amman University

Abstract: This paper describes a systematic approach to assess and fund highways infrastructures project in Jordan. In essence, it focuses on building a framework to implement Public-Private Partnership (PPP) in roadways' Maintenance and Operating (M&O) projects. It presents a methodology to assess the conditions of the highway infrastructures using structural and functional indices. The deterioration in the infrastructure condition with the age is presented, followed by M&O project period classification. Subsequently, identifying the problems confronted in the PPP (M&O) process and the associated factors affecting PPPs in service delivery, and proposing activities contributing to improvements of the M&O performance with the implementation of PPP. Thereafter, a framework to implement the PPP in highway maintenance projects is presented.

Keywords: Highway maintenance, Pavement condition index, Public-private partnership

Introduction

In the contemporary era, transportation assets face a significant challenge due to the escalating demand for traffic. The continual growth in demand results in the deterioration of infrastructure, necessitating maintenance and operation under acceptable conditions. Globally, transportation agencies grapple with the limitation of budgets for maintaining and operating their infrastructure. It has been proven that increasing the capacity of infrastructure is not a viable solution to accommodate traffic demand, especially in densely populated urban areas where space is restricted.

The future planning and vision for the transportation sector address issues such as resource optimization, restricted capacity augmentation of infrastructure, increased traffic due to population growth, declining revenue sources, reduced availability of conventional fuel, and heightened congestion on roadways. Traditional sources of income for highway management include fuel tax, road tax, vehicle registration fees, parking fees, and tolls on certain sections of the infrastructure. However, in developing countries, highway management income depends on dedicated budgeting from authorities like the Ministry of Public Work and Health (MOPWH) or other municipalities. Additionally, external funds from different countries and agencies are often sought to promote infrastructure development. Therefore, the development of a maintenance and operating plan is essential, based on a systematic assessment of road conditions.

One successful model for funding public projects is Public-Private Partnerships (PPPs). PPPs serve as a funding source for highway infrastructure when the government faces financial constraints or funds are unavailable for spending. An exemplary case is the state of Indiana, which received $3.8 billion from a private entity to operate and upgrade its toll roads in exchange for toll revenue over the next seventy-five years (TOLLROADSnews, 2006). Governments can overcome various restrictions, such as legislative constraints and budget allocations, by engaging in PPPs with the private sector to undertake projects that might otherwise be challenging to implement (Engel et al., 2009).

While successful examples of PPPs exist, there have also been instances of misplacement of structure and risk allocation leading to contract failures, renegotiations, or complete breakdowns. For instance, the Dulles Greenway project in Virginia defaulted in its early years due to an overestimation of road demand. Inflexibility in contract structures to accommodate unforeseen circumstances also contributed to failures, as seen in the case of Orange County SR91, where a non-competence clause led to the failure of the PPP. In Jordan, the Queen Alia International Airport (QAIA) stands as the first airport in the Middle East operated under PPP. QAIA received a 25-year concession contract to reconstruct a new terminal, which was opened in 2013 (Biygautane & Jarrar, 2023).

Jordan has predominantly utilized PPPs for energy generation, with few critical infrastructure projects in other industries. The first PPP project in Jordan was the 1995 feasibility study to build the Samra Wastewater Treatment Plant on a PPP basis, although its execution was delayed until 2003 (Oxford Business Group, 2015). Following geopolitical issues like the 2003 Iraq War and the 2007 financial crisis, which strained public finances, Jordan expedited its adoption of PPPs to secure private funding for infrastructure projects (IMF, 2017). The Jordan Education Initiative, the first PPP in MENA education, was implemented in 2003 (Mistarihi et al., 2012). PPP contracts have been awarded for energy, water, sewerage, an airport, a port, and an ICT project, totaling over $7 billion in Jordan. The World Bank Group (2021) reports that 46 projects worth $10,563 have closed. The IMF (2017) estimates that 30% of Jordan's public investment portfolio was procured through PPPs, a significant contrast to 6% in other emerging nations. However, 70% of these contracts, predominantly in the power or water sectors, are government-funded, necessitating government or State-Owned Enterprise (SOE) payments during operation (IMF, 2017). Such agreements transfer most of the risk of early termination or inefficient performance to the government and fail to generate end-user income, thereby increasing the burden on the public budget for project funding.

To this end, this paper aims to develop a framework to implement the PPP in roads' maintenance and operation projects. In essence, this study contributes significantly to state-of-art and state-of-practice by developing a framework to implement the PPP in roads maintenance and operation in Jordan. The developed framework provides an in-depth into how maximizing social benefit, higher quality of service, transparency, and achieve the efficiency in private sector. The proposed framework helps decision makers to foster the rapid development of PPP projects. Following this introduction, the next section presents a thorough review of the road's infrastructure assessment, and the different PPP types. The research methodology/approach is also presented in Section 3. The fourth section discusses the developed framework. The last section elaborates on the implications of the research and presents conclusions, limitations, and recommendations for future research.

Settings

In this section, Public Private Partnership (PPP), the roads infrastructure assessment, followed by the operation and management period and the different PPP types are presented.

Public Private Partnership

There are many types of structures for a PPP, but the primary categorization is based on the type of infrastructure being considered for the PPP venture, i) Existing infrastructure and ii) New infrastructure. When dealing with a delivery structure for existing infrastructure it is labeled as i) Brownfield project which would be the operation and maintenance of an existing asset, while for the development and construction of a new infrastructure it is labeled as ii) Greenfield project. Traditionally the type of contract that has been followed is the design-bid-build, wherein the agency designs the asset by means of in-house staff or external contractors and then bid the project for construction. This traditional arrangement ensures that the design risk, along with the operation and maintenance is retained by the agency while the construction is carried out by an external contractor. Though with time there has been a change in the terms of these traditional contracts to ensure the quality of construction, in the form of performance guarantees for a specific period of time after the construction is finished. The two general types of innovative contracting techniques are for i) non-traditional form of project delivery and ii) project having some form of private debt or equity investment.

Several works have been done to identify the critical factors that affect the implementation of PPP in M&O projects. Hwang, Zhao and Gay (2013) studied cases in Singapore and identified 42 risk factors and 14 factors affecting success of PPP projects. Those factors were assigned to the government authority and the private sector. Similarly, in another research, critical risk factors in the PPP projects were grouped into four aspects

referring to economic, institutional, social and industrial, and project-specific factors (Jin & Zhang, 2011). The most relevant factors are presented in Table 1.

Table1. Factors affect PPP implementation

Group	Factor
policy and governance structures	instability caused by government changes.
	immaturity of relevant legal system.
	unsatisfied distribution of risks and responsibilities between private partner.
obstacles in operating stages	lack of technical experience.
	lack of experiences in M&O long term projects.
financial factors	limited market demand
	financial risks

Road Infrastructure Assessment

The deterioration in facility condition can be mainly categorized into two types: functional deterioration and structural deterioration. Structural condition assesses the infrastructure's capacity to withstand traffic loading, while functional deterioration gauges the quality-of-service provision. Roads' infrastructure, including pavement and bridges, experiences wear and tear with the passage of traffic. The degree of deterioration depends on various factors, such as pavement material, traffic volume and type, and weather conditions. Extending the life of infrastructure involves implementing preventive maintenance before reaching the minimum acceptable pavement performance, as pavement performance starts high and degrades over time.

Common deterioration figures suggest that during 75% of pavement life, pavement performance degrades by 40%. In the second phase, this degradation occurs by only 12% of the pavement lifespan (Johnson, 1983). George et al. (1989) developed a model predicting pavement deterioration, factoring in variables like traffic load, pavement age, strength, and condition. In Jordan, pavement sections predominantly consist of flexible pavement. A predictive model for pavement deterioration in Jordan was developed by Al-Suleiman (2021). Their results indicated that the majority of pavement sections were in an acceptable condition, as per pavement evaluation. However, according to proposed Maintenance and Rehabilitation (M&R) strategies for Jordan's rural roads, around 40% of the evaluated pavement sections require rehabilitation.

Pavement condition is often assessed based on surface condition, expressed by pavement distress that quantifies the impact of traffic loading, environmental effects, and material characteristics. The rating method provides an index reflecting pavement distress in terms of severity, extent, and type of distress as both structural and functional faults. The surface condition is measured by the number, type, extent, and severity of cracks on the pavement surface, which are then summed up to calculate a deducted value from the ideal pavement condition. The quality of driving on the pavement is expressed by the roughness index, influenced by longitudinal and transverse cracks. Both crack roughness and other indices are used to evaluate pavement projects. Evaluating a pavement network requires a predefined minimum acceptable level for pavement condition, usually based on the pavement condition index (PCI) for each roadway. These values are then compared and prioritized based on the lower PCI.

In the United States, several agencies have developed an index to measure pavement condition based on distress or condition, known as the pavement quality index (PQI). For example, Ohio DOT uses pavement condition rating and pavement roughness index to calculate RQI, while Minnesota employs Pavement Riding Quality to calculate the PQI. Nebraska DOT relies on the serviceability index to calculate the PQI, where a combination of visual distress and rut depth or faulting is considered (FHWA, 2013).

Combining PPP in M&O Projects

In identifying the different factors affecting the implementation of PPP in M&O projects, the most critical stage is having obstacles during the operating stage which can be mitigated by enforcing the performance-based contract scheme. Performance-based road maintenance by contracting (PBRMC) is a method under which a contractor has to plan, design, and implement maintenance activities in order to achieve short- and long-term road condition standards for a fixed price, subject to specified risk allocation (Frost and Lithgow, 1998).In essence, the performance based contract shows its ability in reducing maintenance costs through the application

of more effective and efficient technologies and work procedures; providing transparency for road users, road administrations and contractors with regard to the conditions roads have to be maintained; improving control and enforcement of quality standards; and improving overall road conditions. The issues of implementing the PBC has been identified as follows: having performance specification and setting up a standard, expertise of the private sector, deciding the initial project, risk exposures, performance monitoring, employee issue, payment, and termination of the contract.

Performance indicators measure the performance of the contractors in PBMC. Some examples of performance indicators/standards. Commonly, the International Roughness Index to measure the roughness of the road surface, which affects vehicle operating cost; absence of potholes and control of cracks and rutting, which affects safety and pavement performance which could be measured using PCI ; amount of obstruction of the drainage system to avoid destruction of the road structure; friction between tires and road surface for safety reasons; and retro-reflexivity of road signs and markings for safety reasons.

Results

In this section the framework of implementing the PPP within the M&O projects is presented. To implement the PPP within the M&O projects, two main items should be assigned. The contract authority and the public responsibility, the framework is presented in Figure 1.

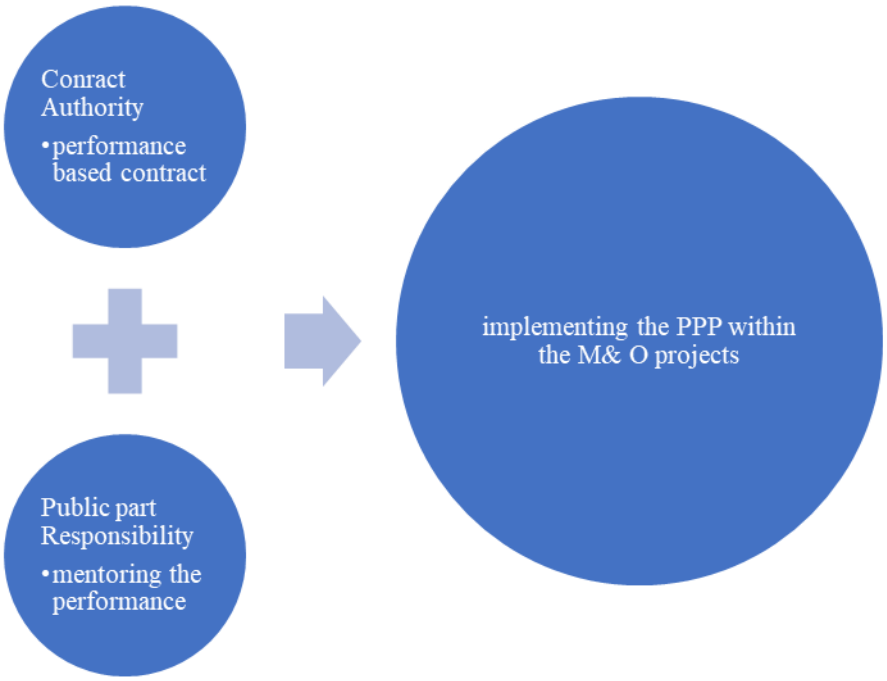

Figure 1. Framework of implementation of PPP within M&O projects

Contractual Authority

In identifying the contractual authorty, assigning the propoer contracutal authority type is the first step. Before implementing the PPP understanding the difference between the different PPP types is presented here**.** Innovative structures for contracts are i) Design and Build, ii) Design-Build-Operate-Maintain, iii) Cost-plus-time bidding (A+B) contracting, iv) Construction Manager/General Contractor, and v) Construction Manager at Risk. The Innovative financing structures are i) Design-Build-Finance-Operate, ii) Build-Operate-Transfer, and iii) Long-term Lease Concessions. The first type of contract, the design and build require the contractor to assume both design and construction and the associated risks, while the public agency pays for the venture by a pre-decided payment structure. The Design-Build-Operate-Maintain type of contract demands that the contractor not only design and build, but also operate and maintain the asset for a predetermined contractual time. Another variant of the contract structure is A+B which has an objective of minimizing the delivery time for projects with priority for fast completion, as in the case of urban and congested areas. The Construction Manager/General Contractor is most suited for speedy bridge construction, by means of hiring two separate

contractors for design and construction, but with the control of design lying with the public agency. The Construction Manager at Risk type of contract requires the need of a contract manager and a design contractor, and then the client and construction manager negotiate a contract as the design process progresses, facilitating better understanding and team relations over the process (NCHRP,2009). The different PPP types, which can be implemented within M&O, are summarized in Table 2.

Table 2. PPP contract types in M&O projects

Type	Subtype	Operating and maintenance
Operation and maintenance (public ownership of the facilities)	Management contract Lease contract	Private investors do not have ownership, but they are responsible only for the risk associated with the M&O over a short time (e.g., 3-5 years)
Concessions (public ownership of the facility)	Rehabilitate-operate transfer Rehabilitate-lease/rent-transfer Build-rehabilitate-operate-transfer	Private investors do not have the ownership rather they are responsible for the M&O risk over a long period (e.g., 20-130 years)
Greenfield projects (private ownership of the facilities)	Build lease transfer Build operate transfer Build own operate Merchant Rental	Private investors have ownership over a long period (e.g., 20-30 years) and are responsible for building operating and maintaining risk during this period.
Management and lease contracts	Management contract: transfer responsibility for managing a utility to a private operator, often for three to five years. Lease contracts: an operator is responsible for operating and maintaining the business, but not for financing investment.	
Concession contracts	Rehabilitate-operate-transfer (rot): a private sponsor rehabilitates an existing facility, then operates and maintains the facility at its own risk for the contract period. Rehabilitate-lease/rent-transfer (RLT): a private sponsor rehabilitates an existing facility at its own risk, leases or rents the facility from the government owner, then operates and maintains the facility at its own risk for the contract period. Build-Rehabilitate-Operate-Transfer (BROT): a private developer builds an addon to an existing facility or completes a partially built facility and rehabilitates existing assets, then operates and maintains the facility at its own risk for the contract period	
Greenfield projects	Build-lease-transfer (BLT): a private sponsor builds a new facility largely at its own risk, transfers ownership to the government, leases the facility from the government and operates it at its own risk, then receives full ownership of the facility at the end of the concession period. Build-operate-transfer (bot): a private sponsor builds a new facility at its own risk, owns and operates the facility at its own risk, then transfers the facility to the government at the end of the contract period. Build-own-operate (boo): a private sponsor builds a new facility at its own risk, then owns and operates the facility at its own risk. Merchant: a private sponsor builds a new facility in a liberalized market in which the government provides no revenue or payment guarantees. The private developer assumes construction, operating, and market risk for the project rental: a private sponsor places a new facility at its own risk, owns and operates the facility at its own risk	

Mentoring the Performance

Pavement performance in its service life cycle is the manifestation of combined effects of traffic loading and non-load factors concerning pavement type, age, climatic features, subgrade material characteristics, drainage conditions, construction quality, and rehabilitation and maintenance treatments. Conventionally, the pavement surface condition for a highway segment can be measured by the present serviceability index (PSI) or pavement

condition index (PCI) which is established on the basis of roughness, cracking, and rutting measurements. The pavement performance trend can be assessed using PSI or PCI values against the cumulative ESALs in its service life-cycle. The PSI or PCI values can be measured according to the pavement design curve and field performance curve, respectively. The area between the horizontal, zero-deterioration line and the design curve in terms of PSI-ESAL or PCI-ESAL losses represents the portion of pavement condition deterioration caused by pure traffic loading (portion a). The area between the design curve and field performance curve as PSI-ESAL or PCI-ESAL losses represents the portion of pavement condition deterioration caused by pure non-load factors (portion b), as well as the load and non-load interactions that can be further split into load-related interaction (portion c) and non load-related interaction (portion d). As such, the overall load portion of pavement condition deterioration is the summation of pure traffic loading and load-related interaction portions (portion a + portion c). Practically, the pavement design and field performance curves and a proportional rule can be employed to derive the individual portions of pavement deterioration (Fwa and Sinha, 1987). Based on the method described in the above, the design curve and field performance curve involving rehabilitation and maintenance treatments can be used to establish the load and non-load portions of pavement rehabilitation and maintenance cost. Similarly, the design curve and field performance curve involving rehabilitation treatments only can be utilized to establish the load and non-load portions of pavement rehabilitation cost. Then, the load portion of the maintenance cost can be computed as the difference between the load portion of pavement rehabilitation and maintenance cost, and the load portion of pavement rehabilitation cost. The ESAL-based and VMT-based/PCE-MT-based procedures can be utilized to separately estimate the shares of load and non-load related pavement rehabilitation cost or maintenance cost attributable to each category of vehicles. The proportionality assumption is illustrated in Figure 2.

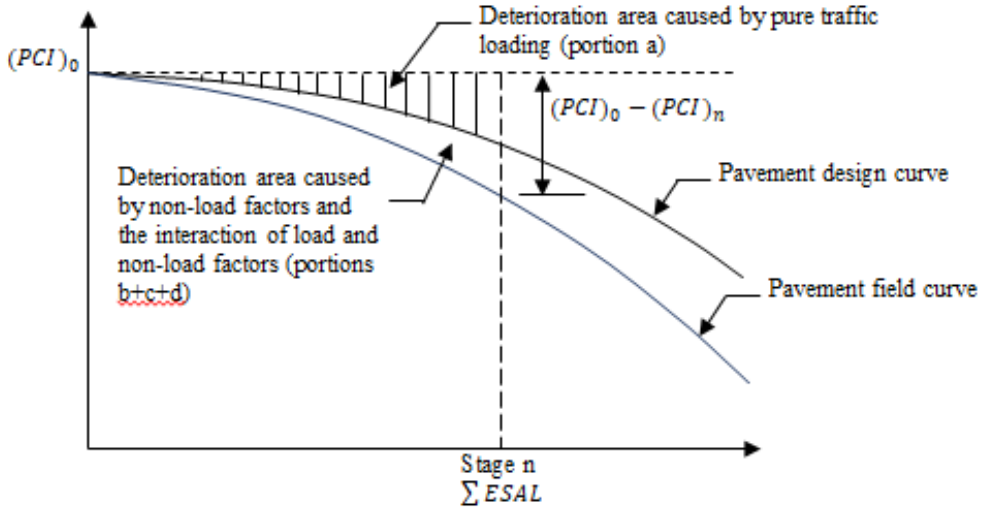

Figure 2. Representation of load and non-load factors shares on pavement condition deterioration

The computation of load and non-load factors on pavement performance is illustrated in Figure 3 below

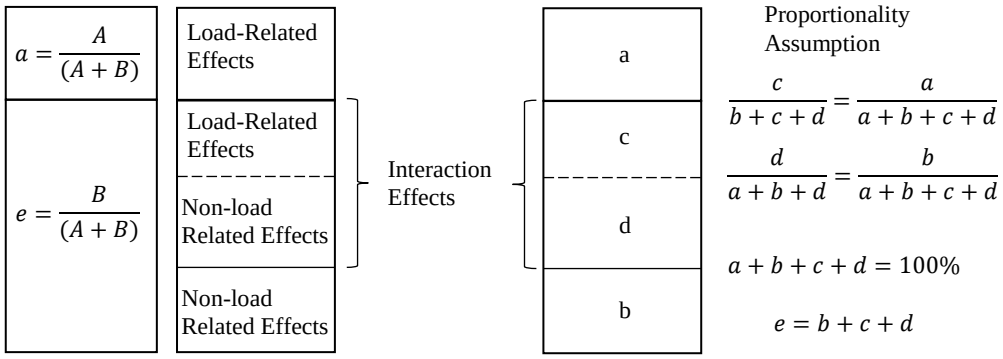

Note: A = area between horizontal line and design curve as PSI-ESAL or PCI-ESAL losses
B = area between design curve and field curve as PSI-ESAL or PCI-ESAL losses

Figure 3. Computation of load and non-load effects on pavement performance

Annual Pavement Maintenance Cost Models for Traffic Loadings

Small et al. (1989) developed the model of maintenance cost for annual ESALs by first determining the overlay interval T as a function of annual traffic loadings Q and number of ESALs that cause pavement to wear out before requiring an overlay N, follow Paterson and Newbery assumption that pavement roughness grows linearly with cumulative ESALs and exponentially over time. The formulation for estimating T is calculated as

$$T = \frac{N}{\lambda Q} e^{-mT} \quad (1)$$

where,

Q: Annual traffic loadings
m: Pavement deterioration rate.
N: Number of standard axle passages before requiring an overlay.
λ: The fraction of one-directional axel passages travelled.
The present value of total pavement maintenance costs during its life cycle is then can be estimated by converting infinite sequence of maintenance cost C every period of T year to present value with a discount rate of r

$$M(Q, W, D) = \frac{C}{(e^{rT}-1)} \quad (2)$$

The annualized maintenance costs given discount rate of r is estimated as rM.
Marginal maintenance cost for traffic loadings
The model of marginal pavement maintenance cost for traffic loadings is derived by differentiating annualized maintenance cost with respect to annual ESALs

$$MC_m = r\frac{\partial M}{\partial Q} = r\frac{\partial M}{\partial T}\frac{\partial T}{\partial Q} = \frac{r^2 e^{rT} C(W)}{(e^{rT}-1)^2}\frac{\partial T}{\partial Q} \quad (3)$$

With T is estimated by Eq. 3, we can find $\frac{\partial T}{\partial Q}$ by differentiating both sides of the equation with respect to Q, corresponding to the case where pavement deterioration rate m is 0 and is not 0. Finally, the marginal pavement maintenance cost of annual ESALs without considering growth of annual ESALs is derived as

$$MC_m = \begin{cases} m = 0, (\frac{(rT)^2 e^{rT}}{(e^{rT}-1)^2}) MC_m^0 \\ m \neq 0, (\frac{(rT)^2 e^{rT}}{(e^{rT}-1)^2})(\frac{e^{mT}}{1+mT}) MC_m^0 \end{cases} \quad (4)$$

PPP in M&O project Framework

In Jordan, to enhance public-private partnership institutions and policies (PPPs) Government, the Jordanian government and the Public-Private Infrastructure Advisory Facility (PPIAF) funded the definition and establishment of a PPP Unit inside the Ministry of Finance, suggestions to strengthen the legislative and regulatory framework for PPPs, a PPP policy, and a pipeline of priority PPP projects. The proposed framework is shown in Figure 4 below.

Discussion

This study provides a framework which will help standardize the practice of PPP in highways maintenance and operation projects. The framework discusses the different types of the PPP contract and the performance-based contract as such, public and private sectors can be beneficial from this study. This accelerate the development and progress of Maintenance and operation projects and ensures that practices are in line with international standards.

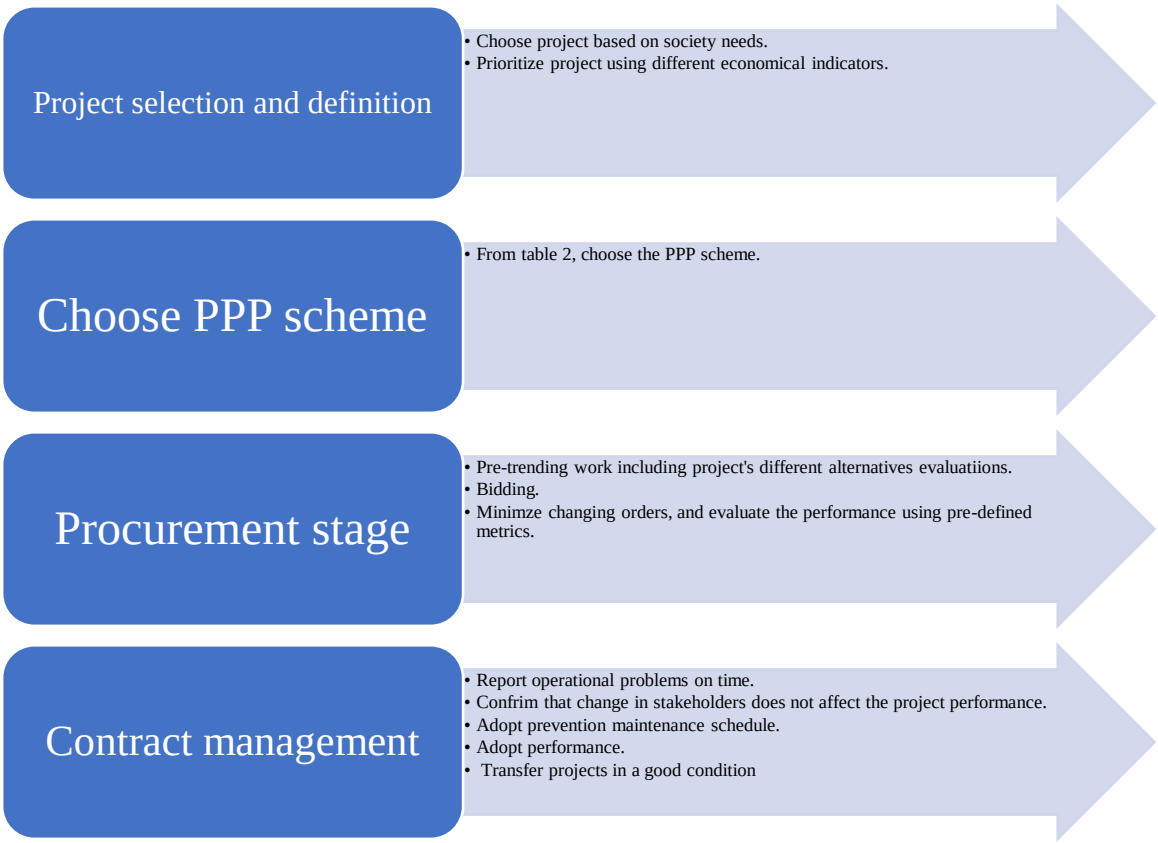

Figure 4. PPP Framework for M&O projects

Initially the framework starts withproject identification and thorough feasibility studies should be done at the PPP initiation stage. Local practitioners should engage opposition political parties and external stakeholders extensively. Transparency is vital in the second PPP stage. Fairness and competitiveness in PPP contract awarding should be ensured. Investors must follow output standards and the contracting authority must oversee the third stage of the PPP process. Private investors should use local materials and prevent building delays. The private partner should prioritize reliable and efficient service delivery at the end of the PPP process. The contracting authority should regularly monitor private partner performance. This suggested framework also gives a framework to standardize PPP in Jordan using different performance indicators including PQI and OCI, also using theoretical backgrounds in predicting the infrastructure conditions using either global standards from FHWA (FHWA, 2007) or using local studies.

This would speed up PPP projects and ensure international standards. The best practise framework provides a th eoretical foundation for developing meaningful hypotheses for empirical research. This approach could be appli ed to a Jordanian or other developing nation project to test its efficacy and efficiency. Finally, the best practice framework serves as a theoretical framework for the formulation of relevant hypothesis for further empirical research. Essentially, the framework could be adopted and tested on a real case project in any developing country to examine its effectiveness and efficiency.

Conclusions

This paper developed a framework for PPP implementation in highway M&O projects. The outputs of this study considerably informs local practitioners in developing countries particularly in Jordan of the best practices that should be carefully observed at M&O projects when implementing PPP projects. In addition, this study expands the existing but limited knowledge on the effective ways of practicing PPP for construction projects in Jordan and developing countries in general. It is hoped that local practitioners in developing countries particularly Jordan, will employ the best practices proposed at each stage of the PPP process in order to ensure a successful PPP implementation and also expedite the implementation of construction PPP projects.

Certainly, a large number of publications would have helped increased the number of best practices. However, considering that the PPP practice is not implemented in Jordan and the fact that few researchers have contributed to PPP discussions using performance-based contract. Nonetheless, the identified best practices should be validated with guidelines issued by the World Bank and state-of-art, thus the results are valid for future reference. Another major limitation is that the best practice framework was not validated using real projects. Apparently, this would have given better assessment results of the validity of the framework. It is suggested that future research studies should adopt the best practice framework and test it on a PPP project throughout its performance-based contract. The outcome of the project that followed the best practice framework should be compared with projects that did not follow the best practice framework. Alternatively, the best practice framework can be tested on a well-established successful PPP project. The applicability of the best practices at each stage can be evaluated by project participants on a Likert scale.

Scientific Ethics Declaration

The author declares that the scientific ethical and legal responsibility of this article published in EPSTEM journal belongs to the author.

Acknowledgements or Notes

* This article was presented as an oral presentation at the International Conference on Technology, Engineering and Science (www.icontes.net) held in Antalya/Turkey on November 16-19, 2023.

*Author acknowledges the financial support from Al-Ahliyya Amman university to present this work at the International Conference on Technology, Engineering and Science.

References

Biygautane, M., & Jarrar, Y. (2023). Public-private partnerships and achievement of public value: The experience of Jordan's Queen Alia international airport. *Journal of Infrastructure, Policy and Development, 7*(1), 1936.

Buxbaum, J. N., & Ortiz, I. N. (2009). *Public sector decision making for public-private partnerships*. (Vol.391).Washington, DC: Transportation Research Board.

Engel. E., R. Fischer, R., & Galetovic, A. (2009). *Soft budgets and renegotiations in public-private partnerships*. (No w15300). Cambridge, MA: National Bureau of Economic Research.

Pierce, L. M., McGovern,, G., Zimmerman, K., &Kathryn, A.(2013). *Practical guide for quality management of pavement condition data collection, federal highway administratio*n. U.S. Department of Transportation. Retrieved from http://www.fhwa.dot.gov/pavement/management/qm/data_qm_guide.pdf

Fwa. T.F., & Sinha, K. C. (1987). Estimation of environmental and traffic loading effects on highway pavements. *Australian Road Research, 17*(4), 256-264.

Hwang, B.G., Zhao, X & Gay, MJS (2013). Public private partnership projects in Singapore: Factors, critical risks and preferred risk allocation from the perspective of contractors. *International Journal of Project Management, 31*(3), 424-433.

IMF. (2017, December 18). *Jordan: Technical assistance report—public ınvestment management assessment (PIMA).* Retrieved from https://www.Imf.Org/En/Publications/CR/Issues/2017/12/18/Jordan-Technical-Assistance-Report-Public-Investment-Management-Assessment-PIMA-45461.

Jin, X., & Zhang, G. (2011).Modelling optimal risk allocation in PPP projects using artificial neural networks', *International Journal of Project Management, 29*(5), 591-603.

Johnson, C (1983) . *Pavement (maintenance) management systems*. American Public Works Association.

Mistarihi, A. M., Al Refai, M. S., Al Qaid, B. A., & Qeed, M. A. (2012). Competency requirements for managing public private partnerships (PPPs): The case of infrastructure projects in Jordan. *International Journal of Business and Management, 7*(12), 60.

Oxford Business Group. (2015). *Government working to increase private sector participation in the conomy*. Retrieved from https://Oxfordbusinessgroup.Com/Analysis/More-Formal-Footing-Public-Private-Partnerships-Benefit-Greater-Legal-Clarity-0.

Tollroad Snews. (2006). *Cintra-Macquarie bid of $3.85b for Indiana TR accepted*. Retrieved from http://www.tollroadsnews.com/node/1420.
World Bank Group. (2021). *PPP knowledge lab*. Retrieved from www.PPPknowledgelab.Com.

Author Information

Taqwa Alhadidi
Al-Ahliyya Amman University
Amman, Jordan
Contact e-mail: *t.alhadidi@ammanu.edu.jo*

To cite this article:

Alhadidi, T. (2023). A framework for implementation public-private partnership in roads' maintenance and operating projects in Jordan. *The Eurasia Proceedings of Science, Technology, Engineering & Mathematics (EPSTEM), 26*, 760-769.

The Eurasia Proceedings of Science, Technology, Engineering & Mathematics (EPSTEM)
ISSN: 2602-3199

The Eurasia Proceedings of Science, Technology, Engineering & Mathematics (EPSTEM), 2023

Volume 26, Pages 770-779

IConTES 2023: International Conference on Technology, Engineering and Science

Metal Artifact Reduction in CT Images through Sinogram Data Inpainting

Abdessalem Benammar
Research Center in Industrial Technologies (CRTI)

Aicha Allag
Research Center in Industrial Technologies (CRTI)

Imad Araar
Research Center in Industrial Technologies (CRTI)

Ahmed Benyahia
Research Center in Industrial Technologies (CRTI)

Redouane Drai
Research Center in Industrial Technologies (CRTI)

Abstract: When metallic implants are present within the human body, they frequently introduce metallic artifacts into X-ray CT images. These artifacts can lead to significant distortions, obscuring critical information and potentially degrading the quality of the CT images, thereby impacting diagnostic accuracy for clinicians. In recent years, there has been extensive research aimed at mitigating the challenges posed by metallic artifacts, resulting in the development of multiple solutions to address this issue. In this study, we present an efficient approach for artifact removal. Our method involves utilizing the image reconstructed from a sinogram affected by artifacts to generate a synthesized sinogram, deviating from the conventional acquisition of sinogram data. The key stages of our approach encompass segmentation, sinogram gap-filling, and subsequent image enhancement. To achieve rapid segmentation, we employed a K-means classification method. For the retrieval of missing data, we utilized an interpolation algorithm based on a penalized least squares method. In the final phase of image reconstruction enhancement, we implemented an advanced contrast equalization technique to restore image intensities to their inherent dynamic range. Through rigorous verification using both simulated and clinical data, our method consistently demonstrates a remarkable improvement in image quality.

Keywords: Computed tomography, Image reconstruction, Metal artifact, Segmentation, Inpainting sinogram, Contrast enhancement.

Introduction

Implanted medical devices like dental fillings and orthopedic implants can give rise to artifacts in computed tomography (CT) images. These artifacts are introduced through processes such as scattering, partial volume effects, aliasing, beam hardening, and photon starvation (Bamberg et al., 2011; King et al., 2022). In the field of medicine, the increasing use of high-density metallic inserts within the human body, such as dental implants, surgical clips, and steel hip or shoulder prostheses, has led to the occurrence of metallic artifacts in tomographic image scans and reconstructions. This phenomenon presents a significant challenge, making it challenging to conduct accurate analyses of specific anatomical regions within the human body (Usman et al., 2020).

Mainly, we can categorize artifacts into the following three forms (Frederique, 2017): a) Streak artifacts, recognizable by the presence of excessive lines in the image. These artifacts stem from errors in mitigation processes resulting from abrupt transitions between two projections or equipment malfunctions. b) Shadow artifacts, marked by a reduction in image intensity. They tend to manifest near high-contrast objects and occur due to deviations in detector responses from expected attenuation values. c) Ring artifacts, characterized by the emergence of ring-shaped patterns within the image. These artifacts arise from errors in one or more detectors, typically due to defects in the detectors themselves or mechanical issues. Typically, the quality of images reconstructed using the conventional filtered back projection algorithm is sufficient for medical diagnosis under normal conditions. However, in specific instances, such as the presence of metal-induced artifacts, the integrity of the scanner signal can be compromised, rendering the assumptions underlying this method inapplicable. Consequently, the resultant image may exhibit pronounced artifacts and provide inaccurate CT data. To address these challenges and minimize such artifacts, various correction methods have been developed over the past two decades. Nevertheless, it's worth noting that this issue remains unresolved to date (Müller et al., 2009). Metal artifact reduction algorithms can typically be categorized into four primary groups: correction of physical effects, interpolation within the projection field, iterative reconstruction, and methods grounded in deep learning techniques (Zhang et al., 2018). In the first group, referred to as direct artifact reduction methods, physical effects are corrected directly. These methods aim to mitigate artifacts caused by phenomena like beam hardening, which occurs in polychromatic X-ray computed tomography when metal is present, without compromising the integrity of the anatomical images. However, in cases involving metals with a high atomic number, the errors can be substantial enough that the aforementioned corrections may not yield satisfactory results (Park et al., 2016). The second group focuses on projections that pass through metallic objects. In these methods, it is assumed that portions of the projections passing through metal objects are missing and are replaced by substitutes, essentially treating metallic objects as completely opaque (Zhang et al., 2011), Mehranian et al., 2013). One commonly used technique in this group is linear interpolation (LI), where the missing data are estimated through linear interpolation from neighboring unaffected projections for each projection view. The third group of methods allows for the iterative reconstruction of images based on weighted or corrected projections (Chang et al., 2019). The fourth group involves metal artifact reduction (MAR) methods that rely on deep learning. These methods apply corrections for metal-induced beam hardening either in the projection domain or in the image domain (Arabi et al., 2021). However, it's important to note that the creation of a successful deep learning model requires a substantial amount of annotated data. Training a deep learning neural network with insufficient data can lead to inaccurate results. Consequently, this process demands significant time and computing power for effective training.

However, given the inherent complexity associated with diverse metal materials, varying sizes, and positions of metallic objects, achieving consistently satisfactory results using a single artifact reduction strategy can be challenging. Therefore, our approach introduces a novel, rapid, and effective method for the removal of metallic artifacts, including streak and shadow artifacts. Our primary contributions lie in the areas of segmentation, gap filling techniques, and image enhancement. In our methodology, we employ a swift segmentation technique based on K-means classification, which takes into account the global characteristics of the entire image. To recover lost data, we utilized an interpolation algorithm based on a penalized least squares method. This technique enables robust smoothing of equidistant data in one dimension and beyond. Furthermore, for enhancing the reconstructed image, we utilize an improved contrast equalization method designed to restore image intensities to their natural dynamic range.

In summary, this article is structured as follows: Section 2 provides an in-depth exploration of the proposed methodology, encompassing segmentation, sinogram inpainting, and the enhancement of the reconstructed image. Section 3 delves into the results achieved through experimentation, encompassing both synthetic and real-world images. Finally, in Section 4, we present our concluding remarks.

Methods

Image Segmentation

The conventional K-means algorithm typically initiates by selecting cluster centers randomly or following specific protocols. Each cluster center serves as a representative for the cluster it encompasses. The K-means method proceeds through iterative steps. In the initial iteration, every data point within the dataset is assigned to a cluster based on its proximity to the cluster centers. Subsequently, in each subsequent iteration, the cluster centers are recalculated, taking into consideration the average values of the features (or values if the feature is a vector) belonging to the cluster elements. Following the recalculation of cluster centers, the memberships for

each data point are updated in accordance with the values of the new cluster centers. If there is no further alteration in the cluster centers, the algorithm concludes its execution.

Let $I_{gray}=\{p_{1G},p_{2G},...,p_{nG}\}$ be the set of the gray level values of the pixels of the input image I, so that p_{iG} is the gray level value of the pixel p_i, where i = 1, 2 ..., n, and $C_G=\{c_{1G},c_{2G},...,c_{kG}\}$ the centers of the clusters in the grayscale space where the specified number of clusters is k. The value of the distance (p_{iG}, C_G) between the gray value of the pixel i^{th} and the cluster center j^{th} is calculated by equation (1).

$$d(p_i^G,c_i^G) = \left|p_i^G - c_i^G\right| \tag{1}$$

An ordinary image comprises a multitude of individual pixels. In accordance with the classical K-means approach, calculating the distance between each pixel and every clustering center during each iteration can be highly time-consuming. A more efficient method involves the utilization of the grayscale image's histogram. The grayscale histogram of a digital image is divided into a set of bins, each representing an integer grayscale value ranging from 0 to 255. Within the histogram, each bin corresponds to a specific integer value, indicating the count of pixels with the same grayscale value (Amorim et al., 2016; Lin et al., 2014). The rapid K-means algorithm, which relies on the grayscale histogram, ensures a significant acceleration of the process. With this approach, the algorithm computes distance values to the cluster centers 256 times, as opposed to n times, for each iteration. A comprehensive breakdown of the steps is provided below:

1.Let's consider the presence of K clusters, with each cluster containing n central vectors

$$c_k = \left(c_{k,1}, c_{k,2}, \ldots, c_{k,n}\right) \tag{2}$$

With *k = 1, 2,..., K.*

2.Calculate the Euclidean distance of each level value to the center of cluster c_k and assign each cluster level value to its nearest center. For example, the Euclidean distance between the value of level r and the cluster center c_k of the k^{th} cluster vector is:

$$d(r, c_k) = \sqrt{\left(r_1 - c_{k,1}\right)^2 + \left(r_2 - c_{k,2}\right)^2 + \cdots + \left(r_n - c_{k,n}\right)^2} \tag{3}$$

Where *k = 1, 2,..., K*. The r value of the gray level scale is assigned to the cluster$c_{\tilde{k}}$ from its nearest center.

3. Calculate the mean value of the levels of each cluster and take it as the new center for each cluster.
4. If the new cluster center is similar to the original one, stop the loop; otherwise, repeat steps 1 to 3.

Sinogram Inpainting

The fast K-means algorithm's output yields segmented images of metallic objects. Subsequently, we project the segmented image of the metallic artifact into the sinogram domain. Then, we subtract the original sinogram, constructed from the unaltered image containing the metallic objects, from the sinogram of the metallic artifact. This subtraction process effectively removes the corrupted projection data. To restore the missing projection data, we employ a gap-filling technique. Our proposed sinogram inpainting technique is an automated smoothing method grounded in penalized least squares regression, specifically based on the discrete cosine transform (DCT-PLS). This technique is utilized for predicting missing values within the sinogram. In this context, we adapt it to fill the gaps, seeking the most suitable sinogram for the restoration of the missing projection data (Wang et al., 2012; Garcia et al., 2010). In a recent study, the author (Bamberg et al., 2011) demonstrated that least squares regression (PLS) can be effectively formulated using DCT, which represents data as a sum of cosine functions oscillating at various frequencies. We provide a brief overview of the DCT-PLS algorithm here, with detailed information available in reference. Consider X as a spatiotemporal dataset containing gaps (missing values), and W as a binary array of identical dimensions indicating the presence or absence of missing values. The DCT-PLS algorithm seeks an $\hat{X}$ that minimizes the following expression:

$$F(\hat{X}) = \left\|W^{1/2}(\hat{X} - X)\right\|^2 + s\left\|\nabla^2 \hat{X}\right\|^2 \tag{4}$$

Where $\|.\|$ is the Euclidean norm, ∇^2 represents the Laplace operator. s is a positive scalar which controls the degree of smoothing: the more s increases, the more the smoothing of $\hat{X}$ increases, W is the diagonal matrix (W_i) which contains the weights $W_i \in [0,1]$ corresponding to the data X_i. Note that in the presence of missing values, W is simply defined by $Wi = 0$ if Xi is missing, while an arbitrary finite value is assigned to Xi. In this case, the algorithm performs both smoothing and interpolation. Unlike conventional methods which generally work with local linear or cubic interpolations, missing data is assigned to values that are estimated using the data set (Wang et al., 2012). The $\hat{X}$ can be easily achieved by rewriting equation (5) in the form.

$$\hat{P} = RF \times IDCTN\left[\Gamma \times DCTN\left(W\left((P-\hat{P})+\hat{P}\right)\right)\right] + (1-RF)\hat{P} \tag{5}$$

$$\Gamma = \frac{1}{1+\lambda \times s_i}$$

Where DCT and IDCT denote the discrete cosine transform and the inverse discrete cosine transform, respectively, RF is a relaxation factor.

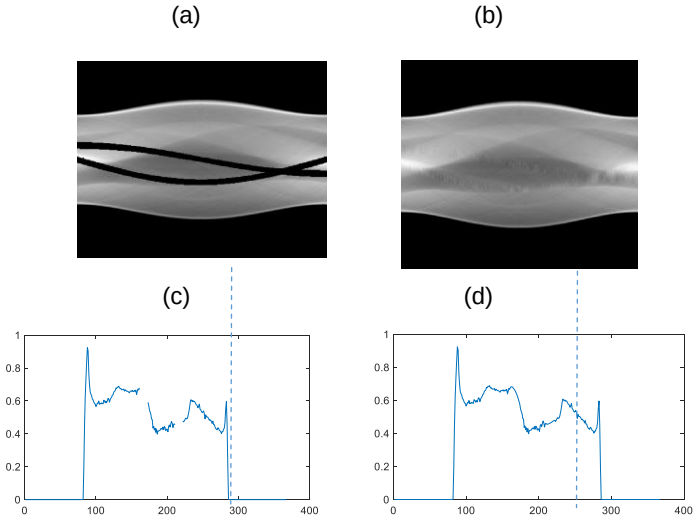

Figure 1. (a) Image of sinogram with removed corrupted projection (metallic objects) from the original sinogram, (b) Inpainted sinogram, The bleu dotted lines in the sinogram images represent the central profiles at the 50th view, (c) corrupted projection at the 50th view, (d) corrected projection.

Enhancement of Reconstructed Images

Images generated by various CT scanners often suffer from reduced contrast effects due to inherent limitations. The contrast equalization technique was originally developed as an integral processing step for a novel face recognition system by (Tan et al., 2010). A refined version of this technique has been introduced to enhance SEM images (scanning electron microscopy) for the purpose of achieving visually appealing results (Al-Ameen, 2018). This modification was carried out through empirical experimentation to afford greater control over the enhancement procedure.

With the use of a single parameter, denoted as μ, the outcome of the two-step regularization process is adjusted in a specific manner. Subsequently, when the subsequent two-step mapping process is applied, it fine-tunes the output to generate results characterized by desirable brightness and contrast. Consequently, the μ parameter plays a crucial role in fine-tuning perceived brightness and contrast, subject to the following conditions: ($\mu > 0$), where a higher μ value contributes to enhanced contrast and brightness regularization, whereas a lower μ value results in outcomes with less-than-ideal brightness and contrast. To achieve optimal results, an operator should manually adjust the μ value, starting with a specific value and gradually increasing it until satisfactory results are attained. This process is operator-dependent. The modified two-step regularization process is computed using equations (6) and (7), as outlined below:

$$K(x,y) = \frac{I(x,y)}{\left(mean(|I(x',y')|^{\mu})\right)^{1/\mu}} \quad (6)$$

where, *I(x,y)* is the input degraded image; *x* and *y* are spatial coordinates; $I(x',y')$ is the transposed version of the image *I(x,y) ; K(x,y)* is the image resulting from the first regularization step:

$$L(x,y) = \frac{K(x,y)}{\left(mean\left(min(\mu,|K(x',y')|)^{\mu}\right)\right)^{1/\mu}} \quad (7)$$

$K(x',y')$ is the transposed version of the image *K (x, y); L (x, y)* is the image resulting from the second regularization step. To further improve the contrast of the regularized image re-map the image intensities in a non-linear and linear fashion, The first step is to use a modified standard logistic function (MSLF), which is a non-linear function for improving contrast. The Conventional Standard Logistics Function (CSLF) is determined using Equation (8):

$$G(x,y) = \frac{exp(L(x,y))}{1+exp(L(x,y))} \quad (8)$$

Where, *G(x, y)* is the resulting image of the CSLF. In this study, an MSLF is used to allow a better control of the apparent brightness and contrast. The modification is curried out to raise the CSLF to the power of μ as in equation (9).

$$\hat{G}(x,y) = \left(\frac{exp(L(x,y))}{1+exp(L(x,y))}\right)^{\mu} \quad (9)$$

Where, Ĝ(x,y) is the resulting image of the MSLF. The output of the above function is an image with altered contrast and attenuated extreme values. To get the final image, the output of equation (9) is normalized to reassign the image intensities to the full dynamic range, which is the second processing step in the proposed new two-step mapping process. This can be done using equation (10).

$$N(x,y) = \frac{\hat{G}(x,y) - min\left(\hat{G}(x,y)\right)}{max\left(\hat{G}(x,y)\right) - min\left(\hat{G}(x,y)\right)} \quad (10)$$

Where, *N(x,y)* is the final image resulting from the proposed technique. The proposed technique comprises two primary phases: The first phase involves a two-step regularization process aimed at standardizing the intensities within the input image. The second phase incorporates a two-step mapping process, designed to enhance contrast and restore the image intensities to their original dynamic range. Figures 2b and 2c visually depict the outcomes of the tomographic image enhancement technique in relation to the parameter μ. Notably, the image quality exhibited significant improvement when the value of μ was set to 2.5 (Figure 2c).

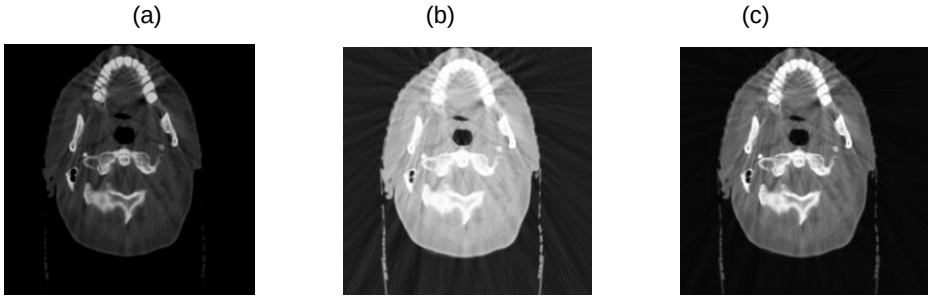

Figure 2. Results obtained by the proposed image enhancement technique, (a) Input image, (b) Enhanced image with μ = 1, (b) Enhanced image with μ = 2.5.

The Proposed Method

The proposed metal artifact reduction algorithm is structured around four fundamental steps:

Step 1: Image Segmentation In the initial step, the input image undergoes segmentation to extract metallic objects. This is achieved through a rapid algorithm grounded in K-means classification, resulting in the isolation of the metallic region within the image.

Step 2: Sinogram Gap Filling In this phase, the metallic area within the image is transformed into the sinogram domain, leading to the acquisition of a metallic trace within the sinogram. Subsequently, by identifying the metallic trace, the corrupted projection data originating from metallic objects is removed from the original sinogram. Finally, a restoration method based on the discrete cosine transform (DCT) is employed to recover the values within the deleted areas.

Step 3: Image Reconstruction and Metallic Object Integration This step involves the reconstruction of the image using the conventional filtered backprojection (FBP) method. Simultaneously, it includes the reintegration of the metallic objects into the reconstructed image.

Step 4: Image Enhancement Through Contrast Equalization The final step focuses on enhancing the reconstructed image by employing a contrast equalization technique. This process is aimed at restoring image intensities to their natural dynamic range.

The overall structure of the proposed algorithm is visually depicted in Figure 3, with each step elaborated in further detail below.

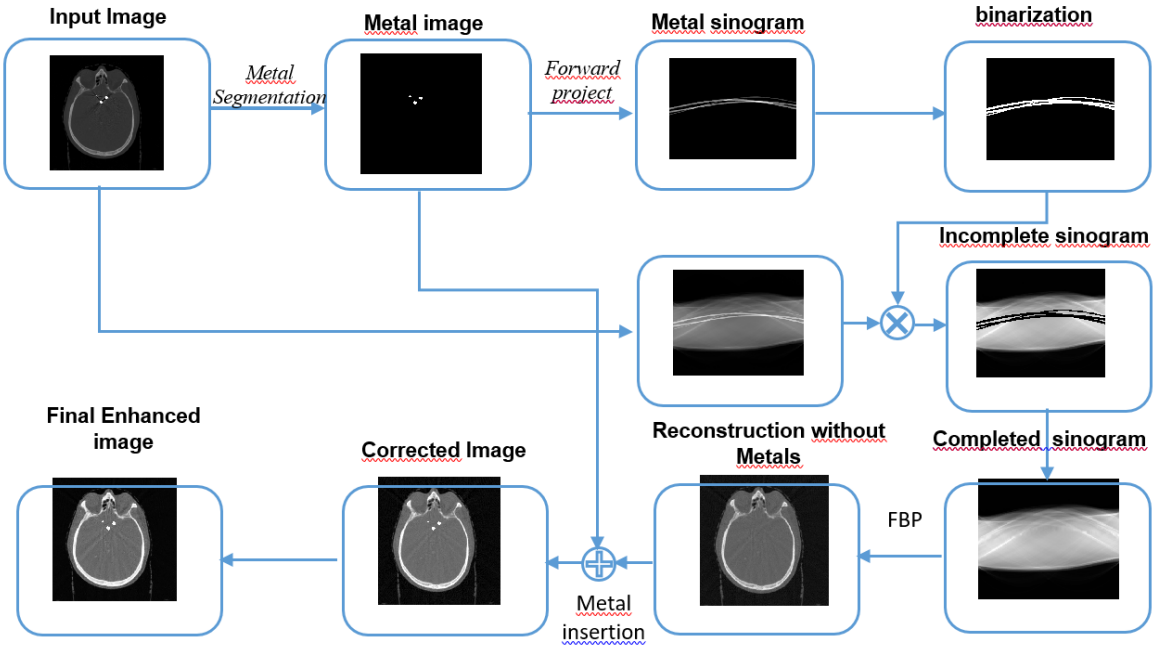

Figure 3. Flowchart of the proposed method

Results and Discussion

To validate the proposed computational approach, a series of experiments were conducted, encompassing both simulated phantom data (utilizing the Shepp-Logan model) and real clinical computed tomography (CT) scans. These tests incorporated images of various dimensions, ranging from 256 × 256 to 512 × 512 pixels. The effectiveness of the newly devised Metal Artifact Reduction (MAR) algorithm was assessed using synthetic images containing metallic implants generated through the Iradon method. The acquisition conditions closely mirrored those found in actual CT scans, aligning with the parallel beam geometry characteristic of simulated CT imagery. In the reconstruction phase of the experiments, the Filtered Back Projection (FBP) technique was employed, incorporating the Shepp-Logan filter to suppress high-frequency components. The algorithm's performance was evaluated across a spectrum of progressively intricate phantoms, with Figure 4a illustrating a 256 × 256 phantom featuring two small artifacts. Figure 4b presents the outcome of the proposed method without any enhancement, while Figure 4c showcases the results achieved with image enhancement techniques applied.

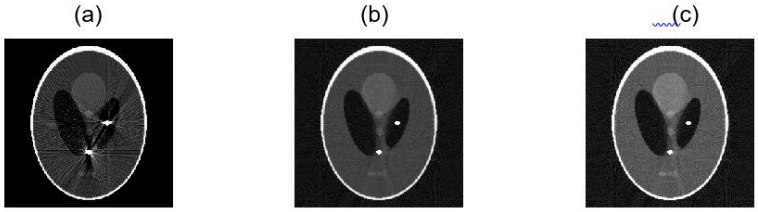

Figure 4. (a) Simulation of a shepp-logan phantom with four metallic artefacts, (b) Result using the proposed correction method, (c) Result of image enhancement technique ($\mu = 2.5$)

Figure 5 depicts the outcomes of our proposed algorithm, with Figure 5(a) showcasing the original phantom containing two substantial metal regions, while Figure 5(b) exhibits the phantom's appearance after being affected by metallic artifacts during the image acquisition process. In our observations, we identified two distinct types of artifacts: hypo-signal and hyper-signal. The results of our algorithmic correction are vividly presented in Figures 5(c) and 5(d). When dealing with multiple metallic regions, the challenge lies in addressing considerably larger gaps in the image, as opposed to the scenario involving a single metallic region. Consequently, a significant amount of information is lost rather than being interpolated. It's worth noting that our proposed algorithm effectively mitigated artifacts in both hypo-signal and hyper-signal areas, as demonstrated in Figure 6.

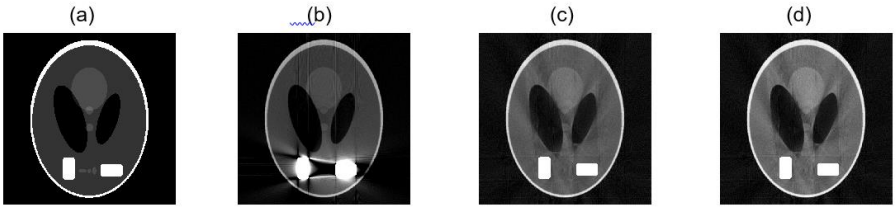

Figure 5. (a) Original Shepp-Logan phantom with two rectangular metallic objects (iron), (b) the original phantom with the influence of metallic artifacts in the acquisition, Results of the proposed algorithm: (c) images corrected without improvement, (d) image corrected with improvement in intensity.

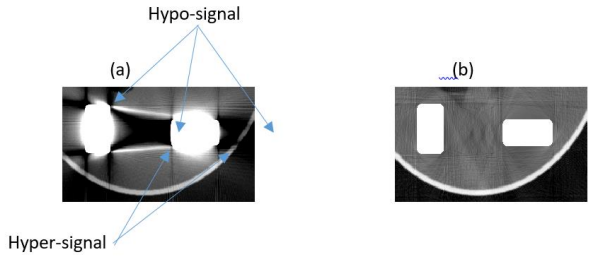

Figure 6. (a) Zoom of Figure 5 on the area of metal artifacts, (b) Results of the proposed algorithm.

In Figure 6a, we present a close-up view of the region affected by the presence of metal during the acquisition process of the tested object. This region experiences a phenomenon where the minimum and maximum absorptions of the two materials overlap, leading to a zone of uncertainty that results in the partial loss of the incident beam. Notably, this issue manifests as a hyper-signal, originating from the subband of lost energies (rays absorbed prematurely within the material), and a hypo-signal, arising due to the measured overcurrent in comparison to the theoretical intensity (visible as shadows in the image). Figure 6b illustrates the compelling results achieved by our proposed method in effectively mitigating both the hyper-signal and hypo-signal artifacts, thereby enhancing the overall image quality. Since there lacks a standardized quantitative approach for assessing CT MAR performance (Zhao et al., 2000), we have employed the peak signal-to-noise ratio (PSNR), a widely accepted criterion in the realm of image inpainting, to evaluate the algorithm's effectiveness.

$$PSNR = 10 \times log_{10}\left(\frac{255^2}{\|Imag - Imag_0\|_2^2}\right) \tag{11}$$

Here, 'Imag' represents the image following inpainting, while '$Imag_0$' denotes the original image.

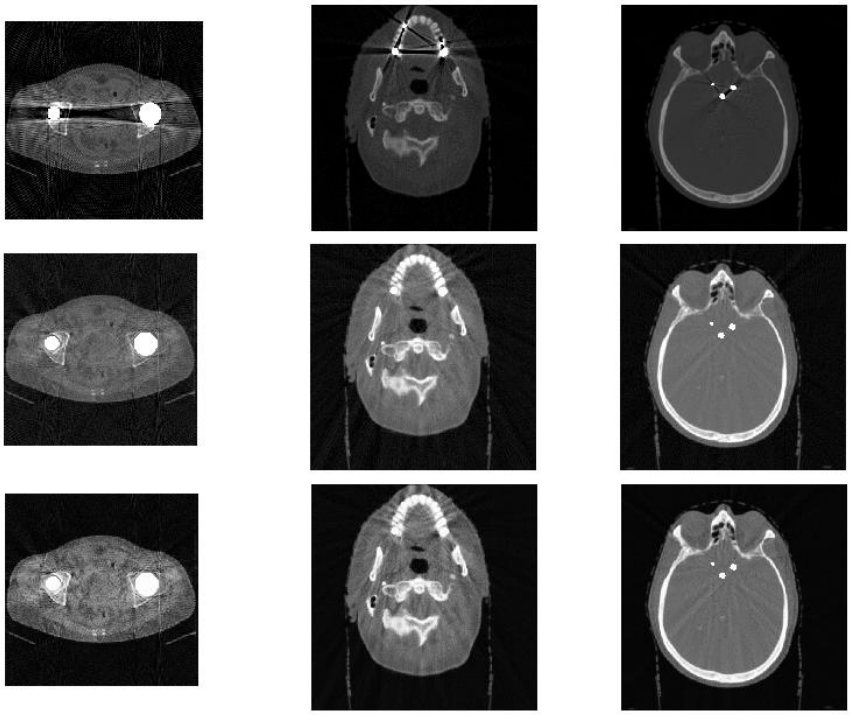

Figure 7. Numerical simulation results using the proposed correction method.

The first, second and third rows respectively show the images with artefacts, images corrected by the proposed method without enhancement and the images corrected with enhancement of their intensities. The first column is clinical CT image of pelvis with the two disk-shaped numerical metallic objects (titanium). Second column: jaw phantom with four disc-shaped metal objects. Third column: clinical CT images of the skull with three metallic objects.

The higher the PSNR value, the more favorable the performance. PSNR serves as a standard metric for quantifying the resemblance between an inpainted image and its genuine counterpart, rendering it a valuable benchmark. The PSNRin value for the image in Figure 5b registers at 14.5. Upon applying the proposed correction method (Figure 5c), we observe an improvement, resulting in a PSNRout of 18.26. Subsequent enhancement further elevates the PSNR to 20.04, as depicted in Figure 5d. Figure 7 illustrates the clinical computed tomography images. We do not know the original images, so it is not possible to calculate their PSNRs. The first, second and third row respectively show the images with artefacts, images corrected by the proposed method without enhancement and the images corrected with enhancement of their intensities. The proposed method makes it possible to successfully remove the streak artifacts without losing the morphological information, as shown in figure 6 (third row).

The outcomes of our study demonstrate the efficacy of the proposed algorithm in mitigating shadow and streak artifacts across various image types. The correction technique we've introduced successfully eradicates beam hardening artifacts without relying on sinogram data. Importantly, it operates independently of any prior knowledge regarding the energy spectra of the incident X-ray beam.

Conclusion

In this article, we have introduced a novel approach to mitigating metallic artifacts in CT images. Our proposed method encompasses four primary steps: image segmentation, gap filling within sinograms, image reconstruction, and enhancement of the reconstructed image. In the initial step, we employ a rapid algorithm based on K-means classification to extract metallic objects, thereby generating an image specifically highlighting metallic regions. The subsequent step involves the transformation of the metallic region image into the sinogram domain, allowing us to derive a trace of metallic elements within the sinogram. Through the identification of this trace, we effectively eliminate the corrupted projection caused by metallic objects from the original sinogram. To restore the values in the deleted regions, we apply a discrete cosine transform (DCT)-based method. Moving on to the third step, we reconstruct the image using the Filtered Back Projection (FBP)

technique while reintroducing the metallic objects into the image. Lastly, in the fourth step, we enhance the reconstructed image by equalizing contrast, thereby restoring the image intensities to their natural dynamic range. Our extensive numerical simulations and clinical applications have convincingly demonstrated the remarkable efficacy of our proposed method in significantly reducing metal artifacts and improving the overall image quality.

Scientific Ethics Declaration

The authors declare that the scientific ethical and legal responsibility of this article published in EPSTEM journal belongs to the authors.

Acknowledgements or Notes

* This article was presented as an poster presentation at the International Conference on Technology, Engineering and Science (www.icontes.net) held in Antalya/Turkey on November 16-19, 2023.

References

Al-Ameen, Z., (2018). An improved contrast equalization technique for contrast enhancement in scanning electron microscopy images, *Wiley Periodicals, Inc. Microsc Res Tech*.1–11.

Amorim, R.C., & Makarenkov, V., (2016). Applying subclustering and Lp distance in weighted K-means with distributed centroids, *Neurocomputing*, (173), 700–707.

Arabi H. & Zaidi H., (2021). Deep learning–based metal artefact reduction in PET/CT imaging, *European Radiology*, https://doi.org/10.1007/s00330-021-07709-z.

Bamberg, F., Dierks, A., Nikolaou, K., Reiser, M.F., Becker, C.R., Johnson T.R., (2011). Metal artefact reduction by dual energy computed tomography using monoenergetic extrapolation, *Eur Radiol, 7*, 1424-1429.

Chang, Z., Ye, D. H., Srivastava, S., Thibault, J. B., Sauer K., & Bouman C. (2019). Prior-guided metal artifact reduction for iterative X-ray computed tomography, *IEEE Transactions on Medical Imaging, 38(6*).

Frederique L., (2017). Identification et réduction de l'artefact métallique en tomographie à rayons X, *Thesis, https://tel.archives-ouvertes.fr/tel-01537663*.

Garcia D., (2010). Robust smoothing of gridded data in one and higher dimensions with missing values", *Comput Stat Data Anal*. *1*, 54(4), 1167–1178.

King, J., Whittam, S., Smith, D., Al-Qaisieh, B., (2022). The impact of a metal artefact reduction algorithm on treatment planning for patients undergoing radiotherapy of the pelvi, *Physics and Imaging in Radiation Oncology, (24),* 138-143.

Lin, C.-H., Chen, C. C., Lee, H. L., & Liao, J. R., (2014). Fast K-means algorithm based on a level histogram for image retrieval, *Expert Systems with Applications, 41(7),* 3276–3283.

Mehranian, A., Ay, M.R., Rahmim, A., & Zaidi, H. (2013). X-ray CT metal artifact reduction using wavelet domain L0 sparse regularization, *IEEE Transactions on Medical Imaging*, *32(9),* 1707–1722

Müller, J., & Buzug, T. M., (2009) Spurious structures created by interpolation-based CT metal artifact reduction, *Medical Imaging 2009: Physics of Medical Imaging*, *72581Y*.

Park, H. S., Hwang, D., & Seo J. K., (2016). Metal artifact reduction for polychromatic X-ray CT based on a beam-hardening corrector, *IEEE Transactions on Medical Imaging*, *35(2).*

Tan, X., & Triggs, B., (2010), Enhanced local texture feature sets for face recognition under difficult lighting conditions, *IEEE Transactions on Image Processing*, *19(6),* 1635–1650.

Usman Ghani, M., & Clem Karl W., (2020). Fast enhanced CT metal artifact reduction using data domain deep learning. *IEEE Transactions on Computational Imaging, (6).*

Wang, G., Garcia, D., Liu, Y., Richard de Jeu, C.D., Johannes Dolman, A., (2012). A three-dimensional gap filling method for large geophysical datasets: Application to global satellite soil moisture observations, *Environmental Modelling & Software, 30,* 139-142.

Zhang, Y., & Yu, H., (2018). Convolutional neural network based metal artifact reduction (et al., 2022) in X-ray computed tomography. *IEEE Trans Med Imaging*, *37*(6), 1370-1381.

Zhang, Y., Pu, Y.F., Hu J.R., Liu, Y., & Zhou, J.-L., (2011). A new ct metal artifacts reduction algorithm based on fractional-order sinogram inpainting, *Journal of X-ray science and technology*, *19(3),* 373–384.

.

Zhao, S., Robertson, D. D., Wang, G., Whiting, B., and Bae, K. T., (2000). X-ray CT metal artifact reduction using wavelets: an application for imaging total hip prostheses, *IEEE Transactions on Medical Imaging*, 19(12), 1238–1247.

Author Information

Abdessalem Benammar
Research Center in Industrial Technologies (CRTI), P.O.Box 64, Cheraga 16014, Algiers, Algeria.
Contact e-mail: a.benammar@crti.dz

Aicha Allag
Research Center in Industrial Technologies (CRTI), P.O.Box 64, Cheraga 16014, Algiers, Algeria.

Imad Araar
Research Center in Industrial Technologies (CRTI), P.O.Box 64, Cheraga 16014, Algiers, Algeria.

Ahmed Benyahia
Research Center in Industrial Technologies (CRTI), P.O.Box 64, Cheraga 16014, Algiers, Algeria.

Redouane Drai
Research Center in Industrial Technologies (CRTI), P.O.Box 64, Cheraga 16014, Algiers, Algeria.

To cite this article:

Benammar, A., Allag, A., Araar, I., Benyahia, A. & Drai, R. (2023). Metal artifact reduction in CT images through sinogram data inpainting. *The Eurasia Proceedings of Science, Technology, Engineering & Mathematics (EPSTEM), 26*, 770-779.

The Eurasia Proceedings of Science, Technology, Engineering & Mathematics (EPSTEM)
ISSN: 2602-3199

The Eurasia Proceedings of Science, Technology, Engineering & Mathematics (EPSTEM), 2023

Volume 26, Pages 780-796

IConTES 2023: International Conference on Technology, Engineering and Science

Application of Information Technology in Human Resource Management

Besnik Hajdari
University of Mitrovica

Hasan Mlinaku
VUZF University

Abstract: This work was carried out in order to inform more about the impact of innovation technology on the development of entrepreneurship. This paper begins with the explanation about the enterprises, starting with their concept, their development over the years, where it elaborates a theory of time about the reasons why the enterprises are opened and exist, continuing with the discussion of who the entrepreneurs are, and what are the tasks theirs, and also gives us a clear picture of how businesses cannot function without business law. This research continues with the most important subject of the time, the history of the development of innovation, showing us different theories about innovation, how it has developed and how it has changed over time, continuing to the division of innovation.Part of the innovation is also the innovation in marketing, where different theories will be examined, including Ansuff's Matrix. Throughout this paper, we have also penetrated the information system, starting from the definition of the terminology of the system, to the types and development of the information system. Then the advantages and disadvantages of virtualization and office automation will be elaborated.

Keywords: IT, E-business, Business engineering, Information systems, Innovation,

Introduction

Enterprises have an important social and economic role, due to their contribution to the functioning of job creation and the functioning of the economic network. In Kosovo, the development of enterprises can contribute to facing the many challenges related to demographic growth, the need for structural change, effects of inequality as well as the high level of unemployment within the region. In business and economics, innovation is the catalyst for economic growth.

Economist Joseph Schumpeter, who has contributed greatly to the study of the innovation economy, argues that industries must constantly revolutionize the economic structure from within, that is, create innovations for better or more effective processes and products, as well as market distribution, such as connecting stores to factories. Schumpeter's (1942) key ideas about entrepreneurship, innovation and economic development are very important for evaluating alternative approaches in contemporary entrepreneurship scholarship. Schumpeter used entrepreneurship as his engine for the dynamic theory of economic development and personified this engine in the theoretical construct of the ideal type of entrepreneurs. This ideal type of actor possessed creative work, the vision of a business idea, the antagonism of non-ovative administrators, the ability to attract investment to lure the capitalist, and to seek out activities that bring about a wide variety of innovations - be they products or

processes. new, creating new market structures (Green & Morgan, 2008). On the other hand, every enterprise relies on information systems to carry out and manage their operations, to interact with their customers and suppliers and to be part of the market.

Application of Information Systems in the Enterprise

Information Systems (IS)

An information system (IS) is a system that collects, stores, stores, processes and sends information important to the organization so that it is understandable and usable by anyone who needs it. The goals of the information system are: to supply the business system with necessary information for the executive subsystem (business process development), the managerial subsystem (business system management) and the information subsystem (cooperation and communication). The parts of the information system are: the system for processing transactions (operating system), the system for supporting decision-making (analytical system), the system for cooperation, communication and individual work (office system) (Beqiri, 2018). The transaction processing system processes a range of transactions, such as:

- Providing accounts for the goods sold,
- Giving accounts for the goods received in the warehouse, as well as
- Sending supplier orders, etc.

The decision support system consists of:

- Unstructured decision making,
- semi-structured decision making,
- Structured decision making.

The system for communication, cooperation and individual work consists of:

- communication,
- Group work support,
- Supporting individual work,
- Content management, as well
- Document search.

General Theory of Information Systems

Never in history has humanity been so flooded with waves of new information and knowledge as it is today. Regardless of where and when it is formed, information is processed and carried in fantastically short intervals, exchanged and used, being exchanged in feedback loops and influencing our own habits and ways of thinking. From its birth, towards the middle of the 20th century, informatics as an interdisciplinary scientific discipline, which deals with the study of all these phenomena and processes, has developed very quickly. All relevant components of informatization: computerization, telecommunications, robotics, artificial intelligence, etc. will be examined in function of their application in business systems, and this means also in function of the development of productive forces. Information represents meaning, which is used very often, both in everyday life and in the fields of many scientific disciplines, theories and different technologies (Beqiri, 2018).

The set of data, meanings or signs, which reduce or eliminate the unpredictability and indeterminacy of the recipient and which enables action by making the most optimal choice from possible events in order to increase the capacity of human knowledge of the chosen event, is called information. For the flow of information, there must be two objects: the giver and receiver of the information. Objects can be different: one-one, one-car, car-one, car-car. The expressions information and news are often taken as the same, but in the field of science that studies information, these two meanings are not the same.

The main characteristic of information is its meaning, purpose and impact on the receiver during the change of his informational state. The news, which does not change the recipient's informational state, has no value, while its value increases if the changes in the informational state caused under the influence of the news content are

greater. Information actually represents the content of a news story. The news may undergo physical changes during transmission, but the information always remains the same. The science that studies the ways of forming, carrying, recording, processing and using information is called informatics. With the application of computers in economic sciences, the application of informatics in economics also began. Its task is to choose problems related to organization, information,

Information theory is a rather complex scientific discipline and is based on probability theory, which was developed as a discipline of mathematics, but has recently been taken as a discipline of informatics. . The most widely cited definition of the enterprise information system is: "the information system is a structured interactive complex of people, machines and actions formed to produce the regulated flow of relevant information collected from internal and external sources of the enterprise , which are used as a basis for making decisions in certain areas, which belong to the management of the enterprise" (Beqiri, 2018).

For comparison, a similar definition can be given for the information system of the enterprise, which is often encountered in the literature: "the information system of the enterprise is a continuous and interactive structure of people, equipment and actions formed for collection, sorting, analysis, evaluation and distribution of appropriate, timely and true information for use by those who bring decisions in decision-making for the purpose of improvement, planning, execution and control of the business.,

If the goals and criteria are defined, then based on them, the management and control bodies can make business decisions, which together with personnel, material and financial resources enter the business process. The result of the business process are: products, services, income, sales, etc. These outputs, due to control, are compared with planned plans (Beqiri, 2018).

Figure 1. Tools for information development

Information Systems in Management

The system which provides necessary information in order to make quality decisions. The inputs of the management information system are smaller than the outputs. The IS components of business management are:

- The material-technical component
- The intangible component
- The human component
- Transmitting component
- Organizational component

The law of minimum quality of management information system (Richard Nolan) says that:

"The quality of the management information system is equal to the quality of its weakest component" (Beqiri, 2018). The structure of the business management information system for management needs: -Decision support system, these systems provide answers to the question: What if?

-Executive information systems (EIS), these systems provide answers to the question: How (should it be done)?
-Transactional systems (TS), these systems give the answer to the question: with whose help can it be realized)?

DSS-They consist of:

- Database
- Database software system
- The base of the models

The model can be: physical model (model of an airplane, ship...), mathematical model (described by equations), verbal model (description of a procedure).

The model that is most often used in DSS is the empathy model, which asks "What if" questions, e.g. What happens if prices increase by 50%, or what happens if we reduce VAT by 5% (Beqiri, 2018).
So, the elements of this system are:

- Hardware – physical equipment of the computer.
- Software - the instructions that direct the operation of the hardware.
- Databases - contain data that is used by application software.
- Procedures are the physical components of brochures, manuals, etc. They can be in the form of instructions for the user or for the preparation of the input by the personnel.
- Personnel - operators, system analysts, data preparation programmers, data administrators, etc (Hajdari & Hajdari, 2021).

Group decision support systems are classified according to two factors:

- The proximity of the participants
- Duration of cooperation in the group

The use of the group decision support system contributes to:

- A better atmosphere during group decision-making
- Increase in productivity
- Generating more ideas
- We allow the individual to organize his work and then present the results to the group (Beqiri, 2018).

Benefits of Information Systems

The benefits of information technology are:

- Visible ease in every operation
- Excellence
- Control
- Presentation of information
- The accuracy
- Data reuse (comparisons, studies)

Likewise, the importance of information systems for the work of the organization, the improvement of the system or the implementation of a new one should be evaluated according to:

- how well the system requirements are understood
- what are the firm's new technology efforts

Every organization must first look at both the benefits and the costs and evaluate the potential investments for information systems. Information systems personnel are the main factor that determines the modification of the system or the development of a new system. In general, the personnel in the information systems department consists of:

- web developer,
- programmers,
- system analysts,
- operators etc.

Utilizer

The users of the company's information system are important resources that can create a real contribution to the fulfillment of strategic objectives and the realization of competitive advantages. In making a decision, the firm will use its sources of information to maximize its benefits and minimize its risk, so the main manager must pay considerable attention to how he should address the final processor (Ansof, 1975).

The end user benefits are:

- It harmonizes opportunities and challenges
- Reduces communication clutter (redundant words)

Figure 2.User

End-user risks of processing are:

- Poorly planned systems
- Poorly documented and designed systems
- Insufficient use of information resources
- Loss of all data
- Loss of security

- Loss of control.

Information Specialists

In the world, the use of Internet services, both from the aspect of communication and from the aspect of absorbing information, is growing for sure. The continuous expansion of computer technology and information systems has enabled the opening of many jobs for specialists in these disciplines. In general, the personnel in the information systems department consists of (Beqiri, 2018):

- System analysts
- Programmers
- Webmaster of
- Operators etc.

System

System is a community of objects, relations between objects and relations between attributes of objects that function as a whole for the given achievement. In other words, the system represents the union of any elements that have common characteristics and form a whole. The whole which represents a system cannot be divided or decomposed into its elements without losing the main properties of the whole. Only the certain community of elements, with mutual connection of action-interaction, ensures the concrete purpose of the system's existence.

So e.g. the supply service in the enterprise has the task of providing certain work equipment and other consumable elements on the basis of which the finished products are created. With the sale of these products, funds are provided, which are used for work tools, as well as for other company needs. This means that each system represents a relatively isolated and rounded community of parts, or mutually interconnected elements, which behave and function according to certain legalities on the basis of which the work and functioning of the system as a whole is ensured (Beqiri, 2018).

Systems can be divided into four main categories: natural systems, organizational systems, technical systems and social systems. Natural systems are based on the natural laws of matter and energy exchange and are unique throughout the world. Organizational systems are built on certain principles and doctrines and their operation is based on the exchange of various information. The main characteristic of organizational systems is their openness to other systems.

Technical systems are created by one, using knowledge of physical laws. Through these systems, one processes nature and makes an impact on nature, adapting the actions of natural processes to one's own needs and goals. Social systems are formed by people as systems of relationships between people. They are formed and function according to the concepts and laws of social and natural sciences. Social systems can be different, such as: economic, social, political, legal, cultural, etc (Beqiri, 2018).

Regarding the exchange of matter and information with the environment, systems can be divided into two characteristics: open systems and closed systems. The system, which exchanges matter and information with the environment in the volume, which affects the characteristics of the system, is called an open system. A closed system is a system that does not combine matter or information with its surroundings in the volume, which affects their characteristics. Business systems must always have the elements, which realize the function of leadership. Sometimes this function is performed by elements, which also perform other activities, but quite often this function is performed by special elements that only have this task.

The elements in the system are connected to each other depending on the algorithm, which refers to the structure of the system. The most common ways of connecting elements in the system are: chain connection, direct re-acting connection and cross-reacting connection. The cross-reactive connection of the elements of the system is realized in the systems, in which the elements are dependent on the action of the other element, not directly, but

with the mediation of the third element. Almost all supersystems, or high-order systems, have such connections. Information systems have the same characteristics as general systems. For this reason, they are defined as a set of components-people, procedures, notes, which are interconnected in such a way that they aim to achieve some common goal (Beqiri, 2018).

Elements of the System

The system has certain parts, or elements, which are called system objects. These elements, or parts of the system in the literature are also called subsystems, segments, or components of the system. Each subsystem can further be decomposed into a certain number of component parts, so that the subsystems can be viewed as separate systems with their own elements. When a large system consists of more subsystems, it is called a supersystem, or higher-order system. Thus, for example: the industry as a system is divided into 35 branches, 85 groups and 185 subgroups, which represent the subsystems of the industry system. Within a given branch of industry, group, or subgroup, enterprises exist as systems. Each enterprise has its subsystems or elements.

The elements of the system are interconnected with certain links within the system itself. Through the connections, certain mutual relationships of the elements in the system are realized and the influence of one element on another is made. There are also certain connections of the elements of the system as a whole with the surroundings, or the surrounding environment. The environment, for the given system, is the set of all objects outside the system for which:

- That changes in the characteristics of the environment affect the system,
- That the behavior of the system affects the changes in the characteristics of the surroundings (Beqiri, 2018).

The effect of each element in the system depends on how it is connected and adapted to the environment. The effect of the system as a whole depends on how each element of the system works separately and how complex they are to achieve the given goal.

Systems Analysts

Figure 1.Systems analysts

Jexpert side in defining problems and compiling written documentation that shows how the computer should help solve identified problems. A successful systems analyst must understand not only programming, databases, networking, and computers, but also business fundamentals, including business strategy, processes, organization, and finance. He/she must be a leader and a manager, well versed in project management. He/she must be able to communicate between business functions and technology professionals and stakeholders (Beqiri, 2018).

Database Administrators

They are responsible for a database. Their tasks are related to the design, implementation, operation and security of the database. A database administrator (sometimes called a DBA) usually has to understand not only the technical side of creating, managing, and maintaining a database, but also the organizational goals behind the functions of each database. After all, it is the role of the database administrator to ensure that the information infrastructure works efficiently and allows users to perform their daily tasks such as: retrieving financial reports or finding information about the customer (Beqiri, 2018).

Figure 3. Database administrators

Below are some common tasks for those who become database administrators:

- Description of coding and writing a database; defining data relationships and attributes.
- Creating and modifying databases according to user needs, maintenance and improvements, understanding organizational goals in order to make recommendations and changes related to the data contained in the database.
- Archiving and retrieval of data, as well as the implementation of security measures to prevent unauthorized access.
- Managing IT staff, such as programmers and analysts, who may work directly on or with databases.
- Estimating cost, time, and other factors in projects involving database development or modifications; development, project scope and guidelines.
- Providing user regulations and permissions, training and support (Beqiri, 2018).

Webmaster is responsible for the content and presentation of the company's website. He must collaborate with network specialists to ensure that the communication network between the firm and its customers and/or its partners is always open. An important task of his is to monitor the visits of the users to the various pages of the website and its continuous improvement. The network specialists cooperate with the system analysts and the users, in the establishment of the data communication networks, which connect distributed computing resources. They combine knowledge from the fields of informatics and telecommunications (Selimaj, nd.).

Figure 4.Webmaster

Programmers

Based on the documentation compiled by system analysts code computer programs. Some firms combine the functions of system analysts with those of programmers, creating the position of analyst programmer. For programmers, a typical workday might involve writing programs in whatever computer language is necessary for their job—Java, for example. Programmers can also debug and troubleshoot programs when they don't work properly. Programmers often work hand-in-hand with software developers, as programmers translate software systems into language that computers can understand. Increasingly, programmers are handling tasks related to mobile applications and other software-based web applications.

Figure 6. Coders

Operators

Voperate large-scale computing equipment, such as mainframes and servers, which are usually located in separate rooms or buildings of the firm. They monitor the control panel. In many ways being a system operator is similar to military service. Time to monitor system conditions is carefully spent in order to anticipate and mitigate potentially dangerous and costly system problems. System operators are constantly trained (prepared), utilizing their skills, and using simulation to practice new situations that expand their expertise. However, when

major system disturbances occur (such as a wind storm or equipment failure), it is the job of the system operator to respond quickly and restore the power grid to safe operating conditions (Hajdari & Hajdari, 2021).

Figure 2. Operators

End-user Computing (EUC) refers to systems in which non-programmers can create working applications. EUC is a set of approaches to computing that aim to better integrate end users into the computing environment. These approaches do their best to realize the potential for high end computing to perform problem solving in a reliable manner. Computing end-users can go from user to complexity by simply clicking a series of buttons, written Scripts in a controlled written language, to be able to change and execute live code. Examples of end-user computing are systems built using fourth-generation programming languages, such as Mapper or SQL, or one of the fifth-generation programming languages, such as ICAD. EUC has evolved due to these key influences.

- **The effect of computer education.** In the early 1980s, the impact of good computer education programs in private and public schools, colleges, and industrial firms became apparent. IT services could not respond quickly enough to user requests, and backlogs piled up with jobs waiting to enter the computer.

Figure 3. The effect of computer education

- **Low hardware cost**. During this time, low-cost computers flooded the market.

Figure 9. The flood of low-cost computers

Virtualization

Virtualization technology is perhaps the most important issue in the field of IT which has started with a total change of the IT industry. The growing awareness of the advantages offered by virtualization technology stems from economic factors, scarce resources, management rules and competition. Virtualization is being used by an increasing number of organizations to reduce energy consumption and air conditioning needs, as well as to reduce the space available in the Server Data Room (Selimaj, nd.).

Figure 10. Virtualization

Virtualization is a combination of hardware and software engineering that creates Virtual Machines (VMs) - an abstraction of computing hardware that allows a single machine to act as if it were many machines at once. Today's IT challenge is the fact that it must always be aware of the latest technological developments. On the

other hand, this allows businesses to adapt a variety of resources, ensuring the infrastructure of the moment and for a much better future. sure.

Advantages of Virtualization

1. Consolidation of the server - A server that supports several VMs (virtual machines) must necessarily have a lot of memory. The CPU and other hardware parts will use a little or a lot of power, and will occupy the same physical space, reducing the cost and spending.
2. Testing and development - The use of virtual machines will rapidly increase development, isolating applications in a known and controlled environment.
3. Dynamic load balancing and disaster coverage - Server workloads are variable. Virtualization provides stability for virtual machines that are using a server's resources.
4. Virtual Desktop - The flexibility provided by virtualization allows a combination of several different operating systems in a single machine, reducing the space occupied by computers in offices, and the costs of hardware.
5. System reliability and security (Hajdari & Hajdari, 2021).

Disadvantages of Virtualization

- The high risk of a physical defect - In virtualization we have a single point of failure or defect. Imagine having five servers and understand very well what effect a single physical defect would have on these five servers, making all five servers fail. were going offline.
- It is not an easy technique.
- Not supported by all applications (Hajdari & Hajdari, 2021).

Virtualization as a term is very broad, but also as an extension, or more precisely as a use, it is also broad. But mainly we will give you some main uses, such as:

- Hardware virtualization
- Virtualization software
- Desktop virtualization
- Application virtualization
- Memory virtualization
- Storage virtualization
- Network virtualization (Hajdari & Hajdari, 2021)

Hardware virtualization or virtualization platform, refers to the creation of a virtual machine that behaves similar to a real computer and that carries an operating system. The concept is as follows: The software that runs in these virtual machines is separated from the hardware resources, so each MV has a part of the capacity of the computer's hardware. So if a computer runs a Microsoft Windows system, it can maintain a phantom virtual machine known as the 'host' from the first view it looks like a computer that runs e.g. in the Linux operating system. In hardware virtualization, the host machine is the actual machine on which the virtualization takes place, and the guest machine is the virtual machine.

Virtualization software It is a virtualization of applications or computer programs. One of the programs that is widely used for software virtualization is SVS (Software Virtualization Solution), developed by Altris. The concept is similar to hardware virtualization, where physical machines are simulated as virtual machines. Software virtualization involves creating a virtual layer or virtual hard drive space where applications can be installed. From this virtual space, applications can be executed, as long as they are installed on a host of an operating system.

When a user has finished using an app, they can 'turn off' it. When an application is turned off, any changes the application made to the host operating system will be completely reversed. This means that the input registry and

installed directories will not leave a trace when the application is installed or run at all. Software virtualization offers several benefits such as:

- The ability to run applications without creating a permanent registry or a changelog.
- The ability to run several versions of the same application.
- The ability to install applications that in one way or another would conflict with each other.
- Ability to test new applications in a single environment (Hajdari & Hajdari, 2021).

So from all these achievements, software virtualization provides many benefits and is easy to implement.

Desktop virtualization is the concept of separating logical desktops from physical machines. One form of desktop virtualization, Virtual Desktop Infrastructure (VDI), can be considered the most advanced form of hardware virtualization. It is based on the direct interaction of a host computer, by means of the keyboard, mouse and monitor connected to it. The user interacts with a 'host' computer through a network connection (LAN or Internet), using a desktop of another computer or mobile device. The 'host' computer in this scenario becomes a server computer, capable of holding several virtual 'host' machines at the same time with several users. For users, this means that they can access their desktop from another location at any time. Using desktop virtualization allows the company to be more flexible, in every last change of technology.

Application virtualization provides portability, management and compatibility of applications, encapsulating them in the underlined form of the operating systems in which they are executed. A full application virtualization is not installed in the first sense of the word, but it runs as if it were.

Advantages of Application Virtualization

- It allows applications to run in an environment that normally does not support that application.
- It can protect the operating system and other applications.
- Uses fewer resources than a separate virtual machine.
- Application virtualization protects operating systems and other applications from the damage that poorly written application code can cause.
- It runs incompatible applications side by side, at the same time and with a minimal increase in testing against each other.
- Reduces system integration and administration cost.
- It implements security and simplicity in the implementation of the operating system (Hajdari & Hajdari, 2021).

Memory virtualization adds the memory resources of individual systems in the data center and aggregates those resources into a memory pool that is made available to every computer in the cluster. The memory pool is accessed by the operating system or by applications running on top of that operating system. This shared memory pool can then be used as a fast cache, as a messaging layer, or as a shared memory resource for CPU or GPU applications.

Memory virtualization allows networked servers in a distributed architecture to share a memory pool between them, thus bypassing the limitations they may have on physical memory. It improves memory utilization by sharing scarce resources. It increases efficiency and reduces execution time for applications that have a lot of data and a lot of I/O operations.

Virtualization of systems of data storage (storage) is a tool by which we get better functionalities and more advanced features in data storage systems. In the context of data storage systems, two basic types of virtualization are distinguished:

1. Block virtualization - refers to the separation of storage from physical storage in such a way that it can be accessed independently of the physical device or the distributed and diverse physical structure. This

separation allows the administrator of the data storage system to have more flexibility in the way he manages storage for end users.

2. File virtualization-eliminates the dependency between the data accessed at the file level and the physical location where these files are stored. This offers the possibility to optimize the use of storage and to carry out easier and problem-free migration of files.

Network virtualization is a process of combining hardware and software network resources and network functionality into a single software-based administrative unit known as a virtual network. Network virtualization is categorized as:

External - combination of several networks, or parts of networks, within a virtual unit or Internal - provides the network as a functionality of software holders in a single system.

The Most Useful Programs for Virtualization

In order to realize the virtualization, it was possible to create several programs, the ones we will mention are:

1. VMware
2. Virtual Box

VMware provides a complete virtualization of a hardware community of the guest operating system. The VMware program virtualizes the hardware for a video adapter, a network adapter and a hard disk adapter. The host provides paths, driver passes, for USB, serial and parallel guest devices. In this way, machines have high transferability between computers, because each host looks almost identical to the guest (Selimaj, nd.). Virtual Box is x86 software that is installed on a host operating system as an application. This host application allows guest operating systems to be loaded and run in a virtual environment.

Office Automation

One of the most encountered terms in the history of computerized business development is office automation, which is about the automatic application of computer technology in office work. Office automation as a process can be dated back to the 1960s when IBM coined the term word processing to express the idea that most office activities are focused on word processing. An advantage of OA (office automation) is the fact that it provides a communication channel between people outside and inside the company.

Tele-Employment

During the 1970s, as a result of the low prices of micro-computers and data communication devices, it became possible for individuals to work from home and thus the virtual office appeared for the first time. The term "tele-employment" was used because it describes precisely the idea that employees are "employed" electronically away from the company or firm).

Advantages of Teleworking

- The flexibility of scheduling work tasks while also accommodating personal tasks,
- The firm pays more attention to the communication needs of teleworkers than in an ordinary office environment, where information is communicated orally (Selimaj, nd.)

Disadvantages of Telecommuting

- Being isolated, they may not feel like important members of the organization
- Fear of job loss or career damage,
- Victims of an "electronic holiday",
- Increased family tension.

The virtual office is a service designed for those who need to have access to offices and business services, but avoiding the costs of opening a traditional office. OA's ability to connect people electronically has opened up new avenues in accomplishing office work. This made working in physical offices unnecessary. Such work can be done wherever the employee is - in a virtual office. The concept of the virtual office has its beginnings in telecommuting and hospitality.

The Meaning of Hospitality

- Tele-routeaccommodation for employees who do their office work at home, while accommodation is partially also in the office when necessary.
- The firm provides a central facility that can be used by employees if they need space or official support.
- Employees make reservations for the facilities they need based on the work they will be performing
- The advantages of hospitality are about a more efficient use of resources and space as well as a better focus on what is required to support the office staff.
- The risks are related to the loss of the "bonuses" of the employee who does not have a private office, loss of the sense of community, and a negative impact on the corporate culture.

Advantages of the Virtual Office

- Reduce the cost of infrastructure,
- Reduce the cost of equipment,
- Reduce the possibility of work interruption,
- Social contribution.

Disadvantages of Virtual Office

- Low morale
- Fear of risks tof security

The virtual office is not for everyone. Only when employees can discipline themselves to do most of the work without control and motivation, the work will not stagnate. The virtual office can be ideal for those employees who prefer to work alone and be their own boss. Office successesvirtual es encouraged the visionaries to extend its application to the entire firm – a virtual organization. In a virtual organization, actions across the firm are designed in such a way that they are not tied to physical events (Selimaj, nd.).

Social Impact of the Virtual Organization

- Industries that are most attracted to the concept of the virtual office and virtual organization are those that increase their value in the form of information, ideas and intelligence, which include education, health, entertainment, sports and consulates.
- The virtual office and virtual organization will reduce the demand for more gradations and people moving from one place to another making our cities quieter and more attractive places to live.
- Today almostall of the firm's activities are based on more information, ideas and intelligence than in the past. For this reason, universities and high schools include computer and informatics knowledge in their programs. IT and IS have become imperative in business processes (Selimaj, nd.)

Conclusions and Recommendations

This study has generally discussed the need for the development of innovation in entrepreneurship. In conclusion, we will list some conclusions that resulted at the end of this paper, as well as some recommendations to be taken into account for increasing the value of innovation that innovation adds.

- Enterprise is the basic unit that deals with the organization and coordination of factors of production. Entrepreneurship is a key factor for the economic and social development of a country.
- Innovation is an effective device, new idea, process, or innovative service which can be seen as the application for the best solution that meets the existing needs of the market or the new demands from the clientele. This is accomplished through the most effective services, products, processes, technologies, or ideas available to society, governments, and markets.
- In business and economics, innovation is a catalyst for economic growth or any type of enterprise. Innovation is a necessary condition for any kind of business, if we want that business to have a successful development and a sustainable life in the market.
- The main component task of innovations is the selection of problems related to organization, information, leadership and placement in the enterprise and in the economy as a whole.
- Online Marketing serves as a bridge between the company and the customers by having a wider scope
- Information systems are now an integral part of every company. These systems are used for collecting, storing, processing and reporting data in the company, serving them in daily operations, in the decision-making process, planning and sending important information for the organization.
- Business systems must always have the elements, which realize the function of leadership.

.recommendation

- There must be innovation in the business model, integrating employees from different backgrounds and from different departments, being open to their ideas can bring innovation.
- For development and innovation in business,mustfor entrepreneurs to be prepared for change and open to learning from others, since the future is already here it's just unevenly distributed.
- Companies must bring innovative services, products, processes and technologies to the market, as it brings the development of efficiency within the company, as well as its financial rise.
- The development and increase in the use of online marketing, increasing the promotion of products in social networks, google ads, or other forms of marketing, since it increases the audience, enabling the internationalization of the service or product.
- The necessary use of information systems within the framework of efficiency development, cost reduction, immediate information supply, better customer service, as well as the enhancement of communication skills & methods.

Scientific Ethics Declaration

The authors declare that the scientific ethical and legal responsibility of this article published in EPSTEM journal belongs to the authors.

Acknowledgements or Notes

* This article was presented as an oral presentation at the International Conference on Technology, Engineering and Science (www.icontes.net) held in Antalya/Turkey on November 16-19, 2023.

References

Ansoff, H. I. (1975). Managing strategic surprise by response to weak signals. *California Management Review 18* (2), 21-33.

Beqiri, E. (2018). The implications of information networking at the pace of business development. *International Journal of Knowledge*, *27*, 17-22.

Gault, F. (2023). The Oslo Manual and standards. In *Handbook of Innovation Indicators and Measurement* (pp. 12-17). Edward Elgar Publishing.

Greene, J. P., & Morgan, P. D. (2008). *Atlantic history: a critical appraisal*. OUP USA.

Hajdarı, B., & Hajdarı, H. (2021). Implementation of inovation in entrepreneurshıp through the application of informaion systems. *International Journal of Management (IJM)*, *12*(10), 8-26.

Schumpeter J.A. (1942). *Capitalism, socialism and democracy*. Allen and Unwin.

Selimaj A. (nd.). *Virtualizimi* https://www.scribd.com/doc/136198392/VIRTUALIZATION

Author Information

Besnik Hajdari
Head of the Economic Engineering Department, Faculty of Mechanical and Computer Engineering, University "Isa Boletini" Mitrovica, Kosovo
Contact e-mail: besnik.hajdari@umib.net

Hasan Mlinaku
VUZF University -Sofje, Bulgaria

To cite this article:

Hajdari, B. & Mlinaku, H. (2023). Application of information technology in human resource management. *The Eurasia Proceedings of Science, Technology, Engineering & Mathematics (EPSTEM), 26,* 780-796.

The Eurasia Proceedings of Science, Technology, Engineering & Mathematics (EPSTEM)
ISSN: 2602-3199

The Eurasia Proceedings of Science, Technology, Engineering & Mathematics (EPSTEM), 2023

Volume 26, Pages 797-809

IConTES 2023: International Conference on Technology, Engineering and Science

Detecting Mixed Gear Faults Using Scalar and Cyclostationary Indicators in an Industrial Settin

Kebabsa Tarek
National Higher School of Technology and Engineering,
University 8 Mai 1945 Guelma

Niou Slimane
National Higher School of Technology and Engineering

Ammar Mrabti
University 8 Mai 1945 Guelma

Abstract: In this paper, an innovative approach is presented to enhance gear fault diagnosis using the cyclostationarity method. The first part of this study focuses on simulating gear signals under various conditions, allowing exploration of signal characteristics in vibration measurements. Spectral analyses and statistical calculations are performed to extract both classical and cyclostationary indicators. In the second part, the cyclostationarity method is applied to signals recorded at the gearbox bearings, clearly revealing the presence of faults. The results from these experiments demonstrate that cyclostationarity indicators can be leveraged to improve the prediction of signal roughness during the production process. This approach thus opens up new possibilities to enhance the reliability of vibration measurements and refine gear fault diagnosis.

Keywords: Scalar indicator, Cyclostationary indicator, Spectral analysis, MID, IMID, Reducer 101 BJT.

Introduction

The control of machines by vibration analysis have been developed considerably due to the evolution of maintenance concepts in order to minimize downtime and revision by adopting the method of conditional preventive maintenance Boulenger, et al (1998), and Pachaud et al (1998). Reducing production costs and increasing the availability of the production tools have indeed become issues that needed to detect and identify all defects at an early stage Heng (2002). The current challenge is not to reveal the importance of using vibration analysis in the field of rotating machines maintenance, but to assimilate the bases and recognize the choice limitations of each technique. It becomes clear that the failures cannot be tolerated because of the complexity of the machine and its criticality in the process Vibro-Meter (1991) and Heng (2005). For efficient conditional preventive maintenance, reliable and accurate measurements of the state of the machine should be made Muller (2005). The best control strategy is to use the most relevant indicators. In addition, misinterpretation of operating conditions often leads to false diagnostic sources, which results in unnecessary repairs and considerable downtime.

Spectral analysis is almost certainly the oldest technique and the most used both. Coming to fill the limits of this technique, several methods have also emerged and generally developed for very specific defects. The "revolution" in the field of vibration diagnostic of machines is probably using periodic methods that allowed the development of more reliable methods based on cyclostationarity (Heng, 2011; Estoque, 2004). And on the separation of cyclical component of the signal (Antoni, 2009; Boustany & Antoni, 2005).

The cyclostationarity formulation presents several advantages for the analysis of such signals over conventional approaches. Firstly it can capture with the same tools a large spectrum of behaviors from simple deterministic periodicity (phenomena of unbalance, misalignment, eccentricity, force inversion, lack of engagement ... etc.) to the non-stationary random (fluid movement, frictional forces, bind ...) (Bonnardot , Randall, & Guillet, 2005; Urbanek, Barszcz, Zimroz, & Antoni, 2012). Then it explicitly incorporates a temporal dimension that lets following the evolution of non-stationarity of the studied systems. This analysis allows to identify the amplitude modulations present in the vibration signals (Urbanek, Barszcz, Sawalhi, & Randall, 2011; Gellermann, 2003). This modulation varies with signal components, these can often provide valuable data. An error occurs when the measurement time is generally insufficient (Antoni, 2007). Several studies have shown that the presence of modulations confirms the existence of defects in rolling bearings and gears (Gardner et al., 1988; Makowski, & Zimroz, 2011; Randall, & Antoni, 2011; Antoni et. Al., 2004).

This paper focuses on the application of two properties of cyclostationarity, commonly, namely spectral correlation and spectral coherence for detecting modulations in intensity distribution of the mechanical signals. First, the proposed method is applied on signal of defective bearing measured on the Machine Faults Simulator (MFS) Spectra Quest. A diagnosis of a turbo-alternator working in real conditions in industrial field based on kinematic study and spectral analysis established. Afterwards, a comparison between the cyclostationarity and spectral analysis performed. Eventually, the influence of the variation of the load on the vibration level change also investigated.

Principle of the Method

The cyclostationarity is a method based mostly on the basis of modulation intensity distribution (MID) for the detection and identification of modulations present in the signal. The MID technique originally designed for defect diagnosis of gears, rolling bearings, and journal bearings. The spectral correlation density is concentrated on the detection of amplitude modulation of sidebands spaced symmetrically in the spectra. It can present values of the modulation indicator on a frequency range of the signal as a function of the carrier frequency f and the modulation frequency α. Several techniques exist such as wavelet and empirical decomposition of modulations that could be used to define the indicator of the modulations presence. Therefore, the proposed method can be customized to specify the properties of different signals to be studied in order to explain the principles of the MID.

A filtered signal in this manner contains, in the idealized case, only the specified component with no additional signals and with a very low noise level Taher F, Fakher C, Mohamed H (2005). In this case, the filtered signal consists of a set of three elements:

$$x_i = x_{\Delta f}\left(t, f - i\alpha\right) \qquad avec \quad i = \left\{-1,0,1\right\} \tag{1}$$

Where xi is the unique value of the signal, $x_{\Delta f}(t, f)$ indicate the filtrated version of x (t) in a side band frequency $\left[f - \frac{\Delta f}{2}, f + \frac{\Delta f}{2}\right]$ with Δf the frequency step.

It may be observed that the symmetric filtration depends on three parameters $f, \alpha, \Delta f$.
The frequency band of the analysis of the MID is calculated as follows:

$$f_{\min} = \frac{\alpha_{\min}}{2} + \frac{\Delta f}{2} \tag{2}$$

and

$$f_{\max} = \frac{f_s}{2} - \frac{\alpha_{\max}}{2} - \frac{\Delta f}{2} \tag{3}$$

Where fs is the sampling frequency of the measured signal.

At the end of the filtering process, the calculated spectral correlation could serve as an indicator of the presence of modulation. According to the concept of the sideband filter, and the notations included in the equation 9, the spectral correlation density between components $x_{\Delta f}(t, f+\alpha)$ and $x_{\Delta f}(t, f)$ are given by:

$$SC_x^{\alpha}\left(f+\frac{\alpha}{2}\right)=\lim_{\Delta f\to 0}\lim_{T\to\infty}\frac{1}{T\Delta f}\int_T x_{\Delta f}(t, f)\, x_{\Delta f}^{*}(t, f+\alpha)e^{-j2\pi\alpha t}dt \tag{4}$$

By analogy, additional spectral correlation density can be calculated between components $x_{\Delta f}(t, f-\alpha)$ and $x_{\Delta f}(t, f)$:

$$SC_x^{\alpha}\left(f-\frac{\alpha}{2}\right)=\lim_{\Delta f\to 0}\lim_{T\to\infty}\frac{1}{T\Delta f}\int_T x_{\Delta f}(t, f)\, x_{\Delta f}^{*}(t, f-\alpha)e^{j2\pi\alpha t}dt \tag{5}$$

In order to inspect the relationship between the three spectral components separated by the cyclic frequency α, the multiplication of two spectral correlation density introduced in equations 4 and 5 should be considered.
The suggestion of the frequency *f* and α, for a given Δ*f*, is commonly called the Modulation Intensity Distribution (MID) that can be expressed by:

$$MID_{\Delta f}^{PSC}(f,\alpha)=SC_x^{\alpha}\left(f+\frac{\alpha}{2}\right)SC_x^{\alpha}\left(f-\frac{\alpha}{2}\right)^{*} \tag{6}$$

Where the superscript PSC is the Product of the Spectral Correlation. The degree of cyclostationarity proposed in D' Elia et al. (2011) and Urbanek et al. (2013) represents the ratio of the energy $\alpha\neq 0$ and $\alpha=0$ for a stationary signal. Its mathematical expression is given by:

$$DSC^{\alpha}=\int\left|R_x^{\alpha}(\alpha)\right|^2 d\alpha \Big/ \left|SC_x^{0}(\alpha)\right|^2 d\alpha \tag{7}$$

In some practical applications of the MID for vibration signals, the multiplication of spectral correlation density as the modulation intensity distribution may not be the most useful measure because of large differences in signal energy in different frequency bands. In this case, the interpretation of the MID plans may be more effective when the absolute value of the spectral correlation density is normalized and varies only between 0 and 1. To this end, the proposal $MID_{\Delta f}^{PSC}$ can easily be extended to the use of coherence spectral density as a modulation intensity distribution. The function of the modulation of the distribution density of spectral coherence is obtained by:

$$MID_{\Delta f}^{PSCoh}(f,\alpha)=\left(\frac{SC_x^{\alpha}(f+\alpha/2)}{\sqrt{SC_x^{0}(f+\alpha/2)}SC_x^{0}(f)}\frac{SC_x^{\alpha}(f-\alpha/2)}{\sqrt{SC_x^{0}(f-\alpha/2)}SC_x^{0}(f)}\right) \tag{8}$$

Integration MID Based on Spectral Correlation

As mentioned above, the MID is a function of the carrier frequency f and the modulation frequency α. However, in some special cases, the user may not be interested in finding the specific range of carrier frequencies, but only in the estimation of the general influence specific modulations of the components on the tested signal. In addition, three-dimensional representations can cause difficulties of interpretation and make automated decisions in the process of monitoring of industrial systems Urbanek J, Barszcz T, and al (2014), and Gardner WA (1986). Based on this observation, it is more convenient to represent the MID not as a surface, but as a curve depending only on the modulation frequency, after integration on a carrier frequency band chosen. In the case of amplitude modulation, such representation could be measured for full modulation.The integration distribution of MID represents the density of spectral correlation, expressed by different sources, is commonly called IMID. This integration will be selected over the entire band carrier frequencies defined by:

$$IMID_{f_1}^{f_2}(\alpha,\Delta f) = \int_{f_1}^{f_2} MID_{\Delta f}(f,\alpha)df \tag{10}$$

Where $MID_{\Delta f}(f;\alpha)$ is a vector calculated in the band carrier frequency from f_1 to f_2. The idea of the IMID.

Case of Bearing of the Machine Faults Simulator MFS Spectra Quest

First, the performances of the cyclostationarity method were tested for the detection of an inner race bearing fault assembled on the Machine Faults Simulator (MFS) Spectra Quest (Figure 1). Table 1 shows the geometrical characteristics of the bearing 6004E and in the Table 2, the defects characteristic frequencies are grouped. The frequency of occurred shocks is usually called ball pass frequency inner (BPFI) and is expressed as follows:

$$BPFI = \frac{nf_r}{2}\left(1+\frac{d}{D_m}\cos\theta\right) \tag{11}$$

with:

$$D_m = \frac{D_1 + D_2}{2} \tag{12}$$

Where *f*r is the rotational frequency in **Hz**, n is the number of bearing balls, **θ** is the contact angle, $\mathbf{D_m}$ indicates the average diameter and d denotes the diameter of a rolling element bearing figure 2.

Table 1 Characteristics of ball bearing 6004E

Diameter of the outer ring	42 mm
Diameter of the inner ring	20 mm
Ball diameter	7.14 mm
Number of balls Nb	08

Table 2 Frequencies characteristic of defect BPFI

Rotation frequency	15 Hz
Frequency characteristic of defect BPFI	72.25 Hz

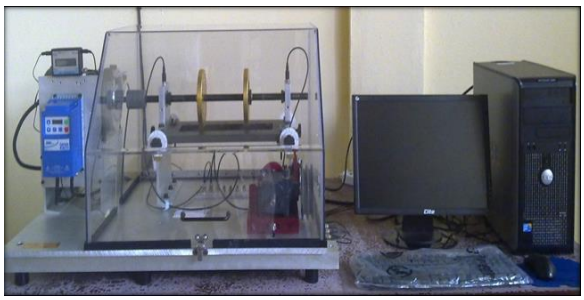

Figure 1. Photograph of simulator MFS Spectra Quest

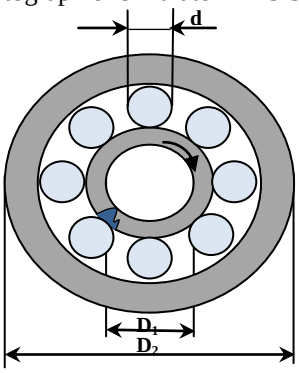

Figure 2. Diagram of a ball bearing with a defect on the inner race

Application of the Cyclostationarity

Shows the result obtained after the application of the MID on the signal measured on the bearing 1. It is clearly noted the appearance of a cyclic frequency at $\alpha = 6.98\times10^{-3}$ *f*s ≈72 Hz and multiple harmonics corresponding to a bearing defect on the inner race (BPFI). This diagnosis was not well clear in the spectral analysis. There is also the occurrence of a carrier frequency at 806 Hz; this value corresponds probably to a resonant frequency of the system see figure 3.a. Shows the result of the use of the integration of the modulation intensity distribution (the IMID) on the same signal. It allows highlighting, by a very clear manner, the cyclic frequency and modulation see figure 3.b.

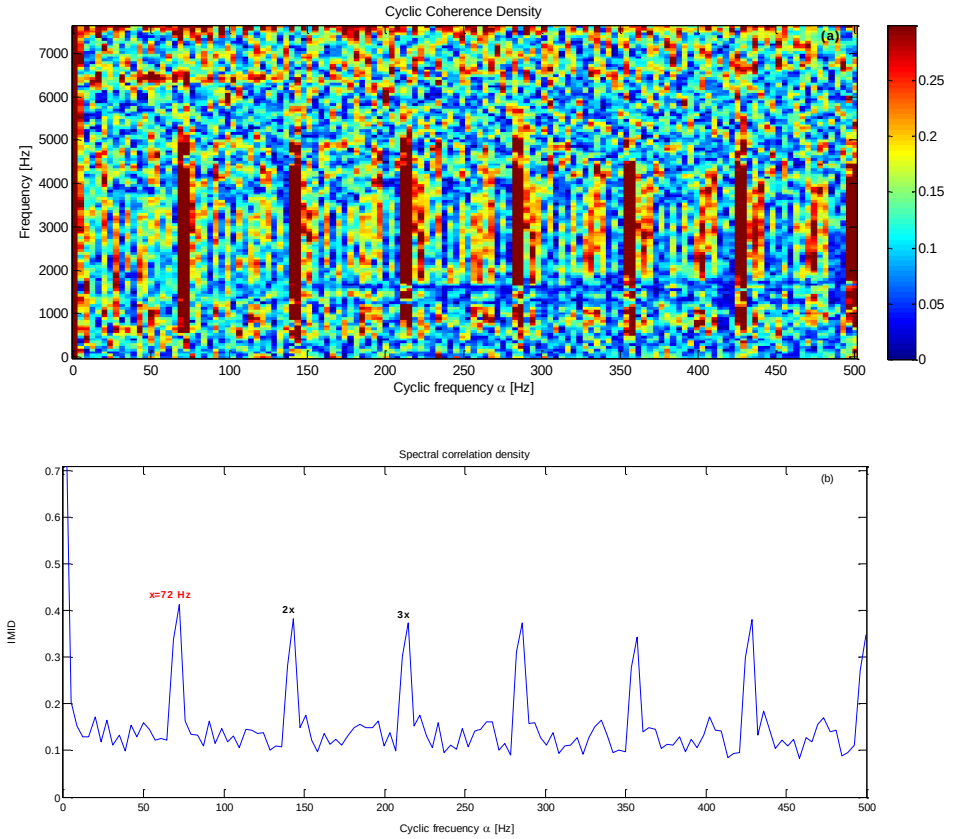

Figure 3. (a) Spectral Correlation (MID) with the corresponding (IMID) (b).

Case of Defects of Turbo-Alternator GZ 1164

Setup Description

The operating principle of the turbo-alternator GZ 1164 comprises introducing superheated vapour at an elevated pressure, commonly called admission vapour, via inlet pipe of the turbine. The latter comprises 16 wheels, each one comprising a number of blades NB (see Table. 3). Each wheel is composed by plurality of eight fixed vanes. The setup comprises a turbine which converts the kinetic energy into mechanical energy that rotates the turbine rotor, a speed reducer in one stage with herringbone teeth, an alternator that rotates at the same output speed of reducer (whatever the load producing electricity), and other accessories figure 4.

Calculation of the Blade Passage Frequency

The passage frequency of the blades of each wheel of the turbine FBP and the frequency of passage of the sets of fixed blades F_{PFBS} can be expressed by the following relationships:

$$F_{BP} = F_{r1} * N_B \tag{12}$$

$$F_{PFBS} = F_{r1} * N_{bW} \quad (13)$$

with N_{bw} = 8 Number of fixed blade in each wheel set.
Fr_1: rotational frequency of the turbine rotor.

Table 3 includes the frequency characteristics of the defect of blade passage for a rotational frequency of the turbine rotor of about150 Hz.

Table 3 Characteristic frequencies of blades passage defects

Number of wheel	Number of blades (NP)	Frequency of the defect (FBP)
1	40	6000 Hz
2	48	7200 Hz
3	48	7200 Hz
4	56	8400 Hz
5	64	9600 Hz
6	88	13200 Hz
7	88	13200 Hz
8	88	13200 Hz
9	88	13200 Hz
10	88	13200 Hz
11	88	13200 Hz
12	88	13200 Hz
13	88	13200 Hz
14	88	13200 Hz
15	80	12000 Hz
16	112	16800 Hz

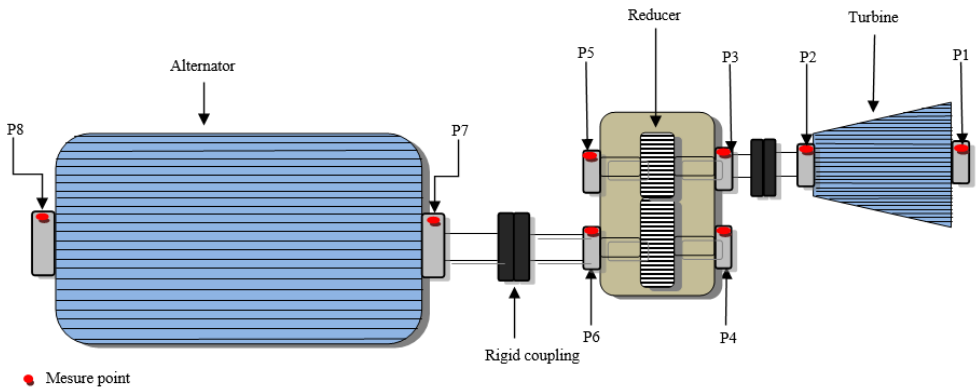

Figure 4. Kinematic diagram of the turbo-alternator GZ1164

Frequency Characteristics of the Reducer

Table 4 shows the technical data of the reducer and its characteristic frequencies. According to the ISO standard 2372 (1974) [34], the studied mechanism is classified in group 3, ie. High power machines (> 300 kW) and mounted on a rigid foundation.

Table 4 Reducer's specifications and its characteristic frequencies

Model / Dimension	GVAB420
nominal power	8300 kW
transmission performance	0.18
input speed (N_1)	9000 RPM say Fr_1=150Hz
output speed (N_2)	1500 RPM say Fr_2=25Hz
Number of pinion's teeth Z_1	41
Number of wheel's teeth Z_2	246
transmission ratio I	6
Meshing frequency F_m=Fr_1 *Z_1 = Fr_2 *Z_2	6125 Hz

Equipment Acquisition and Processing of Measurements

Vibration measurements collected on the eight bearings (P1 to P8) of the turbo-alternator in the three directions. Two accelerometers were used; a mono axial accelerometer B&K type 4511-001 and another triaxial one B&K 4524B-001 (Figure 5.a). For the collection and processing of measurements, the analyzer B&K PULSE 16.1 has been used (Figure 5.b).

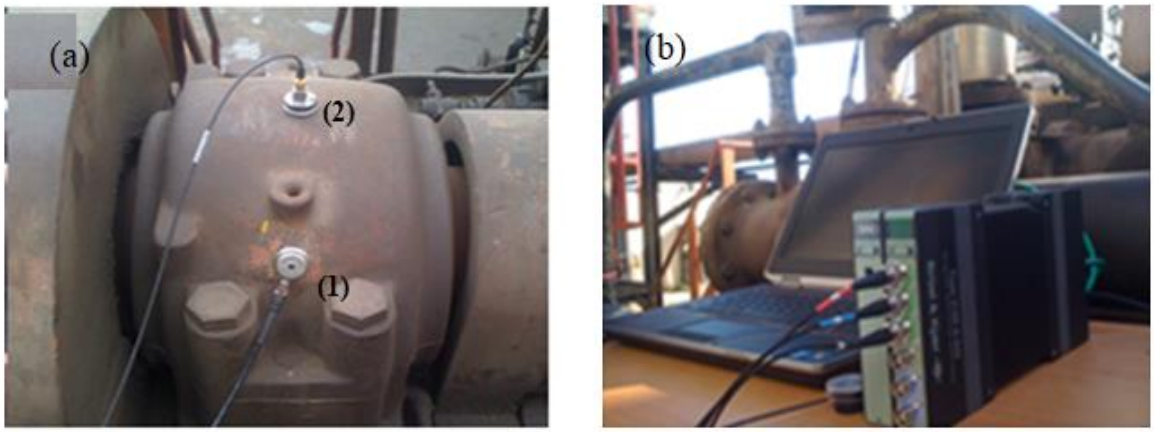

Figure 5. (a) Industrial accelerometer (1) triaxle accelerometer (2), (b) Analyzer pulse 16.1

Data of the Different Sets of Measurements

Because of the importance of the turbo-alternator GZ1164 in the production process of the electrical energy, it requires continuous monitoring. In this study, it was found that this mechanism is simply monitored by periodic tests based on the overall values of the RMS of speed and, time to time, of spectral analysis of speed and of displacement at low and medium frequency respectively [0-200Hz] and [0-1000Hz]. The purpose of the spectral measurements is the detection of any shock into the mechanism, such as shock in gears, shaft friction, bearing wear, etc. Unfortunately, these frequency bands used by the maintenance department of the company do not allow identifying the defects mentioned above, since they are phenomena that mostly occur at high frequency.
Based on RMS overall levels of vibration of measured speed by the company and which show very high levels of vibration up to 14mm / s, we was asked to carry out a global diagnosis of the turbo-alternator. On this basis, it was necessary to launch a series of tests in different frequency bands in order to try to establish a diagnosis of potential defects that cause this increase in the vibration level.

Application of the Cyclostationarity on the Signals Measured on the Reducer's Bearings

Input Bearing of the Reducer

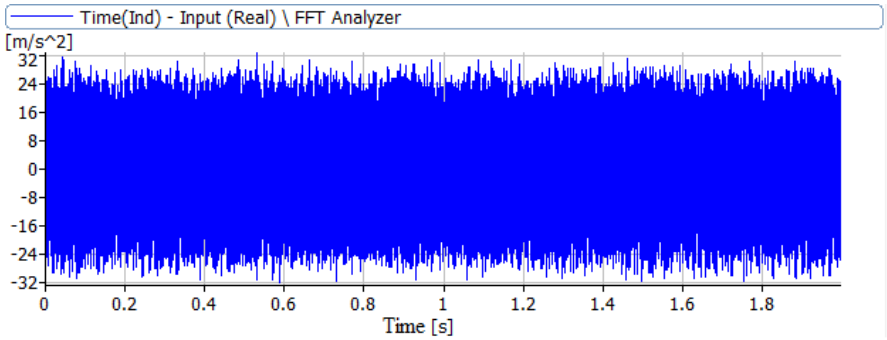

Figure 6. Acceleration signal of the measured on bearing 3 in the frequency band [0-1600 Hz]

The application of the analysis of modulation intensity distribution of the coherence spectral power (with fs=4096 Hz) for each frequency variation $MID_{\Delta f}^{PSCoh}$ of the acceleration signal measured on the bearing 3 figure 6 shows the appearance of two cyclic frequencies: the first $\alpha_2=3\times10^{-3*}f$s ≈12.5 Hz, corresponding to ½ times the

rotation frequency of the reducer's output shaft, and the second, with a very important amplitude, at α_1 = $18.22\times10^{-3*}fs \approx 74.75$ Hz corresponding to ½ times the rotation frequency of the reducer's input shaft, (see figure 7.a). This phenomenon is explained by the presence of an oil whirl defect on the journal bearings see photo 1. We can note also in (figure 7.b) that the use of the integration of the modulation intensity distribution (IMID) allows identifying by a very clear manner the two cyclic frequencies and their modulations.

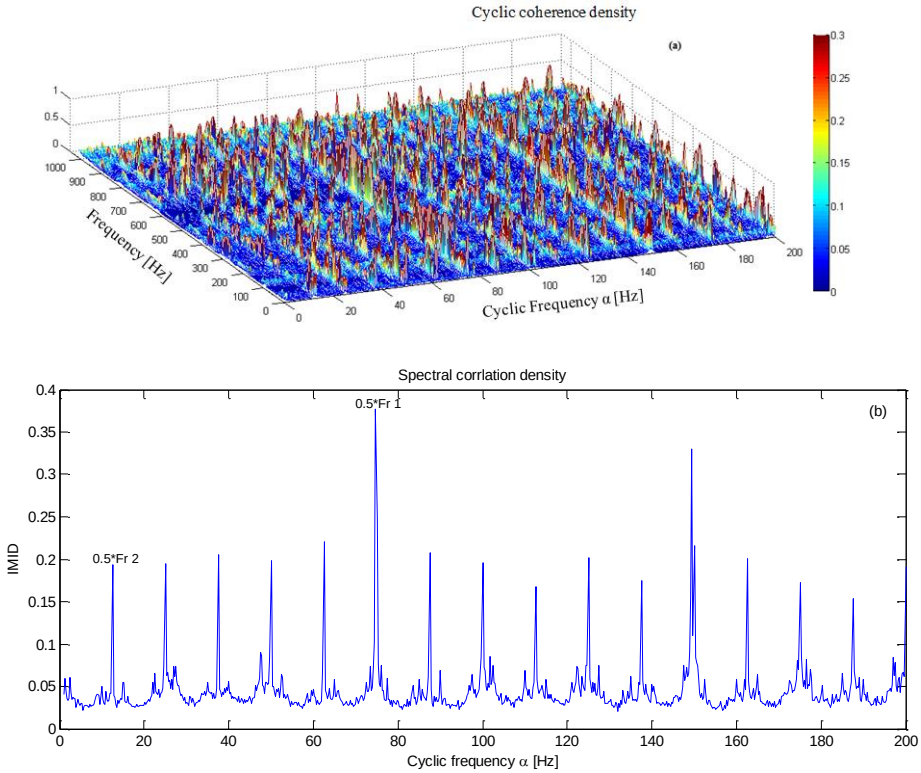

Figure 7. (a) Spectral Correlation (MID) with the corresponding (IMID) (b) of the signal of Fig 6

Output Bearing of the Reducer

The application of the method MID on the signal measured on the output bearing 4 figure 8, gives a spectrum similar to the typological spectrum corresponding to the friction defect in the rotor [35] figure 10. It shows the appearance of a fundamental cyclic frequency $\alpha = 2.4\times10^{-2}$ $fs \approx 12.5$ Hz (with fs= 512 Hz), and its harmonic corresponding to ½ times the rotation frequency of the reducer's output shaft 25 Hz shown on (figure 9. a).
The application of IMID (figure 9. b), allows identifying more clearly the fundamental cyclic frequency α = 12.5 Hz and its harmonic. According to the typological spectrum of the defect (figure 10), the phenomenon presented in (figure 9. b) corresponds to a friction defect in the journal bearing.

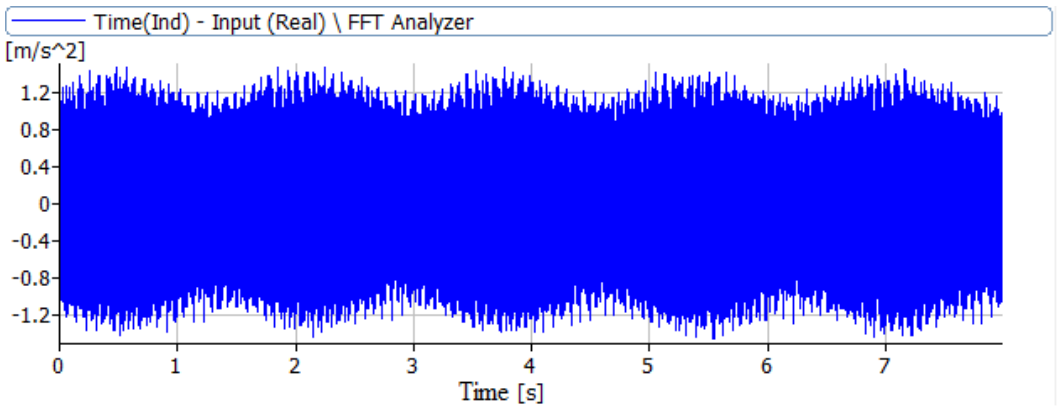

Figure 8. Acceleration signal measured on bearing 4 in the frequency band [0-200 Hz]

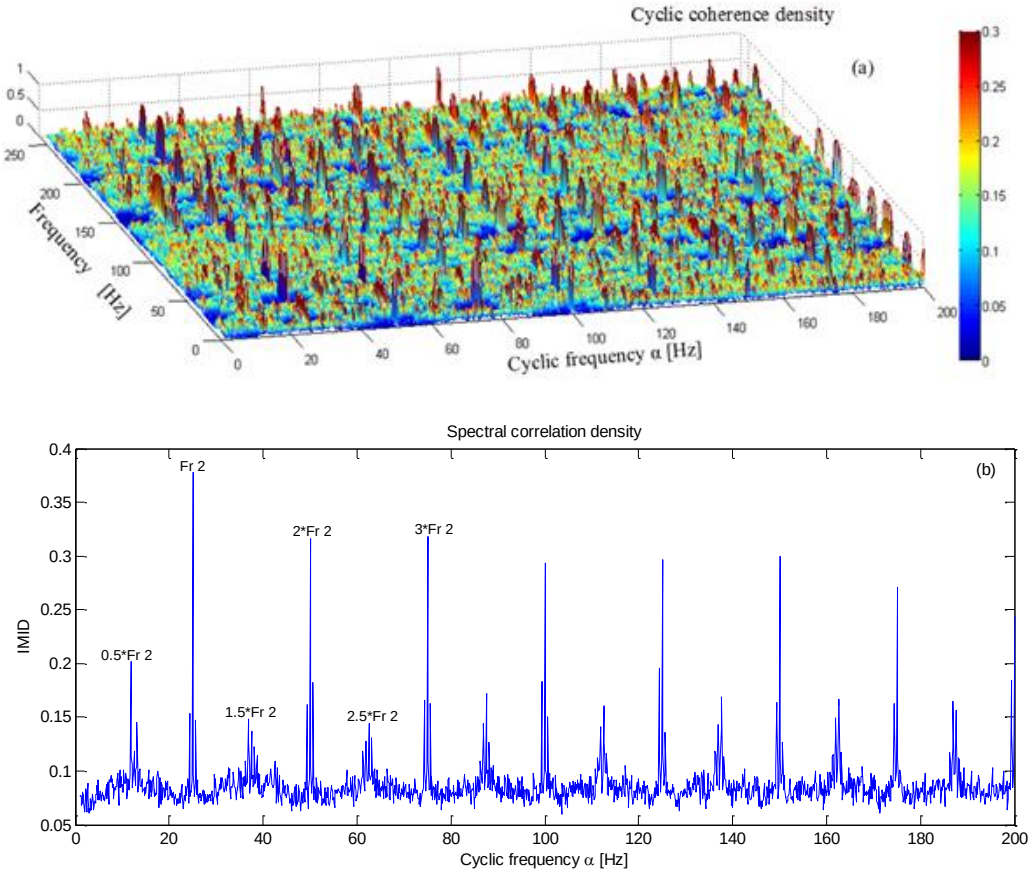

Figure 9. (a) Spectral correlation (MID) with the corresponding (IMID) (b)

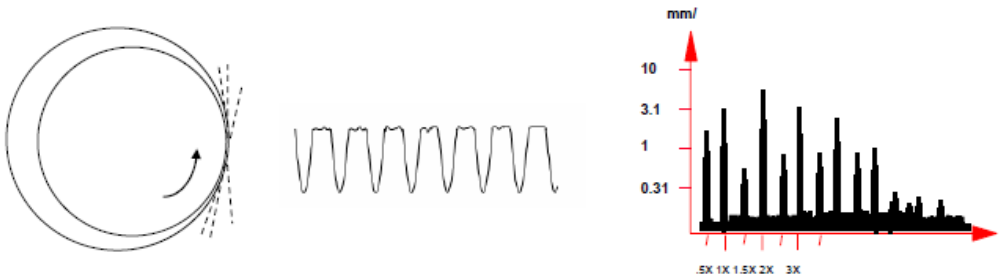

Figure 10. Typological spectrum of oil whirl defect (Brüel & Kjær Vibro) (2005).

Important Remark

The diagnosis presented below is based on the signals measured on March 23th 2022. Department maintenance FERTIAL. A year later, February 04th 2023, a revision was made to the reducer and confirmed the presence of significant wear in the two inputs and output journal bearings, see photo 1, which is confirmed by the present analysis.

Analysis of the Reducer at High Frequency

The treatment of the signals measured on the reducer's bearings at high frequency bands by the spectral analysis allowed highlighting the presence of wear on a large number of teeth of the wheels. We wanted to confirm this result by applying the cyclostationarity. The application of the MID on a signal measured in the frequency band [0-25600Hz] on the bearing 3 of the reducer, see figure 11, shows the appearance of two cyclic frequencies: the first for $\alpha_1=3.81\times10^{-4*}fs\approx25$ Hz corresponding to the rotation frequency of the output shaft and the second one for $\alpha_2=2.28\times10^{-3*}fs \approx150$ Hz (with $fs=65536$ Hz) with very high amplitude corresponding to the rotation

frequency of the input shaft. The modulation of these two cyclical frequencies explains the presence of generalized tooth wear on both wheels, (see figure 12. a) and the photo 2. The application of IMID allowed to highlight, by a very clear and visible way, the both cyclic frequencies and its modulations, (see fig 12.b).

There is also the appearance of a carrier frequency at 1196 Hz, which corresponds to the passage frequency of fixed blades sets and the fifth and sixth harmonics at 5980 Hz and 7176 Hz respectively. These two latter frequencies correspond to the passage frequencies of wheel blades 1 and 2 of the turbine, (see figure 12. a).

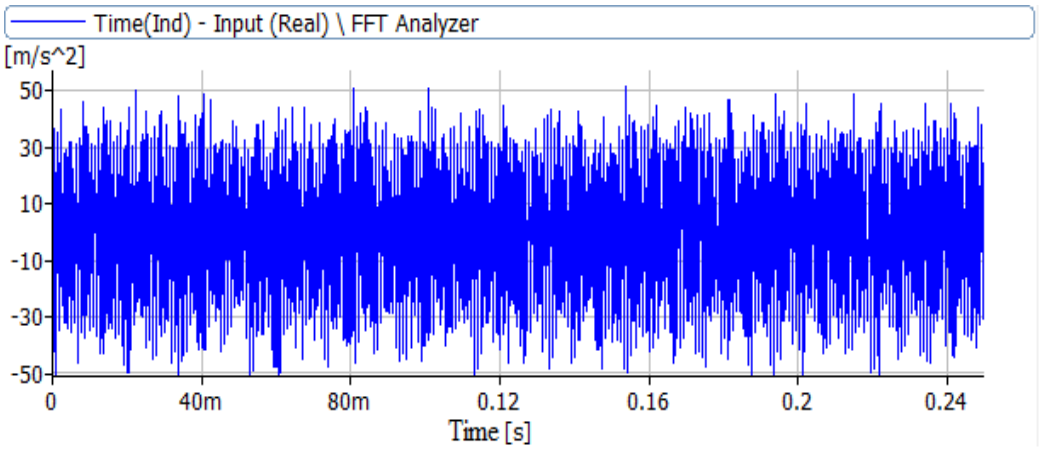

Figure 11. Acceleration of signal measured on the bearing 3 in the frequency band [0-25600 Hz]

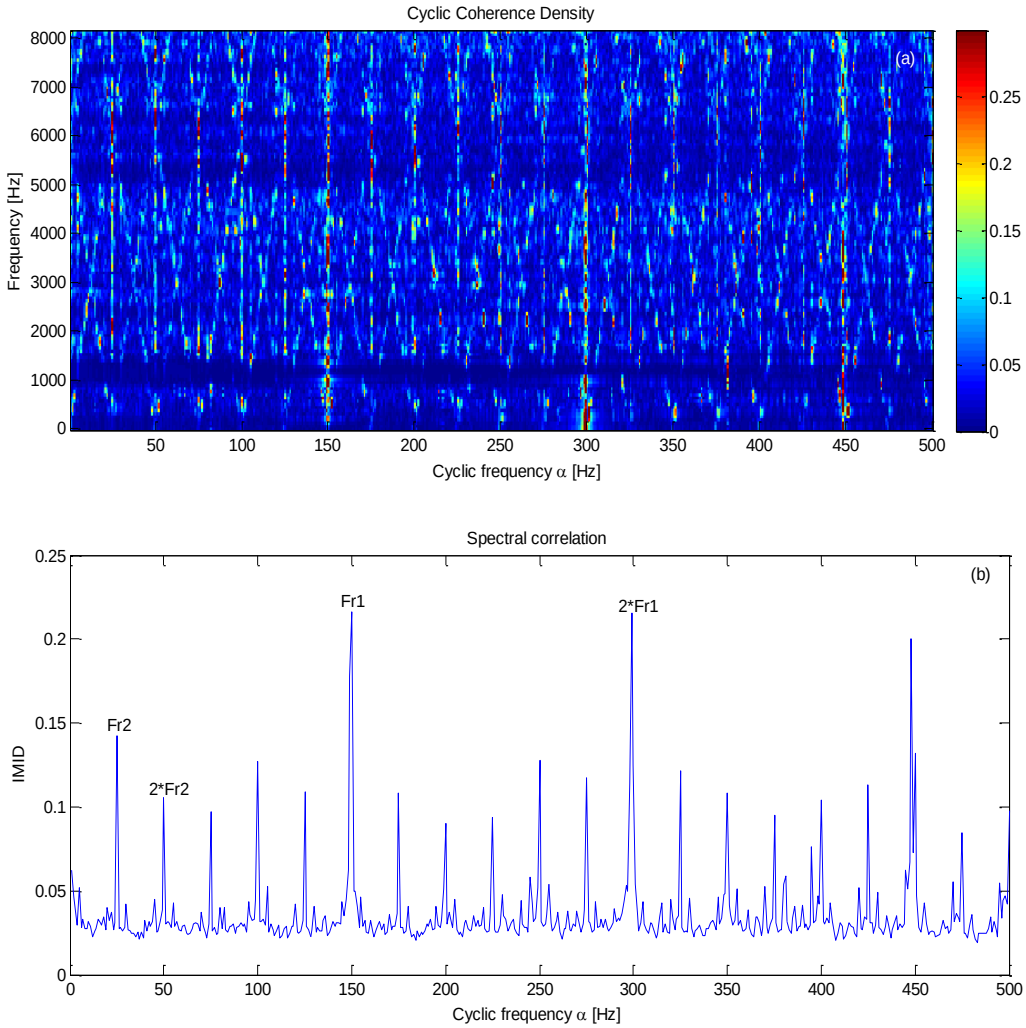

Figure 12. (a) Spectral Correlation (MID) with the corresponding (IMID) (b) of the signal of Fig 14

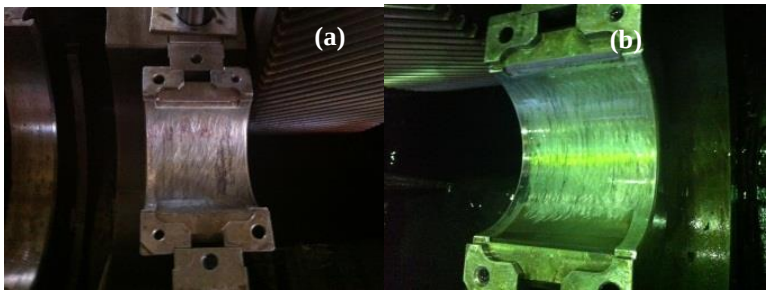

Photo.1 (a) wear in the bearing 3 (b) wear in the bearing 4

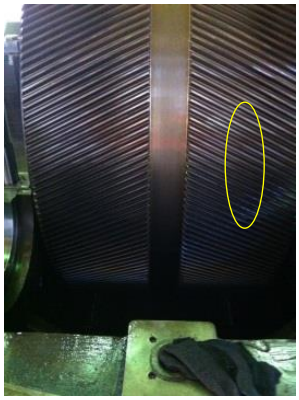

Photo.2 Wear of the gear's teeth

Conclusion

In this paper, it has been shown that the diagnosis of a turbo-machine working in real conditions by the conventional methods of signal processing has shown limitations in the identification of defects which occur at low frequency. To remedy this problem, we used the method of cyclostationarity that has great power to track modulations present in the non-stationary signals. Actually, spectral analysis allowed identifying wear defects on the teeth of the two reducer's wheels by the appearance of a large number of peaks corresponding to two rotation frequencies of the input and the output shafts in addition to the meshing frequency and its harmonics. It also showed the clear appearance of the blade passage frequency F_{BP} and the passage frequency of fixed sets' blades F_{PEFA}. Unfortunately, spectral analysis can't locate the defects in the journal bearings.

The use of cyclostationarity approach through its two indicators (MID and IMID) has highlighted all existing modulations in measured signals whether in low or high frequency. Both indicators allowed identifying the major problem responsible of the vibration level rise in the reducer, which is the presence of the oil whirl and the shaft friction in the journal bearings. The results we found were confirmed by the Maintenance Department of the company almost a year after that the measurements were carried out.

Recommendations

This work was carried out with the material resources of the Laboratory of Mechanics and Structures, University of 8 May 1945 Guelma, with the support of the Algerian ministry of higher education and scientific research, the delegated ministry for scientific research (via PRFU project code : **A14N01EP230220220002**. The authors would also like to thank the company's maintenance crew for their assistance.

Scientific Ethics Declaration

I, Mr. Tarek Kebabsa, corresponding author of the paper "Detecting Mixed Gear Faults Using Scalar and Cyclostationary Indicators in an Industrial Settin", submitted for publication to the in EPSTEM Journal, certify that we have no potential conflict of interest for the mentioned article.Moreover, I certify that the paper follows the ethical rules of good scientific practice mentioned in the "Ethical Responsibilities of Authors" of the journal. Herewith, I confirm, on behalf of all authors, that the information provided is accurate.

Acknowledgements or Notes

* This article was presented as an poster presentation at the International Conference on Technology, Engineering and Science (www.icontes.net) held in Antalya/Turkey on November 16-19, 2023.

* This work was carried out with the material resources of the Laboratory of Mechanics and Structures, University of 8 May 1945 Guelma, with the support of the Algerian ministry of higher education and scientific research, the delegated ministry for scientific research (via PRFU project code : A14N01EP230220220002. The authors would also like to thank the company's maintenance crew for their assistance.

References

Antoni, J., Bonnardot, F., Raad, A., & El Badaoui M (2004) Cyclostationary modelling of rotating machine vibration signals. *Mech Syst Signal Proc 18*(6):1285–314.

Antoni, J. (2007). *Cyclic spectral analysis of rolling-element bearing signals: facts and fictions*. Sound Vib 304:497–529.

Antoni, J. (2009). Cyclostationarity by examples. *Mech Syst Signal Proc 23*:987–1036.

Boulenger, A, Pachaud, C. et al (1998). *Vibratory diagnosis in maintenance préventive*. ISBN 2100041053, Dunod, Paris, pp 239-295

Boustany, R., Antoni, J. (2005) A subspace methode for the blind extraction of a cyclostationary source: Application to rolling element bearing diagnostics. *Mech Syst Signal Proc 19*:1245–1259

Bonnardot, F., Randall, R.B., & Guillet, F. (2005). Extraction of second-order cyclostationary sources application to vibration analysis. *Mech Syst Signal Proc 19*(6) :1230–1244

Brüel & Kjær vibro (2005) *Analyse des vibrations maintenance conditionnelle des machines tournantes*. Brüel & Kjær vibro copyright 0906 v.1-B site www.bkvibro.com.

D' Elia, G., Delvecchio, S., Cocconcelli, M., Dalpiaz, G. (2011). Combining blind separation and cyclostationary techniques for monitoring distributed wear in gearbox rolling bearings. In: *Proc. of surveillance*, Compiegne, France, October 25-26

Estoque, P. (2004) *A methodological approach numerical and experimental support for the detection and monitoring of vibration fault chipping ball bearing*. Ph.D. Thesis, University of Lille

Heng, J. (2002). *Practical of the preventive maintenance*. First edition, Mechanics-Tire-Hydraulics-Electricity-cold, Dunod, Paris

Heng, J. (2005). *Practical of the preventive maintenance*. Second édition, Mechanics-Tire-Hydraulics-Electricity-cold, Dunod, Paris

Heng, J. (2011). *Practical of the preventive maintenance*. Third edition, Mechanics-Tire-Hydraulics-Electricity-cold, Dunod, Paris

Vibro-Meter (1991). *The rotating machinery and vibration b havior*. P / N 561-003 F

Muller, A. (2005) *Contribution to the proactive maintenance of manufacturing system: formalisation of the prognosis process*. Ph.D. Thesis, IAEM & Lorraine University. Henri Poincare

Gardner, W.A., Spooner, C.M. (1988). Cyclic spectral analysis for signal detection and modulation recognition. In: *Proceedings – IEEE military communications conference, vol. 2*, pp 419–24

Gardner, W.A. (1986). Measurement of spectral correlation. *IEEE Trans Acoustic Speech Signal Proc ASSP-34*(5).

Gellermann, T. (2003). *Requirements for condition monitoring systems for wind turbines*. AZT Expertentage, 10-11.11.2003, Allianz

Lie, T-I, Lee, J., Singh, P., Liu, G. (2014). Real-time recognition of ball bearing states for the enhancement of precision, quality, efficiency, safety and automation of manufacturing. *Int J Adv Manuf Technol, 71*, 809-816.

Makowski, R, & Zimroz, R. (2011). Adaptive bearings vibration modeling for diagnosis. *Lect Notes Artif Intell 943*, 248–59.

Randall, R.B., & Antoni, J. (2011). Rolling element bearing diagnostics – a tutorial. *Mech Syst Signal Proc 25*(2):485–520.

Taher, F., Fakher, C., & Mohamed, H. (2005). Numerical and experimental analysis of a gear system with teeth defects. *Int J Adv Manuf Technol 71*, 809-816.

Urbanek, J., Barszcz, T., Zimroz, R., & Antoni, J. (2012). Application of averaged instantaneous power spectrum for diagnostics of machinery operating under non-stationary operational conditions. *Measurement, 45*, 1782–91.

Urbanek, J., Barszcz, T., Sawalhi, N., & Randall, R.B. (2011). Comparison of amplitude based and phase based methods for speed tracking in application to wind turbines. *Metrol Meas Syst XVIII* (2).

.
Urbanek, J., Barszcz, T., & Antoni, J. (2013). Time–frequency approach to extraction of selected second-order cyclostationary vibration components for varying operational conditions. *Measurement*, *46*, 1454–1463

Urbanek, J., Barszcz, T., Zimroz, R., & Antoni, J. (2014) Integrated modulation intensity distribution as a practical tool for condition monitoring. *Appl Acoust*, *77*, 184–194.

Zivanovic, G.D., & Gardner, W.A. (1991). Degrees of cyclostationarity and their application to signal detection and estimation. *Signal Process*, *22* (3), 287–297.

Author Information

Kebabsa Tarek
National Higher School of Technology and Engineering, Annaba, Algeria.
Mechanics and Structures Laboratory (LMS), University 8 Mai 1945 Guelma, Algeria.
Contact e-mail: t.kebabsa@ensti-annaba.dz

Ammar Mrabti
Mechanics and Structures Laboratory (LMS), University 8 Mai 1945 Guelma, Algeria.

Niou Slimane
National Higher School of Technology and Engineering, Annaba, Algeria.

To cite this article:

Tarek, K, Slimane, N, & Mrabti, A. (2023). Detecting mixed gear faults using scalar and cyclostationary indicators in an industrial settin. *The Eurasia Proceedings of Science, Technology, Engineering & Mathematics (EPSTEM), 26*, 797-809.